

## MTA Doktori Értekezés

Ahol a fotoelektrokémia és az anyagtudomány találkoznak:  
egyszerű és összetett fotoelektródok előállítása és  
tulajdonságai

**Dr. Janáky Csaba**

Szegedi Tudományegyetem

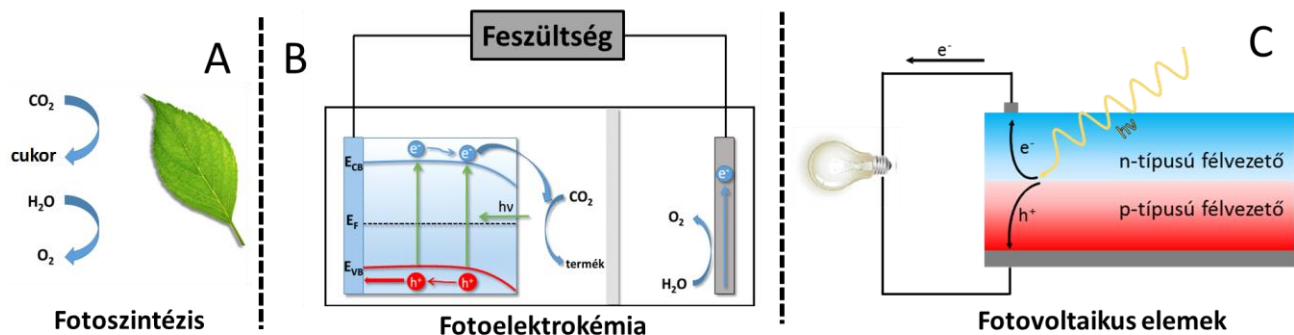
Szeged, 2023

**Tartalomjegyzék**

<b>I. Előszó</b> .....	2
<b>II. Bevezetés és szakirodalmi összefoglaló</b> .....	4
II. 1. Alapfogalmak és főbb kihívások .....	4
II. 2. A fotoelektrokémiáról röviden .....	5
II. 3. Tüzelőanyagok előállítása fotoelektrokémiai módszerekkel .....	6
II. 4. Fotoelektródok fajtái .....	8
II. 5. Fotoelektrokémiai cellák fajtái .....	8
<b>III. Célkitűzés</b> .....	9
<b>IV. A kutatómunka során alkalmazott kísérleti módszerek</b> .....	10
IV. 1. Fém-oxidok elektrokémiai előállítása (anodizáció és leválasztás) .....	10
IV. 2. Fém-oxidok előállítása oldatbelobbantásos szintézissel .....	10
IV. 3. Fém-halogenid fotoelektródok előállítása és vizsgálata .....	12
IV. 4. Szerves polimer alapú elektródok elektrokémiai előállítása .....	12
IV. 5. Szerves/szervetlen hibrid fotoelektródok előállítása .....	13
IV. 6. Félvezető/nanoszén elektródok előállítása .....	15
IV. 7. Anyagtudományi jellemzés .....	17
IV. 8. Fotoelektrokémiai jellemzés .....	17
IV. 9. A képződő termékek detektálása .....	18
IV. 10. Izotópjelzéses mérések .....	20
<b>V. Egyszerű fotoelektródok fotoelektrokémiai tulajdonságai</b> .....	20
V. 1. Oxid félvezetők fotoelektrokémiai tulajdonságai .....	20
V. 2. Fém-halogenid fotoelektródok vizsgálata .....	23
V. 3. Szerves polimer alapú fotoelektródok .....	23
V. 4. Morfológia szerepének vizsgálata .....	24
<b>VI. Összetett fotoelektródok fotoelektrokémiai tulajdonságai</b> .....	27
VI. 1. Szerves/szervetlen hibrid fotoelektródok .....	27
VI. 2. Félvezető/nanoszén elektródok tulajdonságai .....	28
VI. 3. Nanofém/félvezető elektródok .....	29
VI. 4. Szervetlen/szervetlen félvezető elektródok .....	30
<b>VII. Fotokorróziós vizsgálatok</b> .....	31
<b>VIII. Tüzelőanyagok előállítása fotoelektrokémiai módszerekkel</b> .....	34
VIII. 1. A fényelnyelési tartomány növelése .....	34
VIII. 2. A töltéshordozó transzport javítása .....	35
VIII. 3. A katalízis elősegítése .....	36
VIII. 4. Háromkomponensű rendszerek .....	37
<b>IX. In situ mérés technikák</b> .....	39
<b>X. Az eredmények gyakorlati hasznosításának lehetőségei és további kutatási irányok</b> .....	41
<b>XI. Irodalomjegyzék</b> .....	44
<b>XII. Köszönetnyilvánítás</b> .....	50

## I. Előszó

A napenergia hasznosításának számos módja lehetséges, ezek közül néhányat illusztrál az 1. ábra. A különböző félvezető/oldat határfelületen végbemenő folyamatok vizsgálata több évtizedes, ha nem évszázados múltra tekint vissza.<sup>1</sup> Hamar felismerték, hogy a megvilágított félvezetők felületén különböző redoxi reakciók mehetnek végbe. Ezek felhasználhatók környezeti szennyezők ártalmatlanítására (oxidatív és redukív úton egyaránt), tüzelőanyagok előállítására (pl. vízbontás és szén-dioxid redukció), vagy akár szintetikus reakciók végrehajtása (pl. kapcsolási reakciók). Ahhoz, hogy ezeket a folyamatokat célzottan kihasználjuk, pontosan ismernünk kell mind a félvezetők belsejében, mind a félvezető/oldat határfelületen lejátszódó elemi lépéseket. Ezek ismeretében lehet racionálisan tervezett fotoelektrod anyagokat létrehozni,<sup>2</sup> amelyek képesek lehetnek a gyakorlati alkalmazásokhoz szükséges teljesítményparaméterek elérésére. Kutatómunkám középpontjában minden esetben olyan fotoaktív anyagok álltak, amelyeket akár önmagukban vagy hordozó felületén rögzítve, fotoelektrodként alkalmazunk.



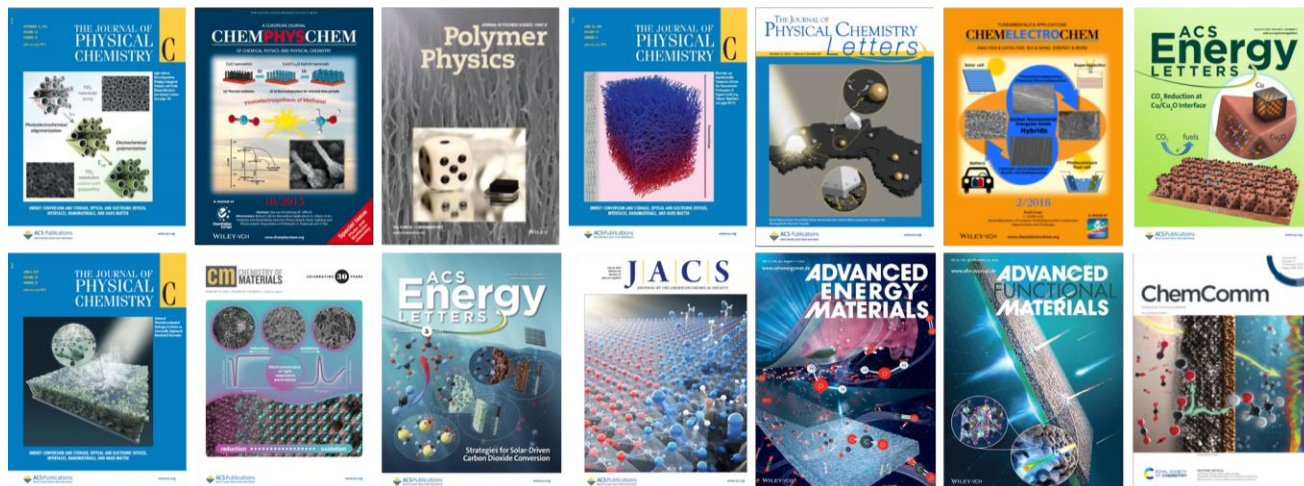
1. ábra A napenergia hasznosításának néhány fontosabb módszere.

Jóllehet a modern fotoelektrokémiai vizsgálatok az 1970-es évek elejére nyúlnak vissza,<sup>3,4</sup> az elmúlt közel 50 év során nem sikerült kereskedelmi forgalomban kapható terméket előállítani (ez alól részleges kivételt képeznek a festékekkel érzékenyített napelemek).<sup>5,6</sup> Ez különösen annak fényében érdekes, hogy a közel egyidőben indult lítiumion-elemeket szerteágazóan használjuk mindennapjainkban. Megítélésem szerint a lassú fejlődés alapvetően két tudományos, és számos egyéb okra vezethető vissza: (1) az új anyagok vizsgálatának/fejlesztésének hiánya (évtizedeken át túlzott titán-dioxid centrikusság), valamint (2) az új, kifinomult szintézismódszerek hiánya (oldatkémiai módszerek dominanciája). Ráadásul a nanotechnológia elmúlt két évtizedes vívmányai csak korlátozott mértékben, úgynevezett „trial and error” alapon épültek be a tudományterület mindennapjaiba. Fontos megemlíteni, hogy a fotoelektrokémia teljes fogalomtárát és elméleti hátterét félvezető egykristályokra dolgozták ki Gerischer és munkatársai,<sup>7</sup> és mindezek az összefüggések a nanostruktúrákra nem, vagy csak korlátozottan érvényesek. Meggyőződésem, hogy amennyiben a fenti pontokban előre lépünk, akkor felgyorsulhat a terület fejlődése, és bizonyos területeken lehetőség nyílna a gyakorlati hasznosításra.<sup>8</sup>

Az értekezés a PhD fokozatom megszerzése óta megjelent 95 db közleményre épül, amelyek között 83 db eredeti és 12 összefoglaló/perspektíva tanulmány található (66 esetben meghatározó szerző vagyok (első vagy levelező)). Ezek közül az értekezéshez szorosan 55 közlemény kapcsolódik. A

kísérleti munkát részben magam végeztem a Marie Curie International Fellowship időszaka alatt (2011–2013) a UT Arlington egyetemen, majd a Szegedi Tudományegyetemen 2013-2014-ben. Ezt követően 2014. július 1-től döntően az újonnan indult Lendület Program, majd a European Research Council (ERC) által támogatott kutatócsoportom tagjaihoz fűződik a kísérletek kivitelezése.

Fontosnak tartom megemlíteni együttműködő partnereink szerepét is. Tekintettel a tudományterület inter- és multidiszciplináris voltára, egy-egy részterületen speciális tudással rendelkező partnerek hozzájárulása nélkül nagyon nehéz élvonalbeli eredményt elérni. Éppen ezért, aktívan kerestem és keresem az előremutató kooperációkat, ami visszaköszön a közlemények szerzőlistáiban. Ugyanakkor hangsúlyozni szeretném, hogy az értekezésben tárgyalt közlemények döntő többségében meghatározó szerző vagyok (első, utolsó vagy levelező). Nem mellékesen, ezen együttműködések lehetőséget teremtettek PhD-hallgatóimnak, hogy hosszabb-rövidebb ideig bekapcsolódhassanak vezető nemzetközi kutatóműhelyek munkájába. Az értekezés alapját képező közlemények mindegyike rangos, lektorált nemzetközi folyóiratban jelent meg (szinte az össze Q1), és ami hasonlóan fontos, jelentős részük kiemelkedően fontos rangos folyóiratban (D1 és top 1%). Az eredmények által kiváltott érdeklődést jelzi, hogy 14 közlemény szerepelt a címlapon, és számos közlemény volt a megjelenést követő időszakban a tudományterület legolvasottabb és legidézettebb közleményei között.



2. ábra A nemzetközi folyóiratok címlapján szerepelt közleményeink.

Azt gondolom, hogy bár mindig lehetne bővíteni és tökéletesíteni a tématerületen rendelkezésre álló ismeretanyagot, az ERC Starting Grant közelmúltbeli lezárása jó apropót szolgáltatott az értekezés megírásához. Különösen igaz ez azért, mert az értekezésben összefoglalt tudásra építve új projekteket indítottam, melyekből született eredmények tárgyalása túlmutatna az értekezés keretein. Végül megemlítem, hogy az értekezésben ismertetett fotoelektrokémiai eredményeken túl az elmúlt évek során számos komoly felismerést tettünk az elektrokatalitikus reakciók vizsgálata terén. Az elektrokémiai vízbontás és a szén-dioxid-redukció terén elért eredményeink nemcsak közleményekben nyilvánultak meg, hanem elindultak az ipari hasznosítás felé partnervállalkozásainkkal együttműködésben.

## II. Bevezetés és szakirodalmi összefoglaló

### II. 1. Alapfogalmak és főbb kihívások

Mind az angol, mind a magyar szaknyelvben gyakran gondot jelent a megfelelő szakkifejezések használata a fény által kiváltott, vagy segített folyamatok leírása során. Itt elsősorban a fotokémia, fotokatalízis, fotoszintézis és fotoelektrokémia kifejezések használatára gondolok, melyek precíz használatát nehezíti, hogy az IUPAC vonatkozó meghatározásai sem teljesen egyértelműek.<sup>9,10</sup>

Az alábbi definíciókat adhatjuk a vonatkozó fogalmakra, és ezeket használom az értekezésben:

**Fotokémia:** fény által kiváltott folyamatok, ahol a fény közvetlenül a reaktánsokat gerjeszti, ezáltal lehetővé téve az adott reakció új reakcióúton való végbemenetelét. Ilyenek lehetnek például különböző szerveskémi-folyamatok: fotocikloaddíció, fotodekarbonilezés, fotoizomerizáció.

**Fotokatalízis:** fényelnyelő molekula, vagy félvezető segítségével végbemenő, termodinamikailag kedvezményezett (exergonikus,  $\Delta G < 0$ ) folyamatok, ahol a fotokatalizátor megvilágításával létrejövő töltéshordozók lehetővé tesznek olyan reakcióutat, amely annak hiányában nem lehetséges. Tipikusan ilyen folyamat a szerves szennyezők fotokatalitikus lebontása (pl. szén-dioxiddá és hidrogénné).

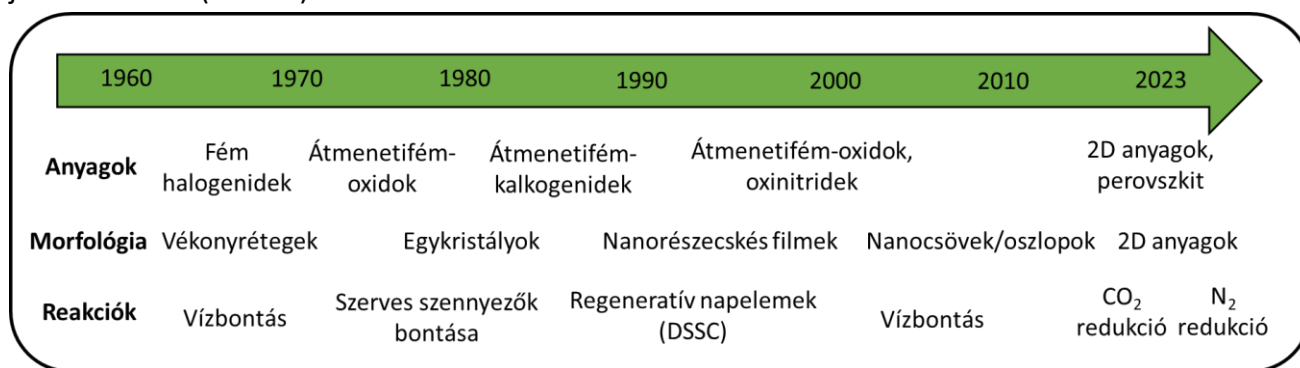
**Fotoszintézis:** fényelnyelő molekula, vagy félvezető segítségével végbemenő termodinamikailag nem kedvezményezett (endergonikus,  $\Delta G > 0$ ) folyamatok, ahol a megvilágító fény energiája fedezi a szükséges energiabefektetést a folyamat végbemeneteléhez. A természetes fotoszintézisen kívül, számos mesterséges fotoszintetikus folyamatot ismerünk, ilyen például a szén-dioxid redukciója szén-monoxiddá vagy etilénné, miközben oxigén fejlődik.

**Fotoelektrokémia:** félvezető fotoelektrod/oldat határfelületen végbemenő, elektronátlépéssel járó folyamatok, amelyek lehetnek katalitikusak (exergonikus,  $\Delta G < 0$ ) vagy szintetikusak (endergonikus,  $\Delta G > 0$ ) egyaránt. Fontos minden esetben megjegyezni, hogy a fotoelektrokémiai folyamatok csak mindkét félreakció (oxidáció és redukció) együttes vizsgálatával értelmezhetőek teljeskörűen.

Bár évente több ezer közlemény jelenik meg, "új" fotokatalizátorokat, fotoelektrodokat, és folyamatokat bemutatva, számos esetben alapvető problémákkal találkozunk. **A tanulmányok többsége csak az egyik félreakcióra összpontosít**, például a CO<sub>2</sub> átalakítására, de a kapcsolt oxidációs/redukciós folyamatot ritkán tárgyalják részletesen. Általános gyakorlat az áldozati reagensek (elektron donorok/akceptorok) bevonása,<sup>11</sup> a nem vizsgált félreakció termodinamikai és kinetikai korlátjainak kiküszöbölésére. Ez a gyakorlat azonban nem csak a kapott eredmények értelmezése és kiterjeszhetősége miatt problémás, de az áldozati reagensek átalakítása hozzájárulhat a reakciótermékeknek tekintett termékek mennyiségéhez.<sup>12</sup> Ezért, ha alkalmazzák, nagyon fontos megvizsgálni ezen áldozati reagensek sorsát és hozzájárulást a termékekhez. Hasonlóan **fontos a megfelelő teljesítményt leíró jellemzők helyes használata.**<sup>13</sup> A Kísérleti Módszerek fejezetben ezeket részletesen tárgyalom, itt csak megjegyzem, hogy egy-egy kiragadott érték ritkán jellemzi a vizsgált rendszert teljes egészében, ezért arra törekedtünk, hogy részleteiben bemutassuk az energiakonverziós folyamatokat jellemző paramétereket.

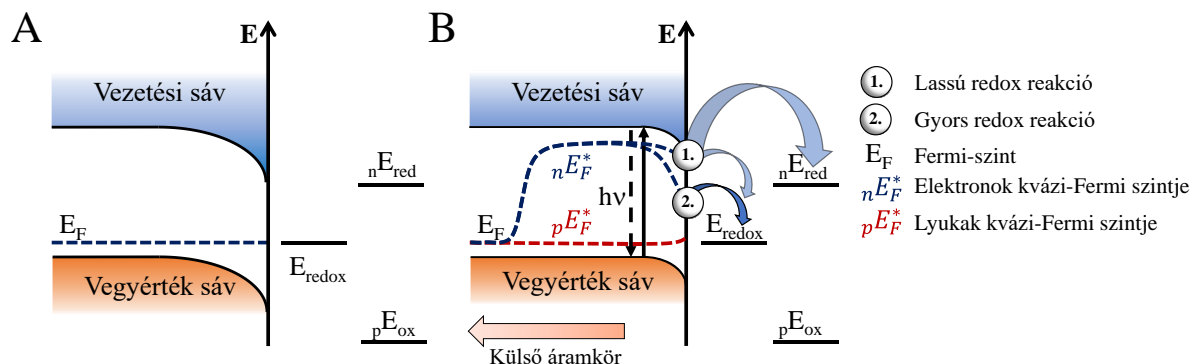
## II. 2. A fotoelektrokémiáról röviden

A fotoelektrokémia nem új tudományterület, a gyökerek egészen Edmond Becquerelig nyúlnak vissza<sup>14</sup>, aki 1839-ben felismerte, hogy egy savas oldatba merülő ezüst-kloriddal vagy ezüst-bromiddal bevont platina elektródok megvilágítása esetén áram mérhető, ezt később fotoelektromos jelenségnek nevezték el. Néhány izolált esetet követően a terület az 1960-as évek közepén indult gyors fejlődésnek, és ezen időszak legfontosabb szereplői Gerischer, Fujishima, Calvin, Fendler voltak.<sup>1,15</sup> Ebben az időszakban használták először a mesterséges fotoszintézis kifejezést, amivel arra utaltak, hogy a napfény energiáját kémiai energiává alakítják. Ezt követően különböző ciklusok jellemezték a tudományterület fejlődését, amelyek nem voltak függetlenek a reálgazdaság folyamataitól (pl. olajár változása, globális felmelegedéssel kapcsolatos aggodalmak, stb.). A különböző időszakok eltérő anyagokkal, tudományos kérdésekkel/jelenségekkel és trendekkel jellemezhetők (3. ábra).



3. ábra A fotoelektrokémia tudományának vázlatos fejlődéstörténete.

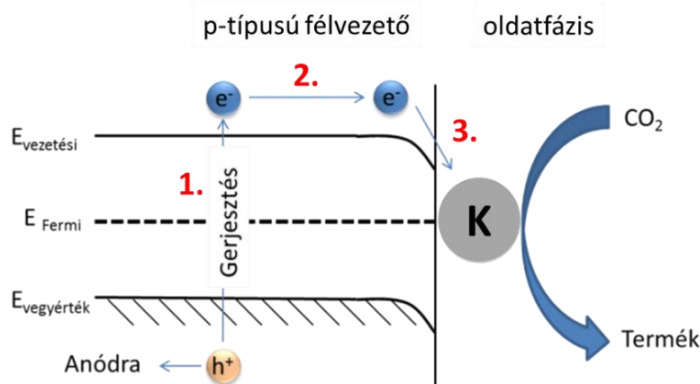
A fotoelektrokémiai folyamatok minden esetben egy félvezető/elektrolit határfelületen játszódnak le, és ennek a határfelületnek kitüntetett szerepe van. A 4. ábra egy p-típusú félvezető sávszerkezetét mutatja, egy egyszerűsített (A) és egy részletesebb (B) séma mentén.<sup>16</sup> Az ábrán jelölt karakterisztikus energiaszintek ismerete kiemelten fontos a félvezető viselkedésének megértésében, ezért számos erre irányuló mérés technikát alkalmaztunk munkánk során. A másik nagyon fontos szempont a különböző lehetséges redoxi folyamatok energiaszintjeinek (redoxi potenciáljainak) ismerete, mivel azok határozzák meg, hogy melyek a potenciálisan végbemenő folyamatok (pl. a szándékolt tüzelőanyag előállítás, fotokorrózió, az elektrolit reakciói, stb.).<sup>17</sup>



4. ábra Egy p-típusú félvezető sávdiaagramja, a legfontosabb karakterisztikus energiaszintek, és a tipikus fotoindukált folyamatok.<sup>16</sup>

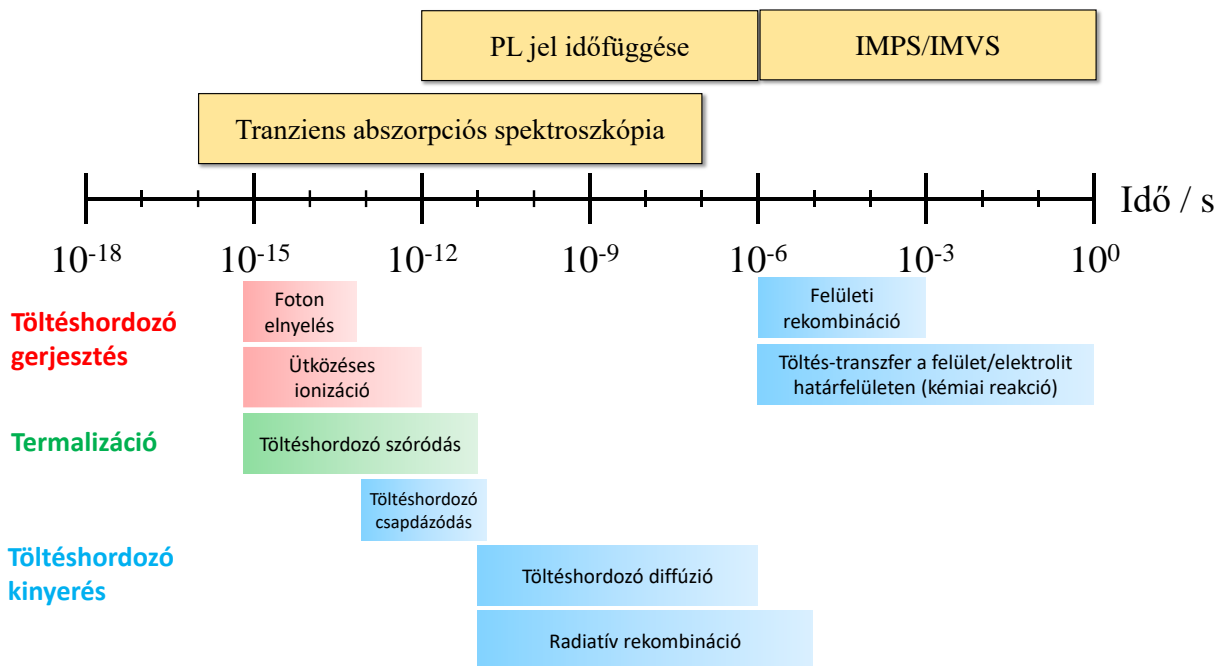
### II. 3. Tüzelőanyagok előállítása fotoelektrokémiai módszerekkel

A fotoelektrokémiai folyamatok egyik célja, hogy a napfény energiáját közvetlenül hasznosítva állítsanak elő nagyenergiájú vagy nagyértékű vegyületeket, olyan nagy mennyiségben elérhető alapanyagokból mint a víz, a szén-dioxid és a nitrogén.<sup>18,19</sup> A katód folyamatok vonatkozásában ez jelenti a hidrogénfejlesztést (HER), CO<sub>2</sub> (CO<sub>2</sub>R) és N<sub>2</sub> redukciót, míg az anódreakció a legtöbb esetben vízoxidáció (OER).<sup>20</sup> A közelmúltban indult el a különböző alternatív anódreakciók vizsgálata,<sup>21</sup> amelyek egyrészt lehetővé tehetik a teljes reakció energiaigényének csökkentését, másrészt pedig



**5. ábra** A fotoelektrokémiai folyamat részlépései. 1. Fényelnyelés, töltéshordozók kialakítása, 2. Töltéshordozó transzport, 3. Töltéshordozó transzfer (kémiai reakció).

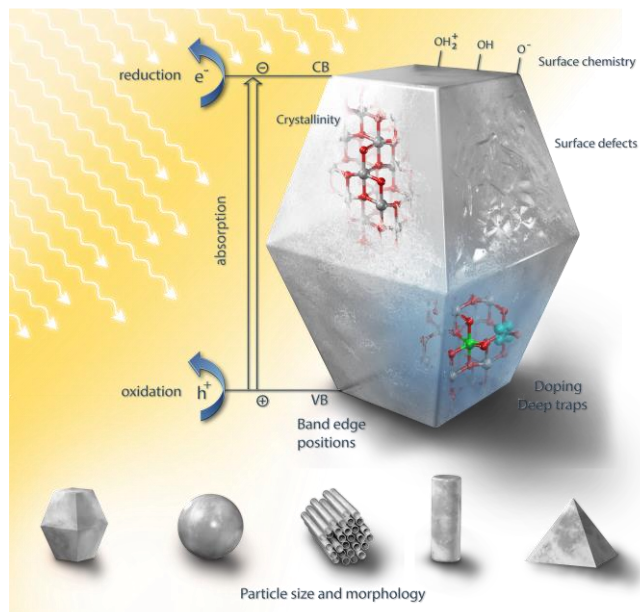
nagyértékű terméket eredményezhetnek az anódon.<sup>21–24</sup> Közös jellemzője ezeknek a félreakcióknak, hogy külső szférás elektrontranszfer folyamatok, amelyek több elektron és proton átmenetével járnak.<sup>25</sup> Éppen ezért jelentős kinetikai gát van a legtöbb esetben, amely miatt a reakciók végrehajtására katalitikusan aktív elektródfelületekre van szükség.<sup>15</sup> Az 5. ábra a fotoelektrokémiai folyamatok részlépéseit mutatja. A félvezetőkben és a félvezető/oldat határfelületen végbemenő, 5. ábrán bemutatott, fotoindukált folyamatok tipikus időskálája (a meghatározásukhoz használt mérés technikákkal együtt) a 6. ábrán látható.



**6. ábra** A félvezetőkben lejátszódó különböző fotoindukált folyamatok jellemző időskálája, valamint a vizsgálatukra alkalmazott módszerek. PL: fotolumineszcencia, IMPS/IMVS: intenzitásmodulált fotoáram/fotofeszültség spektroszkópia.<sup>18</sup>

A 6. ábrán megfigyelhető, hogy a kémiai reakciók időskálája (különös tekintettel a több elektron- és több proton transzferrel járó, energetikai szempontból releváns reakciókra)  $\mu$ s-tartományban van. Ez azt jelenti, hogy hosszú (foto)elektron/lyuk élettartamra van szükség a reakciók végrehajtására.<sup>26</sup> A töltéshordozók rekombinációja ugyanakkor általában sokkal gyorsabban történik (a mechanizmustól függően a ps- $\mu$ s tartományban).<sup>18,27</sup> Ez az eltérés már előrevetíti, hogy a fotoszintetikus és fotelektrokémiai rendszerektől reálisan nem lehet elvárni nagy energiakonverziós hatásfokot, hacsak nem alkalmaznak olyan ko-katalizátorokat, amelyek megfelelően „tárolhatják” az elektronokat/lyukakat. Ugyanakkor a megvilágítás által létrehozott töltéshordozók korróziós folyamatokat is indukálhatnak félvezetőekben, ami komoly kihívást jelent a fotelektrodok stabilitása vonatkozásában.<sup>16</sup>

A fotelektrod anyagok tervezhető előállítására érdekében érdemes összefoglalni azokat a legfontosabb paramétereket, amelyek befolyásolják azok teljesítményét (1. táblázat és 7. ábra).<sup>28</sup> Érdemes hangsúlyozni, hogy a felsorolt tényezők hatása összetett. Például a részecskeméret befolyásolhatja a fényelnyelést a méretkvantálási hatáson keresztül; a fényszórást, és a sávelhajlás befolyásolásán keresztül is a katalitikus aktivitást is.<sup>29</sup> Ezáltal az optikai, szerkezeti és elektromos tényezők összekapcsolódnak. A nanoszerkezetű morfológia a felületi hibahelyekre is hatással lehet, és ezáltal befolyásolhatja az oldott specieszek adszorpcióját.<sup>2,30</sup> Hasonlóképpen, a fotelektrod felületének sav-bázis jellege szabályozhatja az adszorpciót a töltött felületi csoportokkal való elektrosztatikus kölcsönhatásokon keresztül. Ezenkívül, a különböző felületi csoportok is hozzájárulhatnak a félvezető vezetési sávjához és vegyértéksávjához. Éppen ezért, ezen tényezők csoportosítása (1. táblázat) nem vezethet arra a téves következtetésre, hogy azok egymástól függetlenül fejtik ki hatásukat, komplexen kell azokat kezelni.



Kategória	Tényező(k)	Hatás(ok)
Optikai	Tiltottsáv-szélesség	Fényelnyelési hatásfok
Elektromos	Töltéshordozó sűrűség és mobilitás	Kvantumhatásfok
	Sávpozíciók	Transzferhatásfok
Szerkezeti	Kristályosság, kristályorientáció	Sokrétű
	Hibahelyek	Sokrétű
Morfológiai	Felületi érdesség (fajlagos felület)	Adszorpció
	Részecskék dimenziója	Sokrétű
Felületkémiai	Felületi csoportok	Sokrétű
	Hidrofil/hidrofób karakter	Sokrétű
	Sav-bázis karakter	Sokrétű

**7. ábra és 1. táblázat.** A fotelektrokémiai viselkedést meghatározó legfontosabb tényezők.<sup>28</sup>

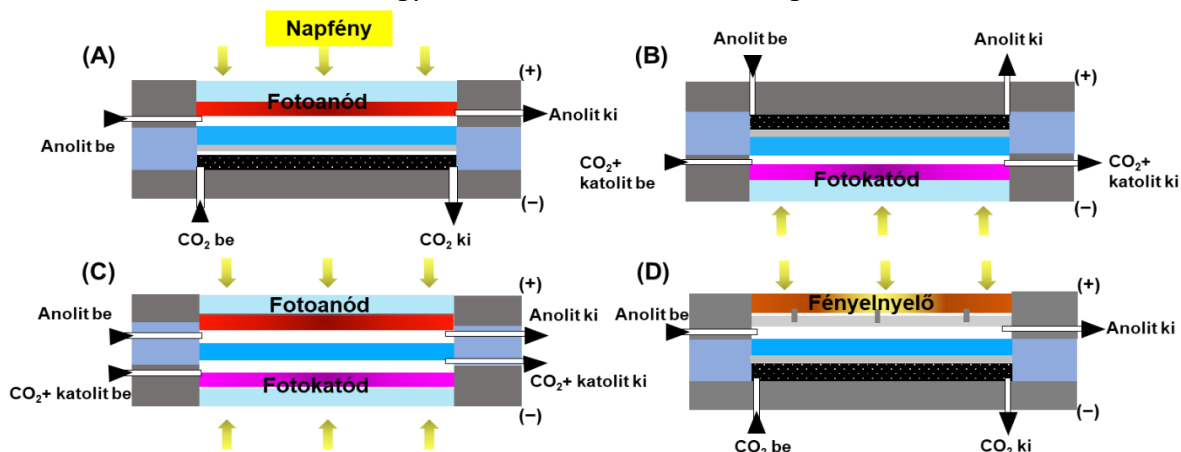


## II. 4. Fotoelektrodok fajtái

Attól függően, hogy oxidációs vagy redukciós folyamatokat kívánunk végrehajtani a fotoelektrod felületén, kell fotoanódot vagy fotokatódot alkalmazni. Előbbinek az n-típusú félvezetők, míg utóbbinak a p-típusú félvezetők alkalmasak.<sup>31,32</sup> Az 5. ábrán bemutatott három folyamat (és ezáltal a teljes fotoelektrokémiai reakció) hatékony végrehajtásához a félvezető fotoelektrodnak a következő tulajdonságokkal kell rendelkeznie: (1) fényelnyelés: elengedhetetlen a napfény spektrumának jelentős részének elnyelése, (2) töltéshordozó transzport: a félvezetőnek nagy a töltőhordozó mobilitással kell rendelkeznie, amihez a tömbi és a felszíni hibahelyek mennyiségét egyaránt minimalizálni kell; (3) töltésátviteli kinetika: gyors töltésátvitel a félvezetőről az oldatban lévő szubsztrát molekulákra vagy a mediátorra (amennyiben alkalmazunk). A stabilitás szintén komoly kihívást jelent, mivel a kémiai-, az elektrokémiai- és a fotokorróziót egyaránt figyelembe kell venni. Tekintve ezeket a sokrétű követelményeket, amelyeket egy fotoelektrodnak teljesítenie kell, nem túl meglepő, hogy mindeddig egyetlen anyag (sem szerves, sem szervetlen félvezető) sem felelt meg egyszerre mindegyiknek. A biológiai fotokonverziós rendszerekben összetett struktúrákat találunk, olyan komponensekkel, amelyek mindegyike meghatározott funkcionalitással és komplementaritással rendelkeznek. Meggyőződésem, hogy a bioinspirált összetett fotoelektrodok<sup>33</sup> hasonlóképpen felülmúlhatják az egyes komponensek önmagukban mutatott teljesítményét, és erre több példát mutatok az értekezésben.

## II. 5. Fotoelektrokémiai cellák fajtái

A fotoelektrod önmagában nem elegendő a fotoelektrokémiai folyamat végrehajtására. A megcélzott reakció, valamint a fotoelektrod tulajdonságai meghatározzák a szükséges cella optimális konfigurációját.<sup>34</sup> Fontos megemlíteni, hogy sok esetben a cella tökéletlenségei limitálják a mérhető fotoelektrokémiai paramétereket (fotoáram, fotopotenciál, szelektivitás), ezért érdemes kellő erőfeszítést fordítani a megfelelő cella kiválasztására/megtervezésére.<sup>35</sup> Tekintettel arra, hogy a disszertáció jelentős részében a CO<sub>2</sub> átalakításra fókuszálok, ezért ennek példáján mutatom be a különböző cellakonstrukciókat. A 8. ábrán látható cellák alapvetően a megvilágított elektród jellegében különböznek (pl. fotoanód, fotokatód, vagy mindkét elektród megvilágított), és a D ábrán látható egy olyan megoldás is, ahol egy napelem van a cellába integrálva.<sup>8</sup> Különlegessége a bemutatott celláknak továbbá, hogy a CO<sub>2</sub> reaktáns közvetlenül gáz formában is bevezethető.<sup>18</sup>

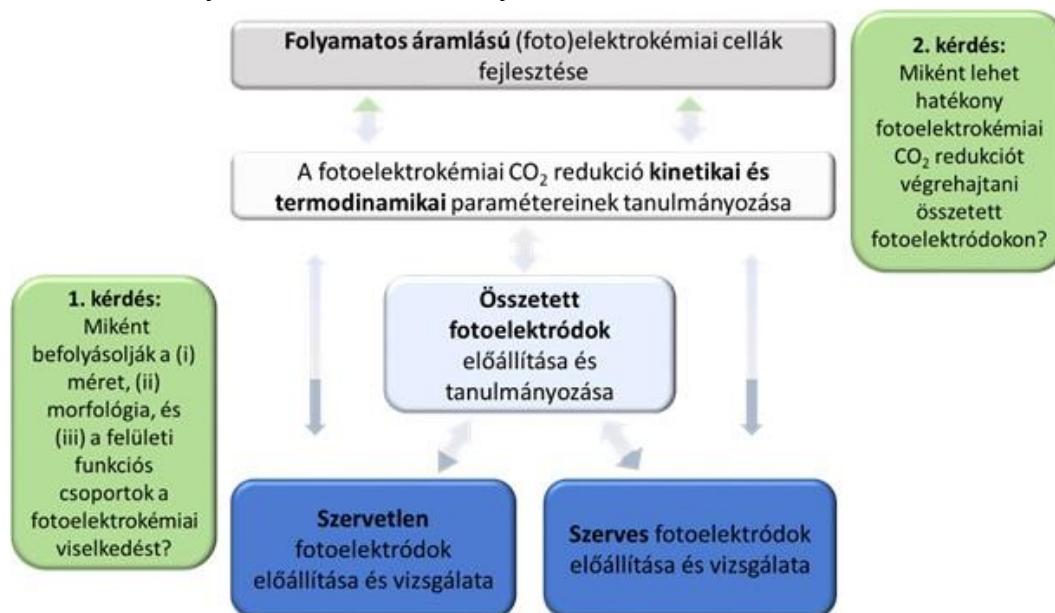


8. ábra Különböző fotoelektrokémiai cellák sematikus illusztrációja.

### III. Célkitűzés

Az előszóban foglaltak szellemében kutatómunkám során egy komplex célegyüttes mentén dolgoztam (9. ábra), amely magában foglalta:

- (i) újgenerációs fotoelektrodok (szerves vezető polimerek, perovszkitok, többfémes oxidok) előállítását és vizsgálatát;
- (ii) összetett elektrodok előállítását, ahol a három alapvető folyamat (a fényelnyelés, a töltéshordozó transzport, valamint a felületi elektrontranszfer) el van választva egymástól, és az ehhez szükséges, főként elektrokémiai, szintézismódszerek kidolgozását;
- (iii) szerkezet–hatás összefüggések felderítését a tüzelőanyagok fotoelektrokémiai előállítása során;
- (iv) *in situ* elektrokémiai jellemzési technikák fejlesztését.



9. ábra A kutatómunka célrendszere.

Hangsúlyozom ugyanakkor, hogy ezen témakörök szorosan és dinamikusan összefüggenek egymással, hiszen a megismert összefüggések ismeretében lehetséges új anyagokat előállítani, amelyhez viszont a szintézismódszerek folyamatos hangolása szükséges (9. ábra). Az értekezés tömörsége és olvashatósága érdekében, valamint a felesleges ismétléseket elkerülendő, eredményeimet a fenti tagolás mentén mutatom be. Ennek megfelelően először hozok példákat a különböző egyszerű és összetett fotoelektrodok előállítására, ott bemutatom a legfontosabb fotoelektrokémiai tulajdonságokat, majd egy külön fejezetben, néhány kiválasztott példán keresztül mutatom be azokat a szerkezet-tulajdonság összefüggéseket, amelyek meghatározzák ezen fotoelektrodok viselkedését tüzelőanyagok előállítása során. Végül bemutatok példákat azon egyedi vagy különleges *in situ* vizsgálati módszerekből, amelyek hozzájárultak a különböző fotoindukált elemi folyamatok jobb megértéséhez. Előfordulnak viszont olyan kulcsfontosságú közlemények, amelyek több szempontból is fontos mondanivalót hordoznak (szintézismódszer, anyagi tulajdonságok és fotoelektrokémia), ezért ezek több fejezetben is előkerülnek. További cél volt az előállított elektrodok azonosított tulajdonságainak vizsgálata egyéb (nem fotoelektrokémiai, pl. elektrokatalitikus, töltéstárolási, optoelektronikai) folyamatokban is, amennyiben azok ígéretesnek tűntek.

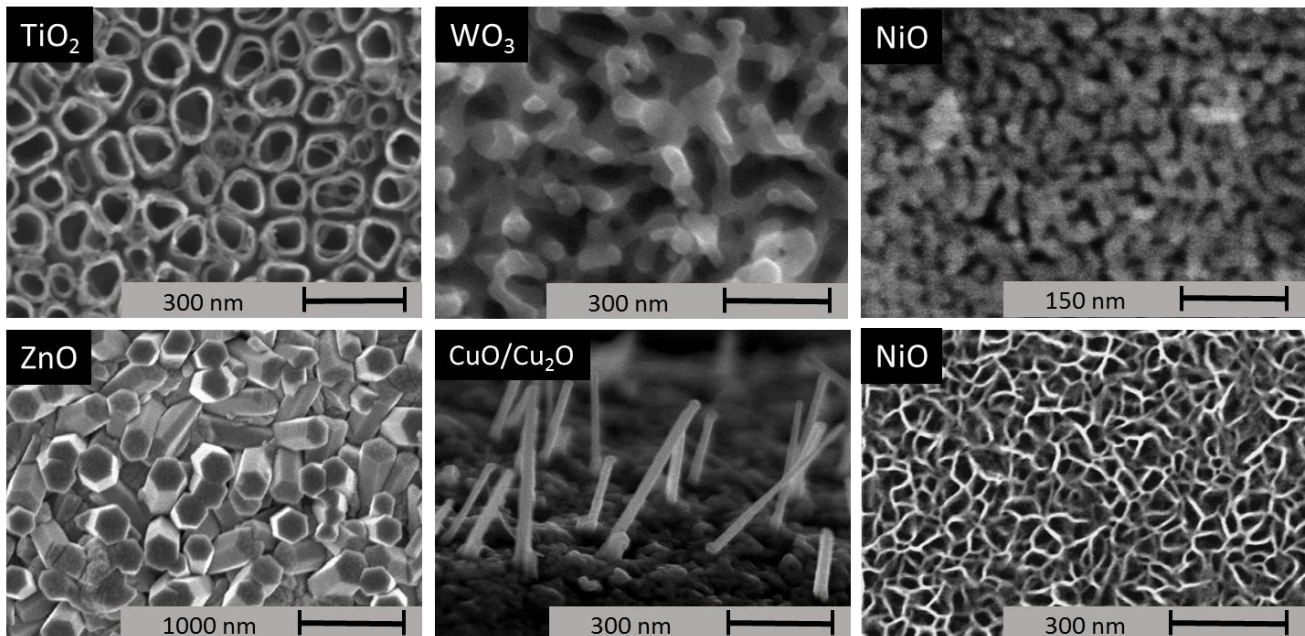
#### IV. A kutatómunka során alkalmazott kísérleti módszerek

Az alkalmazott kísérleti módszereket részleteiben a megfelelő közlemények kísérleti fejezetei tárgyalják. Jelen fejezetben csak a legfontosabb módszerek áttekintő bemutatására vállalkozom. Fontos ugyanakkor kiemelni, hogy sok esetben mi magunk fejlesztettünk ki szintézismódszert, vagy akár vizsgálati módszert is, így ezen fejezet számos része már eredménynek is tekinthető.

##### IV. 1. Fém-oxidok elektrokémiai előállítása (anodizáció és leválasztás)

Számos elektrokémiai leválasztási módszert vizsgáltunk, mely során különböző félvezető oxidokat állítottunk elő (10. ábra). Az egyik az anodizáció módszere, mely során az előállítani kívánt fém-oxidot alkotó fémből (lemez) indulunk ki, és annak felületén, annak anyagából alakítjuk ki az oxidréteget. Az elektrolitoldatban komplexképző ionokat alkalmazva az oxidképződés és az oldódás relatív sebessége szabályozható, így különböző felületi nanostruktúrákat állíthatunk elő.<sup>36</sup> Ezzel az eljárással készítettünk  $\text{TiO}_2$ ,<sup>37,38</sup>  $\text{WO}_3$ ,<sup>39-41</sup>  $\text{NiO}$ , és  $\text{Nb}_2\text{O}_5$  rétegeket, vizsgáltuk fotoelektrokémiai tulajdonságaikat, majd felhasználtuk őket összetett elektródok előállítására.<sup>38</sup>

A másik eljárás a leválasztás módszere. Ennek során az oldatban jelenlevő fémionok elektrokémiai redukciója vagy oxidációja révén alakítjuk ki a fém-oxidot az elektród felületén. Ugyanakkor a pH elektrokémiai változtatása esetében a fémion oxidációs számának változására sincs szükség (pl.  $\text{ZnO}$ ).<sup>42</sup> Ezen módszerek egyik előnyös tulajdonsága, hogy különböző nanoszerkezetű hordozókra is le lehet választani a félvezetőket (ezt aknáztuk ki nanoszen/félvezető elektródok előállítása során). Elektrodepozícióval állítottunk elő  $\text{TiO}_2$ ,<sup>43</sup>  $\text{Cu}_2\text{O}$ ,<sup>44,45</sup>  $\text{ZnO}$ ,<sup>42</sup>  $\text{NiO}$ <sup>46</sup> és  $\text{Fe}_2\text{O}_3$ <sup>47</sup> rétegeket.



10. ábra Példák az elektrokémiai módszerrel előállított félvezető oxid nanoszerkezetekre (SEM felvételek).

##### IV. 2. Fém-oxidok előállítása oldatbelobbantásos szintézissel

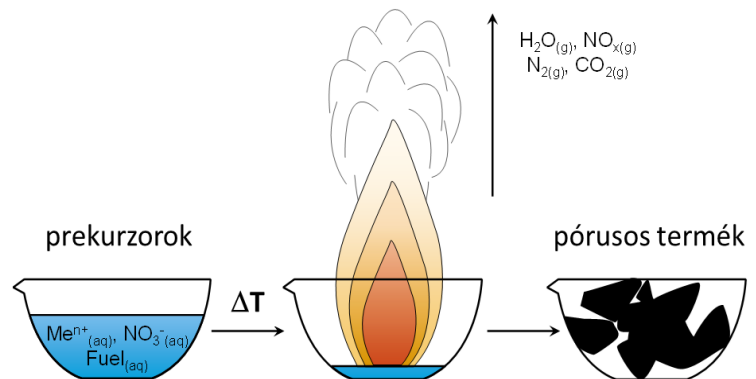
Az oldatbelobbantásos módszer során a prekuzorként használt fém-nitrátot (oxidálószer) és egy szerves üzemanyagot sztöchiometrikus arányban összekeverünk. Ha ezt az elegyet elkezdjük

melegíteni, és az oldószer egy része elpárolog, akkor a fém-nitrát és az üzemanyag között lejátszódó erősen exoterm reakció belobbantja az elegyet, így alakítva ki a kívánt fém-oxidot (11. ábra).<sup>48</sup> Ezt a módszert főleg két- és háromfémű oxidok előállítására használtuk. A módszer főbb előnyei a következők:

- rendkívül gyors (a reakció lejátszódása néhány másodperc alatt bekövetkezik, így egész vegyületcsaládok gyors szintézisére van lehetőség),
- nem igényel nagy energiabefektetést (jó szintézisparaméterek esetén nincs szükség utólagos hőkezelésre, mivel a reakció hőmérséklete elérheti a 3000 °C-ot),
- nagy felületű anyagok előállítására alkalmas (a reakció során az üzemanyag égéséből keletkező és távozó nagy mennyiségű CO<sub>2</sub>, N<sub>2</sub> és vízgőz pórusos struktúrákat eredményez),
- nincs szükség költséges felszerelésekre,
- az alkalmazott vegyszerek könnyen hozzáférhetőek és nem környezetszennyezők,
- a szintézis finomhangolásával metastabil fázisok, adalékolt és összetett anyagok szintézisére is van lehetőségünk.

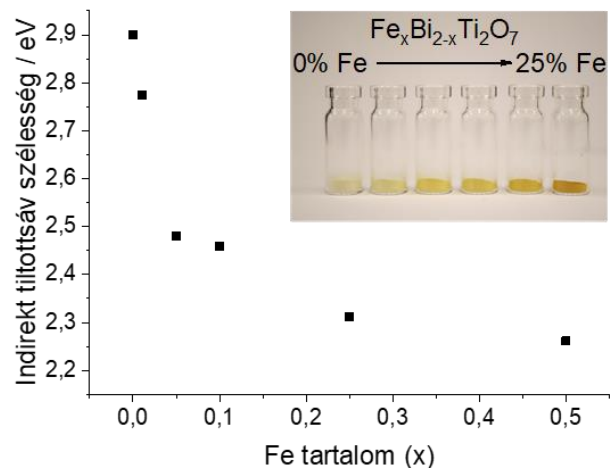
A következő fotoaktív összetett fém-oxidok előállítását valósítottuk meg ezen módszerrel:

- Bi<sub>2</sub>Ti<sub>2</sub>O<sub>7</sub><sup>49</sup>
- M<sub>x</sub>Bi<sub>2-x</sub>Ti<sub>2</sub>O<sub>7</sub>, M: Fe(III), Mn(III)<sup>49</sup>
- Ag<sub>2</sub>WO<sub>4</sub>, CuWO<sub>4</sub>, ZnWO<sub>4</sub><sup>50</sup>
- CuNb<sub>2</sub>O<sub>6</sub>, ZnNb<sub>2</sub>O<sub>6</sub><sup>51</sup>
- AgBiW<sub>2</sub>O<sub>8</sub><sup>52</sup>
- CuBi<sub>2</sub>O<sub>4</sub><sup>53</sup>
- CuCrO<sub>2</sub>, CuFeO<sub>2</sub>, CuCr<sub>x</sub>Fe<sub>1-x</sub>O<sub>2</sub><sup>54,55</sup>



11. ábra Az oldatbelobbantásos szintézis folyamata.

Megvizsgáltuk, hogy az üzemanyag/oxidálószer arányának hatására hogyan változnak az egyes fázisok a termékben, valamint, hogy a szintézist követő hőkezelésnek milyen hatása van a kristályosságra. A röntgendiffraktogramokon a fázisösszetétel megállapítására Rietveld-féle szerkezetfinomítást végeztünk. Megemlítem, hogy ezt az értékelési módszert azóta *meghonosítottuk a kutatócsoportban és rutinszerűen használjuk*. Minden oxid esetén megvalósítottuk a szintézisparaméterek optimalizálását (oxidálószer/üzemanyag arány, hőkezelés) annak érdekében, hogy minél tisztább és kristályosabb anyagot kapjunk.

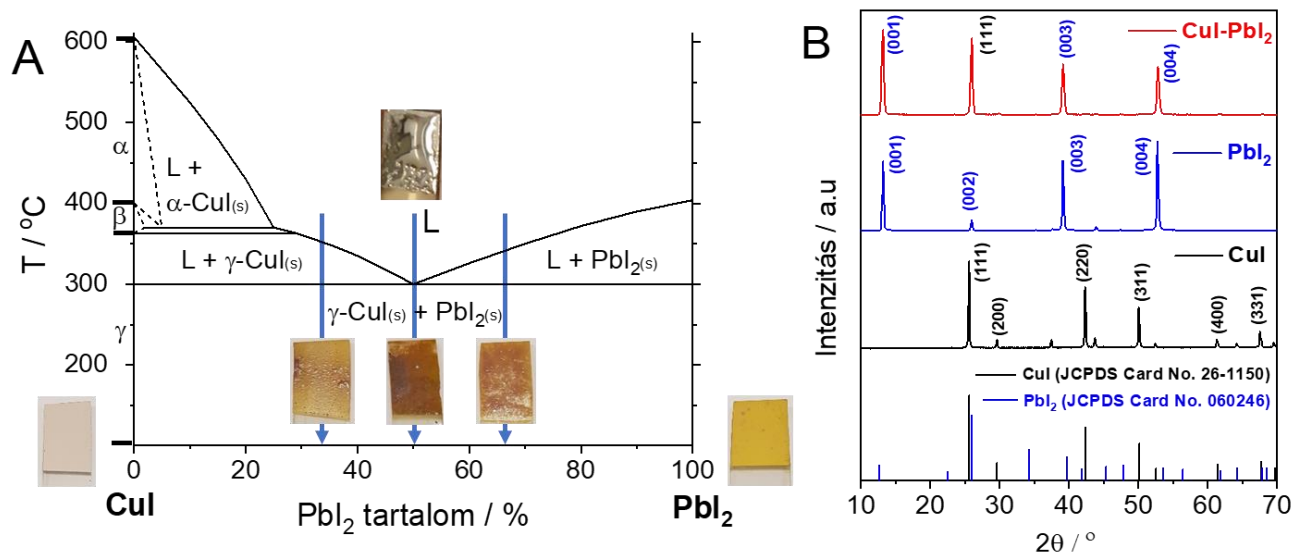


12. ábra A Fe(III)-al adalékolt Bi<sub>2</sub>Ti<sub>2</sub>O<sub>7</sub> minták tiltottsáv-szélességei és fényképei.<sup>49</sup>

További cél volt, hogy különböző fémionokat építsünk be a szintézis során egy adott kétfémes oxid, pl. a  $\text{Bi}_2\text{Ti}_2\text{O}_7$  kristályrácsába.<sup>49</sup> Az ilyen jellegű kristályrács módosításoktól a  $\text{Bi}_2\text{Ti}_2\text{O}_7$  tiltottsáv-szélességének csökkenését vártuk, melytől az anyag a látható fény spektrumának nagyobb tartományát lesz képes hasznosítani. Ezt a módosítást elvégeztük Fe(III), Mn(II), és Ni(II) ionok beépítésével egyaránt. A Fe(III) kristályrácsba történő beépítéséhez különböző összetételű  $\text{Fe}_x\text{Bi}_{2-x}\text{Ti}_2\text{O}_7$  mintákat állítottunk elő, ahol  $x=0,01; 0,05; 0,1; 0,25$  és  $0,50$ . A minták diffúz reflexiós spektrumaiból Tauc-analízis segítségével megfigyelhető, hogy a Fe(III) beépülésével az anyag optikai tiltottsáv-szélessége jelentősen lecsökken, arányosan a beépülő Fe(III) mennyiségével (12. ábra).

#### IV. 3. Fém-halogenid fotelektrodok előállítása és vizsgálata

Oldatkémiai szintézissel állítottunk elő mind egyszerű fém-halogenideket ( $\text{CuI}$  és  $\text{PbI}_2$ ),<sup>56–58</sup> mind összetett perovszkitokat ( $\text{CsPbBr}_3$ ,  $\text{MAPbI}_3$ ,  $\text{MAPbBr}_3$ ).<sup>59–61</sup> Különböző  $\text{CuI-PbI}_2$  nanokompozit elektrodokat is állítottunk elő, amelyek fázisdiagramját a 13. ábrán mutatom be, a különböző összetételű minták fényképével együtt (az olvadt keveréket is bemutatom). Röntgendiffrakciós vizsgálataink igazolták, hogy nem jön létre új vegyület, a kompozit minden esetben  $\gamma\text{-CuI}$  és  $\text{PbI}_2$  keveréke. 50 mol%  $\text{PbI}_2$ -tartalom mellett a rendszernek eutektikus pontja van, ahol az olvadás már  $300^\circ\text{C}$  körül megkezdődik (szemben a tiszta anyagok  $606^\circ\text{C}$  és  $404^\circ\text{C}$ -os olvadáspontjával). A fázisdiagramon jelzett fűtési és hűtési "út" is befolyásolhatja a kapott keverék homogenitását, és a  $\text{CuI-PbI}_2$  nanokompozit leghomogénebb eloszlása eutektikus pontban várható.



13. ábra  $\text{CuI-PbI}_2$  nanokompozit fázisdiagramja és röntgendiffraktogramja.<sup>56</sup>

#### IV. 4. Szerves polimer alapú elektrodok elektrokémiai előállítása

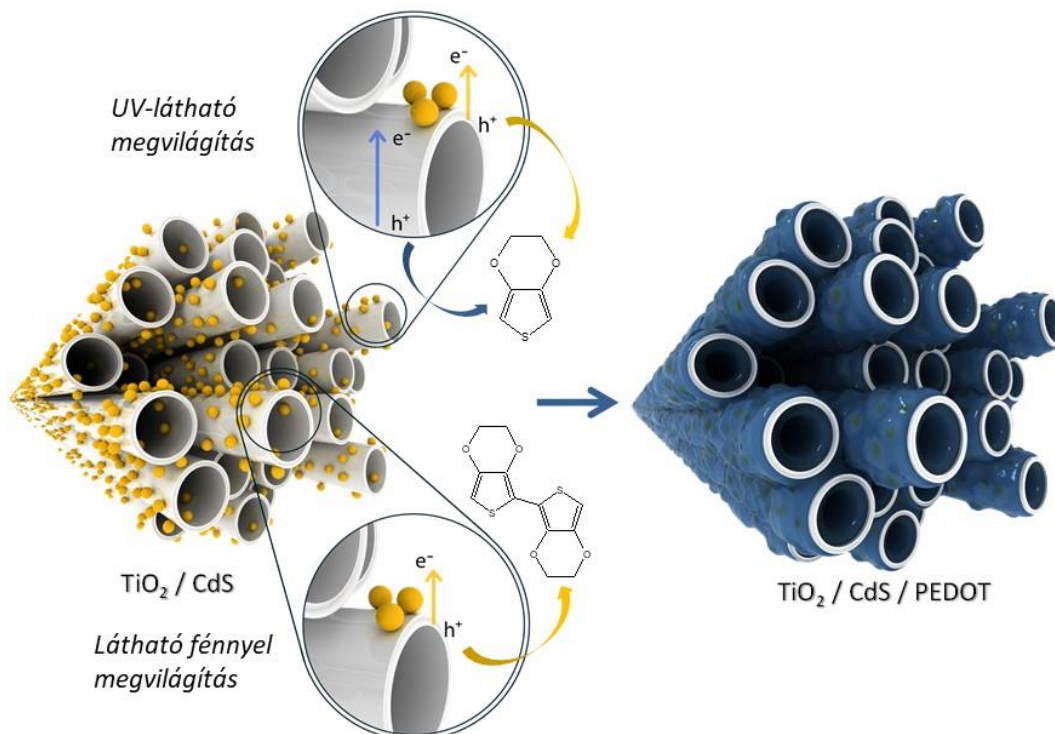
Elektromosan vezető polimer fotelektrodokat is állítottunk elő,<sup>62,63</sup> és vizsgáltunk a  $\text{CO}_2$  fotelektrokémiai redukciójában. A vezető polimereknek a szerepe sokrétű lehet ebben a reakcióban, hiszen azon túl, hogy adszorbeálják a szén-dioxidot, betöltik a fényelnyelő szerepét és molekuláris katalizátorként is funkcionálnak. Ennek vizsgálatára polianilint, polipirrolt, poli(N-metilanilint) és poli(3,4-etiléndioxitifént) állítottunk elő elektrokémiai eljárással. Minden esetben optimalizáltuk a polimerizációs eljárást, hogy az elektrod felületén jól tapadó, stabil elektroaktivitású film keletkezzen.

#### IV. 5. Szerves/szervetlen hibrid fotoelektródok előállításása

Ahhoz, hogy a korábbi pontokban bemutatott szerves és szervetlen félvezetőkből szabályozott szerkezetű és tulajdonságú összetett (kompozit) elektródokat előállítsunk elő, kifinomult szintézismódszerekre van szükség. Vizsgálataink eredményét, egy szakirodalmi áttekintéssel kiegészítve, egy összefoglaló tanulmányban tettük közzé.<sup>38</sup> Főként azon elektrokémiai és fotoelektrokémiai módszereket vettük sorra, amelyek alkalmasak szabályozott nanoszerkezettel rendelkező hibrid anyagok előállítására, összetételük és tulajdonságaik hangolására.

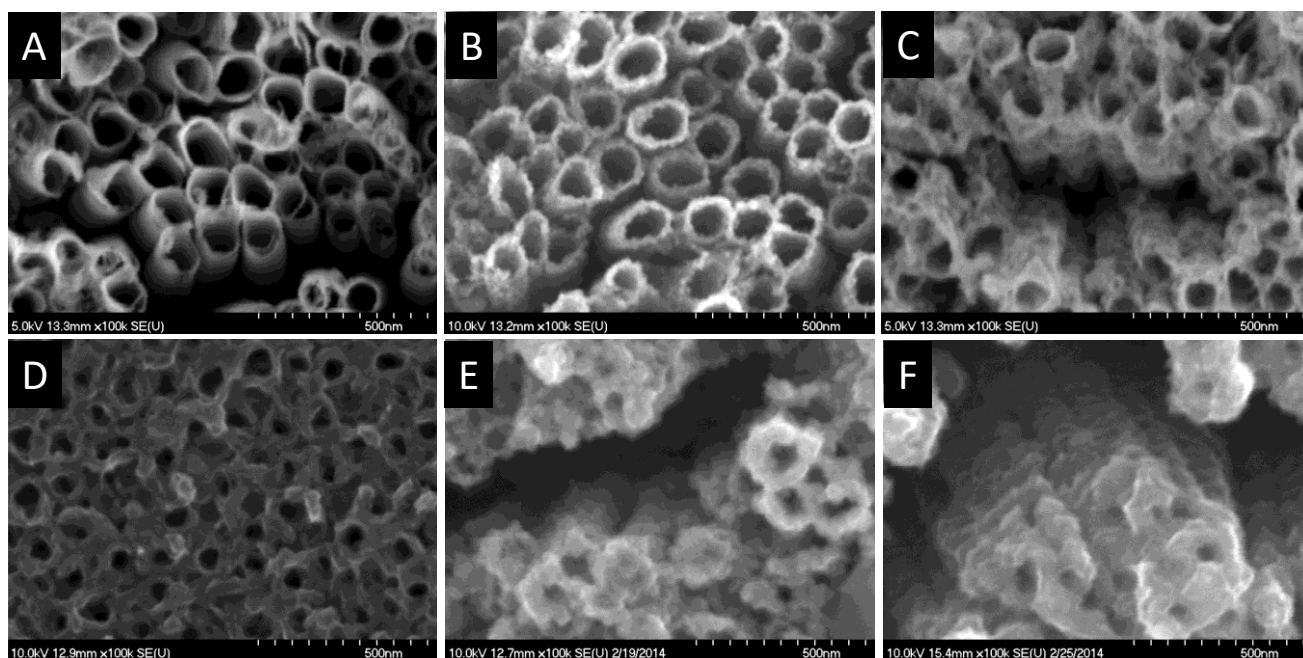
Az előnyök mellett ismertettük az elektrokémiai módszerek korlátait is, amelyek döntően a félvezető munkaelektrodok korlátozott elektromos vezetéséből adódnak. Részletesen tárgyaltuk, hogy miként lehet ebből a hátrányból előnyt kovácsolni azáltal, hogy kihasználják a félvezetők fotoaktivitását, és a megvilágítás során keletkező elektron–lyuk párokból a lyukak segítségével hajtják végre a polimerizációs reakciót (és így a szerves félvezető előállítását).<sup>38</sup> Számos példán keresztül bemutattuk azt is, hogy az előállított kompozitok tulajdonságai és viselkedése hogyan függ az összetételüktől és morfológiájuktól, valamint, hogy az előállítási eljárás hangolásával ezek a paraméterek miként módosíthatók. Végül összehasonlítottuk az elektrokémiai úton előállított kompozitokat az egyéb, hagyományos módszerekkel előállított anyagokkal, ezáltal kiemelve a (foto)elektrokémiai módszerek előnyeit. Munkám ezen részében előállítottuk és vizsgáltuk a következő kompozitokat:

- $\text{WO}_3$ /polianilin<sup>37,40,39</sup>
- $\text{TiO}_2$ /polianilin<sup>37</sup>
- $\text{TiO}_2$ /CdS/PEDOT
- SiC/polianilin<sup>67</sup>
- $\text{WO}_3$ /polipirrol<sup>37</sup>
- $\text{TiO}_2$ /polipirrol<sup>64</sup>
- $\text{TiO}_2$ /CdSe/PEDOT
- SiC/PEDOT<sup>68</sup>
- $\text{TiO}_2$ /PEDOT<sup>65</sup>
- $\text{TiO}_2$ /perovszkit/PEDOT<sup>66</sup>



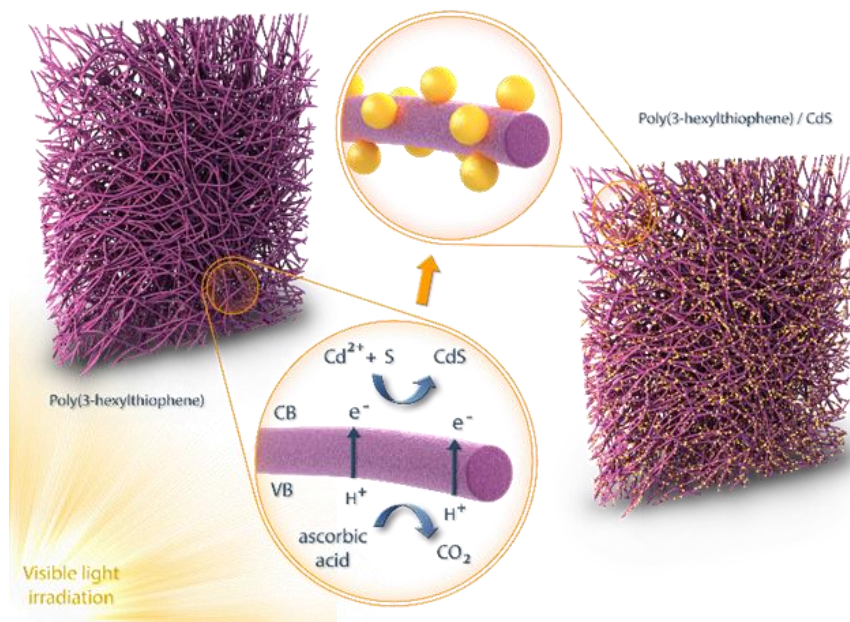
13. ábra A fotoelektrokémiai polimerizáció mechanizmusának sematikus ábrázolása.<sup>65</sup>

A fotelektrokémiai polimerizációs eljárásra példaként bemutatom a PEDOT fotelektrokémiai leválasztását CdS és CdSe-el érzékenyített  $\text{TiO}_2$  nanocsövek felületére (13. ábra). Ezen szintézis során a megvilágítás hatására képződő lyukak képesek oxidálni a monomert, amely elindítja a polimerizációs folyamatot, és kialakul a szerves vezető polimer bevonat. A 14. ábrán a SEM képeken a kialakított polimerbevonat figyelhető meg, amely homogén módon borítja be a szerves templátot. Vizsgáltuk, hogy milyen potenciálon indul el a monomer oxidációja, és hogy milyen optikai tulajdonságú PEDOT rétegek keletkeznek a potenciodynamikus polimerizáció során. Vizsgáltuk a PEDOT bevonatok homogenitását, és megmutattuk, hogy a PEDOT növekedésének sebessége szabályozható az oxidációs potenciállal. Ennek érdekében, hogy a szerves alaprégünket ne roncsoljuk az oxidatív polimerizáció során az EDOT molekula dimerjéből indultunk ki, mivel azt már kevésbé pozitív potenciálon is lehet oxidálni.<sup>65,66</sup> Hasonló eljárással számos kompozitot állítottunk elő  $\text{TiO}_2$  nanocsőköteg, nanopórusos  $\text{WO}_3$  és perovszkit templátok használatával.<sup>37,38</sup>



**14. ábra** SEM felvételek a  $\text{TiO}_2$ ,  $\text{TiO}_2/\text{CdS}$ , és  $\text{TiO}_2/\text{CdSe}$  mintákról PEDOT leválasztás előtt (A, B, C) és után (D, E, F). Paraméterek: UV fény, 10 ciklus,  $50 \text{ mV s}^{-1}$ , 0,01 M EDOT acetonitrilben.<sup>65</sup>

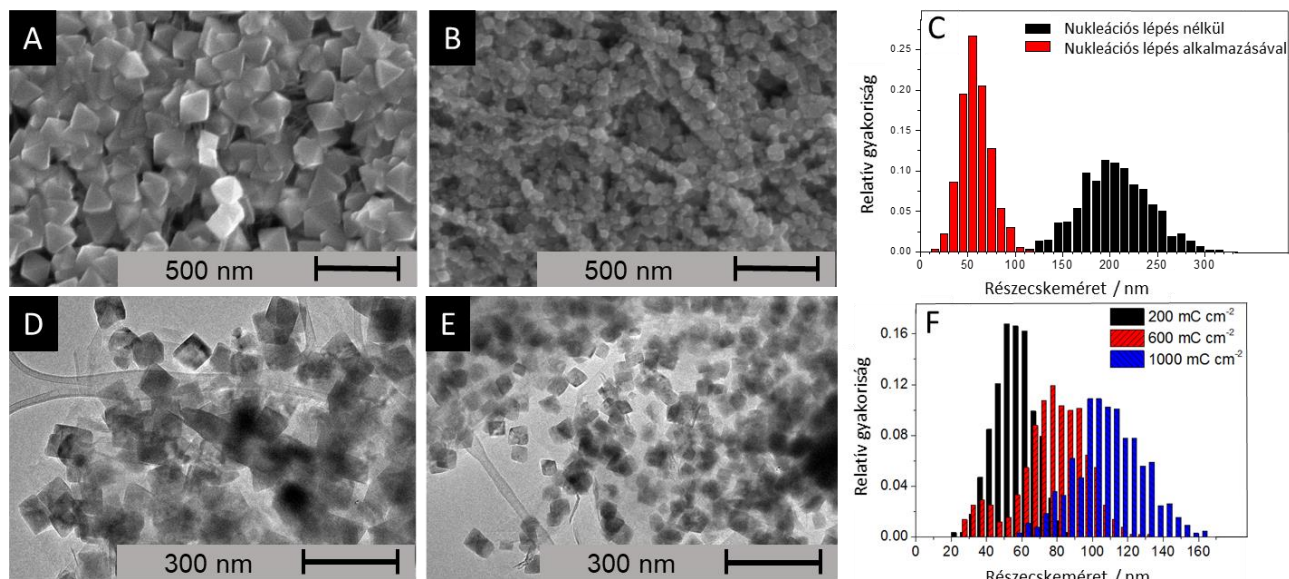
A második példában, az előző eljárás mintegy inverzeként, egydimenziós szerkezetű poli(3-hexiltiofén) nanoszálak felszínére választottunk le fém-kalkogenideket ( $\text{CdS}$ ,  $\text{Sb}_2\text{S}_3$ ) fotokatalitikus úton (15. ábra).<sup>69</sup> Itt arra voltunk kíváncsiak, hogy lehetséges-e szerves nanorészecskéket a vezető polimer saját fotokatalitikus aktivitását kihasználva, *in situ* módon, magán a polimeren létrehozni. Első lépésben a poli(3-hexiltiofén) polimert a megfelelő hullámhosszúságú fényel gerjesztjük. A fotonok az átmenetifémiont vagy az oldatban levő  $\text{S}_8$  molekulákat redukálják (atomos, illetve ionos reakcióút) és így lehetőség van arra, hogy a  $\text{CdS}$  vagy  $\text{Sb}_2\text{S}_3$  leválhasson a polimeren. Igazoltuk, hogy alapvetően az atomos reakcióút a domináns, azaz a fémiont redukáljuk, amely az oldott kénnel fém-kalkogenid nanorészecskét képez.



15. ábra CdS/P3HT kompozitok fotokatalitikus előállításának folyamata.<sup>69</sup>

#### IV. 6. Félvezető/nanoszén elektródok előállítása

Különböző nanoszerkezetű szénelektrodokra (pl. szén nanocső (CNT) és grafén filmek, 3D grafén) is választottunk le félvezetőket elektrokémiai módszerekkel. Ezen témáról írtunk egy összefoglaló tanulmányt, amely során azonosítottuk azokat a körülményeket, amivel szabályozott és homogén félvezető borítottságot érhetünk el nanoszerkezetű szénelektrodok felületén.<sup>70</sup>

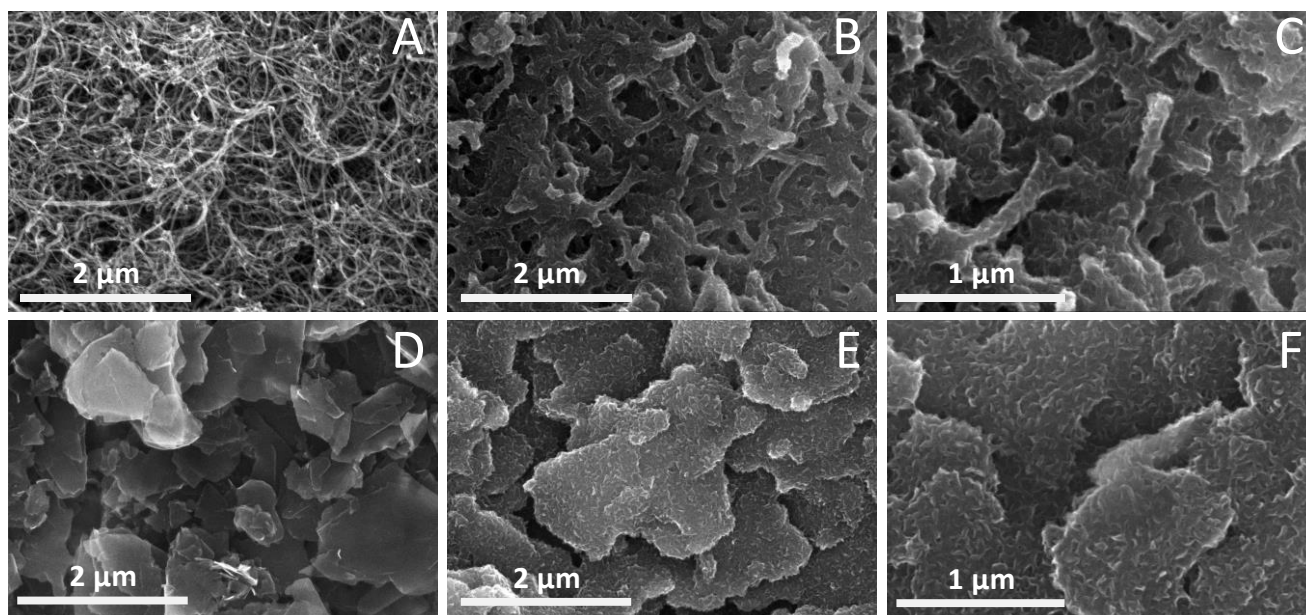


16. ábra Az Cu<sub>2</sub>O/szén nanocső filmek SEM (A, B) és Cu<sub>2</sub>O/grafén filmek TEM (D, E) képei, valamint a Cu<sub>2</sub>O részecskék méreteloszlása (C, F).<sup>71,72</sup>

Ilyen szabályozott módszer lehet a negatívabb kezdőpotenciálon végzett nukleációs lépés és a periodikus szüneteltetés a diffúzió elősegítésére. Példaként említem, hogy szén nanocső filmeket képesek voltunk homogénen feltölteni réz(I)-oxidral, ráadásul a leválasztási idő (és ezáltal az átvitt



töltés) szabályozásával a  $\text{Cu}_2\text{O}$  kristályok méretét is tudtuk hangolni, az 50-120 nm-es tartományban. Grafén filmekre és 3D grafén nanoszerkezetekre is választottunk le elektrokémiai úton szabályozott mennyiségű és méretű  $\text{Cu}_2\text{O}$  nanorészecskéket, melyet a 16. D-F ábra illusztrál. Igazoltuk, hogy megfelelően tervezett elektrokémiai protokollok segítségével grafén lapok esetén homogén borítottságot érhetünk el, és megakadályozható, hogy kizárólag az éleken történjen a kristálynövekedés. Megmutattuk, hogy hasonló kompozitokat elő lehet állítani szerves vezető polimerekkel is, ily módon PEDOT és polianilin tartalmú, grafén és szén nanocső alapú elektródokat készítettünk. Ehhez első lépésben a nanoszén (CNT és illetve grafén) rétegeknek a hordozó elektród felületre történő felvitelét optimaltunk. A nanoszeneket spray-coating technikával fújtuk fel a hordozó üvegszén elektród felületére. Ezt követően a felfújt nanoszén mátrixokra a vezető polimert potenciosztatikus úton választottuk le. A polimerizációs töltéssűrűség értékét variáltuk, így előállítva különféle összetételű PEDOT/nanoszén nanokompozit fotoelektródokat. A 17. ábra ábrán megfigyelhető, hogy a PEDOT réteg homogénen vonta be mindkét nanoszén hordozót.<sup>73</sup>



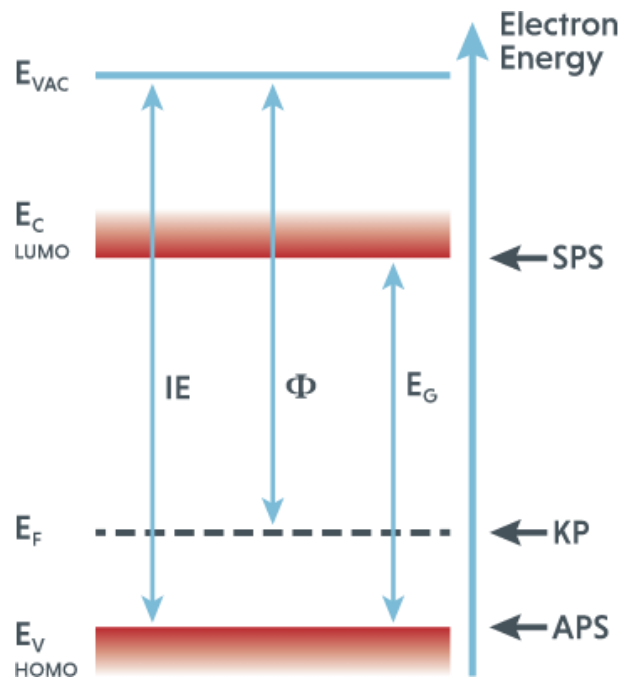
**17. ábra** A CNT és grafén hordozók (A, D), a PEDOT/CNT (B, C), és PEDOT/grafén (E, F) kompozitok SEM felvételei.<sup>73</sup>

A nanoszén tartalmú elektródok előállítását kiterjesztettük a fotoanódok irányába ( $\text{TiO}_2$ ,  $\text{Fe}_2\text{O}_3$ ).<sup>43,47</sup> Első lépésben a jól ismert titán-dioxid példáján vizsgáltuk a kompozitképzést. Az első kitűzött cél egy olyan recept és szintézismódszer kidolgozása volt, mellyel egy lépésben, rögtön az elektrodepozíció után kristályos titán-dioxidot kaphatunk. Titán(III)-klorid savas oldatából anódos leválasztással állítottunk elő  $\text{TiO}_2$ -t, miközben az oldat kémhatását és hőmérsékletét szabályoztuk. Előbbivel a keletkező titán-dioxid összetételét (anatáz és rutil tartalom), utóbbival pedig a leválasztott anyag kristályosságát sikerült szabályozni. Ezen szerkezeti tulajdonságok megmutatkoztak a fotoelektrokémiai viselkedésben is, amely mentén tovább optimalizáltuk a szintézisparamétereket, a homogén borítottság elérése érdekében.<sup>43</sup>

#### IV. 7. Anyagtudományi jellemzés

A klasszikus mikroszkópiás (TEM, SEM), spektroszkópiai (IR, Raman) és röntgenes (XRD, XPS) módszerek bemutatásától itt eltekintenek, mivel ezeket a legtöbb anyagtudományi laboratórium rutinszerűen használja. Hasonló a helyzet az egyszerű elektrokémiai módszerekkel. Mindezek helyett, két olyan módszert és eljárást mutatok be röviden, amelyek használata nem nyilvánvaló, ugyanakkor az általuk nyert információk lényegesek az értekezés mondanivalójának megértéséhez.

A különböző félvezető fotoelektrodok optikai tulajdonságait egy kombinált eszközzel tanulmányoztuk, amely tartalmazott Kelvin szondát (KP), felületi fotofeszültség spektroszkópot (SPS), és légköri fotoelektronspektroszkópot (APS). Ez utóbbi rendszer lehetővé teszi, hogy meghatározzuk az abszolút kilépési munkát akár környezeti, akár szabályozott gáz- vagy vákuumkörnyezetben, és ezáltal a vegyértéksáv pozícióját (és a körülötte levő állapotsűrűséget, density of states). A SPS mérésekből megkapjuk a tiltottsáv-szélességet, és közvetetten az APS-eredmények felhasználásával a vezetési sáv pozícióját. A KP mérésekből pedig megkapjuk a Fermi-szintet.



**18. ábra** Egy félvezető sávpozícióinak meghatározásához alkalmazott módszerek (<https://www.kelvinprobe.com/>).

Beszereztünk és beüzemeltünk egy *in situ* Raman spektroelektrokémiai méréseket és *in situ* röntgendiffraktometriás méréseket lehetővé tevő elektrokémiai cellát.<sup>47</sup> Az első validációs kísérletek után már élesben, valódi mintákhoz használjuk ezen cellát, amelynek segítségével egyrészt a munkaelektrod anyagában bekövetkező változtatásokat tudjuk követni,<sup>46,47,74</sup> másrészt a szén-dioxid redukciós reakció mechanizmusára is tudunk következtetni.<sup>74</sup>

#### IV. 8. Fotoelektrokémiai jellemzés

A fotoelektrokémiai folyamatok vizsgálatának legegyszerűbb eszköze a **fovoltammétria**, amelynek során a munkaelektrod potenciálját állandó sebességgel pásztázzuk egy adott potenciálablakban, miközben a munkaelektrod felületét periodikusan megvilágítjuk. Ugyanazon minta felhasználásával két fovoltammogramot rögzítünk, egyet a célzott szubsztrát (például CO<sub>2</sub>) hiányában, egyet pedig annak jelenlétében. Ha a vizsgált fotoelektrod bármilyen fotoelektrokémiai aktivitást mutat a szubsztrát átalakulása felé, akkor az utóbbi esetben nagyobb fotoáramot mérünk (egyéb körülmények változatlansága mellett). Ez a többlet fotoáram összefüggésbe hozható a szubsztrát molekulák oxidációjával/redukciójával, azonban ezeket az előzetes megfigyeléseket minden esetben termékdetektálási eredményekkel kell alátámasztani. A legfontosabb előnyök és leszűrhető információk a következők:

- A sötét- és fotoáram potenciálfüggése egyazon mérés során meghatározható.
- A félvezető típusa a fotoáram karakterisztikájából azonnal sejthető; katódos fotoáramok – p-típusú félvezető, anódos fotoáramok – n-típusú félvezető.
- A simasáv-potenciál a fotoáram megindulásából határozható meg, amely p-típusú SC esetén az vegyértéksáv potenciáljával, n-típusú félvezető esetén a vezetési sáv pozíciójával korrelálható.
- A fotoáram tranziensek alakja (ún. tüskék) utalhat arra, hogy a félvezető/elektrolit határfelületen jelentős mértékű rekombináció következik be.

A **beeső foton-áram konverziós hatásfok (IPCE)** vagy a külső kvantumhatásfok (EQE) a fotoelektrokémiai rendszerek egyik legfontosabb diagnosztikai értéke. Leírja a beeső fotonfluxusonként kinyert fotoelektronok számát a megvilágítási hullámhossz függvényében. Az IPCE értéke három alapvető folyamat együttes hatásfokát adja meg:

- A fényelnyelés – az egy beeső fotonra jutó elektron-lyuk párok száma.
- A fotogenerált töltéshordozók transzportja az elektród/elektrolit határfelületre.
- A határfelületi töltésátvitel hatásfoka.

A fotoelektrokémiai rendszerekben az IPCE adatok általában kronoamperometriás mérésekből származnak. A munkaelektrodot állandó potenciálon tartjuk (ahol a vizsgált rendszer még stabil, de kellően nagy fotoáram mérhető), majd a felületét periodikusan megvilágítjuk különböző hullámhosszúságú monokromatikus fényel. Az IPCE mérésekből meghatározhatók a következők:

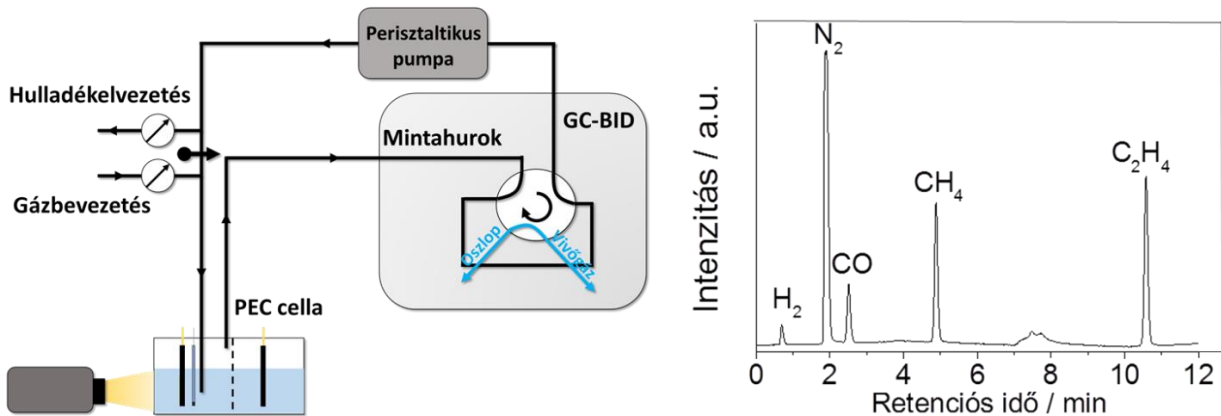
- Az a hullámhossz-tartomány, amelyben a vizsgált minta fotoaktív – ideális a viselkedés, ha ez az ablak és a görbe maximuma átfedésben van az anyag abszorpciós spektrumával,
- Az IPCE értékek abszolút hatásfokot jelentenek, és lehetővé teszik a különböző fotoelektród anyagok összehasonlítását.
- A félvezető tiltotsáv-szélessége meghatározható az IPCE görbe letörési szakaszának illesztésével.
- A napenergia elektronokká való átalakításának kumulatív hatásfoka meghatározható, az IPCE adatok a teljes hullámhossz-tartományon való integrálásával.

Az **intenzitás modulált fotoáram spektroszkópia (IMPS)** az elektrokémiai impedancia spektroszkópia analógja, azzal a különbséggel, hogy itt nem az elektródpotenciált változtatjuk szinuszosan egy egyensúlyi potenciál környezetében, hanem a gerjesztő fény intenzitását. Ezen módszer esetén egy meghatározott és állandó fényintenzitás biztosítja az adott, kvázi-stacionárius körülmények között mérhető fotoáramot, melyre egy szinuszosan változó intenzitású fény szuperponálódik. Ennek eredményeképpen lényegében a rendszert az kvázi-stacionárius fotoáram környezetében moduláljuk. Az IMPS görbéken a fotoáram potenciálfüggését vizsgálva információt kaphatunk a rekombináció mértékéről, illetve a reakció szempontjából lényeges töltéshordozók határfelületen történő átlépésének sebességéről.

#### IV. 9. A képződő termékek detektálása

A különböző fotoelektrokémiai folyamatok során keletkező termékek gyors, pontos és precíz detektálása kulcsfontosságú a különböző elektródok viselkedésének összehasonlítása során. A vízbontás és a CO<sub>2</sub> redukció során keletkező gázfázisú termékeket *on-line* gázkromatográfiával vizsgáltuk egy kisülési ionizációs detektorral (BID) felszerelt Shimadzu 2010 Plus Tracera műszerrel.

Az elektrokémiai cella a gázkromatográffal közvetlen összeköttetésben volt. Mintavétel előtt a cella katódterének gázteréből egy perisztaltikus pumpa segítségével a mintahurokba juttattuk a vizsgálandó gázelegyet, ahonnan a minta egy hatutas szelep átfordításával került gázkromatográf injektorába (19. ábra). Az analizálandó gázelegy elválasztására Shincarbon ST típusú kolonnát használtunk, mely alkalmas a  $H_2$ ,  $O_2$ ,  $N_2$ ,  $CO$ ,  $CO_2$  és könnyű szénhidrogének elválasztására (19. ábra). Az általunk használt BID detektor nagy érzékenyséű, univerzális detektor. Szervetlen gázokra és könnyű szénhidrogénekre a kimutatási határa a ppm tartományban van. Bizonyos mérések során tömegspektrométert használtunk detektorként, akár a gázkromatográfhhoz kapcsolva, akár önmagában. Ez utóbbi esetben gyakorlatilag néhány másodperces csúszással azonnal tudtuk analizálni a képződő termékeket. Az alapvető méréseken túl, kialakítottunk egy izotópjelzéses módszert, amellyel a szén-dioxid redukciós termékek forrását tudjuk egyértelműen azonosítani.



**19. ábra** A gázkromatográfiás termékdetektálás sematikus ábrája, illetve egy hidrogént, szén-monoxidot, metánt, etilént (mindegyik komponens 5 V / V %, vivőgáz:  $N_2$ ) tartalmazó gázelegy kromatogramja Shincarbon ST típusú kolonnán elválasztva GC-BID műszerrel.

A keletkező termékek mennyiségi meghatározását követően az áthaladt töltés ismeretében a Faraday-hatásfokot ( $FE$ ), valamint a parciális áramokat ( $j_p$ ) a következő összefüggésekkel számítottuk:

$$FE(\mathbf{P})\% = \frac{z n(\mathbf{P}) F}{Q} \times 100 \%,$$

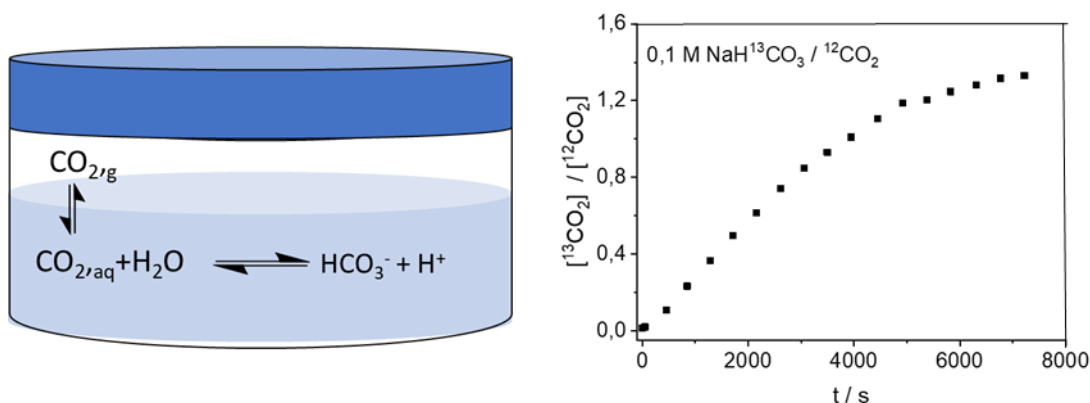
$$j(\mathbf{P}) = j_{tot} \times FE(\mathbf{P})$$

ahol  $z$  a  $\mathbf{P}$  termék képződéséhez szükséges elektronok száma,  $n(\mathbf{P})$  a reakcióban képződött  $\mathbf{P}$  termék anyagmennyisége,  $F$  a Faraday-állandó,  $Q$  a reakció során áthaladt összes töltés,  $j_{tot}$  a mért áramsűrűség.

A folyadékfázisú  $CO_2$  redukciós termékek analízisét általában *ex situ*  $^1H$  NMR spektroszkópiával végeztük egy 500 MHz-es Bruker Advance készülékkel. A mennyiségi meghatározáshoz belső standard-es kalibrációt alkalmaztunk. Az analízis során 450  $\mu L$  vizsgálandó elektrolithoz 50  $\mu L$   $D_2O$ -t adtunk, amely belső standardként 1,3 mM fenolt és 0,8 mM dimetil-szulfoxidot (DMSO) tartalmazott. A kalibrációhoz a termékek és a belső standard komponensek jeléhez tartozó csúcs alatti területek arányát használtuk. A víz jelétől jobbra található komponensek esetén a DMSO, míg az attól balra található komponensek esetén a fenol jeléhez viszonyítottunk. Az alkalmazott módszer kimutatási határa 5 – 10  $\mu M$  (256 scan). Néhány esetben GC-MS módszerrel is vizsgáltuk a folyadéktermékeket, különösen azokat, amelyek kis koncentrációban voltak jelen.

#### IV. 10. Izotópjelzéses mérések

Szén-13 izotópjelzéses vizsgálatokkal arra kerestük a választ, hogy a szén-dioxid redukciója során, az elektród felületén reagáló komponens az oldott szén-dioxid vagy a hidrogén-karbonát ion. Ehhez szelektív izotópjelzést használtunk, vagyis a kísérletek során vagy csak a  $\text{CO}_2$ , vagy csak a  $\text{NaHCO}_3$  volt  $^{13}\text{C}$  jelzett. Mivel az alkalmazott kísérleti körülmények mellett a  $\text{CO}_2$  és a  $\text{HCO}_3^-$  közötti izotópegyensúly beállása nem pillanatszerű (20. ábra), a redukció során keletkező CO izotóptözetételének analízisével (GC-MS) információt szerezhettünk arról, hogy a  $\text{CO}_2$  vagy a  $\text{HCO}_3^-$  reagál-e az elektród felületén. Ezen izotópjelzéses vizsgálatok és különböző pH-jú elektrolitokban végzett kontroll mérések alapján azt állapítottuk meg, hogy az elektród felületen a  $\text{CO}_{2,\text{aq}}$  reagál, azonban a  $\text{HCO}_3^-$  elektrolitnak kulcsszerepe van a  $\text{CO}_2$  pótlásában az elektród felületén („ $\text{CO}_2$ -puffer”).<sup>75</sup> Ezen túlmenően, szén-tartalmú katalizátorok esetében igazolni tudjuk, hogy a képződő termék valóban a betáplált  $\text{CO}_2$ -ból származik és nem a katalizátorból, vagy a hordozóból.

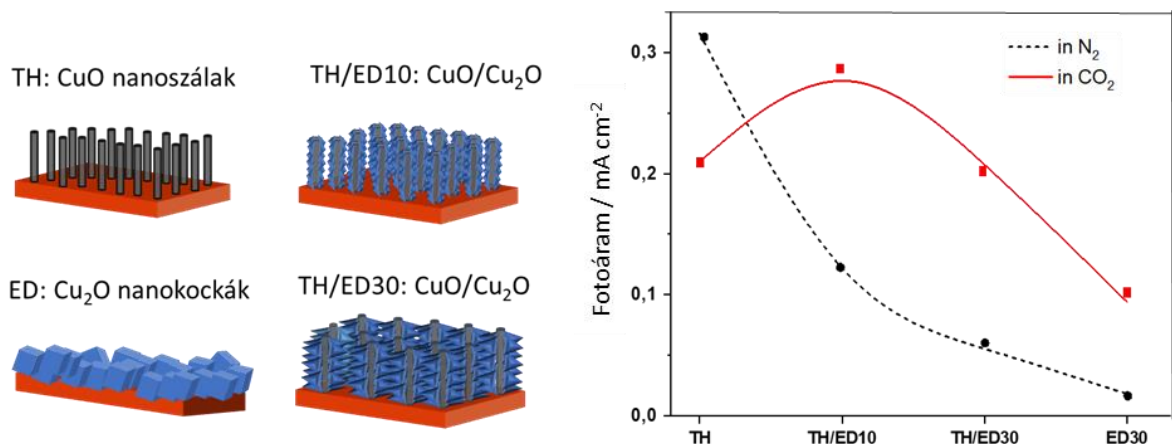


20. ábra A szelektív izotópjelzéses kísérlet vázlatja, és az izotópegyensúly beálltának időskálája.<sup>75</sup>

#### V. Egyszerű fotelektrodok fotelektrokémiai tulajdonságai

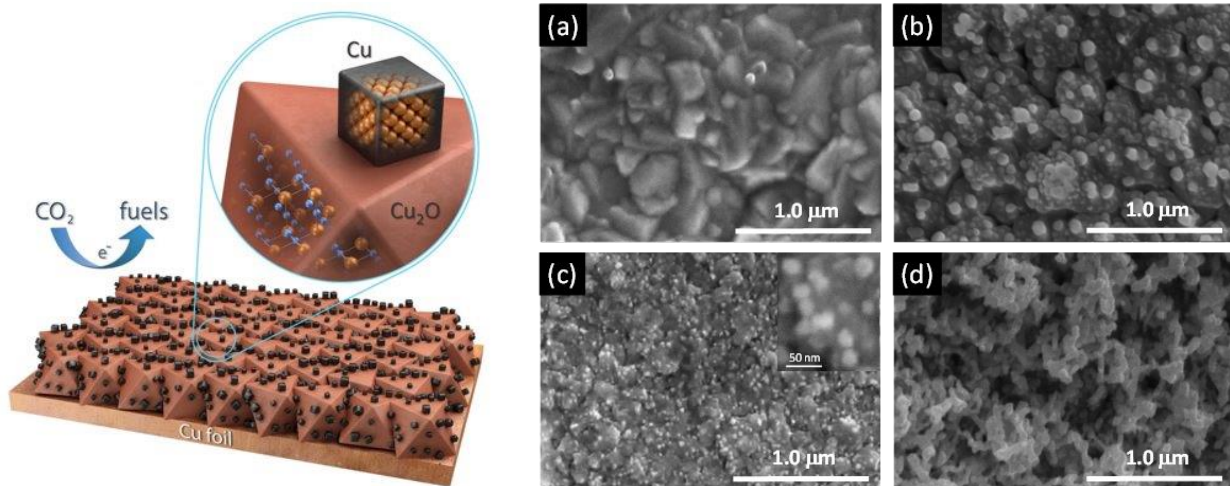
##### V. 1. Oxid félvezetők fotelektrokémiai tulajdonságai

A fotelektrokémiai  $\text{CO}_2$  redukciós vizsgálatokat különböző réz-oxid fotelektrodokon kezdtem el. Ezen kísérletek során, rézlemezen termikus kezeléssel (TH) előállított  $\text{CuO}$  nanoszálakat vontunk be különböző ideig tartó elektrokémiai leválasztással (ED) előállított  $\text{Cu}_2\text{O}$ -al.<sup>44,45</sup>



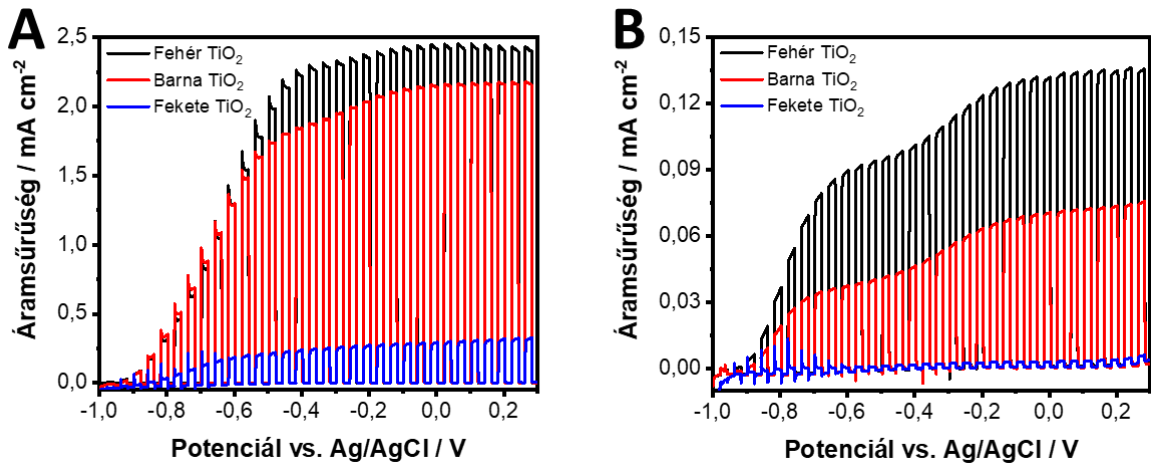
21. ábra Különböző réz-oxid alapú fotelektrodok sematikus ábrázolása és a fotelektrokémiai  $\text{CO}_2$  redukcióban mért fotoáram értékek.<sup>45</sup>

Különböző összetételű és morfológiájú elektródokat állítottunk elő, és megmutattuk, hogy ezen elektródokon a CO<sub>2</sub> fotoelektrokémiai redukciójával metanolt lehet előállítani.<sup>44,45</sup> Azt is igazoltuk, hogy az összetétel változtatásával mind a fotoáram, mind a képződő termékek összetétele változik. Jóllehet ezen kezdeti mérések során viszonylag kis fotoáramokat mérhettünk, ez indított el a későbbi szén-dioxid átalakítási kísérletek irányába. A különböző réz-oxid alapú fotoelektródok kapcsán szerzett tapasztalatainkra építve bemutattuk a Cu/Cu<sub>2</sub>O határfelület kitüntetett szerepét mind az elektrokémiai, mind a fotoelektrokémiai CO<sub>2</sub>-redukciós reakcióban.<sup>76</sup> Azt találtuk, hogy a fotoelektrokémiai korrózió eredményeképpen keletkező réz nanorészecskék megjelenése (ami a 22. ábrán bemutatott SEM felvételeken is látható) segíti a CO<sub>2</sub> redukciós folyamatot (másképp fogalmazva, a Cu nanokocka kokatalizátorok *in situ* képződnek a fotoelektrokémiai folyamat során), ugyanakkor ha a fotokorrózió dominánssá válik, akkor az hátrányosan hat a fotoelektrokémiai tulajdonságokra.<sup>76</sup> További érdekesség, hogy hasonló morfológiájú réteg alakul ki a Cu<sub>2</sub>O fotokorróziója és elektroredukciója során (22. ábra).



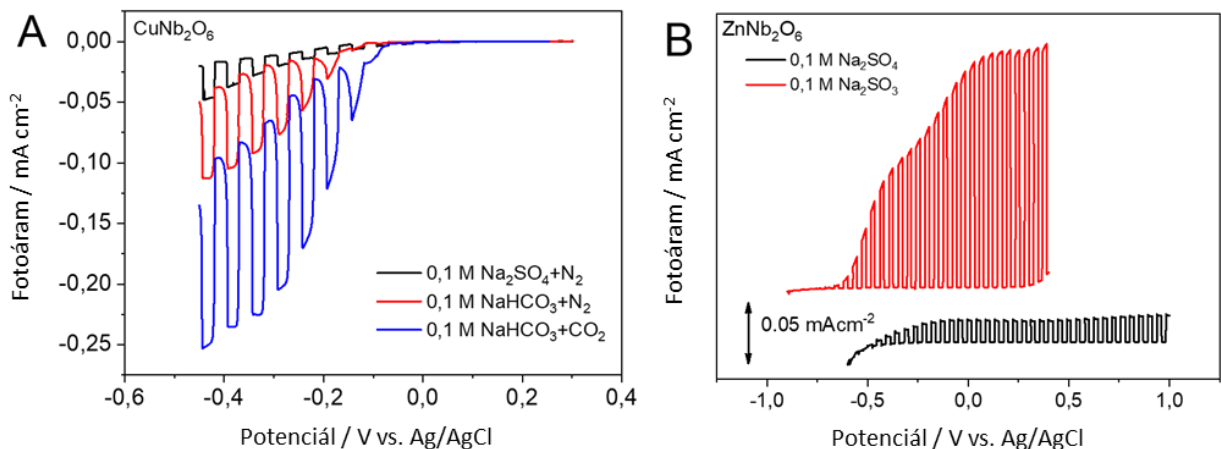
**22. ábra** A fotoelektrokémiai CO<sub>2</sub> redukció során kialakuló Cu/Cu<sub>2</sub>O elektródok sematikus ábrázolása és SEM felvételek: (a) nyers Cu<sub>2</sub>O, (b) Cu<sub>2</sub>O 15 perc szimulált napfényvel való megvilágítás után, (c) 1,5 V (vs. Ag/AgCl) potenciálon 60 percig redukált Cu<sub>2</sub>O, (d) Cu<sub>2</sub>O 60 perc szimulált napfényvel való megvilágítást követően.<sup>76</sup>

A titán-dioxidot (TiO<sub>2</sub>) gyakran használják fényelnyelőként, elektronvezető réteggént és katalizátorként különböző energetikai és környezetvédelmi alkalmazásokban. A hidrogénatmoszférában végzett hőkezelés fekete TiO<sub>2</sub>-t (b-TiO<sub>2</sub>) hoz létre, amely lehetővé teszi a látható fény nagyobb mértékű elnyelését, és ez a b-TiO<sub>2</sub>-t a kutatás élvonalába helyezte.<sup>77</sup> A hidrogénes kezelés ugyanakkor hibahelyeket is létrehoz, amelyek szerepe ellentmondásos, és erősen függ a vizsgált alkalmazástól. Kombinált felületkémi és *in situ* elektrokémiai módszerekkel vizsgáltuk ezen hibahelyek hatását a b-TiO<sub>2</sub> fotoelektrokémiai, elektrokatalitikus és töltéstároló tulajdonságaira. A hibahelyek számának növekedésével kisebb fotoáramot tapasztaltunk, de javultak az elektrokatalitikus és a töltéstárolási tulajdonságok. Azt is megállapítottuk, hogy a fotoelektrokémiai tulajdonságok javíthatók a hibahelyek passziválásával (Li<sup>+</sup> ion interkaláción keresztül egy kétlépéses folyamatban). Megmutattuk, ez a passziválás csak kisméretű kationokat (Li<sup>+</sup>) tartalmazó elektrolitoldattal valósítható meg, nagyméretűekkel (Bu<sub>4</sub>N<sup>+</sup>) nem.<sup>78</sup>



**22. ábra** Fehér, barna és fekete TiO<sub>2</sub> elektródok fotovoltammogramjai (Argonnal öblített 0,1 M Na<sub>2</sub>SO<sub>3</sub> elektrolit, 2 mV s<sup>-1</sup> pásztázási sebesség, 0,1 Hz megvilágítási frekvencia. Fényforrásként (A) UV-lámpát és (B) napfényszimulátort (AM1.5) használtunk.<sup>78</sup>

Számos kétfémes félvezető oxid esetében megmutattuk, hogy ezen oxidok ígéretesek lehetnek akár fotokatódként, akár fotoanódként. Példaként az összetett niobátokat említem: a p-típusú félvezető CuNbO<sub>3</sub> nanorészecskéket vizsgáltuk közvetlen CO<sub>2</sub> redukációs reakcióban alkalmazható fotokatódként, míg a ZnNb<sub>2</sub>O<sub>6</sub> nanorészecskék stabil n-típusú félvezetőként viselkednek (23. ábra).<sup>51</sup>



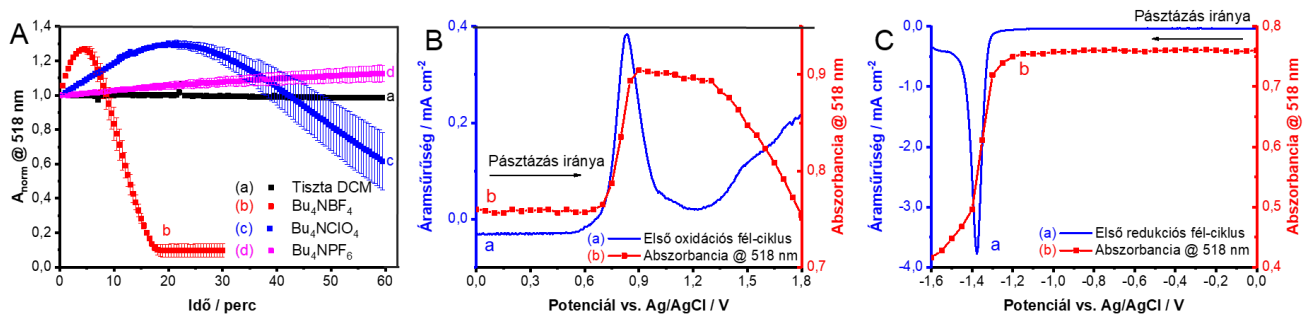
**23. ábra** Oldatbelobbantásos módszerrel előállított CuNb<sub>2</sub>O<sub>6</sub> (A) és ZnNb<sub>2</sub>O<sub>6</sub> (B) fotovoltammogramjai. Fényforrásként napfényszimulátort (AM1.5) használtunk.<sup>51</sup>

CuMO<sub>2</sub> összetételű vegyes oxidok (ún. delafosszitok) előállításával és fotoelektrokémiai vizsgálatával is foglalkoztunk.<sup>79</sup> Az idegen fémion beépítésével (pl. CuFeO<sub>2</sub>, CuCrO<sub>2</sub>, CuRhO<sub>2</sub>), mind a vegyérték, mind a vezetési sáv szerkezete és pozíciója megváltozik a tiszta réz oxidhoz képest. Mitöbb, szakirodalmi tapasztalatok szerint ezen oxidok kémiai és elektrokémiai stabilitása egyaránt meghaladja a Cu<sub>2</sub>O esetében tapasztaltakat. Elektrokémiai mérésekhez az előállított anyagot, szuszpenzióból való felfújás segítségével vittük fel az elektród felszínére. A felfújó rétegek vastagságát optimalizáltuk, valamint a rétegek hőkezelési idejének (0,5–4 h) hatását is tanulmányoztuk. Az így kapott legjobb tulajdonságú CuCrO<sub>2</sub> minta esetében a reprodukálhatóan mérhető fotoáramok

nagysága ( $3 \text{ mA cm}^{-2}$ , UV lámpa használatával) jelentősen meghaladta az általunk akármelyik más fotokatód esetében mértet. Az előállított  $\text{CuCrO}_2$  tiltottsáv-szélessége  $2,83 \text{ eV}$ -nak adódott, ezért ennek csökkentése érdekében  $\text{CuFeO}_2$  és  $\text{CuRhO}_2$ -al való kombinálással is próbálkoztunk.<sup>80</sup>

## V. 2. Fém-halogenid fotelektrodok vizsgálata

Tekintettel a fém-halogenidek számos esetben tapasztalt instabilitására, első lépésben meghatároztuk azokat az elektrolit oldatokat és elektrokémiai stabilitási ablakokat, amelyeken belül ezen félvezetők stabilak, és fotelektrokémiai tulajdonságaik vizsgálhatók (24. ábra). Azonosítottuk a különböző korróziós és fotokorróziós folyamatokat, és a keletkező degradációs termékeket. Megmutattuk, hogy a termodinamikai instabilitás nem minden esetben jár fotokorrózióval, mivel kinetikai stabilizálás elérhető (amennyiben a fotogenerált töltéshordozókat sikerül gyorsan elvezetni az elektródról).<sup>61</sup>



**24. ábra** (A) FTO/TiO<sub>2</sub>/CsPbBr<sub>3</sub> elektród normalizált abszorbancia-változása 518 nm-en különböző elektrolitokat tartalmazó diklórmetánban. A hibásávok három különálló filmen végzett mérésekből származnak. FTO/TiO<sub>2</sub>/CsPbBr<sub>3</sub> filmek 0,1 M Bu<sub>4</sub>NPF<sub>6</sub>/diklór-metán elektrolitban ( $10 \text{ mV s}^{-1}$ ) rögzített spektrumai az (B) oxidációs és (C) redukciós félciklus során, az exciton csúcs abszorbancia-változásával együtt.

## V. 3. Szerves polimer alapú fotelektrodok

Elsők között mutattuk meg, hogy az elektromosan vezető polimereken a CO<sub>2</sub> fotelektrokémiai átalakítása végrehajtható. Polianilin fotelektrodok esetében pufferelt közegben végzett mérések segítségével egyértelműen elkülönítettük egymástól a protonredukciót és a CO<sub>2</sub> redukcióját (25. ábra, A és B). Megállapítottuk, hogy a CO<sub>2</sub> atmoszférában megnövekedett fotoáramokat, illetve a N<sub>2</sub> atmoszférához képest a voltammogramok eltérő alakját egyértelműen a CO<sub>2</sub> fotelektrokémiai redukciója okozza. A jelenség jobb megismerése érdekében hullámhosszfüggő fotoáram méréseket is végeztünk (IPCE). Ahogy a 25. ábra C részén látható, az IPCE görbe jó átfedést mutat a PANI UV-látható elnyelési spektrumával, ami egy újabb bizonyíték a fotelektrokatalitikus hatás eredetére. Hosszú idejű fotelektrolízist végezve redukciós termékként alkoholokat (metil-alkoholt és etil-alkoholt) sikerült kimutatnunk GC-MS technikával.<sup>81</sup>

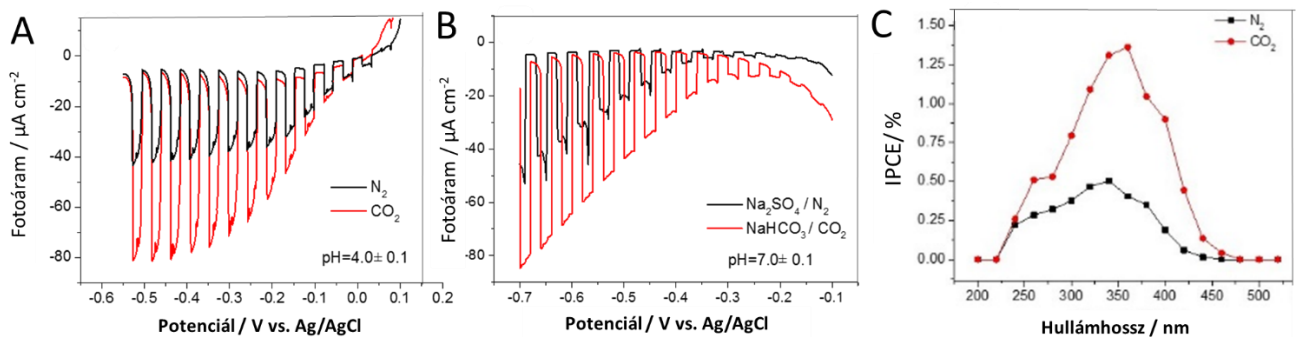
Megállapítottuk, hogy a N-tartalmú polimerek jó CO<sub>2</sub> adszorpciós képességgel rendelkeznek, közülük is azok, melyekben a N atomhoz H atom is kapcsolódik. Összességében elmondható, hogy alapvetően három kritériumnak kell megfelelniük a polimereknek, ahhoz, hogy fotelektrokémiailag aktívak legyenek a CO<sub>2</sub> átalakításában:

1. A vezetési sávjuk (LUMO-pályájuk) potenciálja negatívabb legyen a CO<sub>2</sub> redukciós reakciók termodinamikai potenciáljánál.



2. Azon a potenciáltartományon, ahol a vizsgálatokat végezzük, a polimer teljesen redukált állapotban kell, hogy legyen (a vegyértéksávjának potenciálja megfelelően pozitív legyen). Ellenkező esetben a polimer saját elektrokémiai viselkedése fog dominálni.
3. A polimer rendelkezzen jó CO<sub>2</sub> adszorpciós kapacitással, vagyis tartalmazzon primer vagy szekunder amin-csoportot, amely részvételével kemisorpció történhet.

Amennyiben ezek közül a feltételek közül valamelyik nem teljesül, az adott vezető polimer nem mutat fotoelektrokatalitikus CO<sub>2</sub> redukciós aktivitást. A fenti eredményekből kiindulva különböző N-tartalmú vezető polimereket terveztünk és állítottunk elő, majd vizsgáltuk elektrokémiai tulajdonságaikat.<sup>63</sup> Összességében megállapítottuk, hogy bár ezen anyagcsalád egy érdekes alternatívája lehet a szervesetlen félvezetőknek, mind stabilitásban, mind aktivitásban jelentős növekedésre van szükség.

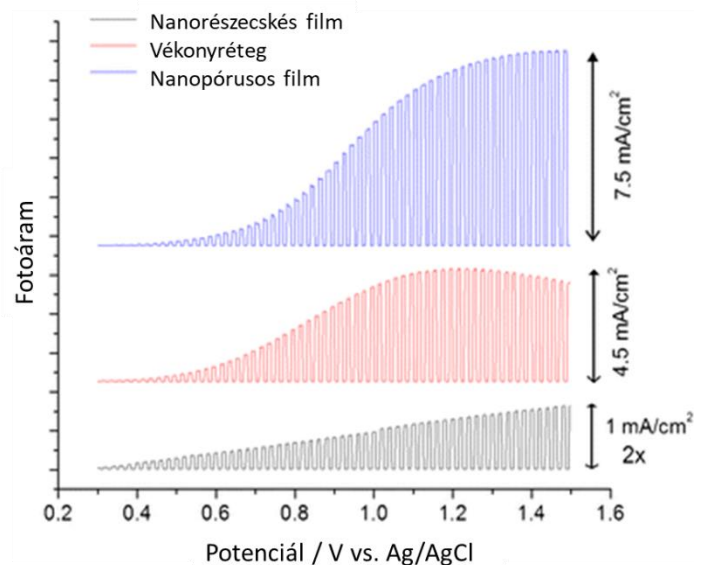


25. ábra Polianilin elektródok fotoelektrokémiai viselkedése különböző közegekben (Xe–Hg lámpa).<sup>81</sup>

#### V. 4. Morfológia szerepének vizsgálata

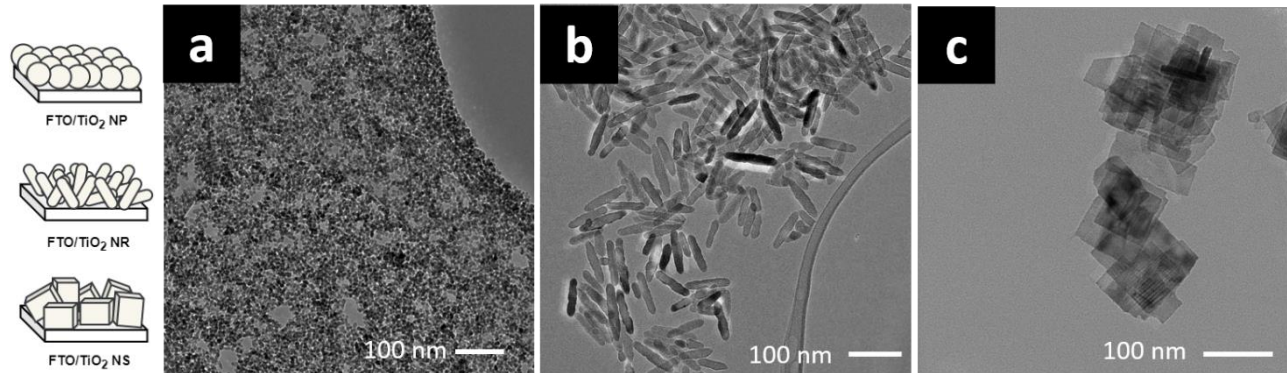
Indirekt módon számos esetben tapasztaltuk (és a szakirodalomban is fellelhető), hogy a fotoelektrodot alkotó félvezető részecskék alakja és az előállított elektród morfológiája döntő befolyást gyakorolnak a fotoelektrokémiai viselkedésre.<sup>30</sup> Először a WO<sub>3</sub> példáján találkoztam ezzel a kérdéssel, amikor három különböző szerkezetű vékonyréteget állítottam elő (kompakt film, nanorészecskés film, koherens nanopórusos film).<sup>41</sup> Savas közegű vízoxidációs folyamatot vizsgáltam, és azt tapasztaltam, hogy a morfológiától függően akár egy nagyságrend különbség is lehet a mérhető fotoáramok nagyságában, egyéb paraméterek változatlansága mellett.

Ugyanakkor ezek a rétegek vastagságban is eltértek egymástól, ezért célul tűztük ki egy jobban definiált modellrendszer vizsgálatát is. Oldatkémiai módszerekkel állítottunk elő 0D (pötty), 1D (rúd),



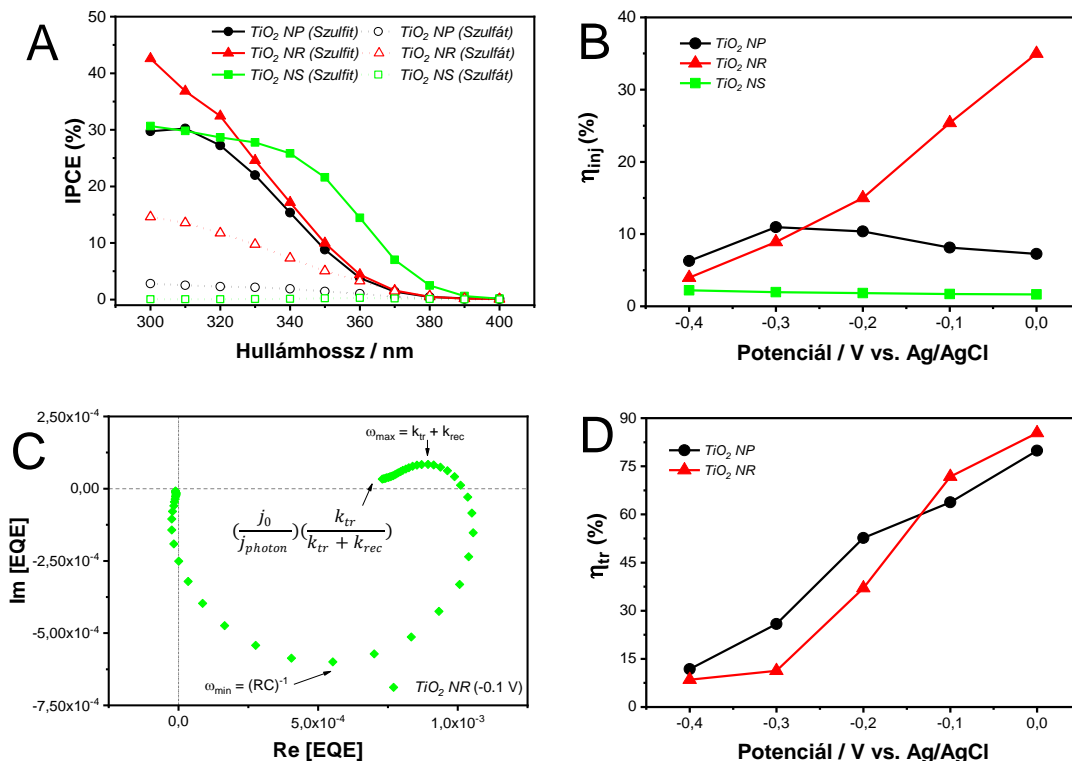
26. ábra Különböző módszerekkel szintetizált WO<sub>3</sub> minták reprezentatív fotovoltammogramja 0,5 M H<sub>2</sub>SO<sub>4</sub> oldatban, 2 mV s<sup>-1</sup> pásztázási sebességgel (150 W-os Xe lámpa).<sup>41</sup>

és 2D (lap)  $\text{TiO}_2$  nanoszerkezeteket (27. ábra), amely nano-kiterjedése (átmérő a pöttyöknél és rudaknál, vastagság a lapok esetében) kb. 10 nm volt.<sup>82</sup> Meggyőződünk arról, hogy ezen anyagok optoelektronikai tulajdonságai nem térnek el jelentős mértékben. Ezt követően fotelektrodokat készítettünk, ügyelve a felvitt mennyiség precíz szabályozására.



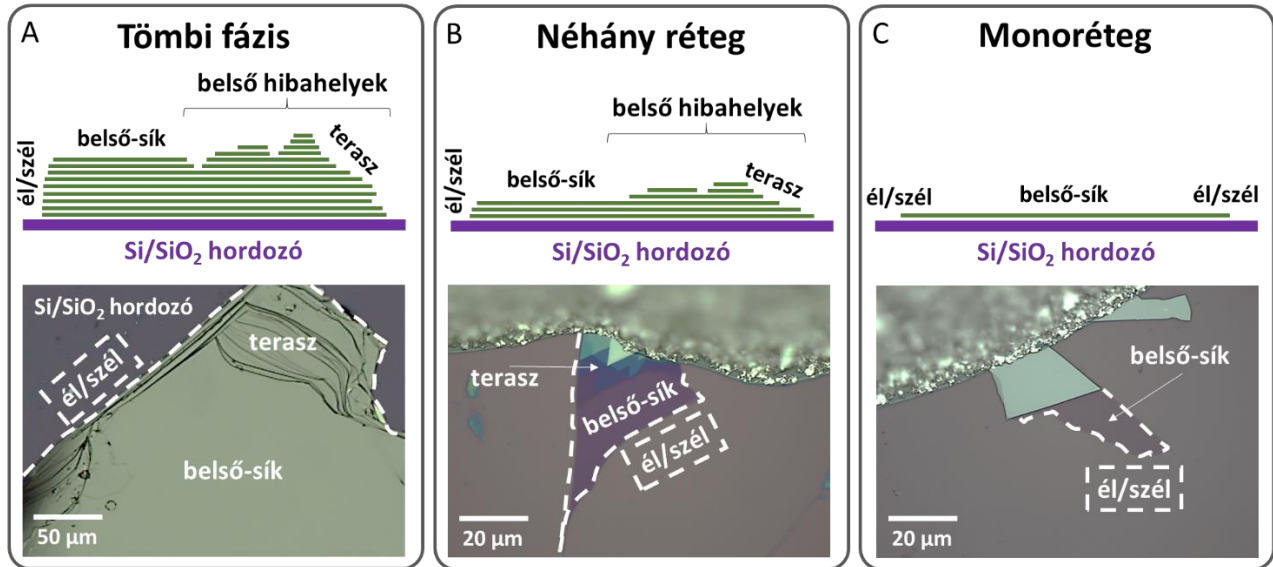
27. ábra Hidrotermális szintézissel előállított 0D, 1D, és 2D  $\text{TiO}_2$  nanoszerkezetek TEM felvételei.<sup>82</sup>

Az így előállított fotelektrodokat vizsgáltuk mind vízoxidációban (ahol van kinetikai gátlás), mind szulfid-ion oxidációban (ahol nincs kinetikai gátlás). ICPE és IMPS mérésekkel igazoltuk, hogy a morfológia a töltéshordozók transzportját és határfelületi transzferét egyaránt befolyásolja (28. ábra), és a nanorudas minták esetében mérhető a legnagyobb fotoáram.



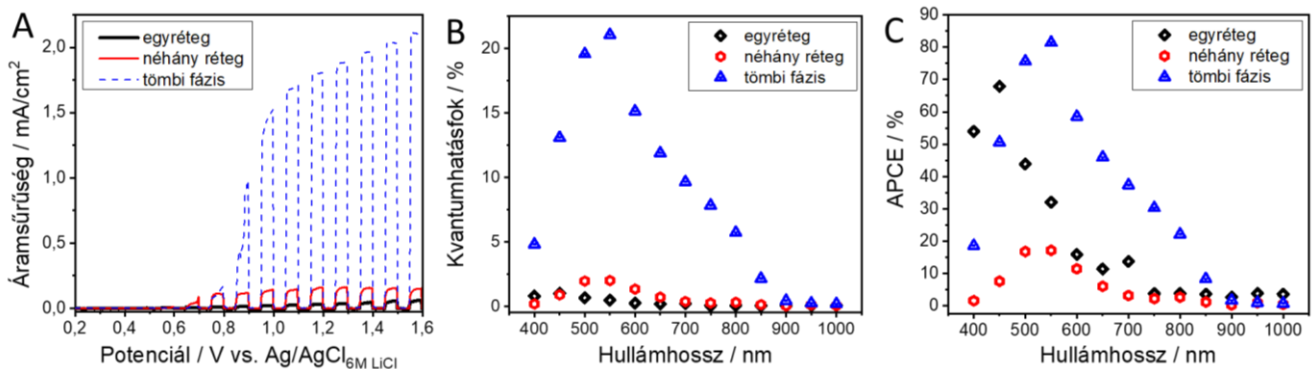
28. ábra (A) A különböző  $\text{TiO}_2$  nanostruktúrák IPCE profiljai (0,2 V vs. Ag/AgCl), (B) töltésátviteli hatásfok értékek  $\text{Na}_2\text{SO}_4$  elektrolitban. (C)  $\text{TiO}_2$  NR filmek reprezentatív IMPS spektruma és (D) a töltésátviteli hatásfok az alkalmazott potenciál függvényében a  $\text{TiO}_2$  NP és NR mintákra  $\text{Na}_2\text{SO}_3$  elektrolitban.<sup>82</sup>

A morfológiai jellemzők szerepét tovább tanulmányoztuk különböző 2D anyagok esetében, egy egyedi fejlesztésű fotoelektrokémiai mikroszkóppal.<sup>83</sup> Mechanikusan exfoliált MoSe<sub>2</sub> elektródok példáján vizsgáltuk a rétegvastagság szerepét, valamint az élek, teraszok, lapsíkok (29. ábra) aktivitását. Ezen vizsgálatokat egy olyan mikropipetta tette lehetővé, amelyben integráltuk az ellen és referencia elektródot, és képes 5-50  $\mu\text{m}$  átmérőjű oldatcseppet a munkaelektrodként alkalmazott 2D anyag meghatározott részére helyezni. A folyadékcsepp/MoSe<sub>2</sub> határfelület nagysága határozta meg az elektrokémiai cellát, amelyet egy fókuszált száloptikás fényforrással világítottuk meg.



29. ábra A különböző 2D MoSe<sub>2</sub> struktúrák fénymikroszkópos felvétele, és a jellemző szerkezeti elemek sematikus bemutatása.<sup>83</sup>

A fotoelektrokémiai vizsgálatok a tömbfázisú lapok esetében mutatták a legjobb aktivitást, még akkor is, ha a nagyobb fényelnyelésből eredő triviális hatással korrigált APCE értékeket nézzük (30. ábra). Megfigyeltük azt is, hogy az élek és teraszok fotoelektrokémiai aktivitása lényegesen kisebb a belső síkokhoz képest. Ez a trend alapvetően a rekombinációs centrumként működő hibahelyek eltérő mennyiségével volt magyarázható.<sup>83</sup> Ezen hibahelyek ugyanakkor megnövekedett elektrokatalitikus aktivitást eredményeztek.

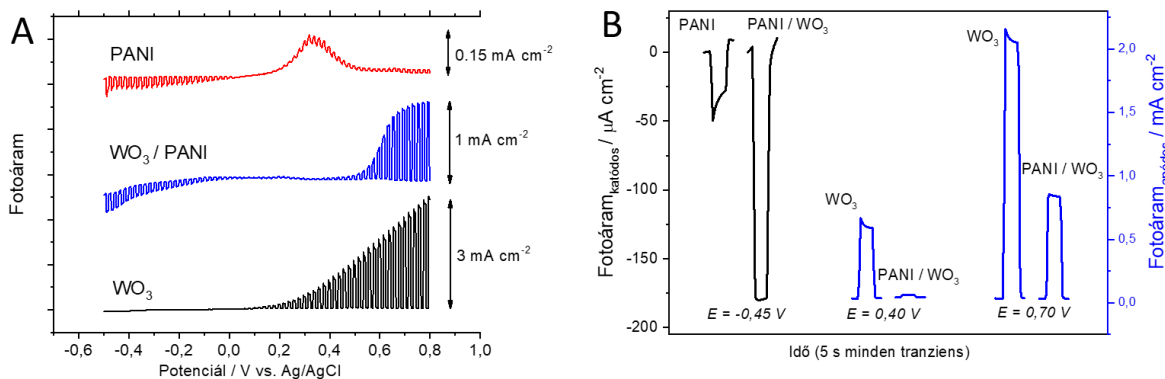


30. ábra Az egy-, néhány rétegű és tömbi MoSe<sub>2</sub> lapok esetében rögzített fotovoltammogramok (A) 6 M LiCl-oldatban (5 mV/s pásztázási sebesség); (B) kvantumhatásfok (IPCE), és (C) APCE-görbék.<sup>83</sup>

## VI. Összetett fotoelektrodok fotoelektrokémiai tulajdonságai

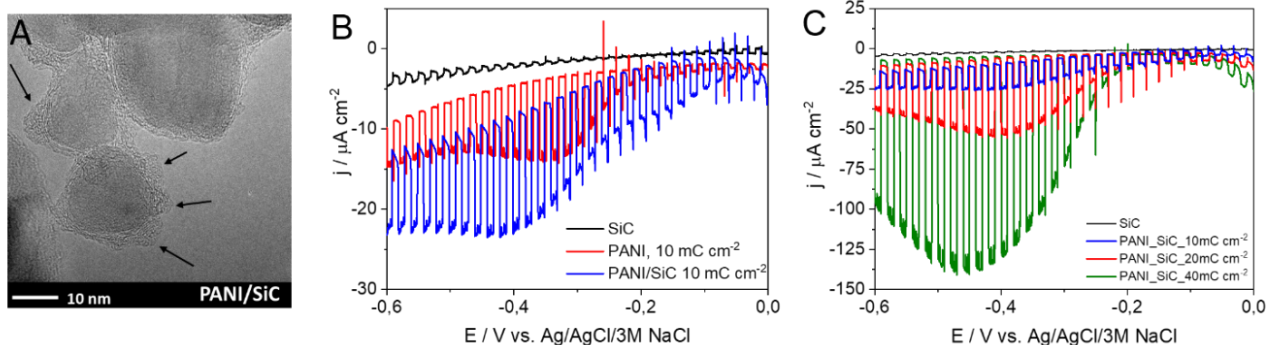
### VI. 1. Szerves/szervetlen hibrid fotoelektrodok

Elsőként egy PANI/WO<sub>3</sub> kompozit fotoelektrokémiai viselkedését mutatom be, mivel korábban mindkét komponens viselkedését bemutattam már. A hibrid elektród fotovoltammogramja mindkét komponensének néhány jellemzőjét mutatja (31. ábra). Míg a katódos fotoáramok megjelenése a polianilin p-típusú fotoaktivitását bizonyítja hibrid konfigurációban, addig pozitív potenciálokon mért anódos fotoáramok a WO<sub>3</sub>-hoz kapcsolódnak. A fotoáramok abszolút értéke azonban meglehetősen érdekes. A polianilinhez kapcsolódó katódos fotoáramok jelentősen (több mint 3-szor) nagyobbak a PANI/WO<sub>3</sub> hibrid esetében, összehasonlítva az Au elektródra azonos töltéssűrűséggel leválasztott PANI filmmel. Ez a hatás a WO<sub>3</sub> elektród nanoszerkezetével magyarázható, amelyet egy homogén, vékony (15 nm) PANI film borít a hibrid fotoelektrodban. Így a fotogenerált lyukak összegyűjtését nem korlátozza a töltéshordozók transzportja a szerves polimerben, mint a tömbi réteg esetében. A fotoáram tranziensek alakjának alapos vizsgálata egy másik jelentős különbséget is feltárt: a katódos fotoáramok esetében a hibrid elektród esetében platót – vagy a potenciáltartománytól függően mérsékelt csökkenést – láttunk a tuskés tranziens profil helyett (mint a tiszta PANI esetében 31/B. ábrán). Ez a töltéshordozók hatékony szétválasztását jelzi, mielőtt azok rekombinálnának.



**31. ábra** A WO<sub>3</sub>, PANI és a PANI/WO<sub>3</sub> hibrid fotoelektrodok reprezentatív fotovoltammogramjai (0,1 M Na<sub>2</sub>SO<sub>4</sub>, 2 mV s<sup>-1</sup> pásztázási sebesség, 150 W-os Xe lámpa, Ag/AgCl referenciaelektrod).<sup>39</sup>

Egy másik példa a PANI/szilícium-karbid (PANI/SiC) kompozitok elektrokémiai szintézise, amelynek során első lépésben a SiC nanorészecskéket rögzítettük üvegszén elektród felületén, majd ezt követően a PANI-t elektrokémiai polimerizációval állítottuk elő (32./A ábra).

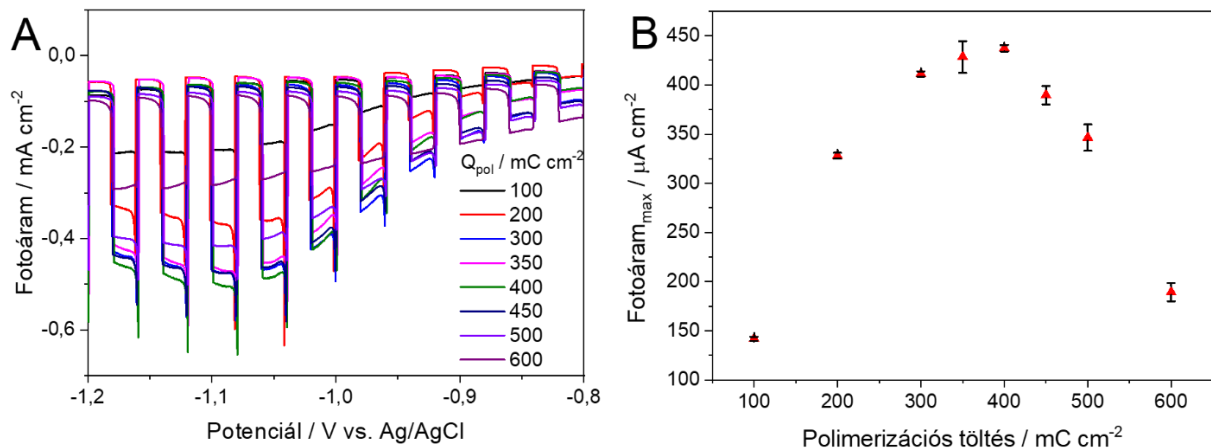


**32. ábra** Az elektrokémiai módszerrel előállított PANI/SiC kompozit TEM képe (a nyilak a PANI réteget jelzik a SiC részecskék felszínén), valamint CO<sub>2</sub> atmoszférában mért fotovoltammogramok összetételüggése.<sup>68</sup>

Az így előállított kompozitok elektroaktívak voltak, és a CO<sub>2</sub> redukciós reakcióban mért fotoáramok meghaladták az egyes komponensek esetében mérteteket (32. B és C ábra). Igazoltuk, hogy a SiC-ban gerjesztett fotoelektronok is részt vesznek a folyamatban, míg a PANI réteg mediátorként funkcionál. Szisztematikusan változtatva a kompozit összetételét meghatároztuk az optimális összetételt. Hosszú távú fotoelektrolízist végezve termékként H<sub>2</sub>-t, CO-t, metanolt és etanolt azonosítottunk GC-MS és NMR technikákkal.<sup>68</sup>

## VI. 2. Félvezető/nanoszén elektródok tulajdonságai

Korábban bizonyítottuk, hogy a vezető polimerek önmagukban is képesek a szén-dioxid fotoelektrokémiai redukciójára. Azonban ezen anyagok, előnyös tulajdonságaik mellett rendelkeznek néhány hátránnyal is: a töltéshordozó mobilitásuk nagyon kicsi, amely erőteljesen befolyásolja a maximálisan kinyerhető fotoáram nagyságát. Ehhez jön még a korlátozott stabilitásuk. A hátrányos sajátságok potenciálisan kiküszöbölhetők, ha a polimereket egy jól vezető, nanoszerkezetű hordozóra választjuk le, mely a fotogenerált töltéshordozókat gyorsan és hatékonyan el tudja vezetni, ezáltal növelve a töltéshordozó mobilitást, illetve esetlegesen növelve ezen kompozit anyagok fotostabilitását. A korábban bemutatott polianilin helyett, ezen kísérletek során egy kis tiltottsáv-szélességgel (1.7 eV) rendelkező igen stabil és robusztus vezető polimert alkalmaztunk, mégpedig a poli(3,4-etiléndioxitiofén)-t (PEDOT). A nanoszeneket spray-coating technikával fújtuk fel a hordozó üvegszén elektród felületére. Ezt követően a felfújt nanoszén mátrixokra a vezető polimert potenciosztatikus úton választottuk le, és közben a polimerizációs töltéssűrűség értékét variáltuk, így előállítva különféle összetételű PEDOT/nanoszén nanokompozit fotoelektródokat.<sup>73</sup>



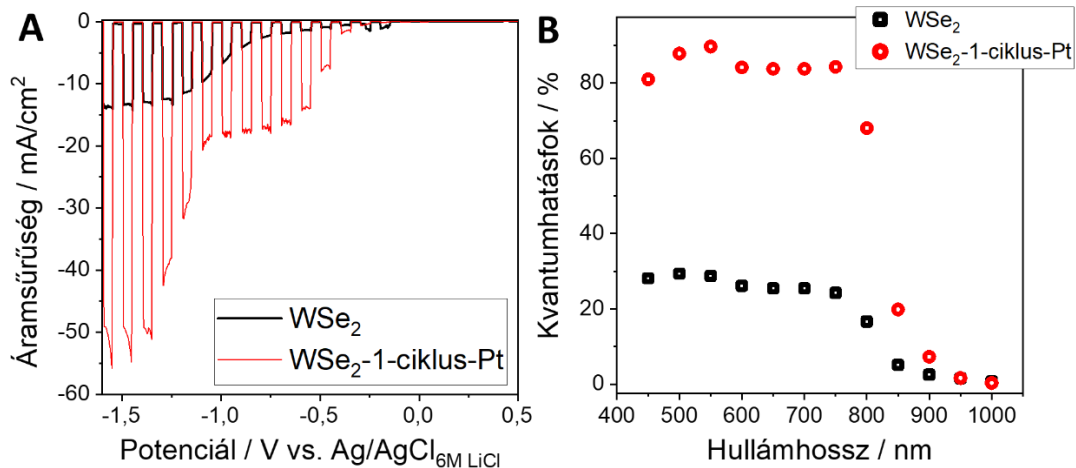
**33. ábra** Különböző PEDOT/CNT aránnyal előállított nanokompozit elektródok esetén felvett fotovoltammogramok, 0,1 mol dm<sup>-3</sup> Na<sub>2</sub>SO<sub>4</sub> oldatban. A megvilágító fényforrásként egy napfényszimulátort alkalmaztunk, melynek fényét 0.1 Hz-es frekvenciával szaggattuk, 2 mV s<sup>-1</sup> pásztázási sebesség mellett. (B) Maximális fotoáram vs. polimerizációs töltéssűrűség görbe, melyet az „A” ábra adatai alapján számítottunk.<sup>73</sup>

A 33. ábrán példaként bemutatok egy fotovoltammogram-sorozatot, melyet különböző összetételű PEDOT/CNT rétegek esetén vettünk fel. A PEDOT/CNT elektródok esetén mintegy maximum négyszeres többletet-, míg a PEDOT/grafén rétegek esetén pedig két és félszeres növekményt tapasztaltunk a sima polimerhez képest. A sima PEDOT-hoz képest jelentősen nagyobb IPCE értékeket kaptunk (33./B ábra), és az értékek sorrendje követte a fotovoltammetriánál

tapasztaltakat. A görbék lefutása hasonló volt, és a fényelnyelési tartomány nem szélesedett ki, mind a három rendszer esetén azonos tiltottsáv-szélesség értékeket tudtunk meghatározni (1,7 eV). A megnövekedett fotoelektrokémiai aktivitás okát tehát nem a fényelnyelés növekedésében, hanem a vezetési sajátságok megváltozásában kell keresni. A fenti hipotézis további vizsgálatára elektrokémiai impedancia spektroszkópiás (EIS) méréseket végeztünk, amelyek igazolták, hogy a nanoszeneket tartalmazó nanokompozit rétegek vezetése a sima polimerhez képest jelentős mértékben megnőtt. Végezetül pedig a fotoelektrodok stabilitását hosszú távú kronoamperometriás-, míg a keletkező termékek minőségét GC–BID és GC–MS technikákkal vizsgáltuk. A nanoszen tartalmú elektródok esetén a stacionárius fotoáram értéke kb. kétszeres volt a sima polimerhez képest. Hidrogéngázt azonosítottunk egyedüli terméként (közel 100%-os Faraday-hatásfok).<sup>73</sup>

### VI. 3. Nanofém/félvezető elektródok

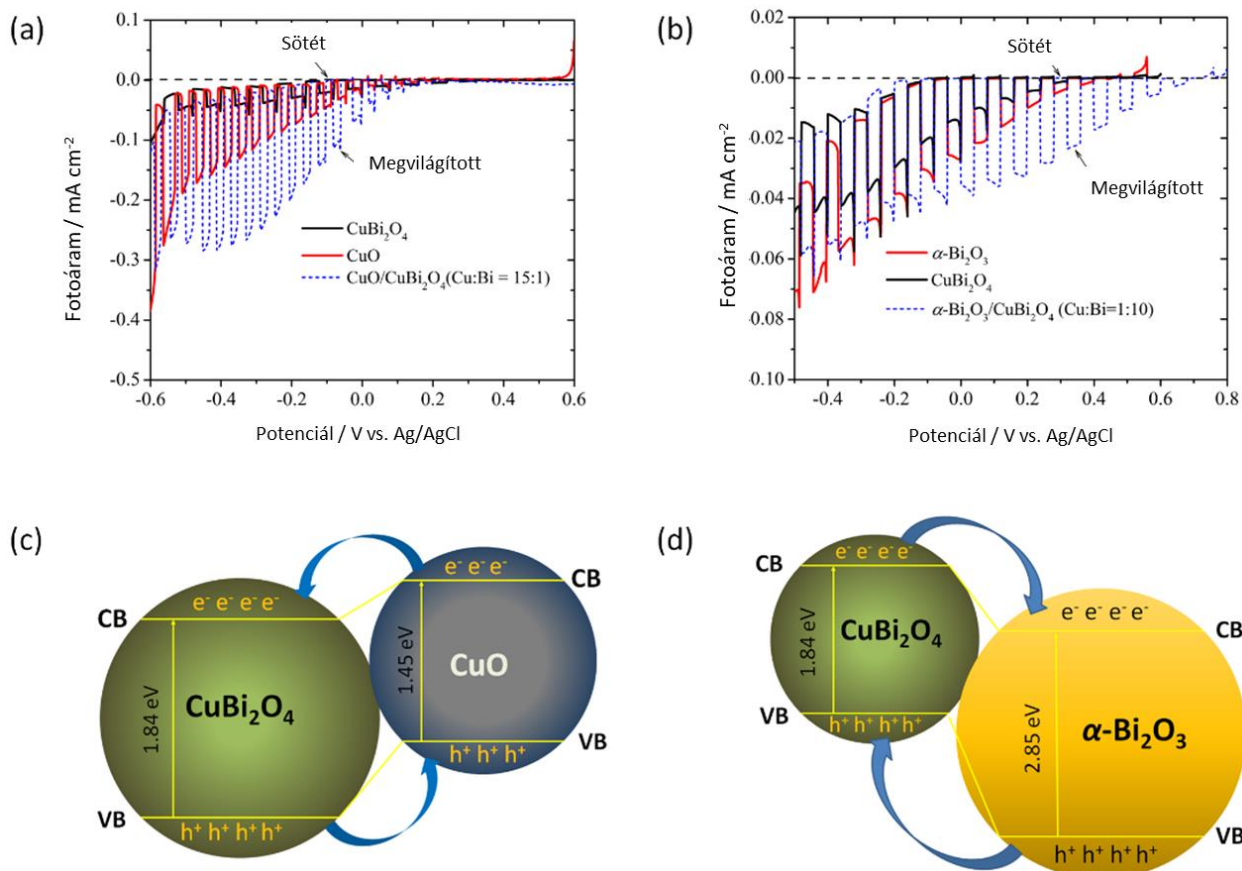
A különböző fém nanorészecskék félvezető fotoelektrodokra való felvitele jellemzően a katalitikus aktivitás növelését célozza. Itt egy példát említek, amelyben a fotoelektrokémiai hidrogénfejlődési reakciót vizsgáltuk Pt nanorészecskékkel dekorált p-WSe<sub>2</sub> nanolapokon, a korábban bemutatott fotoelektrokémiai mikroszkópiás módszerrel. A WSe<sub>2</sub> nanolapok vastagságát atomi erőmikroszkóppal meghatároztuk, a Pt nanorészecskék mennyiségét pedig az alkalmazott ALD ciklusok számával szabályoztuk. Ezekben a Pt/WSe<sub>2</sub> fotokatódokon kivételesen nagy, 49,6 mA cm<sup>-2</sup> fotoáram-sűrűséget (220 mW cm<sup>-2</sup> besugárzási teljesítmény mellett) és IPCE értékeket mértünk (~90% 550 nm-en).<sup>84</sup> Érdekes módon, az IMPS mérések hasonló töltésátviteli és felületi rekombinációs kinetikát mutattak az üres és Pt-dekorált WSe<sub>2</sub> minták esetében, ami azt jelezte, hogy a felületi tulajdonságok önmagában nem magyarázzák a 34. ábrán látott különbségeket, a tömbfázis tulajdonságaiban is van különbség. Röntgen- és ultrabolya fotoelektron-spektroszkópiás módszerekkel jellemeztük az optoelektronikai tulajdonságokat, és azt tapasztaltuk, hogy az ALD folyamat magas hőmérséklete és az *in situ* kialakuló Pt nanorészecskék *együttes jelenléte* segít a hibahelyek passzíválásában, ami jelentősen javította a Pt/WSe<sub>2</sub> elektródok fotoelektrokémiai viselkedését.



**34. ábra** Pt/WSe<sub>2</sub> és WSe<sub>2</sub> fotoelektrokémiai viselkedésének összehasonlítása. A: fotovoltammogramok és B: IPCE görbék 1 M HCl/6 M LiCl oldatban, a fotovoltammogramok esetén a pásztázási sebesség 5 mV s<sup>-1</sup> volt, az IPCE görbéket pedig -1,5 V-on rögzítettük (vs. Ag/AgCl).<sup>84</sup>

## VI. 4. Szervetlen/szervetlen félvezető elektródok

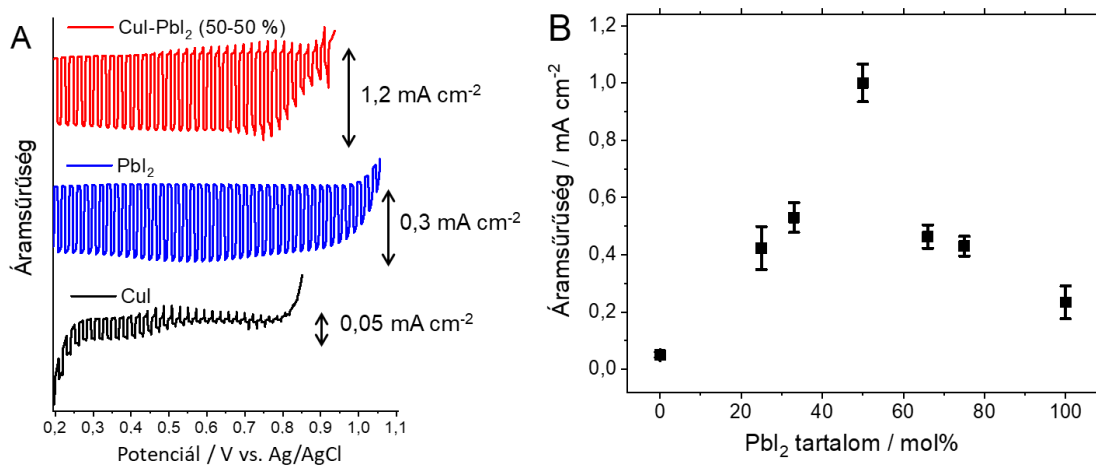
Az összetett oxid félvezetők mellett a különböző oxidok együttes jelenléte is eredményezhet aktív fotoelektrodokat. Az itt bemutatott példában  $\text{CuBi}_2\text{O}_4$ ,  $\text{CuO}$ , és  $\text{Bi}_2\text{O}_3$  oxidokból felépülő fotokatódok viselkedését mutatom be. Igazoltuk, hogy oldatbelobbantásos szintézissel (SCS) nemcsak fázisztiszta  $\text{CuBi}_2\text{O}_4$  állítható elő, hanem annak  $\text{CuO}$ -al vagy  $\text{Bi}_2\text{O}_3$ -al alkotott nanokompozitja is. Ezen oxidok sávszerkezetét és fotoaktivitását lineáris fotovoltammetriával és IPCE görbék felvételével vizsgáltuk.<sup>53</sup> A fotoaktivitás (amely a hidrogénfejlődésnek és a  $\text{CO}_2$  redukciónak tulajdonítható) jelentősen javult a  $\text{CuO}/\text{CuBi}_2\text{O}_4$  nanokompozitokban a  $\text{CuBi}_2\text{O}_4$ -hoz képest, a fotogenerált töltéshordozók  $\text{CuBi}_2\text{O}_4$  és a  $\text{CuO}$  nanorészecskék közötti transzportjának köszönhetően (35. ábra).



**35. ábra** Fotovoltammetriás görbék (a)  $\text{CuBi}_2\text{O}_4$ ,  $\text{CuO}$ , és az optimalizált  $\text{CuO}/\text{CuBi}_2\text{O}_4$  nanokompozit esetén, valamint (b)  $\text{CuBi}_2\text{O}_4$ ,  $\alpha\text{-Bi}_2\text{O}_3$ , és az optimalizált  $\alpha\text{-Bi}_2\text{O}_3/\text{CuBi}_2\text{O}_4$  esetén. A fotovoltammogramokat 0,1 M  $\text{Na}_2\text{SO}_4$  elektrolitban,  $1 \text{ mV s}^{-1}$  potenciál pásztázási sebességgel,  $\text{N}_2$  öblítés mellett rögzítettük. A (c) és (d) ábrák sematikusan illusztrálják a töltéshordozók mozgásának irányát.<sup>53</sup>

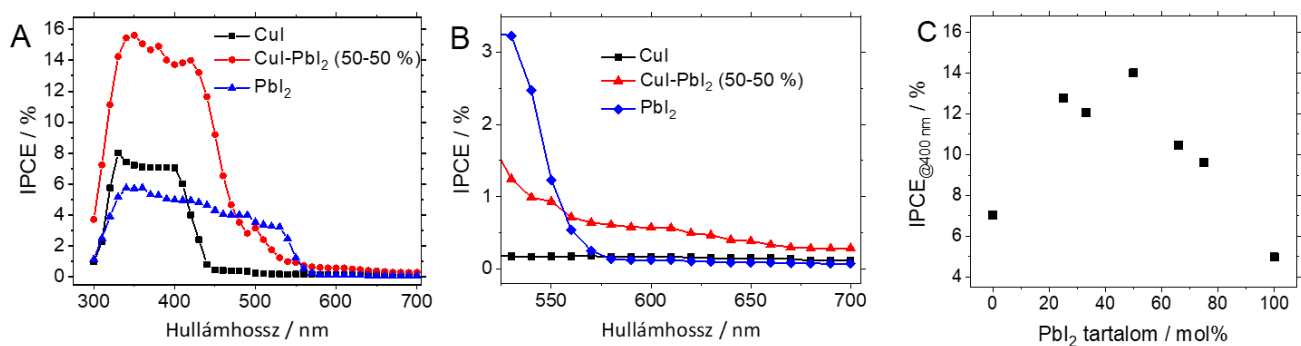
Az elmúlt öt év során robbanásszerűen megnőtt az érdeklődés a perovszkit szerkezetű anyagok iránt, köszönhetően a napelemekben rekordokat döntő hatékonyságú metilammónium-ólom-jodid perovszkitoknak.<sup>85</sup> Szakirodalmi előzmények szerint a  $\text{CuPbI}_3$  összetételű, perovszkit szerkezetű anyag egy keskeny tiltott sávval rendelkező, *p*-típusú félvezető.<sup>86</sup> Igyekeztünk előállítani ezen anyagot,  $\text{PbI}_2$  és  $\text{CuI}$  összeolvasztásával. Röntgendiffrakciós, elektrondiffrakciós, és nagyfelbontású TEM vizsgálatokkal egyértelműen igazoltuk, hogy ilyen vegyület nem keletkezik. A

megjelenő új tulajdonságok a két prekursor nanoszerkezetű ötvözetének képződéséből erednek. Igazoltuk, hogy az ötvözet fotelektrokémiai aktivitása jelentősen meghaladja az egyedi komponensekét (36/A ábra), és az optimális viselkedés 1:1 molaránynál adódott (36/B ábra).<sup>56</sup>



**36. ábra** (A) CuI, PbI<sub>2</sub>, és CuI-PbI<sub>2</sub> (50-50%) fotelektrodok fotovoltammogramjai Ar-nal öblített 0,1 M NaNO<sub>3</sub> oldatban (pásztázási sebesség 2 mV s<sup>-1</sup>, megvilágítási frekvencia: 0,2 Hz). (B) A nanokompozit minták maximális áramsűrűségének összetételfüggése.<sup>56</sup>

Megvizsgálva a szinergikus hatás eredetét, alapvetően két különböző tényezőt azonosítottunk. Az IPCE-görbén (37. ábra) látható, hogy alapvetően az PbI<sub>2</sub> elnyeléséhez kötődő fotoáramok növekedtek meg, ami a CuI ko-katalizátorként való viselkedését jelzi. Ezen túlmenően, az ötvözetben megjelenő új elnyelés (1,8 eV tiltott sáv szélesség tartozik hozzá, 37. ábra), is hozzájárul a fotoáramokhoz. Elméleti számítások azt valószínűsítik, hogy ez az elnyelés a CuI vegyértéksávjából az PbI<sub>2</sub> vezetési sávjába történő gerjesztéshez rendelhető.<sup>56</sup> Hosszú távú fotelektrolízissel igazoltuk, hogy az ötvözet fotokatód alkalmas a NO<sub>3</sub><sup>-</sup> ionok fotelektrokémiai redukciójára, miközben NO<sub>2</sub><sup>-</sup> és N<sub>2</sub> keletkezik.<sup>56</sup>



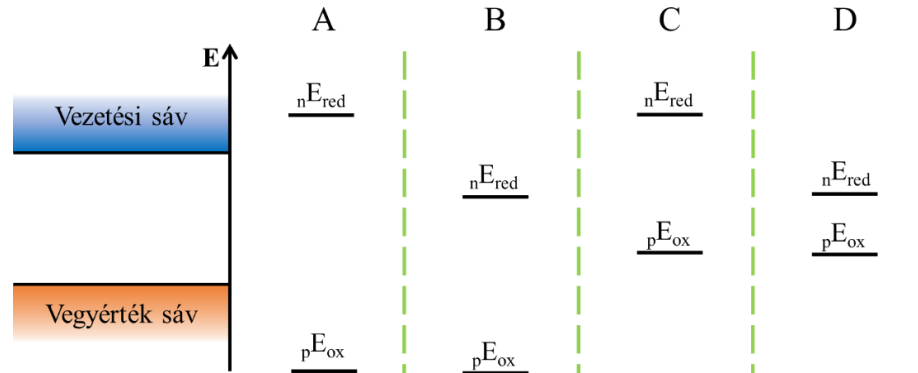
**37. ábra** (A és B): CuI, PbI<sub>2</sub>, és CuI-PbI<sub>2</sub> (50-50%) fotelektrodok IPCE görbéi, (C): CuI, PbI<sub>2</sub>, és CuI-PbI<sub>2</sub> fotelektrodok 400 nm-en rögzített IPCE-értékei. Körülmények: 0,1 M NaNO<sub>3</sub>, 0,61 V vs. RHE.<sup>56</sup>

## VII. Fotokorróziós vizsgálatok

Ahogy már a bevezetésben (4. ábra) és a réz-oxid alapú fotelektrodoknál is említettem, a fotokorróziót komoly kihívást jelent a fotelektrodok stabilitása szempontjából. A 38. ábrán bemutatott sematikus ábrán látható, hogy az anódos és katódos korróziós potenciáloknak a félvezető

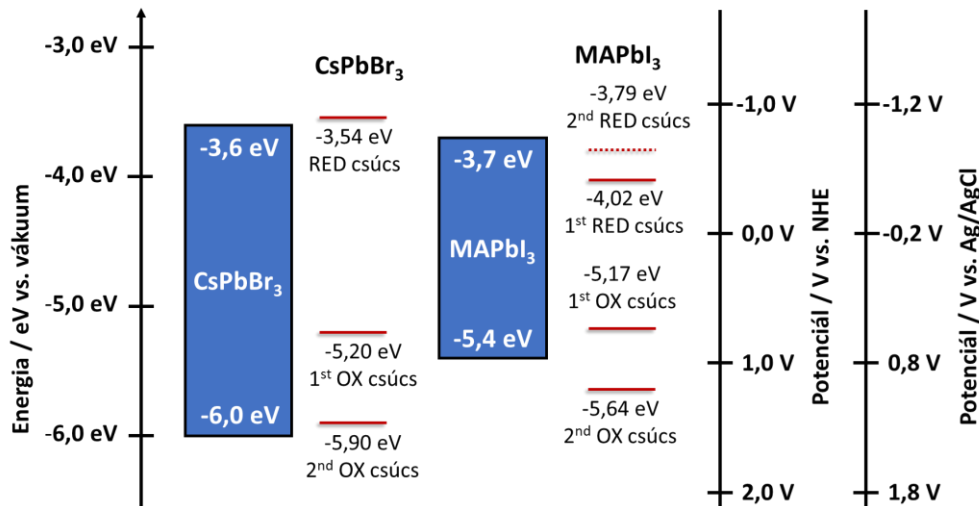


sávpozícióihoz viszonyított értéke alapvetően meghatározza, hogy milyen típusú korrózió várható. Az "A" esetben például várhatóan stabil lesz a fotoelektród, míg a "D" esetben mind katódos, mind anódos fotokorróziót várható. Meg kell jegyezni azonban, hogy ezen pozíciók alapján csak a fotokorrózió termodinamikai lehetőségére kapunk információt, a valóságban a folyamat kinetikája fogja megszabni, hogy a vizsgált félvezető mennyire lesz stabil az adott körülmények között.



38. ábra Egy félvezető sávpozícióinak és a lehetséges korróziós folyamatok potenciáljának ábrázolása.

Ez a kérdéskör további figyelmet kapott azzal, hogy a fém-halogenid perovszkitok az elmúlt évtizedben a kutatást-fejlesztés homlokterébe kerültek. A közelmúltban a fotokatalitikus és fotoelektrokémiai eljárásokban is megvették a lábukat,<sup>87</sup> de a leggyakrabban alkalmazott oldószerekkel és elektrolitokkal szembeni érzékenységük, valamint fotokorróziós tulajdonságaik akadályozzák az ilyen alkalmazásokat. *In situ* és *operando* elektrokémiai technikákat használtunk fel a fotokorrózió elemi lépéseinek vizsgálata érdekében, és tanulmányoztuk a fotokorrózió mérséklésére szolgáló stratégiákat is (pl. felületvédelem és elektrolitok tervezése).<sup>16</sup> Két perovszkit esetében meghatároztuk a 38. ábrán sematikusán illusztrált energiaszinteket (39. ábra).<sup>61</sup>



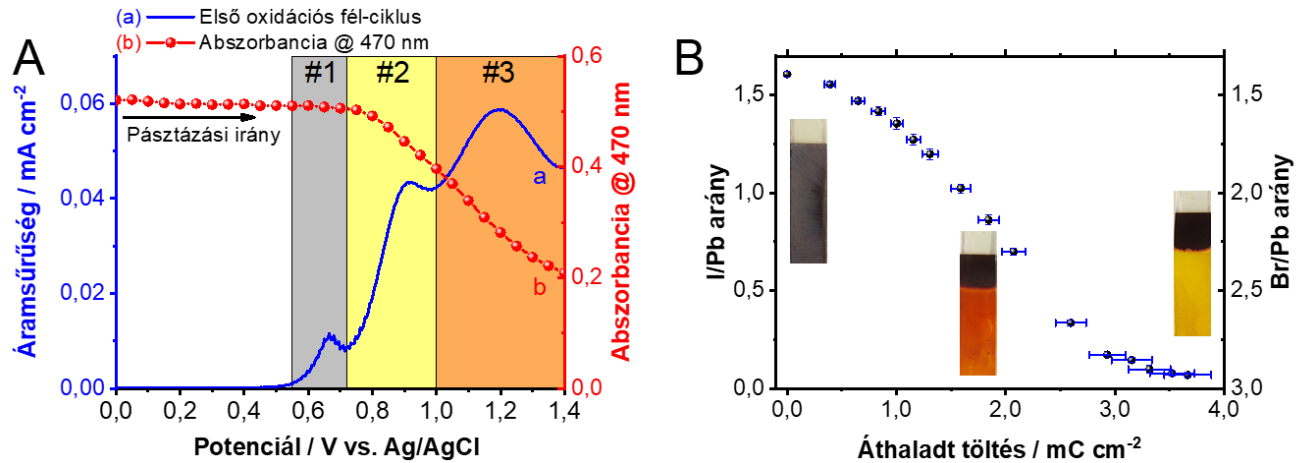
39. ábra A CsPbBr<sub>3</sub> és a MAPbI<sub>3</sub> sávpozícióinak, és a korróziós folyamatok potenciáljának ábrázolása.<sup>61</sup>

A egyes fémhalogenid-perovszkitokban (pl. CH<sub>3</sub>NH<sub>3</sub>PbBr<sub>1,5</sub>I<sub>1,5</sub>) megvilágítás hatására fellépő fázisszegregáció a korrózió egy speciális fajtája.<sup>88</sup> Azáltal, hogy a fotokorrózió mechanizmusának felderítése érdekében elektrokémiai úton oxidáltuk a rétegeket, szelektíven tudtunk lyukakat juttatni az elektródra (szemben a megvilágítással, ahol egyforma mennyiségben képződnek elektronok és lyukak). A 40./A ábrán az 1. és 2. régió a hibahelyeken való lyukcsapdázódáshoz és a vegyértéksávba

való lyuk injektáláshoz kapcsolódik. Azt tapasztaltuk, hogy a rácsban csapdázódó lyukak hatására a jodid ionok fokozatosan kiürülnek a vegyes halogenid filmből (jód és/vagy trijodid ionként), és  $\text{CH}_3\text{NH}_3\text{PbBr}_3$  domének maradnak vissza (40./B ábra).

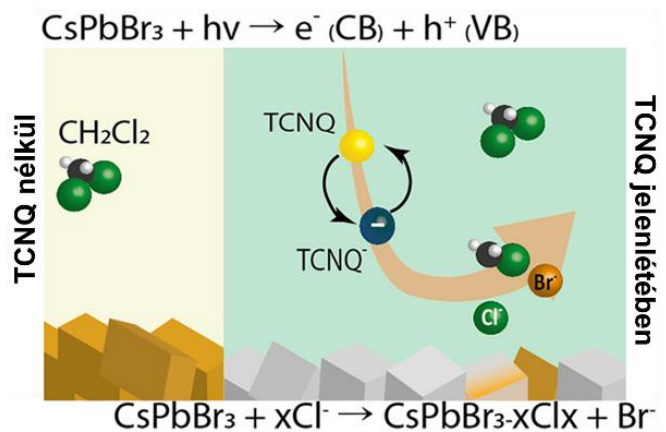


A tranziens abszorpciós spektroszkópiával megmutattuk, hogy a jodid ionok eltávozása egy hibahelyekben gazdag perovszkit rácsot hagy maga után, és újra képződő rácsban a töltéshordozó rekombinációja jelentősen felgyorsul.<sup>89</sup> Igazoltuk, hogy a kationoknak is szerepük van a halogenid ionok mobilitásában: a metil-ammónium ionokat  $\text{Cs}^+$ -ra cserélve a stabilitás megnövekszik.<sup>90</sup>



**40. ábra** Az FTO/MAPbBr<sub>1,5</sub>I<sub>1,5</sub> film lineáris voltammogramja a 470 nm-en mért abszorbanca-változással együtt. B: Az FTO/MAPbBr<sub>1,5</sub>I<sub>1,5</sub> film összetételének változása az áthaladt töltés függvényében a potenciosztatikus mérés során ( $E = 0,9 \text{ V vs. Ag/AgCl}$ ).<sup>89</sup>

Egy további érdekes korróziós jelenséget a  $\text{CsPbBr}_3$  fotelektrodok kapcsán tártunk fel.<sup>60</sup> Megállapítottuk, hogy egy gyakran alkalmazott elektronfogónak (áldozati reagensnek), a TCNQ-nak kettős szerepe van: miközben gyors elektrontranszfert eredményez az elektródról a TCNQ-ra, javítva a fotelektrokémiai viselkedést, közben felgyorsítja a  $\text{CsPbBr}_3$  fotelektrod degradációját is. A filmek fotelektrokémiai instabilitását a TCNQ által mediált halogenidcsere okozza a diklór-metán oldószer és az  $\text{CsPbBr}_3$  film között (41. ábra). *In situ* spektroelektrokémiai és *ex situ* felületjellemzési módszerek alapján töltésátviteli és halogenidcsere-utakat javasoltunk, amelyek útmutatást adnak az ilyen rendszerekkel végzett fotelektrokémiai kísérletek tervezéséhez is.<sup>60</sup>



**41. ábra** A TCNQ-által mediált  $\text{CsPbBr}_3$  korrózió sematikus bemutatása.

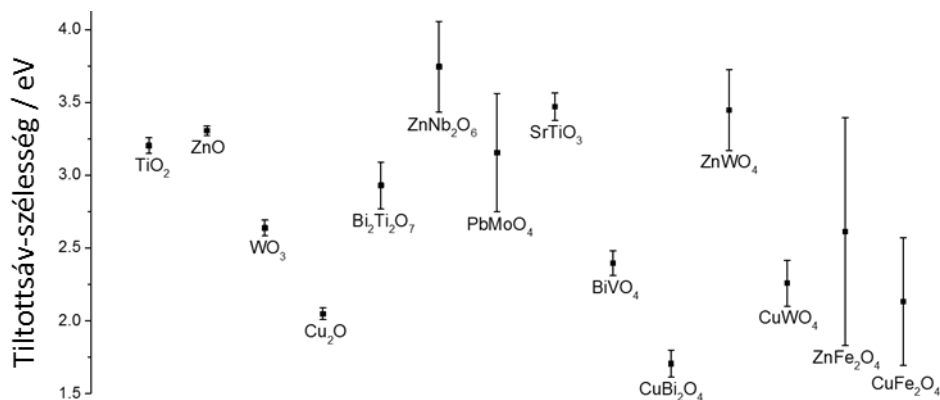
### VIII. Tüzelőanyagok előállítása fotelektrokémiai módszerekkel

A korábban bemutatott szintézismódszerek, fotelektrokémiai, és fotokorróziós vizsgálatok azt a célt szolgálták, hogy olyan fotelektrodákat állítsunk elő, amelyek sikerrel alkalmazhatók energiakonverziós fotelektrokémiai folyamatokban,<sup>91</sup> különösen a CO<sub>2</sub> redukációjában. Ebben a fejezetben arra mutatok példákat, hogy miként lehet ezen tapasztalatokat kihasználni a fotelektrokémiai teljesítmény javítása céljából.

#### VIII. 1. A fényelnyelési tartomány növelése

Az összetett, többfémű oxidok esetében sokszor megfigyelhető, hogy a tiltottsáv-szélességük kisebb, mint az alkotó egyfémű oxidoké.<sup>55,92</sup> Ez döntően az új kristályszerkezet kialakulásához, valamint a vegyérték és vezetési sávot alkotó elektronpályák különbözőségéhez köthető. Ugyanakkor több példán keresztül bemutattuk azt is, hogy a szélesebb tartományon való fényelnyelés nem feltétlenül eredményez jobb fotelektrokémiai tulajdonságokat.<sup>93</sup> Különösen igaz ez azokban az esetekben, ahol az új elnyelés valamiféle hibahelyhez kötődik, ami rekombinációs centrumként funkcionálhat.<sup>94</sup>

Az elmúlt évek munkájának egyik érdekes megfigyelése az volt, hogy sok esetben jelentős eltéréseket tapasztaltunk a tiltottsáv-szélesség nagyságában a szakirodalmi adatokhoz képest. Kíváncsiak voltunk, hogy ennek mi lehet az oka, így elvégeztünk egy alapos szakirodalmi felmérést az oxid félvezetők egy csoportján.<sup>92</sup> Tizennégy tetszőlegesen kiválasztott oxid esetében vizsgáltuk meg a tiltottsáv-szélesség értékét. Minden esetben 10 db, véletlenszerűen kiválasztott közleményt használtunk fel, a feltétel csak az volt, hogy kísérleti módszerrel meghatározott értékek kell lennie, és tudatosan ne legyenek adalékolva (dópolva) a minták. Az eredmény meglepő volt (42. ábra): egyfémű oxidok esetében viszonylag kis szórása volt az értékeknek, addig a kétfémű oxidok esetén többször is nagyon nagy szórással találkoztunk. Alaposan átnézve ezen közleményeket, számos tényezőt azonosítottunk, amely hozzájárul ehhez a jelenséghez. A legfontosabb az volt, hogy nagyon ritkán fordult elő fázisztiszta anyag, és általában a legkisebb tiltottsáv-szélességű komponensre jellemző értéket közölték (ami sokszor valamelyik egyfémű oxid). Szintén jellemző volt a különböző mérési és kiértékelési módszerek (pl. Tauc-analízis) helytelen használata.

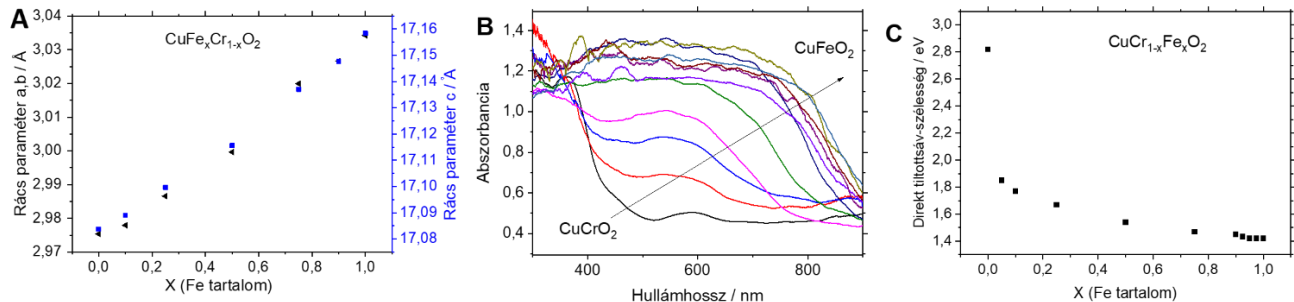


42. ábra Félvezető oxidok tiltottsáv szélessége szakirodalmi adatok alapján.<sup>92</sup>

A fényelnyelés növelésének másik módja, hogy két olyan félvezetőt kapcsolunk egymáshoz, amelyek tiltottsáv-szélessége eltérő. Annak érdekében, hogy kinyerhessük a két félvezetőben keletkező töltéshordozókat, azoknak egymáshoz viszonyított sávpozícióinak megfelelően kell

elhelyezkedniük, az elektródnak pedig megfelelő geometriával kell rendelkeznie. Így lehet vertikális elektrontranszfert elérni, ami az jelenti, hogy mind az elektronok, mind a lyukak a megfelelő irányban vándorolnak. Amennyiben ezek a feltételek nem teljesülnek, akkor jelentős rekombinációval kell számolnunk, és a megnövekedett fényelnyelés nem eredményez javulást a fotelektrokémiai tulajdonságokban.

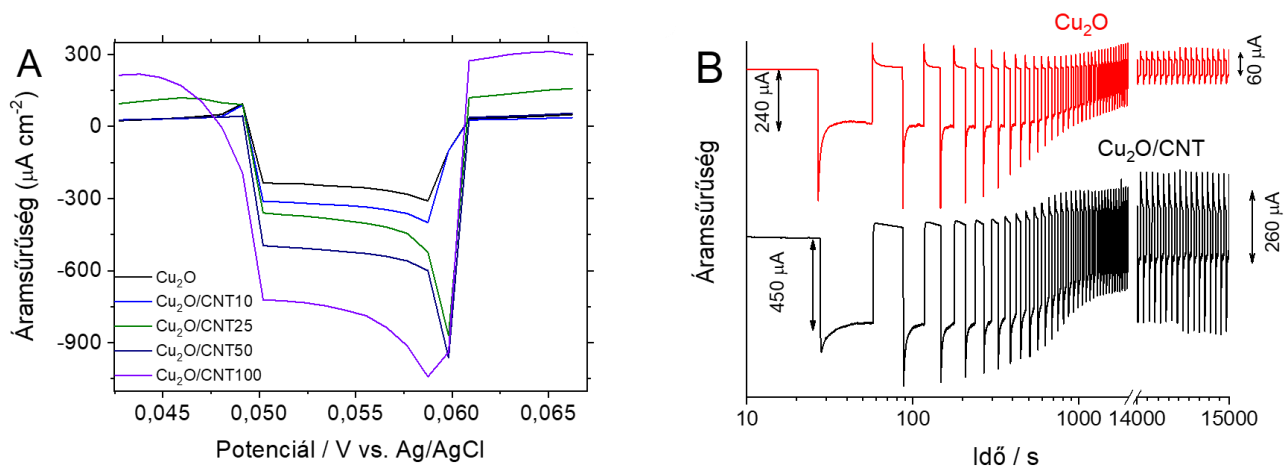
További lehetőség olyan többfémű vegyes oxidok előállítása, amelyben a fémionok egymással helyettesíthetők. A  $\text{CuFe}_x\text{Cr}_{1-x}\text{O}_2$  példáján megmutattuk, hogy a tiltottsáv szélessége a megfelelő kétfémű oxidokra jellemző értékek között hangolható.<sup>55</sup>



**43. ábra**  $\text{CuCrO}_2$ ,  $\text{CuFeO}_2$  és ötvözeteiknek (A) rácsparaméterei és (B) abszorbania-spektrumai különböző összetételnél. (C) A direkt tiltottsáv-szélesség változása az összetétel függvényében.<sup>55</sup>

### VIII. 2. A töltéshordozó transzport javítása

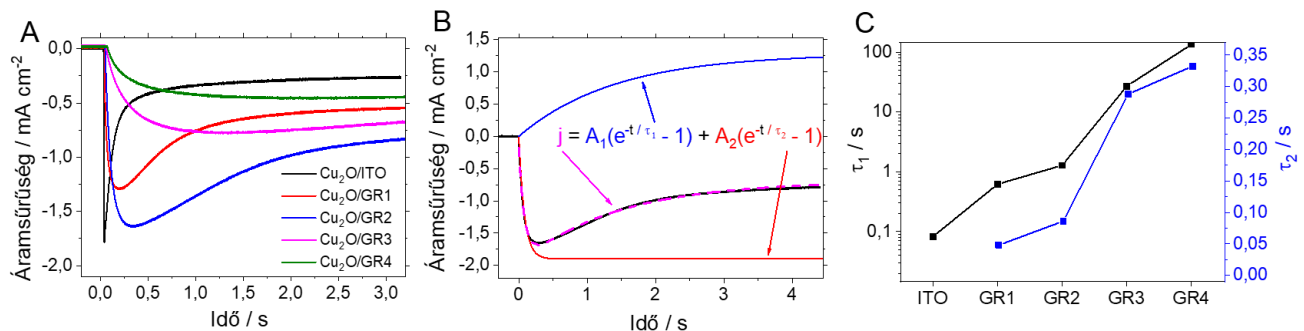
Számos tanulmányozott félvezető esetében azt tapasztaltuk, hogy a töltéshordozó mobilitás kicsi, ami jelentősen befolyásolja a maximálisan kinyerhető fotoáram nagyságát. A hátrányos sajátságok elvben kiküszöbölhetők, ha ezen félvezetőket egy jól vezető, nanoszerkezetű szubsztrátra választjuk le, amely a fotogenerált töltéshordozókat gyorsan és hatékonyan el tudja vezetni, ezáltal növelve a töltéshordozó mobilitást,<sup>70</sup> és esetlegesen javítva a kompozit anyagok fotostabilitását is. Ezt a hipotézist igazoltuk több kompozit elektród esetén, szerves és szervetlen félvezetők esetében egyaránt.<sup>70–73</sup>



**44. ábra** Különböző összetételű  $\text{Cu}_2\text{O}/\text{CNT}$  filmek fotoáram tranziensei, valamint a hosszú távú fotelektrolízis során mért kronoamperometriás görbék,  $\text{CO}_2$ -al telített 0.1 M  $\text{NaHCO}_3$  oldatban.<sup>71</sup>

Példaként megemlítem, hogy a  $\text{Cu}_2\text{O}/\text{CNT}$  vékonyrétegek jelentős fotoáramokat produkáltak  $\text{CO}_2$  redukcióban.<sup>71</sup> Összehasonlítva az eredményeket a CNT-mentes rendszerre kapottakkal, megállapítottuk, hogy a nanocsövek szerepe elsődlegesen a töltésszeparáció és a töltéshordozó-transzport elősegítése, és ezen sajátságok a kompozit összetételével hangolhatók (44./A ábra). Azt is igazoltuk, hogy a jobb töltésszeparáció képes a  $\text{Cu}_2\text{O}$  fotokorrózióját (elemi rézzé való redukcióját) lassítani (44./B ábra), így a bemutatott stratégia a stabilitásnövelés hatékony eszköze lehet.

Továbbá  $\text{Cu}_2\text{O}/\text{grafén}$  elektródokra, a fotoelektrokémiai vizsgálatok megmutatták, hogy a  $\text{Cu}_2\text{O}$  optoelektronikai tulajdonságai nem változtak, ugyanakkor a rendszer aktivitása és stabilitása növekedett.<sup>72</sup> Összehasonlító vizsgálatokat végeztünk különböző vastagságú és morfológiájú grafén hordozókkal, és feltártuk, hogy a különböző nanoszén hordozók elsődleges szerepe a nagy fajlagos felület biztosítása. Gyors fototranziens mérésekkel fél-quantitatívan is jellemezni tudtuk a felületi rekombináció folyamatát (45. ábra). Miután a fajlagos felület hatását kiszűrtük, megállapítottuk, hogy a 3D grafén struktúrát tartalmazó fotoelektródok viselkednek a legjobban, mivel azokban nem található szén–szén határfelület.

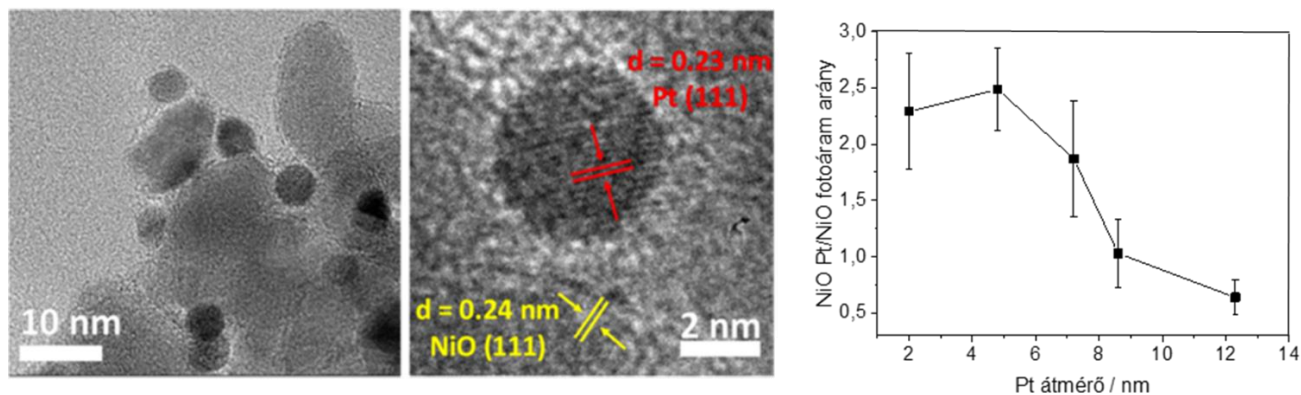


**45. ábra** Gyors fototranziens mérések a különböző összetételű  $\text{Cu}_2\text{O}/\text{grafén}$  elektródok esetén. A B és C ábrák az illetékt exponenciális függvényeket és a meghatározott időállandókat mutatják.<sup>72</sup>

### VIII. 3. A katalízis elősegítése

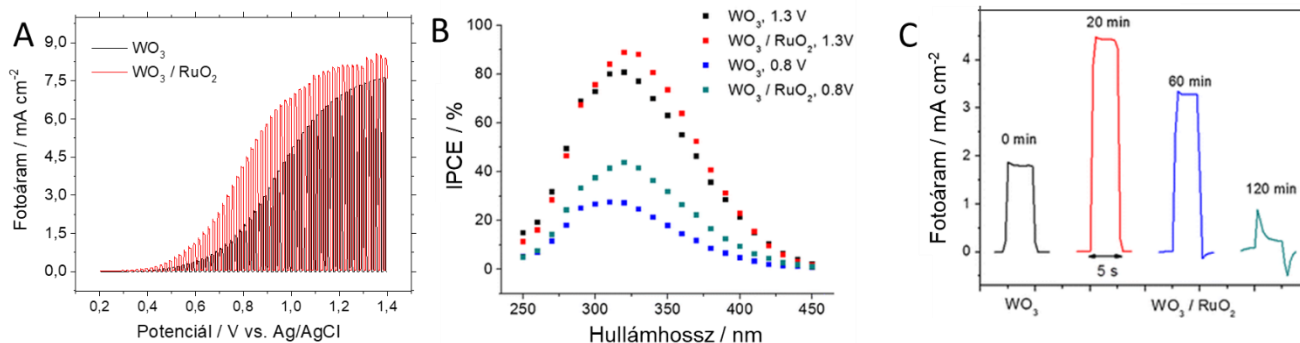
A félvezető fotoelektród felületét elérő kisebbségi töltéshordozók (fotokatódok esetében elektronok) ideális esetben redukálják az oldott  $\text{CO}_2$ -ot. Ezzel az elektrontranszferrel versengő folyamat a töltéshordozók rekombinációja, amely a felületi hibahelyeken nagy valószínűséggel végbe mehet. Ennek az elkerülésére, valamint a reakció szelektív tétel érdekében, a félvezető felületére segédkatalizátor (ko-katalizátor) rögzíthető. Ilyen irányú munkánkból két példát emelnék ki.

Elektrokémiai anodizációval állítottunk elő nanopórusos NiO rétegeket, és vittünk fel rá Pt ko-katalizátorokat 1,5–12,0 nm-es mérettartományban, öt különböző méretben (46. ábra). Az ilyen összetett modellrendszereken azt vizsgáltuk, hogy a ko-katalizátor mérete miként befolyásolja a katalitikus aktivitást fotoelektrokémiai redukciós folyamatokban ( $\text{H}_2$  fejlesztés,  $\text{CO}_2$  redukció). A felderített szerkezet–hatás összefüggések alapján optimalizáltuk a fotoelektródok teljesítményét és vizsgáltuk a hosszú távú fotoelektrolízis hatásfokát. Megállapítottuk, hogy milyen feltételeknek kell megfelelnie egy ilyen kompozit fotoelektródnak. A legfontosabb tanulság az volt, hogy a ko-katalizátor méretének kompatibilisnek kell lennie a félvezető pórusszerkezetével, és esetünkben a 4–5 nm-es részecskék bizonyultak optimálisnak.<sup>95</sup> Ebben az esetben a tiszta NiO-hoz képest 2,5-szer nagyobb fotoáramokat mértünk.



**46. ábra** Pt/NiO nanokompozit elektród TEM felvételei, és a maximálisan mérhető fotoáramok különböző méretű Pt részecskék esetében.<sup>95</sup>

A 26. ábrán bemutatott, különböző morfológiájú  $\text{WO}_3$  fotoanódokon  $\text{RuO}_2$  elektrokatalizátort rögzítettünk, amely lényegesen megnövelte a mért anódos fotoáramokat. A katalitikus hatás az áram megindulási potenciáljának elcsúszásában is megnyilvánult a fotovoltammogramon (47./A ábra). A fotoelektrod összetételének optimalizálása révén az IPCE érték megduplázódott kis potenciáloknál a hatékony felületi töltésátvitelnek köszönhetően, és az elméleti 100%-os határ közelébe emelkedett nagyobb pozitív potenciálértékeknél (47./B ábra). Vizsgáltuk továbbá a  $\text{RuO}_2$  ko-katalizátor mennyiségének a szerepét különböző  $\text{RuO}_2$  borítottaságú hibrid fotoelektrodok előállításával (47./C ábra). Azt tapasztaltuk, hogy már a legrövidebb leválasztási idővel (20 perc) elértük a szükséges felületi mennyiséget. A leválasztási idő további növelésével a fotoáramok csökkenését figyeltük meg, valószínűleg az egyre nagyobb mennyiségben felvitt  $\text{RuO}_2$  árnyékoló hatása miatt.<sup>41</sup>

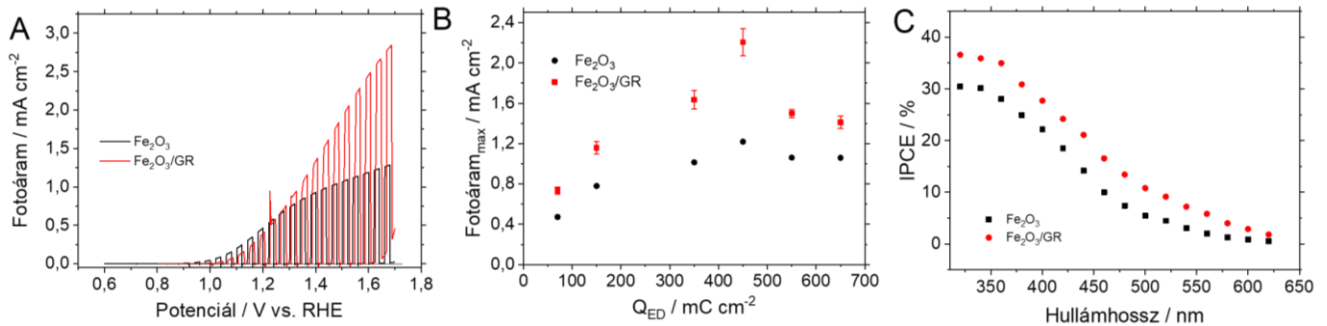


**47. ábra** (A):  $\text{WO}_3$  és a  $\text{WO}_3/\text{RuO}_2$  elektródok reprezentatív fotovoltammogramjai (0,5 M  $\text{H}_2\text{SO}_4$ , 2 mV s<sup>-1</sup> sebesség, 150 W-os Xe lámpa). (B): IPCE értékek, a  $\text{WO}_3$  és  $\text{WO}_3/\text{RuO}_2$  fotoelektrodok esetében (C): Fotoáram tranziensek összehasonlítása  $E = 0,8 \text{ V}$  potenciálon különböző összetételű kompozitok esetében. Minden tranziens 5 másodpercig tartott.<sup>41</sup>

#### VIII. 4. Háromkomponensű rendszerek

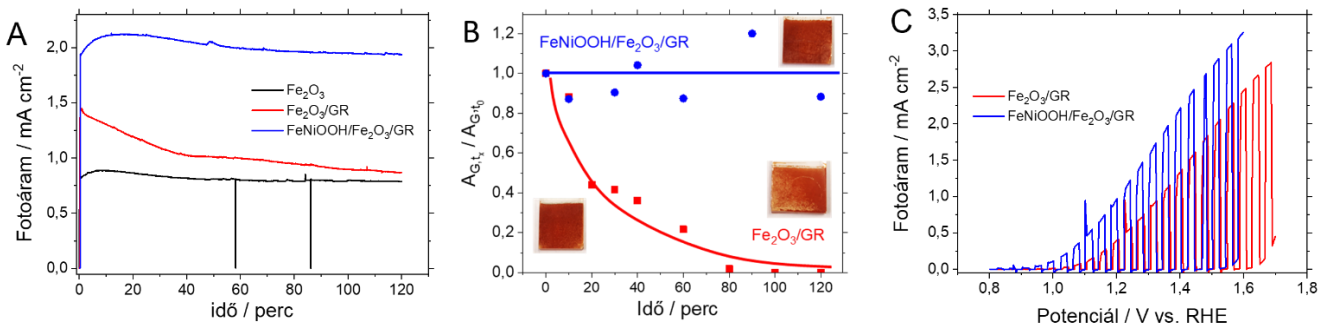
Az előző pontokban bemutatott stratégiák kombinálhatók is. Ezt a  $\text{FeNiOOH}/\text{Fe}_2\text{O}_3/\text{grafén}$  nanohibrid elektródok példáján vizsgáltuk. Ebben a bioinspirált rendszerben minden komponensnek megvolt a maga funkciója: a  $\text{Fe}_2\text{O}_3$  felelős a fényelnyelésért, a grafén váz a megfelelő töltéshordozó-szállításért, míg a  $\text{FeNiOOH}$  réteg a hatékony víz oxidációért (katalízisért). Szabályozott összetétellel és szerkezettel rendelkező hibrid elektródokat állítottunk elő, és a fotoelektrokémiai viselkedést lineáris

fotovoltammetriával (48./A és B ábra), IPCE görbék mérésével (48./C ábra), és hosszútávú fotelektrolízissel vizsgáltuk (49. B és C ábra). 2,6-szor nagyobb fotoáramot kaptunk a legjobban teljesítő FeNiOOH/Fe<sub>2</sub>O<sub>3</sub>/grafén rendszerben, a tiszta Fe<sub>2</sub>O<sub>3</sub>-hoz képest. A tranziens abszorpciós spektroszkópiai mérések megnövelt lyuk-élettartamot mutattak a Fe<sub>2</sub>O<sub>3</sub>/grafén minták esetében.<sup>47</sup>



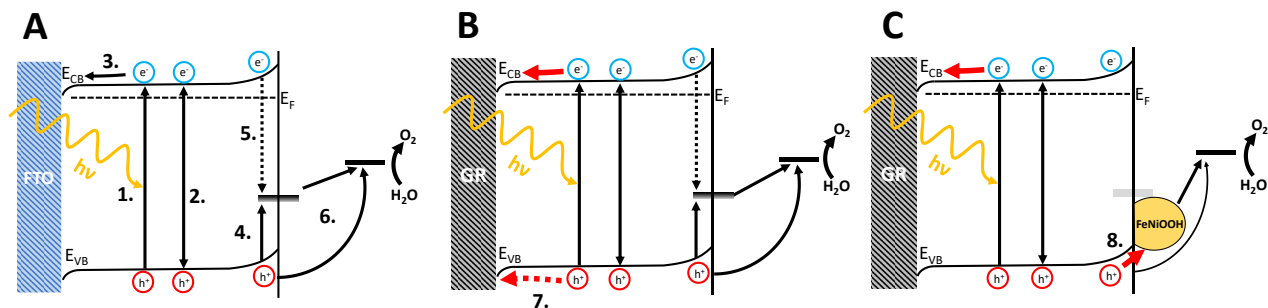
**48. ábra** (A) Fe<sub>2</sub>O<sub>3</sub> és Fe<sub>2</sub>O<sub>3</sub>/GR elektródok esetében rögzített fotovoltammogramok (1 M NaOH, 100 W cm<sup>-2</sup> szimulált napfény). (B) Különböző mennyiségű hematit leválasztásával előállított Fe<sub>2</sub>O<sub>3</sub>/GR elektródok esetében mért maximális fotoáramok. (C) Fe<sub>2</sub>O<sub>3</sub> és Fe<sub>2</sub>O<sub>3</sub>/GR fotelektrodok IPCE görbéi (1,5 V vs. RHE).<sup>47</sup>

A hosszútávú fotelektrolízisek során *in situ* Raman spektroszkópiával igazoltuk, hogy a fotogenerált lyukak oxidálni (korrodálni) tudják a grafén vázat. A felületi FeNiOOH réteg ezen a problémán is segít, mivel gyorsan átveszi a Fe<sub>2</sub>O<sub>3</sub>-ból származó fotogenerált lyukakat, ezzel csökkentve a grafén korrózióját (49. ábra). Ezen túl, a felületi réteg katalitikus aktivitása a kisebb onset potenciálban, és nagyobb fotoáramokban is megnyilvánult (49./C ábra).



**49. ábra** (A) Hosszú távú kronoamperometriás mérések ( $E = 1,45$  V vs. RHE potenciálon), a függőleges vonalak a megvilágítás megszakításakor való áram esést mutatják. (B) A grafén G sávjának normalizált intenzitásának időbeli változása. (C) Fe<sub>2</sub>O<sub>3</sub>/GR és FeNiOOH/Fe<sub>2</sub>O<sub>3</sub>/GR elektródok fotovoltammogramjai. Minden esetben 1 M NaOH-oldat Ar-al öblítve, és 100 mW cm<sup>-2</sup> AM 1,5-es szimulált napfény alkalmazásával.<sup>47</sup>

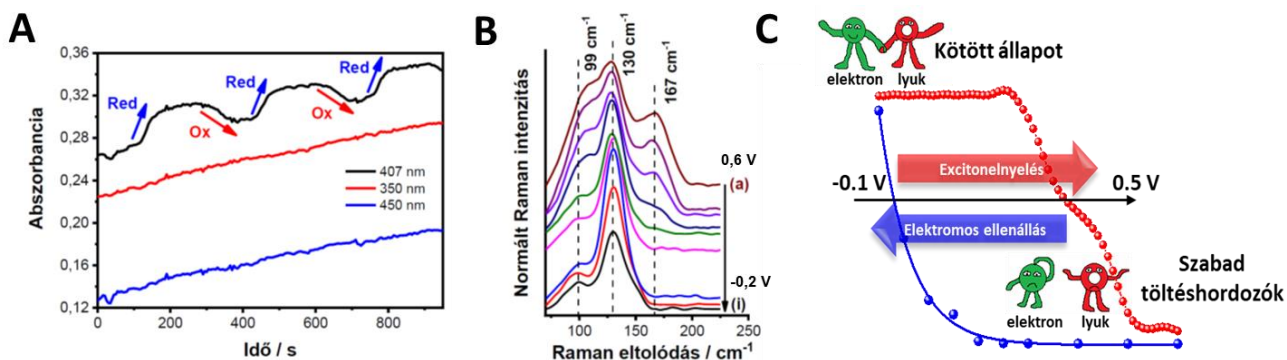
Az 50. ábrán a különböző vizsgált fotelektrodok esetén lezajló elemi folyamatok egyszerűsített modelljeit mutatom be. Ezen elemi folyamatok: 1.) foton abszorpciója és elektron-lyuk pár generálása, 2.) elektron-lyuk pár nem-radiatív rekombinációja, 3.) elektrontranszport a kontaktus felé, 4.) lyukak csapdázódása a felületi hibahelyeken 5.) elektron-lyuk rekombináció felületi hibahelyeken, 6.) lyuktranszfer a vegyértéksávból és a hibahelyekről az elektrolitba, 7.) lyuktranszport a grafénváz felé és 8.) lyuktranszfer az elektrolitba, vagy a FeNiOOH ko-katalizátor rétegre.



50. ábra (A)  $\text{Fe}_2\text{O}_3$ , (B)  $\text{Fe}_2\text{O}_3/\text{GR}$  és (C)  $\text{FeNiOOH}/\text{Fe}_2\text{O}_3/\text{GR}$  fotelektrodok esetében lezajló elemi folyamatok egyszerűsített modelljei.

## IX. *In situ* mérés technikák

A különböző *in situ* elektrokémiai mérések során célunk volt egyrészt az oldatban levő közttermékek és termékek azonosítása, másrészt az elektród anyagában való változások nyomonkövetése. A UV-látható spektroeletrokémiai módszerrel viszonylag egyszerű elektrokémiai cellákban vizsgálhatjuk mind az elektród, mind az elektrolit oldat spektrumának változását az elektródpotenciál változtatásának függvényében. Sokszor azonban figyelmen kívül marad, hogy ezen technika nem korlátozódik a Faraday folyamatokra, segítségével a hibahelyek kimutatására is lehetőség van.<sup>96,97</sup> Ezen energiaszintek különböző töltéshordozókkal történő szelektív betöltése ugyanis könnyen megvalósítható a potenciál változtatásával, a spektrális változások párhuzamos követése pedig lehetőséget biztosít ezen nivók energetikai elhelyezkedésének meghatározására.<sup>97,98</sup>



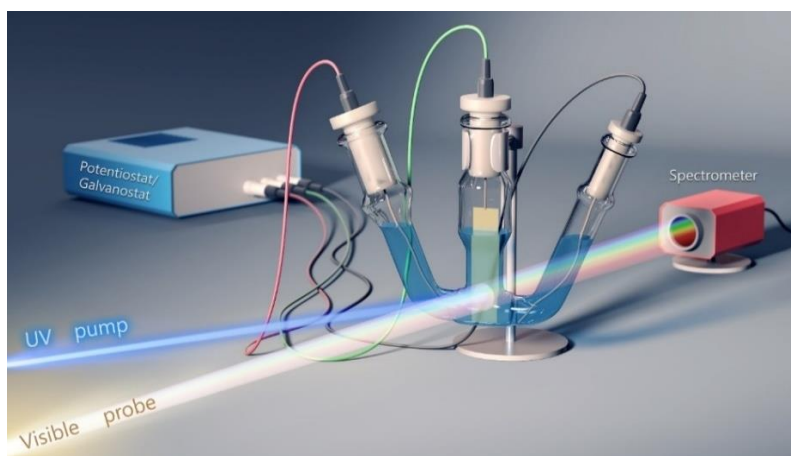
51. ábra  $\text{CuI}$  fotelektrodok (A) UV-látható spektroeletrokémiai görbéi, (B) Raman spektrumai, különböző potenciálértékeken. (C) Az elektródpotenciál fényelnyelésre és elektromos ellenállásra gyakorolt hatásának sematikus ábrázolása.<sup>58</sup>

A  $\text{CuI}$ -ről már többször esett szó az értekezésben, amely nem meglepő, mivel optoelektronikai tulajdonságai a lyukvezető anyagként való felhasználásán túl, alkalmassá teszik rugalmas és átlátszó  $p$ - $n$  diódák, illetve vékonyfilm tranzisztorok gyártására, valamint fotelektrokémiai  $\text{CO}_2$  redukció végrehajtására egyaránt. Spektroeletrokémiai vizsgálataink során azt tapasztaltuk, hogy a  $\text{CuI}$  abszorbanca-spektrumán egy éles csúcs jelenik meg (407 nm maximumnál), mely az anyagban lévő excitonok fényelnyeléséhez köthető. Ezen csúcs nagysága az elektródpotenciál szabályozásával reverzibilisen változtatható (51. ábra). A negatív potenciáltartományban az excitonok koncentrációja, illetve az azokhoz köthető elnyelés megnő. Ennek magyarázata, hogy a vegyértéksáv közelében elhelyezkedő, eredetileg lyukakat tartalmazó hibahelyek a potenciál negatív irányú változtatásával



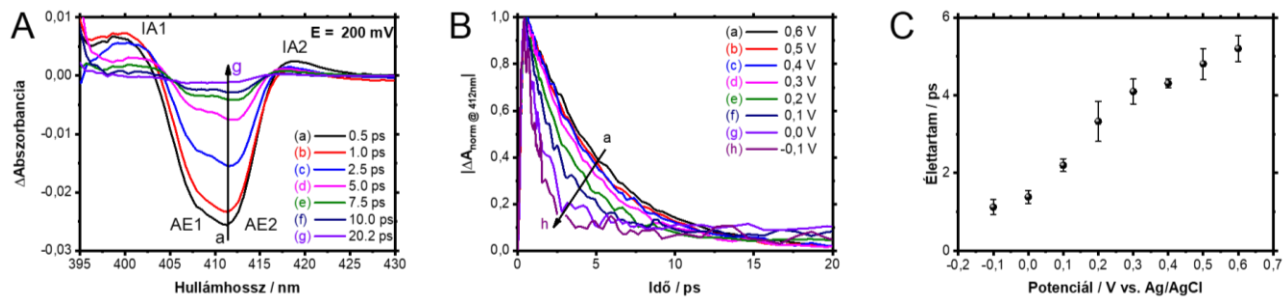
betölthetők elektronokkal, melynek következtében nagyobb valószínűséggel alakulhatnak ki excitonok. Ez a folyamat megfordítható a potenciál ellentétes, azaz pozitív irányú változtatásával, mely a hibahelyek kiürülését, ennek eredményeképpen pedig a fényelnyelés csökkenését vonja maga után. Az *in situ* Raman spektroelektrokémiai vizsgálatok rámutattak arra, hogy pozitívabb potenciálokon a hibahelyek kiürítése egy rendezetlenebb szerkezetet eredményez, amely két rezgési sáv hangsúlyosabbá válásában nyilvánul meg. EIS vizsgálatokkal azt is megmutattuk, hogy a CuI-ban lévő hibahelyek elektronokkal történő reverzibilis betöltése és kiürítése a felelős az elektromos tulajdonságok változásaiért. Az optikai és elektromos tulajdonságok változásai azonban más potenciáltartományon mennek végbe. A tiltotsáv mélyebb részein fekvő hibahelyek felelősek az elektromos tulajdonságok alakulásáért, míg a vegyértéksávhoz közelebb elhelyezkedő hibahelyek optikai változásokért.<sup>58</sup>

Az ultragyors tranzien spektroelektrokémia segítségével a fotolumineszcenciához hasonlóan a gerjesztett töltéshordozók élettartama vizsgálható, azonban itt nem feltétel az, hogy a rekombináció fényemisszióval járjon.<sup>99</sup> Az ultragyors tranzien spektroelektrokémia módszerével az is tanulmányozható, hogy pontosan mi történik a létrehozott töltéshordozókkal a megvilágítást követően. Perovszkitok vizsgálatában elsőként alkalmaztunk ultragyors tranzien abszorpciós spektroszkópiai méréseket *in situ* elektrokémiai kontroll alatt, annak érdekében, hogy megértsük az elektrokémiai polarizáció szerepét a töltéshordozók rekombinációs folyamatai során (52. ábra).



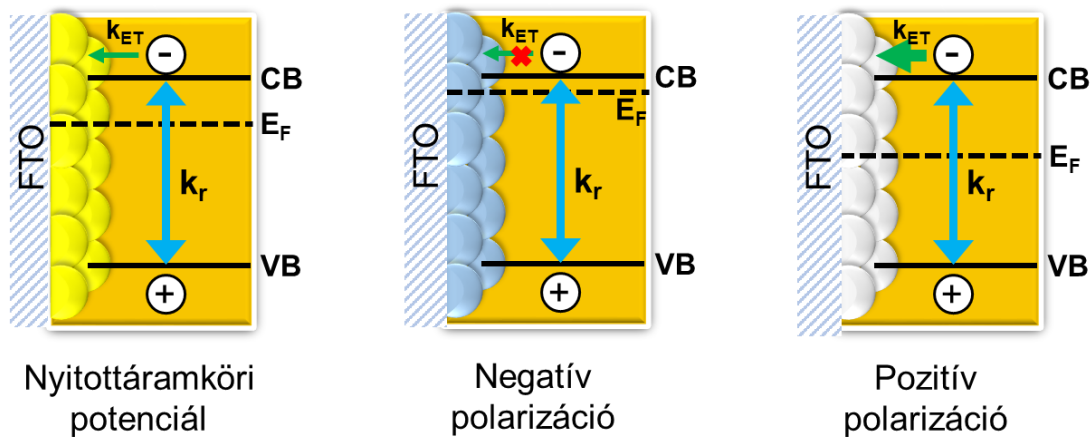
**52. ábra** Az elektrokémiai tranzien abszorpciós spektroszkópia sematikus elrendezése.

Korábban megmutattuk, hogy a CuI-ban található excitonok száma egyre nagyobb az elektródpotenciál csökkenésével (fényelnyelésük is nagyobb a negatív potenciáloknál, 51. ábra). Ultragyors tranzien abszorpciós vizsgálatokkal ugyanakkor igazoltuk, hogy azok élettartama egyre kisebb.<sup>57</sup> Amennyiben a töltéshordozók csapdázódhatnak a tiltott sávon belül elhelyezkedő energiaszinteken, a rekombináció sebessége mindig csökken. Ez azzal magyarázható, hogy az ezen szinteken keresztül megvalósuló rekombinációs folyamat lassabb, mint a töltéshordozók vegyérték- és vezetési sáv közötti közvetlen rekombinációja. Az elektronok növekvő száma a hibahelyeken csökkenti, majd végül teljesen megszünteti a fény általi gerjesztés következtében létrejövő lyukak csapdázódásának lehetőségét. Ez pedig az exciton-rekombináció sebességének növekedésében, és ezáltal azok élettartamának csökkenésében nyilvánul meg (53. ábra).<sup>57</sup>



**53. ábra** Cu/ITO elektródok tranziens abszorpciós spektruma, 0,1 M  $\text{Bu}_4\text{NPF}_6$ /diklór-metán elektrolitban 387 nm-es lézerpulzus-gerjesztést követően ( $4 \mu\text{J cm}^{-2}$ ),  $E = +0,2$  vs. Ag/AgCl alkalmazott potenciál mellett. B: 412 nm-en megfigyelt fehérítő kinetikai görbék különböző alkalmazott potenciáloknál  $-0,1$  és  $+0,6$  V és Ag/AgCl között. C: A "B" ábra görbéiből meghatározott rekombinációs időállandók potenciálfüggése.<sup>57</sup>

Az utolsó *in situ* elektrokémiai TAS mérési példában  $\text{TiO}_2$  rétegen rögzített  $\text{CsPbBr}_3$ -ot vizsgáltunk. A fotoelektrokémiai vizsgálatokon túlmenően, ez a rendszer napelemekben is széleskörben tanulmányozott. Mivel a  $\text{TiO}_2$  réteg feltöltése/kisütése befolyásolhatja a teljes energiaátalakítási folyamat hatásfokát, ennek pontos megértése lényeges. Mezopórusos  $\text{TiO}_2$  filmre vittünk fel  $\text{CsPbBr}_3$ -ot, és az elektrokémiai polarizáció hatását vizsgáltuk a töltéshordozó-rekombinációs, transzport és transzfer folyamatokra (54. ábra). A különböző potenciálokon végzett tranziens abszorpciós spektroszkópiai kísérletek a  $\text{CsPbBr}_3$  töltéshordozók élettartamának csökkenését jelezték, miközben a potenciált  $-0,6$  V-ról  $+0,6$  V-ra növeltük (vs. Ag/AgCl). Fordított irányban, a fordított trendet tapasztaltuk. A jelenség hátterében a  $\text{TiO}_2$  alapréteg betöltöttségi szintjének változása áll (ami az alkalmazott potenciállal szabályozható), ami megszabja a  $\text{CsPbBr}_3$ -ról a  $\text{TiO}_2$ -re való elektrontranszfer sebességét (54. ábra).<sup>59</sup>



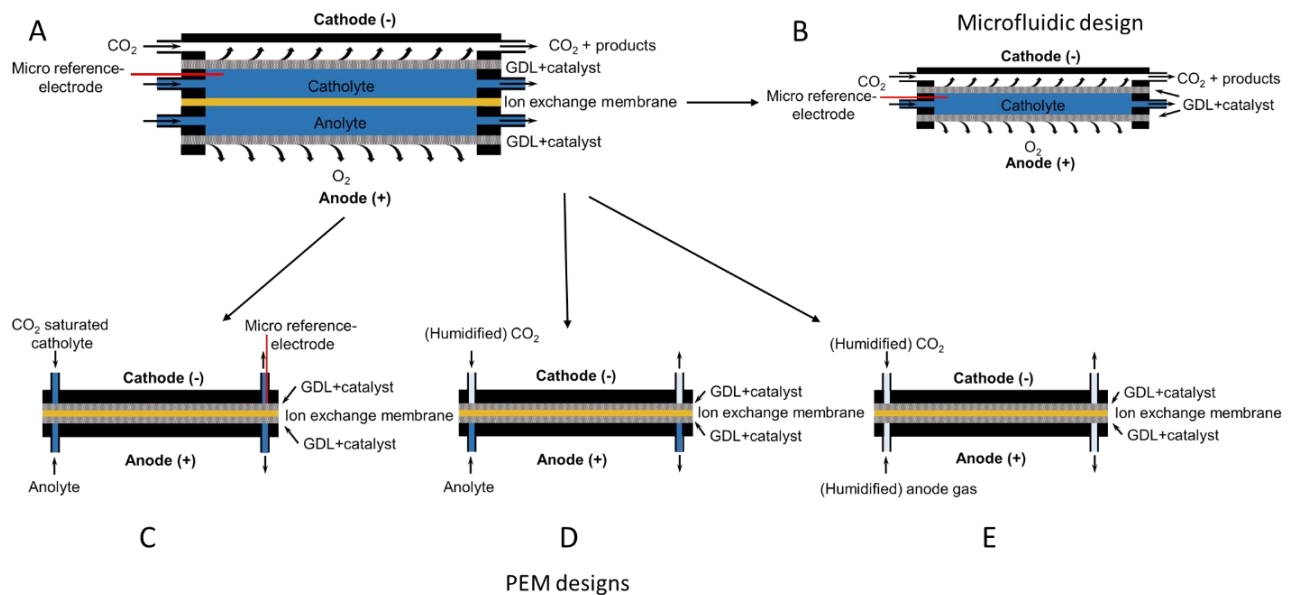
**54. ábra** A  $\text{CsPbBr}_3/\text{TiO}_2$  fotoelektrod sávpozícióit és az alkalmazott potenciáltól függő Fermi-szintet szemléltető sematikus ábrák.<sup>59</sup>

## X. Az eredmények gyakorlati hasznosításának lehetőségei és további kutatási irányok

Az előszóban említettem, hogy az értekezésben nem foglalkozom a  $\text{CO}_2$  elektrokatalitikus átalakításával, amely a kutatócsoportom másik fő iránya. Ugyanakkor kitekintésként fontos megemlíteni a folyamatos áramlású reaktorok fejlesztése irányában tett erőfeszítéseinket, mivel ezen tudást felhasználva jelenleg folyamatos üzemű *fotoelektrokémiai* cellák fejlesztésén dolgozunk. Eddigi

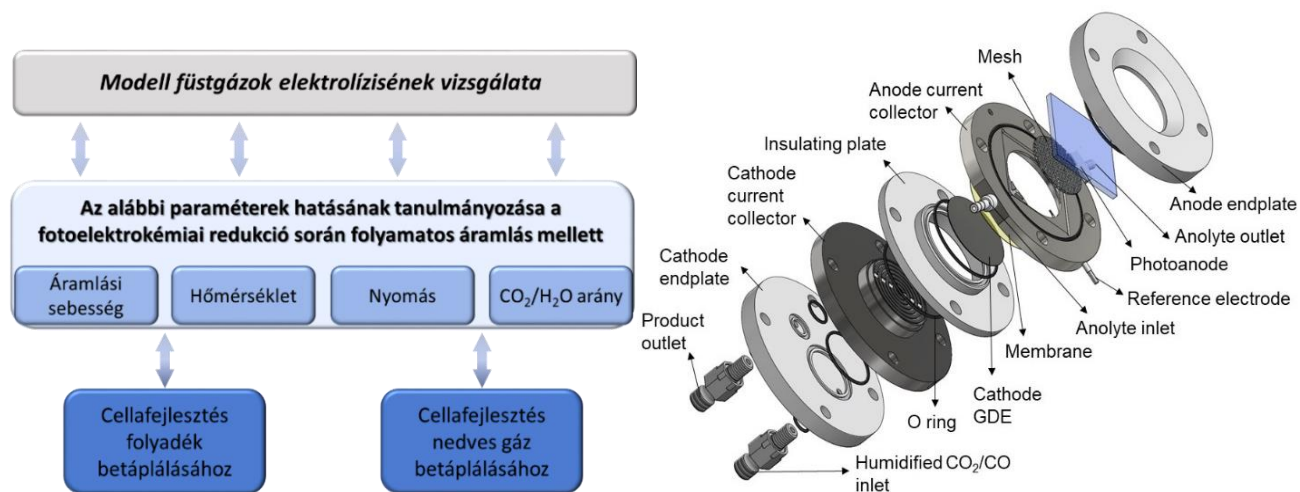
eredményeink azt mutatják, hogy a folyamatos áramlású reaktorokban történő (foto)elektrokémiai vizsgálatok sok esetben gyökeresen más eredményt mutatnak, mint a klasszikus, statikus cellákban mértek.<sup>100</sup> Éppen ezért, már a kutatási tevékenység elejétől fogva fontos, hogy ilyen elrendezésben is vizsgáljuk a különböző elektródokat és foelektrodokat. Így el tudjuk kerülni azt a helyzetet, hogy nagyon sok időt eltöltünk olyan elektródok vizsgálatával, amelyek a folyamatos áramlású cellákban nem mutatnak ígéretes aktivitást és stabilitást.<sup>101</sup>

Első lépésben áttekintettük a szakterület legfrissebb állását,<sup>102</sup> és mindezek alapján azonosítottuk azokat a cellakonstrukciókat, amelyekben a folyamatos szén-dioxid betáplálás megoldható. A 55. ábra foglalja össze a különféle elrendezéseket. Az első fő kérdés, hogy a két félcella terét elválasztjuk-e egymástól egy ioncserélő membránnal, vagy pedig egy mikrofluidikai cellát tervezünk.<sup>103</sup> További kérdés, hogy milyen módon, és melyik elektródot világítjuk meg.



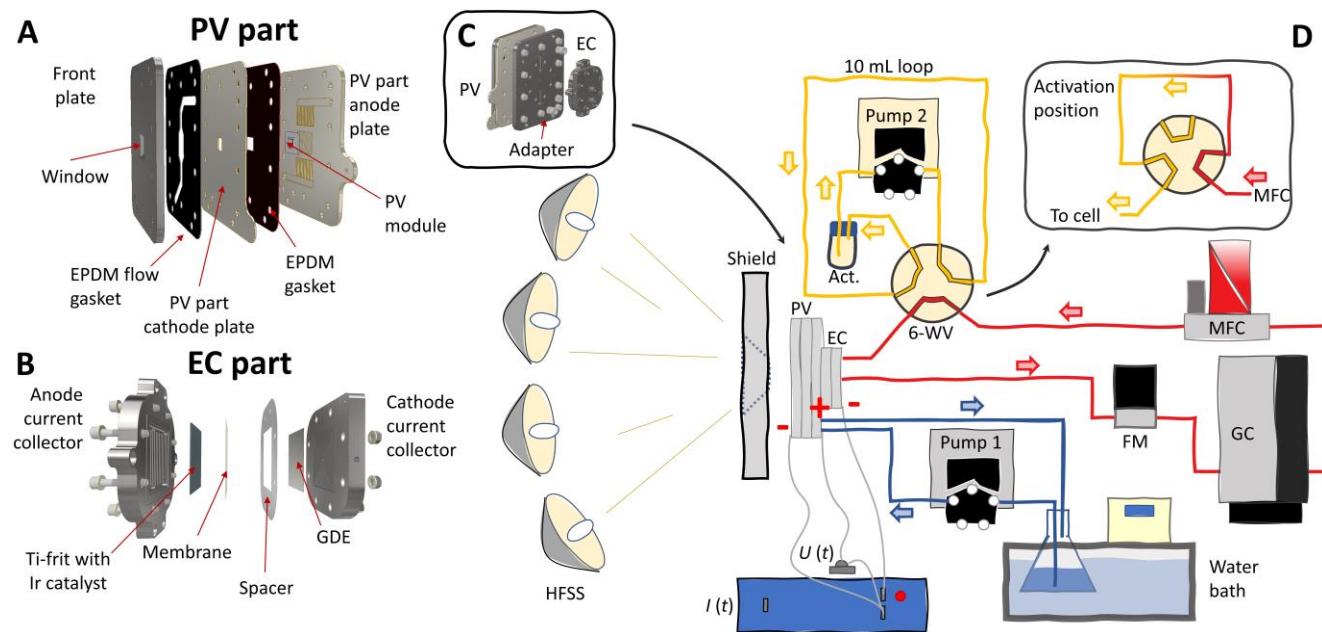
55. ábra A különböző folyamatos áramlású elektrolizáló cellák sémája.<sup>102</sup>

A szakterület eredményeit áttekintve megterveztük első elektrokémiai cellákat, amelyekben a folyamatos CO<sub>2</sub> betáplálás mellett lehet vizsgálni a CO<sub>2</sub> redukcióját, számos paraméter hatásának tanulmányozásával (56. ábra). A legfontosabb kérdés, hogy a szén-dioxidot oldat vagy gáz formájában, vagy egyszerre mindkét formában tápláljuk-e be. Mindhárom eset megvalósítására terveztünk, és gyárttatunk elektrokémiai cellákat. A következő lépés a működtetési körülmények hatásának vizsgálata, amelyek közül itt a nyomás kérdését emelem ki, amely különösen innovatív megoldásokat igényelt. Az így kapott ígéretes eredmények alapján a folyamatos áramlású cellák első generációjának műszaki megoldásai kapcsán az első két alapszabadalmat benyújtottuk,<sup>104,105</sup> és ugyanez várható a közeljövőben a foelektrokémiai cellák kapcsán. Az így létrehozott reaktorok nem csak a földön, de a világűrben is kiemelt fontossággal bírhatnak.<sup>106</sup>



56. ábra A folyamatos áramlású elektrolizáló cellák tesztelésének sémája, valamint egy folyamatos CO<sub>2</sub> betáplálás mellett működtethető, fotoanódot tartalmazó fotoelektrokémiai cella robbantott ábrája.

A közelmúltban ismertettünk egy olyan megoldást, amelyben egy eszközben integráltunk egy fotovoltaikus elemet és egy elektrolizáló cellát. Mindezt olyan módon, hogy alkalmas legyen koncentrált napfényvel való megvilágításra (max. 45 W/cm<sup>2</sup>, 450 nap!), és a két részegység termikusan is integrálva legyen (57. ábra). A koncentrált besugárzás hasznosításának köszönhetően nagy teljesítménysűrűséget kaptunk, a CO képződéshez kötődő parciális áramsűrűség 0,15 A cm<sup>-2</sup> felett volt. A megfelelő anyag- és módszerválasztás lehetővé tették az aktiválási túlfeszültség és az ohmikus veszteségek minimális szinten tartását, így a napfényből-CO átalakítás határfoka meghaladta a 17%-ot. A nagy bemeneti teljesítmény és a nagy konverziós határfok kombinációja eredményezte ezt az első közvetlenül napfény felhasználásával működő, és 1 NL<sub>CO</sub> h<sup>-1</sup> feletti termelési sebességgel működő berendezést.<sup>107</sup>



57. ábra Az egyedi készítésű, integrált PV-EC cella és a kísérleti rendszer sematikus ábrázolása.<sup>107</sup>

A jövőbe tekintve elmondható, hogy a felfedező kutatás területén érdeklődésünk jelenleg a nanoszerkezet és a (foto)elektrokémiai aktivitás kapcsolatára irányul. Ez különösen fontos azért, mert a jelenlegi elméleti háttér és formalizmus (Gerischer, Mott-Schottky, Marcus elmélet stb.) mindegyik makroszkopikus elektród/elektrolit határfelületre vonatkozik, ahol az elektród vastagsága meghaladja a kiürülési réteg vastagságát. Ez nanoszerkezetű anyagok esetében nyilvánvalóan nem teljesül, így a jelenleg használt elméletek alkalmazhatósága is korlátozott. Hasonlóan fontos kérdés a morfológia szerepe, amelynek átfogó és alapos vizsgálata még várat magára. Ráadásul többségében reverzibilis, egy elektronátmenettel járó reakciókat írnak le, szemben a tüzelőanyagok előállítását célzó reakciókkal (CO<sub>2</sub>-redukció, víz-oxidáció). Az Európai Kutatási Tanács által támogatott ERC Consolidator Grant projekt keretén belül ezekre a kérdésekre keressük a választ, újgenerációs félvezetők (vegyes fém-oxidok, fém-halogenidek, és szerves-szerveetlen perovszkit elektródok) felhasználásával készített porózus fotelektrodok vizsgálatával. Az alkalmazott kutatások terén olyan összetett elektródokat, elektrokémiai cellákat, és rendszereket tervezünk és vizsgálunk, amelyekkel különböző (foto)elektroszintetikus folyamatokat lehet környezetbarát módon végrehajtani.

## XI. Irodalomjegyzék

- (1) Gimenez, S.; Bisquert, J. *Photoelectrochemical Solar Fuel Production, From Basic Principles to Advanced Devices*; Giménez, S., Bisquert, J., Eds.; Springer, 2016.
- (2) Lewis, N. S. Developing a Scalable Artificial Photosynthesis Technology through Nanomaterials by Design. *Nat. Nanotechnol.* **2016**, *11*, 1010–1019.
- (3) Fujishima, A.; Honda, K. Electrochemical Photolysis of Water at a Semiconductor Electrode. *Nature* **1972**, *238*, 37–38.
- (4) Calvin, M. Simulating Photosynthetic Quantum Conversion. *Acc. Chem. Res.* **1978**, *11*, 369–374.
- (5) O'Regan, B.; Gratzel, M. A Low-Cost, High-Efficiency Solar Cell Based on Dye-Sensitized Colloidal TiO<sub>2</sub> Films. *Nature* **1991**, *353*, 737–740.
- (6) Kamat, P. V.; Christians, J. A. Solar Cells versus Solar Fuels: Two Different Outcomes. *J. Phys. Chem. Lett.* **2015**, *6*, 1917–1918.
- (7) Heller, A.; Kolb, D.; Rajeshwar, K. The Life and Work of Heinz Gerischer. *Electrochem. Soc. Interface* **2010**, *19*, 37–40.
- (8) Cheng, W. H.; Richter, M. H.; Sullivan, I.; Larson, D. M.; Xiang, C.; Brunschwig, B. S.; Atwater, H. A. CO<sub>2</sub> Reduction to CO with 19% Efficiency in a Solar-Driven Gas Diffusion Electrode Flow Cell under Outdoor Solar Illumination. *ACS Energy Lett.* **2020**, *5*, 470–476.
- (9) *IUPAC. Compendium of Chemical Terminology*, 2nd edition; McNaught, A. D., Wilkinson, A., Eds.; Blackwell Scientific Publications: Oxford, 1997.
- (10) Osterloh, F. E. Photocatalysis versus Photosynthesis: A Sensitivity Analysis of Devices for Solar Energy Conversion and Chemical Transformations. *ACS Energy Lett.* **2017**, *2*, 445–453.
- (11) Schneider, J.; Bahnemann, D. W. Undesired Role of Sacrificial Reagents in Photocatalysis. *J. Phys. Chem. Lett.* **2013**, *4*, 3479–3483.
- (12) Kamat, P. V.; Jin, S. Semiconductor Photocatalysis: "Tell Us the Complete Story!". *ACS Energy Lett.* **2018**, *3*, 622–623.
- (13) Coridan, R. H.; Nielander, A. C.; Francis, S. a; McDowell, M. T.; Dix, V.; Chatman, S. M.; Lewis, N. S. Methods for Comparing the Performance of Energy-Conversion Systems for Use in Solar Fuels and Solar Electricity Generation. *Energy Environ. Sci.* **2015**, *8*, 2886–2901.
- (14) Becquerel, E. Recherches Sur Les Effets de La Radiation Chimique de La Lumière Solaire, Au Moyen Des

- Courants Électriques. *C. R. Hebd. Seances Acad. Sci.* **1839**, *9*, 145–149.
- (15) Rajeshwar, K. Solar Energy Conversion and Environmental Remediation Using Inorganic Semiconductor/Liquid Interfaces: The Road Traveled and the Way Forward. *J. Phys. Chem. Lett.* **2011**, *2*, 1301–1309.
- (16) Samu, G. F.; Janáky, C. Photocorrosion at Irradiated Perovskite/Electrolyte Interfaces. *J. Am. Chem. Soc.* **2020**, *142*, 21595–21614.
- (17) Cendula, P.; Tilley, S. D.; Gimenez, S.; Bisquert, J.; Schmid, M.; Grätzel, M.; Schumacher, J. O. Calculation of the Energy Band Diagram of a Photoelectrochemical Water Splitting Cell. *J. Phys. Chem. C* **2014**, *118*, 29599–29607.
- (18) He, J.; Janáky, C. Recent Advances in Solar-Driven Carbon Dioxide Conversion: Expectations versus Reality. *ACS Energy Lett.* **2020**, *5*, 1996–2014.
- (19) Khan, M. A.; Al-Shankiti, I.; Ziani, A.; Wehbe, N.; Idriss, H. A Stable Integrated Photoelectrochemical Reactor for H<sub>2</sub> Production from Water Attains a Solar-to-Hydrogen Efficiency of 18 % at 15 Suns and 13% at 207 Suns. *Angew. Chemie Int. Ed.* **2020**, *132*, 14912–14918.
- (20) Kumaravel, V.; Bartlett, J.; Pillai, S. C. Photoelectrochemical Conversion of Carbon Dioxide (CO<sub>2</sub>) into Fuels and Value-Added Products. *ACS Energy Lett.* **2020**, *5*, 486–519.
- (21) Vass, Á.; Endrődi, B.; Janáky, C. Coupling Electrochemical Carbon Dioxide Conversion with Value-Added Anode Processes: An Emerging Paradigm. *Curr. Opin. Electrochem.* **2021**, *25*, 100621
- (22) Vass, Á.; Kormányos, A.; Kószo, Z.; Endrődi, B.; Janáky, C. Anode Catalysts in CO<sub>2</sub> Electrolysis: Challenges and Untapped Opportunities. *ACS Catal.* **2022**, *12*, 1037–1051.
- (23) Liu, D.; Liu, J. C.; Cai, W.; Ma, J.; Yang, H. Bin; Xiao, H.; Li, J.; Xiong, Y.; Huang, Y.; Liu, B. Selective Photoelectrochemical Oxidation of Glycerol to High Value-Added Dihydroxyacetone. *Nat. Commun.* **2019**, *10*, 1779
- (24) Barham, J. P.; König, B. Synthetic Photoelectrochemistry. *Angew. Chemie - Int. Ed.* **2020**, *59*, 11732–11747.
- (25) Cukier, R. I.; Nocera, D. G. Proton-Coupled Electron Transfer. *Annu. Rev. Phys. Chem.* **1998**, *49*, 337–369.
- (26) Esposito, D. V.; Baxter, J. B.; John, J.; Lewis, N. S.; Moffat, T. P.; Ogitsu, T.; Neil, G. D. O.; Pham, A.; O'Neil, G. D.; Pham, T. A.; Talin, A. A.; Velazquez, J. M.; Wood, B. Methods of Photoelectrode Characterization with High Spatial and Temporal Resolution. *Energy Environ. Sci.* **2015**, *8*, 2799–3050.
- (27) Hansen, O.; Seger, B.; Vesborg, P. C. K.; Chorkendorff, I. A Quick Look at How Photoelectrodes Work. *Science*, **2015**, *350*, 1030–1031.
- (28) Rajeshwar, K.; Thomas, A.; Janaky, C. Photocatalytic Activity of Inorganic Semiconductor Surfaces: Myths, Hype, and Reality. *J. Phys. Chem. Lett.* **2015**, *6*, 139–147.
- (29) Osterloh, F. E. Inorganic Materials as Catalysts for Photochemical Splitting of Water. *Chem. Mater.* **2008**, *20*, 35–54.
- (30) Wang, S.; Liu, G.; Wang, L. Crystal Facet Engineering of Photoelectrodes for Photoelectrochemical Water Splitting. *Chem. Rev.* **2019**, *119*, 5192–5247.
- (31) Yao, T.; An, X.; Han, H.; Chen, J. Q.; Li, C. Photoelectrocatalytic Materials for Solar Water Splitting. *Adv. Energy Mater.* **2018**, *8*, 1–36.
- (32) Sivula, K. Metal Oxide Photoelectrodes for Solar Fuel Production, Surface Traps, and Catalysis. *J. Phys. Chem. Lett.* **2015**, *6*, 1624–1633.
- (33) Vullev, V. I. From Biomimesis to Bioinspiration: What is the Benefit for Solar Energy Conversion Applications? *J. Phys. Chem. Lett.* **2011**, *2*, 503–508.
- (34) Irtem, E.; Hernández-Alonso, M. D.; Parra, A.; Fàbrega, C.; Penelas-Pérez, G.; Morante, J. R.; Andreu, T. A Photoelectrochemical Flow Cell Design for the Efficient CO<sub>2</sub> Conversion to Fuels. *Electrochim. Acta* **2017**, *240*, 225–230.
- (35) Vesborg, P. C. K.; Seger, B. Performance Limits of Photoelectrochemical CO<sub>2</sub> Reduction Based on Known

- Electrocatalysts and the Case for Two-Electron Reduction Products. *Chem. Mater.* **2016**, *28*, 8844–8850.
- (36) Tsuchiya, H.; Macak, J. M.; Sieber, I.; Taveira, L.; Ghicov, A.; Sirotna, K.; Schmuki, P. Self-Organized Porous WO<sub>3</sub> Formed in NaF Electrolytes. *Electrochem. Commun.* **2005**, *7*, 295–298.
- (37) Janaky, C.; Tacconi, N. de; Chanmanee, W.; Rajeshwar, K. Bringing Conjugated Polymers and Oxide Nanoarchitectures into Intimate Contact: Light Induced Electrodeposition of Polypyrrole and Polyaniline on Nanoporous WO<sub>3</sub> or TiO<sub>2</sub>. *J. Phys. Chem. C* **2012**, *116*, 19145–19155.
- (38) Janáky, C.; Rajeshwar, K. The Role of (Photo)Electrochemistry in the Rational Design of Hybrid Conducting Polymer/Semiconductor Assemblies: From Fundamental Concepts to Practical Applications. *Prog. Polym. Sci.* **2015**, *43*, 96–135.
- (39) Janáky, C.; De Tacconi, N. R.; Chanmanee, W.; Rajeshwar, K.; Janaky, C.; Tacconi, N. R. de; Chanmanee, W.; Rajeshwar, K. Electrodeposited Polyaniline in a Nanoporous WO<sub>3</sub> Matrix: An Organic/Inorganic Hybrid Exhibiting Both p-and n-Type Photoelectrochemical Activity. *J. Phys. Chem. C* **2012**, *116*, 4234–4242.
- (40) Samu, G. F.; Pencz, K.; Janáky, C.; Rajeshwar, K. On the Electrochemical Synthesis and Charge Storage Properties of WO<sub>3</sub>/Polyaniline Hybrid Nanostructures. *J. Solid State Electrochem.* **2015**, *19*, 2741–2751.
- (41) Janáky, C.; Chanmanee, W.; Rajeshwar, K. On the Substantially Improved Photoelectrochemical Properties of Nanoporous WO<sub>3</sub> Through Surface Decoration with RuO<sub>2</sub>. *Electrocatalysis* **2013**, *4*, 382–389.
- (42) Krivan, E. P.; Ungor, D.; Janáky, C.; Németh, Z.; Visy, C. Optimization of the Photoactivity of Conducting Polymer Covered ZnO Nanorod Composite Electrodes. *J. Solid State Electrochem.* **2015**, *19*, 37–44.
- (43) Endrődi, B.; Kecsenovity, E.; Rajeshwar, K.; Janáky, C. One-Step Electrodeposition of Nanocrystalline TiO<sub>2</sub> Films with Enhanced Photoelectrochemical Performance and Charge Storage. *ACS Appl. Energy Mater.* **2018**, *1*, 851–858.
- (44) Ghadimkhani, G.; de Tacconi, N. R.; Chanmanee, W.; Janaky, C.; Rajeshwar, K. Efficient Solar Photoelectrosynthesis of Methanol from Carbon Dioxide Using Hybrid CuO-Cu<sub>2</sub>O Semiconductor Nanorod Arrays. *Chem. Commun.* **2013**, *49*, 1297–1299.
- (45) Rajeshwar, K.; de Tacconi, N. R.; Ghadimkhani, G.; Chanmanee, W.; Janáky, C. Tailoring Copper Oxide Semiconductor Nanorod Arrays for Photoelectrochemical Reduction of Carbon Dioxide to Methanol. *ChemPhysChem* **2013**, *14*, 2251–2259.
- (46) Balog, A.; Janáky, C. The Effect of Trap States on the Optoelectronic Properties of Nanoporous Nickel Oxide. *J. Electrochem. Soc.* **2019**, *166*, H3265
- (47) Kormányos, A.; Kecsenovity, E.; Honarfar, A.; Pullerits, T.; Janáky, C. Hybrid FeNiOOH/ $\alpha$ -Fe<sub>2</sub>O<sub>3</sub>/Graphene Photoelectrodes with Advanced Water Oxidation Performance. *Adv. Funct. Mater.* **2020**, *30*, 2002124
- (48) Rajeshwar, K.; De Tacconi, N. R. Solution Combustion Synthesis of Oxide Semiconductors for Solar Energy Conversion and Environmental Remediation. *Chem. Soc. Rev.* **2009**, *38*, 1984–1998.
- (49) Samu, G. F.; Veres, Á.; Endrődi, B.; Varga, E.; Rajeshwar, K.; Janáky, C. Bandgap-Engineered Quaternary M<sub>x</sub>Bi<sub>2-x</sub>Ti<sub>2</sub>O<sub>7</sub> (M: Fe, Mn) Semiconductor Nanoparticles: Solution Combustion Synthesis, Characterization, and Photocatalysis. *Appl. Catal. B Environ.* **2017**, *208*, 148–160.
- (50) Thomas, A.; Janáky, C.; Samu, G. F.; Huda, M. N.; Sarker, P.; Liu, J. P.; van Nguyen, V.; Wang, E. H.; Schug, K. A.; Rajeshwar, K. Time- and Energy-Efficient Solution Combustion Synthesis of Binary Metal Tungstate Nanoparticles with Enhanced Photocatalytic Activity. *ChemSusChem* **2015**, *8*, 1652–1663.
- (51) Kormányos, A.; Thomas, A.; Huda, M. N.; Sarker, P.; Liu, J. P.; Poudyal, N.; Janáky, C.; Rajeshwar, K. Solution Combustion Synthesis, Characterization, and Photoelectrochemistry of CuNb<sub>2</sub>O<sub>6</sub> and ZnNb<sub>2</sub>O<sub>6</sub> Nanoparticles. *J. Phys. Chem. C* **2016**, *120*, 16024–16034.
- (52) de Tacconi, N. R.; Timmaji, H. K.; Chanmanee, W.; Huda, M. N.; Sarker, P.; Janáky, C.; Rajeshwar, K. Photocatalytic Generation of Syngas Using Combustion-Synthesized Silver Bismuth Tungstate. *ChemPhysChem* **2012**, *13*, 2945–2955.
- (53) Hossain, M. K.; Samu, G. F.; Gandha, K.; Santhanagopalan, S.; Liu, J. P.; Janáky, C.; Rajeshwar, K. Solution

- Combustion Synthesis, Characterization, and Photocatalytic Activity of  $\text{CuBi}_2\text{O}_4$  and Its Nanocomposites with  $\text{CuO}$  and  $\alpha\text{-Bi}_2\text{O}_3$ . *J. Phys. Chem. C* **2017**, *121*, 8252–8261
- (54) Varga, A.; Samu, G. F.; Janáky, C. Rapid Synthesis of Interconnected  $\text{CuCrO}_2$  Nanostructures: A Promising Electrode Material for Photoelectrochemical Fuel Generation. *Electrochim. Acta* **2018**, *272*, 22–32.
- (55) Rajeshwar, K.; Hossain, M. K.; Macaluso, R. T.; Janáky, C.; Varga, A.; Kulesza, P. J. Review—Copper Oxide-Based Ternary and Quaternary Oxides: Where Solid-State Chemistry Meets Photoelectrochemistry. *J. Electrochem. Soc.* **2018**, *165*, H3192–H3206.
- (56) Kecsenovity, E.; Kochuveedu, S. T.; Chou, J. P.; Lukács, D.; Gali, Á.; Janáky, C. Solar Photoelectroreduction of Nitrate Ions on  $\text{PbI}_2/\text{CuI}$  Nanocomposite Electrodes. *Sol. RRL* **2021**, *5*, 2000418.
- (57) Samu, G. F.; Scheidt, R. A.; Balog, Á.; Janáky, C.; Kamat, P. V. Tuning the Excited-State Dynamics of  $\text{CuI}$  Films with Electrochemical Bias. *ACS Energy Lett.* **2019**, *4*, 702–708.
- (58) Balog, Á.; Samu, G. F.; Kamat, P. V.; Janáky, C. Optoelectronic Properties of  $\text{CuI}$  Photoelectrodes. *J. Phys. Chem. Lett.* **2019**, *10*, 259–264.
- (59) Scheidt, R. A.; Samu, G. F.; Janáky, C.; Kamat, P. V. Modulation of Charge Recombination in  $\text{CsPbBr}_3$  Perovskite Films with Electrochemical Bias. *J. Am. Chem. Soc.* **2018**, *140*, 86–89.
- (60) Jeong, H. W.; Zsigmond, T. S.; Samu, G. F.; Janáky, C. Sacrificial Agent Gone Rogue: Electron-Acceptor-Induced Degradation of  $\text{CsPbBr}_3$  Photocathodes. *ACS Energy Lett.* **2022**, *7*, 417–424.
- (61) Samu, G. F.; Scheidt, R. A.; Kamat, P. V.; Janáky, C. Electrochemistry and Spectroelectrochemistry of Lead Halide Perovskite Films: Materials Science Aspects and Boundary Conditions. *Chem. Mater.* **2018**, *30*, 561–569
- (62) Hursán, D.; Kormányos, A.; Rajeshwar, K.; Janáky, C. Polyaniline Films Photoelectrochemically Reduce  $\text{CO}_2$  to Alcohols. *Chem. Commun.* **2016**, *52*, 8858–8861.
- (63) Hursán, D.; London, G.; Olasz, B.; Janáky, C. Synthesis, Characterization, and Electrocatalytic Properties of a Custom-Designed Conjugated Polymer with Pyridine Side Chain. *Electrochim. Acta* **2016**, *217*, 92–99
- (64) Janaky, C.; Chanmanee, W.; Rajeshwar, K. Mechanistic Aspects of Photoelectrochemical Polymerization of Polypyrrole on a  $\text{TiO}_2$  Nanotube Array. *Electrochim. Acta* **2014**, *122*, 303–309.
- (65) Samu, G. F.; Visy, C.; Rajeshwar, K.; Sarker, S.; Subramanian, V. R.; Janáky, C. Photoelectrochemical Infiltration of a Conducting Polymer (PEDOT) into Metal-Chalcogenide Decorated  $\text{TiO}_2$  Nanotube Arrays. *Electrochim. Acta* **2015**, *151*, 467–476.
- (66) Samu, G. F.; Scheidt, R.; Zaiats, G.; Kamat, P. V.; Janáky, C. Electrodeposition of Hole-Transport Layer on Methylammonium Lead Iodide Film: A New Strategy to Assemble Perovskite Solar Cells. *Chem. Mater.* **2018**, *30*, 4202–4206.
- (67) Kormányos, A.; Endrődi, B.; Ondok, R.; Sápi, A.; Janáky, C. Controlled Photocatalytic Synthesis of Core-Shell  $\text{SiC}/\text{Polyaniline}$  Hybrid Nanostructures. *Materials*. **2016**, *9*, 201.
- (68) Kormányos, A.; Ondok, R.; Janáky, C. Electrosynthesis and Photoelectrochemical Properties of Polyaniline/ $\text{SiC}$  Nanohybrid Electrodes. *Electrochim. Acta* **2017**, *256*, 73–80.
- (69) Varga, A.; Endrődi, B.; Hornok, V.; Visy, C.; Janáky, C. Controlled Photocatalytic Deposition of  $\text{CdS}$  Nanoparticles on Poly(3-Hexylthiophene) Nanofibers: A Versatile Approach to Obtain Organic/Inorganic Hybrid Semiconductor Assemblies. *J. Phys. Chem. C* **2015**, *119*, 28020–28027.
- (70) Janáky, C.; Kecsenovity, E.; Rajeshwar, K. Electrodeposition of Inorganic Oxide/Nanocarbon Composites: Opportunities and Challenges. *ChemElectroChem* **2016**, *3*, 181–192.
- (71) Kecsenovity, E.; Endrődi, B.; Pápa, Z.; Hernádi, K.; Rajeshwar, K.; Janáky, C. Decoration of Ultra-Long Carbon Nanotubes with  $\text{Cu}_2\text{O}$  Nanocrystals: A Hybrid Platform for Enhanced Photoelectrochemical  $\text{CO}_2$  Reduction. *J. Mater. Chem. A* **2016**, *4*, 3139–3147.
- (72) Kecsenovity, E.; Endrődi, B.; Toth, P. S.; Zou, Y.; Dryfe, R. A. W.; Rajeshwar, K.; Janáky, C. Enhanced Photoelectrochemical Performance of Cuprous Oxide/Graphene Nanohybrids. *J. Am. Chem. Soc.* **2017**, *139*, 6682–6692.



- (73) Kormányos, A.; Hursán, D.; Janáky, C. Photoelectrochemical Behavior of PEDOT/Nanocarbon Electrodes: Fundamentals and Structure-Property Relationships. *J. Phys. Chem. C* **2018**, *122*, 13682–13690.
- (74) Ismail, A. M.; Samu, G. F.; Balog, Á.; Csapó, E.; Janáky, C. Composition-Dependent Electrocatalytic Behavior of Au-Sn Bimetallic Nanoparticles in Carbon Dioxide Reduction. *ACS Energy Lett.* **2019**, *4*, 48–53.
- (75) Hursán, D.; Janáky, C. Electrochemical Reduction of Carbon Dioxide on Nitrogen-Doped Carbons: Insights from Isotopic Labeling Studies. *ACS Energy Lett.* **2018**, *3*, 722–723
- (76) Janáky, C.; Hursán, D.; Endrődi, B.; Chanmanee, W.; Roy, D.; Liu, D.; De Tacconi, N. R.; Dennis, B. H.; Rajeshwar, K. Electro- and Photoreduction of Carbon Dioxide: The Twain Shall Meet at Copper Oxide/Copper Interfaces. *ACS Energy Lett.* **2016**, *1*, 332–338.
- (77) Chen, X.; Liu, L.; Huang, F. Black Titanium Dioxide (TiO<sub>2</sub>) Nanomaterials. *Chem. Soc. Rev.* **2015**, *44*, 1861–1885.
- (78) Balog, Á.; Samu, G. F.; Pető, S.; Janáky, C. The Mystery of Black TiO<sub>2</sub>: Insights from Combined Surface Science and in Situ Electrochemical Methods. *ACS Mater. Au* **2021**, *1*, 157–168.
- (79) Gu, J.; Yan, Y.; Krizan, J. W.; Gibson, Q. D.; Detweiler, Z. M.; Cava, R. J.; Bocarsly, A. B. *p*-Type CuRhO<sub>2</sub> as a Self-Healing Photoelectrode for Water Reduction under Visible Light. *J. Am. Chem. Soc.* **2014**, *136*, 830–833.
- (80) Hossain, M. K.; Kecsenovity, E.; Varga, A.; Molnár, M.; Janáky, C.; Rajeshwar, K. Solution Combustion Synthesis of Complex Oxide Semiconductors. *Int. J. Self-Propagating High-Temperature Synth.* **2018**, *27*, 129–140.
- (81) Hursán, D.; Kormányos, A.; Rajeshwar, K.; Janáky, C. Polyaniline Films Photoelectrochemically Reduce CO<sub>2</sub> to Alcohols. *Chem. Commun.* **2016**, *52*, 8858–8861.
- (82) Jeong, H. W.; Haihua, W.; Samu, G. F.; Rouster, P.; Szilágyi, I.; Park, H.; Janáky, C. The Effect of Nanostructure Dimensionality on the Photoelectrochemical Properties of Derived TiO<sub>2</sub> Films. *Electrochim. Acta* **2021**, *373*, 137900.
- (83) Tóth, P. S.; Szabó, G.; Janáky, C. Structural Features Dictate the Photoelectrochemical Activities of Two-Dimensional MoSe<sub>2</sub> and WSe<sub>2</sub> Nanostructures. *J. Phys. Chem. C* **2021**, *125*, 7701–7710.
- (84) Tóth, P. S.; Szabó, G.; Bencsik, G.; Samu, G. F.; Rajeshwar, K.; Janáky, C. Peeling off the Surface: Pt-decoration of WSe<sub>2</sub> Nanoflakes Results in Exceptional Photoelectrochemical HER Activity. *SusMat* **2022**, *2*, 749–760.
- (85) Manser, J. S.; Christians, J. A.; Kamat, P. V. Intriguing Optoelectronic Properties of Metal Halide Perovskites. *Chem. Rev.* **2016**, *116*, 12956–13008.
- (86) Kuku, T. A. Ionic Transport and Galvanic Cell Discharge Characteristics of CuPbI<sub>3</sub> Thin Films. *Thin Solid Films* **1998**, *325*, 246–250.
- (87) Huang, H.; Pradhan, B.; Hofkens, J.; Roelofs, M. B. J.; Steele, J. A. Solar-Driven Metal Halide Perovskite Photocatalysis: Design, Stability, and Performance. *ACS Energy Lett.* **2020**, *5*, 1107–1123.
- (88) Samu, G. F.; Janáky, C.; Kamat, P. V. A Victim of Halide Ion Segregation. How Light Soaking Affects Solar Cell Performance of Mixed Halide Lead Perovskites. *ACS Energy Lett.* **2017**, *2*, 1860–1861.
- (89) Samu, G. F.; Balog, Á.; De Angelis, F.; Meggiolaro, D.; Kamat, P. V.; Janáky, C. Electrochemical Hole Injection Selectively Expels Iodide from Mixed Halide Perovskite Films. *J. Am. Chem. Soc.* **2019**, *141*, 10812–10820
- (90) Mathew, P. S.; Mathew, P. S.; Samu, G. F.; Samu, G. F.; Janáky, C.; Kamat, P. V.; Kamat, P. V.; Kamat, P. V. Iodine (I) Expulsion at Photoirradiated Mixed Halide Perovskite Interface. Should it Stay or Should it Go? *ACS Energy Lett.* **2020**, *5*, 1872–1880.
- (91) Spitler, M. T.; Modestino, M. A.; Deutsch, T. G.; Xiang, C. X.; Durrant, J. R.; Esposito, D. V.; Haussener, S.; Maldonado, S.; Sharp, I. D.; Parkinson, B. A.; Ginley, D. S.; Houle, F. A.; Hannappel, T.; Neale, N. R.; Nocera, D. G.; McIntyre, P. C. Practical Challenges in the Development of Photoelectrochemical Solar

- Fuels Production. *Sustain. Energy Fuels* **2020**, *4*, 985–995.
- (92) Roy, D.; Samu, G. F.; Hossain, M. K.; Janáky, C.; Rajeshwar, K. On the Measured Optical Bandgap Values of Inorganic Oxide Semiconductors for Solar Fuels Generation. *Catal. Today* **2018**, *300*, 136–144.
- (93) Wang, G.; Wang, H.; Ling, Y.; Tang, Y.; Yang, X.; Fitzmorris, R. C.; Wang, C.; Zhang, J. Z.; Li, Y. Hydrogen-Treated TiO<sub>2</sub> Nanowire Arrays for Photoelectrochemical Water Splitting. *Nano Lett.* **2011**, *11*, 3026–3033.
- (94) Naldoni, A.; Altomare, M.; Zoppellaro, G.; Liu, N.; Kment, Š.; Zbořil, R.; Schmuki, P. Photocatalysis with Reduced TiO<sub>2</sub>: From Black TiO<sub>2</sub> to Cocatalyst-Free Hydrogen Production. *ACS Catal.* **2019**, *9*, 345–364.
- (95) Sági, A.; Varga, A.; Samu, G. F.; Dobó, D.; Juhász, K. L.; Takács, B.; Varga, E.; Kukovecz, Á.; Kónya, Z.; Janáky, C. Photoelectrochemistry by Design: Tailoring the Nanoscale Structure of Pt/NiO Composites Leads to Enhanced Photoelectrochemical Hydrogen Evolution Performance. *J. Phys. Chem. C* **2017**, *121*, 12148–12158.
- (96) Bedja, I.; Hotchandani, S.; Kamat, P. V. Preparation and Photoelectrochemical Characterization of Thin SnO<sub>2</sub> Nanocrystalline Semiconductor Films and Their Sensitization with Bis(2,2'-Bipyridine)(2,2'-Bipyridine-4,4'-Dicarboxylic Acid)Ruthenium(II) Complex. *J. Phys. Chem.* **1994**, *98*, 4133–4140.
- (97) Świątek, E.; Pilarczyk, K.; Derdzińska, J.; Szaciłowski, K.; Macyk, W. Redox Characterization of Semiconductors Based on Electrochemical Measurements Combined with UV-Vis Diffuse Reflectance Spectroscopy. *Phys. Chem. Chem. Phys.* **2013**, *15*, 14256.
- (98) Nitta, A.; Takase, M.; Takashima, M.; Murakami, N.; Ohtani, B. A Fingerprint of Metal-Oxide Powders: Energy-Resolved Distribution of Electron Traps. *Chem. Commun.* **2016**, *52*, 12096–12099.
- (99) Ponseca, C. S.; Chábera, P.; Uhlig, J.; Persson, P.; Sundström, V. Ultrafast Electron Dynamics in Solar Energy Conversion. *Chem. Rev.* **2017**, *117*, 10940–11024.
- (100) Vilanova, A.; Dias, P.; Azevedo, J.; Wullenkord, M.; Spenke, C.; Lopes, T.; Mendes, A. Solar Water Splitting under Natural Concentrated Sunlight Using a 200 cm<sup>2</sup> Photoelectrochemical-Photovoltaic Device. *J. Power Sources* **2020**, *454*, 227890.
- (101) Burdyny, T.; Smith, W. A. CO<sub>2</sub> Reduction on Gas-Diffusion Electrodes and Why Catalytic Performance Must Be Assessed at Commercially-Relevant Conditions. *Energy Environ. Sci.* **2019**, *12*, 1442–1453.
- (102) Endrődi, B.; Bencsik, G.; Darvas, F.; Jones, R.; Rajeshwar, K.; Janáky, C. Continuous-Flow Electroreduction of Carbon Dioxide. *Prog. Energy Combust. Sci.* **2017**, *62*, 133–154
- (103) Castro, S.; Albo, J.; Irabien, A. Photoelectrochemical Reactors for CO<sub>2</sub> Utilization. *ACS Sustain. Chem. Eng.* **2018**, *6*, 15877–15894.
- (104) Endrődi, B.; Kecsenovity, E.; Samu, A.; Darvas, F.; Jones, R. V.; Török, V.; Danyi, A.; Janáky, C. Modular Electrolyzer Cell and Process to Convert Carbon Dioxide to Gaseous Products at Elevated Pressure with High Conversion Rate, WO2020240218A1, 2019.
- (105) Darvas, F.; Endrődi, B.; Janáky, C.; Jones, R.; Kecsenovity, E.; Samu, A. A Process and System to Enhance and Sustain Electrolyzer Performance of Carbon Dioxide Electrolysers. HU2020050033W, 2020.
- (106) Jones, R.; Darvas, F.; Janáky, C. New Space for Chemical Discoveries. *Nat. Rev. Chem.* **2017**, *1*, 0055.
- (107) Boutin, E.; Patel, M.; Kecsenovity, E.; Suter, S.; Janáky, C.; Haussener, S. Photo-Electrochemical Conversion of CO<sub>2</sub> Under Concentrated Sunlight Enables Combination of High Reaction Rate and Efficiency. *Adv. Energy Mater.* **2022**, *12*, 2200585.

## XII. Köszönetnyilvánítás

Számos embernek tartozom köszönettel azért, hogy az értekezésben bemutatott eredmények és maga az értekezés megszülethettek. Szüleimnek köszönöm a születésem óta való szeretetteljes törődést, töretlen és erőteljes támogatást. Feleségemnek Bíborkának köszönöm a folyamatos türelmet, segítséget és rugalmasságot, valamint a szaknyelvi kérdésekben való hasznos tanácsokat. Kisfiamnak Vilinek köszönöm, hogy mindig elmosolyodok, ha munka közben rá gondolok. Hálás szívvel gondolok vissza középiskolai kémiatanáromra, Meleg Istvánra, akitől a szakma iránti lelkesedést, és a saját munkával szembeni igényességet és önkritikát tanultam meg.

Szakmai szempontból elsőként Visy Csaba professzor úrnak köszönöm, hogy elindított az elektrokémiai pályán, és megismertetett a szerves vezető polimerek világával. Számos együttműködő partnerem közül szeretném név szerint is kiemelni Krishnan Rajeshwar (University of Texas at Arlington) és Prashant V. Kamat (University of Notre Dame) professzorokat, akikre mentorként is tekintek. Előbbi kutatócsoportjában megismerkedtem a fotoelektrokémiai témákkal és vizsgálati módszerekkel. Utóbbtól rengeteget tanultam a tudományos eredmények hatékony és színvonalas disszeminációja terén. Kollégáim és hallgatóim közül mindenképpen név szerint is említenem kell: Dr. Endrődi Balázs, Dr. Samu Gergely Ferenc, Dr. Kormányos Attila, Dr. Varga András, Dr. Hursán Dorottya, Dr. Kecsenovity Egon és Dr. Balog Ádám korábbi PhD hallgatókat, akik a kísérleti munka dandárját végezték. Végül megemlítem Dr. Norma de Tacconi-t és Dr. Wilaiwan Chanmanee-t akiktől az USA-ban töltött évek alatt sokat tanultam a fotoelektrokémia gyakorlati aspektusairól. Végül köszönöm az SZTE TTIK Kémiai Intézetének, különösen a Béke és Bolyai épületekben dolgozó, minden munkatársának a támogató légkört, és a kisebb-nagyobb együttműködések.

**Az értekezés alapját képező közlemények (vastag kijelölés: 20 legjelentősebb cikk)**

1. G. Ghadimkhani, N. R. de Tacconi, W. Chanmanee, **C. Janáky**, K. Rajeshwar: ***Efficient solar photoelectrosynthesis of methanol from carbon dioxide using hybrid CuO/Cu<sub>2</sub>O semiconductor nanorod arrays***  
Chemical Communications, 49 (2013) 1297-1299 DOI: [10.1039/c2cc38068d](https://doi.org/10.1039/c2cc38068d)
2. K. Rajeshwar, N. R. de Tacconi, G. Ghadimkhani, W. Chanmanee, **C. Janáky**: ***Tailoring copper oxide semiconductor nanorod arrays for photoelectrochemical reduction of carbon dioxide to methanol***  
ChemPhysChem, 14 (2013) 2251-2259 DOI: [10.1002/cphc.201300080](https://doi.org/10.1002/cphc.201300080)
3. K. Rajeshwar, **C. Janáky**, W. Y. Lin, D. Roberts, W. Wampler: *Photocatalytically-Prepared Metal Nanocluster-Oxide Semiconductor-Carbon Nanocomposite Electrodes for Driving Multi-electron Processes*  
Journal of Physical Chemistry Letters, 4 (2013) 3468–3478 DOI: [10.1021/jz401455j](https://doi.org/10.1021/jz401455j)
4. **C. Janáky**, N. R. de Tacconi, W. Chanmanee, K. Rajeshwar: ***Electrodeposited Polyaniline in a Nanoporous WO<sub>3</sub> Matrix: An Organic/Inorganic Hybrid Exhibiting Both p- and n-Type Photoelectrochemical Activity***  
Journal of Physical Chemistry C, 116 (2012) 4234-4242 DOI: [10.1021/jp211698j](https://doi.org/10.1021/jp211698j)
5. **C. Janáky**, N. R. de Tacconi, W. Chanmanee, K. Rajeshwar: ***Bringing Conjugated Polymers and Oxide Nanoarchitectures into Intimate Contact: Light Induced Electrodeposition of Polypyrrole and Polyaniline on Nanoporous WO<sub>3</sub> or TiO<sub>2</sub> Nanotube Arrays***  
Journal of Physical Chemistry C, 116 (2012) 19145-19155 DOI: [10.1021/jp305181h](https://doi.org/10.1021/jp305181h)
6. **C. Janáky**, K. Rajeshwar, N. R. de Tacconi, W. Chanmanee, M. Huda: *Tungsten-based oxide semiconductors for solar hydrogen generation*  
Catalysis Today, 199 (2013) 53-64 DOI: [10.1016/j.cattod.2012.07.020](https://doi.org/10.1016/j.cattod.2012.07.020)
7. **C. Janáky**, W. Chanmanee, K. Rajeshwar: *On the substantially improved photoelectrochemical properties of nanoporous WO<sub>3</sub> through surface decoration with RuO<sub>2</sub>*  
Electrocatalysis, 4 (2013) 382-389 DOI: [10.1007/s12678-013-0177-7](https://doi.org/10.1007/s12678-013-0177-7)
8. **C. Janáky**, W. Chanmanee, K. Rajeshwar: *Mechanistic Aspects of Photoelectrochemical Polymerization of Polypyrrole on a TiO<sub>2</sub> Nanotube Array*  
Electrochimica Acta, 122 (2014) 303-309 DOI: [10.1016/j.electacta.2013.12.008](https://doi.org/10.1016/j.electacta.2013.12.008)
9. G. F. Samu, C. Visy, K. Rajeshwar, S. Sarker, V. R. Subramanian and **C. Janáky**: *Photoelectrochemical Infiltration of PEDOT into Metal-Chalcogenide Decorated TiO<sub>2</sub> Nanotube Arrays*  
Electrochimica Acta, 151 (2015) 467-476 DOI: [10.1016/j.electacta.2014.11.094](https://doi.org/10.1016/j.electacta.2014.11.094)
10. K. Rajeshwar, A. Thomas, **C. Janáky**: ***Photocatalytic Activity of Inorganic Semiconductor Surfaces: Myths, Hype, and Reality***  
Journal of Physical Chemistry Letters, 6 (2015), 139-147 DOI: [10.1021/jz502586p](https://doi.org/10.1021/jz502586p)
11. **C. Janáky**, K. Rajeshwar: ***The Role of (Photo)electrochemistry in the Rational Design of Hybrid Conducting Polymer / Semiconductor Assemblies: From Fundamental Concepts to Practical Applications.***  
Progress in Polymer Science, 43 (2015) 96-135 DOI: [10.1016/j.progpolymsci.2014.10.003](https://doi.org/10.1016/j.progpolymsci.2014.10.003)
12. A. Thomas, **C. Janáky**, G. F. Samu, M. N. Huda, P. Sarker, J. P. Liu, V. van Nguyen, K. Rajeshwar: *Time- and Energy-Efficient Solution Combustion Synthesis of Binary Tungstate (Ag<sub>2</sub>WO<sub>4</sub>, CuWO<sub>4</sub>, ZnWO<sub>4</sub>) Nanoparticles with Enhanced Photocatalytic Properties*  
ChemSusChem, 8 (2015) 1652-1663 DOI: [10.1002/cssc.201500383](https://doi.org/10.1002/cssc.201500383)
13. G.F. Samu, K. Pencz, **C. Janáky**, and K. Rajeshwar: *On the electrochemical synthesis and charge storage properties of WO<sub>3</sub>/polyaniline hybrid nanostructures*  
Journal of Solid State Electrochemistry, 19 (2015) 2741-2751 DOI: [10.1007/s10008-015-2820-0](https://doi.org/10.1007/s10008-015-2820-0)
14. A. Varga, B. Endrődi, V. Hornok, C. Visy, **C. Janáky**: *Controlled photocatalytic deposition of CdS nanoparticles on poly(3-hexylthiophene) nanofibers: a versatile approach to obtain organic/inorganic hybrid semiconductor assemblies*  
Journal of Physical Chemistry C, 119 (2015) 28020-28027 DOI: [10.1021/acs.jpcc.5b09029](https://doi.org/10.1021/acs.jpcc.5b09029)

15. C. Janáky, E. Kecszenovity, K. Rajeshwar: *Electrodeposition of Inorganic Oxide/ Nanocarbon Composites: Opportunities and Challenges* ChemElectroChem, 3 (2016) 181-192 DOI: [10.1002/celec.201500460](https://doi.org/10.1002/celec.201500460)
16. E. Kecszenovity, B. Endrődi, Z. Pápa, K. Hernádi, K. Rajeshwar, C. Janáky: **Decoration of ultralong carbon nanotubes with Cu<sub>2</sub>O nanocrystals: a hybrid platform for enhanced photoelectrochemical CO<sub>2</sub> reduction** Journal of Materials Chemistry A, 4 (2016) 3139-3147 DOI: [10.1039/C5TA10457B](https://doi.org/10.1039/C5TA10457B)
17. A. Kormányos, A. Thomas, M. N. Huda, P. Sarker, J. Ping Liu, N. Poudyal, C. Janáky, K. Rajeshwar: *Solution Combustion Synthesis, Characterization, and Photoelectrochemistry of CuNb<sub>2</sub>O<sub>6</sub> and ZnNb<sub>2</sub>O<sub>6</sub> Nanoparticles* Journal of Physical Chemistry C, 120 (2016) 16024–16034 DOI: [10.1021/acs.jpcc.6b13093](https://doi.org/10.1021/acs.jpcc.6b13093)
18. C. Janáky, D. Hursán, B. Endrődi, W. Chanmanee, D. Roy, D. Liu, N. R. de Tacconi, B. H. Dennis and K. Rajeshwar: **Electro- and Photoreduction of Carbon Dioxide: The Twain Shall Meet at Copper Oxide/Copper Interfaces** ACS Energy Letters, 2, (2016) 332–338 DOI: [10.1021/acsenergylett.6b00078](https://doi.org/10.1021/acsenergylett.6b00078)
19. D. Hursán, A. Kormányos, K. Rajeshwar, C. Janáky: **Polyaniline films photoelectrochemically reduce CO<sub>2</sub> to alcohols** Chemical Communications, 52 (2016) 8858-8861 DOI: [10.1039/C6CC04050K](https://doi.org/10.1039/C6CC04050K)
20. D. Hursán, G. London, B. Olasz, C. Janáky: *Synthesis, characterization, and electrocatalytic properties of a custom-designed conjugated polymer with pyridine side-chain* Electrochimica Acta, 217 (2016) 92-99 DOI: [10.1016/j.electacta.2016.09.064](https://doi.org/10.1016/j.electacta.2016.09.064)
21. G.F. Samu, Á. Veres, B. Endrődi, E. Varga, K. Rajeshwar, C. Janáky: **Bandgap-engineered Ternary Bi<sub>2-x</sub>M<sub>x</sub>Ti<sub>2</sub>O<sub>7</sub> (M: Fe, Mn) Semiconductor Nanostructures: Solution Combustion Synthesis, Characterization, and Photocatalysis** Applied Catalysis B Environmental, 208 (2017) 148-160 DOI: [10.1016/j.apcatb.2017.02.036](https://doi.org/10.1016/j.apcatb.2017.02.036)
22. M. K. Hossain, G. Samu, K. Gandha, S. Santhanagopalan, J. P. Liu, C. Janáky, K. Rajeshwar: *Solution Combustion Synthesis, Characterization, and Photocatalytic Activity of CuBi<sub>2</sub>O<sub>4</sub> and its Nanocomposites with CuO and α-Bi<sub>2</sub>O<sub>3</sub>* Journal of Physical Chemistry C, 121 (2017) 8252–8261 DOI: [10.1021/acs.jpcc.6b13093](https://doi.org/10.1021/acs.jpcc.6b13093)
23. A. Sági, A. Varga, D. Dobó, G. F. Samu, B. Takács, E. Varga, Á. Kukovecz, Z. Kónya, and C. Janáky: **Photoelectrochemistry by design: Tailoring the Nanoscale Structure of Pt/NiO Composites Leads to Efficient Photoelectrochemical Hydrogen Evolution** Journal of Physical Chemistry C, 121 (2017) 12148–12158 DOI: [10.1021/acs.jpcc.7b00429](https://doi.org/10.1021/acs.jpcc.7b00429)
24. E. Kecszenovity, B. Endrődi, P. S. Tóth, Y. Zou, R. A. W. Dryfe, K. Rajeshwar, C. Janáky: **Enhanced Photoelectrochemical Performance of Cuprous-oxide/Graphene Nanohybrids** Journal of the American Chemical Society, 139 (2017) 6682-6692 DOI: [10.1021/jacs.7b01820](https://doi.org/10.1021/jacs.7b01820)
25. B. Endrődi, G. Bencsik, F. Darvas, R. Jones, K. Rajeshwar, C. Janáky: **Factors governing the continuous-flow electroreduction of carbon dioxide: Benchmarking electrolyzers and their performance** Progress in Energy and Combustion Science, 62 (2017) 133-154 DOI: [10.1016/j.pecs.2017.05.005](https://doi.org/10.1016/j.pecs.2017.05.005)
26. G. F. Samu, C. Janáky, P. V. Kamat: **A Victim of Halide Ion Segregation. How Light Soaking Affects Solar Cell Performance of Mixed Halide Lead Perovskites.** ACS Energy Letters, 2 (2017) 1860-1861 DOI: [10.1021/acsenergylett.7b00589](https://doi.org/10.1021/acsenergylett.7b00589)
27. A. Kormányos, R. Ondok, C. Janáky: *Electrosynthesis and photoelectrochemical properties of polyaniline/SiC nanohybrid electrodes* Electrochimica Acta, 256 (2017) 73 -80 DOI: [10.1016/j.electacta.2017.10.019](https://doi.org/10.1016/j.electacta.2017.10.019)
28. D. Roy, G. F. Samu, M. Kabir, C. Janáky, K. Rajeshwar: *On the measured optical band gap values of inorganic oxide semiconductors for solar fuels generation* Catalysis Today, 300 (2018) 136-144 DOI: [10.1016/j.cattod.2017.03.016](https://doi.org/10.1016/j.cattod.2017.03.016)

29. R. A. Scheidt, G. F. Samu, **C. Janáky**, P. V. Kamat: *Modulation of Charge Recombination in CsPbBr<sub>3</sub> Perovskite Films with Electrochemical Bias*  
Journal of the American Chemical Society, 140 (2018) 86–89 DOI: [10.1021/jacs.7b10958](https://doi.org/10.1021/jacs.7b10958)
30. G. F. Samu, R. A. Scheidt, P. V. Kamat, **C. Janáky**: *Electrochemistry and Spectroelectrochemistry of Lead Halide Perovskite Films: Materials Science Aspects and Boundary Conditions*  
Chemistry of Materials, 30 (2018) 561–569 DOI: [10.1021/acs.chemmater.7b04321](https://doi.org/10.1021/acs.chemmater.7b04321)
31. B. Endrődi, E. Kecszenovity, K. Rajeshwar, and **C. Janáky**: *One-step Electrodeposition of Nanocrystalline TiO<sub>2</sub> Films with Enhanced (Photo)-electrochemical Performance and Charge Storage*  
ACS Applied Energy Materials, 2 (2018) 851–858 DOI: [10.1021/acsaem.7b00289](https://doi.org/10.1021/acsaem.7b00289)
32. M. K. Hossain, E. Kecszenovity, A. Varga, M. Molnár, **C. Janáky**, K. Rajeshwar: *Solution Combustion Synthesis of Complex Oxide Semiconductors*  
International Journal of Self-Propagating High-Temperature Synthesis 27 (2018) 129–140 DOI: [10.3103/S1061386218030032](https://doi.org/10.3103/S1061386218030032)
33. D. Hursán, **C. Janáky**: *Electrochemical Reduction of Carbon Dioxide on Nitrogen-doped Carbons: Insights from Isotopic Labeling Studies*  
ACS Energy Letters, 3 (2018) 722–723 DOI: [10.1021/acsenergylett.8b00212](https://doi.org/10.1021/acsenergylett.8b00212)
34. K. Rajeshwar, M. K. Hossain, R. T. Macaluso, **C. Janáky**, A. Varga and P. J. Kulesza: *Copper Oxide-Based Ternary and Quaternary Oxides: Where Solid-State Chemistry Meets Photoelectrochemistry*  
Journal of the Electrochemical Society, 165 (2018), H3192–H3206 DOI: [10.1149/2.0271804jes](https://doi.org/10.1149/2.0271804jes)
35. A. Kormányos, D. Hursán, **C. Janáky**: *Photoelectrochemical Behavior of PEDOT/Nanocarbon Electrodes: Fundamentals and Structure–Property Relationships*  
Journal of Physical Chemistry C, 122 (2018) 13682–13690 DOI: [10.1021/acs.jpcc.8b00145](https://doi.org/10.1021/acs.jpcc.8b00145)
36. A. Varga, G. F. Samu, **C. Janáky**: *Rapid Synthesis of Interconnected CuCrO<sub>2</sub> Nanostructures: A Promising Electrode Material for Photoelectrochemical Fuel Generation*  
Electrochimica Acta, 272 (2018) 22–32 DOI: [10.1016/j.electacta.2018.03.185](https://doi.org/10.1016/j.electacta.2018.03.185)
37. G. F. Samu, R. A. Scheidt, G. Zaiats, P. V. Kamat, **C. Janáky**: *Electrodeposition of Hole-transport Layer on Methylammonium Lead Iodide Film: A New Strategy to Assemble Perovskite Solar Cells*  
Chemistry of Materials, 30 (2018) 4202–4206 DOI: [10.1021/acs.chemmater.8b01521](https://doi.org/10.1021/acs.chemmater.8b01521)
38. A. Balog, G. F. Samu, P. V. Kamat, **C. Janáky**: *On the optoelectronic properties of CuI photoelectrodes*  
Journal of Physical Chemistry Letters, 10 (2019) 259–264 DOI: [10.1021/acs.jpcllett.8b03242](https://doi.org/10.1021/acs.jpcllett.8b03242)
39. G. F. Samu, R. Scheidt, A. Balog, **C. Janáky**, P. V. Kamat: *Tuning the Excited State Dynamics of CuI Films with Electrochemical Bias*  
ACS Energy Letters, 4 (2019) 702–708 DOI: [10.1021/acsenergylett.9b00182](https://doi.org/10.1021/acsenergylett.9b00182)
40. A. Balog, **C. Janáky**: *The effect of trap states on the optoelectronic properties of nanoporous NiO*  
Journal of the Electrochemical Society, 166 (2019) H3265–H3270 DOI: [10.1149/2.0361905jes](https://doi.org/10.1149/2.0361905jes)
41. D. Hursán, A. A. Samu, K. Artyushkova, T. Asset, P. Atanassov, **C. Janáky**: *Morphological Attributes Govern Carbon Dioxide Reduction on N-doped Carbon Electrodes*  
Joule, 3 (2019) 1–15 DOI: [10.1016/j.joule.2019.05.007](https://doi.org/10.1016/j.joule.2019.05.007)
42. G. F. Samu, A. Balog, F. de Angelis, P. V. Kamat, **C. Janáky**: *Selective Expulsion of Iodide from Mixed Halide Perovskite Films with Electrochemical Hole Injection*  
Journal of the American Chemical Society, 141 (2019) 10812–10820 DOI: [10.1021/jacs.9b04568](https://doi.org/10.1021/jacs.9b04568)
43. B. Endrődi, E. Kecszenovity, A. Samu, F. Darvas, R. V. Jones, V. Török, A. Danyi, **C. Janáky**: *Multilayer Electrolyzer Stack Converts Carbon Dioxide to Gas Products at High Pressure with High Efficiency*  
ACS Energy Letters, 4 (2019) 1770–1777 DOI: [10.1021/acsenergylett.9b01142](https://doi.org/10.1021/acsenergylett.9b01142)
44. P. S. Mathew, G. F. Samu, **C. Janáky**, P. V. Kamat: *Iodine (I) Expulsion at Photoirradiated Mixed Halide Perovskite Interface. Should I Stay or Should I Go?*  
ACS Energy Letters, 5 (2020) 1872–1880 DOI: [10.1021/acsenergylett.0c00925](https://doi.org/10.1021/acsenergylett.0c00925)

45. J. He, C. Janáky: **Recent Advances in Solar-driven Carbon Dioxide Conversion: Expectations vs. Reality**  
ACS Energy Letters, 5 (2020) 1996-2014 DOI: [10.1021/acsenergylett.0c00645](https://doi.org/10.1021/acsenergylett.0c00645)
46. A. Kormányos, E. Kecsenvity, A. Honarfar, T. Pullerits, C. Janáky: **Hybrid FeNiOOH/ $\alpha$ -Fe<sub>2</sub>O<sub>3</sub>/graphene Photoelectrodes with Advanced Water Oxidation Performance**  
Advanced Functional Materials, 30 (2020) 2002124 DOI: [10.1002/adfm.202002124](https://doi.org/10.1002/adfm.202002124)
47. E. Kecsenvity, S. Kochevedu, K. Horváth, JP Liu, Á. Gali, C. Janáky: **Solar photoelectroreduction of nitrate ions on PbI<sub>2</sub>/CuI nanocomposite electrodes**  
Solar RRL, 5 (2021) 2000418 DOI: [10.1002/solr.202000418](https://doi.org/10.1002/solr.202000418)
48. G.F. Samu, C. Janáky: **Photocorrosion at irradiated perovskite/electrolyte interfaces**  
Journal of the American Chemical Society, 142 (2020) 21595–21614 DOI: [10.1021/jacs.0c10348](https://doi.org/10.1021/jacs.0c10348)
49. Hye Won Jeong, Wu Haihua, G. F. Samu, P. Rouster, I. Szilágyi, Hyunwoong Park, C. Janáky: **Morphology-dependent photoelectrochemical behavior of nanostructured TiO<sub>2</sub> films**  
Electrochimica Acta, 373 (2021) 137900 DOI: [10.1016/j.electacta.2021.137900](https://doi.org/10.1016/j.electacta.2021.137900)
50. P.S. Tóth, G. Szabó, C. Janáky: **Structural Features Dictate the Photoelectrochemical Activities of Two-Dimensional MoSe<sub>2</sub> and WSe<sub>2</sub> Nanostructures**  
Journal of Physical Chemistry C, 125 (2021) 7701–7710 DOI: [10.1021/acs.jpcc.1c01265](https://doi.org/10.1021/acs.jpcc.1c01265)
51. B. Endrődi, A. Samu, E. Kecsenvity, T. Halmágyi, D. Sebők, C. Janáky: **Operando cathode activation with alkali metal cations allows high current density operation of water-fed zero-gap carbon dioxide electrolyzers**  
Nature Energy, 6 (2021) 439–448 DOI: [10.1038/s41560-021-00813-w](https://doi.org/10.1038/s41560-021-00813-w)
52. A. Balog, G. F. Samu, S. Peto, C. Janáky: **The Mystery of Black TiO<sub>2</sub>: Insights from Combined Surface Science and in situ Electrochemical Methods**  
ACS Materials Au, 1 (2021), 157-168 DOI: [10.1021/acsmaterialsau.1c00020](https://doi.org/10.1021/acsmaterialsau.1c00020)
53. H. W. Jeong, T. Zsigmond, G. F. Samu, C. Janáky: **Sacrificial Agent Gone Rogue – Electron Acceptor Induced Degradation of CsPbBr<sub>3</sub> Photocathodes**  
ACS Energy Letters, 7 (2022) 417–424 DOI: [10.1021/acsenergylett.1c02130](https://doi.org/10.1021/acsenergylett.1c02130)
54. E. Boutin, M. Patel, E. Kecsenvity, S. Suter, C. Janáky, S. Haussener: **Photo-electrochemical conversion of CO<sub>2</sub> under concentrated sunlight enables combining high reaction rate and efficiency**  
Advanced Energy Materials, 12 (2022) 2200585 DOI: [10.1002/aenm.202200585](https://doi.org/10.1002/aenm.202200585)
55. P.S. Tóth, G. Szabó, G. Bencsik, G.F. Samu, K. Rajeshwar, C. Janáky: **Peeling off the surface: Pt-decoration of WSe<sub>2</sub> nanoflakes results in exceptional photoelectrochemical HER activity**  
SusMat, 2 (2022) 749-760 DOI: [10.1002/sus2.86](https://doi.org/10.1002/sus2.86)

# Efficient solar photoelectrosynthesis of methanol from carbon dioxide using hybrid CuO–Cu<sub>2</sub>O semiconductor nanorod arrays†

Cite this: *Chem. Commun.*, 2013, **49**, 1297

Received 7th November 2012,  
Accepted 20th December 2012

DOI: 10.1039/c2cc38068d

www.rsc.org/chemcomm

Ghazaleh Ghadimkhani,<sup>a</sup> Norma R. de Tacconi,<sup>\*a</sup> Wilaiwan Chanmanee,<sup>a</sup> Csaba Janaky<sup>ab</sup> and Krishnan Rajeshwar<sup>\*a</sup>

**Solar photoelectrosynthesis of methanol was driven on hybrid CuO–Cu<sub>2</sub>O semiconductor nanorod arrays for the first time at potentials ~800 mV below the thermodynamic threshold value and at Faradaic efficiencies up to ~95%. The CuO–Cu<sub>2</sub>O nanorod arrays were prepared on Cu substrates by a two-step approach consisting of the initial thermal growth of CuO nanorods followed by controlled electrodeposition of p-type Cu<sub>2</sub>O crystallites on their walls. No homogeneous co-catalysts (such as pyridine, imidazole or metal cyclam complexes) were used contrasting with earlier studies on this topic using p-type semiconductor photocathodes. The roles of the core–shell nanorod electrode geometry and the copper oxide composition were established by varying the time of electrodeposition of the Cu<sub>2</sub>O phase on the CuO nanorod core surface.**

Since the pioneering report in 1978,<sup>1</sup> there have been many studies on the use of p-type semiconductors (*e.g.*, CdTe, GaP, GaAs, InP, Si, and FeS<sub>2</sub>) for driving the photoelectrochemical (PEC) reduction of CO<sub>2</sub> in aqueous media; see ref. 2–4 for reviews of this body of work. Given that CO<sub>2</sub> is a greenhouse gas, using sunlight to convert CO<sub>2</sub> to transportation fuel (such as methanol) represents a value-added approach to the simultaneous generation of alternative fuels and environmental remediation of carbon emissions from the continued use of conventional fuels. In this communication, we demonstrate that CuO–Cu<sub>2</sub>O nanorod arrays prepared on Cu substrates by a two-step thermal oxidation–electrodeposition hybrid approach can drive the efficient solar photoelectrosynthetic conversion of CO<sub>2</sub> to methanol. Importantly, unlike in previous studies on this topic,<sup>2,3</sup> no co-catalysts (such as pyridine, imidazole, or Ni cyclam<sup>2+</sup>) were used for this selective conversion process.

Selective conversion of CO<sub>2</sub> to methanol has several redeeming features especially in light of the fact that large amounts of this chemical are manufactured worldwide. For example, in the US

alone there are eighteen methanol production plants with a cumulative annual capacity of over 2.6 billion gallons.<sup>5</sup> However, the current feedstock for this production is hydrocarbon-based with a sizeable carbon footprint. Further, the high operating pressures and temperatures needed for steam reforming translate into correspondingly high capital investment and a long energy pay-back period. Therefore mild methods for producing methanol from environmentally problematic feedstocks such as CO<sub>2</sub> take on added importance.

From the active semiconductor perspective, with the exception of the last compound (pyrite) and elements such as Si and P in the listing above, all the other component elements in these semiconductors are either toxic (As, Cd) or not earth-abundant (Te, Ga, In). Selective photoconversion of CO<sub>2</sub> to methanol without the use of a co-catalyst is also not commonplace in these prior studies, and in such cases, methanol was only photogenerated at very high overpotentials. Two-electron reduction products such as CO<sup>6</sup> and formic acid<sup>7</sup> have been reported in some cases in place of the (more difficult) six-electron conversion to methanol. With the use of semiconductor *colloids* such as CdS or ZnS, photocatalytic reduction of CO<sub>2</sub> yields mostly formate and/or formaldehyde as the products.<sup>8</sup>

Copper oxide exists as a compound semiconductor in two different metal oxidation states, Cu<sub>2</sub>O and CuO; these two compounds have energy band-gaps of ~2.0–2.2 eV and 1.3–1.6 eV respectively.<sup>9</sup> Additionally both oxides have high absorption coefficients over a substantial portion of the solar spectrum and importantly, from a sustainability and toxicity perspective, the component elements are plentiful and relatively less toxic than elements such as Cd or As. The conduction band edge positions lie at very negative potentials (relative to other oxides such as TiO<sub>2</sub> and WO<sub>3</sub>)<sup>10,11</sup> translating into high reducing power for the photogenerated electrons. Given all these favorable attributes and the fact that copper and its oxides have shown high *electrocatalytic* activity for CO<sub>2</sub> reduction,<sup>12–14</sup> it is rather surprising that there are no reports (at least to our knowledge) for the use of copper oxide for the *photoreduction* of CO<sub>2</sub>. On the other hand there are several reports on the utilization of both Cu<sub>2</sub>O and CuO for the

<sup>a</sup> Department of Chemistry and Biochemistry, The University of Texas at Arlington, Arlington, Texas 76019-0065, USA. E-mail: rajeshwar@uta.edu, ntacconi@uta.edu

<sup>b</sup> Department of Physical Chemistry and Materials Science, University of Szeged, Szeged, H6720, Hungary

† Electronic supplementary information (ESI) available. See DOI: 10.1039/c2cc38068d

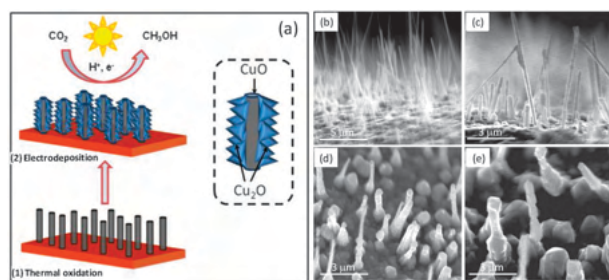


photogeneration of H<sub>2</sub> from water<sup>11,15,16</sup> and very recently, virus-templated CuO “3-D nanorod arrays” were demonstrated<sup>17</sup> to afford high photocurrent densities.

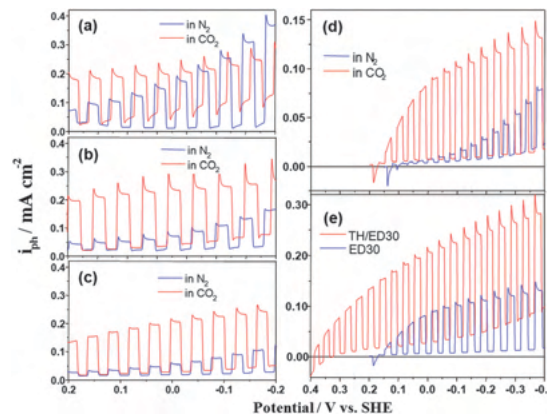
For the preparation of the hybrid CuO–Cu<sub>2</sub>O photocathodes, CuO nanorod arrays were first prepared following a thermal procedure.<sup>18</sup> Cathodic electrodeposition of Cu<sub>2</sub>O was then performed on CuO nanorod arrays from a copper(II) lactate bath.<sup>11,19</sup> The data below thus correspond to electrodeposited Cu<sub>2</sub>O nanocrystallites on CuO nanorods (~100 nm diameter) thermally grown on copper substrates. The electrodeposition was performed at –0.2 V vs. SHE in 0.4 M CuSO<sub>4</sub> + 3 M lactic acid, pH 9 at 60 °C for pre-selected time periods. Electrodes are designated as TH for the thermally grown CuO nanorods, and TH/ED $\tau$  for the CuO–Cu<sub>2</sub>O hybrid samples prepared by electrodeposition for  $\tau$  min ( $\tau$  spanning the range: 1–30 min) on the CuO nanorod surface (see Table S1, ESI<sup>†</sup>). The large area associated with the CuO nanorods provides a surface aspect ratio enhancement factor of 7–8 depending on the electro-synthesis time (Fig. S1, ESI<sup>†</sup>). This morphological factor is the key to the performance of the Cu<sub>2</sub>O–CuO nanorod array photoelectrodes.

Fig. 1a contains a visual representation of the CuO–Cu<sub>2</sub>O nanostructures developed for this study. Fig. 1b–e presents representative SEM pictures for the evolution of the CuO–Cu<sub>2</sub>O nanorods from the starting morphology consisting of thermally grown CuO nanorods (Fig. 1b) to progressively covered CuO–Cu<sub>2</sub>O nanostructures as the Cu<sub>2</sub>O electrodeposition time,  $\tau$ , increased in the sequence: 1 min (Fig. 1c), 10 min (Fig. 1d), and 30 min (Fig. 1e) respectively. By adjusting the  $\tau$  values, the Cu<sub>2</sub>O shell thickness on CuO nanorods was varied between *ca.* 100 and 500 nm, although the resulting CuO–Cu<sub>2</sub>O nanorods were found to be thicker at their bases which is suggestive of a bottom-up growth process for Cu<sub>2</sub>O nanocrystallites.

The photoelectroactivity of selected CuO–Cu<sub>2</sub>O nanorod electrodes is compared in Fig. 2 under chopped AM 1.5 illumination in a 0.1 M Na<sub>2</sub>SO<sub>4</sub> solution for both N<sub>2</sub> and CO<sub>2</sub> saturated conditions. Photocurrent profiles for CuO–Cu<sub>2</sub>O nanorod electrodes, TH/ED10 and TH/ED30, are provided in Fig. 2b and c respectively; the corresponding profile for a thermally prepared photoelectrode (TH, Fig. 2a) is also



**Fig. 1** Schematic illustration of the two-step synthesis of CuO–Cu<sub>2</sub>O hybrid nanorod arrays for solar photoelectrosynthesis of CH<sub>3</sub>OH from CO<sub>2</sub>: (1) thermal growth of CuO nanorods on a Cu foil and (2) cathodic electrodeposition of Cu<sub>2</sub>O for selected time periods from a cupric lactate solution, pH 9 (a). Morphology/composition of a CuO–Cu<sub>2</sub>O nanorod is sketched on the right side of panel (a). SEM images of thermally grown CuO nanorods before (b) and after Cu<sub>2</sub>O electrodeposition on them for 1 (c), 10 (d) and 30 min (e) respectively.



**Fig. 2** Comparison of photocurrent–potential profiles of CuO–Cu<sub>2</sub>O hybrid nanorod arrays obtained with manually-chopped simulated AM 1.5 illumination (70 mW cm<sup>–2</sup>) in 0.1 M Na<sub>2</sub>SO<sub>4</sub> aqueous solution for Cu<sub>2</sub>O electrodeposition times of 0 (TH, a), 10 (TH/ED10, b) and 30 min (TH/ED30, c). Panel d: comparison of PEC activity for the electrodeposited (ED30) Cu<sub>2</sub>O electrode in N<sub>2</sub> and CO<sub>2</sub> saturated solutions. Panel e: comparison of a CuO–Cu<sub>2</sub>O hybrid nanorod film vs. the electrodeposited Cu<sub>2</sub>O electrode in CO<sub>2</sub>-saturated 0.1 M Na<sub>2</sub>SO<sub>4</sub> aqueous solution.

included for comparison. In a N<sub>2</sub> atmosphere, the photocurrent is associated with H<sub>2</sub> photogeneration from water (blue traces in Fig. 2a–c) and we have included these data only for comparative purposes. Importantly, in the CO<sub>2</sub> saturated electrolyte, the photocurrent transients for CuO–Cu<sub>2</sub>O nanorod films are seen to reach ~3 times higher values than in the N<sub>2</sub>-saturated counterpart solution (red traces in Fig. 2b and c). Of all the hybrid CuO–Cu<sub>2</sub>O samples, the TH/ED10 was found to be the best performing for the photoelectroreduction of CO<sub>2</sub>. It is worth noting that for PEC generation of H<sub>2</sub> on the other hand, the thermal film performs the best but at more negative applied potentials (Fig. 2a). For CO<sub>2</sub> photoelectrochemical reduction, the TH films yielded lower photocurrent than any of the TH/ED $\tau$  ( $\tau$  varied between 1 and 30 min) hybrid counterparts.

To further clarify the particular contribution of the two components in the CuO–Cu<sub>2</sub>O nanorod arrays for the photoelectroreduction of CO<sub>2</sub>, Fig. 2d compares photocurrent–potential profiles of a Cu<sub>2</sub>O electrodeposited film (prepared on a polished Cu foil as a substrate) in N<sub>2</sub>- and CO<sub>2</sub>-saturated 0.1 M Na<sub>2</sub>SO<sub>4</sub> solutions. The Cu<sub>2</sub>O film showed a dramatic increase of photocurrent transients in the presence of CO<sub>2</sub> and also a positive shift of the photocurrent onset potential threshold. At –0.25 V vs. SHE, the photocurrent in CO<sub>2</sub> solution was *ca.* 3.2 times higher than in N<sub>2</sub>. At less negative potentials the photocurrent enhancement in the presence of CO<sub>2</sub> was much higher reaching factors of 6–7 at potentials ~–0.1 V thus indicating that CO<sub>2</sub> is a much better electron scavenger (capturing the photoelectrons from Cu<sub>2</sub>O) than water. The comparison of TH/ED30 with ED30 in Fig. 2e sheds important light on the role of the CuO interior core. Observe that throughout the potential range in Fig. 2e, the CuO–Cu<sub>2</sub>O hybrid outperformed the electrodeposited ED30 control sample.

The photocurrent onset potential threshold was ~0.25 V more positive for the CuO–Cu<sub>2</sub>O hybrid than the Cu<sub>2</sub>O ED

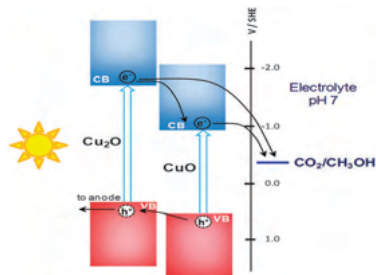


**Fig. 3** Energy band diagram of hybrid CuO–Cu<sub>2</sub>O nanorod arrays for solar photoelectrosynthesis of CH<sub>3</sub>OH from CO<sub>2</sub>. Semiconductor band edges and redox potentials are shown vs. the SHE ref. electrode. CB: conduction band; VB: valence band.

sample (Fig. 2e). This represents an  $\sim 800$  mV shift relative to the standard potential of the CO<sub>2</sub>/CH<sub>3</sub>OH redox couple. Such lowering of the onset potential for CO<sub>2</sub> photoconversion is associated with the CuO component and is unprecedented at least to our knowledge. Photoelectrosynthesis of CH<sub>3</sub>OH was demonstrated with a TH/ED10 CuO–Cu<sub>2</sub>O nanorod photoelectrode (Fig. S2, ESI<sup>†</sup>). The photoelectrode was placed in an aqueous solution saturated with CO<sub>2</sub>, polarized at  $-0.2$  V vs. SHE, and irradiated with visible light provided by a AM 1.5 solar simulator. A gas chromatograph equipped with a mass spectrometer (GC-MS) was used to detect methanol. Methanol photogeneration was monitored at  $m/z = 31$  (CH<sub>2</sub>OH<sup>+</sup>) and was found to reach a concentration of ca. 85  $\mu$ M after 90 min of irradiation. Faradaic efficiencies were in the 94–96% range (considering that 6e<sup>−</sup> are required to form one molecule of CH<sub>3</sub>OH from CO<sub>2</sub>). Note that a potential of  $-0.2$  V vs. SHE represents an “underpotential” greater than at least 150 mV given that the standard potential for the CO<sub>2</sub>/CH<sub>3</sub>OH redox process lies at  $-0.38$  V vs. SHE (see Fig. 3).

X-ray diffraction data corroborate that the photoactive CuO–Cu<sub>2</sub>O nanorods remain intact after a 2 hour photoelectrolysis run (Fig. S2 and S3, ESI<sup>†</sup>). The photogenerated electrons presumably are rapidly transferred to CO<sub>2</sub> before they have an opportunity to substantially photoreduce Cu(I) or Cu(II) in the oxides to the metallic state. The photocurrent–time profile over the 2 h timeframe (Fig. S2, ESI<sup>†</sup>) is also diagnostic of possible slow *self-repair* or *self-healing* of the photocathode assembly as the oxide phases are *regenerated* when the photoelectrons exit the interfacial phase boundary to CO<sub>2</sub>.

The photoreduction of CO<sub>2</sub> to methanol is supported by the band-edge positions of both oxides as depicted in the hypothetical diagram in Fig. 3. Note that the valence band edge of CuO is located at a more positive potential than the corresponding level in Cu<sub>2</sub>O in full agreement with the photocurrent–potential response of a CuO–Cu<sub>2</sub>O hybrid nanorod electrode and that of a single Cu<sub>2</sub>O film (Fig. 2e). Therefore, in a Cu<sub>2</sub>O–CuO core–shell nanorod configuration, the differences in the band edges of the two oxides facilitate the transfer of photogenerated electrons from the Cu<sub>2</sub>O shell to the CuO core. As the Cu<sub>2</sub>O shell is also in contact with the electrolyte, the photogenerated electrons in Cu<sub>2</sub>O are also able to be directly transferred to CO<sub>2</sub> as indicated in Fig. 3. This double pathway for injection of

photoelectrons into CO<sub>2</sub> is likely contributing to the enhanced photoelectrochemical performance of CuO–Cu<sub>2</sub>O nanorod arrays relative to a single Cu<sub>2</sub>O film. An added (morphological) factor is the increased surface area of the CuO–Cu<sub>2</sub>O with respect to a compact Cu<sub>2</sub>O ED film. Importantly note that, to sustain the double injection pathway, the tip of the CuO core has to be in contact with the electrolyte.

In summary, a simple two-step hybrid thermal growth/electrodeposition approach has been employed to prepare and optimize solar photoactive CuO–Cu<sub>2</sub>O nanorod arrays for the photoelectrosynthesis of methanol from CO<sub>2</sub>. Methanol photogeneration was confirmed by GC-MS analyses of product evolved at  $-0.2$  V vs. SHE, *i.e.* at an *underpotential* relative to the standard potential of CO<sub>2</sub>/CH<sub>3</sub>OH. This last feature is an important virtue of the p-type semiconductor based photo-reduction approach as adopted in this study and by other authors<sup>2–4</sup> previously. In contrast the (“dark”) electrocatalytic process counterpart for CO<sub>2</sub> reduction suffers from the electrical energy cost incurred from the need for considerable *overpotentials* to overcome the kinetic barrier associated with this process.<sup>12,14</sup> This cost is simply circumvented in the solar PEC process from the energy inherent in sunlight.

## Notes and references

- M. Halmann, *Nature*, 1978, **275**, 115.
- E. Barton Cole and A. B. Bocarsly, Photochemical, Electrochemical, and Photoelectrochemical Reduction of Carbon Dioxide, in *Carbon Dioxide as Chemical Feedstock*, ed. M. Aresta, Wiley-VCH, 2010, ch. 11.
- B. Kumar, M. Llorente, J. Froelich, T. Dang, A. Sathrum and C. P. Kubiak, *Annu. Rev. Phys. Chem.*, 2012, **63**, 541.
- D. J. Boston, K.-L. Huang, N. R. de Tacconi, F. M. MacDonnell and K. Rajeshwar, Electro- and Photocatalytic Reduction of CO<sub>2</sub>: The Homogeneous and Heterogeneous Worlds Collide? in *Photoelectrochemical Water Splitting Challenges and New Perspectives*, ed. H.-J. Lewerenz and L. M. Peter, RSC Press, 2013.
- (a) <http://www.ttmethanol.com/web/methprocess.html>; (b) <http://www.hpiprojectmanagers.net/methanol>; (c) <http://www.iags.org/methanolsources.htm>.
- B. Kumar, J. M. Smicja and C. P. Kubiak, *J. Phys. Chem. C*, 2010, **114**, 14220.
- H. Yoneyama, K. Sugimura and S. Kuwabata, *J. Electroanal. Chem.*, 1988, **249**, 143.
- B. R. Eggins, P. K. J. Robertson, E. P. Murphy, E. Woods and J. T. S. Irvine, *J. Photochem. Photobiol., A*, 1998, **118**, 31. See also references therein.
- K. Nakaoka, J. Ueyama and K. Ogura, *J. Electrochem. Soc.*, 2004, **151**, C661.
- Y. Hori, K. Kikuchi and S. Susuki, *Chem. Lett.*, 1985, 1695.
- S. Somasundaram, C. R. Chenthamarakshan, N. R. de Tacconi and K. Rajeshwar, *Int. J. Hydrogen Energy*, 2007, **32**, 4661.
- For example: Y. Hori, Electrochemical CO<sub>2</sub> Reduction on Metal Electrodes, in *Modern Aspects of Electrochemistry No. 42*, ed. C. G. Vayenas and R. E. White, Springer, New York, 2008, ch. 3.
- M. Le, M. Ren, Z. Zhang, P. T. Sprunger, R. L. Kurtz and J. C. Flake, *J. Electrochem. Soc.*, 2011, **158**, E45.
- C. W. Li and M. W. Kanan, *J. Am. Chem. Soc.*, 2012, **134**, 7231.
- (a) A. Paracchino, V. Laporte, K. Sivula, M. Gratzel and E. Thimsen, *Nat. Mater.*, 2011, **10**, 456; (b) A. Paracchino, J. C. Brauer, J.-E. Moser, E. Thimsen and M. Gratzel, *J. Phys. Chem. C*, 2012, **116**, 7341.
- Z. Zhang and P. Wang, *J. Mater. Chem.*, 2012, **22**, 2456.
- C.-Y. Chiang, J. Epstein, A. Brown, J. N. Munday, J. N. Culver and S. Ehrman, *Nano Lett.*, 2012, **12**, 6005.
- X. Jiang, T. Herricks and Y. Xia, *Nano Lett.*, 2002, **2**, 1333.
- L. C. Wang, N. R. de Tacconi, C. R. Chenthamarakshan, K. Rajeshwar and M. Tao, *Thin Solid Films*, 2007, **515**, 3090.

# Excellence in Chemistry Research

## Announcing our new flagship journal

- Gold Open Access
- Publishing charges waived
- Preprints welcome
- Edited by active scientists



## Meet the Editors of *ChemistryEurope*



**Luisa De Cola**

Università degli Studi  
di Milano Statale, Italy



**Ive Hermans**

University of  
Wisconsin-Madison, USA



**Ken Tanaka**

Tokyo Institute of  
Technology, Japan

DOI: 10.1002/cphc.201300080

# Tailoring Copper Oxide Semiconductor Nanorod Arrays for Photoelectrochemical Reduction of Carbon Dioxide to Methanol

Krishnan Rajeshwar,<sup>\*[a, b]</sup> Norma R. de Tacconi,<sup>\*[a, b]</sup> Ghazaleh Ghadimkhani,<sup>[b]</sup>  
Wilaiwan Chanmanee,<sup>[a, b]</sup> and Csaba Janáky<sup>[b, c]</sup>

Solar photoelectrochemical reduction of carbon dioxide to methanol in aqueous media was driven on hybrid CuO/Cu<sub>2</sub>O semiconductor nanorod arrays for the first time. A two-step synthesis was designed and demonstrated for the preparation of these hybrid copper oxide one-dimensional nanostructures on copper substrates. The first step consisted in the growth of CuO nanorods by thermal oxidation of a copper foil at 400 °C. In the second step, controlled electrodeposition of *p*-type Cu<sub>2</sub>O crystallites on the CuO walls was performed. The resulting nanorod morphology with controllable wall thickness by adjusting the Cu<sub>2</sub>O electrodeposition time as well as their surface/bulk chemical composition were probed by scanning elec-

tron microscopy, X-ray diffraction and Raman spectroscopy. Photoelectrosynthesis of methanol from carbon dioxide was demonstrated at -0.2 V vs SHE under simulated AM1.5 solar irradiation on optimized hybrid CuO/Cu<sub>2</sub>O nanorod electrodes and without assistance of any homogeneous catalyst (such as pyridine or imidazole) in the electrolyte. The hybrid composition, ensuring double pathway for photoelectron injection to CO<sub>2</sub>, along with high surface area were found to be crucial for efficient performance in methanol generation under solar illumination. Methanol formation, tracked by gas chromatography/mass spectrometry, indicated Faradaic efficiencies of ~95%.

## 1. Introduction

This Full Paper is an elaboration of the results contained in our recent Communication on the efficient solar photoelectrosynthesis of methanol from carbon dioxide (CO<sub>2</sub>) using hybrid CuO/Cu<sub>2</sub>O semiconductor nanorod arrays.<sup>[1]</sup> Copper oxide exists as a compound semiconductor in two different metal oxidation states, Cu<sub>2</sub>O and CuO; these two compounds have energy band-gaps of ~2.0–2.2 eV and 1.3–1.6 eV, respectively.<sup>[2]</sup> Additionally both oxides have high absorption coefficients over a substantial portion of the solar spectrum and importantly, from a sustainability and toxicity perspective, the component elements are plentiful and relatively less toxic than elements such as Cd or As, which are present in other compound semiconductors such as GaAs and CdTe. The conduction band edge positions lie at very negative potentials (relative to other oxides such as TiO<sub>2</sub> and WO<sub>3</sub>)<sup>[3,4]</sup> translating to high reducing power for the photogenerated electrons. These photoelectrons have been utilized for the photogeneration of H<sub>2</sub> from water using both Cu<sub>2</sub>O and CuO.<sup>[4–6]</sup> Recently, both nanowires and

nanorod arrays of these oxides were demonstrated to afford high photocurrent densities for water reduction.<sup>[7,8]</sup> Given all these favorable attributes and the fact that copper and its oxides have shown high electrocatalytic activity for CO<sub>2</sub> reduction,<sup>[9–11]</sup> it is rather surprising that, prior to our communication,<sup>[1]</sup> there were no reports (at least to our knowledge) for the use of copper oxide for the photoreduction of CO<sub>2</sub>. However, semiconductor colloids such as CdS and ZnS have been used by previous authors for the photocatalytic reduction of CO<sub>2</sub>.<sup>[12]</sup> The products in these cases are mostly formate and/or formaldehyde. Selective photoconversion of CO<sub>2</sub> to methanol without the use of a co-catalyst<sup>[13–15]</sup> also is not commonplace in these prior studies, and in the isolated such cases, methanol was only photogenerated at very high overpotentials. Two-electron reduction products such as CO<sup>[16]</sup> and formic acid<sup>[17]</sup> have been reported in some cases in place of the (more difficult) six-electron conversion to methanol. Given that CO<sub>2</sub> is a greenhouse gas, using sunlight to convert CO<sub>2</sub> to transportation fuel (such as methanol) represents a value-added approach to the simultaneous generation of alternative fuels and environmental remediation of carbon emissions from the continued use of conventional fuels.

As briefly presented in our earlier Communication,<sup>[1]</sup> and now further elaborated in this Full Paper with more data, we show below that both morphology and composition in samples derived from our hybrid, two-step thermal oxidation/electrodeposition scheme, are crucial for affording very efficient photoelectrochemical reduction of CO<sub>2</sub> to methanol. Specifically the CuO core/Cu<sub>2</sub>O shell geometry and composition in our

[a] Prof. K. Rajeshwar, Dr. N. R. de Tacconi, Dr. W. Chanmanee  
Center for Renewable Energy Science & Technology (CREST)  
University of Texas at Arlington, Arlington, TX 76019 (USA)  
E-mail: rajeshwar@uta.edu  
ntacconi@uta.edu

[b] Prof. K. Rajeshwar, Dr. N. R. de Tacconi, G. Ghadimkhani,  
Dr. W. Chanmanee, Dr. C. Janáky  
Department of Chemistry & Biochemistry  
University of Texas at Arlington, Arlington, TX 76019 (USA)

[c] Dr. C. Janáky  
Department of Physical Chemistry and Materials Science  
University of Szeged, Szeged, Aradi Sq. 1, H6720 (Hungary)

one-dimensional nanostructures facilitate charge separation across the radial dimension, and subsequent facile transport through the core in the longitudinal direction.

## 2. Results and Discussion

### 2.1. Preparation and Physical Characterization of Hybrid CuO/Cu<sub>2</sub>O Nanorod Arrays

A schematic representation of the preparation of hybrid CuO/Cu<sub>2</sub>O photocathodes is shown in Figure 1. The first step consists of the formation of CuO nanorod arrays obtained by a thermal procedure.<sup>[18]</sup> The second step is the cathodic electrodeposition of Cu<sub>2</sub>O<sup>[4,19]</sup> on CuO nanorod arrays at  $-0.2$  V versus SHE in  $0.4$  M CuSO<sub>4</sub> +  $3$  M lactic acid, pH 9 at  $60$  °C for pre-selected time periods. The resulting photoelectrode samples are designated as TH for the thermally grown CuO nanorods, and TH/ED $\tau$  for the CuO/Cu<sub>2</sub>O hybrid samples prepared by electrodeposition for  $\tau$  min ( $\tau$  spanning the range: 1–30 min) on the CuO nanorod surface. Table 1 provides the nomenclature used to identify the different CuO/Cu<sub>2</sub>O nanorod arrays

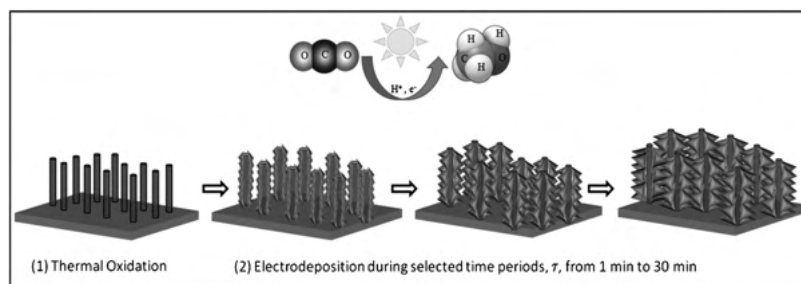


**Figure 1.** Schematic illustration of the two-step synthesis of CuO/Cu<sub>2</sub>O hybrid nanorod arrays for solar photoelectrosynthesis of CH<sub>3</sub>OH from CO<sub>2</sub>: 1) thermal growth of CuO nanorods on a Cu foil and 2) cathodic electrodeposition of Cu<sub>2</sub>O for selected time periods using a pH 9 cupric lactate solution as electrolyte. The figure also includes a sketch of the solar conversion of CO<sub>2</sub> to CH<sub>3</sub>OH.

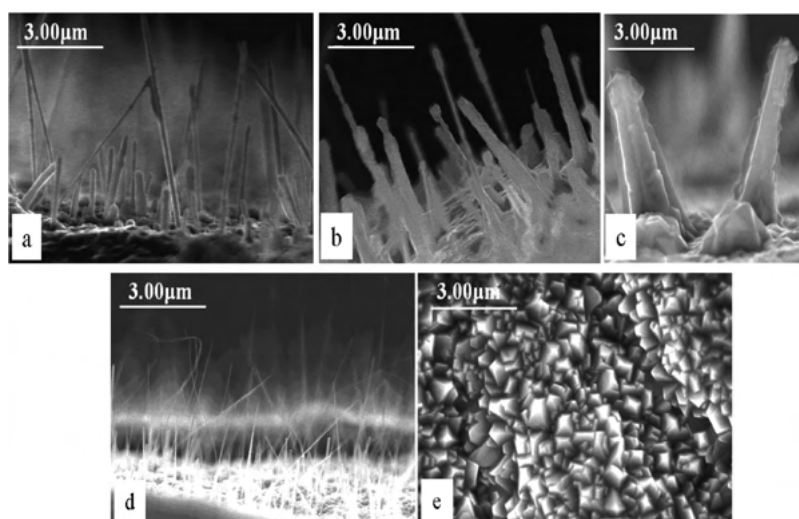


**Figure 2.** SEM images of CuO/Cu<sub>2</sub>O hybrid nanorod arrays obtained by a Cu<sub>2</sub>O electrodeposition coating on thermally grown CuO nanorods for 1 (a), 10 (b) and 30 min (c), respectively. Thermally grown CuO nanorods (indicated as TH) were used as substrate for the preparation of the respective hybrids (d). Electrodeposited Cu<sub>2</sub>O (indicated as ED) on Cu foil without a pre-thermal treatment is included for comparison (e). In all cases, CuO nanorods were grown isothermally ( $400$  °C,  $4$  h) on Cu substrates and Cu<sub>2</sub>O electrodeposition was always performed at  $-0.20$  V (vs. SHE) using an aqueous solution containing  $0.4$  M CuSO<sub>4</sub> and  $3$  M lactic acid adjusted to pH 9.

Photoelectrode name	1) Thermal oxidation (TH)	2) Electrodeposition of Cu <sub>2</sub> O (ED) for selected periods of time
TH/ED1	Cu foil heated at $400$ °C, $4$ h	Cu <sub>2</sub> O electrodeposited for 1 min
TH/ED5	Cu foil heated at $400$ °C, $4$ h	Cu <sub>2</sub> O electrodeposited for 5 min
TH/ED10	Cu foil heated at $400$ °C, $4$ h	Cu <sub>2</sub> O electrodeposited for 10 min
TH/ED15	Cu foil heated at $400$ °C, $4$ h	Cu <sub>2</sub> O electrodeposited for 15 min
TH/ED25	Cu foil heated at $400$ °C, $4$ h	Cu <sub>2</sub> O electrodeposited for 25 min
TH/ED30	Cu foil heated at $400$ °C, $4$ h	Cu <sub>2</sub> O electrodeposited for 30 min
TH	Cu foil heated at $400$ °C, $4$ h	N/A
ED30	N/A	Cu <sub>2</sub> O electrodeposited for 30 min

and their respective preparation conditions. Representative SEM images of the resulting CuO/Cu<sub>2</sub>O hybrid samples prepared with different electrodeposition time  $\tau$  are shown in Figure 2a–c. Corresponding images for the thermally grown free-standing CuO nanorods (designated as “TH”) are presented in Figure 2d, while the morphology of an electrodeposited Cu<sub>2</sub>O sample on a polished Cu substrate (“ED”) is given in Figure 2e for comparison. The average nanorod diameter is in the range:  $0.8$ – $1.0$   $\mu$ m for TH/ED10 and  $1.5$ – $2.0$   $\mu$ m for TH/ED30.

The electrodeposition of Cu<sub>2</sub>O on the Cu substrate without and with previous thermal growth of CuO nanorods shows a remarkable difference in the resulting amount of Cu<sub>2</sub>O electrochemically formed (Figure 3). When the CuO nanorods are thermally pre-formed underneath, much more Cu<sub>2</sub>O is seen to be electrodeposited (Figure 3). This trend is attributable to the much larger surface area of the nanorod array electrode relative to that of a polished Cu substrate. Thus Figure 3 compares the charge evolution associated with Cu<sub>2</sub>O electrodeposition

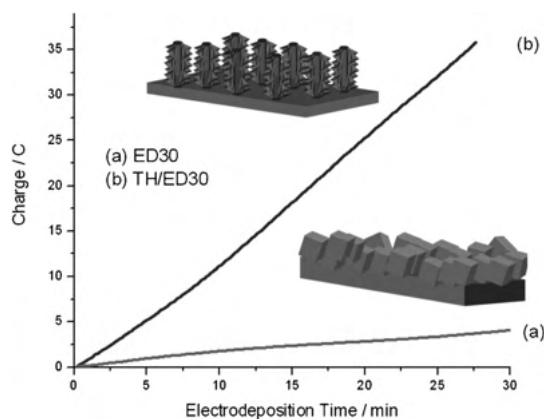


**Figure 3.** Charge evolution during 30 min electrodeposition of  $\text{Cu}_2\text{O}$  on freshly polished Cu foil (ED30) and on thermally oxidized Cu foil (TH/ED30) at  $-0.20$  V (vs. SHE) using a solution containing  $0.4$  M  $\text{CuSO}_4$  and  $3$  M lactic acid adjusted to pH 9. Sketches are included to clarify the two contrasting substrates over which the  $\text{Cu}_2\text{O}$  electrodeposition was performed.

( $\tau=30$  min) on the two contrasting substrates: nanorods versus a flat surface. Note that the electrodeposition charge varies almost linearly with time for both substrates. The morphology of the resulting films is shown in Figure 2c,e, and a schematic representation of the two resulting films is included also in Figure 3. The large area associated with the CuO nanorods provides a surface aspect ratio enhancement factor of 7–8. This morphological factor will be seen to play a key role in the performance of the  $\text{Cu}_2\text{O}/\text{CuO}$  nanorod array photoelectrodes (see below).

The data in Figure 3 clearly indicate that  $\text{Cu}_2\text{O}$  is able to be continuously electrodeposited on the TH film in spite of its semiconductor nature (i.e., CuO is a p-type semiconductor). It is worth recalling that the electrodeposition mechanism of  $\text{Cu}_2\text{O}$  has been reported to hinge on the presence of surface states in the  $\text{Cu}_2\text{O}$  band gap. These surface states are presumed to mediate hole transfer from the  $\text{Cu}^{\text{II}}$  lactate complex to the  $\text{Cu}_2\text{O}$  valence band.<sup>[4,19]</sup> As the CuO nanorods are vertically situated on a dense film of  $\text{Cu}_2\text{O}$ , it can be speculated that electrodeposition on the nanorod surface is initiated bottom-up on the dense  $\text{Cu}_2\text{O}$  layer formed thermally.<sup>[18]</sup> It subsequently advances by progressive upward creep on the CuO nanorods. Evidence may be found in Figure 2 where the diameter of the CuO/ $\text{Cu}_2\text{O}$  nanorods is seen to decrease from bottom to top, consistent with a bottom-up growth mode.

XRD and Raman characterizations of selected copper oxide films are shown in Figures 4 and 5, respectively. Comparison of the XRD patterns for TH, ED30 and TH/ED30 samples is provided in Figure 4. The JCPDS reference patterns for CuO (80-1917),  $\text{Cu}_2\text{O}$  (78-2076) and Cu (04-0836) are also provided in the figure. The thermal film (Figure 4a) is seen to show the underneath Cu substrate as well as CuO and  $\text{Cu}_2\text{O}$  phases. In fact, the pattern is consistent with a dense  $\text{Cu}_2\text{O}$  film topped with CuO nanorods. During thermal oxidation, a dense  $\text{Cu}_2\text{O}$  surface layer is presumably formed first on the Cu foil. It is then oxidized to CuO leading to a compressive stress that drives outward the diffusion of copper cations along the grain bounda-

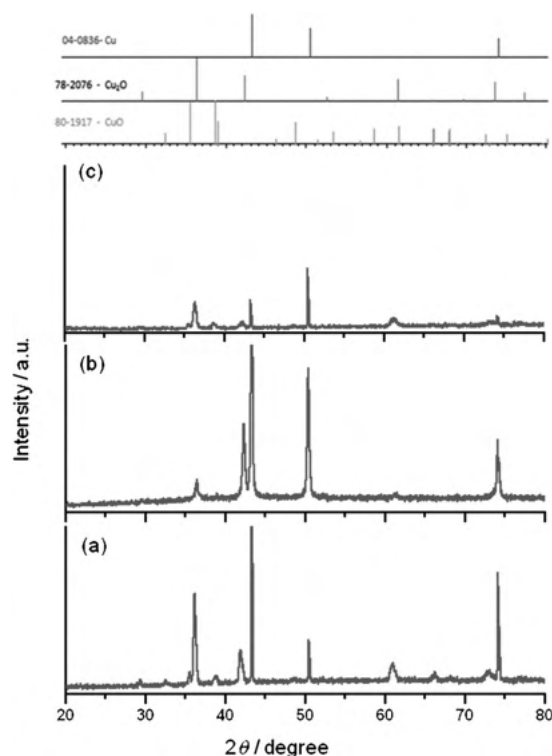


**Figure 4.** XRD spectra of a thermally oxidized [TH, (a)], an electrochemically deposited [ED30, (b)] and a hybrid film [TH/ED30, (c)]. Reference JCPDS patterns for Cu,  $\text{Cu}_2\text{O}$  and CuO are shown at the top of the figure.

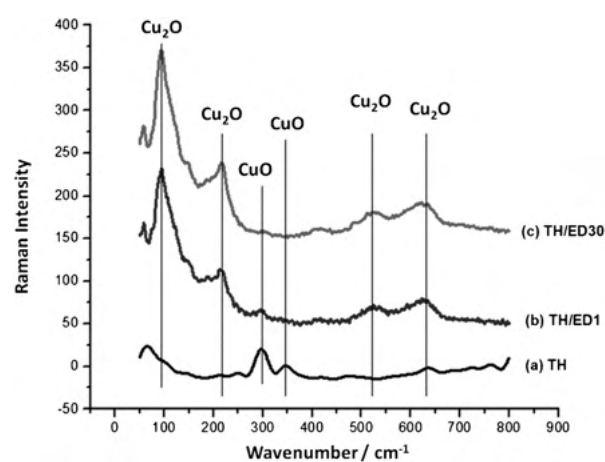


**Figure 5.** Comparison of Raman spectra of thermally oxidized film (a), a hybrid film with cathodic electrodeposition for 1 min (b), and a hybrid film with cathodic electrodeposition for 30 min (c). The nomenclature in the figure legend is that of Table 1.

ries<sup>[18]</sup> thus resulting in CuO nanorod formation. The XRD pattern of an ED30 film shows contributions from  $\text{Cu}_2\text{O}$  on the Cu substrate as expected (Figure 4b) while the TH/ED30 presents three components,  $\text{Cu}_2\text{O}$ , CuO and Cu, although now the  $\text{Cu}_2\text{O}$  phase makes a larger contribution than in the TH film case (Figure 4c). It is worth noting that the Cu signals are seen higher in the pattern for the ED30 sample than in the other two films corroborating that thermal treatment results in

a thick film composed of  $\text{Cu}_2\text{O}$  and  $\text{CuO}$  on which the  $\text{CuO}/\text{Cu}_2\text{O}$  core/shell nanorods are formed.

Figure 5 contains a comparison of Raman spectra of hybrid  $\text{CuO}/\text{Cu}_2\text{O}$  nanorod arrays with that of the thermal precursor film, TH. The assignment of the characteristic Raman peaks for  $\text{Cu}_2\text{O}$  and  $\text{CuO}$ <sup>[20–22]</sup> are also indicated. Observe that the Raman peaks for the TH film are mainly dominated by the contribution of the  $\text{CuO}$  nanorod phase with only minor input from the dense  $\text{Cu}_2\text{O}$  underlayer (Figure 5a). The progressive contribution of vibrations associated with the  $\text{Cu}_2\text{O}$  crystalline structure are clearly seen for TH/ED1 (Figure 5b) and TH/ED30 (Figure 5c) as the shell thickness increases with electrodeposition time. Concomitantly, the phonon peaks due to  $\text{CuO}$  practically disappear in the TH/ED30 film. Therefore, both XRD and Raman data corroborate that the  $\text{CuO}$  nanorods are progressively covered by  $\text{Cu}_2\text{O}$  crystallites in the hybrid samples (Figures 4 and 5).

## 2.2. Photoelectrochemical Performance of Hybrid $\text{CuO}/\text{Cu}_2\text{O}$ Photocathode Samples

Figure 6 compares photocurrent/potential profiles for a TH/ED30 hybrid nanorod film (a) and an electrodeposited ED30 electrode (b) in  $\text{CO}_2$ -saturated 0.1 M  $\text{Na}_2\text{SO}_4$  aqueous solution. The corresponding profile for an electrodeposited  $\text{Cu}_2\text{O}$  sample (ED30) in  $\text{N}_2$ -saturated solution under the same conditions is also included as control (c). The comparison of TH/ED30 (a) with ED30 (b) sheds important light on the role of the  $\text{CuO}$  interior core. Observe that throughout the potential range, the  $\text{CuO}/\text{Cu}_2\text{O}$  hybrid outperformed the electrodeposit-

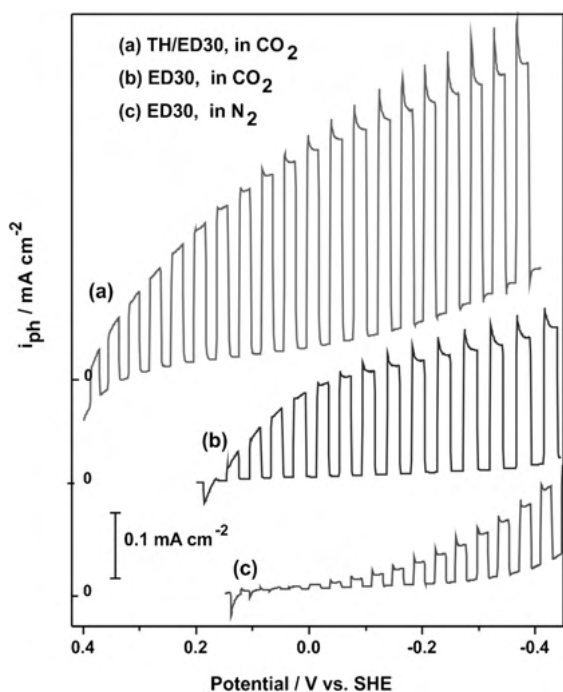


**Figure 6.** Comparison of PEC activity for TH/ED30 hybrid nanorod film (a) versus an electrodeposited ED30 electrode (b) in  $\text{CO}_2$ -saturated 0.1 M  $\text{Na}_2\text{SO}_4$  aqueous solution. The PEC activity for electrodeposited (ED30) in  $\text{N}_2$ -saturated solution (c) is also included for comparison.

ed ED30 control sample. Equally important is the fact that the photocurrent onset potential threshold was  $\sim 0.25$  V more positive for the  $\text{CuO}/\text{Cu}_2\text{O}$  hybrid than the  $\text{Cu}_2\text{O}$  ED sample. The presence of the  $\text{CuO}$  (core) phase in the hybrid film clearly has contributed to this energetically favorable positive shift for the photoreduction reaction.

Another important trend in the data in Figure 6 is that the photocurrent/potential profiles of a  $\text{Cu}_2\text{O}$  electrodeposited film, (ED30, prepared on a polished  $\text{Cu}$  foil as substrate) showed a dramatic increase of photocurrent in the presence of  $\text{CO}_2$  and also a positive shift of the photocurrent onset potential threshold. At  $-0.25$  V vs. SHE, the photocurrent in  $\text{CO}_2$ -saturated solution was ca. 3.2 times higher than in the  $\text{N}_2$  case. At less negative potentials the photocurrent enhancement in presence of  $\text{CO}_2$  was much higher reaching factors of 6–7 at potentials  $\sim -0.1$  V thus indicating that  $\text{CO}_2$  is a much better electron scavenger (capturing the photoelectrons from  $\text{Cu}_2\text{O}$ ) than water.

The photoelectrochemical (PEC) performance of hybrid  $\text{CuO}/\text{Cu}_2\text{O}$  photocathodes prepared with different  $\tau$  (10 and 30 min) at  $-0.1$  V (vs. SHE) is compared in Figure 7 under man-

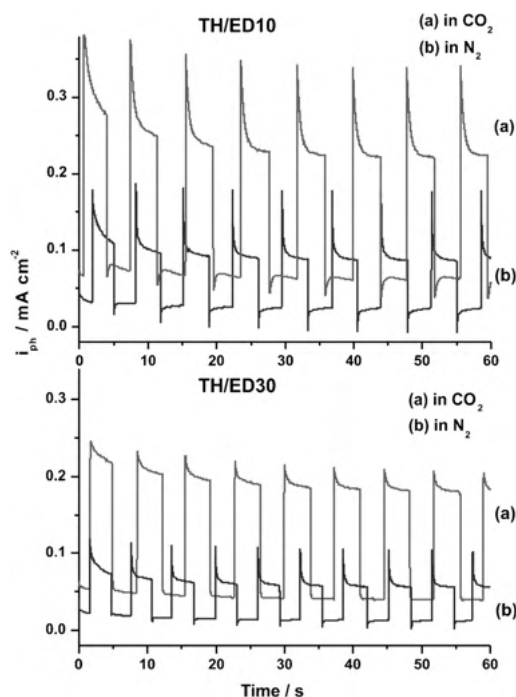


**Figure 7.** Photocurrent transients at  $-0.1$  V (vs. SHE) of  $\text{Cu}_2\text{O}/\text{CuO}$  hybrid nanorod arrays under manually-chopped simulated AM1.5 illumination ( $70 \text{ mW cm}^{-2}$ ) for TH/ED10 and TH/ED30 electrodes in  $\text{CO}_2$ - (a) and  $\text{N}_2$ -saturated (b) aqueous solution containing 0.1 M  $\text{Na}_2\text{SO}_4$  as electrolyte.

ually chopped AM1.5 simulated solar illumination in  $\text{CO}_2$ - (a) and  $\text{N}_2$ -saturated (b) solutions. In the  $\text{N}_2$ -saturated medium, the photocurrent is associated with  $\text{H}_2$  photogeneration from water [(b) in Figure 7]. Importantly, in the  $\text{CO}_2$  saturated electrolyte, the photocurrent transients for  $\text{CuO}/\text{Cu}_2\text{O}$  nanorod films are seen to reach  $\sim 3$  times higher values than in the  $\text{N}_2$ -saturated counterpart solution [(a) in Figure 7]. Of all the

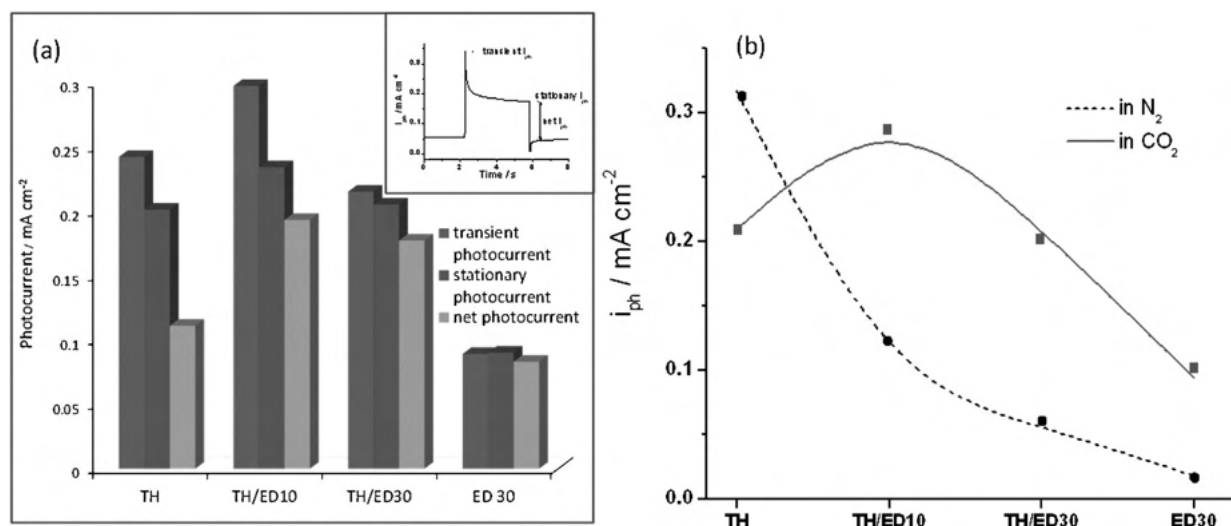


**Figure 8.** a) Comparative bar diagram of transient, stationary and net photocurrent for TH, TH/ED10, TH/ED30 and ED30 photocathodes in CO<sub>2</sub>-saturated 0.1 M Na<sub>2</sub>SO<sub>4</sub> as electrolyte. Applied potential = -0.1 V (vs. SHE). Illumination = AM1.5 solar simulator. The inset clarifies the nomenclature for transient, stationary and net photocurrent. b) Comparative plot of stationary photocurrent for TH, TH/ED10, TH/ED30 and ED30 under N<sub>2</sub> (dash black line) and CO<sub>2</sub> (solid line), respectively.

hybrid CuO/Cu<sub>2</sub>O samples, the TH/ED10 was found to perform the best for the photoelectroreduction of CO<sub>2</sub> although the photocurrent transients have relatively higher spikes than in the TH/ED30 case.

Figure 8a presents a bar diagram comparison of the photoactivity as manifested by transient, stationary and net photocurrents for CuO/Cu<sub>2</sub>O photocathodes in CO<sub>2</sub>-saturated aqueous solution. The hierarchical CuO/Cu<sub>2</sub>O core/shell nanorod arrays all show enhanced photocurrent in CO<sub>2</sub> saturated solutions with respect to the TH film, pointing to efficient removal of photogenerated electrons from Cu<sub>2</sub>O to the CuO core.

Particularly interesting is the fact that for PEC generation of H<sub>2</sub>, the thermal film performs the best and specially at negative applied potentials (data not shown). Figure 8b compares stationary photocurrent at -0.1 V for CO<sub>2</sub> and H<sup>+</sup> photoelectrochemical reduction: the TH films yielded higher photocur-

rent than any of the TH/ED $\tau$  ( $\tau$  varied between 1 and 30 min) hybrid counterparts for H<sub>2</sub> evolution, but the TH films progressively deteriorated in their PEC performance as the CuO nanorods became covered by electrodeposited Cu<sub>2</sub>O.

### 2.3. Performance and Stability of CuO/Cu<sub>2</sub>O Nanorods during the Photoelectrosynthesis of Methanol

Photoelectrosynthesis of CH<sub>3</sub>OH was demonstrated with a TH/ED10 CuO/Cu<sub>2</sub>O nanorod photoelectrode. The photoelectrode was placed in 100 mL electrolyte solution saturated with CO<sub>2</sub>, polarized at -0.2 V vs. SHE, and continually irradiated with visible light provided by a AM1.5 solar simulator. The irradiated electrode area was about 3 cm<sup>2</sup>. Representative photocurrent/time and charge/time profiles recorded during the photoelectrolysis are shown in Figure 9a,b, respectively. To an-

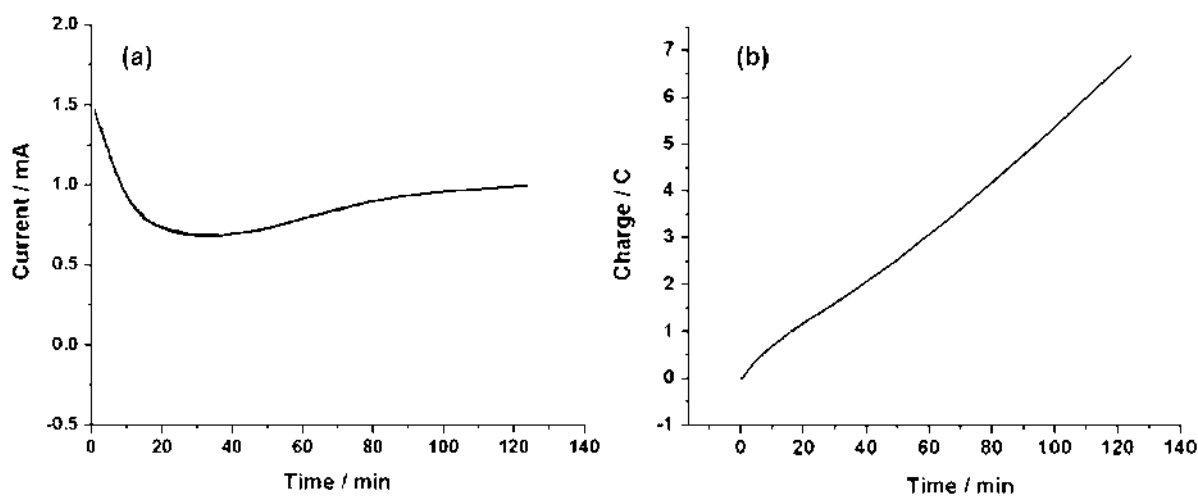


**Figure 9.** Current/time (a) and charge/time (b) profiles under continuous solar irradiation at -0.2 V (vs. SHE) in a sealed two-compartment photoelectrochemical cell containing a TH/ED10 nanorod photocathode. The electrolyte was 0.1 M NaHCO<sub>3</sub> saturated with CO<sub>2</sub> and maintained at room temperature.



alyze the photoelectrogenerated product, liquid samples were periodically withdrawn from the photoelectrochemical cell. A gas chromatograph equipped with a mass spectrometer (GC-MS) was used to detect methanol. Methanol photogeneration was monitored at  $m/z = 31$  ( $\text{CH}_2\text{OH}^+$ ) and was found to reach a concentration of about  $85 \mu\text{M}$  after 90 min of irradiation. Faradaic efficiencies were in the 94–96% range (considering that  $6 e^-$  are required to form one molecule of  $\text{CH}_3\text{OH}$  from  $\text{CO}_2$ ). Note that a potential of  $-0.2 \text{ V}$  (vs. SHE) represents an “underpotential” greater than at least 150 mV given that the standard potential for the  $\text{CO}_2/\text{CH}_3\text{OH}$  redox process lies at  $-0.38 \text{ V}$  (vs. SHE) at pH 7.

Observe in Figure 9 that the photocurrent decreases during the first 30 min and then recovers to reach a constant value of 1.05 mA at  $\sim 2 \text{ h}$  of irradiation. Even if some photocorrosion had occurred leading to formation of metallic copper on the electrode surface, this process did not diminish the performance of the  $\text{CuO}/\text{Cu}_2\text{O}$  photoelectrodes. Note that dark current values at least an order of magnitude lower (0.10 mA) than the photocurrent level corroborate that the electrode remained photoactive throughout the photoelectrolysis duration.

To link stability with photoactivity of the hybrid nanorod photoelectrode during photoelectrogeneration of methanol from  $\text{CO}_2$ , XRD patterns were obtained as a function of photoelectrolysis time and compared with the pattern for the pristine photoelectrode before irradiation (Figure 10). Observe that before photoelectrolysis (Figure 10a), three distinguished crystalline structure are clearly discernible:  $\text{CuO}$ ,  $\text{Cu}_2\text{O}$  and  $\text{Cu}$ . As the hybrid photoelectrode was prepared from a copper foil, the  $\text{Cu}$  metal diffractions, associated with the underlying substrate are also seen in the pattern. When the photoelectrolysis duration reaches 30 min (Figure 10b) the  $\text{Cu}_2\text{O}$  and  $\text{CuO}$  peaks remain unchanged while the  $\text{Cu}^0$  diffraction peaks at  $43.2^\circ$  and  $74.1^\circ$  are higher. It points to incipient formation of metallic  $\text{Cu}$  from self-reduction of the photoelectrode surface. However, as photoelectrolysis continues, the  $\text{Cu}$  peak located at  $74.1^\circ$  shows the largest variation at times of 60 min (Figure 10c) and 120 min (Figure 10d) of photoelectrolysis respectively.

This peak shows a temporal evolution quite similar to the photocurrent evolution in Figure 9a. At shorter times (up to 60 min), the photoelectrode is covered by  $\text{Cu}$  (due to photocorrosion) but then a “self-healing” process counters metal accumulation; i.e., the metal phase undergoes chemical corrosion to regenerate the oxide phases. The photocurrent-time profile over a 2 h time frame (Figure 9a) is also diagnostic of possible slow self-healing of the photocathode assembly as the oxide phases are regenerated when the photoelectrons exit the interfacial phase boundary to  $\text{CO}_2$ . In fact, the photo-generated electrons presumably are rapidly transferred to  $\text{CO}_2$  before they have an opportunity to appreciably photoreduce  $\text{Cu}^{\text{I}}$  or  $\text{Cu}^{\text{II}}$  in the oxides to the metallic state.

One of the reviewers alerted the authors about the possibility that the methanol could originate from decomposition of the lactic acid that may have leached out of the  $\text{Cu}_2\text{O}$  film during the PEC experiments. Their argument rests on the presumed entrapment of lactate species in the oxide film during

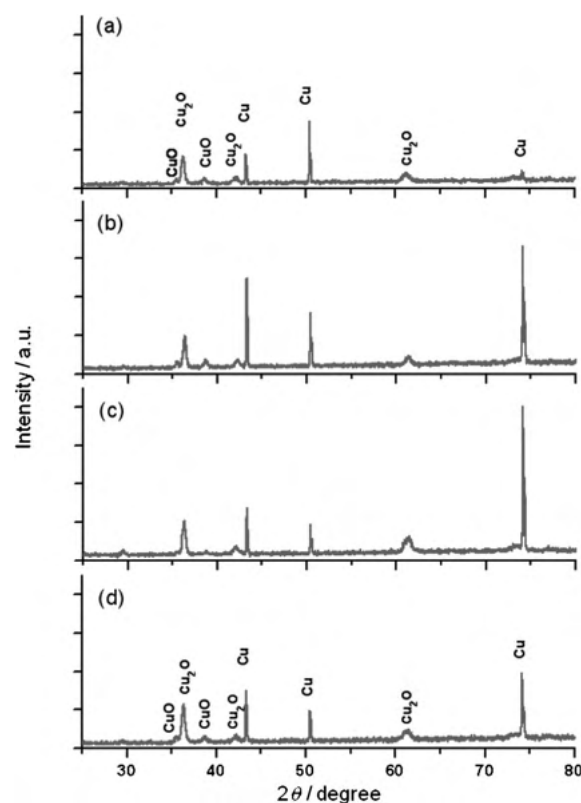


**Figure 10.** XRD spectra of a TH/ED10  $\text{CuO}/\text{Cu}_2\text{O}$  hybrid nanorod film before (a) and after being subjected to photoelectrolysis at  $-0.2 \text{ V}$  (vs. SHE) in a  $\text{CO}_2$ -saturated aqueous solution for 30 (b), 60 (c) and 120 min (d). The  $\text{Cu}/\text{Cu}_2\text{O}$  nanorod film was prepared on a copper foil whose XRD peaks are clearly discernible before and after photoelectrolysis. Because of the photoelectrolysis, the  $\text{Cu}$  peak at  $2\theta = 74.1^\circ$  associated to a (220) orientation is the one seen more affected and it grows progressively at 30 and 60 min and then recede at prolonged electrolysis (120 min). This peak seems therefore to be detecting the formation of surface  $\text{Cu}^0$  by photocorrosion of the respective  $\text{Cu}_2\text{O}$  (220) face seen at  $2\theta = 61.3^\circ$ .

its electrodeposition history. However careful analyses of electrochemically grown  $\text{Cu}_2\text{O}$  films using quartz crystal microgravimetry data<sup>[23]</sup> are unambiguous in the lack of trapped lactate species in the film. Previous authors<sup>[5,24,25]</sup> have also used surface analyses and other means to conclude the lack of lactate (or other electrolyte species such as sulfate, chloride, or phosphate) entrapment in the electrodeposited  $\text{Cu}_2\text{O}$  films.

That the methanol seen in our GC-MS experiments above originated in  $\text{CO}_2$  and not from other adventitious sources such as lactate is unequivocally supported by the following control experiments. Aliquots were withdrawn after 90 min PEC runs in (a) blank in the absence of  $\text{CO}_2$  in  $0.1 \text{ M Na}_2\text{SO}_4$ , (b)  $100 \mu\text{M}$  lactic acid, and (c)  $\text{CO}_2$  in  $0.1 \text{ M}$  sodium bicarbonate and worked up for GC-MS analyses as outlined in the preceding section. Presence of the 1.53 min methanol peak (at  $m/z = 31$ ) was unmistakable in the GC-MS data for (c) but was absent in the other two (a and b) cases. Another set of experiments this time using head-space sampling at  $75\text{--}80^\circ\text{C}$  showed clear evidence that the methanol must have originated from the photoreduction of dissolved  $\text{CO}_2$  and not from the decomposition of any adventitious organic species in the electrolyte. It is

worth noting that methanol has high vapor pressure under these conditions while that of lactic acid (boiling point:  $\sim 200^\circ\text{C}$ ) is virtually negligible.

Thus even in the unlikely scenario (see above) that lactate species leach out from the oxide film during PEC reduction runs, the above data furnish evidence for the fact that they cannot generate methanol either thermally or from the PEC oxidation of lactate (to  $\text{CO}_2$ ). Unlike  $\text{TiO}_2$  for example, the valence band in  $\text{Cu}_2\text{O}$  is situated too "high" to sustain significant PEC oxidation of the lactate species.

## 2.4. Interfacial Charge Transfer in $\text{CuO}/\text{Cu}_2\text{O}$

The photoreduction of  $\text{CO}_2$  to methanol is assisted by the favorable band-edge alignment of both oxide phases, as depicted in the diagram in Figure 11. Note that the valence band of

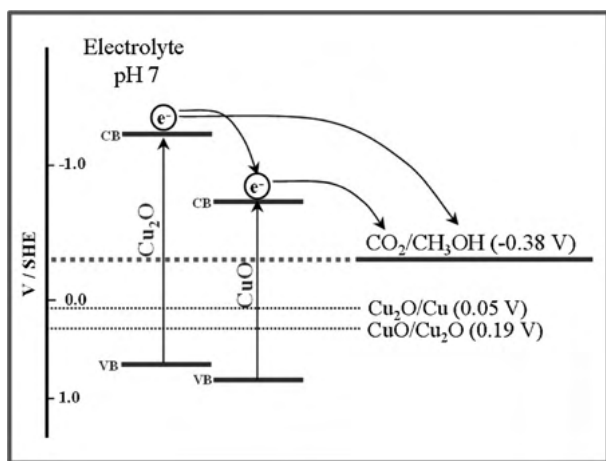


**Figure 11.** Energy-band diagram of hybrid  $\text{CuO}/\text{Cu}_2\text{O}$  nanorod arrays for solar photoelectrosynthesis of  $\text{CH}_3\text{OH}$  from  $\text{CO}_2$ . Semiconductor band edges and redox potentials are shown versus SHE (CB = conduction band and VB = valence band). The oxide photocorrosion potentials were obtained from the data in refs. [27–30].

$\text{CuO}$  is located positive of the corresponding level in  $\text{Cu}_2\text{O}$  in full agreement with the photocurrent/potential response of a  $\text{CuO}/\text{Cu}_2\text{O}$  hybrid nanorod electrode and that of a single  $\text{Cu}_2\text{O}$  film (Figure 6). Therefore, in a  $\text{Cu}_2\text{O}/\text{CuO}$  core/shell nanorod configuration, the differences in the band edges of the two oxides translate to a vectorial transfer of photogenerated electrons from the  $\text{Cu}_2\text{O}$  shell to the  $\text{CuO}$  core. As the  $\text{Cu}_2\text{O}$  shell is also in contact with the electrolyte, the photogenerated electrons in  $\text{Cu}_2\text{O}$  are able to be directly transferred to  $\text{CO}_2$  as indicated in Figure 11. This double pathway for injection of photoelectrons to  $\text{CO}_2$  is likely a contributor to the enhanced photoelectrochemical performance of  $\text{CuO}/\text{Cu}_2\text{O}$  nanorod arrays relative to a single phase  $\text{Cu}_2\text{O}$  film. Additionally, the increased surface area of the  $\text{CuO}/\text{Cu}_2\text{O}$  with respect to a compact  $\text{Cu}_2\text{O}$  ED film is certainly an additional factor in the photocurrent enhancement. Importantly to sustain the double

injection pathway the tip of the  $\text{CuO}$  core has to be in contact with the electrolyte.

The relevant potentials for photocorrosion of  $\text{Cu}_2\text{O}$  and  $\text{CuO}$  are also shown in the same diagram. These data were taken from literature sources<sup>[26–29]</sup> after suitable correction for the reference electrode potential scale. Note that both photocathodic corrosion of  $\text{Cu}_2\text{O}$  (generating metallic  $\text{Cu}$  as the product) and photoanodic oxidation of  $\text{Cu}_2\text{O}$  to  $\text{CuO}$  have been discussed in the literature.

## 3. Conclusions

A simple two-step hybrid thermal growth/electrodeposition approach was employed to prepare and optimize solar photoactive  $\text{CuO}/\text{Cu}_2\text{O}$  nanorod arrays for the photoelectrosynthesis of methanol from  $\text{CO}_2$ . These hybrid photocathodes were shown to possess a suitable geometry and chemical composition consisting of a  $\text{Cu}_2\text{O}$  shell covering the support  $\text{CuO}$  nanorod and with appropriate length and high aspect ratio for optimal transport and collection of photogenerated electrons. Methanol photogeneration was confirmed by GC-MS analyses of the product evolved at  $-0.2\text{ V}$  (vs. SHE), that is, at an underpotential relative to the standard potential of  $\text{CO}_2/\text{CH}_3\text{OH}$ . This last feature is an important virtue of the p-type semiconductor based photoreduction approach as adopted in this study and by other authors<sup>[13–15]</sup> previously. In contrast, the ("dark") electrocatalytic process counterpart for  $\text{CO}_2$  reduction suffers from the electrical energy cost incurred from the need for considerable overpotentials to overcome the kinetic barrier associated with this process.<sup>[30,31]</sup>

## Experimental Section

### Chemicals and Materials

$\text{Cu}$  substrates (foil and mesh) were from Alfa Aldrich and 99.99% purity. The chemical reagents used in the study were of analytical grade and were used without further purification.

### Preparation of $\text{CuO}/\text{Cu}_2\text{O}$ Nanorod Photoelectrodes

The hybrid  $\text{CuO}/\text{Cu}_2\text{O}$  nanorod arrays were fabricated by a two-step process performed on freshly cleaned copper. Thus, copper (foil or mesh) substrates were pretreated with 1.0 M  $\text{HCl}$ , then sonicated in isopropanol, acetone and deionized water, respectively, and finally dried under nitrogen gas. In the first step, freshly cleaned  $\text{Cu}$  substrates were subjected to thermal oxidation in presence of air using a box furnace for 4 h at  $400^\circ\text{C}$ . A temperature program was used and consisted of first heating the sample up to  $400^\circ\text{C}$  (at  $25^\circ\text{ min}^{-1}$ ). After 4 h of isothermal heating, the sample was allowed to return naturally to room temperature.

In the second step,  $\text{Cu}_2\text{O}$  crystallites were electrodeposited on the thermally grown  $\text{CuO}$  nanowires from a basic solution of lactate-stabilized copper sulfate using a potentiostat (CH electrochemical workstation 720C). The electrolytic bath was prepared with deionized (DI) water (Corning Megapure) and contained 0.4 M cupric sulfate and 3 M lactic acid. The bath pH was adjusted to 9 by addition of concentrated sodium hydroxide solution; the temperature of the bath was maintained at  $60^\circ\text{C}$  during electrodeposition. A Pt

foil and a Ag/AgCl (satd. KCl) were used as counterelectrode and reference electrode respectively. The electrodeposition time was varied to investigate the structural attributes, and also the photoactivity of the resulting heterostructures. All potentials were measured vs. Ag/AgCl ref. electrode but they are quoted above with respect to SHE, using  $\text{Ag/AgCl} = -0.197 \text{ V (vs. SHE)}$ .

### Measurement of the Photoelectrochemical Activity

Photocurrent–potential profiles were recorded under solar irradiation (AM1.5) from a solar simulator (Newport 91160-1000). The radiation was interrupted (with a manual chopper) at 0.2 Hz. Bulk photoelectrolysis was also performed in a two-compartment sealed electrochemical cell under continuous light irradiation. The electrolyte used was 0.1 M  $\text{Na}_2\text{SO}_4$ , the solution was saturated with  $\text{N}_2$  and  $\text{CO}_2$  bubbling through the cell. The CH electrochemical workstation 600C was used to apply a constant potential of  $-0.2 \text{ V}$ . Light irradiation (AM 1.5) was provided by the full output of the Newport solar simulator specified and with illumination power of  $70 \text{ mW cm}^{-2}$ .

Long-term photoelectrolysis (Figure 9) was carried out using a CH electrochemical workstation 600C instrument ([www.chinstruments.com](http://www.chinstruments.com)), in a custom-designed two-compartment, three-electrode electrochemical cell. Ag/AgCl (satd. KCl) and Pt foil were used as reference electrode and counter electrode, respectively, although all potentials are quoted with respect to the SHE reference scale. The electrolyte used were 0.1 M  $\text{NaHCO}_3$  (saturated with  $\text{CO}_2$ ) and 0.1 M  $\text{Na}_2\text{SO}_4$  (saturated with  $\text{N}_2$ ) as control experiment.

### Physical Characterization

The surface morphology of the various film samples was characterized using a Hitachi S-5000H field emission scanning electron microscope (SEM) operated at an acceleration voltage of 20.0 kV. Raman spectra were recorded with a HORIBA Jobin Yvon LabRam ARAMIS instrument (incident power  $\leq 300 \text{ mW}$ ) using an excitation wavelength of 532 nm and an 1800 line  $\text{mm}^{-1}$  grating. In all the cases, the slit width was 10  $\mu\text{m}$ , and 32 scans were accumulated for each spectrum. X-ray diffraction (XRD) patterns were obtained on a Siemens D-500 powder diffractometer using  $\text{CuK}\alpha$  as the source radiation.

### Gas Chromatography with Mass Spectrometry Detection

Liquid aliquots were periodically taken during the photoelectrolysis to be analyzed in a gas chromatograph equipped with a mass spectrometer as detector (GC-MS). The aliquots were subjected to supporting electrolyte removal by shaking overnight with Amberlite IRN-150 ion-exchange resin (cleaned and vacuum dried just before use) and then injected into the Shimadzu GC-MS 2010SE chromatograph coupled with a MS QP2010 detector and an AOC-20S sampler. Head space sampling was also used for GC-MS analyses to confirm the photoelectrosynthesis of methanol from  $\text{CO}_2$  by heating the sealed vial at  $75^\circ\text{C}$  water bath for 45 min to let the liquid and volatile organics equilibrate. The chromatographic column was Shimadzu SHRX105 MS (30 m length and 0.25 mm inner diameter, part # 220-94764-02) set at  $45^\circ\text{C}$ . The MS detector was set at  $250^\circ\text{C}$ , and helium was used as the carrier gas. Calibration curves for different methanol concentrations in water showed that the methanol peak eluded at 1.52 min with a corresponding  $m/z = 31$ .

### Acknowledgements

This study was funded in part by a grant from the U.S. Department of Energy. C.J. gratefully acknowledges funding support of the European Union under FP7-PEOPLE-2010-IOF, Grant Number: 274046. The authors thank David J. Boston for help with the GC-MS measurements. This paper is dedicated to Prof. Adam Heller who inspired so many of us with his insights into the importance of surface chemistry on PEC activity, on chemical effects in semiconductor/metal electronic barriers, conjugate reaction kinetics in photocatalytic processes, and so many other aspects of semiconductor–solution interfaces. Equally important he taught at least one of us (KR) that human qualities are as important as intellectual stature. I am forever indebted to him as a mentor and teacher.

**Keywords:** carbon dioxide remediation • electrodeposition • methanol • photoelectrochemistry • semiconductors

- [1] G. Ghadimkhani, N. R. de Tacconi, W. Chanmanee, C. Janaky, K. Rajeshwar, *Chem. Commun.* **2013**, 49, 1297.
- [2] K. Nakaoka, J. Ueyama, K. Ogura, *J. Electrochem. Soc.* **2004**, 151, C661.
- [3] Y. Hori, K. Kikuchi, S. Susuki, *Chem. Lett.* **1985**, 1695.
- [4] S. Somasundaram, C. R. N. Chenthamarakshan, N. R. de Tacconi, K. Rajeshwar, *Int. J. Hydrogen Energy* **2007**, 32, 4661.
- [5] A. Paracchino, V. Laporte, K. Sivula, M. Gratzel, E. Thimsen, *Nat. Mater.* **2011**, 10, 456.
- [6] A. Paracchino, J. C. Brauer, J.-E. Moser, E. Thimsen, M. Gratzel, *J. Phys. Chem. C* **2012**, 116, 7341.
- [7] Z. Zhang, P. Wang, *J. Mater. Chem.* **2012**, 22, 2456.
- [8] C.-Y. Chiang, J. Epstein, A. Brown, J. N. Munday, J. N. Culver, S. Ehrman, *Nano Lett.* **2012**, 12, 6005.
- [9] For example: "Electrochemical  $\text{CO}_2$  Reduction on Metal Electrodes": Y. Hori in *Modern Aspects of Electrochemistry*, Vol. 42 (Eds.: C. G. Vayenas, R. E. White), Springer, New York, **2008**, Chap. 3.
- [10] M. Le, M. Ren, Z. Zhang, P. T. Sprunger, R. L. Kurtz, J. C. Flake, *J. Electrochem. Soc.* **2011**, 158, E45.
- [11] C. W. Li, M. W. Kanan, *J. Am. Chem. Soc.* **2012**, 134, 7231.
- [12] For example: B. R. Eggins, P. K. J. Robertson, E. P. Murphy, E. Woods, J. T. S. Irvine, *J. Photochem. Photobiol. A* **1998**, 118, 31. See also references therein.
- [13] "Photochemical, Electrochemical, and Photoelectrochemical Reduction of Carbon Dioxide": E. B. Cole, A. B. Bocarsly in *Carbon Dioxide as Chemical Feedstock* (Ed.: M. Aresta), Wiley-VCH, Weinheim, **2010**, Chap. 11.
- [14] B. Kumar, M. Llorente, J. Froelich, T. Dang, A. Sathrum, C. P. Kubiak, *Annu. Rev. Phys. Chem.* **2012**, 63, 541.
- [15] Book chapter: "Electro- and Photocatalytic Reduction of  $\text{CO}_2$ : The Homogeneous and Heterogeneous Worlds Collide?": D. J. Boston, K.-L. Huang, N. R. de Tacconi, F. M. MacDonnell, K. Rajeshwar in *Photoelectrochemical Water Splitting: Challenges and New Perspectives* (Eds.: H.-J. Lewerenz, L. M. Peter), Royal Society of Chemistry, *in press*.
- [16] B. Kumar, J. M. Smicja, C. P. Kubiak, *J. Phys. Chem. C* **2010**, 114, 14220.
- [17] H. Yoneyama, K. Sugimura, S. Kuwabata, *J. Electroanal. Chem.* **1988**, 249, 143.
- [18] X. Jiang, T. Herricks, Y. Xia, *Nano Lett.* **2002**, 2, 1333.
- [19] L. C. Wang, N. R. de Tacconi, C. R. Chenthamarakshan, K. Rajeshwar, M. Tao, *Thin Solid Films* **2007**, 515, 3090.
- [20] M. A. Dar, S. H. Nam, Y. S. Kim, W. B. Kim, *J. Solid State Electrochem.* **2010**, 14, 1719.
- [21] N. A. Mohemmed Shanid, M. Abdul Khadar, V. G. Sathe, *J. Raman Spectrosc.* **2011**, 42, 1769.
- [22] Y. Mao, J. He, X. Sun, W. Li, X. Lu, J. Gan, Z. Liu, L. Gong, J. Chen, P. Liu, Y. Tong, *Electrochim. Acta* **2012**, 62, 1.
- [23] N. Myung, N. R. de Tacconi, K. Rajeshwar, *unpublished results*.

- [24] E. W. Bohannon, L.-Y. Huang, F. S. Miller, M. G. Shumsky, J. A. Switzer, *Langmuir* **1999**, *15*, 813.
- [25] S. Haller, J. Jung, J. Rousset, D. Lincot, *Electrochim. Acta* **2012**, *82*, 402.
- [26] L. Wu, I.-K. Tsui, N. Swami, G. Zangari, *J. Phys. Chem. C* **2010**, *114*, 11551.
- [27] L. Huang, F. Peng, H. Yu, H. Wang, *Solid State Sci.* **2009**, *11*, 129.
- [28] Z. Zheng, B. Huang, Z. Wang, M. Guo, X. Qin, X. Zhang, P. Wang, Y. Dai, *J. Phys. Chem. C* **2009**, *113*, 14448.
- [29] Y. Bessekhoud, D. Robert, J. Weber, *Catal. Today* **2005**, *101*, 315.
- [30] J. O. Bockris, J. C. Wass, *J. Electrochem. Soc.* **1989**, *136*, 2521.
- [31] B. A. Rosen, A. Salehi-Khojin, M. R. Thorson, W. Zhu, D. T. Whipple, P. J. A. Kenis, R. I. Masel, *Science* **2011**, *334*, 643.

---

Received: January 25, 2013

Revised: March 8, 2013

Published online on May 24, 2013

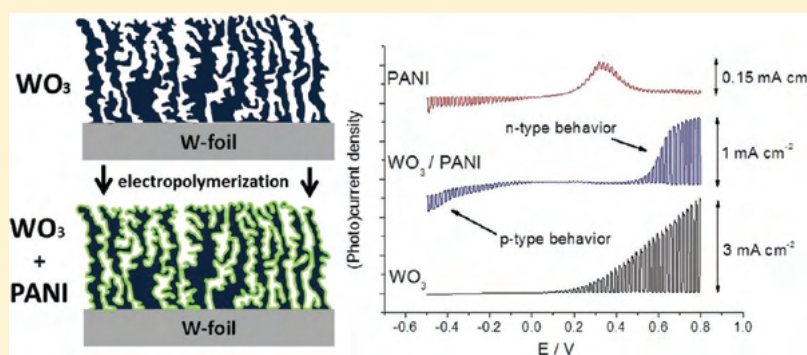
# Electrodeposited Polyaniline in a Nanoporous WO<sub>3</sub> Matrix: An Organic/Inorganic Hybrid Exhibiting Both p- and n-Type Photoelectrochemical Activity

Csaba Janáky,<sup>\*,†,‡</sup> Norma R. de Tacconi,<sup>†</sup> Wilaiwan Chanmanee,<sup>†</sup> and Krishnan Rajeshwar<sup>\*,†</sup>

<sup>†</sup>Department of Chemistry and Biochemistry, University of Texas at Arlington, Arlington, Texas 76019, United States

<sup>‡</sup>Department of Physical Chemistry and Materials Science, University of Szeged, Szeged H6720, Hungary

## S Supporting Information



**ABSTRACT:** This study focuses on the electrodeposition of a conducting polymer such as polyaniline (PANI) into a tungsten trioxide nanoporous host framework. Nanoporous WO<sub>3</sub> films were initially electro synthesized on tungsten foil by anodization at different voltages in a fluoride-containing medium. The PANI layer was electrografted onto the entire surface of the WO<sub>3</sub> using potentiodynamic electrodeposition in sulfuric acid electrolyte. The morphological features of oligomer/polymer formed in the nanoporous oxide template were monitored by field-emission scanning electron microscopy. Systematic changes in the morphology afforded insights into the evolution of the WO<sub>3</sub>/PANI hybrid assembly. This assembly was subsequently characterized by Raman spectroscopy, X-ray photoelectron spectroscopy, cyclic voltammetry, and photoelectrochemical measurements. Photovoltammetric data indicated the complex behavior of the hybrid, featuring the properties of both of its components: namely, p-type behavior in the cathodic polarization regime and n-type behavior at the anodic end. Moreover, much higher cathodic photocurrents were observed for PANI in the hybrid configuration (compared to neat PANI itself), in which effective charge separation manifested in the shape of the photocurrent transients.

## 1. INTRODUCTION

Hybrid materials based on organic conjugated polymers (CP) and inorganic nanostructures have been actively studied in recent years.<sup>1,2</sup> A large variety of composites have been realized, including CP-containing assemblies based on metal nanoparticles, carbon nanostructures, and inorganic compounds. Metal oxide semiconductors are particularly interesting materials in this regard, since a wide range of properties can be combined with complementary properties of the polymer.<sup>3</sup> For example, TiO<sub>2</sub><sup>4,5</sup> and ZnO<sup>6</sup> were combined with thiophene derivatives to form p/n junctions and utilized in solar cells, in organic electronics, or for photocatalysis. Materials with enhanced charge storage capacity were prepared by incorporating RuO<sub>2</sub> and V<sub>2</sub>O<sub>5</sub> into the matrix of CPs such as polyaniline and polypyrrole.<sup>7,8</sup> Combination of MoO<sub>3</sub> and Fe<sub>3</sub>O<sub>4</sub> with CPs has led to hybrid materials with advanced sensing, magnetic, and catalytic properties.<sup>9–11</sup>

Tungsten oxide (WO<sub>3</sub>) is an n-type semiconductor, having an indirect band gap of  $E = 2.7$  eV (for the monoclinic phase);

thus, its absorption edge is in the visible light region.<sup>12,13</sup> It has been successfully utilized in photoelectrocatalytic processes,<sup>14,15</sup> electrochromic devices,<sup>16–18</sup> dye-sensitized solar cells,<sup>19,20</sup> gas sensors,<sup>21,22</sup> and electrocatalysis.<sup>23</sup> Preparation methods involve vapor- and solution-phase procedures, including sputtering, thermal evaporation, sol-gel methods, and others. It is worth mentioning that particular efforts have been devoted to synthesize this oxide with various morphologies covering a wide range of nanostructures including nanoparticles, nanodisks, nanorods, nanowires, nanofibers, nanoplatelets, nanotrees, etc.<sup>13</sup>

A recently developed method is electrochemical etching or anodization of W foil. The process occurs at either constant voltage<sup>24,25</sup> or constant current.<sup>26</sup> For the preparation of inorganic/organic hybrid materials, anodization can be a

**Received:** December 5, 2011

**Revised:** January 11, 2012

**Published:** January 19, 2012

particularly interesting process since the resulted oxide has an ordered nanoscale structure, which greatly increases the specific surface and semiconductor behavior. This opens a route to prepare hybrid materials with a large contact interface and effective p/n junction. Nanoporous  $\text{WO}_3$  prepared via anodization proved to be more efficient compared to materials counterparts synthesized by other methods in terms of photoelectrochemical behavior,<sup>27</sup> sensing properties,<sup>28</sup> water splitting ability,<sup>29</sup> electrocatalytic property,<sup>30</sup> or electrochromism.<sup>31</sup>

Combination of  $\text{WO}_3$  with CPs to form inorganic/organic hybrid materials can be advantageous for numerous reasons. Such composite materials possessing interesting electrical properties<sup>32,33</sup> can be utilized in electrocatalysis,<sup>34</sup> charge storage,<sup>35</sup> electrochromism,<sup>36–38</sup> or for sensing: humidity<sup>39</sup> and gases as hydrogen<sup>40</sup> or  $\text{NO}_2$ .<sup>41</sup> These hybrids have been synthesized by different synthetic procedures ranging from simple mechanical mixing of the components, polymerization in the presence of nanoparticulate  $\text{WO}_3$ , to simultaneous co-deposition of the polymer and the oxide. However, these methods have significant drawbacks and limitations, two most important being the uncontrolled, random distribution of the (nano)particles within the polymer and inadequate electric contact. Thus, use of the hybrid as an electrode (which is the case in most of the applications that have been considered) is hampered by the fact that only the polymer matrix has direct electrical connection to the electrode. In contrast, by infiltrating a conducting polymer into an organized nanoporous  $\text{WO}_3$  framework, hybrid materials with large area of organic/inorganic junction with well-defined morphologies can be obtained where both components have electrical contact with the supporting electrode.

Despite the obvious advantages in using an organized nanostructured  $\text{WO}_3$ , according to the best of our knowledge, there is no precedence in the literature for combination of  $\text{WO}_3$  prepared through anodization with any conjugated polymer. Our aim was to study the feasibility of combining nanoporous tungsten oxide with a semiconducting polymer, namely polyaniline (PANI). This candidate has enjoyed prime importance among CPs, due to its versatile redox behavior (involving many different intrinsic oxidation states), excellent chemical and electrochemical stability, electrochromic properties, and large capacitance.<sup>42–44</sup> Combination of inorganic semiconductors ( $\text{CdS}$ ,  $\text{ZnO}$ ) with polyaniline was recently shown to be useful for photoelectrocatalysis.<sup>45,46</sup> The selection of polyaniline was also motivated by the fact that its ion exchange properties show similarity to  $\text{WO}_3$  in many aspects; most importantly, both of them are electron and proton conductors as well.

Moreover, our study goes one step beyond the state of the art of electrodeposition as well, since electrochemical grafting of conducting polymers into nanostructured semiconductors was heretofore limited to  $\text{TiO}_2$ <sup>47–50</sup> and  $\text{ZnO}$ .<sup>51</sup> Thus, the aim of this study is to prove the feasibility of electrodeposition of PANI onto the nanoporous  $\text{WO}_3$  template, to tune the morphology of the hybrid, and to investigate the photoelectrochemical properties of the resultant organic/inorganic junction.

## 2. EXPERIMENTAL SECTION

**2.1. Chemicals and Materials.** All chemicals were from commercial sources and were of the highest purity available. Deionized water (18 M $\Omega$  cm) was used in all cases for making

solutions. Sodium fluoride (Alfa Aesar, 98.0%) was used as received. Tungsten foil (Alfa Aesar, 0.25 mm thick, 99.95%) was used as the substrate for oxide film growth. Before use, the foil was cut (1.4 cm  $\times$  1.4 cm), mechanically polished to mirror finish using silicon carbide sandpaper of successively finer roughness (220, 240, 400, 800, 1000, and 1500 grit), and cleaned in three 5 min steps in ultrasonicated acetone, 2-propanol, and finally ultrapure water. Subsequently, the substrate was dried in ultrapure  $\text{N}_2$  stream and used immediately.

For polyaniline (PANI) growth, aniline monomer (EM Science, 99.5%) was freshly distilled under vacuum before use. Sulfuric acid (Alfa Aesar, 98.0%) and sodium sulfate (J.T. Baker, 99.0%) were used as received.

**2.2. Anodic Growth of Nanoporous  $\text{WO}_3$ .** Nanoporous films of  $\text{WO}_3$  were grown in a two-electrode electrochemical cell using a large Pt foil as counter electrode and tungsten foil as the working electrode. NaF was used as the electrolyte (0.15 M). The W foil was pressed between a set of O-rings in the electrochemical cell, leaving 0.63 cm<sup>2</sup> exposed to the electrolyte, and the electric contact was located on the backside of the sample. Anodization employed a 420X power supply (The Electrosynthesis Co., Inc., Lancaster, NY). The voltage was held at the preselected level (40 or 60 V) for 3 h. After the oxide film was grown, the anodized W foil was removed from the O-ring assembly, carefully washed by immersion in deionized water, and then dried in a  $\text{N}_2$  stream. Before use as substrates for aniline electropolymerization, the W/ $\text{WO}_3$  electrodes were annealed at 450 °C (under air atmosphere) for 3 h at a heating rate of 20 °C/min (Fisher Scientific, Model 650-14 Isotemp Programmable Muffle Furnace) and allowed to cool gradually back to the ambient temperature. Other details of anodic growth are given elsewhere.<sup>30</sup>

**2.3. Electrosynthesis of PANI/ $\text{WO}_3$  Hybrid.** After a series of optimization experiments, a polymerization medium consisting of 0.2 M aniline monomer and 0.5 M aqueous sulfuric acid was chosen. Optimization of the electrochemical polymerization was carried out in multiple steps. Particular care was devoted to optimize the hybrid morphology (e.g., ensure homogeneous distribution of the polymer) and electroactivity of the deposited polymer simultaneously. As a first step, both potenti- and galvanostatic procedures were utilized, but neither homogeneity nor electroactivity of the resulted hybrid was satisfactory. Then potentiodynamic methods were employed, where the effect of the scan rate was also studied (10, 25, 50, and 100 mV s<sup>-1</sup>), and 100 mV s<sup>-1</sup> was proved to be optimal.

Finally, polymerization of aniline was carried out by a simple, but carefully optimized potential cycling protocol between -0.2 and 1.1 V. As a part of the optimization, both samples containing polyaniline grown by 3, 5, 10, and 20 cycles were prepared. The working electrode was the previously prepared nanoporous  $\text{WO}_3$  in all cases. The reference electrode was Ag/AgCl/satd KCl (Microelectrode Inc., Bedford, NH); all potentials in this paper are given with respect to this reference. For further voltammetric studies, the solution was changed after polymerization to a monomer-free 0.5 M  $\text{H}_2\text{SO}_4$  electrolyte.

**2.4. Characterization Methodology.** The morphology of  $\text{WO}_3$  and the  $\text{WO}_3$ /PANI hybrid samples was studied using a Hitachi S-5000H field emission scanning electron microscope (SEM) at an accelerating voltage of 20 kV. Images were taken at different magnifications between 10K and 200K. Raman

spectra were recorded with a HORIBA Jobin Yvon LabRam ARAMIS instrument (incident power  $\leq 300$  mW) using an excitation wavelength of 473 nm and an 1800 line/mm grating. In all the cases the slit width was 10  $\mu\text{m}$ , and 10 scans were accumulated for each spectrum. X-ray photoelectron spectra (XPS) were recorded on a Kratos Axis Ultra X-ray photoelectron spectrometer at room temperature using an Al source. The gun was operated at 15 kV and 7 mA. Data were acquired with 0.1 eV step size and 0.1 s dwell time. The pass energy for high-resolution spectra (e.g., N 1s, W 4f) was 10 eV. Binding energy data were calibrated using the standard value for C 1s at 285 eV.

All electrochemical measurements were performed on a CHI electrochemical workstation 440A instrument, in a classical one-compartment, three-electrode electrochemical cell. Cyclic voltammograms of the  $\text{WO}_3/\text{PANI}$  hybrid were registered in 0.5 M  $\text{H}_2\text{SO}_4$  solutions at four different potential sweep rates between 10 and 100 mV/s. For the photoelectrochemical measurements a standard single-compartment, three-electrode electrochemical cell was used. A large Pt coil and the reference electrode mentioned earlier, along with the working electrode, completed the cell setup. The light source was a 150 W xenon arc lamp (Oriel, Stratford, CT). The radiation source was placed 8 cm away from the working electrode surface. Photovoltammetry profiles were recorded with the same potentiostat, in 0.1 M  $\text{Na}_2\text{SO}_4$  electrolyte. Photovoltammograms were obtained using a slow potential sweep (2 mV  $\text{s}^{-1}$ ) in conjunction with interrupted irradiation (0.2 Hz) on the semiconductor and hybrid film electrodes. For the chronoamperometric measurements, the working electrode was set at preselected potential values (in the range  $-0.1$  to  $+0.8$  V), and the photocurrent transients under illumination were monitored for 20 s. All procedures described below were performed at the laboratory ambient temperature ( $25 \pm 2$   $^\circ\text{C}$ ).

### 3. RESULTS AND DISCUSSION

**3.1. Potentiodynamic Growth of PANI into the Nanoporous  $\text{WO}_3$  Matrix.** Potentiodynamic deposition is one of the most frequently used methods for the electrochemical synthesis of polyaniline.<sup>44</sup> Since diffusion of the monomer during electrodeposition is usually the limiting step for nanostructured working electrodes,<sup>32</sup> the use of a potentiodynamic growth waveform is indeed effective. Figure 1 contains a series of cyclic voltammograms (10) between  $-0.20$  and  $+1.10$  V, recorded during the electrodeposition of PANI onto the nanostructured  $\text{WO}_3$  electrode. During the first cycle of polymerization, the anodic current starts to increase only above 1.00 V, and then it rises continuously, exhibiting a hysteresis loop on the return scan. This behavior can be explained by the fact that at the beginning of the sweep only monomer oxidation and oligomer formation take place, while after this initial step polymerization also occurs. As the oxidation potential of the oligomers is lower as compared to that of the monomer (and it decreases by the increasing segment number), the currents for monomer and oligomer oxidation cross each other. The initial oxidation potential on the  $\text{W}/\text{WO}_3$  film is  $\sim 0.2$  V more positive than at a Au electrode, presumably stemming from a larger surface resistance on the  $\text{WO}_3$  working electrode. Otherwise, the shapes of the curves are identical to those obtained with gold (not presented here).

**3.2.1. Physical Characterization.  $\text{PANI}/\text{WO}_3$  Hybrid Morphology As Probed by SEM.** To gain insights into the

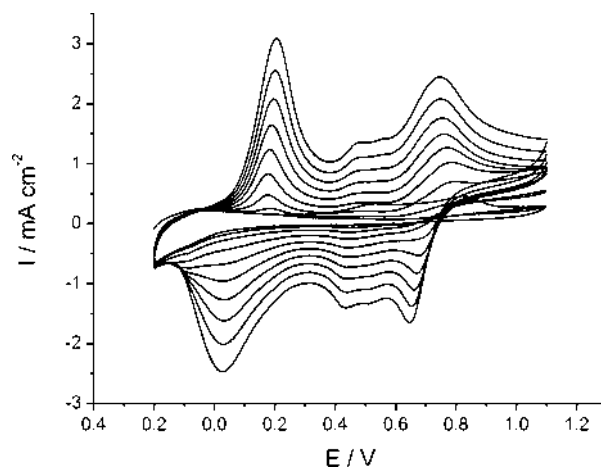


**Figure 1.** Polymerization of aniline over 10 potentiodynamic cycles at a sweep rate of 100 mV  $\text{s}^{-1}$  in a solution containing 0.2 M aniline and 0.5 M aqueous  $\text{H}_2\text{SO}_4$  as electrolyte.

morphological aspects of electrochemical infiltration of the polymer, SEM images were taken at various magnifications, both with the bare  $\text{WO}_3$  nanostructures (prepared at 40 or 60 V) and the hybrid material. In Figure 2A–C and Figure 3A–C, SEM images of the bare oxide materials are presented. As can be clearly seen, the overall morphology of the anodized  $\text{WO}_3$  samples is similar in the two cases. However, some differences in the pore size and porosity of the two oxide materials can be revealed, reflecting more complete overetching of the tungsten surface by the fluoride species at the higher voltage.<sup>30</sup> More precisely, the oxide film obtained by anodization at 40 V gave a nanohole array morphology for the oxide surface. On the other hand, the oxide layer obtained from an anodization voltage of 60 V gave a very porous structure with high surface area.

Figure 2D,E and Figure 3D,E show representative SEM images for the hybrid materials, obtained for the deposition of PANI with five voltammetric cycles onto the tungsten oxide matrix obtained at 40 and 60 V, respectively. During electrochemical polymerization of aniline, the monomers are initially oxidized, and correspondingly, oligomers are formed in the solution phase. After this fast initial step, the formed oligomers are deposited onto the surface of the tungsten oxide nanostructure. When the electrosynthesis proceeds further, chain propagation of the deposited oligomers takes place in the solid phase. This process evolution manifests in the cloudiness seen for the  $\text{WO}_3$  surface on the whole sample. Expansion of the grain size is also seen relative to the parent situation in Figures 2 and 3A–C. It is also important to mention that at this stage the nanostructured support is covered by PANI, and the space between the grains (the pore size) is seen to be much smaller than the neat tungsten oxide case, although most of the grains are not completely fused to one another. The  $\sim 30$  nm difference in the diameter between the neat  $\text{WO}_3$  grains and the coated samples suggests that oligomer/polymer electrodeposition results in a  $\sim 15$  nm thick PANI layer on the surface. Regardless of the different morphology of the  $\text{WO}_3$  substrates anodized at different voltages, the polymer is seen to deposit in a very similar fashion on both samples, resulting in a comparable coating, which covers the entire surface of the nanoporous oxide semiconductor (Scheme 1).

Further advancement of the polymerization process was also investigated. In Figure 4, we present the evolution of the structure of the hybrid material as a series of SEM images, at a

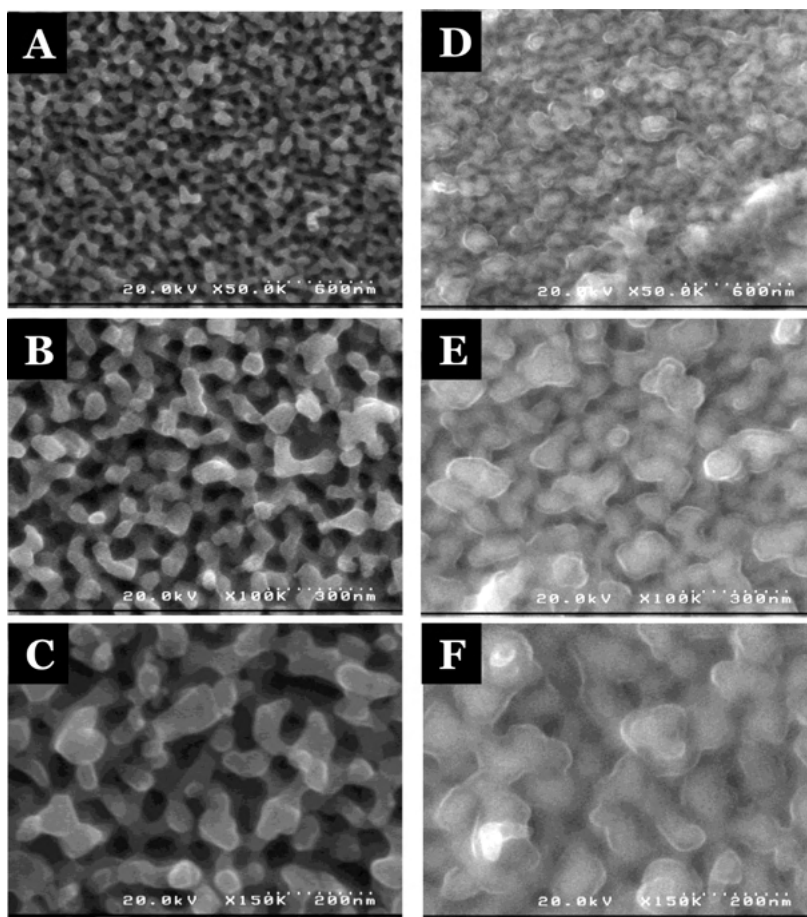


**Figure 2.** SEM images of the bare  $\text{WO}_3$  synthesized at  $E = 40$  V (A–C) and of the corresponding  $\text{WO}_3/\text{PANI}$  hybrid samples (D–F, synthesized using five cycles) at 50K, 100K, and 150K magnification.

**Scheme 1. Illustration of the Two-Step Synthetic Procedure of the  $\text{WO}_3/\text{PANI}$  Hybrid**



selected magnification (25000 $\times$ ). The compared samples contain different amounts of polymer deposited; more specifically, the polymerization was allowed to proceed for 0, 5, 10, and 20 cycles. In Figure 4A, B similar images can be seen as in Figure 3. As the polymeric layers on the grains get progressively thicker, the layers grown on different parts of the substrate abut, and the pores of the  $\text{WO}_3$  template becomes almost completely filled. In this manner, a “skinlike” conjugated polymer network is formed on the oxide template. When all the  $\text{WO}_3$  surface is covered and almost all of the polymer covered grains are attached to each other, the further growth of polyaniline does not result in a compact layer on the top of the substrate as in the case of polymer deposition on  $\text{TiO}_2$  nanotube arrays.<sup>47–49</sup> On the other hand, growth occurs in specific directions, and nanofiber formation can be detected starting from the grains to all directions outward (Figure 4C). Finally, if the polymerization is allowed to progress even further, the density of these nanofibers increases, and the nanoporous substrate gets fully covered with a network of PANI fibers, as can be clearly seen in Figure 4D.

Since the samples prepared by five potentiodynamic cycles (prepared on  $\text{WO}_3$  anodized at 60 V) show the largest electrolyte-exposed area (considered as a prerequisite for many applications), all further characterization is presented for these hybrid samples.

**3.2.2. Raman Spectroscopy.** To confirm the chemical identity of the polymer deposited into the  $\text{WO}_3$  framework, Raman spectra were taken. This method is rather useful for this purpose since both  $\text{WO}_3$  and PANI have characteristic bands, although polyaniline exhibits much higher intensities. Figure 5 contains Raman spectra of a  $\text{WO}_3$  sample and the corresponding  $\text{WO}_3/\text{PANI}$  hybrid. As for the bare oxide material, the existence of typical monoclinic vibrational modes<sup>14</sup> at 272, 325, 715, and 807  $\text{cm}^{-1}$  confirms the formation of  $\text{WO}_3$  during the anodization and the subsequent heat treatment. For the hybrid sample in Figure 5, several new bands can be observed compared to the support oxide framework. All the characteristic bands can be assigned to PANI.<sup>43,44</sup> The appearance of specific bands (see assignments on the spectrum) all confirms the formation of the targeted conducting polymer. Moreover, despite some overlap with the



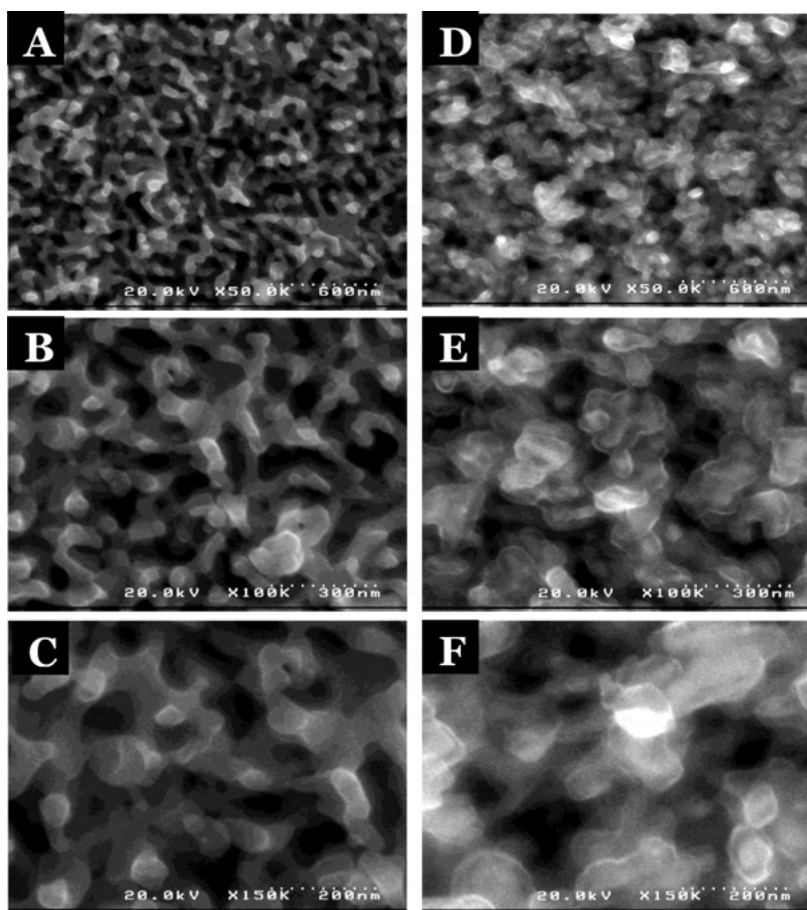


**Figure 3.** SEM images of the bare  $\text{WO}_3$  synthesized at  $E = 60$  V (A–C) and of the corresponding  $\text{WO}_3/\text{PANI}$  hybrid samples (D–F, synthesized by five potentiodynamic cycles) at 50K, 100K, and 150K magnification.

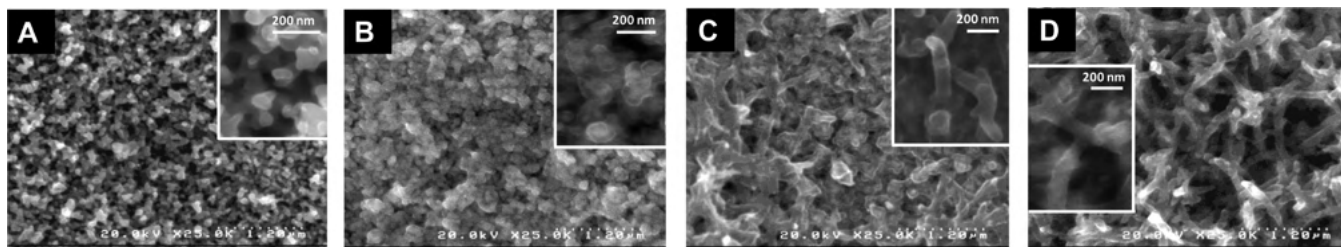


**Figure 4.** Electron microscopic visualization of the morphology development of the  $\text{WO}_3/\text{PANI}$  hybrid (0, 5, 10, and 20 potentiodynamic cycles) at 25000 $\times$  magnification. The insets present representative enlarged areas.

PANI bands, the vibrations from the  $\text{WO}_3$  matrix can be also identified in the spectrum of the hybrid material.

**3.2.3. X-ray Photoelectron Spectroscopy.** In Figure 6, XPS data for three samples are presented: the anodically grown  $\text{WO}_3$  matrix and two hybrid samples (5 and 10 cycles of electropolymerization). In Figure 6A, the W 4f signal is shown, and the well-resolved doublet peaks corresponding to W 4f<sub>5/2</sub> and W 4f<sub>7/2</sub> can be seen. The binding energies of these peaks are 37.8 and 35.8 eV, respectively, indicating that the sample surface is close to the chemical stoichiometry of  $\text{WO}_3$ .<sup>22</sup> Moreover, the peak locations are unchanged diagnosing that the  $\text{WO}_3$  stoichiometry at the surface is not affected by oxidative deposition of the polymer. One can also see the step-by-step diminution of these peak amplitudes by covering the substrate with increasing amounts of PANI. A similar conclusion can be drawn for the gradual development of the

N signal, presented in Figure 6B. The XPS results presented above also suggest that the  $\text{WO}_3$  matrix is *homogeneously* covered by the polymeric film, and uncovered areas are decreased by the longer polymerization time. These observations are coherent with the SEM images presented in Figure 3, where the polymer coverage appears over the entire sample.

**3.3.1. Electrochemical and Photoelectrochemical Measurements. Voltammetric Behavior.** The cyclic voltammograms in Figure 1 above suggest that the deposited polymer exhibits good electroactivity within the nanoporous  $\text{WO}_3$  framework. In order to acquire further information on the electrochemical activity of the hybrid material, cyclic voltammograms were recorded in aqueous  $\text{H}_2\text{SO}_4$ . Cycling in this electrolyte is indeed advantageous, since both  $\text{WO}_3$  and PANI are known as  $\text{H}^+$  exchangers, thus showing a quasi-reversible electroactivity in this media. The data in Figure 7 bear out the

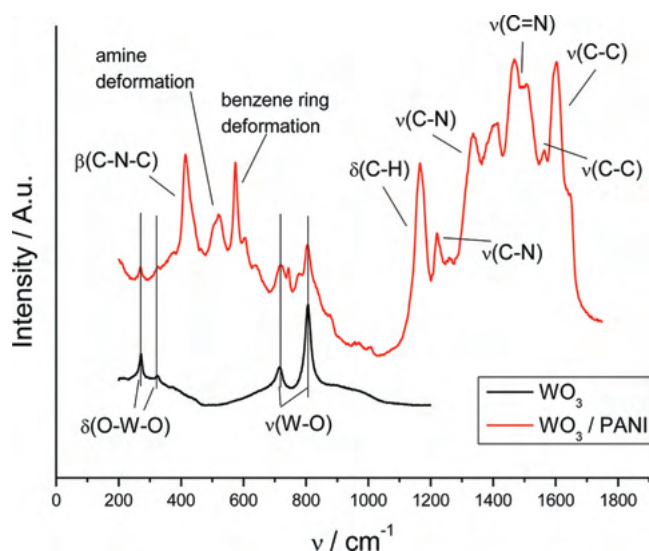


**Figure 5.** Raman spectra of the nanoporous  $\text{WO}_3$  and the  $\text{WO}_3/\text{PANI}$  hybrid prepared by five CVs.

fact that both the  $\text{WO}_3$  support and PANI exhibit well-defined and reversible electroactivity in the hybrid configuration. Moreover the voltammogram of the hybrid translates to the *exact* sum of the electroactivity of its components. It is important to point out that while the inorganic component possesses its redox activity at the cathodic (negative potential) end, the organic part's redox transformation takes place at the anodic (positive potential) end. This separation of the electroactivity within the applied potential window (without losing any electroactivity due to the presence of the other component) is advantageous for the utilization of such hybrids, for example, in electrochromic applications.

In Figure 8A, cyclic voltammograms recorded at four different sweep rates are presented. As for PANI, the peak currents are directly proportional to the potential scan rate for both the anodic and cathodic current flow (Figure 8B), attesting to the lack of diffusion limitations at least for potential sweep rates up to 0.1 V/s.<sup>55</sup> Oppositely, for  $\text{WO}_3$ , the characteristic cathodic currents (at  $E = -0.45$  V) are directly proportional to *square root* of the scan rate (Figure 8C). This

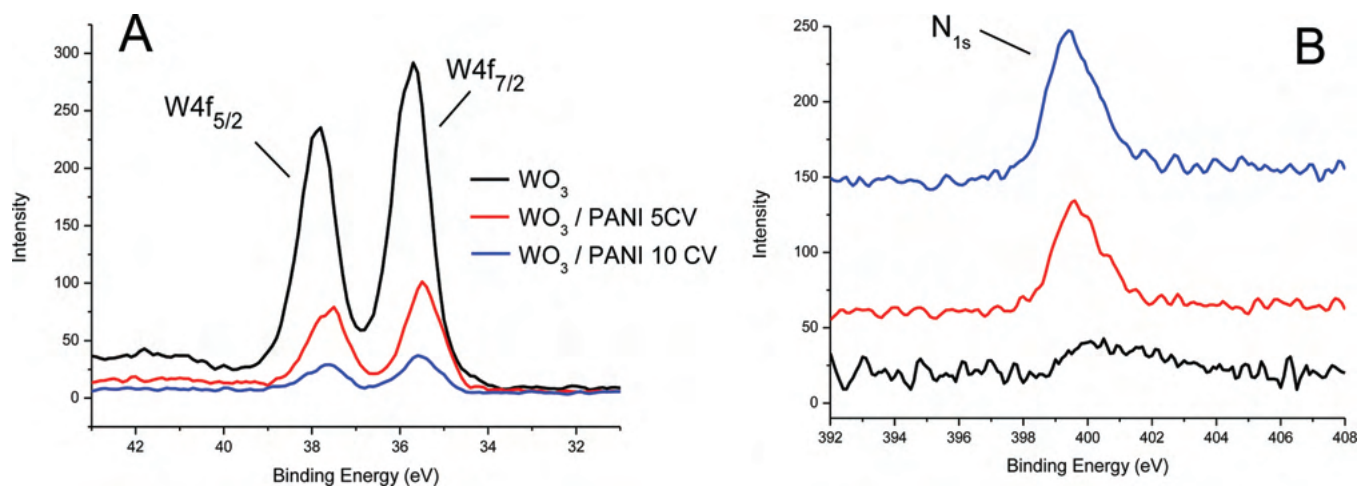


**Figure 6.** Detailed XPS scans of (A) W 4f and (B) N 1s lines for the bare  $\text{WO}_3$  and two  $\text{WO}_3/\text{PANI}$  hybrids (prepared by 5 and 10 CVs).

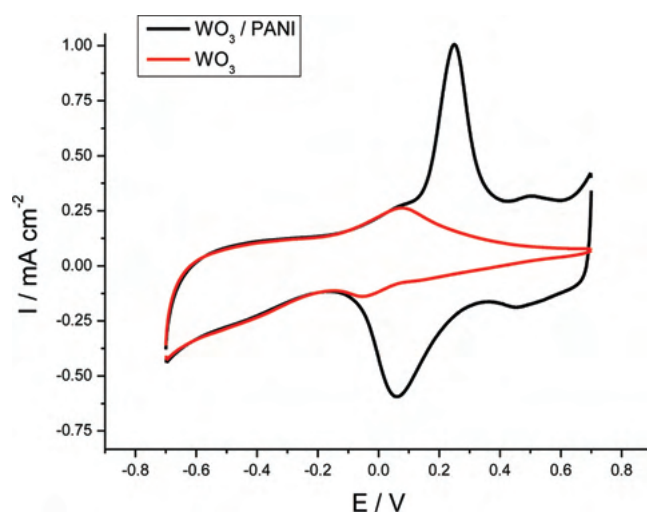


**Figure 7.** Cyclic voltammograms of the  $\text{WO}_3$  substrate and the hybrid layer in 0.5 M sulfuric acid, at a sweep rate of 100  $\text{mV s}^{-1}$ .

indicates the limiting role of mass transport, namely, the diffusion of  $\text{H}^+$  ions within the  $\text{WO}_3$  matrix.<sup>13</sup>

**3.3.2. Photoelectrochemical Characterization.** Figure 9 compares linear sweep photovoltammetry data for the  $\text{WO}_3/\text{PANI}$  hybrid material, with its components namely the bare anodic oxide, and a neat PANI film deposited on Au electrode (with identical charge density). Note that the photovoltammograms are scaled differently to highlight the features of each individual curve. This voltammetry technique is described elsewhere<sup>56</sup> but briefly consists of a slow scan of the potential while the film irradiation is periodically interrupted. In this manner, both the “dark” and the light-induced photoresponse of the samples can be assessed in a single experiment. As for the  $\text{WO}_3$  matrix, the photocurrents are anodic in polarity consistent with the n-type semiconductor behavior of this semiconductor. The photocurrents arise mainly from the photooxidation of adsorbed hydroxyl groups, water molecules, or even the electrolyte sulfate ions. On the other hand, in case of the neat PANI film, at the beginning of the scan, a cathodic photocurrent can be detected at negative potentials, related to the p-type behavior of the polymer. This photocurrent flow is sustained by the reduction of dissolved  $\text{O}_2$ , as was

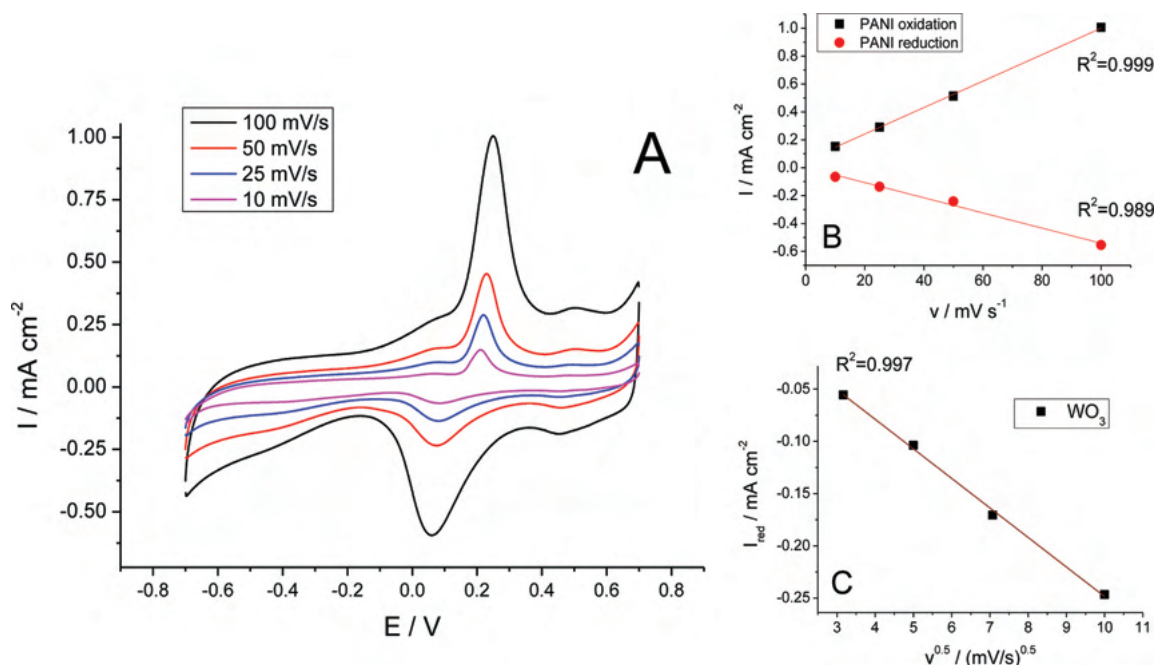


**Figure 8.** (A) Cyclic voltammograms for the  $\text{WO}_3/\text{PANI}$  hybrid in a solution of 0.5 M  $\text{H}_2\text{SO}_4$  at different scan rates. (B, C) Analysis of main anodic and respective cathodic current peak for PANI and a cathodic peak (for  $\text{WO}_3$ ) current vs scan rate data from (A).

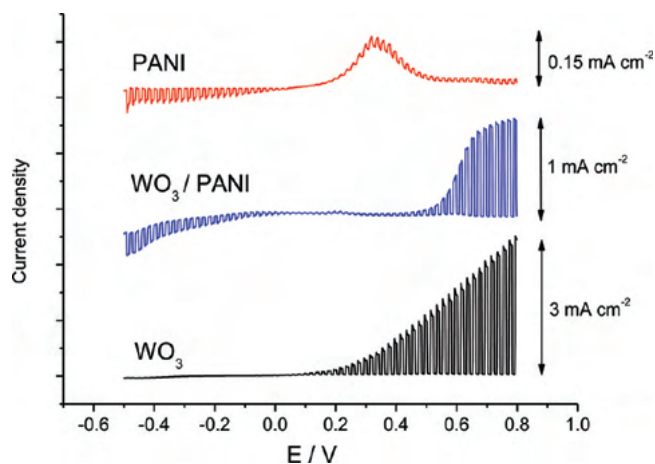


**Figure 9.** Representative photovoltammograms of  $\text{WO}_3$ , PANI, and the  $\text{WO}_3/\text{PANI}$  hybrid, recorded between  $-0.5$  and  $0.8$  V, in  $0.1$  M  $\text{Na}_2\text{SO}_4$ , at a sweep rate of  $2$   $\text{mV s}^{-1}$  using the full output of a  $150$  W Xe arc lamp.

demonstrated for other conducting polymers, such as PEDOT.<sup>57</sup> At positive potentials, superimposed on the dark current related to oxidation of the polymer, some anodic (n-type) photocurrent can also be observed. This is not surprising because although semiconducting polymers (such as PANI) are generally known to be p-type, both p-type and n-type behaviors have been reported depending on its oxidation state.<sup>58–62</sup> The moderate n-type behavior of the oxidized PANI (emeraldine form) was discussed and described by different authors.<sup>58–62</sup>

The photovoltammogram of the hybrid material shows some features of both of its components (Figure 9). While the appearance of the cathodic photocurrents below  $E = 0.0$  V proves the p-type photoactivity of PANI in the hybrid configuration, the n-type behavior with anodic photocurrents at higher potentials is related to the inorganic part. However, the absolute value of these photocurrents is rather interesting,

and this trend is further elaborated in the transient photocurrent data in Figure 10. The cathodic photocurrents related

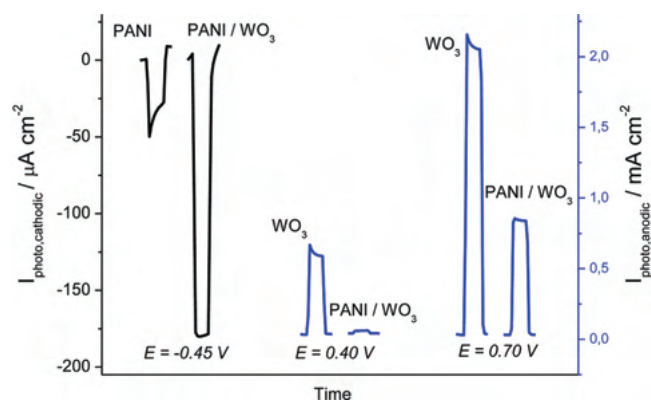


**Figure 10.** Comparison of photocurrent transients at three bias potentials selected from the photovoltammograms presented in Figure 9. Each transient lasted for 5 s.

to polyaniline are significantly (more than 3 times) larger in the  $\text{WO}_3/\text{PANI}$  hybrid, compared to a pure PANI film deposited on the Au electrode. This effect can be interpreted by the nanostructured character of the  $\text{WO}_3$  electrode, which is covered by a homogeneous, thin (15 nm) PANI film (cf. Figure 3). Thus, collection of the photogenerated holes is not limited by transport of the charge carriers in the organic polymer as is the case with a bulk layer. Moreover,  $\text{WO}_3$  is conducting and negatively polarized in this region and is thus able to receive the photogenerated holes, promoting enhancement of the photocurrent.

In addition, beyond the obvious difference in the value of the photocurrents, careful examination of the shape of the photocurrent transients reveals another significant change. Namely, for the cathodic photocurrents, the hybrid sample exhibits a plateau—or a moderately linear decrease, depending

on the potential range—instead of a spiked transient profile as is the case for neat PANI (Figure 10). This is diagnostic of the carriers being effectively separated before they undergo recombination. The plateau-like shape supports the advantage of both the nanostructured semiconductor support and the homogeneous distribution of the deposited polymer. This significant increase of the cathodic photocurrents may be exploited in the future in photoelectrocatalytic applications such as  $O_2$  and  $CO_2$  reduction.

As for the anodic photocurrent magnitude, interestingly a decrease is observed compared to the bare  $WO_3$  case (Figure 10). More careful examination reveals that this decrease is not uniform over the whole potential window. That is, while up to 0.4 V, the photocurrent is almost completely diminished, at a 0.7 V potential bias, only a partial decrease is seen (Figure 10). Note also the coincidence between development of the anodic photocurrent (starting from 0.4 V) and the cessation of dark current flow related to oxidation of the polymer (Figure 9). This indicates that the “quenching” effect of the polymer is strongly dependent on its oxidation state. Moreover, the amount of the deposited polymer plays a key role as well, since the effect is more and more expressed with the gradual increase in the amount of PANI (see Supporting Information Figure S1). The important point to note is that electrochemical infiltration of PANI into a nanoporous  $WO_3$  framework results in a hybrid material exhibiting both p-type and n-type behavior, with relatively large photocurrent densities.

To gain deeper understanding into the unexpected anodic behavior, stationary (chronoamperometric) photocurrent measurements were performed with both the bare oxide and the hybrid material at various potentials (see an example in the inset of Figure 11). In Figure 11, the relative decrease in the

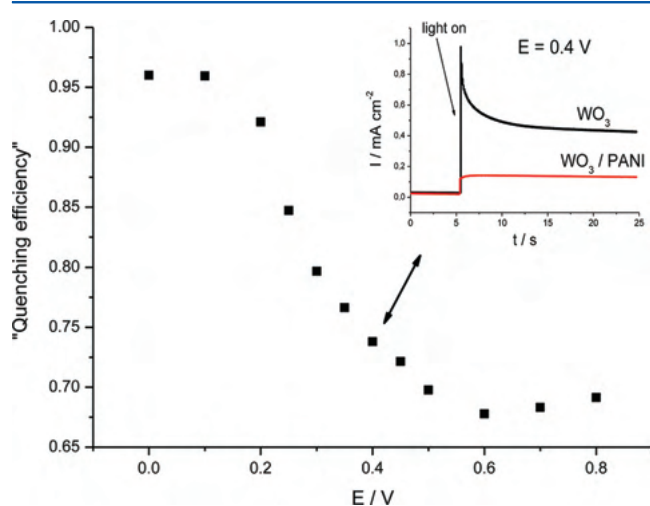


**Figure 11.** Relative decrease in the stationary anodic photocurrent at different potentials in the range 0–0.8 V, as determined by chronoamperometric measurements. The inset shows representative chronoamperometric data at a selected potential ( $E = 0.4$  V).

photocurrents ( $(I_{\text{photo},WO_3} - I_{\text{photo},\text{hybrid}})/I_{\text{photo},WO_3}$ ), measured under chronoamperometric circumstance, is shown as a function of the bias potential. Clearly, at low potentials, there is an almost complete quenching of the photocurrent, while during the oxidation of the polymer (between  $E = 0.2$  and  $0.5$  V) this effect decreases and then remains constant at potentials where PANI is oxidized to its emeraldine form. This trend can

be qualitatively explained by the fact that in its reduced (leucoemeraldine) form PANI is an insulator (with photoconductivity) while in the oxidized form (emeraldine) it is conducting and behaves as an n-type semiconductor. Apparently this dual character results in the interesting behavior presented above: namely, in its reduced form, PANI drains all the photoelectrons from the conduction band of  $WO_3$  (which thus cannot access the back-contact, and consequently no photocurrent can be detected) while in the oxidized form this effect is not expressed anymore, and the holes can reach the solution (since PANI is conducting).

Finally, although the polymeric film deposited on the  $WO_3$  nanostructured matrix is very thin, the decrease in the anodic photocurrent (related to  $WO_3$ ) can be also related to the optical shielding effect from the polymer. It is worth noting that this notion would be in perfect agreement with the data trends seen in the Supporting Information Figure S1). This possibility would be in accordance with the observations presented in Figure 11, since the optical spectrum of the fully reduced polyaniline (leucoemeraldine)<sup>41</sup> almost completely overlaps with the spectrum of  $WO_3$ .<sup>13</sup> On the other hand, after oxidation to emeraldine and coupled with the consequent spectral changes, the overlap is not that significant anymore, and thus the shielding effect is not expressed.

#### 4. CONCLUDING REMARKS

In this study, the feasibility of electrochemical infiltration of a conjugated polymer, namely polyaniline (PANI), into a nanoporous  $WO_3$  host matrix prepared by anodization was demonstrated. Development of the hybrid structure was monitored by SEM, and evidence for a homogeneous distribution of the polymer was presented. Spectroscopic probes such as Raman spectroscopy and XPS not only confirmed the chemical identity of the components of the hybrid material, but the nanoscale homogeneity was also reflected in these data. The hybrid assembly exhibited a quasi-reversible voltammetric behavior, which was the exact sum of its components. Photoelectrochemical data revealed a complex behavior of the  $WO_3$ /PANI composite. Specifically the hybrid exhibited the properties of both individual components: cathodic (p-type) photocurrents at negative potentials and anodic (n-type) photoactivity at positive potentials. Importantly, the cathodic photocurrents related to PANI were ca. 3–4 times larger in the hybrid configuration compared to values obtained for the neat polymeric film on a Au electrode. This enhanced photocurrent may be utilized in applications; for example, the photoelectrocatalytic reduction of  $O_2$  and  $CO_2$  and such studies are in progress.

#### ■ ASSOCIATED CONTENT

##### Supporting Information

Effect of the amount of the deposited polymer on the photovoltammetry data. This material is available free of charge via the Internet at <http://pubs.acs.org>.

#### ■ AUTHOR INFORMATION

##### Corresponding Author

\*Tel: 817 272 5421; e-mail: [cjanaky@uta.edu](mailto:cjanaky@uta.edu) (C.J.), [rajeshwar@uta.edu](mailto:rajeshwar@uta.edu) (K.R.).

##### Notes

The authors declare no competing financial interest.

## ACKNOWLEDGMENTS

C. Janáky gratefully acknowledges the support of the European Union under FP7-PEOPLE-2010-IOF, Grant 274046.

## REFERENCES

- Gomez-Romero, P. *Adv. Mater.* **2001**, *13*, 163–174.
- Gangopadhyay, R.; De, A. *Chem. Mater.* **2000**, *12*, 608–622.
- Rajeshwar, K.; de Tacconi, N. R.; Chenthamarakshan, C. R. *Chem. Mater.* **2001**, *12*, 2765.
- Coakley, K. M.; Liu, Y.; McGehee, M. D.; Frindell, K. L.; Stucky, G. D. *Adv. Funct. Mater.* **2003**, *13*, 301–306.
- Zhang, W.; Cheng, Y.; Yin, X.; Liu, B. *Macromol. Chem. Phys.* **2011**, *212*, 15–23.
- Beek, W. J. E.; Wienk, M. M.; Janssen, R. J. *Adv. Funct. Mater.* **2006**, *16*, 1112–1116.
- Zang, J.; Bao, S. J.; Li, C. M.; Bian, H.; Cui, X.; Bao, Q.; Sun, C. Q.; Guo, J.; Lian, K. *J. Phys. Chem. C* **2008**, *112*, 14843–14847.
- Huguenin, F.; Torresi, R. M. *J. Phys. Chem. C* **2008**, *112*, 2202–2209.
- Kerr, T.; Wu, H.; Nazar, L. *Chem. Mater.* **1996**, *8*, 2005–2015.
- Janáky, C.; Endrődi, B.; Berkesi, O.; Visy, C. *J. Phys. Chem. C* **2010**, *114*, 19338–19344.
- Janáky, C.; Visy, C.; Berkesi, O.; Tombác, E. *J. Phys. Chem. C* **2009**, *113*, 1352–1358.
- Deb, S. K. *Sol. Energy Mater. Sol. Cells* **2008**, *92*, 245–258.
- Zheng, H.; Ou, J. Z.; Strano, M. S.; Kaner, R. B.; Mitchell, A.; Kalantarzadeh, K. *Adv. Funct. Mater.* **2011**, *21*, 2175–2196.
- Monllor-Satoca, D.; Borja, L.; Rodes, A.; Gómez, R.; Salvador, P. *ChemPhysChem* **2006**, *7*, 2540–2541.
- Baeck, S.-H.; Choi, K.-S.; Jaramillo, T. F.; Stucky, G. D.; McFarland, E. W. *Adv. Mater.* **2003**, *15*, 1269–1273.
- Granqvist, C. G. *Sol. Energy Mater. Sol. Cells* **2000**, *60*, 201–262.
- Zhang, J.; Wang, X. L.; Xia, X. H.; Gu, C. D.; Zhao, Z. J.; Tu, J. P. *Electrochim. Acta* **2010**, *55*, 6953–6958.
- Cheng, W.; Baudrin, E.; Dunn, B.; Zink, J. I. *J. Mater. Chem.* **2000**, *11*, 92–97.
- Sadek, A. Z.; Zheng, H.; Breedon, M.; Bansal, V.; Bhargava, S. K.; Latham, K.; Zhu, J.; Yu, L.; Hu, Z.; Spizzirri, P. G.; Wlodarski, W.; Kalantarzadeh, K. *Langmuir* **2009**, *25*, 9545–51.
- Zheng, H.; Tachibana, Y.; Kalantar-Zadeh, K. *Langmuir* **2010**, *26*, 19148–52.
- Akiyama, M.; Tamaki, J.; Miura, N.; Yamazoe, N. *Chem. Lett.* **1991**, *20*, 1611–1614.
- Sun, H.; Cantalini, C.; Lozzi, L.; Passacantando, M.; Santucci, S.; Pelino, M. *Thin Solid Films* **1996**, *287*, 258–265.
- Endo, N.; Miho, Y.; Ogura, K. *J. Mol. Catal.* **1997**, *1169*, xxx.
- Tsuchiya, H.; Macak, J. M.; Sieber, I.; Taveira, L.; Ghicov, A.; Sirotna, K.; Schmuki, P. *Electrochem. Commun.* **2005**, *7*, 295–298.
- de Tacconi, N. R.; Chenthamarakshan, C. R.; Yogeewaran, G.; Watcharenwong, A.; de Zoysa, R. S.; Basit, N.; Rajeshwar, K. *J. Phys. Chem. B* **2006**, *110*, 25347–55.
- Mukherjee, N.; Paulose, M.; Varghese, O.; Mor, G. K.; Grimes, C. A. *J. Mater. Res.* **2003**, *18*, 2296–2299.
- Berger, S.; Tsuchiya, H.; Ghicov, A.; Schmuki, P. *Appl. Phys. Lett.* **2006**, *88*, 203119.
- Kukkola, J.; Mäklin, J.; Halonen, N.; Kyllönen, T.; Tóth, G.; Szabó, M.; Shchukarev, A.; Mikkola, J.-P.; Jantunen, H.; Kordás, K. *Sens. Actuators, B* **2011**, *153*, 293–300.
- Cristino, V.; Caramori, S.; Argazzi, R.; Meda, L.; Marra, G. L.; Bignozzi, C. A. *Langmuir* **2011**, *27*, 7276–84.
- Watcharenwong, A.; Chanmanee, W.; de Tacconi, N. R.; Chenthamarakshan, C. R.; Kajitvichyanukul, P.; Rajeshwar, K. *J. Electroanal. Chem.* **2008**, *612*, 112–120.
- Nah, Y.-C.; Ghicov, A.; Kim, D.; Schmuki, P. *Electrochem. Commun.* **2008**, *10*, 1777–1780.
- Zhu, J.; Wei, S.; Zhang, L.; Mao, Y.; Ryu, J.; Karki, A. B.; Young, D. P.; Guo, Z. *J. Mater. Chem.* **2011**, *21*, 342.
- Lee, K.; Zhang, L.; Lui, H.; Hui, R.; Shi, Z.; Zhang, J. *Electrochim. Acta* **2009**, *54*, 4704–4711.
- Zou, B. X.; Liu, X. X.; Diamond, D.; Lau, K. T. *Electrochim. Acta* **2010**, *55*, 3915–3920.
- Zou, B.-X.; Liang, Y.; Liu, X.-X.; Diamond, D.; Lau, K.-T. *J. Power Sources* **2011**, *196*, 4842–4848.
- Zhang, L.; Xiong, S.; Ma, J.; Lu, X. *Sol. Energy Mater. Sol. Cells* **2009**, *93*, 625–629.
- Kalagi, S. S.; Mali, S. S.; Dalavi, D. S.; Inamdar, I.; Im, H.; Patil, P. S. *Synth. Met.* **2011**, *161*, 1105–1112.
- Zhang, J.; Tu, J. P.; Zhang, D.; Qiao, Y. Q.; Xia, X. H.; Wang, X. L.; Gu, C. D. *J. Mater. Chem.* **2011**, *21*, 17316.
- Parvatikar, N.; Jain, S.; Khasim, S.; Revansiddappa, M.; Bhoraskar, S. V.; Prasad, M. V. N. A. *Sens. Actuators, B* **2006**, *114*, 599–603.
- Sadek, A.; Wlodarski, W.; Shin, K.; Kaner, R.; Kalantarzadeh, K. *Synth. Met.* **2008**, *158*, 29–32.
- Tiwari, A.; Gong, S. *Electroanalysis* **2008**, *20*, 1775–1781.
- Kang, E.; Neoh, K.; Tan, K. *Prog. Polym. Sci.* **1998**, *23*, 277–324.
- Huang, W. S.; Humphrey, B. D.; MacDiarmid, A. G. *J. Chem. Soc., Faraday Trans. 1* **1986**, *82*, 2385.
- Inzelt, G.; Pineri, M.; Schultze, J.; Vorotyntsev, M. *Electrochim. Acta* **2000**, *45*, 2403–2421.
- Zhang, H.; Zong, R.; Zhu, Y. *J. Phys. Chem. C* **2009**, *113*, 4605–4611.
- Zhang, H.; Zhu, Y. *J. Phys. Chem. C* **2010**, 5822–5826.
- Wang, D.; Liu, Y.; Wang, C.; Zhou, F.; Liu, W. *ACS Nano* **2009**, *3*, 1249–57.
- Kowalski, D.; Schmuki, P. *Chem. Commun.* **2010**, *46*, 8585–7.
- Janáky, C.; Bencsik, G.; Rác, A.; Visy, C.; de Tacconi, N. R.; Chanmanee, W.; Rajeshwar, K. *Langmuir* **2010**, *26*, 13697–702.
- Kowalski, D.; Tighineanu, A.; Schmuki, P. *J. Mater. Chem.* **2011**, 17909–17915.
- Döbbelin, M.; Tena-Zaera, R.; Carrasco, P. M.; Sarasua, J.-R.; Cabañero, G.; Mecerreyes, D. *J. Polym. Sci., Part A: Polym. Chem.* **2010**, *48*, 4648–4653.
- Cho, S. I.; Lee, S. B. *Acc. Chem. Res.* **2008**, 699–707.
- Quillard, S.; Louran, G.; Lefrant, S.; MacDiarmid, A. G. *Phys. Rev. B* **1994**, *50*, 496–508.
- Lapkowski, M.; Berrada, K.; Quillard, S.; Louarn, G.; Lefrant, S.; Pron, A. *Macromolecules* **1995**, *28*, 1233–1238.
- Bard, A. J.; Faulkner, L. R. *Electrochemical Methods*, 2nd ed.; John Wiley & Sons: New York, 2001.
- Rajeshwar, K. In *Electron Transfer in Chemistry*; Balzani, V., Ed.; Wiley-VCH: Weinheim, 2001.
- Bencsik, G.; Lukács, Z.; Visy, C. *Analyst* **2010**, *135*, 375–80.
- Miquelino, F. L.; C. Depaoli, M. A.; Genies, E. M. *Synth. Met.* **1994**, *68*, 91–96.
- Kilmartin, P.; Wright, G. *Electrochim. Acta* **1996**, *41*, 1677–1687.
- Kilmartin, P. A.; Wright, G. A. *Electrochim. Acta* **1998**, *43*, 3091–3103.
- Maia, D. J.; Neves, S.; das, Alves, O. L.; Paoli, M.-De *Electrochim. Acta* **1999**, *44*, 1945–1952.
- Dasneves, S.; Dafonseca, C.; Depaoli, M. *Synth. Met.* **1997**, *89*, 167–169.

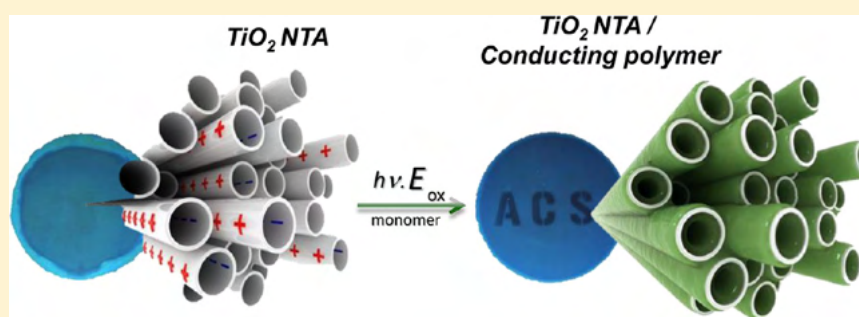
# Bringing Conjugated Polymers and Oxide Nanoarchitectures into Intimate Contact: Light-Induced Electrodeposition of Polypyrrole and Polyaniline on Nanoporous $\text{WO}_3$ or $\text{TiO}_2$ Nanotube Array

Csaba Janáky,<sup>\*,†,‡</sup> Norma R. de Tacconi,<sup>†</sup> Wilaiwan Chanmanee,<sup>†</sup> and Krishnan Rajeshwar<sup>\*,†</sup>

<sup>†</sup>Department of Chemistry and Biochemistry, University of Texas at Arlington, Arlington, Texas 76019, United States

<sup>‡</sup>Department of Physical Chemistry and Materials Science, University of Szeged, Szeged, H6720, Hungary

## S Supporting Information



**ABSTRACT:** This proof-of-concept study focuses on the photocatalytic electrodeposition of two conducting polymers, namely, polyaniline (PANI) and polypyrrole (PPy), in two different nanostructured inorganic semiconductor host matrices, namely, nanoporous tungsten trioxide and nanotubular titanium dioxide. Oxide semiconductor ( $\text{WO}_3$  and  $\text{TiO}_2$ ) films were initially electrosynthesized on tungsten and titanium foils, respectively, by anodization at different voltages in fluoride-containing aqueous media. The conjugated polymer was electrografted onto the entire surface of the photoexcited oxide semiconductor matrix using potentiostatic and potentiodynamic deposition methods. The crucial role of initial photoelectrochemical deposition, preceding the electrochemical polymerization step, was demonstrated. The photoelectrodeposited and electrodeposited hybrid samples were compared from both morphological and electrochemical perspectives. Importantly, through application of the methodology presented in this article, deposition of electroactive polymers can be achieved homogeneously, on both macroscale and nanoscale dimensions. The morphology and structural properties of these assemblies were evaluated by FE-SEM, ATR FT-IR, and Raman spectroscopy, whereas their electroactivity was characterized by cyclic voltammetry.

## INTRODUCTION

Hybrid materials based on organic conducting polymers (CPs) and inorganic nanostructures have been at the leading edge of research and development.<sup>1–4</sup> A wide range of composites has been realized, including the hybridization of metal nanoparticles, carbon nanostructures, and metal chalcogenides (specifically quantum dots) with CPs.<sup>3,4</sup> Oxide semiconductors are remarkably attractive materials in this regard because a wide range of properties can be combined with complementary features of the organic counterpart. Therefore, p/n junctions were formed by combining various polymers (dominantly thiophene derivatives) with  $\text{TiO}_2$ ,  $\text{WO}_3$ , or  $\text{ZnO}$  and deployed in solar cells,<sup>5–8</sup> electrochromic devices,<sup>9</sup> or for photocatalysis.<sup>10</sup> Incorporation of  $\text{MoO}_3$ <sup>11</sup> and  $\text{Fe}_3\text{O}_4$ <sup>12</sup> into CPs has led to hybrid materials with superior sensing, magnetic, and catalytic properties. Composite materials with enhanced charge storage capacity were prepared by embedding  $\text{V}_2\text{O}_5$ ,  $\text{RuO}_2$ , and  $\text{MnO}_2$  into the matrix of CPs such as polypyrrole,<sup>13</sup> polyaniline (PANI),<sup>14</sup> and PEDOT.<sup>15</sup>

Such hybrid materials can be obtained by different synthetic routes ranging from simple mechanical mixing of the components, through chemical or electrochemical polymerization of the monomer in the presence of the inorganic nanoparticles, to simultaneous electrochemical codeposition of the polymer and the oxide (nano)particles. All of these methods possess similar drawbacks and limitations, the three most important being: (i) potential aggregation of the inorganic particles, resulting in a relatively small area of the p/n junction; (ii) uncontrolled, random distribution of the particles within the polymeric matrix; and finally (iii) lack of electrical contact between the inorganic material with the supporting electrode. Therefore, the use of composites prepared thus as electrodes or in electronics (which is the case in most of the applications that have been considered) is hindered by the fact that only the

Received: May 28, 2012

Revised: July 5, 2012

Published: July 11, 2012

conductive polymer matrix has direct electrical connection to the electrode substrate.

Nanostructuring of one or both components of the hybrid assembly is very attractive from both scientific and technological aspects. In fact, the role of morphology and nanoscale structure within organic/inorganic assemblies has been recently highlighted.<sup>16,17</sup> Organized nanostructured frameworks of inorganic semiconductors with well-defined morphologies such as TiO<sub>2</sub> nanotube array (NTA)<sup>18,19</sup> or nanoporous WO<sub>3</sub><sup>20,21</sup> are particularly eminent candidates to overcome the problems listed above. By infiltrating CPs into such nanoarchitectures, hybrid assemblies with ordered structure, large areas of organic/inorganic junctions, and distinct morphologies, can be obtained. In such nanostructured configurations, both components will have better electrical contact with the underlying electrode.

For the preparation of the inorganic part of these hybrid materials, anodization is indeed an attractive method because the resulting oxides fulfill all of the enumerated requirements. Most importantly, they have an ordered nanoscale structure, which greatly enhances semiconductor behavior, particularly improved charge carrier collection due to 1D vectorial e<sup>-</sup> transport.<sup>22–24</sup> Moreover, through simple adjustment of the parameters of the synthetic procedure, several key properties of the nanotubes (length, diameter, wall thickness, conductance, etc.) can be tuned for targeted applications. Because of these favorable properties, TiO<sub>2</sub> NTAs are undoubtedly one of the most intensively studied structures within this class of materials. Accordingly, a wide scale of utilization possibilities have been demonstrated already, such as photocatalysis, electrochromism,<sup>19</sup> solar cells,<sup>22–25</sup> or drug delivery.<sup>26</sup> Similarly, nanoporous WO<sub>3</sub> obtained via anodization of W-foil showed superior efficiency compared with counterparts synthesized by other methods, in terms of photoelectrochemical behavior, electrochromism, sensing, electrocatalytic activity, or water splitting ability.<sup>27–29</sup>

Realization of hybrid materials based on the above organized oxide nanostructures and CPs usually involves spin coating of the solution of the polymer in organic solvents, followed by thermal treatment. However, this approach has limited scope due to simple physical reasons, most importantly because colloidal size polymeric macromolecules are too big to penetrate into the pores of a nanostructured matrix (especially if it is already partially loaded), resulting in insufficient pore filling. The net result is that the organic component resides dominantly at the upper areas of the NTA. Interfacial contact between the inorganic oxide and the infiltrated polymer is rather poor because there is no driving force that would ensure intimate contact between the organic and the inorganic components. Recent studies have underlined the crucial role of the nature of the organic/inorganic interface for different applications.<sup>30,31</sup> Consequently, there are only a few examples for successful application of hybrid assemblies, dominantly as solar cells with<sup>32</sup> or without<sup>33,34</sup> dye sensitization. Importantly by solving the morphological and structural issues listed above, enhanced performance may be expected for organic/inorganic hybrids in a wide range of applications.

In an effort to overcome the above-mentioned obstacles and to achieve homogeneous infiltration of the CP component, different in situ approaches using the corresponding monomer precursor have been deployed. Chemical,<sup>35</sup> thermal,<sup>36</sup> or UV photopolymerization<sup>37</sup> was utilized to synthesize poly(1-methoxy-4-(2-ethylhexyloxy)-p-phenylene-vinylene) (MEH-

PPV), poly(3,4 ethylenedioxythiophene) (PEDOT), or polythiophene, respectively, in the oxide host. Electrodeposition is a particularly versatile method in this regard because it relies on exploitation of the intrinsic electroactivity of the monomer. The most important possible advantage of this approach is that the CPs can be directly electrogenerated on the surface of the inorganic nanostructure, which acts as a working electrode. Therefore, this method has been employed to deposit CPs on different nanostructured semiconductor matrices such as TiO<sub>2</sub>,<sup>38–42</sup> ZnO,<sup>43</sup> Fe<sub>2</sub>O<sub>3</sub>,<sup>44</sup> or WO<sub>3</sub>.<sup>45</sup> Moreover, because of the advancement of the knowledge on inorganic materials, there is a fairly large number of different anodized nanostructures.<sup>19</sup> Therefore, there is a potentially unlimited number of combinations with various CPs. Nonetheless, wide bandgap semiconductors (including TiO<sub>2</sub>) are handicapped by their low electrical conductance, especially in the dark. This results in inhomogeneous deposition of the polymer, either on the top of the substrate, or at the supporting metal electrode interface due to cracks or other defects in the oxide coverage. Importantly, because of inadequate filling of the nanopores the area of the p/n junction is limited, thus deleteriously affecting the performance of the hybrid in different applications.

To underline the role of electroactivity of the oxide semiconductor, Figure 1 presents a comparison of cyclic

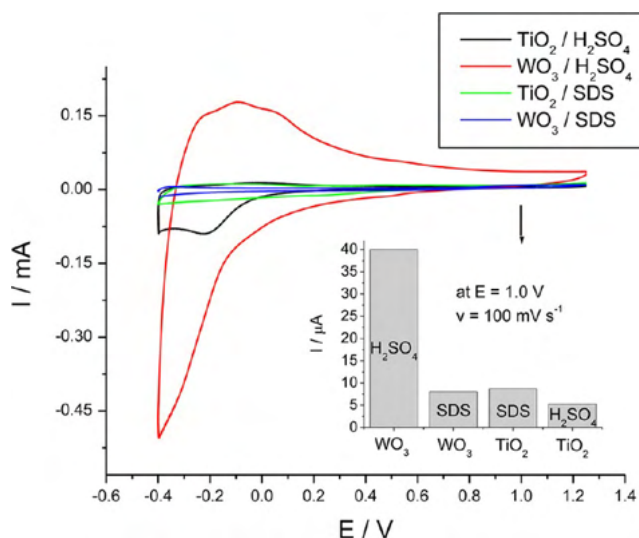


**Figure 1.** Cyclic voltammograms of nanoporous WO<sub>3</sub> and TiO<sub>2</sub> NTA electrodes at a potential sweep rate of 100 mV s<sup>-1</sup> in 0.5 M H<sub>2</sub>SO<sub>4</sub> and in 0.025 M SDS. The inset shows the current values registered at E = 1.0 V.

voltammograms for TiO<sub>2</sub> NTA and nanoporous WO<sub>3</sub> in acidic (H<sub>2</sub>SO<sub>4</sub>) and neutral (sodium dodecyl sulfate, SDS) media. Note that all samples are electroactive in the negative potential regime; however, the *magnitude* of this activity is different for each system. More importantly, as can be clearly seen in the inset in Figure 1, the electroactivity of the materials is very low at the anodic end of the cycles, except in the case of the WO<sub>3</sub>/H<sub>2</sub>SO<sub>4</sub> interface. This enhanced electroactivity of WO<sub>3</sub> in acidic media was rationalized by the formation of tungsten bronze (H<sub>x</sub>WO<sub>3</sub>), assisted by H<sup>+</sup> uptake/release as charge compensation during the (W<sup>6+</sup>/W<sup>5+</sup>) redox process.<sup>27</sup>

Because of the low electroactivity of the oxide semiconductor working electrode, effective and homogeneous anodic electrodeposition can only be achieved under very carefully designed

experimental conditions, both in terms of polymerization electrolyte and procedure. A noteworthy method was reported recently involving several very short steps, employing high current densities and electrode potentials, and was successfully deployed to fill homogeneously either the TiO<sub>2</sub> nanotubes or the interannular space among the nanotubes with polypyrrole.<sup>46,47</sup> This method was developed based on an analogy to metal deposition on nanoporous alumina template.<sup>48</sup> However, the electroactivity of such deposited polymers can be problematic due to potential overoxidation under these rather harsh conditions.

As another example, utilization of specially designed monomers with functional groups, which can be covalently bonded to the inorganic template, can also enhance homogeneity of the hybrid morphology and improve its interfacial properties.<sup>49</sup> Finally, uniform deposition of PANI on nanoporous WO<sub>3</sub><sup>45</sup> was accomplished by recognizing the similarity in their ion exchange properties. That is, both of them are electron and proton conductors resulting in reasonable WO<sub>3</sub> electroactivity, even in the potential regime required for electropolymerization of PANI (see Figure 1).

Because the predominant limitation of these wide bandgap nanostructured oxide matrices is their low electroactivity in the potential regime where CPs are usually electrogenerated and at the same time electronic carriers can be generated in these matrices by photoexcitation, our aim in this study was to study the effect of illumination on the electrochemical deposition of the CP component. We note literature precedent for this notion.<sup>50–56</sup> Some monomers can also be photopolymerized by UV light, even without the presence of a semiconductor<sup>57,58</sup> but usually in the presence of an electron scavenger and often in the presence of a *homogeneous* photocatalyst. Electropolymerization of EDOT was also performed under illumination, and thick PEDOT and PPy layers were deposited on *flat* Nb<sub>2</sub>O<sub>5</sub> and Ta<sub>2</sub>O<sub>5</sub> substrates, respectively, for solid capacitor applications.<sup>59,60</sup>

Notably, to the best of our knowledge, there is no record in the literature of employing illumination to enhance the electrodeposition of CPs on nanostructured oxide hosts, nor are there attempts to improve the interfacial properties of resulting hybrid assemblies based on such oxides. In this article, we present the dramatic effect of illumination on the electrodeposition of two CP candidates in nanostructured oxide semiconductor host frameworks. Moreover, we uncover important mechanistic aspects and clarify the relative contribution of photoelectrochemical deposition and electrochemical polymerization to the overall process.

## EXPERIMENTAL SECTION

**Chemicals and Materials.** All chemicals were from commercial sources and were of the highest purity available. Deionized water (18 MΩ cm) was used in all cases for making solutions. Sodium fluoride (Alfa Aesar, 98.0%), poly(ethylene glycol) (*M<sub>n</sub>* ca. 400, Aldrich), and ammonium fluoride (Alfa Aesar, 98.0%) were used as received. Tungsten (Alfa Aesar, 0.25 mm thick, 99.95%) and titanium (Alfa Aesar, 0.25 mm thick, 99.95%) foils were used as the substrate for oxide film growth. Before use, the foil was cut (1.25 cm × 1.25 cm), mechanically polished to mirror finish using silicon carbide sandpaper of successively finer roughness (220, 400, 600, 1000, 1500, and 2000 grit), and cleaned in three 5 min steps in ultrasonicated acetone, 2-propanol, and finally ultrapure water. Subsequently, the substrate was dried in an ultrapure N<sub>2</sub> stream

and used immediately. For PANI and polypyrrole growth, aniline (EM Science, 99.5%) and pyrrole (Aldrich, 98.0%) monomers were freshly distilled under vacuum before use. Sulfuric acid (Alfa Aesar, 98.0%), sodium dodecyl sulfate (SDS, Sigma-Aldrich, 98.5%), and sodium-sulfate (J.T. Baker, 99.0%) were used as received.

**Anodic Growth of Nanoporous WO<sub>3</sub> and TiO<sub>2</sub> NTA.** Nanoporous WO<sub>3</sub> and nanotubular TiO<sub>2</sub> films were grown in a two-electrode electrochemical cell using a large Pt foil as counter electrode and the respective metal foil as the working electrode. Aqueous NaF was used as the electrolyte (0.15 M) in the case of W, whereas Ti foil was anodized in solutions containing 0.36 M NH<sub>4</sub>F in poly(ethylene glycol) containing a 20% v/v of deionized water. During anodization, the metal foil was pressed between a set of O rings in the electrochemical cell, leaving 0.78 cm<sup>2</sup> exposed to the electrolyte, and the electric contact was located on the backside of the sample. Anodization employed a 420X Power Supply (The Electrosynthesis Company, Lancaster, NY). The voltage was held at a preselected level (60 V in the case of WO<sub>3</sub> and 20 V for TiO<sub>2</sub>, respectively) for 3 h. After the oxide film was grown, the anodized W/Ti foil was removed from the O-ring assembly, carefully washed by immersion in deionized water, and then dried in a N<sub>2</sub> stream. Before use as substrates for aniline/pyrrole polymerization, the W/WO<sub>3</sub> and Ti/TiO<sub>2</sub> electrodes were annealed at 450 °C (under air atmosphere) for 3 h at a heating rate of 20 °C/min (Fisher Scientific, model 650-14 Isotemp Programmable Muffle Furnace) and allowed to cool gradually back to the ambient temperature. Other details of anodic growth are given elsewhere.<sup>21</sup>

**Electrosynthesis of the Hybrid Materials.** A similar experimental setup was used as that during anodization. The working electrode was the previously prepared nanoporous WO<sub>3</sub> or the nanotubular TiO<sub>2</sub> in all cases. The reference electrode was Ag/AgCl/satd. KCl (Microelectrode, Bedford, NH); all potentials in this article are given with respect to this reference. Pt coil was utilized as the counter electrode. The parameters of the performed experiments are summarized in Table 1. Each electrochemical deposition was performed both

**Table 1. Parameters of the Electropolymerization Procedure**

hybrid material	polymerization solution	polymerization method
WO <sub>3</sub> /PANI	0.2 M aniline, 0.5 M H <sub>2</sub> SO <sub>4</sub>	potentiodynamic (−0.2 V – 1.1 V), potentiostatic ( <i>E</i> = 0.85 V)
WO <sub>3</sub> /PPy	0.1 M pyrrole, 25 mM SDS	potentiodynamic (−0.4 V – 1.1 V), potentiostatic ( <i>E</i> = 0.90 V)
TiO <sub>2</sub> /PANI	0.2 M aniline, 0.5 M H <sub>2</sub> SO <sub>4</sub>	potentiodynamic (−0.2 V – 1.1/1.45/2.2 V), potentiostatic ( <i>E</i> = 1.45 V)

in the dark and under illumination, whereas all other circumstances were kept identical. The effect of the applied potential window was also studied, as can be seen in Figure 8. For photoelectrochemical deposition, the light source was a 150 W xenon arc lamp (Oriel, Stratford, CT), and the radiation source was placed 8 cm away from the working electrode surface. The illuminated area was 0.13 cm<sup>2</sup>, whereas the overall electrode surface exposed to solution was 0.39 cm<sup>2</sup>. Selective illumination of the working electrode was performed by using a mask on top of it with a transparent pattern (ACS, see Figure S2 of the Supporting Information). (See Figures 4 and 7 below)



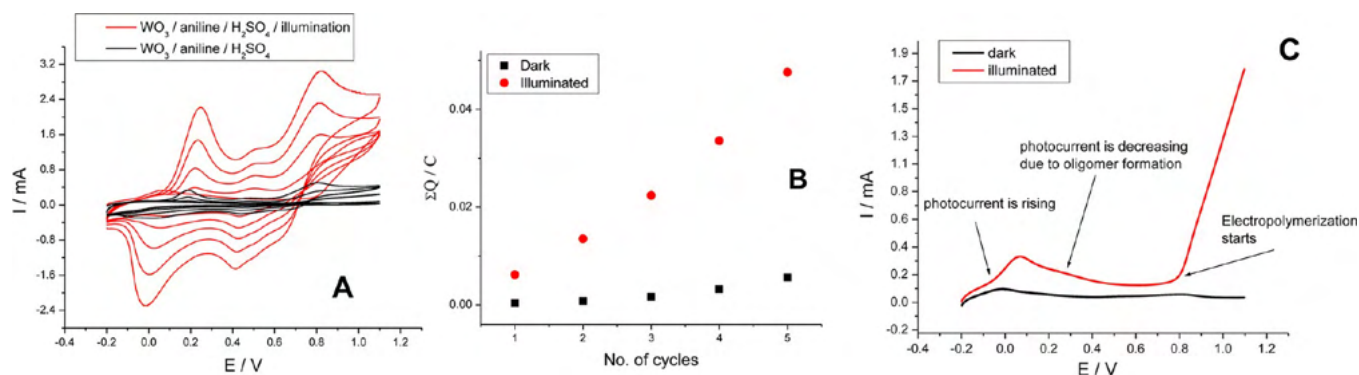


**Figure 2.** Comparison of the electrodeposition of polyaniline on nanoporous  $\text{WO}_3$  with and without illumination (150 W Xe-arc lamp). (A) Potentiodynamic cycles were recorded between  $-0.2$  and  $1.1$  V in a solution of  $0.2$  M aniline in  $0.5$  M  $\text{H}_2\text{SO}_4$ . (B) Cumulative charge flow during the subsequent redox cycles in panel A. (C) Enlargement of the first half-cycles depicted in panel A.

According to our previous study, for the deposition of PANI, a polymerization medium consisting of  $0.2$  M aniline monomer and  $0.5$  M aqueous sulfuric acid was chosen.<sup>45</sup> The solution composition for polypyrrole deposition was adopted from a preceding work.<sup>47</sup> Optimization of the electrochemical polymerization conditions was partially carried out in a previous study (on  $\text{WO}_3/\text{PANI}$ ),<sup>45</sup> and further developed herein. Finally, polymerization of aniline and pyrrole was carried out by simple but carefully optimized potential cycling protocols between different potential ranges adjusted to each system. (See Table 1.) On the basis of the data obtained during the potentiodynamic deposition, potentiostatic polymerization was also performed. For further voltammetric studies, the solution was changed after polymerization to a monomer-free  $0.5$  M  $\text{H}_2\text{SO}_4$  and  $0.1$  M  $\text{Na}_2\text{SO}_4$  electrolyte. All experiments were carried out under ambient conditions at room temperature ( $25 \pm 2$  °C).

**Characterization Methodology.** The morphology of the bare nanostructured oxides ( $\text{WO}_3$ ,  $\text{TiO}_2$ ) and the respective hybrid samples was studied using a Hitachi S-5000H field-emission scanning electron microscope (FE-SEM) at an accelerating voltage of  $15$  and  $20$  kV. Images were taken at different magnifications between  $10\text{k}$  and  $200\text{k}$ . The molecular structure of the deposited CPs was investigated by vibrational spectroscopy. FT-IR spectra were recorded using a Shimadzu IRPrestige-21 Fourier transform infrared spectrometer equipped with a diamond attenuated total reflectance (ATR) accessory. All infrared spectra were recorded between  $4000$  and  $380$   $\text{cm}^{-1}$  at  $4$   $\text{cm}^{-1}$  optical resolution by averaging  $64$  interferograms. Raman spectra were recorded with a Horiba Jobin Yvon LabRam ARAMIS instrument ( $P \leq 300$  mW) using an excitation wavelength of  $473$  nm and  $1800$  line/mm grating. In all of the cases, the slit width was  $10$   $\mu\text{m}$ , and  $10$  scans were accumulated for each spectrum. A Nikon Eclipse optical microscope equipped with a camera was employed to acquire pictures on the hybrid samples. All electrochemical measurements were performed on a CHI Electrochemical Workstation 440A instrument in a classical one-compartment, three-electrode electrochemical cell. Cyclic voltammograms of the  $\text{WO}_3/\text{PANI}$  and  $\text{TiO}_2/\text{PANI}$  hybrid samples were registered in  $0.5$  M  $\text{H}_2\text{SO}_4$  solutions, whereas for  $\text{WO}_3/\text{PPy}$   $0.1$  M  $\text{Na}_2\text{SO}_4$  supporting electrolyte was used at four different potential sweep rates between  $10$  and  $100$  mV/s.

## RESULTS AND DISCUSSION

**Photoelectrodeposition of PANI on  $\text{WO}_3$ .** The effect of illumination was first studied employing a hybrid material described recently,<sup>45</sup> namely, the  $\text{WO}_3/\text{PANI}$  as an example. As we previously presented, because of its  $\text{H}^+$  exchanging (bronze formation) behavior,  $\text{WO}_3$  is sufficiently electroactive for dark electrodeposition on it in strongly acidic media (Figure 1). However, if the electrochemical polymerization is performed under illumination but otherwise identical circumstances, then the overall pattern of current–potential curves registered during potentiodynamic cycling is dramatically different. As can be seen in Figure 2A, rapid growth of the polymer (as diagnosed from the current flow) is striking, although the shapes of the individual voltammograms (cycles) are indeed similar to those obtained in the dark or during electrodeposition on metal electrodes. By integrating the current registered during the subsequent polymerization cycles, more quantitative data may be gleaned on the polymerization process (and the amount of the generated polymer) in the two cases. The cumulative charges are depicted in Figure 2B, where the large difference between the two cases is distinctly visible. Careful examination of the first half-cycles of the polymerizations sheds further light on mechanistic aspects of the oligomer/polymer formation. The curves shown in an enlarged view in Figure 2C are dissimilar in many aspects. For the  $\text{WO}_3$  sample without illumination, very low currents are detected throughout the entire potential window. This trend is typical for CP deposition on semiconductor electrodes because during the first cycle there is only oligomerization at the positive end of the potential range. Growth of the polymer phase proceeds during successive cycles, when the template is already occasionally covered by oligomeric/polymeric nucleating seeds on which the polymer can grow further at even lower potentials. In other words, PANI has an autocatalytic effect on the electropolymerization of aniline.<sup>61,62</sup>

The complexity of the current response under illumination is very distinct. At the beginning of the curve, anodic photocurrent develops at  $\sim E = -0.05$  V, which is consistent with the n-type semiconductor behavior of  $\text{WO}_3$ . The photocurrents arise mainly from the photooxidation of adsorbed water, electrolyte sulfate ions, or more likely the aniline monomer moieties present in the solution. Interestingly the photocurrent does not increase further with increasing bias as expected: in contrast, it starts to decrease from  $E = 0.10$  V onward. This anomalous behavior can be attributed to the photocatalytic

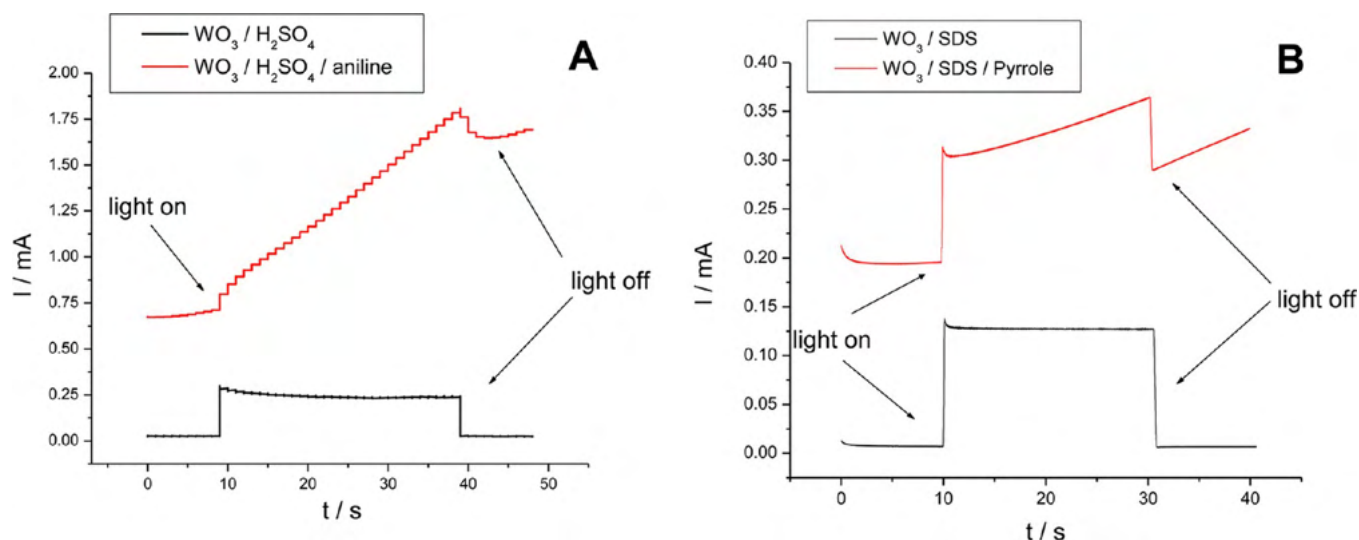


**Figure 3.** Photochronoamperometric curves for nanoporous  $\text{WO}_3$ , recorded in (A) 0.5 M  $\text{H}_2\text{SO}_4$  and 0.2 M aniline and (B) 0.025 M SDS and 0.1 M pyrrole. The curves recorded in the absence of monomers are also shown for comparison at  $E = 0.85$  and 0.9 V, respectively.

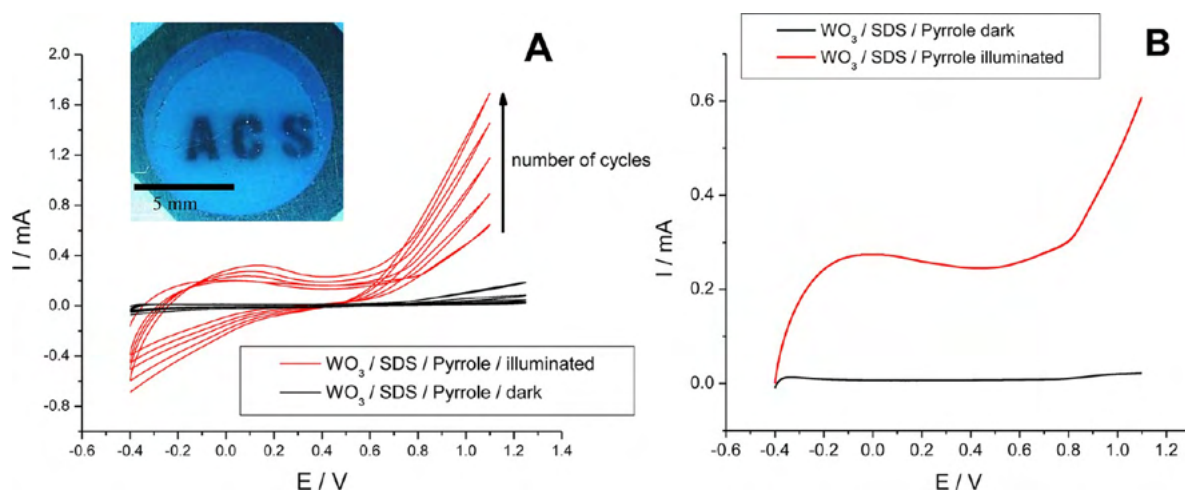


**Figure 4.** Comparison of electrodeposition of polypyrrole on nanoporous  $\text{WO}_3$  with and without illumination. (A) Potentiodynamic cycles recorded between  $-0.2$  to 1.1 and 1.25 V in the dark and under illumination, respectively, in a solution of 0.1 M pyrrole in 0.025 M SDS. (B) Enlargement of the first half-cycles depicted in panel A. The inset shows an optical image of a sample photoelectrodeposited under selective illumination through a mask. (See Figure S2 of the Supporting Information.)

polymerization of aniline, more precisely to the optical (and electric) shielding effect of the photoelectrochemically deposited PANI phase.

As a first step, aniline monomers are oxidized by photo-generated holes on the  $\text{WO}_3$  surface. Then, the radical cation reacts with another radical cation to form dimers that can react further, with either a monomer or an oligomer radical cation.<sup>63</sup> As the oligomers become progressively insoluble, they deposit on the surface of the nanostructured electrode substrate. When the potential is increased further, at a certain threshold value ( $E = 0.80$  V) electrochemical growth of the polymer starts to take place and proceeds rapidly. The striking difference between the two curves in this potential range can be explained by the fact that under illumination oligomer/polymer formation already took place at lower potentials due to photoelectrochemical deposition, thus obviating the need for electrochemical oxidation of the aniline monomer, which requires notably higher potentials. It is worth noting the similarity in the shape of the anodic ends of the cycles for the first cycle under

illumination and the later cycles registered in the dark. This is further indication of the fact that electrochemical growth of the polymer is similar in the two cases, just the formation of the seed layer is different: photoelectrochemically deposited under illumination and electrodeposited in the dark. Data obtained during potentiodynamic experiments suggested that PANI can be photocatalytically polymerized even below the potentials where electrochemical polymerization occurs. However, the external bias potential plays a key role even in this process because it facilitates the separation of the photogenerated charge carriers (by draining the photoelectrons to the back contact and hampering recombination). In this manner, more holes can react with the aniline monomers and oligomers to initiate/facilitate their polymerization through the formation of radical cations.

Chronoamperometric curves under illumination and registered at  $E = 0.85$  V are presented in Figure 3A, both in the presence and in the absence of aniline monomer. The selection of this potential value was motivated by the fact that at this

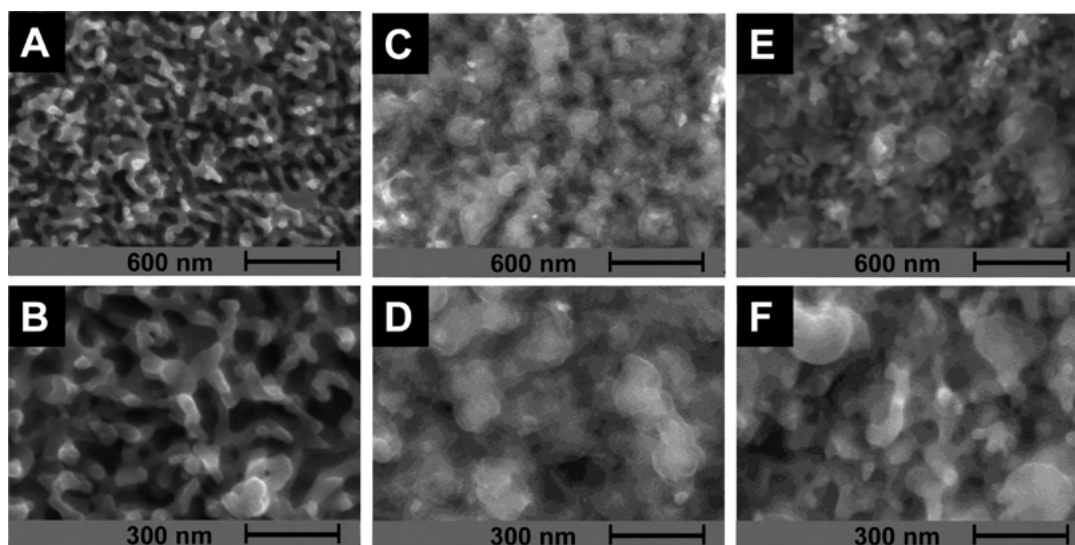


**Figure 5.** SEM images of the bare  $\text{WO}_3$  surface synthesized at  $E = 60$  V (A,B) and of the corresponding  $\text{WO}_3/\text{PPy}$  hybrid samples (synthesized using five cycles with (C,D) and without (E,F) illumination) at 50k and 100k magnification.

potential polymerization cannot be initiated in the dark (monomer oxidation does not take place), but growth of the polymer on a predeposited oligomeric/polymeric film can indeed occur. (See Figure 2.) As can be distinctly seen in Figure 3A, little current response can be obtained without illumination, either in the absence or in the presence of aniline. (Note that the curve registered in the presence of the monomer is vertically shifted, for better visualization.) Under illumination,  $\text{WO}_3$  shows the regular photocurrent transient profile in the absence of aniline, whereas a rather interesting shape can be observed when the monomer is present in the solution. As soon as the light is turned on, the current starts to develop rapidly, but instead of reaching a maximum value, it increases continuously. This pattern is related to the previously described steps of the deposition, namely, that first only photoelectrochemical deposition takes place, but it is immediately followed by electrochemical growth of the polymer. Importantly, after turning off the light, there is only a small drop in the current, indicating that in this stage of the process electropolymerization has the dominant contribution compared with the photocatalytic process.

**$\text{WO}_3/\text{Polypyrrole}$  Hybrid.** Although  $\text{WO}_3/\text{PANI}$  hybrid previously presented is a good system to understand the basic aspects of role of illumination, the real challenge is to exploit this procedure for the preparation of hybrid materials, which cannot be obtained by other methods with the desired properties. As we showed in Figure 1,  $\text{WO}_3$  has much smaller electroactivity in nonacidic medium. However, several polymers (e.g., polypyrrole) cannot be generated in their conducting form in strongly acidic electrolyte. Motivated by these facts, we selected the  $\text{WO}_3/\text{PPy}$  system as a candidate to study the effectiveness of our approach. As shown in Figure 4A, without illuminating the  $\text{WO}_3$  electrode, the anodic growth end of the potential window had to be shifted toward more positive potentials to obtain even a very slight amount of polymer. Moreover, visual examination reveals the distribution of the polymer to be rather inhomogeneous, with polymeric spots on the top of the  $\text{WO}_3$  electrode. In contrast, under illumination, drastically higher currents can be detected, and the formation of conducting PPy can be deduced from the gradual development

of higher currents (electroactivity) in the series of potentiodynamic cycles (Figure 4A).

Consider the first half-cycles enlarged in Figure 4B; although the overall profile is very similar to that presented for  $\text{WO}_3/\text{aniline}$  (Figure 2C), the effect of illumination is even more expressed. The one difference is that photocurrents can be detected from the very beginning of the potential window due to the very good hole scavenging activity of pyrrole and oligopyrroles formed because of UV illumination. Later, a slight decrease in the photocurrent can be noticed due to shielding by the photoelectrochemically deposited PPy, whereas from  $E = 0.7$  V a rapid upturn of the current can be seen, as an indication of the electropolymerization of pyrrole. Notably, under illumination, deposition of PPy takes place only at the illuminated region of the working electrode surface, resulting in homogeneous coverage. As further evidence of the selectivity of the process, by employing a mask, just certain areas of the  $\text{WO}_3$  electrode were illuminated (see the Experimental Section and Figure S2 of the Supporting Information), whereas the whole electrode was exposed to the solution. The result is depicted as an inset of Figure 4A; clearly, polymerization is limited to the areas exposed to light, and thus the pattern of the deposited polymer is identical to the pattern of illumination. Finally, by comparing Figures 2A and 4A, we can conclude that deposition of PPy is less favorable on  $\text{WO}_3$  than that of PANI; however, the illumination plays a very similar role in both cases.

To compare the nanoscale morphological features of the hybrid assemblies and to gain further insight into the effect of illumination, SEM images were taken at various magnifications, with both the bare  $\text{WO}_3$  nanostructure and the hybrid samples. In Figure 5A,B, SEM images of the bare oxide samples are presented. As can be clearly seen,  $\text{WO}_3$  has a very porous structure with high surface area, reflecting effective overetching of the tungsten surface by the fluoride species during anodization. Figure 5C,D shows representative SEM images for the hybrid samples, obtained for the deposition of PPy with five potentiodynamic cycles on the  $\text{WO}_3$  surface under illumination. The most noticeable differences compared with the bare oxide support are (i) the opacity seen for the  $\text{WO}_3$  surface on the whole sample, which can be generally observed for organic polymers; (ii) the expansion of the grain size to the

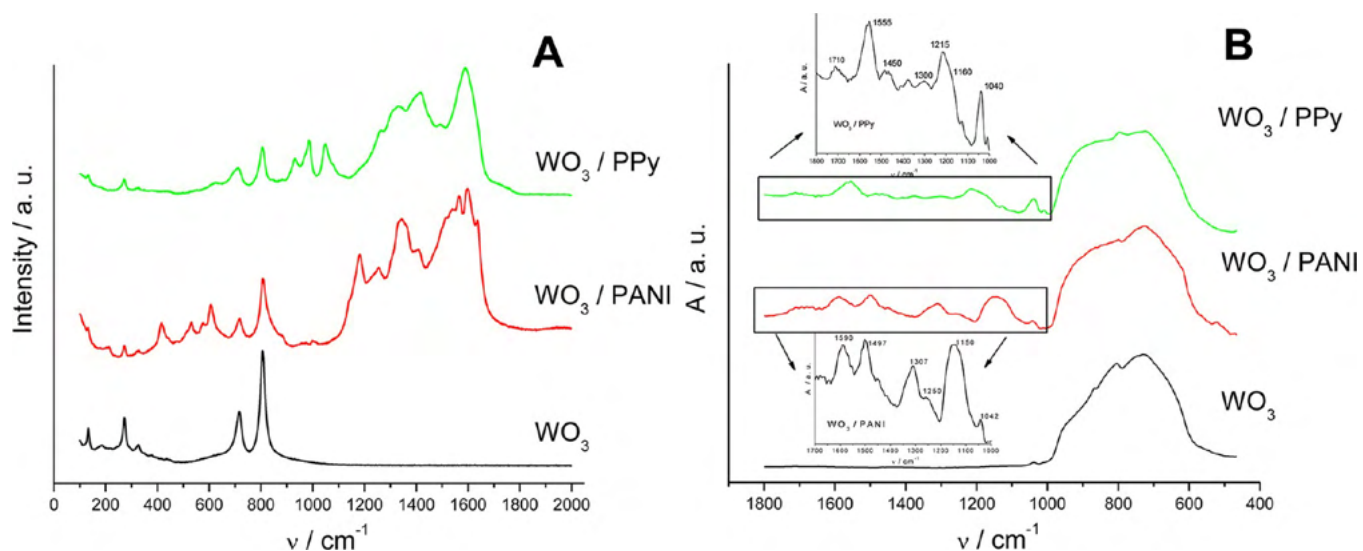


**Figure 6.** Raman (A) and FT-IR (B) spectra of nanoporous  $\text{WO}_3$ ,  $\text{WO}_3/\text{PANI}$ , and  $\text{WO}_3/\text{PPy}$  hybrid samples prepared by five potentiodynamic cycles under illumination. The insets show enlarged images of the areas characteristic for the two polymers.

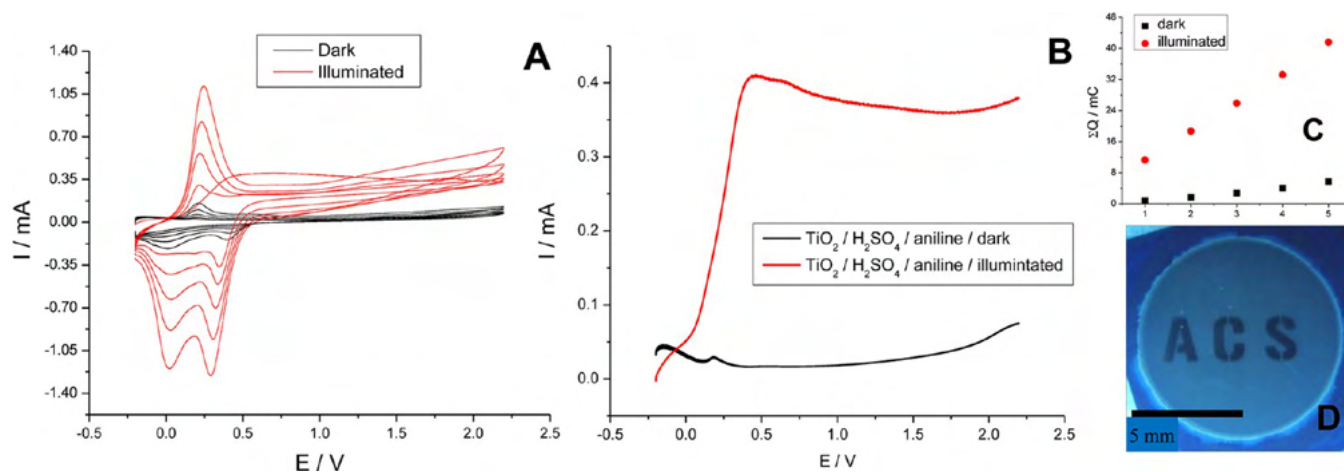


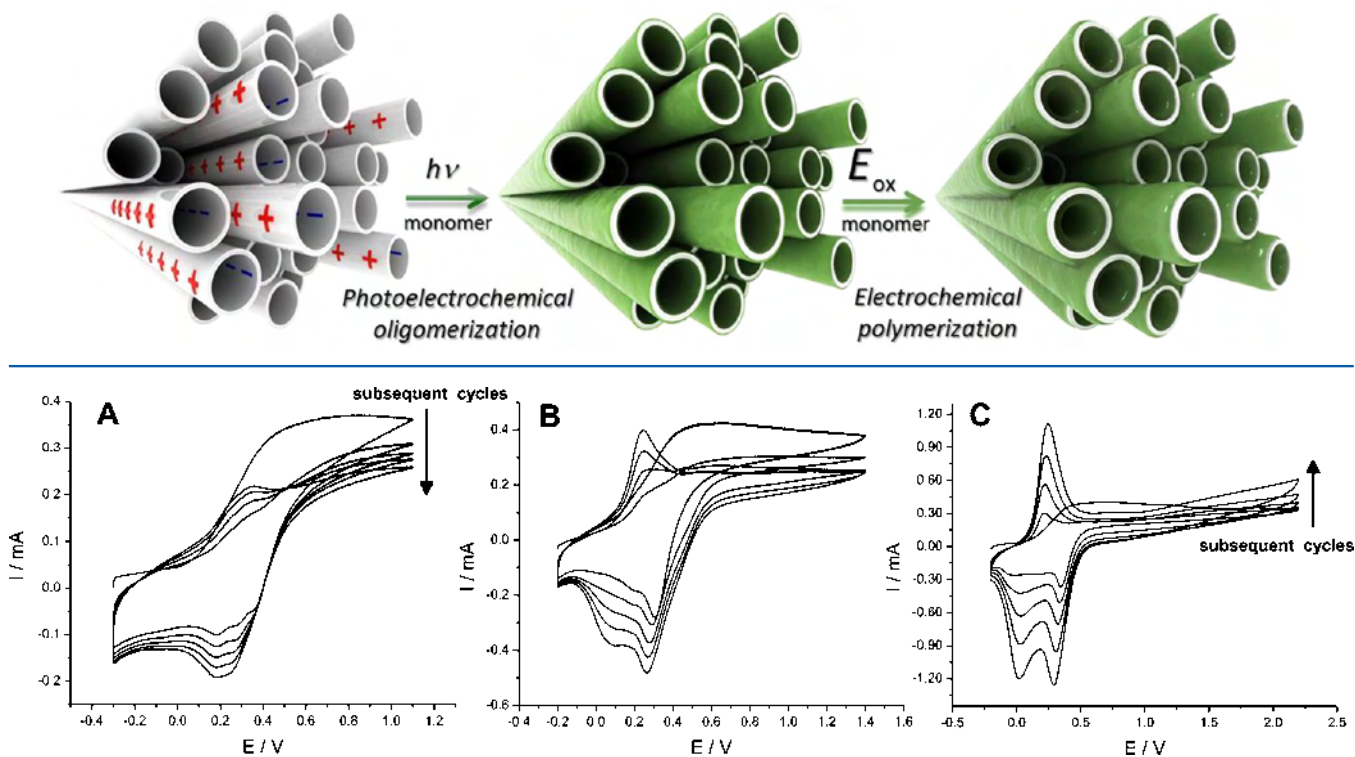
**Figure 7.** Comparison of the electrodeposition of polyaniline on  $\text{TiO}_2$  NTA with and without illumination (150 W Xe-arc lamp). (A) Potentiodynamic cycles were recorded between  $-0.2$  and  $2.2$  V, in a solution of  $0.2$  M aniline in  $0.5$  M  $\text{H}_2\text{SO}_4$ . (B) Enlargement of the first half-cycles depicted in panel A. (C) Cumulative charge flow during the subsequent redox cycles in panel A. (D) Optical image of selectively photoelectrodeposited PANI on the  $\text{TiO}_2$  NTA substrate.

parent situation in Figure 5A,B due to the homogeneous, skin-like coverage by the deposited polypyrrole; and (iii) the decrease in the space between the grains (the pore size).

Closer inspection of the hybrid structure reveals a  $\sim 50$  nm average difference in the diameter between the neat  $\text{WO}_3$  grains and the hybrid sample, which suggests that polymer photoelectrodeposition results in a  $\sim 25$  nm thick PPy film on the surface. Under illumination, PPy is seen to deposit in a very similar fashion on  $\text{WO}_3$  as PANI in the dark,<sup>45</sup> resulting in a comparable coating that covers the entire surface of the nanostructured semiconductor, as seen from both qualitative and quantitative analysis of the images. In contrast, images taken at the few spots where PPy was electrodeposited without illumination show completely different morphological attributes (Figure 5E,F). The two most striking alterations are the following: (i) instead of forming a thin film coverage on the nanoporous matrix, large globular polymeric units can be observed, randomly distributed on the top of the substrate and (ii) the  $\text{WO}_3$  grains have exactly the same average size as that measured for the bare oxide sample, which means that no

polymeric film is deposited on it. On the basis of these observations, the most prominent difference between the two hybrid samples (prepared with and without illumination) is the contact area of the organic/inorganic junction, which is practically equal to the surface area of the inorganic semiconductor matrix in the case of the illuminated sample, whereas it is almost negligible for its counterpart synthesized in the dark.

To confirm the molecular identity of the polymers photoelectrodeposited in the nanoporous  $\text{WO}_3$  framework, we carried out vibrational spectroscopic studies. FT-IR and Raman spectroscopies are rather useful for this purpose because  $\text{WO}_3$ , PPy, and PANI all have characteristic bands. Moreover, beyond simple identification of hybrid components, these complementary techniques can also indicate if any permanent overoxidation of the polymer had occurred during electrodeposition. Figure 6A contains Raman spectra of a  $\text{WO}_3$  sample and the corresponding photoelectrodeposited  $\text{WO}_3/\text{PANI}$  and  $\text{WO}_3/\text{PPy}$  hybrid samples. Existence of vibrational modes<sup>64</sup> at  $133$ ,  $272$ ,  $325$ ,  $715$ , and  $807$   $\text{cm}^{-1}$  confirms the formation of

Scheme 1. Illustration of the Two Steps of the Photo-Electrodeposition of PANI on TiO<sub>2</sub> NTA

**Figure 8.** Effect of the positive end expansion of the potential window on the polymerization of aniline on TiO<sub>2</sub> NTA (five cycles) under illumination in 0.2 M aniline, 0.5 M H<sub>2</sub>SO<sub>4</sub> solution, at a potential scan rate of 100 mV s<sup>-1</sup>.

monoclinic WO<sub>3</sub> during anodization and subsequent heat treatment. Beyond the appearance of the bands originating from the support oxide framework, several new bands can be observed for the hybrid samples in Figure 6A. All characteristic bands can be assigned to the corresponding polymers. (See the assignments in the Supporting Information.)<sup>65–68</sup> As for the PANI-containing hybrid, the overall pattern and the position of the characteristic bands reflects that the deposited PANI is in its emeraldine form, and thus no irreversible formation of pernigraniline had occurred during the polymerization. Similar conclusions can be drawn based on the infrared spectra, depicted in Figure 6B: (i) The broad absorption between 1000 and 600 cm<sup>-1</sup> is characteristic of the different W–O stretching modes in the WO<sub>3</sub> crystal lattice. (ii) Identification of the different additional vibrational bands on the spectra of the hybrids gave further confirmation for the formation of the corresponding CPs. (iii) Importantly, only a  $\nu(\text{C}=\text{O})$  band of moderate amplitude can be observed around 1710 cm<sup>-1</sup>, which indicates a relatively small amount of overoxidized PPy. In the case of significant overoxidation, this band would have been much more expressed.<sup>69</sup>

**Hybrids Based on TiO<sub>2</sub> NTAs.** Prompted by the data presented above for WO<sub>3</sub>, our synthesis concept was extended to TiO<sub>2</sub> NTAs because hybrid materials based on this latter semiconductor may attract significant interest also from a utilization perspective. Very similar experiments were carried out with the TiO<sub>2</sub>/PANI system. To obtain PANI on a TiO<sub>2</sub> NTA working electrode by electrodeposition, very high potentials have to be applied as depicted in Figure 7A. Similar to the examples previously presented, a massive increase in the currents can be observed under illumination. Note that the electroactivity related to the deposited polymer (between  $E =$

$-0.2$  and  $+0.5$  V) is larger even after one potentiodynamic cycle than that of five corresponding cycles in dark. The difference in the overall charge passed through during the subsequent cycles is also striking. As presented in Figure 7C, the slope of the line registered under illumination is more than six times larger than its counterpart obtained without illumination. Comparison of the first half-cycles shows the significant effect of light for this system as well. Photocurrent develops rapidly starting at  $E = 0.1$  V, whereas after reaching its maximum, it starts to decrease owing to optical shielding by the photodeposited PANI (Figure 7B). By increasing further the bias potential, electropolymerization starts to contribute to the current, resulting in its increase at the positive end of the curve (Figure 7B). Hybrid samples obtained by illumination of selected areas of the TiO<sub>2</sub> NTA working electrode provide visual proof of light-induced electrodeposition for PANI, as shown in Figure 7D.

To shed further light on the contribution of photocatalytic and electrochemical polymerization to the formation of PANI (Scheme 1), we studied the role of the positive end of the potential window. More precisely, potentiodynamic cycles were run up to 1.1, 1.45, and 2.2 V, whereas other parameters remained unchanged. By appropriately selecting the applied potential regimes, the contribution of electropolymerization can be separated, which gives information on mechanistic aspects, and also the shape of the curves can be a good indication of the electroactivity of the polymers, obtained under different circumstances. As can be seen in Figure 8, a number of significant differences can be revealed. The most obvious alteration in the series of figures is probably the substantial increase in the magnitude of currents. As the potential window is extended, the contribution of electrochemical polymerization

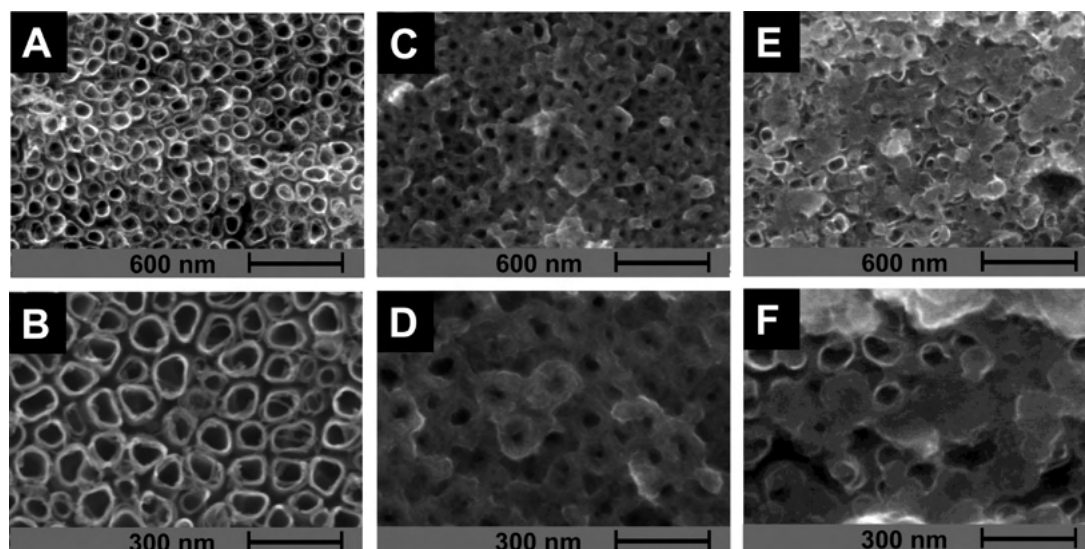


**Figure 9.** SEM images of bare  $\text{TiO}_2$  NTA synthesized at  $E = 20$  V (A,B) and of the corresponding  $\text{TiO}_2/\text{PANI}$  hybrid samples (synthesized using five cycles with (C,D) and without (E,F) illumination) at 50k and 100k magnification.

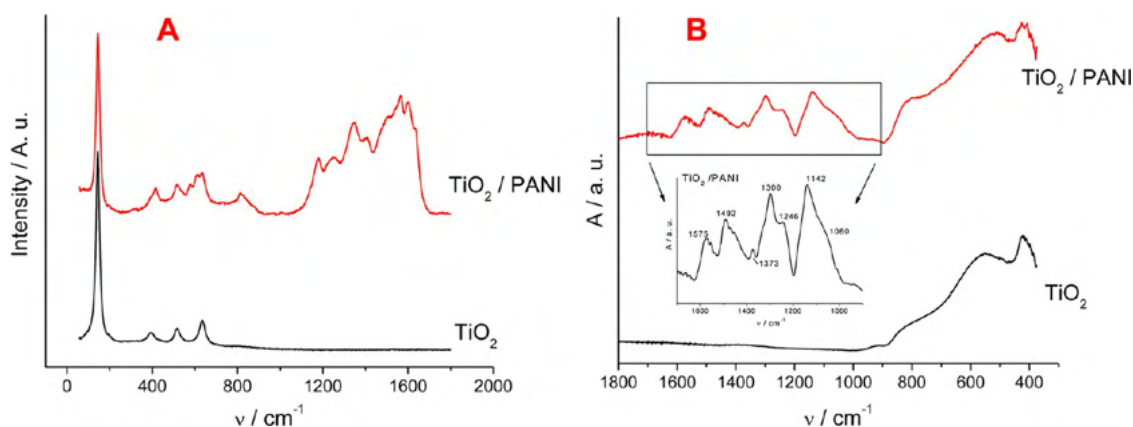


**Figure 10.** Raman (A) and FT-IR (B) spectra of  $\text{TiO}_2$  NTA and the  $\text{TiO}_2/\text{PANI}$  hybrid samples prepared by five potentiodynamic cycles under illumination. The insets show enlarged images of the areas characteristic for polyaniline.

is more and more expressed (compared with Figure 8A, where only photoelectrochemical polymerization occurs), first just causing a moderate enlargement in the registered currents (Figure 8B), whereas in the last case, the dominance of electropolymerization can be deduced (Figure 8C). This change is also reflected in the dissimilar shape of the curves.

As for the anodic end of the curves (where electropolymerization generally occurs), interesting trends can be observed. For the narrowest potential window (Figure 8A), a gradual *decrease* is visible in the photocurrent in the order of cycles, which is dominantly related to the optical shielding effect of the photoelectrochemically deposited PANI. Oppositely, in the case of the widest potential range, a continuous *increase* can be noticed in the series of cycles due to the currents arising from electropolymerization. In the case of the middle potential window (Figure 8B), a *mixed* trend can be seen as a result of the competition between the decreasing photocurrent and the increasing polymerization current. Moreover, note the change in the profile of the curves between  $-0.2$  and  $+0.6$  V, which is related to redox transformation of the generated PANI. As can be seen in Figure 8A, the photodeposited polymer has a less-developed redox activity, the anodic peak around  $E = 0.3$  V is less expressed, whereas only one cathodic peak can be seen

instead of the usually obtained double wave. This inferior electroactivity is in agreement with previous studies related to the photocatalytic deposition of CPs.<sup>52</sup> In contrast, a well-defined, quasi-reversible redox behavior can be seen in the two other cases, where electropolymerization has an important contribution to polymer generation. This is especially true for Figure 8C, where the voltammograms mirror their counterparts on gold electrode. Moreover, the good electroactivity of PANI in the hybrid configuration was confirmed even by cyclic voltammetric studies, performed in monomer-free solution (Figure S1 of the Supporting Information).

Figure 9 contains representative SEM data for both the initial  $\text{TiO}_2$  NTA surface (Figure 9A,B) and the  $\text{TiO}_2/\text{PANI}$  hybrid synthesized under illumination (C,D) and in the dark (E,F). The bare nanotubes exhibit the typical properties for NTAs synthesized under these conditions, in terms of both average tube diameter (85 nm) and wall thickness (15 nm). The morphology of the photoelectrochemically prepared hybrid sample is strikingly different (Figure 9C,D). As can be seen from the expansion of wall thicknesses and from the disappearance of nanoscopic voids in between the tubes, PANI is deposited *all over the illuminated area* of the sample. It should also be noticed that although the nanotubes are

completely covered by the polymeric skin, further growth of the polymer is preferred among the tubes, not inside them (Scheme 1).<sup>47</sup> The hybrid sample obtained in the absence of illumination exhibits a morphology similar to that seen that with the WO<sub>3</sub>/PPy system. PANI is randomly, occasionally deposited on the TiO<sub>2</sub> NTA, forming globular particles on the top of the substrate (note the similarities with precedent literature<sup>41,42</sup>). The individual tubes are not covered, nor is the space among the tubes filled with the conjugated polymer. Completely identical wall thicknesses can be observed with the parent (bare TiO<sub>2</sub> NTA) situation. By comparing the two hybrid samples, the contact area of the junction between the inorganic and organic component is much enhanced, underlining the practical device utility of the concept presented in this paper.

Vibrational spectroscopic measurements were performed to confirm the identity of the photoelectrodeposited polymers in the hybrid configurations. A Raman spectrum of the TiO<sub>2</sub> NTA array indicates that TiO<sub>2</sub> is in the anatase form, which is in agreement with previous reports (Figure 10).<sup>18,70</sup> As for the hybrid sample, the typical vibrations of PANI are superimposed on the vibrations related to the TiO<sub>2</sub> support. Assignment of the bands is given in the Supporting Information. Infrared spectra gave similar conclusions, namely, that the spectral pattern mirrors that measured for electrochemically synthesized polymer on a Au/Pt electrode. Finally, no indication was seen for overoxidation on any of the spectra, similar to the WO<sub>3</sub> case.

## CONCLUDING REMARKS

In this study, proof of concept was presented for photoelectrodeposition of conjugated polymers on nanostructured matrices of wide bandgap inorganic oxide semiconductors. Photocatalytic deposition preceding the electropolymerization step during potentiodynamic synthesis was shown to play a key role in the formation of homogeneous and organized assemblies of these hybrids. Employing illumination to deposit photoelectrochemically a very thin seed layer on the surface of an oxide semiconductor helps to overcome the main challenge, namely, its limited electroactivity. By varying the applied potential window during the potentiodynamic polymerization, the contribution of photoelectrochemical and electrochemical polymerization to the overall process could be separately expressed. Morphological features (as seen by FE-SEM) corroborated the decisive role of illumination in achieving homogeneous deposition of PANI and PPy on nanoporous WO<sub>3</sub> and PANI on nanotubular TiO<sub>2</sub>. This uniform, skin-like polymer coating results in a much larger area of the polymer/oxide semiconductor p/n junction, which is a prerequisite for most of the considered applications for these materials.

Spectroscopic (FT-IR and Raman) studies not only corroborated the molecular identity of both components of the assemblies but also furnished important proof that there was insignificant overoxidation of the polymers during the synthetic procedure. This latter feature was also confirmed by cyclic voltammetric studies, which revealed the typical, quasi-reversible electroactivity for both polymers in the hybrid configuration. Finally, it is believed that bringing the inorganic nanostructures and the organic polymer into intimate contact on both physical and electronic levels (as demonstrated in this study) will facilitate practical applications of these materials, for example, in solar energy conversion.

## ASSOCIATED CONTENT

### Supporting Information

Assignment of the bands in Raman and FT-IR spectra is given. The electroactivity of PANI in the hybrid configuration is shown. This material is available free of charge via the Internet at <http://pubs.acs.org>.

## AUTHOR INFORMATION

### Corresponding Author

\*E-mail: [cjanaky@uta.edu](mailto:cjanaky@uta.edu) (C.J.); [rajeshwar@uta.edu](mailto:rajeshwar@uta.edu) (K.R.), Tel: 817 272 5421.

### Notes

The authors declare no competing financial interest.

## ACKNOWLEDGMENTS

C.J. gratefully acknowledges the support of the European Union under FP7-PEOPLE-2010-IOF, grant number: 274046. We thank the colleagues at RenderNet, Ltd. for their support in the preparation of the artwork of the manuscript.

## ABBREVIATIONS

PPy, polypyrrole; PANI, polyaniline; CP, conducting polymer; ATR FT-IR, attenuated total reflection Fourier-transformed infrared spectroscopy; SEM, scanning electron microscopy; CV, cyclic voltammetry; SHE, standard hydrogen electrode

## REFERENCES

- (1) Gomez-Romero, P. *Adv. Mater.* **2001**, *13*, 163.
- (2) Gangopadhyay, R.; De, A. *Chem. Mater.* **2000**, *12*, 608.
- (3) Nozik, A. J. *Physica E* **2002**, *14*, 115.
- (4) Rajeshwar, K.; de Tacconi, N. R.; Chenthamarakshan, C. R. *Chem. Mater.* **2001**, *12*, 2765.
- (5) Moon, S. J.; Baranoff, E.; Zakeeruddin, S. M.; Yeh, C.-Y.; Diau, E. W.-G.; Grätzel, M.; Sivula, K. *Chem. Commun.* **2011**, *47*, 8244.
- (6) Beek, W. J. E.; Wienk, M. M.; Janssen, R. A. J. *Adv. Funct. Mater.* **2006**, *16*, 1112–1116.
- (7) Bouclé, J.; Ravirajan, P.; Nelson, J. J. *Mater. Chem.* **2007**, *17*, 3141.
- (8) Coakley, K.; McGehee, M. D. *Chem. Mater.* **2004**, *16*, 4533.
- (9) Zhang, J.; Tu, J. P.; Zhang, D.; Qiao, Y. Q.; Xia, X. H.; Wang, X.; Gu, C. D. *J. Mater. Chem.* **2011**, *21*, 17316.
- (10) Zhang, H.; Zong, R.; Zhu, Y. J. *Phys. Chem. C* **2009**, *113*, 4605.
- (11) Kerr, T.; Wu, H.; Nazar, L. *Chem. Mater.* **1996**, *8*, 2005.
- (12) Janáky, C.; Endrődi, B.; Berkesi, O.; Visy, C. *J. Phys. Chem. C* **2010**, *114*, 19338.
- (13) Zang, J.; Bao, S. J.; Li, C. M.; Bian, H.; Cui, X.; Bao, Q.; Sun, C. Q.; Guo, J.; Lian, K. J. *Phys. Chem. C* **2008**, *112*, 14843.
- (14) Huguenin, F.; Torresi, R. M. J. *Phys. Chem. C* **2008**, *112*, 2202.
- (15) Liu, R.; Lee, S. B. *J. Am. Chem. Soc.* **2008**, *130*, 2942.
- (16) Li, S. S.; Chang, C. P.; Lin, C. C.; Lin, Y. Y.; Chang, C. H.; Yang, J. R.; Chu, M. W.; Chen, C. W. *J. Am. Chem. Soc.* **2011**, *133*, 11614.
- (17) Liu, R.; Duay, J.; Lee, S. B. *Chem. Commun.* **2011**, *47*, 1384.
- (18) Chanmanee, W.; Watcharenwong, A.; Chenthamarakshan, C. R.; Kajitvichyanukul, P.; de Tacconi, N. R.; Rajeshwar, K. *J. Am. Chem. Soc.* **2008**, *130*, 965.
- (19) Roy, P.; Berger, S.; Schmuki, P. *Angew. Chem., Int. Ed.* **2011**, *50*, 2904.
- (20) Tsuchiya, H.; Macak, J. M.; Sieber, I.; Taveira, L.; Ghicov, A.; Sirotna, K.; Schmuki, P. *Electrochem. Commun.* **2005**, *7*, 295.
- (21) de Tacconi, N. R.; Chenthamarakshan, C. R.; Yogeeswaran, G.; Watcharenwong, A.; de Zoysa, R. S.; Basit, N. A.; Rajeshwar, K. *J. Phys. Chem. B* **2006**, *110*, 25347.
- (22) Jennings, J. R.; Ghicov, A.; Peter, L. M.; Schmuki, P.; Walker, A. B. *J. Am. Chem. Soc.* **2008**, *130*, 13364.

- (23) Sun, W. T.; Yu, Y.; Pan, H. Y.; Gao, X. F.; Chen, Q.; Peng, L. M. *J. Am. Chem. Soc.* **2008**, *130*, 1124.
- (24) Baker, D. R.; Kamat, P. V. *Adv. Funct. Mater.* **2009**, *19*, 805.
- (25) Mor, G. K.; Shankar, K.; Paulose, M.; Varghese, O. K.; Grimes, C. A. *Nano Lett.* **2006**, *6*, 215.
- (26) Song, Y. Y.; Schmidt-Stein, F.; Bauer, S.; Schmuki, P. *J. Am. Chem. Soc.* **2009**, *131*, 4230.
- (27) Zheng, H.; Ou, J. Z.; Strano, M. S.; Kaner, R. B.; Mitchell, A.; Kalantarzadeh, K. *Adv. Funct. Mater.* **2011**, *21*, 2175.
- (28) Nah, Y. C.; Ghicov, A.; Kim, D.; Schmuki, P. *Electrochem. Commun.* **2008**, *10*, 1777.
- (29) Kukkola, J.; Mäklin, J.; Halonen, N.; Kyllönen, T.; Tóth, G.; Szabó, M.; Shchukarev, A.; Mikkola, J.-P.; Jantunen, H.; Kordás, K. *Sens. Actuators, B* **2011**, *153*, 293.
- (30) Liu, J.; Kadnikova, E. N.; Liu, Y.; McGehee, M. D.; Fréchet, J. M. J. *J. Am. Chem. Soc.* **2004**, *126*, 9486.
- (31) Neyshtadt, S.; Jahnke, J. P.; Messinger, R. J.; Rawal, A.; Segal Peretz, T.; Huppert, D.; Chmelka, B. F.; Frey, G. L. *J. Am. Chem. Soc.* **2011**, *133*, 10119.
- (32) Mor, G. K.; Kim, S.; Paulose, M.; Varghese, O. K.; Shankar, K.; Basham, J.; Grimes, C. A. *Nano Lett.* **2009**, *9*, 4250.
- (33) Shankar, K.; Mor, G. K.; Prakasham, H. E.; Varghese, O. K.; Grimes, C. A. *Langmuir* **2007**, *23*, 12445.
- (34) Lee, J.; Jho, J. Y. *Sol. Energy Mater. Sol. Cells* **2011**, *95*, 3152.
- (35) Atienzar, P.; Ishwara, T.; Horie, M.; Durrant, J. R.; Nelson, J. J. *Mater. Chem.* **2009**, *19*, 5377.
- (36) Koh, J. K.; Kim, J.; Kim, B.; Kim, J. H.; Kim, E. *Adv. Mater.* **2011**, *23*, 1641.
- (37) Tepavcevic, S.; Darling, S. B.; Dimitrijevic, N. M.; Rajh, T.; Sibener, S. J. *Small* **2009**, *5*, 1776.
- (38) Wang, D.; Liu, Y.; Wang, C.; Zhou, F.; Liu, W. *ACS Nano* **2009**, *3*, 1249.
- (39) Mujawar, S. H.; Ambade, S. B.; Battumur, T.; Ambade, R. B.; Lee, S.-H. *Electrochim. Acta* **2011**, *56*, 4462.
- (40) Janáky, C.; Bencsik, G.; Rác, A.; Visy, C.; de Tacconi, N. R.; Chanmanee, W.; Rajeshwar, K. *Langmuir* **2010**, *26*, 13697.
- (41) Liang, H. C.; Li, X. Z. *Appl. Catal. B-Environ.* **2009**, *86*, 8.
- (42) Zhang, Z.; Yuan, Y.; Liang, L.; Cheng, Y.; Xu, H.; Shi, G.; Jin, L. *Thin Solid Films* **2008**, *516*, 8663.
- (43) Döbbelin, M.; Tena-Zaera, R.; Carrasco, P. M.; Sarasua, J.-R.; Cabañero, G.; Mecerreyes, D. *J. Polym. Sci., Part A: Polym. Chem.* **2010**, *48*, 4648.
- (44) Velazquez, J. M.; Gaikwad, A. V.; Rout, T. K.; Rzaev, J.; Banerjee, S. *ACS Appl. Mater. Interfaces* **2011**, *3*, 1238.
- (45) Janaky, C.; Tacconi, N. D.; Chanmanee, W.; Rajeshwar, K. *J. Phys. Chem. C* **2012**, *116*, 4234.
- (46) Kowalski, D.; Schmuki, P. *Chem. Commun.* **2010**, *46*, 8585.
- (47) Kowalski, D.; Tighineanu, A.; Schmuki, P. *J. Mater. Chem.* **2011**, *21*, 17909.
- (48) Nielsch, K.; Müller, F.; Li, A. P.; Gösele, U. *Adv. Mater.* **2000**, *12*, 582.
- (49) Wang, D.; Ye, Q.; Yu, B.; Zhou, F. *J. Mater. Chem.* **2010**, *20*, 6910.
- (50) Chenthamarakshan, C. R.; Ming, Y.; Ming, Y. *Chem. Mater.* **2000**, *12*, 3538.
- (51) Somasundaram, S.; Chenthamarakshan, C. R.; de Tacconi, N. R.; Ming, Y.; Ming, Y.; Rajeshwar, K. *Chem. Mater.* **2004**, *16*, 3846.
- (52) Fox, M. A.; Worthen, K. L. *Chem. Mater.* **1991**, *3*, 253.
- (53) Strandwitz, N. C.; Nonoguchi, Y.; Boettcher, S. W.; Stucky, G. D. *Langmuir* **2010**, *26*, 5319.
- (54) Okano, M.; Kikuchi, E.; Itoh, K.; Fujishima, A. *J. Electrochem. Soc.* **1988**, *135*, 1641.
- (55) de Tacconi, N. R.; Chenthamarakshan, C. R.; Rajeshwar, K.; Tacconi, E. J. *J. Phys. Chem. B* **2005**, *109*, 11953.
- (56) Kim, Y.; Lim, J. W.; Sung, Y. E.; Xia, J. B.; Masaki, N.; Yanagida, S. *J. Photochem. Photobiol., A* **2009**, *204*, 110.
- (57) Breimer, M. A.; Yevgeny, G.; Sy, S.; Sadik, O. A. *Nano Lett.* **2001**, *1*, 305.
- (58) Debarros, R.; Deazevedo, W.; Deaguiar, F. *Mater. Charact.* **2003**, *50*, 131.
- (59) Quarto, F. D.; Figà, V.; Bocchetta, P.; Santamaria, M. *Electrochim. Solid State* **2007**, *10*, H305.
- (60) Di Franco, F.; Bocchetta, P.; Santamaria, M.; Di Quarto, F. *Electrochim. Acta* **2010**, *56*, 737.
- (61) Sapurina, I.; Riede, A.; Stejskal, J. *Synth. Met.* **2001**, *123*, 503.
- (62) Mu, S.; Kan, J. *Electrochim. Acta* **1996**, *41*, 1593.
- (63) Yang, H. J.; Bard, A. J. *J. Electroanal. Chem.* **1992**, *339*, 423.
- (64) Monllor-Satoca, D.; Borja, L.; Rodes, A.; Gómez, R.; Salvador, P. *ChemPhysChem* **2006**, *7*, 2540.
- (65) Lapkowski, M.; Berrada, K.; Quillard, S.; Louarn, G.; Lefrant, S.; Pron, A. *Macromolecules* **1995**, *28*, 1233.
- (66) Quillard, S.; Louran, G.; Lefrant, S.; MacDiarmid, A. G. *Phys. Rev. B* **1994**, *50*, 496.
- (67) Davidson, R. G.; Turner, T. G. *Synth. Met.* **1995**, *72*, 121.
- (68) Duchet, J.; Legras, R.; Demoustier-Champagne, S. *Synth. Met.* **1998**, *95*, 113.
- (69) Ghosh, S.; Bowmaker, G. A.; Cooney, R. P.; Seakins, J. M. *Synth. Met.* **1998**, *95*, 63.
- (70) Hardcastle, F. D.; Ishihara, H.; Sharma, R.; Biris, A. S. *J. Mater. Chem.* **2011**, *21*, 6337.



## Photocatalytic Activity of Inorganic Semiconductor Surfaces: Myths, Hype, and Reality

The notion of driving chemical and biochemical reactions on irradiated inorganic semiconductor surfaces has both fundamental and practical importance. The name “heterogeneous photocatalysis” has been coined for this field of endeavor, and it is hardly surprising that the field has literally exploded during the past couple of decades. Nevertheless, process efficiencies remain poor, and quantum yields have been disappointingly low (amounting only to fractions of a percent) even for well-studied semiconductors such as titanium dioxide,  $\text{TiO}_2$ . Therefore, the time appears ripe to take stock of what we know and what we do not know about photoinduced processes at the molecular level. While impressive advances have been made in the surface science of oxide semiconductors (especially,  $\text{TiO}_2$ ), much of this understanding resides with surfaces as they exist in pristine, ultrahigh vacuum conditions.<sup>1,2</sup> On the other hand, little is known about inorganic semiconductor *surfaces* in contact with air or water and under conditions as they relate to the practical use of such *interfaces*. Here, we will critically examine what we know about the structural and chemical factors related to such interfaces and what knowledge is further needed to move this field forward. However, before we undertake this exercise, it is useful to set the parameters for the discussion.

*Genesis, Concepts, and Confusions.* The field’s growth has been (mistakenly, at least in the authors’ view) associated with the well-cited discovery<sup>3</sup> that irradiated  $\text{TiO}_2$  could assist in the splitting of water. However, oxide semiconductors had long before received considerable scrutiny from the perspective of the electronic theory of chemical catalysis, and this corpus of work dates back at least to the 1960s.<sup>4</sup> Zinc oxide was a particularly popular choice for the oxide semiconductor candidate in these early studies. Oxide semiconductors were also of interest in the geochemical and environmental chemistry literature especially from the perspective of how the combination of sunlight and rocks affected natural remediation processes.<sup>5</sup> Popular recognition that irradiated semiconductor surfaces can indeed break down environmental pollutants (such as chlorinated hydrocarbons, cyanide, etc.) stems from papers that did appear<sup>6–8</sup> just around the time of the Fujishima–Honda discovery; this could offer an explanation for the misplaced identification of the origin of the field of heterogeneous photocatalysis.

Process efficiencies remain poor, and quantum yields have been disappointingly low (amounting only to fractions of a percent) even for well-studied semiconductors such as  $\text{TiO}_2$ .

That heterogeneous photocatalysis can be understood on a fundamental level by using electrochemical principles has been

pointed out by one of us.<sup>9,10</sup> Thus, an irradiated semiconductor particle may be regarded as a short-circuited microelectrochemical cell in which the anodic and cathodic photoprocesses are balanced and the particle attains a (mixed) photopotential that depends on the relative rates of the two “conjugate” half-reactions.<sup>9</sup> Consider the photooxidation of a hydrocarbon; the conjugate process in this case is the photoreduction of dioxygen, and the faster we can make this process, the more facile the hydrocarbon photooxidation.<sup>9</sup> Similarly, consider the photoreduction of a metal ion (i.e., photodeposition of a metal) on an irradiated metal oxide surface. In this case, the conjugate reaction may be the photooxidation of a reducing agent (electron donor) such as formate species. Of course, in all of these cases, the reactions involve the photogenerated electron–hole ( $e^-h^+$ ) pairs in the irradiated semiconductor.

From a thermodynamics perspective, the key point to note is that in both above scenarios, the *overall* chemical reaction, namely, the oxidation of a hydrocarbon (by dioxygen) or the reduction of a metal ion (by a reducing agent) is *thermodynamically “downhill”*. In other words, the overall chemical reaction has a negative free-energy change. However, in the dark, both reactions are *kinetically sluggish*; light therefore serves to accelerate the reaction. Hence, the name “photocatalytic” for the process is entirely appropriate.

At this juncture, it is worth noting the oft-misplaced use of the word “photocatalyst” in the literature even in the cases wherein the overall processes are *thermodynamically uphill*. Examples of these include water splitting (into  $\text{H}_2$  and  $\text{O}_2$ ) and  $\text{CO}_2$  splitting (into a myriad of products depending on the electron stoichiometry; ref 11). Thus,  $\text{TiO}_2$  has been repeatedly (and mistakenly, in our opinion) called a “photocatalyst” for the splitting of water!

It is useful to think of two coupled processes in these cases. Photoexcitation allows the system to be “pumped up” against the free-energy gradient. The second step involves driving multiple electrons across the interface to convert the reactants to products; this is where the catalytic aspect of the inorganic semiconductor comes in.

*Is the Oxide Semiconductor Surface Intrinsically Catalytic?* The fact that strategies such as platinumization of the parent oxide semiconductor surface have been utilized would seem to argue against this possibility. However, recent studies indicate that certain oxide surfaces do appear to have the ability to store electrons even without noble metal (e.g., Pt) islands on them; a case in point is p-type  $\text{Cu}_2\text{O}$ . For example, photoexcitation of this semiconductor results in the  $6e^-$  conversion of  $\text{CO}_2$  to methanol in the absence of any co-catalyst.<sup>12,13</sup> Many of the surface chemical aspects discussed below can only be readily rationalized within the framework that the oxide surface is intrinsically catalytic toward many substrates.

Published: January 2, 2015



**Table 1. Factors Underpinning Photocatalytic Activity of Inorganic Semiconductor Surfaces**

category	factor(s)	impact(s)
optical	energy band gap	photonic efficiency
electronic	carrier mobility	quantum efficiency
structural/morphological	surface area	adsorption
	crystallinity/crystal facet	multiple <sup>a</sup>
	particle size	multiple <sup>a</sup>
	defects	multiple <sup>a</sup>
	crystal phase	multiple <sup>a</sup>
surface chemical	acid–base character	multiple <sup>a</sup>
	surface groups (hydroxyls)	multiple <sup>a</sup>

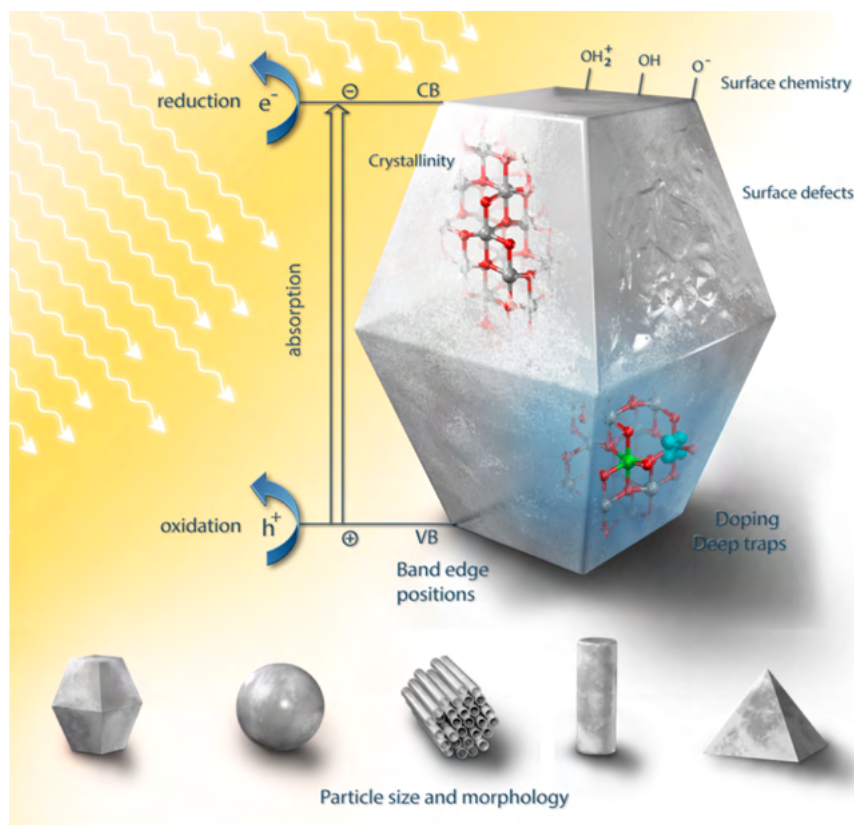
<sup>a</sup>Impacts photocatalytic activity in multiple ways; see the text.

To streamline the discussion, factors underpinning the photocatalytic activity of inorganic semiconductor surfaces are listed in Table 1. It is worth emphasizing that the impact of the factors listed on the photocatalytic activity is complex and convoluted. For example, particle size can influence light absorption via the size quantization effect;<sup>14</sup> it can also influence light-scattering events (see below). Thus, in this sense, optical and structural factors are coupled. Particle size can also impact surface area and hence influence adsorption of solution species. Similarly, the acid–base character of the photocatalyst surface can influence adsorption via electrostatic effects induced by charged surface groups. Grouping of the factors into neat boxes should not lead to the mistaken conclusion that they exert effects independent of one another. The chemometrics community addresses such complications by

implicating that the factors “interact” with one another, and hence, the response surface [i.e., three-dimensional plots of the response variable (in this case, the photocatalytic activity) as a function of the factor level] becomes curved rather than planar.<sup>15</sup>

If the optoelectronic factors are (temporarily) set aside, it is easy to recognize that every other factor listed in the compilation in Table 1 is no different from what is well-established in the heterogeneous catalysis community on the prerequisites of a “good” catalyst. Scheme 1 also highlights the topics addressed below.

**Doping and Metal Modification of Parent Oxide Semiconductor Surfaces.** A major motivation for metal modification is to impart electron storage capacity to the parent semiconductor surface; this is especially useful when the chemical reaction to be driven involves multiple electrons. This chemical modification may be performed either in the semiconductor bulk or on its surface. At this juncture, it is worth noting that the term “doping” has been mistakenly used by many authors in the literature for metal-modified semiconductors. Doping is a very specific phenomenon that in the solid-state chemistry or microelectronics communities means the controlled introduction of trace-level (subppm) impurities (“dopants”) into the host lattice such that they alter its optoelectronic characteristics. On the other hand, even when (a) the metal is present as a distinctly separate phase and/or (b) is present at levels of the order of a few percent (by mass), the term doping has been mistakenly applied. Within the context of this Viewpoint, we mostly consider *metal-modified* cases where the metal phase is present as discontinuous islands on the parent semiconductor surface.

**Scheme 1. Factors Impacting Photocatalytic Activity of a Single (Idealized) Inorganic Semiconductor Particle<sup>a</sup>**

<sup>a</sup>See also Table 1 above.

Recent studies indicate that certain oxide surfaces do appear to have the ability to store electrons even without noble metal (e.g., Pt) islands on them; a case in point is p-type  $\text{Cu}_2\text{O}$ .

Interestingly, a distinction between *doping* and *alloying* has been made<sup>16</sup> in terms of electronic structure consequences. Thus, doping has been used to signal instances where localized electronic states have been added such that the Fermi level shifts but the band edges are not changed. On the other hand, alloying is differentiated by introducing elements having delocalized bands that if sufficiently close in energy to other band edges, hybridize to form a new band with wider dispersion.<sup>16</sup> However, this distinction still does not conform to the solid-state microelectronics/materials science usage where doping signals very low levels (ppm or less) of the foreign element whereas alloying means that the element is present at variable but much higher levels (a few percent) than the case of dopant species.

Another, more recent discovery concerns the possibility of shifting the photoabsorption profile into the visible range of the electromagnetic spectrum by surface plasmon effects when the semiconductor is decorated by metals such as Au.<sup>17</sup>  $\text{TiO}_2$  is not the only semiconductor that has been explored in this regard; others such as bismuth vanadate ( $\text{BiVO}_4$ ) have been modified with metals such as Au.<sup>18</sup> To this end, one of the authors of this Viewpoint has demonstrated the utility of combining anodic electrodeposition with galvanic displacement for preparing Au– $\text{Bi}_2\text{O}_3$ <sup>19</sup> and Au– $\text{BiVO}_4$ <sup>18</sup> nanocomposites. [Bismuth oxide,  $\text{Bi}_2\text{O}_3$ , is an oxide that exists in n- as well as p-type semiconductor forms.] In both cases, the Au-modified photocatalysts exhibited faster kinetics (relative to the parent unmodified surfaces) for the decomposition of a dye probe (Figure 1).

The improvement in photocatalytic activity observed upon Au modification (Figure 1) may be rationalized on both optical and electronic grounds. Surface plasmon effects induced by the

presence of Au islands shift the absorption profile of the parent semiconductor into the visible, resulting in enhanced UV–visible absorption relative to the pristine surface. Second, the photogenerated electrons are siphoned off to the Au islands, thereby diminishing the extent of electron–hole recombination.

*Quantifying Photocatalytic Activity.* Plots such as those contained in Figure 1 have been commonly used by the community to compare the photocatalytic activity of given samples. However, these data shed no light at all on precisely how many of the incident photons were utilized for converting the targeted substrate into products. A well-recognized difficulty pertains to quantifying the number of photons that were absorbed by the semiconductor. Depending on the morphology and other nanoparticle attributes, the light can also be scattered; in fact, multiple scattering events can occur within the reactor confinement. These ideas lead to the notion of a photonic efficiency, that is, how many photons are absorbed versus the number incident on the semiconductor. Related to this parameter is the quantum efficiency, that is, the number of electrons (or holes) utilized in the photochemical process versus the number of photons incident. A large scattering cross section leads to a low photonic efficiency; similarly, facile electron–hole recombination leads to a low quantum efficiency. Facile electron–hole recombination can be caused both by bulk defect states in the semiconductor and by surface trap states (see below).

It is rather unfortunate that the notion of circumventing the above difficulties by defining a relative photonic efficiency<sup>20</sup> has been largely overlooked by practitioners of heterogeneous photocatalysis. The basic tenet of the suggested protocol was that by comparing the performance for the test substrate(s) against corresponding metrics for phenol (a standard secondary actinometer), inherent difficulties with precise knowledge of photon absorption (by the photocatalyst sample) and variations associated with the reactor geometry, light source, and so forth could be factored out.<sup>20</sup>

*Polymorphic Phases and Crystal Facets.* Studies probing the factors underlying the variant photocatalytic activity of the rutile and anatase forms of  $\text{TiO}_2$  have had a long history dating back at least 2 decades. (It is worth noting here that anatase is a *metastable* phase in the thermochemical sense and only reverts

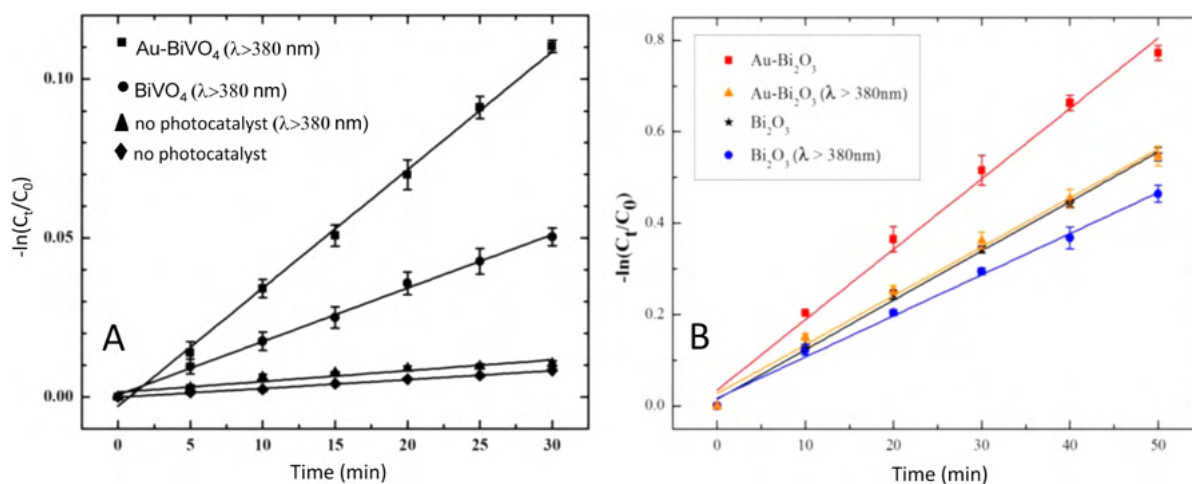


**Figure 1.** Pseudo-first-order kinetics plots showing the enhancement of photocatalytic activity for the decomposition of a dye (methyl orange) upon Au modification of (a)  $\text{BiVO}_4$  and (b)  $\text{Bi}_2\text{O}_3$ . The original papers (refs 18 and 19) may be consulted for further details. Reproduced with permission from Wiley-VCH and the Electrochemical Society. Copyright 2014: VCH (left) and The Electrochemical Society (right).

to rutile by heating up to temperatures in the region of  $\sim 600$  °C).<sup>21</sup> Which of the two phases is more photocatalytically active? The answer depends on the conjugate reaction in the overall photocatalytic process. When O<sub>2</sub> is present in the reaction medium, the anatase phase is always more active; on the other hand, rutile shows significant photocatalytic activity when oxidants other than O<sub>2</sub> are present, such as Ag<sup>+</sup> or H<sub>2</sub>O<sub>2</sub>.<sup>22</sup>

The better photocatalytic activity of anatase relative to rutile is rooted in several (undoubtedly coupled) factors, the more important among them being the (a) higher energy band gap of anatase ( $\sim 3.2$  relative to  $\sim 3.0$  eV for the rutile phase) and conduction band edge location, (b) lower O<sub>2</sub> adsorption capacity for rutile, (c) higher preponderance of surface hydroxyl groups in anatase, (d) enhanced carrier recombination in rutile, (e) higher electron mobility in anatase ( $4 \text{ cm}^2 \text{ V}^{-1} \text{ s}^{-1}$ ) versus rutile ( $0.1 \text{ cm}^2 \text{ V}^{-1} \text{ s}^{-1}$ ),<sup>23</sup> and (f) lower degree of charge separation in rutile because of a lower density of surface-to-bulk trap states. Information on the precise chemical nature of the trap states (surface or bulk) is currently lacking although surface peroxo groups have been implicated by voltammetric measurements.<sup>24</sup> The more stable surface peroxide intermediates generated in situ on the anatase surface during the photo-oxidation process (relative to the rutile surface) would be consistent with the intrinsically higher surface hydroxylation of anatase relative to rutile.

Doping is a very specific phenomenon that in the solid-state chemistry or microelectronics communities means the controlled introduction of trace-level (subppm) impurities ("dopants") into the host lattice such that they alter its optoelectronic characteristics.

Studies<sup>25,26</sup> on rutile TiO<sub>2</sub> synthesized at low temperatures (as opposed to samples obtained by high-temperature calcination of the anatase phase), challenge the long-standing notion for the superior photocatalytic activity of the anatase form of TiO<sub>2</sub>. For example, flower-like rutile "superstructures" were grown by a solution-phase approach at room temperature, and the morphological evolution as a result of calcination was mapped using scanning electron microscopy.<sup>26</sup> Using rhodamine B (RhB) dye as a probe, the room-temperature synthesized samples were observed to have superior photocatalytic activity relative to the calcined ones. A particularly noteworthy aspect of this study was the correlation of surface area and surface charge using active species trapping experiments.<sup>26</sup> Thus, the effects of chemical species selective for scavenging holes (sodium oxalate), electrons (potassium dichromate), O<sub>2</sub><sup>-•</sup> (*p*-benzoquinone), or •OH (isopropanol) were compared for RhB photodegradation.<sup>26</sup>

Studies oriented toward surface chemical and crystal phase effects on the photocatalytic activity of other oxides besides TiO<sub>2</sub> are rather sparse. An interesting potential candidate for such a study is BiVO<sub>4</sub> (see also Figure 1); three phases are known for this material: scheelite-tetragonal, zircon-tetragonal, and scheelite-monoclinic.<sup>27</sup> Crystal form-controlled and highly

crystalline BiVO<sub>4</sub> powder were synthesized, and the photocatalytic properties were reported for the monoclinic and tetragonal phases.<sup>28</sup> The monoclinic form is highly active for O<sub>2</sub> evolution under visible light, and thus, it is not surprising that most of the studies on this material have centered on the O<sub>2</sub> evolution activity (a thermodynamically uphill process; see above) rather than on its photocatalytic attributes.

The O<sub>2</sub> evolution activity was mapped as a function of the postsynthesis calcination temperature ranging from 350 to 800 °C for BiVO<sub>4</sub> synthesized by homogeneous coprecipitation.<sup>29</sup> In all of the cases, only the scheelite-monoclinic phase was observed.<sup>29</sup> Both the V–O bond length (as monitored via Raman spectroscopy) and the energy band gap (as assessed by Tauc plots)<sup>30</sup> monotonically decreased with increasing calcination temperature.<sup>29</sup> Correspondingly, the O<sub>2</sub> evolution photoactivity (using simulated sunlight) increased with increasing calcination temperature.<sup>29</sup> The effect of particle size was also probed, and these results will be addressed in a subsequent section below. Studies comparing the photocatalytic activity of this material for the three crystal forms are still lacking, at least to our knowledge.

Specific crystal facets can have higher photocatalytic activity than others. This is well exemplified by a study on hydrothermally synthesized "starlike" BiVO<sub>4</sub> crystals.<sup>31</sup> These samples were much more active for methylene blue photodecomposition than bulk oxide powder. In particular, this material has a higher atom density on the (010) lattice planes, and therefore, samples exposing more of these family of planes showed higher activity. The photocatalytic activity of this oxide was also attributed to distortion of the Bi–O polyhedron in the monoclinic phase.<sup>31</sup>

Most available anatase TiO<sub>2</sub> crystals are dominated by the thermodynamically stable {101} facets. However, this stability trend can be reversed by tweaking surface chemistry, a paradigm demonstrated by synthesizing fluorine-terminated surfaces where the {001} planes are energetically favored relative to {101} during crystal growth.<sup>32</sup> High photocatalytic activity has been reported for faceted titania particles such as those having decahedral or octahedral shapes (see, for example, ref 33.) In another study, facet-mediated photodegradation of RhB was studied on hematite ( $\alpha$ -Fe<sub>2</sub>O<sub>3</sub>) architectures, namely, 1D nanorods, 2D nanoplates, and 3D nanocubes.<sup>34</sup> The dominant facets in these architectures were {001} and {110} (for the 1D), {001} (2D), and {012} (3D), respectively; the photocatalytic activity was ordered thus 1D > 3D  $\gg$  2D for the dye photodegradation.<sup>34</sup> The observed differences were attributed to the direct consequence of the availability of surface iron sites on the three types of facets in the order {110} > {012}  $\gg$  {001}.

This is an area of heterogeneous photocatalysis deserving further study. Even the photoelectrochemical stability of the material can be influenced by crystal face orientation, as demonstrated recently for electrosynthesized Cu<sub>2</sub>O films.<sup>35</sup>

**Crystallinity and Crystallite Size.** Crystallinity is well-accepted in solid-state science to improve charge-transport dynamics; therefore, this parameter should be crucial in dictating the photocatalytic activity of a given inorganic semiconductor. Thus, amorphous titania has been shown to exhibit negligible activity for several photocatalytic reactions.<sup>36</sup> The general approach for tuning crystallinity (and crystallite size) is by thermal annealing of either the amorphous phase or of small particles. Unfortunately, calcination affects both parameters, complicating clear conclusions to be made about the *individual*

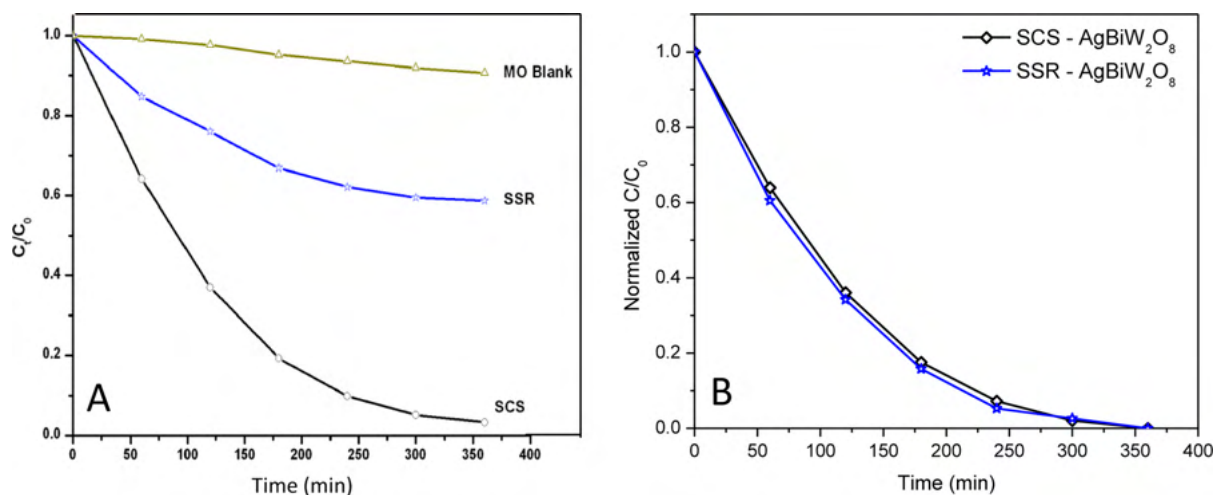


**Figure 2.** Comparison of photocatalytic activity for AgBiW<sub>2</sub>O<sub>8</sub> before (A) and after (B) surface area normalization. The data are for the photocatalytic decomposition of a probe dye (methyl orange or MO; refer to the text) and are compared for a SCS sample and another derived from a SSR by other authors (ref 46). Copyright permission from Wiley-VCH.

effect of crystallinity and crystallite size. The way around this would be to synthesize and characterize a series of samples with well-defined crystallinity and crystallite size without having to resort to thermal pretreatment. This has been done in a study on anatase nanoparticles prepared by supercritical flow synthesis.<sup>37</sup> The crystallite size ranged from 6 to 27 nm (with a fixed crystallinity of ~87%), whereas another series varied the crystallinity from 12 to 82% with a fixed crystallite size of ~9 nm.

Rather surprisingly, the degree of crystallinity was found to exert only a negligible effect on the photodecomposition of phenol.<sup>37</sup> In contrast, crystallite size had a dramatic effect and interestingly influenced the production distribution profiles.<sup>37</sup> When small anatase nanoparticles were used, phenol was selectively photooxidized to benzoquinone as an intermediate.<sup>37</sup> Conversely, hydroquinone was found to be the dominant intermediate product when large anatase nanoparticles were used.<sup>37</sup>

It is well-established in the heterogeneous catalysis community that the catalyst support can exert a key role on the degree of crystallinity and crystallite size of the supported nanoparticles. A corresponding example of such effects in the photocatalysis literature is provided by a study on the effect of porous amorphous silica minerals on supported TiO<sub>2</sub> photocatalysts.<sup>38</sup> Other studies addressing the influence of particle size are also noted,<sup>39,40</sup> although it is not clear to what extent crystallinity variations confounded the effects observed in these studies.

**Defects.** Defects play a critical role in dictating the photocatalytic activity through their role in influencing the optoelectronic characteristics or in affecting carrier transit through the material after photoexcitation. Defects play a role in carrier trapping events both in the material bulk and on its surface. Perhaps a best known defect in the photocatalysis community is Ti<sup>3+</sup> sites in the TiO<sub>2</sub> host lattice; these defect sites may be introduced, for example, by annealing titania powder in a reducing (e.g., hydrogen-containing) environment. The initially white powder immediately turns blue, signaling that “color centers” have been introduced. This color rapidly fades when the reduced material reacts with ambient oxygen. While metal “dopants” have been introduced to modify the optoelectronic characteristics of titania (a topic well reviewed

by previous authors and hence omitted here), a more recent innovation has been the introduction of nonmetals such as N or C. For example, metal oxynitrides show photocatalytic activity under visible light—a manifestation of band edge lowering.<sup>41</sup>

Analyzing the defect structure upon alloying or co-alloying a photocatalytic material is not commonplace. An exception to this trend is furnished by a study on co-alloying of anatase TiO<sub>2</sub> with Nb and N.<sup>16</sup> The resultant material showed a 7-fold increase in the rate of methylene blue photodegradation compared to the parent (unalloyed) TiO<sub>2</sub> phase.<sup>16</sup> Both Ti<sup>3+</sup> and F<sup>+</sup> centers (and oxygen vacancies) were identified as defects in the co-alloyed material that after annealing under ammonia flow appeared as an orange powder with ~2.0 eV band gap.<sup>16</sup>

While X-ray photoelectron spectroscopy provides useful information on the species introduced into the host lattice (and their oxidation states), this information obviously is surface-selective. Low-temperature electron paramagnetic resonance (EPR) is a versatile technique for probing defects in solids and was deployed in the study cited above.<sup>16</sup> Similar EPR studies on TiO<sub>2</sub> have shown the formation of trapped electrons or Ti<sup>3+</sup> states and trapped holes in the crystal lattice and/or surface hydroxyl groups.<sup>42,43</sup> The molar amounts of defect sites ( $M_d$ ) in several TiO<sub>2</sub> photocatalyst powders were determined using photoinduced reactions of electron accumulation in deaerated solutions containing sacrificial hole scavengers.<sup>44</sup>

**Surface Area.** Any discussion of the physical attributes of a given catalyst must start with its surface area, and this is no different for a photocatalyst material. Of course, this parameter manifests most directly in photocatalysis in dictating the amount of substrate species that can be initially bound by adsorption. However, many of the parameters discussed in the previous subsections (e.g., crystallite size) also are inextricably intertwined with surface area. A hierarchical approach serves to parse out the effects of the various factors by normalizing the photocatalytic activity with respect to surface area. Thus, plots of the photocatalytic activity versus time for given series of samples can be renormalized in the vertical direction by factoring out the influence of surface area.

Consider a set of data on combustion-synthesized silver bismuth tungstate, AgBiW<sub>2</sub>O<sub>8</sub>.<sup>45</sup> Figure 2A contains a set of curves for this material in which the activity of a combustion-

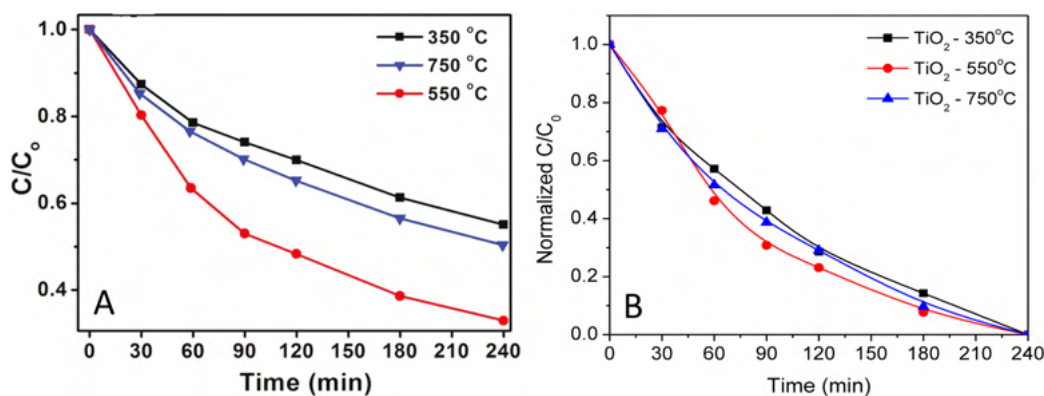


**Figure 3.** Comparison of photocatalytic activity for TiO<sub>2</sub> nanosheet samples before (A) and after (B) surface area normalization. The original data are from ref 47.

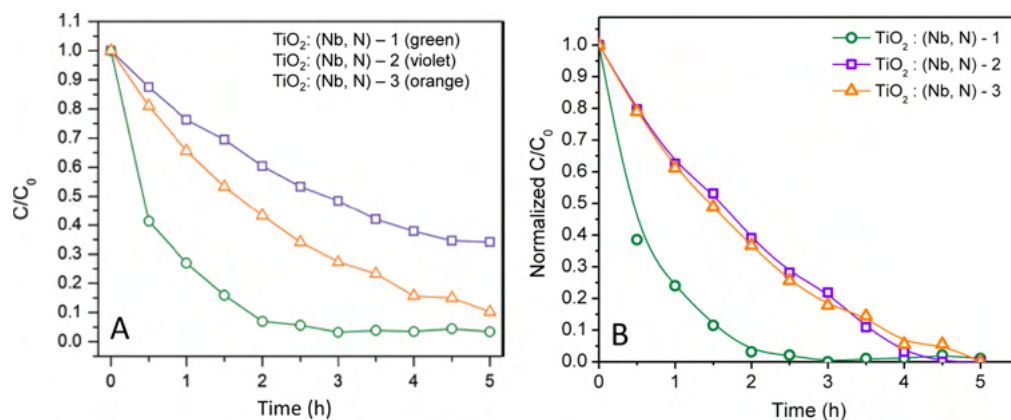


**Figure 4.** Comparison of photocatalytic activity for Nb and N co-alloyed TiO<sub>2</sub> before (A) and after (B) surface area normalization. The original data are from ref 16.

synthesized sample (SCS) for the photodegradation of methyl orange dye is compared with that of another sample (synthesized by previous authors) by a solid-state reaction (SSR) route.<sup>46</sup> A blank is also included to show that the dye degradation is negligible in the absence of the photocatalyst. The activity of the SCS sample is vastly superior to the SSR case. However, to what is this variation in activity attributable? The renormalized curves for the SCS and SSR samples taking into account their variant surface area (Figure 2B) immediately reveal that all of the difference in activity is simply attributable to surface area differences. The two curves now are virtually indistinguishable. Thus, no other factors (as discussed in the earlier subsections above) need be invoked here.

Figure 3A provides another set of data on TiO<sub>2</sub> nanosheets grown by the hydrothermal method;<sup>47</sup> they were subsequently calcined at temperatures indicated in the figure. Renormalization results in a lower degree of dispersion in the conversion curves in the vertical direction (Figure 3B). The differences between the 350 and 750 °C samples virtually disappear, diagnosing that the small difference in performance between them in Figure 3A was *mostly* a manifestation of the surface area difference. On the other hand, the 550 °C set of data do appear to have different photocatalytic activity to a small but perceptible degree (Figure 3B). The 550 °C sample had better reported crystallinity than the 350 °C sample and relative to the 750 °C sample (having the best crystallinity) had a unique bicrystalline network, considered by the original authors of this

study to have a favorable influence on the photocatalytic activity.<sup>47</sup>

As a last example of the interpretative advantages to be accrued by surface area renormalization, consider the data for methylene blue photodegradation from an afore-discussed study on N and Nb co-alloyed TiO<sub>2</sub>.<sup>16</sup> Samples 1–3 in Figure 4A are all derived from sol–gel synthesis but received different postsynthesis treatments. Sample 1 was first annealed in an ammonia atmosphere, sample 2 was then also annealed in an oxygen atmosphere (i.e., after the ammonia treatment), while sample 3 was first annealed in flowing oxygen followed by the same nitrogen treatment in ammonia. The photocatalytic activity obviously is highest for sample 1 in the order (Figure 4A) sample 1  $\gg$  sample 3 > sample 2.<sup>16</sup> Renormalization (for the variant surface area) preserves the superior photocatalytic activity of sample 1, but the differences between the other two samples now become much less pronounced (Figure 4B).

Unlike sample 1, both samples 2 and 3 lacked the defects (Ti<sup>3+</sup> and F<sup>+</sup> centers) as analyzed by EPR in the original study.<sup>16</sup> Further, sample 1 had the lowest-energy band gap ( $\sim$ 2.0 eV) as opposed to  $\sim$ 2.44 and 2.29 eV for samples 2 and 3, respectively.<sup>16</sup> The renormalization approach facilitates better visualization of the importance of defects (and other effects) once the surface area variations are factored out, as in Figure 4B.

Previous authors of photocatalysis studies have factored out surface area variations by renormalizing rate constants with respect to this parameter (see, for example, refs 34 and 48).

This tactic was also employed in studies of nanoparticle dissolution in geochemical environments (for example, ref 49). On the other hand, graphical renormalization of the kinetics data per the methodology prescribed in Figures 2B, 3B, and 4B provides for better visualization of the effects of other parameters (e.g., crystallinity, defect density, etc.). In some (simple) scenarios (e.g., Figure 2B), surface area variations could account for all of the photocatalytic activity differences, while in other (more complicated) situations (e.g., Figures 3B and 4B), other factors are also important for some samples but not in all.

*Photocatalytic Activity–Structural/Physical Property Relationships and Concluding Remarks.* Only limited attention has been paid to the development of quantitative relationships; these studies have almost exclusively focused on TiO<sub>2</sub>. For example, in one such study, empirical reproduction of photocatalytic properties was claimed from a linear combination of six oxide properties.<sup>50</sup> However, as stated at the outset of this Viewpoint, multivariate analyses taking into account factor interactions can provide further insights. This represents an opportunity for the chemometrics community.

It should be abundantly clear from the above paragraphs that attempts to delve into the many factors that govern photocatalytic activity have been largely TiO<sub>2</sub>-centric. This trend ought not to be too surprising given the rich history of study of this material by the heterogeneous photocatalysis community. However, it is the opinion of the authors of this Viewpoint that for tangible (and quantum) progress to be made in securing the photocatalysis process efficiencies at levels that would spur process scale-up efforts and industry adoption, the dragnet for other photocatalyst candidates must be cast wider. Unlike corresponding trends in photoelectrochemical energy conversion,<sup>14</sup> the heterogeneous photocatalysis community has not suffered debilitating swings in research funding; however, the discipline appears to have been mired in a “TiO<sub>2</sub> rut”.

Rather than try and improve the visible wavelength response of TiO<sub>2</sub>, we believe that the photocatalysis community would be better served by systematic efforts to vigorously search for other inorganic semiconductor candidates with comparable robustness but better optoelectronic and surface properties.

Interestingly enough, even for this particular material, the practical applicability of this process for indoor air cleaning and conditioning as well as for surface disinfection applications appears to have surpassed corresponding advances in the development of liquid-based remediation approaches. This trend undoubtedly reflects one handicap of the current state-of-the-science in heterogeneous photocatalysis, securing high reaction fluxes at photocatalyst–liquid interfaces. To improve energy efficiency, the process must also be made solar-compatible so that the electrical cost of driving UV lamps can be circumvented. Rather than try and improve the visible wavelength response of TiO<sub>2</sub>, we believe that the photocatalysis community would be better served by systematic efforts to

vigorously search for other inorganic semiconductor candidates with comparable robustness but better optoelectronic and surface properties. The challenges here are quite different from what the solar photovoltaics community faces in that the intrinsic processes and the materials attributes needed are different in the two application scenarios.

Krishnan Rajeshwar<sup>\*,†</sup>

Abegayl Thomas<sup>†</sup>

Csaba Janáky<sup>‡,§</sup>

<sup>†</sup>Department of Chemistry and Biochemistry, University of Texas at Arlington, Arlington, Texas 76019, United States

<sup>‡</sup>Department of Physical Chemistry and Materials Science, University of Szeged, Szeged H6720, Hungary

<sup>§</sup>MTA-SZTE “Lendület” Photoelectrochemistry Research Group, Rerrich Square 1, 6720 Szeged, Hungary

## AUTHOR INFORMATION

### Notes

Views expressed in this Viewpoint are those of the authors and not necessarily the views of the ACS.

The authors declare no competing financial interest.

### Biographies

**Krishnan Rajeshwar** received his Ph.D. in solid-state chemistry from the Indian Institute of Science in Bangalore, India and completed his postdoctoral training from Colorado State University. His research interests span a broad spectrum of areas related to energy conversion. He is currently a Distinguished University Professor at the University of Texas at Arlington (UT Arlington) and a Vice President of The Electrochemical Society. <http://www.uta.edu/cos/raj/index.html>.

**Abegayl Thomas** is a native of Grenada and migrated to the United States in 2005. She received a B.S. in Chemistry from Midwestern State University in 2008. Presently, she is pursuing her Ph.D. at UT Arlington. Her research focuses on using metal-based oxide semiconductor nanoparticles for environmental remediation.

**Csaba Janáky** is an assistant professor and Principal Investigator of the MTA-SZTE “Momentum” Photoelectrochemistry Research Group at the University of Szeged, Hungary, where he received his Ph.D. in 2010. Subsequently, he spent 2 years at UT Arlington as a Marie Curie Fellow. His research focuses on solar energy conversion, using organic, inorganic, and hybrid semiconductors. <http://www2.sci.u-szeged.hu/physchem/elchem/home.htm>.

## ACKNOWLEDGMENTS

K.R. thanks the National Science Foundation (CHE-1303803) for partial funding support. The authors also thank Rendernet Ltd. for assistance in preparing the artwork in Scheme 1.

## REFERENCES

- (1) Henderson, M. A. A Surface Science Perspective on TiO<sub>2</sub> Photocatalysis. *Surf. Sci. Rep.* **2011**, *66*, 185–297.
- (2) Diebold, U. R. The Surface Science of Titanium Dioxide. *Surf. Sci. Rep.* **2003**, *48*, 53–229.
- (3) Fujishima, A.; Honda, K. Electrochemical Photolysis of Water at a Semiconductor Electrode. *Nature* **1972**, *238*, 37–38.
- (4) Wolkenstein, Th. *The Electron Theory of Catalysis on Semiconductors*; Pergamon Press: Oxford, U.K., 1963.
- (5) Oliver, B. G.; Cosgrove, E. G.; Carey, J. H. Effect of Suspended Sediments on the Photolysis of Sediments in Water. *Environ. Sci. Technol.* **1979**, *13*, 1075–1077.

- (6) Carey, J. H.; Lawrence, J.; Tosine, H. M. Photodechlorination of PCBs in the Presence of Titanium Dioxide in Aqueous Suspensions. *Bull. Environ. Contam. Toxicol.* **1976**, *16*, 697–701.
- (7) Carey, J. H.; Oliver, B. G. The Photochemical Treatment of Wastewater by Ultraviolet Irradiation of Semiconductors. *Water Pollut. Res. J. Canada* **1980**, *15*, 157–185.
- (8) Frank, S. N.; Bard, A. J. Heterogeneous Photocatalytic Oxidation of Cyanide Ion in Aqueous Solution at TiO<sub>2</sub> Powder. *J. Am. Chem. Soc.* **1977**, *99*, 303–304.
- (9) Rajeshwar, K.; Ibáñez, J. G. Electrochemical Aspects of Photocatalysis: Application to Detoxification and Disinfection Scenarios. *J. Chem. Educ.* **1995**, *72*, 1044–1049.
- (10) Rajeshwar, K.; Ibáñez, J. G. *Environmental Electrochemistry*; Academic Press: San Diego, CA, 1997; Ch. 6, pp 499–623.
- (11) Boston, D.; Huang, K.-L.; de Tacconi, N.; Myung, N.; MacDonell, F.; Rajeshwar, K. Electro- and Photocatalytic Reduction of CO<sub>2</sub>: The Homogeneous and Heterogeneous worlds Collide? In *Photoelectrochemical Water Splitting*; Lewerenz, H.-J., Peter, L. M., Eds.; RSC Publishing: Cambridge, U.K., 2013; pp 289–332.
- (12) Ghadimkhani, G.; de Tacconi, N. R.; Chanmanee, W.; Janaky, C.; Rajeshwar, K. Efficient Solar Photoelectrosynthesis of Methanol from Carbon Dioxide Using Hybrid CuO–Cu<sub>2</sub>O Semiconductor Nanorod Arrays. *Chem. Commun.* **2013**, *49*, 1297–1299.
- (13) Rajeshwar, K.; de Tacconi, N. R.; Ghadimkhani, G.; Chanmanee, W.; Janaky, C. Tailoring Copper Oxide Semiconductor Nanorod Arrays for Photoelectrochemical Reduction of Carbon Dioxide to Methanol. *ChemPhysChem* **2013**, *14*, 2251–2259.
- (14) Rajeshwar, K. Solar Energy Conversion and Environmental Remediation Using Inorganic Semiconductor–Liquid Interfaces: The Road Traveled and The Path Forward. *J. Phys. Chem. Lett.* **2011**, *2*, 1301–1309.
- (15) Deming, S. N.; Michotte, Y.; Massart, D. L.; Kaufman, L.; Vandeginste, B. G. M. *Chemometrics: A Textbook*; Elsevier: Amsterdam, The Netherlands, 1988.
- (16) Breault, T. M.; Bartlett, B. M. Lowering the Band Gap of Anatase-Structured TiO<sub>2</sub> by Coalloying with Nb and N: Electronic Structure and Photocatalytic Degradation of Methylene Blue Dye. *J. Phys. Chem. C* **2012**, *116*, 5986–5994.
- (17) For example: Li, Y.; Yu, H.; Zhang, C.; Fu, L.; Li, G.; Shao, Z.; Yi, B. Enhancement of Photoelectrochemical Response by Modified in TiO<sub>2</sub> Nanorods. *Int. J. Hydrogen Energy* **2013**, *38*, 13023–13030; see also references therein.
- (18) Myung, N.; Lee, W.; Lee, C.; Jeong, S.; Rajeshwar, K. Synthesis of Au–BiVO<sub>4</sub> Nanocomposite through Anodic Electrodeposition Followed by Galvanic Replacement and Its Application to the Photocatalytic Decomposition of Methyl Orange. *ChemPhysChem* **2014**, *15*, 2052–2057.
- (19) Lee, C.; Jeong, S.; Myung, N.; Rajeshwar, K. A Facile Method for the Preparation of Au–Bi<sub>2</sub>O<sub>3</sub> and Its Application to Photocatalytic Degradation of Methyl Orange. *J. Electrochem. Soc.* **2014**, *161*, D499–D503.
- (20) Serpone, N. Relative Photonic Efficiencies and Quantum Yields in Heterogeneous Photocatalysis. *J. Photochem. Photobiol., A* **1997**, *104*, 1–12.
- (21) Hanaor, D. A. H.; Sorrell, C. C. Review of the Anatase to Rutile Phase Transformation. *J. Mater. Sci.* **2011**, *46*, 855–874.
- (22) Sclafani, A.; Palmisano, L.; Davi, E. Photocatalytic Degradation of Phenol by TiO<sub>2</sub> Aqueous Dispersions: Rutile and Anatase Activity. *New J. Chem.* **1990**, *14*, 265–268.
- (23) Tang, H.; Prasad, K.; Sanjinés, R.; Schmid, P. E.; Lévy, F. Electrical and Optical Properties of TiO<sub>2</sub> Anatase Thin Films. *J. Appl. Phys.* **1994**, *75*, 2042–2047.
- (24) Augustynski, J. The Role of the Surface Intermediates in the Photoelectrochemical Behavior of Anatase and Rutile TiO<sub>2</sub>. *Electrochim. Acta* **1993**, *38*, 43–46.
- (25) Wang, Y. W.; Zhang, L. Z.; Deng, K. J.; Chen, X. Y.; Zou, Z. G. Low Temperature Synthesis and Photocatalytic Activity of Rutile TiO<sub>2</sub> Nanorod Superstructures. *J. Phys. Chem. C* **2007**, *111*, 2709–2714.
- (26) Ge, S.; Wang, B.; Li, D.; Fa, W.; Yang, Z.; Yang, Z.; Jia, G.; Zheng, Z. Surface Controlled Photocatalytic Degradation of RhB over Flower-Like Rutile TiO<sub>2</sub> Superstructures. *Appl. Surf. Sci.* **2014**, *295*, 123–129.
- (27) Timmaji, H. K.; Chanmanee, W.; de Tacconi, N. R.; Rajeshwar, K. Solution Combustion Synthesis of BiVO<sub>4</sub> Nanoparticles: Effect of Combustion Precursors on the Photocatalytic Activity. *J. Adv. Oxid. Technol.* **2011**, *14*, 93–105.
- (28) Tokunaga, S.; Kato, H.; Kudo, A. Selective Preparation of Monoclinic and Tetragonal BiVO<sub>4</sub> with Scheelite Structure and their Photocatalytic Properties. *Chem. Mater.* **2001**, *13*, 4624–4628.
- (29) Thalluri, S. M.; Suarez, C. M.; Hussain, M.; Hernandez, S.; Virga, A.; Saracco, G.; Russo, N. Evaluation of the Parameters Affecting the Visible-Light-Induced Photocatalytic Activity of Monoclinic BiVO<sub>4</sub> for Water Oxidation. *Ind. Eng. Chem. Res.* **2013**, *52*, 17414–17418.
- (30) Finlayson, A. P.; Tsaneva, V. N.; Lyons, L.; Clark, M.; Glowacki, B. A. Evaluation of Bi-W-Oxides for Visible Light Photocatalysis. *Phys. Status Solidi A* **2006**, *203*, 327–335.
- (31) Sun, S.; Wang, W.; Zhou, L.; Xu, H. Efficient Methylene Blue Removal over Hydrothermally Synthesized Starlike BiVO<sub>4</sub>. *Ind. Eng. Chem. Res.* **2009**, *48*, 1735–1739.
- (32) Yang, H. G.; Sun, C. H.; Qiao, S. Z.; Zou, J.; Liu, G.; Smith, S. C.; Cheng, H. M.; Lu, G. Q. Anatase TiO<sub>2</sub> Single Crystals with a Large Percentage of Reactive Facets. *Nature* **2008**, *453*, 638–642.
- (33) Ohtani, B. Revisiting the Fundamental Physical Chemistry in Heterogeneous Photocatalysis: Its Thermodynamics and Kinetics. *Phys. Chem. Chem. Phys.* **2014**, *16*, 1788–1797.
- (34) Zhou, X.; Lan, J.; Liu, G.; Deng, K.; Yang, Y.; Nie, G.; Yu, J.; Zhi, L. Facet-Mediated Photodegradation of Organic Dye over Hematite Architectures by Visible Light. *Angew. Chem., Int. Ed.* **2012**, *124*, 182–186.
- (35) Sowers, K. L.; Fillingner, A. Crystal Face Dependence of p-Cu<sub>2</sub>O Stability as Photocathode. *J. Electrochem. Soc.* **2009**, *156*, F80–F85.
- (36) Ohtani, B.; Ogawa, Y.; Nishimoto, S.-i. Photocatalytic Activity of Amorphous–Anatase Mixture of Titanium(IV) Oxide Particles Suspended in Aqueous Solutions. *J. Phys. Chem. B* **1997**, *101*, 3746–3752.
- (37) Wang, X.; Se, L.; Su, R.; Wendt, S.; Hald, P.; Mamakhel, A.; Yang, C.; Huang, Y.; Iversen, B. B.; Besenbacher, F. The Influence of Crystallite Size and Crystallinity of Anatase Nanoparticles on the Photo-degradation of Phenol. *J. Catal.* **2014**, *310*, 100–108.
- (38) Sun, Z.; Bai, C.; Zheng, S.; Yang, X.; Frost, R. L. A Comparative Study of Different Porous Amorphous Silica Minerals Supported TiO<sub>2</sub> Catalysts. *Appl. Catal., B* **2013**, *458*, 103–110.
- (39) Xu, N.; Shi, Z.; Fan, Y.; Dong, J.; Shi, J.; Hu, M. Z. C. Effects of Particle Size of TiO<sub>2</sub> on Photocatalytic Degradation of Methylene Blue in Aqueous Suspensions. *Ind. Eng. Chem. Res.* **1999**, *38*, 373–379.
- (40) Tanaka, K.; Lapule, M. F. V.; Hisanaga, T. Effect of Crystallinity of TiO<sub>2</sub> on Its Photocatalytic Action. *Chem. Phys. Lett.* **1991**, *187*, 73–76.
- (41) For example: Le Paven-Thivet, C.; Ishikawa, A.; Ziani, A.; Le Gendre, L.; Yoshida, M.; Kubota, J.; Tessier, F.; Domen, K. Photoelectrochemical Properties of Crystalline Perovskite Lanthanum Titanium Oxynitride Films under Visible Light. *J. Phys. Chem. C* **2009**, *113*, 6156–6162.
- (42) Howe, R. F.; Gratzel, M. EPR Observation of Trapped Electrons in Colloidal Titanium Dioxide. *J. Phys. Chem.* **1985**, *89*, 4495–4499.
- (43) Micic, O.; Zhang, Y.; Cromack, K. R.; Trifunac, A. D.; Thurnauer, M. C. Photoinduced Hole Transfer from Titanium Dioxide to Methanol Molecules in Aqueous Solution Studied by Electron Paramagnetic Resonance. *J. Phys. Chem.* **1993**, *97*, 13284–13288.
- (44) Ikeda, S.; Sugiyama, N.; Murakami, S.; Kominami, H.; Kera, Y.; Noguchi, H.; Uosaki, K.; Torimoto, T.; Ohtani, B. Quantitative Analysis of Defective Sites in Titanium(IV) Oxide Photocatalyst Powders. *Phys. Chem. Chem. Phys.* **2003**, *5*, 778–783.
- (45) de Tacconi, N. R.; Timmaji, H. K.; Chanmanee, W.; Huda, M. N.; Sarker, P.; Janaky, C.; Rajeshwar, K. Photocatalytic Generation of



Syngas Using Combustion-Synthesized Silver Bismuth Tungstate. *ChemPhysChem* **2012**, *13*, 2945–2955.

(46) Tang, J.; Ye, J. Correlation of Crystal Structures and Electronic Structures and Photocatalytic Properties of the W-Containing Oxides. *J. Mater. Chem.* **2005**, *15*, 4246–4251.

(47) Wang, C.; Zhang, X.; Zhang, Y.; Jia, Y.; Yang, J.; Sun, P.; Liu, Y. Hydrothermal Growth of Layered Titanate Nanosheet Arrays on Titanium Foil and their Topotactic Transformation to Heterostructured TiO<sub>2</sub> Photocatalysts. *J. Phys. Chem. C* **2011**, *115*, 22276–22285.

(48) Zhou, X.; Yang, H.; Wang, C.; Mao, X.; Wang, Y.; Yang, Y.; Liu, G. Visible Light Induced Photocatalytic Degradation of Rhodamine B on One-Dimensional Iron Oxide Particles. *J. Phys. Chem. C* **2010**, *114*, 17051–17061.

(49) Anshultz, A.; Penn, R. L. Reduction of Crystalline Iron(III) Oxyhydroxides using Hydroquinone: Influence of Phase and Particle Size. *Geochem. Trans.* **2005**, *6*, 60–66.

(50) Prieto-Mahaney, O.; Murakami, N.; Abe, R.; Ohtani, B. Correlation between Photocatalytic Activities and Structural and Physical Properties of Titanium(IV) Oxide Powders. *Chem. Lett.* **2009**, *38*, 238–239.



Contents lists available at ScienceDirect

## Progress in Polymer Science

journal homepage: [www.elsevier.com/locate/ppolysci](http://www.elsevier.com/locate/ppolysci)

# The role of (photo)electrochemistry in the rational design of hybrid conducting polymer/semiconductor assemblies: From fundamental concepts to practical applications

C. Janáky<sup>a,b,\*</sup>, K. Rajeshwar<sup>c</sup><sup>a</sup> Department of Physical Chemistry and Materials Science, University of Szeged, Szeged H6720, Hungary<sup>b</sup> MTA-SZTE "Lendület" Photoelectrochemistry Research Group, Rerrich Square 1, Szeged 6720, Hungary<sup>c</sup> Department of Chemistry and Biochemistry, University of Texas at Arlington, Arlington, TX 76019, United States

## ARTICLE INFO

## Article history:

Received 28 March 2014

Received in revised form

28 September 2014

Accepted 7 October 2014

Available online 22 October 2014

## Keywords:

Hybrid assembly

Conducting polymer

Semiconductor

Electrochemistry

Photoelectrochemistry

## ABSTRACT

Hybrid materials based on conducting polymers (CPs) and inorganic semiconductors (SCs) undoubtedly constitute one of the most promising classes of new materials. The spectacular progress in this research topic has been driven by the development of novel synthetic procedures and by the large variety of applications. Beyond scientific and fundamental interest, such hybrid assemblies are attractive from technological perspectives as well, for example, in energy conversion and storage, electronics, catalysis, and optics.

This article is designed to be a critical overview for the polymer materials science community on how to employ electrosynthetic methods to obtain hybrid materials with well-designed composition and morphology. As this review illustrates, (photo)electrochemical approaches are versatile and powerful tools in the preparation of conjugated polymer-based composites, containing both elemental and compound semiconductors. Hybridization of CPs with metal oxides (TiO<sub>2</sub>, WO<sub>3</sub>, ZnO, NiO, Cu<sub>2</sub>O, CuO, V<sub>2</sub>O<sub>5</sub>, Fe<sub>2</sub>O<sub>3</sub>, Fe<sub>3</sub>O<sub>4</sub>, MnO<sub>2</sub>, SnO<sub>2</sub>, RuO<sub>2</sub>), metal chalcogenides (CdS, CdTe, CdSe, Bi<sub>2</sub>S<sub>3</sub>), and carbon nanomaterials (nanotubes, graphene, graphene oxide) is presented. We demonstrate that both composition and nanoscale architecture of the hybrid assemblies can be precisely controlled by employing carefully designed electrochemical methods. To achieve the goal of popularizing electro- and photoelectrosynthetic procedures, particular attention will be paid to compare the as-synthesized assemblies with their counterparts obtained from other procedures. The most prominent applications of these electrosynthesized materials are highlighted, with particular focus on energy related utilization pathways.

© 2014 Elsevier Ltd. All rights reserved.

**Abbreviations:** CB, conduction band; CNT, carbon nanotube; CP, conducting polymer; CV, cyclic voltammetry; DS, dodecyl sulfate; DSSC, dye-sensitized solar cell; EQCM, electrochemical quartz crystal microbalance; ERGO, electrochemically reduced graphene oxide; FF, fill factor; GC, glassy carbon; GO, graphene oxide; ITO, indium tin oxide;  $J_{sc}$ , short-circuit current; LPG, liquefied petroleum gas; MIP, molecularly imprinted polymer; MWCNT, multi-walled carbon nanotubes; NP, nanoparticle; NTA, nanotube array; ORR, oxygen reduction reaction; PANI, polyaniline; PCIT, poly(3-chlorothiophene); PDNTD, poly(N,N'-di[p-phenylamino(phenyl)]-1,4,5,8-naphthalene tetra-carboxylic diimide); PDOT, poly(3,4-dioctyloxythiophene); PEDOT, poly(3,4-ethylenedioxythiophene); PHT, poly(3-hexylthiophene); PMT, poly(3-methylthiophene); PNMPy, poly(N-methylpyrrole); POT, poly(3-octylthiophene); PProDOP, poly(3,4-propylenedioxyppyrrrole); PPy, polypyrrole; PSS, poly(styrenesulfonate); PT, polythiophene; PVK, poly(vinylcarbazole); PZC, point of zero charge; RDE, rotating disk electrode; SC, semiconductor; SWCNT, single-walled carbon nanotube; VB, valence band.

\* Corresponding author at: Department of Physical Chemistry and Materials Science, University of Szeged, Szeged H6720, Hungary. Tel.: +36 62544111. E-mail address: [janaky@chem.u-szeged.hu](mailto:janaky@chem.u-szeged.hu) (C. Janáky).

## Contents

1. Introduction .....	97
2. Overview and classification of preparation methods .....	98
3. Electrochemical methods for the preparation of hybrid organic/inorganic assemblies .....	101
3.1. Incorporation of inorganic semiconductors into CPs during electropolymerization .....	101
3.2. Electrodeposition of CPs on inorganic semiconductor (nano)structures .....	105
3.2.1. Electrochemical polymerization on semiconductors .....	106
3.2.2. Photoelectrochemical polymerization .....	112
3.3. Other miscellaneous approaches .....	116
3.3.1. Electrochemical co-deposition .....	116
3.3.2. Deposition of SCs on or inside the CP layer .....	116
4. Selected applications of electrochemically assembled CP/SC hybrids .....	118
4.1. Solar energy harvesting (solar and photoelectrochemical cells) .....	118
4.2. Energy storage .....	121
4.2.1. Supercapacitors .....	121
4.2.2. Lithium-ion batteries .....	123
4.3. Other miscellaneous applications .....	125
4.3.1. Heterogeneous (photo-)catalysis .....	125
4.3.2. Sensors .....	126
4.3.3. Electrochromics .....	126
5. Summary .....	127
Acknowledgements .....	128
References .....	128

## 1. Introduction

The science and technology of conducting polymers (CPs, also called conjugated polymers or synthetic metals) have traveled a long way since the modern discovery of these materials in 1976. The search for new polymers with enhanced stability, processability, and other advanced properties led to the development of subsequent generations of new materials: starting from polyacetylene, through the various heteroaromatic structures (e.g., polythiophenes, polyaniline, polypyrrole), to polymers containing more complex monomeric units [1,2]. This spectacular development was triggered both by the scientific push coming from the relevant R&D communities and a technological pull from emerging applications.

While research has been continuously developing, an increasing interest was devoted to *hybrid assemblies* based on CPs. Combination of CPs with different type of materials, such as non-conducting polymers, metals, carbonaceous materials, and inorganic compounds was successfully achieved [3–5]. Such composites proved their attractive features in a wide range of applications from organic electronics to solar cells [6], energy storage [7], and sensors [8].

In this review article, we focus on one particular segment of this broad field, namely on CP-based hybrid materials containing inorganic semiconductors (SCs). From the very early years of the study of CPs, there were scattered trials to hybridize CPs with inorganic SCs. The really impressive progress of this research field, manifests especially during the last decade, in the exponential growth of research papers published (Fig. 1). CP composites containing metal oxides (TiO<sub>2</sub>, WO<sub>3</sub>, ZnO, NiO, Cu<sub>2</sub>O, CuO, V<sub>2</sub>O<sub>5</sub>, Fe<sub>2</sub>O<sub>3</sub>, Fe<sub>3</sub>O<sub>4</sub>, MnO<sub>2</sub>, SnO<sub>2</sub>, RuO<sub>2</sub>), chalcogenides (CdS, CdTe, CdSe, Bi<sub>2</sub>S<sub>3</sub>), and carbon nanomaterials (nanotubes, graphene, graphene oxide) have been realized. Carbon

nanomaterials are included in this article because they share many similar attributes with SCs (especially related to composite formation), although most of them behave as metallic conductors.

As will be shown later, this research field is rooted in, and has emerged based on the experience gained from *flat* organic/inorganic junctions. However, this was quickly followed by the study of (*nano*)*particulate* systems, and finally, more recent works are almost exclusively devoted to hybrid *organized nano-architectures*. These studies are motivated by the recognition that nanostructured morphology plays a key role in various applications: such as solar cells (facilitating effective exciton dissociation), supercapacitors and Li-ion batteries (faster electrolyte diffusion), electrochromics (fast response), or sensors (enhanced surface area). Therefore in this review, particular focus is on such morphological aspects, both from the fundamental and application perspectives.

There is a large pool of preparation methods that can be deployed to obtain CP/SC assemblies. As presented later, different approaches can be categorized conveniently based on whether the components are synthesized concurrently (one-pot) or separately, and if the polymer is obtained through chemical or electrochemical coupling. In this paper we discuss procedures where at least one component is generated *in situ* in the presence of the other component. Furthermore, from the wealth of synthetic routes we solely focus on electrochemical and photoelectrochemical methods [9,10]. This means that in all the presented procedures in this review, electrochemical or photoelectrochemical oxidation of the monomers is the first step in the formation of the CP.

As can be seen in Fig. 1B, the number of research studies employing electrochemistry to obtain hybrid assemblies follows the same trend as that shown in Fig. 1A. Further, such methods are responsible for about 10% of the overall

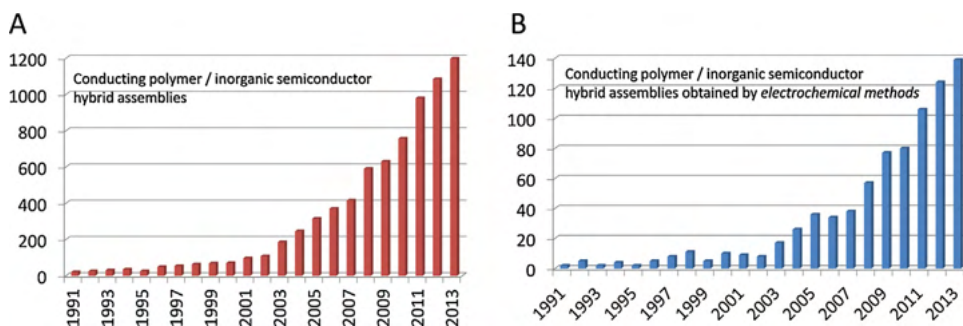


**Fig. 1.** Results from a literature survey using the ISI Web of Knowledge database on the number of articles published on conducting polymer-based hybrid materials; (A) in general, and (B) obtained through electrochemical methods. Note that the search was narrowed to semiconductor-containing hybrids.

number of studies. Importantly, while for certain materials, electrochemical approaches have become the mainstream preparation method (e.g., carbon nanomaterial/CP composites), in other cases (chalcogenide/CP hybrids), they are not considered as widely as other (e.g., wet chemical) procedures. This also means that there are several groups of CP-based composites where electrochemistry has not been fully exploited yet. Therefore we hope that research groups actively involved in various allied areas will gain insights from the forthcoming examples, and may choose to employ electrochemical methods in the future more frequently.

As shown in this review, hybrids obtained by in situ electrochemical methods have several advantages over their ex situ-, and in situ *chemically prepared* counterparts, most importantly that the organic/inorganic interface is formed in one step during the preparation of such assemblies. Using electrodeposition, hybrid materials can be directly formed as a thin film on the electrode surface. Further, the composite structure (e.g., thickness, porosity and other morphological attributes) can be precisely controlled by electrochemical procedures. In addition, such modified electrodes have obvious benefits of strong adherence to the underlying supporting electrode and improved high mechanical stability. Application oriented benefits of the presented synthetic strategies are highlighted through comparative examples in the following sections. At the same time, however, we are aware of the drawbacks of electrochemical methods as well, most importantly that a significant portion of monomers cannot be electropolymerized. This is particularly true in the case of the recently developed bulky monomers, which are specifically designed for targeted applications (e.g., bandgap engineered polymers) [11].

## 2. Overview and classification of preparation methods

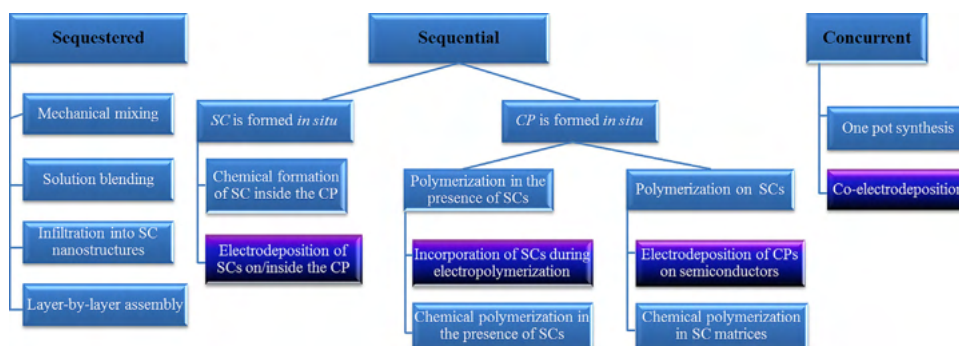
Prior to discussing the electrochemical methods in detail, it is worth briefly to summarize and categorize the various synthetic procedures generally employed to obtain CP/SC assemblies. A classification of variant procedures is shown in Scheme 1, where three main categories can be identified based on the time dimension of the synthesis.

The main feature of all methods in the first category (*sequestered synthesis*) is that both the CP and SC

components are synthesized separately, and the hybrid is assembled during a subsequent step, by simple or more sophisticated blending of the two components [12]. These procedures are the most commonplace due to their simplicity, and due to the fact that the resulted hybrid material is usually solution-processible. This feature in turn facilitates mass production and processing (e.g., roll-to-roll printing using the composite dispersed in solution). Furthermore, in these methods, all the well-established synthetic procedures can be employed for each constituent separately, since their application is not affected by the presence of the other component. As for the assembly process, there is a wealth of strategies available, ranging from simple mechanical mixing of the two powders, to more complex methods such as layer-by-layer build-up or ligand exchange procedures. Last but not least, physical infiltration of CPs into SC nanostructures can also be achieved, resulting in highly ordered organic–inorganic SC architectures.

According to experimental studies, however, such penetration is not that simple, the polymeric guest materials may block the pores of the nanostructured host due to simple physical limitations (e.g., hydrodynamic radius of the polymer), precluding complete pore filling, and therefore pore filling ratios as low as 0.5% have been obtained (this phenomenon will be discussed later in detail) [13]. Finally, the difference in the hydrophilic/hydrophobic nature of the two components can further hamper the application of such procedures.

In the second category of methods (*sequential*), one component of the hybrid material is generated in situ in the presence of its counterpart. These techniques can be further sorted on the basis of the in situ formed component. We focus here on strategies where the CP is synthesized in situ in the presence of the SC; however, the opposite sequence is also possible, namely the SC component is generated in situ inside the CP, either through chemical (co-precipitation) or electrochemical methods (stripping). As for the in situ polymerization, two distinctly different strategies can be followed. In the first group, polymerization is carried out in the presence of dispersed SC particles (either dots or other structures such as nanotubes, nanowires and nanorods), and depending on the synthesis method, either composite particles (typical for chemical polymerization), or hybrid thin films, containing SC particles are obtained (typical for electropolymerization).



**Scheme 1.** Summary of the preparation routes employed to synthesize SC-containing CP-based composite materials. Darker color indicates electrochemical methods, which are discussed in this review in greater detail.

For the chemical synthesis, formation of the nanocomposite is rather straightforward, because during chemical synthesis of a CP, coexisting nanoparticles act as nuclei, thus the forming insoluble oligomer chains are deposited on them. On the other hand, in the case of electrochemical synthesis, formation of the hybrid is not that obvious, since it usually relies on the exploitation of specific interactions between the monomer/oligomer and the nanoparticles (see Section 3.1). The second major group consists of tactics where CP is in situ deposited either on SC electrodes, or on electrode surfaces on which SCs are immobilized.

As for the third category (*concurrent* procedures) in Scheme 1, probably the easiest (and the most uncontrolled) methods belong to this group. These “one pot” methods are simply based on the in situ formation of *both* components, in/from one solution. Both chemical and electrochemical procedures belong to this group; however, co-electrodeposition is more frequently used. The most important drawback of this method is the very limited control over structure and morphology of the resultant composite material.

CPs are usually synthesized through oxidative coupling. In most polymerization reactions, the first step is the oxidation of the monomer, resulting in the formation of a radical cation, which reacts with another monomer or radical cation, forming a dimer. Therefore, another obvious dimension along which methods can be categorized is the way of initiation (and maintenance) of the polymerization. The two most generally applied routes are *chemical* and *electrochemical* oxidation. In the first, chemical oxidants (such as  $\text{FeCl}_3$  or  $(\text{NH}_4)_2\text{S}_2\text{O}_8$ ) are used to oxidize the monomer, whereas in the second one, monomers are oxidized electrochemically. Other, miscellaneous approaches, such as heat initiated polymerization [14], photopolymerization [15], or ultrasound-assisted methods [16] are also available. Note, however, that these methods are restricted to certain, special esoteric monomers.

Finally, although the particular advantages of each electrochemical method will be presented later, we briefly note that using electrodeposition composites can be directly formed as a thin film on the electrode surface. Furthermore, the film thickness, porosity and morphological features can be precisely controlled by electrochemical procedures. Also, such modified electrodes have obvious advantages of high mechanical stability and strong adherence to the

underlying supporting electrode surface. For comparison, note the typical drawbacks and limitations of corresponding materials derived from chemical methods: (i) possible aggregation of the inorganic particles, resulting in a relatively small area of the organic/inorganic interface; (ii) uncontrolled, random distribution of the particles within the polymeric matrix; and finally (iii) lack of electrical contact between the inorganic material and the supporting electrode (this hampers the application of the hybrids in many applications, e.g., electronics).

Before describing the particular electrochemical strategies to obtain CP based hybrid assemblies, it is useful to discuss some of the general aspects of electrochemical polymerization [17,18]. Therefore, electrochemical protocols, which are mostly employed to electropolymerize CPs are summarized and compared in Table 1; typical examples for each technique are given in Fig. 2. By sorting the listed approaches, two major groups can be identified: static and dynamic methods. Depending on the controlled variable, we can also distinguish between potential- and current-controlled techniques. Some of their advantages and disadvantages of these approaches are listed Table 1. At this point it is important to clarify a terminological issue which is problematic in many publications, namely that cyclic voltammetry (CV) is an *electroanalytical* tool, not a *synthetic* procedure. Therefore, when potential cycling is employed to electrogenerate a CP, the correct nomenclature is either “potentiodynamic electropolymerization”, or polymerization by “potential cycling” (instead of using the term CV).

As may be seen from Table 1, as well as in Fig. 2, the different methods of electrochemical polymerization have markedly different features. Depending on the complexity of the procedure, a number of parameters can be varied in order to tailor the properties of the forming CP toward a targeted application. Optimization of these circumstances (e.g., potential window, sweep rate, current density, time of each potential step) is crucially important in light of the competing processes [19]. Concurrent nucleation and growth, or in other words, the formation and growth of insoluble oligomers, control the relative contribution of solution phase and solid phase polymerization. Furthermore, depending on the above listed parameters, polymer formation can also be controlled either by the polymerization kinetics or by monomer (or even dopant ion) mass

**Table 1**

Summary and comparison of various electrochemical polymerization methods employed to obtain CPs.

Method	Controlled variable	Measured response	Advantages	Disadvantages
<b>Static</b>				
Galvanostatic	Current density kept constant	Potential	The polymerization rate as well as overall charge density can be easily controlled and continuous growth ensured	Potential may reach high values to keep the current constant, which can cause overoxidation. It is difficult to normalize the current in the case of nanostructured electrodes
Potentiostatic	Potential kept constant	Current density	As the potential is controlled, overoxidation can be avoided	Possible inhomogeneous growth of the polymer, especially for thicker layers. The current may drop significantly in the case of longer procedures
<b>Dynamic</b>				
Current pulses	Current density periodically varied	Potential	The overall charge density can be easily controlled	There are rest periods between the polymerization steps; therefore problems caused by diffusion limitation can be avoided
Potential step	Potential periodically varied	Current density	Polymerization can be precisely controlled	Electrochemical double layer may get charged/discharged at every step
Potential cycling (potentiodynamic)	Potential cyclically varied	Current density	Polymer is under permanent electrochemical stimulus	There is a large (and uncontrolled) current spike at the beginning of each step Formed polymer may get overoxidized during subsequent polymerization cycles

transport. Note that these processes become even more important when either nanoparticles are used as dopants, or CPs are electrodeposited on nanostructured SC matrices.

Beyond the employed electrochemical technique, several other factors influence the polymerization process (Table 2), such as solvent, electrolyte, electrode material, monomer etc. All these have crucial impact on the properties of the CP ranging from molecular structure to supramolecular morphology [20]. For a hybrid, the picture gets even murkier. Two examples suffice for the challenges

which have to be overcome: (i) selection of the appropriate potential window, where the monomer gets oxidized (but the polymer will not suffer overoxidation), and at the same time the solvent, the electrolyte ions, and the SC remain chemically intact; (ii) optimization of the polymerization medium, both in terms of the conducting electrolyte, as well as the solvent. Further, several monomers can only be polymerized in organic solvents; while in aqueous solutions, special emphasis should be given to the pH (it has to be optimal for both components).

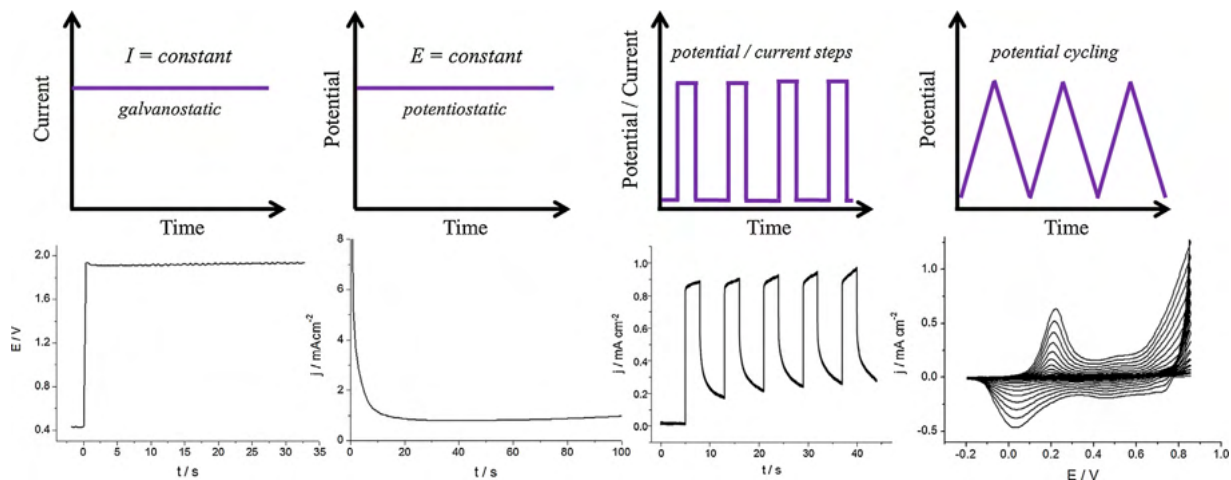


**Fig. 2.** Comparison of frequently employed electrochemical polymerization techniques. The controlled variables upper drawings, as well as the measured experimental responses measured data at the bottom, are shown for the various cases.

**Table 2**

Factors that affect electrochemical polymerization of CPs.

	General considerations, and properties it affects	Possible threat	Typical examples
Electrochemical method	It affects both the molecular and supramolecular structure of the polymer. By varying the synthesis parameters the thickness and the morphology of the polymer can be controlled	Careful selection of the applied potential window is indeed important to avoid overoxidation of the polymer Mass transport limitation is usually also not favored	Static: Potentiostatic, galvanostatic Dynamic: multiple potential steps, potentiodynamic cycling
Monomer	Some monomers (especially the bulky ones) are not electropolymerizable Often dimers or trimers are used as precursor, due to their lower oxidation potential Monomers with $-\text{COOH}$ and $-\text{NH}_2$ moieties are generally useful for composite preparation	Low solubility causing mass transport limitation High oxidation potential may hamper electrodeposition on SCs	Our review is restricted to the classic heteroaromatic monomers and their derivatives (pyrrole, thiophene, aniline). Larger monomers with fused rings are not discussed here
Supporting electrolyte	Ion exchange behavior of the polymer is strongly dependent of the electrolyte used during the electropolymerization (mobile vs. immobile anions) Doping level, and electroactivity is also affected Morphology, the compactness and porosity is also linked to the nature of the electrolyte	Highly electronegative and nucleophile anions may assist overoxidation of the polymer Note that some anions are effective dopants, others are not (especially true for multivalent anions)	Immobile anions ( $\text{PSS}^-$ , $\text{DS}^-$ ) Mobile anions ( $\text{ClO}_4^-$ , $\text{BF}_4^-$ , $\text{PF}_6^-$ ) Small cations ( $\text{Li}^+$ , $\text{Na}^+$ ) Bulky cations ( $\text{Bu}_4\text{N}^+$ , cetyl-) Ionic liquids can be solvent and dopant at the same time
Solvent	Aqueous solutions are generally preferred, due to economic and environmental consideration. pH of the solution is crucial to obtain the conducting form of the polymer For certain, thiophene-type monomers, non-aqueous solvents have to be utilized The solvent affects the morphology, and even the electroactivity (memory effect)	Formation of non-conducting polymer Oxidation/reduction of the solvent	Water, acetonitrile, nitrobenzene, propylene carbonate, nitromethane, various ionic liquids
Electrode material	Adhesion of the polymer, interactions are possible between the monomer and the electrode Interfacial properties of the polymer/electrode junction	Oxidation of the electrode material Detachment of the CP Low conductivity hampering the electrodeposition of the polymer	Classical inert electrodes are: Pt, Au, glassy carbon, ITO coated glass Examples for SC electrodes are presented in this review

### 3. Electrochemical methods for the preparation of hybrid organic/inorganic assemblies

#### 3.1. Incorporation of inorganic semiconductors into CPs during electropolymerization

In the following examples, SC *particles* are embedded into the matrix of various CPs, through electropolymerization of the respective monomers in the presence of SCs. In these methods, compared with conventional electrogeneration of CPs, the only difference is having the (nano)particles in the polymerization media. Otherwise, similar inert working electrodes (Au, Pt, ITO, glassy carbon) and electrochemical procedures (see Table 2) are used. This one-step procedure is very attractive, because the composite can directly form in situ on an electrode surface, which can then be readily used as a chemically modified electrode.

The first trials in this manner relied on the simple physical entrapment of colloidal particles. Different metal oxide particles ( $\text{MnO}_2$ ,  $\text{SnO}_2$ ,  $\text{TiO}_2$  and  $\text{WO}_3$ ) were incorporated into both polypyrrole (PPy) and polyaniline (PANI) [21–26]. The role of anions in the solution, the concentration of the SC particles, and the crucial influence of vigorous stirring, was demonstrated. The need for stirring can be rationalized by the large (micrometer) size of the SC particle,

which would otherwise sediment. As for the role of pH and anions being present in the polymerization solution, detailed studies revealed that successful synthesis (e.g., high particle content in the deposited polymeric matrix) is based on optimizing interactions between the polymer and the SC particles. This interaction is usually electrostatic in nature, which means that the SC particles bearing negatively charged surfaces are incorporated into the polymer as dopants, compensating the positive charges generated in the polymer during the anodic electropolymerization. In other words, without such strong interactions, synthesis usually leads to small loadings of the built-in component, due to some occasional physical or weak chemical (dipole–dipole) interactions between the polymer and the SC particles.

Metal oxides can have different surface charge depending on the solution pH. Thus their surface  $-\text{OH}$  groups can be neutral, protonated (positive surface charge), or deprotonated (negative surface charge). Some oxides (e.g.,  $\text{SnO}_2$ ,  $\text{WO}_3$ ) have very low point of zero charge (PZC), consequently the pH of the oxide suspension (*without any additional electrolyte*) results in negative charges on the oxide surface. For these materials no external anions are needed as dopants, although the lack of other anions may result in lower doping levels, and thus poor electroactivity.

In other cases, most importantly for TiO<sub>2</sub>, basic conditions would be needed to ensure negative surface charge. Formation of CPs in basic solutions, however, is hampered by the presence of nucleophile OH<sup>-</sup> ions which lead to the formation of non-conducting polymeric species. To overcome this problem, addition of different anions (e.g., I<sup>-</sup> and SO<sub>4</sub><sup>2-</sup>), having good adsorbability on the particle surface, may lead to a negatively charged surface, without disturbing electrochemical growth of the CP [22].

The effect of presence of a conducting electrolyte, however, is complex: (i) anions being adsorbed on the SC particle surface may enable their incorporation as dopants (ii) the anions can act as dopants themselves, therefore hampering incorporation of the oxide particles. In light of the possibility of such competitive doping, it is not surprising that the loaded amounts of the oxide decrease with increasing electrolyte concentration [23]. There is also good correlation between the amount of particles in the solution and in the composite, which indicates that incorporation is limited by mass transport of the SC particles. This feature was also confirmed by the fact that a slower polymerization procedure (e.g., lower current densities during the galvanostatic polymerization) results in a higher amount of the SC particle [23]. Finally, incorporation of the photoactive SC particles was confirmed by the photoelectrochemical behavior of the composite [23]. However, the anodic photocurrents were rather low (compared to both neat SC surfaces and hybrids with organized nanoscale structures, as shown in Section 3.2) predominantly due to the fact that only the CP had electrical contact with the supporting electrode (and the solution) resulting in inefficient charge carrier transport.

Based on the previous observations, and recognizing the importance of surface charge, further sophisticated surface treatments have been developed. Various small sized, and also macroions have been employed to cover the surface of the particles. It is important to emphasize that after the initial studies (mentioned above), where colloidal sized particles were incorporated, the interest turned toward *nanoparticles* (NPs) and other structures with nanosized dimensions. The most important features of using nano objects are the increased specific surface area, the lack of sedimentation in the suspension, and the novel properties related to the nanometer scale size of the various compounds. Besides additional studies on TiO<sub>2</sub> [27–33] and WO<sub>3</sub> [34], the group of embedded SC particles has been extended to include Bi<sub>2</sub>S<sub>3</sub> [35,36], CdS [37–39], CdTe [40], Fe<sub>2</sub>O<sub>3</sub> [41–43], Fe<sub>3</sub>O<sub>4</sub> [44–46], MnO<sub>2</sub> [24], V<sub>2</sub>O<sub>5</sub> [47,48], ZnO [49], and ZrO<sub>2</sub> [50], as listed in Table 3.

All the methods presented in Section 3.1 share at least one common attribute, namely that the incorporated SCs were prepared *before* the electrochemical polymerization. NPs of SC compounds are generally synthesized by wet chemistry. The principal advantage of these methods is that both the size and size distribution of the NPs can be carefully controlled in the synthesis. Note that NPs are often grown in the presence of a surfactant, to prevent the nanosized particles from aggregation. Moreover, encapsulating agents may facilitate the incorporation of the coated NPs during anodic electrodeposition of the respective polymer through various interactions, as discussed earlier. Such

coating species, however, may also affect the reactivity, solubility and dimension of the resulting NPs, therefore careful selection of encapsulating ions is indeed important. Despite the above advantages, application of surfactants has also an unintended effect, namely separating the inorganic and the organic semiconducting phase. In the case of electrochemically inactive surfactants, this separation may cause insulation (series resistance) between the polymer and the NPs. The existence of such an electrical barrier is particularly disadvantageous in applications based on charge transfer and/or charge separation at the organic/inorganic interface. To overcome this problem, the use of electroactive coatings has been introduced, and their effectiveness was thoroughly demonstrated [58,59].

Going another step further, nanoparticles were coated by the electroactive monomer molecules *themselves*. In this manner electropolymerization can start right at the NP surface; an intimate contact is thus ensured while aggregation is also avoided. Also note that here the driving force for the encapsulation of SC nanoparticles is not doping but the chemical interaction between the SC and the monomer/polymer components. Such chemical interactions can be facilitated through various moieties, such as –OH/–COOH, Au/S and –COOH/–NH<sub>2</sub>, etc. This strategy was followed for preparing hybrid thin films of Fe<sub>3</sub>O<sub>4</sub> and poly(3-thiophene-acetic-acid) [60]. Magnetite nanoparticles were stabilized in a non-aqueous solution through chemisorption of the monomer on their surface. The interaction of surface –OH groups of the oxide NP and the carboxyl moieties of the monomer was utilized. By this method, through simple variation of the magnetite content of the polymerization mixture, the amount of encapsulated oxide could be easily tuned, and increased up to 80% (w/w), as corroborated from electrochemical quartz crystal microbalance (EQCM) data [60]. In addition, by covering the NPs with an organic coating it was possible to carry out the electropolymerization in organic media (which is a prerequisite for certain thiophene-type monomers).

In an even more sophisticated variant of this method, a thin primary layer of the polymer/oligomer was electrodeposited on the electrode surface (shown in Fig. 3). Subsequently, electrochemical capture of CdSe semiconductor nanocrystals, with thiophene-terminated carboxylic acid capping ligands, took place at the surface of electrodeposited polythiophene film [51,52]. Due to the large size, and consequently the low diffusion coefficient of the monomer coated NPs, a multiple potential step method was employed. Initially a very short step of high potential is applied, when electrodeposition is kinetically controlled. Subsequently, a longer rest pulse is included, when the solution got enriched around the electrode surface (depletion layer). These two steps can be applied multiple times to increase the film thickness, and thus the NP loading.

A very similar approach has been followed to electrochemically attach p-aminothiophenol-functionalized CdS nanoparticles to a Au electrode, which was pre-modified with a monolayer of the monomer [61]. Interestingly even *ternary* hybrids were realized through this approach by adding either gold NPs [62] or carbon nanotubes (CNTs) [63] to the CdS/PANI system. Importantly, these hybrids showed improved photoelectrochemical properties



**Table 3**

Representative examples for the incorporation of inorganic SCs into CPs during electropolymerization.

Semiconductor	Polymer	Method	Comments/important message	Refs.
Bi <sub>2</sub> S <sub>3</sub>	PPy	Potentiodynamic	The lack of interaction between the components led to low inorganic content embedded in the polymer	[35,36]
CdS	PANI	Galvanostatic	The effect of the agitation of the solution was shown	[37]
		Potentiostatic	Electrolyte dependence was observed and described	[38]
CdSe	PPy	Potentiodynamic	Role of stirring was emphasized	[39]
	Thiophenes	Potentiostatic	Role of electroactive protecting shell (of the monomers) was shown	[51,52]
CdSe@ZnS	PDMDT	Potentiodynamic	The NPs were protected with —NH <sub>2</sub> functionalized molecules, which can be coupled with the monomer	[53]
CdTe	PPy	Galvanostatic	A thin pre-layer of the polymer was advantageous, to avoid the need for high potential (degradation of the inorganic component was thus avoided)	[40]
CuMnO	PPy	Galvanostatic	The role of anions was shown, in light of the difference in the conductivity of the obtained hybrid	[54]
Fe <sub>2</sub> O <sub>3</sub>	PPy	Galvanostatic	Role of the surface adsorbed anions was demonstrated	[42]
		Potentiostatic	Different anionic chelating agents were used to facilitate incorporation. Conductivity of the hybrids was compared	[43]
		Galvanostatic	Incorporation of NPs was achieved by chemical etching of the NP surface, endowing negative charge to them	[41,44]
Fe <sub>3</sub> O <sub>4</sub>	PANI	Galvanostatic	The previous method was extended for another polymer	[55]
	PEDOT	Galvanostatic	The role of pH on the polymer formation was shown	[55]
	PPy	Galvanostatic	The mechanism was uncovered, doping type incorporation was evidenced	[44–46]
MnO <sub>2</sub>	PPy	Galvanostatic	The mechanism was summarized, emphasizing the role of interactions between the components	[24]
NiCoO	PPy	Galvanostatic	The polymer was immediately overoxidized during the synthesis	[56]
TiO <sub>2</sub>	PANI	Galvanostatic	The role of stirring was evaluated	[27]
		Potentiostatic	The polymer was immediately overoxidized	[32]
			The role of stirring, as well as the pre-deposition of a polymeric layer was studied	[31]
	Polyazulene	Potentiodynamic	The influence of TiO <sub>2</sub> concentration on the incorporated amount was shown	[33]
	PPy	Galvanostatic	The crucial role of different anions, potentially adsorbed on the NP surface, was demonstrated	[22]
		Galvanostatic	Oxalic acid was used as electrolyte during the deposition	[28,29]
V <sub>2</sub> O <sub>5</sub>	PEDOT	Potentiodynamic	Thermal stability of the hybrid was discussed	[30]
		Potentiostatic	Titanate nanotubes were incorporated	[57]
		Galvanostatic	Good discussion on the mechanical properties of the hybrid	[47]
WO <sub>3</sub>	PPy	Potentiostatic	Inorganic nanobeams were incorporated	[48]
	PANI	Potentiostatic	Role of stirring was studied	[21]
ZnO	PDMDT	Potentiostatic	H-bonding contributed to the immobilization of the NPs	[34]
		Potentiodynamic	Detailed analysis of the effect synthesis parameters on the hybrid composition and properties was given	[26]
ZnO	PPy	Galvanostatic	The role of a surfactant in the solution was shown	[49]
ZrO <sub>2</sub>	NMPy	Potentiodynamic	The hybrid formed a strongly adherent layer	[50]
ZrO <sub>2</sub>	Polymer	Potentiodynamic		

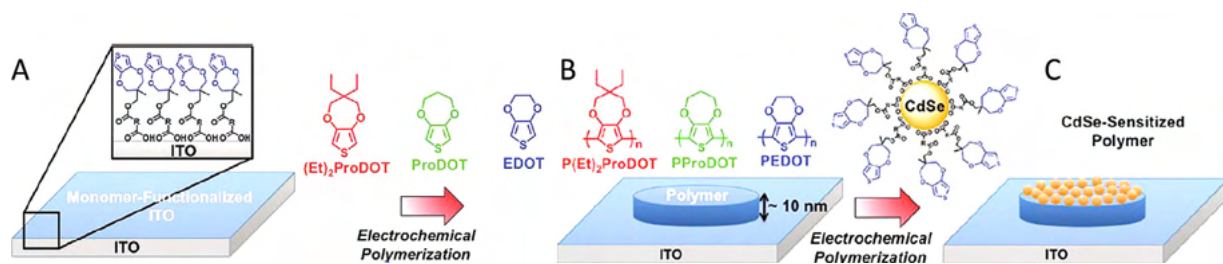


**Fig. 3.** Schematic illustration of the formation of different polythiophene/CdSe hybrids, using monomer coated nanoparticles, and the pre-deposited thin polymeric film (A–C). [52], Copyright 2010, Adapted with permission from the American Chemical Society.

compared with its CNT-, and Au free counterpart due to better charge separation and charge carrier collection.

Another remarkable group of polymerization methods uses carbazole containing *dendrons* as precursor of the CP and as coating agent for chalcogenide NPs. Polymerization in such configuration was shown to be successful for a TiO<sub>2</sub>/PPy system already, with the use of pyrrole-coated TiO<sub>2</sub> nanoparticles at the supporting electrode surface as a precursor [64]. Polymer formation is based on electrochemical crosslinking, and therefore it is different from the previously shown examples in various aspects [65,66]. As seen in Fig. 4A, monomer-coated particles were cast on the electrode surface which was subsequently exposed to potentiodynamic cycling (no additional monomers or monomer-coated NPs are available in the solution). In this procedure, the carbazole units are crosslinked both intra-molecularly and inter-molecularly within the film structure. In contrast to the previous examples, the higher current densities detected here with the increasing number of cycles do not mean increasing amount of material on the electrode, but rather step-by-step formation of the electroactive *polymer* as corroborated from the gradually developing electrochemical activity (Fig. 4A). Importantly, the bandgap of the organic SC can be tuned by the number of cycles (Fig. 4B).

All the previous examples share the same attribute in the sense that an external coating (either a negatively charged surfactant or an electroactive monomer) was introduced to facilitate the incorporation of the SC NPs. A somewhat different approach uses a special electrolyte or reagent for chemically modifying the SC NP surface, which subsequently leads to an interaction with the polymeric chain. This is illustrated in Fig. 5, for the specific example of chemically etched Fe<sub>3</sub>O<sub>4</sub> nanoparticles, leading to a negatively charged surface. By using potassium tetraoxalate as electrolyte the magnetite nanoparticles are partially dissolved, and their surface is covered by Fe-oxalate moieties. Importantly, careful optimization of the electrolyte concentration and magnetite amount is required, to endow negative charge to the particles, but not to dissolve them completely [41,44,45].

In the case of carbon nanostructures, surface modification is even more facile. Both carbon nanotubes and graphene sheets can be chemically modified to introduce different functional groups, such as –OH, C=O, –COOH, or –NH<sub>2</sub>. Oxygen containing moieties are usually formed by oxidative acid treatment at elevated temperatures,

whereas other groups are often introduced by chemical coupling reactions [67,68]. Such modifications make these materials more hydrophilic, which allows them to be dispersed in aqueous media. Note that this is a prerequisite for their subsequent incorporation into CPs during electrosynthesis in aqueous solutions. Furthermore, these moieties can facilitate either doping type incorporation, or immobilization based on the interaction between the monomer/polymer and the surface-functionalized carbon nanomaterial [69].

In the case of graphene, the starting material is frequently graphene-oxide (GO) (note that it has a wealth of different oxygen containing moieties), which is subsequently reduced electrochemically *inside the composite material*. Representative functional groups and their respective interactions are shown in Fig. 6. Note that due to the easy surface modification, and therefore the large variety of possible interactions, this approach is widely used, so only a few representative examples are shown in Table 4.

As a partial summary, we may conclude that a wealth of examples was shown above for the incorporation of SCs into CPs, while they were electrogenerated on the surface of conventional electrodes. All these methods, however, share some significant drawbacks and limitations, the two most important being the uncontrolled, random distribution of the (nano)particles within the polymer, and the fact that only the polymer phase has electrical contact with the supporting electrode. Consequently, use of the hybrid

**Table 4**  
Representative examples for the incorporation of carbon nanomaterials into CPs during their electrochemical polymerization.

Carbon	CP	Refs.
C60	PEDOT	[72]
	POT	[73]
Carbon black	PPy	[74,75]
Graphene	PANI	[76]
	PEDOT	[77]
	Polypyrene	[78]
	PPy	[71,79–81]
MWCNT	PANI	[70,82,83]
	PEDOT	[84–88]
	PPy	[89–92]
	PMT	[93]
SWCNT	PPy	[94]
	PANI	[95,96]

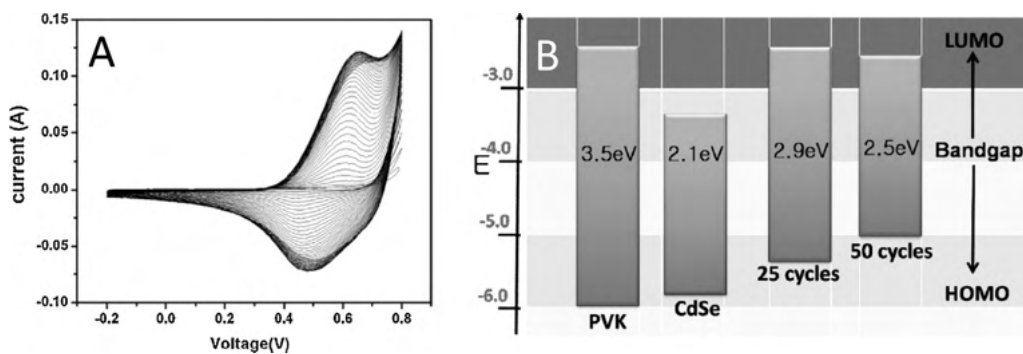


**Fig. 4.** Potentiodynamic curves registered during the electrochemical crosslinking of carbazole-dendron covered CdSe NPs. B: Bandgap tuning through electropolymerization. For comparison, band positions of the monomer PVK, and CdSe, are also shown. [65]. Copyright 2008, Adapted with permission from John Wiley & Sons Inc.

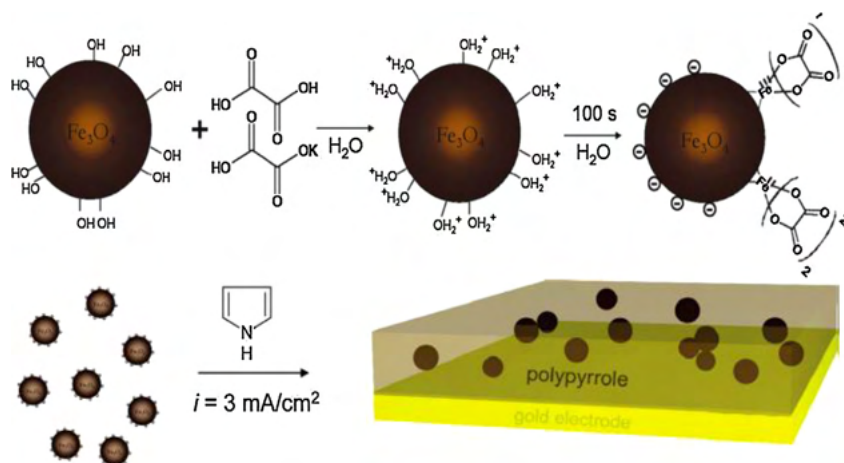


**Fig. 5.** Illustration of the surface modification of magnetite nanoparticles with potassium tetraoxalate electrolyte top, and of nanocomposite formation during the electrochemical polymerization bottom. [45]. Copyright 2010, Reproduced with permission from the American Chemical Society.

as an *electrode* is handicapped by both inefficient charge separation and propagation. The tactics outlined in the following sections aim at overcoming these problems, by using well-ordered SC arrays, in which both components have electrical contact with the supporting electrode.

### 3.2. Electrodeposition of CPs on inorganic semiconductor (nano)structures

Beyond the generally used noble metal (Pt, Au), glassy carbon (GC) and ITO-coated glass electrodes,

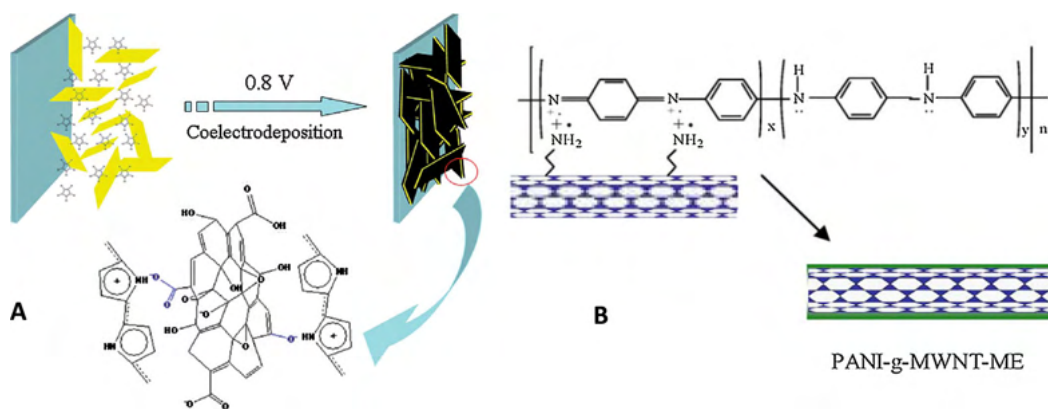


**Fig. 6.** Illustration of interaction between surface-modified carbon nanomaterials and CPs. Sources, respectively: [70], Copyrights 2006, Reproduced with permission from Elsevier Ltd.; [71], Copyrights 2012, the Royal Society of Chemistry.

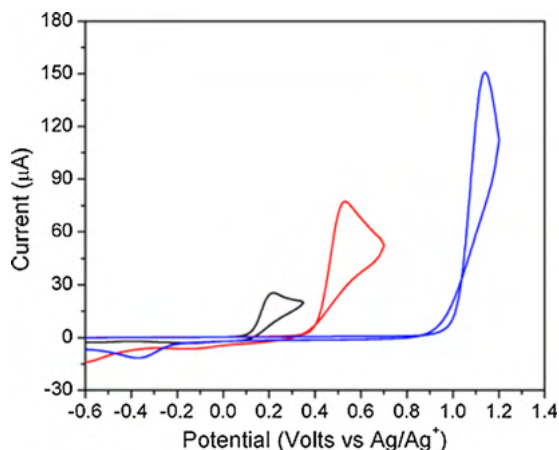


**Fig. 7.** Comparison of potentiodynamic polymerization curves for EDOT, bi-EDOT, tri-EDOT. [112], Copyright 2011, Reproduced with permission from Springer.

semiconductor materials can also be used as working electrodes for the electrochemical polymerization of CPs. Such approaches are motivated by various applications, ranging from the simple protection of inorganic SC electrodes (e.g., CdS, Si) from either corrosion or photocorrosion, to photo-sensitization of oxide SCs, most importantly, TiO<sub>2</sub>. Employing SC electrodes, however, is hampered by various facts, most importantly by their limited stability and lower conductivity, compared to their previously mentioned metal counterparts. Therefore, careful optimization of the polymerization procedure is indeed required, as demonstrated in this section. The first successful studies were carried out using flat SC surfaces; however, our particular focus is on nanostructured SCs, because the advantages of these tactics become really prominent in the case of such architectures.

### 3.2.1. Electrochemical polymerization on semiconductors

In this section, electrosynthetic methods, in which SCs are used as working electrodes, are described. Importantly, in all the presented examples, electrochemical polymerization was carried out without illumination, in the dark. Studies exploiting the photoelectrochemical behavior of the SC electrode are presented in Section 3.2.2. In the early studies, CPs were electropolymerized on flat SC surfaces. In this vein, electrodeposition of CPs on elemental SCs (e.g., Si) [97], phosphides (e.g., InP) [98], metal oxides (e.g., CuO, MnO<sub>2</sub> or TiO<sub>2</sub>) [99–102], different chalcogenides (including CdS, CdSe, CdTe and PbS) [103–109], as well as ternary compounds (CuInS<sub>2</sub> and CuInSe<sub>2</sub>) [110,111] was accomplished.

The most important lessons learned from these studies include appreciation of the need for careful selection of the potential window, especially for those SCs which are prone to electrochemical corrosion. A notable trick to keep the SC electrode material stable is to use organic dimer or trimer instead of using the respective monomer. As mentioned earlier, the oxidation potential gradually decreases with increasing segment number due to the extended conjugation length (Fig. 7) [112]. This way, the polymerization

**Table 5**

Examples of electrodeposited CPs on carbon nanomaterials.

Carbon	CP	Refs.
Carbon rods	PPy	[113]
Graphene	PANI	[114–116]
	PPy	[117–120]
MWCNT	PANI	[121–123]
	PEDOT	[124,125]
	PMT	[126]
	PPy	[127–129]
	PVK	[130,131]
Porous carbon	PANI	[132]
	PPy	[133]
SWCNT	PANI	[134–136]
	PDOP	[137]
	PHT	[138]
	PPy	[139]
	PT	[140]
	PVK	[130,131]

can start at notably lower potentials, minimizing the risk of oxidizing the electrode material. Furthermore, the use of non-aqueous solutions, and especially ionic liquids, may also be viable strategies to keep the SC electrode stable.

For electrodeposition of CPs on *nanostructured* oxide matrices, multiple challenges have to be tackled simultaneously, namely issues with mass transport limitations, and difficulties related to the low conductivity of the SC matrix. Carbon nanomaterials exhibit far the highest conductivity within the studied group, which means, that for this class of materials, the limited conductivity is not an issue. Furthermore, beyond the sufficiently high conductivity, there is also a catalytic effect of carbon nanomaterials toward the electropolymerization of CPs, presumably due to  $\pi$ - $\pi$  stacking between them and the heteroaromatic monomers. Because of this catalytic effect, deposition of CPs is favored on CNTs compared to the supporting electrode, and oxidation of the monomer (and consequently the polymerization as well) will occur at lower potentials compared to the generally used noble metal, or glassy carbon (GC) electrodes. Also note that no pretreatment of the nanocarbon is required, in contrast to the methods presented earlier, where surface groups have to be formed to ensure interaction with the polymer phase. Furthermore, there is no risk of aggregation of the nanomaterials during polymerization since they are not in the solution phase during the procedure. Table 5 lists representative examples of electrodeposited CPs on carbon nanomaterials.

In the early studies in this group, CNT films were obtained from simple drop- or spin coating of their solutions on an inert conductive surface (noble metal, ITO, GC), and were then used as working electrode for the subsequent electropolymerization of a monomer. This configuration is useful for some of the targeted applications (e.g., sensors or electrochromics), but is handicapped by both the rigidity of the supporting electrode, as well as the poor adhesion of the carbon nanomaterials, which can eventually lead to their partial desorption from the substrate. More recently, well-ordered arrays of CNTs were grown on flexible thin metal foils and used as template to electrodeposit CPs on them [122,123,127,129,139].

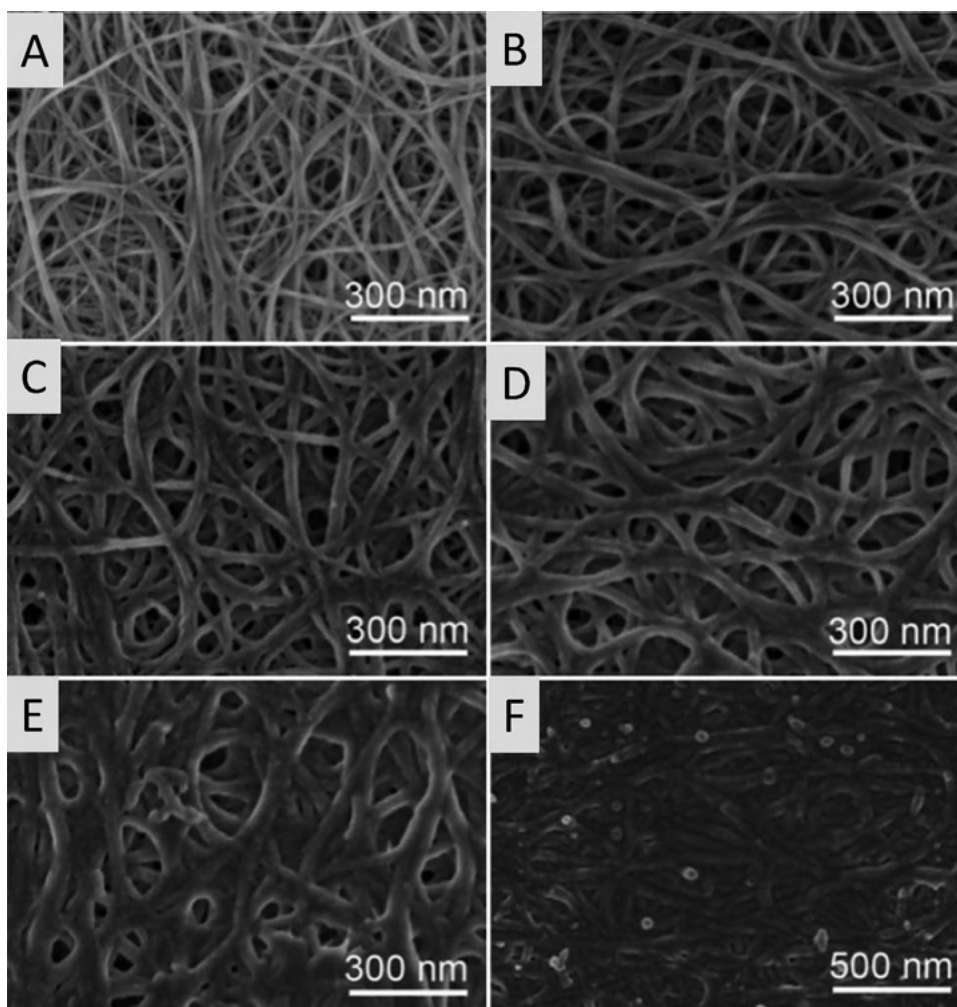


**Fig. 8.** Development of SWCNT/PANI structures with increasing deposition time. The evolution in the morphology can be followed from frames A to F. [136], Copyright 2012, Reproduced with permission from the Royal Society of Chemistry.

Such nanoarchitectures bear the advantage that every single nanotube is in direct electrical contact with the supporting electrode. Furthermore, the density of these nanotube arrays (NTAs, also called as forests or carpets) can be tuned by the synthetic parameters, and adjusted to the targeted application needs. Finally, composites based on free-standing films of CNTs and graphene have also come to the forefront of research recently. In this configuration, there is no additional supporting electrode, but self-supported films of the carbon nanomaterials are used as working electrodes (e.g., graphene or CNT papers) [114,117,136].

As for the polymerization methods, for thin films (generally up to few hundred nm, but also strongly depends on the porosity) mass transport limitation is not really an issue, therefore even static methods can be employed. To illustrate the development of a hybrid structure, we show the electrodeposition of PANI onto a continuous thin 2D film of firmly connected SWCNT bundles [136]. Such an interconnected network structure is indeed beneficial for facile electron transport and high mechanical strength of

the film. As can be seen in Fig. 8, the polymer coating on the SWCNT bundles gets progressively thicker (skeleton/skin architecture), and in parallel, the pore size decreases during polymerization. As the polymerization proceeds further, the pores get filled and finally they disappear altogether.

As for thicker and dense carbon matrices, potentiodynamic protocols are generally favored because of the nanostructured character of the carbon film, which often makes diffusion of the monomer and counterion, the rate-limiting step in the electropolymerization. During continuous polymerization, all the monomer being present in the nanoporous carbon structure at the beginning of the synthesis is consumed, leading to significantly reduced electropolymerization inside the nanostructured matrix. Instead, polymerization may occur on top of the nanostructured layer, where there is a continuous supply of monomer from the bulk solution. Such top surface layer morphology of the CP is unfortunate, as it may block the functional capabilities of CNTs. Both potential cycling and current/potential pulses have been employed to ensure even distribution of the polymer within the nanostructured

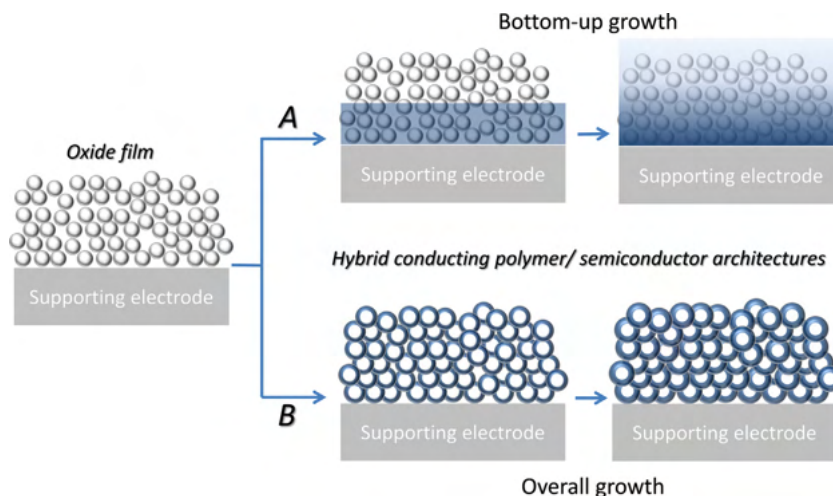


**Fig. 9.** Illustration of (A) bottom-up growth and (B) surface deposition of CPs on nanostructured SC matrices.

template [117,122,127,129]. The key point in all these methods is the introduction of rest periods between the deposition steps, which allow for the monomer to diffuse into the carbon matrix.

If we move one step further to inorganic nanostructures, one has to tackle the challenges originating from the nanostructured character and the limited conductivity of the oxide matrix *simultaneously*. Due to the second feature we have to distinguish between two distinctly different mechanisms in this group (Fig. 8). In the first group, SC nanoparticles or nanostructures are grown, or immobilized on an underlying electrode surface (e.g., metal or ITO). As SCs are usually not as conductive as the supporting electrode, the growth of the polymer usually starts from the bottom of the immobilized SC layer, at the underlying electrode. In these cases the CP fills up the matrix gradually, and SC particles get entrapped in the growing polymeric layer.

Oppositely, under special conditions, electropolymerization may occur directly on the surface of the SC nanostructure. Such deposition can be envisioned for example when (i) a compact oxide layer exists underneath the nanostructured film, (ii) the SC is very conductive, (iii) the SC has a large affinity toward the monomer, (iv) monomers are chemically linked to the SC surface. Importantly, these latter methods ensure intimate contact between the two components of the hybrid assembly (vs. those in the first category) since they are in both electrical and physical contact *already during formation of the polymer* (Fig. 9).

Even if the previously mentioned two methods cannot be completely separated, in the following examples, the dominance of the bottom-up growth approach, starting at the underlying electrode can be seen [141–147]. In these arrangements, SC nanoparticles (usually  $\text{TiO}_2$ ) are immobilized on a conducting substrate, such as ITO-coated glass electrode. As a next step, the electrodes are soaked in the monomer- and electrolyte-containing solutions (often ionic liquids, due to their inertness and favorable wetting properties), and subsequently electropolymerization

is carried out. Morphological studies confirmed [142,143] deposition of the polymer inside the mesoporous SC layer, albeit, with an uneven distribution, with a densely packed layer close to the ITO substrate, and much less complete pore fillings closer to the top of the layer. This clearly reflects a disadvantage of this method, namely that the CP is growing from the *substrate only* and not on the SC throughout the nanoporous matrix.

Note the similarities of this configuration with that of dye-sensitized solar cells (DSSCs) [148]. This is not a coincidence, since most of these studies were motivated by the possible use of these assemblies in solid state DSSCs, where the CP may act as sensitizer or hole-transport agent or both. Finally, beyond mesoporous  $\text{TiO}_2$  layers, similar bottom-up growth was observed for other SC/CP pairs, such as CdS nanorod array, grown on conducting gold film, with remarkably high filling ratios (with PANI, up to 76%) [149] or mesoporous film of  $\text{IrO}_x$  either immobilized on gold substrate, or grown on Ir [150].

Table 6 lists representative examples, where CPs were electrochemically deposited directly on nanostructured SC surfaces. Beyond listing the components, the employed electrochemical method, and some interesting attributes of the hybrid assemblies are also shown. Note that although a range of SCs appear in Table 6, the vast majority of the studies deal with either  $\text{TiO}_2$  or  $\text{ZnO}$ . From a morphology perspective, SCs with various structures were studied, including interconnected configurations, such as nanoporous layers, as well as *arrays* of nanoflakes, nanopillars, nanorods, nanotubes, and nanowires. Such SC architectures are eminently attractive candidates for various applications due to their ordered nanoscale structure, which greatly enhances semiconductor behavior, particularly through improved charge carrier collection due to one-dimensional vectorial  $e^-$  transport [151]. Moreover, through simple adjustment of the parameters of the synthetic procedures (e.g., electrochemical anodization) several key properties of the nanostructures (length, diameter, wall thickness, conductance, etc.) can be tailored toward targeted applications [152,153].

**Table 6**  
Selected examples for direct electrodeposition of CPs on nanostructured SCs.

SC	CP	Polymerization method	SC morphology	Comments	Refs.
Co <sub>3</sub> O <sub>4</sub>	PANI, PEDOT	Galvanostatic	Nanowire/nanoflake array	The morphology of the hybrid was controlled by the polymerization time (coaxial vs. branched)	[154]
Fe <sub>2</sub> O <sub>3</sub> GaAs	PPy PEDOT	Galvanostatic	Nanowire array	Role of monomer concentration was shown	[155]
		Potentiodynamic	Nanopillar array	The effect of dopant anions was demonstrated	[156]
MnO <sub>2</sub>	PEDOT	Potentiostatic	Nanorod array	Coaxial structures were obtained, and the method was compared with other procedures	[157]
	PPy	Potentiostatic	Nanoporous	Deposition on two different oxide morphologies was compared	[158]
NiO	PANI	Potentiodynamic	Nanoflakes	Showed how porosity changes by the PANI formation	[159]
	PEDOT	Potentiodynamic	Nanoflakes	Good description on the benefits of the hybrids morphology	[160,161]
RuO <sub>2</sub>	PANI	Potentiodynamic	Porous	Beneficial effects of the PANI coating on the film stability was shown	[162]
Si	PPy	Galvanostatic	Nanoporous	Pore filling as well as the mechanistic details were studied	[163,164]
TiN	PANI	Galvanostatic	Nanotube array	PANI was deposited both inside, and among the nanotubes	[165]
TiO <sub>2</sub>	PANI	Potentiodynamic	Nanotube array	Inhomogeneous polymer deposition was observed Effect of various synthesis parameters was studied	[166,167]
	PPy	Potentiodynamic	Nanorod array	Core-shell structures were obtained	[154,168]
		Galvanostatic	Nanowire array	Uniform PPy shell was deposited on long TiO <sub>2</sub> nanowires	[169]
		Potentiodynamic	Nanotube array	Sophisticated method to prepare MIP sensors	[170]
		Potential steps	Nanotube array	Carefully designed multiple step protocol. Site selective deposition was also shown	[171,172]
		Potentiostatic	Nanotube array	Morphology of the hybrid was not very uniform	[173]
	PEDOT	Potentiodynamic	Mesoporous	EQCM was used to study the hybrid	[174]
		Potentiostatic	Nanotube array	Role of polymerization potential in controlling nucleation and growth was shown	[175,176]
	PEDOT PHT	Potentiodynamic	Mesoporous	TiO <sub>2</sub> film was deposited onto EQCM crystal	[174]
		Potentiostatic	Nanotube array	Very slow process seemed to result in homogenous deposition	[177]
PCIT PT	Galvanostatic	Mesoporous	Ionic liquid was employed	[178]	
	Potentiostatic	Nanotube array	Thiophenes with different side chains were studied	[179]	
WO <sub>3</sub>	PANI	Potentiodynamic	Mesoporous	Role of electrolyte was shown	[180]
ZnO	PPy	Potentiostatic	Nanorod array	Good discussion on the limiting steps of the polymerization	[181]
		Potentiostatic	Nanorod array	Role of diffusion vs. kinetics was discussed	[181]
	PEDOT	Nanorod array	The thickness of the deposited PANI film was monitored	[182]	
	PANI	Galvanostatic	Nanorod array	Dense array of ZnO was filled to form p/n junction	[183]
	Potentiodynamic	Nanowire array		[183]	
ZnO@CdSe	PHT	Potentiostatic	Nanorod array	ZnO nanorods were sensitized with CdSe prior to polyhexylthiophene (PHT) electrodeposition	[184]
ZnO@CdS	PHT	Potentiostatic	Nanotube array	CdS was deposited on ZnO first	[185]
ZnCoO	PPy	Potentiodynamic	Nanorod array	An example for doped ZnO	[186]

When nanostructured hosts are used as working electrodes, potentiodynamic methods are favored, due to the previously shown favorable attributes. As seen in Table 6, most of the successful approaches involve either dynamic or slow static methods, which are preferred because they afford more time to continuously replenish the solution in monomer during the polymerization, adjacent to the SC surface. In Fig. 10, representative examples of different SC/CP hybrids made by direct electropolymerization are shown. All images share similar attributes: (i)

cloudiness of the images in the hybrid case, and (ii) expansion of the dimensions of the nanoobjects (grain size, rod diameter, and wall-thickness) compared to the parent situation.

We intend to demonstrate the effect of the various synthesis parameters (see Table 2), using a different system to show the role of each parameter separately. First, to understand the role of the monomer concentration, consider the mechanism of polymer formation. As the first step, electrochemical oxidation of the pyrrole monomers leads to

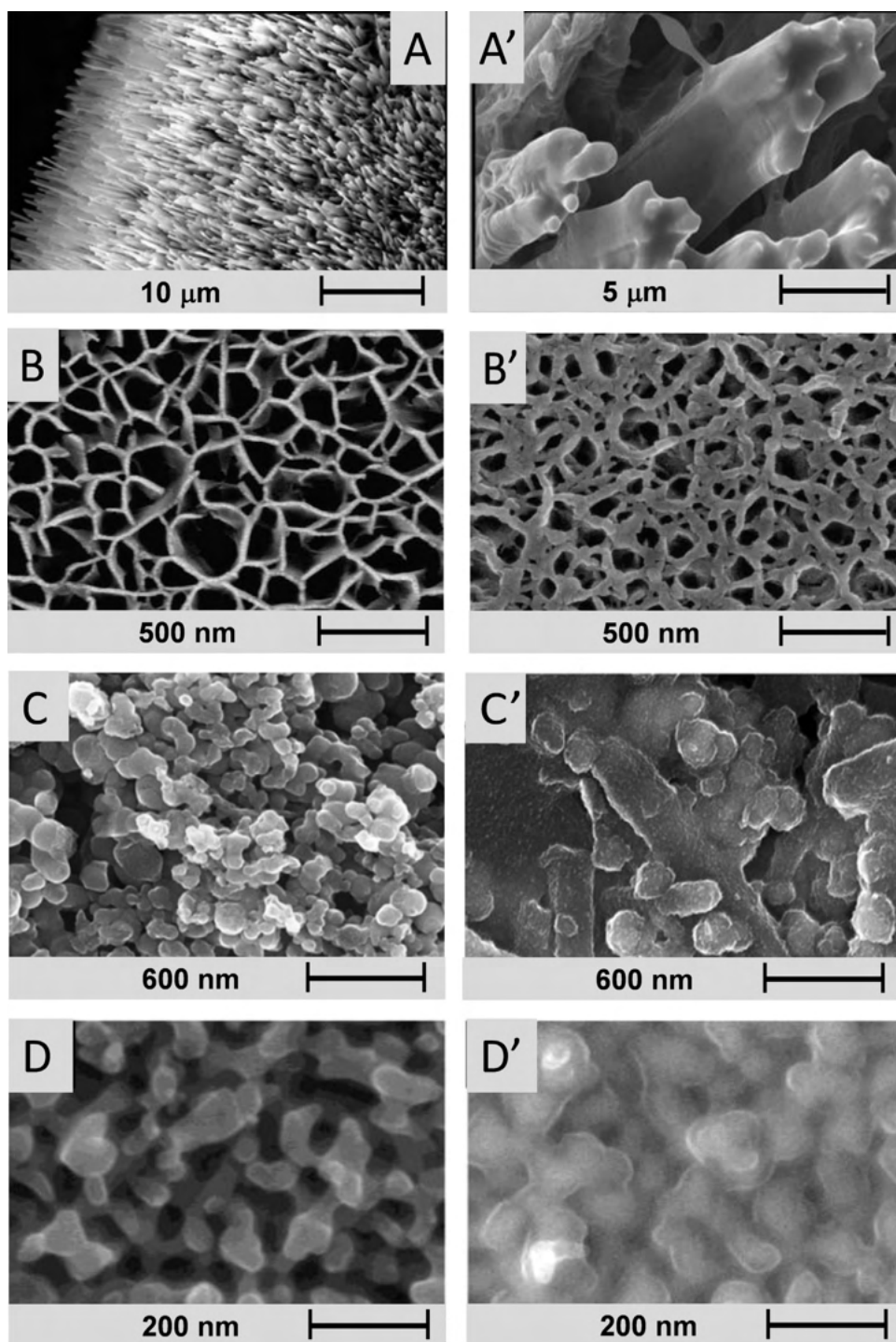


**Fig. 10.** Representative examples of the morphological development of CP based assemblies. The images on the left always show the parent oxide, whereas those on the right show the respective hybrid materials. (A)  $\text{Fe}_2\text{O}_3/\text{PPy}$ , (B)  $\text{NiO}/\text{PEDOT}$ , (C)  $\text{RuO}_2/\text{PANI}$ , (D)  $\text{WO}_3/\text{PANI}$ . Sources (A–D), respectively: [155], Copyrights 2011, Reproduced with permission from the American Chemical Society; [160], Copyrights 2009, Elsevier Ltd.; [162], Copyrights 2011, Springer; [180], Copyrights 2012, the American Chemical Society.

the formation of soluble oligomers around the electrode surface, therefore the solution inside the SC nanostructure gets saturated (note that insoluble oligomers are also forming). Subsequently, nucleation and growth begins first at

favorable sites in the nanostructure, then possibly everywhere. As the next step, solid-state growth of the polymer continues and the forming polymer gradually fills the SC structure.



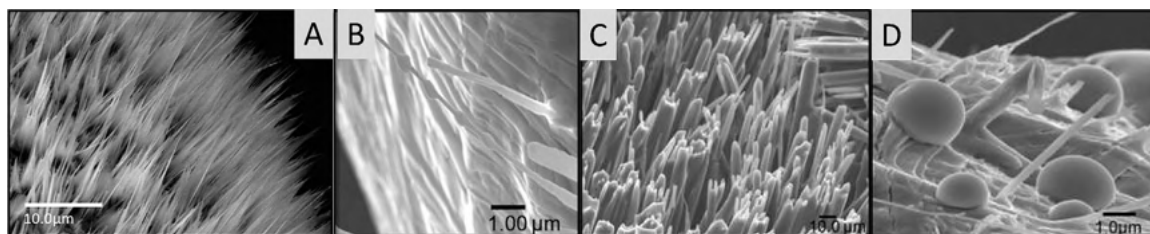


**Fig. 11.** Morphology of (A) the bare  $\text{Fe}_2\text{O}_3$  nanowires and the (B–D)  $\text{Fe}_2\text{O}_3/\text{PPy}$  nanostructures obtained by electrodeposition at identical current densities but with different monomer concentration, (B) 0.01 M, (C) 0.05 M, (D) 0.5 M. Note that the images are at different magnification for better visualization. [155], Copyright 2011, Reproduced with permission from the American Chemical Society.

As nicely demonstrated for the example of  $\text{Fe}_2\text{O}_3$  nanowires and PPy, at low monomer concentrations ( $\sim 10$  mM), polymerization is limited by the mass transport of the monomer and therefore PPy is deposited only at some favorable spots of the nanowires (such as tapered tips and kinks). If the monomer concentration is increased to medium values ( $\sim 50$  mM), polymer deposition results in a uniform, conformal coating on the individual nanowires. Finally, at rather high concentrations of pyrrole ( $\sim 500$  mM), fast and uncontrolled electropolymerization leads not only to extensive aggregation of polymer-coated nanowires, but also to the formation of large globular PPy particles attached to the nanowire surface (Fig. 11) [155].

The competition between diffusion vs. kinetics can be visualized for the example of electrodepositing PEDOT on ZnO nanowires [181]. In a very simple and demonstrative set of experiments, PEDOT was electrodeposited potentiostatically in one step and in 9 steps employing otherwise identical conditions (e.g., polymerization potential and overall charge density). The difference is striking, while in the one-step experiment PEDOT was preferably formed on the top of the ZnO nanowires, in the second case, homogenous deposition can be witnessed along the nanowires. Very similar result (namely having the polymer mostly at the top of the nanowires) was obtained even with shorter ZnO nanowires, while fast growth of the polymer was provoked by employing higher deposition currents. Importantly, in both diffusion-limited cases, mushroom-like morphologies were obtained, instead of the homogenous coating observed for the kinetically limited experiments (Fig. 12). Similar conclusions have been drawn when diffusion limitation occurred because of using a static polymerization method instead of a dynamic one [187].

The nature of the electrolyte may also play a key role in the electropolymerization procedure. The  $\text{WO}_3/\text{PANI}$  hybrid system is a good example, since uniform deposition of PANI on nanoporous  $\text{WO}_3$  was accomplished by recognizing the similarity in their ion-exchange properties [180]. Both components of the hybrid system are electron and proton conductors, resulting in reasonable  $\text{WO}_3$  electroactivity in acidic solutions even in the positive potential regime, required for electropolymerization of PANI. The enhanced electroactivity of  $\text{WO}_3$  was rationalized by the formation of tungsten-bronze phases ( $\text{H}_x\text{WO}_3$ ), assisted by  $\text{H}^+$  uptake/release as charge compensation during the ( $\text{W}^{6+}/\text{W}^{5+}$ ) redox process. Note that electropolymerization of pyrrole in a pH-neutral medium, under otherwise

identical circumstances (same  $\text{WO}_3$  substrate), was hampered by the low electroactivity of the SC matrix [188].

Finally, the nature of the solvent also has a substantial effect on the formation of the hybrid material. Solvent molecules with higher polarity are considered to interact more closely with polar SC surfaces (e.g., ZnO or  $\text{TiO}_2$ ), which hampers adsorption of the monomer molecules (thus impeding the polymerization). Furthermore, the solubility of the forming oligomers also varies in different solvents, therefore saturation (and consequent deposition on the SC) occurs in a different manner [189]. The polarity of the solvent not only affects wetting of the SC nanostructure and solubility of the oligomers, but also limits the solubility of certain monomers. Employing micellar solutions is an elegant way to overcome solubility issues, because it also facilitates transport of the monomers inside the SC host matrix [190].

Hybrids based on  $\text{TiO}_2$  nanotube arrays (NTA) obtained by anodization deserve special consideration for multiple reasons. Notably,  $\text{TiO}_2$  has fairly high resistance which hinders direct electrodeposition of CPs. In addition, there is an insulating compact barrier layer below the nanotubes, unlike in the examples presented above, where  $\text{TiO}_2$  nanoparticles are immobilized directly on the conducting substrate (ITO). Despite this fact, there are a considerable number of papers published on the electrodeposition of different CPs (most importantly PPy and PANI) on  $\text{TiO}_2$  NTAs. Most of these examples, however, suffer from major drawbacks such as uneven distribution of the polymer, and consequently the small area of the forming p/n junction [166,167,173,177,179,191].

Recent studies demonstrated, however, that homogeneous deposition of PPy onto  $\text{TiO}_2$  NTA can be achieved by employing a carefully designed multiple potential step protocol. Each step consisted of a short anodic pulse of very high current density ( $+26$  mA/cm<sup>2</sup>) to ensure high nucleation density, followed by a relatively long rest period to let the solution in the NTA refill with both monomer and the electrolyte by their diffusion, and to let possible side products diffuse away. A very short cathodic step ( $-26$  mA/cm<sup>2</sup>) was introduced to prevent change of the local pH. Note that the anodic step is short enough (10 ms) to avoid 3-dimensional growth of PPy after the nucleation step [171,172,192]. Employing high current densities (consequently high potentials), however, involves the risk of overoxidizing the forming polymer. Overoxidation means irreversible oxidation of the polymer, introducing oxygen-containing functional groups to the polymeric chains.

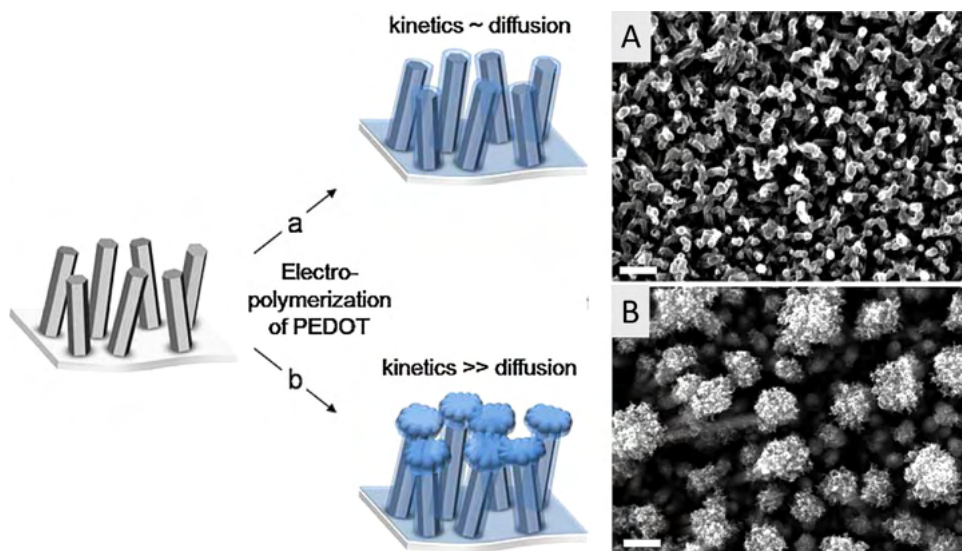


**Fig. 12.** Schematic and SEM illustration of the competition of kinetics and diffusion, for the example of PEDOT electropolymerization on ZnO nanowires. [181], Copyright 2010, Adapted with permission from Wiley.

Formation of such moieties interrupts conjugation of the polymer backbone, thus hampering its applicability in most of the considered applications due to decreased electroactivity [193,194].

The role of the template structure was also brought out by electrosynthesizing PPy on various TiO<sub>2</sub> NTA templates with different geometrical attributes. As depicted in Fig. 13, polymer deposition can occur *inside* the nanotubes, in the space *among* the tubes, and on top of the NTA. In principle, if the space between the tube walls is reasonably large, electropolymerization leads to filling the voids between the tubes. This behavior was rationalized by the nanoscale wetting behavior of NTA, which showed preferential wetting of the space between the nanotubes. By tailoring the properties of the TiO<sub>2</sub> NTA, PPy can be deposited even inside the nanotubes, if the space between the nanotubes is sufficiently reduced (this can be done by decreasing the water content of the anodization medium) and wetting inside the tubes is activated by thermal treatment [171,172].

Similarly, PEDOT was electrografted onto TiO<sub>2</sub> NTA by a simple but carefully optimized two-step potentiostatic growth protocol in acetonitrile-containing supporting electrolyte [195]. During a short pre-polymerization period, a relatively high constant potential ( $E = 1.35$  V, vs. Ag/AgCl) was applied to induce homogeneous oligomer formation. At the end of this period, electrodeposition was continued, without interrupting the current, at a lower potential (1.20 V) for longer periods. The morphology of the hybrid assembly was similar to that shown before for the TiO<sub>2</sub>/PPy system (i.e., polymer is dominantly deposited in between the tubes). More recently it has been shown that site selective deposition of the PEDOT can be controlled by changing the polymerization parameters [175,176]. At relatively low potential, polymerization led to deposition of PEDOT inside the tubes, as well as into the void spaces. In contrast, at higher potentials, polymerization occurs in the spaces between the nanotubes *only*. Such variant

behavior was rationalized by the differences in nucleation density and rate of polymerization, and a model of 3D-instantaneous and 3D-progressive nucleation and growth was proposed [175].

### 3.2.2. Photoelectrochemical polymerization

In the case of some oxides (including TiO<sub>2</sub>), electrodeposition is often hampered by the low conductivity of the inorganic matrix; therefore high potentials must be applied, consequently the electrogenerated polymer is prone to overoxidation. In the quest to overcome this issue, it was recognized soon that such challenge related to the semiconducting nature of an electrode material can be turned to an opportunity. Namely, light has at least two beneficial effects with respect to the deposition of CPs on SCs. First, by illuminating the electrode (employing bandgap irradiation) the conductivity of the SC increases (photoconductivity). In addition, photogenerated holes can directly oxidize the monomer and initiate polymerization. Since this type of photoelectrochemical polymerization of electroactive monomers has not been reviewed yet, we briefly summarize the history and evolution of this approach. Note that photo-initiated polymerization of other, non electron-conducting polymers has been reviewed recently [196].

Photoelectrochemical polymerization dates back to the early 1980s when flat Si [197–199] and GaAs [200] surfaces were covered by PPy employing UV illumination and constant bias potential. Later the concept was extended to other SCs and CPs; thus assemblies such as CdS/PPy [201], CdS/PMT [202], GaAs/PMT [203,204], GaAs/PVP [205], and CuInS<sub>2</sub>/PPy [206] have been realized. Subsequently hybrids based on *flat* oxide SCs, initially TiO<sub>2</sub>/PPy [207,208], ZnO/PPy [209], and more recently Nb<sub>2</sub>O<sub>5</sub> [210], Ta<sub>2</sub>O<sub>5</sub> [211], WO<sub>3</sub> [212] based composites were also obtained.

In these methods, photoelectrochemical polymerization occurs at the irradiated SC/electrolyte interface. When

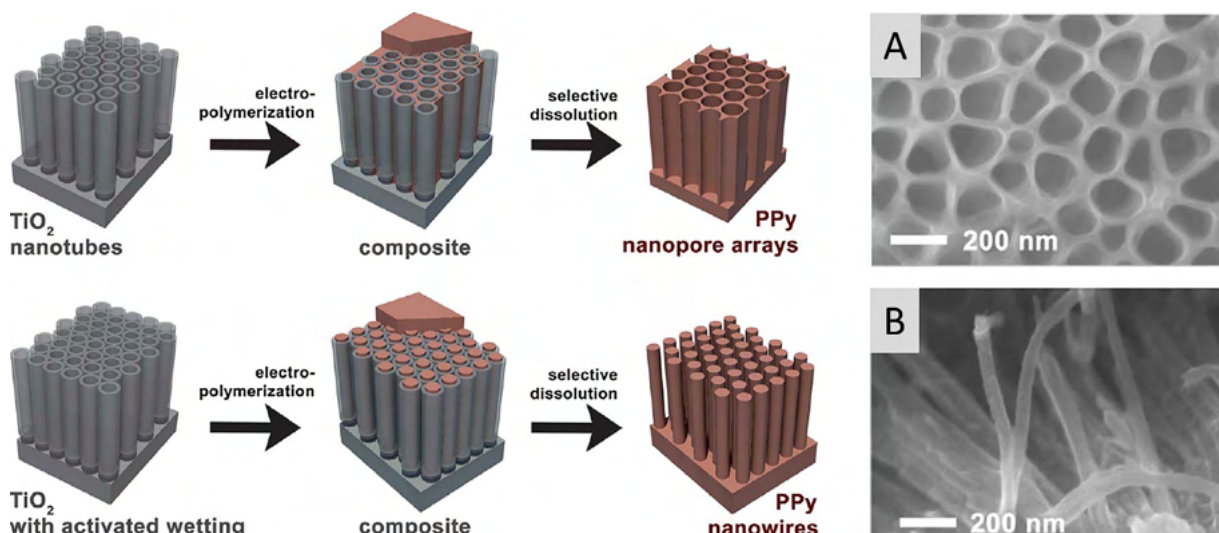


**Fig. 13.** Illustration of site selective electrodeposition of PPy onto TiO<sub>2</sub> NTA with different geometrical parameters. [172], Copyright 2011, Adapted with permission from the Royal Society of Chemistry.

light is incident on the SC electrode, electrons from the valence band (VB) are promoted to the conduction band (CB). These electrons are drained into the external circuit by the applied external bias potential, while the photo-generated holes react with species in the solution (solvent, electrolyte anion, or monomer). The polymerization is successful if this particular species is the monomer, which gets oxidized and the polymerization starts (Fig. 14B). Then, the radical cation reacts with another radical cation (or monomer) to form dimers which can react further, either with a monomer- or oligomer radical cation and the polymer is formed. Therefore, it was recognized soon that band edge positions of the SC, as well as the oxidation potential of the species in the solution are of prime importance for the success of this method. The different process variants, the role photoexcitation, external bias potential, and that of using  $e^-$  scavengers, are shown in Fig. 14.

As for the role of the bias potential, note that the applied potential values are not high enough to *electrochemically oxidize* the monomer, its role is to suppress the recombination of the photogenerated charge carriers. Another parameter to consider is that some of the SCs are prone to photocorrosion under anodic conditions, which not only

leads to possible degradation of the electrode, but also lowers the efficiency of the polymerization, because only a fraction of the photogenerated holes can now oxidize the monomer. For example in the case of ZnO, much more polymer can be generated with the same charge density by electrochemical- than by photoelectrochemical polymerization [209]. Careful adjustment of the solution pH and application of additional hole-scavengers may help to suppress photocorrosion in such cases.

After the early studies on flat electrode surfaces, the concept was extended to particulate systems, more precisely to colloidal or nanoparticulate TiO<sub>2</sub> slurries [213,214]. In such configurations the (nano)particles are dispersed in the solution of the monomer, and possibly supporting electrolyte. Light is incident on the slurry under continuous stirring, and a thin polymeric film deposits on the surface of the NPs. Note that in these experiments no external bias potential is applied, the only driving force for charge separation is the hole scavenging property of the monomer (Fig. 14A). Sacrificial electron acceptors may also be used to enhance the effectiveness of charge separation, thus the solution is usually saturated with O<sub>2</sub>. As a result of polymerization, coverage (only a few nm) of a thin film is formed

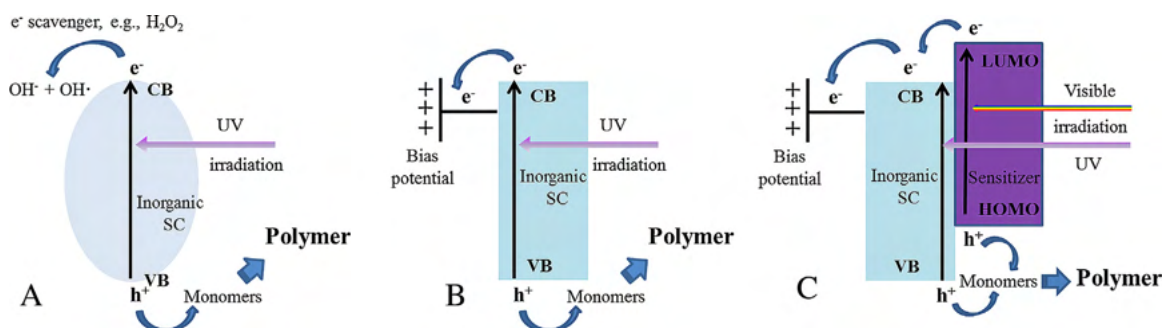


**Fig. 14.** Schematic illustration of (A) the photocatalytic, (B and C) photoelectrochemical polymerization of a monomer on bare and dye-sensitized semiconductor electrodes, respectively.

on the NP surface. The growth of the polymer is finally terminated by both electrical and optical shielding of the deposited CP. Additional studies demonstrated the use of this method with other SCs such as CdS, CdTe [215], and (CdSe@ZnS) [216] and polymers (PEDOT) [217] as well as yielded further mechanistic details [218].

In a comparison of photoelectrochemically generated polymers with their electrochemically prepared counterparts, photoelectrochemical polymerization was found to be less dependent on the nature of the electrolyte, both in terms of the morphology and the conductivity of the formed polymer [214]. This latter was inferior compared to its electrochemically polymerized counterpart, a conclusion in accordance with earlier studies [209]. The morphology also showed significant differences, namely a more compact CP film was observed in the case of photoelectrochemical deposition, presumably due to the considerably slower polymerization procedure.

After these pioneering studies, this versatile method was somewhat forgotten, and the new wave of research was triggered by a demand for solid-state hole transporters in DSSCs, which arose after the discovery of mesoscopic DSSCs in 1991 [148]. In such solar cells, a CP can act as both sensitizer (electron donor) and even more importantly as a solid-state hole transporter [6,219,220]. From a polymerization perspective, the benefits of the previously described geometries are merged in this configuration, namely the large surface area of the nanoparticulate film, and electrochemical control with over the polymerization. In this vein, TiO<sub>2</sub>/PPy [221–223], TiO<sub>2</sub>/PEDOT [224,225], TiO<sub>2</sub>/PT [15,226], and ZnO/PMT [227] hybrids were realized. In some cases, carboxyl group-containing thiophene-derivatives were initially grafted onto the TiO<sub>2</sub> surface and subsequent polymer growth was initiated through these moieties. Therefore, better electrical contact is envisioned between the organic and inorganic components. Interestingly, in some of the cases, polymer formation was witnessed even when UV-light was filtered out, consequently the SC component cannot be excited. In these cases, the precursor of the polymer (e.g., a dimer or oligomer) linked to the SC surface is photoexcited, and while the photogenerated e<sup>-</sup> is transferred to the SC, the oxidized precursor reacts with a further monomer/dimer [226,228].

These observations bring up the next point, a more interesting variant of this method, namely when the TiO<sub>2</sub> NPs are already dye-sensitized before formation of the CP (Fig. 14C). In such a procedure, photoexcitation of TiO<sub>2</sub> and the anchored dye may occur simultaneously (under white light irradiation), or in contrast, the components can be selectively excited by irradiating with illumination of properly selected wavelengths. In practice, in most of the studies, the UV component is filtered out to avoid excitation of the SC, and only the holes, generated by the photoexcited dye are exploited (Fig. 14C). This trick not only ensures intimate contact between the photosensitizer (dye) and the hole transporter (polymer), but also avoids photodegradation of dye by the holes from TiO<sub>2</sub>, which have high oxidation power due to its valence band position. This is a real threat, realizing that a prominent application of such SCs is the degradation of organic dyes [229]. Studies, however,

have indicated that the dye fortuitously does not decompose during photoelectrochemical polymerization [230].

In the first successful trial within this group, polypyrrole was photoelectrochemically generated onto mesoporous TiO<sub>2</sub> matrix on which a Ru-containing dye was immobilized by chemical bonding through its carboxyl function [231]. As a next step, a novel ruthenium dye was designed bearing pyrrole-, or thiophene functions as well as dicarboxylic acid groups as ligands. Therefore the polymerization can directly start at the dye molecule itself, bringing the dye and the hole-transporter polymer into close molecular contact. Such close contact was proven to be beneficial in terms of photoelectrochemical behavior, compared to a counterpart using a dye without monomeric moieties [232–236].

More recent efforts almost exclusively focus on PEDOT, because it possesses many favorable attributes such as high chemical stability (especially in the oxidized or doped state), small band gap energy, and good optical transparency in the electronically conducting state. For this polymer, however, the problem with the higher oxidation potential of the EDOT monomer (1.0 V vs. Ag/AgCl) means that it cannot be oxidized by the ruthenium dye (HOMO potential: 0.59 V vs. Ag/AgCl) [237]. Therefore, use of bis-EDOT [112,238] or its derivatives [239], having a lower oxidation potential (0.4 V vs. Ag/AgCl) becomes a better option.

The critical role of the dye was brought out when photoelectrochemical polymerization of bis-EDOT was carried out with two different Ru-dyes but otherwise identical circumstances [240]. Under potentiostatic conditions, the D149-sensitized TiO<sub>2</sub> layer gave a higher polymerization current than the Z907-sensitized TiO<sub>2</sub> layer. Such a difference can be rooted in the more effective charge transfer from the dye molecule to the monomer and to TiO<sub>2</sub>. Importantly, the nature of the dye has a crucial influence on the polymerization procedure, consequently it affects the properties of the TiO<sub>2</sub>/dye/polymer interface as well as penetration of the polymer into the mesoporous TiO<sub>2</sub> layer (pore filling ratio) [240].

Finally, recent progress was achieved in photoelectrochemical polymerization on *organized* SC nanostructures. In this vein, deposition of PPy and PANI on nanoporous WO<sub>3</sub> and TiO<sub>2</sub> NTA was successfully carried out [188,241]. The most important feature of this approach is that it results in homogenous deposition of polymer, which covers the entire surface of the nanostructured SC, as can be seen both from the expansion of wall thickness and from the disappearance of nanoscopic voids in between the tubes (Fig. 15). On the other hand, the hybrid sample obtained in the absence of illumination exhibits a morphology similar to that seen in many of the papers employing general electrochemical methods in the dark, namely that the CP (in this case PANI) is randomly deposited on the substrate, even forming globular particles on the top of the TiO<sub>2</sub> NTA (Fig. 15). Importantly, such an alteration in the morphology results in a huge difference in the contact area of the organic/inorganic junction, which is practically equal to the surface area of the inorganic semiconductor matrix in the case of the illuminated sample, whereas it is almost negligible the its counterpart synthesized in the dark.

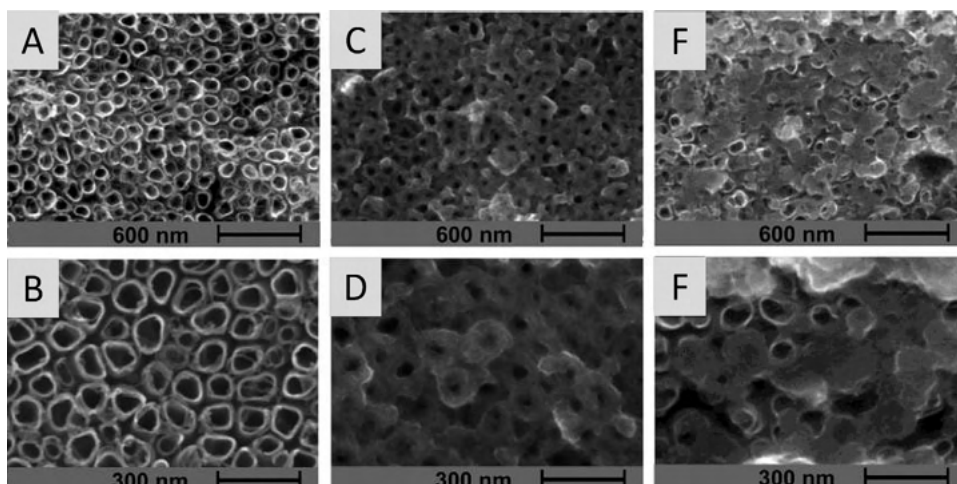


**Fig. 15.** SEM images of (A and B) bare TiO<sub>2</sub> NTA anodized at  $E=20\text{V}$ ; (C and D) of the corresponding TiO<sub>2</sub>/PANI hybrid samples synthesized using 5 potentiodynamic polymerization cycles with illumination, at 50k and 100k magnification; and (E and F) without that illumination. [188], Copyright 2012, Reproduced with permission from the American Chemical Society.

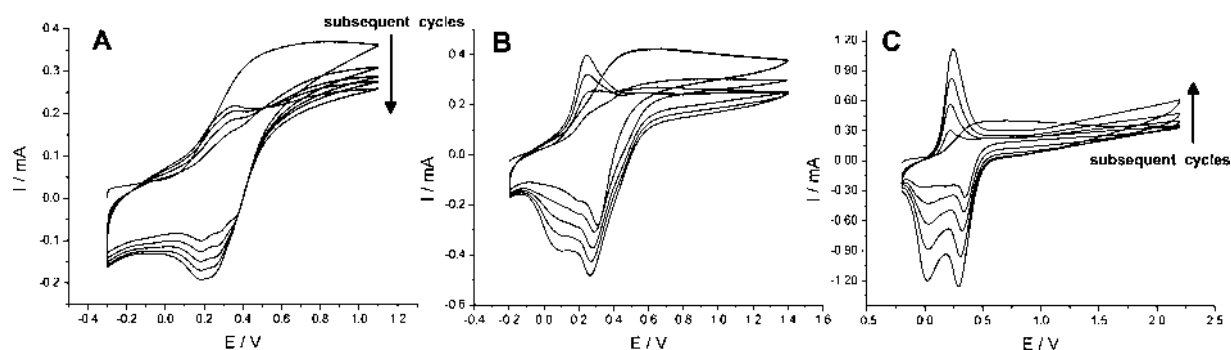


**Fig. 16.** Effect of the positive end expansion of the potential window, on the polymerization of aniline on TiO<sub>2</sub> NTA under illumination (5 cycles). [188], Copyright 2012, Reproduced with permission from the American Chemical Society.

To rationalize the remarkable difference shown above, the contribution of electrochemical and photoelectrochemical polymerization to the formation of CP was separated, and the multiple role of external bias potential was demonstrated [188,241]. To this end, potentiodynamic polymerization cycles were run to three different potential values (1.1, 1.45 and 2.2 V), while other parameters remained unchanged (Fig. 16). Note that in the first case

no direct electropolymerization occurs, whereas its gradually increasing contribution can be revealed as the potential window is extended. The increasing electroactivity can be deduced from both the increased current densities and the more expressed shape of the voltammograms. Further experiments showed the complexity of the current response under illumination, from which the mechanism of the deposition was clarified (Fig. 17). As a first step, the



**Fig. 17.** Illustration of the two steps of the photo-electrodeposition of PANI on TiO<sub>2</sub> NTA. [188], Copyright 2012, Reproduced with permission from the American Chemical Society.

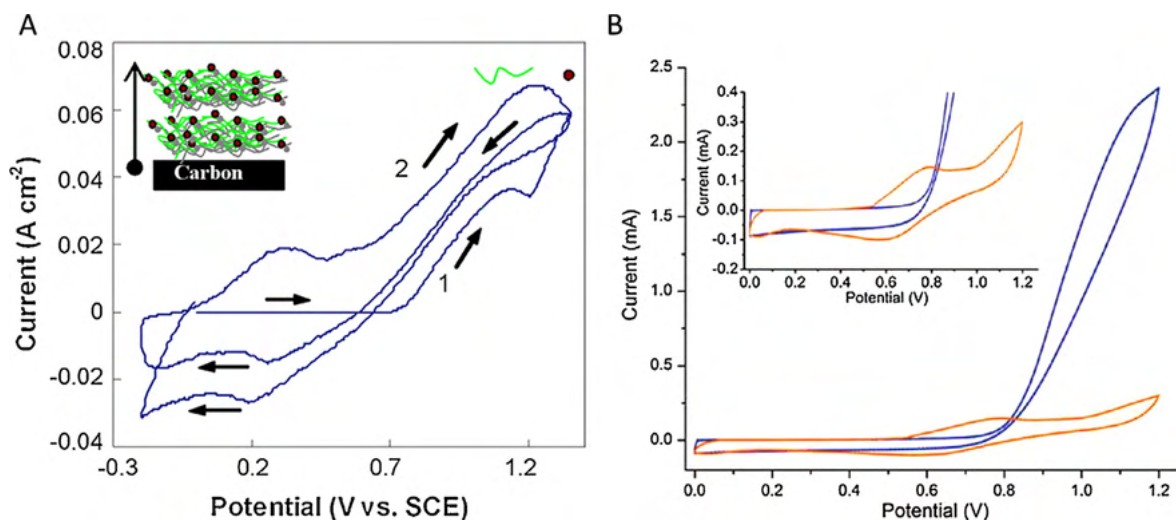


**Fig. 18.** Examples for electrochemical co-deposition of CP/SC hybrids, by potentiodynamic cycling. (A) MnO<sub>2</sub>/PANI on carbon substrate. (B) MnO<sub>2</sub>/PEDOT in alumina template. Sources, respectively: [243], Copyright 2008, Reproduced, with permission from Elsevier Ltd; [247], Copyright 2011, Reproduced, with permission from the American Chemical Society.

aniline monomer is oxidized by photogenerated holes on the SC surface. Here the external bias potential facilitates the separation of the photogenerated excitons (by draining the photoelectrons to the back contact); hence more holes can react with the aniline monomer and oligomer to facilitate polymerization. When the potential is increased, at a certain threshold value, *electrochemical* growth of the polymer starts to take place. Note, however, that this threshold potential is lower than in the dark, because under illumination oligomer/polymer formation already took place at lower potentials due to photoelectrochemical deposition, thus obviating the need for electrochemical oxidation of the aniline monomer, which requires notably higher potentials. This two-step procedure is illustrated in Fig. 17.

### 3.3. Other miscellaneous approaches

#### 3.3.1. Electrochemical co-deposition

In this sub-section we show examples where the precursor of each constituent is present in the initial polymerization solution. Subsequently, both components, and therefore the hybrid itself is electrogenerated in the same process in one single step. This approach has been exploited to obtain hybrids with PPy, PEDOT, and most importantly PANI; containing Fe<sub>2</sub>O<sub>3</sub> [242], MnO<sub>2</sub> [243–248], MoO<sub>3</sub> [249], NiO<sub>x</sub> [250–252], and WO<sub>3</sub> [253,254]. The main advantage of this approach is its simplicity and time efficiency. Also note that it is typically applied for oxide SCs, which can be anodically generated from their precursors in aqueous solutions. The drawback on the other hand, is limited control over simultaneously occurring processes, which results in uncontrolled size and size distribution of the SC particles, and poorly defined morphology of the hybrid.

Potentiodynamic cycling is useful to identify the potential values where polymerization and oxide formation take place. The example of PANI/MnO<sub>2</sub> is shown in Fig. 18A,

where during the positive potential scan, electropolymerization of aniline occurs first (from 0.7 V vs. SCE during the first scan). Upon further increase of potential up to 1.35 V vs. SCE, MnO<sub>2</sub> is electrogenerated on the previously formed PANI according to the following reaction:  $\text{Mn}^{2+} + 2\text{H}_2\text{O} \rightarrow \text{MnO}_2 + 4\text{H}^+ + 2\text{e}^-$ . This procedure is repeated during subsequent cycles, leading to the formation of the hybrid layer on the electrode surface. Importantly, the mechanistic picture gets more complex when the potential regimes for formation of the constituents overlap, as can be seen for the example of MnO<sub>2</sub>/PEDOT hybrid (Fig. 18B). Under such circumstances, careful control of the electrodeposition potential is indeed required. Note that for such a system, very small changes in the electrochemical bias potential can favor one process over the other. In this manner, the ratio of the components within the electrogenerated hybrid material can be tuned [247]. Finally, control of pH is important because it has to be optimal for polymerization, while at the same time, formation of the SC particles should not be hindered (for example by hydroxide formation).

#### 3.3.2. Deposition of SCs on or inside the CP layer

As opposed to most of the previously described approaches, the CP component can also be synthesized as a first step, and subsequently hybridized with the inorganic component. Such composite formation can be facilitated either by the electroactivity of the CP film or by that of the underlying supporting electrode. In the first case the SC is generated inside the CP, assisted by its electrochemical transformation. In the second case, the inorganic component grows from the substrate and fills the pores of the CP (note that this procedure mirrors that where the CP fills the nanoparticulate TiO<sub>2</sub> matrix, see Section 3.2.1). This second method is especially attractive for SCs which are not stable at the highly positive potentials where CPs are usually electrosynthesized.

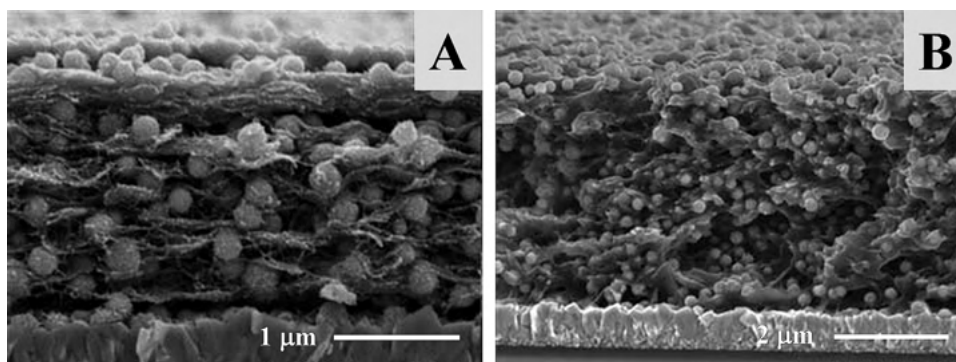


**Fig. 19.** Electrodeposited CdS particles inside the PEDOT host matrix from an ionic liquid solution (A) without, (B) with a pre-wetting step. [257], Copyright 2012, Reproduced with permission from the Royal Society of Chemistry.

As mentioned earlier, CdS is prone to both electrochemical and photocorrosion. Therefore its formation within a previously deposited CP film is favored vs. the previously shown approaches. In this manner, the cation exchange behavior of a PPy/PSS layer was exploited first. Having a large immobile polyion ( $\text{PSS}^-$ ) as dopant,  $\text{Cd}^{2+}$  ions can be incorporated in the polymer upon cathodic polarization. Note that by applying a carefully selected potential, only the polymer is reduced (and not the  $\text{Cd}^{2+}$  ions), and therefore the metal cations can be incorporated to compensate the negative charges of the built-in macroanions. Subsequently, addition of bisulfide ions ( $\text{HS}^-$ ) led to the formation of CdS particles at various sites throughout the PPy matrix [255].

CdS formation was achieved in the opposite order as well, namely exposing the bisulfide ion-doped PPy to  $\text{Cd}^{2+}$  containing solutions [255]. Alternatively, Cd was electrodeposited onto poly(3,4-dioctyloxythiophene) (PDOT) and subsequently chemically transformed into CdS [256]. Finally, direct electrodeposition of CdS from its precursors (cadmium acetate and sodium thiosulfate) in an ionic liquid was also achieved, under galvanostatic conditions at elevated temperatures ( $120^\circ\text{C}$ ). The synthesis resulted in relatively large-sized CdS particles throughout the whole PEDOT host matrix (Fig. 19) [257].

Cuprous oxide ( $\text{Cu}_2\text{O}$ ) is a good example of an oxide in which the metal can have different oxidation states. Importantly, electropolymerization is hampered on this SC, since the formation of  $\text{CuO}$  (cupric oxide) is favored under oxidative conditions. Therefore the opposite strategy was followed:  $\text{Cu}_2\text{O}$  was cathodically electrodeposited in the porous CP layer. At the same time, however, under cathodic polarization most CPs are in their neutral, insulating state, thus the growth of the SC occurs from the substrate electrode, and the forming oxide fills the pores of the CP. By careful adjustment of the deposition potential, the formation of different Cu-species (Cu,  $\text{Cu}_2\text{O}$ ,  $\text{CuO}$ ) can be tuned [258–260] as well as hybrids with various morphologies can be obtained [261].

Oppositely, when SCs are electrogenerated anodically, the electroactivity of the CP template can be exploited, as they are conductive in their oxidized (doped) state. For example electrodeposition of  $\text{SnO}_2$  nanocrystals on PPy

nanowire was carried out under galvanostatic conditions ( $\text{Sn}^{2+} - 2e^- \rightarrow \text{Sn}^{4+} + 4\text{OH}^- \rightarrow \text{Sn}(\text{OH})_4 \rightarrow \text{SnO}_2 + \text{H}_2\text{O}$ ). The such formed 3D nanostructured  $\text{SnO}_2@\text{PPy}$  composite exhibits a rough surface indicating that the PPy nanowires are covered with  $\text{SnO}_2$  nanoparticles [262].

Similarly,  $\text{RuO}_2$  can be oxidatively deposited from solutions containing  $\text{Ru}^{3+}$  ions.  $\text{RuO}_2/\text{PEDOT}$  composite nanotubes were electrogenerated using porous alumina template [263]. As the first step, EDOT was electropolymerized and PEDOT nanotubes were formed. Subsequently,  $\text{RuO}_2$  was formed inside the nanotubes through potential cycling; more precisely,  $\text{RuO}_2$  was electrodeposited on the inner walls of the polymeric tubes [263].  $\text{RuO}_2$  electrodeposition was achieved on PANI films as well, both under potentiodynamic [264] and galvanostatic [265] conditions. In the same vein,  $\text{MnO}_2$  was hybridized with PANI [266], PEDOT [267], PMT [268] and even PEDOT-PANI assemblies [269].

The previous approach can be followed by subsequent deposition of another polymeric layer, obtaining a sandwich structure [270]. Through tuning the deposition conditions, the thickness of each layer, and consequently the properties of the hybrid assembly can be controlled. Furthermore, even sequential deposition can be achieved, by subsequently repeating the deposition steps for the SC and the polymer [271]. If a template is also used, then nanostructures containing multiple heterojunctions can be obtained (Fig. 20A and B) [247]. Such a multilayer formation can be also seen on the example of a graphene/PEDOT system, where graphene layers were introduced between PEDOT layers of different thickness (Fig. 20C) [272].

An interesting and also promising variant of this method is when both the CP and graphene are deposited on the electrode surface at the anodic and cathodic ends of the potentiodynamic cycles respectively. This approach is enabled by the fact that graphene oxide (GO) can be reduced at negative potentials, whereas oxidative polymerization of aniline takes place in the anodic regime. This separation of the two processes allows layer-by-layer formation of the hybrid assembly. Furthermore, just by switching the direction of the potentiodynamic cycle, the order of the layers can be controlled [273].

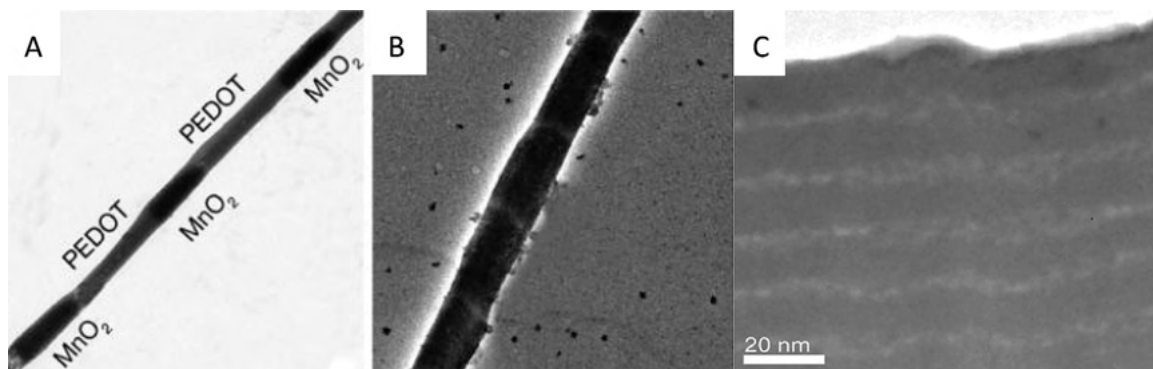


**Fig. 20.** Formation of multiple heterojunctions by sequential electrodeposition. (A and B) MnO<sub>2</sub>/PEDOT, (C) graphene/PEDOT.

Source: (A and B) [247] Copyright 2011, Adapted with permission from the American Chemical Society; (C) [272], Copyright 2012, Adapted with permission from the Royal Society of Chemistry.

#### 4. Selected applications of electrochemically assembled CP/SC hybrids

##### 4.1. Solar energy harvesting (solar and photoelectrochemical cells)

Finding alternative earth abundant solar cell materials beyond Si has been at the leading edge of research for many years. There are three distinctly different solar cell configurations in which assemblies of organic and inorganic SCs can be deployed (Fig. 21). First, the high absorption coefficient of CPs makes them possible candidates to be used in a combination with n-type inorganic SCs (typically TiO<sub>2</sub>, ZnO, and CdSe) to form simple and inexpensive hybrid organic–inorganic solar cells [274–276]. In such arrangements, the p-type semiconductor polymer acts both as an electron donor and as a hole transporter. The theoretically achievable efficiencies are predicted to be as high as 12% [275], but until now the performances obtained for real cells remain well below these expectations (1–4%). It is also worth noting that for the preparation of materials in this group, chemical methods dominate over electrochemical processes, most importantly due to the larger variety of possible polymers that can be combined with the SC NPs [276].

In the second case (Fig. 21B), CPs are employed as solid-state hole transporter materials in DSSCs [219,277]. This is an attractive approach, because by replacing the homogeneous redox couple (I<sup>-</sup>/I<sub>3</sub><sup>-</sup>) by a solid-state hole conductor,

it is possible to avoid use of the liquid electrolyte. This is indeed important, since many of the drawbacks of conventional DSSCs, such as leakage, low thermal stability, and corrosion of the counterelectrode are related to the presence of the liquid electrolyte. What is equally important, a steep rise in the power conversion efficiencies was witnessed during the last decade for this type of solar cell. Note that while the first trials resulted in efficiencies only about 0.1% [231], the latest cells exhibit 7.1% [278], which is in the range of values obtained with molecular hole transporters (7.2% with Spiro-OmeMAD [279]). Molecular dyes can be either the regularly employed Ru-containing benchmark dyes (N3 or Z907) or other, more environmentally friendly candidates (porphyrins). The rapid rise depicted in Fig. 22 is predominantly rooted in the development of photoelectrochemical polymerization techniques, achieving careful interfacial engineering in the hybrid materials.

Most recently, quantum-dot [280,281] and perovskite sensitized solar cells [282,283] have come to the forefront of research. Impressive power conversion efficiencies were obtained (over 15%) using perovskite sensitizer and solid state hole-transporter [282,283]. Although CPs were proven to be efficient in this configuration as well [220,284], their use has been restricted to the infiltration of the polymer, and no in situ electrochemical or photoelectrochemical polymerization methods have been employed yet. Such studies are in progress in our research groups, with particular focus on the structure/property relationships of oxide/perovskite/CP interfaces.

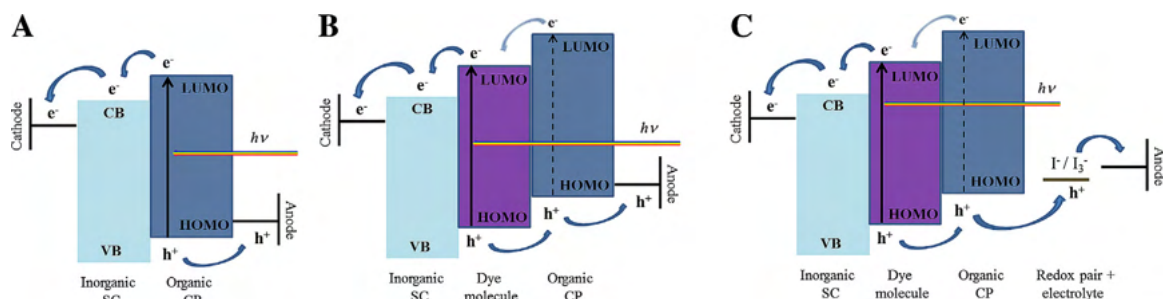


**Fig. 21.** Illustration of different solar cell configurations containing inorganic SCs and CPs.



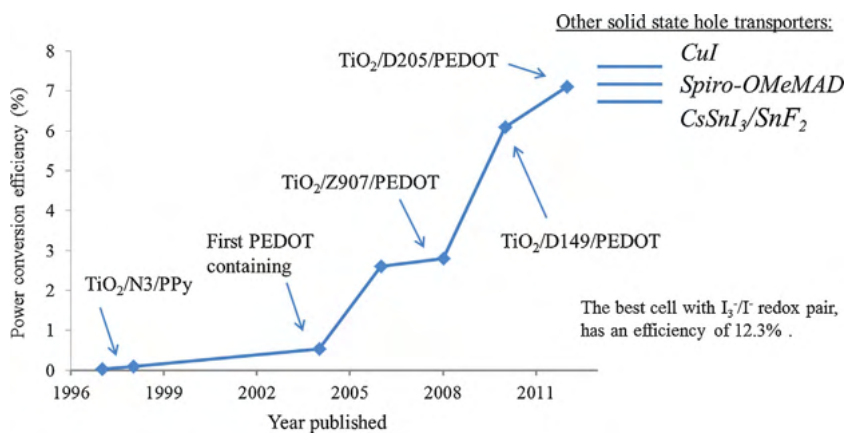


**Fig. 22.** Development of power conversion efficiencies in solid-state DSSCs, using CP as a hole transporter. Highest efficiencies obtained with solid-state inorganic as well as molecular hole transporters are shown as benchmarks.

In some cases, both polymer and the redox electrolyte are present in the cell (Fig. 21C), and in such configurations CP acts as a surface modifier to enhance interfacial charge transfer, and thus suppress recombination [184,185,285,286]. Finally, electrodeposited CNT/CP and graphene/CP hybrids are also used as the counterelectrode in DSSCs [125,287–289]. This research is fueled by the high price of Pt, and aims to find cheap alternatives with high specific surface area, and reasonable catalytic activity toward the reduction of  $I_3^-$ .

It is well known that nanostructuring play a key role in the performance: laminar device structures only show limited efficiencies (<1%) due to the small interfacial area. Also, as the exciton diffusion length in most CPs is in the range of 5–10 nm, enlargement of the interfacial area is of prime importance to avoid extensive carrier recombination. In this vein, various strategies have been developed to create nanostructured heterojunctions with large area, ensuring efficient charge separation at the interface and charge carrier transport [290]. One such method is to make bulk heterojunctions by blending inorganic NPs with the CP [274]. This approach works for CdS and CdSe, however, for oxide NPs, most importantly for TiO<sub>2</sub>, it usually results in devices with low performance, due to the small area of the heterojunction, caused by NP agglomeration.

As an alternative approach, CPs can be infiltrated into nanostructured SC matrices, using solutions of the pre-synthesized CP. However, as mentioned earlier, this approach is hampered by the large size of the CP, and by the difference in the hydrophilic/hydrophobic character of the two components. Consequently, often very low pore-filling ratios have been observed [13]. Various studies have dealt with the role of pore filling, and although the conclusions are controversial in the sense whether the nanostructured oxide host has to be fully filled or not, there is an agreement that uniform distribution of the infiltrated CP is crucially important [291–293]. Due to these facts, in situ approaches are favored to generate CPs inside nanostructured oxide matrices, bringing the organic and inorganic component into intimate contact both at the physical and electronic level [294,295]. As an example, short circuit currents ( $J_{sc}$ ) of a solid-state DSSC

containing photoelectrochemically generated PEDOT was about 20 times higher than that of its counterpart having chemically polymerized PEDOT as hole transporter [237].

As already shown in the previous sections, the nature of the doping ion plays a key role in determining the properties of the electrogenerated CP, and this has substantial impact on the solar cell devices as well. For example, solid-state DSSCs have been fabricated based on TiO<sub>2</sub>, and employing PEDOT as a hole transporter, using various anions [296,297]. Importantly, the anions already affect the photoelectrochemical polymerization procedure, as can be deduced from the overall charge passed through during the synthesis. These variances, however cannot fully explain the differences observed in the solar cell performance. It was found that dopant anions in the PEDOT hole-conductor have great influences on  $I$ - $V$  curves, conductivity, and impedance as well. The most vital finding of these studies is probably the linear dependence of conversion efficiency on the logarithm of the conductivity of the hole transporting polymer [296,297].

The strong effect of the anions was also demonstrated for hybrids synthesized by dark electrodeposition [104,156]. For example, in a recent study a nanostructured organic/inorganic solar cell was constructed by electrodepositing PEDOT on a GaAs nanopillar array using potentiodynamic cycling [156]. Five different dopant ions were studied (dodecyl-sulfate, poly(styrenesulfonate),  $ClO_4^-$ ,  $BF_4^-$ ,  $PF_6^-$ ), and it was found that both the properties of the CP, as well as that of the organic/inorganic interface are affected by the nature of the dopant anion. Most importantly, charge transport properties of electrogenerated PEDOT exhibited a strong dependence on the dopant ion, and the conductivity values ranged between 21 and 116  $S\ cm^{-1}$ . As depicted in Fig. 23, all the important parameters describing solar cell performance are strongly influenced by the properties of the CP, thus short circuit current ( $J_{sc}$ ), fill factor (FF), external quantum efficiency (EQE) and the open circuit voltage ( $V_{oc}$ ) show a clear and strong dependence on the nature of the dopant ion.

Parameters of the employed electrochemical method also exert an important effect on the solar cell performance. As discussed before, in the case of photoelectrochemical

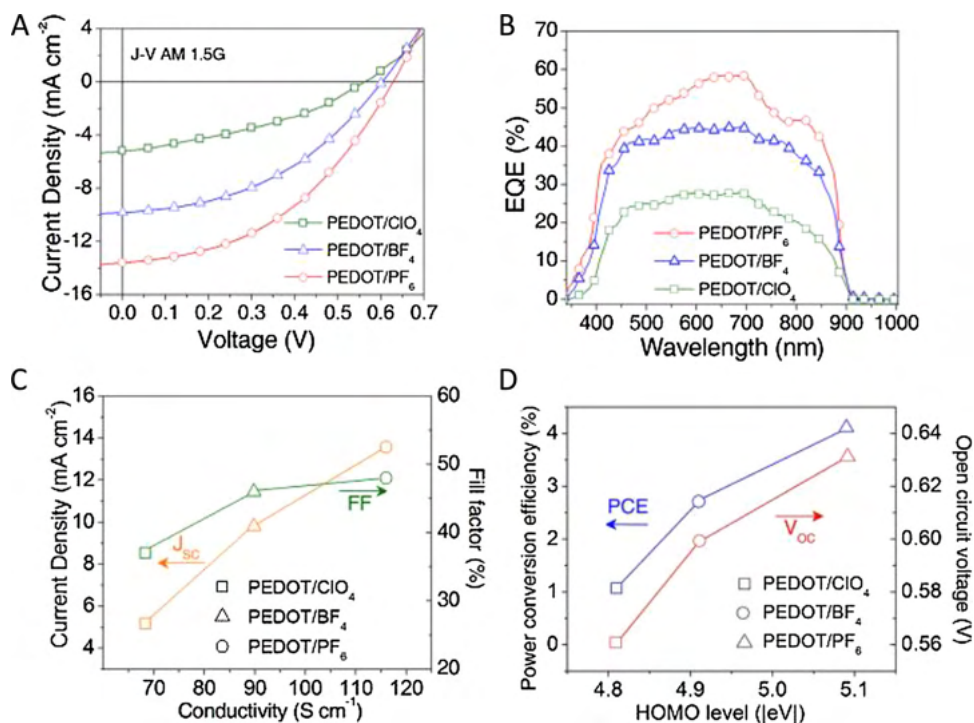


**Fig. 23.** Dependence of solar cell parameters of GaAs/PEDOT devices on the dopant ion. [156], Copyright 2012, Reproduced with permission from the American Chemical Society.

polymerization methods, the applied external bias potential may have dual contribution to the polymer formation. Such involvement can be envisioned either through direct electrochemical polymerization, or by draining the photo-generated electrons, therefore providing more holes to oxidize the monomer. In most of the studies where actual solar cell devices are fabricated, bias potential values are selected where only the second mechanism contributes to the polymerization [298]. This is mainly because in these configurations TiO<sub>2</sub> NPs were immobilized on conducting glass, and therefore electrochemical growth of the CP would occur on that, possibly causing short circuit in the cell. On the other hand, in Section 3.2.2, we showed that electropolymerization results in polymers with superior conductivity and electroactivity compared to counterparts generated purely by photoelectrochemical polymerization. Therefore future studies along this avenue may be useful, with oxide structures where short circuiting is not an issue (e.g., NTAs, having a compact barrier layer below the tubes).

To illustrate the complexity of such systems and the role of multiple parameters, we show another example, namely the role of thickness of the hybrid layer. In conventional DSSCs, relatively thick TiO<sub>2</sub> layers (up to 10 μm) are used, to ensure sufficient light absorption. At such thicknesses mass transport limitation of bis-EDOT (or any other) monomer may hamper the polymerization at the deeper regions of the layer. This limitation not only results in inadequate pore filling, but also in an uneven distribution of PEDOT throughout the oxide matrix. Such effect was observed, when increasing thickness of the TiO<sub>2</sub> film first resulted

in higher power conversion efficiencies, but after a certain threshold, the opposite trend was observed [240]. Solubility of the monomer can be increased by using organic solvents or aqueous micellar solutions. This latter method in an environmentally friendly and cheap alternative, and relies on the solubilization of the monomers using micelles (e.g., sodium dodecyl sulfate) [299].

Furthermore, a recent study [278] demonstrates that the picture is even more complicated, since diffusion of the monomer is not the only factor which hinders polymerization at the deeper areas of relatively thick TiO<sub>2</sub> films. Hybrid layers obtained under monochromatic illumination outperformed their counterparts synthesized under continuous wavelength illumination. Interestingly, for different thickness different wavelengths were shown to be optimal. Such behavior was shown to be related to the difference in the absorption properties of the TiO<sub>2</sub>/dye layer for the different wavelengths. The consequence of this decrease is shown in Fig. 24; the optimal illumination wavelength is seen to be different for each layer thickness [278].

Overall, we may conclude that all solid-state solar cell devices will receive more and more attention in the future. The importance of high polymer loading is underlined by the fact that in solid-state DSSC using PEDOT as hole transporter, dye regeneration kinetics was found to be orders of magnitude slower than its counterparts having either I<sup>-</sup>/I<sub>3</sub><sup>-</sup> redox couple or small molecule hole transporters [300]. Such slow dye regeneration limits the short circuit current, and this was attributed to low pore-filling (approximately 20%), and thus a low polymer/sensitizer ratio.

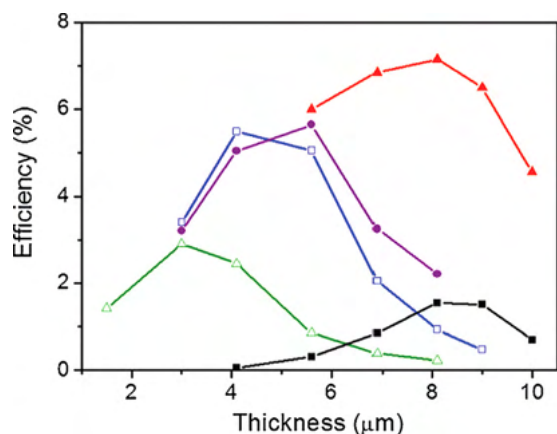


**Fig. 24.** Power conversion efficiencies of PEDOT based solid-state DSSCs with different mesoporous  $\text{TiO}_2$  film thicknesses, synthesized under different light illumination black: 740 nm, red: 670 nm, blue: 605 nm, green: 540 nm and purple: continuous spectral light. (For interpretation of the references to color in this figure legend, the reader is referred to the web version of the article.) [278], Copyright 2012, Reproduced with permission from the PCCP owner societies.

## 4.2. Energy storage

### 4.2.1. Supercapacitors

CP-based hybrids are eminently attractive candidates for energy storage. CPs have very good prospects in this application because of their pseudocapacitive behavior. This potential, however, has not been fully exploited yet, due to some handicaps of CPs, most importantly related to their relatively low cycling stability and limited mobility of anions in bulk CP layers. Hybridization with different inorganic materials aims to overcome these limitations. In most of the available examples, both components can contribute with their intrinsic electroactivity but the real synergy stems from other aspects of hybrid formation.

Two distinctly different categories can be identified: there are hybrids where both constituents exhibit electroactivity in the same potential regime (e.g., MWCNT/PHT, see Fig. 25A), while in other cases the components have complementary electroactivity, therefore the hybrid is

electroactive in a wider potential window (e.g.,  $\text{WO}_3/\text{PANI}$ , see Fig. 25B). Importantly, in the case of appropriately designed composites, the specific capacitance of the hybrid is not just a linear combination of that of the constituents, but in optimal cases the specific capacity of the hybrid can be higher than that of its components. What is equally important, the composites usually have smaller charge transfer resistance than the pure polymer, which further enhances the performance in electrochemical capacitors.

As excellent reviews are available on this body of research [7,301], we only cite studies where electrochemical synthesis methods have contributed to some special, application-related benefit. As seen in Table 7, dominantly carbon nanomaterials (e.g., nanotubes or graphene) and metal oxides (such as  $\text{MnO}_2$  or  $\text{RuO}_2$ ) are combined with CPs for the purpose of electrochemical charge storage. This is not a surprise given that these are the most frequently applied materials in their own right.

In general, the advantage of electrochemical polymerization is the lack of added oxidants and binders as CPs and their hybrids are directly formed on the electrode. Consequently, the resistance between the CP-based active material and the current collector is smaller than in their chemically prepared counterparts. These notions have been realized in a pioneering study, where among the three methods used for preparing CNT/PEDOT composites (mechanical mixing, chemical polymerization, electrodeposition) the electrochemical method gave the best capacitor performance [84]. Table 7 compiles various hybrid assemblies with possible use as electrochemical capacitors. The highest specific capacitance values obtained in each study are also compared.

First-generation hybrids incorporated the carbon component into the CP matrix during electrodeposition [309]. Besides the contribution of the intrinsic capacitive behavior of the carbons, the enhanced behavior (especially in terms of durability) of the hybrid is generally attributed to the higher conductivity and stability of the composites compared to their bare CP counterparts. Such improvement is due to better charge-transfer and the porous structure of composites, facilitating rapid ionic transport. However, co-polymerization suffers from aggregation of the nanomaterials, as well as from the uneven distribution

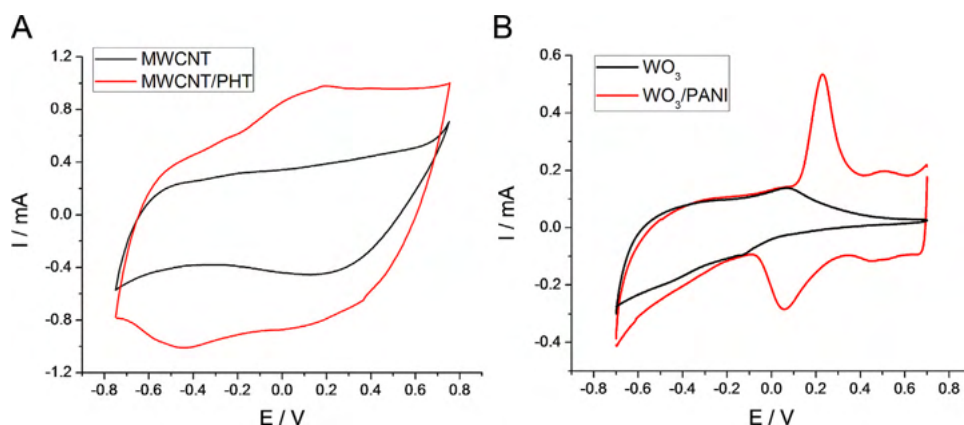


**Fig. 25.** Examples for hybrid charge-storage materials where the constituents have (A) overlapping, (B) complementary electroactivity.

**Table 7**  
Electrogenerated CP-based assemblies as electrochemical capacitors.

Carbon	CP	Comment	Capacity	Refs.
GO	PPy	Free standing electrodes were obtained by doping type incorporation of GO	356 F/g at 0.5 A/g	[71]
Graphene	PANI	PANI nanorods were electrodeposited onto a self-standing graphene paper	763 F/g at 1 A/g	[302]
Graphene	PANI	3D porous structure was filled with increasing amounts of PANI	716 F/g at 0.47 A/g	[115]
Graphene	PANI	Free standing and flexible electrode. The effect of PANI amount was also shown	233 F/g	[114]
Graphene	PANI	This flexible electrode had high capacity and excellent stability	970 F/g at 2.5 A/g	[116]
Graphene	PANI	Attractive one step electrodeposition	640 F/g at 0.1 A/g	[303]
Graphene	PANI	Fast doping/dedoping of PANI was observed due to the morphology of the hybrid	725 F/g at 10 A/g	[76]
Graphene	PPy	Structure–property relationship for hybrids obtained by continuous and pulsed electrodeposition was evaluated	237 F/g at 10 mV/s	[117]
Graphene	PPy	Sulfonated graphene sheets were incorporated, resulting in improved electrical properties	285 F/g at 0.5 A/g	[80]
MWCNT	PANI	PANI was infiltrated into fibers of aligned carbon nanotubes	274 F/g at 2 A/g	[304]
MWCNT	PANI	The advantages of highly ordered NTAs were demonstrated. The role of filling ratio on the capacitance as well as the stability was also discussed	1030 F/g at 5.9 A/g	[122,123]
MWCNT	PEDOT	Several different compositions were studied, and the superior performance of electrodeposited hybrids was demonstrated	150 F/g	[84]
MWCNT	PPy	The contribution of increasing amounts of PPy was shown for this self-supporting membrane	427 F/g at 5 mV/s	[128]
MWCNT	PPy	Very thick NTA films are used and defects were introduced before polymer deposition	587 F/g at 3 A/g	[129]
MWCNT	PPy, PANI, PEDOT	Different polymers were studied, and the PANI containing composite showed the best durability	No data	[83]
Porous carbon	PANI	Hierarchically porous carbon monolith was used as an effective support for PANI deposition	360 F/g at 20 mA/g	[132]
SWCNT	PANI	The effect of hybrid composition on the capacitance and conductivity was studied	473 F/g at 5 mA/cm <sup>2</sup>	[135]
SWCNT	PANI	Skeleton/skin morphology, effect of the change in porosity on the capacitance was shown	236 F/g at 20 mV/s	[136]
SWCNT	PDOP	An adhesive layer was introduced between the CP and the CNTs	151 F/g	[137]
MnO <sub>2</sub>	PEDOT	Electrochemical behavior was correlated with the morphology and crystal structure of the hybrid electrodes	285 F/g at 20 mV/s	[157]
MnO <sub>2</sub>	PMT	Role of polymeric underlayer was studied, and compared with MnO <sub>2</sub> deposited onto Ti	218 F/g at 20 mV/s	[268]
MnO <sub>2</sub>	PEDOT	Morphological considerations on the performance were given	199 F/g at 10 mV/s	[267]
MnO <sub>2</sub>	PANI	Contribution of the individual components to the capacitance in the hybrid configuration was studied	715 F/g at 5 mA/cm <sup>2</sup>	[266]
MnO <sub>2</sub>	PEDOT	Sequential deposition of multilayers was achieved, and capacitive properties of the various structures were compared	487.5 F/g at 1 mA/cm <sup>2</sup>	[270]
MnO <sub>2</sub>	PEDOT	Hybrid coaxial nanowires were formed, and both symmetric and asymmetric capacitor devices were assembled	210 F/g	[305,248]
MnO <sub>2</sub>	PPy	Redox performance of the hybrid significantly exceeded that of its constituents	620 F/g at 5 mV/s	[245]
MnO <sub>2</sub>	PANI	Dependence of the specific capacitance on the hybrid composition was shown	532 F/g at 2.4 mA/cm <sup>2</sup>	[244]
MnO <sub>2</sub> .C	PANI	The hybrid was deposited on activated carbon, and performance was studied in organic electrolyte	413 F/g at 5 mV/s	[246]
RuO <sub>2</sub>	PEDOT	Hybrid nanotubes were formed in Al <sub>2</sub> O <sub>3</sub> template, and RuO <sub>2</sub> had very high contribution in the hybrid configuration	664 F/g at 5 mA/cm <sup>2</sup>	[263]

Table 7 (Continued)

Carbon	CP	Comment	Capacity	Refs.
RuO <sub>2</sub>	PPy	Vertically well-aligned cone-shaped nanostructures of PPy were coated by a thin film of RuO <sub>2</sub>	302 F/g at 0.5 mA/cm <sup>2</sup>	[306]
RuO <sub>2</sub>	PANI	Porous PANI provided a high surface area substrate for RuO <sub>2</sub> growth	605 F/g at 10 mV/s	[265]
RuO <sub>2</sub> .C	PANI	Specific capacitance significantly decreased at higher scan rates	708 F/g at 5 mV/s	[162]
RuO <sub>2</sub> .C	PANI	RuO <sub>2</sub> and PANI were co-immobilized on porous double-shelled carbon spheres	531 F/g at 1 mA/cm <sup>2</sup>	[264]
TiO <sub>2</sub>	PPy	TiO <sub>2</sub> NTA was used, and PPy did not have well defined electroactivity in the hybrid	179 F/g at 1.85 mA/cm <sup>2</sup>	[192]
TiO <sub>2</sub>	PT	Polythiophene was infiltrated into TiO <sub>2</sub> NTA, therefore it had high surface area	640 F/g at 5 mV/s	[307]
WO <sub>3</sub>	PANI	Good performance in asymmetric capacitor configuration	168 F/g at 1.28 mA/cm <sup>2</sup>	[254]
WO <sub>3</sub>	PANI	Interaction of PANI with WO <sub>3</sub> improved stability	No data	[308]

of the carbon component within the polymer matrix. Furthermore, due to lack of connection between the incorporated conductive materials, large electrode resistances are observed. To overcome these drawbacks, and to gain additional benefits from the hybridization, CPs were electrodeposited on *nanostructured* carbon substrates. The advantages of this method were shown for example on different highly porous carbon/PANI composites, and summarized as follows [132]:

- Easy handling compared with powdered carbon,
- Binder-free and conductive-agent-free electrode preparation,
- Facile synthesis,
- Controlled growth of active materials by limited pore spaces,
- Optimal performance (specific capacitance, power and energy densities, excellent cycling stability).

Importantly, all these characteristics apply for other nanostructured carbon hosts as well, such as CNT arrays or three-dimensional graphene structures. The capacitance of an electrode depends among other factors, on the resistance of electron transfer between the electroactive material and current collector and the ease of electrolyte migration. Consequently, a good compromise has to be found between the deposited amount of polymer and the pore size and density. This latter is an important parameter, because it ensures that all the deposited polymer is accessible to the electrolyte phase, as demonstrated by the example of interconnected SWCNT/PANI hybrid [136]. In another example, the amount of PANI electrodeposited inside a three-dimensional matrix of electrochemically reduced graphene oxide (ERGO) was varied, by increasing the number of potentiodynamic deposition cycles [115]. As seen in Fig. 26, there is an optimal loading of PANI, over which the capacitance does not increase further, and even decreases mainly due to pore blocking.

Among metal oxides, MnO<sub>2</sub> and especially RuO<sub>2</sub> are very attractive for charge storage, as they have an extraordinary high charge capacity. When combining them with CPs, the aim is generally to obtain hybrids with high

surface area using nanoscale distribution of the components. For example, a co-deposited MnO<sub>2</sub>/PPy composite outperformed both of its components in terms of specific capacitance, with reasonable stability at the same time [245]. Careful study of sequential electrodeposition of different MnO<sub>2</sub>/PEDOT hybrids proved the importance of both under- and over-laying PEDOT film, below, and above a MnO<sub>2</sub> layer respectively [246]. Such a sandwich structure was beneficial from two aspects: the thin inner layer of PEDOT acted as a flexible binder to the current collector, whereas the outer film protected MnO<sub>2</sub> from being detached. Due to these favorable contributions, the hybrid held 95.5% of its charge capacity over 1500 cycles [246].

In the case of RuO<sub>2</sub>, higher specific capacitance values are often obtained for the hybrid than for its components, due to the large surface area of the oxide in the hybrid configuration [162]. Very similar trends were revealed for PPy nanotubes having an ultrathin coating of RuO<sub>2</sub> on their surface [306]. Ternary composites have also been fabricated by depositing both the CP and RuO<sub>2</sub> on high surface area carbon substrate [162,264]. In another study, both the inner and outer surfaces of PEDOT nanotubes were decorated with RuO<sub>2</sub> NPs. In these configurations, the mechanical properties of the components are mutually reinforced: the flexible PEDOT prevents the RuO<sub>2</sub> detaching from the current collector while the rigid oxide avoids collapse and aggregation of the nanotubes [263]. The charge-storage mechanism of RuO<sub>2</sub>/PEDOT composite nanotubes as well as the advantages of the organized nanoscale structure is schematically shown in Fig. 27A.

More recently, other oxides (WO<sub>3</sub> and TiO<sub>2</sub>) have also been studied in this manner (see Table 7). TiO<sub>2</sub> NTAs appear to be particularly promising in this respect, due to their high surface area and chemical/electrochemical stability. Such composites may offer short migration path for the dopant ions and also improve the effectiveness of electron transfer, resulting in a high electrochemical capacitance (e.g., 640 F/g for TiO<sub>2</sub>/PT hybrid) [169,307].

#### 4.2.2. Lithium-ion batteries

This application area is not as well developed as those discussed before, but there are still some notable examples

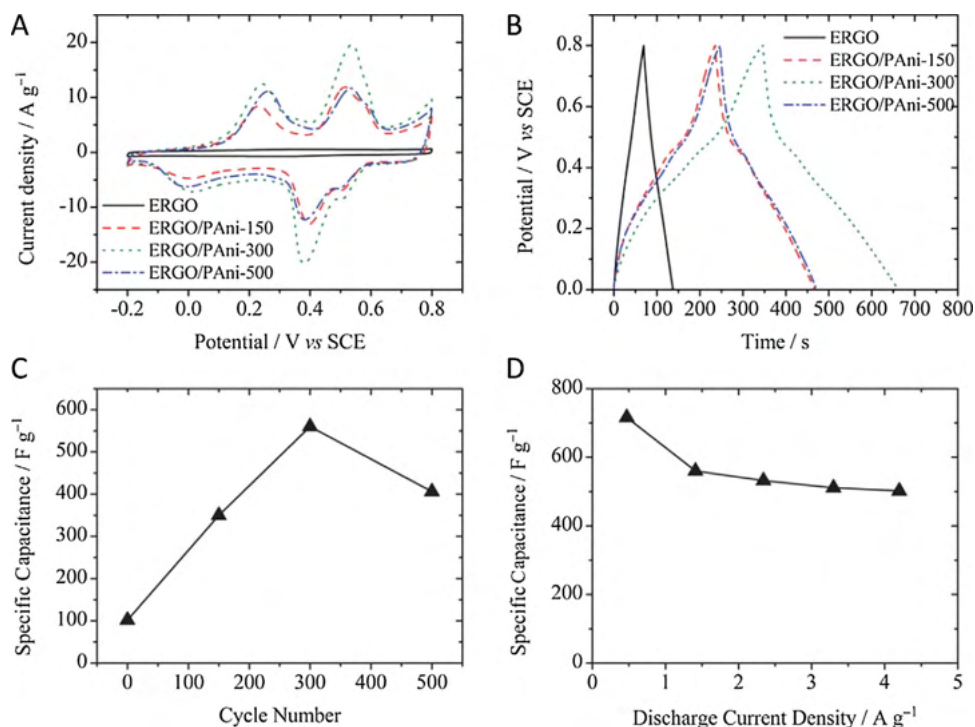


**Fig. 26.** Electrochemical properties of electrochemically reduced graphene oxide ERGO, and ERGO–PANI composite electrodes. (A) CV curves at the scan rate of 5 mV/s; (B) galvanostatic charge–discharge curves at a current density of 1.4 A/g; (C) specific capacitance at current density of 1.4 A/g; (D) specific capacitance of ERGO–PANI-300 at different charge/discharge current densities. [115], Copyright 2012, Reproduced with permission from the Royal Society of Chemistry.

as presented below. There are also emerging concepts, such as combining solar cells with Li-ion batteries in one electrochemical cell resulting in a solar rechargeable battery [225,310]. In general, transition metal oxides are attractive candidates as active materials in Li-ion batteries due to their high capacity (over 700 mAh/g) even at high charge–discharge current density. However, in most of the cases, a very quick decrease in their capacity can be observed during repeated discharge–charge cycles, due to the low conductivity of these oxide SCs. Therefore, hybrids with carbons, metals or even CPs have been developed.

In such composites CPs improve both Li-ion intercalation capacity and accessibility, mechanical stability, and conductivity of the electrode compared to the parent oxide. Furthermore, CPs have an additional advantage, as they not only act as the conducting network but also as the active material, because of their ion-exchange properties.

For example,  $\text{MnO}_2$  particles in a PPy film worked well as an active material, giving an increase in the charge–discharge capacity over that of PPy itself. These electrodes had only one potential plateau during both charge and discharge cycles, which indicated that the

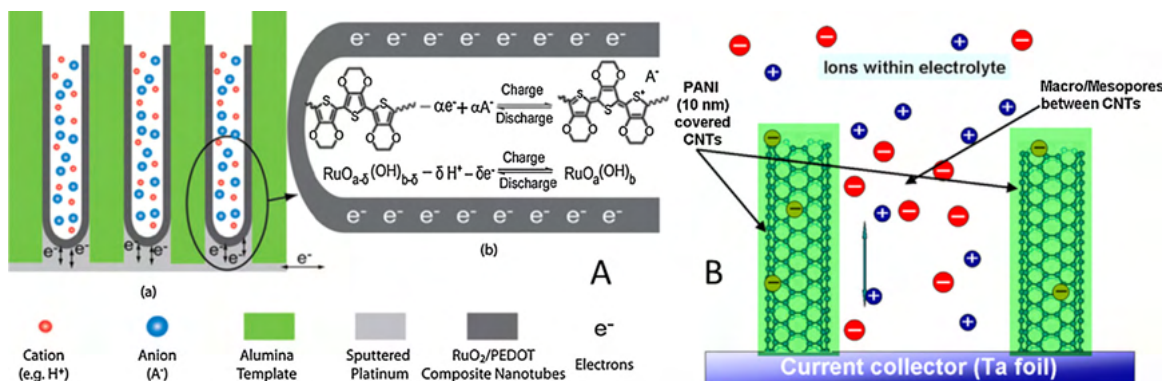


**Fig. 27.** Role of organized nanostructures in enhanced capacitive properties due to effective ion transport. (A) RuO<sub>2</sub>/PEDOT composite nanotubes, (B) CNT array/PANI hybrid. Sources, respectively: [263], Copyright 2010, Reproduced with permission from the PCCP owner societies; [123], Copyright 2009, Reproduced with permission from Elsevier Ltd.

redox transformation of both components take place in the same potential regime [24,311]. NiO/PEDOT films were also studied, and exhibited weaker polarization and better cycling performance as compared to the bare oxide (best specific capacity: 520 mAh/g) [161]. Importantly, the presence of PEDOT enhanced the conductivity of the electrode, and contributed to the improved stability of the porous NiO during the cycling [161]. PPy nanowires were uniformly decorated by SnO<sub>2</sub> nanocrystals forming organized nanostructures to be applied in Li-ion batteries. This assembly exhibited a reversible capacity of 690 mAh/g, and what is equally important, most of its electroactivity (622 mAh/g) was retained even after 80 cycles. The advanced properties were enabled by multiple factors, most importantly by the advantages of the three-dimensional architecture of the PPy nanowire support, in terms of facile charge carrier transport, high porosity, and enhanced stability [262].

Lithium ion intercalation/de-intercalation of TiO<sub>2</sub>/PPy and TiO<sub>2</sub>/PEDOT hybrids was studied [174]. The improved Li-ion intercalation was attributed to the higher conductivity of the hybrid compared to mesoporous TiO<sub>2</sub> [174]. Vanadium pentoxide is probably one of the most extensively studied materials, and its hybrids with PPy, PANI and PEDOT have been evaluated for their application in this vein. In all the cases, a better mechanical flexibility during the expanding/shrinking cycles of discharge/charge was observed. V<sub>2</sub>O<sub>5</sub>/PANI composite films showed a specific capacity of 270 mAh/g, with very small fading (ca., 3.4%) [312]. As for V<sub>2</sub>O<sub>5</sub>/PPy composites (294 mAh/g), the performance of electrodeposited and chemically generated samples was compared, and the electrochemically assembled electrode displayed superior performance in terms of both cycle stability and specific capacity [313]. Finally, V<sub>2</sub>O<sub>5</sub> nanobeams were embedded into PEDOT and the kinetics of lithium transport was analyzed [47].

Most recently, a novel ternary composite anode composed of Si NPs embedded in a three-dimensional hierarchically porous PPy framework containing SWCNTs has been realized [314]. This Si/PPy/CNT showed high-performance, because of exploiting the benefits of each component, namely the high surface area of the CP, the ultrahigh specific capacity of Si, and the high electric conductivity of the SWCNTs. The as-prepared ternary electrode exhibited long-term stability because of the presence of the CP helped to avoid major degradation of the Si particles during lithium insertion/extraction [314].

#### 4.3. Other miscellaneous applications

##### 4.3.1. Heterogeneous (photo-)catalysis

CPs can be used as a support for both photo- and electrocatalysts, due to their porosity and potentially high surface area, especially in their nanostructured form. Metal NPs are the most frequently used additives for such purposes, but studies with inorganic SCs and carbon nanostructures can also be found in the literature. Furthermore, CPs have intrinsic electrocatalytic activity toward different reactions, for example, oxygen reduction reaction (ORR) [315]. Such activity can be synergistically combined with that of the immobilized inorganic NPs, as shown in the following examples.

A wide range of ternary transition metal oxides have been incorporated into CPs in this vein, including Cu<sub>1.4</sub>Mn<sub>1.6</sub>O<sub>4</sub> or Ni<sub>x</sub>Co<sub>3-x</sub>O<sub>4</sub> [54,56], and their improved efficiency in ORR was demonstrated. In addition, it was found that the presence of oxide NPs avoids degradation of the polymeric matrix, caused by the formation of HO<sub>2</sub><sup>-</sup> during ORR. This is a vital point in view of applications because chemical and mechanical degradation is a major drawback of polymeric materials in these applications (note the similarity with PEMFCs [316]). The nature and concentration of the dopant anions play a key role in ORR, due to their effect on the structural, morphological, and electronic properties of the hybrid assembly. Electrocatalytic reduction of other species, such as ClO<sub>3</sub><sup>-</sup> and BrO<sub>3</sub><sup>-</sup> were performed on WO<sub>3</sub>/PANI [317] and MoO<sub>3</sub>/PANI [249] composites, respectively. With the purpose of possible fuel cell applications, electrooxidation of different fuels, such as methanol [251], ethanol [251,252], and also polyhydroxyl compounds [250] were tested on NiO<sub>x</sub>-containing CP electrodes. In all the cases the catalytic activity was facilitated by the Ni(II)/Ni(III) redox transition of the NiO<sub>x</sub> nanoparticles, dispersed in the CP matrix.

In some cases, the catalytic efficiency can be further enhanced by illumination, due to the semiconductor properties of either the CP, or the embedded NPs, or occasionally both. For example, CPs (being p-type SCs) are known to photoreduce dissolved oxygen [318]. In the case of a Fe<sub>3</sub>O<sub>4</sub>/PPy composite, the built-in oxide resulted in higher currents, because of the electroreduction of H<sub>2</sub>O<sub>2</sub>, formed in the reaction between the photogenerated electron and oxygen. Rotating disk electrode (RDE) studies indicated the dominance of the 4 e<sup>-</sup> reduction pathway for O<sub>2</sub> for the overall process. In addition, electrocatalytic reduction of H<sub>2</sub>O<sub>2</sub> (as the intermediate of the ORR) was also studied, and the Fe<sub>3</sub>O<sub>4</sub>/PPy hybrid showed 7.5 times larger catalytic activity compared to neat PPy [45,46].

CPs can also be used as sensitizers of inorganic photocatalysts (similar to their application in hybrid organic/inorganic solar cells). In this manner TiO<sub>2</sub> NTAs were decorated by various thiophene derivatives [179] and PANI [166], and tested under visible light irradiation for photoelectrochemical degradation of 2,3-dichlorophenol and Rhodamine B, respectively. One particularly important finding was that the side chain of the polymer affects the photocatalytic efficiency, due to differences in interfacial properties, and consequently in the charge transfer. Again, electrodeposition is particularly useful here, since it directly results in better electronic contact between the two components (see above).

As for carbon nanomaterials, their incorporation can also enhance the catalytic performance related to the polymer, because such hybrids exhibit improved electrical conductivity, electrochemical capacitance, and mechanical strength. SWCNT/PPy were used in ORR and, a mixture of two-electron and four-electron processes was observed [94]. Electrodeposited composites (having a thin net-like structure) were found to outperform their chemically synthesized counterparts, because of morphological differences [94]. Similar conclusions were drawn for MWCNT/PMT hybrids for the electrooxidation of NADH [126]. The real advantages of carbon nanomaterials

however, can be exploited in *ternary* hybrids, in which beyond the CP and the carbon, a third, catalytically active component (e.g., metal NPs) is also present. In such configurations, the advantages of each constituent are mutually reinforced: CP provides a common flexible platform, the carbon nanomaterial enhances the electronic conductivity, and metal/inorganic nanoparticles contribute with their catalytic activity. In this manner among others, SWCNT/PANI/Pt [319,320], MWCNT/PANI/Au [321] and graphene/PEDOT/Co [322] assemblies were realized through electrodeposition, and tested for the oxidation of formic acid, methanol, ascorbic acid and nitrite-ions, respectively.

#### 4.3.2. Sensors

The first applications of CP-based assemblies in this area were demonstrated in *conductivity sensors*, where the interaction between the analyte and the electrode material (usually in the gas phase) results in a change of the electrical conductivity. Chemical reactions (doping/dedoping) as well as physical (e.g., solvation/desolvation) changes are responsible for the observed resistivity alterations. Hybridization aims to extend sensing to a wider range of analytes: to enhance sensitivity, and to achieve better selectivity [8].

For example, photoelectrochemically generated TiO<sub>2</sub>/PPy was demonstrated to outperform its bare polymeric counterpart as a humidity sensor [323]. The surface morphology as well as the interaction between PPy and doped TiO<sub>2</sub> NPs resulted in higher sensitivity (impedance changed almost two orders of magnitude), and much better linearity in the semi-logarithmic response curve. The PPy component has much higher surface area in the hybrid configuration, which is indeed important when sensing is based on the reduced conductivity due to water adsorption. Co-deposited graphene oxide/polypyrrole composite films were employed for the detection of volatile organic compounds [78]. The presence of the carbon component improved the mechanical properties of the polymer and ensured a continuous and porous morphology. A chemoresistor-type vapor sensor demonstrated fast, linear and reversible response to toluene with high sensitivity and selectivity [78]. Detection of liquefied petroleum gas (LPG) was performed using a series of SC/PANI heterojunctions, containing CdTe [107], CdS [105] and PbS [109] respectively. In these studies, changes in the *I*-*V* curves were correlated with the LPG concentration and the response alteration were rationalized in terms of the modification of the organic/inorganic interface.

In *electrochemical sensors*, application of CP-modified electrodes was first demonstrated in potentiometric sensors, most importantly in ion selective electrodes [324]. As for voltammetric/amperometric detection, considerable interest manifested toward hybrid materials due to their selectivity, sensitivity and homogeneity, strong adherence to electrode surface and chemical stability [325]. We omit examples from this last group for two reasons: (i) these hybrids are very similar to those shown in the previous section, used as electrocatalysts, (ii) this topic has been reviewed recently [326]. The conclusion of the review was that electrodeposited composites exhibited superior

performance both in terms of sensitivity and detection limits compared to that of the chemically synthesized samples [326].

#### 4.3.3. Electrochromics

Many of the widely utilized electrochromic materials are either inorganic oxide SCs (most importantly WO<sub>3</sub>) [327] or CPs. Note that the whole color palette has been covered using CPs by now [328]. The main advantages of inorganic materials are the relatively fast color switching, durability, and long term stability, but their use is hampered by their narrow color variation and low coloration efficiencies. This latter, together with the high contact resistance in the device, results in the need of high electrical power input to reach the required color change. On the other hand, CPs exhibit high coloration efficiencies at relatively lower redox switching potentials, on a short timescale. Their relatively low environmental stability (especially in the oxidized state) and mechanical strength, however, are important drawbacks from an application perspective. Therefore, it was soon recognized that in hybrids, the complementary properties can be exploited, and the synergies fully utilized [329]. Such synergies predominantly stem from the combination of the flexibility and functionality of the CP with the mechanical strength and chemical stability of the inorganic SC [330]. The assembling method, as well as the resulted (nanoscale) morphology is of prime importance as shown in the examples below.

The first realization of electrochromic hybrid assemblies relied on the incorporation of WO<sub>3</sub> particles into both PPy [23] and PANI [253]. The composite films were blue in color at negative potentials (due to the color of the inorganic component) and multicolored from green to violet at positive potentials. Importantly, there is an electrochromic window between the WO<sub>3</sub> coloration and PANI coloration, which opens an opportunity to their use in multicolor displays. In this vein, WO<sub>3</sub> particles were embedded to additional polymers [34], and PANI was also electrodeposited on the WO<sub>3</sub> surface [308,331]. TiO<sub>2</sub>-containing hybrids have also been obtained, containing PANI [168], and various thiophene derivatives [142,146,178]. In these cases a major advantage is the increased stability of the CP in the hybrid configuration.

The improved stability during the redox transformation is predominantly related to the hybrid architecture (CP is infiltrated into mesoporous TiO<sub>2</sub>), as the nanoparticulate matrix acts as a skeleton, keeping the polymer intact and avoiding its detachment. Notably, use of ionic liquid as an electrolyte is also likely to contribute to the enhanced lifetime. In addition, significantly faster electrochromic response was obtained in the case of a nanostructured TiO<sub>2</sub>/PPy hybrid compared to the neat PPy layer [223]. Similarly, an interconnected array of NiO nanoflakes was employed as the host matrix for both PANI and PEDOT, and subsequently used as electrochromic materials [159,160].

In summary, the most important lessons learned from the previous studies can be summarized as follows:

- The inorganic compound may contribute with its intrinsic electroactivity coupled with the color change. This may



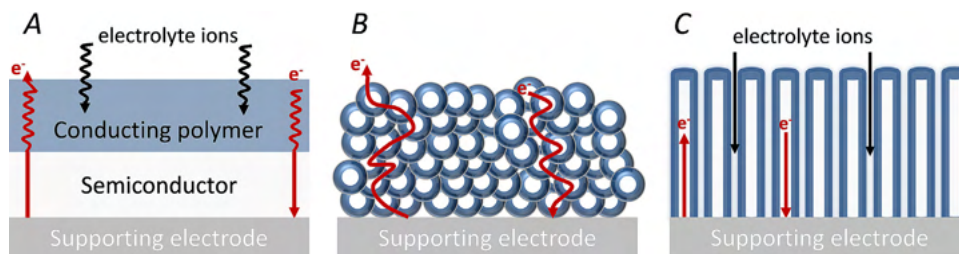


**Fig. 28.** Comparison of (A) flat, (B) nanoparticulate and (C) nanostructured device configuration for electrochromic applications. The possible ion and electron transport routes are also shown.

- or may not coincide with the polymer properties in terms of coloration window (potential) and the resulting colors.
- Improved stability of the polymer because of the intimate contact with the inorganic component.
  - Better charge carrier transport due to the organized network structure, which can act as a “freeway” for the charge carriers (see also Fig. 28). Also the nano-dimension of the polymer can avoid limitations from the small exciton diffusion length in CPs.
  - Porous hybrid structures facilitating diffusion/migration of ions and resulting in faster coloration times (Fig. 28B and C).

Finally a related phenomenon, namely, photochromism of SC-containing CP films is noted. In the case of TiO<sub>2</sub>

[27,332] or CdS [37] containing films, their coloration was observed upon illumination. In this case, alteration of the PANI oxidation level (and the coupled color change) was not caused by external electrochemical stimulus (bias potential) but by photogenerated electrons from the SC particles. Upon generation of excitons, the photoelectrons reduce the oxidized PANI, while the photoholes are consumed by a hole scavenger (methanol) in the solution phase.

## 5. Summary

Introduction of new functional materials into CPs, or deposition of CPs on SC surfaces aims to result in advanced properties in various aspects. The success of such

**Table 8**

Direct examples of performance enhancement in selected applications of electrogenerated conducting polymer–inorganic semiconductor nanocomposites relative to cases when other, non-electrochemical synthesis methods were applied.

Hybrid material	Application	Remarks	Refs.
TiO <sub>2</sub> /dye/PEDOT	Hole-transporter in solid state DSSC	Short circuit currents ( $J_{SC}$ ) of a solid-state DSSC containing photoelectrochemically generated PEDOT was about 20 times higher, than that of its counterpart having chemically polymerized PEDOT as hole transporter	[237]
CNT/PEDOT	Supercapacitor	Because of the lack of added oxidants and binders, resistance between the CP-based active material and the current collector is smaller than in their chemically prepared counterparts. For example among three compositionally identical CNT/PEDOT composites made by different methods (mechanical mixing, chemical polymerization, electrodeposition) the electrochemical method gave the best capacitance results	[84]
V <sub>2</sub> O <sub>5</sub> /PPy	Li-ion battery	The performance of electrodeposited and chemically generated V <sub>2</sub> O <sub>5</sub> /PPy composite samples was compared, and the electrochemically assembled electrode displayed superior performance in terms of both cycle stability and specific capacity	[313]
SWCNT/PPy and MWCNT/PMT	Electrocatalysis	Electrodeposited SWCNT/PPy composites (having a thin net-like structure) were found to outperform their chemically synthesized counterparts in ORR, because of morphological differences and enhanced mechanical strength. Similar conclusions were drawn for MWCNT/PMT for the electrooxidation of NADH	[94,124]
Various CNT/CP and SC/CP hybrids	Electrochemical sensing	By comparing similar composite materials prepared by different techniques, those obtained through electrochemical methods show superior performance to their chemically synthesized counterparts in electrochemical sensing. Almost all the composites that exhibit the lowest detection limits within their group toward the sensing of a certain benchmark analyte have been obtained electrochemically	[326]

hybridization however, critically depends on the control attained over the composition and nanoscale morphology of the hybrid assembly and especially the interface between the components. In this review we have demonstrated the power of electrochemistry for obtaining hybrid materials based on CPs and SCs. Through careful control over the electrochemical synthesis parameters, the resultant hybrid can be tuned toward a targeted application. What is equally important, electrochemistry is a relatively mild method, and it does not require use of additional chemicals for the polymer synthesis. As demonstrated in this review, there is a wealth of possible electrochemical approaches to be employed, each of them having particular advantages and drawbacks. Opportunities with less frequently used approaches, such as photoelectrochemical polymerization, may attract increasing interest in the future, especially in light of its usefulness for less conductive SC electrode substrates.

The above listed attractive attributes of CP/SC composites have re-sparked much attention on such hybrid assemblies to be deployed in various applications ranging from solar energy conversion, energy storage, sensors, and electrochromics. Particular stress was given to applications, in which the hybrid can be directly used as a modified electrode. Table 8 highlights a set of CP/SC nanocomposite systems where the electrogenerated hybrids outperformed counterparts obtained by other synthetic procedures. Examples of performance enhancement in selected applications are by no means exhaustive but only representative of the range examined. It is impressive that these nanocomposites show superior performance whether the application considered is solar energy conversion (solar and photoelectrochemical cells), electrochromics (smart windows), (photo)catalysis (environmental remediation, solar fuel generation, or sensors), or charge storage (electrochemical capacitor, Li-ion battery).

## Acknowledgements

CJ is grateful to his former PhD advisor and mentor Prof. Csaba Visy, who inspired him to enter the fascinating world of conducting polymer based hybrid assemblies. Equally important he taught that human qualities are as important as intellectual stature and that training of younger generations of emerging researchers and new scientific achievements must go hand in hand. CJ also gratefully acknowledges funding support of the European Union under FP7-PEOPLE-2010-IOF, Grant Number: 274046. This research was also supported in the framework of TÁMOP 4.2.4.A/2-11-1-2012-001 “National Excellence Program-Elaborating and operating an inland student and research personal support system” key project. KR thanks the National Science Foundation (CHE-1303803) for partial funding support.

## References

- [1] Heeger AJ. Semiconducting polymers: the Third Generation. *Chem Soc Rev* 2010;39:2354–71.
- [2] Inzelt G, Pineri M, Schultze J, Vorotyntsev M. Electron and proton conducting polymers: recent developments and prospects. *Electrochim Acta* 2000;45:2403–21.
- [3] Gangopadhyay R, De A. Conducting polymer nanocomposites: a brief overview. *Chem Mater* 2000;12:608–22.
- [4] Rajeshwar K, de Tacconi NR, Chenthamarakshan CR. Semiconductor-based composite materials: preparation, properties, and performance. *Chem Mater* 2001;13:2765–82.
- [5] Gomez-Romero P. Hybrid organic–inorganic materials – in search of synergic activity. *Adv Mater* 2001;13:163–74.
- [6] Skompska M. Hybrid conjugated polymer/semiconductor photovoltaic cells. *Synth Met* 2010;160:1–15.
- [7] Wang G, Zhang L, Zhang J. A review of electrode materials for electrochemical supercapacitors. *Chem Soc Rev* 2012;41:797–828.
- [8] Hatched DW, Josowicz M. Composites of intrinsically conducting polymers as sensing nanomaterials. *Chem Rev* 2008;108:746–69.
- [9] Malinauskas A, Malinauskienė J, Ramanavicius A. Conducting polymer-based nanostructured materials: electrochemical aspects. *Nanotechnology* 2005;16:R51–62.
- [10] Li C, Bai H, Shi G. Conducting polymer nanomaterials: electro-synthesis and applications. *Chem Soc Rev* 2009;38:2397–409.
- [11] Liang Y, Yu L. Development of semiconducting polymers for solar energy harvesting. *Polym Rev* 2010;50:454–73.
- [12] Reiss P, Couderc E, Girolamo J, Pron A. Conjugated polymers/semiconductor nanocrystals hybrid materials – preparation, electrical transport properties and applications. *Nanoscale* 2011;3:446–89.
- [13] Bartholomew GP, Heeger AJ. Infiltration of regioregular poly[2,2-(3-hexylthiophene)] into random nanocrystalline TiO<sub>2</sub> networks. *Adv Funct Mater* 2005;15:677–82.
- [14] Koh JK, Kim J, Kim B, Kim JH, Kim E. Highly efficient, iodine-free dye-sensitized solar cells with solid-state synthesis of conducting polymers. *Adv Mater* 2011;23:1641–6.
- [15] Huisman CL, Huijser A, Donker H, Schoonman J, Goossens A. UV polymerization of oligothiophenes and their application in nanostructured heterojunction solar cells. *Macromolecules* 2004;37:5557–64.
- [16] Kowsari E, Faraghi G. Ultrasound and ionic-liquid-assisted synthesis and characterization of polyaniline/Y<sub>2</sub>O<sub>3</sub> nanocomposite with controlled conductivity. *Ultrason Sonochem* 2010;17:718–25.
- [17] Rajeshwar K. Electrochemistry of conducting polymers. In: Skotheim T, Elsenbaumer RL, Reynolds JR, editors. *Handbook conducting polymers*. 2nd ed. New York: Marcel Dekker Inc.; 1998. p. 531–89.
- [18] Heinze J, Frontana-Urbe B, Ludwigs S. Electrochemistry of conducting polymers – persistent models and new concepts. *Chem Rev* 2010;110:4724–71.
- [19] Zhou M, Heinze J. Electropolymerization of pyrrole and electrochemical study of polypyrrole: 1. Evidence for structural diversity of polypyrrole. *Electrochim Acta* 1999;44:1733–48.
- [20] Sabouraud G, Sadki S, Brodie N. The mechanisms of pyrrole electropolymerization. *Chem Soc Rev* 2000;29:283–93.
- [21] Yoneyama H, Hirao S, Kuwabata S. Preparation and electrochemical properties of WO<sub>3</sub>-incorporated polyaniline films. *J Electrochem Soc* 1992;139:3141–6.
- [22] Kawai K, Mihara N, Kuwabata S, Yoneyama H. Electrochemical synthesis of polypyrrole films containing TiO<sub>2</sub> powder particles. *J Electrochem Soc* 1990;137:1793–6.
- [23] Yoneyama H, Shoji Y. Incorporation of WO<sub>3</sub> into polypyrrole, and electrochemical properties of the resulting polymer films. *J Electrochem Soc* 1990;137:3826–30.
- [24] Kuwabata S, Kishimoto A, Tanaka T, Yoneyama H. Electrochemical synthesis of composite films of manganese dioxide and polypyrrole and their properties as an active material in lithium secondary batteries. *J Electrochem Soc* 1994;141:10–5.
- [25] Beck F, Dahlhaus M, Zahedi N. Anodic codeposition of polypyrrole and dispersed TiO<sub>2</sub>. *Electrochim Acta* 1992;37:1265–72.
- [26] Beck F, Dahlhaus M. Anodic formation of polypyrrole/tungsten trioxide composites. *J Appl Electrochem* 1993;23:781–9.
- [27] Kuwabata S, Takahashi N, Hirao S, Yoneyama H. Light image formations on deprotonated polyaniline films containing titania particles. *Chem Mater* 1993;5:437–41.
- [28] Ferreira C, Domenech S, Lacaze P. Synthesis and characterization of polypyrrole/TiO<sub>2</sub> composites on mild steel. *J Appl Electrochem* 2001;31:49–56.
- [29] Lenz D, Delamar M, Ferreira C. Application of polypyrrole/TiO<sub>2</sub> composite films as corrosion protection of mild steel. *J Electroanal Chem* 2003;540:35–44.
- [30] Liu YC, Huang JM, Tsai CE, Chuang TC, Wang CC. Effect of TiO<sub>2</sub> nanoparticles on the electropolymerization of polypyrrole. *Chem Phys Lett* 2004;387:155–9.

- [31] Ilieva M, Ivanov S, Tsakova V. Electrochemical synthesis and characterization of TiO<sub>2</sub>-polyaniline composite layers. *J Appl Electrochem* 2007;38:63–9.
- [32] Zubillaga O, Cano FJ, Azkarate I, Molchan IS, Thompson GE, Skeldon P. Synthesis of anodic films in the presence of aniline and TiO<sub>2</sub> nanoparticles on AA2024-T3 aluminium alloy. *Thin Solid Films* 2009;517:6742–6.
- [33] Latonen RM, Meana Esteban B, Kvarnström C, Ivaska A. Electrochemical polymerization and characterization of a poly(azulene)-TiO<sub>2</sub> nanoparticle composite film. *J Appl Electrochem* 2008;39:653–61.
- [34] Wei H, Yan X, Li Y, Gu H, Wu S, Ding K, Wei S, Guo Z. Electrochromic poly(DNTD)/WO<sub>3</sub> nanocomposite films via electropolymerization. *J Phys Chem C* 2012;116:16286–93.
- [35] Rincón M, Hu H, Martínez G. Effect of Bi<sub>2</sub>S<sub>3</sub> nanoparticles in the protection mechanism of polypyrrole thin films. *Synth Met* 2003;139:63–9.
- [36] Rincon M, Hu H, Martínez G, Suarez R, Banuelos JG. Bi<sub>2</sub>S<sub>3</sub> nanoparticles in polypyrrole thin films electropolymerized on chemically deposited bismuth sulfide electrodes: synthesis and characterization. *Sol Energy Mater Sol Cells* 2003;77:239–54.
- [37] Yoneyama H, Tokuda M, Kuwabata S. Photo-induced electrochromic reactions of deprotonated polyaniline containing cadmium sulfide particles. *Electrochim Acta* 1994;39:1315–20.
- [38] Pethkar S, Patil R, Kher J, Vijayamohan K. Deposition and characterization of CdS nanoparticle/polyaniline composite films. *Thin Solid Films* 1999;349:105–9.
- [39] Madani A, Nessark B, Boukherroub R, Chehimi MM. Preparation and electrochemical behaviour of PPy–CdS composite films. *J Electroanal Chem* 2011;650:176–81.
- [40] Gaponik NP, Talapin DV, Rogach AL, Eychmüller A. Electrochemical synthesis of CdTe nanocrystal/polypyrrole composites for optoelectronic applications. *J Mater Chem* 2000;10:2163–6.
- [41] Garcia B, Lamzoudi A, Pillier F, Nguyen H, Le T, Deslouis C. Oxide/polypyrrole composite films for corrosion protection of iron. *J Electrochem Soc* 2002;149:B560–6.
- [42] Bidan G, Jarjayes O, Fruchart J, Hannecart E. New nanocomposites based on “tailor dressed” magnetic particles in a polypyrrole matrix. *Adv Mater* 1994;6:152–5.
- [43] Jarjayes O, Fries P, Bidan C. New nanocomposites of polypyrrole including  $\gamma$ -Fe<sub>2</sub>O<sub>3</sub> particles: electrical and magnetic characterizations. *Synth Met* 1995;69:343–4.
- [44] Pailleret A, Hien NTL, Thanh DTM, Deslouis C. Surface reactivity of polypyrrole/iron-oxide nanoparticles: electrochemical and CS-AFM investigations. *J Solid State Electrochem* 2007;11:1013–21.
- [45] Janáky C, Endrodi B, Berkesi O, Visy C. Visible-light-enhanced electrocatalytic activity of a polypyrrole/magnetite hybrid electrode toward the reduction of dissolved dioxygen. *J Phys Chem C* 2010;114:19338–44.
- [46] Bencsik G, Janáky C, Endrodi B, Visy C. Electrocatalytic properties of the polypyrrole/magnetite hybrid modified electrode towards the reduction of hydrogen peroxide in the presence of dissolved oxygen. *Electrochim Acta* 2012;73:53–8.
- [47] Song HM, Yoo DY, Hong SK, Kim JS, Cho WI, Mho SI. Electrochemical impedance analysis of V<sub>2</sub>O<sub>5</sub> and PEDOT composite film cathodes. *Electroanalysis* 2011;23:2094–102.
- [48] Kim Y, Ta Q, Dinh H, Aum PK, Yeo I, Cho II W, Mho S. Cyclic stability of electrochemically embedded nanobeam V<sub>2</sub>O<sub>5</sub> in polypyrrole films for Li battery cathodes. *J Electrochem Soc* 2011;158:A133–8.
- [49] Mahmoudian MR, Basirun WJ, Alias Y, Khorsand Zak A. Electrochemical characteristics of coated steel with poly(N-methyl pyrrole) synthesized in presence of ZnO nanoparticles. *Thin Solid Films* 2011;520:258–65.
- [50] Chaudhari S, Patil P. Use of poly(o-toluidine)/ZrO<sub>2</sub> nanocomposite coatings for the corrosion protection of mild steel. *J Appl Polym Sci* 2007;106:220–9.
- [51] Shallcross RC, D’Ambruoso GD, Korth BD, Hall HK, Zheng Z, Pyun J, Armstrong NR. Poly(3,4-ethylenedioxythiophene)-semiconductor nanoparticle composite thin films tethered to indium tin oxide substrates via electropolymerization. *J Am Chem Soc* 2007;129:11310–1.
- [52] Shallcross RC, D’Ambruoso GD, Pyun J, Armstrong NR. Photoelectrochemical processes in polymer-tethered CdSe nanocrystals. *J Am Chem Soc* 2010;132:2622–32.
- [53] Wei H, Yan X, Li Y, Wu S, Wang A, Wei S, Guo Z. Hybrid electrochromic fluorescent poly(DNTD)/CdSe/ZnS composite films. *J Phys Chem C* 2012;116:4500–10.
- [54] Nguyencong H, Elabbassi K, Gautier J, Chartier P. Oxygen reduction on oxide/polypyrrole composite electrodes: effect of doping anions. *Electrochim Acta* 2005;50:1369–76.
- [55] Janáky C, Kormányos A, Visy C. Magnetic hybrid modified electrodes, based on magnetite nanoparticle containing polyaniline and poly(3,4-ethylenedioxythiophene). *J Solid State Electrochem* 2011;15:2351–9.
- [56] Cong HN, de la Garza Guadarrama V, Gautier JL, Chartier P. Ni<sub>x</sub>Co<sub>3-x</sub>O<sub>4</sub> mixed valence oxide nanoparticles/polypyrrole composite electrodes for oxygen reduction. *J New Mater Electrochem Syst* 2002;40:35–40.
- [57] Herrasti P, Kulak AN, Bavykin DV, de Léon CP, Zekonyte J, Walsh FC. Electrodeposition of polypyrrole-titanate nanotube composites coatings and their corrosion resistance. *Electrochim Acta* 2011;56:1323–8.
- [58] Milliron D, Alivisatos A, Pitois C, Edder C, Frechet J. Electroactive surfactant designed to mediate electron transfer between CdSe nanocrystals and organic semiconductors. *Adv Mater* 2003;15:58–61.
- [59] Mitsumori M, Nakhado T, Fujihara H. Synthesis of chiral hybrid nanotubes of magnetite nanoparticles and conducting polymers. *Nanoscale* 2012;4:117–9.
- [60] Janáky C, Visy C, Berkesi O, Tombácz E. Conducting polymer-based electrode with magnetic behavior: electrochemical synthesis of poly(3-thiophene-acetic-acid)/magnetite nanocomposite thin layers. *J Phys Chem C* 2009;113:1352–8.
- [61] Granot E, Patolsky F, Willner I. Electrochemical assembly of a CdS semiconductor nanoparticle monolayer on surfaces: structural properties and photoelectrochemical applications. *J Phys Chem B* 2004;108:5875–81.
- [62] Yildiz HB, Tel-Vered R, Willner I. Solar cells with enhanced photocurrent efficiencies using oligoaniline-crosslinked Au/CdS nanoparticles arrays on electrodes. *Adv Funct Mater* 2008;18:3497–505.
- [63] Ovits O, Tel-Vered R, Baravik I, Wilner OI, Willner I. Photoelectrochemical cells based on bis-aniline-crosslinked CdS nanoparticle-carbon nanotube matrices associated with electrodes. *J Mater Chem* 2009;19:7650–65.
- [64] Roux S, Soler-Illia GJ, Demoustier-Champagne S, Audebert P, Sanchez C. Titania/polypyrrole hybrid nanocomposites built from in-situ generated organically functionalized nanoanatase building blocks. *Adv Mater* 2003;15:217–21.
- [65] Park Y, Taraneekar P, Park JY, Baba A, Fulghum T, Ponnappati R, Advincula RC. Hybrid CdSe nanoparticle-carbazole dendron boxes: electropolymerization and energy-transfer mechanism shift. *Adv Funct Mater* 2008;18:2071–8.
- [66] Frau AF, Park Y, Pernites RB, Advincula RC. Nanocomposite p-n junction polycarbazole CdSe/TiO<sub>2</sub> thin films on ITO via electrochemical crosslinking. *Macromol Mater Eng* 2012;297:875–86.
- [67] Okpalugo TIT, Papakonstantinou P, Murphy H, McLaughlin J, Brown NMD. High resolution XPS characterization of chemical functionalised MWCNTs and SWCNTs. *Carbon* 2005;43:153–61.
- [68] Chua CK, Pumera M. Covalent chemistry on graphene. *Chem Soc Rev* 2013;42:3222–33.
- [69] Oueiny C, Berlioz S, Perrin FX. Carbon nanotube-polyaniline composites. *Prog Polym Sci* 2013;39:707–48.
- [70] Santhosh P, Manesh K, Gopalan A, Lee K. Fabrication of a new polyaniline grafted multi-wall carbon nanotube modified electrode and its application for electrochemical detection of hydrogen peroxide. *Anal Chim Acta* 2006;575:32–8.
- [71] Zhu C, Zhai J, Wen D, Dong S. Graphene oxide/polypyrrole nanocomposites: one-step electrochemical doping, coating and synergistic effect for energy storage. *J Mater Chem* 2012;22:6300–6.
- [72] Nasybulin E, Cox M, Kymissis I, Levon K. Electrochemical codeposition of poly(thieno[3,2-b]thiophene) and fullerene: an approach to a bulk heterojunction organic photovoltaic device. *Synth Met* 2012;162:10–7.
- [73] Kim SY, Lee KH, Chin BD, Yu JW. Network structure organic photovoltaic devices prepared by electrochemical copolymerization. *Sol Energy Mater Sol Cells* 2009;93:129–35.
- [74] Wampler WA, Wei C, Rajeshwar K. Electrocomposites of polypyrrole and carbon black. *J Electrochem Soc* 1994;141:L13–5.
- [75] Wampler WA, Wei C, Rajeshwar K. Composites of polypyrrole and carbon black. 2. Electrolysis, characterization and influence of carbon black characteristics. *Chem Mater* 1995;7:585–92.
- [76] Hu L, Tu J, Jiao S, Hou J, Zhu H, Fray DJ. In situ electrochemical polymerization of a nanorod-PANI-graphene composite in a reverse

- micelle electrolyte and its application in a supercapacitor. *Phys Chem Chem Phys* 2012;14:15652–6.
- [77] Österholm A, Lindfors T, Kauppila J, Damlin P, Kvarnström C. Electrochemical incorporation of graphene oxide into conducting polymer films. *Electrochim Acta* 2012;83:463–70.
- [78] Zhang L, Li C, Liu A, Shi G. Electrosynthesis of graphene oxide/polypyrrole composite films and their applications for sensing organic vapors. *J Mater Chem* 2012;22:8438–43.
- [79] Scott CL, Zhao G, Pumeras M. Stacked graphene nanofibers doped polypyrrole nanocomposites for electrochemical sensing. *Electrochem Commun* 2010;12:1788–91.
- [80] Liu A, Li C, Bai H, Shi G. Electrochemical deposition of polypyrrole/sulfonated graphene composite films. *J Phys Chem C* 2010;114:22783–9.
- [81] Si P, Chen HL, Kannan P, Kim DH. Selective and sensitive determination of dopamine by composites of polypyrrole and graphene modified electrodes. *Analyst* 2011;136:5134–8.
- [82] Guo D, Li H. Well-dispersed multi-walled carbon nanotube/polyaniline composite films. *J Solid State Electrochem* 2005;9:445–9.
- [83] Peng C, Jin J, Chen GZ. A comparative study on electrochemical co-deposition and capacitance of composite films of conducting polymers and carbon nanotubes. *Electrochim Acta* 2007;53:525–37.
- [84] Lota K, Khomenko V, Frackowiak E. Capacitance properties of poly(3,4-ethylenedioxythiophene)/carbon nanotubes composites. *J Phys Chem Solids* 2004;65:295–301.
- [85] Bhandari S, Deepa M, Srivastava AK, Lal C, Kant R. Poly(3,4-ethylenedioxythiophene) (PEDOT)-coated MWCNTs tethered to conducting substrates: facile electrochemistry and enhanced coloring efficiency. *Macromol Rapid Commun* 2008;29:1959–64.
- [86] Bhandari S, Deepa M, Srivastava AK, Joshi AG, Kant R. Poly(3,4-ethylenedioxythiophene)-multiwalled carbon nanotube composite films: structure-directed amplified electrochromic response and improved redox activity. *J Phys Chem B* 2009;113:9416–28.
- [87] Mousavi Z, Bobacka J, Lewenstam A, Ivaska A. Poly(3,4-ethylenedioxythiophene) (PEDOT) doped with carbon nanotubes as ion-to-electron transducer in polymer membrane-based potassium ion-selective electrodes. *J Electroanal Chem* 2009;633:246–52.
- [88] Luo X, Weaver CL, Zhou DD, Greenberg R, Cui XT. Highly stable carbon nanotube doped poly(3,4-ethylenedioxythiophene) for chronic neural stimulation. *Biomaterials* 2011;32:5551–7.
- [89] Chen G, Shaffer M, Coleby D, Dixon G, Zhou W, Fray DJ, Windle AH. Carbon nanotube and polypyrrole composites: coating and doping. *Adv Mater* 2000;12:522–6.
- [90] Hughes M, Chen G, Shaffer M, Fray DJ, Windle AH. Electrochemical capacitance of a nanoporous composite of carbon nanotubes and polypyrrole. *Chem Mater* 2002;14:1610–3.
- [91] Wang J, Musameh M. Carbon-nanotubes doped polypyrrole glucose biosensor. *Anal Chim Acta* 2005;539:209–13.
- [92] Zhang X, Zhang J, Liu Z. Conducting polymer/carbon nanotube composite films made by in situ electropolymerization using an ionic surfactant as the supporting electrolyte. *Carbon* 2005;43:2186–91.
- [93] Hughes M, Chen GZ, Shaffer MSP, Fray DJ, Windle AH. Controlling the nanostructure of electrochemically grown nanoporous composites of carbon nanotubes and conducting polymers. *Compos Sci Technol* 2004;64:2325–31.
- [94] Wei P, Tanabe H. Synergy effects between single-walled carbon nanotubes and polypyrrole on the electrocatalysis of their composites for the oxygen reduction reaction. *Carbon* 2011;49:4877–89.
- [95] Huang J, Li X, Xu J, Li H. Well-dispersed single-walled carbon nanotube/polyaniline composite films. *Carbon* 2003;41:2731–6.
- [96] Wei D, Kvarnstrom C, Lindfors T, Ivaska A. Electrochemical functionalization of single walled carbon nanotubes with polyaniline in ionic liquids. *Electrochem Commun* 2007;9:206–10.
- [97] Intelmann CM, Syrjitski V, Tsankov D, Hinrichs K, Rappich J. Ultrathin polypyrrole films on silicon substrates. *Electrochim Acta* 2008;53:4046–50.
- [98] Aydoğan Ş, Sağlam M, Türüt A. Current–voltage and capacitance–voltage characteristics of polypyrrole/p-InP structure. *Vacuum* 2005;77:269–74.
- [99] Wang X, Shi G, Liang Y. Low potential electropolymerization of thiophene at a copper oxide electrode. *Electrochem Commun* 1999;1:536–9.
- [100] Bahloul A, Nessark B, Chelali NE, Groult H, Mauger A, Julien CM. New composite cathode material for Zn/MnO<sub>2</sub> cells obtained by electro-deposition of polybithiophene on manganese dioxide particles. *Solid State Ionics* 2011;204–205:53–60.
- [101] Bahloul A, Nessark B, Habelhames F, Julien CM. Preparation and characterization of polybithiophene/β-MnO<sub>2</sub> composite electrode for oxygen reduction. *Ionics* 2010;17:239–46.
- [102] Idla K, Inganäs O, Strandberg M. Good adhesion between chemically oxidised titanium and electrochemically deposited polypyrrole. *Electrochim Acta* 2000;45:2121–30.
- [103] Cong HN, Sene C, Chartier P. Cadmium sulfide thickness effect on the photoresponse of the CdS spray/poly(3-methylthiophene) solid state junction. *Sol Energy Mater Sol Cells* 1993;29:209–19.
- [104] Cong HN, Dieng M, Sene C, Chartier P. Hybrid organic–inorganic solar cells: case of the all thin film PMeT(Y)/CdS(X) junctions. *Sol Energy Mater Sol Cells* 2000;63:23–35.
- [105] Dhawale DS, Dubal DP, Jamadade VS, Salunkhe RR, Joshi SS, Lokhande CD. Room temperature LPG sensor based on n-CdS/p-polyaniline heterojunction. *Sens Actuators B* 2010;145:205–10.
- [106] Chartier P, Cong HN, Sene C. Hybrid organic–inorganic photovoltaic junctions: case of the all thin-film CdSe/poly(3-methylthiophene) junction. *Sol Energy Mater Sol Cells* 1998;52:413–21.
- [107] Joshi SS, Gujar TP, Shinde VR, Lokhande CD. Fabrication of n-CdTe/p-polyaniline heterojunction-based room temperature LPG sensor. *Sens Actuators B* 2008;132:349–55.
- [108] Gamboa SA, Sebastian PJ, Mathew X, Nguyen-Cong H, Chartier P. A CdTe/PMeT photovoltaic structure formed by electrodeposition and processing. *Sol Energy Mater Sol Cells* 1999;59:115–24.
- [109] Patil SV, Deshmukh PR, Lokhande CD. Fabrication and liquefied petroleum gas (LPG) sensing performance of p-polyaniline/n-PbS heterojunction at room temperature. *Sens Actuators B* 2011;156:450–5.
- [110] Bereznev S, Konovalov I, Öpik A, Kois J, Mellikov E. Hybrid copper–indium disulfide/polypyrrole photovoltaic structures prepared by electrodeposition. *Sol Energy Mater Sol Cells* 2005;87:197–206.
- [111] Bereznev S, Kois J, Golovtsov I, Öpik A, Mellikov E. Electrodeposited (Cu–In–Se)/polypyrrole PV structures. *Thin Solid Films* 2006;511–512:425–9.
- [112] Cai L, Liu X, Wang L, Liu B. Iodine-free organic dye sensitized solar cells with in situ polymerized hole transporting material from alkoxy-substituted TriEDOT. *Polym Bull* 2011;68:1857–65.
- [113] Min HS, Park BY, Taherabadi L, Wang C, Yeh Y, Zaouk R, Madou MJ, Dunn B. Fabrication and properties of a carbon/polypyrrole three-dimensional microbattery. *J Power Sources* 2008;178:795–800.
- [114] Wang D, Li F, Zhao J, Ren W, Chen Z, Tan J, Wu ZS, Gentle I, Lu GQ, Cheng HM. Fabrication of graphene/polyaniline composite paper via in situ anodic electropolymerization for high-performance flexible electrode. *ACS Nano* 2009;3:1745–52.
- [115] Chen K, Chen L, Chen Y, Bai H, Li L. Three-dimensional porous graphene-based composite materials: electrochemical synthesis and application. *J Mater Chem* 2012;22:20968–76.
- [116] Xue M, Li F, Zhu J, Song H, Zhang M, Cao T. Structure-based enhanced capacitance: in situ growth of highly ordered polyaniline nanorods on reduced graphene oxide patterns. *Adv Funct Mater* 2012;22:1284–90.
- [117] Davies A, Audette P, Farrow B, Hassan F, Chen Z, Choi JY, Yu A. Graphene-based flexible supercapacitors: pulse-electropolymerization of polypyrrole on free-standing graphene films. *J Phys Chem C* 2011;115:17612–20.
- [118] Zhang S, Shao Y, Liu J, Aksay IA, Lin Y. Graphene-polypyrrole nanocomposite as a highly efficient and low cost electrically switched ion exchanger for removing ClO<sub>4</sub><sup>-</sup> from wastewater. *ACS Appl Mater Interfaces* 2011;3:3633–7.
- [119] Qu L, Liu J, Wang Z, Zhao Y, Cheng H, Hu C, Jiang L, Qu L. Three-dimensional graphene/polypyrrole hybrid electrochemical actuator. *Nanoscale* 2012;4:7563–8.
- [120] Song Y, Xu JL, Liu XX. Electrochemical anchoring of dual doping polypyrrole on graphene sheets partially exfoliated from graphite foil for high-performance supercapacitor electrode. *J Power Sources* 2014;249:48–58.
- [121] Lin Y, Cui X. Electrosynthesis, characterization, and application of novel hybrid materials based on carbon nanotube–polyaniline–nickel hexacyanoferrate nanocomposites. *J Mater Chem* 2006;16:585–92.
- [122] Zhang H, Cao G, Wang Z, Yang Y, Shi Z, Gu Z. Tube-covering-tube nanostructured polyaniline/carbon nanotube array composite electrode with high capacitance and superior rate performance as well as good cycling stability. *Electrochem Commun* 2008;10:1056–9.
- [123] Zhang H, Cao G, Wang W, Yuan K, Xu B, Zhang W, Cheng J, Yang Y. Influence of microstructure on the capacitive performance

- of polyaniline/carbon nanotube array composite electrodes. *Electrochim Acta* 2009;54:1153–9.
- [124] Chen Y, Gao H, Luo Y. Coaxial carbon nanotube–polythiophene core–shell nanowire for efficient hole transport in heterojunction photovoltaic device. *Appl Phys Lett* 2011;99:143309/1–3.
- [125] Xiao Y, Lin JY, Tai SY, Chou SW, Yue G, Wu J. Pulse electropolymerization of high performance PEDOT/MWCNT counter electrodes for Pt-free dye-sensitized solar cells. *J Mater Chem* 2012;22:19919–25.
- [126] Agui L, Penafaral C, Yanezsedeno P, Pingarron J. Poly-(3-methylthiophene)/carbon nanotubes hybrid composite-modified electrodes. *Electrochim Acta* 2007;52:7946–52.
- [127] Gao M, Huang S, Dai L, Wallace G, Gao R, Wang Z. Aligned coaxial nanowires of carbon nanotubes sheathed with conducting polymers. *Angew Chem Int Ed* 2000;112:3810–3.
- [128] Fang Y, Liu J, Yu DJ, Wickstedt JP, Kalkan K, Topal CO, Flanders BN, Wu J, Li J. Self-supported supercapacitor membranes: polypyrrole-coated carbon nanotube networks enabled by pulsed electrodeposition. *J Power Sources* 2010;195:674–9.
- [129] Hu Y, Zhao Y, Li Y, Li H, Shao H, Qu L. Defective super-long carbon nanotubes and polypyrrole composite for high-performance supercapacitor electrodes. *Electrochim Acta* 2012;66:279–86.
- [130] Baibarac M, Lira-Cantú M, Oró-Solé J, Casañ-Pastor N, Gomez-Romero P. Electrochemically functionalized carbon nanotubes and their application to rechargeable lithium batteries. *Small* 2006;2:1075–82.
- [131] Baibarac M, Lira-Cantú M, Oró Sol J, Baltog I, Casañ-Pastor N, Gomez-Romero P. Poly(N-vinyl carbazole) and carbon nanotubes based composites and their application to rechargeable lithium batteries. *Compos Sci Technol* 2007;67:2556–63.
- [132] Fan LZ, Hu YS, Maier J, Adelhelm P, Smarsly B, Antonietti M. High electroactivity of polyaniline in supercapacitors by using a hierarchically porous carbon monolith as a support. *Adv Funct Mater* 2007;17:3083–7.
- [133] Moghaddam RB, Pickup PG. Electrochemical impedance study of the polymerization of pyrrole on high surface area carbon electrodes. *Phys Chem Chem Phys* 2010;12:4733–41.
- [134] Baibarac M, Baltog I, Godon C, Lefrant S, Chauvet O. Covalent functionalization of single-walled carbon nanotubes by aniline electrochemical polymerization. *Carbon* 2004;42:3143–52.
- [135] Gupta V, Miura N. Polyaniline/single-wall carbon nanotube (PANI/SWCNT) composites for high performance supercapacitors. *Electrochim Acta* 2006;52:1721–6.
- [136] Niu Z, Luan P, Shao Q, Dong H, Li J, Chen J, Zhao D, Cai L, Zhou W, Chen X, Xie S. A “skeleton/skin” strategy for preparing ultrathin free-standing single-walled carbon nanotube/polyaniline films for high performance supercapacitor electrodes. *Energy Environ Sci* 2012;5:8726–33.
- [137] Ertas M, Walczak RM, Das RK, Rinzler AG, Reynolds JR. Supercapacitors based on polymeric dioxyppyroles and single walled carbon nanotubes. *Chem Mater* 2012;24:433–43.
- [138] Patel RJ, Tighe TB, Ivanov IN, Hickner MA. Electro-optical properties of electropolymerized poly(3-hexylthiophene)/carbon nanotube composite thin films. *J Polym Sci B Polym Phys* 2011;49:1269–75.
- [139] Mukai K, Yamato K, Asaka K, Hata K, Oike H. Actuator of double layer film composed of carbon nanotubes and polypyrroles. *Sens Actuators B* 2012;161:1010–7.
- [140] Baibarac M, Baltog I, Lefrant S. Raman spectroscopic evidence for interfacial interactions in poly(bithiophene)/single-walled carbon nanotube composites. *Carbon* 2009;47:1389–9138.
- [141] Lin YJ, Wang L, Chiu WY. Novel poly(3-methylthiophene)-TiO<sub>2</sub> hybrid materials for photovoltaic cells. *Thin Solid Films* 2006;511–512:199–202.
- [142] Ma L, Li Y, Yu X, Yang Q, Noh CH. Using room temperature ionic liquid to fabricate PEDOT/TiO<sub>2</sub> nanocomposite electrode-based electrochromic devices with enhanced long-term stability. *Sol Energy Mater Sol Cells* 2008;92:1253–9.
- [143] Latonen RM, Kvarnström C, Ivaska A. Electrochemical preparation of oligo(azulene) on nanoporous TiO<sub>2</sub> and characterization of the composite layer. *J Appl Electrochem* 2010;40:1583–91.
- [144] Wu CT, Chen PY, Chen JG, Suryanarayanan V, Ho KC. Detection of nicotine based on molecularly imprinted TiO<sub>2</sub>-modified electrodes. *Anal Chim Acta* 2009;633:119–26.
- [145] Yoon JH, Kim DM, Yoon SS, Won MS, Shim YB. Comparison of solar cell performance of conducting polymer dyes with different functional groups. *J Power Sources* 2011;196:8874–80.
- [146] Cecchet F, Bignozzi CA, Paolucci F, Marcaccio M. Electrochemical and electrochromic investigation of poly-bithiophene films on a mesoporous TiO<sub>2</sub> surface. *Synth Met* 2006;156:27–31.
- [147] Hao Y, Yang M, Li W, Qiao X, Zhang L, Cai S. A photoelectrochemical solar cell based on ZnO/dye/polypyrrole film electrode as photoanode. *Sol Energy Mater Sol Cells* 2000;60:349–59.
- [148] O'Regan B, Grätzel M. A low-cost, high-efficiency solar cell based on dye-sensitized colloidal TiO<sub>2</sub> films. *Nature* 1991;353:737–40.
- [149] Xi D, Zhang H, Furst S, Chen B, Pei Q. Electrochemical synthesis and photovoltaic property of cadmium sulfide–polybithiophene interdigitated nanohybrid thin films. *J Phys Chem C* 2008;112:19765–9.
- [150] Elzanowska H, Miasek E, Birss VI. Electrochemical formation of Ir oxide/polyaniline composite films. *Electrochim Acta* 2008;53:2706–15.
- [151] Chen X, Li C, Grätzel M, Kostecki R, Mao SS. Nanomaterials for renewable energy production and storage. *Chem Soc Rev* 2012;41:7909–37.
- [152] De Tacconi NR, Chenthamarakshan C, Yogeewaran G, Watcharenwong A, de Zoysa R, Basit N, Rajeshwar K. Nanoporous TiO<sub>2</sub> and WO<sub>3</sub> films by anodization of titanium and tungsten substrates: influence of process variables on morphology and photoelectrochemical response. *J Phys Chem B* 2006;110:25347–55.
- [153] Roy P, Berger S, Schmuki P. TiO<sub>2</sub> nanotubes: synthesis and applications. *Angew Chem Int Ed* 2011;50:2904–39.
- [154] Xia X, Chao D, Qi X, Xiong Q, Zhang Y, Tu J, Zhang H, Fan HJ. Controllable growth of conducting polymers shell for constructing high-quality organic/inorganic core/shell nanostructures and their optical-electrochemical properties. *Nano Lett* 2013;13:4562–8.
- [155] Velazquez JM, Gaikwad AV, Rout TK, Rzaevy J, Banerjee S. A substrate-integrated and scalable templated approach based on rusted steel for the fabrication of polypyrrole nanotube arrays. *ACS Appl Mater Interfaces* 2011;3:1238–44.
- [156] Mariani G, Wang Y, Wong PS, Lech A, Hung CH, Shapiro J, Prikhodko S, El-Kady M, Kaner RB, Huffaker DL. Three-dimensional core–shell hybrid solar cells via controlled in situ materials engineering. *Nano Lett* 2012;12:3581–6.
- [157] Babakhani B, Ivey DG. Improved capacitive behavior of electrochemically synthesized Mn oxide/PEDOT electrodes utilized as electrochemical capacitors. *Electrochim Acta* 2010;55:4014–24.
- [158] Bahloul A, Nessark B, Briot E, Groult H, Mauger A, Zaghbi K, Julien CM. Polypyrrole-covered MnO<sub>2</sub> as electrode material for supercapacitor. *J Power Sources* 2013;240:267–72.
- [159] Xia XH, Tu JP, Zhang J, Wang XL, Zhang WK, Huang H. A highly porous NiO/polyaniline composite film prepared by combining chemical bath deposition and electro-polymerization and its electrochromic performance. *Nanotechnology* 2008;19, 465701/1–7.
- [160] Xia XH, Tu JP, Zhang J, Huang XH, Wang XL, Zhang WK, Huang H. Multicolor and fast electrochromism of nanoporous NiO/poly(3,4-ethylenedioxythiophene) composite thin film. *Electrochem Commun* 2009;11:702–5.
- [161] Huang XH, Tu JP, Xia XH, Wang XL, Xiang JY, Zhang L. Porous NiO/poly(3,4-ethylenedioxythiophene) films as anode materials for lithium ion batteries. *J Power Sources* 2010;195:1207–10.
- [162] Nam HS, Kim KM, Kim SH, Kim BC, Wallace GG, Ko JM. Supercapacitive properties of polyaniline/hydrous RuO<sub>2</sub> composite electrode. *Polym Bull* 2011;68:553–60.
- [163] Concepción Arenas M, Hu H, Antonio del Río J, Sánchez A, Nicho ME. Electrical properties of porous silicon/polypyrrole heterojunctions. *Sol Energy Mater Sol Cells* 2006;90:2413–20.
- [164] Harraz FA, Salem MS, Sakka T, Ogata YH. Hybrid nanostructure of polypyrrole and porous silicon prepared by galvanostatic technique. *Electrochim Acta* 2008;53:3734–40.
- [165] Peng X, Huo K, Fu J, Zhang X, Gao B, Chu PK. Coaxial PANI/TiN/PANI nanotube arrays for high-performance supercapacitor electrodes. *Chem Commun* 2013;49:10172–4.
- [166] Li X, Teng W, Zhao Q, Wang L. Efficient visible light-induced photoelectrocatalytic degradation of rhodamine B by polyaniline-sensitized TiO<sub>2</sub> nanotube arrays. *J Nanopart Res* 2011;13:6813–20.
- [167] Su L, Gan YX. Experimental study on synthesizing TiO<sub>2</sub> nanotube/polyaniline (PANI) nanocomposites and their thermoelectric and photosensitive property characterization. *Composites B* 2012;43:170–82.
- [168] Cai G, Tu J, Zhou D, Zhang J, Xiong Q, Zhao X, Guo Z. Multicolor electrochromic film based on TiO<sub>2</sub>@polyaniline core/shell nanorod array. *J Phys Chem C* 2013;117:15967–75.
- [169] Yu M, Zeng Y, Zhang C, Lu X, Zeng C, Yao C, Yang Y, Tong Y. Titanium dioxide@polypyrrole core–shell nanowires for all solid-state flexible supercapacitors. *Nanoscale* 2013;5:10806–10.
- [170] Shi H, Zhao G, Liu M, Zhu Z. A novel photoelectrochemical sensor based on molecularly imprinted polymer modified TiO<sub>2</sub> nanotubes and its highly selective detection of 2,4-dichlorophenoxyacetic acid. *Electrochem Commun* 2011;13:1404–7.

- [171] Kowalski D, Schmuki P. Polypyrrole self-organized nanopore arrays formed by controlled electropolymerization in TiO<sub>2</sub> nanotube template. *Chem Commun* 2010;46:8585–7.
- [172] Kowalski D, Tighineanu A, Schmuki P. Polymer nanowires or nanopores? Site selective filling of titania nanotubes with polypyrrole. *J Mater Chem* 2011;21:17909–15.
- [173] Jia Y, Xiao P, He H, Yao J, Liu F, Wang Z, Li Y. Photoelectrochemical properties of polypyrrole/TiO<sub>2</sub> nanotube arrays nanocomposite under visible light. *Appl Surf Sci* 2012;258:6627–31.
- [174] Dzięwoński PM, Grzeszczuk M. Towards TiO<sub>2</sub>-conducting polymer hybrid materials for lithium ion batteries. *Electrochim Acta* 2010;55:3336–47.
- [175] Kowalski D, Schmuki P. Advanced geometries of PEDOT formed in titania nanotubes. *ChemPhysChem* 2012;13:3790–3.
- [176] Kowalski D, Albu SP, Schmuki P. Current dependent formation of PEDOT inverse nanotube arrays. *RSC Adv* 2013;3:2154–7.
- [177] Wang D, Liu Y, Wang C, Zhou F, Liu W. Highly flexible coaxial nanohybrids made from porous TiO<sub>2</sub> nanotubes. *ACS Nano* 2009;3:1249–57.
- [178] Pang Y, Li X, Shi G, Wang F, Jin L. Electrochromic properties of poly(3-chlorothiophene) film electrodeposited on a nanoporous TiO<sub>2</sub> surface via a room temperature ionic liquid and its application in an electrochromic device. *Thin Solid Films* 2008;516:6512–6.
- [179] Liang H, Li X. Visible-induced photocatalytic reactivity of polymer-sensitized titania nanotube films. *Appl Catal B Environ* 2009;86:8–17.
- [180] Janáky C, de Tacconi NR, Chanmanee W, Rajeshwar K. Electrodeposited polyaniline in a nanoporous WO<sub>3</sub> matrix: an organic/inorganic hybrid exhibiting both p- and n-type photoelectrochemical activity. *J Phys Chem C* 2012;116:4234–42.
- [181] Döbbelin M, Tena-Zaera R, Carrasco PM, Sarasua JR, Cabañero G, Mecerreyes D. Electrochemical synthesis of poly(3,4-ethylenedioxythiophene) nanotube arrays using ZnO templates. *J Polym Sci A Polym Chem* 2010;48:4648–53.
- [182] Wang ZL, Guo R, Li GR, Lu HL, Liu ZQ, Xiao FM, Zhang M, Tong YX. Polyaniline nanotube arrays as high-performance flexible electrodes for electrochemical energy storage devices. *J Mater Chem* 2012;22:2401–4.
- [183] Tang Q, Lin L, Zhao X, Huang K, Wu J. p–n heterojunction on ordered ZnO nanowires/polyaniline microrods double array. *Langmuir* 2012;28:3972–8.
- [184] Hao Y, Pei J, Wei Y, Cao Y, Jiao S, Zhu F, Li J, Xu D. Efficient semiconductor-sensitized solar cells based on poly(3-hexylthiophene)/CdSe@ZnO core-shell nanorod arrays. *J Phys Chem C* 2010;114:8622–5.
- [185] Sun B, Hao Y, Guo F, Cao Y, Zhang Y, Li Y, Xu D. Fabrication of poly(3-hexylthiophene)/CdSe/ZnO core-shell nanotube array for semiconductor-sensitized solar cell. *J Phys Chem C* 2012;116:1395–400.
- [186] Mohan Kumar G, Raman V, Kawakita J, Ilanchezhiyan P, Jayavel R. Fabrication of polypyrrole/ZnCoO nanohybrid systems for solar cell applications. *Dalton Trans* 2010;39:8325–30.
- [187] Kateb M, Ahmadi V, Mohseni M. Fast switching and high contrast electrochromic device based on PEDOT nanotube grown on ZnO nanowires. *Sol Energy Mater Sol Cells* 2013;112:57–64.
- [188] Janáky C, de Tacconi N, Chanmanee W, Rajeshwar K. Conjugated polymers and oxide nanoarchitectures into intimate contact: light induced electrodeposition of polypyrrole and polyaniline on nanoporous WO<sub>3</sub> or TiO<sub>2</sub>. *J Phys Chem C* 2012;116:19145–55.
- [189] Feng W, Wan AS, Garfunkel E. Interfacial bonding and morphological control of electropolymerized polythiophene films on ZnO. *J Phys Chem C* 2013;117:9852–63.
- [190] Sakmeche N, Aeiayach S, Aaron J, Jouini M, Lacroix J, Lacaze P. Improvement of the electrocatalysis and physicochemical properties of poly(3,4-ethylenedioxythiophene) using a sodium dodecyl sulfate micellar aqueous medium. *Langmuir* 1999;15:2566–74.
- [191] Zhang Z, Yuan Y, Liang L, Cheng Y, Xu H, Shi G, Jin L. Preparation and photoelectrochemical properties of a hybrid electrode composed of polypyrrole encapsulated in highly ordered titanium dioxide nanotube array. *Thin Solid Films* 2008;516:8663–7.
- [192] Xie Y, Du H. Electrochemical capacitance performance of polypyrrole–titania nanotube hybrid. *J Solid State Electrochem* 2012;16:2683–9.
- [193] Debienne-Chouvy C, Tran TTM. An insight into the overoxidation of polypyrrole materials. *Electrochem Commun* 2008;10:947–50.
- [194] Tóth PS, Janáky C, Berkesi O, Tamm T, Visy C. On the unexpected cation exchange behavior, caused by covalent bond formation between PEDOT and Cl<sup>-</sup> ions: extending the conception for the polymer–dopant interactions. *J Phys Chem B* 2012;116:5491–500.
- [195] Janáky C, Bencsik G, Rácz A, Visy C, de Tacconi NR, Chanmanee W, Rajeshwar K. Electrochemical grafting of poly(3,4-ethylenedioxythiophene) into a titanium dioxide nanotube host network. *Langmuir* 2010;26:13697–702.
- [196] Bella F, Bongiovanni R. Photoinduced polymerization: an innovative, powerful and environmentally friendly technique for the preparation of polymer electrolytes for dye-sensitized solar cells. *J Photochem Photobiol C* 2013;16:1–21.
- [197] Noufi R, Frank AJ, Nozik AJ. Stabilization of n-type silicon photoelectrodes to surface oxidation in aqueous electrolyte solution and mediation of oxidation reaction by surface attached organic conducting polymer. *J Am Chem Soc* 1981;103:1849–50.
- [198] Fan FRF, Wheeler BL, Bard AJ, Noufi R. Semiconductor electrodes: XXXIX. Techniques for stabilization of n-silicon electrodes in aqueous solution photoelectrochemical cells. *J Electrochem Soc* 1981;128:2042–5.
- [199] Skotheim T, Lundstrom I, Prejza J. Stabilization of n-Si photoanodes to surface corrosion in aqueous electrolyte with a thin film of polypyrrole. *J Electrochem Soc* 1981;128:1625–6.
- [200] Noufi R, Tench D, Warren LF. Protection of n-GaAs photoanodes with photoelectrochemically generated polypyrrole films. *J Electrochem Soc* 1980;127:2310–1.
- [201] Frank A, Honda K. Oxygen and hydrogen generation from water on polymer-protected CdS photoanodes. *J Electroanal Chem* 1983;150:673–8.
- [202] Frank A, Glenis S, Nelson A. Conductive polymer–semiconductor junction: characterization of poly(3-methylthiophene); cadmium sulfide based photoelectrochemical and photovoltaic cells. *J Phys Chem* 1989;38:18–25.
- [203] Horowitz G, Tourillon G, Garnier F. Protection of n-GaAs photoanodes by photoelectrochemical grafting of poly(3-methylthiophene) and poly(3,4-dimethylthiophene) films. *J Electrochem Soc* 1984;131:151–6.
- [204] Horowitz G, Garnier F. Polythiophene–GaAs p–n heterojunction solar cells. *Sol Energy Mater* 1986;13:47–55.
- [205] Kamat PV, Basheer R, Fox MA. Polymer-modified electrodes. Electrochemical and photoelectrochemical polymerization of 1-vinylpyrene. *Macromolecules* 1985;18:1367–71.
- [206] Bereznev S, Konovolov I, Öpik A, Kois J. Hybrid CuInS<sub>2</sub>/polypyrrole and CuInS<sub>2</sub>/poly(3,4-ethylenedioxythiophene) photovoltaic structures. *Synth Met* 2005;152:81–4.
- [207] Okano M, Itoh K, Fujishima A, Honda K. Generation of organic conducting patterns on semiconductors by photoelectrochemical polymerization of pyrrole. *Chem Lett* 1986:469–72.
- [208] Okano M, Itoh K, Fujishima A, Honda K. Photoelectrochemical polymerization of pyrrole on TiO<sub>2</sub> and its application to conducting pattern generation. *J Electrochem Soc* 1987;134:837–41.
- [209] Okano M, Kikuchi E, Itoh K, Fujishima A. Photoelectrochemical polymerization of pyrrole on ZnO and its application to conducting pattern generation. *J Electrochem Soc* 1988;135:1641–5.
- [210] Di Franco F, Bocchetta P, Santamaria M, Di Quarto F. Light induced electropolymerization of poly(3,4-ethylenedioxythiophene) on niobium oxide. *Electrochim Acta* 2010;56:737–44.
- [211] Di Quarto F, Figà V, Bocchetta P, Santamaria M. Photoelectrochemical synthesis of polypyrrole on anodic Ta<sub>2</sub>O<sub>5</sub> films. *Electrochem Solid-State Lett* 2007;10:H305–8.
- [212] Yang Z, Ni X. Photovoltaic hybrid films with polythiophene growing on monoclinic WO<sub>3</sub> semiconductor substrates. *Langmuir* 2012;28:4829–34.
- [213] Yildiz A, Sobczynski A, Bard A, Campion A, Fox MA, Mallouk TE, Webber SE, White JM. Sensitized polypyrrole-coated semiconducting powders as materials in photosystems for hydrogen generation. *Langmuir* 1989;5:148–9.
- [214] Fox MA, Worthen KL. Comparison of the physical properties of polypyrrole produced by anodic oxidation and by photoelectrochemical activation of TiO<sub>2</sub>. *Chem Mater* 1991;3:253–7.
- [215] Jarkov A, Bereznev S, Volobujeva O, Traksmaa R, Tverjanovich A, Öpik A, Mellikov E. Photo-assisted electrodeposition of polypyrrole back contact to CdS/CdTe solar cell structures. *Thin Solid Films* 2013;535:198–201.
- [216] Ramanavicius A, Karabanovas V, Ramanaviciene A, Rotomskis R. Stabilization of (CdSe)/ZnS quantum dots with polypyrrole formed by UV/Vis irradiation initiated polymerization. *J Nanosci Nanotechnol* 2009;9:1909–15.
- [217] Goubard F, Aubert PH, Boukerma K, Pauthe E, Chevrot C. Elaboration of nanohybrid materials by photopolymerisation of 3,4-ethylenedioxythiophene on TiO<sub>2</sub>. *Chem Commun* 2008;3139–41.

- [218] Weng Z, Ni X. Oxidative polymerization of pyrrole photocatalyzed by TiO<sub>2</sub> nanoparticles and interactions in the composites. *J Appl Polym Sci* 2008;110:109–16.
- [219] Zhang W, Cheng Y, Yin X, Liu B. Solid-state dye-sensitized solar cells with conjugated polymers as hole-transporting materials. *Macromol Chem Phys* 2011;212:15–23.
- [220] Heo JH, Im SH, Noh JH, Mandal TN, Lim CS, Chang JA, Lee YH, Kim HJ, Sarkar A, Nazeeruddin MK, Grätzel M, Seok S. Efficient inorganic–organic hybrid heterojunction solar cells containing perovskite compound and polymeric hole conductors. *Nat Photonics* 2013;7:486–91.
- [221] Wang J, Ni X. Photoresponsive polypyrrole-TiO<sub>2</sub> nanoparticles film fabricated by a novel surface initiated polymerization. *Solid State Commun* 2008;146:239–44.
- [222] Strandwitz NC, Nonoguchi Y, Boettcher SW, Stucky GD. In situ photopolymerization of pyrrole in mesoporous TiO<sub>2</sub>. *Langmuir* 2010;26:5319–22.
- [223] Takagi S, Makuta S, Veamatahau A, Otsuka Y, Tachibana Y. Organic/inorganic hybrid electrochromic devices based on photoelectrochemically formed polypyrrole/TiO<sub>2</sub> nanohybrid films. *J Mater Chem* 2012;22:22181–9.
- [224] Dehaut J, Beouch L, Peralta S, Plesse C, Aubert PH, Chevrot C, Goubard F. Facile route to prepare film of poly(3,4-ethylene dioxythiophene)-TiO<sub>2</sub> nanohybrid for solar cell application. *Thin Solid Films* 2011;519:1876–81.
- [225] Liu P, Yang HX, Ai XP, Li GR, Gao XP. A solar rechargeable battery based on polymeric charge storage electrodes. *Electrochem Commun* 2012;16:69–72.
- [226] Otsuka Y, Okamoto Y, Akiyama HY, Umekita K, Tachibana Y, Kuwabata S. Photoinduced formation of polythiophene/TiO<sub>2</sub> nanohybrid heterojunction films for solar cell applications. *J Phys Chem C* 2008;112:4767–75.
- [227] Sydorov D, Smertenko P, Piryatinski Y, Yoshida T, Pud A. Electrochemically assembled planar hybrid poly(3-methylthiophene)/ZnO nanostructured composites. *Electrochim Acta* 2012;81:83–9.
- [228] Senadeera R, Fukuri N, Saito Y, Kitamura T, Wada Y, Yanagida S. Volatile solvent-free solid-state polymer-sensitized TiO<sub>2</sub> solar cells with poly(3,4-ethylenedioxythiophene) as a hole-transporting medium. *Chem Commun* 2005;2259–61.
- [229] Rajeshwar K, Osugi ME, Chanmanee W, Chenthamarakshan CR, Zanon MVB, Kajitvichyanukul P, Krishnan-Ayer R. Heterogeneous photocatalytic treatment of organic dyes in air and aqueous media. *J Photochem Photobiol C* 2008;9:171–92.
- [230] Manseki K, Jareerboon W, Youhai Y, Jiang KJ, Suzuki K, Masaki N, Kim Y, Xia J, Yanagida S. Solid-state dye-sensitized solar cells fabricated by coupling photoelectrochemically deposited poly(3,4-ethylenedioxythiophene) (PEDOT) with silver-paint on cathode. *Chem Commun* 2011;47:3120.
- [231] Murakoshi K, Kogure R, Wada Y, Yanagida S. Solid state dye-sensitized TiO<sub>2</sub> solar cell with polypyrrole as hole transport layer. *Chem Lett* 1997:471–2.
- [232] Murakoshi K, Kogure R, Wada Y, Yanagida S. Fabrication of solid-state dye-sensitized TiO<sub>2</sub> solar cells combined with polypyrrole. *Sol Energy Mater Sol Cells* 1998;55:113–25.
- [233] Saito Y, Azechi T, Kitamura T, Hasegawa Y, Wada Y, Yanagida S. Photo-sensitizing ruthenium complexes for solid state dye solar cells in combination with conducting polymers as hole conductors. *Coord Chem Rev* 2004;248:1469–78.
- [234] Mozer AJ, Wada Y, Jiang KJ, Masaki N, Yanagida S, Mori SN. Efficient dye-sensitized solar cells based on a 2-thiophen-2-yl-vinyl-conjugated ruthenium photosensitizer and a conjugated polymer hole conductor. *Appl Phys Lett* 2006;89, 043509/1–3.
- [235] Caramori S, Cazzanti S, Marchini L, Argazzi R, Bignozzi CA, Martineau D, Gros PC, Beley M. Dye-sensitized solar cells based on PEDOP as a hole conductive medium. *Inorg Chim Acta* 2008;361:627–34.
- [236] Kim HS, Wamser CC. Photoelectropolymerization of aniline in a dye-sensitized solar cell. *Photochem Photobiol Sci* 2006;5:955–60.
- [237] Saito Y, Fukuri N, Sanadeera R, Kitamura T, Wada Y, Yanagida S. Solid state dye sensitized solar cells using in situ polymerized PEDOTs as hole conductor. *Electrochem Commun* 2004;6:71–4.
- [238] Yanagida S, Yu Y, Manseki K. Iodine/iodide-free dye-sensitized solar cells. *Acc Chem Res* 2009;42:1827–38.
- [239] Song IY, Park SH, Lim J, Kwon YS, Park T. A novel hole transport material for iodine-free solid state dye-sensitized solar cells. *Chem Commun* 2011;47:10395–7.
- [240] Liu X, Zhang W, Uchida S, Cai L, Liu B, Ramakrishna S. An efficient organic-dye-sensitized solar cell with in situ polymerized poly(3,4-ethylenedioxythiophene) as a hole-transporting material. *Adv Mater* 2010;22:E150–5.
- [241] Janáky C, Chanmanee W, Rajeshwar K. Mechanistic aspects of photoelectrochemical polymerization of polypyrrole on a TiO<sub>2</sub> nanotube array. *Electrochim Acta* 2014;122:303–9.
- [242] Fonseca L, Rinaldi A, Rubira A, Cotica L, Medeiros S, Paesano A, Santos IA, Girotto EM. Structural, magnetic, and electrochemical properties of poly(o-anisidine)/maghemite thin films. *Mater Chem Phys* 2006;97:252–5.
- [243] Prakash GKS, Suresh P, Viva F, Olah GA. Novel single step electrochemical route to  $\gamma$ -MnO<sub>2</sub> nanoparticle-coated polyaniline nanofibers: thermal stability and formic acid oxidation on the resulting nanocomposites. *J Power Sources* 2008;181:79–84.
- [244] Sun LJ, Liu XX. Electrodepositions and capacitive properties of hybrid films of polyaniline and manganese dioxide with fibrous morphologies. *Eur Polym J* 2008;44:219–24.
- [245] Sharma RK, Rastogi AC, Desu SB. Manganese oxide embedded polypyrrole nanocomposites for electrochemical supercapacitor. *Electrochim Acta* 2008;53:7690–5.
- [246] Zou W, Wang W, He B, Sun M, Yin Y. Supercapacitive properties of hybrid films of manganese dioxide and polyaniline based on active carbon in organic electrolyte. *J Power Sources* 2010;195:7489–93.
- [247] Liu R, Duay JW, Lee SB. Electrochemical formation mechanism for the controlled synthesis of heterogeneous MnO<sub>2</sub>/poly(3,4-ethylenedioxythiophene) nanowires. *ACS Nano* 2011;5:5608–19.
- [248] Duay J, Gillette E, Liu R, Lee SB. Highly flexible pseudocapacitor based on freestanding heterogeneous MnO<sub>2</sub>/conductive polymer nanowire arrays. *Phys Chem Chem Phys* 2012;14:3329–37.
- [249] Liu XX, Bian LJ, Zhang L, Zhang LJ. Composite films of polyaniline and molybdenum oxide formed by electrocodeposition in aqueous media. *J Solid State Electrochem* 2007;11:1279–86.
- [250] Peng X, Li W, Liu X, Hua P. Electrodeposition of NiO<sub>x</sub>/PANI composite film and its catalytic properties towards electrooxidations of polyhydroxyl compounds. *J Appl Polym Sci* 2007;105:2260–4.
- [251] Peng XY, Liu XX, Hua PJ, Diamond D, Lau KT. Electrochemical codeposition of nickel oxide and polyaniline. *J Solid State Electrochem* 2009;14:1–7.
- [252] Ehsani A, Mahjani MG, Jafarian M, Naemy A. Electrosynthesis of polypyrrole composite film and electrocatalytic oxidation of ethanol. *Electrochim Acta* 2012;71:128–33.
- [253] Shen PK, Huang HT, Tseung ACC. A study of tungsten trioxide and polyaniline composite films. *J Electrochem Soc* 1992;139:1840–5.
- [254] Zou BX, Liang Y, Liu XX, Diamond D, Lau KT. Electrodeposition and pseudocapacitive properties of tungsten oxide/polyaniline composite. *J Power Sources* 2011;196:4842–8.
- [255] Hepel M, Seymour E, Yogev D, Fendler JH. Electrochemical quartz crystal microbalance monitoring of cadmium sulfide generation in polypyrrole and polypyrrole-poly(styrenesulfonate) thin films. *Chem Mater* 1992;4:209–16.
- [256] Refczynska M, Mieczkowski J, Skompska M. Synthesis, characterization and photoelectrochemical properties of poly(3,4-dioxythiophene)-CdS hybrid electrodes. *Electrochim Acta* 2008;53:2984–93.
- [257] Arnel V, Winther-Jensen O, Kerr R, MacFarlane DR, Winther-Jensen B. Designed electrodeposition of nanoparticles inside conducting polymers. *J Mater Chem* 2012;22:19767–73.
- [258] Guascito M, Boffi P, Malitesta C. Conducting polymer electrodes modified by metallic species for electrocatalytic purposes – spectroscopic and microscopic characterization. *Mater Chem Phys* 1996;44:17–24.
- [259] Cioffi N, Torsi L, Losito I, Di Franco C, De Bari I, Chiavarone L, Scamarcio G, Tsakova V, Sabbatini L, Zamboni PG. Electrosynthesis and analytical characterisation of polypyrrole thin films modified with copper nanoparticles. *J Mater Chem* 2001;11:1434–40.
- [260] Xue T, Loo LS, Wang X, Kyu Kwak S, Lee JM. Electrodeposition of mesoporous bilayers of polyaniline supported Cu<sub>2</sub>O semiconductor films from lyotropic liquid crystalline phase. *Chem Eng Sci* 2012;80:452–9.
- [261] Andreoli E, Annibaldi V, Rooney DA, Breslin CB. Electrochemical fabrication of copper-based hybrid microstructures and mechanism of formation of related hierarchical structures on polypyrrole films. *J Phys Chem C* 2011;115:20076–83.
- [262] Du Z, Zhang S, Jiang T, Wu X, Zhang L, Fang H. Facile synthesis of SnO<sub>2</sub> nanocrystals coated conducting polymer nanowires for enhanced lithium storage. *J Power Sources* 2012;219:199–203.
- [263] Liu R, Duay J, Lane T, Lee SB. Synthesis and characterization of RuO<sub>2</sub>/poly(3,4-ethylenedioxythiophene) composite nanotubes for supercapacitors. *Phys Chem Chem Phys* 2010;12:4273–84.

- [264] Zhao D, Guo X, Gao Y, Gao F. An electrochemical capacitor electrode based on porous carbon spheres hybridized with polyaniline and nanoscale ruthenium oxide. *ACS Appl Mater Interfaces* 2012;4:5583–9.
- [265] Li X, Gan W, Zheng F, Li L, Zhu N, Huang X. Preparation and electrochemical properties of RuO<sub>2</sub>/polyaniline electrodes for supercapacitors. *Synth Met* 2012;162:953–7.
- [266] Prasad K, Miura N. Polyaniline–MnO<sub>2</sub> composite electrode for high energy density electrochemical capacitor. *Electrochem Solid-State Lett* 2004;7:A425–8.
- [267] Rios EC, Correa AA, Cristovan FH, Pocrifka LA, Rosario AV. Poly(3,4-ethylenedioxythiophene)/MnO<sub>2</sub> composite electrodes for electrochemical capacitors. *Solid State Sci* 2011;13:1978–83.
- [268] Rios EC, Rosario AV, Mello RMQ, Micaroni L. Poly(3-methylthiophene)/MnO<sub>2</sub> composite electrodes as electrochemical capacitors. *J Power Sources* 2007;163:1137–42.
- [269] Liu FJ. Electrodeposition of manganese dioxide in three-dimensional poly(3,4-ethylenedioxythiophene)–poly(styrene sulfonic acid)–polyaniline for supercapacitor. *J Power Sources* 2008;182:383–8.
- [270] Tang P, Zhao Y, Xu C. Step-by-step assembled poly(3,4-ethylenedioxythiophene)/manganese dioxide composite electrodes: tuning the structure for high electrochemical performance. *Electrochim Acta* 2013;89:300–9.
- [271] Lu SY, Lin IH. Characterization of polypyrrole–CdSe/CdTe nanocomposite films prepared with an all electrochemical deposition process. *J Phys Chem B* 2003;107:6974–8.
- [272] Lee S, Cho MS, Lee H, Nam JD, Lee Y. A facile synthetic route for well defined multilayer films of graphene and PEDOT via an electrochemical method. *J Mater Chem* 2012;22:1899–903.
- [273] Tang Y, Wu N, Luo S, Liu C, Wang K, Chen L. One-step electrodeposition to layer-by-layer graphene-conducting-polymer hybrid films. *Macromol Rapid Commun* 2012;33:1780–6.
- [274] Huynh WU, Dittmer JJ, Alivisatos P. Hybrid nanorod–polymer solar cells. *Science* 2002;295:2425–7.
- [275] Xu T, Qiao Q. Conjugated polymer–inorganic semiconductor hybrid solar cells. *Energy Environ Sci* 2011;4:2700–20.
- [276] Zhao L, Lin Z. Crafting semiconductor organic–inorganic nanocomposites via placing conjugated polymers in intimate contact with nanocrystals for hybrid solar cells. *Adv Mater* 2012;24:4353–68.
- [277] Nogueira AF, Longo C, De Paoli MA. Polymers in dye sensitized solar cells: overview and perspectives. *Coord Chem Rev* 2004;248:1455–68.
- [278] Liu X, Cheng Y, Wang L, Cai L, Liu B. Light controlled assembling of iodine-free dyesensitized solar cells with poly(3,4-ethylenedioxythiophene) as a hole conductor reaching 7.1% efficiency. *Phys Chem Chem Phys* 2012;14:7098–103.
- [279] Cells SDS, Burschka J, Dualé A, Kessler F, Baranoff E, Yi C, Nazeeruddin MK, Grätzel M. Tris(2-(1H-pyrazol-1-yl)pyridine)cobalt(III) as p-type dopant for organic semiconductors and its application in highly efficient solid-state dye-sensitized solar cells. *J Am Chem Soc* 2011;133:18042–5.
- [280] Im SH, Lim CS, Chang JA, Lee YH, Maiti N, Kim HJ, Nazeeruddin MDK, Grätzel M, Seok S. Toward interaction of sensitizer and functional moieties in hole-transporting materials for efficient semiconductor-sensitized solar cells. *Nano Lett* 2011;11:4789–93.
- [281] Kamat P. Quantum dot solar cells. The next big thing in photovoltaics. *J Phys Chem Lett* 2013;4:908–18.
- [282] Burschka J, Pellet N, Moon S-J, Humphry-Baker R, Gao P, Nazeeruddin MK, Grätzel M. Sequential deposition as a route to high-performance perovskite-sensitized solar cells. *Nature* 2013;499:316–9.
- [283] Park NG. Organometal perovskite light absorbers toward a 20% efficiency low-cost solid-state mesoscopic solar cell. *J Phys Chem Lett* 2013;4:2423–9.
- [284] Bi D, Yang L, Boschloo G, Hagfeldt A, Johansson EMJ. Effect of different hole transport materials on recombination in CH<sub>3</sub>NH<sub>3</sub>PbI<sub>3</sub> perovskite-sensitized mesoscopic solar cells. *J Phys Chem Lett* 2013;4:1532–6.
- [285] Lee W, Roh SJ, Hyung KH, Park J, Lee SH, Han SH. Photoelectrochemically polymerized polythiophene layers on ruthenium photosensitizers in dye-sensitized solar cells and their beneficial effects. *Sol Energy* 2009;83:690–5.
- [286] Lim I, Yoon SJ, Lee W, Nah YC, Shrestha NK, Ahn H, Han SH. Interfacially treated dye-sensitized solar cell with in situ photopolymerized iodine doped polythiophene. *ACS Appl Mater Interfaces* 2012;4:838–41.
- [287] Zhang J, Li X, Guo W, Hreid T, Hou J, Su H, Yuan Z. Electropolymerization of a poly(3,4-ethylenedioxythiophene) and functionalized, multi-walled, carbon nanotubes counter electrode for dye-sensitized solar cells and characterization of its performance. *Electrochim Acta* 2011;56:3147–52.
- [288] Guan G, Yang Z, Qiu L, Sun X, Zhang Z, Ren J, Peng H. Oriented PEDOT: PSS on aligned carbon nanotubes for efficient dye-sensitized solar cells. *J Mater Chem A* 2013;1:13268–73.
- [289] Yue G, Wu J, Xiao Y, Lin J, Huang M, Lan Z, Fan L. Functionalized graphene/poly(3,4-ethylenedioxythiophene): polystyrenesulfonate as counter electrode catalyst for dye-sensitized solar cells. *Energy* 2013;54:315–21.
- [290] McGehee MD. Nanostructured organic–inorganic hybrid solar cells. *MRS Bull* 2009;34:95–100.
- [291] Grant CD, Schwartzberg AM, Smestad GP, Kowalik J, Tolbert LM, Zhang JZ. Characterization of nanocrystalline and thin film TiO<sub>2</sub> solar cells with poly(3-undecyl-2,2-bithiophene) as a sensitizer and hole conductor. *J Electroanal Chem* 2002;522:40–8.
- [292] Coakley KM, Liu Y, McGehee MD, Frindell KL, Stucky GD. Infiltrating semiconducting polymers into self-assembled mesoporous titania films for photovoltaic applications. *Adv Funct Mater* 2003;13:301–6.
- [293] Olson DC, Lee YJ, White MS, Kopidakis N, Shaheen SE, Ginley DS, Voigt JA, Hsu JWP. Effect of polymer processing on the performance of poly(3-hexylthiophene)/ZnO nanorod photovoltaic devices. *J Phys Chem C* 2007;111:16640–5.
- [294] Tepavcevic S, Darling SB, Dimitrijevic NM, Rajh T, Sibener SJ. Improved hybrid solar cells via in situ UV polymerization. *Small* 2009;5:1776–83.
- [295] Atienzar P, Ishwara T, Horie M, Durrant JR, Nelson J. Hybrid polymer–metal oxide solar cells by in situ chemical polymerization. *J Mater Chem* 2009;19:5377–80.
- [296] Xia J, Masaki N, Lira-Cantu M, Kim Y, Jiang K, Yanagida S. Influence of doped anions on poly(3,4-ethylenedioxythiophene) as hole conductors for iodine-free solid-state dye-sensitized solar cells. *J Am Chem Soc* 2008;130:1258–63.
- [297] Xia J, Masaki N, Lira-Cantu M, Kim Y, Jiang K, Yanagida S. Effect of doping anions' structures on poly(3,4-ethylenedioxythiophene) as hole conductors in solid-state dye-sensitized solar cells. *J Phys Chem C* 2008;112:11569–74.
- [298] Kim Y, Sung YE, Xia JB, Lira-Cantu M, Masaki N, Yanagida S. Solid-state dye-sensitized TiO<sub>2</sub> solar cells using poly(3,4-ethylenedioxythiophene) as substitutes of iodine/iodide electrolytes and noble metal catalysts on FTO counter electrodes. *J Photochem Photobiol A* 2008;193:77–80.
- [299] Yang L, Zhang J, Shen Y, Park B, Bi D, Haggman L, Johansson EMJ, Boschloo G, Hagfeldt A, Vlachopoulos N, Snedden A, Kloo L, Jarboui A, Chams A, Perruchot C, Jouini M. New approach for preparation of efficient solid-state dye-sensitized solar cells by photoelectrochemical polymerization in aqueous micellar solution. *J Phys Chem Lett* 2013;4:4026–31.
- [300] Mozer AJ, Panda DK, Gambhir S, Winther-Jensen B, Wallace GG. Microsecond dye regeneration kinetics in efficient solid state dye-sensitized solar cells using a photoelectrochemically deposited PEDOT hole conductor. *J Am Chem Soc* 2010;132:9543–5.
- [301] Snook GA, Kao P, Best AS. Conducting-polymer-based supercapacitor devices and electrodes. *J Power Sources* 2011;196:1–12.
- [302] Cong HP, Ren XC, Wang P, Yu SH. Flexible graphene–polyaniline composite paper for high-performance supercapacitor. *Energy Environ Sci* 2013;6:1185–91.
- [303] Feng XM, Li RM, Ma YW, Chen RF, Shi NE, Fan QL, Huang W. One-step electrochemical synthesis of graphene/polyaniline composite film and its applications. *Adv Funct Mater* 2011;21:2989–96.
- [304] Cai Z, Li L, Ren J, Qiu L, Lin H, Peng H. Flexible, weavable and efficient microsupercapacitor wires based on polyaniline composite fibers incorporated with aligned carbon nanotubes. *J Mater Chem A* 2013;1:258–61.
- [305] Liu R, Lee SB. MnO<sub>2</sub>/poly(3,4-ethylenedioxythiophene) coaxial nanowires by one-step coelectrodeposition for electrochemical energy storage. *J Am Chem Soc* 2008;130:2942–53.
- [306] Zang J, Bao SJ, Li CM, Bian H, Cui X, Bao Q, Sun CQ, Guo J, Lian K. Well-aligned cone-shaped nanostructure of polypyrrole/RuO<sub>2</sub> and its electrochemical supercapacitor. *J Phys Chem C* 2008;112:14843–7.
- [307] Ambade RB, Ambade SB, Shrestha NK, Nah YC, Han SH, Lee W, Lee SH. Polythiophene infiltrated TiO<sub>2</sub> nanotubes as high-performance supercapacitor electrodes. *Chem Commun* 2013;49:2308–10.
- [308] Wei H, Yan X, Wu S, Luo Z, Wei S, Guo Z. Electropolymerized polyaniline stabilized tungsten oxide nanocomposite films: electrochromic behavior and electrochemical energy storage. *J Phys Chem C* 2012;116:25052–64.



- [309] Pieta P, Obratsov I, D'Souza F, Kutner W. Composites of conducting polymers and various carbon nanostructures for electrochemical supercapacitors. *ECS J Solid State Sci Technol* 2013;2:M3120–34.
- [310] Nagai H, Segawa H. Energy-storable dye-sensitized solar cell with a polypyrrole electrode. *Chem Commun* 2004:974–5.
- [311] Yoneyama H, Kishimoto A, Kuwabata S. Charge–discharge properties of polypyrrole films containing manganese dioxide particles. *J Chem Soc Chem Commun* 1991:986–7.
- [312] Park KI, Song HM, Kim Y, Mho S, Cho II W, Yeo IH. Electrochemical preparation and characterization of  $V_2O_5$ /polyaniline composite film cathodes for Li battery. *Electrochim Acta* 2010;55:8023–9.
- [313] Boyano I, Bengoechea M, de Meaza I, Miguel O, Cantero I, Ochoteco E, Rodriguez J, Lira-Cantu M, Gomez-Romero P. Improvement in the PPy/ $V_2O_5$  hybrid as a cathode material for Li ion batteries using PSA as an organic additive. *J Power Sources* 2007;166:471–7.
- [314] Liu B, Soares P, Checkles C, Zhao Y, Yu G. Three-dimensional hierarchical ternary nanostructures for high-performance Li-ion battery anodes. *Nano Lett* 2013;13:3414–9.
- [315] Winther-Jensen B, Winther-Jensen O, Forsyth M, Macfarlane DR. High rates of oxygen reduction over a vapor phase-polymerized PEDOT electrode. *Science* 2008;321:671–4.
- [316] Rajeshwar K, Janáky C, Lin WY, Roberts DA, Wampler W. Photocatalytically prepared metal nanocluster-oxide semiconductor-carbon nanocomposite electrodes for driving multielectron transfer. *J Phys Chem Lett* 2013;4:3468–78.
- [317] Zou BX, Liu XX, Diamond D, Lau KT. Electrochemical synthesis of  $WO_3$ /PANI composite for electrocatalytic reduction of iodate. *Electrochim Acta* 2010;55:3915–20.
- [318] Bencsik G, Lukács Z, Visy C. Photo-electrochemical sensor for dissolved oxygen, based on a poly(3,4-ethylenedioxythiophene)/iron oxalate hybrid electrode. *Analyst* 2010;135:375–80.
- [319] Shi J, Guo D, Wang Z, Li H. Electrocatalytic oxidation of formic acid on platinum particles dispersed in SWNT/PANI composite film. *J Solid State Electrochem* 2005;9:634–8.
- [320] Wu G, Li L, Li JH, Xu BQ. Methanol electrooxidation on Pt particles dispersed into PANI/SWNT composite films. *J Power Sources* 2006;155:118–27.
- [321] Wang Z, Yuan J, Li M, Han D, Zhang Y, Shen Y, Niu L, Ivaska A. Electropolymerization and catalysis of well-dispersed polyaniline/carbon nanotube/gold composite. *J Electroanal Chem* 2007;599:121–6.
- [322] Wang Q, Yun Y. A nanomaterial composed of cobalt nanoparticles, poly(3,4-ethylenedioxythiophene) and graphene with high electrocatalytic activity for nitrite oxidation. *Microchim Acta* 2012;177:411–8.
- [323] Su PG, Huang LN. Humidity sensors based on  $TiO_2$  nanoparticles/polypyrrole composite thin films. *Sens Actuators B* 2007;123:501–7.
- [324] Bobacka J, Ivaska A, Lewenstam A. Potentiometric ion sensors based on conducting polymers. *Electroanalysis* 2003;15:366–74.
- [325] Ramanavicius A, Ramanaviciene A, Malinauskas A. Electrochemical sensors based on conducting polymer–polypyrrole. *Electrochim Acta* 2006;51:6025–37.
- [326] Janáky C, Visy C. Conducting polymer-based hybrid assemblies for electrochemical sensing: a materials science perspective. *Anal Bioanal Chem* 2013;405:489–511.
- [327] Granqvist CG. Electrochromic tungsten oxide films: review of progress 1993–1998. *Sol Energy Mater Sol Cells* 2000;60:201–62.
- [328] Amb CM, Dyer AL, Reynolds JR. Navigating the color palette of solution-processable electrochromic polymers. *Chem Mater* 2011;23:397–415.
- [329] Kobayashi N, Teshima K, Hirohashia R. Conducting polymer image formation with photoinduced electron transfer reaction. *J Mater Chem* 1998;8:497–506.
- [330] Thakur VK, Ding G, Ma J, Lee PS, Lu X. Hybrid materials and polymer electrolytes for electrochromic device applications. *Adv Mater* 2012;24:4071–96.
- [331] Cai GF, Tu JP, Zhou D, Zhang JH, Wang XL, Gu CD. Dual electrochromic film based on  $WO_3$ /polyaniline core/shell nanowire array. *Sol Energy Mater Sol Cells* 2014;122:51–8.
- [332] Yoneyama H, Takahashi N, Kuwabata S. Formation of a light image in a polyaniline film containing titanium (IV) oxide particles. *Chem Commun* 1992:716–7.


 CrossMark  
click for updates

 Cite this: *J. Mater. Chem. A*, 2016, 4, 3139

## Decoration of ultra-long carbon nanotubes with Cu<sub>2</sub>O nanocrystals: a hybrid platform for enhanced photoelectrochemical CO<sub>2</sub> reduction†

 E. Kecsenovity,<sup>ad</sup> B. Endrődi,<sup>ab</sup> Zs. Pápa,<sup>e</sup> K. Hernádi,<sup>d</sup> K. Rajeshwar<sup>\*c</sup> and C. Janáky<sup>\*ab</sup>

Photoelectrochemical reduction of CO<sub>2</sub> to form useful chemicals is an increasingly studied avenue for harnessing and storing solar energy. In the quest for efficient and stable photocathode materials, nanostructured hybrid assemblies are eminently attractive candidates, because they exhibit multiple favorable properties that cannot be expected from a single material. One possible direction is to combine p-type inorganic semiconductors with highly conductive large surface area electrodes such as carbon nanotube networks. In this work, the controlled synthesis and photoelectrochemical behavior of CNT/Cu<sub>2</sub>O films was reported for the first time for CO<sub>2</sub> reduction applications. A carefully designed, multiple-step electrodeposition protocol was developed that ensured homogeneous coating of CNTs with Cu<sub>2</sub>O nanocrystals. The hybrid materials were characterized by electron microscopy, X-ray diffraction, Raman spectroscopy, electrochemical impedance spectroscopy, and photoelectrochemical methods. The hybrid films had five-fold higher electrical conductivity compared to their pure Cu<sub>2</sub>O counterparts. This enhanced charge transport property resulted in a drastic increase in the photocurrents measured for CO<sub>2</sub> reduction. In addition to this superior performance, long term photoelectrolysis measurements proved that the CNT/Cu<sub>2</sub>O hybrids were more stable than the oxide alone. These observations, together with the established structure/property relationships, may contribute to the rational design of nanocarbon/inorganic semiconductor hybrid photocathodes for deployment in photoelectrochemical cells.

Received 20th December 2015

Accepted 4th January 2016

DOI: 10.1039/c5ta10457b

[www.rsc.org/MaterialsA](http://www.rsc.org/MaterialsA)

## Introduction

Semiconductor photoelectrochemistry is an intensely studied approach for solar fuel generation.<sup>1,2</sup> Photoelectrochemical (PEC) water splitting,<sup>3</sup> and more recently, CO<sub>2</sub> reduction,<sup>4</sup> have been at the forefront of research because of their promise to simultaneously remove a greenhouse gas, and to harness and store the energy of sunlight in the form of useful fuels. In the simplest case, the semiconductor itself acts as the light absorber as well as the catalyst as was first shown for p-GaP as an example.<sup>5</sup> To efficiently drive a thermodynamically uphill reaction at the semiconductor/electrolyte interface, however,

the employed photoelectrode needs to fulfil multiple criteria at the same time.<sup>6</sup> Light absorption, charge carrier transport, surface chemical properties, chemical/electrochemical/photo-stability, and cost: these are only some of the factors that need to be optimized. Perhaps this is the reason that although several different semiconductors were tested since the first reports,<sup>7</sup> much remains to be done to achieve similar progress to what the solar cell photovoltaics community has witnessed for electricity generation.<sup>8</sup>

Since our proof-of-concept studies on the solar photoelectrosynthesis of methanol using hybrid CuO/Cu<sub>2</sub>O nanorod arrays,<sup>9,10</sup> different laboratories have employed Cu<sub>2</sub>O as a photocathode material in CO<sub>2</sub> reduction.<sup>11,12</sup> In addition, further progress has been achieved in terms of (i) analyzing the potential dependent product distribution,<sup>13</sup> (ii) realizing the reaction in a continuous flow reactor,<sup>14</sup> and (iii) gaining mechanistic understanding of CO<sub>2</sub> adsorption using quantum chemical calculations.<sup>15</sup> The instability of Cu<sub>2</sub>O towards photoelectrochemical corrosion (*i.e.*, metallic copper formation) was already found to be a major problem in earlier reports on PEC water splitting using this material.<sup>16,17</sup> Application of surface coating was demonstrated as a possible strategy to increase the photoelectrode lifetime, either by employing a carbon coating<sup>17</sup> or other *via* atomic layer deposition of Al-

<sup>a</sup>MTA-SZTE "Lendület" Photoelectrochemistry Research Group, Rerrich Square 1, Szeged, H-6720, Hungary. E-mail: janaky@chem.u-szeged.hu

<sup>b</sup>Department of Physical Chemistry and Materials Science, University of Szeged, Rerrich Square 1, Szeged, H-6720, Hungary

<sup>c</sup>Department of Chemistry and Biochemistry, University of Texas at Arlington, Arlington, Texas 76019, USA. E-mail: rajeshwar@uta.edu

<sup>d</sup>Department of Applied and Environmental Chemistry, University of Szeged, Rerrich Square 1, Szeged, H-6720, Hungary

<sup>e</sup>Department of Optics and Quantum Electronics, University of Szeged, Dóm Square 9, Szeged, H-6720, Hungary

† Electronic supplementary information (ESI) available: The synthesis and characterization of the photoelectrode. See DOI: 10.1039/c5ta10457b

doped zinc oxide and titanium oxide nanolayers.<sup>18,19</sup> Employing a surface coating on the Cu<sub>2</sub>O surface, however, is not necessarily useful in CO<sub>2</sub> reduction, where Cu surface clusters play a specific catalytic role in the reaction as was shown in different electrocatalytic reaction schemes.<sup>20</sup>

In addition to instability, two other factors, namely, surface area and charge carrier mobility, are also critical issues limiting the performance of photocathodes. To address the above challenges together as a whole, nanostructuring of the electrode may offer a viable avenue of attack.<sup>21</sup> In addition, nanocarbon/inorganic semiconductor hybrids offer a promising platform in different solar energy application schemes, by uniting the high electrical conductivity of the carbon component with the photoactive behavior of the inorganic material.<sup>22</sup> There are different studies in the literature, proving the above concept in both binary<sup>23,24</sup> and ternary hybrid configurations.<sup>25,26</sup> As for Cu<sub>2</sub>O specifically, it has been combined with both carbon quantum dots<sup>27</sup> and reduced graphene oxide sheets<sup>28</sup> recently to perform the photo-driven reduction of CO<sub>2</sub> to fuels. These studies used a slurry of the composite material. To the best of our knowledge, however, there is no precedence in the literature, where such hybrids were employed as photocathodes in a photoelectrochemical cell.

To efficiently exploit these possible synergies in a PEC configuration, however, carefully designed synthetic protocols are required, which allow us to tailor the composition and morphology of the hybrid material toward the targeted reaction. Electrochemical deposition of inorganic semiconductors on carbon nanostructures is an emerging topic with high applicability in various application avenues.<sup>29</sup> This preparation method can be particularly useful for PEC applications, where electronic communication between the components is a prerequisite. In this study we accordingly present the tailored electrodeposition of Cu<sub>2</sub>O nanocrystals on high quality ultra-long carbon nanotubes (CNTs). To the best of our knowledge, this is the first time when photoelectrochemical CO<sub>2</sub>-reduction was driven at a nanocarbon/inorganic semiconductor hybrid electrode material. It is demonstrated that efficient charge carrier transport and rapid charge carrier extraction contribute to both remarkably higher photocurrents and higher stability. The effects of the composition and morphology on the PEC performance are also discussed and structure–property relationships are established.

## Experimental

### CVD synthesis of CNT arrays

High quality, ultra-long (1–1.5 mm) carbon nanotube arrays were grown following a previously optimized chemical vapor deposition (CVD) process, detailed elsewhere.<sup>30</sup> The Al<sub>2</sub>O<sub>3</sub> support layer and the mixed Fe–Co catalyst layer were deposited subsequently on silicon substrates using a pulsed laser deposition method, by focusing the laser beam (LLG TWINAMP ArF excimer laser,  $\lambda = 193$  nm, pulse length 18 ns, and repetition rate 10 Hz) on pressed Al<sub>2</sub>O<sub>3</sub> and Fe–Co (1 : 1 molar ratio) targets, respectively.

The catalyst-coated silicon wafers were placed in a fixed-bed flow quartz tube reactor (20 mm diameter, 800 mm length). The reaction chamber was heated to 750 °C under nitrogen purging (100 mL min<sup>-1</sup>). After 5 min, hydrogen gas (with a flow rate of 80 mL min<sup>-1</sup>) was added to the nitrogen, and the catalysts were activated for 5 min in this mixture. Subsequently, an ethylene carbon source (100 mL min<sup>-1</sup>) and moisturized nitrogen (25 mL min<sup>-1</sup>, bubbled through 25 °C water to achieve ~2 ppm water content in the reaction chamber) were also introduced into the quartz tube for the 30 min CVD process.

### Electrode preparation

Arrays of CNTs were dispersed in ethanol by ultrasonic treatment. The formed dispersion ( $c \sim 10$   $\mu\text{g mL}^{-1}$ ) was spray-coated on preheated indium doped tin oxide covered glass (ITO) electrodes, using an Alder AD320 type airbrush, operated with 1 bar compressed air. To remove traces of the solvent and to enhance adhesion of the CNTs, the thin layers were kept in an oven (180 °C) for 1 h. Carbon nanotube loading of the electrodes was controlled with the number of spray steps (5–100  $\mu\text{g cm}^{-2}$ , denoted as CNT5, CNT10, *etc.*), and quantified by quartz crystal microbalance (QCM) measurements using a Stanford Research System QCM-200 type instrument.

### Cu<sub>2</sub>O electrodeposition

Cu<sub>2</sub>O was electrodeposited from an alkaline solution of lactate-stabilized copper sulfate, containing 0.4 mol dm<sup>-3</sup> cupric sulfate and 3 mol dm<sup>-3</sup> lactic acid in deionized water (Millipore Direct Q3-UV, 18.2 M $\Omega$  cm). The bath pH was adjusted to 9 with concentrated sodium hydroxide solution. The temperature of the solution was maintained at 60 °C, and it was constantly stirred by using a magnetic stirrer during the electrodeposition.

All the electrochemical measurements were performed on a Metrohm Autolab PGSTAT302N type potentiostat/galvanostat. The electrodeposition was performed in a classic three electrode cell, using Pt sheet and Ag/AgCl/3 M NaCl counter and reference electrodes, respectively. For Cu<sub>2</sub>O electrodeposition, after carefully studying the linear sweep voltammetry curves, a potentiostatic method was applied by adjusting previous procedures.<sup>31,32</sup> To ensure complete coverage of the CNTs, nuclei formation was initialized by introducing a seed nucleation step at more negative potential (–0.35 V) until the first 50 mC cm<sup>-2</sup> charge was passed (~15 s) (Fig. 1b). The deposition was then continued at a less negative potential ( $E = -0.25$  V, ~20 s each step) to achieve uniform and homogenous crystal growth. After each 50 mC of passed charge, the deposition was interrupted for 60 s to avoid depletion of the solution.

### Electrochemical impedance spectroscopy (EIS) and Mott–Schottky analysis

Impedance spectra of the Cu<sub>2</sub>O and CNT/Cu<sub>2</sub>O layers were recorded in a 0.1 mol dm<sup>-3</sup> sodium acetate solution at open circuit potential, in the 0.1 Hz to 1 MHz frequency range, using a sinusoidal excitation signal (10 mV RMS amplitude). For Mott–Schottky analysis, impedance spectra of the electrodes

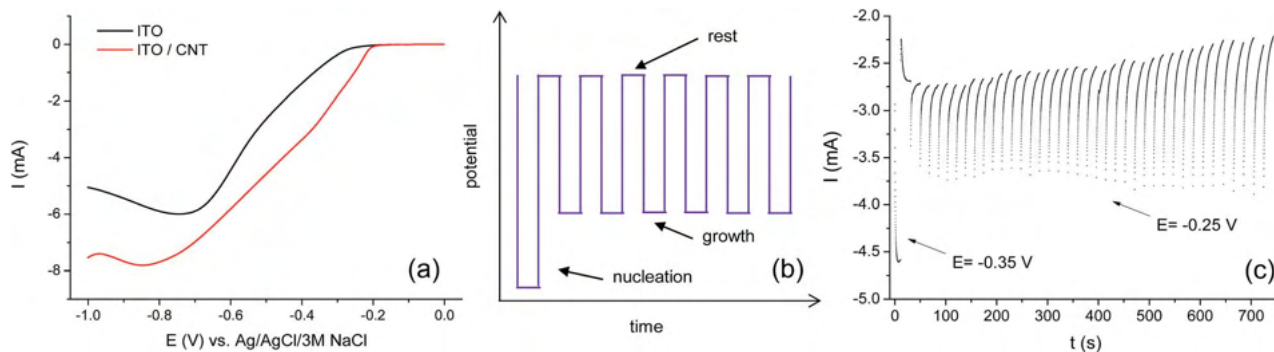


**Fig. 1** (a) Linear sweep voltammograms recorded in 0.4 M Cu–lactate solution (pH = 9), at a sweep rate of  $25 \text{ mV s}^{-1}$ , on both ITO and ITO/CNT electrodes, (b) schematic illustration of the multiple potential-step protocol, employed for electrodeposition and (c) current response of an ITO/CNT electrode ( $100 \mu\text{g cm}^{-2}$ ) while applying the potential waveform shown in (b).

were recorded at 6 frequencies (1 kHz–75 kHz) between  $E = 0.10$  and  $0.42 \text{ V}$  potentials.

### Photoelectrochemical measurements

Photovoltammograms were recorded in a two-compartment, sealed electrochemical cell in a  $0.1 \text{ mol dm}^{-3} \text{ Na}_2\text{SO}_4$  solution. The solution was saturated with  $\text{N}_2$  or  $\text{CO}_2$  by bubbling the gases through the cell for 30 min before, and forming gas pillows above the solutions during the measurements. The photovoltammograms were recorded under periodically interrupted (0.2 Hz, with an automated chopper) solar irradiation, using a Newport LCS-100 type solar simulator (100 W), operated at full output with a UV-cutoff filter ( $<400 \text{ nm}$ ).

Long-term carbon dioxide photoelectrolysis (and consequently constant potential stability) tests were performed using the same arrangement. The electrode potential was kept at  $+0.05 \text{ V}$  (vs. Ag/AgCl/3 M NaCl), and was irradiated with the above described light source (periodically interrupted at 0.033 Hz). Liquid aliquots were taken at the end of photoelectrolysis to be analyzed in a gas chromatograph equipped with a mass spectrometer as the detector (GC-MS). The aliquots were injected into the Shimadzu GC-MS 2010SE chromatograph coupled with a MS QP2010 detector. The chromatographic column was a Stabilwax-DA (30 m length and 0.32 mm inner diameter) set at  $40 \text{ }^\circ\text{C}$ , and the injection port temperature was  $220 \text{ }^\circ\text{C}$ . The MS detector was set at  $200 \text{ }^\circ\text{C}$ , and helium was used as the carrier gas. Product detection was afforded by selective ion monitoring (SIM)-MS, while the total ion chromatogram was used for the quantification of methanol, ethanol, and formic acid.

### Structural characterization

Raman spectroscopic studies were performed on a DXR Raman Microscope using a green laser ( $\lambda = 532 \text{ nm}$ ), operating at 1 mW laser power. A FEI Tecnai G2 20 X-Twin type instrument, operating at an acceleration voltage of 200 kV, was used for transmission electron microscopy (TEM) investigations. Scanning electron microscopy (SEM) images were recorded by using a Hitachi S-4700 field emission scanning electron microscope (coupled with a Röntec EDX detector), operating at an acceleration voltage of 10 kV. X-Ray diffraction (XRD) data were

recorded in the range,  $2\theta = 30\text{--}80^\circ$ , at  $1^\circ \text{ minute}^{-1}$  scan rate by using a Rigaku Miniflex II instrument, operating with a Cu  $K_{\alpha,1}$  radiation source ( $\lambda = 0.1541 \text{ nm}$ ).

## Results and discussion

As the first step, ordered arrays of ultra-long CNTs were synthesized by the CVD method (Fig. S1†). These nanostructures can be used as electrode materials without any additional treatment, and we performed electrodeposition of  $\text{Cu}_2\text{O}$  on these carbon nanotubes.<sup>29</sup> For PEC applications however, the large thickness of the electrode ( $\sim 1 \text{ mm}$ ) is not suitable, considering the penetration depth of solar irradiation. Therefore, the synthesized nanocarbon arrays were sonicated, and the obtained suspension was spray-coated on ITO electrodes. *Via* this method, an interconnected nanonet structure was reproducibly obtained (see, for example, Fig. 2a below), where the thickness was controlled by the number of the spray-coat cycles.

Prior to electrodeposition of the  $\text{Cu}_2\text{O}$  crystals, an electrochemical conditioning step was carried out in the Cu–lactate solution, to remove any entrapped gas and to ensure proper wetting of the CNT film. This step consisted of multiple cyclic voltammetry scans in a potential window ( $E = 0.0 \text{ V} \text{--} 0.5 \text{ V}$ ), where the lower vertex potential was more positive than the potential required for the reduction of  $\text{Cu}^{2+}$ . During these cycles we observed that the evolution of the capacitance dominated the electrochemical behavior of the CNTs (Fig. S2†), with parallel desorption of the entrapped gases ( $\text{N}_2$  and  $\text{O}_2$ ). In the case of thicker CNT films, we found this step to be essential for achieving high  $\text{Cu}_2\text{O}$  loadings in the subsequent electrodeposition process.

Based on earlier literature studies,<sup>9,31,32</sup> we aimed to employ slow potentiostatic deposition, to minimize the metallic Cu content of the deposited oxide phase. To determine the deposition potential, linear sweep voltammograms (LSVs) were recorded. As seen in Fig. 1a, the two curves have a very similar pattern, but the cathodic currents start to develop at markedly less negative potential values ( $E \approx -0.2 \text{ V}$ ) on the CNTs than at the bare ITO coated glass electrode. This shift indicates that

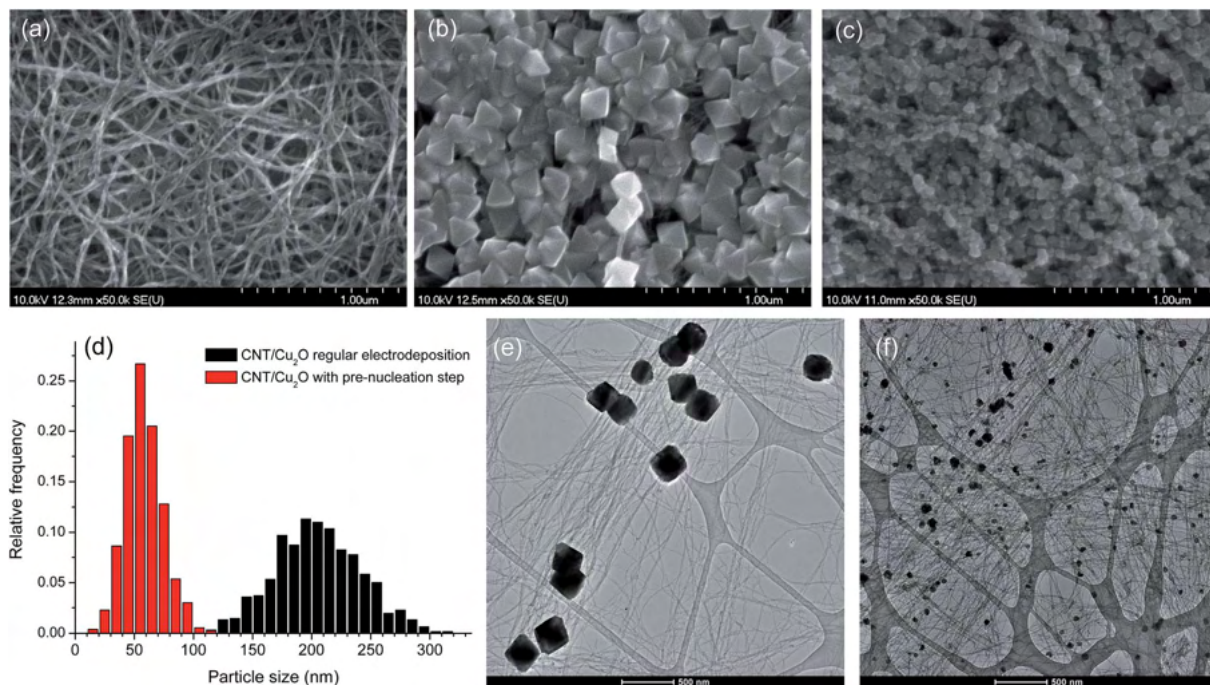


Fig. 2 SEM images of the bare CNT nanonet (a), a CNT/Cu<sub>2</sub>O hybrid obtained at constant  $E = -0.25$  V potential,  $Q = 200$  mC (b), and with a short pre-deposition step at  $E = -0.35$  V potential  $Q = 200$  mC (c). Particle size distribution (d) and TEM images are also shown for the same samples (e and f).

oxide formation is favored on the CNTs, and by appropriately selecting the potential value, Cu<sub>2</sub>O crystals could be exclusively deposited on the CNTs (this was also confirmed by the SEM images, see below). The composition and morphology of the CNT/Cu<sub>2</sub>O hybrid greatly affect its electrical- and photoelectrochemical properties (for example, a complete filling of the nanocarbon template may hinder the accessibility of Cu<sub>2</sub>O in the deeper regions). To establish structure–property relationships, and to find the best performing material in PEC CO<sub>2</sub> reduction, the thickness of the CNT film ( $5\text{--}100\ \mu\text{g cm}^{-2}$ ), as well as the amount of the electrodeposited Cu<sub>2</sub>O, was systematically varied ( $50\text{--}2000\ \text{mC cm}^{-2}$ ).

It was found that simple potentiostatic growth results in homogeneous films without, or with very small amounts of CNTs. On the other hand, for thicker CNT films, more sophisticated methods are indeed required. Therefore, we developed an approach consisting of multiple potentiostatic deposition steps, as well as rest periods interspersed among them, to allow for continuous supply of the copper ions from the bulk solution (Fig. 1b). An initial nucleation step at a more negative potential ( $-0.35$  V) was also found to be beneficial for achieving homogeneous coating on the ITO/CNT electrode. The length of this nucleation step, however, cannot be too long, because formation of metallic copper also occurs at this potential. Accordingly, the subsequent Cu<sub>2</sub>O growth was performed at less negative potential ( $-0.25$  V). This protocol is summarized in Fig. 1b, whereas the observed response is shown in Fig. 1c. As seen in Fig. 1c, the rapid nucleation occurs during the first step (as deduced from the high currents), while a steady growth is indicated during the subsequent phase.

The above observations were also confirmed at the sub-microscopic level. Scanning electron microscopic studies showed the bare CNT nanonet (Fig. 2a) and the formation of typical octahedral Cu<sub>2</sub>O crystals on the CNT surface (Fig. 2b and c). Importantly, while some bare carbon nanotubes can be spotted on the sample synthesized without the pre-nucleation step (Fig. 2b), perfect coverage is seen when the optimized protocol was employed (Fig. 2c). This better homogeneity was a general trend, observed in all the cases when the pre-nucleation step was applied. In addition, a striking difference can be seen in the size of the Cu<sub>2</sub>O particles deposited, namely they are much smaller in the latter case. This is not a surprise considering the equal amount of deposition charge ( $200\ \text{mC}$ ), and the larger number of nuclei formed during the nucleation step at a more negative potential. This difference was also quantified by obtaining the particle size distribution. As shown in the histograms in Fig. 2d, the particles are massively larger in the first case ( $d_{\text{av}} = 200\ \text{nm}$  vs.  $60\ \text{nm}$ ). We note here that these particle sizes serve only for comparative purposes, since they can be widely tuned by the deposition charge. TEM images (Fig. 2e and f) confirmed the above conclusions, and very similar particle sizes were obtained.

Structural properties of the hybrid assemblies were investigated using Raman spectroscopy and X-ray diffraction (XRD), and both techniques confirmed the formation of Cu<sub>2</sub>O nanocrystals on the CNTs (Fig. 3a and b, respectively). The spectrum of the CNT film shows the typical D and G-bands at  $1346$  and  $1588\ \text{cm}^{-1}$ , respectively. The bands at  $150$ ,  $212$ , and  $630\ \text{cm}^{-1}$  all confirm the formation of cuprite (Cu<sub>2</sub>O) crystals.<sup>33</sup> Importantly, the absence of the phonon peak around  $300\ \text{cm}^{-1}$  proves the

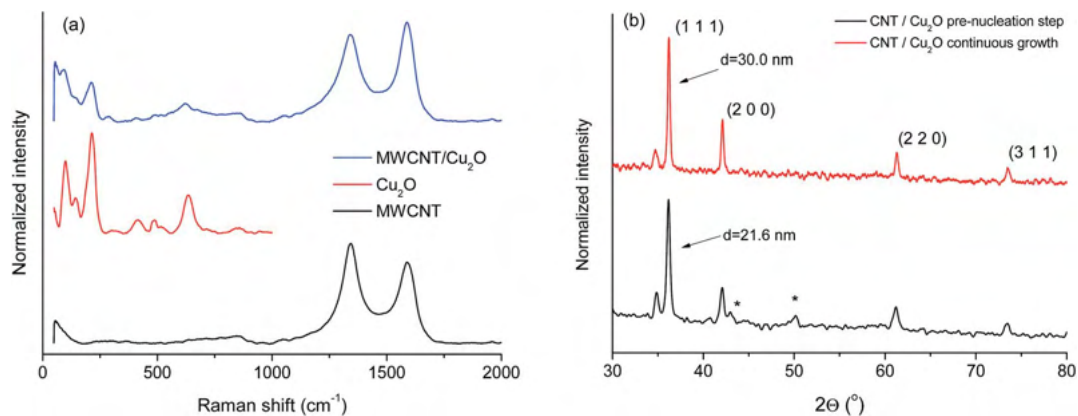


Fig. 3 (a) Raman spectra of a CNT film, an electrodeposited  $\text{Cu}_2\text{O}$  film, and a hybrid CNT/ $\text{Cu}_2\text{O}$  sample. (b) XRD patterns of two different CNT/ $\text{Cu}_2\text{O}$  samples synthesized with and without a pre-nucleation step respectively. \* indicates the reflection from the metallic Cu phase.

absence of CuO in the film. On the spectrum of the hybrid sample, beyond the obvious appearance of the bands of its constituents, an interesting phenomenon can be spotted. The decrease in the D/G band ratio after the cathodic synthesis indicates an improved quality of the CNTs (most likely because of the electrochemical reduction of certain oxygen-functional groups). XRD data furnished further evidence for the formation of  $\text{Cu}_2\text{O}$ . Comparison of the XRD patterns of two CNT/ $\text{Cu}_2\text{O}$  samples (with and without a nucleation step) is provided in Fig. 3b. Both patterns are consistent with the presence of a  $\text{Cu}_2\text{O}$  phase, except two minor diffractions (marked with asterisks) which originate from the presence of metallic copper traces. The Scherrer equation was employed to estimate the size of the crystalline domains using the most intensive reflection (111). As seen in Fig. 3b, in line with the electron microscopic observations (see above), a markedly smaller value was obtained for the sample obtained with a pre-nucleation step (21 nm vs. 30 nm).

Electrochemical impedance spectroscopy was employed to probe the electrical properties of the bare  $\text{Cu}_2\text{O}$  and the CNT/ $\text{Cu}_2\text{O}$  electrodes deposited with identical charge density (1C). Nyquist plots are presented in Fig. 4, together with the fit obtained using the equivalent circuit shown in Fig. S3.† The most important point from the analysis of these EIS data was that the CNT/ $\text{Cu}_2\text{O}$  electrode shows a 4–5 times lower charge transfer

resistance compared to the bare  $\text{Cu}_2\text{O}$  electrode (440  $\Omega$  vs. 1.9 k $\Omega$ ), while the other circuit parameters were practically the same. This massive decrease can be attributed to the presence of a well-connected, highly conductive pathway under and between the  $\text{Cu}_2\text{O}$  nanocrystallites.<sup>22,34</sup> Importantly, this architecture may lead to suppressed charge carrier recombination, and rapid charge carrier extraction, and therefore to better catalytic activity and longer lifetime of the catalyst. The flat-band potentials were determined for both samples using Mott-Schottky analyses. For the bare  $\text{Cu}_2\text{O}$ , this was found to be 0.29 V ( $\sim 0.5$  V vs. SHE), which agrees well with previously reported values.<sup>11</sup> Upon introducing the CNT network, only a slight positive shift can be witnessed, which means that the deposited  $\text{Cu}_2\text{O}$  has a very similar flat-band potential in both cases ( $\sim 0.55$  V vs. SHE).

Fig. 5a compares linear sweep photovoltammetry data of the CNT/ $\text{Cu}_2\text{O}$  hybrid material (CNT10, 200 mC  $\text{Cu}_2\text{O}$ ), both in the presence and absence of dissolved  $\text{CO}_2$ . This voltammetry technique consists of a slow scan of the potential (2 mV  $\text{s}^{-1}$ ) while the film irradiation is periodically chopped. In this manner, both the dark and light-induced photoresponses of the hybrid samples can be assessed in a single experiment. As seen in Fig. 5, cathodic photocurrents can be detected for all the samples, diagnostic of the p-type semiconductor behavior of the

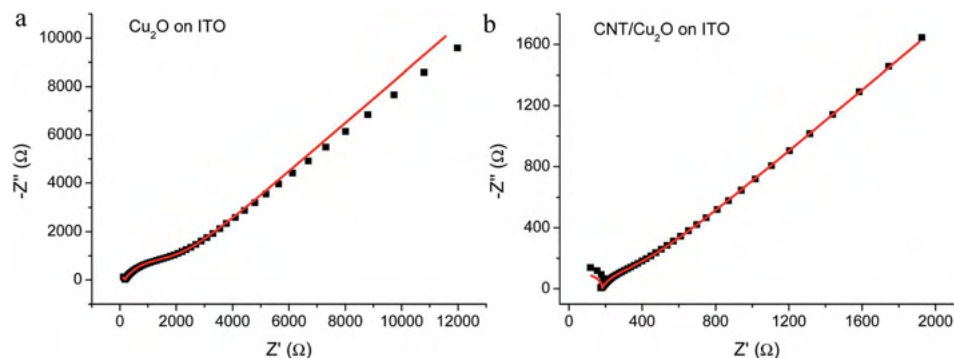


Fig. 4 Measured (points) and simulated (solid lines) Nyquist plots of (a)  $\text{Cu}_2\text{O}$  and (b) CNT/ $\text{Cu}_2\text{O}$ , recorded in 0.1 mol  $\text{dm}^{-3}$  sodium acetate solution at open circuit potential, in the 0.1 Hz to 1 MHz frequency range.

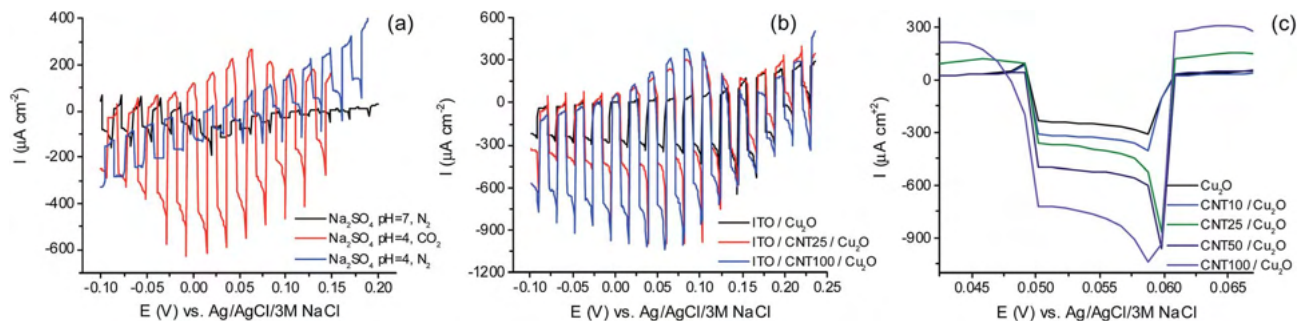


Fig. 5 (a) LSV curves of a CNT10/Cu<sub>2</sub>O hybrid sample registered at 2 mV s<sup>-1</sup>, in 0.1 M Na<sub>2</sub>SO<sub>4</sub> solution under N<sub>2</sub> (both at pH = 4.0 and 7.0) and CO<sub>2</sub> (pH = 4.0) atmospheres, with the full output of a 100 W solar simulator, employing a UV cut-off filter (<400 nm); (b) comparison of the photovoltammograms registered for hybrid samples with different CNT-contents (1C Cu<sub>2</sub>O in all the cases) in CO<sub>2</sub> saturated 0.1 M Na<sub>2</sub>SO<sub>4</sub> solution; (c) enlarged view of a photocurrent transient from (b).

electrodeposited Cu<sub>2</sub>O. This observation is entirely consistent with the negative slope of the Mott–Schottky plots, obtained from EIS measurements (Fig. S4†). The photocurrent flow is sustained by the reduction of either H<sup>+</sup> ions (H<sub>2</sub>-evolution), or dissolved CO<sub>2</sub>, as was demonstrated for the CuO/Cu<sub>2</sub>O hybrids earlier.<sup>9,10</sup> As seen in Fig. 5a, much higher currents were measured in the presence of CO<sub>2</sub>, indicating that the latter process is favored on this photocathode. To deconvolute the effect of the more acidic environment (and thus the enhanced H<sub>2</sub>-evolution) in the CO<sub>2</sub> saturated case, a photovoltammogram recorded in a N<sub>2</sub> atmosphere, but at pH = 4, is also included. As seen in Fig. 5a, there was an increase compared to the neutral solution, but the photocurrents were still much smaller than those in the CO<sub>2</sub> case.

The effect of the hybrid architecture was studied by comparing and contrasting photoelectrochemical (PEC) data gathered with and without the presence of CNTs. Fig. 5b shows the photovoltammograms of the bare Cu<sub>2</sub>O, and two hybrid films with different CNT-contents. The most obvious difference was the striking increase of the photocurrent values in the case of the hybrid films, compared to the bare oxide. This effect can be interpreted by the structure of the nanohybrid, in which small (~50–100 nm, see again, Fig. 2c) Cu<sub>2</sub>O crystals cover the highly conductive carbon nanonet. Thus, collection of the photogenerated holes (as well as their transport to the supporting electrode) is neither limited by transport, nor hampered by recombination of the charge carriers as is the case with a bulk film. Moreover, the CNT network is very conductive and capable of accepting the photogenerated holes, thus minimizing charge recombination and promoting enhancement of the photocurrent. We note here that the CNT film alone showed no photocurrent when probed under identical conditions. A careful study of the shape of these curves also revealed the development of a small, but significant, anodic peak in the dark, in the range,  $E = 0.0$ – $0.15$  V, for the hybrid samples. This effect is interesting, considering that the CNT support has no redox peak in that region (see Fig. S2†). Analysis of the Pourbaix-diagrams of Cu (Fig. S5†) suggests that the peak is assignable to the electrooxidation of Cu traces to Cu<sub>2</sub>O.

The PEC behavior of the CNT/Cu<sub>2</sub>O assemblies was systematically studied by varying the composition. As the first step, the

effect of the CNT presence was quantified by synthesizing a series of samples, with a fixed Cu<sub>2</sub>O content (1C), but deposited on gradually thicker CNT films. As seen in Fig. 5c and 6a, the photocurrents increased steadily with the CNT film thickness. To eliminate the possible effect of the increased surface area on the photocurrent magnitude, the surface roughness of the neat Cu<sub>2</sub>O and CNT/Cu<sub>2</sub>O hybrid films must be considered. As a first step, the SEM images of these photoelectrodes were compared (Fig. S6†). It can be seen that both films are built up from nanoparticles of a similar size. This suggests that introduction of the CNT film does not alter the overall morphology. To quantify this effect, the double layer capacitance of the electrodes was determined by both CV-analysis (recorded at various sweep rates) and EIS (see Fig. S3† for the employed equivalent circuits).

As deduced from these studies, there was a slight increase in the overall charge capacitance that mostly stemmed from the contribution of the uncoated CNTs. This conclusion is supported by the observation that the capacitance value related to the Cu<sub>2</sub>O surface remained unchanged in the hybrid configuration. In addition, careful examination of the shape of the photocurrent transients in Fig. 5 revealed another significant change, confirming that something else beyond the surface area contributed to the increased photocurrents. Namely, the spike/plateau ratio showed a decrease with increasing CNT-content. This is diagnostic of the charge carriers being effectively separated in the composite structure before they undergo recombination.

In Fig. 6a, the plateau current is plotted vs. the thickness of the CNT film for various hybrid samples, containing relatively little Cu<sub>2</sub>O (0.2C deposition charge). Clearly, there was a steep increase in the currents until a certain thickness; however, further increase had only a moderate effect. If the CNT film thickness was kept fixed (10 μg cm<sup>-2</sup>), and the amount of electrodeposited Cu<sub>2</sub>O was varied, similar interesting trends could be seen. In Fig. 6b, the ratio of the stationary photocurrent values (measured at  $E = 0.1$  V) between the bare and CNT-containing Cu<sub>2</sub>O is compared as a function of Cu<sub>2</sub>O amount. The trend is clear, the largest effect occurred when the Cu<sub>2</sub>O content was small. This is not surprising, since the gradually increasing amounts of Cu<sub>2</sub>O covered the thin CNT film, and the

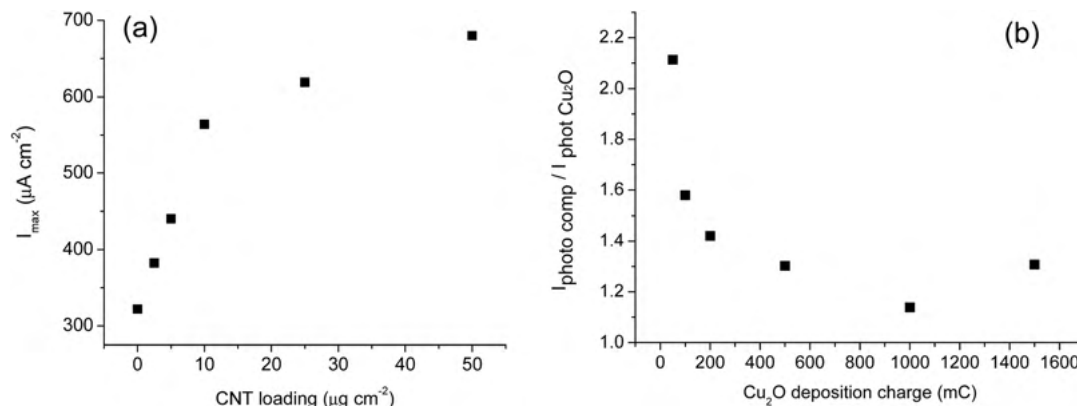


Fig. 6 Comparison of the photoelectrochemical performance of different CNT/ $\text{Cu}_2\text{O}$  electrodes. (a) Maximum of the stationary photocurrents measured at  $E = 0.1$  V, and (b) the ratio of the maximum photocurrents measured with and without CNTs.

sample behaved more and more similarly to the bulk film. Taking all these observations into consideration as a whole, we conclude that parallel optimization of the CNT thickness and  $\text{Cu}_2\text{O}$  amount is necessary to obtain high performance photocathodes.

Long term PEC measurements were performed for both a bare  $\text{Cu}_2\text{O}$  and a CNT/ $\text{Cu}_2\text{O}$  film (Fig. 7). Chronoamperometric curves were registered at  $E = 0.05$  V under periodically chopped solar irradiation, for 15 000 s (over 4 h, note the logarithmic scale in the figure). While the shape of the curves is very similar, important differences can be spotted. While the bare  $\text{Cu}_2\text{O}$ , consistently with earlier reports, retains only 25% of its initial photoactivity (60  $\mu\text{A}$  vs. 240  $\mu\text{A}$ ), this ratio is 60% for the CNT/ $\text{Cu}_2\text{O}$  hybrid sample (260  $\mu\text{A}$  vs. 450  $\mu\text{A}$ ). This is a key observation of this study, because it proves that by introducing a highly conductive nanostructured scaffold into the  $\text{Cu}_2\text{O}$  film, the stability of the photocathode can be increased. At this juncture, it is important to emphasize that the choice of the potential to

drive the photoelectrolysis was deliberate. At this potential (see again the Pourbaix-diagram in Fig. S5<sup>†</sup>), the eventually forming metallic Cu moieties can be electrochemically re-oxidized to  $\text{Cu}_2\text{O}$  (self-healing). In fact, the slow development of small anodic dark currents in Fig. 7 supports this hypothesis. Finally, we note that a similar stability increase was witnessed in a sensing application when  $\text{Cu}_2\text{O}$  nanocubes were immobilized on graphene.<sup>35</sup>

The liquid products formed during the long term photoelectrolysis were monitored using GC-MS. A typical chromatogram recorded for the CNT/ $\text{Cu}_2\text{O}$  electrode is shown in Fig. 8, along with that of the calibration standard. As seen in the figure, methanol, ethanol, and formic acid were detected in the solution for  $\text{CO}_2$ -saturated samples. Semi-quantitative analysis of the products afforded faradaic efficiencies of 9%, 24% and 18%, respectively. The rest of the charge was related to  $\text{H}_2$  formation (this was the only product detected in the gas phase), and the reduction of  $\text{Cu}_2\text{O}$  to Cu as discussed above. We also note that no such products (except  $\text{H}_2$ ) could be detected for samples

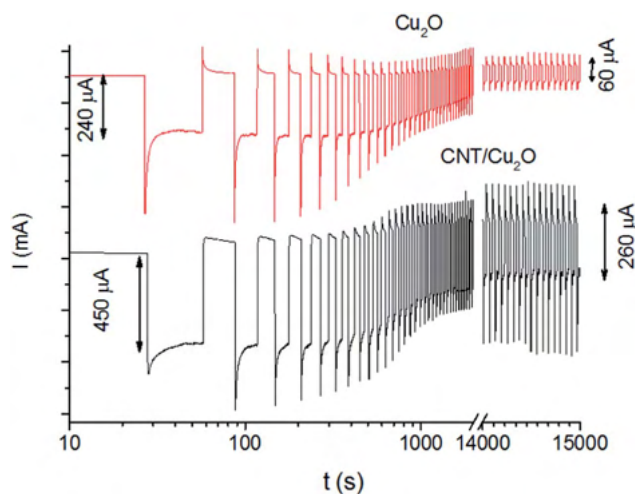


Fig. 7 Long-term chronoamperometry data of a  $\text{Cu}_2\text{O}$  and a CNT100/ $\text{Cu}_2\text{O}$  film with an identical  $\text{Cu}_2\text{O}$  content (1C), registered at 0.05 V potential (vs.  $\text{Ag}/\text{AgCl}/3$  M  $\text{NaCl}$ ), in  $\text{CO}_2$  saturated 0.1 M  $\text{Na}_2\text{SO}_4$  solution.

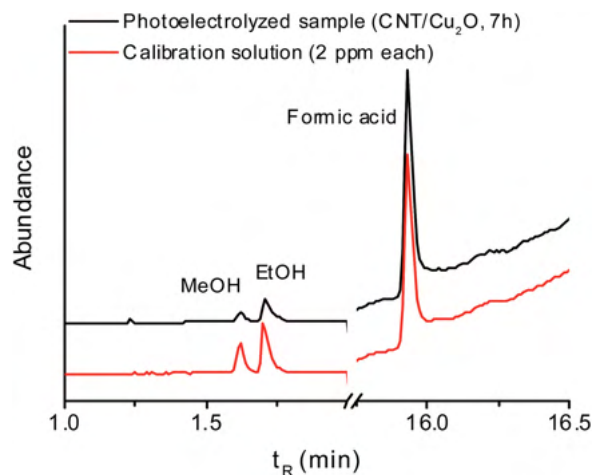


Fig. 8 GC-MS profiles registered using selective ion monitoring (SIM) for the sample after 7 h photoelectrolysis (similarly to Fig. 7), as well as for a standard solution containing 2.0 ppm methanol, ethanol, and formic acid respectively.



obtained from the experiments under N<sub>2</sub>-saturation. As for the comparison with the bare Cu<sub>2</sub>O photoelectrodes, we can conclude that the formation of the same products was observed with a similar overall faradaic efficiency, although their relative ratio was slightly different.

## Conclusions

An interconnected network (nanonet) of ultra-long CNTs was employed as a highly conductive template for the controlled electrodeposition of Cu<sub>2</sub>O nanoparticles. The homogeneous coating (together with control over the particle size) was ensured by a first nucleation step, followed by several growth steps that were interspersed by rest periods. SEM and TEM images demonstrated that by employing the optimized protocol, the oxide nanoparticles were exclusively deposited on the CNTs, resulting in complete coverage of the conductive scaffold. Raman spectroscopy and XRD showed the formation of Cu<sub>2</sub>O, with the presence of minor traces of metallic Cu. Beyond corroborating the p-type behavior of the photoelectrodes, EIS indicated a fivefold increase in the electrical conductivity of the CNT/Cu<sub>2</sub>O hybrid, compared to that of the bare oxide. This enhancement is indeed very beneficial for all photoelectrochemical applications, where transport and recombination of the photogenerated charge carriers is a limiting factor.

By comparing photovoltammetry curves registered under N<sub>2</sub> and CO<sub>2</sub> atmospheres, the drastically enhanced photocurrents in the latter case proved the activity of the photocathode towards the reduction of CO<sub>2</sub>. To understand the contribution of both components to the photoelectrochemical performance of the hybrid material, and maximize the possible synergies, both the CNT film thickness and the electrodeposited Cu<sub>2</sub>O amount were varied systematically. Under optimal conditions, an almost threefold increase was achieved in the maximum photocurrents, compared to the bare oxide film. What is equally important, the hybrid electrodes showed a markedly improved stability during long term (over 4 h) photoelectrolysis. We note here that careful analysis of the Pourbaix-diagram for Cu enabled selection of an optimal potential, where electrochemical self-healing also contributed to the observed stability. All these beneficial properties can be explained by the introduction of the nanostructured conductive framework (the CNT nanonet) into the photoelectrode.

Firstly, the faster transport of photogenerated electrons to the Cu<sub>2</sub>O/electrolyte interface is ensured by the fact that instead of having a bulk Cu<sub>2</sub>O layer, Cu<sub>2</sub>O nanoparticles are present in the system. Secondly, transport of the photogenerated holes from the Cu<sub>2</sub>O crystals to the supporting electrode is facilitated by the highly conductive carbon nanotube network. These factors reduce charge carrier recombination, as diagnosed from the change in the photocurrent transient profiles, resulting in better photoelectrochemical performance. GC-MS analysis proved unambiguously that the cathodic photocurrents led to the formation of liquid fuels such as methanol, ethanol, and formic acid.

Finally, we note that the demonstrated concept (*i.e.*, electrodeposition of semiconductors on nanostructured carbon electrodes for solar fuel generation) points well beyond the studied system. There is a wealth of possible combinations, where precise control over the composition and morphology of these hybrid photoelectrodes may lead to major breakthroughs in the future.

## Acknowledgements

C. J. gratefully acknowledges the support from the Hungarian Academy of Science, through its "Momentum" Excellence Program (LP2014-3). E. K., Zs. P., and K. H. appreciate the financial support of NKFI under the NN 114463 grant. K. R. acknowledges partial funding support for this work from the National Science Foundation (CHE-1303803). The authors thank Dr B. Kmellar (Simkon Ltd) for assistance with the GC-MS measurements. We thank the three anonymous reviewers for constructive criticisms on an earlier version of this manuscript.

## References

- 1 K. Sivula, *J. Phys. Chem. Lett.*, 2013, **4**, 1624.
- 2 K. Rajeshwar, *J. Appl. Electrochem.*, 2007, **37**, 765.
- 3 A. Fujishima and K. Honda, *Nature*, 1972, **238**, 37.
- 4 D. J. Boston, K. L. Huang, N. R. de Tacconi, N. Myung, F. M. MacDonnell and K. Rajeshwar, in *Photoelectrochemical Water Splitting: Materials, Processes and Architectures*, 2013, p. 289.
- 5 M. Halmann, *Nature*, 1978, **275**, 115.
- 6 K. Rajeshwar, A. Thomas and C. Janáky, *J. Phys. Chem. Lett.*, 2015, **6**, 139.
- 7 B. Kumar, M. Llorente, J. Froehlich, T. Dang, A. Sathrum and C. P. Kubiak, *Annu. Rev. Phys. Chem.*, 2012, **63**, 541.
- 8 K. Rajeshwar, *J. Phys. Chem. Lett.*, 2011, **2**, 1301.
- 9 G. Ghadimkhani, N. R. de Tacconi, W. Chanmanee, C. Janaky and K. Rajeshwar, *Chem. Commun.*, 2013, **49**, 1297.
- 10 K. Rajeshwar, N. R. de Tacconi, G. Ghadimkhani, W. Chanmanee and C. Janáky, *ChemPhysChem*, 2013, **14**, 2251.
- 11 D. H. Won, C. H. Choi, J. Chung and S. I. Woo, *Appl. Catal., B*, 2014, **158–159**, 217.
- 12 X. Ba, L. Yan, S. Huang, J. Yu, X. Xia and Y. Yu, *J. Phys. Chem. C*, 2014, **118**, 24467.
- 13 J. F. de Brito, A. Da Silva, A. Cavalheiro and B. Zaroni, *Int. J. Electrochem. Sci.*, 2014, **9**, 5961.
- 14 H. Homayon, C. Wilaiwan, N. R. de Tacconi, B. H. Dennis and K. Rajeshwar, *J. Electrochem. Soc.*, 2015, **162**, E115.
- 15 L. Bendavid and E. Carter, *J. Phys. Chem. C*, 2013, **117**, 26048.
- 16 S. Wu, Z. Yin, Q. He, G. Lu, X. Zhou and H. Zhang, *J. Mater. Chem.*, 2011, **21**, 3467.
- 17 Z. Zhang, R. Dua, L. Zhang, H. Zhu, H. Zhang and P. Wang, *ACS Nano*, 2013, **7**, 1709.
- 18 A. Paracchino, V. Laporte, K. Sivula, M. Grätzel and E. Thimsen, *Nat. Mater.*, 2011, **10**, 456.
- 19 A. Paracchino, N. Mathews, T. Hisatomi, M. Stefik, S. D. Tilley and M. Grätzel, *Energy Environ. Sci.*, 2012, **5**, 8673.

- 20 C. W. Li and M. W. Kanan, *J. Am. Chem. Soc.*, 2012, **134**, 7231.
- 21 F. E. Osterloh, *Chem. Soc. Rev.*, 2013, **42**, 2294.
- 22 W.-D. Zhang, B. Xu and L.-C. Jiang, *J. Mater. Chem.*, 2010, **20**, 6383.
- 23 J. Young Kim, J.-W. Jang, D. Hyun Youn, J. Yul Kim, E. Sun Kim and J. Sung Lee, *RSC Adv.*, 2012, **2**, 9415.
- 24 X. Huang, X. Qi, F. Boey and H. Zhang, *Chem. Soc. Rev.*, 2012, **41**, 666.
- 25 K. Rajeshwar, C. Janaky, W.-Y. Lin, D. A. Roberts and W. Wampler, *J. Phys. Chem. Lett.*, 2013, **4**, 3468.
- 26 I. V. Lightcap and P. V. Kamat, *Acc. Chem. Res.*, 2013, **46**, 2235.
- 27 H. Li, X. Zhang and D. R. MacFarlane, *Adv. Energy Mater.*, 2014, **5**, 1401077.
- 28 X. An, K. Li and J. Tang, *ChemSusChem*, 2014, **7**, 1086.
- 29 C. Janaky, E. Kecszenovity and K. Rajeshwar, *ChemElectroChem*, DOI: 10.1002/celec.201500460, in press.
- 30 D. Fejes, Z. Pápa, E. Kecszenovity, B. Réti, Z. Toth and K. Hernadi, *Appl. Phys. A*, 2015, **118**, 855.
- 31 Y. Zhou and J. A. Switzer, *Scr. Mater.*, 1998, **38**, 1731.
- 32 L. C. Wang, N. R. de Tacconi, C. R. Chenthamarakshan, K. Rajeshwar and M. Tao, *Thin Solid Films*, 2007, **515**, 3090.
- 33 N. A. Mohemmed Shanid, M. Abdul Khadar and V. G. Sathe, *J. Raman Spectrosc.*, 2011, **42**, 1769.
- 34 W. Aolan, L. Xueshan, Z. Yibo, W. Wei, C. Jianfeng and M. Hong, *Powder Technol.*, 2014, **261**, 42.
- 35 M. Liu, R. Liu and W. Chen, *Biosens. Bioelectron.*, 2013, **45**, 206.

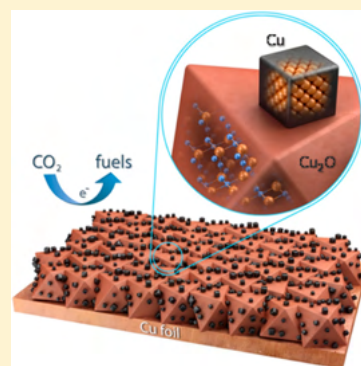
# Electro- and Photoreduction of Carbon Dioxide: The Twain Shall Meet at Copper Oxide/Copper Interfaces

C. Janáky,<sup>†,‡</sup> D. Hursán,<sup>†,‡</sup> B. Endrődi,<sup>†,‡</sup> W. Chanmanee,<sup>⊥</sup> D. Roy,<sup>§</sup> D. Liu,<sup>§</sup> N. R. de Tacconi,<sup>§</sup> B. H. Dennis,<sup>⊥</sup> and K. Rajeshwar<sup>\*,§</sup>

<sup>†</sup>MTA-SZTE, Lendület Photoelectrochemistry Research Group and <sup>‡</sup>Department of Physical Chemistry and Materials Science, University of Szeged, Rerrich Square 1, Szeged H-6720, Hungary

<sup>§</sup>Department of Chemistry and Biochemistry and <sup>⊥</sup>Department of Mechanical and Aerospace Engineering, University of Texas at Arlington, Arlington, Texas 76019, United States

**ABSTRACT:** Of the myriad electrode materials that have been used for electrochemical (EC) and photoelectrochemical (PEC) reduction of carbon dioxide in aqueous media, copper oxide/copper interfaces have shown a remarkable range of hydrocarbon and oxygenated products including acids, aldehydes, ketones, and alcohols. This Perspective highlights experimental evidence for the fact that both EC and PEC reduction scenarios have similar chemical and morphological underpinnings in the in situ formation of copper nano- or microcubes on the (photo)cathode surface. Recent rapid developments in our fundamental understanding of these interfaces and areas requiring further studies are discussed in light of recent studies in the authors' laboratories and elsewhere.



Much has been written already about the technological relevance of carbon dioxide (CO<sub>2</sub>) conversion and utilization.<sup>1–3</sup> Whether it makes sense from an overall energy balance and practical feasibility perspective, it is hardly debatable that electrochemical (EC) reduction and subsequent hydrogenation/oxygenation of an inert molecule such as CO<sub>2</sub> has considerable fundamental appeal. On the other hand, the energy input needed for the process is considerably ameliorated by the addition of solar excitation of the active material (a photoresponsive semiconductor) such that the CO<sub>2</sub> reduction now occurs at 700 mV positive of the thermodynamic threshold. Both process variants are hardly new, and the electroreduction concept was first published some 150 years ago.<sup>4</sup> The modern era of CO<sub>2</sub> electroreduction, however, can be traced back to the 1970s and 1980s. The photoelectrochemical (PEC) approach first surfaced around the same time, with the seminal paper appearing in 1978.<sup>5</sup> Since then, interest in both the EC and PEC approaches has been frenetic, especially during the past 5 years.

The one-electron reduction of CO<sub>2</sub> to the radical anion is a high-energy pathway and occurs at a standard potential of  $-1.90$  V in water.<sup>6</sup> On the other hand, the two-electron reduction generates CO via a pathway that is shared by enzymatic processes and metal electrode surfaces. Subsequent conversion to hydrocarbons and oxygenates, however, requires the use of a catalyst and cogeneration of hydrogen. A wide range of electrode materials and electrolytes have been deployed for the EC and

PEC conversion of CO<sub>2</sub>; many reviews and book chapters exist.<sup>6–13</sup> In terms of sustainability and process scalability, however, only a limited range of candidates are worthy of serious consideration for technological deployment. Thus, the use of earth-abundant and nontoxic electrode materials has considerable appeal relative to noble metals (e.g., Pt, Ru, Rh, etc.) or nonabundant elements (e.g., Ga, In, etc.). Likewise, notwithstanding the limited solubility of CO<sub>2</sub> in water (0.033 M at 298 K and 1 atm), the use of aqueous electrolytes presents considerable practical advantages relative to aprotic solvents and ionic liquids. Approaches involving semiconductor suspensions and sacrificial reagents (the so-called “photocatalytic” (PC) processes),<sup>14,15</sup> while extremely simple and attractive from an initial materials screening perspective, will not be practical. For example, (a) the products are cogenerated in close proximity in PC reactors rather than in separate compartments as in the EC and PEC counterparts, (b) recovery and reuse of the photocatalyst necessitates an additional step in PC reactors, and (c) back-reactions are especially prevalent and the system attains a photostationary state. This Perspective thus focuses on the EC/PEC process variant involving one such intriguing electrode material, namely, copper oxide decorated with copper nano- or

Received: April 20, 2016

Accepted: May 11, 2016

Published: May 11, 2016

micrometer-sized particles. This rather complex electrode material henceforth is simply designated as  $\text{Cu}_x\text{O}/\text{Cu}$ .

*Peculiar Case of Copper Oxide/Nanoparticulate Copper.* Of all the myriad metals that have been used for EC reduction of  $\text{CO}_2$ ,

Of all the myriad metals that have been used for EC reduction of  $\text{CO}_2$ , only copper has shown a proclivity to generate C1–C3 hydrocarbons and oxygenated products.

only copper has shown a proclivity to generate C1–C3 hydrocarbons and oxygenated products. Copper oxide is a semiconductor, and both  $\text{Cu}_2\text{O}$  and  $\text{CuO}$  are known to exhibit p-type semiconductor behavior. The so-called “oxide-derived”  $\text{Cu}^{16,17}$  has been shown to have much higher selectivity toward  $\text{CO}_2$  electroreduction (relative to the hydrogen evolution reaction or HER) than does polycrystalline copper. Thus, the  $\text{Cu}_x\text{O}/\text{Cu}$  interface is unusual in that it can be deployed for both EC and PEC reduction of  $\text{CO}_2$ . Finally, while demand for copper metal generally has soared because of power transmission and microelectronics industry needs, it still is an earth-abundant and nontoxic material. For all of these reasons, the liquid junction formed by this composite interface forms the focus of this Perspective.

Interest in  $\text{Cu}_2\text{O}$  first began in the 1920s, and subsequently both oxides of copper were evaluated for use in solid-state photovoltaic devices.<sup>18</sup> The earliest report on the use of these metal oxides in PEC devices dates back to the 1970s.<sup>19</sup> The first report of the use of hydrous  $\text{Cu}_2\text{O}$  suspensions for  $\text{CO}_2$  photoreduction occurred much later in 1989.<sup>20</sup> The use of  $\text{Cu}_2\text{O}$  photocathodes began soon thereafter, and there has been explosive growth of interest in this PEC approach, particularly since ~2010. The various aspects of the preparation, characterization, and use of  $\text{Cu}_2\text{O}$  have been reviewed.<sup>18</sup>

The oxide layers are generally grown by thermal annealing of polycrystalline copper foils in air. Both the annealing time and annealing temperature are crucial variables in dictating the subsequent behavior of the oxides, as discussed later. Thermal growth of copper oxide nanowires on copper foil has been reviewed.<sup>21</sup> Electrosynthesis is another powerful tool for preparing  $\text{Cu}_x\text{O}$  layers or nanoparticles;<sup>22–24</sup> modifications in deposition bath can be used to tune the nanoparticle morphology, as demonstrated in these studies. This aspect is further addressed below within the context of product selectivity in  $\text{CO}_2$  reduction.

*Both Oxide Phases Are Important in the PEC Activity for  $\text{CO}_2$  Reduction.* Thermal annealing of a copper foil generates both

Thermal annealing of a copper foil generates both copper oxides (i.e.,  $\text{Cu}_2\text{O}$  and  $\text{CuO}$ ), whose relative dominance can be tracked by X-ray powder diffraction (XRD).

copper oxides (i.e.,  $\text{Cu}_2\text{O}$  and  $\text{CuO}$ ), whose relative dominance can be tracked by X-ray powder diffraction (XRD). As shown in Figure 1a, high aspect ratio (>200), dense, vertically standing copper oxide heterojunction nanowires were fabricated by simply heating a copper substrate in air. Interestingly, the PEC

activity for  $\text{CO}_2$  reduction for these fabricated materials appears to be closely correlated with the relative dominance of the two formed phases,  $\text{Cu}_2\text{O}$  and  $\text{CuO}$ , as established by quantitative analyses of XRD data (Figure 1b,c). The sample with the more dominant  $\text{Cu}_2\text{O}$  phase (500 °C, Figure 1b; 4 h, Figure 1c) was seen to afford the highest photocurrent for  $\text{CO}_2$  reduction.

*In Situ Formation of Copper on Cuprous Oxide Photocathodes and Consequences in Terms of PEC Activity.* On the notion that copper that is formed in situ on the  $\text{Cu}_2\text{O}$  surface during photoirradiation in  $\text{CO}_2$ -containing solutions plays a key role in the PEC activity, the following series of comparative experiments were performed. The  $\text{Cu}_2\text{O}$  films were electrodeposited on Cu foils and glassy carbon electrodes<sup>24</sup> and irradiated with simulated sunlight for different time periods (5, 10, 30, 60 min) in 0.1 M  $\text{NaHCO}_3/\text{satd. CO}_2$  solution (to mimic the conditions in  $\text{CO}_2$  photoelectrolysis). No external bias potential was applied to the photocathode in these experiments. As a control measurement, an identical  $\text{Cu}_2\text{O}$  film was electroreduced (for 60 min) at  $E = -1.5$  V (vs Ag/AgCl reference) to obtain  $\text{Cu}_2\text{O}$ -derived metallic copper. The first striking difference was the color of the samples (Figure 2), namely, the oxide film became progressively darker with increasing irradiation time (in fact, the sample irradiated for 60 min was completely black). XRD patterns were recorded to prove that this change in the color was coupled with the increasing Cu content of the samples (note that no  $\text{CuO}$  was detected). Rietveld refinement of the XRD patterns proved that the  $\text{Cu}_2\text{O}:\text{Cu}$  ratio systematically increased in the series of samples and it reached 4:1 after 60 min of irradiation.

Scanning electron microscopy (SEM) images (Figure 3) were taken to study the morphological changes associated with Cu formation in the samples. While the bare  $\text{Cu}_2\text{O}$  layer showed the characteristic nanocrystal morphology (Figure 3a),<sup>24</sup> important changes were observed even after only 5 min of irradiation. In this case, the initial crystallites could still be seen, but they lost their sharp edges, and Cu nanocubes (50–80 nm) were formed on the surface. When continuing the irradiation, the initial morphology changed and a porous Cu film was obtained (Figure 3d). The morphology of an electroreduced Cu oxide sample was also studied for comparison (Figure 3c). A relatively compact structure was found in this case, where the surface was decorated with small-sized (~20 nm) nanocubes. Note that this morphology is rather similar to the one shown for the  $\text{Cu}_2\text{O}$  sample irradiated for short timeframes (Figure 3b), although the nanoparticle size was distinctly smaller for the electroreduced sample. Irradiation for longer times (e.g., 60 min, Figure 3d) resulted in markedly altered morphology from that in panel (b), reflecting further chemical changes of the oxide layer. This corresponds to the blackened layer visually seen in Figure 2.

The distinct morphological differences highlighted above are also reflected in the electrocatalytic properties of the samples. The first striking variance is manifested in the electroactive surface area (as deduced from cyclic voltammetry, Figure 4). While the electroreduced samples had 3–4 times higher surface roughness compared with the flat Cu electrode, the same ratio was around 6–7 for the photoreduced sample (Figure 4a). Subsequently, linear sweep voltammograms were recorded in  $\text{HCO}_3^-/\text{CO}_2$  solution to assess the electrocatalytic activity of the samples. The most important observation was the shift in the onset potential. While for the bulk Cu foil  $\text{CO}_2$  reduction started at  $E = -1.0$  V (vs Ag/AgCl reference), the onset potential was notably more positive for the  $\text{Cu}_2\text{O}$ -derived Cu samples (–0.85 and –0.90 V for the electroreduced and photoreduced samples, respectively; Figure 4b).

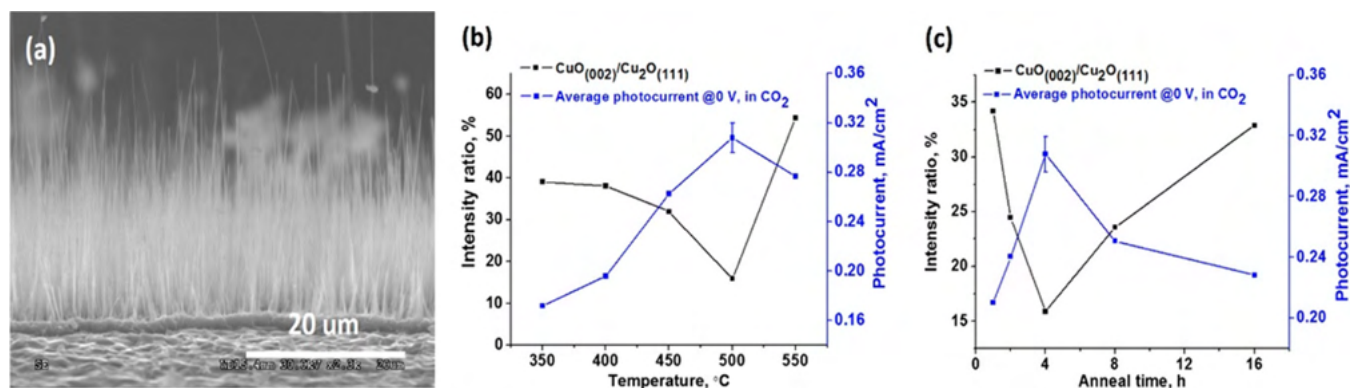


Figure 1. Side view (a) SEM images of copper-supported oxide layers grown by thermal annealing at 500 °C for 4 h. Panels b and c map the correlation between the relative fraction of CuO and Cu<sub>2</sub>O (as established by powder XRD analyses) and the average photocurrent for CO<sub>2</sub> reduction as a function of thermal annealing temperature (at a fixed 4 h time) (b) and time (at fixed 500 °C anneal temperature) (c). The photocurrents were measured in CO<sub>2</sub>-saturated 0.1 M sodium sulfate at zero applied bias (i.e., at short-circuit). The error bars in (b) and (c) were obtained from measurements on eight separate samples.

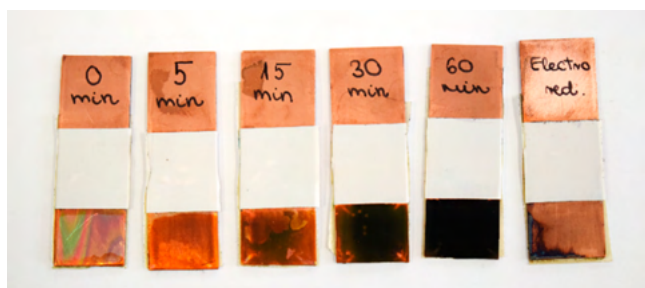


Figure 2. Photographs of slides containing Cu<sub>2</sub>O layers irradiated in CO<sub>2</sub>-containing solutions for varying times without an externally applied bias potential. An electroreduced control sample (refer to the text) is also shown for comparison.

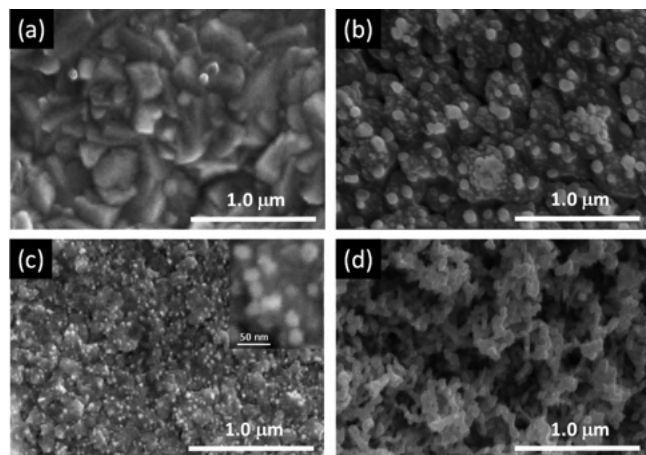


Figure 3. SEM images of the various Cu<sub>2</sub>O-derived films. (a) Bare Cu<sub>2</sub>O, (b) Cu<sub>2</sub>O irradiated with simulated sunlight for 15 min, (c) Cu<sub>2</sub>O electroreduced at  $-1.5$  V (vs Ag/AgCl/3 M NaCl) for 60 min, and (d) Cu<sub>2</sub>O irradiated with simulated sunlight for 60 min.

This latter observation is consistent with literature data where a 150–200 mV shift was seen in the onset potential when comparing bulk and oxide-derived Cu.<sup>16</sup> To prove that these increased currents were related to CO<sub>2</sub> reduction, and not to the reduction of Cu<sub>2</sub>O traces present in the samples, long-term electrolysis was also performed on both Cu<sub>2</sub>O and Cu electrodes (Figure 4c,d). While at the initial stage of the electrolysis the

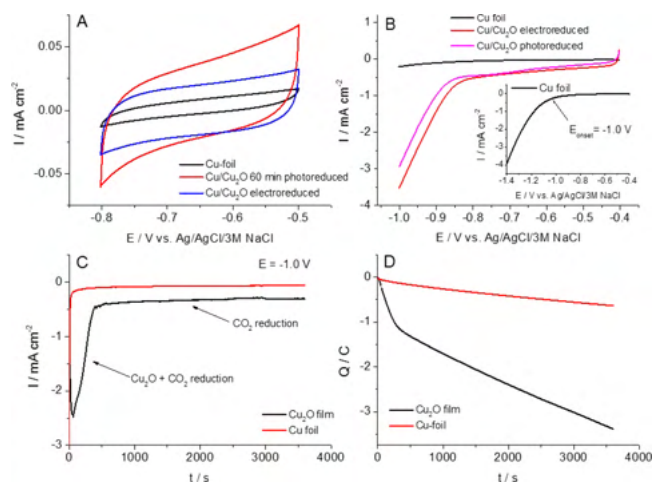


Figure 4. (a) Cyclic voltammograms of the different Cu<sub>2</sub>O-derived films, registered in 0.1 M phosphate buffer solution (pH = 7) at a sweep rate of 25 mV s<sup>-1</sup>. (b) Linear sweep voltammetry curves recorded for the different Cu<sub>2</sub>O-derived films in 0.1 M NaHCO<sub>3</sub>/satd. CO<sub>2</sub> solution at a sweep rate of 25 mV s<sup>-1</sup>. (c,d) Current–time and charge–time curves registered for a Cu foil and Cu<sub>2</sub>O film in 0.1 M NaHCO<sub>3</sub>/satd. CO<sub>2</sub> solution at E =  $-1.0$  V potential (vs Ag/AgCl reference).

reduction of Cu<sub>2</sub>O and CO<sub>2</sub> occurred in parallel, after the oxide was completely reduced (note that the necessary charge perfectly matches the stoichiometric amount, 1 C), CO<sub>2</sub> reduction was sustained on the oxide-derived metal surface. Thus, the difference between the two samples cannot be simply ascribed to the difference in surface area; rather, other structural factors (nanoparticle size, crystal facets, interparticle grain boundaries, etc.) also must contribute to the enhanced activity (see below).

The gradual conversion of Cu<sub>2</sub>O to metallic copper during the PEC processes has at least two effects on PEC performance. First, the formation of traces of Cu (cf. Figure 3b) enhances the PEC activity due to the intrinsic catalytic activity of the Cu nanocubes. Existence of a Schottky junction between Cu<sub>2</sub>O and Cu can also facilitate e<sup>-</sup>/h<sup>+</sup> separation, thus enhancing the catalytic activity. On the other hand, especially after longer irradiation, gradual consumption of the Cu<sub>2</sub>O semiconductor component (because of photocorrosion) leads to a decrease in light absorption and consequently results in the cessation of PEC activity. Note,

however, that the photoreduction studies presented here were performed in the absence of any external bias potential.

The photocorrosion of  $\text{Cu}_x\text{O}$  in this system is not a fatal flaw because the electrode material can be regenerated, as demonstrated by our recent study on  $\text{Cu}_2\text{O}/\text{CNT}$  photoelectrodes.<sup>24</sup> Electro-oxidation of the photogenerated Cu (to  $\text{Cu}_2\text{O}$ ) occurred during the dark periods periodically inserted into the photoelectrolysis protocol. It is worth noting that this EC self-healing was enabled by selection of an optimal potential after careful analysis of the Pourbaix diagram for Cu.

*Reduction Products, Causal Factors in Product Distribution, and Crystal Engineering.* The  $\text{Cu}_x\text{O}/\text{Cu}$  interface is remarkable in the

The  $\text{Cu}_x\text{O}/\text{Cu}$  interface is remarkable in the range of products that have been reported from EC and PEC reduction of  $\text{CO}_2$ .

range of products that have been reported from EC and PEC reduction of  $\text{CO}_2$ . Table 1 collates the various reduction steps possible and corresponding redox potentials. Discounting the one-electron radical pathway, anywhere from 2 electrons up to 18 electrons can be delivered to the  $\text{CO}_2$  molecule (Table 1). Clearly, carbon–carbon bond formation upon deeper reduction is predicated upon initial binding of intermediates such as CO at active sites on the solid surface. It is hardly surprising that the surface morphology plays a key role in product selectivity. While many mechanistic details still remain to be elucidated, high-energy steps and edges on the crystal surface are currently believed to stabilize and afford the chemisorbed C1 and C2 intermediates to undergo intermolecular C–C coupling.

As many as 16 reaction products were observed in one EC reduction study on Cu, and of these, 12 were C2 or C3 species, comprised of a range of oxygenated species including hydrocarbons, ketones, aldehydes, carboxylic acids, and alcohols.<sup>25</sup> In our own PEC reduction studies on hybrid  $\text{CuO}/\text{Cu}_2\text{O}$  photocathodes, clean conversion of  $\text{CO}_2$  exclusively to methanol was initially observed.<sup>26,27</sup> However, our two later studies involving a different set of experimental conditions also revealed the additional formation of ethanol and isopropanol<sup>28</sup> and ethanol, formaldehyde, acetaldehyde, and acetone<sup>29</sup> in addition to methanol.

Theoretical insights<sup>30,31</sup> considerably aid in guiding experimentation and also for rationalizing the experimentally observed product selectivity trends. Thus, analysis of trends in the binding

energies for the  $\text{CO}_2$  reduction intermediates revealed the protonation of adsorbed CO as the most important step in dictating the overpotential magnitude.<sup>31</sup> Density functional theory (DFT) calculations have also been presented to this end.<sup>30</sup>

Ethylene and ethanol have higher energy densities and commercial value than the C1 counterparts. Thus, much effort has focused on optimizing, for example, the  $\text{C}_2\text{H}_4/\text{CH}_4$  product ratio in EC reduction schemes. In this vein, copper microcubes containing a large number of exposed (100) facets (see Figure 5)

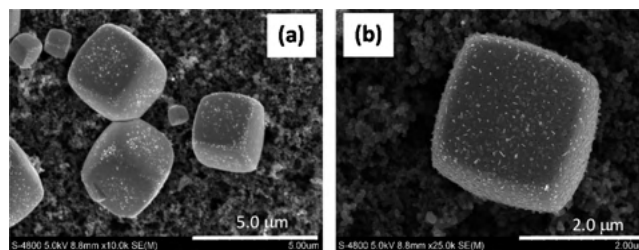


Figure 5. Representative SEM images at two magnifications of a  $\text{Cu}_x\text{O}/\text{Cu}$  microcube layer electrodeposited on a gas diffusion electrode (GDE) at  $-0.4$  V ( $60$  °C) from a pH 7 solution of  $0.2$  M  $\text{CuSO}_4 + 0.1$  M  $\text{CuBr} + 2$  M lactic acid.

have shown a much higher ratio than unstructured polycrystalline copper.<sup>32–36</sup> Their manifestation in PEC reduction was addressed above (cf. Figure 4b). While this morphology is derived from the use of copper(I) halides (chloride and bromide) as precursors (cf. Figure 5), in situ X-ray absorption spectroscopy (XAS) has revealed that copper(I) oxide, formed by the initial hydrolysis of the halide, is really the precursor to copper nanocube formation.<sup>35</sup> Undoubtedly, the deployment of new in situ probes such as XAS along with online mass spectrometry and techniques such as nuclear magnetic resonance (NMR) spectroscopy should continue to provide insights into deposition mechanisms and reaction pathways. Careful isotope labeling studies will also contribute to further mechanistic insights.

The electrolytes used, the potentials applied, and the crystal topology all have a major influence on EC reduction and, by extension, the PEC reduction product selectivity. The oxide layer thickness on copper is another crucial factor as is the local pH at the oxide/copper/electrolyte interface. A high local pH, for example, could suppress the HER and promote C2 coupling.<sup>36</sup> Finally, “crystal engineering” could be used to tune product

Table 1. Nonradical Reduction Pathways for Carbon Dioxide

product	reaction	standard reduction potential (V vs SHE, at pH = 7)
carbon monoxide	$\text{CO}_2 + 2\text{H}^+ + 2\text{e}^- = \text{CO} + \text{H}_2\text{O}$	−0.51
	Hydrocarbons	
methane	$\text{CO}_2 + 8\text{H}^+ + 8\text{e}^- = \text{CH}_4 + 2\text{H}_2\text{O}$	−0.24
ethane	$2\text{CO}_2 + 14\text{H}^+ + 14\text{e}^- = \text{C}_2\text{H}_6 + 4\text{H}_2\text{O}$	−0.27
ethylene	$2\text{CO}_2 + 12\text{H}^+ + 12\text{e}^- = \text{C}_2\text{H}_4 + 4\text{H}_2\text{O}$	−0.34
	Oxygenates	
formic acid	$\text{CO}_2 + 2\text{H}^+ + 2\text{e}^- = \text{HCOOH}$	−0.58
oxalic acid	$2\text{CO}_2 + 2\text{H}^+ + 2\text{e}^- = (\text{COOH})_2$	−0.87
formaldehyde	$\text{CO}_2 + 4\text{H}^+ + 4\text{e}^- = \text{HCHO} + \text{H}_2\text{O}$	−0.48
methanol	$\text{CO}_2 + 6\text{H}^+ + 6\text{e}^- = \text{CH}_3\text{OH} + \text{H}_2\text{O}$	−0.39
ethanol	$2\text{CO}_2 + 12\text{H}^+ + 12\text{e}^- = \text{C}_2\text{H}_5\text{OH} + 3\text{H}_2\text{O}$	−0.33
isopropanol	$3\text{CO}_2 + 18\text{H}^+ + 18\text{e}^- = \text{C}_3\text{H}_7\text{OH} + 5\text{H}_2\text{O}$	−0.32

selectivity. Two examples of this may be cited. Controlled chemical etching has been demonstrated<sup>37</sup> as a strategy for exposing high-energy (110) facets on copper nanocubes; the resultant EC reduction activity was significantly enhanced. The grain boundary density has been shown to be correlated to CO reduction activity for oxide-derived metals, suggesting another route for externally manipulating the catalytic activity of the surface.<sup>38</sup>

*Electrode and Reactor Designs for EC and PEC Reduction of CO<sub>2</sub>.* The vast majority of the initial studies were confined to stationary laboratory-scale batch reactors in both cases. Electrode designs also come into play. For example, a porous hollow fiber copper electrode with a compact three-electrode geometry has been shown to provide a large-area three-phase boundary for CO<sub>2</sub> EC reduction.<sup>39</sup> Borrowing from the fuel cell playbook, a GDE provides for operation at pressures higher than the ambient.<sup>9</sup> Solid-oxide fuel cells also provide for a matrix for performing CO<sub>2</sub> electrolysis at higher temperatures with concomitant improvements in process thermodynamics and kinetics.<sup>9</sup> Energy efficiencies for various CO<sub>2</sub> electrolyzer designs have been compared.<sup>3</sup> The challenge here is to simultaneously secure high values of energy efficiency and cathodic current density. Reactor designs for PEC reduction of CO<sub>2</sub> have been reviewed.<sup>13</sup> In our own studies of a continuous-flow PEC reactor (CFPR) for CO<sub>2</sub> reduction, interesting shifts in product distribution away from C1 (methanol) to longer chain products were observed because of the small volume in the cathode microchannel and consequential ease of coupling of the initial electrogenerated precursors.<sup>28</sup>

*Future Outlook.* In summary, this Perspective has highlighted the important fact that morphological evolution of the (photo)-cathode during the complex steps involved in the addition of electrons and protons to CO<sub>2</sub> has similar underpinnings in both EC and PEC reduction scenarios. Nonetheless and as pointed out earlier, the chemical changes undergone by the copper oxide surface during CO<sub>2</sub> (photo)reduction need not be considered a fatal flaw in the use of this intriguing material. Many natural assemblies (e.g., the plant photosynthesis apparatus) do indeed undergo self-repair mechanisms after exposure to high photon fluxes. In a similar fashion, a periodic reactivation step to regenerate CO<sub>2</sub> reduction activity may be built into the overall process design to combat too deep of a reduction of the copper oxide layer.

Interestingly, however, the behavior of copper-based electrodes calls into question our traditional notion of a chemical catalyst as an agent that does not itself undergo chemical change! This aspect certainly is not the only puzzle that the Cu<sub>2</sub>O/Cu/liquid interface holds; many more surprises undoubtedly await the intense EC and PEC scrutiny of it in the coming months and years. Finally, the features of copper oxide/copper interfaces as noted here may not be unique; recent studies highlighting similar trends in other metal oxide/metal interfaces, including Au, Sn, and even Co, are worthy of note.<sup>40–42</sup>

The behavior of copper-based electrodes calls into question our traditional notion of a chemical catalyst as an agent that does not itself undergo chemical change!

Finally, notwithstanding the remarkable strides that have been made in the past 5 years in our understanding of copper-based

electrodes and photoelectrodes for CO<sub>2</sub> (photo)reduction, the product fluxes need to be boosted significantly to levels that are sufficiently high for reactor scale-up and engineering. There are promising avenues, including the incorporation of additional metal ions into the copper oxide host framework (e.g., CuFeO<sub>2</sub> and CuNb<sub>2</sub>O<sub>6</sub>)<sup>43,44</sup> or the use of 3D electrode architectures of highly conductive nanocarbons such as aligned carbon nanotubes or graphene foams. Finally, further advances in electrode and reactor designs also have to occur to translate the laboratory-scale findings to technological readiness.

## ■ AUTHOR INFORMATION

### Corresponding Author

\*E-mail: [rajeshwar@uta.edu](mailto:rajeshwar@uta.edu).

### Notes

The authors declare no competing financial interest.

### Biographies

**Csaba Janáky** obtained his Ph.D. at the University of Szeged in 2011. Subsequently, he was a Marie Curie Fellow at the University of Texas at Arlington between 2011 and 2013. Since 2014, he has been the Principal Investigator of the MTA-SZTE “Momentum” Photoelectrochemistry Research Group, supported by the excellence program of the Hungarian Academy of Sciences. His scientific interests include various aspects of energy-oriented semiconductor electrochemistry and photoelectrochemistry.

**Dorottya Hursán** is a Ph.D. student at the University of Szeged, under the supervision of Prof. Janáky. Her research focuses on the electrochemical and photoelectrochemical conversion of CO<sub>2</sub>.

**Balázs Endrődi** completed his education at the University of Szeged, where he obtained his Ph.D. in 2015. Currently he is an assistant professor at his alma mater, focusing on electrochemical energy conversion.

**Wilaiwan Chanmanee** received her M.Sc. degree in Environmental Engineering at Kasetsart University (Thailand) in 2005 and went on to receive her Ph.D. degree in Environmental Science at Chulalongkorn University (Thailand) in 2008. She is a postdoctoral researcher at the Center for Renewable Energy and Science Technology at the University of Texas at Arlington.

**Daipayan Roy**, a native of India, is currently a first-year graduate student at the University of Texas, Arlington. He completed his Master’s degree from the University of Pune with a specialization in inorganic chemistry in 2015.

**Dong Liu** received his Ph.D. in Materials Science and Engineering from the University of Texas at Arlington in 2015. He is a postdoctoral researcher at the Center for Renewable Energy and Science Technology at the University of Texas at Arlington.

**Norma R. de Tacconi** received her Ph.D. in Electrochemistry (1975) from the University of La Plata and INIFTA, Argentina. After postdoctoral research (1977–1978) at the University of Paris VII, France, she was scientist of INIFTA/CONICET until 1991 when she moved to the United States. She is a Research Associate Professor at the University of Texas at Arlington, and her current research interests are on metal and semiconductor nanostructures and nanocomposites for (photo)electroreduction of carbon dioxide.

**Brian H. Dennis** received his Ph.D. in Aerospace Engineering (2000) from the Pennsylvania State University where he focused on the development of numerical methods for simulating the interaction of conducting fluids with electromagnetic fields. He is currently a Professor of Mechanical & Aerospace Engineering at the University of Texas at Arlington. His current research interests are on the design, numerical

simulation, and fabrication of electrochemical and photoelectrochemical reactors.

**Krishnan Rajeshwar** completed his Masters and Ph.D. degrees in solid-state chemistry at the Indian Institute of Technology (Kharagpur, India) and Indian Institute of Science (Bengaluru, India), respectively. After postdoctoral training at Colorado State University (Fort Collins, CO) in the area of energy R&D, he joined the faculty of the University of Texas at Arlington in 1983, where he is currently Distinguished University Professor. He is also Senior Vice President and President-Elect of the Electrochemical Society. His research interests span a broad spectrum in materials chemistry and design for thermal, electrochemical, and photoelectrochemical energy conversion.

## ACKNOWLEDGMENTS

We thank the following agencies for partial funding support of the research described herein: the National Science Foundation (CHE-1303803) (to K.R.); Hungarian Academy of Science, "Momentum" Excellence Program (LP2014-3) (to C.J.); and NASA (Award No. NNL15AA08C to K.R., N.d.T., and B.H.D.). The authors also thank Rendernet Ltd. for assistance in preparing the artwork in the TOC. The constructive criticisms provided by three anonymous reviewers on an initial version of this manuscript are much appreciated.

## REFERENCES

- Olah, G. A.; Prakash, G. K. S.; Goepfert, A. Anthropogenic Chemical Carbon Cycle for a Sustainable Future. *J. Am. Chem. Soc.* **2011**, *133*, 12881–12898.
- Oloman, C.; Li, H. Electrochemical Processing of Carbon Dioxide. *ChemSusChem* **2008**, *1*, 385–391.
- Whipple, D. T.; Kenis, P. J. A. Prospects of CO<sub>2</sub> Utilization via Direct Heterogeneous Electrochemical Reduction. *J. Phys. Chem. Lett.* **2010**, *1*, 3451–3458.
- Royer, M. E. Réduction de L'acide Carbonique En Acide Formique. *C. R. Hebd. Séanc. Acad. Sci., Paris* **1870**, *70*, 731–732.
- Halmann, M. Photoelectrochemical Reduction of Aqueous Carbon Dioxide on p-Type Gallium Phosphide in Liquid Junction Solar Cells. *Nature* **1978**, *275*, 115–116.
- Costentin, C.; Robert, M.; Savéant, J.-M. Catalysis of the Electrochemical Reduction of Carbon Dioxide. *Chem. Soc. Rev.* **2013**, *42*, 2423–2436.
- Hori, Y. Electrochemical CO<sub>2</sub> Reduction on Metal Electrodes. In *Modern Aspects of Electrochemistry*; Vayenas, C. G., White, R. E., Gamboa-Aldeco, M. E., Eds.; Springer, 2008; pp 89–189.
- Roy, S. C.; Varghese, O. K.; Paulose, M.; Grimes, C. A. Toward Solar Fuels: Photocatalytic Hydrocarbons. *ACS Nano* **2010**, *4*, 1259–1278.
- Kondratenko, E. V.; Mul, G.; Baltrusaitis, J.; Larrazabal, G. O.; Perez-Ramirez, J.; Larrazabal, G. O.; Pérez-Ramírez, J. Status and Perspectives of CO<sub>2</sub> Conversion into Fuels and Chemicals by Catalytic, Photocatalytic and Electrocatalytic Processes. *Energy Environ. Sci.* **2013**, *6*, 3112–3135.
- Ogura, K. Electrochemical Reduction of Carbon Dioxide to Ethylene: Mechanistic Approach. *Journal of CO<sub>2</sub> Utilization* **2013**, *1*, 43–49.
- Lu, Q.; Rosen, J.; Jiao, F. Nanostructured Metallic Electrocatalysts for Carbon Dioxide Reduction. *ChemCatChem* **2015**, *7*, 38–47.
- Chang, X.; Wang, T.; Gong, J. CO<sub>2</sub> Photo-Reduction: Insights into CO<sub>2</sub> Activation and Reaction on Surfaces of Photocatalysts. *Energy Environ. Sci.* **2016**, DOI: 10.1039/C6EE00383D.
- Li, K.; An, X.; Park, K. H.; Khraisheh, M.; Tang, J. A Critical Review of CO<sub>2</sub> Photoconversion: Catalysts and Reactors. *Catal. Today* **2014**, *224*, 3–12.
- Rajeshwar, K.; Thomas, A.; Janaky, C. Photocatalytic Activity of Inorganic Semiconductor Surfaces: Myths, Hype, and Reality. *J. Phys. Chem. Lett.* **2015**, *6*, 139–147.
- Inoue, T.; Fujishima, A.; Konishi, S.; Honda, K. Photoelectrocatalytic Reduction of Carbon Dioxide in Aqueous Suspensions of Semiconductor Powders. *Nature* **1979**, *277*, 637–638.
- Li, C. W.; Kanan, M. W. CO<sub>2</sub> Reduction at Low Overpotential on Cu Electrodes Resulting from the Reduction of Thick Cu<sub>2</sub>O Films. *J. Am. Chem. Soc.* **2012**, *134*, 7231–7234.
- Li, C. W.; Ciston, J.; Kanan, M. W. Electroreduction of Carbon Monoxide to Liquid Fuel on Oxide-Derived Nanocrystalline Copper. *Nature* **2014**, *508*, 504–507.
- Rakhshani, A. E. Preparation, Characteristics and Photovoltaic Properties of Cuprous Oxide - a Review. *Solid-State Electron.* **1986**, *29*, 7–17.
- Hardee, K. L.; Bard, A. J. Semiconductor Electrodes X. Photoelectrochemical Behavior of Several Polycrystalline Metal Oxide Electrodes in Aqueous Solutions. *J. Electrochem. Soc.* **1977**, *124*, 215–224.
- Tennakone, K.; Jayatissa, A. H.; Punchihewa, S. Selective Photoreduction of Carbon Dioxide with Hydrous Cuprous Oxide. *J. Photochem. Photobiol., A* **1989**, *49*, 369–375.
- Filipič, G.; Cvelbar, U. Copper Oxide Nanowires: A Review of Growth. *Nanotechnology* **2012**, *23*, 194001.
- Wang, L. C.; de Tacconi, N. R.; Chenthamarakshan, C. R.; Rajeshwar, K.; Tao, M. Electrodeposited Copper Oxide Films: Effect of Bath pH on Grain Orientation and Orientation-Dependent Interfacial Behavior. *Thin Solid Films* **2007**, *515*, 3090–3095.
- Siegfried, M. J.; Choi, K. S. Elucidation of an Overpotential-Limited Branching Phenomenon Observed during the Electrocrystallization of Cuprous Oxide. *Angew. Chem., Int. Ed.* **2008**, *47*, 368–372.
- Kecsenovity, E.; Endrodi, B.; Pápa, Z.; Hernadi, K.; Rajeshwar, K.; Janaky, C. Ultralong Carbon Nanotubes Decorated with Cu<sub>2</sub>O Nanocrystals: A Hybrid Platform for Enhanced Photoelectrochemical CO<sub>2</sub> Reduction. *J. Mater. Chem. A* **2016**, *4*, 3139–3147.
- Kuhl, K. P.; Cave, E. R.; Abram, D. N.; Jaramillo, T. F. New Insights into the Electrochemical Reduction of Carbon Dioxide on Metallic Copper Surfaces. *Energy Environ. Sci.* **2012**, *5*, 7050–7059.
- Ghadimkhani, G.; de Tacconi, N. R.; Chanmanee, W.; Janaky, C.; Rajeshwar, K. Efficient Solar Photoelectrosynthesis of Methanol from Carbon Dioxide Using Hybrid CuO-Cu<sub>2</sub>O Semiconductor Nanorod Arrays. *Chem. Commun.* **2013**, *49*, 1297–1299.
- Rajeshwar, K.; de Tacconi, N. R.; Ghadimkhani, G.; Chanmanee, W.; Janáky, C. Tailoring Copper Oxide Semiconductor Nanorod Arrays for Photoelectrochemical Reduction of Carbon Dioxide to Methanol. *ChemPhysChem* **2013**, *14*, 2251–2259.
- Homayoni, H.; Chanmanee, W.; de Tacconi, N. R.; Dennis, B. H.; Rajeshwar, K. Continuous Flow Photoelectrochemical Reactor for Solar Conversion of Carbon Dioxide to Alcohols. *J. Electrochem. Soc.* **2015**, *162*, E115–E122.
- de Brito, J. F.; Araujo, A. R.; Rajeshwar, K.; Zanon, M. V. B. Photoelectrochemical Reduction of CO<sub>2</sub> on Cu/Cu<sub>2</sub>O Films: Product Distribution and pH Effects. *Chem. Eng. J.* **2015**, *264*, 302–309.
- Shi, C.; Hansen, H. A.; Lausche, A. C.; Nørskov, J. K. Trends in Electrochemical CO<sub>2</sub> Reduction Activity for Open and Close-Packed Metal Surfaces. *Phys. Chem. Chem. Phys.* **2014**, *16*, 4720–4727.
- Peterson, A. A.; Nørskov, J. K. Activity Descriptors for CO<sub>2</sub> Electroreduction to Methane on Transition-Metal Catalysts. *J. Phys. Chem. Lett.* **2012**, *3*, 251–258.
- Lee, S.; Kim, D.; Lee, J. Electrocatalytic Production of C3-C4 Compounds by Conversion of CO<sub>2</sub> on a Chloride-Induced Bi-Phase Cu<sub>2</sub>O-Cu Catalyst. *Angew. Chem.* **2015**, *127*, 14914–14918.
- Roberts, F. S.; Kuhl, K. P.; Nilsson, A. High Selectivity for Ethylene from Carbon Dioxide Reduction over Copper Nanocube Electrocatalysts. *Angew. Chem., Int. Ed.* **2015**, *54*, 5179–5182.
- Ren, D.; Wong, N. T.; Handoko, A. D.; Huang, Y.; Yeo, B. S. Mechanistic Insights into the Enhanced Activity and Stability of Agglomerated Cu Nanocrystals for the Electrochemical Reduction of Carbon Dioxide to n-Propanol. *J. Phys. Chem. Lett.* **2016**, *7*, 20–24.
- Eilert, A.; Roberts, F. S.; Friebe, D.; Nilsson, A. Formation of Copper Catalysts for CO<sub>2</sub> Reduction with High Ethylene/Methane



Product Ratio Investigated with In Situ X-Ray Absorption Spectroscopy.

*J. Phys. Chem. Lett.* **2016**, *7*, 1466–1470.

(36) Raciti, D.; Livi, K. J.; Wang, C. Highly Dense Cu Nanowires for Low-Overpotential CO<sub>2</sub> Reduction. *Nano Lett.* **2015**, *15*, 6829–6835.

(37) Wang, Z.; Yang, G.; Zhang, Z.; Jin, M.; Yin, Y. Selectivity on Etching: Creation of High-Energy Facets on Copper Nanocrystals for CO<sub>2</sub> Electrochemical Reduction. *ACS Nano* **2016**, *10*, 4559–4564.

(38) Feng, X.; Jiang, K.; Fan, S.; Kanan, M. W. Grain-Boundary-Dependent CO<sub>2</sub> Electroreduction Activity. *J. Am. Chem. Soc.* **2015**, *137*, 4606–4609.

(39) Kas, R.; Hummadi, K. K.; Kortlever, R.; de Wit, P.; Milbrat, A.; Luiten-Olieman, M. W. J.; Benes, N. E.; Koper, M. T. M.; Mul, G. Three-Dimensional Porous Hollow Fibre Copper Electrodes for Efficient and High-Rate Electrochemical Carbon Dioxide Reduction. *Nat. Commun.* **2016**, *7*, 10748–10754.

(40) Chen, Y.; Li, C. W.; Kanan, M. W. Aqueous CO<sub>2</sub> Reduction at Very Low Overpotential on Oxide-Derived Au Nanoparticles. *J. Am. Chem. Soc.* **2012**, *134*, 19969–19972.

(41) Dutta, A.; Kuzume, A.; Rahaman, M.; Vesztergom, S.; Broekmann, P. Monitoring the Chemical State of Catalysts for CO<sub>2</sub> Electroreduction: An In Operando Study. *ACS Catal.* **2015**, *5*, 7498–7502.

(42) Gao, S.; Lin, Y.; Jiao, X.; Sun, Y.; Luo, Q.; Zhang, W.; Li, D.; Yang, J.; Xie, Y. Partially Oxidized Atomic Cobalt Layers for Carbon Dioxide Electroreduction to Liquid Fuel. *Nature* **2016**, *529*, 68–71.

(43) Gu, J.; Wuttig, A.; Krizan, J. W.; Hu, Y.; Detweiler, Z. M.; Cava, R. J.; Bocarsly, A. B. Mg-Doped CuFeO<sub>2</sub> Photocathodes for Photoelectrochemical Reduction of Carbon Dioxide. *J. Phys. Chem. C* **2013**, *117*, 12415–12422.

(44) Kormányos, A.; Thomas, A.; Huda, M. N.; Sarker, P.; Liu, J. P.; Poudyal, N.; Janáky, C.; Rajeshwar, K. Solution Combustion Synthesis, Characterization, and Photoelectrochemistry of CuNb<sub>2</sub>O<sub>6</sub> and ZnNb<sub>2</sub>O<sub>6</sub> Nanoparticles. *J. Phys. Chem. C* **2016**, DOI: [10.1021/acs.jpcc.5b12738](https://doi.org/10.1021/acs.jpcc.5b12738).



Cite this: *Chem. Commun.*, 2016, 52, 8858

Received 13th May 2016,  
Accepted 16th June 2016

DOI: 10.1039/c6cc04050k

www.rsc.org/chemcomm

## Polyaniline films photoelectrochemically reduce CO<sub>2</sub> to alcohols†

Dorottya Hursán,<sup>ab</sup> Attila Kormányos,<sup>abc</sup> Krishnan Rajeshwar<sup>\*cd</sup> and Csaba Janáky<sup>\*ab</sup>

**In this communication, we demonstrate that polyaniline, the very first example of an organic semiconductor, is a promising photocathode material for the conversion of carbon dioxide (CO<sub>2</sub>) to alcohol fuels. CO<sub>2</sub> is a greenhouse gas; thus using solar energy to convert CO<sub>2</sub> to transportation fuels (such as methanol or ethanol) is a value-added approach to simultaneous generation of alternative fuels and environmental remediation of carbon emissions. Insights into its unique behavior obtained from photoelectrochemical measurements and adsorption studies, together with spectroscopic data, are presented. Through a comparative study involving various conducting polymers, a set of criteria is developed for an organic semiconductor to function as a photocathode for generation of solar fuels from CO<sub>2</sub>.**

Sunlight is undoubtedly one of the most valuable resources in the quest for a diversified and sustainable energy supply.<sup>1,2</sup> Photoelectrochemistry has been proven to be a promising, albeit, challenging avenue for solar water splitting.<sup>3</sup> Solar splitting of CO<sub>2</sub>, however, is even more kinetically daunting, and requires the use of carefully designed photocathode surfaces to accelerate electron transfer rates to levels that make practical sense in terms of the overall energy balance.<sup>4,5</sup> A wide range of inorganic p-type semiconductors (SCs) (*e.g.*, Si, CdTe, InP, GaAs, GaP, FeS<sub>2</sub>, ZnTe, Cu<sub>2</sub>O, and CuFeO<sub>2</sub><sup>2,6–12</sup>) have been employed for photoelectrochemically reducing CO<sub>2</sub> either directly at the SC/electrolyte interface, or indirectly, employing a redox mediator.<sup>13</sup> At the same time, the use of an inorganic SC (with optoelectronically-acceptable properties) often necessitates the use of relatively high temperatures for its synthesis/processing and consequently long energy

payback time. Organic SCs are attractive from this perspective since they can be synthesized and processed *via* mild (low-temperature) routes; consequently, their energy payback time is much shorter. In this communication, we show that polyaniline (PANI), a prominent member of the organic conducting polymer family, is eminently attractive as a photocathode material for CO<sub>2</sub> reduction. Importantly our proof-of-concept data below show that: (a) no co-catalyst is needed for sustaining the photoconversion to alcohol products; and (b) PANI shows the requisite surface selectivity for chemical interactions with CO<sub>2</sub>. Interestingly, the findings of the present study would be in line with the fact that N-rich organic polymers (*e.g.*, polyimines) are currently among the best solid-state adsorbents for CO<sub>2</sub>.<sup>14–16</sup> Furthermore, conducting polymers such as polypyrrole (PPy) and PANI have shown electrocatalytic activity towards CO<sub>2</sub> reduction.<sup>17,18</sup> These polymers have also been deployed in conjunction with inorganic SCs such as Si<sup>19</sup> and ZnTe<sup>20</sup> for the photoelectrochemical (PEC) reduction of CO<sub>2</sub>. Conducting polymer-based hybrid organic photocathodes showed unprecedentedly high photocurrents, and high rates of PEC H<sub>2</sub>-generation with the use of a (homogeneous) co-catalyst;<sup>21</sup> in addition water oxidation was also demonstrated employing a special ladder-type conjugated polymer.<sup>22</sup> Finally, N-containing heterocycles such as pyridine<sup>11,23</sup> have been shown to be effective co-catalysts for the PEC reduction of CO<sub>2</sub> when used with SCs such as p-GaP.

The photovoltammograms presented in Fig. 1 bear all the hallmarks associated with the behavior of a p-type SC.<sup>24</sup> The photocurrents are cathodic in polarity, originating from the reduction of either H<sup>+</sup> ions or CO<sub>2</sub> at the conducting polymer/electrolyte interface. Photoexcitation of an electron from the valence band to the conduction band (*via* UV or visible light irradiation) is followed by electric-field separated photoelectrons being driven to the surface of the p-type SC where they can react with solution-confined species such as protons or CO<sub>2</sub>.

The CO<sub>2</sub>-reducing ability of the photogenerated electrons is dictated by the position of their surface quasi-Fermi level and the SC conduction band edge (Fig. S1, ESI†). Therefore it is possible to photoreduce CO<sub>2</sub> at a less negative potential (“underpotential”)

<sup>a</sup> Department of Physical Chemistry and Materials Science, University of Szeged, Szeged, Hungary. E-mail: janaky@chem.u-szeged.hu

<sup>b</sup> MTA-SZTE “Lendület” Photoelectrochemistry Research Group, Rerrich Square 1, 6720, Szeged, Hungary

<sup>c</sup> Department of Chemistry and Biochemistry, University of Texas at Arlington, Arlington, Texas, USA. E-mail: rajeshwar@uta.edu

<sup>d</sup> Center for Renewable Energy Science & Technology, University of Texas at Arlington, Arlington, Texas, USA

† Electronic supplementary information (ESI) available. See DOI: 10.1039/c6cc04050k

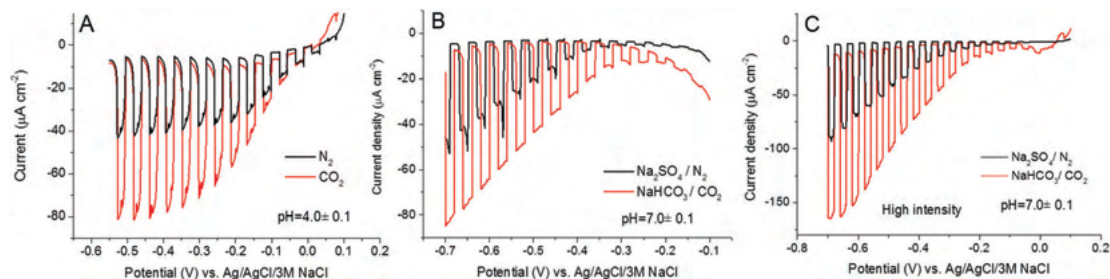


**Fig. 1** Representative photocurrent–potential profiles of an electrodeposited PANI layer under chopped UV-vis illumination (Xe–Hg arc lamp, 100 W output) in (A)  $N_2$ - and  $CO_2$ -saturated 0.1 M  $Na_2SO_4$  aqueous solution where the  $N_2$ -saturated solution was buffered to pH = 4.0; (B)  $N_2$ -saturated 0.1 M  $Na_2SO_4$  and  $CO_2$ -saturated  $NaHCO_3$  aqueous solutions (pH = 7.0); (C) photocurrent–potential profiles of an electrodeposited PANI layer under chopped UV-vis illumination (Xe–Hg arc lamp, 300 W output) in the same solution as (B).

relative to the thermodynamic reduction potential; the principal role of external bias potential is to augment the built-in electric field to separate the photogenerated charge carriers. This observation highlights the benefit of the PEC method over its “dark” electrochemical counterpart where usually a high overpotential (thus high energy input) is needed to drive the reaction due to the kinetic constraints of  $CO_2$  reduction.

Comparing the two curves in Fig. 1A, a two-fold increase was seen in the cathodic photocurrents in the plateau region in the presence of  $CO_2$ . What is also important is that the onset potential (+0.1 V vs. Ag/AgCl/3 M NaCl) observed at the maximum light intensity (Fig. 1C) was several hundred mV below the thermodynamic potential of most of the  $CO_2$  reduction processes, and in particular the  $CO_2/CH_3OH$  redox process (see Fig. S1, ESI†) which lies at  $-0.41$  V vs. Ag/AgCl/3 M NaCl at pH = 4. The pH strongly affects both the (photo)electroactivity of PANI<sup>25</sup> as well as the  $H^+$  reduction ( $H_2$ -evolution) process.

Notably, to separate the intrinsic contribution of  $CO_2$  from the more trivial pH-effect (caused by the increased  $H^+$  concentration because of the  $CO_2$  dissolution), the control measurement under an  $N_2$  atmosphere was recorded in a buffered solution having exactly the same pH as measured in  $CO_2$  saturated solution (pH =  $4.0 \pm 0.1$ , Fig. 1A). A similar comparison was made in  $NaHCO_3/CO_2$  solution (pH =  $7.0 \pm 0.1$ , Fig. 1B), and very similar conclusions were drawn, together with the observation of a 150 mV shift in the onset potential, which indicated the participation of  $H^+$  ions in the  $CO_2$  reduction. Finally, the photon flux was increased to the maximum output of the lamp (300 W), which resulted in an almost three-fold increase of the photocurrents (with a maximum of  $170 \mu A cm^{-2}$ , see Fig. 1C). This proportional increase in the photoconversion rate with the photon flux suggests that carrier-recombination processes are not yet rate-limiting in the overall process.

To further examine the photoreduction process, photoaction spectra were measured to determine internal photon to electron conversion efficiencies (IPCEs) both under  $N_2$  and  $CO_2$  saturation. As seen in Fig. 2A the obtained photoaction spectra perfectly corresponded to the UV-vis spectrum of PANI (Fig. 2B), recorded under identical circumstances (*i.e.*,  $E = -0.4$  V external bias potential). The threshold energy determined from the photoaction spectra (440 nm, 2.8 eV) nicely agreed with the bandgap energy (2.8 eV) obtained from the UV-vis spectra using the Tauc

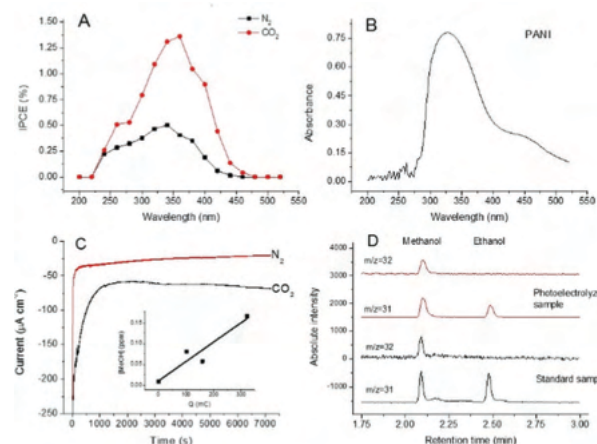


**Fig. 2** (A) Photoaction spectra of PANI registered at  $E = -0.4$  V in  $N_2$ - and  $CO_2$ -saturated 0.1 M  $Na_2SO_4$  aqueous solution. (B) UV-vis spectrum of PANI registered at  $E = -0.4$  V in  $CO_2$ -saturated 0.1 M  $Na_2SO_4$  aqueous solution. (C) Current/time profiles under continuous UV-vis light irradiation (100 W) at  $-0.4$  V vs. Ag/AgCl/3 M NaCl in a sealed two-compartment photoelectrochemical cell containing a PANI layer photocathode. Electrolyte was 0.1 M  $NaHCO_3$  saturated with  $CO_2$  (pH = 7). The inset shows the increasing methanol concentration with the transferred charge, as deduced from data shown in (D). (D) GC-MS profiles registered using selective ion monitoring (SIM) for the sample after photoelectrolysis shown in (C), as well as for a standard solution containing 0.5 ppm methanol and ethanol respectively.

plot (not shown). Photovoltammograms were also recorded by irradiating the photocathode with simulated sunlight yielding very similar profiles both in terms of shape and absolute photocurrent values (Fig. S2, ESI†).

Long term constant-potential electrolysis was performed at  $E = -0.4$  V (Fig. 2C), and the formed products were analyzed using GC and GC-MS (Fig. 2D) for the gas and liquid phases, respectively. The striking difference in the stationary currents ( $20 \mu A$  vs.  $70 \mu A$ ) recorded after 2 h in the two cases suggests that the PANI layer, at least partially, maintained its PEC efficacy for the studied time period. While in the gas phase only  $H_2$  was detected as the product in both cases (through proton reduction), methanol and ethanol (together with some minor traces of formaldehyde) were detected in the solution for  $CO_2$ -saturated samples. Importantly, no such products could be detected under  $N_2$ -saturation. In the  $CO_2$ -saturated case, it was

found that 20% of the transferred charge (Faradaic efficiency) accounts for H<sub>2</sub> formation, while the rest is responsible for the alcohol formation with an approximately 2 : 1 methanol/ethanol molar ratio (~43% and ~20%) indicating that the measured photocurrent is related to the formation of the listed products.

During the long term photoelectrolysis, an initial decrease in the photocurrents was always observed (see also in Fig. 2C). At the same time, the intrinsic electroactivity of the PANI films did not change significantly (as probed by cyclic voltammetry before and after photoelectrolysis, see Fig. S3, ESI†). This fact confirms that the decrease of the PEC performance is not a consequence of molecular or supramolecular degradation of PANI. Scanning electron microscopy (SEM) images furnished insights into this peculiar phenomenon, namely that the decrease in the PEC activity is predominantly rooted in the melting of the polymer (Fig. S4, ESI†). Melting of the PANI film causes a decrease in the surface area, thus the majority of the photoactive material becomes inaccessible for the CO<sub>2</sub> saturated solution. Such light-induced melting was reported earlier for PANI,<sup>26</sup> and in our case the local heating, induced by charge carrier recombination, is responsible for this phenomenon.

To further probe the factors behind the PEC activity, similar data to those in Fig. 1 are contained in Fig. S5 (ESI†) for PPy and poly(3,4-ethylenedioxythiophene) (PEDOT); these show that both these conducting polymers afford only negligible photoeffects from CO<sub>2</sub> reduction. The conduction band edge positions of these polymers were located negative enough to reduce CO<sub>2</sub> (Fig. S1, ESI†). Therefore the lack of photoactivity clearly does not reside with reduced driving force for photoinduced electron transfer in these other cases relative to PANI. In other words, factor(s) beyond thermodynamics must control the rather unique ability of PANI to photoelectroreduce CO<sub>2</sub>. With the notion that the chemical environment of the N-atom in PANI must be of special importance, similar experiments (as in Fig. 1) were carried out with poly(*N*-methylaniline) (PNMANI). The only difference here from PANI is the lack of H-substituents on the N-atom in the conjugated structure, the hydrogen being substituted by a methyl group. Importantly, the enhanced PEC behavior seems to be unique to PANI, because no such increase can be seen for its -CH<sub>3</sub> derivative (Fig. S5, ESI†); clearly this small structural difference exerts a huge impact on CO<sub>2</sub> photo-reduction efficacy.

Fig. 3A compares three adsorption/desorption sequences for the above-discussed polymers on supporting gold electrodes, as derived from quartz crystal microgravimetry (QCM) measurements. The largest adsorbed amounts were detected for PANI, and also somewhat surprisingly for PPy. In addition, a careful comparison of the desorption portion of these data revealed striking differences: while for PNMANI, the mass decreased rapidly upon N<sub>2</sub> purging (10–15 s), in the case of PANI it took 300 s to reach the original mass value. Note that all these polymer films were electrodeposited with identical charge density; therefore their thickness was also very similar. Consequently we have to assume that there is specific chemical interaction between PANI (and PPy) and the CO<sub>2</sub> molecules which clearly does not exist for PEDOT and PNMANI beyond simple physisorption.

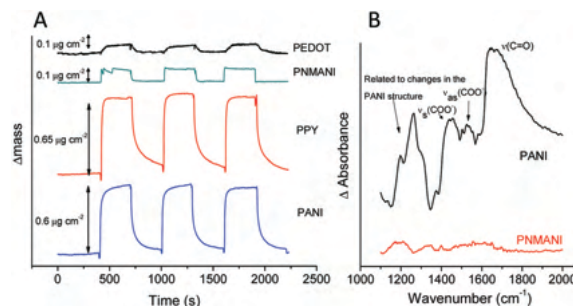
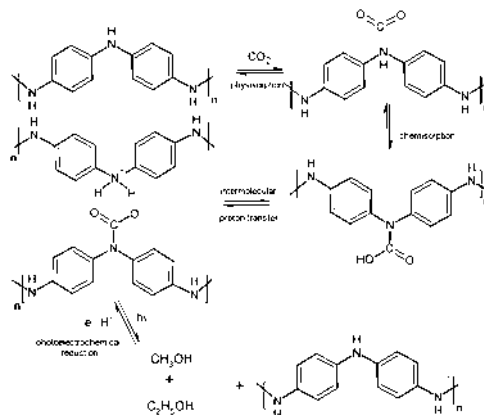


Fig. 3 (A) Subsequent mass changes upon CO<sub>2</sub> and N<sub>2</sub> exposure for the various conducting polymer films, as registered by QCM. (B) Changes in the FT-IR spectra of PANI and PNMANI upon exposure to CO<sub>2</sub> for 5 min; the background was the respective polymer pre-treated in He in both cases (refer to text).

To shed further light on the underlying surface chemistry, a series of diffuse reflectance FT-IR spectra were recorded for both PANI and PNMANI, both before and after being in contact with CO<sub>2</sub> (Fig. 3B). The difference is striking: while a set of new vibrations is visible for PANI, there is no change for PNMANI (Fig. 3B). The changes observed for PANI are the superposition of the alteration of the original PANI spectrum (because of protonation, see Scheme 1)<sup>27</sup> and the bands related to the chemisorbed CO<sub>2</sub>. The appearance of the ν(C=O) at 1680 cm<sup>-1</sup> (in carbamic acid) as well as the ν<sub>as</sub>(COO<sup>-</sup>) and ν<sub>s</sub>(COO<sup>-</sup>) vibrations at around 1530 cm<sup>-1</sup> and 1450 cm<sup>-1</sup>, respectively,<sup>28,29</sup> confirms the formation of carbamic acid and carbamate (see Scheme 1) as reported for primary and secondary amine-containing (non-conductive) polymers<sup>29</sup> and PANI-based composite materials.<sup>30,31</sup> Importantly, the vibrations related to physisorbed CO<sub>2</sub> are of very similar intensity in the two cases.

Taking all the findings from this study together, the following reaction scheme is suggested for the PEC reduction of CO<sub>2</sub> by PANI. The formation of protonated PANI rationalizes the observed color change upon CO<sub>2</sub> adsorption and is a necessary but not sufficient criterion. Adsorption of CO<sub>2</sub>, while important, is also not enough as seen by the example of PPy. The polymer band edge positions (see Fig. S1, ESI†) are critical in at least two respects: (i) the CB edge (LUMO band position) of the conducting polymer



Scheme 1 Possible mechanistic pathway for CO<sub>2</sub> adsorption and photoelectroreduction on PANI.

has to be negative enough for the photogenerated electrons to reduce CO<sub>2</sub> and (ii) the VB edge (HOMO band position) has to be positive enough to make the conducting polymer behave as a SC (rather than as a semi-metal) at the potential where the PEC experiment is performed. In the latter case, the polymer electroactivity would dominate, as exemplified here by the PPy case (Fig. S6, ESI†).

In summary, the present study underlines the rather different prerequisites for a given conducting polymer to behave as an electrocatalyst (as demonstrated by previous authors in the literature) or as a photocathode capable of reducing CO<sub>2</sub> as demonstrated in this study. In a PEC process designed to drive a given reaction thermodynamically uphill (as in the CO<sub>2</sub> reduction case), photoexcitation of the cathode material initially serves to “pump” the species against the free-energy gradient. The reversible chemical interaction between the PANI surface and CO<sub>2</sub> then fulfills the catalytic role where multiple electrons are stored and transferred. The above-described chemisorption plays a key role in protonating/binding CO<sub>2</sub>, as well as possibly the intermediate products in the initial reduction step, thereby increasing their residence time on the electrode surface.

It is also worth noting that PANI was seen here to be able to photoreduce CO<sub>2</sub> in the absence of a co-catalyst. In this sense, the choice of PANI as a candidate photocathode material has practical significance in that aniline is among the commodity chemicals produced in the largest amounts globally (well over 4 million tons per year). Consequently, large quantities are available at an economically viable price (about 2 USD per kg) (vs. Si-based photoelectrodes). In addition, PANI can be obtained by simple chemical or electrochemical polymerization. The proof-of-concept data in this communication were collected for PANI films under unoptimized conditions. PANI films with high surface area in a nanocomposite configuration may result in even higher photoconversion rates and improved stability. For example, depositing PANI on a carbon nanotube network (see Fig. S7, ESI†, for SEM images)<sup>32</sup> further enhances the process efficiency through better charge separation/transport, as shown in Fig. S8 (ESI†). Using an identical PANI amount, strikingly higher photocurrents (up to 0.5 mA cm<sup>-2</sup>) were obtained, underlining the promise to practically exploit the proof-of-concept presented herein.

The authors thank K. Baán for recording the FT-IR spectra, B. Endrődi for the technical assistance in the CO<sub>2</sub> adsorption measurement using QCM, and Prof. J. Balla for confirming our own GC-MS results at the Technical University of Budapest. The authors are grateful for the valuable discussions with Profs. C. Visy and A. Erdőhelyi.

## Notes and references

- N. Lewis and D. Nocera, *Proc. Natl. Acad. Sci. U. S. A.*, 2006, **104**, 15729–15735.
- A. M. Appel, J. E. Bercaw, A. B. Bocarsly, H. Dobbek, D. L. Dubois, M. Dupuis, J. G. Ferry, E. Fujita, R. Hille, P. J. A. Kenis, C. A. Kerfeld, R. H. Morris, C. H. F. Peden, A. R. Portis, S. W. Ragsdale, T. B. Rauchfuss, J. N. H. Reek, L. C. Seefeldt, R. K. Thauer and G. L. Waldrop, *Chem. Rev.*, 2013, **113**, 6621–6658.
- K. Rajeshwar, *J. Phys. Chem. Lett.*, 2011, **2**, 1301–1309.
- D. J. Boston, K. L. Huang, N. R. de Tacconi, N. Myung, F. M. MacDonnell and K. Rajeshwar, *Photoelectrochemical Water Splitting: Materials, Processes and Architectures*, 2013, pp. 289–332.
- K. Sivula, *J. Phys. Chem. Lett.*, 2015, **6**, 1624–1633.
- J.-W. Jang, S. Cho, G. Magesh, Y. J. Jang, J. Y. Kim, W. Y. Kim, J. K. Seo, S. Kim, K.-H. Lee and J. S. Lee, *Angew. Chem., Int. Ed.*, 2014, **53**, 5852–5857.
- U. Kang, S. K. Choi, D. J. Ham, S. M. Ji, W. Choi, D. S. Han, A. A. Wahab and H. Park, *Energy Environ. Sci.*, 2015, **8**, 2638–2643.
- M. Halmann, *Nature*, 1978, **275**, 115–116.
- J. Bockris and J. C. Wass, *Mater. Chem. Phys.*, 1989, **22**, 249–280.
- B. Kumar, M. Llorente, J. Froehlich, T. Dang, A. Sathrum and C. P. Kubiak, *Annu. Rev. Phys. Chem.*, 2012, **63**, 541–569.
- E. Barton, D. M. Rampulla and A. B. Bocarsly, *J. Am. Chem. Soc.*, 2008, **130**, 6342–6344.
- G. Ghadimkhani, N. R. de Tacconi, W. Chanmanee, C. Janaky and K. Rajeshwar, *Chem. Commun.*, 2013, **49**, 1297–1299.
- Y. Oh and X. Hu, *Chem. Soc. Rev.*, 2013, 2253–2261.
- A. Goepfert, M. Czaun, G. K. Surya Prakash and G. A. Olah, *Energy Environ. Sci.*, 2012, **5**, 7833.
- J. Wang, L. Huang, R. Yang, Z. Zhang, J. Wu, Y. Gao, Q. Wang, D. O'Hare and Z. Zhong, *Energy Environ. Sci.*, 2014, **7**, 3478–3518.
- Y. Xie, T.-T. Wang, X.-H. Liu, K. Zou and W.-Q. Deng, *Nat. Commun.*, 2013, **4**, 1960.
- A. Zhang, W. Zhang, J. Lu, G. G. Wallace and J. Chen, *Electrochem. Solid-State Lett.*, 2009, **12**, E17–E19.
- R. D. L. Smith and P. G. Pickup, *Electrochem. Commun.*, 2010, **12**, 1749–1751.
- B. Aurian-Blajeni, I. Taniguchi and J. Bockris, *J. Electroanal. Chem.*, 1983, **149**, 291–293.
- D. Won, J. Chung, S. Park, E. Kim and S. Woo, *J. Mater. Chem. A*, 2015, **3**, 1089–1095.
- A. Guerrero, M. Haro, S. Bellani, M. R. Antognazza, L. Meda, S. Gimenez and J. Bisquert, *Energy Environ. Sci.*, 2014, **7**, 3666–3673.
- P. Bornoz, M. S. Prevot, X. Yu, N. Guijarro, K. Sivula, P. Bornoz, M. S. Prevot, X. Yu, N. Guijarro and K. Sivula, *J. Am. Chem. Soc.*, 2015, **137**, 15338–15341.
- E. B. Cole, P. S. Lakkaraju, D. M. Rampulla, A. J. Morris, E. Abelev and A. B. Bocarsly, *J. Am. Chem. Soc.*, 2010, **132**, 11539–11551.
- K. Rajeshwar, in *Electron Transfer in Chemistry*, ed. V. Balzani, Wiley-VCH, Weinheim, 2001.
- P. Kilmartin and G. Wright, *Electrochim. Acta*, 1996, **41**, 1677–1687.
- J. X. Huang and R. B. Kaner, *Nat. Mater.*, 2004, **3**, 783–786.
- S. Quillard, G. Louran, S. Lefrant and A. G. MacDiarmid, *Phys. Rev. B: Condens. Matter Mater. Phys.*, 1994, **50**, 496–508.
- A. Danon, P. Stair and E. Weitz, *J. Phys. Chem. C*, 2011, **115**, 11540–11549.
- W. C. Wilfong, C. S. Srikanth and S. S. C. Chuang, *ACS Appl. Mater. Interfaces*, 2014, **6**, 13617–13626.
- A. K. Mishra and S. Ramaprabhu, *J. Mater. Chem.*, 2012, **22**, 3708–3712.
- S. Khalili, B. Khoshandam and M. Jahanshahi, *RSC Adv.*, 2016, **6**, 35692–35704.
- C. Janáky and K. Rajeshwar, *Prog. Polym. Sci.*, 2015, **43**, 96–135.

# Enhanced Photoelectrochemical Performance of Cuprous Oxide/Graphene Nanohybrids

Egon Kecsenovity,<sup>†,‡</sup> Balázs Endrődi,<sup>†,‡</sup> Péter S. Tóth,<sup>§</sup> Yuqin Zou,<sup>§</sup> Robert A. W. Dryfe,<sup>§,ID</sup> Krishnan Rajeshwar,<sup>||,ID</sup> and Csaba Janáky<sup>\*,†,‡,§,||,ID</sup>

<sup>†</sup>MTA-SZTE “Lendület” Photoelectrochemistry Research Group, Rerrich Square 1, Szeged H-6720, Hungary

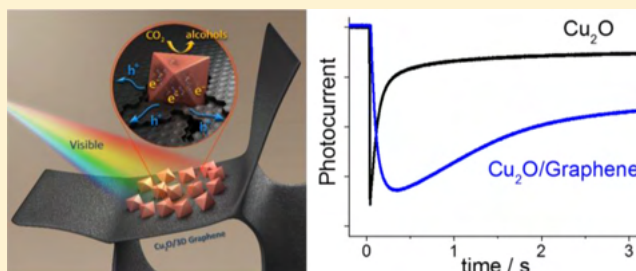
<sup>‡</sup>Department of Physical Chemistry and Materials Science, University of Szeged, Rerrich Square 1, Szeged H-6720, Hungary

<sup>§</sup>School of Chemistry, University of Manchester, Oxford Road, Manchester M13 9PL, United Kingdom

<sup>||</sup>Department of Chemistry and Biochemistry, The University of Texas at Arlington, Arlington, Texas 76019, United States

## Supporting Information

**ABSTRACT:** Combination of an oxide semiconductor with a highly conductive nanocarbon framework (such as graphene or carbon nanotubes) is an attractive avenue to assemble efficient photoelectrodes for solar fuel generation. To fully exploit the possible synergies of the hybrid formation, however, precise knowledge of these systems is required to allow rational design and morphological engineering. In this paper, we present the controlled electrochemical deposition of nanocrystalline p-Cu<sub>2</sub>O on the surface of different graphene substrates. The developed synthetic protocol allowed tuning of the morphological features of the hybrids as deduced from electron microscopy. (Photo)electrochemical measurements (including photovoltammetry, electrochemical impedance spectroscopy, photocurrent transient analysis) demonstrated better performance for the 2D graphene containing photoelectrodes, compared to the bare Cu<sub>2</sub>O films, the enhanced performance being rooted in suppressed charge carrier recombination. To elucidate the precise role of graphene, comparative studies were performed with carbon nanotube (CNT) films and 3D graphene foams. These studies revealed, after allowing for the effect of increased surface area, that the 3D graphene substrate outperformed the other two nanocarbons. Its interconnected structure facilitated effective charge separation and transport, leading to better harvesting of the generated photoelectrons. These hybrid assemblies are shown to be potentially attractive candidates in photoelectrochemical energy conversion schemes, namely CO<sub>2</sub> reduction.



## INTRODUCTION

The increasing demand for efficient technologies to harvest the energy of the Sun is a major current driver of materials chemistry.<sup>1</sup> In addition to batteries and supercapacitors,<sup>2</sup> chemical fuels<sup>3,4</sup> (such as H<sub>2</sub> or methanol) are an attractive option for energy storage, especially given the intermittent nature of renewable sources. Photoelectrochemistry, which relies on chemical reactions initiated at the semiconductor/electrolyte interface<sup>5</sup> by photogenerated charge carriers, offers a viable avenue for the direct generation of solar fuels. Photoelectrochemical (PEC) water splitting, on an irradiated TiO<sub>2</sub> surface is the pioneering example,<sup>6</sup> and the field has grown rapidly during the past decades since the first discovery in the late 1960s.<sup>5</sup> On the other hand, CO<sub>2</sub> conversion is specifically challenging, because this reaction is multielectron in nature (e.g., 8 e<sup>-</sup> to CH<sub>4</sub>) and thus requires long-lived charge carriers<sup>7</sup> and good electrocatalysts to obtain the targeted reduction product(s).<sup>8,9</sup> While several materials were tested in this vein, ranging from elemental semiconductors (e.g., p-Si)<sup>10</sup> to the most frequently studied oxides (mainly Cu-based binary and ternary oxides: e.g., Cu<sub>2</sub>O,<sup>11,12</sup> CuFeO<sub>2</sub>,<sup>13–15</sup> CuBi<sub>2</sub>O<sub>4</sub>,<sup>16</sup> and CuNb<sub>2</sub>O<sub>6</sub><sup>17</sup>), to other compound semiconductors (e.g.,

GaP, CdTe, InP, GaAs, GaP, FeS<sub>2</sub>, ZnTe),<sup>5,18–23</sup> none have reached the performance level required for practical utilization.

Considering the very complex requirements that have to be met by a photoelectrode (good light absorption, efficient charge carrier transport, rapid charge transfer kinetics, stability, etc.), it is not too surprising that no single “magic bullet” material has emerged so far.<sup>5,24</sup> Consequently, there are ample arguments in favor of assembling and studying intricate architectures with components that have precisely defined functionality and complementarity. There is literature precedence for composite materials outperforming their singular counterparts in PEC applications.<sup>25,26</sup> In particular, by providing a highly conductive scaffold, carbon nanotube and graphene-based composite materials are particularly attractive for photocatalytic<sup>27,28</sup> and PEC<sup>29–31</sup> applications in that they facilitate exciton dissociation and charge carrier transport.<sup>32</sup> Coherent, interconnected structures have additional benefits, rooted in the lack of carbon/carbon interfaces.<sup>33–37</sup>

Received: February 21, 2017

Published: May 1, 2017

As further, specific examples, enhanced anodic photocurrents were registered in a bioinspired ZnO/graphene assembly, where ZnO nanowires were obtained on honeycomb reduced graphene oxide (rGO).<sup>38</sup> Similarly, efficient charge transfer and suppressed electron–hole recombination was reported for a Cu<sub>2</sub>O/rGO system.<sup>39</sup> Liquid phase exfoliated (LPE) graphene nanoplatelets were combined with TiO<sub>2</sub> nanoparticles, and improved photocatalytic efficiency was found for both CH<sub>3</sub>CHO oxidation and CO<sub>2</sub> reduction.<sup>40</sup> As yet another example, BiVO<sub>4</sub>/rGO hybrids were employed in PEC water oxidation, and showed 10-times higher anodic photocurrent, compared to BiVO<sub>4</sub> alone.<sup>41</sup> Similar to the other cases reported, the enhanced activity was rationalized by the instantaneous electron injection to the rGO component from the photo-excited BiVO<sub>4</sub>. The example of Fe<sub>2</sub>O<sub>3</sub>/rGO was used to demonstrate the different time scale of the various processes involved in a PEC reaction.<sup>30</sup> Most recently, we demonstrated how ultralong carbon nanotubes could be used as a scaffold for Cu<sub>2</sub>O nanocrystals to boost the PEC conversion of CO<sub>2</sub> to alcohols and formic acid.<sup>42</sup> Finally, the combination of carbon nanotubes (CNTs) and graphene can also be employed as conductive platforms, as demonstrated for a hematite (Fe<sub>2</sub>O<sub>3</sub>) containing composite, which was successfully employed for PEC water oxidation.<sup>43</sup> Notably, the reverse strategy was also demonstrated, where a carbon coating on the semiconductor surface acted both as stabilizer and cocatalyst.<sup>44–46</sup>

Despite the promising examples above, there is still much to be done to completely understand the effect of the nanocarbon scaffold, and thus to efficiently harness the synergy of the components in the hybrid configurations. Interestingly, there are many examples in the literature for photodriven (sometimes also referred as photocatalytic) reduction of CO<sub>2</sub> using suspensions of Cu<sub>2</sub>O/nanocarbon hybrids,<sup>47–49</sup> but only a very few for the corresponding PEC scenario. In our opinion, this trend is rooted in the increased complexity of this latter configuration, where the most important two bottlenecks are (i) the lack of precise control over the composition and morphology in the hybrid architectures, which may deleteriously affect the PEC properties; and (ii) the lack of high quality nanocarbon electrodes with organized, interconnected three-dimensional (3D) structure. Consequently, there are only a few examples in the literature where 3D graphene nanostructures (such as foams) were used as a scaffold for different inorganic oxides. Nanorods of ZnO were hydrothermally deposited on a chemical vapor deposition (CVD)-grown 3D graphene foam and tested as electrochemical sensors.<sup>50</sup> Nanosheets of Ni(OH)<sub>2</sub> were hydrothermally grown on 3D graphene, and the hybrid was employed for the electrochemical sensing of glucose.<sup>51</sup> Finally, a mesoporous Co<sub>3</sub>O<sub>4</sub> nanosheet array was deposited on a graphene foam to obtain high performance charge storage materials.<sup>52</sup> Importantly, none of these studies focused on the PEC performance of these nanocomposites.

Electrochemistry is a particularly versatile tool for the controlled synthesis of different semiconductors on nanostructured carbon surfaces. As shown in our recent Minireview article<sup>26</sup> it is possible to tailor the composition, particle size and morphology, and the crystallinity of the electrodeposited semiconductor toward specific applications. Similarly, much experience has accumulated on graphene electrochemistry,<sup>53,54</sup> which suggests that high quality graphene (or few-layer graphene), obtained by CVD, will be a more versatile electrode

materials than their liquid phase exfoliated and partially reduced counterparts (rGO).

In this contribution, we aim to uncover the reasons behind the improved PEC performance of nanocarbon based photoelectrodes, compared to the bare semiconductor counterpart. To this end, various nanostructured carbon electrodes were prepared, including CNT networks, spray-coated graphene films (using LPE few-layer graphene platelets), and 3D graphene foams. Variable amounts of p-Cu<sub>2</sub>O was loaded on their surface via controlled electrochemical deposition, to explore a broad compositional and morphological space. By comparing and contrasting the PEC behavior of these hybrid photocathodes, we present a comprehensive analysis of the beneficial effects of various nanocarbon scaffolds, with primary focus on graphene. The main outcome of this study is that both the high surface area and the improved charge carrier separation and transport contribute to the enhanced PEC properties. After allowing for the effect of the different surface areas, it was possible to compare the nanocarbons with different morphology. Importantly, the 3D graphene architecture significantly outperformed its random/nonoriented counterparts. This trend was semiquantitatively supported by transient photocurrent measurements, where the magnitude of charge carrier recombination at the surface was estimated. The presented structure–property relationships can be exploited in the rational design of hybrid photoelectrodes *in general*, to obtain potentially attractive candidates for PEC energy conversion schemes, such as water splitting or CO<sub>2</sub> reduction.

## ■ EXPERIMENTAL SECTION

**3D Graphene Foam Synthesis.** 3D graphene (3D-GR) foam was prepared via a CVD process using methane as the carbon source. The nickel foam (MTI Corporation, surface density: 350 g m<sup>-2</sup>) was cleaned by successive sonication for 20 min in ethanol and water. A 1 cm × 3 cm piece of cleaned nickel foam was placed at the center of a fused quartz tube furnace (Lindberg Blue M, inner diameter 22 mm). The furnace tube was evacuated and then heated to 1000 °C with a 40 sccm H<sub>2</sub> gas flow under atmospheric pressure. After annealing for 20 min under these conditions, methane was introduced into the reactor. The temperature and gas flows were maintained in the furnace tube for 2 h. After the growth period, the Ar gas flow was stopped and the sample was cooled to room temperature under 40 sccm H<sub>2</sub> gas flow. Finally, the samples were immersed in 1 mol dm<sup>-3</sup> FeCl<sub>3</sub> overnight to dissolve the Ni foam and isolate the free-standing 3D graphene.<sup>52</sup>

**Electrode Preparation.** Premium-quality graphene powder (exfoliated graphene platelets from Elicarb) or home-grown arrays of CNTs<sup>42</sup> were dispersed in absolute ethanol by ultrasonic treatment. The formed dispersion (graphene:  $c = 1 \text{ mg mL}^{-1}$ , CNT:  $c \approx 100 \text{ } \mu\text{g mL}^{-1}$ ) was spray-coated on ultrasonically cleaned (5–5 min in acetone and ethanol) and preheated indium doped tin oxide-coated glass (ITO) electrodes, using an Alder AD320 type airbrush with a custom-made fully automated spray coater machine (operated with 1 bar compressed air). During the spray-coating process, the electrodes were masked to have an exposed surface area of 1 cm<sup>2</sup>. To remove ethanol traces and to enhance adhesion of the graphene platelets or the CNTs, the electrodes were kept in an oven (180 °C) for 30 min. Graphene and CNT loading of the electrodes was controlled with the number of spray steps (GR1–6, 30–560  $\mu\text{g cm}^{-2}$ , CNT: 35–690  $\mu\text{g cm}^{-2}$ , see also Table S1), and quantified by quartz crystal microbalance (QCM) measurements using a Stanford Research System QCM-200 type instrument. The 3D graphene samples were fixed on a glass sheet by a small piece of a double-sided tape, and were contacted at the top by graphite adhesive to form the working electrode.

**Cu<sub>2</sub>O Electrodeposition.** All chemicals used were of analytical grade and were used as received. CuSO<sub>4</sub> × 5H<sub>2</sub>O and Na<sub>2</sub>SO<sub>4</sub> were purchased from Alfa Aesar, NaOH from VWR International, lactic acid

was from Sigma-Aldrich. Ultrapure water ( $\rho = 18.2 \text{ M}\Omega \text{ cm}$ , produced with a Millipore Direct Q3-UV instrument) was used for the preparation of all aqueous solutions. The nanocarbon electrodes were employed as the working electrode, while a Pt sheet and a Ag/AgCl/3 M NaCl were used as counter and reference electrodes, respectively.  $\text{Cu}_2\text{O}$  was electrodeposited from an alkaline solution of lactate-stabilized copper sulfate, containing  $0.4 \text{ mol dm}^{-3}$  cupric sulfate and  $3 \text{ mol dm}^{-3}$  lactic acid in deionized water.<sup>42</sup> The pH was adjusted to 9 by the addition of concentrated sodium hydroxide solution. The electrodeposition was performed in a temperature-controlled classical three electrode electrochemical cell. The temperature of the solution was maintained at  $60 \text{ }^\circ\text{C}$ , and the solution was constantly stirred by a magnetic stirrer during the electrodeposition. After recording linear sweep voltammetry data (Figure S2), multiple step potentiostatic electrodeposition protocols were employed (Figure 1).

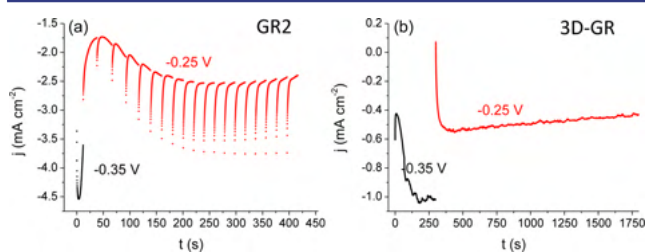


**Figure 1.** (a) Current response of a GR2/ITO electrode, while applying the multiple-potential step protocol. (b) Current–time curves, registered during the two-step potentiostatic electrodeposition of  $\text{Cu}_2\text{O}$  on a 3D-GR electrode. Both syntheses were performed in  $0.4 \text{ mol dm}^{-3}$  cupric sulfate and  $3 \text{ mol dm}^{-3}$  lactate solution, at  $\text{pH} = 9$  and  $T = 60 \text{ }^\circ\text{C}$ .

All electrochemical measurements were performed on a Metrohm Autolab PGSTAT302 type potentiostat/galvanostat, equipped with an FRA32 type module for the impedance spectroscopic and the current transient measurements. To establish structure–property relationships, the thickness of the nanocarbon films (CNT:  $35\text{--}690 \mu\text{g cm}^{-2}$ , graphene  $30\text{--}560 \mu\text{g cm}^{-2}$ ), as well as the amount of the electrodeposited  $\text{Cu}_2\text{O}$  was systematically varied ( $50\text{--}2000 \text{ mC cm}^{-2}$ ). Cyclic voltammograms were recorded to estimate the actual surface area of the electrodes (see further discussion in the SI).

**Physical Characterization.** Raman spectroscopy was performed on a DXR Raman Microscope using a green laser ( $\lambda = 532 \text{ nm}$ ), operating at  $10 \text{ mW}$  laser power. A FEI Tecnai G<sup>2</sup> 20 X-Twin type instrument, operating at an acceleration voltage of  $200 \text{ kV}$ , was used for transmission electron microscopy (TEM). Scanning electron microscopy (SEM) images were recorded on a Hitachi S-4700 field emission scanning electron microscope (coupled with a Röntec EDX detector), operating at an acceleration voltage of  $10 \text{ kV}$ . X-ray diffraction (XRD) patterns were recorded between  $2\theta = 20\text{--}80^\circ$  at  $1^\circ$  per minute scan rate on a Rigaku Miniflex II instrument, operating with a  $\text{Cu K}\alpha_1$  radiation source ( $\lambda = 0.1541 \text{ nm}$ ). Diffuse reflectance UV–visible (DR UV–vis) spectra were recorded on an Avantes AVASpec-2048 type instrument, equipped with an AvaSphere-30 type integrating sphere. X-ray photoelectron spectra were recorded with a SPECS instrument equipped with a PHOIBOS 150 MCD 9 hemispherical analyzer. The analyzer was operated in the fixed analyzer transmission (FAT) mode with  $20 \text{ eV}$  pass energy. The Al  $\text{K}\alpha$  radiation ( $h\nu = 1486.6 \text{ eV}$ ) of a dual anode X-ray gun was used as the excitation source. The gun was operated at  $210 \text{ W}$  power ( $14 \text{ kV}$ ,  $15 \text{ mA}$ ). The binding energy scale was corrected by fixing the main C 1s component to  $285.0 \text{ eV}$ , corresponding to adventitious carbon. For spectrum acquisition and evaluation both manufacturers (SpecsLab2) and commercial (CasaXPS, Origin) software packages were used. Electrochemical impedance spectra (EIS) of the hybrid films were recorded at open-circuit potential in the  $10 \text{ Hz}$  to  $10 \text{ kHz}$  frequency range, using a sinusoidal excitation signal ( $10 \text{ mV RMS}$  amplitude). Modulus weighted fitting was performed using the Nova Software of the Autolab Instrument. For Mott–Schottky analysis, the full

impedance spectra of the electrodes were recorded at different potentials ( $E = 0.1\text{--}0.35 \text{ V}$  vs Ag/AgCl/3 M NaCl).

**Photoelectrochemical Measurements.** Photovoltammograms were recorded in a sealed electrochemical cell made of quartz. To eliminate the effect of pH, photovoltammograms were recorded in  $\text{N}_2$ -saturated phosphate buffer ( $\text{pH} = 4.0$ , equal to the pH of the  $\text{CO}_2$  saturated  $0.1 \text{ mol dm}^{-3} \text{ Na}_2\text{SO}_4$ ) solutions as well. The solutions were saturated with  $\text{N}_2$  or  $\text{CO}_2$  by bubbling the gases through the cell for  $30 \text{ min}$  before and during the measurements (by forming a gas pillow above the solutions in the latter case). Linear sweep photovoltammograms were recorded under periodically interrupted light irradiation, using a Newport LCS-100 type solar simulator, operated at full output with a UV-cutoff filter ( $<400 \text{ nm}$ ), always placed at a fixed distance of  $8 \text{ cm}$  from the working electrode. Fast photocurrent transient measurements were performed using the same arrangement. During this measurement, data collection frequency was  $20 \text{ kHz}$  at five different potentials. Long-term  $\text{CO}_2$  photoelectrolysis tests were performed in a two-compartment, sealed electrochemical cell (separated by a Nafion-117 membrane). The electrode potential was kept at a given value ( $-0.05$  and  $+0.05 \text{ V}$  vs Ag/AgCl/3 M NaCl), and the electrode was irradiated with the above-described periodically interrupted light source (at  $0.033 \text{ Hz}$ ). Incident photon-to-electron conversion efficiency (IPCE) measurements were performed on a Newport Quantum Efficiency Measurement System (QEPVSI-B) in a single-compartment, three electrode quartz electrochemical cell. The wavelength range was  $360\text{--}600 \text{ nm}$  ( $\Delta\lambda = 10 \text{ nm}$  step size). The IPCE profiles were recorded at  $E = 0.0 \text{ V}$ , in  $\text{CO}_2$  saturated  $0.1 \text{ mol dm}^{-3} \text{ Na}_2\text{SO}_4$  solution.

Liquid and gas aliquots were taken regularly during photoelectrolysis. The  $\text{CO}_2$  reduction products in the gas phase were analyzed with a Shimadzu GC-2010 Plus gas-chromatograph equipped with a barrier discharge ionization detector (BID). A HP-PLOT Molisieve column was used for the separation. Samples from the gas phase were taken at  $5, 25, 50,$  and  $70 \text{ min}$  with a gastight syringe and injected into the GC with split injection. Heating procedure:  $40 \text{ }^\circ\text{C}$  ( $6 \text{ min}$ ) to  $30 \text{ }^\circ\text{C/min}$   $-200 \text{ }^\circ\text{C}$  ( $4 \text{ min}$ ), injection temperature:  $250 \text{ }^\circ\text{C}$ , linear velocity:  $45.6 \text{ cm/s}$ , split ratio:  $40$ . The liquid-phase products were analyzed with a Shimadzu GC–MS QP 2010S gas chromatograph–mass spectrometer (column: ZB-FFAP) after removing the electrolyte ions with an Amberlite IRN-150 ion-exchange resin. Liquid samples were taken a few seconds after the gas samples. Heating procedure:  $40 \text{ }^\circ\text{C}$  ( $3.5 \text{ min}$ ) to  $50 \text{ }^\circ\text{C/min}$   $-70 \text{ }^\circ\text{C}$  to  $10 \text{ }^\circ\text{C/min}$   $170 \text{ }^\circ\text{C}$  to  $50 \text{ }^\circ\text{C/min}$   $-250 \text{ }^\circ\text{C}$  ( $5 \text{ min}$ ), injection temperature:  $200 \text{ }^\circ\text{C}$ , linear velocity:  $40 \text{ cm/s}$ , split ratio:  $10$ .

## RESULTS AND DISCUSSION

### Electrodeposition of $\text{Cu}_2\text{O}$ /Graphene Composites.

Electrodeposition of the  $\text{Cu}_2\text{O}$  nanoparticles on the nanocarbon substrates was realized by a multiple-step potentiostatic method (Figure 1). On the basis of linear sweep voltammetric data (Figure S2), a first nucleation step was conducted at  $E = -0.35 \text{ V}$  to initialize the formation of small seed particles, followed by one or more slow crystal growth steps at a less negative potential ( $E = -0.25 \text{ V}$ ). For the spray-coated graphene samples, multiple growth steps were applied to introduce rest periods allowing for continuous supply of copper ions from the bulk solution. We emphasize that although the prenucleation step leads to some copper traces in the formed cuprous oxide, it was found to be essential to reach homogeneous coverage of the nanocarbon supports.

When this step was omitted, crystal formation occurred *exclusively* on the edges of graphene sheets (see the inset in Figure 4d). In agreement with our earlier results on  $\text{Cu}_2\text{O}$  decorated carbon nanotubes,<sup>26,42</sup> we can conclude that homogeneous coverage of carbon nanostructures necessitates the application of a larger driving force (i.e., deposition potential), otherwise only the energetically preferred defect



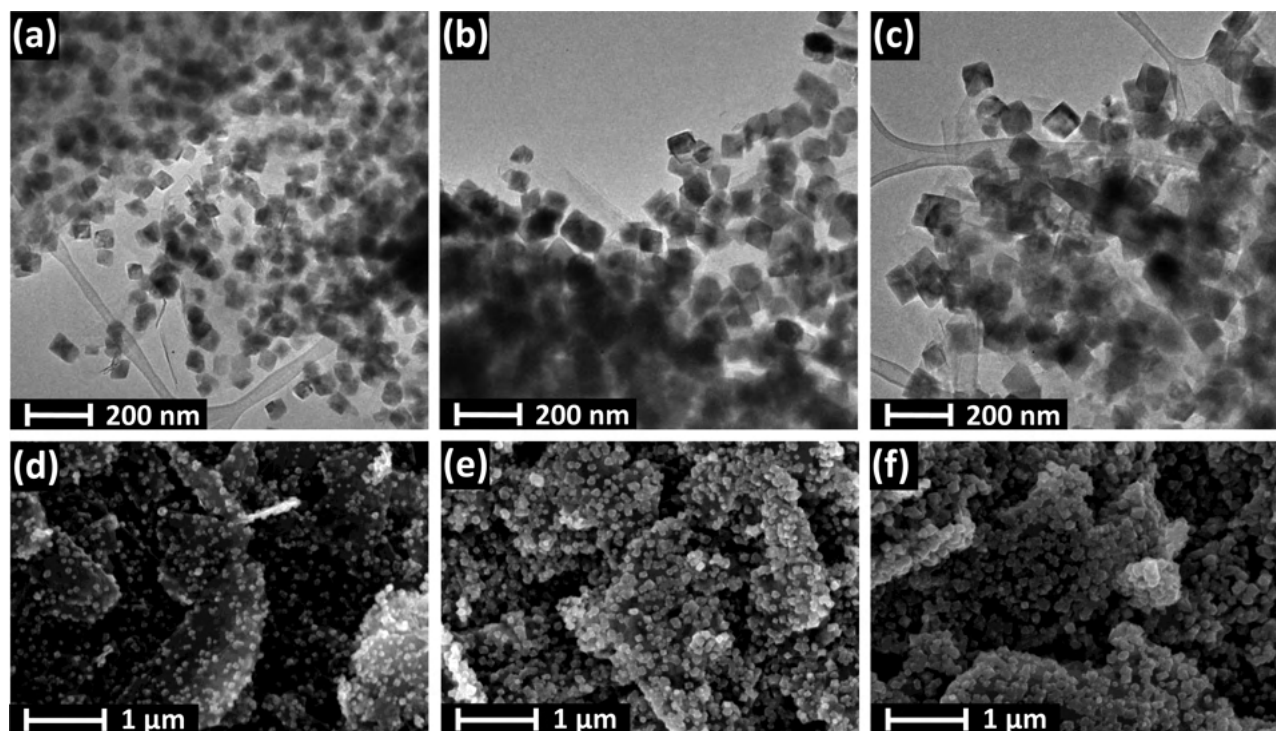


**Figure 2.** TEM images of  $\text{Cu}_2\text{O}/\text{GR4}$  hybrids obtained with the deposition protocol shown in Figure 1a. The deposition charges were (a)  $200 \text{ mC cm}^{-2}$ , (b)  $600 \text{ mC cm}^{-2}$ , and (c)  $1000 \text{ mC cm}^{-2}$ . SEM images are also shown for the same samples (d–f).

places (e.g., edges, amorphous carbon traces, and grain boundaries) are covered by the electrodeposited  $\text{Cu}_2\text{O}$ .

Electron microscopy images were taken for the hybrid  $\text{Cu}_2\text{O}/\text{GR}$  samples with various compositions to probe their morphological attributes. TEM images confirmed that the  $\text{Cu}_2\text{O}$  nanocrystallites are evenly dispersed on the graphene flakes (see Figure 2 and also Figure S3 for more images at both lower and higher magnifications). Additionally, it was also demonstrated that both the size and density of the nanoparticles can be effectively controlled by tuning the deposition protocol (i.e., the transferred charge). As seen in Figure 2 (from left to right), the growing deposition charge (from  $200 \text{ mC cm}^{-2}$  to  $1 \text{ C cm}^{-2}$ ) resulted in a gradual increase in both the surface coverage and the particle size. Specifically, the mean particle diameter shifted from 50 to 110 nm as deduced from the histograms in Figure 3. SEM images further confirmed the even dispersion of  $\text{Cu}_2\text{O}$  nanoparticles on the graphene platelets (Figure 2d,e). SEM images were also taken for the bare  $\text{Cu}_2\text{O}$  film on an ITO electrode (Figure S4). Most importantly, the crystallite sizes were much larger in this case, due to the smaller actual electrode surface area (note that the amount of the deposited  $\text{Cu}_2\text{O}$  was identical).

For the 3D graphene-based hybrids, the graphene platelets were homogeneously and almost completely covered with octahedral  $\text{Cu}_2\text{O}$  nanoparticles (see also Figure S5 for elemental mapping by EDX), having a size in the range of 100–150 nm (Figure 4). For this system, the initial nucleation step was indeed required to avoid specific deposition at the edge of the graphene platelets (compare with the inset in Figure 4d). Finally, we note that the original structure of the 3D graphene support was preserved in the nanocomposite; it did not suffer any major damage during the electrochemical deposition.

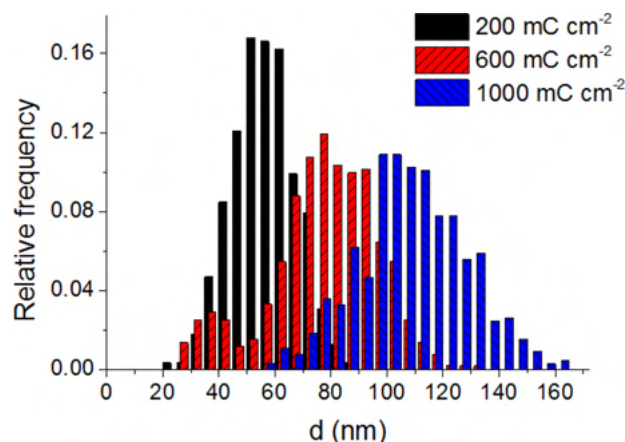


**Figure 3.** Particle size distribution for the same samples presented in Figure 2. The data were gathered from the TEM images, by measuring the size of 300 particles in each case.

Physical characterization was performed for all the prepared composite systems. The results were very similar for all the samples, confirming that there is no difference in the physicochemical properties of the deposited  $\text{Cu}_2\text{O}$  in the different hybrid configurations. For the sake of brevity, we only present the results obtained for the  $\text{Cu}_2\text{O}/3\text{D-GR}$  composite, and emphasize any differences for the other hybrids. XRD patterns of the  $\text{Cu}_2\text{O}/\text{graphene}$  composites were recorded to identify the crystal structure and composition of the deposited oxide. The four most intense reflections of the  $\text{Cu}_2\text{O}$  can be recognized (Figure 5a).<sup>55</sup> Although the presence of some copper traces cannot be completely excluded, the fact that reflections related to copper cannot be identified confirmed that this amount was negligible, if any. We note here that XPS data also confirmed that no Cu was formed during electro-

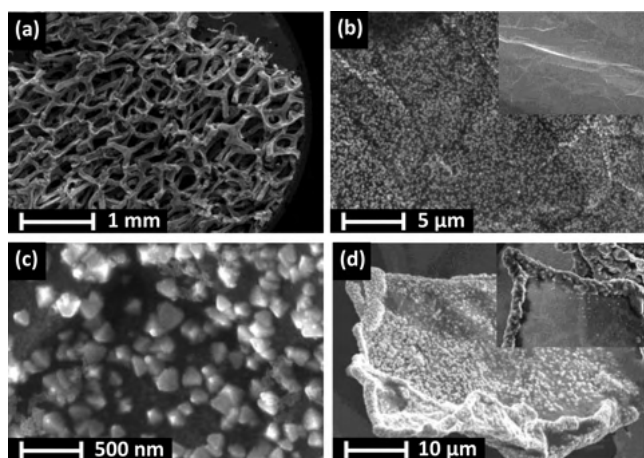


**Figure 4.** SEM images of a  $\text{Cu}_2\text{O}/3\text{D-GR}$  composite (deposited with  $1 \text{ C cm}^{-2}$  charge density) at different magnifications. The inset on (b) shows the bare graphene surface while in (d) it shows the structure of the composite formed without the pre-nucleation step.

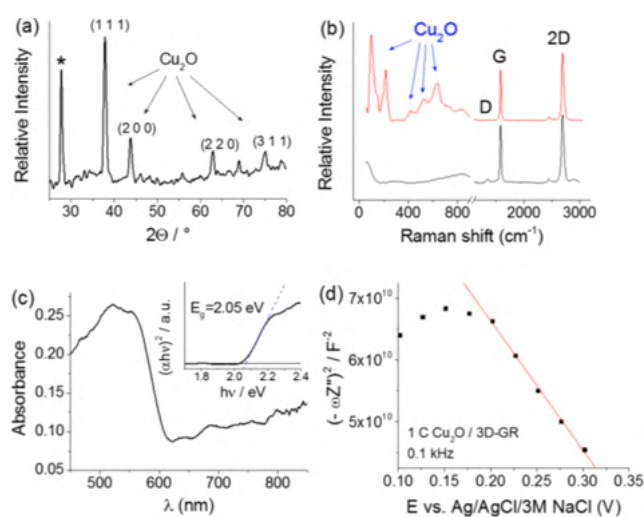


**Figure 5.** (a) XRD pattern, (b) Raman spectrum (also for the bare 3D-GR sample), (c) Diffuse-reflectance UV-vis spectrum (together with Tauc representation as inset), and (d) Mott-Schottky plot (recorded in  $0.1 \text{ M NaAc}$  solution), of a  $\text{Cu}_2\text{O}/3\text{D-GR}$  composite, deposited with  $1 \text{ C cm}^{-2}$  charge density. The diffraction marked with asterisk in (a) corresponds to the graphene substrate.

deposition of  $\text{Cu}_2\text{O}$  (see the lack of  $\text{Cu}$  (0) peak around  $918.6 \text{ eV}$  at the Auger spectrum, Figure S6B).

The appearance of the diffraction at  $2\theta = 27.8^\circ$  (marked with asterisk in Figure 5a) indicated that we have a multilayer graphene structure instead of a graphene monolayer, as the CVD-grown 3D graphene samples typically consist of both one- and few-layer domains.<sup>52</sup> This observation is typical for CVD-grown 3D graphene samples and contributes to the mechanical stability of the 3D electrode.<sup>56</sup>

The Raman spectrum of the composite showed all the characteristic Raman active vibration modes of  $\text{Cu}_2\text{O}$  (Figure 5b). The appearance of the peaks at  $145, 220, 416, 532,$  and  $631 \text{ cm}^{-1}$  proves that  $\text{Cu}_2\text{O}$  was formed during the deposition.<sup>57,58</sup> The lack of the characteristic vibration modes of  $\text{CuO}$  at  $297$  and  $350 \text{ cm}^{-1}$  proved that the formed oxide is exclusively  $\text{Cu}_2\text{O}$  and not  $\text{CuO}$  (confirming XRD results).<sup>59</sup> At  $1582.5 \text{ cm}^{-1}$ , the G-band of the graphene substrate, associated

with the  $E_{2g}$  vibration mode of the  $sp^2$  framework,<sup>60</sup> can be discerned on the Raman spectrum.<sup>61</sup> The presence of a very small D-band at  $1374 \text{ cm}^{-1}$  indicated that only trace amounts of defects were present in the nanocarbon template. Importantly, these defects were already present before synthesis of the composites, as seen from the spectrum of the bare 3D-GR sample. The intense 2D band centered at  $2698 \text{ cm}^{-1}$  confirmed the few-layer character of the 3D-GR sample.

The optical bandgap of the  $\text{Cu}_2\text{O}/3\text{D-GR}$  composite was determined by diffuse reflectance UV-vis spectroscopy, and the spectrum was analyzed using a Tauc plot (see an example for the 3D-GR support in Figure 5c). The determined  $E_g = 2.05 \text{ eV}$  was in good agreement with values reported for  $\text{Cu}_2\text{O}$ .<sup>62</sup> Similar data were collected for all  $\text{Cu}_2\text{O}/\text{nanocarbon}$  samples (not shown here). The most important conclusions were the following: (i) the absorption edge (related to  $\text{Cu}_2\text{O}$ ,  $E_g = 2.05 \text{ eV}$ , see also Figure 5c) of the samples did not alter with the varying graphene content and (ii) there was a massively increased noncharacteristic absorption related to graphene (especially in the vis-NIR region<sup>30,63</sup>).

Electrochemical impedance spectroscopic (EIS) measurements were carried out to determine the flatband potential of the composite (Figure 5d). By performing the Mott-Schottky analysis on the measured data, a flatband potential of  $E = +0.51 \text{ V}$  (vs  $\text{Ag}/\text{Ag}/3 \text{ M NaCl}$ ) was obtained for the  $\text{Cu}_2\text{O}/3\text{D-GR}$  sample, a value slightly higher compared to data reported for electrodeposited  $\text{Cu}_2\text{O}$  at neutral pH.<sup>64,65</sup> To compare the flatband potential (and thus the apparent Fermi level) of the various photoelectrodes, Table S2 summarizes the onset potential of the photovoltammetry profiles, the open circuit potentials with and without illumination, and the flatband potential obtained from the Mott-Schottky plots. The most important trend observed in these comparisons was the slight positive shift in the flatband potential (apparent Fermi level) in the case of the composite samples (compared to the bare  $\text{Cu}_2\text{O}$ ). The magnitude of this shift increased with increasing nanocarbon loading, and had a maximum of  $100 \text{ mV}$  for the spray-coated carbons and  $200 \text{ mV}$  for the 3D-GR sample. These shifts indicate the intimate contact between the constituents, similar to trends in other studies in the literature on different semiconductor/nanocarbon assemblies.<sup>29,30,32,63</sup>

**Photoelectrochemical Properties.** To evaluate the PEC properties of the  $\text{Cu}_2\text{O}/\text{graphene}$  composites, the photo-reduction of  $\text{CO}_2$  was performed as a model reaction of practical significance (Figure 6a). The most important conclusions to be drawn from these initial measurements are the following: (i) The nanocomposite showed PEC activity toward  $\text{CO}_2$  reduction, as confirmed by the enhanced photocurrents in the presence of  $\text{CO}_2$  (note that the pH-effect was deconvoluted by performing control measurements in  $\text{N}_2$  saturated solution, buffered to  $\text{pH} = 4.0$ , the pH of the  $\text{CO}_2$  saturated solution); (ii) There was an increased photocurrent for the GR containing samples as compared to the bare oxide (Figure 6b); and (iii) The overall shape of the photovoltammograms was similar in the presence/absence of the carbon scaffold, except the development of a dark current in the case of the hybrids.

Additionally, both the onset potential of the  $\text{CO}_2$  reduction and the maximum photocurrent were very similar to those determined earlier for  $\text{Cu}_2\text{O}/\text{CNT}$  composites,<sup>42</sup> but the shape of the linear sweep voltammetry (LSV) curve was somewhat different. In this case, the photocurrent did not decrease after a certain potential; it was stable in the presented potential

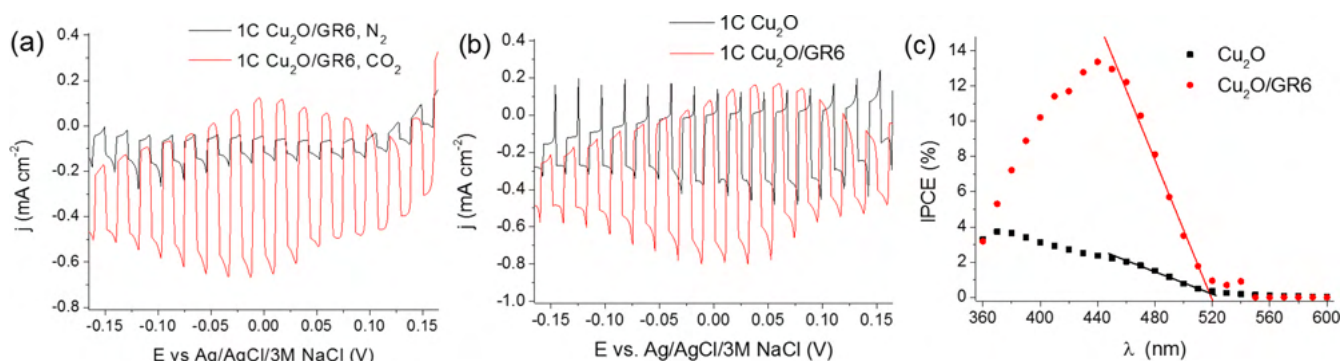


**Figure 6.** Linear sweep photovoltammograms recorded for (a) a  $\text{Cu}_2\text{O}/\text{GR6}$  hybrid sample ( $1 \text{ C cm}^{-2} \text{ Cu}_2\text{O}$ ) in  $\text{CO}_2$  or  $\text{N}_2$  saturated  $0.1 \text{ mol dm}^{-3} \text{ Na}_2\text{SO}_4$  (having the same  $\text{pH} = 4.0$ ). (b) LSV curves for a  $\text{Cu}_2\text{O}/\text{GR6}$  hybrid and a  $\text{Cu}_2\text{O}$  film ( $1 \text{ C cm}^{-2} \text{ Cu}_2\text{O}$ ) in  $\text{CO}_2$  saturated  $0.1 \text{ mol dm}^{-3} \text{ Na}_2\text{SO}_4$  solution. The sweep rate was kept at  $2 \text{ mV s}^{-1}$ , while the light-chopping frequency was  $0.2 \text{ Hz}$ . A solar simulator was used employing a UV cutoff filter ( $<400 \text{ nm}$ ). (c) Photoaction spectra for the two electrodes presented in (b), recorded at  $E = 0.0 \text{ V}$  (vs  $\text{Ag}/\text{AgCl}/3 \text{ M NaCl}$ ) in  $\text{CO}_2$  saturated  $0.1 \text{ mol dm}^{-3} \text{ Na}_2\text{SO}_4$  solution.

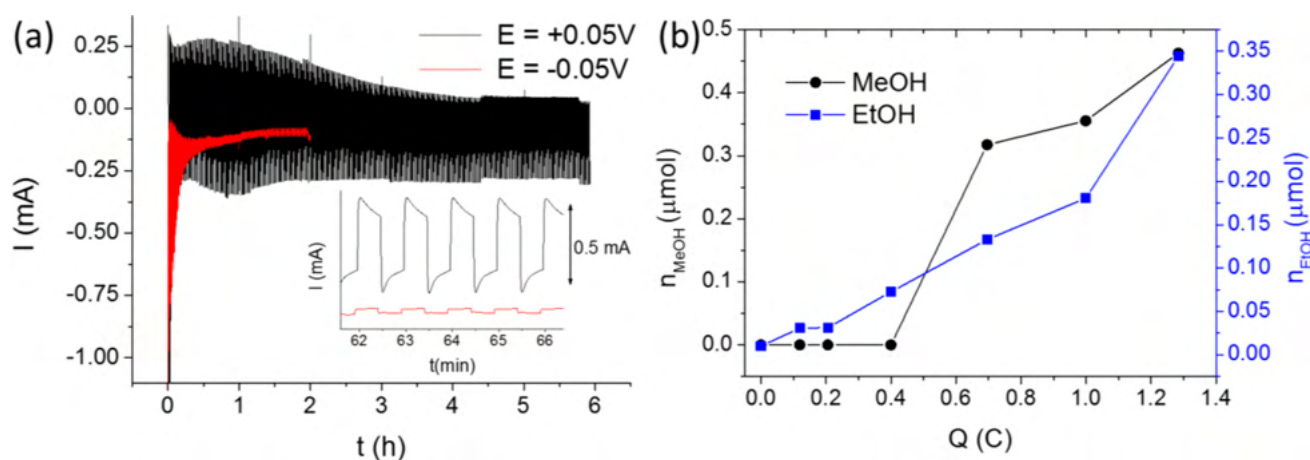


**Figure 7.** (a) Long-term chronoamperometry data of two  $\text{Cu}_2\text{O}/\text{GR6}$  electrodes with an identical  $\text{Cu}_2\text{O}$  content ( $1 \text{ C}$ ), registered at  $E = +0.05 \text{ V}$  and  $E = -0.05 \text{ V}$  potential (vs  $\text{Ag}/\text{AgCl}/3 \text{ M NaCl}$ ), in  $\text{CO}_2$  saturated  $0.1 \text{ M Na}_2\text{SO}_4$  solution. A solar simulator was used employing a UV cutoff filter ( $<400 \text{ nm}$ ). (b) Formation of alcohols during the photoelectrolysis presented in (a).

regime. Photoaction spectra (incident photon to current efficiency (IPCE) vs wavelength) were recorded, and a massive increase in the IPCE values was observed on the photoaction spectrum (Figure 6c). The identical wavelength threshold value confirmed that the enhanced photocurrents were not related to some new absorption or bandgap shift, but indeed to the better charge carrier extraction in the hybrid (note that the amount of  $\text{Cu}_2\text{O}$  was the same).

Long-term photoelectrolysis was performed at different potentials to assess the stability of the  $\text{Cu}_2\text{O}/\text{GR}$  electrode. As shown in Figure 7a, even a  $100 \text{ mV}$  shift in the external bias potential can cause a massive alteration in the overall shape. Specifically, at  $E = -0.05 \text{ V}$ , the rapid cessation of the photocurrents was seen, as a result of photocorrosion (i.e., formation of metallic  $\text{Cu}$ ).<sup>12</sup> On the other hand, at  $E = +0.05 \text{ V}$ , stable photoactivity was reached after an initial decrease. This enhanced PEC behavior is attributed to the dark reoxidation of metallic copper moieties, formed via photocorrosion.<sup>12</sup> This hypothesis is supported by the initially observed dark anodic currents at this potential. Notably, a steady-state was reached after  $2.5 \text{ h}$ , with stable photocurrents and minor dark currents.

To verify that the increased photocurrents in the presence of  $\text{CO}_2$  (see Figure 6a) were related to its conversion to useful products, aliquots were taken periodically both from the liquid and gas phases. Importantly, in the gas phase only minor traces

of  $\text{H}_2$  were detected and no  $\text{CO}$  formation was confirmed. As for the liquid phase, methanol, ethanol and minor amounts of formic acid were detected; similarly to earlier studies on  $\text{Cu}_2\text{O}$ -containing photoelectrodes.<sup>42,66</sup> Interestingly, while the ethanol concentration increased continuously, the methanol formation only started after the steady-state PEC behavior was reached (Figure 7b). Quantitatively, the two alcohols accounted for a Faradaic efficiency of  $50\text{--}60\%$  (with a  $2:3$  FE ratio for methanol/ethanol) while the rest of the charge was related to  $\text{H}_2$  and formate production, and the photoreduction of  $\text{Cu}_2\text{O}$  to  $\text{Cu}$  as detailed above. Comparative studies were performed with a bare  $\text{Cu}_2\text{O}$  electrode, deposited with identical charge density (Figure S7). The formation of methanol and ethanol was witnessed, although with a different ratio (see additional discussion in the SI).

Degradation of the  $\text{Cu}_2\text{O}/3\text{D-GR}$  electrode structure during long-term photoelectrolysis is a relevant concern. We found that major degradation of the 3D structure only occurred when the photoelectrolysis was performed at more negative potentials, where water splitting (and thus  $\text{H}_2$  bubble formation) also occurred. SEM images were taken for samples after photoelectrolysis, and are shown in Figure S9.

**Factors Behind the Improved PEC Properties.** To explore a broad range of the composition and morphology, the effect of the GR thickness and the deposited  $\text{Cu}_2\text{O}$  amount

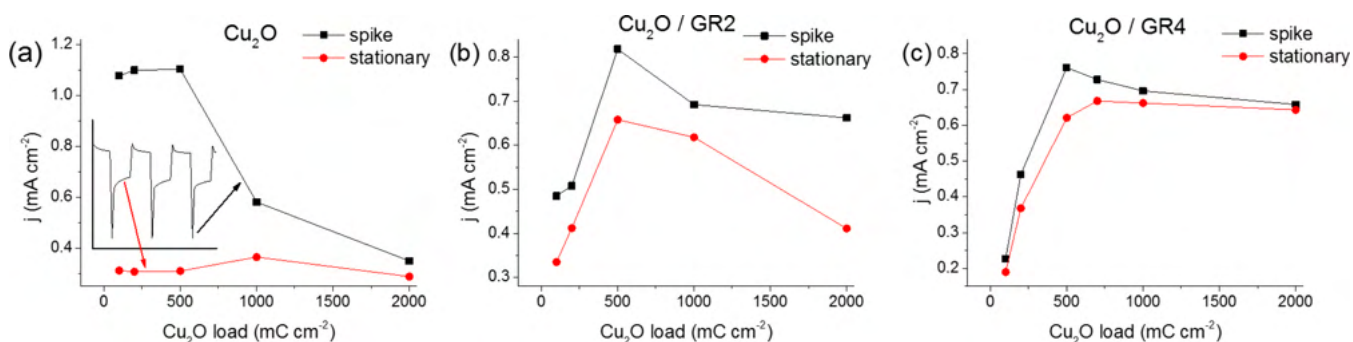


**Figure 8.** Comparison of the transient and stationary photocurrents at  $E = +0.05$  V, for five different Cu<sub>2</sub>O loadings (100–2000 mC cm<sup>-2</sup>), on (a) a bare ITO and (b,c) two different GR/ITO supports. The inset in (a) shows how the data points were determined. The lines among the data points serve only to guide the eye.

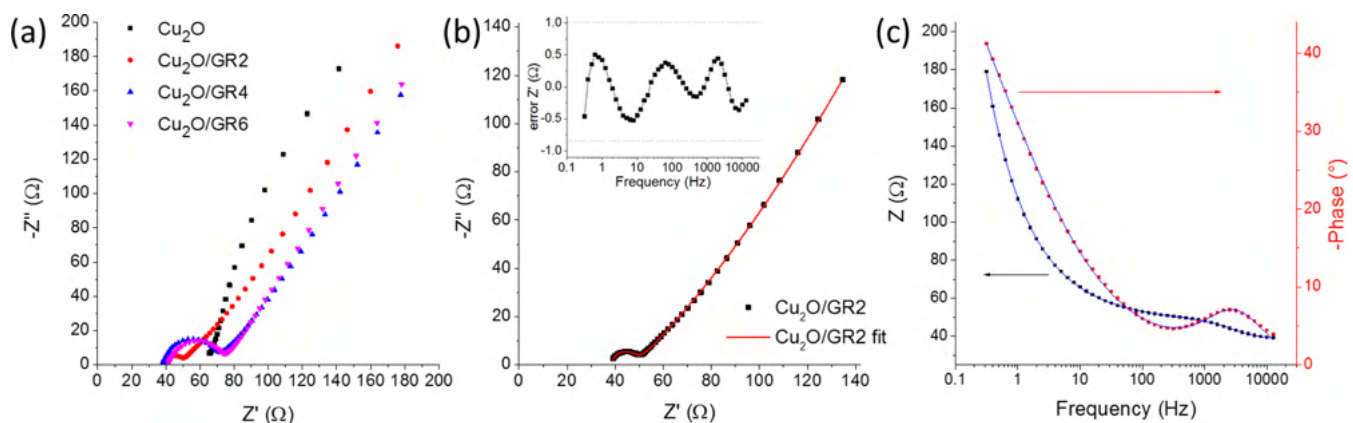


**Figure 9.** (a) Nyquist plots recorded for pristine Cu<sub>2</sub>O and three different Cu<sub>2</sub>O/GR composites deposited with 1 C cm<sup>-2</sup> charge density, in 0.1 M sodium acetate solution at open circuit potential, in the 0.1 Hz to 10 kHz frequency range. (b) Measured (points) and simulated (solid line) Nyquist and (c) Bode-plots of a Cu<sub>2</sub>O/GR electrode. The inset in (b) shows the error associated with the Bode plot fit (i.e., difference between the measured and calculated value).

were both varied systematically. Figure 8 compares the measured photocurrents (both the initial current spike and the stationary plateau; as shown in the inset of Figure 8a) for the bare Cu<sub>2</sub>O (on an ITO electrode) and composites (GR supports of three different thicknesses and five different Cu<sub>2</sub>O loadings for each support). As for the bare Cu<sub>2</sub>O, there was a huge difference between the initial and the stationary photocurrent values. This observation suggests the insufficient charge carrier extraction in the case of the bare oxide (see below for detailed discussion of this point). In addition, the stationary photocurrents seemed to be independent of the Cu<sub>2</sub>O loading (film thickness), at least in the studied regime. This constant current suggests that the reacting photoelectrons come from a distinct region of the Cu<sub>2</sub>O film, independently from the thickness. The overall pattern was totally different for the Cu<sub>2</sub>O/graphene composites (Figure 8b–c): (i) The transient and the stationary values were much closer to each other, confirming our assumption that the highly conductive graphene support facilitates effective charge separation and charge carrier extraction; (ii) The maximum photocurrent gradually shifts to higher Cu<sub>2</sub>O loadings with increasing graphene thickness. Similar experiments were carried out with the 3D graphene samples and the composition dependent PEC behavior was also confirmed (Figure S8). These trends suggest that there is an optimal composition (i.e., Cu<sub>2</sub>O/graphene ratio) in the hybrid configuration.

While the effect of GR thickness can be studied by comparing samples with identical Cu<sub>2</sub>O content, their optical behavior might be different. In fact, this increased light absorption with higher GR thicknesses explains the decrease in the photocurrents at high GR thicknesses, where light absorption of Cu<sub>2</sub>O is hindered by the presence of GR. This trend is also reflected in Figure 10 below.

The question, however, still holds: what are the reasons behind the improvement in the PEC properties? EIS measurements were performed to scrutinize the electronic properties of the synthesized photoelectrodes. From qualitative analysis of the Nyquist plots depicted in Figure 9a, one can see the large decrease of semicircle size for the graphene-containing composites. Additionally, there is a higher series resistance for the Cu<sub>2</sub>O/ITO sample compared to its graphene-containing counterparts (most likely rooted in the resistance of the Cu<sub>2</sub>O/ITO interface). To quantify these trends an equivalent circuit (see the circuit and its description in the SI, Figure S10) was employed to fit the measured data (Figures 9b and c). The most important conclusions are the following: (i) There was a huge decrease (from 500 Ω to 10 Ω) in the charge transfer resistance ( $R_{ct}$ ) when Cu<sub>2</sub>O was electrodeposited on the GR support instead of the bare ITO; (ii) When the GR thickness was increased the  $R_{ct}$  value also increased to 30 Ω, and then remained constant at higher GR thicknesses; (iii) The very high surface area of the hybrid electrodes was reflected in the high double-layer capacitance values ( $C_1$ , 10–30 mF cm<sup>-2</sup>). Overall,

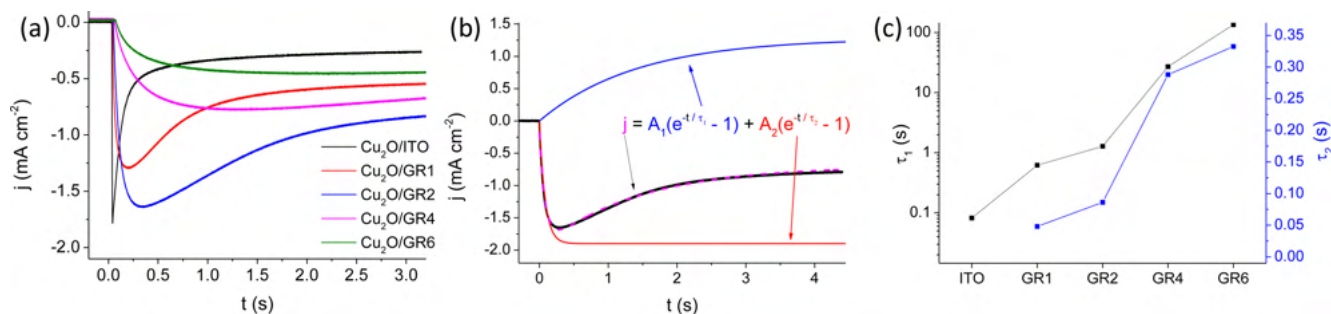


**Figure 10.** (a) Photocurrent transients of a pristine  $\text{Cu}_2\text{O}$  film and four different  $\text{Cu}_2\text{O}/\text{GR}$  composites deposited with  $0.5 \text{ C cm}^{-2}$  charge density, in  $\text{CO}_2$  saturated  $0.1 \text{ M Na}_2\text{SO}_4$  solution at  $E = 0.05 \text{ V}$  potential. A solar simulator was used employing a UV cutoff filter ( $<400 \text{ nm}$ ). (b) Dual exponential fit of a transient photocurrent response of the  $\text{Cu}_2\text{O}/\text{GR2}$  sample. (c) Time constant values obtained for the samples shown in (a). The lines among the data points serve only to guide visualization.

these results confirm that the improved electrical conductivity, facilitating better charge carrier transport, is an important contributor to the superior PEC properties of the hybrid electrodes.

To get a better understanding on the charge carrier recombination process, transient photocurrent measurements were performed.<sup>67–69</sup> In these measurements the photocurrent was followed after the light was switched on (chopped illumination). The first important observation in all experiments was the slow relaxation of the cathodic photocurrents (on the order of seconds, see Figures 10 and 11). Similarly to

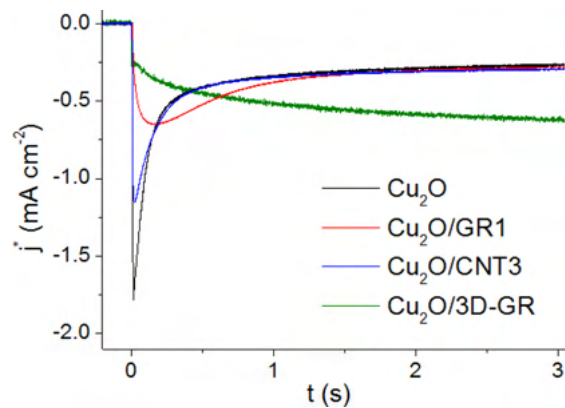


**Figure 11.** Photocurrent transient analysis of a pristine  $\text{Cu}_2\text{O}$  film and three different  $\text{Cu}_2\text{O}/\text{nanocarbon}$  composites deposited with  $0.5 \text{ C cm}^{-2}$  charge density. The measurements were performed in  $\text{CO}_2$  saturated  $0.1 \text{ M Na}_2\text{SO}_4$  solution at  $E = 0.05 \text{ V}$  potential. A solar simulator was used employing a UV cutoff filter ( $<400 \text{ nm}$ ). Photocurrent normalization was performed using the relative surface area data in Table S1.

previous water oxidation studies,<sup>68,69</sup> this slow charge transfer can be attributed to the kinetically hindered, multielectron nature of  $\text{CO}_2$  reduction (i.e., it involves  $6 \text{ e}^-$  and  $6 \text{ H}^+$  to form methanol). The competition between electron transfer to  $\text{CO}_2$  at electrode/electrolyte interface and electron–hole recombination within the space charge layer and at the surface means that only a portion of the photogenerated electrons can react with  $\text{CO}_2$ . Consequently, the achieved solar to chemical conversion efficiencies are much smaller than what could be expected from the optoelectronic properties of  $\text{Cu}_2\text{O}$ . Extensive recombination is particularly problematic close to the Fermi level, and while higher external bias potentials can help to suppress it, there is a trade off because of the needed additional

energy input. Also note that the stability of the photoelectrode was much lower at higher bias potentials, see also Figure 7.

Transient photocurrent curves recorded for the different samples are compared and contrasted in Figure 10a. While for the bare  $\text{Cu}_2\text{O}$  there was a sharp transient, this feature gradually disappeared in the series of  $\text{Cu}_2\text{O}/\text{GR}$  samples with progressively higher GR content. As for  $\text{Cu}_2\text{O}$ , the photocurrent developed instantaneously after the light was turned on, followed by an exponential decay to a steady-state cathodic value. These cathodic photocurrent transients can be attributed to accumulation of the photogenerated electrons in the  $\text{Cu}_2\text{O}$  space charge layer and recombination of bulk holes with these electrons.<sup>67–69</sup> At longer time scales, a steady-state photocurrent was reached, the magnitude of which was dictated by the relative rates of recombination and charge transfer to redox species.<sup>67</sup>

As for the graphene containing samples, the pattern was more complex. First, the initial spike got gradually smaller and finally disappeared as the graphene thickness increased. Meanwhile, an opposite (i.e., increasing) pattern developed, dictated by charge carrier transport through the relatively thick  $\text{Cu}_2\text{O}/\text{GR}$  electrode architecture (note that no such behavior was observed for thin nanocarbon supports or bare  $\text{Cu}_2\text{O}$ , see also Figures 11 and S11). The relative contribution of these processes is clearly correlated with the graphene content (note that the  $\text{Cu}_2\text{O}$  amount was identical in all cases). The ratio of the steady-state and the peak photocurrent increased with the graphene thickness, because of the increasing magnitude of  $\text{Cu}_2\text{O}/\text{GR}$  junction area (see also Figure 8). This suppressed recombination, however, did not result in constantly growing steady-state currents, mostly because of changing optoelectronic properties in the series of samples (i.e., light absorption of graphene (see above), increased resistance (see Figure 9)).

To facilitate quantitative comparison, the transient photocurrent curves were fitted and time constants were determined for all systems with different composition and morphology. The transient photocurrent curves could be well-fit to a sum of two exponential functions, one related to surface recombination (characterized by  $\tau_1$ ) and another one dictated by hole-transport through the electrode assembly (characterized by  $\tau_2$ )<sup>70</sup> (see the fitted equation and an example of the fitting in Figure 10b). While  $A_2$  gives the absolute value of the maximum achievable photocurrent (i.e., in the absence of recombination),  $A_1$  shows the maximal contribution of the recombination process to the decrease in the photocurrent. As seen in Figure 10c, both time constants increased with the growing GR thickness, although at vastly different extents (note the

logarithmic scale for  $\tau_1$ ). The time constant related to recombination increased rapidly with the higher graphene thicknesses. Note that the  $\text{Cu}_2\text{O}$  amount was fixed, therefore this trend is related to the gradually thinner  $\text{Cu}_2\text{O}$  coverage on the graphene platelets.

Upon light irradiation the photogenerated electrons (minority carriers) are driven toward the electrode/electrolyte interface by band bending, while the holes are rapidly siphoned off by the graphene phase (note that this process occurs on the nanosecond time scale).<sup>71</sup> As a net result, the time constant related to recombination increased by three orders of magnitude for the composite sample with the highest graphene content, compared to the bare  $\text{Cu}_2\text{O}$  film. On the other hand,  $\tau_2$  changed almost proportionally with the GR loading (thickness), which is not too surprising considering that this time constant is related to the transport of holes to the current collector (ITO). We also note here that there are several other processes which contribute to the charge carrier dynamics of the presented photoelectrodes. However, exciton generation, charge carrier separation in  $\text{Cu}_2\text{O}$ , and charge transfer from  $\text{Cu}_2\text{O}$  to GR occur on a much shorter (fs–ns) time scale, so that their effect cannot be important here.<sup>30,72</sup> Pump–probe transient absorption laser spectroscopic studies are planned in the future to study these processes in operando. From these results taken as a whole, we may conclude that both the enhanced specific surface area and improved charge carrier transport result in suppressed recombination, so that a higher fraction of the photogenerated electrons can react with  $\text{CO}_2$ .

**Comparison of Graphene, 3D Graphene, and CNT as Photoelectrode Support.** Finally, to further elucidate the role of the nanocarbon scaffold and possible morphological aspects, the PEC behavior of different nanocarbon containing hybrid samples were compared. To deconvolute the effect of the different surface areas, samples with similar charge capacitance are compared in Figure 11, and the slight differences in the surface area were taken into account by normalizing the photocurrent values (see also Figure S1 and Table S1). The  $\text{Cu}_2\text{O}$  content was identical in all cases ( $0.5 \text{ C cm}^{-2}$ , with respect to the geometrical surface area). What is immediately striking is that steady-state currents on the three curves ( $\text{Cu}_2\text{O}$ ,  $\text{Cu}_2\text{O}/\text{CNT3}$ , and  $\text{Cu}_2\text{O}/\text{GR1}$ ) almost overlap after normalization, although they have significantly different time constants (slower recombination for CNT and especially the GR-containing composite, compared to the bare  $\text{Cu}_2\text{O}$ ). These trends suggest that in these instances the improved PEC activity shown above (e.g., Figures 6 and 8) is predominantly rooted in the increased surface area (and the resultant high  $\text{Cu}_2\text{O}/\text{carbon}$  junction area), provided by the highly conductive nanocarbon scaffold. After factoring out this effect, very similar behavior is seen, at least in terms of the steady-state photocurrents (see also Figure S12a).

On the other hand, much higher normalized steady-state photocurrent flow could be seen for the 3D-GR support, most likely because of the superior charge transport properties rooted in the lack of particle–particle interfaces (also consider that the size of graphene platelets is much higher in this case, compared to the spray-coated samples, see Figure 4 and Figure S3). Note that while this support had relatively small surface area, at the same time, it has a higher thickness. This manifested in the large time constant for the photocurrent development ( $\tau_2$ ).

Finally, we recognize that the light penetration depth was limited in this macroscopic architecture. Consequently, design

of other 3D architectures, where benefits of the presented 3D graphene structure could be maintained while simultaneously ensuring sufficient light harvesting, would be highly desirable; such studies are in progress in our laboratories.

## CONCLUSIONS

A broad compositional and morphological space was explored to assemble hybrid photoelectrodes based on a highly conductive nanocarbon support (graphene) and a p-type inorganic semiconductor ( $\text{Cu}_2\text{O}$ ). A multiple potential-step electrodeposition protocol was employed to control the amount and size (thus the overall coverage) of the  $\text{Cu}_2\text{O}$  nanocrystallites on the graphene surface. The PEC activity of the composites was proved in  $\text{CO}_2$  reduction (to form alcohol products), as a model multielectron transfer reaction of practical significance. It was found that the graphene-containing photoelectrodes outperformed the pure  $\text{Cu}_2\text{O}$ , both in terms of the achieved current densities and stability. Composition-dependent PEC studies revealed that there was an optimal loading for both components. Transient photocurrent measurements revealed that the main contribution of the graphene substrate in such structures was the facilitation of effective charge separation and transport, leading to better harvesting of the generated photoelectrons. An added bonus is enhanced stability and durability of the semiconductor components.

A phenomenological model was developed involving: (i) electron transfer from  $\text{Cu}_2\text{O}$  to  $\text{CO}_2$ , (ii) recombination of the photoelectrons with holes in the space charge layer, (iii) hole transfer from  $\text{Cu}_2\text{O}$  to graphene, and (iv) hole transport through the electrode architecture to the current collector. By fitting the transient photocurrent curve, semiquantitative assessment could be made, for the first time, for the graphene contribution to the enhanced PEC activity of the hybrid photoelectrodes. The presented approach also afforded study of the effect of the nanocarbon morphology: after deconvoluting the effect of the increased surface area, we demonstrated that an interconnected 3D graphene structure (as a new promising member of the self-standing, highly conductive carbon derivative family) has further benefits compared to its nonorganized counterparts (spray-coated graphene and CNT films), because of the lack of carbon–carbon boundaries in the structure. Importantly, the presented design elements for the new family of photoelectrode materials in this study can be utilized for solar fuels generation *in general*, by assembling hybrid architectures with complementary function and optimized nanomorphology.

## ASSOCIATED CONTENT

### Supporting Information

The Supporting Information is available free of charge on the ACS Publications website at DOI: 10.1021/jacs.7b01820.

Additional synthetic details, morphological studies, EIS data, and photoelectrochemical analysis (PDF)

## AUTHOR INFORMATION

### Corresponding Author

\*janaky@chem.u-szeged.hu

### ORCID

Robert A. W. Dryfe: 0000-0002-9335-4451

Krishnan Rajeshwar: 0000-0003-4917-7790

Csaba Janáky: 0000-0001-5965-5173

## Notes

The authors declare no competing financial interest.

## ACKNOWLEDGMENTS

This project has received funding from the European Research Council (ERC) under the European Union's Horizon 2020 research and innovation programme (grant agreement No 716539). The authors also thank Rendernet Ltd. for assistance in preparing the artwork in the TOC. This research was partially supported by the "Széchenyi 2020" program in the framework of GINOP-2.3.2-15-2016-00013 "Intelligent materials based on functional surfaces—from syntheses to applications" project. Authors from the University of Manchester were supported by EPSRC grants (EP/K007033/1 and EP/K016954/1). The authors thank Dr. Tamás Pajkossy (Research Center for Natural Sciences of the Hungarian Academy of Sciences) for the valuable discussions on the EIS results, Dorottya Hursán for the support with the GC–MS analysis, and Dr. Albert Oszkó (University of Szeged) for recording the XPS spectra during the peer review cycle. Finally, the authors thank the three anonymous reviewers for their constructive and insightful criticisms of an earlier manuscript version.

## REFERENCES

- (1) Lewis, N. S.; Nocera, D. G. *Proc. Natl. Acad. Sci. U. S. A.* **2006**, *103*, 15729–15735.
- (2) Wang, H.; Dai, H. *Chem. Soc. Rev.* **2013**, *42*, 3088–3113.
- (3) Joshi, U. A.; Palasyuk, A.; Arney, D.; Maggard, P. A. *J. Phys. Chem. Lett.* **2010**, *1*, 2719–2726.
- (4) Sivula, K. *J. Phys. Chem. Lett.* **2015**, *6*, 1624–1633.
- (5) Rajeshwar, K. *J. Phys. Chem. Lett.* **2011**, *2*, 1301–1309.
- (6) Fujishima, A.; Honda, K. *Nature* **1972**, *238*, 37–38.
- (7) Cowan, A. J.; Durrant, J. R. *Chem. Soc. Rev.* **2013**, *42*, 2281–2293.
- (8) Boston, D.; Huang, K.-L.; de Tacconi, N.; Myung, N.; MacDonell, F.; Rajeshwar, K. Chapter 11. Electro- and Photocatalytic Reduction of CO<sub>2</sub>: The Homogeneous and Heterogeneous Worlds Collide? In *Photoelectrochemical Water Splitting: Materials, Processes and Architectures*; Lewerenz, H.-J., Peter, L., Eds.; The Royal Society of Chemistry, 2013.
- (9) Kumar, B.; Llorente, M.; Froehlich, J.; Dang, T.; Sathrum, A.; Kubiak, C. P. *Annu. Rev. Phys. Chem.* **2012**, *63*, 541–569.
- (10) Taniguchi, I.; Aurian-Blajeni, B.; Bockris, J. *Electrochim. Acta* **1984**, *29*, 923–932.
- (11) Ghadimkhani, G.; de Tacconi, N. R.; Chanmanee, W.; Janaky, C.; Rajeshwar, K. *Chem. Commun.* **2013**, *49*, 1297–1299.
- (12) Janaky, C.; Hursán, D.; Endrodi, B.; Chanmanee, W.; Roy, D.; Liu, D.; Tacconi, N. R. De; Dennis, B. H.; Rajeshwar, K. *ACS Energy Lett.* **2016**, *1*, 332–338.
- (13) Read, C. G.; Park, Y.; Choi, K. S. *J. Phys. Chem. Lett.* **2013**, *3*, 1872–1876.
- (14) Gu, J.; Wuttig, A.; Krizan, J. W.; Hu, Y.; Detweiler, Z. M.; Cava, R. J.; Bocarsly, A. B. *J. Phys. Chem. C* **2013**, *117*, 12415–12422.
- (15) Prévot, M. S.; Guijarro, N.; Sivula, K. *ChemSusChem* **2015**, *8*, 1359–1367.
- (16) Sharma, G.; Zhao, Z.; Sarker, P.; Nail, B. A.; Wang, J.; Huda, M. N.; Osterloh, F. E. *J. Mater. Chem. A* **2016**, *4*, 2936–2942.
- (17) Kormányos, A.; Thomas, A.; Huda, M. N.; Sarker, P.; Liu, J. P.; Poudyal, N.; Janáky, C.; Rajeshwar, K. *J. Phys. Chem. C* **2016**, *120*, 16024–16034.
- (18) Jang, J.-W.; Cho, S.; Magesh, G.; Jang, Y. J.; Kim, J. Y.; Kim, W. Y.; Seo, J. K.; Kim, S.; Lee, K.-H.; Lee, J. S. *Angew. Chem., Int. Ed.* **2014**, *53*, 5852–5857.
- (19) Kang, U.; Choi, S. K.; Ham, D. J.; Ji, S. M.; Choi, W.; Han, D. S.; Abdel-Wahab, A.; Park, H. *Energy Environ. Sci.* **2015**, *8*, 2638–2643.
- (20) Halmann, M. *Nature* **1978**, *275*, 115–116.
- (21) Bockris, J.; Wass, J. C. *Mater. Chem. Phys.* **1989**, *22*, 249–280.
- (22) Barton, E.; Rampulla, D. M.; Bocarsly, A. B. *J. Am. Chem. Soc.* **2008**, *130*, 6342–6344.
- (23) Appel, A. M.; Bercaw, J. E.; Bocarsly, A. B.; Dobbek, H.; Dubois, D. L.; Dupuis, M.; Ferry, J. G.; Fujita, E.; Hille, R.; Kenis, P. J. A.; Kerfeld, C. A.; Morris, R. H.; Peden, C. H. F.; Portis, A. R.; Ragsdale, S. W.; Rauchfuss, T. B.; Reek, J. N. H.; Seefeldt, L. C.; Thauer, R. K.; Waldrop, G. L. *Chem. Rev.* **2013**, *113*, 6621–6658.
- (24) Sivula, K. *J. Phys. Chem. Lett.* **2015**, *6*, 975–976.
- (25) Janáky, C.; Rajeshwar, K. *Prog. Polym. Sci.* **2015**, *43*, 96–135.
- (26) Janáky, C.; Kecszenovity, E.; Rajeshwar, K. *ChemElectroChem* **2016**, *3*, 181–192.
- (27) Thangavel, S.; Krishnamoorthy, K.; Krishnaswamy, V.; Raju, N.; Kim, S. J.; Venugopal, G. *J. Phys. Chem. C* **2015**, *119*, 22057–22065.
- (28) Thangavel, S.; Krishnamoorthy, K.; Kim, S.; Venugopal, G. *J. Alloys Compd.* **2016**, *683*, 456–462.
- (29) Kongkanand, A.; Martínez Domínguez, R.; Kamat, P. V. *Nano Lett.* **2007**, *7*, 676–680.
- (30) Meng, F.; Li, J.; Cushing, S. K.; Bright, J.; Zhi, M.; Rowley, J. D.; Hong, Z.; Manivannan, A.; Bristow, A. D.; Wu, N. *ACS Catal.* **2013**, *3* (4), 746–751.
- (31) Meng, F.; Cushing, S. K.; Li, J.; Hao, S.; Wu, N. *ACS Catal.* **2015**, *5*, 1949–1955.
- (32) Xiang, Q.; Yu, J.; Jaroniec, M. *Chem. Soc. Rev.* **2012**, *41*, 782–796.
- (33) Yang, M.-Q.; Zhang, N.; Pagliaro, M.; Xu, Y.-J. *Chem. Soc. Rev.* **2014**, *43*, 8240–8254.
- (34) Xiang, Q.; Cheng, B.; Yu, J. *Angew. Chem., Int. Ed.* **2015**, *54*, 11350–11366.
- (35) Lightcap, I. V.; Kamat, P. V. *Acc. Chem. Res.* **2013**, *46*, 2235–2243.
- (36) Yokomizo, Y.; Krishnamurthy, S.; Kamat, P. V. *Catal. Today* **2013**, *199*, 36–41.
- (37) Pathak, P.; Gupta, S.; Grosulak, K.; Imahori, H.; Subramanian, V. *J. Phys. Chem. C* **2015**, *119*, 7543–7553.
- (38) Yin, S.; Men, X.; Sun, H.; She, P.; Zhang, W.; Wu, C.; Qin, W.; Chen, X. *J. Mater. Chem. A* **2015**, *3*, 12016–12022.
- (39) An, X.; Li, K.; Tang, J. *ChemSusChem* **2014**, *7*, 1086–1093.
- (40) Liang, Y. T.; Vijayan, B. K.; Gray, K. A.; Hersam, M. C. *Nano Lett.* **2011**, *11*, 2865–2870.
- (41) Ng, Y. H.; Iwase, A.; Kudo, A.; Amal, R. *J. Phys. Chem. Lett.* **2010**, *1*, 2607–2612.
- (42) Kecszenovity, E.; Endródi, B.; Pápa, Z.; Hernádi, K.; Rajeshwar, K.; Janáky, C. *J. Mater. Chem. A* **2016**, *4*, 3139–3147.
- (43) Young Kim, J.; Jang, J.-W.; Hyun Youn, D.; Yul Kim, J.; Sun Kim, E.; Sung Lee, J. *RSC Adv.* **2012**, *2*, 9415.
- (44) Zhang, Z.; Dua, R.; Zhang, L.; Zhu, H.; Zhang, H.; Wang, P. *ACS Nano* **2013**, *7*, 1709–1717.
- (45) Yu, L.; Li, G.; Zhang, X.; Ba, X.; Shi, G.; Li, Y.; Wong, P. K.; Yu, J. C.; Yu, Y. *ACS Catal.* **2016**, *6*, 6444–6454.
- (46) Hou, J.; Cheng, H.; Takeda, O.; Zhu, H. *Angew. Chem., Int. Ed.* **2015**, *54*, 8480–8484.
- (47) Yang, M.-Q.; Xu, Y.-J. *Nanoscale Horiz.* **2016**, *1*, 185–200.
- (48) Low, J.; Yu, J.; Ho, W. *J. Phys. Chem. Lett.* **2015**, *6*, 4244–4251.
- (49) Low, J.; Cheng, B.; Yu, J.; Jaroniec, M. *Energy Storage Mater.* **2016**, *3*, 24–35.
- (50) Dong, X.; Cao, Y.; Wang, J.; Chan-Park, M. B.; Wang, L.; Huang, W.; Chen, P. *RSC Adv.* **2012**, *2*, 4364–4369.
- (51) Zhan, B. B.; Liu, C. B.; Chen, H. P.; Shi, H. X.; Wang, L. H.; Chen, P.; Huang, W.; Dong, X. C. *Nanoscale* **2014**, *6*, 7424–7429.
- (52) Zou, Y.; Kinloch, I. A.; Dryfe, R. A. W. *ACS Appl. Mater. Interfaces* **2015**, *7*, 22831–22838.
- (53) Ambrosi, A.; Chua, C. K.; Bonanni, A.; Pumera, M. *Chem. Rev.* **2014**, *114*, 7150–7188.
- (54) Valota, A. T.; Toth, P. S.; Kim, Y.-J.; Hong, B. H.; Kinloch, I. A.; Novoselov, K. S.; Hill, E. W.; Dryfe, R. A. W. *Electrochim. Acta* **2013**, *110*, 9–15.
- (55) Zhang, H.; Zhu, Q.; Zhang, Y.; Wang, Y.; Zhao, L.; Yu, B. *Adv. Funct. Mater.* **2007**, *17*, 2766–2771.

- (56) Cao, X.; Yin, Z.; Zhang, H. *Energy Environ. Sci.* **2014**, *7*, 1850–1865.
- (57) Huang, M.; Wang, T.; Chang, W.; Lin, J.; Wu, C.; Chen, I.-C.; Peng, K.; Lee, S. *Appl. Surf. Sci.* **2014**, *301*, 369–377.
- (58) Mohemmed Shanid, N. A.; Abdul Khadar, M.; Sathe, V. G. *J. Raman Spectrosc.* **2011**, *42*, 1769–1773.
- (59) Dar, M. A.; Kim, Y. S.; Kim, W. B.; Sohn, J. M.; Shin, H. S. *Appl. Surf. Sci.* **2008**, *254*, 7477–7481.
- (60) Ferrari, A. C.; Meyer, J. C.; Scardaci, V.; Casiraghi, C.; Lazzeri, M.; Mauri, F.; Piscanec, S.; Jiang, D.; Novoselov, K. S.; Roth, S.; Geim, A. K. *Phys. Rev. Lett.* **2006**, *97*, 187401–187404.
- (61) Malard, L. M.; Pimenta, M. A.; Dresselhaus, G.; Dresselhaus, M. S. *Phys. Rep.* **2009**, *473*, 51–87.
- (62) Nakano, Y.; Saeki, S.; Morikawa, T. *Appl. Phys. Lett.* **2009**, *94*, 22111.
- (63) Gao, E.; Wang, W.; Shang, M.; Xu, J. *Phys. Chem. Chem. Phys.* **2011**, *13*, 2887–2893.
- (64) Paracchino, A.; Brauer, J. C.; Moser, J. E.; Thimsen, E.; Graetzel, M. J. *Phys. Chem. C* **2012**, *116*, 7341–7350.
- (65) Wang, L. C.; de Tacconi, N. R.; Chenthamarakshan, C. R.; Rajeshwar, K.; Tao, M. *Thin Solid Films* **2007**, *515*, 3090–3095.
- (66) de Brito, J. F.; Araujo, A. R.; Rajeshwar, K.; Zannoni, M. V. B. *Chem. Eng. J.* **2015**, *264*, 302–309.
- (67) Peter, L. M. *Chem. Rev.* **1990**, *90*, 753–769.
- (68) Ma, Y.; Pendlebury, S. R.; Reynal, A.; Le Formal, F.; Durrant, J. R. *Chem. Sci.* **2014**, *5*, 2964.
- (69) Klahr, B.; Gimenez, S.; Fabregat-Santiago, F.; Bisquert, J.; Hamann, T. W. *Energy Environ. Sci.* **2012**, *5*, 7626.
- (70) Noack, V.; Weller, H.; Eychmuller, A. *J. Phys. Chem. B* **2002**, *106*, 8514–8523.
- (71) Pu, Y. C.; Chou, H. Y.; Kuo, W. S.; Wei, K. H.; Hsu, Y. J. *Appl. Catal., B* **2017**, *204*, 21–32.
- (72) Hansen, O.; Seger, B.; Vesborg, P. C. K.; Chorkendorff, I. *Science* **2015**, *350*, 1030–1031.





Contents lists available at ScienceDirect

## Progress in Energy and Combustion Science

journal homepage: [www.elsevier.com/locate/pecs](http://www.elsevier.com/locate/pecs)

## Continuous-flow electroreduction of carbon dioxide

B. Endrődi<sup>a,b</sup>, G. Bencsik<sup>a,b</sup>, F. Darvas<sup>c</sup>, R. Jones<sup>c</sup>, K. Rajeshwar<sup>d</sup>, C. Janáky<sup>a,b,\*</sup><sup>a</sup> MTA-SZTE "Lendület" Photoelectrochemistry Research Group, Rerrich Square 1, Szeged, H-6720, Hungary<sup>b</sup> Department of Physical Chemistry and Materials Science, University of Szeged, Rerrich Square 1, Szeged, H-6720, Hungary<sup>c</sup> ThalesNano Inc., Záhony u. 7, Budapest 1031, Hungary<sup>d</sup> Department of Chemistry and Biochemistry, University of Texas at Arlington, Arlington, TX 76019, USA

## ARTICLE INFO

## Article History:

Received 23 February 2017

Accepted 31 May 2017

Available online 13 June 2017

## Keywords:

Electrolysis  
CO<sub>2</sub> conversion  
Renewable energy  
Syngas  
Solar fuels

## ABSTRACT

Solar fuel generation through electrochemical CO<sub>2</sub> conversion offers an attractive avenue to store the energy of sunlight in the form of chemical bonds, with the simultaneous remediation of a greenhouse gas. While impressive progress has been achieved in developing novel nanostructured catalysts and understanding the mechanistic details of this process, limited knowledge has been gathered on continuous-flow electrochemical reactors for CO<sub>2</sub> electroreduction. This is indeed surprising considering that this might be the only way to scale-up this fledgling technology for future industrial application. In this review article, we discuss the parameters that influence the performance of flow CO<sub>2</sub> electrolyzers. This analysis spans the overall design of the electrochemical cell (microfluidic or membrane-based), the employed materials (catalyst, support, etc.), and the operational conditions (electrolyte, pressure, temperature, etc.). We highlight R&D avenues offering particularly promising development opportunities together with the intrinsic limitations of the different approaches. By collecting the most relevant characterization methods (together with the relevant descriptive parameters), we also present an assessment framework for benchmarking CO<sub>2</sub> electrolyzers. Finally, we give a brief outlook on photoelectrochemical reactors where solar energy input is directly utilized.

© 2017 The Authors. Published by Elsevier Ltd.

This is an open access article under the CC BY license. (<http://creativecommons.org/licenses/by/4.0/>)

## Contents

1. Introduction .....	134
2. Reactor designs .....	135
3. Materials .....	137
3.1. Electrocatalysts .....	137
3.2. Effects of catalyst size and morphology .....	137
3.3. Role of the catalyst support .....	139
3.4. Catalyst immobilization .....	140
3.5. The role of ion-exchange membranes .....	141
3.6. The role of the current collectors, bipolar plates, and cell body .....	142
4. Operation .....	142
4.1. Feedstock .....	142
4.2. Liquid/gas flow rate .....	144
4.3. Temperature and pressure .....	145
4.4. Effect of the applied potential/voltage .....	146

**Abbreviations:** BID, Barrier ionization discharge detector; CO<sub>2</sub>, Carbon dioxide; R<sub>cell</sub>, Cell resistance; R<sub>ct</sub>, Charge transfer resistance; CB, Conduction band; CV, Cyclic voltammetry; DEMS, Differential electrochemical mass spectrometry; EIS, Electrochemical impedance spectroscopy; EC, Electrochemical; EDX, Energy-dispersive X-ray spectroscopy; FE, Faradaic efficiency; FT-IR, Fourier transform infrared spectroscopy; GC, Gas chromatography; GDEs, Gas diffusion electrodes; GDL, Gas diffusion layer; LSV, Linear sweep voltammetry; MEAs, Membrane electrode assemblies; NMR, Nuclear magnetic resonance; OER, Oxygen evolution reaction; PC, Photochemical; PEC, Photoelectrochemical; PV, Photovoltaic; PVA, Poly(vinyl alcohol); PEM, Polymer electrolyte membrane; SEM, Scanning electron microscopy; SC, Semiconductor; STH, Solar-to-hydrogen; SOE, Solid-oxide electrolyzers; Rs, Solution resistance; SCCM, Standard cubic centimeters per minute; SPEEK, Sulfonated poly(ether ether ketone); 3D, Three-dimensional; TEM, Transmission electron microscopy; UV, Ultraviolet; R<sub>u</sub>, Uncompensated resistance; VB, Valence band; XRF, X-ray fluorescence spectroscopy; XPS, X-ray photoelectron spectroscopy; XRD, X-ray powder diffraction

\* Corresponding author.

E-mail address: [janaky@chem.u-szeged.hu](mailto:janaky@chem.u-szeged.hu) (C. Janáky).<http://dx.doi.org/10.1016/j.pecs.2017.05.005>10360-1285/© 2017 The Authors. Published by Elsevier Ltd. This is an open access article under the CC BY license. (<http://creativecommons.org/licenses/by/4.0/>)

4.5. Timescale of the experiments .....	146
5. How to benchmark a CO <sub>2</sub> electrolyzer correctly? .....	147
5.1. Pre-operational characterization .....	147
5.2. In operando characterization .....	148
5.3. Post-operational characterization .....	149
5.4. Most important metrics to report .....	149
6. Photoelectrochemical reduction of CO <sub>2</sub> in continuous-flow .....	149
7. Summary and outlook .....	151

## 1. Introduction

Finding adequate solutions for a diversified and sustainable energy supply is undoubtedly one of the grand challenges of our society today [1]. It is imperative that renewable energy sources and solar/wind energy in particular, are increasingly used to improve the security of energy supplies and also ameliorate the environmental impact from carbon-based energy production and consumption. While solar and wind electricity generation already enjoy an important, and impressively increasing role in the global (and especially European) energy mix, *storage* is still an issue because of the intermittency of most renewable energy sources [2]. At the same time, the steeply rising level of carbon dioxide (CO<sub>2</sub>) in the atmosphere calls for conceptually new approaches to capture and utilize this greenhouse gas. A solar fuels-based economy tackles the above parallel challenges admirably well, although many challenges remain before widespread use of such energy carriers (e.g., H<sub>2</sub>, methanol, ethanol, and methane) sees the light of day.

CO<sub>2</sub> is a greenhouse gas; therefore using renewable energy to convert CO<sub>2</sub> to transportation fuels and commodity chemicals is a value-added approach to simultaneous generation of products and environmental remediation of carbon emissions. The large amounts of chemicals produced worldwide (Fig. 1) that can be potentially derived from the hydrogenation of CO<sub>2</sub>, highlights further the importance of this strategy. Several industrial entities are interested in such technologies, ranging from energy/utilities companies through cement producing and processing firms to oil and gas companies.

There are numerous routes for converting CO<sub>2</sub> to transportation fuels and other chemicals. The following three major pathways delineate how *sunlight* can be used to generate such products (e.g., CH<sub>4</sub> or CH<sub>3</sub>OH) from CO<sub>2</sub> (Fig. 1) [2–7].

**Photochemical (PC) or photosynthetic methods:** Directly use sunlight to photochemically convert CO<sub>2</sub> to fuels using molecular- or suspended semiconductor (SC) photocatalysts [8–10].

**Electrochemical (EC) approaches:** Here sunlight is first converted to electricity by a photovoltaic solar cell (PV) and CO<sub>2</sub> is then reduced electrochemically [11,12].

**Photoelectrochemical (PEC) route:** Photogenerated electrons are utilized to reduce CO<sub>2</sub> either directly at a SC/electrolyte interface or indirectly employing a redox mediator [13].

With the recent rapid drop in the cost of Si solar cells, the price of solar electricity has decreased to a level that in over 20 countries translates to grid parity. A recent study concluded that on a 20–25 year term it is not likely that any solar energy utilization pathways other than Si solar photovoltaic panels will have an industrially-relevant role [14]. Another techno-economic analysis suggested that PV+EC conversion setups may attain ~14% solar to H<sub>2</sub> efficiency (20% PV, 70% EC) in an economically feasible manner as the electricity price drops (which is clearly the case for both solar and wind power) [4]. These factors suggest that CO<sub>2</sub> conversion, at least on a short to intermediate term, will be driven in an EC configuration (note also the availability of other renewable electricity sources, such as wind). On a longer term basis, the PEC strategy also cannot be ruled out and in fact, further extensive research work is highly encouraged [4].

Electrochemical (EC) and photoelectrochemical (PEC) conversion of CO<sub>2</sub> are multi-electron in nature (up to 8 e<sup>-</sup> for conversion to methane) with considerable kinetic barriers to electron transfer. It therefore requires the use of carefully designed electrode surfaces to accelerate electron transfer rates to levels that make practical sense. In this vein, much has been written about the electrochemical, solid-state physics, theoretical, catalytic, and general materials science aspects of EC/PEC CO<sub>2</sub> reduction [15–17]. During the past 5 years, however, an accelerated progress has occurred, reflected in the number of published research articles and the citations they attracted (Fig. 2). Most of this work has focused on the development of new catalysts [18] and the enhancement of product selectivity [11,19]. Excitingly, we appear to be at the very cusp of a new era of electrochemical CO<sub>2</sub> conversion studies, which hopefully will lead to efficient CO<sub>2</sub> electrolyzers on a practical scale.

At this juncture, however, it has to be noted that CO<sub>2</sub> reduction is a lot more complex than water splitting, simply because many different products can be formed via proton-coupled multi-electron transfer [20]. To drive this process in an economically attractive way, it is important to produce (i) any product as selectively as possible; (ii) products of economic value; and (iii) products that are easy to separate. A recently-performed techno-economic analysis on the process suggested that the picture is even murkier, because co-producing a low value product (such as methanol or ethylene) together with a high value product (such as formic acid or carbon-monoxide) can be a better strategy than producing them alone. In fact, the optimal scenario would be to co-produce two products that are in different phases (i.e., one in the liquid phase and the other in the gas phase) as the separation process becomes straightforward in this case [21].

In addition, since the redox potential for proton to H<sub>2</sub> transformation is very close to the redox potential of the desired CO<sub>2</sub> reduction processes, there is always a competition between these two processes. Furthermore, although thermodynamic considerations would allow reduction of CO<sub>2</sub> at moderately negative potentials, electrochemical reduction of CO<sub>2</sub> is kinetically daunting with high overpotentials needed for its conversion to hydrocarbons and alcohols. Finally, in a simple batch reactor, the maximum achievable rate

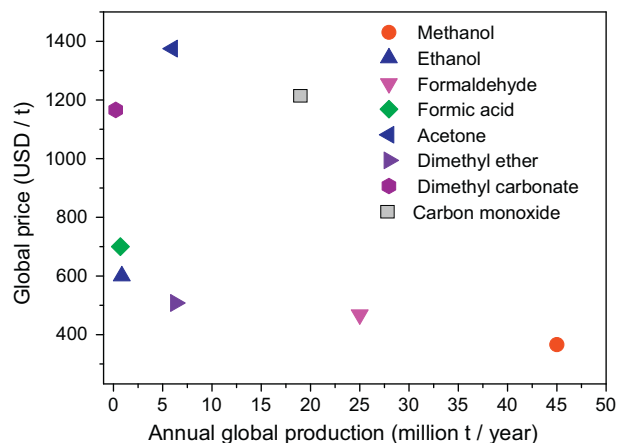
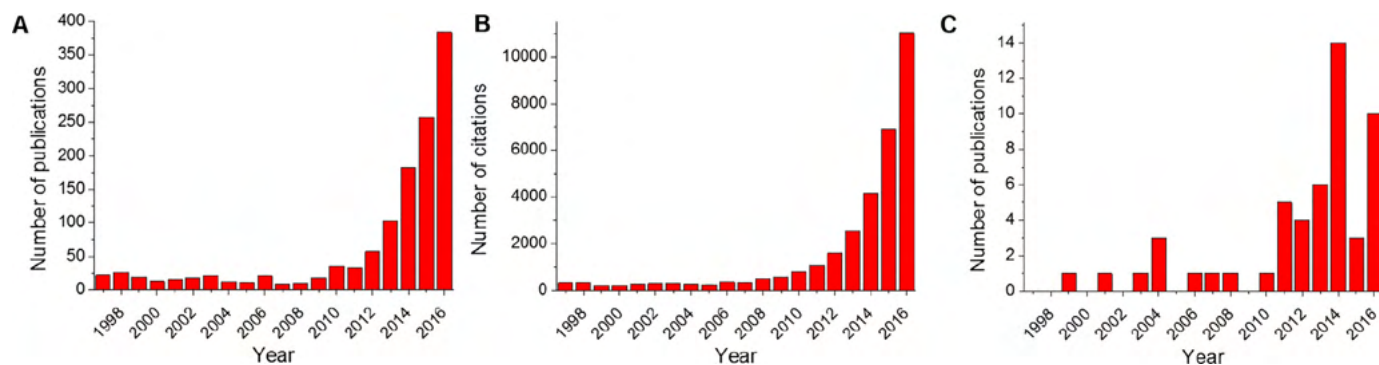


Fig. 1. Global market of the most important CO<sub>2</sub>-utilization products.



**Fig. 2.** Results of a literature survey on electrochemical and photoelectrochemical CO<sub>2</sub> reduction. A: number of papers published, B: the citations gathered by these papers, C: papers claimed to use a flow-setup (this is a subset of Fig. 2A).

for the reaction is often limited by the low solubility ( $\sim 30$  mM) of CO<sub>2</sub> in water. Using a simple semi-infinite diffusion model, the limiting current density attainable at this concentration is approximately  $I_L = 60 \text{ mA cm}^{-2}$  under vigorous stirring [22]. Importantly, the solubility of CO<sub>2</sub> strongly depends on the temperature, the solution pH, and the ionic strength as well, which should be taken into account when comparing data measured in different solutions [23].

To increase the CO<sub>2</sub> conversion rate to a level of practical significance, EC CO<sub>2</sub> reduction must be performed in a continuous-flow setup to overcome mass-transport limitations. We note that there is a striking difference here compared to water splitting, where ample amounts of water molecules (55.5 M!) are available for the reaction. Interestingly, despite some successful pioneering studies [24], very little attention has been devoted to EC CO<sub>2</sub> reduction *in continuous flow mode*. Only a minor fraction ( $\sim 5\%$ ) of the articles (see Fig. 2C) report on studies performed under such flow conditions. In fact, this trend can also be very problematic in the sense that conclusions drawn from batch experiments cannot be directly translated to flow situations (unlike for water splitting).

There are a few reviews on electrochemical cell designs for CO<sub>2</sub> reduction: namely microfluidic reactors [25,26] and polymer electrolyte membrane (PEM) electrolyzers [27]. Solid-oxide electrolyzers, while an important category, fall outside the purview of the present study, because of their vastly different operational principles and conditions (high temperature, single CO product, etc.) [28]. In a continuous flow CO<sub>2</sub> electrolyzer, multiple parameters have to be simultaneously tailored to possibly achieve an economically viable process [21]. In two recent articles careful modeling on the effect of the various operational parameters (pH, concentration, temperature) was carried out, mostly through studying the CO<sub>2</sub>/carbonate family equilibrium [29,30]. In this review, we focus on real operational cells: materials aspects, device-related features, together with operational parameters are the three main categories forming the crux of this article. We compare various reports in the literature, to identify the role of the individual parameters, and to set guidelines for future studies. We also incorporate the lessons learned from the fuel cell and water electrolyzer communities, while highlighting also the most important differences.

The prematurity of the field is also reflected in the lack of precise definition of electrochemical flow cells. A simple literature search for “flow-electrochemical cell” or “continuous-flow electrolyzer” can easily mislead the reader. For example, some studies in which the liquid phase is continuously purged with systematically varied flux of CO<sub>2</sub> during the measurement are claimed to be on “flow” systems. Although very important conclusions can be drawn from these studies on the effect of the different reaction parameters (e.g., gas flow-rate, electrode composition, pH), these setups significantly differ from those – constituting the core of this study – in which a fresh solution/gas phase is fed to the electrodes continuously as detailed later [31]. Similarly, while in some cases both the catholyte and the

anolyte is continuously pumped (and thus refreshed), in other instances only one of them. It is also common that the circumstances of the measurements are not precisely defined, and therefore it is very difficult to determine whether the experiments were performed in a real flow electrolyzer or not.

Finally, in our opinion, there is a strong need for setting the proper measurement protocol for assessing the properties of continuous flow EC cells for CO<sub>2</sub> reduction and for specifying a set of parameters for benchmarking purposes. Such an exercise is particularly relevant because researchers from diverse specialties (e.g., heterogeneous/homogeneous catalysis, fuel cells, water splitting, etc.) and even disciplines (chemistry, physics, and engineering) have congregated in the EC CO<sub>2</sub> reduction arena. These disparate communities often use very different terminologies. Hark back to the history of the fuel cells and water electrolyzer communities where it took decades to establish generally-accepted testing protocols and benchmarking parameters. In the interim period, literally hundreds/thousands of reports accumulated in the literature describing results that could not be reliably intercompared with one another.

## 2. Reactor designs

Whether we consider technology scale-up or reliable rapid screening of materials in the laboratory, continuous-flow reactors have multiple benefits compared to their batch counterparts. Among others, these include increased mass transfer and improved mixing of different phases, better temperature and heat transfer control, and more precise influence on reaction mixture residence time in the reactor [32]. When moving from batch-type experiments to continuous-flow cells, the architecture and design of the reactor (electrochemical cell) must be first clearly defined. Note that this includes: the type of electrolyte used (liquid/gas), reactor material-reaction mixture compatibility, whether it can be pressurized or not, the applicable temperature and flow rate, and the possibility of using a reference electrode.

Schematic drawings of the most frequently studied cell configurations are presented in Fig. 3. Before discussing each of them individually, we would like to emphasize the importance of the number of electrodes employed in the setup. Many designs only involve two electrodes (a working and a counter electrode); thus only current or voltage (not potential) control is possible in these cases. There is a considerable number of electrolyzer setups where a reference electrode is also integrated into the cell, close to the working electrode surface, to ensure the possibility of *potential* control. A four-electrode setup is also possible (with two reference electrodes), if the water oxidation step is complicated, and thus the monitoring of both half-cells becomes important. Potential control is especially important in electrolyzers in which the catalysts (e.g., copper oxides [20]) change their chemical composition (or surface properties)

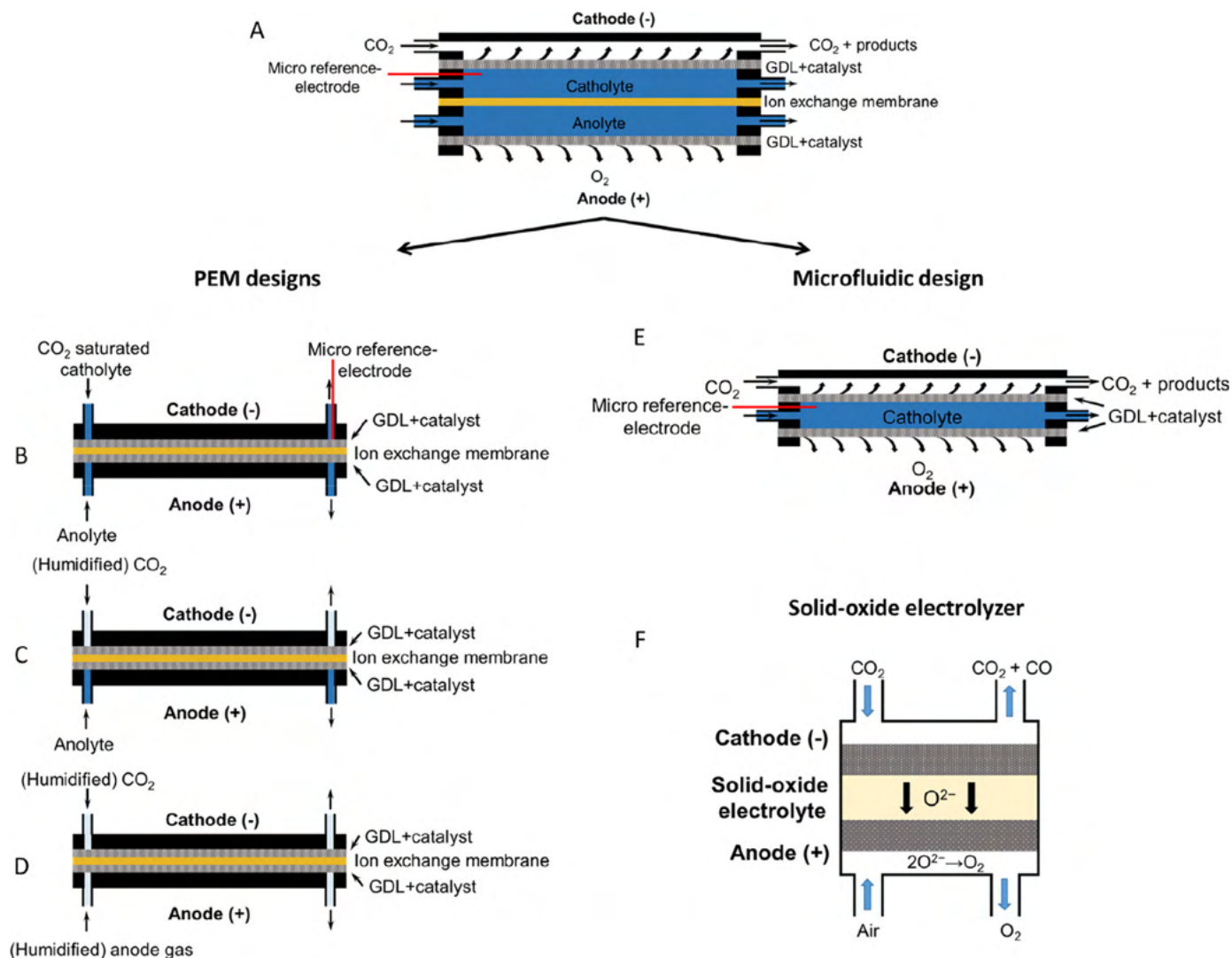


**Fig. 3.** Sketch and operating principle of the most frequently studied cell configurations in continuous-flow EC CO<sub>2</sub> reduction. (A): general design used to derive: a classical microfluidic setup (E), and three different configurations containing a polyelectrolyte membrane (B–D). (GDL: gas diffusion layer) F: Solid-oxide electrolyzer.

during operation (i.e., aging). This often results in a change in the product distribution with time, as discussed in what follows.

Fig. 3A shows the most universal architecture, from which all other setups can be derived. This parent configuration consists of two flow channels, one for the anolyte and another for the catholyte, separated by an ion-exchange membrane. The cathode electrocatalyst is immobilized on a gas diffusion layer (GDL), which is in contact with the flowing catholyte from one side, while CO<sub>2</sub> gas is directly fed on the other side [33]. This arrangement overcomes most of the problems associated with the other setups, namely: (i) current limitation due to the low concentration of CO<sub>2</sub> at the electrode; (ii) H<sup>+</sup> crossover from the anode and the consequent acidification of the catholyte; (iii) difficulty of inserting a reference electrode; (iv) diffusion of liquid-phase products to the anode, where they are oxidized (product crossover). Although no such instrument is commercially available on the industrial scale at the moment, most components of this setup (i.e., GDLs and catalysts) are available and ready for scale-up already. We note here that it seems to be very challenging to build large stacks based on this concept mostly because of the pressure sensitivity of this structure [34]. We expect therefore that the parallel operation of these instruments (the scale-out concept) will constitute the main track of industrialization in this case – at least in the near future. The other experimental devices (Fig. 3B–E) can be derived by “removing” different elements of this general setup, thus

simplifying the overall architecture. By applying a single, undivided channel for flow of the common electrolyte, we get a typical microfluidic reactor (Fig. 3E). In this setup, the electrodes are separated by a thin spacer (usually well below 1 mm in thickness) and no membrane is included [35–39]. The reference electrode can be inserted in the electrolyte flow stream and the excess protons formed on the anode are drained from the cathode vicinity by electrolyte flow (although not as effectively as in the case of separated electrolyte channels).

A popular class of devices feature separation of the two electrodes by an ion-exchange membrane (typically Nafion™, but see also Section 3.5. for others) (Fig. 3B–D). Usually the electrodes are pressed together and no flow channels are formed between them (zero gap cells). The electrolyte/gas is fed to the electrodes (mostly gas diffusion electrodes (GDEs), formed by immobilizing the catalyst on a GDL), and remains in the cell until reaching the exit point. The greatest advantage of these setups, compared to the microfluidic arrangements, is that it is relatively easy to pressurize the reactant and product flows. Furthermore, based on the similarity of these devices to PEM water electrolyzers, the scale-up of these setups to the industrial scale and construction of large sized stacks seems to be more straightforward.

Variants of these setups differ in the type of electrolytes used. The reactants fed to the cathode and anode compartment can be (i) both

in liquid phase (Fig. 3B) [40]; (ii) CO<sub>2</sub> gas on the cathode and liquid phase anolyte (Fig. 3C) [41,42]; (iii) humidified gases on both electrodes (Fig. 3D) [43,44]. Although this may look like a minor difference at first sight, the reactant type has an important and complex effect on cell performance. When feeding pure CO<sub>2</sub> to the cathode, the reactant concentration remains very high on the catalyst, and therefore high reaction rate (current) can be achieved. In this case however, trustworthy measurement of the individual electrode potentials is far from trivial, although several promising attempts were made with all-gas fuel cells [45–48]. Previous studies have shown that the product distribution changes parallel to continuous ageing of certain catalysts during long-term operation [49,50]. The lack of a reference electrode complicates this situation even more, since in this case the change in the cell voltage/current stems from either anode or cathode degradation (or both), whose effects cannot be separated.

The main drawback of these membrane-separated zero-gap devices paradoxically is the same as their main advantage, namely the proximity of the two electrodes to one another. This decreases the cell resistance and consequently, the IR-drop to a minimum level, but on the other hand, ion exchange leads to acidification of the catholyte and therefore to increased production of H<sub>2</sub> (instead of reduction of CO<sub>2</sub>). Including a buffer layer between the electrodes can circumvent this effect, but at the same time, leads to increased cell resistance [51]. Although most studies on PEM CO<sub>2</sub> electrolyzers focus on the use of cation exchange membranes, anion exchange membranes may also bear considerable scope in CO<sub>2</sub> conversion. In such arrangements, OH<sup>-</sup> ions are transported through the membrane, which results in a different product distribution compared to cation exchange membrane containing systems [52]. A new anion-exchange membrane based electrolyzer was recently developed for both CO<sub>2</sub> conversion and water splitting [53]. The reactors, using the new anion exchange membrane based on polymers containing imidazolium and pyridinium groups, exhibited high durability at industrially relevant current densities (100 mA cm<sup>-2</sup> for CO formation) [53]. Detailed discussion on the role of the ion-exchange membrane is given in Section 3.5.

It is very important to underline that for industrial applications, large-sized, multiple-stack electrolyzers are required. The current status of this field is very far from this level, since aside from a few examples, all studies were carried out on 1–10 cm<sup>2</sup> sized electrodes [54,55]. Consequently, a grand challenge for future research and development is to construct experimental setups that can be readily translated to *real* industrial technologies.

The operational principle of solid oxide electrolyzers is shown in Fig. 3F. Detailed discussion however, is omitted because of their completely different properties compared to both their microfluidic and PEM counterparts [28].

### 3. Materials

As outlined in the previous section, various device architectures can be used for the continuous-flow electroreduction of CO<sub>2</sub>. There are certain components, however, which are common to all electrolyzer designs, and they are discussed in what follows (also see Table 1 for an overview).

#### 3.1. Electrocatalysts

As it dictates both the kinetics and thermodynamics of the electrolysis process, the electrocatalyst is the heart of such devices. The most extensively scrutinized cathode catalysts and their most important features are summarized in Table 1. When comparing and contrasting these to the catalysts employed in batch experiments we can conclude that (i) the catalyst candidates that proved to be promising in batch setups show similar, or even, higher

electrochemical activity in the corresponding flow setup; (ii) the formed products are very similar for both batch and flow experiments; (iii) the reported potential values differ significantly in many cases. The most intensively studied electrocatalysts are Sn, on which formate is produced almost exclusively; Ag with preferred CO formation; and Cu, on which a wide variety of products is formed, depending on the experimental circumstances. Several catalysts (e. g., metal alloys) that were promising in batch experiments however, are still waiting to be tested in flow cells. An example of new generation catalysts is metal organic frameworks (MOFs), which were very recently studied in flow-reactors [56]. Much less effort has been devoted to the anode catalyst, where mostly IrO<sub>x</sub> and Pt was employed to facilitate water oxidation (O<sub>2</sub> evolution) [57]. In the outlook section, we present some possible future R&D avenues, where the anode electrocatalyst gets higher importance.

The amount of the electrocatalyst in these devices varies in a relatively broad range, from 0.2 to 10 mg cm<sup>-2</sup>. The most commonly applied catalyst loading however, is around 1 mg cm<sup>-2</sup>, independently of the catalyst used. This latter fact is indeed very surprising, since the molar mass, density, and specific surface area of the different catalysts can differ severely. This may cause *several orders of magnitude* difference in the number of electrocatalyst atoms, and more specifically in that of the surface atoms, which can interact with the CO<sub>2</sub> molecules. To get a meaningful comparison on the electrocatalytic properties of different catalysts, one must therefore always normalize the measured current values in terms of either the electrochemically active surface area, or with the number of surface atoms, but not with respect to the geometric surface area or electrode mass. This is even more important in the case of thick porous electrodes, where the current density can be influenced by electrode thickness, without affecting the electrode kinetics.

At this juncture, however we note that researchers need to make sure that all measurements were taken in the kinetically-controlled regime and not the mass transfer-limited regime, before they compare reaction rates across different catalytic systems. Different strategies can be employed to determine mass transfer limitations, for example obtaining breakthrough curves (current density vs. catalyst loading) [78]. An example is shown in Fig. 4, where LSV curves are shown for Sn-based GDEs with different Sn-loading. As seen in Fig. 4A, after a certain Sn-content, the mass-transport limited regime is reached. This trend is directly visualized in Fig. 4B, where the partial current density related to CO<sub>2</sub> reduction is plotted vs. the catalyst loading (note the constant FE values, confirming that the chemical process is identical).

It should also be noted that although attempts were made to directly compare the results of batch experiments with those measured in flow setups, such a comparison is not straightforward because of several reasons [33]. The continuously refreshed solution, reaching the electrode surface leads to striking differences as it has a massive influence on the (i) mass-transport (diffusion layer thickness); (ii) local pH effects; (iii) product accumulation in the close vicinity of the cathode; (iv) residence time of CO<sub>2</sub> molecules at the electrode surface. When applying (humidified) CO<sub>2</sub> gas as “catholyte,” its effective concentration on the surface is obviously higher than in the case of aqueous solutions, which leads to higher current densities at the same “potential”. Here we refer to our earlier point, namely that defining and measuring electrode potential in such arrangements is also problematic.

#### 3.2. Effects of catalyst size and morphology

Particle size effects [79] have not been extensively studied in flow cells; however, there are some nice examples on copper nanoparticles and thin films (3–21 nm thick) [80]. First it was shown that nanoparticulate Cu (n-Cu) behaves differently than Cu foils (Fig. 5A). In addition, from the film thickness dependent methanation Faradaic

**Table 1**  
Materials properties of champion continuous-flow CO<sub>2</sub> electrolyzers.

Catalyst	Catalyst size	Electrocatalyst loading	Electrode support	Electrode thickness	Current density (mA cm <sup>-2</sup> )	Main Products (FE)	Ref.
Ag	<100 nm	0.75 mg cm <sup>-2</sup>	Sigracet 35 BC	325 μm	100	CO (80–95)	[58]
Ag	–	–	GDE (Silflon, Gaskatel)	n/a	100	CO (30–90)	[59]
Ag	<100 nm	2 mg cm <sup>-2</sup>	Sigracet 35 BC	325 μm	340	CO (95+)	[39]
Ag	<100 nm	0.2 mg cm <sup>-2</sup> (+0.8 mg cm <sup>-2</sup> MWCNT)	Sigracet 35 BC	325 μm	350	CO (95)	[38]
Ag-complex	–	1 mg cm <sup>-2</sup>	Sigracet 35 BC	325 μm	95	CO (90)	[36]
Ag	–	n/a	GDE (Silflon, Gaskatel)	n/a	275	CO (80)	[60]
Ag	10 nm on TiO <sub>2</sub> nanoparticles	1 mg cm <sup>-2</sup>	Sigracet 35BC	325 μm	100	CO (90)	[61]
Au	Foil	–	–	–	2.8	CO (92)	[62]
Au	av. 60 nm	–	Porous membrane	–	3–30	CO (38)	[63]
Cu	2–4 μm, 8–15 μm	2 mg cm <sup>-2</sup> , 10 mg cm <sup>-2</sup>	Nafion-117	180 μm	15	C <sub>2</sub> H <sub>4</sub> (12–13)	[64]
Cu	Plate	–	–	1 mm	20	CH <sub>4</sub> (40)	[19]
Cu	n/a	n/a	Toray TGP-H-120	370 μm	11	CH <sub>4</sub> (5)	[52]
Cu	10–50 nm	1 mg cm <sup>-2</sup>	Sigracet 35 BC	325 μm	150	CO (57)	[33]
CuO/Cu	20–40 nm	1 mg cm <sup>-2</sup>	Sigracet 35 BC	325 μm	11	CO (~20), formate (~20)	[65]
Cu <sub>2</sub> O/Cu	n/a	2 mg cm <sup>-2</sup>	Toray TGP-H-120	370 μm	5.4	CH <sub>4</sub> (32)	[66]
Cu <sub>2</sub> O or Cu <sub>2</sub> O/ZnO	Cu <sub>2</sub> O < 5 μm, ZnO < 45 μm	1 mg cm <sup>-2</sup>	Toray TGP-H-60	190 μm	10	MeOH (42)	[67]
CuO/Cu <sub>2</sub> O	Nanorod arrays	–	Cu foil	n/a	20	EtOH (~50)	[68]
Sn	2.39 mm shot and 0.252 mm granules	n/a	Sn sheet	n/a	310	Formate (63–91)	[54]
Sn	0.3 mm (granules)	n/a	Sn sheet	3 mm	300	Formate (60–90)	[55]
Sn	Nanopowder	2–5 mg cm <sup>-2</sup>	E-TEK “S”-type GDE	n/a	100	Formate (89)	[35]
Sn	Sn-loaded brass mesh	1.5 mg cm <sup>-2</sup>	GDL: conductive carbon black+PTFE (3:7)	ca. 0.2 mm	17.6	Formate (79)	[69]
Sn/Cu	–	–	30 # or 60 # copper mesh	610 (30 #) and 380 (60 #) μm	130	Formate (86)	[70]
Sn/Cu	Nanoparticles	–	30 # copper mesh	600 μm	100	Formate (13–86)	[71]
SnO <sub>2</sub>	Nanoparticles	0.87 mg cm <sup>-2</sup>	GDE (acetylene black:PTFE 65:35)	n/a	30 (3 V) 120 (6 V)	Formate (74–84)	[72]
Pb	2–5 μm	0.5 mg cm <sup>-2</sup>	Toray 170	n/a	46	Formate (65)	[73]
Pb	–	5 mg cm <sup>-2</sup>	Polytetrafluoroethylene - carbon paper	n/a	143–345	Formate (95)	[37,74]
Fe, Cu, Co, Pt, Fe-Co, Fe-Cu, Fe-Co-Cu	Nanoparticles	0.5 mg cm <sup>-2</sup>	CNT/Sigracet 24 BC	235 μm	20	–	[75]
In	–	–	Cu mesh	n/a	–	Formate (67)	[76]
Pt	3–5 nm	0.4–0.6 mg cm <sup>-2</sup>	E-TEK carbon cloth	n/a	20	>C5	[77]

efficiency and gravimetric methanation current experiments, it was demonstrated that thin evaporated films behaved like the n-Cu/C electrodes while thick evaporated films behaved like copper foils (Fig. 5B). In this study, it was also suggested that n-Cu was ideal for preparing GDLs with lowered polarization losses, thus maximizing the energy efficiency of the electrolyzer [80].

In another study, Cu electrodes with different morphologies were prepared [81]. The first important observation was that higher active surface area resulted in an improved total FE compared to the smooth Cu plate. As for the product selectivity: (i) electroplated Cu

(on Cu foil) favored the production of formate; (ii) electrofaceting of the Cu foil moved the selectivity towards CH<sub>4</sub> formation; (iii) deposition of Cu onto carbon cloth resulted in the formation of C<sub>2</sub>H<sub>4</sub> [81]. The effect of tin loading and particle size were studied in a filter-press cell for CO<sub>2</sub> reduction [82]. Tin particles of different sizes (150 nm, 10 μm, and 150 μm) were studied, and certain size effects were reported with an optimal behavior for the smallest particles. Again, meaningful normalization is a mandatory exercise in such studies, to deconvolute the simple surface area effect from other, chemical underpinnings.

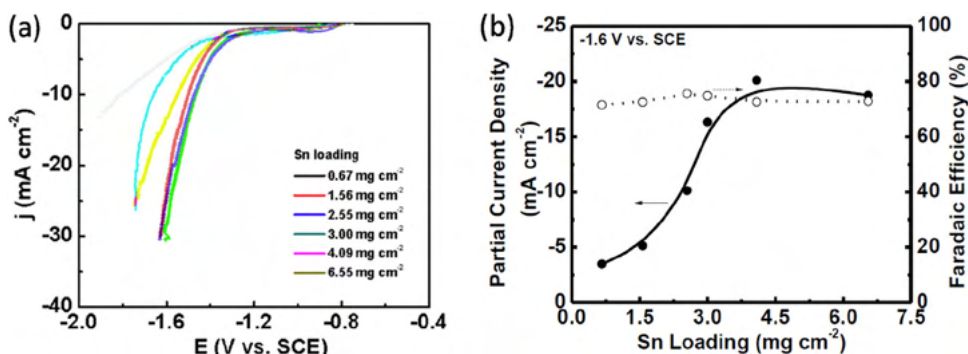


**Fig. 4.** Current density vs. catalyst loading curves for a Sn/C gas diffusion electrode. Adapted with permission from ref. [78].

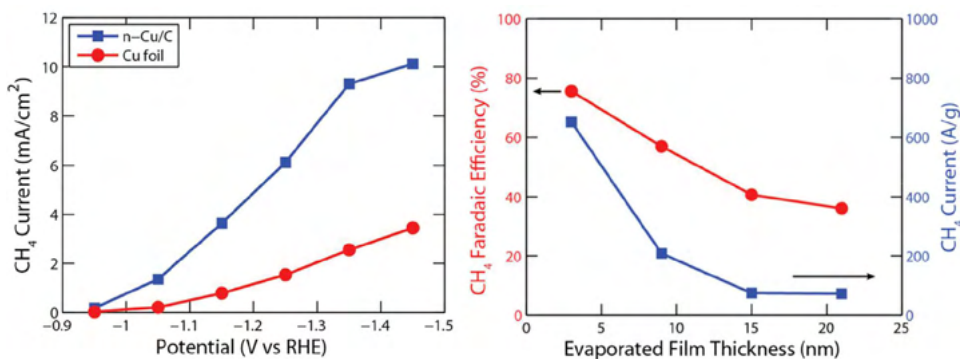


**Fig. 5.** The effect of Cu film thickness on the Faradaic efficiency and specific current density of CH<sub>4</sub> formation in a continuous-flow electrolyzer. Reproduced with permission from ref. [80].

### 3.3. Role of the catalyst support

To achieve current densities of practical relevance, it is vital to increase the electroactive surface area of the electrocatalyst. Moreover, in the case of flow electrolyzers, one must also consider that the electrolyte flow continuously removes the products (or intermediates) from the electrode surface, leading to relatively short residence time. This severely influences both the Faradaic efficiency and product distribution. Therefore, the CO<sub>2</sub> containing electrolyte must be forced to travel through a long path, while it remains in contact with the electrocatalyst for a sufficiently long time period. This can be achieved by immobilizing the catalyst on a GDL, which is a porous substrate with large surface area. The GDL has a dual function in the cell by allowing transport of materials between the catalyst and the flow channel while also maintaining proper electronic communication between the current collector and the electrocatalyst. The most frequently (almost exclusively) applied GDLs are porous carbon supports, formed from carbon fibers or pressed carbon particles. These carbon cloths and carbon papers are

frequently used supports in fuel cells and water electrolyzers on the cathode side. Interestingly, although several attempts were made to employ different metal foils or meshes as catalyst supports in CO<sub>2</sub> flow electrolysis cells, the use of different carbonaceous substrates is reported in almost all the recent studies. As a specific example, we mention the comparison of two continuous-flow electrolyzers, where an In metal foil electrode was compared with In nanoparticles (100–300 nm) immobilized on a carbon GDL. Seven-fold higher partial current densities towards HCOOH formation were detected in the latter case, compared to the simple indium foil [83].

Fig. 6 summarizes the typical components of a GDE, which includes the GDL, the microporous layer, and the catalyst (possibly together with an ionomer) [78]. The importance of the tri-phasic solid/liquid/gas interface is also highlighted. The effect of GDE structure (e.g., thickness, porosity, and density) on the electrocatalytic properties was extensively studied in fuel cells and water electrolyzers; much less attention has been dedicated to these parameters in the case of flow CO<sub>2</sub> electrolyzers so far. As an exception, optimization of the gas diffusion electrodes consisting of a carbon fiber

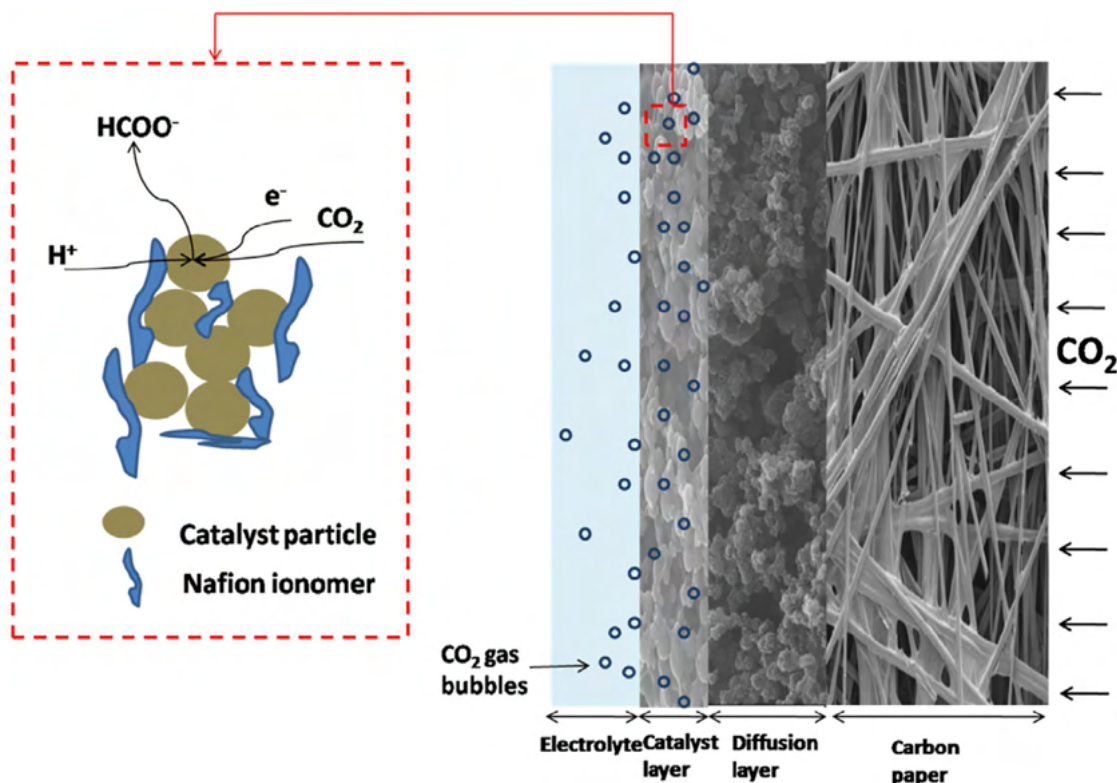


**Fig. 6.** Schematic composition of a gas diffusion electrode (GDE) and the three-phase interface. Reproduced with permission from ref. [78].

substrate, a microporous layer, and a catalyst layer was performed very recently [84]. The optimized electrode exhibited a higher partial current density for CO production than Sigracet 35BC, a commercially available GDE. Overall, we are convinced that there is a significant opportunity for the rational design of GDEs for further improvement of such devices.

Another very important aspect in the case of flow electrolyzers working with liquid electrolytes is the hydrophobic/hydrophilic properties of the GDL. In the case of fuel cells, an important role of the hydrophobic GDL is the removal of excess water. The case is however different for flow CO<sub>2</sub> electrolyzers: the solution must be kept in contact with the catalyst surface for a sufficiently long time. Proper wetting of the top of the carbon support therefore is a prerequisite, but too much hydrophilicity should also be avoided, because H<sub>2</sub> evolution would be favored in that case. Different ionomers are employed to circumvent the above contradiction, which in turn also contributes to the fixation of the catalyst on the surface of the gas diffusion electrodes (Fig. 6). We also note that controlling the interfacial chemistry between the components of the electrode assembly is of prime importance to ensure high performance and stability at the same time.

### 3.4. Catalyst immobilization

The technique employed for the catalyst immobilization has a decisive influence on the performance of flow electrolysis setups. The most often used techniques include two steps: first the

electrocatalyst is prepared and subsequently, it is transferred to the GDL (or other substrate) or more frequently to the membrane to form the so-called membrane electrode assembly (MEA), via a physical method. We note here that no “standard” catalyst immobilization method exists, but paint- and air-brush techniques are the most common ones. As demonstrated in a recent study, the immobilization technique influences both the measured current values and the product distribution (Fig. 7) [58]. In addition, according to our own experience, the catalyst deposition method affects the stability of the cell as well: channel formation and degradation can be observed if the catalyst is not evenly dispersed, rooted in the uneven distribution of the current flow (see also Fig. 7 for catalyst distribution details).

In situ deposition methods, in which the catalyst is directly formed on the substrate, constitute the other large, but less frequently applied class of immobilization techniques. Electrochemical deposition of different catalysts, exploiting the conductive nature of the carbonaceous GDLs is a particularly promising avenue to form such architectures. The catalyst/GDL structure is thus formed in a single step, and intimate electrical and physical contact between the electrocatalyst and the carbon substrate is ensured. Further, after careful pretreatment of the GDL layer (to tune its hydrophobic/hydrophilic character) not only the top of the GDL is decorated with catalyst (nano)particles, but the inner regions as well. This can lead to increased current values because of the enlarged electrochemically active surface area. A recent study presented the electrodeposition of Sn on carbon fibers thus forming a GDE as a promising

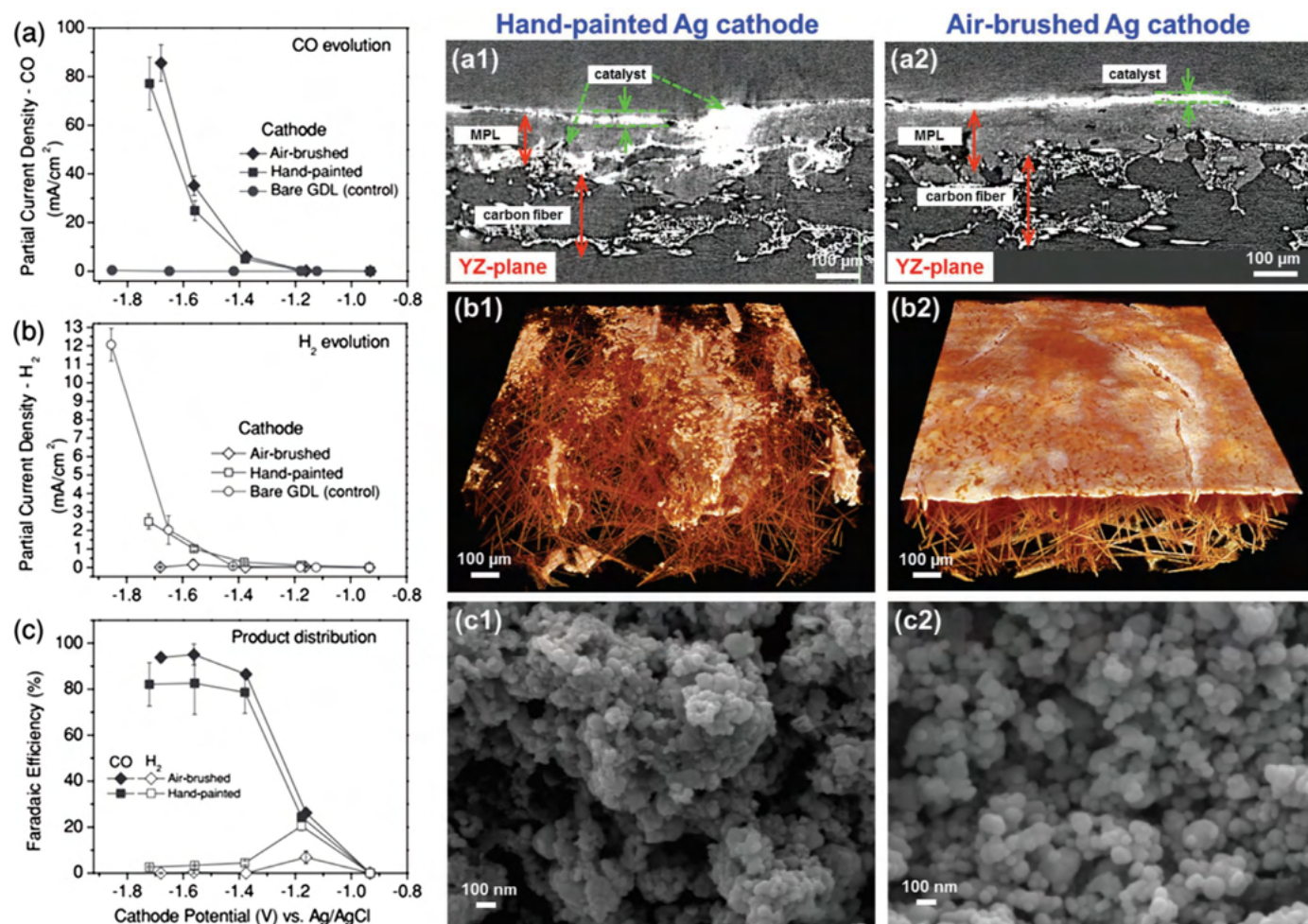


Fig. 7. The effect of the immobilization method on the Faradaic efficiency and specific current density of CO and H<sub>2</sub> formation in a continuous flow electrolyzer with Ag/C cathode. Reproduced with permission from ref. [58].





properties of the membrane towards  $\text{CO}_2$  electroreduction (or even towards specific product formation) [66,90]. Chemical modification of well-known polymers with new organic mediators may open up a new avenue in the future [91,92]. Finally, in addition to chemical factors, durability and pressure handling are two equally important physical attributes to consider.

Four different membranes (Nafion™, SPEEK, alkali-doped PVA, and Amberlyst/SPEEK) were compared in a continuous-flow cell using Pt/C anode and Cu/C cathode for  $\text{CO}_2$  reduction [52]. Both the measured current density as well as the relative amounts of the products showed a notable variation as a function of the chemical properties of the membrane. This distinction was rationalized predominantly by the vastly different ionic conductivity of the membranes [52]. In another recent study several chemically different membranes were compared, and an ionic-liquid inspired polymer (anion exchanging Sustainion™) was introduced, providing both high efficiency and stability [93]. For those applications where  $\text{H}_2$  formation is to be avoided (e.g., space utilization, see also the Outlook section) the use of anion exchange membranes may help by suppressing proton reduction. This trend was demonstrated when an anion- and cation exchange membranes were compared using a Ag-cathode [94]. Most recently, bipolar membranes have offered enhanced water splitting via steady-state pH gradients and product separation, and these novel materials may be worth exploiting for  $\text{CO}_2$  reduction studies as well [95,96]. Finally, we note that product crossover is an important factor to be considered for these membranes from the early development stage.

### 3.6. The role of the current collectors, bipolar plates, and cell body

The mechanical stability of an electrolyzer is ensured by the cell body, the current collectors (end-plates), and the bipolar plates. As the cell body is a passive element in the setup, the most important requirements to fulfill are chemical inertness and mechanical stability, hence it must not change its shape or dimensions during the electrolysis. This is particularly relevant when the cell operates at high pressure and/or high temperature conditions. The cell body is therefore most frequently made of stainless steel, and its two parts are pressed and held together by several steel screws.

When considering the industrial application of continuous-flow  $\text{CO}_2$  electrolyzers, we must distinguish between the microfluidic and the PEM arrangements (see again Fig. 3). While for the first group the scale-out strategy (and therefore the parallel operation of large surface area setups) seems to be favored, the scale-up strategy seems to be the best way of industrial application of PEM  $\text{CO}_2$  electrolyzers – very similarly to PEM water electrolyzer and PEM fuel-cells. In this case, several electrocatalyst layers and membranes (MEAs) are coupled in series, separated by bipolar plates, functioning

as anode on one side and cathode on the other side (see a typical PEM fuel cell setup in Fig. 9 as an example). The function of these bipolar plates and end-plates is complex: (i) they form the electrodes which are in contact with the catalyst layers, (ii) as the reactants are fed to the catalyst layer through the channels formed in these plates, they are responsible for the reactants supply to the cell active area, and for the proper outlet of the products. Furthermore, they play a significant role in the water and heat management of the cell (most importantly in the case of PEM setups, fed with humidified gases) [98]. To serve this purpose, flow-channels are formed on these plates to increase the surface area, and to help the transport processes [97]. As it was shown for PEM fuel-cells, the different flow-field designs (e.g., straight flow channels, single- or multiple serpentine channels, etc.) have both pros and cons, and therefore this pattern must be always optimized towards the targeted application in the employed setup. The use of current collectors with flow-patterns in continuous-flow  $\text{CO}_2$  electrolyzers needs extensive investigations and use of different flow-patterns might contribute to the scale-up and industrialization of this process.

## 4. Operation

All factors governing the performance on a sub-reactor level were summarized in the previous sections. Now we turn the focus to the operation of the *complete* electrochemical cell, and review parameters that affect the EC  $\text{CO}_2$  reduction reaction in the continuous-flow mode. Note that the effects of the discussed parameters are not independent of each other. In fact, their influences are rather complex and convoluted; therefore it is often difficult to carry out studies where only one parameter is varied. Table 2 lists selected examples of continuous-flow  $\text{CO}_2$  electroreduction studies from the literature, where the effect of the most important factors is highlighted.

### 4.1. Feedstock

The first question related to the input flow turns back to the reactor design (see also Fig. 3). It seems that in most studies there is a parallel feed of liquid electrolyte and  $\text{CO}_2$  gas; however, there are reports with liquid or gas feed only. Here the reader must be very careful, because certain articles claim solution+gas flow, although when examined closely, only liquid flow (which was previously saturated with  $\text{CO}_2$ ) was deployed. It is also worth noting that all those studies where notably high currents were reported employed *both* gas and solution feed. While the gas feed was almost always pure  $\text{CO}_2$  (see discussion later on pressure effects and an exception where Ar/ $\text{CO}_2$  mixtures were studied [85]), the composition of the liquid electrolyte varied massively throughout the studies (Table 2). This

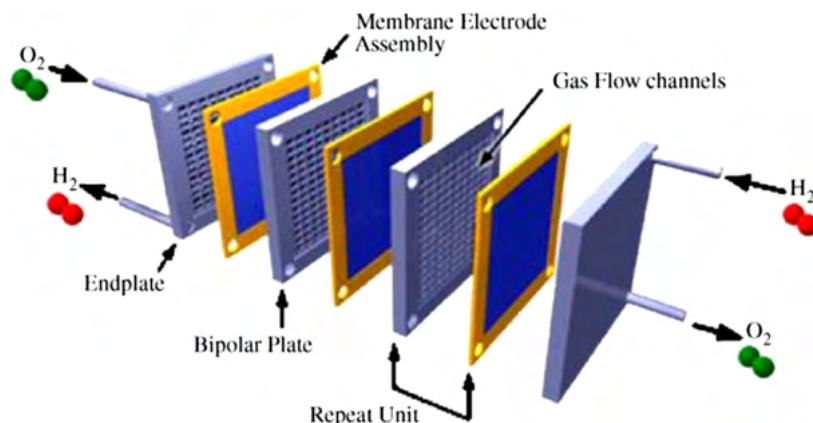


Fig. 9. Stack components of typical fuel cell. Reproduced with permission from ref. [97].

**Table 2**The role of operational conditions in the continuous-flow electroreduction of CO<sub>2</sub>. The sorting factor was the achieved current density.

Setup	Electroactive material	Electrolyte type	Electrolyte composition	Temperature	Pressure	Current density (mA cm <sup>-2</sup> )	Main Products (FE)	Time	Ref.
Microfluidic	Ag	Solution + CO <sub>2</sub> gas	KCl, KOH, KHCO <sub>3</sub> , EMIM Cl, Choline Cl	RT	Ambient	440	CO (95+)	n/a	[39]
Microfluidic	Ag	Solution + CO <sub>2</sub> gas	1 M KOH	RT	Ambient	350	CO (95)	7 min	[38]
Microfluidic	Pb	Solution + CO <sub>2</sub> gas	0.5 M K <sub>2</sub> SO <sub>4</sub> (0.5 M H <sub>2</sub> SO <sub>4</sub> )	RT	Ambient	345	Formate (95)	500 min	[37]
PEM	Sn	Solution + CO <sub>2</sub> gas	0.5 M KHCO <sub>3</sub> + 2 M KCl	314 K	600 kPa	310	Formate (61)	100 min	[54]
PEM	Sn	Solution + CO <sub>2</sub> gas	0.5 M KHCO <sub>3</sub> + 2 M KCl	RT	Ambient	300	Formate (70)	4 h	[55]
Microfluidic	Ag	Solution	1 M KOH	RT	Ambient	280	CO (90)	4 h	[84]
PEM	Ag	Solution + CO <sub>2</sub> gas	0.5 M K <sub>2</sub> SO <sub>4</sub> or 0.5 M K <sub>2</sub> SO <sub>4</sub> :1.0 M KHCO <sub>3</sub>	333 K, 363 K	24.6 atm	350/275	CO (80)	70 min	[60]
Microfluidic	Ag	Solution + CO <sub>2</sub> gas	1 M KOH	RT	Ambient	250	CO (90)	n/a	[101]
PEM	Sn	Solution	0.1 M KHCO <sub>3</sub>	RT	Ambient	250	Formate (80–90)	5 h	[102]
PEM	Ag	Solution + CO <sub>2</sub> gas	0.5 M K <sub>2</sub> SO <sub>4</sub>	333 K	20 atm	225	CO (90)	90 min	[103]
PEM	La <sub>1.8</sub> Sr <sub>0.2</sub> CuO <sub>4</sub>	Solution + CO <sub>2</sub> gas	0.5 M KOH	–	Ambient	180	EtOH (30)	3.5 h	[104]
PEM	Cu	Solution + CO <sub>2</sub> gas	1 M KOH	RT	Ambient	150	CO (57)	4 h	[33]
Microfluidic	Pb	Solution + CO <sub>2</sub> gas	0.5 M K <sub>2</sub> SO <sub>4</sub> (0.5 M H <sub>2</sub> SO <sub>4</sub> )	RT	Ambient	143	Formate (95)	n/a	[74]
PEM	Sn	Solution + CO <sub>2</sub> gas	0.5 M KHCO <sub>3</sub> + 0.5 M KCl	RT	120 kPa	130	Formate (86)	10 min	[54]
PEM	Ag	CO <sub>2</sub> gas	–	RT	Ambient	100	CO	250 h	[53]
Microfluidic	Ag	Solution + CO <sub>2</sub> gas	1 M KCl	RT	Ambient	100	CO (80–95)	n/a	[58]
Microfluidic	Sn	Solution + CO <sub>2</sub> gas	0.5 M KHCO <sub>3</sub>	RT	Ambient	100	Formate (89)	n/a	[35]
PEM	Ag	Solution + CO <sub>2</sub> gas	0.8 M K <sub>2</sub> SO <sub>4</sub>	343 K	Ambient	100	CO (30–90)	4 h	[59]
PEM	Sn/Cu	Solution + CO <sub>2</sub> gas	0.45 M KHCO <sub>3</sub>	RT	115 kPa	100	Formate (13–86)	3 h	[71]
Microfluidic	Ag	Solution + CO <sub>2</sub> gas	1 M KOH	RT	Ambient	100	CO (90)	n/a	[61]
PEM	Sn	CO <sub>2</sub> sat. Solution	CO <sub>2</sub> sat. 0.5 M NaOH + 1 M NaClO <sub>4</sub>	RT	Ambient	97	Formate (58)	10 min	[105]
Microfluidic	Ag	Solution + CO <sub>2</sub> gas	1 M KOH	RT	Ambient	95	CO (90)	n/a	[36]
PEM	Sn	Solution + CO <sub>2</sub> gas	0.45 M KHCO <sub>3</sub> + 0.5 M KCl	RT	Ambient	90	Formate (70)	90 min	[82]
Microfluidic	pyrolyzed CN/CNT	Solution + CO <sub>2</sub> gas	1 M KCl	RT	Ambient	90	CO (98)	n/a	[106]
PEM	Ag	Solution	1 M Li <sup>+</sup> /Na <sup>+</sup> /K <sup>+</sup> /Cs <sup>+</sup> /Cl <sup>-</sup> /Br <sup>-</sup> /I <sup>-</sup> /OH <sup>-</sup>	RT	Ambient	80	CO (60–95)	n/a	[100]
PEM	Ag	Solution + CO <sub>2</sub> gas	0.5 M KHCO <sub>3</sub>	RT	Ambient	80	CO (30–80)	285 min	[107]

variation is quite surprising, considering the prominent role the electrolyte may play in the electrochemical process [39].

The role of the electrolyte, by varying both concentration and chemical makeup, was investigated using a Ag-based gas diffusion electrode as cathode [39]. It was found that anions play a significant role in the process, as reflected in the onset potential for CO formation shifting in the order OH<sup>-</sup> < HCO<sub>3</sub><sup>-</sup> < Cl<sup>-</sup> (Fig. 10A and B). This trend was explained by the interplay of several factors such as pH, conductivity, and, more importantly, specific adsorption of certain anions on the electrode surface. Similar conclusions were drawn for a Sn-based electrolyzer, where OH<sup>-</sup>, HCO<sub>3</sub><sup>-</sup>, Cl<sup>-</sup>, and HSO<sub>4</sub><sup>-</sup> anions were studied [99]. The effect of electrolyte anions and cations was further elucidated, by investigating four cations (Na<sup>+</sup>, K<sup>+</sup>, Rb<sup>+</sup>, Cs<sup>+</sup>) and four anions (i.e., Cl<sup>-</sup>, Br<sup>-</sup>, I<sup>-</sup>, OH<sup>-</sup>) [100]. A major size dependence was observed for the cations, namely an increased CO<sub>2</sub> reduction (and decreased H<sub>2</sub> evolution) activity was detected when larger cations were present in the solution. This trend was rationalized by the better hydration of smaller cations which thus are less likely to adsorb on an electrode surface. The larger cations were thought to adsorb on the cathode repelling H<sup>+</sup> ions from the cathode and stabilizing the “CO<sub>2</sub><sup>-</sup>” intermediate on the electrode surface [100].

As for the effect of electrolyte concentration, a monotonic increase in the current density (as well as the energy efficiency) with increasing electrolyte concentration was noted (Fig. 10C and D). Electrochemical impedance spectroscopy (EIS) showed that both the charge transfer resistance (R<sub>ct</sub>) and the cell resistance (R<sub>cell</sub>) decreased with increasing KOH concentration [39]. The effect of catholyte concentration (varied in the range: from 0.1 mol dm<sup>-3</sup> to 2.0 mol dm<sup>-3</sup>) on product (formate) selectivity was also studied using a tinned copper mesh electrode [54]. An optimal intermediate KHCO<sub>3</sub> concentration (0.45 mol dm<sup>-3</sup>) was found, and rationalized in terms of the competing effects of surface speciation, ionic conductivity, and CO<sub>2</sub> solubility. We note here that CO<sub>2</sub>-saturated

KOH and KHCO<sub>3</sub> solutions are very similar in nature, only the species distribution and the pH being different. As seen in Table 2, there are examples for the addition of an inert electrolyte (e.g., KCl or NaClO<sub>4</sub>) to such solutions, further improving the electrical (ionic) conductivity without severely affecting the other parameters mentioned above [54,55,82,100]. As a general conclusion, we can state that higher electrolyte concentration leads to higher current densities, unless there is a specific adsorptive interaction with the electrode surface.

Ionic liquids are an emerging class of solvents in CO<sub>2</sub> electroreduction [108]. These materials are special in many aspects, for example they can even stabilize the formed reaction intermediates in CO<sub>2</sub> reduction. Synthetic chemistry allows considerable latitude for tailoring the molecular structure of these liquids, and thereby enhance CO<sub>2</sub> solubility via specific chemical interactions [53,108,109]. The chemistry learned for ionic liquids might be exploited as either surface modifiers or ionomers in membrane electrode assemblies (MEAs) discussed below.

The effect of solution pH is also rather complex and the conclusions cannot be generalized for different electrocatalysts and targeted reduction products. In general, at lower pH values, the formation of H<sub>2</sub> is more favored. However, to form hydrogenated CO<sub>2</sub> reduction products (e.g., formate and methanol), a lower pH is beneficial, while higher pH is suitable for CO formation. The pH effect was studied in a microfluidic reactor, employing a Sn cathode and a Pt black anode [35]. Experiments were carried out at three different pH values, and the cell voltage, the electrode potentials, and the efficiencies (energy and Faradaic) were monitored (Fig. 11). The pH is seen to exert a more prominent effect on the cathode process. At lower pH, the formation of formic acid was favored, both in terms of higher current density and selectivity [35]. This study also calls attention to the importance of having two reference electrodes in the cell, enabling the monitoring of both half-cell processes separately.

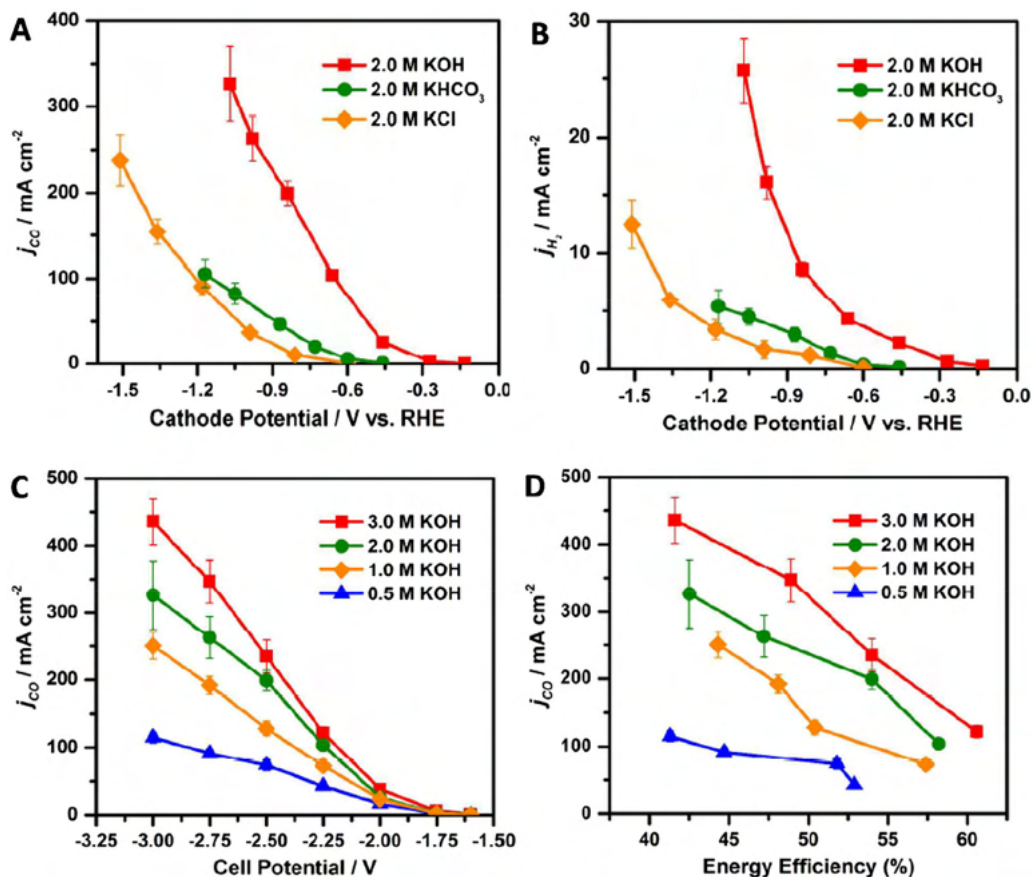


Fig. 10. The effect of electrolyte nature and concentration on the CO<sub>2</sub> reduction current density and energy efficiency in a continuous-flow electrochemical cell. Adapted with permission from ref. [39].

More recently, a dual electrolyte microfluidic reactor was designed, and the effect of using anolyte and catholyte of different pH was systematically studied. A set of electrocatalysts was investigated, and it was concluded that catholyte pH=2 and anolyte pH=14 resulted in an optimal cell performance. Furthermore, a three-fold increase was witnessed in the overall performance, compared to the single neutral (pH=7) electrolyte arrangement [37].

#### 4.2. Liquid/gas flow rate

With the aim of converting large amounts of CO<sub>2</sub>, the question occurs instantly: how does the flow rate of the liquid/gas input influence the current density and the Faradaic efficiency (and thus the overall CO<sub>2</sub> conversion process)? Considering the importance

of this parameter, it is very surprising that there is no precise definition to meaningfully present the CO<sub>2</sub> flux in the electrolyzer. In almost all the cases, the unit of standard cubic centimeters per minute (sccm) was employed to characterize the gas flow, which equals cm<sup>3</sup>/min at standard temperature and pressure. While this unit sufficiently describes the overall gas flow, it gives only very limited information on the actual flux of CO<sub>2</sub> reaching the electrocatalyst surface in the electrolyzer. Consequently, it is very difficult to compare studies performed in different laboratories on electrolyzers of different size. It seems to be a useful exercise to normalize the flow rate with the *electrochemically-active* surface area of the electrode, and/or to the free volume of the cathode compartment of the electrolyzer, thus obtaining the actual flux of CO<sub>2</sub> (see below). In addition, the fact that more often than not,

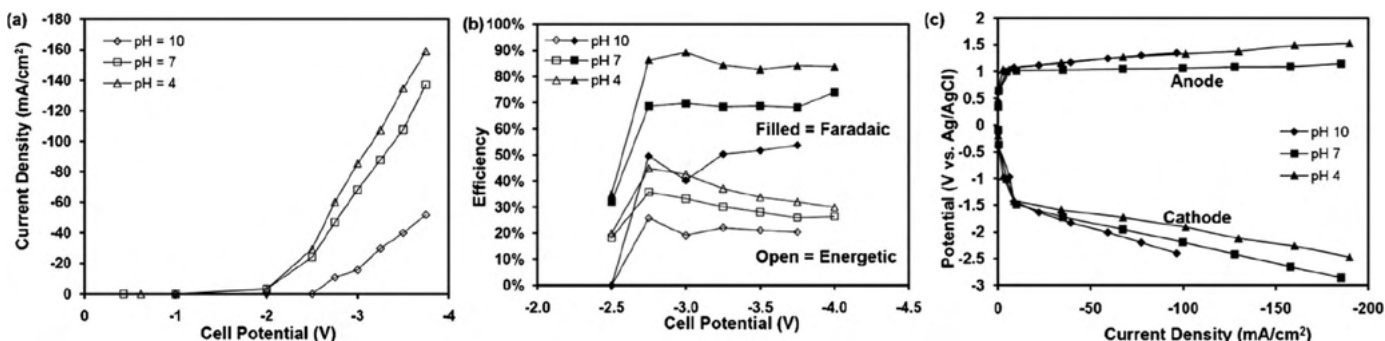
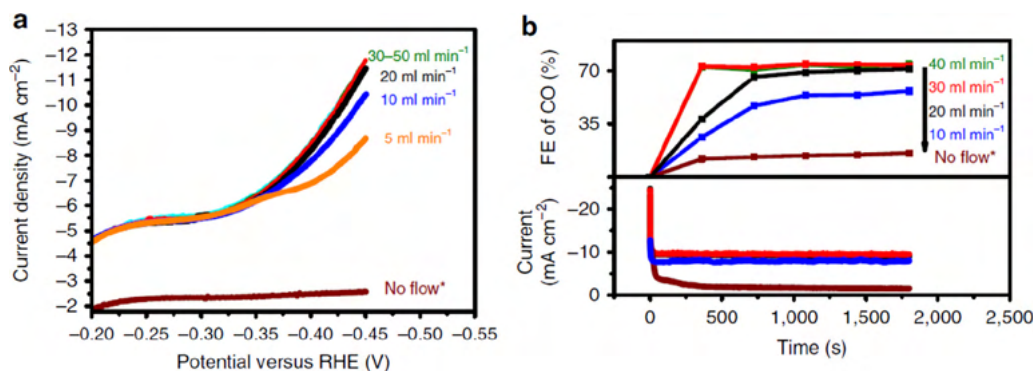


Fig. 11. The effect of pH on the performance of a microfluidic continuous-flow electrolyzer, employing Sn cathode and Pt anode. Adapted with permission from ref. [35].



**Fig. 12.** Effect of CO<sub>2</sub> flow rate on the performance of a batch electrolyzer, but under continuous CO<sub>2</sub> purge. The applied potential was  $E = -0.4$  versus RHE in (b). Reproduced with permission from ref. [31].

pure CO<sub>2</sub> (or solutions with different CO<sub>2</sub> concentrations) is fed to the cathode, implies that the flow rate should be also normalized with respect to the CO<sub>2</sub> content. This exercise was nicely performed in a recent study on Sn-GDE electrodes, where the Ar/CO<sub>2</sub> ratio was systematically varied, while the flow rate was kept constant [85].

In a very recent study, copper hollow fiber electrodes were employed as both the gas diffusion layer and cathode electrocatalyst; and the effect of CO<sub>2</sub> flow rate on the cell performance was studied [31]. As presented in Fig. 12, there is a considerable effect on both the overall current density and the FE for CO generation. The enhancement in FE towards CO as a function of CO<sub>2</sub> flow rate is consistent with a concurrent increase in current density, suggesting that the FE of CO strongly depends on the efficiency of mass transfer of CO<sub>2</sub> to the electrode surface. After reaching a certain flow rate, the achieved steady behavior suggests that most active catalyst sites are involved in the reaction and the kinetically controlled regime was reached [31]. The importance of CO<sub>2</sub> transport in nanostructured electrodes was also demonstrated for electrodeposited Cu nanofoams, where a thickness-dependent selectivity was observed for the formation of formic acid and CO (vis-a-vis hydrogen evolution) [110].

A similar trend was reported for a dual microfluidic reactor, where after reaching a certain threshold, further increase of the flow rate had no effect on cell performance [37]. Over this flow rate, mass transfer rate of CO<sub>2</sub> through the GDE becomes the bottleneck. A higher porosity and smaller thickness of the GDL may help to improve the performance, however, its coherent structure has to be maintained to sustain its mechanical stability and its electronic communication with the current collector.

Besides the achievable current density, product distribution can also be tailored by the flow rate. For example, the effect of flow rate on the H<sub>2</sub>/CO ratio was studied in a hybrid PEM/microfluidic reactor, having a Ag cathode and Ru anode [59]. It was demonstrated that by controlling the current density and the CO<sub>2</sub> flow, it was possible to tailor the H<sub>2</sub>:CO product ratio between 1:4 and 9:1. Not surprisingly, by limiting the amount of CO<sub>2</sub> reaching the electrode surface, an increase in the H<sub>2</sub>:CO ratio was seen. At the same time, this increase in the ratio was not accompanied by any change in the cell voltage or cathode potential [59]. Importantly, after a short induction period, the product ratio was maintained for a relatively long time (5 h). These data suggest that there is considerable scope for tailoring the product ratio, for syngas formation, simply by optimizing the flow rate. Notably, such output can be directly utilized in different chemical processes, for example in the Fischer–Tropsch synthesis.

Finally, we highlight a study where considerable attempt was made to normalize the flow rate, although with the geometrical surface area. Experiments were carried out at three different electrolyte flow (Q) / electrode area (A) ratios and both the amount of the

formed products, as well as their distribution varied [50]. Even more interestingly, a Cu electrocatalyst with two different morphologies (Cu plate and Cu<sub>2</sub>O derived Cu on carbon support) were compared, and different behavior was seen (Fig. 13). This may be rooted, at least partially, in the different electrochemically-active surface area in the two cases, further highlighting the importance of the suggested normalization protocol (see Section 5).

#### 4.3. Temperature and pressure

As seen in Table 2, there are only few examples where the pressure and temperature were varied from ambient values. The number of systematic studies is even smaller [59,60,103,111], but it seems that higher operating temperatures correlate with higher currents (Fig. 14). This effect however is also complex, because higher temperature leads to lower CO<sub>2</sub> solubility (causing also a change in the pH), but higher diffusion coefficient and reactivity [29]. In these studies the temperature had little effect on the selectivity [103], but this is likely to vary a lot depending on the electrocatalyst. Over a certain temperature, current increase is associated with a decrease in FE of CO<sub>2</sub> conversion, and thus increased H<sub>2</sub> evolution [60]. Our own, currently ongoing work suggests that lower temperatures (e.g., 3 °C) promote ethylene formation over methane for copper-based cathodes in a GDL-configuration. Considering the complex effects of temperature, many more studies are needed in this direction with in situ monitoring of the temperature in the electrolyzer, which is not trivial.

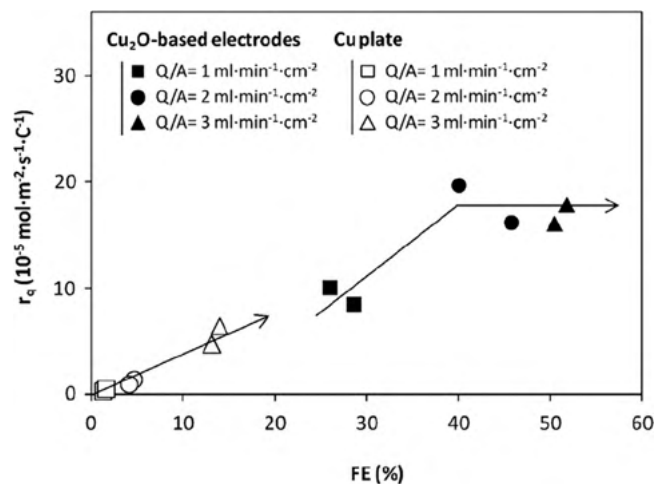


**Fig. 13.** Comparison of the product formation rate and FE for two different electrodes at three different surface area normalized flow rates. Reproduced with permission from ref. [50].

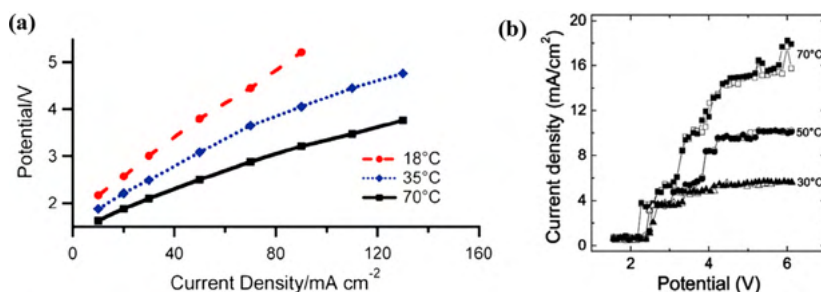


Fig. 14. The effect of temperature on the operation of two CO<sub>2</sub> electrolyzers with Ag (a) and Cu felt (b) cathode. Reproduced with permission from refs. [59,111].

The effect of pressure is even less studied although increased pressure: (i) increases the solubility of CO<sub>2</sub> according to Henry's law; (ii) enables work at higher temperatures; (iii) makes it easier to store, or to react the products (e.g., syngas) further to value-added products. The pressure was gradually increased in a combined PEM + microfluidic reactor setup (see Fig. 3A) from atmospheric to 20 atm. A five-fold increase in FE towards CO evolution was seen both at room temperature and at 60 °C (Fig. 15) [60].

#### 4.4. Effect of the applied potential/voltage

The potential/current dependent product distribution has been extensively studied in batch reactors. Much less is known about continuous-flow setups, but a comprehensive study using a PEM electrolyzer (Cu cathode, Pt anode) was able to detect as many as 16 reaction products (Fig. 16). At low overpotentials, only hydrogen, CO, and formate were observed, with the dominance of hydrogen formation at very low overpotentials. As the overpotential increased, cumulative FE of CO<sub>2</sub> reduction products increased versus H<sub>2</sub> formation. First hydrocarbons (methane and ethane) were formed, while at even higher voltages, C<sub>2</sub>–C<sub>3</sub> products were produced [19].

The effect of the applied potential is less complex in those cases where only one product (e.g., formate, CO) is formed [38,112,113]. Note however that H<sub>2</sub> evolution is a competing reaction even in these instances. As the external driving force (potential/voltage) is increased, this latter becomes more and more prominent, leading to a volcano-type plot for the Faradaic efficiency of the product with the applied potential. One hand, this is disadvantageous, since the production rate of the intended product cannot be increased while maintaining a high energy-efficiency. On the other hand, this gives the opportunity to form specific product mixtures. For example, using a silver containing GDE cathode, the H<sub>2</sub>/CO ratio was tuned to form readily processable syngas simply by varying the applied current density (and hence the potential) [59].

#### 4.5. Timescale of the experiments

As seen in Table 2, the timeframe of the electrolysis experiments span a few minutes to a few hours. Interestingly, in many cases, no

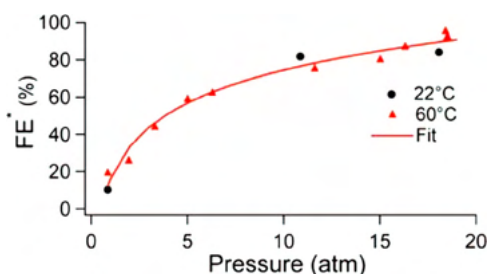


Fig. 15. The effect of pressure on the FE value for a combined PEM + microfluidic CO<sub>2</sub> electrolyzer with a Ag GDE cathode. Reproduced with permission from ref. [60].

stationary electrolysis was performed, and the current values were gathered from linear sweep voltammetry (LSV) experiments. There are only a few studies where the product distribution was reported as a function of time. This information would be crucially important in assessing the stability of the electrocatalyst and the entire electrolyzer assembly. For example, the H<sub>2</sub>/CO ratio was monitored during a galvanostatic experiment (Fig. 17), using a silver GDE. The monotonic increase in the H<sub>2</sub> evolution ratio (and the decrease of FE<sub>CO</sub>) was rationalized by alteration of the electrode, in particular increased wetting of the GDL [103]. A recent study, employing a solid catholyte and an anion-exchange membrane showed stable selectivity and cell voltage over 250 hours of operation at 100 mA cm<sup>-2</sup> [53].

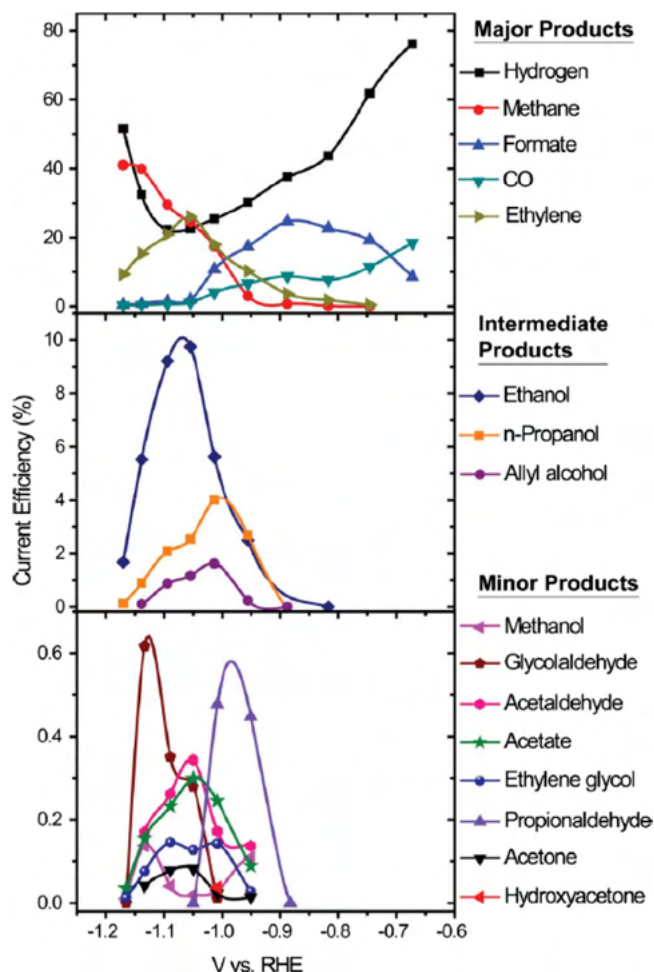


Fig. 16. Effect of applied voltage on the product distribution in a continuous-flow CO<sub>2</sub> electrolyzer with a Cu cathode. Adapted with permission from ref. [19].

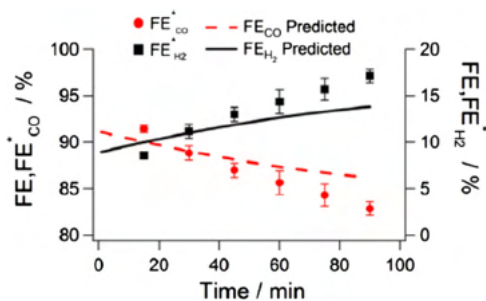


Fig. 17. Alteration of the product selectivity with time in a pressurized PEM electrolyzer with a silver cathode. Reproduced with permission from ref. [103].

## 5. How to benchmark a CO<sub>2</sub> electrolyzer correctly?

As data-mining turns into a major component of every research project, it is now more important than ever to report experimental data (and the drawn conclusions) in a manner where comparisons from laboratory to laboratory can be easily made. According to lessons learned from allied R&D fields (most importantly fuel cells and electrochemical water electrolysis), setting up a proper benchmarking protocol leads to a more coherent knowledge of these systems, and consequently to an accelerated development of these fields

Table 3

Proposed benchmarking protocol for continuous-flow CO<sub>2</sub> electrolyzers.

Characterization method	Requirements	Data to report	
Physical and chemical characterization methods (XRD, XPS, TEM, SEM, EDS, Contact angle, and surface area measurements, etc.)	Multiple scale analysis has to be performed both for the electrocatalyst and the support.	Chemical composition, size distribution, shape, dominant crystal orientation, surface properties	PRE operation
Cyclic voltammetry and linear sweep voltammetry of the individual electrodes. Measurement of Tafel-plots	No Faraday process shall occur during CV, reference electrode is needed. Both separately for the two electrodes, and before operation inside the cell. IR-compensation shall be carried out	Electrochemically active surface area, onset potential value at a given current density.	
Electrochemical impedance spectroscopy	Multiple voltage values shall be used.	$R_{ss}$ , $R_{ct}$ , C	
Linear sweep voltammetry	Multiple scan rates. Several subsequent scans, till the stationary behaviour is reached. Comparison of measurements with and without CO <sub>2</sub> shall be carried out, with solutions of the same pH.	LSV curves, current density normalized to both geometric and electrochemically active surface area. Onset potential value at a given current density.	Operation
Stationary electrolysis (chronoamperometry/chronopotentiometry) coupled with product analysis	Online analysis of both gas and liquid phase products. Measure on multiple current/voltage values (at least 5).	Faradaic efficiencies for ALL products, including H <sub>2</sub> (for all current/voltage values).	
Long term stationary electrolysis (chronoamperometry/chronopotentiometry) coupled with product analysis	Online analysis of both gas and liquid phase products after selected time periods.	Faradaic efficiencies for ALL products, including H <sub>2</sub> (for all current/voltage values) with respect to the elapsed time.	
Electrochemical impedance spectroscopy	Multiple voltage values shall be used.	$R_{ss}$ , $R_{ct}$ , C	POST operation
Cyclic voltammetry and linear sweep voltammetry of the individual electrodes. Measurement of Tafel-plots	The same measurements as before operation both inside and outside the cell	Electrochemically active surface area	
Physical and chemical characterization methods (XRD, XPS, TEM, SEM, EDS, Contact angle, and surface area measurements, etc.)	The same measurements as before operation	Chemical composition, size distribution, shape, dominant crystal orientation, surface properties	

	Data to report
Parameters related to the operation of the electrolyzer	pH, temperature, pressure, electrolyte concentration, surface area/free volume normalized flow rate
Parameters describing the cell setup	Cell configuration and size, properties and dimensions of the individual components (e.g., membrane and GDL thickness), catalyst loading

[114–118]. Such a protocol should include characterization of both the electrochemical cell-forming components separately as well as the complete cell itself, via a set of systematic studies. We suggest the following benchmarking experiments to be carried out and a list of figures-of-merit to report, as a framework for testing a new electrolyzer setup. Table 3 briefly summarizes these items, and each of them is further elaborated in what follows.

Reporting the exact details of the cell is of prime importance. This should cover the dimensions of the cell components, their physical and chemical properties (e.g., membrane and GDL type and thickness, chemical composition, pretreatment method), and the degree of compression. We reiterate our earlier point, that without this information, the flow rate of the electrolyte (or the gas)—which is usually provided in units such as sccm or ml/min—gives only very limited information on the retention time of CO<sub>2</sub> in the cell. The flow rate of the electrolyte therefore should be always normalized by either the free volume of the half-cell or with respect to the electrochemically-active surface area of the electrode (or both).

### 5.1. Pre-operational characterization

The electrocatalyst is the core component of any electrochemical setup, therefore its comprehensive physical and chemical characterization must be the first step of every experimental work. These

studies must involve physical, chemical, and surface characterization via different spectroscopic techniques (FT-IR, Raman Spectroscopy), electron microscopy (TEM, SEM), elemental composition analyses (EDX, XRF), surface composition and functional groups analysis (XPS) and crystal phase determination (XRD). Similar characterization of the supporting layer (GDL) must be also performed, supplemented with the characterization of its pore structure (e.g.,  $N_2$  adsorption/desorption).

Although the catalyst morphology is one of the most important factors after the chemical composition, often little information could be found in the different articles. We recommend multi-level analysis to be performed before and after immobilizing the catalyst on the substrate, revealing crystallite size, crystallinity of the material, degree of aggregation, and surface properties of the particles. The geometric surface area of the immobilized catalyst can be estimated from the recorded microscopic images, but it must be kept in mind that the electrochemically-active surface area can immensely differ from this value. Therefore this latter parameter has to be calculated from EIS measurements, or by simply recording cyclic voltammograms in a potential window where no Faradaic process interferes [119]. For certain electrocatalysts, the use of model redox active compounds can also be useful.

The activity of an electrocatalyst is most usually characterized by recording linear sweep or cyclic voltammograms. As these are non-stationary measurements (even at low polarization rates), the values of derived kinetic parameters from these, must be treated with caution. Recording of polarization curves provides complementary data. In this case, the stationary potential is recorded at different current densities (spanning several orders of magnitude), and then plotted versus the logarithm of the current densities to afford Tafel plots (Fig. 18). The linear region of the curve is fitted to give the Tafel-slope, which – together with the onset potential of the process – is the most important parameter describing the electrocatalyst.

By performing LSV measurements for the single electrodes in a classical three-electrode electrochemical cell and in the assembled electrolyzer under otherwise identical circumstances (electrolyte concentration, pH, temperature etc.), the effect of the cell construction method (hot pressing, mechanical fixation, etc.) on the catalyst properties can be studied directly. EIS measurements are very useful at this early stage of investigating the cell, as they can reveal any additional resistances ( $R_s$ ,  $R_{ct}$ ), arising from failure of the cell assembly and leading to severe losses due to IR-drops in the system. Note, that during electrolysis, as a current ( $I$ ) is driven between the working and the counter electrode, a potential drop ( $IR$ ) develops in the setup; originating from the resistance of the cell constituents, the electrolyte, and the membrane. In a three-electrode electrochemical setup, the potential of the working electrode is measured against a stable reference electrode. Although these electrodes are placed very close to each other, some portion of this potential drop is still present between them, which is caused by the so called

uncompensated resistance ( $R_u$ ). The  $IR_u$ -drop is dictated by the cell geometry and is dependent on the applied current and its presence leads to distortion of the electrochemical measurements [78]. To secure reliable data on the catalyst activity, the measured potentials must be always corrected for the value of this uncompensated potential drop. For this purpose, the uncompensated resistance has to be measured, which is typically done by either EIS or by the current-interruption technique [121,122]. Overall, the discrepancy between actual and applied voltage requires the use of IR compensation to get reproducible data that is comparable between different laboratories for the various cells, especially those operating at high current densities.

## 5.2. In operando characterization

The most important part of these studies is the investigation of the assembled flow cell during operation. To study the kinetics of  $CO_2$  reduction in the given setup, LSV measurements should be carried out at multiple scan rates. Note that measurements at the first sweep rate must be repeated until steady-state electrochemical behavior is reached. Information gathered from the first cycles can often be misleading, because the measured current can originate from multiple sources, including the reduction of the electrode support or the electrocatalyst itself—as it was observed for the case of  $Cu_2O$  derived Cu catalysts [20]. The LSV curves must be always normalized to the geometric surface area and/or to the electrochemically active surface area of the cathode. Comparison of such data to results measured with chemically-equivalent, but different sized catalyst particles can help to understand different size effects beyond the trivial increased surface area/volume ratio. Here we refer to the discussion on the importance of having one or more reference electrodes in the cell (see Fig. 3).

The estimation of the onset potential of a process is always a difficult question. Some researchers derive this value graphically from the LSV curves, while others give the potential value at which the current reaches a certain threshold value. Consequently, the comparison of these data is difficult and often misleading. To avoid confusion, we suggest 1 and 10  $mA\ cm^{-2}$  as a benchmarking current density (note the similarities with solar powered water oxidation and  $H_2$  evolution) [118]. The LSV measurements serve as a decent guide for choosing the proper potential/current region, where  $CO_2$  reduction studies have practical relevance. Subsequently performed stationary measurements, either at constant current or constant potential/voltage give real insights into the performance of a given setup. These time-dependent experiments must be coupled with in situ product analysis, both for the liquid and the gas phases, since these are better tools for determining the onset voltage (potential) than just using LSV curves.

Designing a proper product-detection setup, however is not straightforward, because there is no single analytical method which can characterize both quantitatively and qualitatively all reduction products generated from  $CO_2$ . First, for the analysis of the gas and liquid phase products, we generally need different analysis tools. An online sampling system should be connected to a gas chromatograph (for gas phase analyses) and sealed to avoid any leakage. We highlight a recent development, the barrier ionization discharge (BID) detector, which is universal with greater sensitivity than both the thermal conductivity- (TCD), and flame ionization detectors (FID). Consequently, there is no need for two different detectors to measure  $H_2$  gas and the  $CO_2$  derived products [123].

Analysis of the liquid phase is a little more complicated, because the electrolyte ions must be either removed for the most sensitive GC-MS analysis, or higher sample concentrations are needed for NMR analysis. The performance of the NMR analysis, however, can be improved by special cell design with high surface area working electrode and very low electrolyte volume [124]. Differential

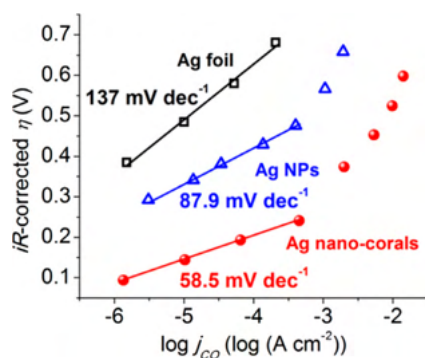


Fig. 18. Tafel plot of different Ag electrocatalysts in a 0.1 M  $KHCO_3$  solution purged with  $CO_2$ . Reproduced with permission from ref. [120].



electrochemical mass spectrometry (DEMS) is an effective tool for the real-time detection of electrochemical reduction products, however, the interpretation of the results can be complicated for a reaction which gives a mixture of different products [125]. For example, DEMS cannot be used for detection of CO, because CO<sub>2</sub> gives the same ionization fragments. The quantitative detection of formic acid, because of its deprotonation, is challenging by GC and DEMS as well. The amount of formate can be reliably quantified by ion chromatography. By this technique, however, other solution compounds (e.g. different alcohols) cannot be analyzed [126]. It is therefore of utmost importance to follow the reaction with different instrumental techniques, and to account for all the charge passed during the electrolysis.

It is recommended to clearly state in every manuscript: (i) detection limit for the employed analytical instrument and (ii) the partial current density for the observed product at the onset voltage. We emphasize that because of the frequent use of carbon-based catalyst supports, studies with <sup>13</sup>C labeled CO<sub>2</sub> should be performed to clarify the origin of the carbon-containing products. Finally, we note that the selected analytical methods have to be compatible with the electrolyzer setup, possibly limiting the application of certain (otherwise promising) techniques.

The Faradaic efficiency (FE) for all the formed compounds as well as the overall FE has to be reported. Note that FE as defined is strictly the ratio of the charge consumed on a given process and the passed total charge. Some authors—without analyzing the liquid or the gas phase products—mistakenly and misleadingly refer to the ratio of the given product amount and the detected total amount of all the products as the Faradaic efficiency. Similarly, H<sub>2</sub> is also a product (although not CO<sub>2</sub>-derived), therefore must be taken into account for these calculations.

The operation of the electrolyzer must be also characterized on a longer timescale. Therefore, the above listed measurements—or at least those which were promising in the sense of current density and product distribution—has to be conducted for several days, while the product distribution is traced after regular time periods. Keep in mind that water electrolyzer cells, working on very similar principles and built from almost identical materials have a reported lifetime in the range of 10,000 h [127], and similarly long lifetimes are required for CO<sub>2</sub> electrolyzers in practical applications.

### 5.3. Post-operational characterization

After the long-term operation, degradation of the electrochemical cell must be investigated at every level, by repeating the same measurements as before operation, in the reversed order. Thus, an EIS measurement of the cell can reveal corrosion of the cell constituents, while change in the onset potential (derived from LSV measurements) can indicate chemical change of the catalyst. After disassembling the cell, the catalysts must be characterized separately with the formerly used experimental techniques, revealing changes in the catalyst particle size, aggregation, composition, and in the structure of the membrane or the GDL, etc. [128].

### 5.4. Most important metrics to report

Talking about the efficiency of the cell, one must distinguish among current-, electrical-, and energy efficiency. The current efficiency (or Faradaic efficiency,  $\epsilon_{\text{Faradaic}}$ ) of the process is a direct relation between the number of electrons consumed in a given electrode process and the total amount of the charge passed during the electrolysis. Energy efficiency of a given cell is somewhat more complex concept, as it is not only influenced by the thermodynamics and kinetics of the electrode processes, but electrical parameters of the cell as well. The measurement conditions and heat exchange efficacy during the process may also be important parameters. These

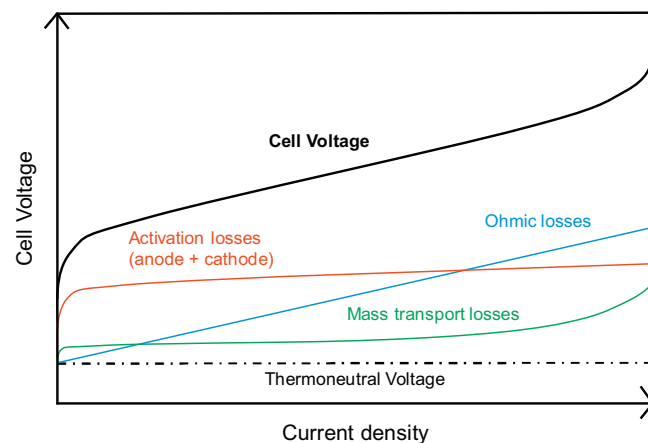


Fig. 19. Different loss-mechanisms potentially affecting the performance of an electrolyzer.

can be defined in different ways, and therefore are a common source of confusion [129].

The most commonly applied, and most straightforward definition is the voltage efficiency of the cell, which gives a good approximation on its operation. This is calculated as the ratio of the thermodynamic voltage needed to drive the given electrochemical process (given by the redox potential of the half-reactions) and the total voltage applied to the electrolysis cell ( $V_{\text{cell}}$ ). Beyond the thermodynamic requirements of the reaction, this latter value is dictated by different energy losses, related to the catalysts (anodic and cathodic overpotential,  $\eta_i$ ), to mass-transport, and to the cell itself (IR-drop). Fig. 19 summarizes the most common mechanisms, which lead to an increased cell voltage. Note that the shape of the curves may also be useful for diagnostic purposes when an electrolyzer fails. In addition, these factors can be separated by the above described benchmarking protocol, thus uncovering future development avenues [130].

The above-mentioned efficiency units alone, however, are of low industrial relevance. To give an exact measure on its operation, the energy efficiency of the cell must be calculated during long-term operation. The energy efficiency is most commonly calculated as the product of the voltage- and Faradaic-efficiencies [15]. This is only true, however, if only one single product is formed. If this is not the case (i.e., multiple products are formed in parallel), the individual redox potentials (e.g.,  $E^{\circ}_{\text{CO}_2/\text{CH}_4}$ ) have to be taken into consideration Eq. (2).

$$V_{\text{cell}} = E^{\circ}_{\text{anode}} - E^{\circ}_{\text{cathode}} + \sum_i \eta_i + IR_{\text{cell}} \quad (1)$$

$$\epsilon_{\text{energy}} = \frac{\sum_i (E^{\circ}_{\text{anode},i} - E^{\circ}_{\text{cathode},i}) \times \epsilon_{\text{Faradaic},i}}{V_{\text{cell}}} \quad (2)$$

The energy efficiency can be also defined as the energy content ( $E_{\text{content}}$ ) of the given product over the electrical energy consumed during electrolysis, where  $t$  is the time of electrolysis to form unity amount of the product. The chemical energy of the produced molecules can be expressed by their Gibbs free energy per mole ( $\Delta G_0$ ). In some articles, the heat of combustion, or enthalpy, has been used to represent the energy content:

$$\epsilon_{\text{energy}} = \frac{E_{\text{content}}}{E_{\text{input}}} = \frac{E_{\text{content}}}{V_{\text{cell}} \times I_{\text{cell}} \times t} \quad (3)$$

## 6. Photoelectrochemical reduction of CO<sub>2</sub> in continuous-flow

As a possible alternative on a longer horizon, we would like to briefly mention a few examples of continuous flow

photoelectrochemical (PEC) cells, demonstrated in CO<sub>2</sub> conversion. Historically, PEC solar fuel generation was predominantly focused on water splitting (H<sub>2</sub> evolution), and much less attention was paid to CO<sub>2</sub> reduction, mainly because of kinetic constraints [131]. In direct PEC CO<sub>2</sub> reduction, upon excitation of an electron from the valence band to the conduction band (by UV or visible light irradiation) of a p-type semiconductor (SC) the separated photoelectrons are driven to the surface of the SC and react with CO<sub>2</sub> (or a redox mediator/co-catalyst present either on the surface or in the solution). The CO<sub>2</sub>-reducing ability of the photo-electrocatalyst is dictated by the position of the conduction band (CB) edge: it has to be at a more negative potential than the targeted CO<sub>2</sub> reduction reaction. In such a procedure, it is possible to reduce CO<sub>2</sub> at less negative potential relative to the thermodynamic potential (vs. electrochemical reduction). The indirect PEC approach is also possible, where an n-type semiconductor photoanode is employed, and CO<sub>2</sub> reduction takes place at the cathode in the dark [132]. By employing either PEC approach, the necessary energy input (cell voltage) can be decreased by the photopotential, which is dictated by the CB edge of the SC photocathode and the redox potential of the CO<sub>2</sub> reduction process (or the VB edge of the photoanode and the water oxidation potential, for the indirect approach).

To enhance the current densities to a level which makes practical significance, however, photoelectrodes with large specific surface area are needed. This necessitates the use of nanostructured photoelectrodes, which is a surprisingly unexplored area, in fact, the long-standing theory of PEC builds on thick electrode films (with film thickness of over several micrometers) [133]. To efficiently drive CO<sub>2</sub> reduction reactions, these carriers need to reach the photoelectrodes interfaces at the electrolyte and at the back contact. Therefore it will be very important to understand the effect of nanostructuring on carrier generation and collection, surface recombination, and on the size of space charge layers [134].

There are only a few examples in the literature, which at least demonstrate the concept of continuous-flow PEC CO<sub>2</sub> conversion. In a recent proof-of-concept study, hybrid CuO/Cu<sub>2</sub>O nanorod arrays were incorporated as the photocathode in a new continuous-flow design [68]. The performance of the photocathode was compared to a conventional two-compartment batch type PEC cell. The primary products were alcohols, with a yield which was ~6 times higher than the batch design, and significantly enough, also showed longer-chain alcohol products up to C2–C3 (ethanol and isopropanol). The high surface area-to-volume ratio resulting from the narrow

reaction channels resulted in an enhance photocurrent density and Faradaic efficiency.

Even more recently, NASA researchers reported a PEC conversion device, operated at room temperature and ambient pressure with only ultraviolet radiation [135]. They used a nanocomposite electrode which combines a photocatalyst and an electrocatalyst, capable of reducing gaseous CO<sub>2</sub> to methane without the need of external electricity input. Considering the typical solar flux, the achievable current densities are typically lower for these cells (~10 mA cm<sup>-2</sup>) compared to the electrolyzers presented earlier. In addition, long term stability is an addition hurdle to face, therefore stability tests are even more important in these instances. In other instances, the indirect approach was employed, where the oxidation half reaction took place on a photoexcited n-type semiconductor (specifically, TiO<sub>2</sub>). As shown in Fig. 20, the overall cell design is very similar to the conventional PEM electrolyzers, except that the anode is irradiated [132,136]. The principal benefit of this setup is that all the knowledge gathered for the cathode reaction (CO<sub>2</sub> conversion) can be implemented, while the solar energy input is harnessed.

In the case of PEC cells, the photon to product conversion efficiency is defined as the output power, namely, the product of voltage, partial current densities, and Faradaic efficiency for the formation of different products, divided by the denominator, namely, the solar energy input from sunlight:

$$\eta_{PEC} = \frac{j_{photo} \times \sum_i (V_{redox,i} - V_{bias}) \times \epsilon_{Faradaic,i}}{P_{light}} \quad (4)$$

where  $j_{photo}$  is the photocurrent density (mA cm<sup>-2</sup>) normalized to the illuminated electrode area,  $V_{redox}$  is the thermodynamic potential of the given process,  $V_{bias}$  is the applied voltage,  $\epsilon_{Faradaic,i}$  are the partial Faradaic efficiencies for the different products, and  $P_{light}$  is the power of the incident illumination [137,138].

Alternatively, Eq. (5) uses the chemical energy of the products formed divided by the solar energy input from sunlight incident on the electrode. In this expression, the nominator is directly related to the formation rate of a given product, establishing a direct relation to product analysis during the measurements. Note that this definition is similar to that conventionally used for solar to hydrogen (STH) conversion [139], and is only applicable if no external bias is employed (i.e., at short circuit conditions).

$$\eta_{PEC} = \frac{\sum_i v_i \times \Delta G_i}{P_{light} \times A} \quad (5)$$

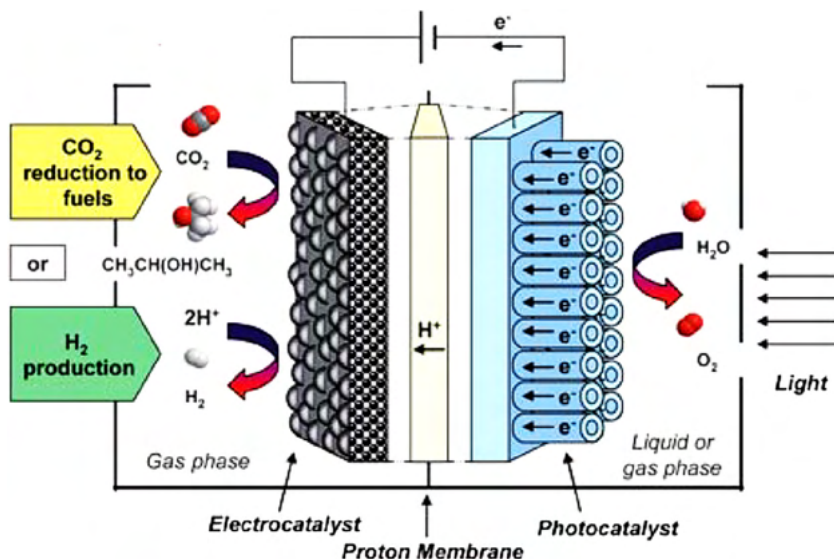


Fig. 20. Schematic illustration of the indirect PEC approach with a PEM cell. Reproduced with permission from ref. [136].

where  $v_i$  is the formation rate of a given product ( $\text{mmol s}^{-1}$ ),  $\Delta G_i$  is the Gibbs free energy per mole of a given product ( $\text{J mol}^{-1}$ ),  $P_{\text{total}}$  is the incident illumination power density ( $\text{mW cm}^{-2}$ ), and  $A$  is the illuminated electrode area ( $\text{cm}^2$ ).

## 7. Summary and outlook

As demonstrated in this review article, multiple parameters have to be optimized simultaneously to efficiently perform continuous-flow electroreduction of  $\text{CO}_2$ . Some of them are well understood, while others still need to be carefully studied. The effects of high pressure and temperature are of particular interest to achieve reasonable current density and selectivity. These parameters will also affect the surface of the catalysts [140], which is another factor to be studied in continuous-flow cells. Computational modeling can contribute to the rational design of electrolyzer configuration. In this vein, the reactor performance can be numerically simulated to unravel the influence of flow rate and channel geometry on  $\text{CO}_2$  conversion and consumption rate. Similarly, recent advances in 3D printing allows rapid prototyping of different cell geometries and thus will be a powerful tool in the hand of electrochemists [141]. Furthermore, we believe that successful studies in vapor phase will open up the opportunity to use industrial exhaust fume (rich in both  $\text{CO}_2$  and  $\text{H}_2\text{O}$ ) directly as feedstock for solar fuel generation. Accordingly, different model gases containing typical impurities should be studied in the future.

As for future development avenues, we would like to emphasize two directions. One is coming from the materials perspective: the need for intricate architectures where the elements of the GDE are simultaneously optimized. As shown in Sections 3.3–3.5, rationally designed interfaces are required for efficient  $\text{CO}_2$  conversion. In this endeavor, the cooperation of chemists, materials scientists, and engineers is highly recommended. The second R&D path is rooted in the fact that the anode reaction was oxygen evolution (water oxidation, OER) in almost all the presented studies. In such cases the formed oxygen is considered as a non-harmful by-product, and is simply let to the atmosphere without using it for any purpose. We also note that OER as the anode process can be important in Space applications, namely as a root for the recovery of  $\text{O}_2$  from  $\text{CO}_2$ . With the interest of deep space exploration (i.e., possible prolonged missions to Mars), it is of high importance to improve such key enabling technologies. As for terrestrial applications, the formed oxygen can be compressed and sold, but driving a more beneficial electrochemical procedure on the anode could be a value-added approach. In this manner,  $\text{CO}_2$  electrolyzers could be easily integrated in other industrial processes, in which the main product is formed on the anode.

There are several candidates, for example, using the oxidation of organic pollutants on the anode, which is a kinetically-facile reaction. Thus the electrolyzer can be employed as both  $\text{CO}_2$  converter and water purifier (i.e., wastewater treatment with a net zero  $\text{CO}_2$  emission) adding value to the overall process [142]. This can be envisioned by either directly oxidizing the organic pollutants, or indirectly, by generating ozone on the anode. This concept is well-known for water electrolyzers, in which hydrogen is produced on the cathode, while oxidation of water pollutant occurs on the anode [143]. Chlorine ( $\text{Cl}_2$ ) evolution is another technologically relevant reaction, which might be worth coupling with  $\text{CO}_2$  reduction (also called chlor-syngas process, see Fig. 21) [144]. Importantly, the redox potential of chloride oxidation matches with that for the water oxidation; therefore, this approach does not lead to an increased cell voltage [145]. In this case, however, important precursors of some commodity chemicals are formed on both the electrodes. As these products are all in the gas phase, it is easy to separate them from the aqueous electrolyte during a subsequent technological step. This concept is very similar to the so called oxygen

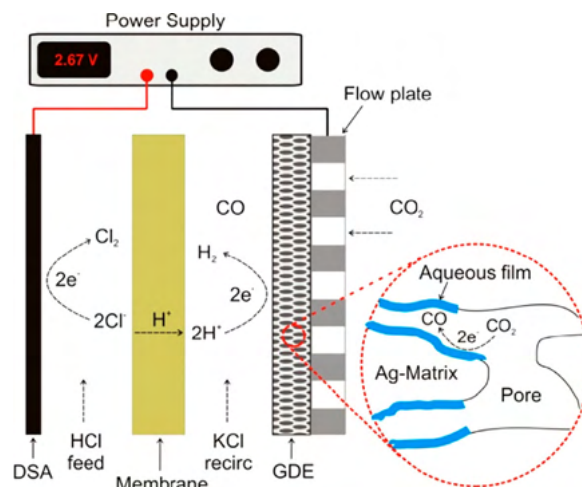


Fig. 21. Schematic illustration of the chlor-syngas electrochemical process. Reproduced with permission from ref. [144].

depolvanized cathode chlor-alkali cells, where chlorine is formed on the anode, while oxygen gas is reduced on the cathode [146]. Plants operating on this concept have been in operation for years; and therefore the infrastructure and technological know-how are readily available. Finally, while  $\text{H}_2$  oxidation at the anode is not a value-added approach, it allows for gas feed on both sides, which can be beneficial in certain instances [44,147].

We are also convinced that concentrated efforts need to be devoted to scale-up and scale-out, to achieve reactor sizes which are at least similar to industrially used water electrolyzers (2 MW). It is worth emphasizing that conclusions drawn for electrochemical cells offering very low current densities are not necessarily valid for those with high currents. Consequently, analyzing electrodes/cells under conditions which are far removed from those which are necessary for practical applications, is a futile exercise. Finally, we hope that the proposed benchmarking protocol will provide insightful guidelines to researchers involved in this endeavor and will lead to more comparable results.

## Acknowledgments

This project has received funding from the European Research Council (ERC) under the European Union's Horizon 2020 Research and Innovation Programme (grant agreement No 716539). This work was partly supported by the Momentum Program of the Hungarian Academy of Sciences (LP-2014/3) and the GINOP 2.3.2/2015-13 project. The authors are very thankful to Prof. Paul J. Kenis (University of Illinois at Urban Champaign) for his constructive criticism and insightful comments on an earlier version of this manuscript.

## References

- [1] Lewis NS, Nocera DG. Powering the planet: Chemical challenges in solar energy utilization. *Proc Natl Acad Sci* 2006;103:15729–35. doi: 10.1073/pnas.0603395103.
- [2] Lewis NS. Research opportunities to advance solar energy utilization. *Science* 2016;351:353–62. doi: 10.1126/science.aad1920.
- [3] Kumar B, Llorente M, Froehlich J, Dang T, Sathrum A, Kubiak CP. Photochemical and photoelectrochemical reduction of  $\text{CO}_2$ . *Annu Rev Phys Chem* 2012;63:541–69. doi: 10.1146/annurev-physchem-032511-143759.
- [4] Herron JA, Kim J, Upadhye A, Huber GW, Maravelias CT. A general framework for the assessment of solar fuel technologies. *Energy Environ Sci* 2015;8:126–57. doi: 10.1039/C4EE01958J.
- [5] Centi G, Perathoner S. Perspectives and state of the art in producing solar fuels and chemicals from  $\text{CO}_2$ . In: Centi G, Perathoner S, editors. *Green carbon dioxide advances in CO utilization*. Wiley Online Library; 2014. p. 1–24. doi: 10.1002/9781118831922.ch1.
- [6] Ganesh I. Conversion of carbon dioxide into methanol – a potential liquid fuel: Fundamental challenges and opportunities (a review). *Renew Sustain Energy Rev* 2014;31:221–57. doi: 10.1016/j.rser.2013.11.045.

- [7] Herron JA, Maravelias CT. Assessment of solar-to-fuels strategies: photocatalysis and electrocatalytic reduction. *Energy Technol* 2016;4:1369–91. doi: [10.1002/ente.201600163](https://doi.org/10.1002/ente.201600163).
- [8] Nocera DG. The artificial leaf. *Acc Chem Res* 2012;45:767–76. doi: [10.1021/ar2003013](https://doi.org/10.1021/ar2003013).
- [9] Osterloh FE. Photocatalysis versus photosynthesis: a sensitivity analysis of devices for solar energy conversion and chemical transformations. *ACS Energy Lett* 2017; 445–53. doi: [10.1021/acsenerylett.6b00665](https://doi.org/10.1021/acsenerylett.6b00665).
- [10] Usubharatana P, Mccartin D, Veawab A, Tontiwachwuthikul P. Photocatalytic process for CO<sub>2</sub> emission reduction from industrial flue gas streams. *Ind Eng Chem Res* 2006;45:2558–68. doi: [10.1021/ie0505763](https://doi.org/10.1021/ie0505763).
- [11] “Molly” Jhong H-R, Ma S, Kenis PJ. Electrochemical conversion of CO<sub>2</sub> to useful chemicals: current status, remaining challenges, and future opportunities. *Curr Opin Chem Eng* 2013;2:191–9. doi: [10.1016/j.coche.2013.03.005](https://doi.org/10.1016/j.coche.2013.03.005).
- [12] Costentin C, Robert M, Savéant J-M. Catalysis of the electrochemical reduction of carbon dioxide. *Chem Soc Rev* 2013;42:2423–36. doi: [10.1039/c2cs35360a](https://doi.org/10.1039/c2cs35360a).
- [13] Boston DJ, Huang KL, de Tacconi NR, Myung N, MacDonnell FM, Rajeshwar K. Electro- and photocatalytic reduction of CO<sub>2</sub>: the homogeneous and heterogeneous worlds collide? Photoelectrochemical water splitting: materials, processes and architectures; 2013289–332. doi: [10.1039/9781849737739-00289](https://doi.org/10.1039/9781849737739-00289).
- [14] Schmalensee R. *The future of solar energy, an interdisciplinary MIT study*. Massachusetts Institute of Technology ISBN (978-0-928008-9-8); 2015.
- [15] Whipple DT, Kenis PJA. Prospects of CO<sub>2</sub> utilization via direct heterogeneous electrochemical reduction. *J Phys Chem Lett* 2010;1:3451–8. doi: [10.1021/jz1012627](https://doi.org/10.1021/jz1012627).
- [16] Jones JP, Prakash GKS, Olah GA. Electrochemical CO<sub>2</sub> reduction: recent advances and current trends. *Isr J Chem* 2014;54:1451–66. doi: [10.1002/ijch.201400081](https://doi.org/10.1002/ijch.201400081).
- [17] Kortlever R, Shen J, Schouten KJP, Calle-Vallejo F, Koper MTM. Catalysts and reaction pathways for the electrochemical reduction of carbon dioxide. *J Phys Chem Lett* 2015;6:4073–82. doi: [10.1021/acs.jpcclett.5b01559](https://doi.org/10.1021/acs.jpcclett.5b01559).
- [18] Qiao J, Liu Y, Hong F, Zhang J. A review of catalysts for the electroreduction of carbon dioxide to produce low-carbon fuels. *Chem Soc Rev* 2014;43:631–75. doi: [10.1039/c3cs60323g](https://doi.org/10.1039/c3cs60323g).
- [19] Kuhl KP, Cave ER, Abram DN, Jaramillo TF. New insights into the electrochemical reduction of carbon dioxide on metallic copper surfaces. *Energy Environ Sci* 2012;5:7050–9. doi: [10.1039/c2ee21234j](https://doi.org/10.1039/c2ee21234j).
- [20] Janaky C, Hursán D, Endrődi B, Channaneew W, Roy D, Liu D, et al. Electro- and photoreduction of carbon dioxide: the twain shall meet at copper oxide/copper nanocube interfaces. *ACS Energy Lett* 2016;1:332–8. doi: [10.1021/acsenerylett.6b00078](https://doi.org/10.1021/acsenerylett.6b00078).
- [21] Verma S, Kim B, “Molly” JhongH-R, Ma S, Kenis PJA. A gross-margin model for defining techno-economic benchmarks in the electroreduction of CO<sub>2</sub>. *ChemSusChem* 2016;9:1972–9. doi: [10.1002/cssc.201600394](https://doi.org/10.1002/cssc.201600394).
- [22] Martín AJ, Larrazábal GO, Pérez-Ramírez J. Towards sustainable fuels and chemicals through the electrochemical reduction of CO<sub>2</sub>: lessons from water electrolysis. *Green Chem* 2015;17:5114–30. doi: [10.1039/C5GC01893E](https://doi.org/10.1039/C5GC01893E).
- [23] Wong CS, Tishchenko PY, Johnson WK. Solubility of carbon dioxide in aqueous HCl and NaHCO<sub>3</sub> solutions from 278 to 298 K. *J Chem Eng Data* 2005;50:817–21. doi: [10.1021/je049716q](https://doi.org/10.1021/je049716q).
- [24] Dewulf DW, Bard AJ. The electrochemical reduction of CO<sub>2</sub> to CH<sub>4</sub> and C<sub>2</sub>H<sub>4</sub> at Cu/Nafion electrodes (solid polymer electrolyte structures). *Catal Letters* 1988;1:73–80. doi: [10.1007/BF00765357](https://doi.org/10.1007/BF00765357).
- [25] Bevilacqua M, Filippi J, Miller HA, Vizza F. Recent technological progress in CO<sub>2</sub> electroreduction to fuels and energy carriers in aqueous environments. *Energy Technol* 2015;3:197–210. doi: [10.1002/ente.201402166](https://doi.org/10.1002/ente.201402166).
- [26] Albo J, Alvarez-Guerra M, Castaño P, Irabien A. Towards the electrochemical conversion of carbon dioxide into methanol. *Green Chem* 2015;17:2304–24. doi: [10.1039/C4GC02453B](https://doi.org/10.1039/C4GC02453B).
- [27] Merino-García I, Alvarez-Guerra E, Albo J, Irabien A. Electrochemical membrane reactors for the utilisation of carbon dioxide. *Chem Eng J* 2016;305:104–20. doi: [10.1016/j.cej.2016.05.032](https://doi.org/10.1016/j.cej.2016.05.032).
- [28] Kondratenko E V, Mul G, Baltrusaitis J, Larrazabal GO, Perez-Ramirez J, Larrazábal GO, et al. Status and perspectives of CO<sub>2</sub> conversion into fuels and chemicals by catalytic, photocatalytic and electrocatalytic processes. *Energy Environ Sci* 2013;6:3112–35. doi: [10.1039/c3ee41272e](https://doi.org/10.1039/c3ee41272e).
- [29] Lobaccaro P, Singh MR, Clark L, Kwon Y, Bell AT, Ager JW. Effects of temperature and gas – liquid mass transfer on the operation of small electrochemical cells for the quantitative evaluation of CO<sub>2</sub> reduction electrocatalysts. *Phys Chem Chem Phys* 2016;18:26777–85. doi: [10.1039/C6CP05287H](https://doi.org/10.1039/C6CP05287H).
- [30] Singh MR, Clark EL, Bell AT. Effects of electrolyte, catalyst, and membrane composition and operating conditions on the performance of solar-driven electrochemical reduction of carbon dioxide. *Phys Chem Chem Phys* 2015;17:18924–36. doi: [10.1039/C5CP03283K](https://doi.org/10.1039/C5CP03283K).
- [31] Kas R, Hummadi KK, Kortlever R, de Wit P, Milbrat A, Luiten-Olieman MWJ, et al. Three-dimensional porous hollow fibre copper electrodes for efficient and high-rate electrochemical carbon dioxide reduction. *Nat Commun* 2016;7:10748–54. doi: [10.1038/ncomms10748](https://doi.org/10.1038/ncomms10748).
- [32] Darvas F, Hessel V, György D. *Flow chemistry - Fundamentals*. 1st ed. De Gruyter ISBN 978-3-11-028916-9; 2014.
- [33] Ma S, Sadakiyo M, Luo R, Heima M, Yamauchi M, Kenis PJA. One-step electro-synthesis of ethylene and ethanol from CO<sub>2</sub> in an alkaline electrolyzer. *J Power Sources* 2016;301:219–28. doi: [10.1016/j.jpowsour.2015.09.124](https://doi.org/10.1016/j.jpowsour.2015.09.124).
- [34] Hereijgers J, Ottevaere H, Breugelmans T, De Malsche W. Membrane deflection in a flat membrane microcontact: experimental study of spacer features. *J Membr Sci* 2016;504:153–61. doi: [10.1016/j.memsci.2016.01.015](https://doi.org/10.1016/j.memsci.2016.01.015).
- [35] Whipple DT, Finke EC, Kenis PJA. Microfluidic reactor for the electrochemical reduction of carbon dioxide: the effect of pH. *Electrochim Solid-State Lett* 2010;13:B109–11. doi: [10.1149/1.3456590](https://doi.org/10.1149/1.3456590).
- [36] Tornow CE, Thorson MR, Ma S, Gewirth AA, Kenis PJA. Nitrogen-based catalysts for the electrochemical reduction of CO<sub>2</sub> to CO. *J Am Chem Soc* 2012;134:19520–3. doi: [10.1021/ja308217w](https://doi.org/10.1021/ja308217w).
- [37] Lu X, Leung DYC, Wang H, Xuan J. A high performance dual electrolyte microfluidic reactor for the utilization of CO<sub>2</sub>. *Appl Energy* 2017;194:549–59. doi: [10.1016/j.apenergy.2016.05.091](https://doi.org/10.1016/j.apenergy.2016.05.091).
- [38] Ma S, Luo R, Gold JI, Yu AZ, Kim B, Kenis PJA. Carbon nanotube containing Ag catalyst layers for efficient and selective reduction of carbon dioxide. *J Mater Chem A* 2016;4:8573–8. doi: [10.1039/C6TA00427J](https://doi.org/10.1039/C6TA00427J).
- [39] Verma S, Lu X, Ma S, Masel RI, Kenis PJA. The effect of electrolyte composition on the electroreduction of CO<sub>2</sub> to CO on Ag based gas diffusion electrodes. *Phys Chem Chem Phys* 2015;18:7075–84. doi: [10.1039/C5CP05665A](https://doi.org/10.1039/C5CP05665A).
- [40] Alvarez-Guerra M, Del Castillo A, Irabien A. Continuous electrochemical reduction of carbon dioxide into formate using a tin cathode: Comparison with lead cathode. *Chem Eng Res Des* 2014;92:692–701. doi: [10.1016/j.cherd.2013.11.002](https://doi.org/10.1016/j.cherd.2013.11.002).
- [41] Merino García I, Albo J, Irabien A. Productivity and selectivity of gas phase CO<sub>2</sub> electroreduction to methane at Cu nanoparticle-based electrodes. *Energy Technol* 2017. in press doi: [10.1002/ente.201600616](https://doi.org/10.1002/ente.201600616).
- [42] Cook RL, MacDuff RC, Sammells AF. High rate gas phase CO<sub>2</sub> reduction to ethylene and methane using gas diffusion electrodes. *J Electrochem Soc* 1990;137:607–8. doi: [10.1149/1.2086515](https://doi.org/10.1149/1.2086515).
- [43] Gutierrez-Guerra N, Moreno-Lopez L, Serrano-Ruiz JC, Valverde JL, de Lucas-Consuegra A. Gas phase electrocatalytic conversion of CO<sub>2</sub> to syn-fuels on Cu based catalysts-electrodes. *Appl Catal B Environ* 2016;188:272–82. doi: [10.1016/j.apcatb.2016.02.010](https://doi.org/10.1016/j.apcatb.2016.02.010).
- [44] Pérez-Rodríguez S, Barreras F, Pastor E, Lázaro MJ. Electrochemical reactors for CO<sub>2</sub> reduction: From acid media to gas phase. *Int J Hydrogen Energy* 2016;41:19756–65. doi: [10.1016/j.ijhydene.2016.06.130](https://doi.org/10.1016/j.ijhydene.2016.06.130).
- [45] Li G, Pickup PG. Measurement of single electrode potentials and impedances in hydrogen and direct methanol PEM fuel cells. *Electrochim Acta* 2004;49:4119–26. doi: [10.1016/j.electacta.2004.04.005](https://doi.org/10.1016/j.electacta.2004.04.005).
- [46] Herrera OE, Merida W, Wilkinson DP. New reference electrode approach for fuel cell performance evaluation. *ECS Trans* 2008;16:1915–26. doi: [10.1149/1.2982032](https://doi.org/10.1149/1.2982032).
- [47] Kulikovskiy AA, Berg P. Positioning of a reference electrode in a PEM fuel cell. *J Electrochem Soc* 2015;162:F843–8. doi: [10.1149/2.0231508jes](https://doi.org/10.1149/2.0231508jes).
- [48] Liu Z, Wainright JS, Huang W, Savinell RF. Positioning the reference electrode in proton exchange membrane fuel cells: calculations of primary and secondary current distribution. *Electrochim Acta* 2004;49:923–35. doi: [10.1016/j.electacta.2003.10.004](https://doi.org/10.1016/j.electacta.2003.10.004).
- [49] Garg G, Basu S. Studies on degradation of copper nano particles in cathode for CO<sub>2</sub> electrolysis to organic compounds. *Electrochim Acta* 2015;177:359–65. doi: [10.1016/j.electacta.2015.03.161](https://doi.org/10.1016/j.electacta.2015.03.161).
- [50] Albo J, Sáez A, Solla-Gullón J, Montiel V, Irabien A. Production of methanol from CO<sub>2</sub> electroreduction at Cu<sub>2</sub>O and Cu<sub>2</sub>O/ZnO-based electrodes in aqueous solution. *Appl Catal B Environ* 2015;176:709–17. doi: [10.1016/j.apcatb.2015.04.055](https://doi.org/10.1016/j.apcatb.2015.04.055).
- [51] Wu J, Risalvato FG, Sharma PP, Pellechia PJ, Ke F-S, Zhou X-D. Electrochemical reduction of carbon dioxide: II. Design, assembly, and performance of low temperature full electrochemical cells. *J Electrochem Soc* 2013;160:F953–7. doi: [10.1149/2.030309jes](https://doi.org/10.1149/2.030309jes).
- [52] Aeshala LM, Rahman SU, Verma A. Effect of solid polymer electrolyte on electrochemical reduction of CO<sub>2</sub>. *Sep Purif Technol* 2012;94:131–7. doi: [10.1016/j.seppur.2011.12.030](https://doi.org/10.1016/j.seppur.2011.12.030).
- [53] Liua Z, Masel RI, Chen Q, Kutz R, Yang H, Lewinski K, et al. Electrochemical generation of syngas from water and carbon dioxide at industrially important rates. *J CO<sub>2</sub> Util* 2016;15:50–6. doi: [10.1016/j.jcou.2016.04.011](https://doi.org/10.1016/j.jcou.2016.04.011).
- [54] Li H, Oloman C. Development of a continuous reactor for the electro-reduction of carbon dioxide to formate – Part 2: Scale-up. *J Appl Electrochem* 2007;37:1107–17. doi: [10.1007/s10800-007-9371-8](https://doi.org/10.1007/s10800-007-9371-8).
- [55] Oloman C, Li H. Electrochemical processing of carbon dioxide. *ChemSusChem* 2008;1:385–91. doi: [10.1002/cssc.200800015](https://doi.org/10.1002/cssc.200800015).
- [56] Albo J, Vallejo D, Beobide G, Castillo O, Castaño P, Irabien A. Copper-based metal-organic porous materials for CO<sub>2</sub> electrocatalytic reduction to alcohols. *ChemSusChem* 2017;10:1100–9. doi: [10.1002/cssc.201600693](https://doi.org/10.1002/cssc.201600693).
- [57] Luc W, Rosen J, Jiao F. An Ir-based anode for a practical CO<sub>2</sub> electrolyzer. *Catal Today* 2016; 1–6. doi: [10.1016/j.cattod.2016.06.011](https://doi.org/10.1016/j.cattod.2016.06.011).
- [58] Jhong HRQ, Brushett FR, Kenis PJA. The effects of catalyst layer deposition methodology on electrode performance. *Adv Energy Mater* 2013;3:589–99. doi: [10.1002/aenm.201200759](https://doi.org/10.1002/aenm.201200759).
- [59] Dufek EJ, Lister TE, McIlwain ME. Bench-scale electrochemical system for generation of CO<sub>2</sub> and syn-gas. *J Appl Electrochem* 2011;41:623–31. doi: [10.1007/s10800-011-0271-6](https://doi.org/10.1007/s10800-011-0271-6).
- [60] Dufek EJ, Lister TE, Stone SG, McIlwain ME. Operation of a pressurized system for continuous reduction of CO<sub>2</sub>. *J Electrochem Soc* 2012;159:514–7. doi: [10.1149/2.011209jes](https://doi.org/10.1149/2.011209jes).
- [61] Ma S, Lan Y, Perez GMJ, Moniri S, Kenis PJA. Silver supported on titania as an active catalyst for electrochemical carbon dioxide reduction. *ChemSusChem* 2014;7:866–74. doi: [10.1002/cssc.201300934](https://doi.org/10.1002/cssc.201300934).
- [62] Shi J, Li Q-Y, Shi F, Song N, Jia Y-J, Hu Y-Q, et al. Design of a two-compartment electrolysis cell for the reduction of CO<sub>2</sub> to CO in tetrabutylammonium perchlorate/propylene carbonate for renewable electrical energy storage. *J Electrochem Soc* 2016;163:G82–7. doi: [10.1149/2.1381607jes](https://doi.org/10.1149/2.1381607jes).

- [63] Stevens GB, Reda T, Raguse B. Energy storage by the electrochemical reduction of CO<sub>2</sub> to CO at a porous Au film. *J Electroanal Chem* 2002;526:125–33. doi: [10.1016/S0022-0728\(02\)00688-5](https://doi.org/10.1016/S0022-0728(02)00688-5).
- [64] Komatsu S, Tanaka M, Okumura A, Kungi A. Preparation of Cu-solid polymer electrolyte composite electrodes and application to gas-phase electrochemical reduction of CO<sub>2</sub>. *Electrochim Acta* 1995;40:745–53. doi: [10.1016/0013-4686\(94\)00325-U](https://doi.org/10.1016/0013-4686(94)00325-U).
- [65] Lan Y, Gai C, Kenis PJA, Lu J. Electrochemical reduction of carbon dioxide on Cu/CuO core/shell catalysts. *ChemElectroChem* 2014;1:1577–82. doi: [10.1002/celc.201402182](https://doi.org/10.1002/celc.201402182).
- [66] Aeshala LM, Uppaluri RG, Verma A. Effect of cationic and anionic solid polymer electrolyte on direct electrochemical reduction of gaseous CO<sub>2</sub> to fuel. *J CO<sub>2</sub> Util* 2013;3–4:49–55. doi: [10.1016/j.jcou.2013.09.004](https://doi.org/10.1016/j.jcou.2013.09.004).
- [67] Albo J, Irbaien A. Cu<sub>2</sub>O-loaded gas diffusion electrodes for the continuous electrochemical reduction of CO<sub>2</sub> to methanol. *J Catal* 2016;343:232–9. doi: [10.1016/j.jcat.2015.11.014](https://doi.org/10.1016/j.jcat.2015.11.014).
- [68] Homayoni H, Chammanee W, de Tacconi NR, Dennis BH, Rajeshwar K, Homayon H, et al. Continuous flow photoelectrochemical reactor for solar conversion of carbon dioxide to alcohols. *J Electrochem Soc* 2015;162:E115–22. doi: [10.1149/2.0331508jes](https://doi.org/10.1149/2.0331508jes).
- [69] Wang Q, Dong H, Yu H, Yu H, Liu M. Enhanced electrochemical reduction of carbon dioxide to formic acid using a two-layer gas diffusion electrode in a microbial electrolysis cell. *RSC Adv* 2015;5:10346–51. doi: [10.1039/C4RA14535F](https://doi.org/10.1039/C4RA14535F).
- [70] Li H, Oloman C. Development of a continuous reactor for the electro-reduction of carbon dioxide to formate - Part 1: Process variables. *J Appl Electrochem* 2006;36:1105–15. doi: [10.1007/s10800-007-9371-8](https://doi.org/10.1007/s10800-007-9371-8).
- [71] Li H, Oloman C. The electro-reduction of carbon dioxide in a continuous reactor. *J Appl Electrochem* 2005;35:955–65. doi: [10.1007/s10800-005-7173-4](https://doi.org/10.1007/s10800-005-7173-4).
- [72] Kopljär D, Wagner N, Klemm E. Transferring electrochemical CO<sub>2</sub> reduction from semi-batch into continuous operation mode using gas diffusion electrodes. *Chem Eng Technol* 2016;39:2042–50. doi: [10.1002/ceat.201600198](https://doi.org/10.1002/ceat.201600198).
- [73] MacHunda RL, Lee J, Lee J. Microstructural surface changes of electrodeposited Pb on gas diffusion electrode during electroreduction of gas-phase CO<sub>2</sub>. *Surf Interface Anal* 2010;42:564–7. doi: [10.1002/sia.3245](https://doi.org/10.1002/sia.3245).
- [74] Lu X, Leung DYC, Wang H, Maroto-Valer MM, Xuan J. A pH-differential dual-electrolyte microfluidic electrochemical cells for CO<sub>2</sub> utilization. *Renew Energy* 2016;95:277–85. doi: [10.1016/j.renene.2016.04.021](https://doi.org/10.1016/j.renene.2016.04.021).
- [75] Genovese C, Ampelli C, Perathoner S, Centi G. Electrochemical conversion of CO<sub>2</sub> on carbon nanotube-based electrodes for producing solar fuels. *J Catal* 2013;308:237–49. doi: [10.1016/j.jcat.2013.08.026](https://doi.org/10.1016/j.jcat.2013.08.026).
- [76] White JL, Herb JT, Kaczur JJ, Majsztrik PW, Bocarsly AB. Photons to formate: Efficient electrochemical solar energy conversion via reduction of carbon dioxide. *J CO<sub>2</sub> Util* 2014;7:1–5. doi: [10.1016/j.jcou.2014.05.002](https://doi.org/10.1016/j.jcou.2014.05.002).
- [77] Centi G, Perathoner S, Wine G, Gangeri M. Electrochemical conversion of CO<sub>2</sub> to long carbon-chain hydrocarbons. *Green Chem* 2007;9:671–8. doi: [10.1039/b615275a](https://doi.org/10.1039/b615275a).
- [78] Wu J, Sharma PP, Harris BH, Zhou X. Electrochemical reduction of carbon dioxide: IV dependence of the Faradaic efficiency and current density on the microstructure and thickness of tin electrode. *J Power Sources* 2014;258:189–94. doi: [10.1016/j.jpowsour.2014.02.014](https://doi.org/10.1016/j.jpowsour.2014.02.014).
- [79] Lu Q, Rosen J, Jiao F. Nanostructured metallic electrocatalysts for carbon dioxide reduction. *ChemCatChem* 2015;7:38–47. doi: [10.1002/cctc.201402669](https://doi.org/10.1002/cctc.201402669).
- [80] Manthiram K, Beberwyck BJ, Alivisatos AP. Enhanced electrochemical methanation of carbon dioxide with a dispersible nanoscale copper catalyst. *J Am Chem Soc* 2014;136:13319–25. doi: [10.1021/ja5065284](https://doi.org/10.1021/ja5065284).
- [81] Bevilacqua M, Filippi J, Folliero M, Lavacchi A, Miller HA, Marchionni A, et al. Enhancement of the efficiency and selectivity for carbon dioxide electroreduction to fuels on tailored copper catalyst architectures. *Energy Technol* 2016;4:1020–8. doi: [10.1002/ente.201600044](https://doi.org/10.1002/ente.201600044).
- [82] Del Castillo A, Alvarez-Guerra M, Solla-Gullón J, Sáez A, Montiel V, Irbaien A. Electrochemical reduction of CO<sub>2</sub> to formate using particulate Sn electrodes: Effect of metal loading and particle size. *Appl Energy* 2015;157:165–73. doi: [10.1016/j.apenergy.2015.08.012](https://doi.org/10.1016/j.apenergy.2015.08.012).
- [83] Bitar Z, Fecant A, Trela-Baudot E, Chardon-Noblat S, Pasquier D. Electrochemical reduction of carbon dioxide on indium coated gas diffusion electrodes-Comparison with indium foil. *Appl Catal B Environ* 2016;189:172–80. doi: [10.1016/j.apcatb.2016.02.041](https://doi.org/10.1016/j.apcatb.2016.02.041).
- [84] Kim B, Hillman F, Ariyoshi M, Fujikawa S, Kenis PJA. Effects of composition of the micro porous layer and the substrate on performance in the electrochemical reduction of CO<sub>2</sub> to CO. *J Power Sources* 2016;312:192–8. doi: [10.1016/j.jpowsour.2016.02.043](https://doi.org/10.1016/j.jpowsour.2016.02.043).
- [85] Irtem E, Andreu T, Parra A, Hernandez-Alonso MD, García-Rodríguez S, Riesco García JM, et al. Low-energy formate production from CO<sub>2</sub> electroreduction using electrodeposited tin on GDE. *J Mater Chem A* 2016;4:13582–8. doi: [10.1039/C6TA04432H](https://doi.org/10.1039/C6TA04432H).
- [86] Antolini E, Giorgi L, Pozio A, Passalacqua E. Influence of Nafion loading in the catalyst layer of gas-diffusion electrodes for PEFC. *J Power Sources* 1999;77:136–42. doi: [10.1016/S0378-7753\(98\)00186-4](https://doi.org/10.1016/S0378-7753(98)00186-4).
- [87] Jeon S, Lee J, Rios GM, Kim H-J, Lee S-Y, Cho E, et al. Effect of ionomer content and relative humidity on polymer electrolyte membrane fuel cell (PEMFC) performance of membrane-electrode assemblies (MEAs) prepared by decal transfer method. *Int J Hydrogen Energy* 2010;35:9678–86. doi: [10.1016/j.ijhydene.2010.06.044](https://doi.org/10.1016/j.ijhydene.2010.06.044).
- [88] Liu Y, Murphy MW, Baker DR, Gu W, Ji C, Jorne J, et al. Proton conduction and oxygen reduction kinetics in PEM fuel cell cathodes: Effects of ionomer-to-carbon ratio and relative humidity. *J Electrochem Soc* 2009;156:B970–80. doi: [10.1149/1.3143965](https://doi.org/10.1149/1.3143965).
- [89] Wilson MS, Gottesfeld S. Thin-film catalyst layers for polymer electrolyte fuel cell electrodes. *J Appl Electrochem* 1992;22:1–7. doi: [10.1007/BF01093004](https://doi.org/10.1007/BF01093004).
- [90] Narayanan SR, Haines B, Soler J, Valdez TI. Electrochemical conversion of carbon dioxide to formate in alkaline polymer electrolyte membrane cells. *J Electrochem Soc* 2011;158:A167–73. doi: [10.1149/1.3526312](https://doi.org/10.1149/1.3526312).
- [91] Oh Y, Hu X. Organic molecules as mediators and catalysts for photocatalytic and electrocatalytic CO<sub>2</sub> reduction. *Chem Soc Rev* 2013;42:2253–61. doi: [10.1039/c2cs35276a](https://doi.org/10.1039/c2cs35276a).
- [92] Xia Z, Qiu W, Bao H, Yang B, Lei L, Xu Z, et al. Electrochemical reduction of gaseous CO<sub>2</sub> with a catechol and polyethyleneimine co-deposited polypropylene membrane. *Electrochem Commun* 2016;71:1–4. doi: [10.1016/j.elecom.2016.07.009](https://doi.org/10.1016/j.elecom.2016.07.009).
- [93] Robert A, Kutz B, Chen Q, Yang H, Dawar S, Liu Z, et al. Sustainion™ imidazolium functionalized polymers for CO<sub>2</sub> electrolysis. *Energy Technol* 2017. doi: [10.1002/ente.201600636](https://doi.org/10.1002/ente.201600636) in press.
- [94] Hori Y, Ito H, Okano K, Nagasu K, Sato S. Silver-coated ion exchange membrane electrode applied to electrochemical reduction of carbon dioxide. *Electrochim Acta* 2003;48:2651–7. doi: [10.1016/S0013-4686\(03\)00311-6](https://doi.org/10.1016/S0013-4686(03)00311-6).
- [95] Sun K, Liu R, Chen Y, Verlage E, Lewis NS, Xiang C. A stabilized, intrinsically safe, 10% efficient, solar-driven water-splitting cell incorporating earth-abundant electrocatalysts with steady-state pH gradients and product separation enabled by a bipolar membrane. *Adv Energy Mater* 2016;6:1600379. doi: [10.1002/aenm.201600379](https://doi.org/10.1002/aenm.201600379).
- [96] Luo J, Vermaas DA, Bi D, Hagfeldt A, Smith WA, Grätzel M. Bipolar membrane-assisted solar water splitting in optimal pH. *Adv Energy Mater* 2016;6:1600100. doi: [10.1002/aenm.201600100](https://doi.org/10.1002/aenm.201600100).
- [97] Li X, Sabir I. Review of bipolar plates in PEM fuel cells: Flow-field designs. *Int J Hydrogen Energy* 2005;30:359–71. doi: [10.1016/j.ijhydene.2004.09.019](https://doi.org/10.1016/j.ijhydene.2004.09.019).
- [98] Ito H, Maeda T, Nakano A, Hasegawa Y, Yokoi N, Hwang CM, et al. Effect of flow regime of circulating water on a proton exchange membrane electrolyzer. *Int J Hydrogen Energy* 2010;35:9550–60. doi: [10.1016/j.ijhydene.2010.06.103](https://doi.org/10.1016/j.ijhydene.2010.06.103).
- [99] Kim H-Y, Choi I, Ahn SH, Hwang SJ, Yoo SJ, Han J, et al. Analysis on the effect of operating conditions on electrochemical conversion of carbon dioxide to formic acid. *Int J Hydrogen Energy* 2014;39:16506–12. doi: [10.1016/j.ijhydene.2014.03.145](https://doi.org/10.1016/j.ijhydene.2014.03.145).
- [100] Thorson MR, Siil KI, Kenis PJA. Effect of cations on the electrochemical conversion of CO<sub>2</sub> to CO. *J Electrochem Soc* 2013;160:F69–74. doi: [10.1149/2.052301jes](https://doi.org/10.1149/2.052301jes).
- [101] Ma S, Luo R, Moniri S, Lan Y, Kenis PJA. Efficient electrochemical flow system with improved anode for the conversion of CO<sub>2</sub> to CO. *J Electrochem Soc* 2014;161:F1124–31. doi: [10.1149/2.1201410jes](https://doi.org/10.1149/2.1201410jes).
- [102] Kopljär D, Inan A, Vindayer P, Wagner N, Klemm E. Electrochemical reduction of CO<sub>2</sub> to formate at high current density using gas diffusion electrodes. *J Appl Electrochem* 2014;44:1107–16. doi: [10.1007/s10800-014-0731-x](https://doi.org/10.1007/s10800-014-0731-x).
- [103] Dufek EJ, Lister TE, Stone SG. Sampling dynamics for pressurized electrochemical cells. *J Appl Electrochem* 2014;44:849–55. doi: [10.1007/s10800-014-0693-z](https://doi.org/10.1007/s10800-014-0693-z).
- [104] Schwartz M, Cook RL, Kehoe VM, MacDuff RC, Patel J, Sammells AF. Carbon dioxide reduction to alcohols using perovskite-type electrocatalysts. *J Electrochem Soc* 1993;140:614–8. doi: [10.1149/1.2056131](https://doi.org/10.1149/1.2056131).
- [105] Bumroongsakulsawat P, Kelsall GH. Tinned graphite felt cathodes for scale-up of electrochemical reduction of aqueous CO<sub>2</sub>. *Electrochim Acta* 2015;159:242–51. doi: [10.1016/j.electacta.2015.01.209](https://doi.org/10.1016/j.electacta.2015.01.209).
- [106] Jhong H-RM, Tornow CE, Smid B, Gewirth AA, Lyth SM, Kenis PJA. A nitrogen-doped carbon catalyst for electrochemical CO<sub>2</sub> conversion to CO with high selectivity and current density. *ChemSusChem* 2017;10:1094–9. doi: [10.1002/cssc.201600843](https://doi.org/10.1002/cssc.201600843).
- [107] Delacourt C, Ridgway PL, Kerr JB, Newman J. Design of an electrochemical cell making syngas (CO+H<sub>2</sub>) from CO<sub>2</sub> and H<sub>2</sub>O reduction at room temperature. *J Electrochem Soc* 2008;155:B42–9. doi: [10.1149/1.2801871](https://doi.org/10.1149/1.2801871).
- [108] Alvarez-Guerra M, Albo J, Alvarez-Guerra E, Irbaien A. Ionic liquids in the electrochemical valorisation of CO<sub>2</sub>. *Energy Environ Sci* 2015;8:2574–99. doi: [10.1039/C5EE01486G](https://doi.org/10.1039/C5EE01486G).
- [109] Rosen BA, Salehi-khojin A, Thorson MR, Zhu W, Whipple DT, Kenis PJA, et al. Ionic liquid-mediated selective conversion of CO<sub>2</sub> to CO at low overpotentials. *Science* 2011;334:643–4. doi: [10.1126/science.1209786/DC1](https://doi.org/10.1126/science.1209786/DC1).
- [110] Sen S, Liu D, Palmore TR. Electrochemical reduction of CO<sub>2</sub> at copper nanofoams. *ACS Catal* 2014;4:3091–5. doi: [10.1021/cs500522g](https://doi.org/10.1021/cs500522g).
- [111] Kriescher SMA, Kugler K, Hosseiny SS, Gendel Y, Wessling M. A membrane electrode assembly for the electrochemical synthesis of hydrocarbons from CO<sub>2(g)</sub> and H<sub>2</sub>O<sub>(g)</sub>. *Electrochem Commun* 2015;50:64–8. doi: [10.1016/j.elecom.2014.11.014](https://doi.org/10.1016/j.elecom.2014.11.014).
- [112] Wang Q, Dong H, Yu H. Development of rolling tin gas diffusion electrode for carbon dioxide electrochemical reduction to produce formate in aqueous electrolyte. *J Power Sources* 2014;271:278–84. doi: [10.1016/j.jpowsour.2014.08.017](https://doi.org/10.1016/j.jpowsour.2014.08.017).
- [113] Agarwal AS, Zhai Y, Hill D, Sridhar N. The electrochemical reduction of carbon dioxide to formate/formic acid: engineering and economic feasibility. *ChemSusChem* 2011;4:1301–10. doi: [10.1002/cssc.201100220](https://doi.org/10.1002/cssc.201100220).
- [114] McCrory CCL, Jung S, Peters JC, Jaramillo TF. Benchmarking heterogeneous electrocatalysts for the oxygen evolution reaction. *J Am Chem Soc* 2013;135:16977–87. doi: [10.1021/ja407115p](https://doi.org/10.1021/ja407115p).

- [115] Gasteiger HA, Kocha SS, Sompalli B, Wagner FT. Activity benchmarks and requirements for Pt, Pt-alloy, and non-Pt oxygen reduction catalysts for PEMFCs. *Appl Catal B Environ* 2005;56:9–35. doi: [10.1016/j.apcatb.2004.06.021](https://doi.org/10.1016/j.apcatb.2004.06.021).
- [116] Makharia R, Kocha S, Yu P, Sweikart MA, Gu W, Wagner F, et al. Durable PEM fuel cell electrode materials: Requirements and benchmarking methodologies. *ECS Trans* 2006;1:3–18. doi: [10.1149/1.2214540](https://doi.org/10.1149/1.2214540).
- [117] Chen Z, Jaramillo TF, Deutsch TG, Kleiman-Shwarscstein A, Forman AJ, Gaillard N, et al. Accelerating materials development for photoelectrochemical hydrogen production: Standards for methods, definitions, and reporting protocols. *J Mater Res* 2010;25:3–16. doi: [10.1557/jmr.2010.0020](https://doi.org/10.1557/jmr.2010.0020).
- [118] McCrory CCL, Jung S, Ferrer IM, Chatman SM, Peters JC, Jaramillo TF. Benchmarking hydrogen evolving reaction and oxygen evolving reaction electrocatalysts for solar water splitting devices. *J Am Chem Soc* 2015;137:4347–57. doi: [10.1021/ja510442p](https://doi.org/10.1021/ja510442p).
- [119] Doña Rodríguez JM, Herrera Melián JA, Pérez Peña J. Determination of the real surface area of Pt electrodes by hydrogen adsorption using cyclic voltammetry. *J Chem Educ* 2000;77:1195–7. doi: [10.1021/ed077p1195](https://doi.org/10.1021/ed077p1195).
- [120] Hsieh Y-C, Senanayake SD, Zhang Y, Xu W, Polyansky DE. Effect of chloride anions on the synthesis and enhanced catalytic activity of silver nanocoral electrodes for CO<sub>2</sub> electroreduction. *ACS Catal* 2015;5:5349–56. doi: [10.1021/acscatal.5b01235](https://doi.org/10.1021/acscatal.5b01235).
- [121] Yuan X, Wang H, Colinsun J, Zhang J. AC impedance technique in PEM fuel cell diagnosis—a review. *Int J Hydrogen Energy* 2007;32:4365–80. doi: [10.1016/j.ijhydene.2007.05.036](https://doi.org/10.1016/j.ijhydene.2007.05.036).
- [122] van der Vliet D, Strmcnik DS, Wang C, Stamenkovic VR, Markovic NM, Koper MTM. On the importance of correcting for the uncompensated Ohmic resistance in model experiments of the Oxygen Reduction Reaction. *J Electroanal Chem* 2010;647:29–34. doi: [10.1016/j.jelechem.2010.05.016](https://doi.org/10.1016/j.jelechem.2010.05.016).
- [123] Pougin A, Dilla M, Strunk J. Identification and exclusion of intermediates of photocatalytic CO<sub>2</sub> reduction on TiO<sub>2</sub> under conditions of highest purity. *Phys Chem Chem Phys* 2016;18:3–4. doi: [10.1039/C5CP07148H](https://doi.org/10.1039/C5CP07148H).
- [124] Huang L, Sorte EG, Sun S, Tong YY. A straightforward implementation of in situ solution electrochemical <sup>13</sup>C NMR spectroscopy for studying reactions on commercial electrocatalysts: ethanol oxidation. *Chem Commun* 2015;51:8086–8. doi: [10.1039/C5CC00862J](https://doi.org/10.1039/C5CC00862J).
- [125] Clark EL, Singh MR, Kwon Y, Bell AT. Differential electrochemical mass spectrometer cell design for online quantification of products produced during electrochemical reduction of CO<sub>2</sub>. *Anal Chem* 2015;87:8013–20. doi: [10.1021/acs.analchem.5b02080](https://doi.org/10.1021/acs.analchem.5b02080).
- [126] Del Castillo A, Alvarez-Guerra M, Irabien A. Continuous electroreduction of CO<sub>2</sub> to formate using Sn gas diffusion electrodes. *AIChE J* 2014;60:3557–64. doi: [10.1002/aic.14544](https://doi.org/10.1002/aic.14544).
- [127] Shao Y, Yin G, Gao Y. Understanding and approaches for the durability issues of Pt-based catalysts for PEM fuel cell. *J Power Sources* 2007;171:558–66. doi: [10.1016/j.jpowsour.2007.07.004](https://doi.org/10.1016/j.jpowsour.2007.07.004).
- [128] Wu J, Sun SG, Zhou XD. Origin of the performance degradation and implementation of stable tin electrodes for the conversion of CO<sub>2</sub> to fuels. *Nano Energy* 2016;27:225–9. doi: [10.1016/j.nanoen.2016.06.028](https://doi.org/10.1016/j.nanoen.2016.06.028).
- [129] Zeng K, Zhang D. Recent progress in alkaline water electrolysis for hydrogen production and applications. *Prog Energy Combust Sci* 2010;36:307–26. doi: [10.1016/j.pecs.2009.11.002](https://doi.org/10.1016/j.pecs.2009.11.002).
- [130] Ferreira RB, Falcão DS, Oliveira VB, Pinto AMFR. Experimental study on the membrane electrode assembly of a proton exchange membrane fuel cell: effects of microporous layer, membrane thickness and gas diffusion layer hydrophobic treatment. *Electrochim Acta* 2017;224:337–45. doi: [10.1016/j.electacta.2016.12.074](https://doi.org/10.1016/j.electacta.2016.12.074).
- [131] White JL, Baruch MF, Pander JE, Hu Y, Fortmeyer IC, Park JE, et al. Light-driven heterogeneous reduction of carbon dioxide: photocatalysts and photoelectrodes. *Chem Rev* 2015;115:12888–935. doi: [10.1021/acs.chemrev.5b00370](https://doi.org/10.1021/acs.chemrev.5b00370).
- [132] Ampelli C, Centi G, Passalacqua R, Perathoner S. Electrolyte-less design of PEC cells for solar fuels: prospects and open issues in the development of cells and related catalytic electrodes. *Catal Today* 2016;259:246–58. doi: [10.1016/j.cattod.2015.07.020](https://doi.org/10.1016/j.cattod.2015.07.020).
- [133] Rajeshwar K. Electron transfer at semiconductor–electrolyte interfaces. In: Balzani V, editor. *Electron transfer in chemistry*. Weinheim: Wiley-VCH; 2001. doi: [10.1002/9783527618248.ch53](https://doi.org/10.1002/9783527618248.ch53).
- [134] Gimenez S, Bisquert J. Photoelectrochemical solar fuel production, from basic principles to advanced devices. Springer; 2016. doi: [10.1007/978-3-319-29641-8](https://doi.org/10.1007/978-3-319-29641-8).
- [135] Thompson JF, Chen B, Kubo M, Londono N, Minuzzo J. Artificial photosynthesis device development for CO<sub>2</sub> photoelectrochemical conversion. *MRS Adv* 2016;1:447–52. doi: [10.1557/adv.2016.111](https://doi.org/10.1557/adv.2016.111).
- [136] Ampelli C, Centi G, Passalacqua R, Perathoner S. Synthesis of solar fuels by a novel photoelectrocatalytic approach. *Energy Environ Sci* 2010;3:292–301. doi: [10.1039/c003390c](https://doi.org/10.1039/c003390c).
- [137] Parkinson B. On the efficiency and stability of photoelectrochemical devices. *Acc Chem Res* 1984;17:431–7. doi: [10.1021/ar00108a004](https://doi.org/10.1021/ar00108a004).
- [138] Walter MG, Warren EL, McKone JR, Boettcher SW, Mi Q, Santori EA, et al. Solar water splitting cells. *Chem Rev* 2010;110:6446–73. doi: [10.1021/cr1002326](https://doi.org/10.1021/cr1002326).
- [139] Chen Z, Dinh HN, Miller E. Photoelectrochemical water splitting. *New York: Springer Briefs in Energy*; 2013. doi: [10.1007/978-1-4614-8298-7](https://doi.org/10.1007/978-1-4614-8298-7).
- [140] Herranz J, Durst J, Fabbri E, Patru A, Cheng X, Permyakova AA, et al. Interfacial effects on the catalysis of the hydrogen evolution, oxygen evolution and CO<sub>2</sub>-reduction reactions for (co-)electrolyzer development. *Nano Energy* 2016;29:4–28. doi: [10.1016/j.nanoen.2016.01.027](https://doi.org/10.1016/j.nanoen.2016.01.027).
- [141] Hudkins JR, Wheeler DG, Pen B, Berlinguette CP. Rapid prototyping of electrolyzer flow field plates. *Energy Environ Sci* 2016;9:3417–23. doi: [10.1039/C6EE01997H](https://doi.org/10.1039/C6EE01997H).
- [142] Sabatino S, Galia A, Saracco G, Scialdone O. Development of an electrochemical process for the simultaneous treatment of wastewater and the conversion of carbon dioxide to higher value products. *ChemElectroChem* 2017;4:150–9. doi: [10.1002/celec.201600475](https://doi.org/10.1002/celec.201600475).
- [143] Martínez-Huitle CA, Ferro S. Electrochemical oxidation of organic pollutants for the wastewater treatment: direct and indirect processes. *Chem Soc Rev* 2006;35:1324–40. doi: [10.1039/B517632H](https://doi.org/10.1039/B517632H).
- [144] Lister TE, Dufek EJ. Chlor-syngas: Coupling of electrochemical technologies for production of commodity chemicals. *Energy Fuels* 2013;27:4244–9. doi: [10.1021/ef302033j](https://doi.org/10.1021/ef302033j).
- [145] Karlsson RKB, Cornell A. Selectivity between oxygen and chlorine evolution in the chlor-alkali and chlorate processes. *Chem Rev* 2016;116:2982–3028. doi: [10.1021/acs.chemrev.5b00389](https://doi.org/10.1021/acs.chemrev.5b00389).
- [146] Moussallem I, Jorissen J, Kunz U, Pinnow S, Turek T. Chlor-alkali electrolysis with oxygen depolarized cathodes: history, present status and future prospects. *J Appl Electrochem* 2008;38:1177–94. doi: [10.1007/s10800-008-9556-9](https://doi.org/10.1007/s10800-008-9556-9).
- [147] Wu J, Risalvato FG, Ma S, Zhou X-D. Electrochemical reduction of carbon dioxide III. The role of oxide layer thickness on the performance of Sn electrode in a full electrochemical cell. *J Mater Chem A* 2014;2:1647–51. doi: [10.1039/c3ta13544f](https://doi.org/10.1039/c3ta13544f).

# A Victim of Halide Ion Segregation. How Light Soaking Affects Solar Cell Performance of Mixed Halide Lead Perovskites

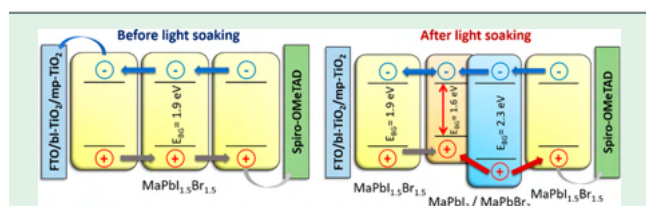
Gergely F. Samu,<sup>†,§,||</sup> Csaba Janáky,<sup>§,||</sup> and Prashant V. Kamat<sup>\*,†,‡,||</sup>

<sup>†</sup>Radiation Laboratory and <sup>‡</sup>Department of Chemistry and Biochemistry, University of Notre Dame, Notre Dame, Indiana 46556, United States

<sup>§</sup>Department of Physical Chemistry and Materials Science, University of Szeged, Rerrich Square 1, Szeged H-6720, Hungary

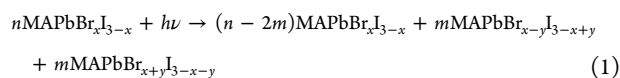
<sup>||</sup>MTA-SZTE “Lendület” Photoelectrochemistry Research Group, Rerrich Square 1, Szeged H-6720, Hungary

**S** Supporting Information



**ABSTRACT:** Photoinduced segregation in mixed halide perovskites has a direct influence on decreasing the solar cell efficiency as segregated I-rich domains serve as charge recombination centers. The changes in the external quantum efficiency mirror the spectral loss in the absorption; however, the time scale of the IPCE recovery in the dark is slower than the absorption recovery, showing the intricate nature of the photoinduced halide segregation and charge collection in solar cell devices.

The ability to tune the bandgap of mixed halide perovskites through halide composition is attractive to design solar cells with tailored response.<sup>1–3</sup> Halide ion migration in perovskite solar cells plays an important role in determining the overall photovoltaic performance.<sup>4–7</sup> Light soaking, for example, leads to migration of ions and vacancies toward the oxide interface, influencing the observed photovoltage.<sup>8</sup> Another property of the mixed halide lead perovskite is its ability to undergo phase segregation under continuous illumination.<sup>4,9–13</sup> For example, when methylammonium lead halide (Br/I, 1:1 ratio) is subjected to longer-term (>20 min) visible irradiation, it undergoes phase segregation to yield iodide-rich and bromide-rich domains (reaction 1)



Upon stopping the illumination, the segregated phase is restored to the original mixed phase.<sup>12–14</sup> It was also found that the excitation intensity and duration of irradiation determine the dark recovery.<sup>12,13</sup> These intriguing behaviors of mixed halide perovskites have led us to probe halide ion segregation on the

solar cell performance. The obvious question is, *What is the impact of longer-term light irradiation (or light soaking) on the performance of mixed halide perovskite cells?*

We prepared two sets of cells, one with a partial assembly excluding top gold contact and the other complete solar cell assembly using the same mixed halide perovskite deposition on a mesoporous TiO<sub>2</sub> film (see Scheme S1). The methylammonium lead halide films were cast using a stoichiometric composition with a Br/I ratio of 1:1. The partially assembled cell was used for absorption measurements. The absorption spectra recorded before and after 30 min of irradiation with visible light (100 mW/cm<sup>2</sup>) are shown in Figure 1A. The decrease in absorbance at 620 nm suggests the diminution of the mixed halide phase. The concurrent increase in the absorption at shorter and longer wavelengths represents formation of bromide-rich and iodide-rich phases. To better visualize this process, the difference absorption spectra were recorded during the dark recovery (Figure 1B). In about 3 h, we saw almost complete recovery of the mixed halide phase. Details of the absorption changes and recovery can be found in our earlier studies.<sup>12,13</sup>

The next step was to evaluate the photovoltaic performance of fully assembled solar cells. The champion cell we tested for these measurements yields a power conversion efficiency of 4.4%, an open-circuit voltage of 1.04 V, a short circuit current of 6.4 mA/cm<sup>2</sup>, and a fill factor of 66%. The cell was then subjected to visible light irradiation (100 mW/cm<sup>2</sup>) for 30 min under open-circuit conditions. This allowed us to induce halide ion segregation through visible light excitation (identical to the conditions in Figure 1A). Upon evaluation of *J–V* curves (Figure S1), we found a significant decrease in the solar cell performance with a *V*<sub>oc</sub> of 0.91 V and *J*<sub>sc</sub> of 4.2 mA/cm<sup>2</sup>, resulting in a net photoconversion efficiency of 1.4%. This phenomenon was also observable for different cells irradiated for 15 and 30 min (as seen in Figure S2).

We also recorded IPCE spectra at different times as the cell recovered in the dark (Figure 1C). The IPCE spectrum recorded immediately after 30 min of irradiation shows a nearly 50% drop

Received: July 5, 2017

Accepted: July 24, 2017

Published: July 24, 2017

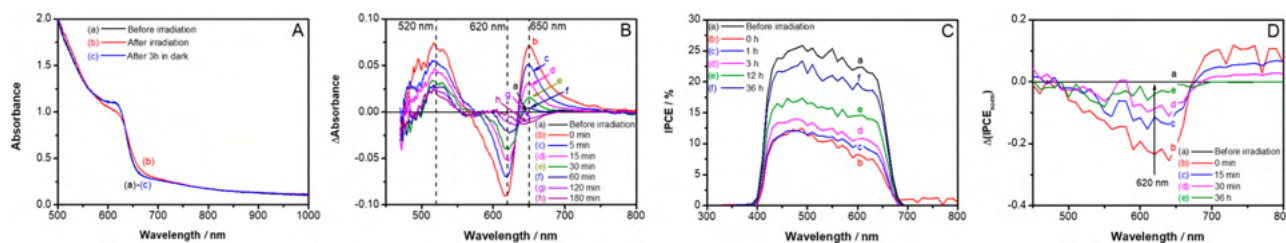


**Figure 1.** (A) Absorption spectra of a mixed halide perovskite film (a) before and (b) after irradiation for 30 min. (c) Dark recovery after 3 h. (B) Difference absorption spectra after 30 min of light soaking show dark recovery. (C) External quantum efficiency (IPCE) of a mixed halide perovskite solar cell (a) before light soaking and (b–f) during dark recovery following 30 min of light soaking. (A 420 nm cutoff filter was used for IPCE measurements, and residual dark currents were corrected for IPCE measurements). (D) Difference IPCE spectra showing the recovery of the solar cell response in the 600–700 nm region. (The spectra were normalized at 470 nm, and the IPCE was recorded before the continuous irradiation was used as the reference.)

in IPCE. The IPCE spectra were seen to recover slowly as we left the cell in the dark. Almost 90% of the recovery was seen in 36 h. This recovery time is notably longer than the recovery time scale we see in the absorption spectra (see Figure S3). The quick absorption recovery is indicative of the fact that the majority of the segregated phases have reversed back. However, the slower recovery in IPCE indicates that a few remaining charge carrier traps that are not captured through absorption changes are responsible for poor charge carrier extraction. This difference in the recovery time thus suggests the necessity of longer time to alleviate residual traps following light-induced halide ion segregation.

The drop in the IPCE response at longer wavelengths appears to be greater than that at shorter wavelengths. To obtain a closer look at this phenomenon, we recorded difference IPCE spectra at different recovery times following normalization (Figure 1D). The difference IPCE spectra recorded immediately after the 30 min irradiation of the solar cell shows depletion in the 550–680 nm region with a maximum at around 620 nm. This depletion in IPCE matches closely the decreased absorbance seen in the absorption spectrum after irradiation. This result confirms that the loss of contribution in the IPCE at longer wavelengths arises from the fraction of mixed halide that is lost in the segregation process. As we continue the recovery process in the dark, this depleted IPCE (500–670 nm) region recovers. This recovery of IPCE performance parallels the reversibility seen in the photoinduced segregation (see, for example, Figure 1A, B). It is important to note that the irradiated MAPbI<sub>3</sub> solar cells do not show such loss of IPCE response in the red region (see Figure S4).

The observed decrease in IPCE following 30 min of light soaking of mixed halide film arises from halide ion segregation and not from film degradation (both the absorption properties and IPCE recover almost completely when left in the dark). As noted in our previous study, the low-lying I-rich phase serves as a sink for photogenerated electrons and holes.<sup>12</sup> The gain in the IPCE at wavelengths greater than 700 nm is rather small and cannot account for the loss that we see in the 500–670 nm region. We attribute this discrepancy to the halide ion segregated domains within the film that block the flow of charge carriers. While the conduction bands of mixed halide and segregated phases are isoenergetic, the valence bands show an energy gradient causing the I-rich region to favor the hole accumulation (see the abstract graphic). The I-rich domains thus serve as recombination centers resulting in an eventual decrease in the IPCE and overall photoconversion efficiency.<sup>10,12,15</sup> As the mixed films recover in the dark, these recombination centers are removed and we see recovery of photovoltaic performance.

To summarize, the photoinduced segregation seen in mixed halide films makes the photovoltaic performance of perovskite solar cells less efficient as I-rich domains block the flow of charge carriers and promote charge carrier recombination. The dark reversibility is a silver lining here, and one should focus on speeding up the dark recovery time. Indeed, increased halide concentration is one way to speed up the dark recovery and minimize segregation effects.

## ■ ASSOCIATED CONTENT

### Supporting Information

The Supporting Information is available free of charge on the ACS Publications website at DOI: 10.1021/acsenergylett.7b00589.

Experimental methods including film preparation, solar cell fabrication, and related spectroscopic and photovoltaic measurements (PDF)

## ■ AUTHOR INFORMATION

### Corresponding Author

\*E-mail: pkamat@nd.edu. Twitter: @kamatlabND.

### ORCID

Csaba Janáky: 0000-0001-5965-5173

Prashant V. Kamat: 0000-0002-2465-6819

### Notes

The authors declare no competing financial interest.

## ■ ACKNOWLEDGMENTS

See the Supporting Information.

## ■ REFERENCES

- (1) McMeekin, D. P.; et al. *Science* **2016**, *351*, 151–155.
- (2) Jesper Jacobsson, T.; et al. *Energy Environ. Sci.* **2016**, *9*, 1706–1724.
- (3) Klein-Kedem, N.; et al. *Acc. Chem. Res.* **2016**, *49*, 347–354.
- (4) Slotcavage, D. J.; et al. *ACS Energy Lett.* **2016**, *1*, 1199–1205.
- (5) Mosconi, E.; et al. *ACS Energy Lett.* **2016**, *1*, 182–188.
- (6) Eames, C.; et al. *Nat. Commun.* **2015**, *6*, 7497.
- (7) Barker, A. J.; et al. *ACS Energy Lett.* **2017**, *2*, 1416–1424.
- (8) Hu, J.; et al. *ACS Energy Lett.* **2017**, *2*, 950–956.
- (9) Brivio, F.; et al. *J. Phys. Chem. Lett.* **2016**, *7*, 1083–1087.
- (10) Hoke, E. T.; et al. *Chem. Sci.* **2015**, *6*, 613–617.
- (11) Hentz, O.; et al. *Nano Lett.* **2016**, *16*, 1485–1490.
- (12) Yoon, S. J.; et al. *ACS Energy Lett.* **2016**, *1*, 290–296.
- (13) Yoon, S. J.; et al. *ACS Energy Lett.* **2017**, *2*, 1507–1514.
- (14) Bischak, C. G.; et al. *Nano Lett.* **2017**, *17*, 1028–1033.
- (15) Hoffman, J. B.; et al. *J. Am. Chem. Soc.* **2016**, *138*, 8603–8611.



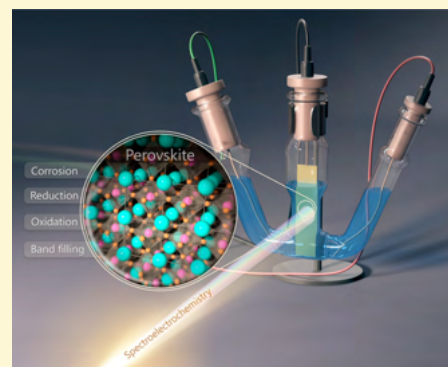


# Electrochemistry and Spectroelectrochemistry of Lead Halide Perovskite Films: Materials Science Aspects and Boundary Conditions

Gergely F. Samu,<sup>†,‡</sup> Rebecca A. Scheidt,<sup>†,§</sup> Prashant V. Kamat,<sup>\*,†,§,||</sup> and Csaba Janáky<sup>\*,†,§,||</sup><sup>†</sup>Radiation Laboratory, University of Notre Dame, Notre Dame, Indiana 46556, United States<sup>‡</sup>Department of Physical Chemistry and Materials Science, University of Szeged, Rerrich Square 1, Szeged, H-6720, Hungary<sup>§</sup>Department of Chemistry and Biochemistry, University of Notre Dame, Notre Dame, Indiana 46556, United States<sup>||</sup>ELI-ALPS Research Institute, Szeged, Dugonics sq. 13, 6720, Hungary

## Supporting Information

**ABSTRACT:** The unique optoelectronic properties of lead halide perovskites have triggered a new wave of excitement in materials chemistry during the past five years. Electrochemistry, spectroelectrochemistry, and photoelectrochemistry could be viable tools both for analyzing the optoelectronic features of these materials and for assembling them into hybrid architectures (e.g., solar cells). At the same time, the instability of these materials limits the pool of solvents and electrolytes that can be employed in such experiments. The focus of our study is to establish a stability window for electrochemical tests for all-inorganic CsPbBr<sub>3</sub> and hybrid organic–inorganic MAPbI<sub>3</sub> perovskites. In addition, we aimed to understand the reduction and oxidation events that occur and to assess the damage done during these processes at extreme electrochemical conditions. In this vein, we demonstrated the chemical, structural, and morphological changes of the films in both reductive and oxidative environments. Taking all these results together as a whole, we propose a set of boundary conditions and protocols for how electrochemical experiments with lead halide perovskites should be carried out and interpreted. The presented results will contribute to the understanding of the electrochemical response of these materials and lead to a standardization of results in the literature so that comparisons can more easily be made.



## INTRODUCTION

The discovery of the intriguing optoelectronic properties of lead halide perovskites has created excitement in various fields of materials science, especially in solar energy conversion.<sup>1,2</sup> While the most prominent application avenue for these materials is in solar cells, where the current certified record efficiency is held at 22.1%,<sup>3</sup> they have shown great promise as light-emitting diodes,<sup>4</sup> photodetectors,<sup>5</sup> and lasers.<sup>6</sup> The common virtue of all these applications is that charge carrier generation and transport are involved. Although electrochemistry is a simple tool to probe charge carrier formation and transport, there is surprisingly little precedence in the literature on this matter. Electrochemical experiments would be powerful tools to study the rich solid state chemistry aspects of perovskites,<sup>7</sup> where defects and grain boundaries as well as presence of minority phases could be monitored. In addition, investigation of the optoelectronic properties—including determination of band edge positions and trap state density mapping—would be possible to perform using spectroelectrochemistry. Electrochemical measurements could also contribute to the better understanding of chemical changes occurring at the various interfaces in perovskite solar cells.<sup>8</sup> Finally, electrochemical synthetic techniques could provide new

opportunities to assemble complex perovskite based architectures.

The infancy of perovskite electrochemistry is most likely rooted in the instability of the material in *almost all* commonly used solvents and electrolytes. Recently, a few studies employed electrochemistry for different purposes, such as probing Li<sup>+</sup> intercalation/deintercalation<sup>9,10</sup> and electrochemiluminescence measurements.<sup>11–13</sup> It was observed that charging/discharging studies need to be conducted with extreme caution because unintended side reactions may take place which would cause inaccuracies in the determined charge capacitance values.<sup>9,10,14,15</sup> Electrogenerated luminescence was reported with such materials, although the phenomenon is not fully understood yet.<sup>11–13</sup> In another recent paper, a solvent toolkit was proposed for these Li<sup>+</sup> intercalation experiments.<sup>16</sup> A very thorough study investigated the electron injection process into formamidinium lead halide perovskite using spectroelectrochemistry.<sup>17</sup> It was demonstrated in this study that it is very difficult, yet possible, to probe band edge positions via charge

Received: October 16, 2017

Revised: December 1, 2017

Published: December 5, 2017

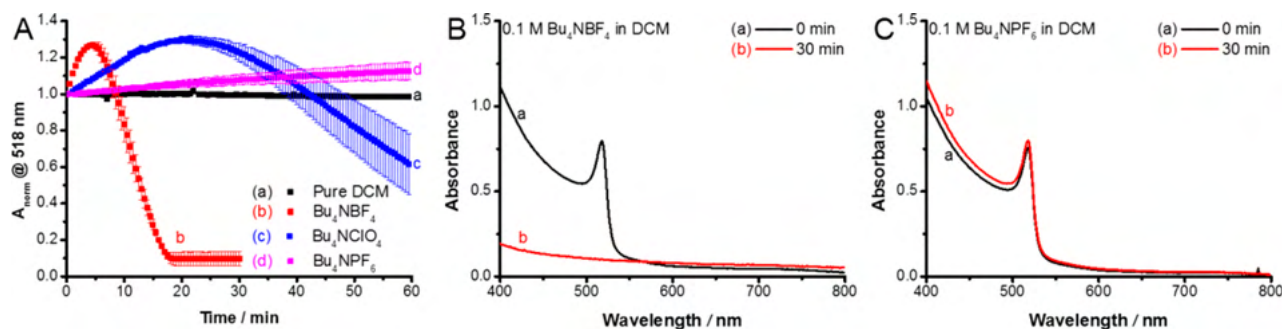


**Figure 1.** (A) Normalized absorbance change at 518 nm of FTO/TiO<sub>2</sub>/CsPbBr<sub>3</sub> electrode in DCM containing different electrolytes. The error bars were derived from measurements on three separate films. (B) and (C) show representative UV-vis spectra recorded before and after 30 min exposure to 0.1 M Bu<sub>4</sub>NBF<sub>4</sub>/DCM and 0.1 M Bu<sub>4</sub>NPF<sub>6</sub>/DCM solutions, respectively.

carrier injection. During these experiments, however, an irreversible electrochemical reduction occurred, thus making the picture even murkier.<sup>17</sup> An overview of the possible solution chemistry events was given, although without taking into account the likely contribution of the electrolyte ions. A similar approach was followed for mixed CsPbX<sub>3</sub> (X = Cl, Br, and I) perovskites, where it was assumed that band edge positions can be simply determined from voltammetric data.<sup>18</sup> The photoelectrochemical behavior of methylammonium lead iodide (MAPbI<sub>3</sub>) was probed in dichloromethane, in the presence of different reversible redox couples (e.g., ferrocene and benzoquinone). Cells showed high open-circuit voltage and remarkable stability for prolonged irradiation time in these systems.<sup>19,20</sup> Electrochemical impedance spectroscopy and Mott-Schottky analysis was also performed to estimate the charge carrier density and flatband potential of different optically active perovskites.<sup>19,21</sup> Most recently, we demonstrated the use of transient absorption spectroscopy under electrochemical control.<sup>22</sup>

Despite the above examples, solid and coherent knowledge about the fundamental electrochemical behavior of these materials is missing. Thus, the interpretation of results can be challenging. In this paper, the electrochemical behavior of the two most frequently studied perovskites (MAPbI<sub>3</sub> and CsPbBr<sub>3</sub>) is scrutinized in conventional electrolytes. The stability window was established, and the products formed during the redox transformation of these materials were analyzed. Elaborating on these results, guidelines are given to perform different (photo)electrochemical experiments, which can be later exploited in solar fuel generation or for the electrodeposition of a hole transporter material.

## EXPERIMENTAL SECTION

**Electrode Preparation.** To study practically relevant electrodes as model systems, CsPbBr<sub>3</sub> and MAPbI<sub>3</sub> were immobilized on TiO<sub>2</sub>-coated fluorine doped tin oxide (FTO) glass electrodes, thus mimicking the commonly used architecture in perovskite solar cells. During the electrochemical experiments, dichloromethane (DCM) was used as solvent while tetrabutyl ammonium tetrafluoroborate (Bu<sub>4</sub>NBF<sub>4</sub>), tetrabutyl ammonium perchlorate (Bu<sub>4</sub>NClO<sub>4</sub>), and tetrabutyl ammonium hexafluorophosphate (Bu<sub>4</sub>NPF<sub>6</sub>) were used as conducting electrolytes. All of these chemicals were carefully dried before use as described in the Supporting Information.

The electrode preparation process is detailed in the Supporting Information. Briefly, it comprises the following

steps. First, a TiO<sub>2</sub> blocking layer followed by a mesoporous TiO<sub>2</sub> layer was spin-coated on FTO slides. Subsequently, the FTO/bl-TiO<sub>2</sub>/mp-TiO<sub>2</sub> samples<sup>23</sup> were subjected to a TiCl<sub>4</sub> treatment step. The fabrication of the FTO/TiO<sub>2</sub>/MAPbI<sub>3</sub> electrodes followed the Lewis base adduct method.<sup>24</sup> The perovskite layers were obtained via the one-step method where the precursors were dissolved in dimethylformamide and were then spin-coated onto the FTO/bl-TiO<sub>2</sub>/mp-TiO<sub>2</sub> substrates. A hot injection method was used with Cs-oleate and PbBr<sub>2</sub> precursors to synthesize CsPbBr<sub>3</sub> nanocrystals (NCs).<sup>25</sup> Finally, bulk films were formed using subsequent deposition of the NCs on the substrate as demonstrated in previous reports.<sup>25</sup> The perovskite-coated electrodes were freshly prepared and kept in a glovebox before use.

**Characterization Methods.** Steady state UV-vis absorption spectra of the prepared electrodes were recorded with a Cary 50 Bio spectrophotometer (Varian). X-ray diffraction (XRD) patterns were collected using a Bruker D8 DISCOVER instrument with Cu K $\alpha$  X-ray source ( $\lambda = 1.5406\text{ \AA}$ ), in the 20–80° range, with a 2° min<sup>-1</sup> scan rate. Top-down and cross-sectional scanning electron microscopic (SEM) images were captured using a FEI Helios NanoLab DualBeam instrument. X-ray photoelectron spectra were acquired with a PHI VersaProbe II system. The binding energy scale was corrected by fixing the main C 1s component to 284.8 eV, corresponding to the adventitious carbon. For spectrum acquisition and evaluation, the MultiPak software was used. To fit the XP spectra and determine the elemental composition of the different samples a Shirley background was used. First the spectra of the pure CsPbBr<sub>3</sub> samples was fitted. From these fittings the profile shape, position, and full width at half maximum (FWHM) of the fitting functions were determined. For the electrochemically treated samples these fittings functioned as starting parameters, from which the shape and FWHM was held constant for each subsequent fitting. Small variation in the peak position was allowed for each fit. If the fitting was inadequate, another component was added to the process.

The electrochemical measurements were carried out with a Gamry potentiostat in a standard three-electrode setup (see the schematics of the setup in Scheme S1.). The FTO/TiO<sub>2</sub>/perovskite electrodes functioned as the working electrode, a Pt mesh (1 cm<sup>2</sup>) as the counterelectrode (cleaned by “Piranha solution”, water, and finally DCM), and a Ag/AgCl wire as a pseudoreference electrode. The homemade Ag/AgCl pseudoreference electrode was a Ag wire having AgCl deposited on its surface. This is generally applied in organic media, because it

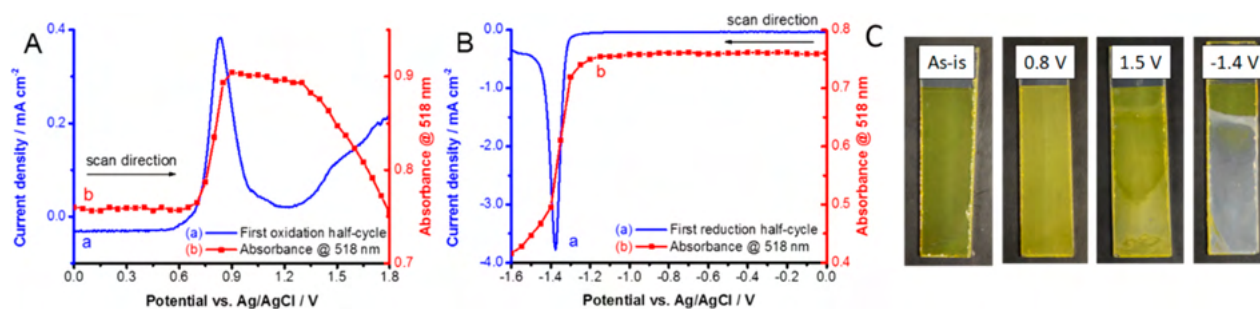


**Figure 2.** Spectroelectrochemical data, recorded for FTO/TiO<sub>2</sub>/CsPbBr<sub>3</sub> films in 0.1 M Bu<sub>4</sub>NPF<sub>6</sub>/dichloromethane electrolyte (10 mV s<sup>-1</sup> sweep rate), during the (A) oxidation and (B) reduction half cycle together with the absorbance change at the excitonic peak. (C) shows photographs of electrodes treated at selected potential values for 30 s.

can be considered as a secondary electrode, with very low chloride ion concentration. Its potential was calibrated before and after the experiments, by measuring the formal potential of the ferrocene/ferrocenium redox couple in dichloromethane (0.01 M ferrocene and 0.1 M Bu<sub>4</sub>NPF<sub>6</sub>). Cyclic voltammetry was used, and the formal potential was found to be  $E = 0.45 \pm 0.04$  V vs our Ag/AgCl. All cells were assembled in a glovebox (N<sub>2</sub> atmosphere, H<sub>2</sub>O < 0.1 ppm, O<sub>2</sub> < 0.1 ppm) and sealed hermetically to ensure inert conditions.

## RESULTS AND DISCUSSION

After screening a large pool of solvents and electrolytes, we concluded that dichloromethane (DCM) is a viable candidate. Most perovskites are stable in this medium, and it readily dissolves commonly employed electrolytes. To probe the stability of the films, a series of UV-vis spectra was recorded in pure DCM as well as in each electrolyte for a period of 60 min (Figure S1). Normalized absorbance traces, measured at 518 nm (the excitonic peak of CsPbBr<sub>3</sub>), are compared in Figure 1A for the different electrolytes. After an initial absorbance increase, where the film becomes cloudy and slightly opaque, the films begin to dissolve. The rate of dissolution is related to the complexing ability of the anions as well as the specific interactions between the different anions in the solution and the cations in the perovskite lattice.<sup>26,27</sup> The following definite trend was found in the dissolution rate: BF<sub>4</sub><sup>-</sup> > ClO<sub>4</sub><sup>-</sup> ≫ PF<sub>6</sub><sup>-</sup>. Based on these observations, we have chosen Bu<sub>4</sub>NPF<sub>6</sub> for all further experiments. We note here that even trace amounts of water can completely ruin the stability of these samples (in our experiments the water content was always kept below 10 ppm). Therefore, electrochemical experiments involving lead halide perovskites should be conducted in an inert environment. This can be achieved by completing measurements either inside of a glovebox or inside of a sealed electrochemical cell that has been thoroughly purged. The latter option was used for all experiments discussed in this paper. Additionally, the water content of not only the pure solvents but also the solutions needs to be checked (e.g., by Karl Fischer titration), and additional drying steps should be employed if necessary.

In the next step, two separate spectroelectrochemical experiments were carried out, where the potential was scanned from the open circuit potential (OCP) value to both anodic and cathodic directions. Under positive (anodic) bias, the first oxidation wave was situated at 0.8 V, followed by a second oxidation peak starting at 1.3 V. In fact, this second wave is a sum of two peaks, as seen from the shoulder in Figure 2A. These redox events are reflected in distinct changes that occur in the optical behavior. During oxidation, the absorbance

increased below 530 nm in the first oxidation step with the onset of ~0.6 V. The shape of the absorbance increase (i.e., difference absorbance spectrum) mirrors the initial spectrum of the electrode which indicates that the perovskite structure is preserved in the film even with a surface etching phenomenon occurring which causes this increase in absorbance (Figure S2). In addition, the absorbance increase (and opacity) witnessed upon immersion into 0.1 M Bu<sub>4</sub>NPF<sub>6</sub> is also very similar (Figure S2). Overall, we think that this absorbance increase is not rooted in the formation of a new material, but in other physical factors (e.g., scattering) which enhance the absorption of the perovskite film. The absorbance drastically decreased during the second step (onset ~1.3 V). As for the reduction, there was a single redox peak centered at -1.4 V, where notably higher current densities were measured compared to the oxidative events. As a result of the reduction, there was a rapid decrease in the absorbance at the excitonic peak characteristic to the perovskite material (Figure 2B). In parallel, there was an increased noncharacteristic absorption in the whole wavelength range (Figure S3), which was also confirmed by the reflective metallic appearance of the film (Figure 2C).

The question naturally comes whether these peaks correspond to Faradaic events (i.e., reduction of ions) or they are simply related to electron and hole injection into the conduction and valence bands (CB and VB), respectively, and, thus, represent band energy values. To probe the possible changes in the CsPbBr<sub>3</sub> structure, the electrodes were polarized at  $E = -1.4$  V, +0.8 V, and +1.5 V for 30 s in 0.1 M Bu<sub>4</sub>NPF<sub>6</sub>/DCM solution. After carefully washing the electrodes with DCM and drying them in an argon stream, XPS measurements were carried out to analyze the chemical composition of the surface. Several important trends can be revealed by the careful analysis of the XPS spectra (Figure 3): (i) the intensity of the Br<sup>-</sup>-related signal decreased during all treatments and a new species developed during the reduction; (ii) the F<sup>-</sup> signal emerged upon oxidation and this trend was more pronounced for samples treated at more positive potentials; (iii) in parallel, a new electron-rich form of Cs<sup>+</sup> developed for the oxidized samples; and (iv) a new form of oxygen arose in the reduced sample (in addition to the adsorbed oxygen moieties).

Taking these trends together as a whole, we propose the following explanations. The obvious reduction reaction is the formation of Pb at negative potentials (as also confirmed by SEM-EDX analysis, shown later). Pb is partially reoxidized to PbO upon air exposure while preparing the electrode for XPS measurements, confirmed by both the Pb and the O signals. During oxidation, the Br<sup>-</sup> and Pb<sup>2+</sup> content is gradually lost due to the destruction of the CsPbBr<sub>3</sub> structure. In parallel the F<sup>-</sup>

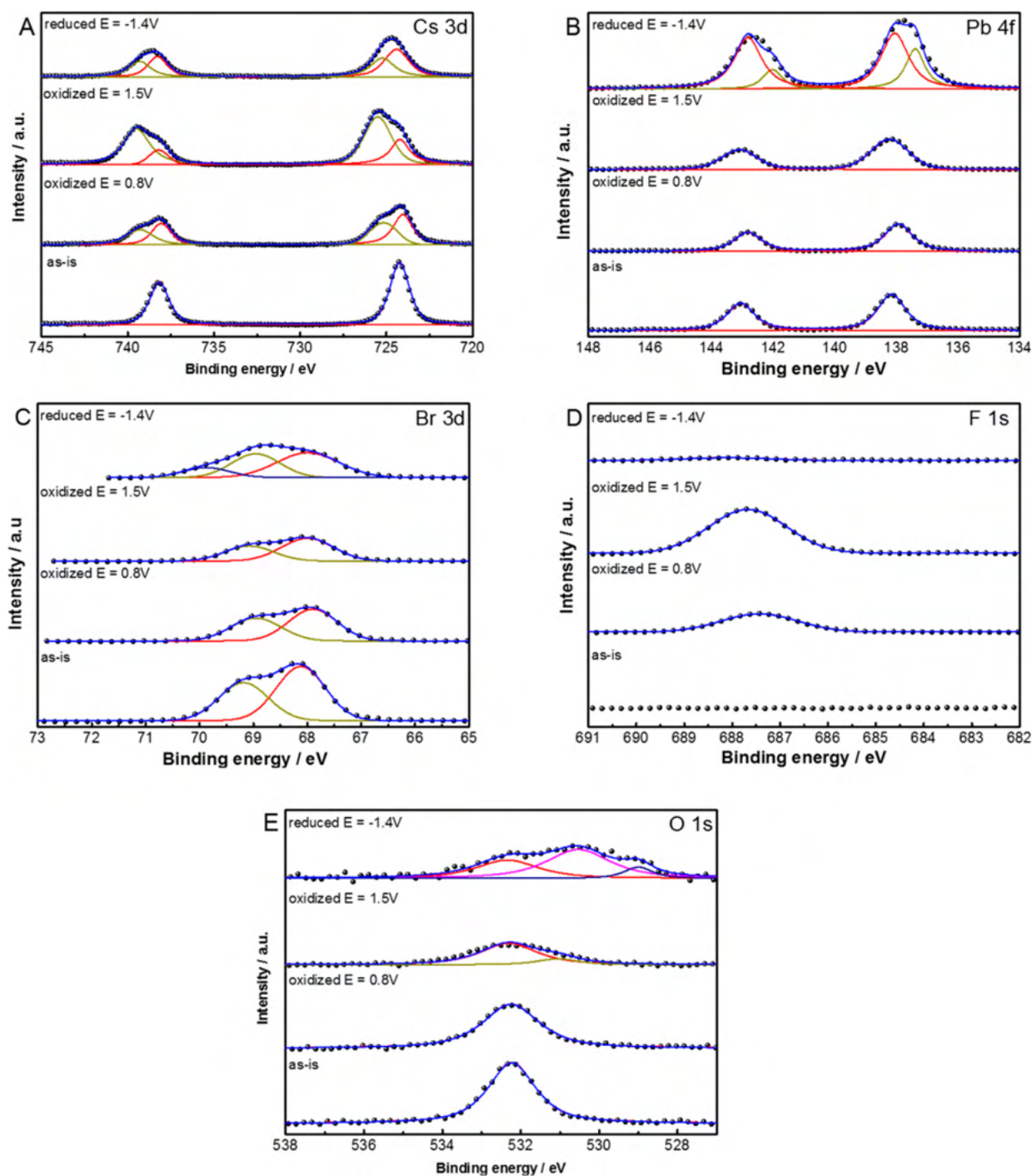


**Figure 3.** High resolution XPS data for the FTO/TiO<sub>2</sub>/CsPbBr<sub>3</sub> electrodes treated at selected potential values (as is, −1.4 V, +0.8 V, +1.5 V), for 30 s in 0.1 M Bu<sub>4</sub>NPF<sub>6</sub>/dichloromethane solution.

content (with a binding energy typical for PF<sub>6</sub><sup>−</sup>) increased significantly, suggesting the formation of CsPF<sub>6</sub> on the surface. This notion was further confirmed by SEM–EDX, which demonstrated the P content in the oxidized samples. These trends are quantified in Table 1, where the surface composition of the various samples is presented. The larger dispersion in the case of the reduced electrodes further confirmed the inhomogeneity of these samples, to be shown later on the SEM images.

To quantify the above-mentioned trends, we deconvoluted the spectra in Figure 3, which allowed for quantitative analysis

of the surface composition, and specifically to determine the amount of the various species. For example, upon the oxidation of CsPbBr<sub>3</sub>, we assume the formation of CsPF<sub>6</sub>. By analyzing the Cs 3d region, two distinct species were identified. By assigning the ones at 738.3 and 724.3 eV to CsPbBr<sub>3</sub> and the ones at 739.6 and 725.2 eV to CsPF<sub>6</sub>, we calculated the theoretical Br<sup>−</sup>, F<sup>−</sup>, and Pb<sup>2+</sup> content (Table S2). As seen in Table S2, a very good match was found between the measured and the calculated data.

To further confirm the above conclusions, XRD analysis was also performed. We consider XPS analysis to be more

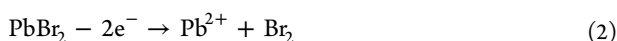
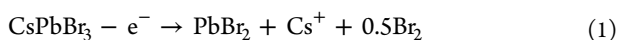
**Table 1.** Compositional Analysis of the Surface of the Electrochemically Treated FTO/TiO<sub>2</sub>/CsPbBr<sub>3</sub> Electrodes Using XPS<sup>a</sup>

sample	Br, atomic %	Cs, atomic %	Pb, atomic %	F, atomic %
as-is	59.9 ± 0.6	22.6 ± 1.0	17.5 ± 0.4	0
reduced (-1.4 V)	40.7 ± 2.7	20.6 ± 0.8	26.9 ± 5.7	11.8 ± 7.5
oxidized (0.8 V)	22.2 ± 1.8	15.9 ± 1.0	8.4 ± 0.7	53.6 ± 2.1
oxidized (1.5 V)	9.6 ± 1.0	14.3 ± 0.5	5.2 ± 0.9	71.0 ± 1.5

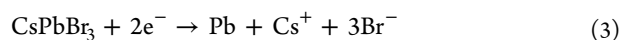
<sup>a</sup>The STD values were derived from analyzing XPS spectra captured from three different spots of the sample.

informative, due to the very small thickness of the films employed in this study. In addition, because of the complexity of the system and the large number of possible corrosion products, there are notable overlaps among the various diffractions. Because of these two factors, we only make qualitative conclusions, which are in line with the XPS data presented above. Figure 4 shows the XRD patterns of FTO/TiO<sub>2</sub>/CsPbBr<sub>3</sub> electrodes, held at the same potential values as those presented in Figure 3. The characteristic diffraction peaks of CsPbBr<sub>3</sub> were identified on all diffractograms at 15.3°, 21.7°, 26.6°, 30.8°, and 33.8° 2θ values.<sup>25</sup> Upon oxidation, a gradual decrease was witnessed in the intensity of these diffractions (Figure 4A), although because of the overlap of several diffractions this is not trivial for the first view. In addition, low intensity diffractions related to CsPF<sub>6</sub> developed at 2θ = 21.6, 30.7, and 36.4 (PDF: 00-034-0506). Note that the elemental composition deduced from XPS data semiquantitatively confirmed the formation of CsPF<sub>6</sub>. A substantial decrease in the intensity of the diffractions associated with CsPbBr<sub>3</sub> was seen as a result of the cathodic treatment. In addition, PbO-related diffraction peaks appeared (PDF: 00-085-1288), suggesting that the formed Pb is readily reoxidized to PbO upon air exposure.<sup>28</sup> Based on the above observations, the plausible reactions 1–3 are summarized below:

Oxidation:



Reduction:



To validate that the observed chemical changes are direct consequences of the redox events identified on the voltammetric scans (Figure 2A,B), control measurements were carried out at milder conditions, of which -0.4 V, 0.4 V, and simple immersion were chosen. As seen in Figure S4, there was no change when the electrode was placed into the solution and when only moderate bias was employed. Most importantly, only negligible amounts of F<sup>-</sup> were detected (due to physisorbed PF<sub>6</sub><sup>-</sup>), and the Br, Cs, Pb, and O elements were of identical chemical nature to those in the pristine sample (Figure S4). The quantitative surface composition analysis also supported these qualitative observations (Table S3).

The morphological changes that occurred during the redox events were visualized using SEM and SEM–FIB (to capture side-view images). The top view and cross-section images are compiled in Figure 5. The pristine sample has the granular morphology typically seen for CsPbBr<sub>3</sub> (Figure 5A), and it remains almost intact under mild electrochemical conditions (Figure S5). When the electrodes were exposed to more extreme electrochemical conditions (under the same circumstances as the samples discussed above), notable changes happened. Upon reduction, the particulate morphology disappeared and a compact film was formed at certain areas of the electrode (Figure 5B and Figure S6). At lower magnification, we could even observe formation of dendrites, and EDX analysis confirmed that the dendrites are made of Pb (Figure S6). During oxidation, rectangular particles were formed, which grew with the increasing potential (Figure 5C,D). For the sample held at 1.5 V bias potential, the underlying mesoporous TiO<sub>2</sub> became visible because of the destruction of the original perovskite film (Figure 5D). What is common in all cases is that the initial compact film turns into a porous one. Thus, the applied potential impacts the morphological changes to different extents (Figure 5 E–H). The side-view images provide similar insights: (i) the CsPbBr<sub>3</sub> disappears at certain areas and the TiO<sub>2</sub> becomes visible and (ii) a hollow structure is formed upon oxidation (Figure 5G and H), due to the dissolution of the perovskite.

To better understand the nature of these redox transformations, control experiments were carried out with FTO/

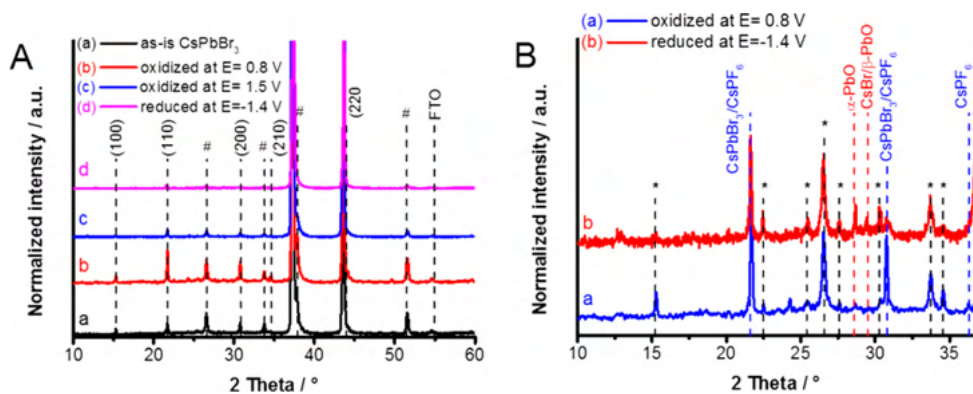


**Figure 4.** (A) XRD patterns for the FTO/TiO<sub>2</sub>/CsPbBr<sub>3</sub> electrodes treated at selected potential values (as is, -1.4 V, +0.8 V, +1.5 V) for 30 s in 0.1 M Bu<sub>4</sub>NPF<sub>6</sub>/dichloromethane solution. The peaks marked with # represent overlapping diffractions of CsPbBr<sub>3</sub> and the FTO/TiO<sub>2</sub> substrate. (B) Magnified regions of the diffraction patterns of the samples held at -1.4 V and +0.8 V. The peaks marked with \* belong to the untreated FTO/TiO<sub>2</sub>/CsPbBr<sub>3</sub> electrodes.

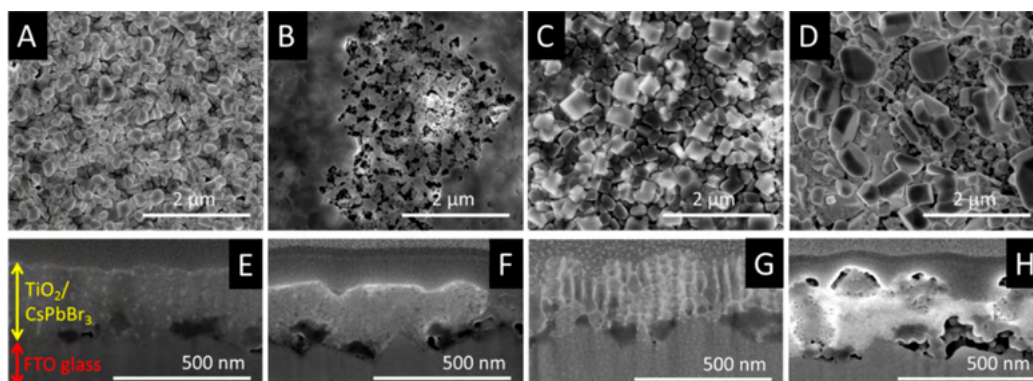


**Figure 5.** SEM images of CsPbBr<sub>3</sub> films both from the top and side views. (A, E) Pristine; (B, F) reduced at  $E = -1.4$  V; (C, G) oxidized at  $E = 0.8$  V, (D, H) oxidized at  $E = 1.4$  V. All treatments lasted 30 s in 0.1 M Bu<sub>4</sub>NPF<sub>6</sub>/dichloromethane solution.

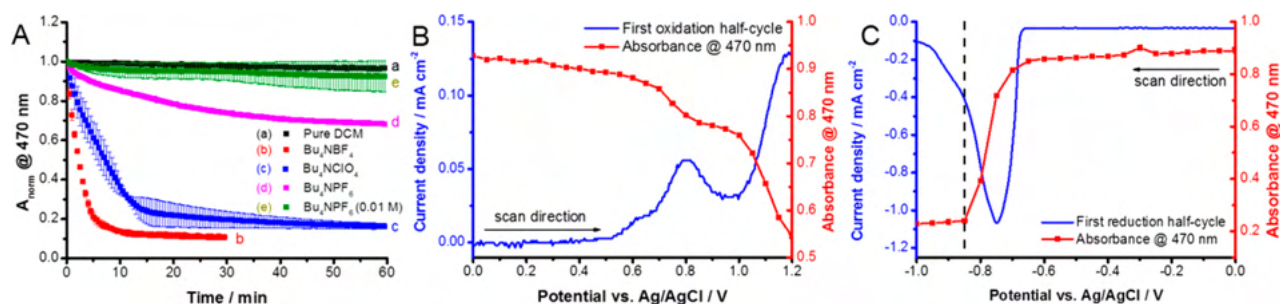


**Figure 6.** (A) Kinetic curves of the normalized absorbance change at 470 nm, recorded for FTO/TiO<sub>2</sub>/MAPbI<sub>3</sub> in different electrolytes. The error bars were derived from the measurement of three separate films. Spectroelectrochemical data, recorded for FTO/TiO<sub>2</sub>/MAPbI<sub>3</sub> films in 0.1 M Bu<sub>4</sub>NPF<sub>6</sub>/dichloromethane solution (10 mV s<sup>-1</sup> sweep rate), during the (B) oxidation and (C) reduction half cycles together with the absorbance changes at 470 nm.

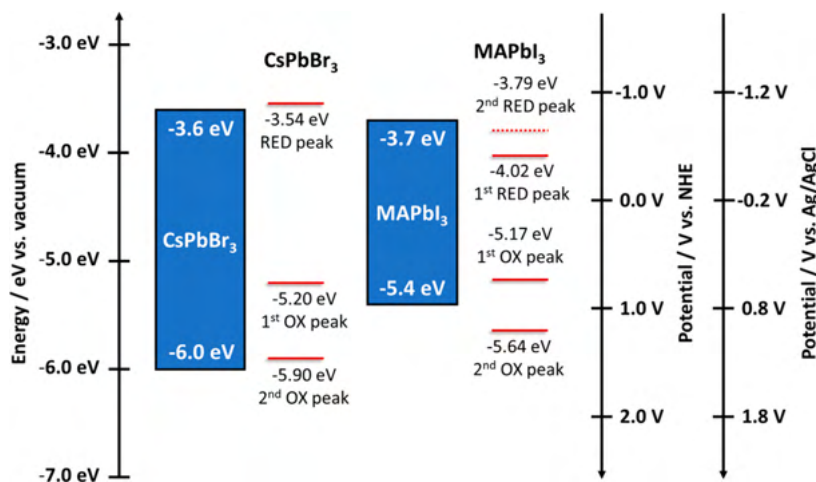


**Figure 7.** Comparison of the band edge positions and the potential of various redox events detected for the studied two lead halide perovskites.

TiO<sub>2</sub> and FTO/TiO<sub>2</sub>/PbBr<sub>2</sub> films (Figure S7). The PbBr<sub>2</sub> was more resistant toward oxidation, as the FTO/TiO<sub>2</sub>/PbBr<sub>2</sub> was stable up to 1.6 V (vs 0.7 V in the case of CsPbBr<sub>3</sub>). This suggests that only the third oxidation peak in Figure 2A is related to either PbBr<sub>2</sub> or the substrate, while the other two waves (at less positive potentials) are characteristic to CsPbBr<sub>3</sub>. As for the reduction, a more interesting trend was seen: the CsPbBr<sub>3</sub> was more stable than PbBr<sub>2</sub>, as this latter was reduced at 450 mV less negative potential.

To see whether the observed behavior is unique to CsPbBr<sub>3</sub> or if it is more general, we extended our study to MAPbI<sub>3</sub>. Largely, the stability of the films was worse in all electrolytes

studied in the present investigation (Figure 6A and Figure S8). However, the degradation trend at both positive and negative bias was the same as in the case of CsPbBr<sub>3</sub>. In addition, the initial absorbance increase (and any opacity) was not seen in this case. Since the stability obtained in 0.1 M Bu<sub>4</sub>NPF<sub>6</sub> solution was still not ideal, the electrolyte concentration was decreased to 0.01 M through which a reasonable lifetime was ensured (Figure 6A). Spectroelectrochemical studies revealed two oxidation and one reduction steps, at  $E = +0.8$  V,  $+1.1$  V, and  $-0.75$  V, respectively. Careful inspection of the cathodic wave revealed a shoulder at  $E = -0.95$  V. These redox events were coupled with a massive decrease in the absorbance related

to MAPbI<sub>3</sub>, and the degradation rate was especially high during reduction (Figure 6C and Figure S9). Similar to the previous example, control experiments were carried out with the PbI<sub>2</sub> films (Figure S10). Interestingly, PbI<sub>2</sub> was less resistant to oxidation compared to MAPbI<sub>3</sub>. Pb<sup>2+</sup> was reduced at the same potential in the case of each film (see Figures S9B and S10B), indicating the similar chemical nature of Pb<sup>2+</sup> in the two compounds. Further details related to the MAPbI<sub>3</sub> system are given in the Supporting Information.

Taking the above results together, we constructed a potential diagram (Figure 7) to compare the potentials of the various redox events, deduced from the spectroelectrochemical studies. The position of the redox events was always calculated from the onset potential of the redox waves. The band edge positions of the perovskite materials were obtained from previous literature data and serve semiquantitative comparison, because the film preparation methods were not identical.<sup>29,30</sup> This representation, together with the previously demonstrated structural analysis, allows the initial question of whether the currents measured during the voltammetric curves are related to charge carrier injection into the materials and/or to real Faradaic events to be answered. As for CsPbBr<sub>3</sub>, a good match can be revealed between the potential of the reduction peak and the CB edge as well as the second oxidation peak and the VB edge. More interestingly, the first oxidation peak occurs at a less positive potential than the VB, meaning that the CsPbBr<sub>3</sub> is irreversibly oxidized before hole injection can take place. Based on all the evidence gathered in this study, these potential values should be considered as cathodic and anodic corrosion potentials, respectively. There is a comparable situation in the case of MAPbI<sub>3</sub>, but here the second reduction peak matches the potential of the CB. This means that an irreversible chemical transformation occurs before the CB can be populated with electrons. These observations highlight the difference between the solar- and electrochemical cell scenarios because, in a solar cell, the photogenerated holes (in the case of CsPbBr<sub>3</sub>) and the electrons (in the case of MAPbI<sub>3</sub>) do not corrode the electrode material as they are transferred quickly to electron and hole transport layers (ETL and HTL). If not scavenged quickly, these electrons and holes can induce degradation based on the energy levels illustrated in Figure 7. Addition of an electron acceptor (redox mediator) to the solution can also increase the stability in a similar manner.<sup>17</sup>

**Best Practice for Pursuing Electrochemical Experiments with Metal Halide Perovskites.** To conduct electrochemical studies with metal halide perovskites in a reliable manner, the experiments need to comply with the basic principles of electrochemistry. One needs to carefully make the choice of the solvent, electrolyte, and electrochemical window to ensure the stability of the electrode within the time frame of the experiment. Given the sensitivity of perovskite films to polar solvents, one needs to exercise caution while drawing conclusions from the studies performed in aqueous media.<sup>11,12</sup> It should also be noted that conclusions obtained with certain special electrolytes, such as Li<sup>+</sup> or reversible redox couples<sup>19</sup> which are pertinent to certain specific applications, cannot be simply generalized. The researchers should provide data to support the stability test by monitoring the absorption and/or performing surface spectroscopy measurements before and after electrochemical measurements. This is the only way to ensure that the observed redox processes are chemically reversible. However, there is a safe electrochemical window to conduct electrochemical experiments. Based on our findings

one should be able to conduct the electrochemical or spectroelectrochemical experiments reliably by adopting the conditions presented in Table 2. Note that the records in this table are based on a wealth of experiments, of which only a minor fraction is presented in this paper.

**Table 2. Parameters to Conduct (Spectro)Electrochemical Experiments**

parameter	CsPbBr <sub>3</sub>	MAPbI <sub>3</sub>
electrochemical window	−1.0 to +0.6 V vs Ag/AgCl	−0.65 to +0.55 V vs Ag/AgCl
solvent	dichloromethane	dichloromethane
electrolyte	Bu <sub>4</sub> NPF <sub>6</sub> , ≤0.1 M	Bu <sub>4</sub> NPF <sub>6</sub> , ≤0.01 M
time window (maximum)	two hours	one hour
electrode substrate	FTO, FTO/TiO <sub>2</sub> , glassy carbon	FTO, FTO/TiO <sub>2</sub> , glassy carbon

In addition to the experimental considerations, careful analysis of the results is equally important. First of all, the electrochemical processes behind the measured redox waves must be clearly identified to draw meaningful conclusions. It should be decided whether the current response reflects a chemical (faradaic) process or simple charging/discharging (i.e., electron or hole injection). If it is a chemical process, one should study its chemical and electrochemical reversibility. Similarly, it should be clarified whether it is a redox process limited by mass-transport from the solution or a surface confined one. If there is certainly no process other than charge injection, then voltammetric curves can be employed to determine band edge positions. Similar to organic semiconductors,<sup>31</sup> however, the onsets of the redox peaks<sup>17</sup> and not the position of the peak maxima<sup>18</sup> have to be correlated with the respective band edge positions. Finally, during prolonged experiments migration of mobile ions within the perovskite structure might also happen thus complicating the picture even further.<sup>32</sup>

## CONCLUSIONS

In this study, we assessed the stability window of two different lead halide perovskites (CsPbBr<sub>3</sub> and MAPbI<sub>3</sub>) and analyzed the chemical changes during the anodic and cathodic redox waves. This is a crucially important exercise to perform before conducting any electrochemical experiment, such as Li<sup>+</sup> ion incorporation or photoelectrochemical studies. The two representative optically active perovskites show the importance of a case by case analysis that is necessary for each perovskite–electrolyte–solvent system. The complex solution and solid-state chemistry dictates the stability window of the given system. It is very important to underline that simple CV scans alone can hardly be employed to determine the band edge positions of these materials. To do so, one must be convinced that there is no other redox event associated with the redox peaks. Overall, under carefully planned conditions it is possible to study the electrochemical behavior of these materials and to gain a better understanding of their unique optoelectronic properties.

## ■ ASSOCIATED CONTENT

### Supporting Information

The Supporting Information is available free of charge on the ACS Publications website at DOI: [10.1021/acs.chemmater.7b04321](https://doi.org/10.1021/acs.chemmater.7b04321).

UV-vis spectra recorded in different electrolytes, additional spectroelectrochemical data, additional SEM images and XPS data, and control measurements with  $\text{PbBr}_2$  and  $\text{PbI}_2$  (PDF)

## ■ AUTHOR INFORMATION

### Corresponding Authors

\*(P.V.K.) E-mail: [pkamat@nd.edu](mailto:pkamat@nd.edu).

\*(C.J.) E-mail: [janaky@chem.u-szeged.hu](mailto:janaky@chem.u-szeged.hu).

### ORCID

Prashant V. Kamat: 0000-0002-2465-6819

Csaba Janáky: 0000-0001-5965-5173

### Notes

The authors declare no competing financial interest.

## ■ ACKNOWLEDGMENTS

The authors thank Dr. Tatyana Orlova for taking the SEM images, Steven M. Kobosko for recording the XPS spectra, and Dr. Allen G. Oliver for recording the XRD patterns. We thank the ND Energy Materials Characterization Facility (MCF) for the use of the PHI VersaProbe II system. The MCF is funded by the Sustainable Energy Initiative (SEI), which is part of the Center for Sustainable Energy at Notre Dame (ND Energy). This project has received funding from the European Research Council (ERC) under the European Union's Horizon 2020 research and innovation program (Grant Agreement No. 716539). ELI-ALPS is supported by the European Union and cofinanced by the European Regional Development Fund (GOP-1.1.1-12/B-2012-000, GINOP-2.3.6-15-2015-00001). The authors also thank Rendernet Ltd. for assistance in preparing the artwork in the TOC. P.V.K. acknowledges the support by the Division of Chemical Sciences, Geosciences, and Biosciences, Office of Basic Energy Sciences, of the U.S. Department of Energy, through award DE-FC02-04ER15533. R.A.S. acknowledges the support of King Abdullah University of Science and Technology (KAUST) through Award OCF-2014-CRG3-2268. This is NDRL No. 5190 from Notre Dame Radiation Laboratory.

## ■ REFERENCES

- (1) Manser, J. S.; Christians, J. A.; Kamat, P. V. Intriguing Optoelectronic Properties of Metal Halide Perovskites. *Chem. Rev.* **2016**, *116*, 12956–13008.
- (2) Park, N.-G. Organometal Perovskite Light Absorbers Toward a 20% Efficiency Low-Cost Solid-State Mesoscopic Solar Cell. *J. Phys. Chem. Lett.* **2013**, *4*, 2423–2429.
- (3) Yang, W. S.; Park, B.-W.; Jung, E. H.; Jeon, N. J.; Kim, Y. C.; Lee, D. U.; Shin, S. S.; Seo, J.; Kim, E. K.; Noh, J. H.; Seok, S. Il. Iodide Management in Formamidinium-Lead-Halide-based Perovskite Layers for Efficient Solar Cells. *Science* **2017**, *356*, 1376–1379.
- (4) Cho, H.; Jeong, S.-H.; Park, M.-H.; Kim, Y.-H.; Wolf, C.; Lee, C.-L.; Heo, J. H.; Sadhanala, A.; Myoung, N.; Yoo, S.; Im, S. H.; Friend, R. H.; Lee, T.-W. Overcoming the Electroluminescence Efficiency Limitations of Perovskite Light-Emitting Diodes. *Science* **2015**, *350*, 1222–1225.
- (5) Fang, Y.; Dong, Q.; Shao, Y.; Yuan, Y.; Huang, J. Highly Narrowband Perovskite Single-Crystal Photodetectors Enabled by Surface-Charge Recombination. *Nat. Photonics* **2015**, *9*, 679–686.

(6) Zhu, H.; Fu, Y.; Meng, F.; Wu, X.; Gong, Z.; Ding, Q.; Gustafsson, M. V.; Trinh, M. T.; Jin, S.; Zhu, X.-Y. Lead Halide Perovskite Nanowire Lasers with Low Lasing Thresholds and High Quality Factors. *Nat. Mater.* **2015**, *14*, 636–642.

(7) Manser, J. S.; Saidaminov, M. I.; Christians, J. A.; Bakr, O. M.; Kamat, P. V. Making and Breaking of Lead Halide Perovskites. *Acc. Chem. Res.* **2016**, *49*, 330–338.

(8) Zhao, L.; Kerner, R. A.; Xiao, Z.; Lin, Y. L.; Lee, K. M.; Schwartz, J.; Rand, B. P. Redox Chemistry Dominates the Degradation and Decomposition of Metal Halide Perovskite Optoelectronic Devices. *ACS Energy Lett.* **2016**, *1*, 595–602.

(9) Dawson, J. A.; Naylor, A. J.; Eames, C.; Roberts, M.; Zhang, W.; Snaith, H. J.; Bruce, P. G.; Islam, M. S. Mechanisms of Lithium Intercalation and Conversion Processes in Organic-Inorganic Halide Perovskites. *ACS Energy Lett.* **2017**, *2*, 1818–1824.

(10) Jiang, Q.; Chen, M.; Li, J.; Wang, M.; Zeng, X.; Besara, T.; Lu, J.; Xin, Y.; Shan, X.; Pan, B.; Wang, C.; Lin, S.; Siegrist, T.; Xiao, Q.; Yu, Z. Electrochemical Doping of Halide Perovskites with Ion Intercalation. *ACS Nano* **2017**, *11*, 1073–1079.

(11) Huang, Y.; Fang, M.; Zou, G.; Zhang, B.; Wang, H. Monochromatic and Electrochemically Switchable Electrochemiluminescence of Perovskite  $\text{CsPbBr}_3$  Nanocrystals. *Nanoscale* **2016**, *8*, 18734–18739.

(12) Tan, X.; Zhang, B.; Zou, G. Electrochemistry and Electrochemiluminescence of Organometal Halide Perovskite Nanocrystals in Aqueous Medium. *J. Am. Chem. Soc.* **2017**, *139*, 8772–8776.

(13) Huang, Y.; Long, X.; Shen, D.; Zou, G.; Zhang, B.; Wang, H. Hydrogen Peroxide Involved Anodic Charge Transfer and Electrochemiluminescence of All-Inorganic Halide Perovskite  $\text{CsPbBr}_3$  Nanocrystals in an Aqueous Medium. *Inorg. Chem.* **2017**, *56*, 10135–10138.

(14) Vicente, N.; Garcia-Belmonte, G. Methylammonium Lead Bromide Perovskite Battery Anodes Reversibly Host High Li-Ion Concentrations. *J. Phys. Chem. Lett.* **2017**, *8*, 1371–1374.

(15) Tathavadekar, M.; Krishnamurthy, S.; Banerjee, A.; Nagane, S.; Gawli, Y.; Suryawanshi, A.; Bhat, S.; Puthusseri, D.; Mohite, A. D.; Ogale, S. Low-Dimensional Hybrid Perovskites as High Performance Anodes for Alkali-Ion Batteries. *J. Mater. Chem. A* **2017**, *5*, 18634–18642.

(16) Hasan, M.; Venkatesan, S.; Lyashenko, D.; Slinker, J. D.; Zakhidov, A. Solvent Toolkit for Electrochemical Characterization of Hybrid Perovskite Films. *Anal. Chem.* **2017**, *89*, 9649–9653.

(17) Shallcross, R. C.; Zheng, Y.; Saavedra, S. S.; Armstrong, N. R. Determining Band-Edge Energies and Morphology-Dependent Stability of Formamidinium Lead Perovskite Films Using Spectroelectrochemistry and Photoelectron Spectroscopy. *J. Am. Chem. Soc.* **2017**, *139*, 4866–4878.

(18) Ravi, V. K.; Markad, G. B.; Nag, A. Band Edge Energies and Excitonic Transition Probabilities of Colloidal  $\text{CsPbX}_3$  ( $X = \text{Cl}, \text{Br}, \text{I}$ ) Perovskite Nanocrystals. *ACS Energy Lett.* **2016**, *1*, 665–671.

(19) Hsu, H.; Ji, L.; Ahn, H. S.; Zhao, J.; Yu, E. T.; Bard, A. J. A Liquid Junction Photoelectrochemical Solar Cell Based on p-Type  $\text{MeNH}_3\text{PbI}_3$  Perovskite with 1.05 V Open-Circuit Photovoltage. *J. Am. Chem. Soc.* **2015**, *137*, 14758–14764.

(20) Hsu, H.; Ji, L.; Du, M.; Zhao, J.; Yu, E. T.; Bard, A. J. Optimization of  $\text{PbI}_2/\text{MAPbI}_3$  Perovskite Composites by Scanning Electrochemical Microscopy. *J. Phys. Chem. C* **2016**, *120*, 19890–19895.

(21) Li, Z.; Mercado, C. C.; Yang, M.; Palay, E.; Zhu, K. Electrochemical Impedance Analysis of Perovskite-electrolyte Interfaces. *Chem. Commun.* **2017**, *53*, 2467–2470.

(22) Scheidt, R. A.; Samu, G. F.; Janáky, C.; Kamat, P. V. Modulation of Charge Recombination in  $\text{CsPbBr}_3$  Perovskite Films with Electrochemical Bias. *J. Am. Chem. Soc.* **2017**, DOI: [10.1021/jacs.7b10958](https://doi.org/10.1021/jacs.7b10958).

(23) Neale, N. R.; Frank, A. J. Size and Shape Control of Nanocrystallites in Mesoporous  $\text{TiO}_2$  Films. *J. Mater. Chem.* **2007**, *17*, 3216–3221.



- (24) Ahn, N.; Son, D.-Y.; Jang, I.-H.; Kang, S. M.; Choi, M.; Park, N.-G. Highly Reproducible Perovskite Solar Cells with Average Efficiency of 18.3% and Best Efficiency of 19.7% Fabricated via Lewis Base Adduct of Lead(II) Iodide. *J. Am. Chem. Soc.* **2015**, *137*, 8696–8699.
- (25) Hoffman, J. B.; Schleper, A. L.; Kamat, P. V. Transformation of Sintered CsPbBr<sub>3</sub> Nanocrystals to Cubic CsPbI<sub>3</sub> and Gradient CsPbBr<sub>x</sub>I<sub>3-x</sub> through Halide Exchange. *J. Am. Chem. Soc.* **2016**, *138*, 8603–8611.
- (26) Strauss, S. H. The Search for Larger and More Weakly Coordinating Anions. *Chem. Rev.* **1993**, *93*, 927–942.
- (27) Krossing, I.; Raabe, I. Noncoordinating Anions - Fact or Fiction? A Survey of Likely Candidates. *Angew. Chem., Int. Ed.* **2004**, *43*, 2066–2090.
- (28) Sawatani, S.; Ogawa, S.; Yoshida, T.; Minoura, H. Formation of Highly Crystallized  $\beta$ -PbO Thin Films by Cathodic Electrodeposition of Pb and Its Rapid Oxidation in Air. *Adv. Funct. Mater.* **2005**, *15*, 297–302.
- (29) Akkerman, Q. A.; Gandini, M.; Di Stasio, F.; Rastogi, P.; Palazon, F.; Bertoni, G.; Ball, J. M.; Prato, M.; Petrozza, A.; Manna, L. Strongly Emissive Perovskite Nanocrystal Inks for High-Voltage Solar Cells. *Nat. Energy* **2016**, *2*, 16194.
- (30) Schulz, P.; Edri, E.; Kirmayer, S.; Hodes, G.; Cahen, D.; Kahn, A. Interface Energetics in Organo-Metal Halide Perovskite-Based Photovoltaic Cells. *Energy Environ. Sci.* **2014**, *7*, 1377–1381.
- (31) Cardona, C. M.; Li, W.; Kaifer, A. E.; Stockdale, D.; Bazan, G. C. Electrochemical Considerations for Determining Absolute Frontier Orbital Energy Levels of Conjugated Polymers for Solar Cell Applications. *Adv. Mater.* **2011**, *23*, 2367–2371.
- (32) Bandiello, E.; Ávila, J.; Gil-Escrig, L.; Tekelenburg, E.; Sessolo, M.; Bolink, H. J. Influence of Mobile Ions on the Electroluminescence Characteristics of Methylammonium Lead Iodide Perovskite Diodes. *J. Mater. Chem. A* **2016**, *4*, 18614–18620.



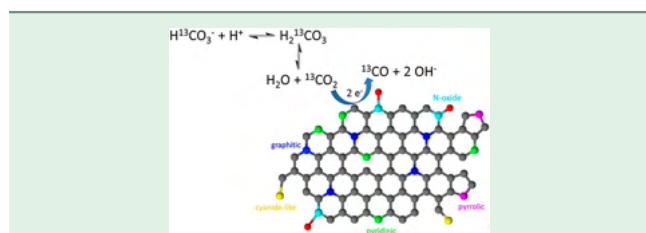
# Electrochemical Reduction of Carbon Dioxide on Nitrogen-Doped Carbons: Insights from Isotopic Labeling Studies

Dorottya Hursán<sup>†,‡</sup> and Csaba Janáky<sup>\*,†,‡,§</sup>

<sup>†</sup>Department of Physical Chemistry and Materials Science, University of Szeged, Rerrich Square 1, Szeged H-6720, Hungary

<sup>‡</sup>MTA-SZTE “Lendület” Photoelectrochemistry Research Group, Rerrich Square 1, Szeged H-6720, Hungary

**S** Supporting Information



**ABSTRACT:** Isotopic labeling experiments were performed to better understand the electrochemical reduction of carbon dioxide on nitrogen-doped porous carbon electrodes. By using nonequilibrated solutions of selectively labeled initial carbon sources (i.e.,  $^{13}\text{CO}_2$  and  $\text{H}^{13}\text{CO}_3^-$ ), bicarbonate anion was identified as the predominant source of the carbon monoxide reduction product.

Nitrogen-doped carbon materials are increasingly studied in energy-oriented electrochemical and photoelectrochemical reactions as active materials and conductive scaffolds.<sup>1</sup> After demonstrating their catalytic activity in the electrochemical oxygen reduction reaction,<sup>2,3</sup> there is growing interest toward  $\text{H}_2$  evolution<sup>4</sup> and  $\text{CO}_2$  conversion, too.<sup>5–9</sup> Impressive activities were reported in  $\text{CO}_2$  reduction, which makes these cheap materials potential rivals to their more expensive inorganic counterparts. Both experimental and theoretical studies investigated mechanistic aspects to identify the active center. The chemical nature of the C–N moiety seems to be a decisive factor, where pyridinic N and a C atom next to pyridinic N were the most active.<sup>6</sup> Despite the steeply growing number of papers on  $\text{CO}_2$  electroreduction using carbon-based electrodes, there are only a very few papers where any kind of isotopic labeling was performed to confirm the source of  $\text{CO}_2$  reduction products.<sup>5,9,10</sup> On the other hand, detailed studies were carried out on gold<sup>11</sup> and copper<sup>12</sup> electrodes, where the electroreduction process was monitored by surface-sensitive infrared spectroscopy and mass spectrometry. In other instances, NMR spectroscopy was employed to identify  $^{13}\text{C}$  in the liquid phase reduction products on gold and copper electrodes.<sup>13,14</sup> At the same time, the question still holds, what is the source of the assumed  $\text{CO}_2$  reduction products in such cases? The dissolved

$\text{CO}_2$ , the bicarbonate ions,  $\text{CO}_2$  furnished through the carbon dioxide–bicarbonate equilibrium, or the electrode material itself? To answer this question, we performed the *first systematic isotopic labeling study employing a N-doped carbon electrode*. The fact that it takes around 2 h to reach the equilibrium conditions between the bicarbonate ions and  $\text{CO}_2$  (Figure S2) allowed selective or joint labeling of the carbon sources ( $\text{CO}_2$  and  $\text{HCO}_3^-$ ), and electrogenerated CO was analyzed by GC–MS.

A highly porous, high surface area N-doped carbon catalyst (HPG-PPy) was synthesized by adaptation of a literature procedure<sup>15</sup> (see details in the SI). Product analysis during potentiostatic electrolysis revealed the formation of CO and  $\text{H}_2$  as main products (Figure S1D). The amounts of CO and  $\text{H}_2$  were similar at moderate overpotentials (–0.61 and –0.71 V) and scaled linearly with the reduction charge (Figure 1A). First, joint isotopic labeling experiments (i.e., both the  $\text{CO}_2$  gas- and bicarbonate-labeled) were carried out, and the exclusive formation of  $^{13}\text{CO}$  confirmed that indeed the  $\text{CO}_2$ /bicarbonate feedstock was converted (Figure S3). To have a deeper understanding of the  $\text{CO}_2$  reduction mechanism on the carbon catalyst, especially to find out whether the bicarbonate or the aqueous  $\text{CO}_2$  is the reacting species, the two carbon sources were selectively labeled. When the bicarbonate was the labeled component and we were operating under nonequilibrium conditions (see SI section 1.3 for details), in the first hour of electrolysis, the majority of the CO was  $^{13}\text{C}$ -labeled. Within this time frame, the isotopic equilibrium was not yet established between bicarbonate ions and  $\text{CO}_2$  gas (Figure S2). The  $^{13}\text{CO}/^{12}\text{CO}$  ratio gradually decreased and approached the ratio characteristic of the equilibrium conditions during the 2 h electrolysis (Figure 1B). On the other hand, when the  $\text{CO}_2$  gas was labeled, the opposite trend was observed (Figure 1C). As in the case of nonequilibrated precursor solution, the isotopic composition of the CO product mirrored that of bicarbonate ions; it seems that CO either originates directly from the reduction of bicarbonate or from the aqueous  $\text{CO}_2$  supplied through the fast equilibrium with the bicarbonate ions (but not from the dissolved  $\text{CO}_2$  in the bulk solution). This latter mechanism was suggested for Au and Cu electrodes.<sup>11,12</sup>

Received: February 7, 2018

Accepted: February 19, 2018

Published: February 19, 2018

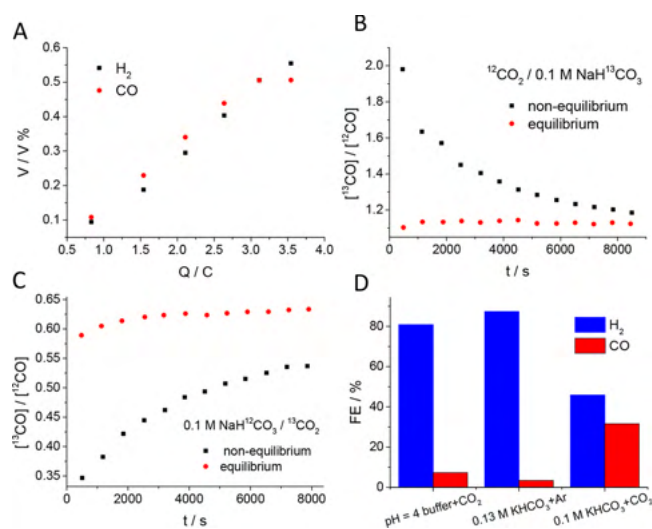


**Figure 1.** (A) Concentration of CO and H<sub>2</sub> generated on the HPG-PPy electrode with increasing reduction charge during potentiostatic electrolysis at  $-0.71$  V (vs RHE) in a CO<sub>2</sub>-saturated 0.1 M KHCO<sub>3</sub> electrolyte. (B) Ratio of the concentration of <sup>13</sup>CO to <sup>12</sup>CO formed during potentiostatic electrolysis at  $-0.71$  V (vs RHE) in a <sup>13</sup>CO<sub>2</sub>-saturated 0.1 M NaH<sup>13</sup>CO<sub>3</sub> electrolyte under nonequilibrium and equilibrium conditions. (C) Ratio of the concentration of <sup>13</sup>CO to <sup>12</sup>CO formed during potentiostatic electrolysis at  $-0.71$  V (vs RHE) in a <sup>13</sup>CO<sub>2</sub>-saturated 0.1 M NaH<sup>12</sup>CO<sub>3</sub> electrolyte under nonequilibrium and equilibrium conditions. (D) Faradaic efficiencies of H<sub>2</sub> and CO formation at the 75th minute of electrolysis at  $-0.61$  V (vs RHE) in different electrolytes: (i) CO<sub>2</sub>-saturated 0.1 M phosphate buffer (pH = 3.8); (ii) Ar-saturated 0.13 M KHCO<sub>3</sub> (pH = 8.8); (iii) CO<sub>2</sub>-saturated 0.1 M KHCO<sub>3</sub> (pH = 6.6).

To decide whether the CO<sub>2</sub> or the HCO<sub>3</sub><sup>-</sup> is the actual reacting species, a set of control experiments was performed. The concentration of bicarbonate ions and CO<sub>2, aq</sub> and the pH cannot be controlled independently because of the existing equilibrium. We can operate at pH values, however, where dominantly only one species is present. If the pH is below 5, almost all of the dissolved CO<sub>2</sub> is in the form of CO<sub>2, aq</sub> while between pH 7 and 9, mainly bicarbonate is present in the solution.<sup>16</sup> Thus, we performed electrolysis in (i) CO<sub>2</sub>-saturated 0.1 M phosphate buffer (pH = 3.8), (ii) 0.13 M KHCO<sub>3</sub> solution saturated with Ar (pH = 8.8), and (iii) CO<sub>2</sub>-saturated 0.1 M KHCO<sub>3</sub> (pH = 6.6), at  $-0.61$  V vs RHE in all cases (Figure 1D). The Faradaic efficiency of CO formation (FE<sub>CO</sub>) was 31.6% in the CO<sub>2</sub>-saturated 0.1 M KHCO<sub>3</sub>, while it was only 3.4% in the Ar-saturated 0.13 M KHCO<sub>3</sub>. Although the total dissolved CO<sub>2</sub> content of the two electrolytes is approximately the same, the CO<sub>2, aq</sub> concentration is around 40 times higher for the CO<sub>2</sub>-saturated 0.1 M KHCO<sub>3</sub> (see SI section S). In the CO<sub>2</sub>-saturated pH = 3.8 buffer, the FE<sub>CO</sub> was 7.3%, higher than that in the case of the Ar-saturated electrolyte, probably because of the much higher CO<sub>2, aq</sub> concentration. The fact that FE<sub>CO</sub> in the CO<sub>2</sub>-saturated pH = 3.8 buffer is *much* lower than in the CO<sub>2</sub>-saturated 0.1 M KHCO<sub>3</sub> solution suggests the vital role of bicarbonate ions acting as a CO<sub>2</sub> source. Notably, a very similar trend was seen in the partial current densities to what was presented for the FE values.

Overall, findings from selective isotopic labeling and pH-dependent studies demonstrated that the reacting species at the surface of a N-C electrode is most likely CO<sub>2, aq</sub>. Dissolved

CO<sub>2</sub> at the electrode surface, however, is rapidly supplied by bicarbonate ions (acting as a “CO<sub>2</sub> buffer”), if present, rather than gas-phase CO<sub>2</sub> or that dissolved in bulk solution. This assumption explains why the isotopic composition of the CO product is similar to that of bicarbonate when the isotopic equilibrium is not yet established. The fact that the highest FE<sub>CO</sub> was obtained for the bicarbonate/CO<sub>2</sub> system and that it was significantly lower when CO<sub>2, aq</sub> was present without bicarbonate further supports this hypothesis. Direct bicarbonate reduction is unlikely as only very small amounts of CO were produced when practically only bicarbonate ions were present. This mechanism was also suggested for a Ni-N-C catalyst based on the dependence of the CO partial current density on bicarbonate concentration.<sup>17</sup> Further efforts are ongoing to elucidate the mechanism of the electrochemical CO<sub>2</sub> reduction on N-doped carbon electrodes because these insights are very important in designing new electrode and electrochemical cell configurations to scale up this promising technology.<sup>18,19</sup>

## ■ ASSOCIATED CONTENT

### 📄 Supporting Information

The Supporting Information is available free of charge on the ACS Publications website at DOI: 10.1021/acsenenergylett.8b00212.

Electrode preparation, electrochemical measurements, and related mass spectrometry data (PDF)

## ■ AUTHOR INFORMATION

### ✉ Corresponding Author

\*E-mail: janaky@chem.u-szeged.hu. Twitter: @JanakyLab.

### ORCID

Csaba Janáky: 0000-0001-5965-5173

### Notes

The authors declare no competing financial interest.

## ■ ACKNOWLEDGMENTS

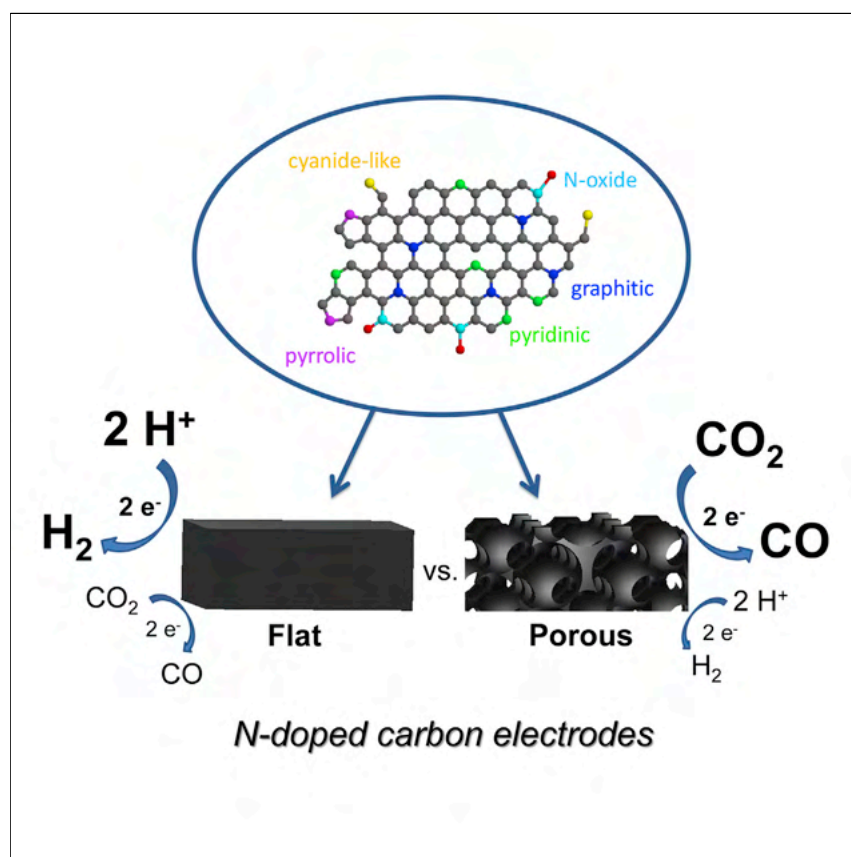
This project received funding from the European Research Council (ERC) under the European Union’s Horizon 2020 programme (Grant 716539). This work was supported by the GINOP-2.2.1-15-2017-00041 project.

## ■ REFERENCES

- (1) Yang, N.; et al. *ACS Appl. Mater. Interfaces* **2016**, *8*, 28357–28371.
- (2) Pan, F.; et al. *J. Mater. Chem. A* **2017**, *5*, 13104–13111.
- (3) Zhu, C.; et al. *Chem. Soc. Rev.* **2016**, *45*, 517–531.
- (4) Lai, J.; et al. *Energy Environ. Sci.* **2016**, *9*, 1210–1214.
- (5) Wu, J.; et al. *Nat. Commun.* **2016**, *7*, 13869.
- (6) Duan, X.; et al. *Adv. Mater.* **2017**, *29*, 1701784.
- (7) Liu, T.; et al. *J. Mater. Chem. A* **2017**, *5*, 21596–21603.
- (8) Ju, W.; et al. *Nat. Commun.* **2017**, *8*, 944.
- (9) Song, Y.; et al. *Angew. Chem., Int. Ed.* **2017**, *56*, 10840–10844.
- (10) Jiang, K.; et al. *Chem.* **2017**, *3*, 950–960.
- (11) Dunwell, M.; et al. *J. Am. Chem. Soc.* **2017**, *139*, 3774–3783.
- (12) Zhu, S.; et al. *J. Am. Chem. Soc.* **2017**, *139*, 15664–15667.
- (13) Han, Z.; et al. *ACS Cent. Sci.* **2017**, *3*, 853–859.
- (14) Cave, E. R.; et al. *Phys. Chem. Chem. Phys.* **2017**, *19*, 15856–15863.
- (15) To, J. W. F.; et al. *ACS Cent. Sci.* **2015**, *1*, 68–76.
- (16) Zhong, H.; et al. *J. Phys. Chem. C* **2015**, *119*, 55–61.
- (17) Zhao, C.; et al. *J. Am. Chem. Soc.* **2017**, *139*, 8078–8081.
- (18) Endrődi, B.; et al. *Prog. Energy Combust. Sci.* **2017**, *62*, 133–154.
- (19) Janáky, C.; et al. *ACS Energy Lett.* **2016**, *1*, 332–338.

## Article

## Morphological Attributes Govern Carbon Dioxide Reduction on N-Doped Carbon Electrodes



Nitrogen-doped carbon materials are attracting increasing interest as inexpensive and efficient electrocatalysts for carbon dioxide reduction.  $CO_2$  reduction selectivity (versus the hydrogen evolution reaction) was increased three times just by introducing porosity into the carbon structure (with an optimal pore size of 27 nm). This effect was quantitatively analyzed by systematically varying the porosity of the electrodes while fixing all other chemical and structural parameters.  $CO_2$  adsorption properties, wetting characteristics, and geometric effects are jointly responsible for the observed differences.

Dorottya Hursán, Angelika A. Samu, László Janovák, Kateryna Artyushkova, Tristan Asset, Plamen Atanassov, Csaba Janáky

janaky@chem.u-szeged.hu

## HIGHLIGHTS

The role of morphology in  $CO_2$  reduction was studied on N-doped carbon electrodes

All chemical and structural properties were set to be identical except the morphology

Both electrocatalytic activity and selectivity was tuned by changing the porosity

Wettability, adsorption strength, and geometric effects were dictating factors

Hursán et al., *Joule* 3, 1719–1733  
 July 17, 2019 © 2019 The Author(s). Published by Elsevier Inc.  
<https://doi.org/10.1016/j.joule.2019.05.007>



## Article

# Morphological Attributes Govern Carbon Dioxide Reduction on N-Doped Carbon Electrodes

Dorottya Hursán,<sup>1,2</sup> Angelika A. Samu,<sup>1,2</sup> László Janovák,<sup>1</sup> Kateryna Artyushkova,<sup>3</sup> Tristan Asset,<sup>3,4</sup> Plamen Atanassov,<sup>3,4</sup> and Csaba Janáky<sup>1,2,5,\*</sup>

## SUMMARY

The morphology of electrode materials is often overlooked when comparing different carbon-based electrocatalysts for carbon dioxide reduction. To investigate the role of morphological attributes, we studied polymer-derived, interconnected, N-doped carbon structures with uniformly sized meso or macropores, differing only in the pore size. We found that the carbon dioxide reduction selectivity (versus the hydrogen evolution reaction) increased around three times just by introducing the porosity into the carbon structure (with an optimal pore size of 27 nm). We attribute this change to alterations in the wetting and CO<sub>2</sub> adsorption properties of the carbon catalysts. These insights offer a new platform to advance CO<sub>2</sub> reduction performance by only morphological engineering of the electrocatalyst.

## INTRODUCTION

Electrochemical reduction of CO<sub>2</sub> (CO<sub>2</sub>R) is a promising method for converting a greenhouse gas into value-added products, utilizing renewable energy. Novel catalysts, electrode assemblies, and cell configurations are all necessary to achieve economically appealing performance.<sup>1–3</sup> Nitrogen-doped carbon (N-C) materials are attracting increasing interest as inexpensive and efficient electrocatalysts of this process.<sup>4–9</sup> Despite the rapid progress, summarized in recent review articles,<sup>10–13</sup> there are still several open questions related to the mechanistic insights. The nature of active centers and the role of different heteroatoms on the catalytic performance have been studied,<sup>8,14,15</sup> but the exact nature of the catalytic sites is still under debate. In addition, the composition and structure of these electrode materials are not well defined. The material can contain more than one active center and the distribution of heteroatoms and morphology can also change. Finally, several structural properties vary through these studies, such as the level of graphitization, surface functional groups, surface area, or metal impurities.<sup>8,16,17</sup> This makes it very difficult (if not impossible) to compare the results of precedent art. This issue was highlighted recently since several factors, other than the inherent properties of the catalysts, can severely influence the measured activity.<sup>18</sup>

From a morphological perspective, a wide range of carbon structures such as nanofibers, nanotubes, nanospheres, nano-onions, and graphene was investigated.<sup>15,19,20</sup> Furthermore, catalyst layers are prepared through different methods (e.g., dip-coating, brush painting, spray-coating, and drop-casting),<sup>5,7,15,21</sup> which usually result in a different porosity of the electrode for even the same catalyst

## Context & Scale

Producing fuels and commodity chemicals from carbon dioxide using electrochemical methods is a promising way to transform a greenhouse gas into value-added products. Scaling up this process to an industrial level, however, requires efficient, stable, and cheap electrocatalysts. One such group of materials is nitrogen-doped carbons, as demonstrated by their impressive performance improvements in recent years. Factors dictating their catalytic behavior, however, have yet to be understood to make further progress. Here, we show that both the catalytic activity and product selectivity are greatly varied by tuning the pore size of the carbon catalyst while keeping all other chemical and structural features identical. With these findings, we would like to highlight that structure-activity-stability relationships should be scrutinized before reporting on the electrocatalytic activity of different nanostructured carbons, as simple morphological factors can dictate the overall performance.



material.<sup>22</sup> The electrode configurations also vary from work to work, being catalysts supported on flat substrates, gas diffusion electrodes, or employed as self-supported catalysts.<sup>7,21,23,24</sup> Several mass transport limitation scenarios<sup>25,26</sup> can be envisioned in these structures, leading to differences in the overall activity and selectivity.<sup>27</sup> Yet, only a few studies suspected the determinant role of catalyst morphology and porosity on the CO<sub>2</sub>R performance of carbon-based electrodes,<sup>21,24,28,29</sup> and to the best of our knowledge, no systematic studies were performed on this subject up to now.

In the case of metal electrodes, CO<sub>2</sub>R performance was shown to be affected by the catalyst morphology, particle size, and loading. Alterations in the product distribution were attributed to (1) an increased residence time of products and intermediates in the pores of the nanostructured catalyst layers,<sup>30,31</sup> (2) differences in mass transport requirements for hydrogen evolution (HER) and CO<sub>2</sub>R reactions,<sup>32</sup> (3) CO<sub>2</sub> transport enhancement induced by gas evolution,<sup>33</sup> (4) size and morphology-dependent surface coordination effects,<sup>34–36</sup> and (5) a field-induced reagent concentration on highly curved surfaces.<sup>37</sup>

The role of porosity was systematically studied in the oxygen reduction reaction (ORR) on N–C electrodes using well-defined porous carbon structures. Macroporous graphitic C<sub>3</sub>N<sub>4</sub>/Carbon composites outperformed its mesoporous counterpart because of the facile reactant transport in the larger pores.<sup>38</sup> In the mesopore range, an intermediate pore size (around 22 nm in diameter) was the best,<sup>39</sup> while the performance was further enhanced by introducing microporosity and modifying surface functionalities.<sup>40</sup> Transport effects in ORR and CO<sub>2</sub>R, however, are different: ORR results in water formation, which can undergo condensation, while gas-phase products are common in CO<sub>2</sub>R. Furthermore, the solution chemistry of the reactants is largely different in the two cases.

The above trends gave us the motivation of this study, where we aimed to deconvolute the effect of various structural parameters and thus focus only on the role of the porosity in the CO<sub>2</sub>R process. This study aims to shine light on the morphology-activity-stability relationships in CO<sub>2</sub>R electrocatalysis with well-defined carbon-based catalysts materials as an object. In this work, we will show that variations in the porosity of N–C electrodes *alone* can result in massive differences in the electrocatalytic behavior in both activity and selectivity. We will also demonstrate that altered CO<sub>2</sub> adsorption and wetting properties, along with a curvature effect, are jointly responsible for this intriguing phenomenon.

## RESULTS AND DISCUSSION

### Catalyst Synthesis and Characterization

As the first step, we have synthesized a series of N–C electrodes by a *totally metal-free* sacrificial support method (Scheme 1). The *o*-phenylenediamine (oPD) monomer was chemically polymerized in the presence of monodisperse silica nanoparticles. The resulting SiO<sub>2</sub>/PoPD composite was carbonized (pyrolyzed) at 900°C in neat N<sub>2</sub> flow, followed by the etching of the silica template with hydrogen fluoride (HF). By this “hard templating method,” we prepared three N–C samples having pores with 13, 27, and 90 nm nominal diameters (denoted as NC-13, NC-27, and NC-90, respectively) based on the mean size of the silica template used. A nonporous catalyst (NC), without using a silica template, was also prepared for comparison. We used the same oPD/SiO<sub>2</sub> mass ratio through the synthesis of the porous catalysts, thus fixing the total pore volume for the samples. This synthetic approach

<sup>1</sup>Department of Physical Chemistry and Materials Science, Interdisciplinary Excellence Centre, University of Szeged, Aradi sq. 1, Szeged 6720, Hungary

<sup>2</sup>MTA-SZTE “Lendület” Photoelectrochemistry Research Group, Rerrich sq. 1, Szeged 6720, Hungary

<sup>3</sup>Department of Chemical and Biological Engineering, Center Micro-Engineered Materials, University of NewMexico Albuquerque, Albuquerque, NM 87131, USA

<sup>4</sup>Department of Chemical and Biomolecular Engineering, National Fuel Cell Research Center, University of California, Irvine, Irvine, CA 92697, USA

<sup>5</sup>Lead Contact

\*Correspondence: [janaky@chem.u-szeged.hu](mailto:janaky@chem.u-szeged.hu)  
<https://doi.org/10.1016/j.joule.2019.05.007>



**Scheme 1. Scheme of the Catalyst Synthesis**

Catalysts were synthesized by a sacrificial support method, starting from poly(o-phenylenediamine) polymers and using silica nanoparticles with different diameters as templates. High-temperature carbonization of the silica/polymer composites was followed by etching of the template particles with hydrogen fluoride solution.

allowed us to control the morphological attributes of the electrodes while keeping all other parameters unchanged, as shown in what follows.

The formation of interconnected carbon structures with uniformly sized pores was verified by transmission electron microscopy (TEM) and scanning electron microscopy (SEM) (Figure 1). The average diameter of the pores (determined from the TEM images) was  $12.7 \pm 2.1$ ,  $26.4 \pm 3.9$ , and  $94.8 \pm 9.4$  nm for the NC-13, NC-27, and NC-90 samples, respectively, mirroring the size of the template silica particles. In contrast, the NC appeared to be smooth, absent of meso- or macropores (Figure S1). The size of the template particles also affected the carbon wall thickness. Semi-quantitatively, the smaller the particles, the thinner the wall size (5–8 nm for NC-13, 10–12 nm for NC-27, and 15–20 nm for NC-90). High-resolution (HR) TEM images, however, revealed similar graphitic structures for all four samples (Figure S2).

N<sub>2</sub> adsorption and desorption isotherms (Figure S3) of NC-13 and NC-27 showed dominantly mesoporous features with the characteristic hysteresis loops, while the less pronounced capillary condensation for NC-90 (also shifted to higher relative pressures) confirmed its rather macroporous structure. The pore size distribution curves peaked at 13, 30, and 78 nm for NC-13, NC-27, and NC-90, respectively (Figure S4), and further confirmed that uniformly sized pores formed. Specific surface areas were  $957 \text{ m}^2 \text{ g}^{-1}$  for NC-13,  $899 \text{ m}^2 \text{ g}^{-1}$  for NC-27,  $665 \text{ m}^2 \text{ g}^{-1}$  for NC-90, and only  $104 \text{ m}^2 \text{ g}^{-1}$  for NC. The trend in the roughness factors of the electrodes ( $1 \text{ mg cm}^{-2}$  loadings), determined from the double layer capacitance values, were in line with the BET specific surface areas (Figures S6–S8).

X-ray diffraction (XRD) and Raman spectroscopic analysis indicated very similar carbon structures for the catalysts (Figure S5). The intensity ratio of D and G bands in the Raman spectra (characteristic of the defects and the graphitic structure) was  $0.89 \pm 0.01$  for all four samples, indicating an identical density of defect sites.

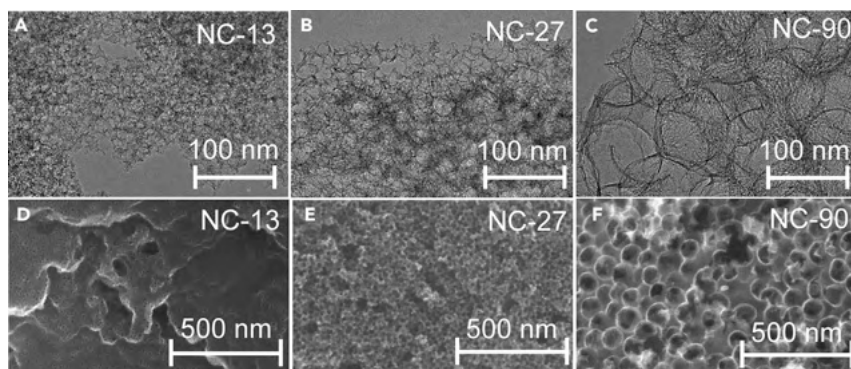


**Figure 1. Morphology of the Studied Porous Catalysts**

Transmission (A: NC-13, B: NC-27, C: NC-90) and scanning (D: NC-13, E: NC-27, F: NC-90) electron microscopy images of the porous N-C catalysts. See also Figures S1 and S2.

The broad and very weak diffraction at  $25^\circ$  and  $43^\circ$  in the XRD pattern are typical for amorphous carbons. The surface chemical composition of the electrodes was studied by X-ray photoelectron spectroscopy (XPS) (Figure 2). The relative amounts of carbon, nitrogen, and oxygen atoms were very similar for all N-C samples: the composition was 80–85 atom % C, 6–8 atom % N, and 6–11 atom % O (Table S1). Similarly, the distribution of nitrogen moieties<sup>41,42</sup> in different chemical environments was almost identical (Figure 2B; Table S2) for all studied catalysts and was in good accordance with previous results on related materials.<sup>43,44</sup> Overall, the N-C catalysts were very similar both in terms of the surface functional groups (chemical properties) and the electronic features. Therefore, they offer a platform to systematically study the effect of morphology on the CO<sub>2</sub>R performance.

### Electrochemical CO<sub>2</sub> Reduction Performance

The CO<sub>2</sub>R activity of the N-C electrodes with the same catalyst loading ( $1.00 \pm 0.07 \text{ mg cm}^{-2}$ ) was first tested by linear sweep voltammetry (LSV) in a CO<sub>2</sub>-saturated KHCO<sub>3</sub> solution (Figure 3A). NC-27 and NC-13 showed the highest current densities, exceeding  $25 \text{ mA cm}^{-2}$  at  $-1.0 \text{ V}$  (versus RHE). Only half of this current was recorded for NC-90, while currents stayed below  $5 \text{ mA cm}^{-2}$  for NC. The onset potential for the reduction was  $-0.27 \pm 0.03 \text{ V}$  (versus RHE) for all samples (Figure S9), further confirming that the chemical features of the active centers are

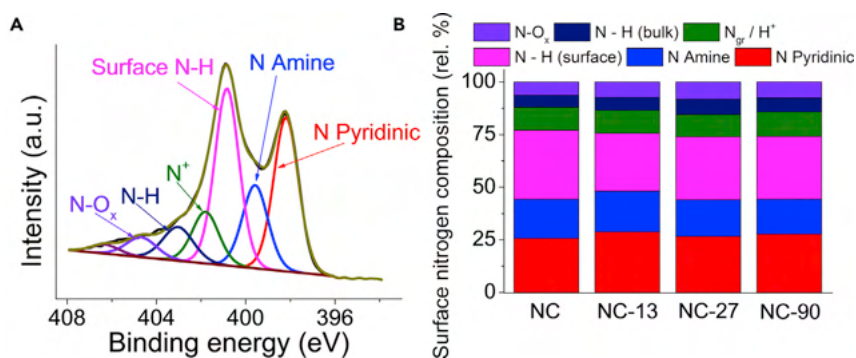


**Figure 2. X-Ray Photoelectron Spectroscopic Data for the NC-90 Sample**

(A) N1s XPS pattern for the NC-90 catalyst.

(B) Distribution of the N species in different chemical environments.

See also Table S1 and S2.



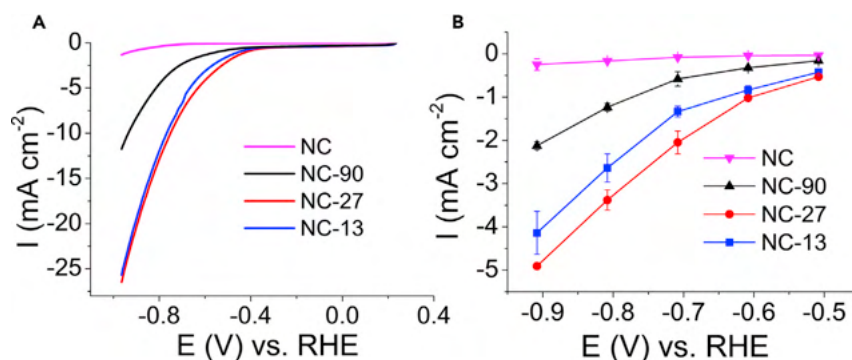


**Figure 3. Electrochemical Reduction Performance of the Studied Catalysts**

(A) Linear sweep voltammograms of the catalysts recorded in a  $\text{CO}_2$ -saturated 0.5 M  $\text{KHCO}_3$  solution with  $5 \text{ mV s}^{-1}$  sweep rate.

(B) Total current densities recorded in the 40<sup>th</sup> min of the potentiostatic electrolysis in a 0.1 M  $\text{KHCO}_3$  solution, saturated with  $\text{CO}_2$ . Currents are normalized by the geometrical surface area of the electrodes. Error bars reflect the average of three parallel measurements for different samples, and data are represented as mean  $\pm$  SEM.

See also Figure S10.

identical. To deconvolute the evident surface area effect, currents were normalized by the roughness factors too (Figure S10). The trend in the current densities remained the same among the porous samples, implying that structural features other than the variations in the specific surface area are responsible for the differences in the catalytic performance.

Product selectivity was studied by *on-line* gas chromatography (GC) and *ex situ* nuclear magnetic resonance (NMR) spectroscopic analysis of the gas and liquid-phase products during potentiostatic electrolysis. We detected the formation of  $\text{CO}$  and  $\text{H}_2$  accounting for more than 95% of the total products (in some cases, trace amounts of methane and formate were also seen). The total current density versus potential curves is plotted in Figure 3B. The order in the total currents followed the same trend as during the LSV measurements normalized either by the geometric surface areas or by the roughness factors (Figure S10).

The porosity of the N-C electrodes immensely affected the selectivity, too (Figure 4C). While the  $\text{CO}/\text{H}_2$  ratio went through a maximum peaking at  $-0.6 \text{ V}$  (versus RHE) for NC-27 and NC-13; NC-90 and NC showed a continuous decrease in this ratio in the studied potential window. A general trend in decreasing  $\text{CO}$  selectivity with increasing pore size was observed at all potentials; however, differences in the product distribution were more obvious above  $-0.7 \text{ V}$  (i.e., where  $\text{CO}_2\text{R}$  dominated over HER). The highest  $\text{CO}$  selectivity was achieved for NC-27 at all potentials, peaking at  $-0.6 \text{ V}$  with 76%.

$\text{H}_2$  partial current densities ( $I_{\text{HER}}$ ) exponentially increased with increasing overpotential, indicating a purely kinetic process (Figure 4A).  $I_{\text{HER}}$  was practically the same for NC-27 and NC-13 but showed a 2- to 3-fold decrease for NC-90. In contrast,  $\text{CO}$  partial currents ( $I_{\text{CO}}$ ) increased in the order of  $\text{NC-90} < \text{NC-13} < \text{NC-27}$  and showed distinct potential dependences for the various samples (Figure 4B). While  $I_{\text{CO}}$  increased continuously with more negative potentials for NC-90 and NC, it declined at  $-1.0 \text{ V}$  in case of NC-27 and NC-13. This suggests that besides the charge transfer kinetics, other complications arise in the  $\text{CO}_2\text{R}$ , which are also dependent on the porosity. The superior  $\text{CO}$  production activity of NC-27 among the studied catalysts

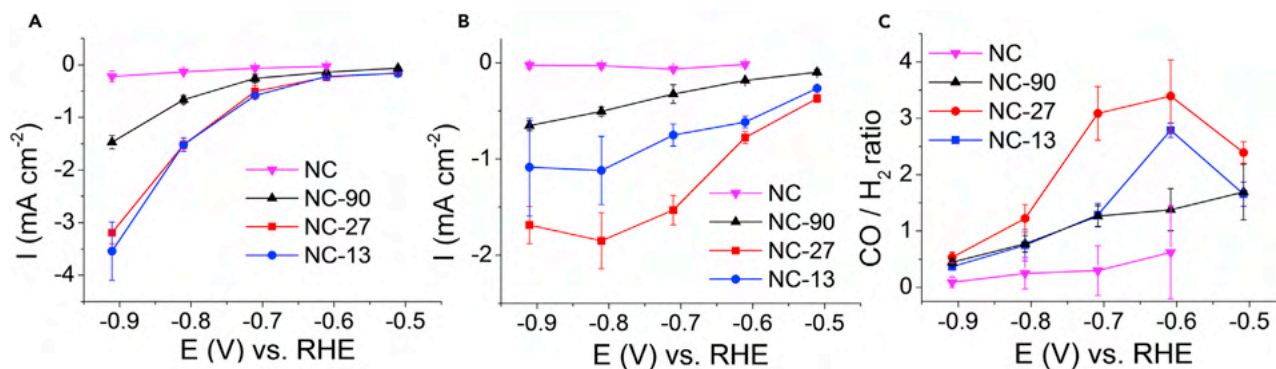


**Figure 4. Electrochemical CO<sub>2</sub> Reduction Selectivity of the Studied Catalysts**

(A and B) Partial current densities for H<sub>2</sub> (A) and CO (B) formation on the N-C catalysts during potentiostatic electrolysis in a CO<sub>2</sub>-saturated 0.1 M KHCO<sub>3</sub> solution.

(C) Molar ratio of the CO and H<sub>2</sub> products as a function of the electrode potential. Data points are measured in the 40<sup>th</sup> min of the electrolysis, and currents are normalized by the geometric surface areas. Error bars reflect the average of three parallel measurements for different samples, and data are represented as mean ± SEM.

See also Figure S11.

was even more pronounced when we normalized the partial currents by the roughness factors (Figure S11). Overall, the mesoporous NC-27 performed best both in terms of total activity and CO selectivity, which is in line with a recent report on similar catalysts.<sup>29</sup> The decreased catalytic performance of NC-13 was because of the decreased CO<sub>2</sub>R, while for NC-90, it was the effect of the simultaneous attenuation of the HER and the CO<sub>2</sub>R. In this case, the CO selectivity approached the bulk-like behavior. Also, note that *not* the best performing NC-27 catalyst contains the highest amount of pyridinic and graphitic N-moieties, which sites are supposed to be the active sites in CO<sub>2</sub>R for such materials.<sup>13</sup> This further supports our notion, namely that the observed trends in catalytic activity are more likely rooted in the different morphology as discussed below, and the contribution of the slightly different chemical properties is inferior.

Overall, the performance of the N-C catalyst described in this study is comparable to that of the other carbon-based CO-selective electrodes reported earlier (see an extensive compilation of precedent art in Table S4). The highest CO production activity was reached for NC-27 at -0.8 V with -1.85 mA cm<sup>-2</sup> partial current density, which falls in the activity range of metal-free N-doped carbon catalysts measured under similar conditions (electrolyte, substrate electrode, and cell type). Preliminary experiments in a membrane-separated continuous-flow cell (data not shown) resulted in 70 mA cm<sup>-2</sup> CO<sub>2</sub>R partial current density, which is also in the range measured for similar catalysts (see Table S4). Furthermore, the activity of our best performing catalyst is also close to many metal-nitrogen-doped carbons (M-N-Cs). The advantage of incorporating atomically dispersed metals into the carbon structure is evident from the literature comparison, especially in the case of Ni-N-C materials. The optimization of the carbon framework, however, is also crucial in the M-N-C catalysts. Taking into account these considerations, our set of catalysts is a relevant *model* system for the investigation of the morphological effects of the carbon structure in CO<sub>2</sub>R. Moreover, as data on rate-controlling steps in CO<sub>2</sub>R are scarce and under dispute, this work provides a baseline and a *low-parameter variability* study on the effect of morphology in this electrochemical process. This allows us to separate the adsorption steps in catalyst reactivity and demonstrate that a “holistic materials design,” which includes porosity at several length scales is needed for successful implementation of electrochemical processes for CO<sub>2</sub> valorization.

### Control Experiments

To prove that the above observations are not the results of the unlikely variation in the layer thicknesses for the different catalysts with the same mass loadings, we studied the product distributions for NC-27 with three different loadings (0.50, 1.00, and 1.50 mg cm<sup>-2</sup>). The total and partial current densities increased with increasing mass (Figure S12); however, the specific activity (currents normalized by the roughness factors) diminished for the thicker layers (Figure S13). This might be the result of the higher mass transfer resistance of the thicker layers. The CO/H<sub>2</sub> selectivity was similar for the layers with 0.50 and 1.00 mg cm<sup>-2</sup> loadings at all studied potentials. For the layers with 1.50 mg cm<sup>-2</sup> loadings, it was around 1.3 times lower than the thinner layers above -0.7 V, while slightly higher at more negative potentials. Changes in the layer thickness influenced slightly the product distribution; however, its effect was far not as pronounced as that of the variations in the pore size.

### Factors behind the Changing Selectivity

The differences in the CO<sub>2</sub>R activity and selectivity can be rationalized by taking into account three main factors: (1) wettability of the catalysts, (2) CO<sub>2</sub> adsorption in the differently sized pores, and (3) curvature effects. The wetting properties of the NC samples were investigated by measuring the dynamic (advancing and receding) contact angles of the thin layers (Figure S14). The surface energies (Figure 5A) were calculated from the contact angle hysteresis.<sup>45</sup> The nonporous NC catalyst was the least hydrophobic ( $\Theta = 128.5^\circ$ ) and presented the highest hysteresis, resulting in the highest surface energy ( $\gamma_{s,tot} = 6.35 \pm 2.31$  mJ m<sup>-2</sup>). Introducing pores into the carbon framework decreased the surface energy to about 2 mJ m<sup>-2</sup> (ideal porosity) independently of the pore size. This effect is in line with previous morphology-surface energy correlations.<sup>46,47</sup> Importantly, this trend in the surface energies may partially account for the enhanced CO<sub>2</sub>R performance (versus HER) of the porous samples, compared to the flat NC, in the absence of flooding water.<sup>27</sup>

As the dynamics of gas bubble formation on the electrode surface depend on the wettability and morphology (among others), the size of the bubbles was analyzed along with their residence time during potentiostatic electrolysis (Figure S15). Such analysis is important because the release of gas bubbles can enhance mass transport of the reactant by inducing convective flow, hence reducing the diffusion layer thickness, leading to higher catalytic current density.<sup>33</sup> In addition, large bubbles, which remain on the electrode surface for a longer time, can partially block the active area resulting in lower current density.<sup>48</sup> The departing bubbles were relatively large on all N-C catalysts (few hundred  $\mu$ m) because of the hydrophobic character of the samples. The increase in the overpotential (hence the current density), reduced both the departure diameters and the residence time (Figure S16A). The residence time decreased drastically for the porous samples, compared to the nonporous NC. Comparing the porous samples, both the residence times and the departure diameters decreased with the reduction of the pore size (Figure S16B) (i.e., in the order of NC-90 > NC-27 > NC-13). This finding is in agreement with previous reports, where enhanced bubble release was observed in nanostructures with smaller dimensions.<sup>33,48</sup> The distribution diagrams also revealed that polydispersity of the bubble size and residence time increased with increasing pore size (Figure S17) suggesting progressive nucleation. The differences in residence time can be an additional reason for the superiority of the porous catalysts compared to the flat NC and also for the better performance of NC-27 and NC-13 than NC-90. In contrast, these findings do not explain NC-27 being the best performing

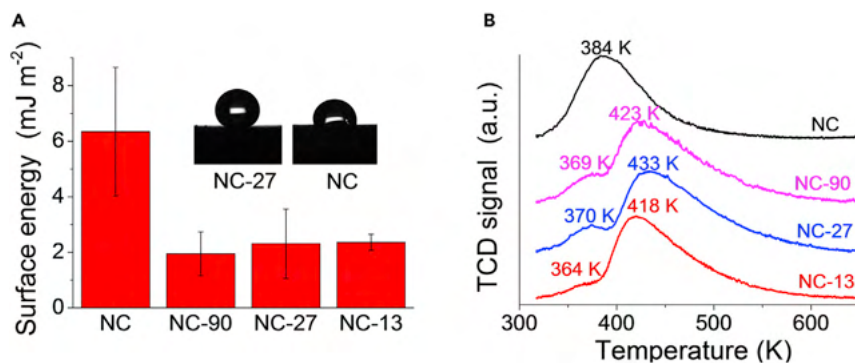


**Figure 5. Wettability and CO<sub>2</sub> Adsorption Measurements to Reveal the Factors behind the Changing Selectivity**

(A) Surface energies of the studied catalysts calculated from dynamic contact angle measurements. The inset shows the representative images of water drops on the surface of the catalyst layers used for the determination of contact angles for NC-27 and NC.

(B) Temperature-programmed CO<sub>2</sub> desorption profiles of the studied catalysts.

See also [Figure S14](#).

electrode, as the bubble-induced CO<sub>2</sub> transport enhancement effect is expected to be the highest in the case of NC-13.

Temperature-programmed desorption was employed to study the CO<sub>2</sub> adsorption strength of the catalysts ([Figure 5B](#)). While only one desorption peak was present in case of the NC, CO<sub>2</sub> desorption from the porous samples happened in two distinct steps. We assume that the first step at a lower temperature (< 400 K) is connected to the adsorbed CO<sub>2</sub> on the outer surface of the catalyst layers, and the second step is linked to the desorption of CO<sub>2</sub> from the inner surface of the pores (which is absent for NC). The temperature of the desorption from the pores was the highest (433 K) for NC-27, implying the highest CO<sub>2</sub> adsorption strength. As NC-27 performed best also in the CO<sub>2</sub> conversion, we assume a link between the CO<sub>2</sub> adsorption and reduction activity. Considering that the studied N–C catalysts are practically identical in terms of N-containing moieties, we suggest that the distinct CO<sub>2</sub> adsorption strengths arise from the differences in the pore structure. In this case, the strain induced on the CO<sub>2</sub> adsorption sites by the differently curved surfaces is optimal for the 27 nm pores. This curvature-dependent binding strength of CO<sub>2</sub> is similar to what was reported for both graphene and N–C materials, based on computational methods.<sup>49,50</sup> Additionally, the importance of differently curved adsorption sites was highlighted in ORR for N–C materials, based on experimental evidence.<sup>51</sup>

We also note that the presented N–C structures are not ideal and present several levels of chemical and morphological defects. These are defects in the carbon structure; therefore, the contribution of edge-site-exposed defects versus in-plane sites might be of importance. The differently curved pores may indeed contribute to a different ratio of in-plane versus edge defects. For smaller pores, we may expect more edge site defects than in-plane ones, resulting in higher catalytic activity. High-resolution C1s XPS indeed revealed a higher amount of graphitic carbon in the NC than the porous samples ([Figure S18](#); [Table S3](#)). This is probably because of the lower concentration of defects and edge sites in the case of a flat structure compared to the curved ones. Carbon speciation of all three porous catalysts, however, was identical based on the XPS (within the experimental error). Finally, we note that higher curvature (i.e., smaller pore diameter) can also lead to field-induced CO<sub>2</sub>

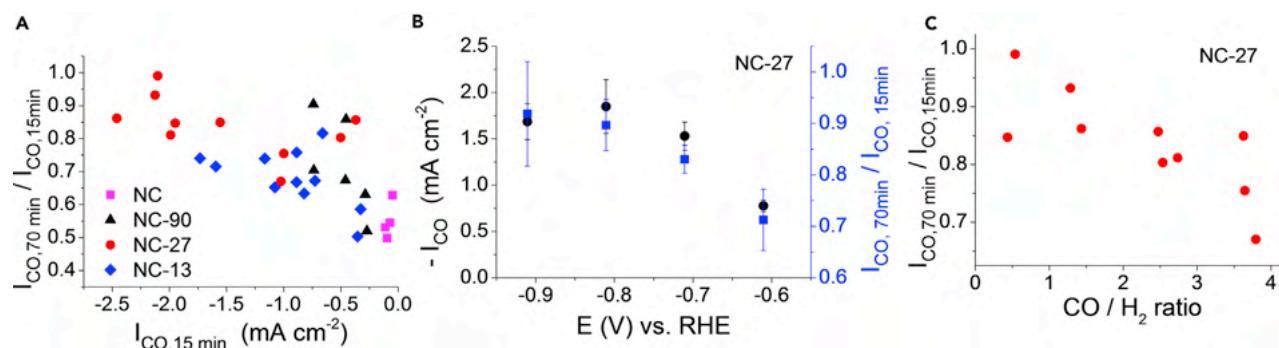


**Figure 6. CO<sub>2</sub> Reduction Activity-Stability-Selectivity Correlations**

(A) Stability of the CO partial currents during 70 min of operation as a function of the CO partial currents in the 15<sup>th</sup> min of the potentiostatic electrolysis for the different samples.

(B) CO partial currents (left) and stability of CO partial currents (right) during 70 min of electrolysis as a function of the electrode potential for NC-27. (C) Stability of the CO partial currents during 70 min of operation as a function of the CO selectivity for NC-27. Error bars reflect the average of three parallel measurements for different samples, and data are represented as mean  $\pm$  SEM.

See also Figures S19–S21.

accumulation (condensation), which can also contribute to the enhanced CO<sub>2</sub> reduction performance of NC-27 and NC-13, as demonstrated earlier in the case of metal electrodes.<sup>37</sup>

### Activity-Selectivity-Stability Correlations

Stability of the catalytic performance is a key point in catalyst development, especially from the perspective of future application. This is a particularly intriguing issue for a nano-engineered catalyst, where the morphology might alter during operation, thus causing changes in the catalytic properties.<sup>52</sup> To find the key parameters dictating the stability of the N–C catalysts, the decay of the catalytic currents, for both HER and CO<sub>2</sub>R, was studied as a function of potential, catalyst activity ( $I_{\text{CO}}$  and  $I_{\text{H}_2}$ ), and selectivity (CO/H<sub>2</sub> ratio). We found that the higher the CO production rate ( $I_{\text{CO}}$ ), the more stable the CO<sub>2</sub>R activity (Figure 6A). Importantly, all data points fell on the same trendline, irrespective from the sample studied. Notably, the data points are clustered: NC-27 is the most stable, followed by NC-13, NC-90, and finally NC. Another representation of the same data for the most active and stable NC-27 sample is shown in Figure 6B. This interpretation further confirms that stability correlates with activity, and they both increase with the overpotential.

We were also interested to see the relationship between stability and selectivity. Interestingly, a clear trend was witnessed for all porous samples, and the example of NC-27 is shown in Figure 6C. The stability rapidly decreased with the increasing CO<sub>2</sub>R selectivity (i.e., CO/H<sub>2</sub> ratio). Although this dataset highlights the trade-off between selectivity and stability for the N–C catalyst, the underlying mechanistic insights still have to be uncovered.

Overall, we identified that higher CO formation activity and lower CO selectivity resulted in more stable CO production in time, independently of the porosity. In the HER, however, no such unambiguous correlations were found (Figure S19), and even some HER performance increase was seen, while the CO<sub>2</sub>R activity decreased. Finally, we also tested the morphological stability of NC-27. No major changes in the porosity could be observed after a 4 h long potentiostatic electrolysis at  $-0.6$  V, as seen on the SEM images taken before and after CO<sub>2</sub> reduction (Figure S20).

Changes in the HER and CO<sub>2</sub>R currents followed that same pattern as discussed above (Figure S21).

In summary, we found that CO<sub>2</sub>R activity, selectivity, and stability of N–C electrodes are highly dependent on their porosity. The presence of mesopores was demonstrated to be beneficial in achieving high CO selectivity and current density, with an optimal pore size around 27 nm. Even after convoluting factors other than morphology (e.g., surface chemistry, level of graphitization, surface area), the reasons behind the observed trends are complex. CO<sub>2</sub> adsorption properties, wetting characteristics, and geometric effects are jointly responsible for the massive difference in the CO<sub>2</sub>R performance. All these properties must be taken into consideration when we aim to understand the reduction mechanism on different catalysts and while improving the performance further to a technologically relevant level (as alternatives to precious metal catalysts).

## EXPERIMENTAL PROCEDURES

### Catalyst Synthesis and Electrode Preparation

All chemicals were used as received, without further purification. Aqueous solutions were prepared using deionized water (Millipore Direct Q3-UV, 18.2 MΩ cm).

The catalysts were synthesized by a sacrificial support method using oPD as the carbon and nitrogen precursors. A solution containing 0.58 M oPD (C<sub>6</sub>H<sub>8</sub>O<sub>2</sub>, Merck, 108.14 g/mol), 0.72 M hydrochloric acid (HCl; VWR International, 37%, 36.46 g/mol), 0.19 g/cm<sup>3</sup> silica nanoparticle (see Table 1) was vigorously stirred for ~15 min to adsorb the monomer molecules on the silica surface. A solution of 2.7 M ammonium persulfate (APS; (NH<sub>4</sub>)<sub>2</sub>S<sub>2</sub>O<sub>8</sub>, Acros Organics, 228.19 g/mol) in 1 M HCl was dropwise added to the oPD solution (n(oPD) / n(APS) = 0.8) at 0°C (ice bath) and stirred for 24 h to complete the polymerization process. The obtained PoPD / SiO<sub>2</sub> composites were dry-frozen, then pyrolyzed at 900°C in a tube furnace in N<sub>2</sub> flow (110 cm<sup>3</sup>/min). Heating program: room temperature (RT)–5°C/min–180°C (1 h)–5°C/min–900°C (2 h). The silica nanoparticles were etched out overnight with an excess amount of 15 wt % HF (VWR, 40 wt %, 20.01 g/mol) solution. Finally, the nitrogen-doped carbon catalysts were washed thoroughly with ultrapure water, until close to neutral pH (>5) was reached. The nonporous (NC) sample was prepared by the same procedure but without the use of silica colloid.

For the electrochemical measurements, the catalysts were spray-coated onto the surface of glassy carbon plates. The substrates were polished with 0.05 μm MicroPolish Alumina (Buehler), rinsed, and sonicated in acetone (C<sub>3</sub>H<sub>6</sub>O, 58.08 g/mol, VWR), ethanol (C<sub>2</sub>H<sub>6</sub>O, 46.07 g/mol, 99%, VWR), and ultrapure water before spray-coating. The catalyst ink consisted of 5 mg/mL catalyst dispersed in 10 mL ethanol-ultrapure water mixture (50 V/V%) containing 100 μL Nafion dispersion (FuelCell Store, 10%). Spray-coating was performed with a homemade automated spray-coating equipment at 110°C until the desired catalyst loading was achieved. The exact amount of catalyst coated was always measured with a microbalance.

**Table 1. Silica Colloids Used as Templates in the Synthesis of the N–C Catalysts**

Silica colloid	Mean diameter/nm	wt %
LUDOX-HS40 (Aldrich)	13	40%
LUDOX-TM50 (Aldrich)	27	50%
LEVASIL CT3-PL (AkzoNobel)	90	50%

### Electrochemical Measurements

Electrochemical measurements were carried out using an Autolab PGSTAT 204 instrument. Potentials were measured against an Ag/AgCl/3 M NaCl reference electrode, but they are given versus the reversible hydrogen electrode (RHE) in the text ( $E_{\text{RHE}} = E_{\text{Ag/AgCl}} + 0.20 \text{ V} + 0.059 \text{ V} \times \text{pH}$ ).

Cyclic voltammograms (for the determination of the electrochemically active surface areas of the electrodes) were recorded in a one-compartment three-electrode setup using the catalyst-coated glassy carbon substrates as the working electrodes, a Pt foil as the counter electrode and the Ag/AgCl/3 M NaCl electrode as the reference. These measurements were carried out in an Ar-saturated (Messer, 99.995 %) 1 M sodium sulfate solution ( $\text{Na}_2\text{SO}_4$  anhydrous, 142.04 g/mol, 99% Alfa Aesar).

Linear sweep voltammetric and chronoamperometric electrolysis measurements were performed in a two-compartment sealed electrochemical cell with the cathode and anode compartments separated by a Nafion-117 membrane. For the analysis of gas-phase products, the cathode compartment of the cell was directly connected to the inlet of the gas chromatograph via a six-port valve. In the  $\text{CO}_2$  reduction experiments,  $\text{CO}_2$ -saturated (Messer; 99.995%) potassium hydrogen carbonate ( $\text{KHCO}_3$ , 100.12 g/mol, VWR) solutions were used. The error bars on the figures reflect the average of three parallel measurements for different catalyst layers.

Roughness factors of the N-C electrodes were calculated from the electrochemical double layer capacitance ( $Q_{\text{dl}}$ ) values determined by cyclic voltammetry. Cyclic voltammograms were recorded in an Ar-saturated 1 M  $\text{Na}_2\text{SO}_4$  solution between  $-0.21$  and  $0.61$  V (versus RHE) applying different sweep rates. The double layer current ( $I_{\text{dl}}$ ) was determined at  $0.41$  V as the difference between the anodic and cathodic currents ( $I_{\text{dl}} = I_{\text{a}} - I_{\text{c}}$ ).  $I_{\text{dl}}$  was plotted as a function of the sweep rate ( $v$ ) and  $Q_{\text{dl}}$  was calculated from the slope ( $s$ ) of this curve ( $Q_{\text{dl}} = s/2$ ). The  $Q_{\text{dl}}$  values obtained for the N-C electrodes were compared to that of a bare, smooth glassy carbon electrode (assuming surface roughness of 1). Roughness factors were given by the ratio of these two values.

### $\text{CO}_2$ Reduction Products Analysis

Gas-phase  $\text{CO}_2$  reduction products were analyzed by *on-line* GC, using a Shimadzu-2010 Plus GC equipped with a barrier ionization discharge detector. A Shincarbon ST column was used for the separation. During electrolysis, 0.5 mL of the headspace gas was injected into the GC at around 15, 40, and 68 min. Analysis parameters were the following: carrier gas: helium; oven program:  $T_{\text{start}} = 35^\circ\text{C}$  (2.5 min),  $\Delta T_{\text{ramp}} = 20^\circ\text{C min}^{-1}$ ,  $T_{\text{end}} = 270^\circ\text{C}$  (3 min); injection temperature:  $T = 150^\circ\text{C}$ ; linear velocity was controlled by the pressure  $p_{\text{start}} = 250 \text{ kPa}$  (2.5 min)  $\Delta p_{\text{ramp}} = 15 \text{ kPa min}^{-1}$   $p_{\text{end}} = 400 \text{ kPa}$  (7.5 min); and split ratio: 10.

Liquid-phase products were analyzed by NMR spectroscopy acquired on a Bruker NMR Avance 500 MHz instrument. Water suppression was used to eliminate the peak of the water. 450  $\mu\text{L}$  of the electrolyte sample was mixed with 50  $\mu\text{L}$   $\text{D}_2\text{O}$  (Sigma Aldrich, 99.9 atom% D) containing dimethyl-sulfoxide (DMSO,  $\text{C}_2\text{H}_6\text{SO}$ , 78.13 g/mol, Alfa Aesar) and phenol ( $\text{C}_6\text{H}_6\text{O}$ , 94.11 g/mol 99.5% Sigma Aldrich) as the internal standards. The ratio of peak areas of the products and the internal standards were used for the calibration. Peak areas of the products right to the water peak were compared to the peak area of the DMSO, while peak areas of products left to that were compared to the peak area of the phenol.

Error bars were determined from at least three parallel measurements for separate electrodes.

### Materials Characterization Techniques

XPS spectra were acquired on a Kratos Axis Ultra DLD spectrometer. A monochromatic Al K $\alpha$  source operated at 300 W. No charge neutralization was needed. CasaXPS was used for the data analysis (three regions were analyzed per sample). The survey patterns were acquired at 80 eV pass energy. The high-resolution patterns for C 1s and N 1s were acquired at 20 eV pass energy and fitted with a 70% Gaussian-30% Lorentzian line shape with fixed full-width half maximum of 1.0–1.2 eV for C and of 1.3–1.5 eV for N. For consistency, the positions and width of peaks used in the curve-fit was adapted from previously established protocol.<sup>43,53</sup>

XRD patterns were recorded between  $2\theta = 10^\circ$ – $80^\circ$  at  $1^\circ$  per min scan rate on a Rigaku Miniflex II instrument, operating with a Cu K $\alpha$ ,1 radiation source ( $\lambda = 0.1541$  nm)

For the determination of the BET surface areas, the samples were outgassed under N<sub>2</sub> flow at 120°C overnight using a Micromeritics flow prep system. The surface area was then measured using N<sub>2</sub> adsorption at 77 K in a Micromeritics Gemini 2360 multipoint BET analyzer.

N<sub>2</sub> adsorption/desorption isotherms were recorded at 77.4 K on a Quantachrome Nova 3000e instrument. Samples were outgassed at 200°C for 2 h before measurement. Pore size distribution curves were calculated using the Barrett-Joyner-Halenda method excluding points below 0.35 relative pressure.

Raman spectroscopy was measured with a Senterra II Compact Raman microscope (Bruker), using 532 nm laser excitation wavelength, operating at a power of  $\leq 2.5$  mW, and a 50 $\times$  objective.

Transmission electron microscopic (TEM) images were recorded by using a FEI Tecnai G2 20 X-Twin type instrument, operating at an acceleration voltage of 200 kV. A Hitachi S4700 field emission scanning electron microscope (SEM) was operated at an accelerating voltage of 10 kV.

The dynamic advancing ( $\theta_{adv}$ ) and receding ( $\theta_{rec}$ ) contact angles of the layers were measured applying an EasyDrop drop shape analysis system (Krüss GmbH, Hamburg, Germany) controlled with the DSA100 software, equipped with a Peltier temperature chamber ( $T = 25.0^\circ\text{C} \pm 0.5^\circ\text{C}$ , under atmospheric pressure and constant humidity) and a steel syringe needle of 0.5 mm diameter. During the measurements, distilled water was used as a test liquid. The total apparent surface free energies ( $\gamma_{s,tot}$ ) of the layers were calculated from these dynamic contact angle data, knowing the surface tension of the distilled water, ( $\gamma_l$ , 72.1 mN m<sup>-1</sup> at 25°C) and the contact angle hysteresis, which is defined as the difference between the  $\theta_{adv}$  and  $\theta_{rec}$  as shown by Equation 1.<sup>45</sup>

$$\gamma_s^{tot} = \left( \frac{\gamma_l(1 + \cos\theta_{adv})^2}{(2 + \cos\theta_{rec} + \cos\theta_{adv})} \right). \quad (\text{Equation 1})$$

*In-situ* bubble formation during potentiostatic electrolysis was recorded with a digital microscope (500  $\times$  magnification) at different potentials in a CO<sub>2</sub>-saturated 0.1 M KHCO<sub>3</sub>-solution. The size of the bubbles—right before their departure from the electrode surface—was determined with the ImageJ image processing and analysis software.



Temperature-programmed CO<sub>2</sub> desorption (TPD) profiles were recorded with a BELCAT-A instrument. Samples were heated to 500°C for 1 h in N<sub>2</sub> atmosphere prior to the measurements to remove all the adsorbed species from the surface. The catalysts were cooled in He atmosphere to 50°C, and CO<sub>2</sub> was adsorbed at this temperature for 30 min. This was followed by a He rinsing step (15 min), when the excess (not adsorbed) CO<sub>2</sub> was removed. In these steps, the flow rate of the gases was 50 mL min<sup>-1</sup>. For the CO<sub>2</sub> desorption step samples were heated in He with 10°C min<sup>-1</sup> heating rate (30 mL min<sup>-1</sup> flow rate). The desorbed CO<sub>2</sub> was analyzed with a TCD detector.

## SUPPLEMENTAL INFORMATION

Supplemental Information can be found online at <https://doi.org/10.1016/j.joule.2019.05.007>.

## ACKNOWLEDGMENTS

This project has received funding from the European Research Council (ERC) under the European Union's Horizon 2020 research and innovation program (grant agreement no. 716539). This work was supported by the GINOP-2.3.2-15-2016-00013 project. Ministry of Human Capacities, Hungary grant 20391-3/2018/FEKUSTRAT is also acknowledged. K.A., T.A., and P.A. would like to thank the Army Research Office MURI grant for financial support (#W911NF1410263). D.H. acknowledges the support of the New National Excellence Program of the Ministry of Human Capacities (grant UNKP-18-3). The authors are thankful to AkzoNobel for the donation of the LEVASIL silica colloid. The authors also thank Kornélia Ábrahámné Baán for performing the temperature programmed desorption measurements, László Nagy for the help with the N<sub>2</sub> adsorption and desorption measurements, Egon Kecsenovity for taking the TEM, Dr. Attila Kormányos for taking the SEM images, and Dr. Biborka Janáky-Bohner for her help with the manuscript preparation.

## AUTHOR CONTRIBUTIONS

P.A. and C.J. conceived the research and designed the experiments. D.H. and A.S. synthesized the samples and performed all electrochemical measurements. K.A. supervised, designed, and analyzed XPS experiments. T.A. performed the XPS and some BET measurements. L.J. carried out and analyzed the contact angle measurements. All authors discussed the results and assisted during manuscript preparation, which was completed by D.H. and C.J.

## DECLARATION OF INTERESTS

The authors declare no competing interests.

Received: January 18, 2019

Revised: March 18, 2019

Accepted: May 7, 2019

Published: May 30, 2019

## REFERENCES

- Endrődi, B., Bencsik, G., Darvas, F., Jones, R., Rajeshwar, K., and Janáky, C. (2017). Continuous-flow electroreduction of carbon dioxide. *Prog. Energy Combust. Sci.* 62, 133–154.
- Seh, Z.W., Kibsgaard, J., Dickens, C.F., Chorkendorff, I., Nørskov, J.K., and Jaramillo, T.F. (2017). Combining theory and experiment in electrocatalysis: insights into materials design. *Science* 355, eead4998.
- Bushuyev, O.S., De Luna, P., Dinh, C.T., Tao, L., Saur, G., van de Lagemaat, J., Kelley, S.O., and Sargent, E.H. (2018). What should we make with CO<sub>2</sub> and how can we make it? *Joule* 2, 825–832.
- Hursán, D., and Janáky, C. (2018). Electrochemical reduction of carbon dioxide on nitrogen-doped carbons: insights from isotopic labeling studies. *ACS Energy Lett.* 3, 722–723.
- Roy, A., Hursán, D., Artyushkova, K., Atanassov, P., Janáky, C., and Serov, A. (2018).

- Nanostructured metal-N-C electrocatalysts for CO<sub>2</sub> reduction and hydrogen evolution reactions. *Appl. Catal. B* 232, 512–520.
- Ju, W., Bagger, A., Hao, G.P., Varela, A.S., Sinev, I., Bon, V., Roldan Cuenya, B., Kaskel, S., Rossmeisl, J., and Strasser, P. (2017). Understanding activity and selectivity of metal-nitrogen-doped carbon catalysts for electrochemical reduction of CO<sub>2</sub>. *Nat. Commun.* 8, 944.
  - Leonard, N., Ju, W., Sinev, I., Steinberg, J., Luo, F., Varela, A.S., Roldan Cuenya, B., and Strasser, P. (2018). The chemical identity, state and structure of catalytically active centers during the electrochemical CO<sub>2</sub> reduction on porous Fe–nitrogen–carbon (Fe–N–C) materials. *Chem. Sci.* 9, 5064–5073.
  - Wu, J., Liu, M., Sharma, P.P., Yadav, R.M., Ma, L., Yang, Y., Zou, X., Zhou, X.D., Vajtai, R., Yakobson, B.I., et al. (2016). Incorporation of nitrogen defects for efficient reduction of CO<sub>2</sub> via two-electron pathway on three-dimensional graphene foam. *Nano Lett.* 16, 466–470.
  - Zheng, T., Jiang, K., Ta, N., Hu, Y., Zeng, J., Liu, J., and Wang, H. (2019). Large-scale and highly selective CO<sub>2</sub> electrocatalytic reduction on nickel single-atom catalyst. *Joule* 3, 265–278.
  - Varela, A.S., Ju, W., and Strasser, P. (2018). Molecular nitrogen–carbon catalysts, solid metal organic framework catalysts, and solid metal/nitrogen-doped carbon (MNC) catalysts for the electrochemical CO<sub>2</sub> reduction. *Adv. Energy Mater.* 8, 1703614.
  - Vasileff, A., Zheng, Y., and Qiao, S.Z. (2017). Carbon solving carbon's problems: recent progress of nanostructured carbon-based catalysts for the electrochemical reduction of CO<sub>2</sub>. *Adv. Energy Mater.* 7, 1700759.
  - Lai, J., Nsabimana, A., Luque, R., and Xu, G. (2018). 3D porous carbonaceous electrodes for electrocatalytic applications. *Joule* 2, 76–93.
  - Duan, X., Xu, J., Wei, Z., Ma, J., Guo, S., Wang, S., Liu, H., and Dou, S. (2017). Metal-free carbon materials for CO<sub>2</sub> electrochemical reduction. *Adv. Mater.* 29, 1701784.
  - Daiyan, R., Tan, X., Chen, R., Saputera, W.H., Tahini, H.A., Lovell, E., Ng, Y.H., Smith, S.C., Dai, L., Lu, X., et al. (2018). Electroreduction of CO<sub>2</sub> to CO on a mesoporous carbon catalyst with progressively removed nitrogen moieties. *ACS Energy Lett.* 3, 2292–2298.
  - Liu, S., Yang, H., Huang, X., Liu, L., Cai, W., Gao, J., Li, X., Zhang, T., Huang, Y., and Liu, B. (2018). Identifying active sites of nitrogen-doped carbon materials for the CO<sub>2</sub> reduction reaction. *Adv. Funct. Mater.* 28, 1800499.
  - Lum, Y., Kwon, Y., Lobaccaro, P., Chen, L., Clark, E.L., Bell, A.T., and Ager, J.W. (2016). Trace levels of copper in carbon materials show significant electrochemical CO<sub>2</sub> reduction activity. *ACS Catal.* 6, 202–209.
  - Zhao, Y., Liang, J., Wang, C., Ma, J., and Wallace, G.G. (2018). Tunable and efficient tin modified nitrogen-doped carbon nanofibers for electrochemical reduction of aqueous carbon dioxide. *Adv. Energy Mater.* 8, 1702524.
  - Clark, E.L., Resasco, J., Landers, A., Lin, J., Chung, L.-T., Walton, A., Hahn, C., Jaramillo, T.F., and Bell, A.T. (2018). Standards and protocols for data acquisition and reporting for studies of the electrochemical reduction of carbon dioxide. *ACS Catal.* 8, 6560–6570.
  - Zhang, S., Kang, P., Ubnoske, S., Brennaman, M.K., Song, N., House, R.L., Glass, J.T., and Meyer, T.J. (2014). Polyethylenimine-enhanced electrocatalytic reduction of CO<sub>2</sub> to formate at nitrogen-doped carbon nanomaterials. *J. Am. Chem. Soc.* 136, 7845–7848.
  - Liu, T., Ali, S., Lian, Z., Si, C., Su, D.S., and Li, B. (2018). Phosphorus-doped onion-like carbon for CO<sub>2</sub> electrochemical reduction: the decisive role of the bonding configuration of phosphorus. *J. Mater. Chem. A* 6, 19998–20004.
  - Song, Y., Chen, W., Zhao, C., Li, S., Wei, W., and Sun, Y. (2017). Metal-free nitrogen-doped mesoporous carbon for electroreduction of CO<sub>2</sub> to ethanol. *Angew. Chem. Int. Ed.* 56, 10840–10844.
  - Jhong, H.R., Brushett, F.R., and Kenis, P.J.A. (2013). The effects of catalyst layer deposition methodology on electrode performance. *Adv. Energy Mater.* 3, 589–599.
  - Wu, J., Ma, S., Sun, J., Gold, J.I., Tiwary, C., Kim, B., Zhu, L., Chopra, N., Odeh, I.N., Vajtai, R., et al. (2016). A metal-free electrocatalyst for carbon dioxide reduction to multi-carbon hydrocarbons and oxygenates. *Nat. Commun.* 7, 13869.
  - Yang, H., Wu, Y., Lin, Q., Fan, L., Chai, X., Zhang, Q., Liu, J., He, C., and Lin, Z. (2018). Composition tailoring via N & S co-doping and structure tuning by constructing hierarchical pores: metal-free catalysts for high-performance electrochemical reduction of CO<sub>2</sub>. *Angew. Chem. Int. Ed.* 130, 15702–15706.
  - Jaouen, F., and Lindbergh, G. (2003). Transient techniques for investigating mass-transport limitations in gas diffusion electrodes: I. Modeling the PEFC cathode. *J. Electrochem. Soc.* 150, A1699–A1717.
  - Kong, C.S., Kim, D.-Y., Lee, H.-K., Shul, Y.-G., and Lee, T.-H. (2002). Influence of pore-size distribution of diffusion layer on mass-transport problems of proton exchange membrane fuel cells. *J. Power Sources* 108, 185–191.
  - Weng, L.C., Bell, A.T., and Weber, A.Z. (2018). Modeling gas-diffusion electrodes for CO<sub>2</sub> reduction. *Phys. Chem. Chem. Phys.* 20, 16973–16984.
  - Yamamoto, T., Tryk, D.A., Hashimoto, K., Fujishima, A., and Okawa, M. (2000). Electrochemical reduction of CO<sub>2</sub> in the micropores of activated carbon fibers. *J. Electrochem. Soc.* 147, 3393–3400.
  - Wang, H., Jia, J., Song, P., Wang, Q., Li, D., Min, S., Qian, C., Wang, L., Li, Y.F., Ma, C., et al. (2017). Efficient electrocatalytic reduction of CO<sub>2</sub> by nitrogen-doped nanoporous carbon/carbon nanotube membranes: a step towards the electrochemical CO<sub>2</sub> refinery. *Angew. Chem. Int. Ed.* 56, 7847–7852.
  - Dutta, A., Rahaman, M., Luedi, N.C., Mohos, M., and Broekmann, P. (2016). Morphology matters: tuning the product distribution of CO<sub>2</sub> electroreduction on oxide-derived Cu foam catalysts. *ACS Catal.* 6, 3804–3814.
  - Sen, S., Liu, D., and Palmore, G.T.R. (2014). Electrochemical reduction of CO<sub>2</sub> at copper nanofoams. *ACS Catal.* 4, 3091–3095.
  - Hall, A.S., Yoon, Y., Wuttig, A., and Surendranath, Y. (2015). Mesostructure-induced selectivity in CO<sub>2</sub> reduction catalysis. *J. Am. Chem. Soc.* 137, 14834–14837.
  - Burdyny, T., Graham, P.J., Pang, Y., Dinh, C.-T., Liu, M., Sargent, E.H., and Sinton, D. (2017). Nanomorphology-enhanced gas-evolution intensifies CO<sub>2</sub> reduction electrochemistry. *ACS Sustain. Chem. Eng.* 5, 4031–4040.
  - Reske, R., Mistry, H., Beharid, F., Roldan Cuenya, B., and Strasser, P. (2014). Particle size effects in the catalytic electroreduction of CO<sub>2</sub> on Cu nanoparticles. *J. Am. Chem. Soc.* 136, 6978–6986.
  - Tang, W., Peterson, A.A., Varela, A.S., Jovanov, Z.P., Bech, L., Durand, W.J., Dahl, S., Nørskov, J.K., and Chorkendorff, I. (2012). The importance of surface morphology in controlling the selectivity of polycrystalline copper for CO<sub>2</sub> electroreduction. *Phys. Chem. Chem. Phys.* 14, 76–81.
  - Lu, Q., Rosen, J., Zhou, Y., Hutchings, G.S., Kimmel, Y.C., Chen, J.G., and Jiao, F. (2014). A selective and efficient electrocatalyst for carbon dioxide reduction. *Nat. Commun.* 5, 3242.
  - Liu, M., Pang, Y., Zhang, B., De Luna, P., Voznyy, O., Xu, J., Zheng, X., Dinh, C.T., Fan, F., Cao, C., et al. (2016). Enhanced electrocatalytic CO<sub>2</sub> reduction via field-induced reagent concentration. *Nature* 537, 382–386.
  - Liang, J., Zheng, Y., Chen, J., Liu, J., Hulicova-Jurcakova, D., Jaroniec, M., and Qiao, S.Z. (2012). Facile oxygen reduction on a three-dimensionally ordered macroporous graphitic C<sub>3</sub>N<sub>4</sub>/carbon composite electrocatalyst. *Angew. Chem. Int. Ed.* 51, 3892–3896.
  - Wei, W., Liang, H., Parvez, K., Zhuang, X., Feng, X., and Müllen, K. (2014). Nitrogen-doped carbon nanosheets with size-defined mesopores as highly efficient metal-free catalyst for the oxygen reduction reaction. *Angew. Chem. Int. Ed.* 53, 1570–1574.
  - Liang, H.W., Zhuang, X., Brüller, S., Feng, X., and Müllen, K. (2014). Hierarchically porous carbons with optimized nitrogen doping as highly active electrocatalysts for oxygen reduction. *Nat. Commun.* 5, 4973.
  - Chen, Y., Artyushkova, K., Rojas-Carbonell, S., Serov, A., Matanovic, I., Santoro, C., Asset, T., and Atanassov, P. (2018). Inhibition of surface chemical moieties by tris(hydroxymethyl) aminomethane: a key to understanding oxygen reduction on iron–nitrogen–carbon catalysts. *ACS Appl. Energy Mater.* 1, 1942–1949.
  - Matanovic, I., Artyushkova, K., and Atanassov, P. (2018). Understanding PGM-free catalysts by linking density functional theory calculations and structural analysis: perspectives and challenges. *Curr. Opin. Electrochem.* 9, 137–144.
  - Kabir, S., Artyushkova, K., Serov, A., and Atanassov, P. (2018). Role of nitrogen moieties in N-doped 3D-graphene nanosheets for oxygen electroreduction in acidic and alkaline media. *ACS Appl. Mater. Interfaces* 10, 11623–11632.

44. Kabir, S., Artyushkova, K., Serov, A., Kiefer, B., and Atanassov, P. (2016). Binding energy shifts for nitrogen-containing graphene-based electrocatalysts – Experiments and DFT calculations. *Surf. Interface Anal.* **48**, 293–300.
45. Chibowski, E. (2003). Surface free energy of a solid from contact angle hysteresis. *Adv. Colloid Interface Sci.* **103**, 149–172.
46. Wenzel, R.N. (1949). Surface roughness and contact angle. *J. Phys. Chem.* **53**, 1466–1467.
47. Bico, J., Thiele, U., and Quéré, D. (2002). Wetting of textured surfaces. *Colloids Surf. A Physicochem. Eng. Asp.* **206**, 41–46.
48. Faber, M.S., Dziedzic, R., Lukowski, M.A., Kaiser, N.S., Ding, Q., and Jin, S. (2014). High-Performance Electrocatalysis using metallic cobalt pyrite (CoS<sub>2</sub>) micro- and nanostructures. *J. Am. Chem. Soc.* **136**, 10053–10061.
49. Dutta, D., Wood, B.C., Bhide, S.Y., Ayappa, K.G., and Narasimhan, S. (2014). Enhanced gas adsorption on graphitic substrates via defects and local curvature: a density functional theory study. *J. Phys. Chem. C* **118**, 7741–7750.
50. Chai, G.L., and Guo, Z.X. (2016). Highly effective sites and selectivity of nitrogen-doped graphene/CNT catalysts for CO<sub>2</sub> electrochemical reduction. *Chem. Sci.* **7**, 1268–1275.
51. Yadav, R.M., Wu, J., Kochandra, R., Ma, L., Tiwary, C.S., Ge, L., Ye, G., Vajtai, R., Lou, J., and Ajayan, P.M. (2015). Carbon nitrogen nanotubes as efficient bifunctional electrocatalysts for oxygen reduction and evolution reactions. *ACS Appl. Mater. Interfaces* **7**, 11991–12000.
52. Grosse, P., Gao, D., Scholten, F., Sinev, I., Mistry, H., and Roldan Cuenya, B. (2018). Dynamic changes in the structure, chemical state and catalytic selectivity of Cu nanocubes during CO<sub>2</sub> electroreduction: size and support effects. *Angew. Chem.* **57**, 6192–6197.
53. Workman, M.J., Dzara, M., Ngo, C., Pylypenko, S., Serov, A., McKinney, S., Gordon, J., Atanassov, P., and Artyushkova, K. (2017). Platinum group metal-free electrocatalysts: effects of synthesis on structure and performance in proton-exchange membrane fuel cell cathodes. *J. Power Sources* **348**, 30–39.

# Electrochemical Hole Injection Selectively Expels Iodide from Mixed Halide Perovskite Films

Gergely F. Samu,<sup>†,‡,§,¶</sup> **Ádám Balog,**<sup>†</sup> Filippo De Angelis,<sup>||,⊥,#</sup> **Daniele Meggiolaro,**<sup>⊥,#</sup>  
 Prashant V. Kamat,<sup>\*,§,¶</sup> and **Csaba Janáky**<sup>\*,†,‡,¶</sup>

<sup>†</sup>Department of Physical Chemistry and Materials Science, Interdisciplinary Excellence Centre, University of Szeged, Rerrich Square 1, Szeged, H-6720, Hungary

<sup>‡</sup>ELI-ALPS Research Institute, Dugonics Square 13, Szeged, 6720, Hungary

<sup>§</sup>Department of Chemistry and Biochemistry, University of Notre Dame, Notre Dame, Indiana 46556, United States

<sup>||</sup>Department of Chemistry, Biology and Biotechnology, University of Perugia, Via Elce di Sotto, 8I-06123 Perugia, Italy

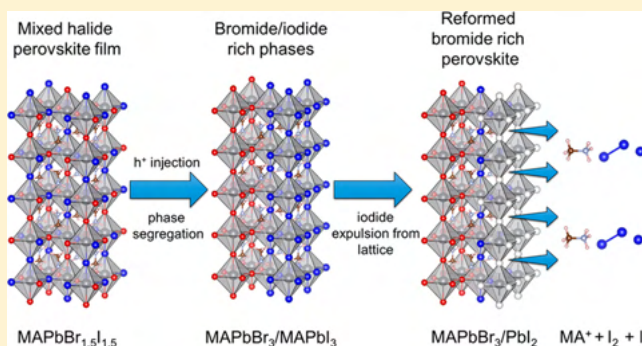
<sup>⊥</sup>Computational Laboratory for Hybrid/Organic Photovoltaics (CLHYO), CNR-ISTM, Via Elce di Sotto 8, 06123 Perugia, Italy

<sup>#</sup>CompuNet, Istituto Italiano di Tecnologia, Via Morego 30, 16163 Genova, Italy

<sup>¶</sup>Radiation Laboratory, University of Notre Dame, Notre Dame, Indiana 46556, United States

**S** Supporting Information

**ABSTRACT:** Halide ion mobility in metal halide perovskites remains an intriguing phenomenon, influencing their optical and photovoltaic properties. Selective injection of holes through electrochemical anodic bias has allowed us to probe the effect of hole trapping at iodide (0.9 V) and bromide (1.15 V) in mixed halide perovskite ( $\text{CH}_3\text{NH}_3\text{PbBr}_{1.5}\text{I}_{1.5}$ ) films. Upon trapping holes at the iodide site, the iodide gradually gets expelled from the mixed halide film (as iodine and/or triiodide ion), leaving behind re-formed  $\text{CH}_3\text{NH}_3\text{PbBr}_3$  domains. The weakening of the Pb–I bond following the hole trapping (oxidation of the iodide site) and its expulsion from the lattice in the form of iodine provided further insight into the photoinduced segregation of halide ions in mixed halide perovskite films. Transient absorption spectroscopy revealed that the iodide expulsion process leaves a defect-rich perovskite lattice behind as charge carrier recombination in the re-formed lattice is greatly accelerated. The selective mobility of iodide species provides insight into the photoinduced phase segregation and its implication in the stable operation of perovskite solar cells.



## INTRODUCTION

The ability to tune the bandgap of mixed halide perovskites (MHPs) by controlling the halide composition generated a wave of interest toward studying their optical and photovoltaic properties.<sup>1,2</sup> Their potential application in tandem solar cells employing multilayered MHP films with a bandgap gradient is of particular interest.<sup>3–6</sup> Challenges, however, remain in their utilization in such photovoltaic devices.<sup>7</sup> The ease of exchange of halide ions between two perovskite layers with different halide composition<sup>8–11</sup> as well as photo-,<sup>12–14</sup> current-, or voltage-induced<sup>14–17</sup> segregation burdens their utilization. For example, we have recently shown that the photoinduced segregation in mixed halide lead perovskite films leads to a drop in photovoltaic performance.<sup>18</sup> Strategies exist to mitigate the extent of segregation including varying crystallite domain size,<sup>19–24</sup> defect concentration,<sup>12,13</sup> nature of A-site cation in the  $\text{ABX}_3$  structure,<sup>1,5,19,25,26</sup> or charge carrier generation profile.<sup>27–29</sup>

The photoinduced segregation in mixed halide films (e.g.,  $\text{MAPbBr}_{1.5}\text{I}_{1.5}$  where  $\text{MA}^+ = \text{CH}_3\text{NH}_3^+$ ) results in phase demixing, whereby iodide-rich and bromide-rich domains form during steady state illumination.<sup>30,31</sup> Interestingly, this phenomenon is reversible, as the original mixed halide composition is restored in the dark. Different models have been proposed to explain this behavior including defect-driven<sup>26–28,32</sup> and polaron-induced lattice strain driven<sup>25,33,34</sup> segregation of halide ions. There are two points that all these models have in common: the importance of the long charge carrier lifetime<sup>35–37</sup> and the migration of halide ions (which is even observable in pure  $\text{MAPbI}_3$  and  $\text{MAPbBr}_3$ ) through the dynamically changing perovskite structure.<sup>38–40</sup>

In a photovoltaic cell, the charge carrier separation upon bandgap excitation leads to the transport of electrons and holes

Received: April 29, 2019

Published: June 19, 2019

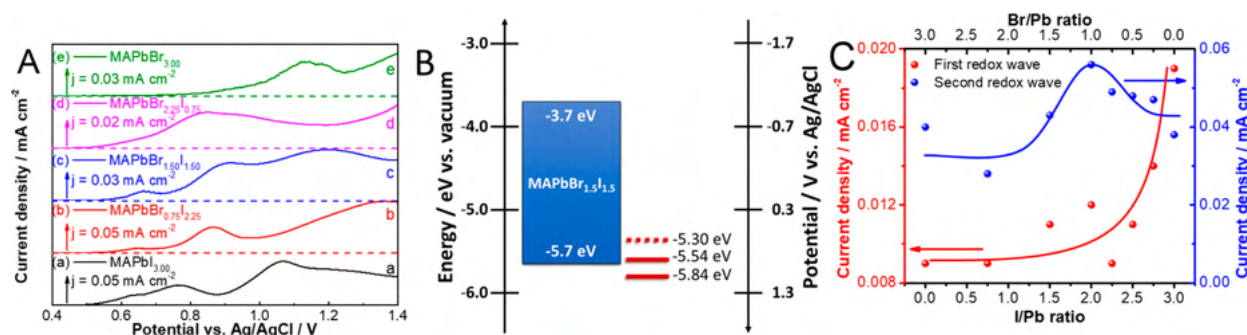


**Figure 1.** (A) Linear sweep voltammograms of FTO/MAPbBr<sub>x-1.5</sub>I<sub>1.5</sub> films in 0.1 M Bu<sub>4</sub>NPF<sub>6</sub>/DCM electrolyte (5 mV s<sup>-1</sup> sweep rate). (B) Band diagram of MAPbBr<sub>1.5</sub>I<sub>1.5</sub> together with the peak onset of the observed Faradaic events. (C) Variation of the peak currents of the first two redox waves as a function of MHP composition, with solid lines to guide the eye.

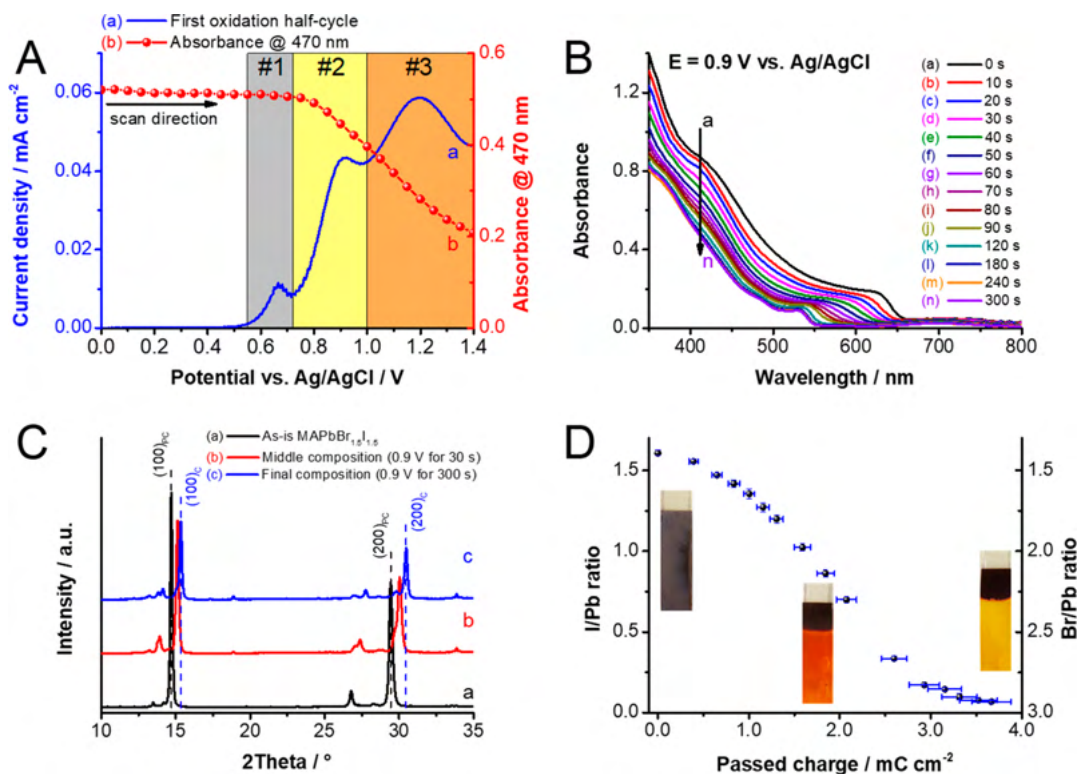


**Figure 2.** (A) Linear sweep voltammogram of a FTO/MAPbBr<sub>1.5</sub>I<sub>1.5</sub> film in 0.1 M Bu<sub>4</sub>NPF<sub>6</sub>/DCM electrolyte (5 mV s<sup>-1</sup> sweep rate) plotted together with the absorbance change at 470 nm. Region #1 is where hole trapping occurs, and region #2 is where hole injection to the valence band occurs. (B) UV-vis spectra of FTO/MAPbBr<sub>1.5</sub>I<sub>1.5</sub> films during potentiostatic treatment at 0.9 V vs Ag/AgCl. (C) XRD patterns of thick FTO/MAPbBr<sub>x-1.5</sub>I<sub>1.5</sub> electrodes before and after potentiostatic treatment at 0.9 V vs Ag/AgCl in 0.1 M Bu<sub>4</sub>NPF<sub>6</sub>/DCM electrolyte. PC and C denote pseudocubic and cubic lattice, respectively. (D) Alteration of the optically active perovskite composition as a function of passed charge during potentiostatic treatment at 0.9 V vs Ag/AgCl. The photographs show the color change of the electrode at two stages of the potentiostatic treatment. The standard deviation was determined from measurements on three separate FTO/MAPbBr<sub>1.5</sub>I<sub>1.5</sub> electrodes.

toward the collecting electrodes placed on the opposite sides of the cell. A significant fraction of these charge carriers undergo recombination as well as trapping at the various defect sites. In fact, we can show the consequences of charge carrier trapping through probing their recombination using time-resolved transient absorption<sup>12,41</sup> and emission spectroscopies.<sup>11,21</sup> While these techniques have provided some useful information on the defect sites and their role in dictating excited state dynamics, it is difficult to establish the contribution of electron- or hole-trapping selectively.

In most studies, where the aim is to understand charge carrier dynamics, light excitation is solely responsible for charge carrier generation, which always results in a comparable

density of electrons and holes. Recently, we have shown that the excited state dynamics of metal halide perovskite films can be probed through ultrafast spectroelectrochemistry.<sup>42</sup> This technique also provides us an opportunity to inject holes into perovskite films *selectively*, through applied anodic bias. We discuss here the effect of electrochemical hole injection into mixed halide lead perovskite films and the consequential effect of hole trapping by the halide ions in the structure.

## RESULTS AND DISCUSSION

**Selective Hole Injection via Electrochemistry.** On the basis of the electrochemical protocols outlined in our previous study<sup>43</sup> we recorded linear sweep voltammograms (LSVs) in

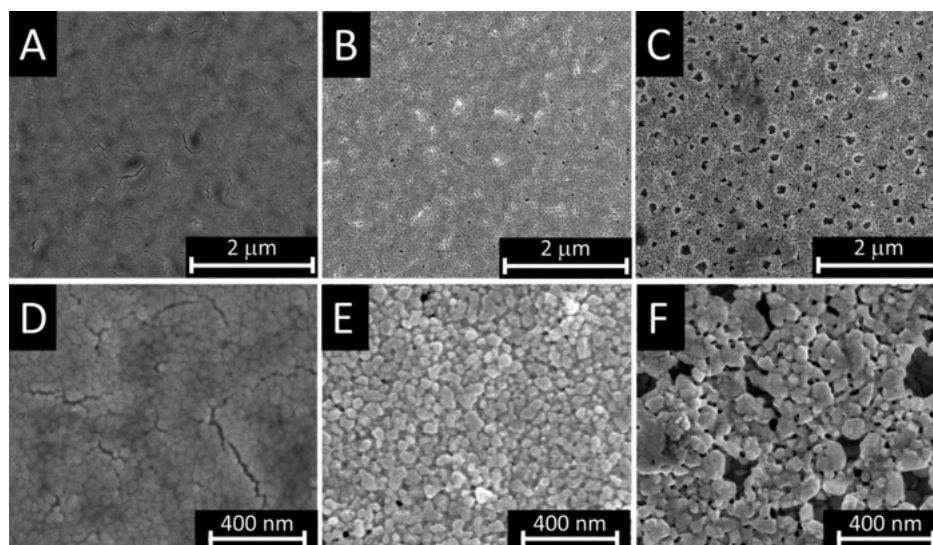


**Figure 3.** Top-down SEM images of FTO/MAPbBr<sub>1.5</sub>I<sub>1.5</sub> films at different magnifications. (A, D) Pristine films, (B, E) films treated at 0.9 V vs Ag/AgCl for 30 s (until 1.3 mC cm<sup>-2</sup> charge density was passed), (C, F) films treated at 0.9 V vs Ag/AgCl for 300 s (until 3.7 mC cm<sup>-2</sup> charge density is passed).

0.1 M Bu<sub>4</sub>NPF<sub>6</sub> dichloromethane (DCM) electrolyte for various MHP films. The LSVs show a composition dependency in the position (and magnitude) of the distinct oxidation waves (Figure 1A, Figure S1, and Table S1). Considering the redox potential of halide oxidation in lead halides<sup>43</sup> and solution phase (i.e., bromide (+1.26 V) and iodide (+0.86 V) oxidation in this medium (Figure S2)), the more positive events on the LSV scans can be assigned to these reactions (Figure 1A and Figure S1). The MHP films are stable below these potentials, so the first two waves can be attributed to the electrochemistry of the intact MHP layers. These oxidation waves show a gradual shift to more positive potentials with increasing bromide content (Table S1), as one would expect from their increased stability in the series. We can attribute the oxidation wave in the region #1 to the trapping of holes and the subsequent movement of iodide ions in the lattice in these materials, as shown by electrochemical impedance spectroscopy (Figure S3). Note that these states barely exist in the case of MAPbBr<sub>3</sub>. The position of the #2 oxidation wave at higher potential matches the respective valence band edge position (Figure 1B) and corresponds to hole injection into the perovskite structure (i.e., to the valence band). From the magnitude of the current density related to process #1 it is apparent that all MHP phases show decreased trap state density compared to the pure MAPbI<sub>3</sub> phase (Figure 1C). Notably, the rate (i.e., the current density) of process #2 peaks at approximately equimolar Br/I ratio (Figure 1C).

**Selective Expulsion of Iodide from MAPbBr<sub>1.5</sub>I<sub>1.5</sub> Films.** Spectroelectrochemistry was used to track the spectral changes following the hole injection into MAPbBr<sub>1.5</sub>I<sub>1.5</sub> films. During the initial step of hole trapping no change of the spectral features was observed (region #1 in Figure 2A). As sufficient electrochemical driving force (with increased electrode potential) is reached to induce hole injection into the valence band of MAPbBr<sub>1.5</sub>I<sub>1.5</sub> (region #2 in Figure 2A), we observe a decrease in the overall absorbance (Figure S4). Interestingly, this process is coupled with the monotonic shift of the absorption edge (i.e., bandgap) to shorter wavelengths. This irreversible shift in absorption edge suggests enrichment of the MHP phase with bromide-rich domains through the

selective expulsion of iodide into the solution from the perovskite lattice. The higher affinity of Pb(II) to bromide as compared to iodide in the perovskite lattice is likely to be the reason for the enrichment of bromide-rich domains after the electrochemical hole injection.<sup>12,44</sup>

Similar trends were revealed during potentiostatic experiments. At moderately positive potentials, where no Faradaic event occurs (i.e., 0.5 V and below), the UV-vis absorbance remains unaltered (Figure S5). However, when the applied potential was increased to 0.9 V vs Ag/AgCl, we observe a gradual decrease in absorbance, coupled with the shift in the absorption edge from 660 nm to 545 nm in 300 s. Thus, the shift in the bandgap to a higher energy region becomes evident as iodide was expelled from the perovskite lattice (Figure 2B). During the intermediate times, the absorbance onset becomes less sharp, as residual contribution from varying degree of mixed phases is seen during the expulsion process. Once iodide expulsion from the lattice is completed, the spectrum reflects the optical features of MAPbBr<sub>3</sub>. Further anodic polarization at this potential does not change the spectrum, confirming the stability of MAPbBr<sub>3</sub> (as predicted from the LSV traces in Figure 1A).

The effect of the iodide expulsion process on the crystal structure of the MHP films was monitored by X-ray diffraction (XRD) measurements (Figure 2C). A gradual shift of the MAPbBr<sub>1.5</sub>I<sub>1.5</sub>-related reflections was observed to higher 2θ values upon oxidation, which translates to the contraction of the pseudocubic perovskite crystal lattice. At an intermediate treatment time this results in the formation of MAPbBr<sub>2.6</sub>I<sub>0.4</sub>.<sup>2</sup> Closer inspection of the pattern reveals that an additional intermediate MHP phase is also present in the films (MAPbBr<sub>2.3</sub>I<sub>0.7</sub>). The presence of multiple perovskite phases is consistent with the less sharp nature of the absorption onset seen previously on the UV-vis spectra (Figure 2B). Interestingly, at the end of the potentiostatic treatment a slightly contracted MAPbBr<sub>3</sub> lattice was formed, which is possibly caused by the presence of defects in the re-formed crystal lattice. Reflections from both PbI<sub>2</sub> and PbBr<sub>2</sub> phases are also present in all cases (as also deduced from X-ray photoelectron spectroscopy, XPS), however only weakly.

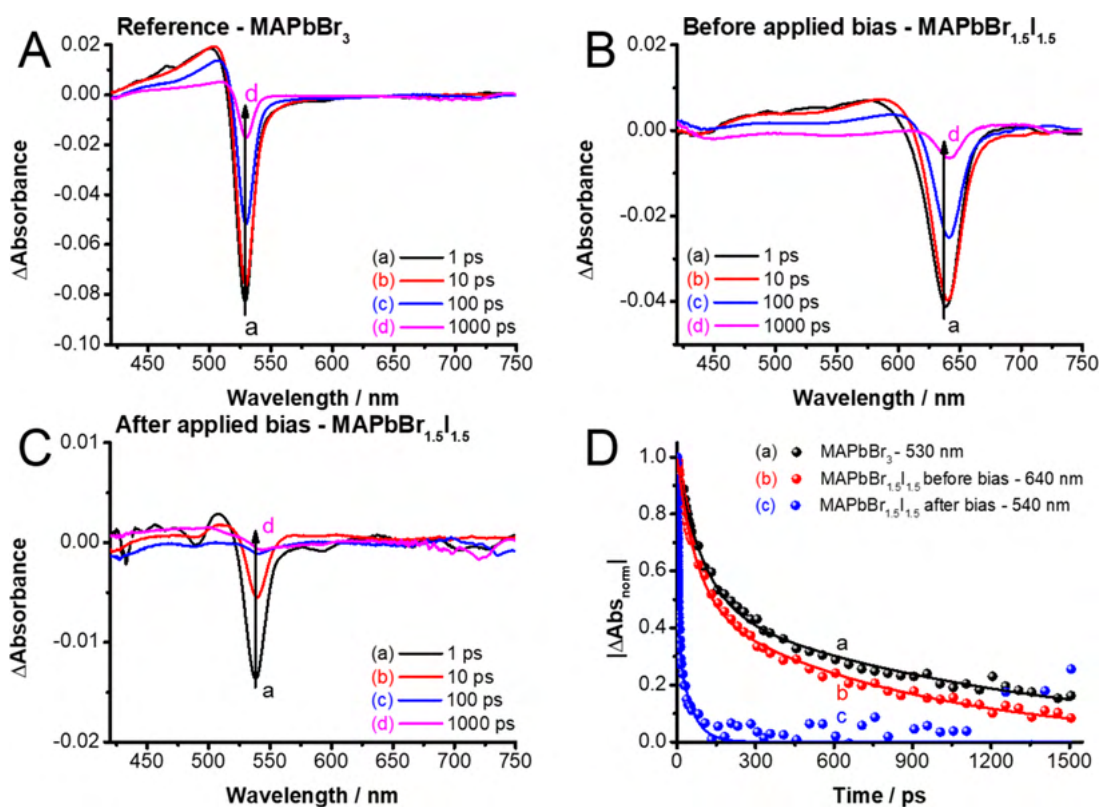


**Figure 4.** Time-resolved transient absorption spectra recorded following 387 nm laser pulse excitation ( $4 \mu\text{J cm}^{-2}$ ) of (A) pristine FTO/MAPbBr<sub>3</sub> films, (B) pristine FTO/MAPbBr<sub>1.5</sub>I<sub>1.5</sub> films, and (C) FTO/MAPbBr<sub>1.5</sub>I<sub>1.5</sub> films after potentiostatic treatment at 0.9 V vs Ag/AgCl for 300 s under vacuum. (D) Recovery profiles of the perovskite films monitored at their ground state bleach maxima and the corresponding biexponential fits.

This signals that their formation is confined to the surface of the MHP films (or that their crystal domain size is rather small and not continuous) and the bulk of the material retains the perovskite crystal lattice. The XRD data strengthen the notion that the iodide expulsion process is accompanied by the dynamic re-formation of the perovskite lattice, and not just the destruction and ultimate dissolution of the material are achieved.<sup>45</sup> In situ Raman spectroelectrochemistry (Figures S6–S8) further confirmed the formation of iodide- and bromide-rich domains as the first step of the iodide expulsion process. As the applied electrochemical bias was increased (until the point where iodide migration starts in the films), a broad fluorescence signal was observed (Figure S7B). This can be attributed to the formation of domains capable of absorbing (and emitting) the exciting laser light ( $\lambda = 780 \text{ nm}$ ).

To quantify the electrochemically induced iodide expulsion process, we determined the composition of the films from Tauc plots using the recorded UV–vis spectra and a previously obtained bandgap–composition relationship (Figure S9). The Pb/halide composition of the film was found to be dependent on the net charge injected into the MAPbBr<sub>1.5</sub>I<sub>1.5</sub> films (Figure 2D). To minimize the contribution of charging/discharging of the electrical double layer, a preconditioning step (at 0.5 V vs Ag/AgCl for 30 s, Figure S10) was employed, when calculating the charge during the potentiostatic treatment. The effect of electrochemical iodide expulsion was also visually observed, as the dark appearance of the MAPbBr<sub>1.5</sub>I<sub>1.5</sub> films slowly changed, ultimately resulting in a yellow-colored bromide-rich film when the process was completed (Figure 2D).

**Morphological Changes.** With the expulsion of iodide upon hole injection, one would expect morphological changes

associated with the spectral changes. Top-down SEM images were recorded to visualize these changes of the MAPbBr<sub>1.5</sub>I<sub>1.5</sub> films (Figure 3). The alteration of the initially smooth surface to a rougher one was observed with increasing time of the electrochemical biasing. This process is accompanied by the formation of voids in the films. Both the size of the voids and their number increase with the injected charge into the MAPbBr<sub>1.5</sub>I<sub>1.5</sub> film ( $31 \pm 15 \text{ nm}$  at  $1.3 \text{ mC cm}^{-2}$  and  $116 \pm 31 \text{ nm}$  at  $3.7 \text{ mC cm}^{-2}$  injected charge density). The voids in the film further confirm the loss of iodide as the crystal structure re-forms. The evolution of the morphology suggests that MAPbBr<sub>1.5</sub>I<sub>1.5</sub> continuously undergoes structural changes, ultimately yielding the MAPbBr<sub>3</sub> structure.

**Compositional Analysis.** Since the electrode/electrolyte interface plays a pivotal role in the iodide expulsion process, XPS measurements were carried out to probe the alteration of the surface composition of the MAPbBr<sub>1.5</sub>I<sub>1.5</sub> films during the potentiostatic treatment (Table S2). The surface of the MAPbBr<sub>1.5</sub>I<sub>1.5</sub> film was enriched in iodide even before electrochemical treatment. In the intermediate step of the electrochemical treatment we continue to see this excess iodide that remains at the surface, but with a concomitant decrease in the bromide content. This is indicative of the MAPbBr<sub>1.5</sub>I<sub>1.5</sub> surface becoming rich in PbI<sub>2</sub>. This trend signals that iodide constantly migrates to the surface of the film, before getting expelled to the solution. Bromide remains preferentially in the deeper regions of the film. As the electrochemical treatment process was completed, a decrease of PbI<sub>2</sub> on the surface of the films was observed. The final depletion of iodide on the surface signals that the composition of the perovskite phase located on

the surface is approaching that of pure MAPbBr<sub>3</sub> as the electrochemical treatment progresses.

Additionally, we tracked compositional changes of the bulk films by energy-dispersive X-ray spectroscopy (EDX) (Table S3) and that of the solution by inductively coupled plasma optical emission spectrometry (ICP-OES) (for Pb<sup>2+</sup>) and ion-chromatography (IC) (for Br<sup>-</sup> and I<sup>-</sup>) measurements (Table S4), at different stages of the electrochemical biasing. The analysis confirmed a greatly reduced iodide amount in the films, while the amount of lead and bromide remained unchanged. Notably, these measurements suggest that after the potentiostatic treatments there is still remnant iodide left in the films. A plausible explanation for this is the formation of a PbI<sub>2</sub> intermediate during the expulsion process (see also additional absorbance at 450–500 nm in Figure 2B compared to Figure S6A). A detailed discussion on the cross-correlation of the determined compositions can be found in the SI.

**Excited State Dynamics.** We also probed the excited state behavior of MAPbBr<sub>1.5</sub>I<sub>1.5</sub> films to see the effect of iodide expulsion on the charge carrier recombination dynamics. The transient absorption spectra of MHP films were recorded before and after electrochemical treatment (holding the electrode at +0.9 V vs Ag/AgCl), as well as for a pure MAPbBr<sub>3</sub> film (Figure 4A). The intact MAPbBr<sub>1.5</sub>I<sub>1.5</sub> films showed an intense bleach signal centered at 640 nm and recovered within 1.6 ns after excitation (Figure 4B). This transient behavior has been discussed in detail elsewhere.<sup>12,41</sup>

After the electrochemical treatment, a blue-shifted ground state bleach was seen, in accordance with the expulsion of iodide from the perovskite lattice (Figure 4C). Specifically, the maximum of this bleach signal appears at shorter wavelengths (540 nm), which is close to the ground state bleach maximum (530 nm) of pure MAPbBr<sub>3</sub> films (Figure 4A). Furthermore, the maximum intensity of the bleach signal of the MHP film after the electrochemical treatment is decreased in accordance with the decreased absorbance following the iodide expulsion.

Figure 4D compares the recovery kinetics of the bleach signal of MAPbBr<sub>1.5</sub>I<sub>1.5</sub> films before and after electrochemical treatment and the pristine MAPbBr<sub>3</sub> film. The charge carrier lifetime of the two untreated perovskite films are similar (571 ± 68 ps in MAPbBr<sub>3</sub> and 381 ± 28 ps in untreated MAPbBr<sub>1.5</sub>I<sub>1.5</sub>). After the electrochemical treatment (following complete iodide expulsion from the MAPbBr<sub>1.5</sub>I<sub>1.5</sub> film) the recovery becomes faster (16 ± 8 ps). As the iodide is expelled, we expect to see an increase in the number of defect sites. A significant change in the surface morphology seen on the SEM images further supports this notion. These defect sites are responsible for the observed enhancement in the recombination of charge carriers.

**Mechanistic Insights.** The results presented above highlight the effect of hole injection on the compositional, structural, and morphological features of MAPbBr<sub>1.5</sub>I<sub>1.5</sub> films. However, the mechanism behind iodide expulsion remains an intriguing question. To elucidate the form in which iodide leaves the lattice (I<sup>-</sup> or I<sub>2</sub>), we recorded the UV–vis absorbance spectra of the electrolyte after various amounts of charge injection into the MAPbBr<sub>1.5</sub>I<sub>1.5</sub> films. We found that the predominant species formed in the solution phase is I<sub>3</sub><sup>-</sup>, which points toward either the direct expulsion of I<sub>3</sub><sup>-</sup> from the layer or the parallel I<sup>-</sup> and I<sub>2</sub> injection to the solution. In terms of the net redox reaction (eq 1), the trapping of two holes on the iodide sites of four perovskite units results in the formation of one I<sub>2</sub> molecule. To check the validity of the proposed

mechanism, we tracked the evolution of I<sub>3</sub><sup>-</sup> concentration in the electrolyte solution (Figure 5). A linear relationship was

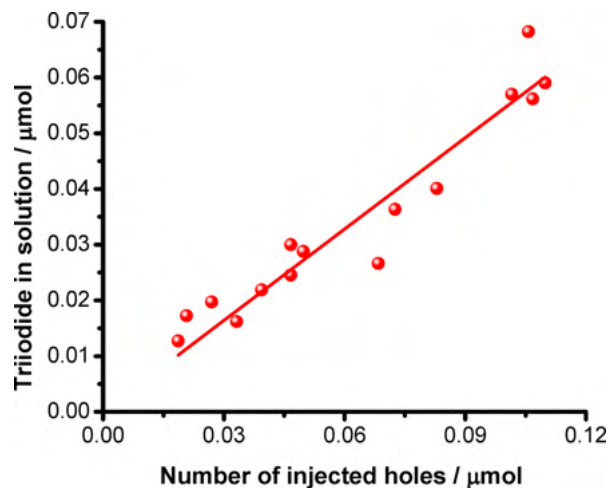


**Figure 5.** Dependence of the formed triiodide amount in the solution phase (0.1 M Bu<sub>4</sub>NPF<sub>6</sub> in DCM) on the amount of injected charge to thick MAPbBr<sub>1.5</sub>I<sub>1.5</sub> films. The films were subjected to potentiostatic treatment at 0.9 V vs Ag/AgCl, while the UV–vis absorbance of the electrolyte was measured. The triiodide concentration was determined from the absorption peak located at 364 nm.

found between the number of injected holes and the amount of I<sub>3</sub><sup>-</sup> in the solution. Furthermore, the slope of the fitted line was  $0.55 \pm 0.02$ , which is in close agreement with the proposed reaction (i.e., 0.5 theoretical value, meaning a 10% deviation).

At the same time, during the re-formation of the structure after hole trapping and iodide oxidation, partial dissolution of the MAPbBr<sub>1.5</sub>I<sub>1.5</sub> structure also occurs (eq 2), thus leaching I<sup>-</sup> ions into the solution, which can form the triiodide complex with I<sub>2</sub>. Note that without electrochemical bias the films are stable within the time frame of the experiments; therefore physical dissolution cannot account for the presence of I<sup>-</sup> ions in the solution. Overall, these three processes together can explain the absence of I<sub>2</sub> species in the solution and the exclusive presence of I<sub>3</sub><sup>-</sup>.

To gain further insight into the mechanistic features, we carried out first-principles calculations employing a hybrid DFT+SOC computational approach; see SI for details. We focus on the nature of hole traps in MAPbI<sub>3</sub>, MAPbBr<sub>3</sub>, and MAPbBr<sub>x</sub>I<sub>3-x</sub>. The defect chemistry of lead halide perovskites is dominated by lead vacancies (V<sub>Pb</sub>) and interstitial halides (X<sub>i</sub>, X = I, Br),<sup>46,47</sup> which are stable defects that can trap holes through the (-2/-) and (-/0) transitions, respectively, both in MAPbI<sub>3</sub> and MAPbBr<sub>3</sub> (see Figure 6A). Despite the apparently different nature, the two types of defects are quite similar, being related to the presence of undercoordinated iodine atoms in the lattice, either because of a lack of lead (V<sub>Pb</sub>) or added halide (X<sub>i</sub>).

In MAPbI<sub>3</sub>, the (-/0) transition of I<sub>i</sub>, corresponding to hole trapping at negatively charged interstitial iodine (I<sub>i</sub><sup>-</sup> → I<sub>i</sub><sup>0</sup>), is calculated at 0.29 eV above the valence band (VB), similar to the (-2/-) transition of V<sub>Pb</sub>, calculated at 0.13 eV. The calculated transition energies nicely match the energy difference measured by voltammetry for traps and VB oxidation in MAPbI<sub>3</sub>, 0.62 and 0.77 V vs Ag/AgCl, respectively; see Table S1 and Figure 1A. In MAPbBr<sub>3</sub> a similar picture is predicted, although both transition levels are somehow shallower,



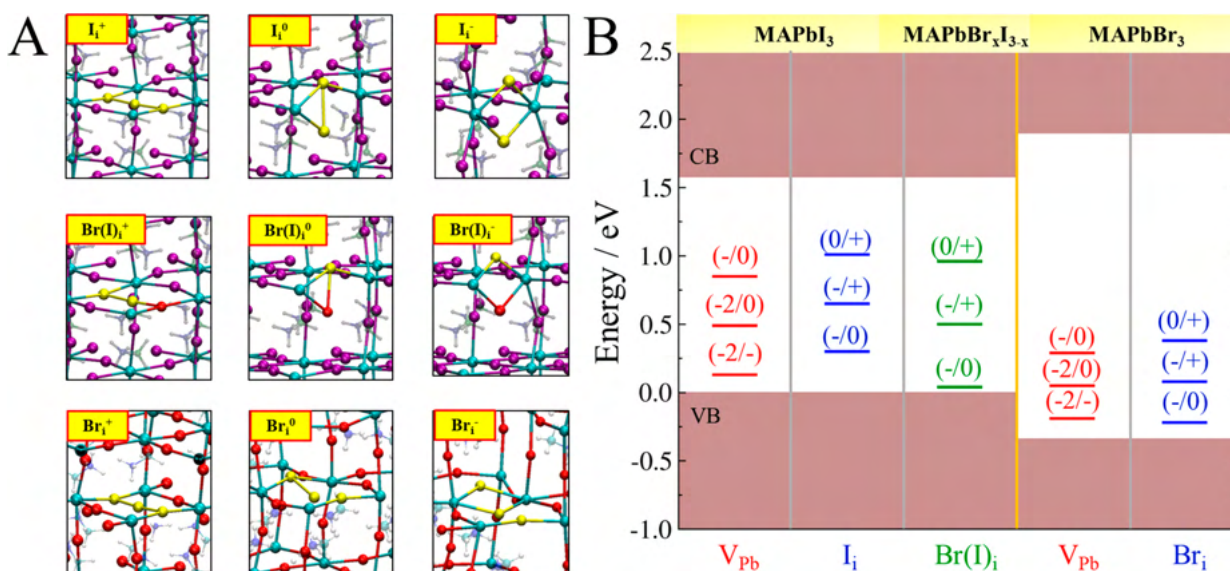
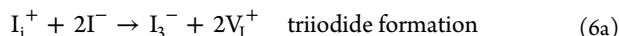
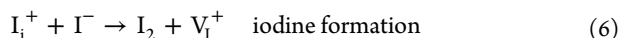
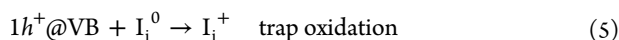
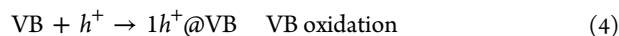
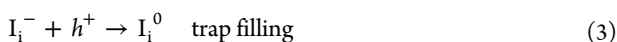
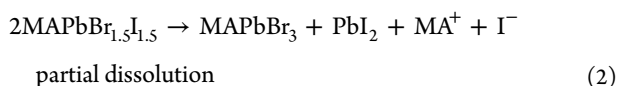
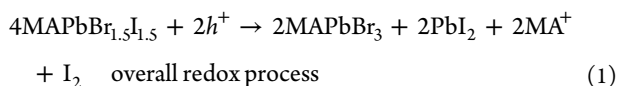


**Figure 6.** (A) Structures and (B) transition energies of stable hole-trapping defects in MAPbI<sub>3</sub>, MAPbBr<sub>3</sub>, and MAPbBr<sub>x</sub>I<sub>3-x</sub>. The zero of the energy scale is set to the MAPbI<sub>3</sub> VB maximum.

consistent with the merging of the trap oxidation peaks into the signal of VB oxidation; see Table S1 and Figure 1A. Interestingly, in the case of MAPbBr<sub>x</sub>I<sub>3-x</sub> we predict substitution of interstitial iodide by bromide to be favored by 0.1 eV compared to substitution of lattice iodide. This behavior means that in the presence of interstitial iodide in MAPbI<sub>3</sub> Br incorporation will preferentially lead to a mixed I/Br interstitial defect (Figure 6A, middle row), whose (-/0) transition energy level is calculated at 0.03 eV above the VB. Thus, while the VB edge becomes significantly more positive upon increasing Br incorporation into the lattice (0.77 → 1.15 V vs Ag/AgCl), oxidation of the trap states only slightly drifts toward more positive potentials, remaining always close to its value in MAPbI<sub>3</sub> (0.62 → 0.67 V vs Ag/AgCl, see Table S1 and Figure 1A). The overall picture extracted from theory is thus fully consistent with the experimental results and suggests that the energetics of trap states are mainly contributed by iodine even in mixed I/Br perovskites, whereby the (-/0) transition of the mixed I/Br interstitial defect remains almost constant while the VB deepens (Figure 6B).

Most notably, experiments clearly indicate that hole injection into the trap states is not sufficient to promote iodide expulsion from the lattice (see Figure 2A). Nevertheless, traps are filled at less positive potentials than the VB; thus they are filled before iodide expulsion is observed and likely contribute to this reaction. In particular, defects are known to promote ion migration in perovskites (and in general in ionic conductors), and significant ion migration has to take place upon hole injection to lead to iodide expulsion. Based on this analysis, a possible mechanism can be sketched as follows:



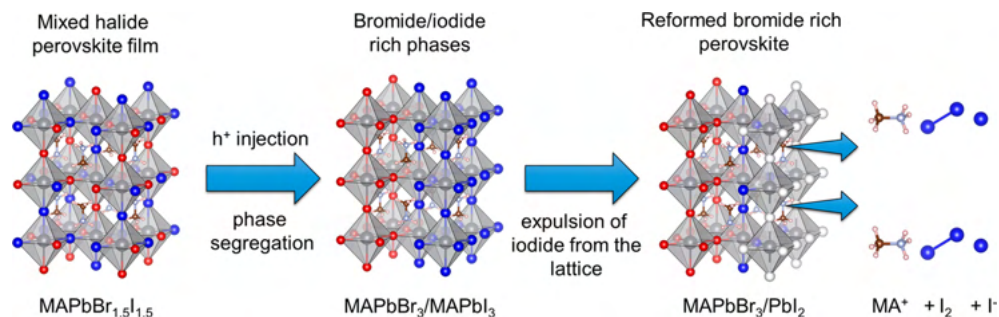
where I<sub>1</sub><sup>-</sup>, I<sub>1</sub><sup>0</sup>, and I<sub>1</sub><sup>+</sup> denote a negatively charged, a neutral, and a positively charged interstitial iodine, I<sup>-</sup> is a lattice iodide, and V<sub>1</sub><sup>+</sup> is an iodine vacancy.

Equations 3 and 4 correspond to the sequential hole injection into the traps and the VB. Under prolonged electrochemical bias, a hole is transferred from the VB to the filled trap, leading to oxidation of I<sub>1</sub><sup>0</sup> to I<sub>1</sub><sup>+</sup>, eq 5. I<sub>1</sub><sup>+</sup> has a trimer structure<sup>48</sup> typical of I<sub>3</sub><sup>-</sup>. Equation 6 corresponds to the attack of I<sub>1</sub><sup>+</sup> to lattice iodide (I<sup>-</sup>) to generate molecular iodine (I<sub>2</sub>) and an iodine vacancy, V<sub>1</sub><sup>+</sup>. Alternatively, in eq 6a I<sub>1</sub><sup>+</sup> abstracts two iodine atoms from the lattice to exit in the form of I<sub>3</sub><sup>-</sup>. In eq 6 I<sub>2</sub> can be formed either in the bulk or at surfaces/grain boundaries. Molecular iodine is unstable in the lattice;<sup>49</sup> if formed in the bulk, I<sub>2</sub> thus tends to migrate to the surface, where it can be easily abstracted to the solution. The reaction in eq 6 is calculated to be energetically unfavorable by 0.39 eV when I<sub>1</sub><sup>+</sup> and V<sub>1</sub><sup>+</sup> are bulk defects and I<sub>2</sub> is formed as a gas phase molecule (neglecting thermal corrections to enthalpy and entropy). I<sub>2</sub> surface stabilization and its subsequent solvation with consequent energetic and entropic gain, however, provide energetically favorable pathways for iodide expulsion.

## CONCLUSIONS

As noted earlier, the halide ions within the perovskite exhibit mobility with relatively low activation energy.<sup>50</sup> When subjected to steady state light irradiation, the single-anion-containing phases in mixed halides segregate. The diffusion length of the charge carriers is an important parameter that dictates the phase segregation in MHP films.<sup>21</sup> Cathode luminescence studies have shown that iodide ions selectively accumulate near the grain boundaries.<sup>33</sup> In contrast to

Scheme 1. Illustration of the Structural Changes Induced by Hole Injection into the MHP Lattice



photoirradiation (where equal amounts of electrons and holes are formed), we have employed selective injection of holes through electrochemical treatment to deconvolute the complex effect of different charge carriers. While in single-anion-containing perovskites hole injection causes the direct degradation of the structure, the situation is more complex for MHPs. The trapped holes at the iodide sites first cause the phase segregation and subsequently the disintegration of the crystal structure, through intermediate crystal phases (Scheme 1). The blue shift in the absorption feature is indicative of the loss of methylammonium ion as the accomplice of iodine (or triiodide) during their expulsion. Overall, the electrochemically induced phase segregation with ultimate expulsion of iodine provides new evidence of hole trapping as the driving force for the halide ion mobility. What is further important, simple electrochemical measurements can provide a new tool to assess the stability of different MHPs in a rapid way, thus avoiding the need of long-term initial testing during materials screening.

## ■ ASSOCIATED CONTENT

### 📄 Supporting Information

The Supporting Information is available free of charge on the ACS Publications website at DOI: 10.1021/jacs.9b04568.

(Complete experimental section (including used materials, characterization methods, electrode preparation), additional electrochemical measurements (LSVs, EIS, in situ Raman spectroelectrochemistry), complete compositional analysis (XPS, EDX, ICP-OES, IC results) together with discussion and lifetime calculations PDF)

## ■ AUTHOR INFORMATION

### Corresponding Authors

\*pkamat@nd.edu; Twitter: @KamatLab

\*janaky@chem.u-szeged.hu; Twitter @Janakylab

### ORCID

Gergely F. Samu: 0000-0002-3239-9154

Filippo De Angelis: 0000-0003-3833-1975

Daniele Meggiolaro: 0000-0001-9717-133X

Prashant V. Kamat: 0000-0002-2465-6819

Csaba Janáky: 0000-0001-5965-5173

### Notes

The authors declare no competing financial interest.

## ■ ACKNOWLEDGMENTS

The authors thank the Notre Dame Integrated Imaging Facility and Dr. Tatyana Orlova for taking the SEM images. We thank Dr. Allen G. Oliver for recording the XRD patterns and the valuable discussion. We thank the Center for Environmental

Science and Technology at the University of Notre Dame for the use of their instrumentation and the help of Jon Loftus and Jeffrey DuBose with the ICP-OES and ion chromatography measurements. We are grateful for the help of Sylwia Ptasinska and Pitambar Sapkota with the XPS measurements and the evaluation, as well as to Rebecca A. Scheidt for the support in the TAS measurements. P.V.K. acknowledges support by the Division of Chemical Sciences, Geosciences, and Biosciences, Office of Basic Energy Sciences of the U.S. Department of Energy (award DE-FC02-04ER15533). This collaborative research received funding from the European Research Council (ERC) under the EU's Horizon 2020 research and innovation program (G.F.S., A.B., and C.J., grant agreement No. 716539). ELI-ALPS is supported by the EU and cofinanced by the European Regional Development Fund (GOP-1.1.1-12/B-2012-000, GINOP-2.3.6-15-2015-00001). This is contribution number NDRL No. 5250 from the Notre Dame Radiation Laboratory. F.D.A. acknowledges support from the Italian "Ministero per l'Università e la Ricerca Scientifica e Tecnologica", MIUR (Rome, Italy), and the University of Perugia, under the "Dipartimenti di Eccellenza 2018-2022" (grant AMIS) and from the European Union's Horizon 2020 research and innovation program, under grant agreement No. 764047.

## ■ REFERENCES

- (1) McMeekin, D. P.; Sadoughi, G.; Rehman, W.; Eperon, G. E.; Saliba, M.; Horantner, M. T.; Haghighirad, A.; Sakai, N.; Korte, L.; Rech, B.; Johnston, M. B.; Herz, L. M.; Snaith, H. J. A Mixed-Cation Lead Mixed-Halide Perovskite Absorber for Tandem Solar Cells. *Science* **2016**, *351*, 151–155.
- (2) Noh, J. H.; Im, S. H.; Heo, J. H.; Mandal, T. N.; Seok, S. I. Chemical Management for Colorful, Efficient, and Stable Inorganic–Organic Hybrid Nanostructured Solar Cells. *Nano Lett.* **2013**, *13* (4), 1764–1769.
- (3) Bush, K. A.; Palmstrom, A. F.; Yu, Z. J.; Boccard, M.; Cheacharoen, R.; Mailoa, J. P.; McMeekin, D. P.; Hoyer, R. L. Z.; Bailie, C. D.; Leijtens, T.; Peters, I. M.; Minichetti, M. C.; Rolston, N.; Prasanna, R.; Sofia, S.; Harwood, D.; Ma, W.; Moghadam, F.; Snaith, H. J.; Buonassisi, T.; Holman, Z. C.; Bent, S. F.; McGehee, M. D. 23.6%-Efficient Monolithic Perovskite/Silicon Tandem Solar Cells with Improved Stability. *Nat. Energy* **2017**, *2*, 17009.
- (4) Zhao, D.; Wang, C.; Song, Z.; Yu, Y.; Chen, C.; Zhao, X.; Zhu, K.; Yan, Y. Four-Terminal All-Perovskite Tandem Solar Cells Achieving Power Conversion Efficiencies Exceeding 23%. *ACS Energy Lett.* **2018**, *3*, 305–306.
- (5) Beal, R. E.; Slotcavage, D. J.; Leijtens, T.; Bowring, A. R.; Belisle, R. A.; Nguyen, W. H.; Burkhard, G. F.; Hoke, E. T.; McGehee, M. D. Cesium Lead Halide Perovskites with Improved Stability for Tandem Solar Cells. *J. Phys. Chem. Lett.* **2016**, *7*, 746–751.
- (6) Eperon, G. E.; Leijtens, T.; Bush, K. A.; Prasanna, R.; Green, T.; Wang, J. T.-W.; McMeekin, D. P.; Volonakis, G.; Milot, R. L.; May,

- R.; Palmstrom, A.; Slotcavage, D. J.; Belisle, R. A.; Patel, J. B.; Parrott, E. S.; Sutton, R. J.; Ma, W.; Moghadam, F.; Conings, B.; Babayigit, A.; Boyen, H.; Bent, S.; Giustino, F.; Herz, L. M.; Johnston, M. B.; McGehee, M. D.; Snaith, H. J. Perovskite-Perovskite Tandem Photovoltaics with Optimized Band Gaps. *Science* **2016**, *354*, 861–865.
- (7) Leijtens, T.; Bush, K. A.; Prasanna, R.; McGehee, M. D. Opportunities and Challenges for Tandem Solar Cells Using Metal Halide Perovskite Semiconductors. *Nat. Energy* **2018**, *3*, 828–838.
- (8) Hoffman, J. B.; Schleper, A. L.; Kamat, P. V. Transformation of Sintered CsPbBr<sub>3</sub> Nanocrystals to Cubic CsPbI<sub>3</sub> and Gradient CsPbBr<sub>x</sub>I<sub>3-x</sub> through Halide Exchange. *J. Am. Chem. Soc.* **2016**, *138*, 8603–8611.
- (9) Zhou, C.; Ou, Q.; Chen, W.; Gan, Z.; Wang, J.; Bao, Q.; Wen, X.; Jia, B. Illumination-Induced Halide Segregation in Gradient Bandgap Mixed-Halide Perovskite Nanoplatelets. *Adv. Opt. Mater.* **2018**, *6*, 1801107.
- (10) Ravi, V. K.; Scheidt, R. A.; Nag, A.; Kuno, M.; Kamat, P. V. To Exchange or Not to Exchange. Suppressing Anion Exchange in Cesium Lead Halide Perovskites with PbSO<sub>4</sub>-Oleate Capping. *ACS Energy Lett.* **2018**, *3*, 1049–1055.
- (11) Pan, D.; Fu, Y.; Chen, J.; Czech, K. J.; Wright, J. C.; Jin, S. Visualization and Studies of Ion-Diffusion Kinetics in Cesium Lead Bromide Perovskite Nanowires. *Nano Lett.* **2018**, *18*, 1807–1813.
- (12) Yoon, S. J.; Kuno, M.; Kamat, P. V. Shift Happens. How Halide Ion Defects Influence Photoinduced Segregation in Mixed Halide Perovskites. *ACS Energy Lett.* **2017**, *2*, 1507–1514.
- (13) Belisle, R. A.; Bush, K. A.; Bertoluzzi, L.; Gold-Parker, A.; Toney, M. F.; McGehee, M. D. Impact of Surfaces on Photoinduced Halide Segregation in Mixed-Halide Perovskites. *ACS Energy Lett.* **2018**, *3*, 2694–2700.
- (14) Duong, T.; Mulmudi, H. K.; Wu, Y.; Fu, X.; Shen, H.; Peng, J.; Wu, N.; Nguyen, H. T.; Macdonald, D.; Lockrey, M.; White, T. P.; Weber, K.; Catchpole, K. Light and Electrically Induced Phase Segregation and Its Impact on the Stability of Quadruple Cation High Bandgap Perovskite Solar Cells. *ACS Appl. Mater. Interfaces* **2017**, *9*, 26859–26866.
- (15) Braly, I. L.; Stoddard, R. J.; Rajagopal, A.; Uhl, A. R.; Katahara, J. K.; Jen, A. K.-Y.; Hillhouse, H. W. Current-Induced Phase Segregation in Mixed Halide Hybrid Perovskites and Its Impact on Two-Terminal Tandem Solar Cell Design. *ACS Energy Lett.* **2017**, *2*, 1841–1847.
- (16) Lin, Y.; Chen, B.; Fang, Y.; Zhao, J.; Bao, C.; Yu, Z.; Deng, Y.; Rudd, P. N.; Yan, Y.; Yuan, Y.; Huang, J. Excess Charge-Carrier Induced Instability of Hybrid Perovskites. *Nat. Commun.* **2018**, *9*, 4981.
- (17) Ruf, F.; Rietz, P.; Aygüler, M. F.; Kelz, I.; Docampo, P.; Kalt, H.; Hetterich, M. The Bandgap as a Moving Target: Reversible Bandgap Instabilities in Multiple-Cation Mixed-Halide Perovskite Solar Cells. *ACS Energy Lett.* **2018**, *3*, 2995–3001.
- (18) Samu, G. F.; Janáky, C.; Kamat, P. V. A Victim of Halide Ion Segregation. How Light Soaking Affects Solar Cell Performance of Mixed Halide Lead Perovskites. *ACS Energy Lett.* **2017**, *2*, 1860–1861.
- (19) Braly, I. L.; Stoddard, R. J.; Rajagopal, A.; Uhl, A. R.; Katahara, J. K.; Jen, A. K.-Y.; Hillhouse, H. W. Current-Induced Phase Segregation in Mixed Halide Hybrid Perovskites and Its Impact on Two-Terminal Tandem Solar Cell Design. *ACS Energy Lett.* **2017**, *2*, 1841–1847.
- (20) Tang, X.; van den Berg, M.; Gu, E.; Horneber, A.; Matt, G. J.; Osvet, A.; Meixner, A. J.; Zhang, D.; Brabec, C. J. Local Observation of Phase Segregation in Mixed-Halide Perovskite. *Nano Lett.* **2018**, *18*, 2172–2178.
- (21) Draguta, S.; Shariya, O.; Yoon, S. J.; Brennan, M. C.; Morozov, Y. V.; Manser, J. S.; Kamat, P. V.; Schneider, W. F.; Kuno, M. Rationalizing the Light-Induced Phase Separation of Mixed Halide Organic–inorganic Perovskites. *Nat. Commun.* **2017**, *8*, 200.
- (22) Gualdrón-Reyes, A. F.; Yoon, S. J.; Barea, E. M.; Agouram, S.; Muñoz-Sanjosé, V.; Meléndez, Á. M.; Niño-Gómez, M. E.; Mora-Seró, I. Controlling the Phase Segregation in Mixed Halide Perovskites through Nanocrystal Size. *ACS Energy Lett.* **2019**, *4*, 54–62.
- (23) Mao, W.; Hall, C. R.; Chesman, A. S. R.; Forsyth, C.; Cheng, Y.-B.; Duffy, N. W.; Smith, T. A.; Bach, U. Visualizing Phase Segregation in Mixed-Halide Perovskite Single Crystals. *Angew. Chem., Int. Ed.* **2019**, *58*, 2893–2898.
- (24) Hu, M.; Bi, C.; Yuan, Y.; Bai, Y.; Huang, J. Stabilized Wide Bandgap MAPbBr<sub>x</sub>I<sub>3-x</sub> Perovskite by Enhanced Grain Size and Improved Crystallinity. *Adv. Sci.* **2016**, *3*, 1500301.
- (25) Bischak, C. G.; Wong, A. B.; Lin, E.; Limmer, D. T.; Yang, P.; Ginsberg, N. S. Tunable Polaron Distortions Control the Extent of Halide Demixing in Lead Halide Perovskites. *J. Phys. Chem. Lett.* **2018**, *9*, 3998–4005.
- (26) Oranskaia, A.; Yin, J.; Bakr, O. M.; Brédas, J.-L.; Mohammed, O. F. Halogen Migration in Hybrid Perovskites: The Organic Cation Matters. *J. Phys. Chem. Lett.* **2018**, *9*, 5474–5480.
- (27) Knight, A. J.; Wright, A. D.; Patel, J. B.; McMeekin, D. P.; Snaith, H. J.; Johnston, M. B.; Herz, L. M. Electronic Traps and Phase Segregation in Lead Mixed-Halide Perovskite. *ACS Energy Lett.* **2019**, *4*, 75–84.
- (28) Barker, A. J.; Sadhanala, A.; Deschler, F.; Gandini, M.; Senanayak, S. P.; Pearce, P. M.; Mosconi, E.; Pearson, A. J.; Wu, Y.; Srimath Kandada, A. R.; Leijtens, T.; De Angelis, F.; Dutton, S. E.; Petrozza, A.; Friend, R. H. Defect-Assisted Photoinduced Halide Segregation in Mixed-Halide Perovskite Thin Films. *ACS Energy Lett.* **2017**, *2*, 1416–1424.
- (29) Yang, X.; Yan, X.; Wang, W.; Zhu, X.; Li, H.; Ma, W.; Sheng, C. Light Induced Metastable Modification of Optical Properties in CH<sub>3</sub>NH<sub>3</sub>PbI<sub>3-x</sub>Br<sub>x</sub> Perovskite Films: Two-Step Mechanism. *Org. Electron.* **2016**, *34*, 79–83.
- (30) Hoke, E. T.; Slotcavage, D. J.; Dohner, E. R.; Bowring, A. R.; Karunadasa, H. I.; McGehee, M. D. Reversible Photo-Induced Trap Formation in Mixed-Halide Hybrid Perovskites for Photovoltaics. *Chem. Sci.* **2015**, *6*, 613–617.
- (31) Slotcavage, D. J.; Karunadasa, H. I.; McGehee, M. D. Light-Induced Phase Segregation in Halide-Perovskite Absorbers. *ACS Energy Lett.* **2016**, *1*, 1199–1205.
- (32) Ruth, A.; Brennan, M. C.; Draguta, S.; Morozov, Y. V.; Zhukovskiy, M.; Janko, B.; Zapol, P.; Kuno, M. Vacancy-Mediated Anion Photo-segregation Kinetics in Mixed Halide Hybrid Perovskites: Coupled Kinetic Monte Carlo and Optical Measurements. *ACS Energy Lett.* **2018**, *3*, 2321–2328.
- (33) Bischak, C. G.; Hetherington, C. L.; Wu, H.; Aloni, S.; Ogletree, D. F.; Limmer, D. T.; Ginsberg, N. S. Origin of Reversible Photoinduced Phase Separation in Hybrid Perovskites. *Nano Lett.* **2017**, *17*, 1028–1033.
- (34) Miyata, K.; Meggiolaro, D.; Trinh, M. T.; Joshi, P. P.; Mosconi, E.; Jones, S. C.; De Angelis, F.; Zhu, X.-Y. Large Polarons in Lead Halide Perovskites. *Sci. Adv.* **2017**, *3*, No. e1701217.
- (35) Stranks, S. D.; Eperon, G. E.; Grancini, G.; Menelaou, C.; Alcocer, M. J. P.; Leijtens, T.; Herz, L. M.; Petrozza, A.; Snaith, H. J. Electron-Hole Diffusion Lengths Exceeding 1 Micrometer in an Organometal Trihalide Perovskite Absorber. *Science* **2013**, *342*, 341–344.
- (36) de Quilletes, D. W.; Vorpahl, S. M.; Stranks, S. D.; Nagaoka, H.; Eperon, G. E.; Ziffer, M. E.; Snaith, H. J.; Ginger, D. S. Impact of Microstructure on Local Carrier Lifetime in Perovskite Solar Cells. *Science* **2015**, *348*, 683–686.
- (37) Xing, G.; Mathews, N.; Sun, S.; Lim, S. S.; Lam, Y. M.; Grätzel, M.; Mhaisalkar, S.; Sum, T. C. Long-Range Balanced Electron- and Hole-Transport Lengths in Organic-Inorganic CH<sub>3</sub>NH<sub>3</sub>PbI<sub>3</sub>. *Science* **2013**, *342*, 344–347.
- (38) Eames, C.; Frost, J. M.; Barnes, P. R. F.; O'Regan, B. C.; Walsh, A.; Islam, M. S. Ionic Transport in Hybrid Lead Iodide Perovskite Solar Cells. *Nat. Commun.* **2015**, *6*, 7497.
- (39) Kim, G. Y.; Senocrate, A.; Yang, T.-Y.; Gregori, G.; Grätzel, M.; Maier, J. Large Tunable Photoeffect on Ion Conduction in Halide

Perovskites and Implications for Photodecomposition. *Nat. Mater.* **2018**, *17*, 445–449.

(40) Peng, W.; Aranda, C.; Bakr, O. M.; Garcia-Belmonte, G.; Bisquert, J.; Guerrero, A. Quantification of Ionic Diffusion in Lead Halide Perovskite Single Crystals. *ACS Energy Lett.* **2018**, *3*, 1477–1481.

(41) Yoon, S. J.; Draguta, S.; Manser, J. S.; Sharia, O.; Schneider, W. F.; Kuno, M.; Kamat, P. V. Tracking Iodide and Bromide Ion Segregation in Mixed Halide Lead Perovskites during Photoirradiation. *ACS Energy Lett.* **2016**, *1*, 290–296.

(42) Scheidt, R. A.; Samu, G. F.; Janáky, C.; Kamat, P. V. Modulation of Charge Recombination in CsPbBr<sub>3</sub> Perovskite Films with Electrochemical Bias. *J. Am. Chem. Soc.* **2018**, *140*, 86–89.

(43) Samu, G. F.; Scheidt, R. A.; Kamat, P. V.; Janáky, C. Electrochemistry and Spectroelectrochemistry of Lead Halide Perovskite Films: Materials Science Aspects and Boundary Conditions. *Chem. Mater.* **2018**, *30*, 561–569.

(44) Yoon, S. J.; Stamplecoskie, K. G.; Kamat, P. V. How Lead Halide Complex Chemistry Dictates the Composition of Mixed Halide Perovskites. *J. Phys. Chem. Lett.* **2016**, *7*, 1368–1373.

(45) Manser, J. S.; Saidaminov, M. I.; Christians, J. A.; Bakr, O. M.; Kamat, P. V. Making and Breaking of Lead Halide Perovskites. *Acc. Chem. Res.* **2016**, *49*, 330–338.

(46) Meggiolaro, D.; De Angelis, F. First-Principles Modeling of Defects in Lead Halide Perovskites: Best Practices and Open Issues. *ACS Energy Lett.* **2018**, *3*, 2206–2222.

(47) Meggiolaro, D.; Motti, S. G.; Mosconi, E.; Barker, A. J.; Ball, J.; Andrea Riccardo Perini, C.; Deschler, F.; Petrozza, A.; De Angelis, F. Iodine Chemistry Determines the Defect Tolerance of Lead-Halide Perovskites. *Energy Environ. Sci.* **2018**, *11*, 702–713.

(48) Du, M.-H. Density Functional Calculations of Native Defects in CH<sub>3</sub>NH<sub>3</sub>PbI<sub>3</sub>: Effects of Spin–Orbit Coupling and Self-Interaction Error. *J. Phys. Chem. Lett.* **2015**, *6*, 1461–1466.

(49) Meggiolaro, D.; Mosconi, E.; De Angelis, F. Modeling the Interaction of Molecular Iodine with MAPbI<sub>3</sub>: A Probe of Lead-Halide Perovskites Defect Chemistry. *ACS Energy Lett.* **2018**, *3*, 447–451.

(50) Yuan, Y.; Huang, J. Ion Migration in Organometal Trihalide Perovskite and Its Impact on Photovoltaic Efficiency and Stability. *Acc. Chem. Res.* **2016**, *49*, 286–293.



# Multilayer Electrolyzer Stack Converts Carbon Dioxide to Gas Products at High Pressure with High Efficiency

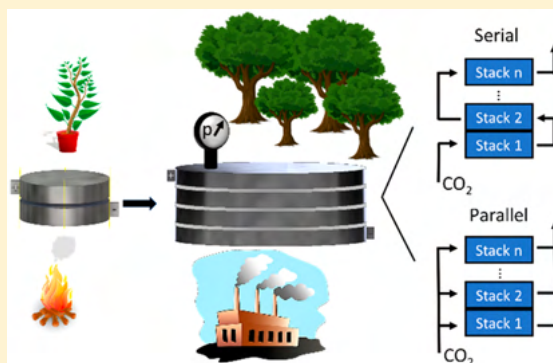
B. Endrődi,<sup>\*,†</sup> E. Kecsenovity,<sup>†</sup> A. Samu,<sup>†</sup> F. Darvas,<sup>‡</sup> R. V. Jones,<sup>‡</sup> V. Török,<sup>‡</sup> A. Danyi,<sup>‡</sup> and C. Janáky<sup>\*,†</sup>

<sup>†</sup>Department of Physical Chemistry and Materials Science, Interdisciplinary Excellence Centre, University of Szeged, Rerrich Square 1, Szeged H-6720, Hungary

<sup>‡</sup>ThalesNano Inc., Záhony u. 7, Budapest 1031, Hungary

**S** Supporting Information

**ABSTRACT:** Electrochemical reduction of CO<sub>2</sub> is a value-added approach to both decrease the atmospheric emission of carbon dioxide and form valuable chemicals. We present a zero gap electrolyzer cell, which continuously converts gas phase CO<sub>2</sub> to products without using any liquid catholyte. This is the first report of a multilayer CO<sub>2</sub> electrolyzer stack for scaling up the electrolysis process. CO formation with partial current densities above 250 mA cm<sup>-2</sup> were achieved routinely, which was further increased to 300 mA cm<sup>-2</sup> (with ~95% faradic efficiency) by pressurizing the CO<sub>2</sub> inlet (up to 10 bar). Evenly distributing the CO<sub>2</sub> gas among the layers, the electrolyzer operates identically to the sum of multiple single-layer electrolyzer cells. When passing the CO<sub>2</sub> gas through the layers consecutively, the CO<sub>2</sub> conversion efficiency increased. The electrolyzer *simultaneously* provides high partial current density, low cell voltage (−3.0 V), high conversion efficiency (up to 40%), and high selectivity for CO production.



With either considering carbon dioxide as a feedstock for transportation fuels and commodity chemicals or aiming to reduce its atmospheric emission, electrochemical reduction of CO<sub>2</sub> (CO<sub>2</sub>RR) is one of the major scientific and engineering challenges.<sup>1,2</sup> Various catalysts have been investigated in literally thousands of scientific works, identifying active and selective candidates and revealing important structure–property relationships with regard to catalyst size, shape, morphology, etc. As important examples of CO<sub>2</sub>RR, selective carbon monoxide formation was demonstrated on Ag electrodes, while multitudes of different alcohols and hydrocarbons form on copper catalysts.<sup>3</sup> The large differences in the activities and selectivities of different catalysts in CO<sub>2</sub>RR are better understood by now and are also supported by theoretical studies on the reaction mechanism.<sup>4</sup>

The industrial implementation of this technology necessitates the transformation of CO<sub>2</sub> to products at a high rate (i.e., current density,  $|j_{\text{product}}| > 200 \text{ mA cm}^{-2}$ ),<sup>5,6</sup> which is inherently hampered in aqueous solutions by the low solubility of CO<sub>2</sub>. Continuous-flow gas-fed electrolyzers might offer the only viable technological solution to overcome this limitation.<sup>7,8</sup> Apart from the high reactant concentration on the

catalyst surface ensured by the continuous CO<sub>2</sub> flow, it is also crucial to provide a high surface area for the electrochemical reaction. Hence, porous, gas diffusion electrodes (GDEs) are used in these electrolyzers, in which the triple phase boundary among the reactant gas, the catalyst, and the solid ionomer is maximized.<sup>9–11</sup>

To drive CO<sub>2</sub>RR in an economically feasible way, electrolyzer cells must be developed, which operate (i) at high current density (conversion rate), (ii) at low cell voltage (i.e., high energy efficiency), (iii) with high faradic efficiency (selectivity), and (iv) with high conversion efficiency. Notably, even though these four parameters *together* describe the overall performance of an electrolyzer cell, very seldom are all of these reported in the scientific literature.

Over the past decade, a remarkable advancement was achieved with continuous-flow electrolyzers,<sup>7,8,12,13</sup> most importantly with electrolyzers applying a dual (electrolyte + CO<sub>2</sub> gas) feed on the cathode (e.g., in microfluidic cells) and electrolyte feed at the anode.<sup>14,15</sup> Cation<sup>16</sup> or anion<sup>17–20</sup>

Received: May 26, 2019

Accepted: June 27, 2019

Published: June 27, 2019

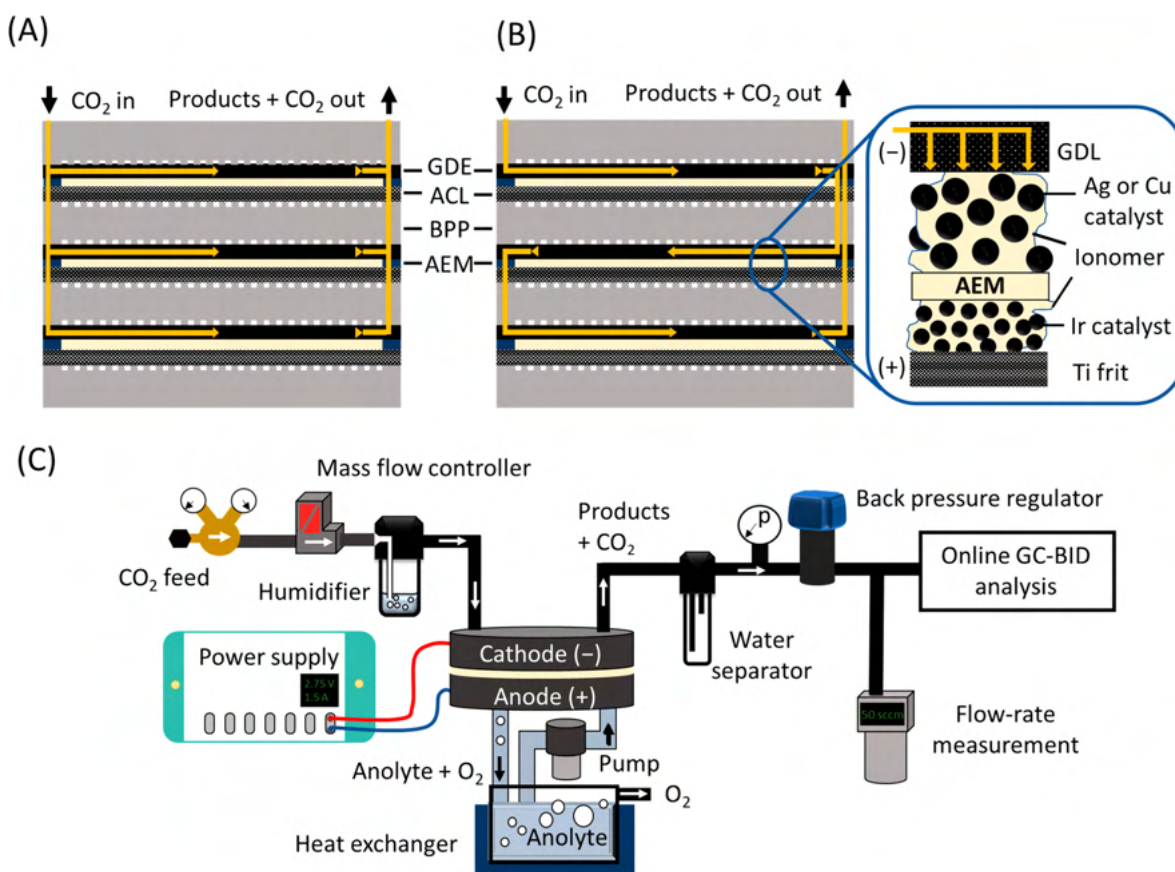


**Figure 1.** CO<sub>2</sub> gas channel structure in an electrolyzer stack consisting of three layers in the (A) parallel and (B) serial connection configurations. BPP: bipolar plate; ACL: anode catalyst layer; GDE: gas diffusion electrode; GDL: gas diffusion layer; AEM: anion exchange membrane. (C) Schematic flowchart of the measurement setup.

exchange membranes, bipolar membranes,<sup>21–23</sup> (PEM, AEM, and BPM, accordingly), and even an inorganic diaphragm<sup>24</sup> were proved to be applicable separators between the cell compartments. The effects of several parameters were scrutinized: electrolyte composition (e.g., electrolyte type, concentration, pH, etc.),<sup>14,23,25–27</sup> structure of the microporous layer,<sup>28</sup> catalyst morphology,<sup>29</sup> and immobilizing the catalysts on different high surface area supports.<sup>30–32</sup> Some of these studies were performed applying pressurized CO<sub>2</sub> inlets (although not in the zero-gap configuration),<sup>16,25,33</sup> further improving the performance. As a result, industrially relevant current densities, above  $j_{\text{product}} = 200 \text{ mA cm}^{-2}$ , have become a reality with both Cu<sup>34–38</sup> and Ag<sup>30,32,39</sup> catalysts. Achieving high CO<sub>2</sub> conversion efficiency, however, is a substantial challenge in such electrolyzers because of (i) the typically large gas head space above the GDEs and (ii) the CO<sub>2</sub> losses due to its dissolution in the catholyte.

Considerably less attention has been devoted to zero gap membrane electrolyzers, in which CO<sub>2</sub> gas is directly fed to the cathode.<sup>40–46</sup> These cells offer a simple technological solution, in which (i) the cell resistance can be very low (which translates to high energy efficiency), (ii) the inlet can be pressurized relatively easily, (iii) no catholyte is used and, hence, no liquid catholyte circulation loop is required, and finally, (iv) the losses due to CO<sub>2</sub> dissolution in the catholyte are minimal. The knowledge gathered with fuel cells and PEM water electrolyzers might contribute to future scale-up of this technology, as these are mature electrochemical technologies with cells of similar structure. Constructing large size and

multilayer stacks is a common practice in both above-mentioned fields;<sup>47,48</sup> nonetheless, it has not been demonstrated for CO<sub>2</sub> reduction yet. Implementation of this concept to CO<sub>2</sub> electrolyzers can accelerate technology development, to scale up electrochemical CO<sub>2</sub> reduction to an industrially relevant level. Here we present a zero gap CO<sub>2</sub> electrolyzer stack, which consists of multiple electrolyzer layers and can operate with a pressurized CO<sub>2</sub> gas feed, without the need for any liquid catholyte. Furthermore, the flexibility of the presented design allows different connections between the layers of the electrolyzer regarding the distribution of the reactant CO<sub>2</sub> gas. Connecting the cells in parallel (Figure 1A), the gas is equally distributed among them; hence, pure CO<sub>2</sub> is fed to each cathode. On the other hand, when connecting the gas channels in series (Figure 1B), the total gas flux enters the first layer, and the off-gas (remnant CO<sub>2</sub> + products) continues to the subsequent layer(s), hence allowing very high conversion efficiencies. From an electric perspective, the cells are connected in series in both cases (i.e., the same current flows through them). While the presented cell is completely scalable, the presented data were recorded with a cell which contained up to three electrolyzer units (having 61 cm<sup>2</sup>/cell active area), connected through bipolar plates. For testing the operation of the electrolyzer cell and to analyze the formed products, a test station was designed (Figure 1C) that was used throughout the experiments presented here. Further information regarding the cell (Figure S1) and the electrolyzer station is provided in the Supporting Information.

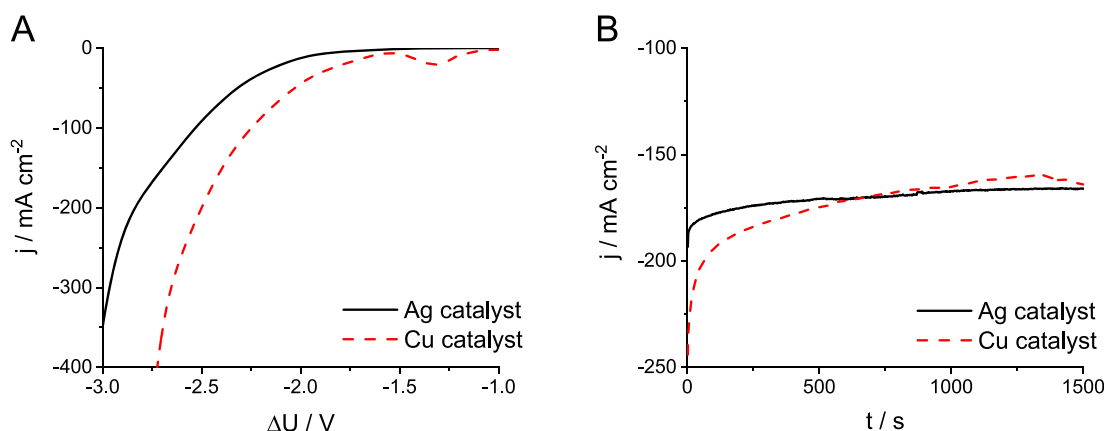


Figure 2. (A) LSV curves recorded at  $\nu = 10 \text{ mV s}^{-1}$  sweep rate and (B) chronoamperometric curves recorded at  $\Delta U = -2.75 \text{ V}$  with different catalyst containing cathode GDEs. The cathode compartment was purged with humidified  $\text{CO}_2$  at a flow rate of  $u = 150 \text{ cm}^3 \text{ min}^{-1}$ .

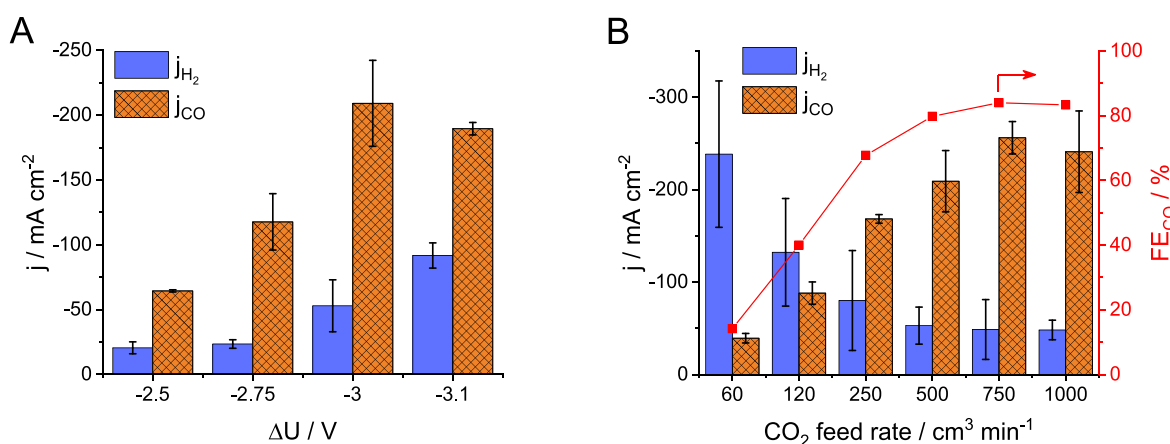


Figure 3. Partial current densities for CO and  $\text{H}_2$  formation (A) at different cell voltages, at a  $\text{CO}_2$  feed rate of  $u = 500 \text{ cm}^3 \text{ min}^{-1}$ , and (B) at  $\Delta U = -3.00 \text{ V}$ , as a function of the  $\text{CO}_2$  feed rate to the cathode.

*Electrochemical  $\text{CO}_2$  Reduction to Gas Phase Products Using Ag and Cu Catalysts.* Ag nanoparticles and electrodeposited Cu nanocubes,<sup>49,50</sup> immobilized on separate gas diffusion layers, were used to validate the operation of the electrolyzer in a single layer setup (see SEM images in Figures S2 and S3). The onset of a faradic process, read at  $10 \text{ mA cm}^{-2}$  current density, was observed at  $-1.71 \text{ V}$  with the Cu nanocube catalyst and  $-2.01 \text{ V}$  with the Ag nanoparticles on the linear sweep voltammetry curves (LSVs, Figure 2A). At voltages between  $-1.2$  and  $-1.5 \text{ V}$ , a reduction peak, related to the reduction of copper oxide, was observed for the Cu nanocube catalyst in line with our previous study.<sup>51</sup>

Chronoamperometric curves were recorded for both catalysts at  $-2.75 \text{ V}$ , where a stable operation was observed (Figure 2B). Gas chromatographic analysis of the composition of the product stream during electrolysis showed the formation of  $\text{C}_2\text{H}_4$ ,  $\text{CH}_4$ ,  $\text{CO}$ , and  $\text{H}_2$  for the Cu nanocube catalyst, while only  $\text{CO}$  and  $\text{H}_2$  formed on the Ag catalyst (Figure S4A,B). The cumulative faradic efficiency calculated for these products approached 100% in both cases, which suggests that the possible formation of other products is negligible. These results agree with earlier literature reports<sup>30,34</sup> and confirm that the  $\text{CO}_2$  gas enters the GDE and reaches the catalyst surface; hence, the structure of the electrolyzer cell is appropriate for such studies. In the following, the detailed study on the effect of different experimental conditions and cell parameters is presented for the silver nanoparticle catalyst. Notably, in this

study we focus on the operation of the electrolyzer; hence, the cathode GDEs were formed from commercially available components (GDL, Ag catalyst, ionomer), based on earlier reports.<sup>17,19,20</sup>

*Effect of the Operational Parameters.* The effect of the cell voltage on the conversion rate and selectivity of  $\text{CO}_2\text{RR}$  was investigated at constant  $\text{CO}_2$  feed rate (Figure 3A). Increasing the cell voltage leads to an increase in the overall current density. The  $\text{CO}$  partial current density ( $j_{\text{CO}}$ ) peaks at  $-3 \text{ V}$ , while the partial current density for  $\text{H}_2$  production ( $j_{\text{H}_2}$ ) grows monotonously with the cell voltage; hence, the hydrogen evolution reaction (HER) becomes dominant at higher cell voltages.

Regarding the  $\text{CO}_2$  gas feed rate, HER is dominant over  $\text{CO}_2\text{RR}$  at lower values. The  $j_{\text{H}_2}$  decreases and reaches a minimum value, while  $j_{\text{CO}}$  (together with the faradic efficiency of  $\text{CO}$  formation) increases and then peaks with the increasing  $\text{CO}_2$  feed rate. Importantly, a partial current density for  $\text{CO}$  formation above  $-250 \text{ mA cm}^{-2}$  was achieved (this is an average of multiple measurements on five different cell assemblies, where the champion cell resulted in  $-300 \text{ mA cm}^{-2}$ ), while the faradic efficiency (FE<sub>CO</sub>) was around 85%. We emphasize that only hydrogen was formed as a byproduct; no liquid or other gas phase products were detected. This simplifies the further processing of the product stream, as this syngas mixture can be directly used in the Fischer–Tropsch

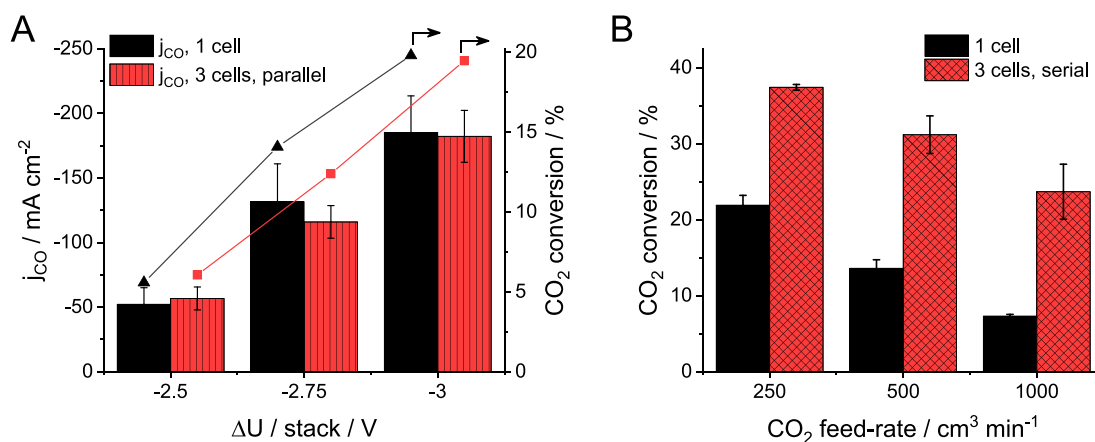


Figure 4. (A) CO partial current density and CO<sub>2</sub> conversion with a one-cell electrolyzer and an electrolyzer stack consisting of three cells, in the parallel configuration during electrolysis at different cell voltages with 433 cm<sup>3</sup> min<sup>-1</sup> CO<sub>2</sub> feed rate per cell at the cathode. (B) CO<sub>2</sub> conversion with a single-cell electrolyzer and an electrolyzer stack consisting of three cells, in the serial configuration, at different CO<sub>2</sub> feed rates, at  $\Delta U = -2.75$  V/cell.

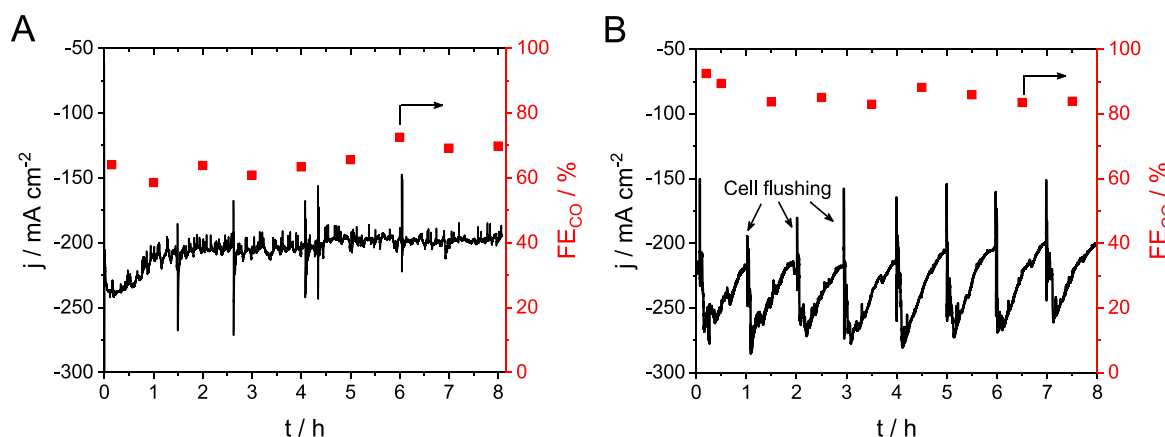


Figure 5. Chronoamperometric curves recorded at  $\Delta U = -3.00$  V with  $u = 750$  cm<sup>3</sup> min<sup>-1</sup> CO<sub>2</sub> flow rate, humidified at (A)  $T = 85$  °C and (B)  $T = 60$  °C, while the cell was rinsed with ca. 50 cm<sup>3</sup> deionized water at the beginning of each hour. The CO faradic efficiency values were calculated from the analysis of the gas products by gas chromatography.

synthesis, after adjusting the proper CO to H<sub>2</sub> ratio using an external hydrogen source, such as a water electrolyzer cell.<sup>52</sup>

**Electrolysis of CO<sub>2</sub> to CO in a Multilayer Electrolyzer Stack.** Assembling multilayer electrolyzer stacks, in which the cathode compartments are connected in parallel, is a way to increase the electrochemically active surface area without having to increase the lateral size of the electrolyzer. Comparing the results obtained with a single-cell electrolyzer and a stack cell consisting of three layers in parallel connection, the partial current density for CO formation and the CO<sub>2</sub> conversion were very similar at all studied cell voltages (Figure 4A). This indicates that the CO<sub>2</sub> gas is evenly split among the layers in the stack and all individual cells operate with the same performance. We note again that the layers are connected in series electrically, and therefore the overall stack voltage can be controlled. Measuring the individual cell voltages during electrolysis, we found that the overall stack voltage is split evenly among them. Furthermore, the onset voltage (note that the stack voltage is normalized with the number of electrolyzer layers) and currents on the LSV curves recorded with a single-cell electrolyzer and a 3-layer electrolyzer stack in the parallel configuration are also comparable (Figure S4). The faradic efficiencies were also very similar: around 85% at lower cell voltages in both cases, which decreased to 75% at  $-3.0$  V/layer

voltage. From a technological perspective, assembling multiple-layer electrolyzer stacks instead of parallelly operating multiple, single-cell electrolyzers decreases the capital investment costs, as the electrolyzer frame and the anolyte circulation loop only has to be built once and any further cell only requires an extra bipolar plate, insulation, and a membrane electrode assembly.

Connecting the cells in series is a completely different story. In this case, the off-gas of the first electrolyzer layer is fed to the subsequent layers, where (part) of the remnant CO<sub>2</sub> is transformed to products. Comparing the results measured with an electrolyzer stack consisting of three cells in serial configuration with that recorded for a single-layer cell, a large increase (ca. 70%) in CO<sub>2</sub> conversion was achieved even at low CO<sub>2</sub> feed rates, where the CO<sub>2</sub> conversion is already over 20% for the single-cell electrolyzer; hence, a CO<sub>2</sub> stream, diluted with CO and H<sub>2</sub>, reached the subsequent layers of the stack (Figure 4B). When increasing the gas feed rate, the difference increases drastically. At the highest studied gas feed rate, the CO<sub>2</sub> conversion was three times higher in the electrolyzer stack, indicating the comparable operation of three individual cells. Furthermore, the faradic efficiency for CO production was above 95% in this case. We note that achieving high conversion decreases the separation and handling costs



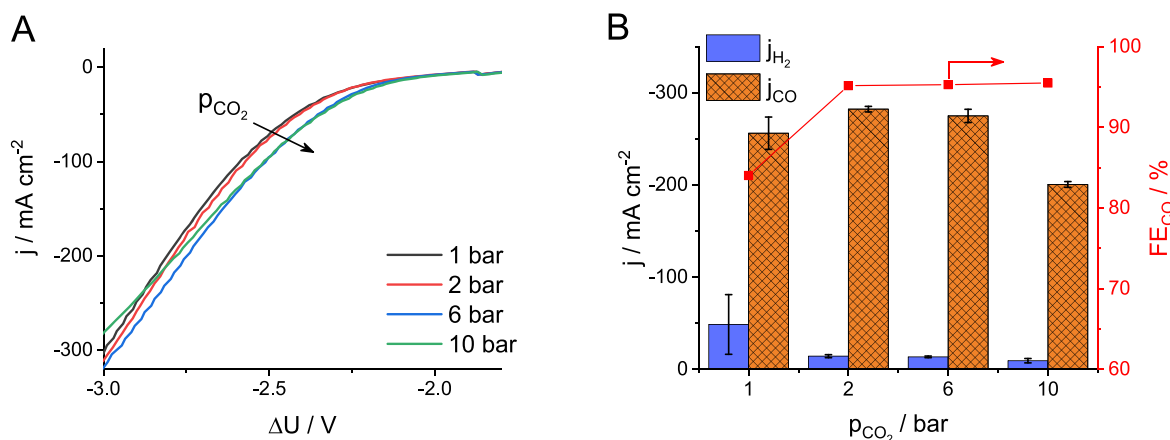


**Figure 6.** (A) LSV curves recorded at  $\nu = 10 \text{ mV s}^{-1}$  sweep rate and (B) partial current densities for CO and H<sub>2</sub> formation, and the ratio of these during electrolysis at  $\Delta U = -3.00 \text{ V}$ , both as a function of the differential CO<sub>2</sub> pressure. The cathode compartment was purged with humidified CO<sub>2</sub> at a flow rate of  $u = 750 \text{ ncm}^3 \text{ min}^{-1}$ .

and, therefore, increases the value of the final gas mixture, strongly supporting the industrial implementation of CO<sub>2</sub>RR.

**Stationary Operation of the CO<sub>2</sub> Electrolyzer.** When using anion exchange membranes and concentrated KOH solution in CO<sub>2</sub>RR, the precipitation of K<sub>2</sub>CO<sub>3</sub> at the cathode side is a common issue, decreasing the performance of the electrolyzer by blocking the gas channels and the active catalyst sites.<sup>53</sup> Different approaches can be envisioned to overcome this challenge. The first and most obvious one is to use pure deionized water as anolyte instead of strong alkaline solutions. This tactic is feasible for some AEMs,<sup>54</sup> and with the rapid development in this field, we envision that other membranes will also be available to be used with pure water (just like Nafion in water electrolyzer cells). For cells working with KOH, dissolving the precipitated K<sub>2</sub>CO<sub>3</sub> during operation must be solved (without disassembling the cell), but as of yet, no ultimate engineering solution has been developed.

We present two possible avenues here. One is to increase the temperature of the humidified CO<sub>2</sub> inlet and, thus, continuously feed more water vapor into the cell (Figure 5A). The other approach is to periodically flush the cell with liquid water (Figure 5B). In the first case, the temperature of the water humidifier was increased to 85 °C, which led to the stable operation of the cell after a 30 min transient period at the beginning of the experiment. The FE<sub>CO</sub> however, was considerably smaller (65–70%) throughout the measurement, compared to previous studies at lower inlet temperature (Figure 3). This trend can be attributed to the increased amount of water in the cell (i.e., higher probability of the HER). On the other hand, when the humidification was performed at lower temperature, a continuous current decay was observed during the measurements, due to K<sub>2</sub>CO<sub>3</sub> precipitation. Therefore, the cell was flushed with deionized water at the beginning of each hour for 10 s. This rapid washing step healed the electrolyzer stack and restored the current to its original value (~250–275 mA cm<sup>-2</sup>). The FE<sub>CO</sub> was around 85% through the whole electrolysis. Comparing the current values at the end and at the beginning of each hour, no systematic decrease and, hence, no irreversible degradation were observed during the 8 h. Overall, both approaches avoid the accumulation of K<sub>2</sub>CO<sub>3</sub> precipitate. In the first case, the elevated temperature increases both the water amount in the CO<sub>2</sub> stream and the solubility of K<sub>2</sub>CO<sub>3</sub>. In the second case, K<sub>2</sub>CO<sub>3</sub> is washed out before larger plaque could build up.

**Pressurized Electrolysis of CO<sub>2</sub> to CO.** Performing CO<sub>2</sub>RR with a pressurized CO<sub>2</sub> inlet is technologically important from multiple aspects. Some of the industrial CO<sub>2</sub> point sources are already under pressure, so the technology can be easily implemented. In addition, a pressurized product stream can be more easily transported, handled, and utilized.

Pressurizing the cathodic CO<sub>2</sub> feed leads to the positive shift of the onset potential on the LSV curves (Figure 6A), indicating a thermodynamically more favored CO<sub>2</sub>RR process. The current also increases slightly with the applied pressure. In line with this, the CO formation partial current density during potentiostatic measurements initially increases from ~-250 mA cm<sup>-2</sup> above -285 mA cm<sup>-2</sup> with the applied pressure and then decreases at 10 bar (Figure 6B). The decrease at high pressure might be related to the enhanced crossover of CO<sub>2</sub> (and possibly CO) through the employed anion exchange membrane; a notable decrease (above 20%) was observed in the gas flow rate during these measurements, even without any electrochemical polarization. More importantly, the selectivity for CO formation increases remarkably under pressure; a faradaic efficiency of 95% (as compared to ~85% at atmospheric pressure) was found for CO<sub>2</sub>RR even at 1 bar CO<sub>2</sub> overpressure, which is not influenced by the further pressure increase. The operation of the electrolyzer was stable under intermediate pressure (4–6 bar) during the tests, for tens of hours.

The effect of pressure on the electrochemical properties of the electrolyzer cell is rather complex. The most important factors are the following: (i) the applied pressure presses the GDE on the membrane surface, hence ensuring better contact between them, (ii) the CO<sub>2</sub> gas is forced to enter into the GDE structure, (iii) smaller relative amounts of water enter the cell with the humidified, pressurized CO<sub>2</sub> stream, and (iv) the concentration (activity) of the CO<sub>2</sub> increases. As one can see, some of these effects are simply mechanical while others are chemical, and it is not trivial to deconvolute them.

To further emphasize the complex effect of pressure, measurements similar to what is shown Figure 6 were performed with an electrolyzer built of the same components, but which was significantly underperforming compared to the average cells. Surprisingly, the effect of pressure was much larger in this case! A great current increase was seen in the currents on the LSV curves with increasing pressure (Figure 7A). The  $j_{\text{CO}}$  showed a volcano type dependency, while the

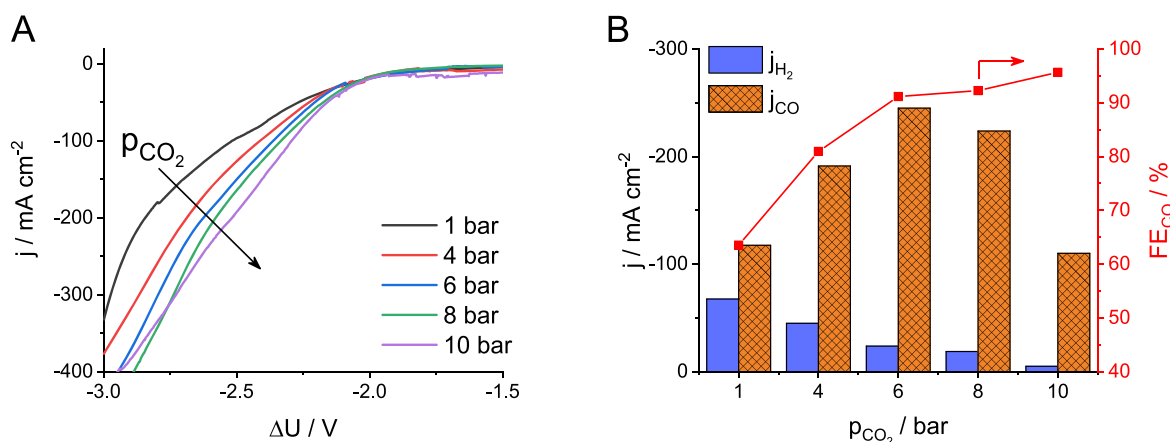


Figure 7. (A) LSV curves recorded at  $\nu = 10 \text{ mV s}^{-1}$  sweep rate and (B) partial current densities for  $\text{CO}$  and  $\text{H}_2$  formation and the ratio of these during electrolysis at  $\Delta U = -2.75 \text{ V}$ , both as a function of the differential  $\text{CO}_2$  pressure for a cell underperforming at atmospheric pressure. The cathode compartment was purged with humidified  $\text{CO}_2$  at a flow rate of  $u = 750 \text{ ncm}^3 \text{ min}^{-1}$ .

reaction selectivity increased continuously with the pressure (Figure 7B). Interestingly, the  $j_{\text{CO}}$  and the  $\text{FE}_{\text{CO}}$  is very similar to what was shown for the well performing electrolyzer cells at intermediate pressure ( $p = 6 \text{ bar}$ ).

Two important conclusions can be drawn from these observations. First, when reporting the effect of pressure, it is very important to investigate and exclude all trivial effects (e.g., the compression of the GDE) and study cells which already have good performance at atmospheric pressure. Second, an electrolyzer cell underperforming at atmospheric pressure, in which the dimensions of the components are not perfectly matched, can function the same way under pressure as a properly assembled cell.

In summary, we developed a direct  $\text{CO}_2$  gas-fed, zero gap electrolyzer cell, which can operate with different catalysts. By employing GDEs formed of commercially available components,  $\text{CO}$  formation partial current densities above  $-250 \text{ mA cm}^{-2}$  were routinely achieved. By pressurizing the  $\text{CO}_2$  inlet, this could be increased close to  $-300 \text{ mA cm}^{-2}$ , and the  $\text{CO}$  to  $\text{H}_2$  ratio was extraordinarily high in this case (above 20). The assembly and operation of a multilayer electrolyzer stack of any  $\text{CO}_2$  electrolyzer was demonstrated for the first time. We highlighted two possible scenarios for assembling multiple cells in an electrolyzer stack: one in which the electrolyzer layers are connected in parallel in terms of the gas feed, where hence the operation of electrolyzer stack is identical to the sum of multiple single-cell electrolyzers, and another one, where, when connecting the layers in series, the conversion rate increased significantly compared to a single-cell electrolyzer. These insights might trigger further development in scaling-up this fledging technology, which will bring us closer to its industrial implementation.

## ■ ASSOCIATED CONTENT

### Supporting Information

The Supporting Information is available free of charge on the ACS Publications website at DOI: 10.1021/acseenergylett.9b01142.

Experimental details and the following additional data: schematic structure of the electrolyzer stack, SEM images of the electrodeposited Cu nanocube layers, SEM images of the spray-coated Ag nanoparticle layers, gas chromatographs recorded during potentiostatic

measurements with the Ag and Cu catalysts, and additional electrochemical measurements with the electrolyzer stack (PDF)

## ■ AUTHOR INFORMATION

### Corresponding Authors

\*E-mail: janaky@chem.u-szeged.hu (C. Janáky).

\*E-mail: endrodib@chem.u-szeged.hu (B. Endrődi).

### ORCID

B. Endrődi: 0000-0003-3237-9222

C. Janáky: 0000-0001-5965-5173

### Notes

The authors declare the following competing financial interest(s): There is a patent application pending, filed by the authors of this paper and their institutions. Application number: PCT/HU2019/095001. Specifically, the patent application covers the details of the cell architecture, description of the individual components of the cell, and the electrolysis process.

## ■ ACKNOWLEDGMENTS

This project has received funding from the European Research Council (ERC) under the European Union's Horizon 2020 research and innovation programme (Grant Agreement No. 716539). E.K. acknowledges the support of the New National Excellence Program of the Ministry of Human Capacities (Grant UNKP-18-3). This research was also supported by the "Széchenyi 2020" program in the framework of the GINOP-2.2.1-15-2017-00041 project.

## ■ REFERENCES

- (1) Chen, C.; Khosrowabadi Kotyk, J. F.; Sheehan, S. W. Progress toward Commercial Application of Electrochemical Carbon Dioxide Reduction. *Chem.* **2018**, *4* (11), 2571–2586.
- (2) De Luna, P.; Hahn, C.; Higgins, D.; Jaffer, S. A.; Jaramillo, T. F.; Sargent, E. H. What Would It Take for Renewably Powered Electrosynthesis to Displace Petrochemical Processes? *Science* **2019**, *364* (6438), No. eaav3506.
- (3) Jones, J. P.; Prakash, G. K. S.; Olah, G. A. Electrochemical  $\text{CO}_2$  Reduction: Recent Advances and Current Trends. *Isr. J. Chem.* **2014**, *54* (10), 1451–1466.
- (4) Kortlever, R.; Shen, J.; Schouten, K. J. P.; Calle-Vallejo, F.; Koper, M. T. M. Catalysts and Reaction Pathways for the

Electrochemical Reduction of Carbon Dioxide. *J. Phys. Chem. Lett.* **2015**, *6* (20), 4073–4082.

(5) Verma, S.; Kim, B.; Jhong, H.-R.; Ma, S.; Kenis, P. J. A. A Gross-Margin Model for Defining Technoeconomic Benchmarks in the Electroreduction of CO<sub>2</sub>. *ChemSusChem* **2016**, *9* (15), 1972–1979.

(6) Jouny, M.; Luc, W.; Jiao, F. General Techno-Economic Analysis of CO<sub>2</sub> Electrolysis Systems. *Ind. Eng. Chem. Res.* **2018**, *57* (6), 2165–2177.

(7) Endrődi, B.; Bencsik, G.; Darvas, F.; Jones, R.; Rajeshwar, K.; Janáky, C. Continuous-Flow Electroreduction of Carbon Dioxide. *Prog. Energy Combust. Sci.* **2017**, *62*, 133–154.

(8) Merino-Garcia, I.; Alvarez-Guerra, E.; Albo, J.; Irabien, A. Electrochemical Membrane Reactors for the Utilisation of Carbon Dioxide. *Chem. Eng. J.* **2016**, *305*, 104–120.

(9) Higgins, D.; Hahn, C.; Xiang, C.; Jaramillo, T. F.; Weber, A. Z. Gas-Diffusion Electrodes for Carbon Dioxide Reduction: A New Paradigm. *ACS Energy Lett.* **2019**, *4* (1), 317–324.

(10) Liu, K.; Smith, W. A.; Burdyny, T. Introductory Guide to Assembling and Operating Gas Diffusion Electrodes for Electrochemical CO<sub>2</sub> Reduction. *ACS Energy Lett.* **2019**, *4* (3), 639–643.

(11) Burdyny, T.; Smith, W. A. CO<sub>2</sub> Reduction on Gas-Diffusion Electrodes and Why Catalytic Performance Must Be Assessed at Commercially-Relevant Conditions. *Energy Environ. Sci.* **2019**, *12*, 1442–1453.

(12) Weekes, D. M.; Salvatore, D. A.; Reyes, A.; Huang, A.; Berlinguette, C. P. Electrolytic CO<sub>2</sub> Reduction in a Flow Cell. *Acc. Chem. Res.* **2018**, *51* (4), 910–918.

(13) Jeanty, P.; Scherer, C.; Magori, E.; Wiesner-Fleischer, K.; Hinrichsen, O.; Fleischer, M. Upscaling and Continuous Operation of Electrochemical CO<sub>2</sub> to CO Conversion in Aqueous Solutions on Silver Gas Diffusion Electrodes. *J. CO<sub>2</sub> Util.* **2018**, *24*, 454–462.

(14) Whipple, D. T.; Finke, E. C.; Kenis, P. J. A. Microfluidic Reactor for the Electrochemical Reduction of Carbon Dioxide: The Effect of pH. *Electrochem. Solid-State Lett.* **2010**, *13* (9), B109.

(15) Dufek, E. J.; Lister, T. E.; McIlwain, M. E. Bench-Scale Electrochemical System for Generation of CO and Syn-Gas. *J. Appl. Electrochem.* **2011**, *41* (6), 623–631.

(16) Dufek, E. J.; Lister, T. E.; Stone, S. G.; McIlwain, M. E. Operation of a Pressurized System for Continuous Reduction of CO<sub>2</sub>. *J. Electrochem. Soc.* **2012**, *159* (9), F514–F517.

(17) Kaczur, J. J.; Yang, H.; Liu, Z.; Sajjad, S. D.; Masel, R. I. Carbon Dioxide and Water Electrolysis Using New Alkaline Stable Anion Membranes. *Front. Chem.* **2018**, *6*, 263.

(18) Lee, J.; Lim, J.; Roh, C.-W.; Whang, H. S.; Lee, H. Electrochemical CO<sub>2</sub> Reduction Using Alkaline Membrane Electrode Assembly on Various Metal Electrodes. *J. CO<sub>2</sub> Util.* **2019**, *31*, 244–250.

(19) Kutz, R. B.; Chen, Q.; Yang, H.; Sajjad, S. D.; Liu, Z.; Masel, R. I. Sustainion Imidazolium-Functionalized Polymers for Carbon Dioxide Electrolysis. *Energy Technology* **2017**, *5*, 929–936.

(20) Yang, H.; Kaczur, J. J.; Sajjad, S. D.; Masel, R. I. Electrochemical Conversion of CO<sub>2</sub> to Formic Acid Utilizing Sustainion<sup>TM</sup> Membranes. *J. CO<sub>2</sub> Util.* **2017**, *20*, 208–217.

(21) Li, Y. C.; Zhou, D.; Yan, Z.; Gonçalves, R. H.; Salvatore, D. A.; Berlinguette, C. P.; Mallouk, T. E. Electrolysis of CO<sub>2</sub> to Syngas in Bipolar Membrane-Based Electrochemical Cells. *ACS Energy Lett.* **2016**, *1* (6), 1149–1153.

(22) Salvatore, D. A.; Weekes, D. M.; He, J.; Dettelbach, K. E.; Li, Y. C.; Mallouk, T. E.; Berlinguette, C. P. Electrolysis of Gaseous CO<sub>2</sub> to CO in a Flow Cell with a Bipolar Membrane. *ACS Energy Lett.* **2018**, *3* (1), 149–154.

(23) Dinh, C. T.; Garcia De Arquer, F. P.; Sinton, D.; Sargent, E. H. High Rate, Selective, and Stable Electroreduction of CO<sub>2</sub> to CO in Basic and Neutral Media. *ACS Energy Lett.* **2018**, *3* (11), 2835–2840.

(24) Haas, T.; Krause, R.; Weber, R.; Demler, M.; Schmid, G. Technical Photosynthesis Involving CO<sub>2</sub> Electrolysis and Fermentation. *Nat. Catal.* **2018**, *1* (1), 32–39.

(25) Gabardo, C. M.; Seifitokaldani, A.; Edwards, J. P.; Dinh, C.-T.; Burdyny, T.; Kibria, M. G.; O'Brien, C. P.; Sargent, E. H.; Sinton, D.

Combined High Alkalinity and Pressurization Enable Efficient CO<sub>2</sub> Electroreduction to CO. *Energy Environ. Sci.* **2018**, *11* (9), 2531–2539.

(26) Ma, L.; Fan, S.; Zhen, D.; Wu, X.; Liu, S.; Lin, J.; Huang, S.; Chen, W.; He, G. Electrochemical Reduction of CO<sub>2</sub> in Proton Exchange Membrane Reactor: The Function of Buffer Layer. *Ind. Eng. Chem. Res.* **2017**, *56* (37), 10242–10250.

(27) Verma, S.; Lu, X.; Ma, S.; Masel, R. I.; Kenis, P. J. A. The Effect of Electrolyte Composition on the Electroreduction of CO<sub>2</sub> to CO on Ag Based Gas Diffusion Electrodes. *Phys. Chem. Chem. Phys.* **2016**, *18* (10), 7075–7084.

(28) Kim, B.; Hillman, F.; Ariyoshi, M.; Fujikawa, S.; Kenis, P. J. A. Effects of Composition of the Micro Porous Layer and the Substrate on Performance in the Electrochemical Reduction of CO<sub>2</sub> to CO. *J. Power Sources* **2016**, *312*, 192–198.

(29) Hursán, D.; Samu, A. A.; Janovák, L.; Artyushkova, K.; Asset, T.; Atanassov, P.; Janáky, C. Morphological Attributes Govern Carbon Dioxide Reduction on N-Doped Carbon Electrodes. *Joule* **2019**, DOI: 10.1016/j.joule.2019.05.007.

(30) Ma, S.; Luo, R.; Gold, J. I.; Yu, A. Z.; Kim, B.; Kenis, P. J. A. Carbon Nanotube Containing Ag Catalyst Layers for Efficient and Selective Reduction of Carbon Dioxide. *J. Mater. Chem. A* **2016**, *4* (22), 8573–8578.

(31) Möller, T.; Ju, W.; Bagger, A.; Wang, X.; Luo, F.; Ngo Thanh, T.; Varela, A. S.; Rossmeisl, J.; Strasser, P. Efficient CO<sub>2</sub> to CO Electrolysis on Solid Ni–N–C Catalysts at Industrial Current Densities. *Energy Environ. Sci.* **2019**, *12* (2), 640–647.

(32) Ma, S.; Lan, Y.; Perez, G. M. J.; Moniri, S.; Kenis, P. J. A. Silver Supported on Titania as an Active Catalyst for Electrochemical Carbon Dioxide Reduction. *ChemSusChem* **2014**, *7* (3), 866–874.

(33) Ramdin, M.; Morrison, A. R. T.; De Groen, M.; Van Haperen, R.; De Kler, R.; Van Den Broeke, L. J. P.; Trusler, J. P. M.; De Jong, W.; Vlugt, T. J. H. High Pressure Electrochemical Reduction of CO<sub>2</sub> to Formic Acid/Formate: A Comparison between Bipolar Membranes and Cation Exchange Membranes. *Ind. Eng. Chem. Res.* **2019**, *58* (5), 1834–1847.

(34) Lan, Y.; Gai, C.; Kenis, P. J. A.; Lu, J. Electrochemical Reduction of Carbon Dioxide on Cu/CuO Core/Shell Catalysts. *ChemElectroChem* **2014**, *1* (9), 1577–1582.

(35) Dinh, C.; Burdyny, T.; Kibria, M. G.; Seifitokaldani, A.; Gabardo, C. M.; Garcia de Arquer, F. P.; Kiani, A.; Edwards, J. P.; De Luna, P.; Bushuyev, O. S.; et al. CO<sub>2</sub> Electroreduction to Ethylene via Hydroxide-Mediated Copper Catalysis at an Abrupt Interface. *Science* **2018**, *360* (6390), 783–787.

(36) Ma, S.; Sadakiyo, M.; Luo, R.; Heima, M.; Yamauchi, M.; Kenis, P. J. A. One-Step Electrosynthesis of Ethylene and Ethanol from CO<sub>2</sub> in an Alkaline Electrolyzer. *J. Power Sources* **2016**, *301*, 219–228.

(37) Hoang, T. T. H.; Ma, S.; Gold, J. I.; Kenis, P. J. A.; Gewirth, A. A. Nanoporous Copper Films by Additive-Controlled Electrodeposition: CO<sub>2</sub> Reduction Catalysis. *ACS Catal.* **2017**, *7* (5), 3313–3321.

(38) Mistry, H.; Varela, A. S.; Bonifacio, C. S.; Zegkinoglou, I.; Sinev, I.; Choi, Y. W.; Kisslinger, K.; Stach, E. A.; Yang, J. C.; Strasser, P.; et al. Highly Selective Plasma-Activated Copper Catalysts for Carbon Dioxide Reduction to Ethylene. *Nat. Commun.* **2016**, *7*, 12123.

(39) Ma, S.; Liu, J.; Sasaki, K.; Lyth, S. M.; Kenis, P. J. A. Carbon Foam Decorated with Silver Nanoparticles for Electrochemical CO<sub>2</sub> Conversion. *Energy Technol.* **2017**, *5* (6), 861–863.

(40) Delacourt, C.; Ridgway, P. L.; Kerr, J. B.; Newman, J. Design of an Electrochemical Cell Making Syngas (CO+H<sub>2</sub>) from CO<sub>2</sub> and H<sub>2</sub>O Reduction at Room Temperature. *J. Electrochem. Soc.* **2008**, *155* (1), B42–B49.

(41) Hori, Y.; Ito, H.; Okano, K.; Nagasu, K.; Sato, S. Silver-Coated Ion Exchange Membrane Electrode Applied to Electrochemical Reduction of Carbon Dioxide. *Electrochim. Acta* **2003**, *48*, 2651–2657.

(42) Lee, W.; Kim, Y. E.; Youn, M. H.; Jeong, S. K.; Park, K. T. Catholyte-Free Electrocatalytic CO<sub>2</sub> Reduction to Formate. *Angew. Chem., Int. Ed.* **2018**, *57*, 6883–6887.

(43) Ma, C.; Hou, P.; Wang, X.; Wang, Z.; Li, W.; Kang, P. Carbon Nanotubes with Rich Pyridinic Nitrogen for Gas Phase CO<sub>2</sub> Electroreduction. *Appl. Catal., B* **2019**, *250*, 347–354.

(44) Liu, Z.; Masel, R. I.; Chen, Q.; Kutz, R.; Yang, H.; Lewinski, K.; Kaplun, M.; Luopa, S.; Lutz, D. R. Electrochemical Generation of Syngas from Water and Carbon Dioxide at Industrially Important Rates. *J. CO<sub>2</sub> Util.* **2016**, *15*, 50–56.

(45) Wang, G.; Pan, J.; Jiang, S. P.; Yang, H. Gas Phase Electrochemical Conversion of Humidified CO<sub>2</sub> to CO and H<sub>2</sub> on Proton-Exchange and Alkaline Anion-Exchange Membrane Fuel Cell Reactors. *J. CO<sub>2</sub> Util.* **2018**, *23*, 152–158.

(46) Aeshala, L. M.; Rahman, S. U.; Verma, A. Effect of Solid Polymer Electrolyte on Electrochemical Reduction of CO<sub>2</sub>. *Sep. Purif. Technol.* **2012**, *94*, 131–137.

(47) Millet, P.; Ngameni, R.; Grigoriev, S. a.; Mbemba, N.; Brisset, F.; Ranjbari, A.; Etiévant, C. PEM Water Electrolyzers: From Electrocatalysis to Stack Development. *Int. J. Hydrogen Energy* **2010**, *35*, 5043–5052.

(48) Marx, N.; Boulon, L.; Gustin, F.; Hissel, D.; Agbossou, K. A Review of Multi-Stack and Modular Fuel Cell Systems: Interests, Application Areas and on-Going Research Activities. *Int. J. Hydrogen Energy* **2014**, *39* (23), 12101–12111.

(49) Grosse, P.; Gao, D.; Scholten, F.; Sinev, I.; Mistry, H.; Roldan Cuenya, B. Dynamic Changes in the Structure, Chemical State and Catalytic Selectivity of Cu Nanocubes during CO<sub>2</sub> Electroreduction: Size and Support Effects. *Angew. Chem., Int. Ed.* **2018**, *57* (21), 6192–6197.

(50) Gao, H.; Wang, Y.; Xiao, F.; Ching, C. B.; Duan, H. Growth of Copper Nanocubes on Graphene Paper as Free-Standing Electrodes for Direct Hydrazine Fuel Cells. *J. Phys. Chem. C* **2012**, *116* (14), 7719–7725.

(51) Janáky, C.; Hursán, D.; Endrődi, B.; Chanmanee, W.; Roy, D.; Liu, D.; de Tacconi, N. R.; Dennis, B. H.; Rajeshwar, K. Electro- and Photoreduction of Carbon Dioxide: The Twain Shall Meet at Copper Oxide/Copper Interfaces. *ACS Energy Lett.* **2016**, *1* (2), 332–338.

(52) Van Der Laan, G. P.; Beenackers, A. A. C. M. Kinetics and Selectivity of the Fischer–Tropsch Synthesis: A Literature Review. *Catal. Rev.: Sci. Eng.* **1999**, *41* (3–4), 255–318.

(53) Weng, L.-C.; Bell, A. T.; Weber, A. Z. Towards Membrane-Electrode Assembly Systems for CO<sub>2</sub> Reduction: A Modeling Study. *Energy Environ. Sci.* **2019**, *12* (6), 1950–1968.

(54) Yin, Z.; Peng, H.; Wei, X.; Zhou, H.; Gong, J.; Huai, M.; Xiao, L.; Wang, G.; Lu, J.; Zhuang, L. An Alkaline Polymer Electrolyte CO<sub>2</sub> Electrolyzer Operated with Pure Water. *Energy Environ. Sci.* **2019**, DOI: 10.1039/C9EE01204D.

# Recent Advances in Solar-Driven Carbon Dioxide Conversion: Expectations versus Reality

Jie He and Csaba Janáky\*

Cite This: *ACS Energy Lett.* 2020, 5, 1996–2014

Read Online

ACCESS |



Metrics &amp; More

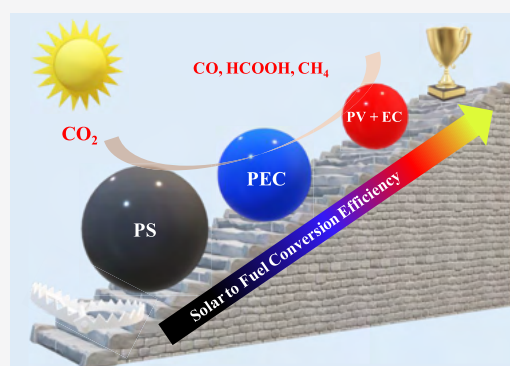


Article Recommendations



Supporting Information

**ABSTRACT:** Solar-driven carbon dioxide (CO<sub>2</sub>) conversion to fuels and high-value chemicals can contribute to the better utilization of renewable energy sources. Photosynthetic (PS), photocatalytic (PC), photoelectrochemical (PEC), and photovoltaic plus electrochemical (PV+EC) approaches are intensively studied strategies. We aimed to compare the performance of these approaches using unified metrics and to highlight representative studies with outstanding performance in a given aspect. Most importantly, a statistical analysis was carried out to compare the differences in activity, selectivity, and durability of the various approaches, and the underlying causes are discussed in detail. Several interesting trends were found: (i) Only the minority of the studies present comprehensive metrics. (ii) The CO<sub>2</sub> reduction products and their relative amount vary across the different approaches. (iii) Only the PV+EC approach is likely to lead to industrial technologies in the midterm future. Last, a brief perspective on new directions is given to stimulate discussion and future research activity.



Carbon dioxide (CO<sub>2</sub>) is one of the main greenhouse gases contributing to global climate change.<sup>1</sup> According to the National Oceanic and Atmospheric Administration (United States), the global mean CO<sub>2</sub> level reached 410 ppm in 2019.<sup>2</sup> To cope with climate challenge, more than 170 nations signed the Paris agreement in 2016, committing to fight climate change by cutting CO<sub>2</sub> emissions.<sup>3</sup> Such a political ambition requires a paradigm shift, supported by technological breakthroughs. One such change is to consider CO<sub>2</sub> as an abundant carbon source, instead of a pollutant. The turn-waste-into-wealth strategy will certainly play a key role in the green transformation of the chemical industry.<sup>4–6</sup> There are numerous routes to convert CO<sub>2</sub> to fuels and other chemicals. From the overall energy payback perspective, however, the most promising methods are those employing renewable energy. In this Focus Review, we focus on solar energy, which is regarded as a clean, abundant, and free renewable energy source. About 10% of the solar energy received on 0.3% of the Earth's surface would be enough to fulfill the expected energy needs in 2050.<sup>7</sup> Therefore, the combination of solar energy utilization and CO<sub>2</sub> resources can be expected to produce fuels as well as value-added chemicals. Moreover, beyond their cost-effectiveness, such processes are environmentally friendly and carbon-neutral.<sup>8</sup>

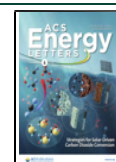
The conversion of CO<sub>2</sub> can lead to several different chemical/fuel products depending on the materials and/or methods employed, including carbon monoxide (CO), formic acid (HCOOH), methane (CH<sub>4</sub>), methanol (CH<sub>3</sub>OH), ethylene (C<sub>2</sub>H<sub>4</sub>), ethane (C<sub>2</sub>H<sub>6</sub>), propane (C<sub>3</sub>H<sub>8</sub>), ethanol (CH<sub>3</sub>CH<sub>2</sub>OH), acetic acid (CH<sub>3</sub>COOH), acetone, *n*-propanol, acetaldehyde, allyl alcohol, dimethyl ether, glycolaldehyde, hydroxyacetone, ethylene glycol, propionaldehyde, and glycerol.<sup>9</sup> Although the carbon content of these products, at the current production level, accounts for only a fraction of the emitted CO<sub>2</sub>,<sup>10</sup> the concept of solar-driven CO<sub>2</sub> can be extended to fuel production in the future (especially for aviation where high energy density is inevitable), which accounts for a much larger carbon footprint.<sup>5</sup>

Since the discovery of photoinduced reduction of CO<sub>2</sub> on semiconductors,<sup>11</sup> enormous research efforts have been devoted to the solar-driven conversion of CO<sub>2</sub>, and the field has witnessed a renaissance in the past few years.<sup>7,8,12–30</sup> We

Received: March 23, 2020

Accepted: May 15, 2020

Published: May 15, 2020



collected the number of papers published between 2014 and 2019 from the Web of Science database. There is a 3-fold increase in the number of published papers since 2014 (Figure 1), indicating the continuously growing research interest.

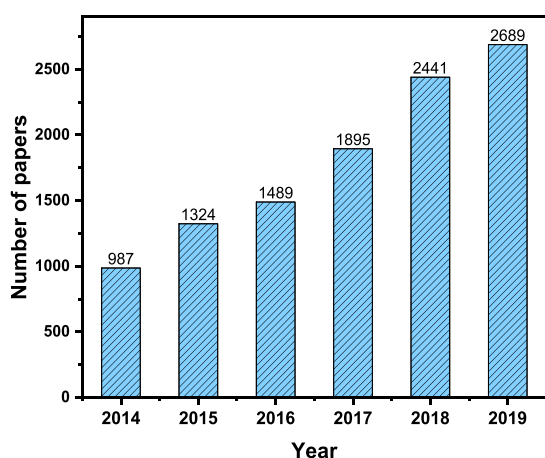


**Figure 1.** Number of papers published in the years of 2014–2019. Data collected from Web of Science Core Collection on 2020-03-06; topic: (photo\* or solar) and (CO<sub>2</sub> or carbon dioxide) and (conversion or reduction).

In fact, this trend also follows the policy orientation of national governments and international funding agencies. Energy-X<sup>5</sup> and Sunrise<sup>31</sup> started as independent projects, supported by the European Union's Horizon 2020 research and innovation program, focusing on the science and technology enabling efficient conversion of solar energy into chemicals. They are now merged into the "SUN-ERGY" program, to join forces under the umbrella of Horizon Europe, also in line with the Solar-Driven Chemistry Initiative of the European Chemical Society (EuChemS).<sup>32</sup> In the United States, the Joint Center for Artificial Photosynthesis (JCAP) was established in 2010, aiming to find new and effective ways to produce fuels using only sunlight, water, and CO<sub>2</sub>. It is the largest research program in the United States dedicated to the advancement of solar-fuels generation science and technology.<sup>33</sup> Other national programs are being implemented around the world, focusing on both fundamental science and technology development.

Considering the current momentum of the field and the expectations of the funders (ultimately the society), there is a need to scrutinize the recent scientific and technological

achievements. This exercise can shed light on what is competitive (and what remains in the land of promise) and also help to identify the most promising directions for newcomers to the field. There are a lot of books, book chapters, and review articles focusing on solar-driven CO<sub>2</sub> reduction topics, and the aim of this Focus Review is not to repeat such information. In contrast, our approach is to compare precedent results, based on metrics that can be employed as overarching benchmarks through the various solar-driven CO<sub>2</sub> conversion technologies. In addition, we highlight a few studies in which outstanding performances were achieved for a given metric.

**Different Solar-Driven CO<sub>2</sub> Conversion Approaches.** Solar-driven CO<sub>2</sub> conversion methods can be categorized into biophotosynthetic, photothermal, microbial-photoelectrochemical, photosynthetic (PS), photocatalytic (PC), photoelectrochemical (PEC), photovoltaic plus electrochemical (PV+EC), etc. The classification and definitions of solar-driven CO<sub>2</sub> conversion approaches involved in this review article are summarized in Table 1. The schematic illustrations of these systems together with the operational principles are also shown in Figure 2. Biophotosynthetic CO<sub>2</sub> conversion mimics natural photosynthesis and therefore usually involves redox enzyme molecules as photocatalysts or artificial microbes for photosynthesis.<sup>34–40</sup> The photothermal CO<sub>2</sub> conversion approach uses high-temperature solar reactors, typically concentrated solar radiation, to split CO<sub>2</sub>, potentially offering high product formation rate.<sup>41–50</sup> Microbial PEC CO<sub>2</sub> conversion combines the advantages of semiconductor nanodevices and the high-selectivity biocatalysts, directly converting CO<sub>2</sub> into fuels or chemicals.<sup>51–53</sup> Among the above-mentioned pathways, PS, PC, PEC, and PV+EC approaches are more commonly studied, because they are mostly carried out under relatively mild conditions, such as low temperature and ambient pressure. These strategies will be discussed in detail later; here, only a brief overview is provided.

Our approach was to compare precedent results, based on metrics which can be employed as overarching benchmarks through the various solar-driven CO<sub>2</sub> conversion technologies.

**Table 1.** Classifications and Definitions of Solar-Driven CO<sub>2</sub> Conversion Approaches

category	definition
Biophotosynthetic	An approach that mimics natural photosynthesis, which usually involves redox enzyme molecules as photocatalysts or artificial microbes for photosynthesis
Photothermal	An approach that uses high-temperature solar reactors, typically employing concentrated solar radiation, to split CO <sub>2</sub> , potentially utilizing the entire solar spectrum and offering high product formation rate
Microbial-photoelectrochemical	Combines the advantages of semiconductor photoelectrodes and the high-selectivity microbe-based biocatalysts, directly converting CO <sub>2</sub> into fuels or chemicals
Photosynthetic and photocatalytic (PS/PC)	Two sister approaches using particulate or molecular photocatalysts, either in solution or immobilized on a surface. This category includes both PC ( $\Delta G < 0$ ) and PS ( $\Delta G > 0$ ) processes, depending on the oxidation half reaction. Because of many similarities, they are discussed together herein, but in the light-to-fuel efficiency comparison (Figure 9b), only PS processes were selected to ensure fair comparison.
Photoelectrochemical (PEC)	Either one or both electrodes of the electrochemical cell is/are semiconductor photoelectrode(s). Photogenerated charge carriers drive either one or both half reactions. We included studies using the "buried junction" concept here, where a solar cell is covered by one or more catalyst(s) (and possibly a protecting layer) and this whole assembly acts as a photoelectrode.
Photovoltaic plus electrochemical (PV+EC)	The combination of PV cells with CO <sub>2</sub> electrolysis in one device. This approach decouples the light-harvesting and the electrochemical conversion steps.

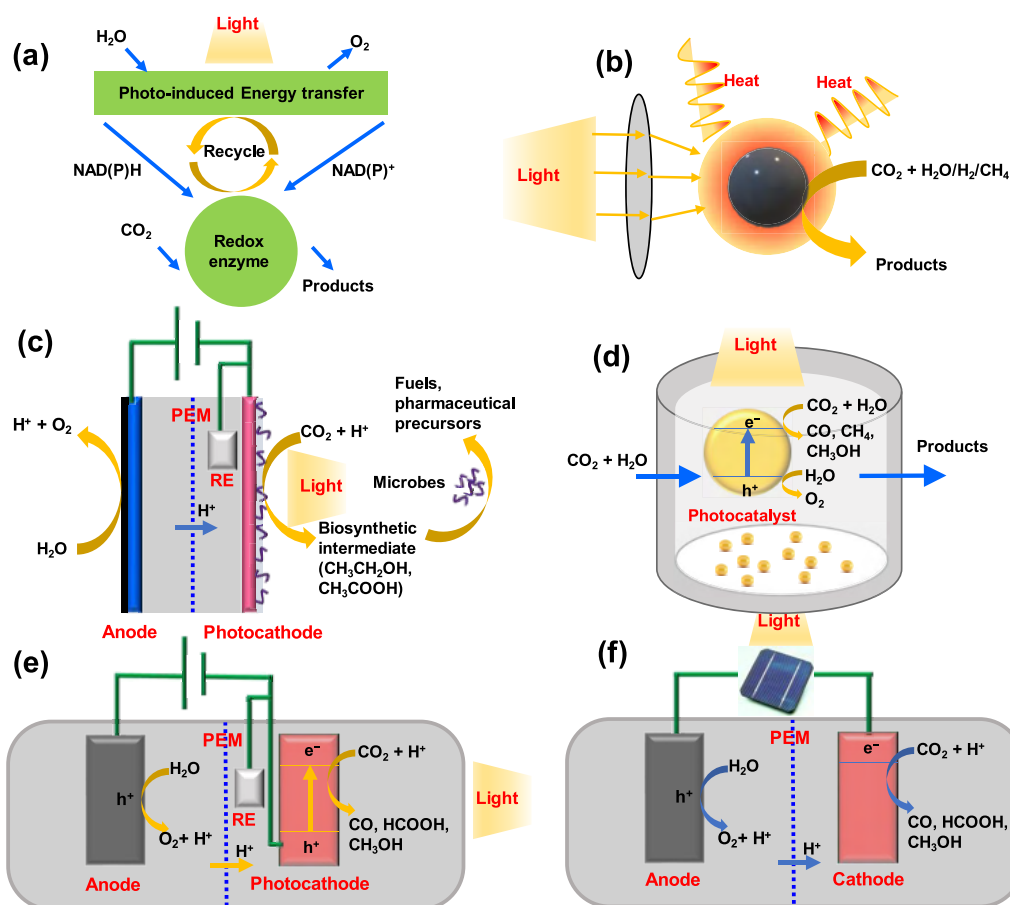


**Figure 2.** Schematic illustration of (a) biophotosynthetic, (b) photothermal, (c) microbial-photoelectrochemical, (d) photosynthetic and photocatalytic (PS/PC), (e) photoelectrochemical (PEC), and (f) photovoltaic plus electrochemical (PV+EC) approaches for CO<sub>2</sub> conversion.

There are many studies using sunlight to convert CO<sub>2</sub> over molecular or semiconductor photocatalysts, the so-called photosynthetic (PS) and photocatalytic (PC) processes. Notably, relevant chemical literature often does not differentiate between these two, although these reactions differ in their thermodynamics. PC processes are thermodynamically downhill ( $\Delta G < 0$ ) and are purely accelerated by the catalyst, whereas PS processes are thermodynamically unfavorable ( $\Delta G > 0$ ) and require photochemical energy input to occur. When CO<sub>2</sub> reduction is paired with the oxygen evolution reaction, it is an uphill reaction ( $\Delta G > 0$ ); thus, it should be defined as a PS process.<sup>54,55</sup> In contrast, if it is coupled with an anode process where a hole-scavenger is present, it can indeed be a PC process. This distinction is important, because there are different descriptors defining the performance in the two scenarios.<sup>54</sup> While similar solar light harvesting, charge separation, and transportation processes occur, the surface reactions and recombination are very different in the two cases.<sup>19,55,56</sup> Because of the many similarities, they are discussed together herein, except for the light-to-fuel conversion efficiency comparison.

Although hundreds of photocatalysts are reported yearly to demonstrate their effectiveness, many of these studies suffer from fundamental problems. Most of these studies focus only on the reduction part of the process such as the transformation of CO<sub>2</sub> to CO, CH<sub>4</sub>, and HCOOH, but the coupled oxidation process (the other half of the story) is seldom discussed in

detail. It has been a common practice to include sacrificial electron donors such as triethanolamine in a PC reaction to overcome both thermodynamic and kinetic limitations of the oxidation process. This practice, however, requires careful attention: (1) the process should be defined as PC rather than PS (see above); (2) the reported light-to-fuel conversion efficiencies might be inaccurate; (3) the oxidation of sacrificial donors may contribute to the products that are being considered as CO<sub>2</sub>-reduction products. There are at least two possible ways how a sacrificial donor can “contribute” to assumed CO<sub>2</sub>-reduction products: either the oxidation of the sacrificial electron donors directly produces C<sub>1</sub> products, or the radical intermediates produced in the oxidation process have reductive abilities, which help to convert CO<sub>2</sub>. Therefore, if applied, it is very important to evaluate the fate of these sacrificial donors and their contributions to the overall yield of the products in the PC CO<sub>2</sub> reduction reactions.<sup>57,58</sup>

Compared with the particle suspension-based PS and PC process, the photoelectrode-based PEC reduction of CO<sub>2</sub> can integrate the advantages of photosynthesis and electrocatalysis.<sup>59</sup> Based on which electrode acts as the light absorber, three different PEC configurations can be envisioned: photocathode–dark anode (shown in Figure 2e as an example), photoanode–dark cathode, and photocathode–photoanode. The fact that each photoelectrode can consist of multiple absorber layers to better cover the solar spectrum complicates the picture further. A sophisticated variant is the

Table 2. Summarized Performance Metrics for PS/PC, PEC, and PV+EC Systems

	PS/PC	PEC	PV+EC
Performance metrics	Formation rate	Formation rate (current density)	Formation rate (current density)
	Conversion	Potential/voltage	Potential/voltage
	Turnover number (TON)	Selectivity (Faradic efficiency, FE)	Selectivity (Faradic efficiency, FE)
	Selectivity	Solar-to-fuel conversion efficiency (SFE)	Solar-to-fuel conversion efficiency (SFE)
	Quantum efficiency (QE)	Incident photon-to-current conversion efficiency (IPCE)	Durability
	Durability	Absorbed photon-to-current conversion efficiency (APCE)	
		Durability	

Table 3. Selected Studies on PS/PC CO<sub>2</sub> Conversion

		PS							
catalyst	illumination conditions	reactant/solution	products	QE (%)	selectivity (%)	formation rate normalized (mmol e <sup>-</sup> g <sub>cat</sub> <sup>-1</sup> h <sup>-1</sup> )	maximum test time (h)	ref.	
Surface S and Br modified CoO/Co <sub>3</sub> O <sub>4</sub>	300 W Xe lamp, IR water filter, 500 mW cm <sup>-2</sup>	H <sub>2</sub> O	CH <sub>4</sub>	2.3 at 405 nm	98	~80	9	99	
CuIn <sub>3</sub> S <sub>8</sub> single-unit-cell layers	AM 1.5G filter, λ ≥ 400 nm, ~50 mW cm <sup>-2</sup>	H <sub>2</sub> O	CH <sub>4</sub>	0.79	100	0.0696	120	100	
(Ag@Cr)/Ga <sub>2</sub> O <sub>3</sub>	400 W high-pressure mercury lamp with a quartz filter	H <sub>2</sub> O	CO		85.2	2.1	5	101	
		PC							
catalyst	illumination conditions	reactant/solution	products	QE (%)	selectivity (%)	formation rate normalized (mmol e <sup>-</sup> g <sub>cat</sub> <sup>-1</sup> h <sup>-1</sup> ) or TON	maximum test time (h)	ref.	
Co–Co <sub>2</sub> P@NPC	200 W white LED lamp	TEOA/H <sub>2</sub> O/MeCN, [Ru(bpy) <sub>3</sub> ]Cl <sub>2</sub> ·6H <sub>2</sub> O	CO		79.1	~70	18	102	
RuP/C <sub>3</sub> N <sub>4</sub>	400 W Hg lamp, λ > 400 nm	DMA/TEOA	HCOOH	5.7 at 400 nm		TON > 1000		103	
Iridium(III) complexes	Blue LED light, 0.43 mW cm <sup>-2</sup>	TEOA/MeCN	CO	10		TON > 265	10 days	104	

“buried junction” concept, where a solar cell is covered by one or more catalyst(s) (and possibly a protecting layer) and this whole assembly acts as a photoelectrode.<sup>60–63</sup>

Development in photovoltaic (PV) technologies over the past 5–10 years is eye-catching, with the record of light-to-electrical power conversion efficiency (PCE, which is the ratio between the incident solar photon energy and the electrical energy output) being continuously renewed.<sup>64</sup> For example, the silicon-based single-junction PV cell could achieve the PCE of 26.7%; the III–V single-junction cells, such as GaAs, reached the PCE of as high as 29.1%, while the burgeoning perovskite-based cells could also achieve 21.6%. The multi-junction cells, such as AlGaInP/AlGaAs/GaAs/GaInAs further increased the PCE to 47.1%.<sup>65,66</sup> What is equally important, with the rapid growth of the PV industry, the price of the Si-based PV cells has declined sharply.<sup>67</sup> Therefore, these low-cost and reliable silicon-based PV modules are widely available. PV cells can be combined with an electrolyzer, thus decoupling the light-harvesting (current generation) and the electrochemical conversion steps (PV+EC system). For the PV+EC systems discussed in this Focus Review, we excluded those studies where a solar cell covered by a catalyst acts as a photoelectrode for one half reaction (those are discussed in the PEC field). Only those scenarios are considered where the PV panel is the sole supplier of the electrochemical bias, and the CO<sub>2</sub> conversion takes place on an electrode wired to the PV cell.<sup>63</sup> The separation of the optical and electrical components allows a greater selection of materials and eliminates concerns of processing compatibilities and solution stability of the light-active components. Furthermore, in principle, it allows the use of high-quality (and expensive) electrocatalysts, because of the much higher operational current densities. This strategy has

been successfully applied for water splitting to produce hydrogen. The price of renewable hydrogen has dropped to about €3.23 kg<sup>-1</sup> considering the parameters relevant to Germany, which is already competitive with small and medium-size operations of conventional, fossil fuel-based processes. Considering the trend in the cost, €2.50 kg<sup>-1</sup> seems realistic within a decade, which will be competitive with petrochemical approaches.<sup>63</sup> We envision similar opportunities for PV+EC CO<sub>2</sub> conversion, once mature electrolyzer technologies will be available.

*Performance Metrics for PS/PC, PEC, and PV+EC Approaches.* As data-mining becomes a major component of every research project, it is now more important than ever to report experimental data (and the drawn conclusions) in a manner that comparisons among laboratories can be easily made.<sup>68</sup> While analyzing the papers from the past 5 years, we collected a broad set of performance metrics (Table 2), to see which ones allow the most meaningful comparisons for PS/PC, PEC, and PV+EC studies.

Activity, selectivity, and durability are usually the main three aspects to evaluate the performance of different solar-driven CO<sub>2</sub> conversion approaches. In PS/PC studies, product formation rate is the most commonly reported metric for evaluating the activity. In most cases, the formation rate is normalized over the weight of the catalyst or the geometrical area if it is immobilized on a substrate. Products, however, may vary in different catalytic systems. It is a worthwhile exercise to normalize the formation rate with the reaction stoichiometry (i.e., numbers of electrons transferred in the reaction); thus, comparisons can be reasonably made among different products (such analysis will be shown later). Quantum efficiency (QE) is another important component of the light-to-fuel efficiency,



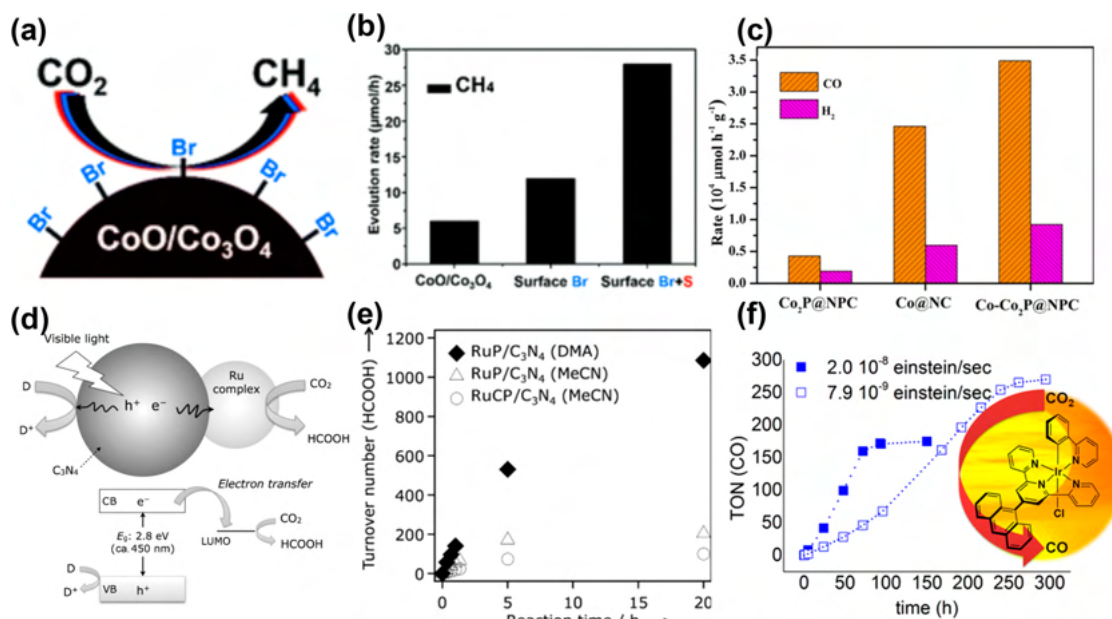


Figure 3. (a) Schematic illustration of N-bromosuccinimide treated cobalt oxide nanoparticles and (b) CH<sub>4</sub> formation rate over catalysts with different surface treatments. Reprinted with permission from ref 99. Copyright 2019 Royal Society of Chemistry. (c) Comparison of CO<sub>2</sub> reduction performances of different catalysts. Reprinted with permission from ref 102. Copyright 2019 Wiley-VCH. (d) Schematic illustration of CO<sub>2</sub> reduction using a Ru complex/C<sub>3</sub>N<sub>4</sub> hybrid photocatalyst and (e) the turnover number of HCOOH production as a function of irradiation time using different photocatalysts and solvents. Reprinted with permission from ref 103. Copyright 2019 Wiley-VCH. (f) The turnover number of CO evolution as a function of irradiation time over modified iridium(III) photocatalyst. Reprinted from ref 104. Copyright 2017 American Chemical Society.

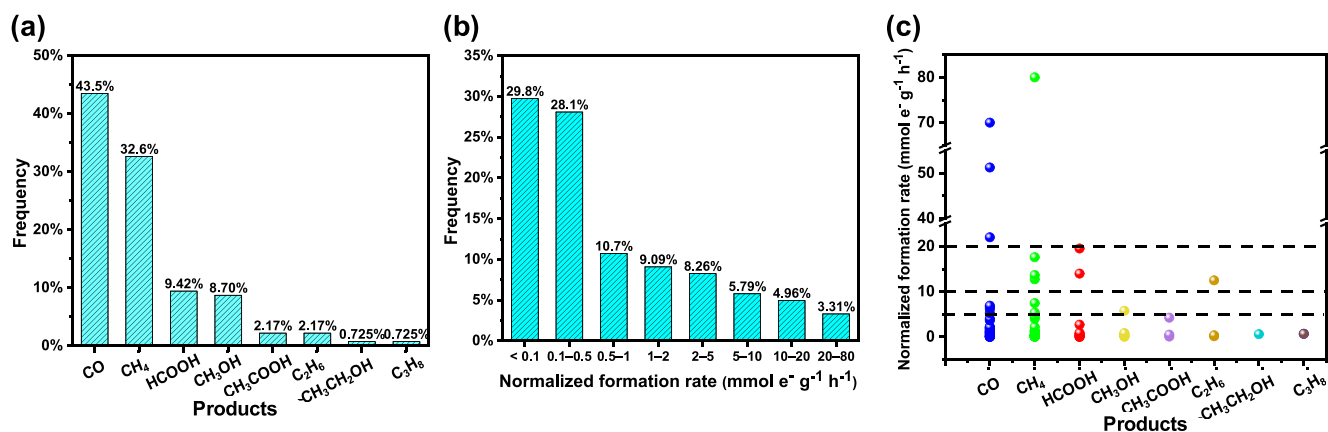


Figure 4. Statistical analysis of PS/PC CO<sub>2</sub> conversion studies: (a) product distribution, (b) normalized formation rate distribution, and (c) normalized formation rate distribution of different products.

but it is not provided in all reports. For the PEC approach, the Faradaic efficiency (FE) is the most reported metric, often misleadingly interpreted as an activity descriptor. In addition, the onset potential of the reduction process (the potential/voltage at which the product detection measurement was carried out) and the corresponding normalized current density are also important metrics to be reported. Solar-to-fuel conversion efficiency (SFE) is a key metric, which is less reported in PEC systems. Strictly speaking, SFE is applicable only if no external bias is employed. Incident photon-to-current conversion efficiency (IPCE) and absorbed photon-to-current conversion efficiency (APCE) can also reflect the efficiency from different aspects.<sup>69</sup> In PV+EC related systems, the performance metrics are similar to those of the PEC. The

operation points (including voltage and current density) are usually provided, and SFE is more commonly reported.

*Recent Development in PS/PC CO<sub>2</sub> Conversion.* In the past 5 years, numerous research articles have been published focusing on further improving the activity, selectivity, and durability for PS/PC CO<sub>2</sub> reduction. There are also a lot of reviews and perspectives, such as a summary of photocatalyst development,<sup>7,8,16,20–22,24,27,28,70–91</sup> design strategies for reactors,<sup>18,92,93</sup> and the possibilities and challenges of solar fuel production.<sup>8,14,17,19,27,28,94–98</sup> Here, we highlighted three studies on PS and PC CO<sub>2</sub> conversion with outstanding performance in some regard (see bold values in Table 3).

CO<sub>2</sub> reduction to CH<sub>4</sub> with high formation rate and selectivity was reported, when surface activated cobalt oxide nanoparticles were used as catalyst.<sup>99</sup> As shown in Figure 3a,

Table 4. Selected Studies on PEC CO<sub>2</sub> Conversion

Photocathode–Dark Anode									
cathode	anode	illumination conditions	electrolyte	potential and current density	products	FE (%)	SFE (%)	maximum test time (h)	ref
Bi Nanosheets	Graphite	1 Sun	NaHCO <sub>3</sub>	−1.1 V vs RHE, 18 mA cm <sup>−2</sup>	HCOOH	~100	1.5	12	105
In <sub>0.4</sub> Bi <sub>0.6</sub> /MAPbI <sub>3</sub>	Pt	1 Sun	KHCO <sub>3</sub>	−0.6 V vs RHE, ~5.5 mA cm <sup>−2</sup>	HCOOH	~100		1.5	106
TiO <sub>2</sub> -protected Cu <sub>2</sub> O–Re(tBu-bipy)(CO) <sub>3</sub> Cl	Pt	Xe lamp with KG 3 and AM 1.5 G filters	Re(tBu-bipy)(CO) <sub>3</sub> Cl and MeOH	−1.73 V vs Fc <sup>+</sup> /Fc, ~1.5 mA cm <sup>−2</sup>	CO	~100		5.5	107
Li-doped CuFeO <sub>2</sub>	Graphite	1 Sun	pyridine acetate buffer	−0.63 V vs SCE, ~0.6 mA cm <sup>−2</sup>	CH <sub>3</sub> OH	96.7		1.5	108
CuFeO <sub>2</sub> /CuO	Pt	1 Sun	KHCO <sub>3</sub>	0.15 V vs RHE, ~1.5 mA cm <sup>−2</sup>	HCOOH	>90	1–1.2	7 days	109

Photoanode–Dark Cathode									
cathode	anode	illumination condition	electrolyte	potential and current density	products	FE (%)	SFE (%)	maximum test time (h)	ref
Pd/C-coated Ti mesh	GaAs/InGaP/TiO <sub>2</sub> /NiO <sub>x</sub>	1 Sun	Anolyte: KOH; catholyte: KHCO <sub>3</sub>	Cathode: ~−0.8 V vs Ag/AgCl, 8.5 mA cm <sup>−2</sup>	HCOOH	>94	~10	3	9

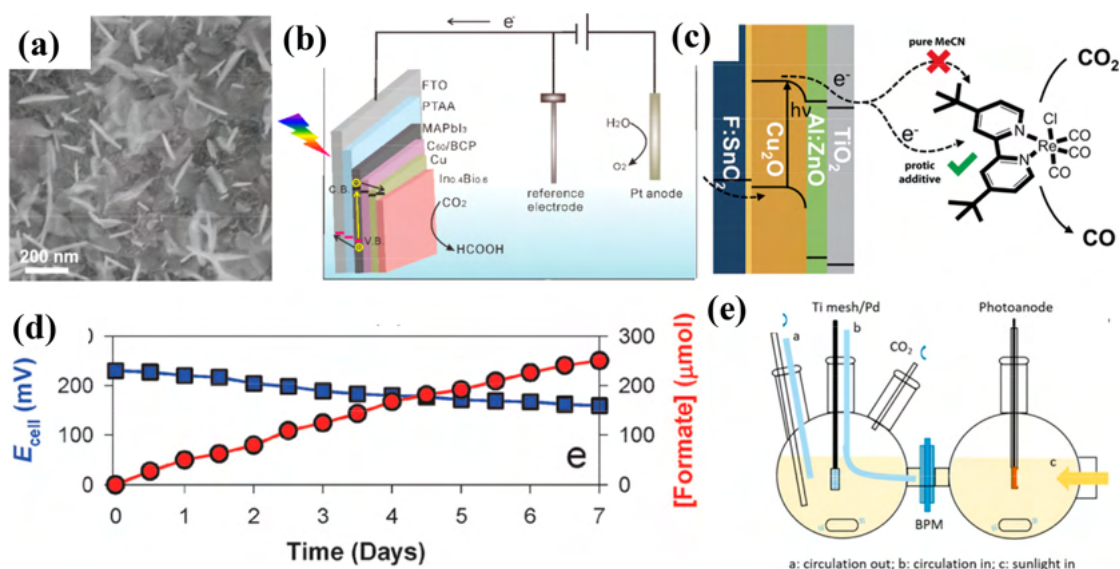


Figure 5. (a) SEM image of reduced mesoporous Bi nanosheets. Reprinted with permission from ref 105. Copyright 2018 Wiley-VCH. (b) Full cell configuration containing In<sub>0.4</sub>Bi<sub>0.6</sub>-coated perovskite photocathode. Reprinted from ref 106. Copyright 2019 American Chemical Society. (c) Schematic of the PEC CO<sub>2</sub> reduction process involving protected Cu<sub>2</sub>O photocathodes and a Re-based molecular catalyst. Reprinted with permission from ref 107. Copyright 2015 Royal Society of Chemistry. (d) Changes in  $E_{\text{cell}}$  and HCOOH production with a wired CuFeO<sub>2</sub>/CuO and Pt couple under illumination without external bias. Reprinted with permission from ref 109. Copyright 2015 Royal Society of Chemistry. (e) The scheme of photoanode-dark anode configuration for CO<sub>2</sub> conversion. Reprinted from ref 9. Copyright 2016 American Chemical Society.

treatment with N-bromosuccinimide resulted in the formation of Co<sub>3</sub>O<sub>4</sub> with coordinated Br on the surface, therefore enhancing the catalytic efficiency. The formation rate of CH<sub>4</sub> was further enhanced by surface modification with sulfur, reaching 10 mmol g<sup>−1</sup> h<sup>−1</sup> (normalized formation rate of 80 mmol e<sup>−</sup> g<sup>−1</sup> h<sup>−1</sup>) with a QE of 2.3% at 405 nm and a selectivity of 98% (Figure 3b). In another study, a heterogeneous hybrid catalyst of Co and Co<sub>2</sub>P nanoparticles was embedded in carbon nanolayers codoped with N and P (activities shown in Figure 3c) which was combined with a homogeneous Ru-based complex photosensitizer, allowing high CO formation rate.<sup>102</sup> In atomically thin layers of sulfur-deficient CuIn<sub>3</sub>S<sub>8</sub> (containing charge-enriched Cu–In dual sites), the formation of a stable Cu–C–O–In intermediate at the Cu–In dual sites was the key feature

determining selectivity.<sup>100</sup> As a result, the CuIn<sub>3</sub>S<sub>8</sub> single-unit-cell layers achieved nearly 100% selectivity for visible-light-driven CO<sub>2</sub> reduction to CH<sub>4</sub>, with a formation rate of 8.7 μmol g<sup>−1</sup> h<sup>−1</sup>. A hybrid system of a ruthenium complex and carbon nitride (C<sub>3</sub>N<sub>4</sub>) was shown to selectively convert CO<sub>2</sub> to HCOOH (Figure 3d,e).<sup>103</sup> As for molecular systems, terpyridine modifications of an iridium(III) photocatalysts with a combined 2-phenylpyridine (ppy) and 2,2′:6′,2′′-terpyridine (tpy) ligand have been investigated and yielded a turnover number (TON) of up to 265 with a QE of 0.10 (Figure 3f).<sup>104</sup> It is worth pointing out that this catalytic system showed high durability (over 10 day operation without obvious decay of activity).

To get a statistically validated picture of PS/PC CO<sub>2</sub> conversion studies, 138 cases were analyzed among those

papers published since 2014. The selection criterion was the availability of two or more of the important performance indicators in the study. The majority of these studies (>100) employed various sacrificial agents; therefore, they belong to the PC category. The results are shown in Figure 4. For the product distribution, only the major products (selectivity > 30%) of each study were counted. The most common products formed are CO and CH<sub>4</sub>, which together account for over 75% of the major products. In addition, HCOOH and CH<sub>3</sub>OH also represent 9.4% and 8.7%, respectively. Other products, such as CH<sub>3</sub>COOH, C<sub>2</sub>H<sub>6</sub>, CH<sub>3</sub>CH<sub>2</sub>OH, and C<sub>3</sub>H<sub>8</sub>, were seldom reported as major products, which is consistent with the results in the selected studies we have highlighted. To transparently compare the activity of the catalysts in these studies, the reported formation rates have been normalized with the electron-transfer number of the given product, enabling comparisons among different products. Among the above 138 cases, 121 demonstrated unambiguous formation rate data, which were selected for the subsequent analysis. As shown in Figure 4b, the formation rates concentrated within a lower range of 0–0.5 mmol e<sup>-</sup> g<sup>-1</sup> h<sup>-1</sup>, accounting for about 50% of the studies. There are 4 cases reported formation rates ranging from 20 to 80 mmol e<sup>-</sup> g<sup>-1</sup> h<sup>-1</sup>. We further analyzed the normalized formation rate distribution of different products (Figure 4c and Table S1). Only CO and CH<sub>4</sub> have been produced with a formation rate greater than 20 mmol e<sup>-</sup> g<sup>-1</sup> h<sup>-1</sup>. Interestingly, although almost 10% of the cases had HCOOH as the major product, most of them reported the formation rate lower than 5 mmol e<sup>-</sup> g<sup>-1</sup> h<sup>-1</sup>. This pattern suggests that there is a greater chance of reoxidation of HCOOH to CO<sub>2</sub> (back reaction on the very same catalyst, driven by the photogenerated holes), compared to that for the gas-phase products, which rapidly move away from the catalyst surface.

**Recent Development in PEC CO<sub>2</sub> Conversion.** The number of studies employing PEC CO<sub>2</sub> conversion approach has also grown rapidly in the past 5 years. Some outstanding examples are highlighted in Table 4.

Mesoporous bismuth nanosheets have been prepared by the cathodic transformation of atomic-thick bismuth oxycarbonate nanosheets, which showed selective CO<sub>2</sub> reduction to HCOO<sup>-</sup> with high current density (-1.1 V vs RHE, ~18 mA cm<sup>-2</sup>, FE ≈ 100%) and operation stability (12 h). Moreover, Bi nanosheets were integrated with Ir/C dark anode in full cells and achieved a solar-to-formate conversion efficiency of 1.5%. The CO<sub>2</sub> reduction performance was rationalized by the 2D mesoporous nanosheet morphology with an enlarged surface, abundant under-coordinated Bi sites, and structural robustness (Figure 5a).<sup>105</sup>

The application of hybrid organic–inorganic and fully inorganic perovskites in PEC processes has also been a hot topic. For example, a novel photocathode was prepared by coating an In<sub>0.4</sub>Bi<sub>0.6</sub> alloy layer on a MAPbI<sub>3</sub> PV cell (as illustrated in Figure 5b), which achieved a current density of 5.5 mA cm<sup>-2</sup> at -0.6 V vs RHE, producing HCOOH at nearly 100% FE for 1.5 h.<sup>106</sup> A TiO<sub>2</sub>-protected Cu<sub>2</sub>O photocathode

The selectivity toward a given product is affected more by the electrode material and the PEC condition, rather than the product itself.

was paired with a molecular rhenium bipyridyl catalyst. At -1.73 V vs Fc<sup>+</sup>/Fc, the system showed a current density of ~1.5 mA cm<sup>-2</sup> and FE<sub>CO</sub> of nearly 100% (Figure 5c).<sup>107</sup> This kind of configuration is not a standard PEC system as we discussed above because the light absorber and active sites are

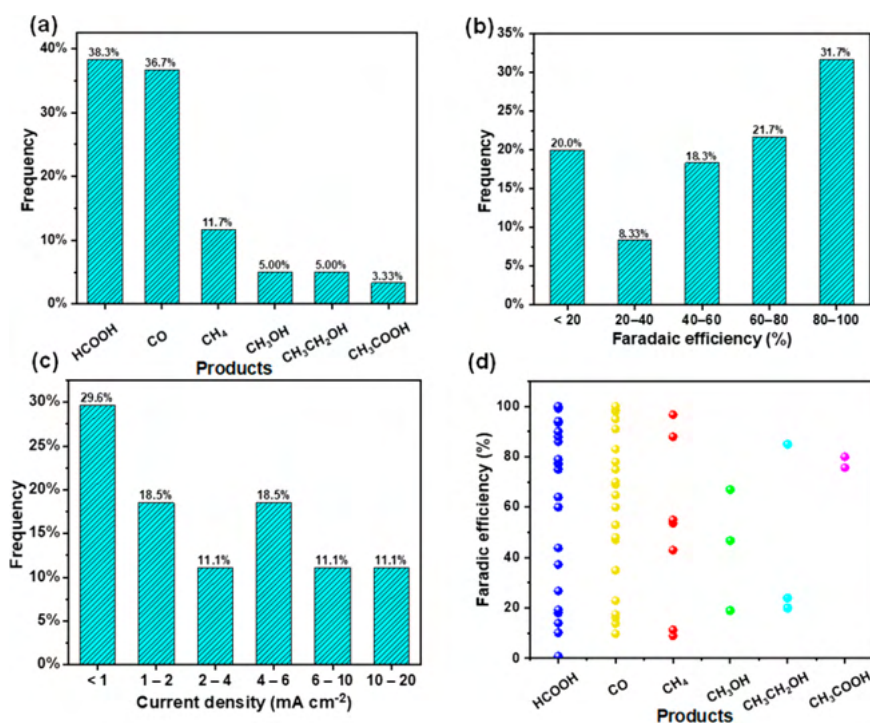


Figure 6. Statistical analysis of PEC CO<sub>2</sub> conversion studies: (a) product distribution, (b) FE distribution, (c) current density (under 1 Sun) distribution, and (d) FE distribution of different products.

Table 5. Representative Studies on PV+EC CO<sub>2</sub> Conversion

light absorber	anode	cathode	illumination conditions	electrolyte	products	operation point	FE (%)	SFE (%)	maximum test time (h)	ref
GaInP/GaInAs/Ge	CuO/SnO <sub>2</sub>	CuO/SnO <sub>2</sub>	1 Sun	Anolyte: CsOH, Catholyte: CsHCO <sub>3</sub>	CO	2.38 V, -0.55 V vs RHE, 11.6 mA cm <sup>-2</sup>	81	14.4	5	111
GaInP/GaInAs/Ge	Sr <sub>2</sub> GaCoO <sub>3</sub>	Ag	1 Sun	NaNO <sub>3</sub>	CO	2.26 V, 3.54 mA cm <sup>-2</sup>	85–89	15.6	19	112
Triple-junction GaAs (InGaP/GaAs/Ge) solar cell	Zn	Au	1 Sun	Anolyte: KOH with zinc acetate, catholyte: KHCO <sub>3</sub>	CO	1.96 V, 10 mA cm <sup>-2</sup>	~92	~16.9	24	113
GaInP/GaInAs/Ge	Ni or Pt	Ag/GDE	1 Sun	Anolyte: KOH; Catholyte: KOH	CO	2.23 V, -0.6 V vs RHE, 14.4 mA cm <sup>-2</sup>	~100	19.1	150	114

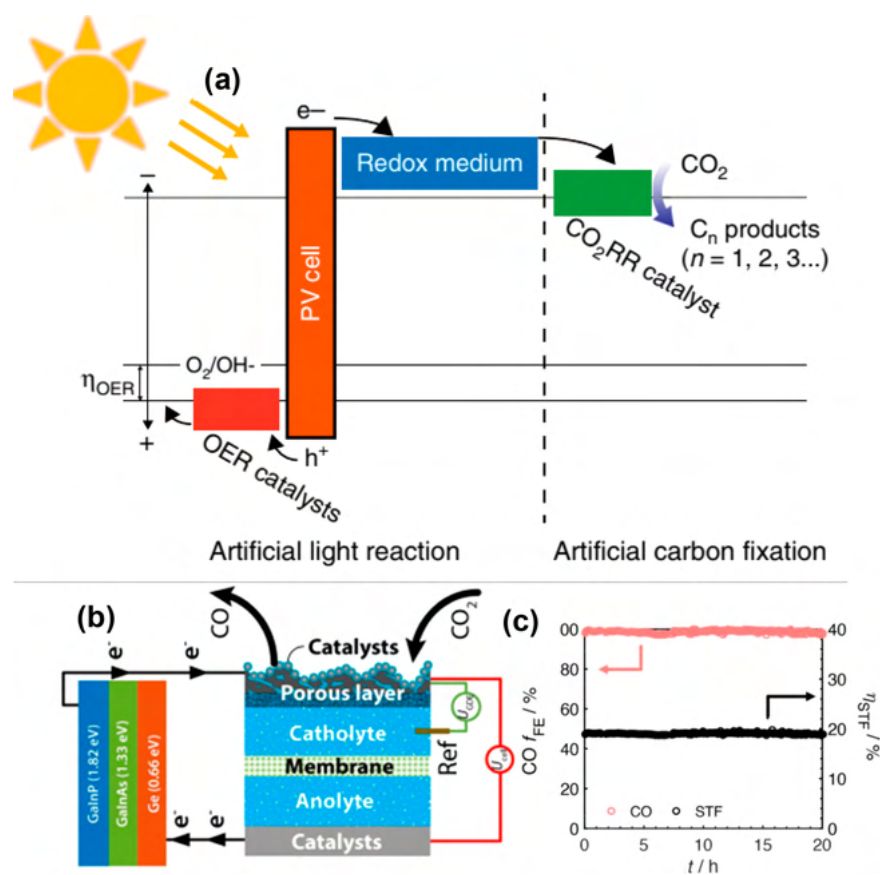


Figure 7. (a) Energy diagram of each part in a redox-medium-assisted system. Reprinted with permission from ref 113. Copyright 2018 Springer Nature. (b) Illustration of a wire connection between the triple-junction cell and GDE cell and (c) CO Faradaic efficiency and solar-to-fuel efficiency over 20 h duration. Reprinted from ref 114. Copyright 2020 American Chemical Society.

separated, and the buried junction together with the external electric power provides the bias.

There are also reports on PEC CO<sub>2</sub> reduction to alcohols, for example, CH<sub>3</sub>OH was synthesized at a Li-doped CuFeO<sub>2</sub> thin-film photocathode with a FE<sub>CH<sub>3</sub>OH</sub> of 96.7% at -0.63 V vs SCE.<sup>108</sup> Durability is another objective of the studies: a PEC cell, containing CuFeO<sub>2</sub>/CuO photocathode and Pt anode couples, could produce HCOOH for over 1 week at a solar-to-formate energy conversion efficiency of ~1% (FE > 90%) without any external bias (Figure 5d).<sup>109</sup> CuFeO<sub>2</sub>/CuO bulk heterojunction films were also capable of converting CO<sub>2</sub> into C1–C6 aliphatic acid anions under simulated sunlight in the absence of any sacrificial chemicals or electrical bias, which shows that larger molecules can also be formed via PEC C–C

coupling.<sup>110</sup> The photoanode–dark cathode configuration has also been heavily investigated. For example, a solar-driven CO<sub>2</sub> reduction cell was constructed encompassing a tandem GaAs/InGaP/TiO<sub>2</sub>/Ni photoanode, a Pd/C nanoparticle-coated Ti mesh cathode,<sup>9</sup> and a bipolar membrane to allow for steady-state operation with a separate catholyte and anolyte. At the operational current density of 8.5 mA cm<sup>-2</sup> without external bias, the cathode exhibited <100 mV overpotential and >94% FE for the reduction of CO<sub>2</sub> to formate with SFE as high as 10%.

What is common in most of the highlighted studies is the very high selectivity. Note that almost 100% FE was reported for three different products (CO, HCOOH, and CH<sub>3</sub>OH). To further elaborate on this matter, statistical analysis of the PEC CO<sub>2</sub> conversion studies has also been conducted (Figure 6).

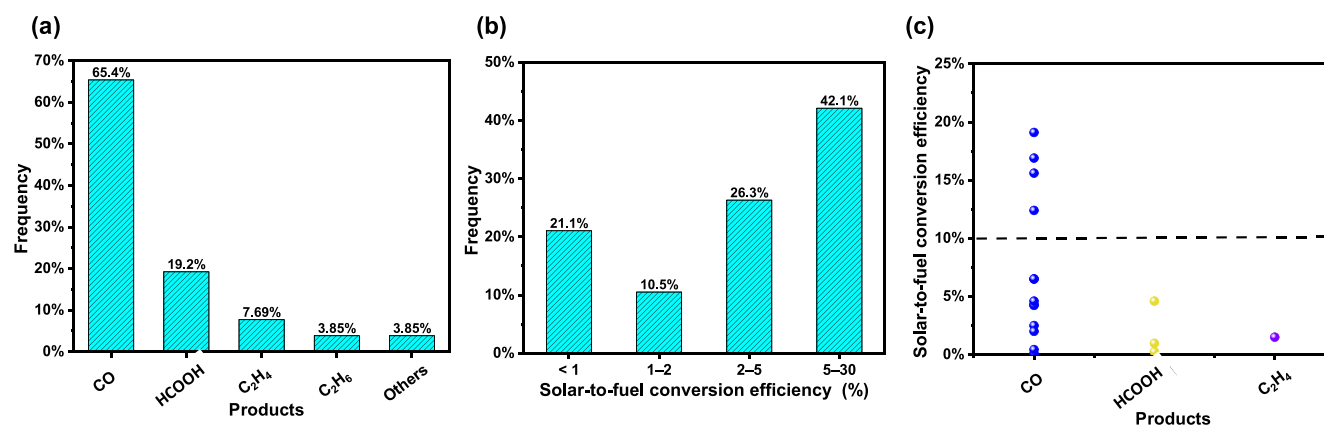


Figure 8. Statistical analysis of PV+EC CO<sub>2</sub> conversion studies: (a) product distribution, (b) SFE distribution, and (c) SFE distribution of different products.

Sixty cases were collected that provided clear FE data for corresponding CO<sub>2</sub> conversion products, which is employed as the key metric for comparing the PEC behavior herein.

For product distribution, HCOOH and CO are the most common major products reported, together accounting for 75% of the studies, followed by CH<sub>3</sub>OH (11.7%), CH<sub>4</sub> (5%), CH<sub>3</sub>CH<sub>2</sub>OH (5%), and CH<sub>3</sub>COOH (3.33%), which is consistent with the results of the highlighted studies. For the FE of the product formed in the largest amount, most of the studies reported FE higher than 60%, in which there are 32% with FE higher than 80%. There are still 20% of the studies reported, with FEs lower than 20%. To compare the activity, we also analyzed the current density distribution. More than 45% of the studies reported current density lower than 2 mA cm<sup>-2</sup>, while only 11% reported higher than 10 mA cm<sup>-2</sup>. For the FE distribution for different products, we do not see any cluster formation, which means that none of the products tends to form more selectively than others. In fact, there is a rather even distribution of the FE values for all products, which suggests that the selectivity of a given product is affected more by the electrode material and the PEC condition, rather than the product itself. It is easy to understand that different electrode materials greatly affect the product because the reducing power of the electrons in the PEC system is defined by the conduction band energy of the photocathode. The PEC condition, such as the electrolyte, also affect the surface chemistry and the intermediate species. Note that similarly high FE values were found for the highly reduced products (e.g., CH<sub>3</sub>OH, C<sub>2</sub>H<sub>5</sub>OH, CH<sub>4</sub>, etc.) to those obtained for CO and HCOOH. The detailed product distribution of PEC CO<sub>2</sub> conversion studies within different FE ranges is shown in Table S2.

**Recent Development in PV+EC CO<sub>2</sub> Conversion.** Based on the successful H<sub>2</sub> evolution studies employing PV+EC systems, this configuration has attracted much attention also for CO<sub>2</sub> reduction, especially in the past two years. Here we must make a distinction between (i) integrated systems, where the two functions are incorporated in the same unit, and those (ii) coupled ones, where regular PV panels are DC–DC connected to regular electrochemical cells. In our analysis, only the integrated systems were considered to ensure a fair comparison with the PS/PC and PEC approaches. In Table 5, we highlight some representative studies with high SFE and/or durability.

Atomic layer deposition of SnO<sub>2</sub> was performed on CuO nanowires for narrowing the product distribution of CO<sub>2</sub>

reduction, thus yielding predominantly CO. The prepared catalyst was employed as both the cathode and anode for complete CO<sub>2</sub> electrolysis. In the resulting device, the electrodes were separated by a bipolar membrane, and a GaInP/GaInAs/Ge photovoltaic cell was used to drive the solar-driven splitting of CO<sub>2</sub> into CO and oxygen with a solar-to-CO efficiency of 13.4% and overall SFE of 14.4%. The operating current density, selectivity toward CO, and solar-to-CO efficiency remained almost stable during 5 h of electrolysis.<sup>111</sup> In another study, a CO<sub>2</sub> reduction system was integrated, achieving an average solar-to-CO efficiency of 13.9% and SFE of 15.6% with no appreciable performance degradation in 19 h of operation.<sup>112</sup>

In another example, a two-step, redox-medium-assisted solar-driven CO<sub>2</sub> electroreduction system was developed by incorporating a Zn/Zn(II) redox mediator that acts as the electron carrier during the photosynthesis. In the light reaction, the solar-driven oxygen evolution and Zn(II) reduction store electrons in the Zn/Zn(II) medium. The carbon fixation releases the stored electrons and leads to an unassisted electrochemical reduction of CO<sub>2</sub>. The energy diagram of each reaction part is shown in Figure 7a.<sup>113</sup> This redox-medium-assisted system enables a solar-to-CO conversion efficiency of 15.6% under 1 Sun illumination. In addition, in a very recent study, solar-driven CO<sub>2</sub> reduction to CO with 19% solar-to-CO efficiency under 1 Sun illumination in a gas diffusion electrode (GDE) flow cell has been reported.<sup>114</sup> The use of a reverse assembled GDE (Figure 7b) prevented transition from a wetted to a flooded catalyst bed and allowed the device to operate stably for >150 h with no loss in efficiency. The FE<sub>CO</sub> and SFE over a 20 h duration are shown in Figure 7c.

As also highlighted by one of the Reviewers, the relative surface areas of PV and EC components are often significantly different, but this is often not clearly explained in the papers. In a practical device, the PV cells with a much larger area will be required compared to the area of the EC component, because of the relatively low energy density of solar irradiation. Importantly, an EC component can be cost-effective when it is smaller and runs at higher current densities (such as those with GDE cells). This mismatch, however, can bring confusion to the readers if the reported values are not concise. There have been some bad practices in reporting current density and SFE in the PV+EC systems. PV cells with a much larger area were integrated with electrodes with a smaller area, while the current density was improperly normalized with the area of the

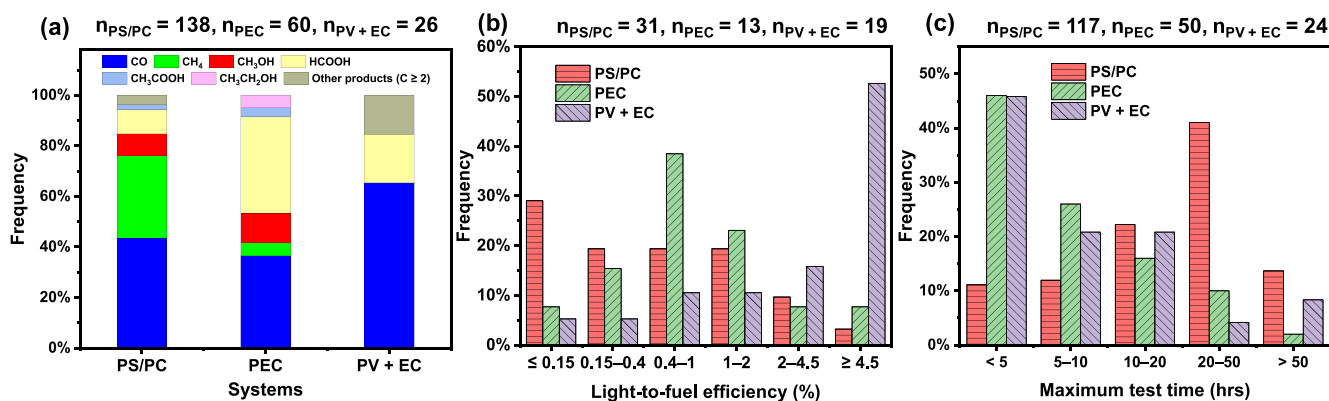


Figure 9. Comparisons of (a) product distribution, (b) light-to-fuel conversion efficiency, and (c) longest measurements in PS/PC, PEC, and PV+EC systems.

electrodes, resulting in misleadingly large current densities or SFEs. On the other hand, it is also possible to use electrodes with an area larger than that of the PV cells, especially when using expensive PV cells and relatively cheap electrode materials. In these cases, the overpotential can be very small, because of operating at low current density. Finally, in some cases the SFE was obtained under irradiance significantly lower than 1 Sun, resulting in higher SFE values, which is unlikely to scale with the light intensity.

The above highlighted studies all reported CO as the main product with high SFEs. As for the statistics, 26 cases were collected, in which 19 cases demonstrated clear SFEs (Figure 8). For the product distribution, CO is the most common product, accounting for 65.4% alone. It is followed by HCOOH with 19.2%. Most of the studies reported SFE greater than 5%, accounting for 42.1%. Only 21.1% of the cases reported SFE less than 1%. For those reporting SFEs greater than 10%, all the main products are CO, which are highlighted in the above discussion. The statistical data is shown in Table S3.

*Comparisons of the Key Performance Metrics between PS/PC, PEC, and PV+EC Approaches for Solar-Driven CO<sub>2</sub> Conversion.* We have not found any literature precedence that compared the performance metrics among different approaches for solar-driven CO<sub>2</sub> reduction. These subdisciplines, however, cannot be considered as isolated fields, and their comparison is of great importance to analyze intrinsic differences and similarities. As demonstrated in the above sections, there are different performance metrics for PS/PC, PEC, and PV+EC systems, among which, product distribution, light-to-fuel conversion efficiency, and maximum test time were selected as the indicators of selectivity, activity, and durability, respectively.

Inclusion and exclusion criteria:

- (i) Product Distribution. The inclusion criterion follows that of the above statistical studies: only the major products (selectivity > 30%) of a given study were counted.
- (ii) Light-to-fuel Efficiency. In principle, the cases included in the product distribution analysis were included here except those that did not provide clear light-to-fuel conversion efficiency data. In many PS/PC studies, measurements were performed under monochromatic illumination making the efficiency metrics higher than that measured under simulated sunlight or full-arc

illumination. These issues, however, had only a negligible effect on the comparison, as shown in the following discussion. Those studies using sacrificial agents in the performance evaluation were excluded in the comparison of light-to-fuel efficiency, to ensure that water oxidation is the other half reaction. For PEC studies, only studies without external bias were taken into account in the light-to-fuel conversion efficiency comparison. For PV+EC studies, SFE (or light-to-fuel efficiency in some cases) data were already obtained in the above sections.

- (iii) Maximum Reported Test Time. All cases were included here except those that did not provide clear maximum test time data.

The comparison of product distribution is shown in Figure 9a. Overall, the products of PS/PC and PEC studies are more broadly distributed than those in PV+EC studies with a distinctly higher frequency of CO. The reason for this is that most of the PV+EC studies are proof of concept focusing on device fabrication or system validation, using commercial electrocatalysts, such as Ag<sup>115</sup> and Au<sup>116</sup> on which selective CO<sub>2</sub> reduction to CO has been widely reported. The gas products (mainly CO and CH<sub>4</sub>) together account for nearly 80% in PS/PC studies, while they account for only about 40% in PEC studies, which might be associated with the factor that in PS/PC systems, both reduction and oxidation happen on the same particle, while in PEC systems they are spatially separated. The unfavored generation of liquid products in the PS/PC system may be plausibly further consumed by the photogenerated holes involving oxidation reaction conducted at the same particle surface. In addition, the frequency of HCOOH in PS/PC studies is lower than those of PEC and PV+EC plausibly because HCOOH, as one of the thermodynamically prior products, might be oxidized by the photogenerated holes or derived oxidizing intermediates, whereas this process is avoided to a great extent in PEC and PV+EC systems.

The activities of the three approaches are compared by light-to-fuel efficiencies, as shown in Figure 9b. The differences are striking! Most of the light-to-fuel efficiencies in PS studies (PC were not included in this analysis) are located in low-value ranges, with 29.0% located between 0 and 0.15% and 19.4% located between 0.15 to 0.4%, accounting for 48.4% together. For the PEC studies, the majority is less than 2%, accounting for 61.6%. While for that of PV+EC, the light-to-fuel efficiencies are more concentrated in the high-value range

( $\geq 4.5\%$ ). There is an obvious trend that PS studies frequently reported relatively lower light-to-fuel efficiencies while those of PEC are somewhat higher, and those of PV+EC are further improved.

For the comparison of durability (shown in Figure 9c), most of the PEC and PV+EC studies reported the longest measurement with the maximum test time less than 10 h, accounting for more than 50%. Although fewer cases reported more than 50 h of durability, some of those still have good stability. Moreover, we found that PS/PC studies reported a higher frequency of more than 20 h durability. Generally, the instability in PS/PC systems is caused by photocorrosion resulting from the reduction/oxidation of the photoactive material by photogenerated electrons and holes. For that of PEC systems, not only photocorrosion but also electrocorrosion and electrolyte degradation are considerable challenges for long-term durability. The lack of many long-duration PV+EC studies is somewhat surprising, because PV cells have a very long lifetime, while over 100–1000 h stability was also demonstrated for EC systems. We speculate that more work has to be done on the integration to realize achievable durability for the combined system.

For the sake of simplicity, we compare the most important descriptors behind these trends in Table 6. As seen, the reasons are complex and convoluted; therefore, at this point, we discuss only one overarching aspect of all these areas, namely, the timescale of the different elementary processes. In Figure 10, we present the typical timescale of photoinduced processes occurring in semiconductors and at semiconductor interfaces. Most importantly, the timescale of the chemical reactions (especially the  $\text{CO}_2$  reduction reactions involving multi-electron and multiproton transfer) is in the microsecond-to-second regime. This means that a substantially long (photo)-electron lifetime is necessary for this process. Unfortunately, charge carrier recombination occurs at a much faster timescale (depending on the mechanism from subpicosecond to microsecond). This mismatch already indicates that high light-to-fuel conversion efficiencies cannot be realistically expected from PS and PEC systems, unless cocatalysts can be found, which can properly “store” electrons. There is precedence in the literature, where complex PS/PC assemblies allowed charge carrier lifetime on the order of microseconds.<sup>117</sup> This lifetime enabled different redox reactions, although not those involving the transfer of multiple electrons and protons. Specifically, in a recent study on  $\text{CsPbBr}_3$  perovskite, nanocubes facilitated photodriven C–C coupling, where both charge carriers were rapidly ( $\sim 50$  ps) extracted from the photoexcited perovskite NCs to reactant molecules. The separated charge carriers lived for more than  $0.8 \mu\text{s}$ , enabling a radical mechanism to form the C–C bonds.<sup>118</sup> At the same time, corrosion processes are also induced in the semiconductors via charge carrier trapping, posing a great threat for PS and PEC methods.<sup>119</sup> Such corrosive processes inside the semiconductors are typically faster than the  $\text{CO}_2$  reduction reaction, where charge transfer is required from the electrode surface to the substrate. This is not the case for the PV+EC method, where charge carriers are rapidly extracted from the PV cell (on the nanosecond–picosecond) timescale.

Finally, we also found that often different products formed via the different approaches even with similar catalysts. Taking  $\text{Cu}_x\text{O}$ -based catalysts as an example, several studies are listed in Table 7. There is a variety of products including  $\text{CO}$ ,  $\text{CH}_4$ ,  $\text{C}_2\text{H}_4$ ,  $\text{C}_2\text{H}_6$ ,  $\text{HCOOH}$ ,  $\text{CH}_3\text{COOH}$ , and  $\text{CH}_3\text{OH}$ . In PS and

**Table 6. Summary of the Differences among PS/PC, PEC, and PV+EC Systems from Six Aspects**

	PS/PC systems	PEC systems	PV+EC systems
Light absorption	One or more light absorbers are needed (see tandem and z-scheme configurations).	Either one (photocathode or photoanode) or two photoactive electrodes. The individual photoelectrodes can also be multicomponent.	Tailored photovoltaic cells can be designed (from single- to multijunction cells), to provide the necessary cell voltage.
Charge carrier collection	No need for carrier collection, but photogenerated holes and electrons need to reach the respective surface sites.	Charge carrier trapping at defect sites at the electrode/electrolyte interface hinders charge carrier collection.	Rapid charge carrier collection is achieved in the PV cell.
Charge transfer (reaction)	Both reactions proceed on the same particles. Preferably different sites for the two half reactions. Back reactions are possible. The rates of the two half reactions have to match.	Slow charge carrier transfer to the substrate or mediator from the electrode surface, compared to the timescale of charge carrier recombination.	A separate electrochemical interface is responsible for the chemical reaction. Well-known stable and active electrocatalysts can be employed.
Nano aspects	A high surface area is necessary to provide enough active sites for the reaction. High probability of surface recombination.	A high surface area is necessary to provide enough active sites for the reaction. High probability of surface recombination.	Nanostructured electrocatalysts can be used, without the detrimental surface recombination in the light absorber.
Stability	Intermediate stability, because of the presence of the solid/liquid interface.	Very difficult to achieve reasonable stability, because of the presence of current flow and the electrode/electrolyte interface. Different protective coatings seem to ensure certain improvements.	The stability is dictated only by the stability of the electrolyzer, as PV panels are stable for ages. Examples on the order of hundreds of hours are available.
Cost	Cheap experimental setup or device, but expensive multifunctional catalyst materials are needed.	More expensive and sophisticated cell designs are necessary, especially in the case of continuous flow processes. If a cocatalyst is employed, large amounts are needed because of the identical surface area of the light absorber and the electrochemical interface.	Relatively expensive system cost. Much smaller electrochemically active area is needed (compared to the size of the PV) and thus less electrocatalysts, membranes, etc. have to be used. It is also possible to select high-performance PV cells with a smaller area (under concentrated light) and electrodes with a larger area.

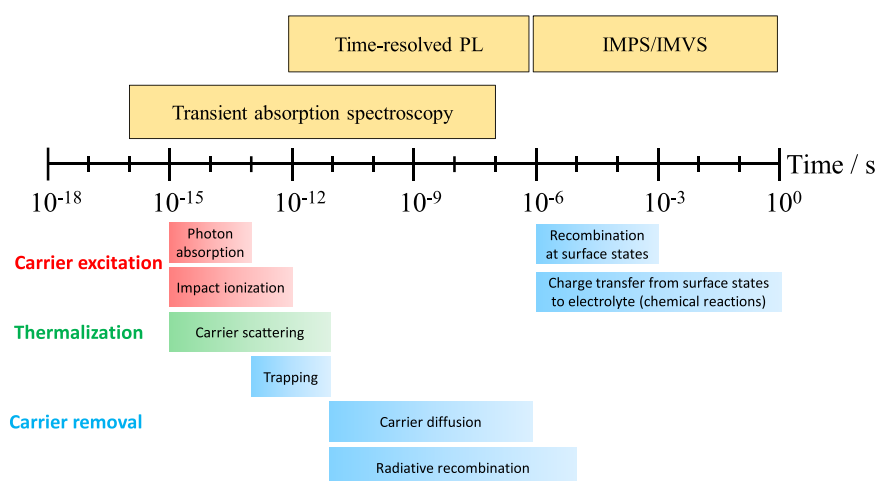


Figure 10. Typical timescale of different photoinduced processes in semiconductors, together with the methods that are employed to monitor them. PL, photoluminescence; IMPS/IMVS, intensity-modulated photocurrent/photovoltage spectroscopy.

Table 7. Representative Studies on Solar-Driven CO<sub>2</sub> Conversion Using Cu<sub>x</sub>O-Based Catalysts

system	catalyst	main product(s)	formation rate (mmol e <sup>-</sup> g <sub>cat</sub> <sup>-1</sup> h <sup>-1</sup> )	FE (%)	SFE (%)	ref
PS	carbon quantum dots/Cu <sub>2</sub> O	CH <sub>3</sub> OH	0.336			121
PEC	Cu <sub>2</sub> O–Cu	HCOOH		14		122
		CH <sub>3</sub> COOH		76		123
		CH <sub>4</sub>		47		124
PV+EC	Cu/Cu <sub>2</sub> O	CH <sub>3</sub> OH		53.6		125
	CuO	C <sub>2</sub> H <sub>4</sub>		34		126
		C <sub>2</sub> H <sub>6</sub>		6.5		126
	Cu <sub>x</sub> O wire arrays	CO			2.5	126
		HCOOH			0.25	

Table 8. Representative Studies on Solar-Driven CO<sub>2</sub> Conversion Using Au-Based Catalysts

system	catalyst	main product(s)	selectivity (%)	FE (%)	SFE (%)	ref
PS (Plasmonic catalysis)	Au	C <sub>1</sub> –C <sub>3</sub> hydrocarbons	50% (C <sub>2+</sub> hydrocarbons)			127
PEC	Cathode	Au/Si	CO	91		60
		Au/B doped g-C <sub>3</sub> N <sub>4</sub>	CH <sub>3</sub> CH <sub>2</sub> OH	47		128
		Au	CO	~92	15.6	113

PEC systems, the conduction band energy of the photocathode defines the energy of the photoelectrons, while in the PV+EC systems, it is dictated by the electrode potential. This important difference also means that while in electrocatalysis the reaction rate (i.e., current density) and the reducing power of the electrons (i.e., the electrode potential) are inherently coupled (see the Butler–Volmer equation), this is not the case for PEC.<sup>120</sup> This simple fact can be a major contributor to the observed differences in the product distributions and a major opportunity for PEC-based methods in the future.

The same catalyst may play different roles in different scenarios. Taking Au-based catalysts as an example, three studies are shown in Table 8. In a PS study, Au nanoparticles (NPs) were used as a catalyst for the conversion of CO<sub>2</sub> and H<sub>2</sub>O into C<sub>1</sub>–C<sub>3</sub> hydrocarbons under visible light irradiation.<sup>127</sup> The Au NPs possess a strong localized surface plasmon resonance (LSPR) band centered around 520 nm, which enables the generation of energetic electron–hole carriers under green light for the reduction of CO<sub>2</sub> and oxidation of H<sub>2</sub>O, resulting in the main products of hydrocarbons. In two PEC studies, Au cocatalyst can lead to

main products CO and CH<sub>3</sub>CH<sub>2</sub>OH in different studies.<sup>60,128</sup> In such cases, beyond facilitating charge transfer, the cocatalyst also affects the energetics of the electrode/electrolyte interface. In the highlighted PV+EC study, the main product is CO, where Au acted as an electrocatalyst.<sup>113</sup>

At this stage only the PV+EC approach shows a performance (especially in terms of activity and durability) that can lead to industrial technologies in the near future.

*Summary.* Over the past years, the fundamental understanding of the solar-driven CO<sub>2</sub> conversion reaction has improved substantially,<sup>129–136</sup> and deactivation mechanisms have also been studied.<sup>137,138</sup> Integration and validation of reactors and systems are also ongoing.<sup>111,114,125,139–146</sup> With this Focus Review, our aim was to provide an overview of the state-of-the-art solar-driven CO<sub>2</sub> conversion approaches. We



have presented for the first time a statistical analysis of activity, selectivity, and durability of PS/PC, PEC, and PV+EC systems. The results indicate that (i) only the minority of studies present all those metrics, which fully describe the performance of a given system; (ii) the CO<sub>2</sub> reduction products and their distribution are different in the different scenarios, and (iii) at this stage only the PV+EC approach shows a performance (especially in terms of activity and durability), which can lead to industrial technologies in the near future (see Figure 9 and Table 6).

Based on the statistical analysis, several questions and problems were raised:

- (i) **Unbalanced research efforts.** More than 80% of the studies focused on PS/PC CO<sub>2</sub> conversion, most of which discussed catalyst synthesis and the corresponding laboratory performance evaluation. Very recently, critical comments were made on the doping of graphene with a plethora of elements for enhanced electrocatalytic effect.<sup>147</sup> We see a very similar trend in solar-driven PS/PC CO<sub>2</sub> conversion, namely that hundreds of “doped photocatalysts” are being tested with little outcome.
- (ii) **Avoid the pitfalls.** As discussed in the introduction of PC systems, many studies employ sacrificial electron donors, without evaluating the fate of these agents. It is strongly required to carry out a complete study on the overall solar-driven reactions, not only the CO<sub>2</sub> reduction half of it. Another critical issue is to confirm that CO<sub>2</sub> is the actual source of the carbon-containing products. Isotopic <sup>13</sup>CO<sub>2</sub> labeling is an efficient technique for this purpose. Quantitative detection of the evolved oxygen can also help quantifying the performance. Moreover, a control test without CO<sub>2</sub> but in the presence of H<sub>2</sub>O would be a cost-effective, yet preliminary approach to confirm/exclude participation of carbon residues (on active sites) in CO<sub>2</sub> reduction.
- (iii) **Lack of complete data set.** Only a minority of the studies contain metrics which fully describe the performance of a given system. While it is encouraging to see many studies being carried out in this area, telling the whole story is essential. This not only demonstrates the reliability of the work but also ensures reproducibility. Finally, reporting the appropriate metrics helps to make clear comparisons with other studies, shows the research status we have reached, and reminds how far we are from industrial applications.

By taking a careful look at the metrics presented above (especially concerning SFE values), we have to conclude that only the PV+EC systems have the potential to become an industrial technology in the near and midterm future.<sup>148</sup> Several trends support this notion, most importantly: (i) The rapid improvements of PCE and a decrease in the cost of PV cells. In fact, the price of solar electricity has decreased to a level that in over 20 countries translates to grid parity. (ii) The continuous progress in developing practical CO<sub>2</sub> electrolyzers.<sup>149</sup> Particularly, there are emerging trends in the employment of gas diffusion electrodes (GDEs), aiming to eliminate limitations arising from slow mass transport and small turnover number at the active sites.<sup>150,151</sup> The use of GDEs enabled the achievement of operational parameters of great industrial significance; unfortunately, not yet all of them

are for the same system. These are (i) current densities higher than 300 mA cm<sup>-2</sup>, (ii) cell voltages in the 2.5–3.0 V range (translating to energy efficiencies higher than 50%), (iii) close to 100% FE for CO and HCOOH, and (iv) over 5000 h durability.

**Future Directions.** **Selectivity** is the metric which seems to be the most addressable if we better understand the nature of active sites.<sup>152–158</sup> Atomic-level understanding of the active sites and transformation mechanisms under realistic working conditions is a prerequisite for the rational design of photoactive materials with high selectivity. For example, the (110) facet of a single-crystal Cu<sub>2</sub>O particle is active for photodriven CO<sub>2</sub> reduction to methanol while the (100) facet is inert. The oxidation state of the active sites changes from Cu(I) toward Cu(II) because of CO<sub>2</sub> and H<sub>2</sub>O coadsorption and changes back to Cu(I) after CO<sub>2</sub> conversion under visible light illumination.<sup>156</sup>

**Hybrid photoelectrode assemblies** offer a platform to rationally design materials for solar-driven CO<sub>2</sub> conversion. We need to consider the following processes. (i) Light absorption: it is essential to harness a reasonable portion of the solar spectrum. (ii) Charge transport: the semiconductor shall have high charge carrier mobility. The amount of bulk and surface traps shall also be minimized. (iii) Charge transfer kinetics: facile charge transfer from the semiconductor to either the CO<sub>2</sub> molecules in the solution, or to a mediator (either immobilized or in the solution), is required. (iv) Stability and robustness are definitely major concerns, where chemical, electrochemical, and photocorrosion all have to be considered. Considering these very complex requirements, which have to be met by a photoelectrode, it is not too surprising that no single material could meet all of these so far. In biological systems, one can find complex architectures with components that have precisely defined functionality and complementarity. As a bioinspired approach, some of the limitations of the individual components can be overcome by the rational design and assembly of hybrid PS/PC and PEC materials, where the different functionalities are decoupled. For example, CsPbBr<sub>3</sub>@zeolitic imidazolate framework nanocomposites have been reported to exhibit enhanced CO<sub>2</sub> reduction activity due to the addition of zeolitic imidazolate framework with its original CO<sub>2</sub> capturing ability and the role of acting as a cocatalyst.<sup>159</sup> In addition, it was demonstrated by the example of Cu<sub>2</sub>O that when a highly conductive scaffold is introduced into the photoelectrode, the charge carrier transport can be enhanced, and larger photocurrents can be harvested.<sup>160,161</sup> Similar trends have also been discovered in organic photoelectrodes.<sup>162</sup> This strategy greatly broadened the range of the catalyst and light absorber selection by reasonably combining the attractive features of each component.

**Nanoscale aspects** are important to enhance the current density to a level that makes practical significance. The field of nanostructured photoelectrodes is surprisingly an unexplored area. While the PS/PC<sup>163</sup> and the EC communities have built solid and coherent knowledge on the effect of catalyst size at the nanoscale, there is no systematic study on this matter for PEC processes. In fact, the long-standing theory of PEC builds on thick electrode films (with film thickness of over several micrometers).<sup>164</sup> Systematic study of nanoscale effects in PEC would be indeed important, because they affect all the important processes, such as light absorption, charge carrier transport, band bending, and charge transfer. Similar considerations are also valid for the effect of morphology.

Despite some very informative studies on Si micro-<sup>165,166</sup> and nanowires,<sup>167</sup> there is a lack of knowledge whether there is an ideal morphology for PEC applications. In addition, the consequence of drastically increased surface/bulk ratio (which is the case for nanomaterials) on the contribution of surface functional groups to the materials' property has remained unknown.

**Plasmonic catalysis** has become an emerging avenue in CO<sub>2</sub> conversion by the promise of these particles to harness visible light as hot carriers and their intrinsic catalytic activity toward CO<sub>2</sub> reduction. Noble metal NPs, in particular, allow the integration of strong visible-wavelength plasmonic excitation with surface activation of CO<sub>2</sub> and therefore represent a novel and promising class of photocatalysts for CO<sub>2</sub> reduction.<sup>8</sup> The fundamental understanding of plasmon-assisted CO<sub>2</sub> reduction processes, however, is still lacking. In plasmonic CO<sub>2</sub> reduction reaction, catalytic activity, reaction pathways, and selectivity are expected to not only depend on the properties of the metal and metal/adsorbate interactions but also possibly be tuned by light excitation.<sup>168–170</sup>

**Buried junction** is another promising approach, because if properly designed, it can integrate the benefits of PV and EC technologies.<sup>71</sup> In practice, the employment of buried junction in integrated PEC cells can overcome the instability issue. The PV components in the buried junction can act as more efficient and stable light absorbers than most of the single semiconductors when physical contact with the aqueous environment is avoided.<sup>172</sup> This strategy might provide a new direction toward the enhanced durability of PEC systems.

**Concentrated sunlight** can enable high current density operation for both the PEC and PV+EC approaches. In these cases, the solar power input can be concentrated up to 500 Suns, which in combination with proper PV cells or photoelectrodes can allow current densities similar to those in industrial electrolyzers. For water splitting, 0.88 A cm<sup>-2</sup> current density was demonstrated with an STH efficiency of over 15%, under concentrated solar irradiation (up to 474 kW m<sup>-2</sup>).<sup>173</sup> Similar integration of photoanodes or PV cells can be envisioned with CO<sub>2</sub> reduction GDEs on the cathode side. Such studies are in progress in our laboratory and will be communicated soon.

**Value-added anode processes** are also worth more consideration. Most CO<sub>2</sub> reduction approaches couple cathodic CO<sub>2</sub> reduction with the anodic oxygen evolution reaction (OER), resulting in approximately 90% of the electricity input being consumed by the OER in the EC scenario.<sup>174</sup> This issue can be addressed by coupling other anodic oxidation reactions with less electricity needs and probably higher-value products. For example, oxidation of glycerol (a byproduct of biodiesel and soap production) can lower electricity consumption up to 53%, thus reducing the operating costs and carbon footprint. In addition, value-added products can be produced, including glyceraldehyde and lactic acid.<sup>174</sup> This strategy might also offer opportunities to the PC and PEC approaches as well, because there will be no need to cope with the difficult OER, and in fact, thermodynamically downhill processes can be designed.

**PV+EC systems** can be further improved through component development, because to date, the focus was mostly on catalysts. A recent study has demonstrated that the largest voltage losses may occur at the membrane or the membrane electrode assembly rather than at the catalyst layers in their flow cell.<sup>175</sup> As another example, we note that a solid

electrolyte may be a better alternative, because the formed liquid products are in a mixture with the dissolved salts in liquid electrolytes, requiring energy-intensive downstream separation. However, in the solid electrolyte, the generated cations (such as H<sup>+</sup>) and anions (such as HCOO<sup>-</sup>) are combined to form pure product solutions without mixing with other ions.<sup>154</sup> In addition, the development of reactors for EC CO<sub>2</sub> utilization is also required, to optimize such characteristics as geometrical configuration, construction material, heat exchange, and mixing and flow characteristics.<sup>18,176</sup>

## ■ ASSOCIATED CONTENT

### Supporting Information

The Supporting Information is available free of charge at <https://pubs.acs.org/doi/10.1021/acsenerylett.0c00645>.

Statistical data of PS, PEC, and PV+EC systems (PDF)

## ■ AUTHOR INFORMATION

### Corresponding Author

**Csaba Janáky** – Department of Physical Chemistry and Materials Science, Interdisciplinary Excellence Centre, University of Szeged, Szeged H-6720, Hungary; [orcid.org/0000-0001-5965-5173](https://orcid.org/0000-0001-5965-5173); Phone: +36-62-546-393; Email: [janaky@chem.u-szeged.hu](mailto:janaky@chem.u-szeged.hu)

### Author

**Jie He** – Department of Physical Chemistry and Materials Science, Interdisciplinary Excellence Centre, University of Szeged, Szeged H-6720, Hungary

Complete contact information is available at:

<https://pubs.acs.org/doi/10.1021/acsenerylett.0c00645>

### Notes

The authors declare no competing financial interest.

### Biographies

**Dr. Jie He** is a postdoctoral research fellow at the University of Szeged, Hungary. He obtained his Ph.D. from Hunan University, China in 2018. His research interest includes integration and validation of continuous flow photoelectrochemical CO<sub>2</sub> conversion cell and development of novel photoactive materials for water splitting. <https://orcid.org/0000-0001-5481-6986>

**Prof. Csaba Janáky** is an associate professor and Principal Investigator of the Photoelectrochemistry Research Group at the University of Szeged, Hungary. His research group focuses on converting CO<sub>2</sub> to useful chemicals, utilizing solar energy. His ERC supported activity spans through the materials aspects of photoelectrochemistry to electrochemical cell development. <https://orcid.org/0000-0001-5965-5173>

## ■ ACKNOWLEDGMENTS

This project has received funding from the European Research Council (ERC) under the European Union's Horizon 2020 research and innovation programme (Grant Agreement Nos. 716539 and 899747). This research was partially supported by the "Széchenyi 2020" program in the framework of GINOP-2.3.2-15-2016-00013 "Intelligent materials based on functional surfaces—from syntheses to applications" project. The authors thank Dr. Biborka Janáky-Bohner for her help with manuscript preparation and Prof. Krishnan Rajeshwar (UT Arlington, United States and Prof. Balázs Endrődi (University of Szeged,

Hungary) for their comments on an earlier version of the manuscript.

## REFERENCES

- Jacobson, T. A.; Kler, J. S.; Hernke, M. T.; Braun, R. K.; Meyer, K. C.; Funk, W. E. Direct Human Health Risks of Increased Atmospheric Carbon Dioxide. *Nat. Sustain.* **2019**, *2* (8), 691–701.
- ESRL Global Monitoring Division - Global Greenhouse Gas Reference Network. <https://www.esrl.noaa.gov/gmd/ccgg/trends/global.html> (accessed 2020-03-19).
- Rogelj, J.; Den Elzen, M.; Höhne, N.; Fransen, T.; Fekete, H.; Winkler, H.; Schaeffer, R.; Sha, F.; Riahi, K.; Meinshausen, M. Paris Agreement Climate Proposals Need a Boost to Keep Warming Well below 2°C. *Nature* **2016**, *534* (7609), 631–639.
- De Luna, P.; Hahn, C.; Higgins, D.; Jaffer, S. A.; Jaramillo, T. F.; Sargent, E. H. What Would It Take for Renewably Powered Electrosynthesis to Displace Petrochemical Processes? *Science* **2019**, *364* (6438), 3506.
- Nørskov, J. K.; Weckhuysen, B.; Centi, G.; et al. *Research Needs towards Sustainable Production of Fuels and Chemicals*; Energy X, 2019 September. Downloaded from: [https://www.energy-x.eu/wp-content/uploads/2019/09/Energy\\_X\\_Research-needs-report.pdf](https://www.energy-x.eu/wp-content/uploads/2019/09/Energy_X_Research-needs-report.pdf).
- Villadsen, S. N. B.; Fosbøl, P. L.; Angelidaki, I.; Woodley, J. M.; Nielsen, L. P.; Møller, P. The Potential of Biogas; the Solution to Energy Storage. *ChemSusChem* **2019**, *12* (10), 2147–2153.
- Ran, J.; Jaroniec, M.; Qiao, S. Z. Cocatalysts in Semiconductor-Based Photocatalytic CO<sub>2</sub> Reduction: Achievements, Challenges, and Opportunities. *Adv. Mater.* **2018**, *30* (7), 1704649.
- Yu, S.; Wilson, A. J.; Kumari, G.; Zhang, X.; Jain, P. K. Opportunities and Challenges of Solar-Energy-Driven Carbon Dioxide to Fuel Conversion with Plasmonic Catalysts. *ACS Energy Lett.* **2017**, *2* (9), 2058–2070.
- Zhou, X.; Liu, R.; Sun, K.; Chen, Y.; Verlage, E.; Francis, S. A.; Lewis, N. S.; Xiang, C. Solar-Driven Reduction of 1 Atm of CO<sub>2</sub> to Formate at 10% Energy-Conversion Efficiency by Use of a TiO<sub>2</sub>-Protected III-V Tandem Photoanode in Conjunction with a Bipolar Membrane and a Pd/C Cathode. *ACS Energy Lett.* **2016**, *1* (4), 764–770.
- Grim, R. G.; Huang, Z.; Guarnieri, M. T.; Ferrell, J. R.; Tao, L.; Schaidle, J. A. Transforming the Carbon Economy: Challenges and Opportunities in the Convergence of Low-Cost Electricity and Reductive CO<sub>2</sub> Utilization. *Energy Environ. Sci.* **2020**, *13* (2), 472–494.
- Halmann, M. Photoelectrochemical Reduction of Aqueous Carbon Dioxide on P-Type Gallium Phosphide in Liquid Junction Solar Cells. *Nature* **1978**, *275*, 115–116.
- Kim, W.; McClure, B. A.; Edri, E.; Frei, H. Coupling Carbon Dioxide Reduction with Water Oxidation in Nanoscale Photocatalytic Assemblies. *Chem. Soc. Rev.* **2016**, *45* (11), 3221–3243.
- White, J. L.; Baruch, M. F.; Pander, J. E.; Hu, Y.; Fortmeyer, I. C.; Park, J. E.; Zhang, T.; Liao, K.; Gu, J.; Yan, Y.; Shaw, T. W.; Abelev, E.; Bocarsly, A. B. Light-Driven Heterogeneous Reduction of Carbon Dioxide: Photocatalysts and Photoelectrodes. *Chem. Rev.* **2015**, *115* (23), 12888–12935.
- Tu, W.; Zhou, Y.; Zou, Z. Photocatalytic Conversion of CO<sub>2</sub> into Renewable Hydrocarbon Fuels: State-of-the-Art Accomplishment, Challenges, and Prospects. *Adv. Mater.* **2014**, *26* (27), 4607–4626.
- Ulmer, U.; Dingle, T.; Duchesne, P. N.; Morris, R. H.; Tavasoli, A.; Wood, T.; Ozin, G. A. Fundamentals and Applications of Photocatalytic CO<sub>2</sub> Methanation. *Nat. Commun.* **2019**, *10* (1), 3169.
- Li, C.; Tong, X.; Yu, P.; Du, W.; Wu, J.; Rao, H.; Wang, Z. M. Carbon Dioxide Photo/Electroreduction with Cobalt. *J. Mater. Chem. A* **2019**, *7* (28), 16622–16642.
- Wang, C.; Sun, Z.; Zheng, Y.; Hu, Y. H. Recent Progress in Visible Light Photocatalytic Conversion of Carbon Dioxide. *J. Mater. Chem. A* **2019**, *7* (3), 865–887.
- Khan, A. A.; Tahir, M. Recent Advancements in Engineering Approach towards Design of Photo-Reactors for Selective Photo-catalytic CO<sub>2</sub> Reduction to Renewable Fuels. *J. CO<sub>2</sub> Util.* **2019**, *29*, 205–239.
- Chang, X.; Wang, T.; Gong, J. CO<sub>2</sub> Photo-Reduction: Insights into CO<sub>2</sub> Activation and Reaction on Surfaces of Photocatalysts. *Energy Environ. Sci.* **2016**, *9* (7), 2177–2196.
- Liu, X.; Inagaki, S.; Gong, J. Heterogeneous Molecular Systems for Photocatalytic CO<sub>2</sub> Reduction with Water Oxidation. *Angew. Chem., Int. Ed.* **2016**, *55* (48), 14924–14950.
- Xiong, J.; Song, P.; Di, J.; Li, H. Ultrathin Structured Photocatalysts: A Versatile Platform for CO<sub>2</sub> Reduction. *Appl. Catal., B* **2019**, *256*, 117788.
- Ye, L.; Deng, Y.; Wang, L.; Xie, H.; Su, F. Bismuth-Based Photocatalysts for Solar Photocatalytic Carbon Dioxide Conversion. *ChemSusChem* **2019**, *12* (16), 3671–3701.
- Xia, T.; Long, R.; Gao, C.; Xiong, Y. Design of Atomically Dispersed Catalytic Sites for Photocatalytic CO<sub>2</sub> Reduction. *Nanoscale* **2019**, *11* (23), 11064–11070.
- Wu, H. L.; Li, X. B.; Tung, C. H.; Wu, L. Z. Semiconductor Quantum Dots: An Emerging Candidate for CO<sub>2</sub> Photoreduction. *Adv. Mater.* **2019**, *31* (36), 1900709.
- Marques Mota, F.; Kim, D. H. From CO<sub>2</sub> Methanation to Ambitious Long-Chain Hydrocarbons: Alternative Fuels Paving the Path to Sustainability. *Chem. Soc. Rev.* **2019**, *48* (1), 205–259.
- Yang, J.; Guo, Y.; Lu, W.; Jiang, R.; Wang, J. Emerging Applications of Plasmons in Driving CO<sub>2</sub> Reduction and N<sub>2</sub> Fixation. *Adv. Mater.* **2018**, *30* (48), 1802227.
- Sun, Z.; Talreja, N.; Tao, H.; Texter, J.; Muhler, M.; Strunk, J.; Chen, J. Catalysis of Carbon Dioxide Photoreduction on Nanosheets: Fundamentals and Challenges. *Angew. Chem., Int. Ed.* **2018**, *57* (26), 7610–7627.
- Stolarczyk, J. K.; Bhattacharyya, S.; Polavarapu, L.; Feldmann, J. Challenges and Prospects in Solar Water Splitting and CO<sub>2</sub> Reduction with Inorganic and Hybrid Nanostructures. *ACS Catal.* **2018**, *8* (4), 3602–3635.
- Wu, J.; Huang, Y.; Ye, W.; Li, Y. CO<sub>2</sub> Reduction: From the Electrochemical to Photochemical Approach. *Adv. Sci.* **2017**, *4* (11), 1700194.
- Li, K.; Peng, B.; Peng, T. Recent Advances in Heterogeneous Photocatalytic CO<sub>2</sub> Conversion to Solar Fuels. *ACS Catal.* **2016**, *6* (11), 7485–7527.
- Faber, C.; Allahverdiyeva, R.; Artero, V.; Baraton, L.; Barbieri, A.; Bercegol, H.; Fleischer, M.; Huynhthi, H.; Kargul, J.; Lepaumier, H.; Lopez, L.; Magnuson, A. *Solar Energy for a Circular Economy: Technological Roadmap*; SUNRISE, 2020. Downloaded from: [https://sunriseaction.com/wp-content/uploads/2020/02/Roadmap\\_February\\_2020.pdf](https://sunriseaction.com/wp-content/uploads/2020/02/Roadmap_February_2020.pdf).
- EuChemS Call for Proposals: Solar-driven chemistry 2019/2020. <https://www.euchems.eu/proposals-solar-driven-chemistry/> (accessed 2020-03-19).
- Yano, J.; Haber, J. A.; Gregoire, J. M.; Friebe, D.; Nilsson, A.; Houle, F. JCAP Research on Solar Fuel Production at Light Sources. *Synchrotron Radiat. News* **2014**, *27* (5), 14–17.
- Kuk, S. K.; Ham, Y.; Gopinath, K.; Boonmongkolras, P.; Lee, Y.; Lee, Y. W.; Kondaveeti, S.; Ahn, C.; Shin, B.; Lee, J. K.; Jeon, S.; Park, C. B. Continuous 3D Titanium Nitride Nanoshell Structure for Solar-Driven Unbiased Biocatalytic CO<sub>2</sub> Reduction. *Adv. Energy Mater.* **2019**, *9* (25), 1900029.
- Ye, J.; Yu, J.; Zhang, Y.; Chen, M.; Liu, X.; Zhou, S.; He, Z. Light-Driven Carbon Dioxide Reduction to Methane by Methanosarcina barkeri-CdS Biohybrid. *Appl. Catal., B* **2019**, *257*, 117916.
- Shen, Q.; Huang, X.; Liu, J.; Guo, C.; Zhao, G. Biomimetic Photoelectrocatalytic Conversion of Greenhouse Gas Carbon Dioxide: Two-Electron Reduction for Efficient Formate Production. *Appl. Catal., B* **2017**, *201*, 70–76.
- Amao, Y.; Kataoka, R. Methanol Production from CO<sub>2</sub> with the Hybrid System of Biocatalyst and Organo-Photocatalyst. *Catal. Today* **2018**, *307*, 243–247.
- Yadav, R. K.; Oh, G. H.; Park, N. J.; Kumar, A.; Kong, K. J.; Baeg, J. O. Highly Selective Solar-Driven Methanol from CO<sub>2</sub> by a

Photocatalyst/Biocatalyst Integrated System. *J. Am. Chem. Soc.* **2014**, *136* (48), 16728–16731.

(39) Yaashikaa, P. R.; Senthil Kumar, P.; Varjani, S. J.; Saravanan, A. A Review on Photochemical, Biochemical and Electrochemical Transformation of CO<sub>2</sub> into Value-Added Products. *J. CO<sub>2</sub> Util.* **2019**, *33*, 131–147.

(40) Yadav, R. K.; Baeg, J. O.; Kumar, A.; Kong, K. J.; Oh, G. H.; Park, N. J. Graphene-BODIPY as a Photocatalyst in the Photocatalytic-Biocatalytic Coupled System for Solar Fuel Production from CO<sub>2</sub>. *J. Mater. Chem. A* **2014**, *2* (14), 5068–5076.

(41) Wang, L.; Wang, Y.; Cheng, Y.; Liu, Z.; Guo, Q.; Ha, M. N.; Zhao, Z. Hydrogen-Treated Mesoporous WO<sub>3</sub> as a Reducing Agent of CO<sub>2</sub> to Fuels (CH<sub>4</sub> and CH<sub>3</sub>OH) with Enhanced Photothermal Catalytic Performance. *J. Mater. Chem. A* **2016**, *4* (14), 5314–5322.

(42) Meng, X.; Wang, T.; Liu, L.; Ouyang, S.; Li, P.; Hu, H.; Kako, T.; Iwai, H.; Tanaka, A.; Ye, J. Photothermal Conversion of CO<sub>2</sub> into CH<sub>4</sub> with H<sub>2</sub> over Group VIII Nanocatalysts: An Alternative Approach for Solar Fuel Production. *Angew. Chem., Int. Ed.* **2014**, *53* (43), 11478–11482.

(43) Jia, J.; O'Brien, P. G.; He, L.; Qiao, Q.; Fei, T.; Reyes, L. M.; Burrow, T. E.; Dong, Y.; Liao, K.; Varela, M.; Pennycook, S. J.; Hmadeh, M.; Helmy, A. S.; Kherani, N. P.; Perovic, D. D.; Ozin, G. A. Visible and Near-Infrared Photothermal Catalyzed Hydrogenation of Gaseous CO<sub>2</sub> over Nanostructured Pd@Nb<sub>2</sub>O<sub>5</sub>. *Adv. Sci.* **2016**, *3* (10), 1600189.

(44) Ha, M. N.; Lu, G.; Liu, Z.; Wang, L.; Zhao, Z. 3DOM-LaSrCoFeO<sub>6-δ</sub> as a Highly Active Catalyst for the Thermal and Photothermal Reduction of CO<sub>2</sub> with H<sub>2</sub>O to CH<sub>4</sub>. *J. Mater. Chem. A* **2016**, *4* (34), 13155–13165.

(45) Xu, M.; Hu, X.; Wang, S.; Yu, J.; Zhu, D.; Wang, J. Photothermal Effect Promoting CO<sub>2</sub> Conversion over Composite Photocatalyst with High Graphene Content. *J. Catal.* **2019**, *377*, 652–661.

(46) Ghossoub, M.; Xia, M.; Duchesne, P. N.; Segal, D.; Ozin, G. Principles of Photothermal Gas-Phase Heterogeneous CO<sub>2</sub> Catalysis. *Energy Environ. Sci.* **2019**, *12* (4), 1122–1142.

(47) Chen, G.; Gao, R.; Zhao, Y.; Li, Z.; Waterhouse, G. I. N.; Shi, R.; Zhao, J.; Zhang, M.; Shang, L.; Sheng, G.; Zhang, X.; Wen, X.; Wu, L.; Tung, C.; Zhang, T. Alumina-Supported CoFe Alloy Catalysts Derived from Layered-Double-Hydroxide Nanosheets for Efficient Photothermal CO<sub>2</sub> Hydrogenation to Hydrocarbons. *Adv. Mater.* **2018**, *30* (3), 1704663.

(48) O'Brien, P. G.; Ghuman, K. K.; Jelle, A. A.; Sandhel, A.; Wood, T. E.; Loh, J. Y. Y.; Jia, J.; Perovic, D.; Singh, C. V.; Kherani, N. P.; Mims, C. A.; Ozin, G. A. Enhanced Photothermal Reduction of Gaseous CO<sub>2</sub> over Silicon Photonic Crystal Supported Ruthenium at Ambient Temperature. *Energy Environ. Sci.* **2018**, *11* (12), 3443–3451.

(49) Wu, D.; Deng, K.; Hu, B.; Lu, Q.; Liu, G.; Hong, X. Plasmon-Assisted Photothermal Catalysis of Low-Pressure CO<sub>2</sub> Hydrogenation to Methanol over Pd/ZnO Catalyst. *ChemCatChem* **2019**, *11* (6), 1598–1601.

(50) Ren, J.; Ouyang, S.; Xu, H.; Meng, X.; Wang, T.; Wang, D.; Ye, J. Targeting Activation of CO<sub>2</sub> and H<sub>2</sub> over Ru-Loaded Ultrathin Layered Double Hydroxides to Achieve Efficient Photothermal CO<sub>2</sub> Methanation in Flow-Type System. *Adv. Energy Mater.* **2017**, *7* (5), 1601657.

(51) Guzman, M. S.; Rengasamy, K.; Binkley, M. M.; Jones, C.; Ranaivoarisoa, T. O.; Singh, R.; Fike, D. A.; Meacham, J. M.; Bose, A. Phototrophic Extracellular Electron Uptake Is Linked to Carbon Dioxide Fixation in the Bacterium *Rhodospseudomonas Palustris*. *Nat. Commun.* **2019**, *10* (1), 1355.

(52) Woo, H. M. Solar-to-Chemical and Solar-to-Fuel Production from CO<sub>2</sub> by Metabolically Engineered Microorganisms. *Curr. Opin. Biotechnol.* **2017**, *45*, 1–7.

(53) Liu, C.; Gallagher, J. J.; Sakimoto, K. K.; Nichols, E. M.; Chang, C. J.; Chang, M. C. Y.; Yang, P. Nanowire-Bacteria Hybrids for Unassisted Solar Carbon Dioxide Fixation to Value-Added Chemicals. *Nano Lett.* **2015**, *15* (5), 3634–3639.

(54) Osterloh, F. E. Photocatalysis versus Photosynthesis: A Sensitivity Analysis of Devices for Solar Energy Conversion and Chemical Transformations. *ACS Energy Lett.* **2017**, *2* (2), 445–453.

(55) Rajeshwar, K.; Thomas, A.; Janaky, C. Photocatalytic Activity of Inorganic Semiconductor Surfaces: Myths, Hype, and Reality. *J. Phys. Chem. Lett.* **2015**, *6* (1), 139–147.

(56) Xiao, M.; Wang, Z.; Luo, B.; Wang, S.; Wang, L. Enhancing Photocatalytic Activity of Tantalum Nitride by Rational Suppression of Bulk, Interface and Surface Charge Recombination. *Appl. Catal., B* **2019**, *246*, 195–201.

(57) Kamat, P. V.; Jin, S. Semiconductor Photocatalysis: “Tell Us the Complete Story! *ACS Energy Lett.* **2018**, *3* (3), 622–623.

(58) Kramm, U. I.; Marschall, R.; Rose, M. Pitfalls in Heterogeneous Thermal, Electro- and Photocatalysis. *ChemCatChem* **2019**, *11* (11), 2563–2574.

(59) Chang, X.; Wang, T.; Yang, P.; Zhang, G.; Gong, J. The Development of Cocatalysts for Photoelectrochemical CO<sub>2</sub> Reduction. *Adv. Mater.* **2019**, *31* (31), 1804710.

(60) Song, J. T.; Ryoo, H.; Cho, M.; Kim, J.; Kim, J. G.; Chung, S.-Y.; Oh, J. Nanoporous Au Thin Films on Si Photoelectrodes for Selective and Efficient Photoelectrochemical CO<sub>2</sub> Reduction. *Adv. Energy Mater.* **2017**, *7* (3), 1601103.

(61) Pastor, E.; Le Formal, F.; Mayer, M. T.; Tilley, S. D.; Francàs, L.; Mesa, C. A.; Grätzel, M.; Durrant, J. R. Spectroelectrochemical Analysis of the Mechanism of (Photo)Electrochemical Hydrogen Evolution at a Catalytic Interface. *Nat. Commun.* **2017**, *8* (1), 14280.

(62) Zhang, D.; Shi, J.; Zi, W.; Wang, P.; Liu, S. F. Recent Advances in Photoelectrochemical Applications of Silicon Materials for Solar-to-Chemicals Conversion. *ChemSusChem* **2017**, *10* (22), 4324–4341.

(63) Rongé, J.; Bosserez, T.; Martel, D.; Nervi, C.; Boarino, L.; Taulelle, F.; Decher, G.; Bordiga, S.; Martens, J. A. Monolithic Cells for Solar Fuels. *Chem. Soc. Rev.* **2014**, *43* (23), 7963–7981.

(64) Nayak, P. K.; Mahesh, S.; Snaith, H. J.; Cahen, D. Photovoltaic Solar Cell Technologies: Analysing the State of the Art. *Nat. Rev. Mater.* **2019**, *4* (4), 269–285.

(65) Green, M. A.; Dunlop, E. D.; Hohl-Ebinger, J.; Yoshita, M.; Kopidakis, N.; Ho-Baillie, A. W. Y. Solar Cell Efficiency Tables (Version 55). *Prog. Photovoltaics* **2020**, *28* (1), 3–15.

(66) Best Research-Cell Efficiency Chart | Photovoltaic Research. <https://www.nrel.gov/pv/cell-efficiency.html> (accessed 2020-03-19).

(67) Liu, Z.; Sofia, S. E.; Laine, H. S.; Woodhouse, M.; Wieghold, S.; Peters, I. M.; Buonassisi, T. Revisiting Thin Silicon for Photovoltaics: A Technoeconomic Perspective. *Energy Environ. Sci.* **2020**, *13* (1), 12–23.

(68) Endrődi, B.; Bencsik, G.; Darvas, F.; Jones, R.; Rajeshwar, K.; Janáky, C. Continuous-Flow Electroreduction of Carbon Dioxide. *Prog. Energy Combust. Sci.* **2017**, *62*, 133–154.

(69) Kumaravel, V.; Bartlett, J.; Pillai, S. C. Photoelectrochemical Conversion of Carbon Dioxide (CO<sub>2</sub>) into Fuels and Value-Added Products. *ACS Energy Lett.* **2020**, *5* (2), 486–519.

(70) Akhundi, A.; Habibi-Yangjeh, A.; Abitorabi, M.; Rahim Pouran, S. Review on Photocatalytic Conversion of Carbon Dioxide to Value-Added Compounds and Renewable Fuels by Graphitic Carbon Nitride-Based Photocatalysts. *Catal. Rev.: Sci. Eng.* **2019**, *61* (4), 595–628.

(71) Hiragond, C.; Ali, S.; Sorcar, S.; In, S.-I. In Hierarchical Nanostructured Photocatalysts for CO<sub>2</sub> Photoreduction. *Catalysts* **2019**, *9* (4), 370.

(72) Christoforidis, K. C.; Fornasiero, P. Photocatalysis for Hydrogen Production and CO<sub>2</sub> Reduction: The Case of Copper-Catalysts. *ChemCatChem* **2019**, *11* (1), 368–382.

(73) Tjandra, A. D.; Huang, J. Photocatalytic Carbon Dioxide Reduction by Photocatalyst Innovation. *Chin. Chem. Lett.* **2018**, *29* (6), 734–746.

(74) Ma, Y.; Wang, Z.; Xu, X.; Wang, J. Review on Porous Nanomaterials for Adsorption and Photocatalytic Conversion of CO<sub>2</sub>. *Chin. J. Catal.* **2017**, *38* (12), 1956–1969.

(75) Huang, Z.; Teramura, K.; Asakura, H.; Hosokawa, S.; Tanaka, T. Recent Progress in Photocatalytic Conversion of Carbon Dioxide

over Gallium Oxide and Its Nanocomposites. *Curr. Opin. Chem. Eng.* **2018**, *20*, 114–121.

(76) Sun, H.; Wang, S. Research Advances in the Synthesis of Nanocarbon-Based Photocatalysts and Their Applications for Photocatalytic Conversion of Carbon Dioxide to Hydrocarbon Fuels. *Energy Fuels* **2014**, *28* (1), 22–36.

(77) Low, J.; Cheng, B.; Yu, J.; Jaroniec, M. Carbon-Based Two-Dimensional Layered Materials for Photocatalytic CO<sub>2</sub> Reduction to Solar Fuels. *Energy Storage Mater.* **2016**, *3*, 24–35.

(78) Chen, X.; Jin, F. Photocatalytic Reduction of Carbon Dioxide by Titanium Oxide-Based Semiconductors to Produce Fuels. *Front. Energy* **2019**, *13* (2), 207–220.

(79) Abdullah, H.; Khan, M. M. R.; Ong, H. R.; Yaakob, Z. Modified TiO<sub>2</sub> Photocatalyst for CO<sub>2</sub> Photocatalytic Reduction: An Overview. *J. CO<sub>2</sub> Util.* **2017**, *22*, 15–32.

(80) Shehzad, N.; Tahir, M.; Johari, K.; Murugesan, T.; Hussain, M. A Critical Review on TiO<sub>2</sub> Based Photocatalytic CO<sub>2</sub> Reduction System: Strategies to Improve Efficiency. *J. CO<sub>2</sub> Util.* **2018**, *26*, 98–122.

(81) Xie, H.; Wang, J.; Ithisuphalap, K.; Wu, G.; Li, Q. Recent Advances in Cu-Based Nanocomposite Photocatalysts for CO<sub>2</sub> Conversion to Solar Fuels. *J. Energy Chem.* **2017**, *26* (6), 1039–1049.

(82) Xiong, Z.; Lei, Z.; Li, Y.; Dong, L.; Zhao, Y.; Zhang, J. A Review on Modification of Facet-Engineered TiO<sub>2</sub> for Photocatalytic CO<sub>2</sub> Reduction. *J. Photochem. Photobiol., C* **2018**, *36*, 24–47.

(83) Chen, D.; Zhang, X.; Lee, A. F. Synthetic Strategies to Nanostructured Photocatalysts for CO<sub>2</sub> Reduction to Solar Fuels and Chemicals. *J. Mater. Chem. A* **2015**, *3* (28), 14487–14516.

(84) Razzaq, A.; In, S. TiO<sub>2</sub> Based Nanostructures for Photocatalytic CO<sub>2</sub> Conversion to Valuable Chemicals. *Micromachines* **2019**, *10* (5), 326.

(85) Yang, M. Q.; Xu, Y. J. Photocatalytic Conversion of CO<sub>2</sub> over Graphene-Based Composites: Current Status and Future Perspective. *Nanoscale Horiz.* **2016**, *1* (3), 185–200.

(86) Shen, M.; Zhang, L.; Shi, J. Converting CO<sub>2</sub> into Fuels by Graphitic Carbon Nitride-Based Photocatalysts. *Nanotechnology* **2018**, *29*, 412001.

(87) Zeng, S.; Kar, P.; Thakur, U. K.; Shankar, K. A Review on Photocatalytic CO<sub>2</sub> Reduction Using Perovskite Oxide Nanomaterials. *Nanotechnology* **2018**, *29*, 052001.

(88) Voiry, D.; Shin, H. S.; Loh, K. P.; Chhowalla, M. Low-Dimensional Catalysts for Hydrogen Evolution and CO<sub>2</sub> Reduction. *Nat. Rev. Chem.* **2018**, *2* (1), 105.

(89) Li, X.; Wen, J.; Low, J.; Fang, Y.; Yu, J. Design and Fabrication of Semiconductor Photocatalyst for Photocatalytic Reduction of CO<sub>2</sub> to Solar Fuel. *Sci. China Mater.* **2014**, *57* (1), 70–100.

(90) Shi, R.; Waterhouse, G. I. N.; Zhang, T. Recent Progress in Photocatalytic CO<sub>2</sub> Reduction Over Perovskite Oxides. *Sol. RRL* **2017**, *1* (11), 1700126.

(91) Low, J.; Cheng, B.; Yu, J. Surface Modification and Enhanced Photocatalytic CO<sub>2</sub> Reduction Performance of TiO<sub>2</sub>: A Review. *Appl. Surf. Sci.* **2017**, *392*, 658–686.

(92) Ola, O.; Maroto-Valer, M. M. Review of Material Design and Reactor Engineering on TiO<sub>2</sub> Photocatalysis for CO<sub>2</sub> Reduction. *J. Photochem. Photobiol., C* **2015**, *24*, 16–42.

(93) Das, S.; Wan Daud, W. M. A. Photocatalytic CO<sub>2</sub> Transformation into Fuel: A Review on Advances in Photocatalyst and Photoreactor. *Renewable Sustainable Energy Rev.* **2014**, *39*, 765–805.

(94) Kumar, S.; Jain, S.; Yadav Lamba, B.; Kumar, P. Epigrammatic Status and Perspective of Sequestration of Carbon Dioxide: Role of TiO<sub>2</sub> as Photocatalyst. *Sol. Energy* **2018**, *159*, 423–433.

(95) Ali, S.; Flores, M. C.; Razzaq, A.; Sorcar, S.; Hiragond, C. B.; Kim, H. R.; Park, Y. H.; Hwang, Y.; Kim, H. S.; Kim, H.; Gong, E. H.; Lee, J.; Kim, D.; In, S. Gas Phase Photocatalytic CO<sub>2</sub> Reduction, “A Brief Overview for Benchmarking. *Catalysts* **2019**, *9* (9), 727.

(96) Roy, N.; Suzuki, N.; Terashima, C.; Fujishima, A. Recent Improvements in the Production of Solar Fuels: From CO<sub>2</sub> Reduction to Water Splitting and Artificial Photosynthesis. *Bull. Chem. Soc. Jpn.* **2019**, *92* (1), 178–192.

(97) Neațu, Ș.; Maciá-Agulló, J. A.; Garcia, H. Solar Light Photocatalytic CO<sub>2</sub> Reduction: General Considerations and Selected Bench-Mark Photocatalysts. *Int. J. Mol. Sci.* **2014**, *15* (4), 5246–5262.

(98) Ganesh, I. Conversion of Carbon Dioxide into Methanol - A Potential Liquid Fuel: Fundamental Challenges and Opportunities (a Review). *Renewable Sustainable Energy Rev.* **2014**, *31*, 221–257.

(99) Choi, J. Y.; Lim, C. K.; Park, B.; Kim, M.; Jamal, A.; Song, H. Surface Activation of Cobalt Oxide Nanoparticles for Photocatalytic Carbon Dioxide Reduction to Methane. *J. Mater. Chem. A* **2019**, *7* (25), 15068–15072.

(100) Li, X.; Sun, Y.; Xu, J.; Shao, Y.; Wu, J.; Xu, X.; Pan, Y.; Ju, H.; Zhu, J.; Xie, Y. Selective Visible-Light-Driven Photocatalytic CO<sub>2</sub> Reduction to CH<sub>4</sub> Mediated by Atomically Thin CuIn<sub>3</sub>S<sub>8</sub> Layers. *Nat. Energy* **2019**, *4* (8), 690–699.

(101) Pang, R.; Teramura, K.; Asakura, H.; Hosokawa, S.; Tanaka, T. Effect of Thickness of Chromium Hydroxide Layer on Ag Cocatalyst Surface for Highly Selective Photocatalytic Conversion of CO<sub>2</sub> by H<sub>2</sub>O. *ACS Sustainable Chem. Eng.* **2019**, *7* (2), 2083–2090.

(102) Xu, Y.; Mo, J.; Fu, Z. C.; Liu, S.; Yang, Z.; Fu, W. F. An Exceptionally Efficient Co-Co<sub>2</sub>P@N, P-Codoped Carbon Hybrid Catalyst for Visible Light-Driven CO<sub>2</sub>-to-CO Conversion. *Chem. - Eur. J.* **2018**, *24* (34), 8596–8602.

(103) Kuriki, R.; Sekizawa, K.; Ishitani, O.; Maeda, K. Visible-Light-Driven CO<sub>2</sub> Reduction with Carbon Nitride: Enhancing the Activity of Ruthenium Catalysts. *Angew. Chem., Int. Ed.* **2015**, *54* (8), 2406–2409.

(104) Genoni, A.; Chiridon, D. N.; Boniolo, M.; Sartorel, A.; Bernhard, S.; Bonchio, M. Tuning Iridium Photocatalysts and Light Irradiation for Enhanced CO<sub>2</sub> Reduction. *ACS Catal.* **2017**, *7* (1), 154–160.

(105) Yang, H.; Han, N.; Deng, J.; Wu, J.; Wang, Y.; Hu, Y.; Ding, P.; Li, Y.; Li, Y.; Lu, J. Selective CO<sub>2</sub> Reduction on 2D Mesoporous Bi Nanosheets. *Adv. Energy Mater.* **2018**, *8* (35), 1801536.

(106) Chen, J.; Yin, J.; Zheng, X.; Ait Ahsaine, H.; Zhou, Y.; Dong, C.; Mohammed, O. F.; Takanabe, K.; Bakr, O. M. Compositionally Screened Eutectic Catalytic Coatings on Halide Perovskite Photocathodes for Photoassisted Selective CO<sub>2</sub> Reduction. *ACS Energy Lett.* **2019**, *4* (6), 1279–1286.

(107) Schreiber, M.; Gao, P.; Mayer, M. T.; Luo, J.; Moehl, T.; Nazeeruddin, M. K.; Tilley, S. D.; Grätzel, M. Efficient and Selective Carbon Dioxide Reduction on Low Cost Protected Cu<sub>2</sub>O Photocathodes Using a Molecular Catalyst. *Energy Environ. Sci.* **2015**, *8* (3), 855–861.

(108) Yuan, J.; Yang, L.; Hao, C. Communication—Lithium-Doped CuFeO<sub>2</sub> Thin Film Electrodes for Photoelectrochemical Reduction of Carbon Dioxide to Methanol. *J. Electrochem. Soc.* **2019**, *166* (14), H718–H720.

(109) Kang, U.; Choi, S. K.; Ham, D. J.; Ji, S. M.; Choi, W.; Han, D. S.; Abdel-Wahab, A.; Park, H. Photosynthesis of Formate from CO<sub>2</sub> and Water at 1% Energy Efficiency via Copper Iron Oxide Catalysis. *Energy Environ. Sci.* **2015**, *8* (9), 2638–2643.

(110) Kang, U.; Yoon, S. H.; Han, D. S.; Park, H. Synthesis of Aliphatic Acids from CO<sub>2</sub> and Water at Efficiencies Close to the Photosynthesis Limit Using Mixed Copper and Iron Oxide Films. *ACS Energy Lett.* **2019**, *4* (9), 2075–2080.

(111) Schreiber, M.; Héroguel, F.; Steier, L.; Ahmad, S.; Luterbacher, J. S.; Mayer, M. T.; Luo, J.; Grätzel, M. Solar Conversion of CO<sub>2</sub> to CO Using Earth-Abundant Electrocatalysts Prepared by Atomic Layer Modification of CuO. *Nat. Energy* **2017**, *2* (7), 17087.

(112) Zhou, L. Q.; Ling, C.; Zhou, H.; Wang, X.; Liao, J.; Reddy, G. K.; Deng, L.; Peck, T. C.; Zhang, R.; Whittingham, M. S.; Wang, C.; Chu, C.; Yao, Y.; Jia, H. A High-Performance Oxygen Evolution Catalyst in Neutral-pH for Sunlight-Driven CO<sub>2</sub> Reduction. *Nat. Commun.* **2019**, *10* (1), 4081.

(113) Wang, Y.; Liu, J.; Wang, Y.; Wang, Y.; Zheng, G. Efficient Solar-Driven Electrocatalytic CO<sub>2</sub> Reduction in a Redox-Medium-Assisted System. *Nat. Commun.* **2018**, *9* (1), 5003.

(114) Cheng, W.; Richter, M. H.; Sullivan, I.; Larson, D. M.; Xiang, C.; Brunschwigg, B. S.; Atwater, H. A.; Xiang, C.; Brunschwigg, B. S.;

Atwater, H. A. CO<sub>2</sub> Reduction to CO with 19% Efficiency in a Solar-Driven Gas Diffusion Electrode Flow Cell under Outdoor Solar Illumination. *ACS Energy Lett.* **2020**, *5* (2), 470–476.

(115) Ma, M.; Liu, K.; Shen, J.; Kas, R.; Smith, W. A. In Situ Fabrication and Reactivation of Highly Selective and Stable Ag Catalysts for Electrochemical CO<sub>2</sub> Conversion. *ACS Energy Lett.* **2018**, *3* (6), 1301–1306.

(116) Zhao, S.; Jin, R.; Jin, R. Opportunities and Challenges in CO<sub>2</sub> Reduction by Gold- and Silver-Based Electrocatalysts: From Bulk Metals to Nanoparticles and Atomically Precise Nanoclusters. *ACS Energy Lett.* **2018**, *3* (2), 452–462.

(117) Kodaimati, M. S.; McClelland, K. P.; He, C.; Lian, S.; Jiang, Y.; Zhang, Z.; Weiss, E. A. Viewpoint: Challenges in Colloidal Photocatalysis and Some Strategies for Addressing Them. *Inorg. Chem.* **2018**, *57* (7), 3659–3670.

(118) Wang, K.; Lu, H.; Zhu, X.; Lin, Y.; Beard, M. C.; Yan, Y.; Chen, X. Ultrafast Reaction Mechanisms in Perovskite Based Photocatalytic C-C Coupling. *ACS Energy Lett.* **2020**, *5* (2), 566–571.

(119) Samu, G. F.; Balog, A.; De Angelis, F.; Meggiolaro, D.; Kamat, P. V.; Janáky, C. Electrochemical Hole Injection Selectively Expels Iodide from Mixed Halide Perovskite Films. *J. Am. Chem. Soc.* **2019**, *141* (27), 10812–10820.

(120) Beranek, R. Selectivity of Chemical Conversions: Do Light-Driven Photoelectrocatalytic Processes Hold Special Promise? *Angew. Chem., Int. Ed.* **2019**, *58* (47), 16724–16729.

(121) Li, H.; Zhang, X.; MacFarlane, D. R. Carbon Quantum Dots/Cu<sub>2</sub>O Heterostructures for Solar-Light-Driven Conversion of CO<sub>2</sub> to Methanol. *Adv. Energy Mater.* **2015**, *5* (5), 1401077.

(122) Brito, J. F.; Genovese, C.; Tavella, F.; Ampelli, C.; Boldrin Zanoni, M. V.; Centi, G.; Perathoner, S. CO<sub>2</sub> Reduction of Hybrid Cu<sub>2</sub>O-Cu/Gas Diffusion Layer Electrodes and Their Integration in a Cu-based Photoelectrocatalytic Cell. *ChemSusChem* **2019**, *12* (18), 4274–4284.

(123) Kim, J. H.; Magesh, G.; Kang, H. J.; Banu, M.; Kim, J. H.; Lee, J.; Lee, J. S. Carbonate-Coordinated Cobalt Co-Catalyzed BiVO<sub>4</sub>/WO<sub>3</sub> Composite Photoanode Tailored for CO<sub>2</sub> Reduction to Fuels. *Nano Energy* **2015**, *15*, 153–163.

(124) Chang, X.; Wang, T.; Zhao, Z. J.; Yang, P.; Greeley, J.; Mu, R.; Zhang, G.; Gong, Z.; Luo, Z.; Chen, J.; Cui, Y.; Ozin, G. A.; Gong, J. Tuning Cu/Cu<sub>2</sub>O Interfaces for the Reduction of Carbon Dioxide to Methanol in Aqueous Solutions. *Angew. Chem., Int. Ed.* **2018**, *57* (47), 15415–15419.

(125) Huan, T. N.; Dalla Corte, D. A.; Lamaison, S.; Karapinar, D.; Lutz, L.; Menguy, N.; Foldyna, M.; Turren-Cruz, S. H.; Hagfeldt, A.; Bella, F.; Fontecave, M.; Mougel, V. Low-Cost High-Efficiency System for Solar-Driven Conversion of CO<sub>2</sub> to Hydrocarbons. *Proc. Natl. Acad. Sci. U. S. A.* **2019**, *116* (20), 9735–9740.

(126) Deb Nath, N. C.; Choi, S. Y.; Jeong, H. W.; Lee, J. J.; Park, H. Stand-Alone Photoconversion of Carbon Dioxide on Copper Oxide Wire Arrays Powered by Tungsten Trioxide/Dye-Sensitized Solar Cell Dual Absorbers. *Nano Energy* **2016**, *25*, 51–59.

(127) Yu, S.; Jain, P. K. Plasmonic Photosynthesis of C<sub>1</sub>-C<sub>3</sub> Hydrocarbons from Carbon Dioxide Assisted by an Ionic Liquid. *Nat. Commun.* **2019**, *10* (1), 2022.

(128) Sagara, N.; Kamimura, S.; Tsubota, T.; Ohno, T. Photoelectrochemical CO<sub>2</sub> Reduction by a P-Type Boron-Doped g-C<sub>3</sub>N<sub>4</sub> Electrode under Visible Light. *Appl. Catal., B* **2016**, *192*, 193–198.

(129) Mateo, D.; Asiri, A. M.; Albergo, J.; García, H. The Mechanism of Photocatalytic CO<sub>2</sub> Reduction by Graphene-Supported Cu<sub>2</sub>O Probed by Sacrificial Electron Donors. *Photochem. Photobiol. Sci.* **2018**, *17* (6), 829–834.

(130) Ci, C.; Carbó, J. J.; Neumann, R.; Graaf, C. De; Poblet, J. M. Photoreduction Mechanism of CO<sub>2</sub> to CO Catalyzed by a Rhenium(I)-Polyoxometalate Hybrid Compound. *ACS Catal.* **2016**, *6* (10), 6422–6428.

(131) Zheng, Y.; Zhang, W.; Li, Y.; Chen, J.; Yu, B.; Wang, J.; Zhang, L.; Zhang, J. Energy Related CO<sub>2</sub> Conversion and Utilization: Advanced Materials/Nanomaterials, Reaction Mechanisms and Technologies. *Nano Energy* **2017**, *40*, 512–539.

(132) Poudyal, S.; Laursen, S. Photocatalytic CO<sub>2</sub> Reduction by H<sub>2</sub>O: Insights from Modeling Electronically Relaxed Mechanisms. *Catal. Sci. Technol.* **2019**, *9* (4), 1048–1059.

(133) Karamian, E.; Sharifnia, S. On the General Mechanism of Photocatalytic Reduction of CO<sub>2</sub>. *J. CO<sub>2</sub> Util.* **2016**, *16*, 194–203.

(134) Kang, H. Y.; Nam, D. H.; Yang, K. D.; Joo, W.; Kwak, H.; Kim, H. H.; Hong, S. H.; Nam, K. T.; Joo, Y. C. Synthetic Mechanism Discovery of Monophase Cuprous Oxide for Record High Photoelectrochemical Conversion of CO<sub>2</sub> to Methanol in Water. *ACS Nano* **2018**, *12* (8), 8187–8196.

(135) Uzunova, E. L.; Seriani, N.; Mikosch, H. CO<sub>2</sub> Conversion to Methanol on Cu(I) Oxide Nanolayers and Clusters: An Electronic Structure Insight into the Reaction Mechanism. *Phys. Chem. Chem. Phys.* **2015**, *17* (16), 11088–11094.

(136) Yin, G.; Huang, X.; Chen, T.; Zhao, W.; Bi, Q.; Xu, J.; Han, Y.; Huang, F. Hydrogenated Blue Titania for Efficient Solar to Chemical Conversions: Preparation, Characterization, and Reaction Mechanism of CO<sub>2</sub> Reduction. *ACS Catal.* **2018**, *8* (2), 1009–1017.

(137) Meister, S.; Reithmeier, R. O.; Tschurl, M.; Heiz, U.; Rieger, B. Unraveling Side Reactions in the Photocatalytic Reduction of CO<sub>2</sub>: Evidence for Light-Induced Deactivation Processes in Homogeneous Photocatalysis. *ChemCatChem* **2015**, *7* (4), 690–697.

(138) Sommers, J. M.; Alderman, N. P.; Viasus, C. J.; Gambarotta, S. Revisiting the Behaviour of BiVO<sub>4</sub> as a Carbon Dioxide Reduction Photo-Catalyst. *Dalt. Trans.* **2017**, *46* (19), 6404–6408.

(139) Sriramagiri, G. M.; Ahmed, N.; Luc, W.; Dobson, K. D.; Hegedus, S. S.; Jiao, F. Toward a Practical Solar-Driven CO<sub>2</sub> Flow Cell Electrolyzer: Design and Optimization. *ACS Sustainable Chem. Eng.* **2017**, *5* (11), 10959–10966.

(140) Endrődi, B.; Kecsenovity, E.; Samu, A.; Darvas, F.; Jones, R. V.; Török, V.; Danyi, A.; Janáky, C. Multilayer Electrolyzer Stack Converts Carbon Dioxide to Gas Products at High Pressure with High Efficiency. *ACS Energy Lett.* **2019**, *4* (7), 1770–1777.

(141) Urbain, F.; Tang, P.; Carretero, N. M.; Andreu, T.; Gerling, L. G.; Voz, C.; Arbiol, J.; Morante, J. R. A Prototype Reactor for Highly Selective Solar-Driven CO<sub>2</sub> Reduction to Synthesis Gas Using Nanosized Earth-Abundant Catalysts and Silicon Photovoltaics. *Energy Environ. Sci.* **2017**, *10* (10), 2256–2266.

(142) Haas, T.; Krause, R.; Weber, R.; Demler, M.; Schmid, G. Technical Photosynthesis Involving CO<sub>2</sub> Electrolysis and Fermentation. *Nat. Catal.* **2018**, *1* (1), 32–39.

(143) Ren, D.; Loo, N. W. X.; Gong, L.; Yeo, B. S. Continuous Production of Ethylene from Carbon Dioxide and Water Using Intermittent Sunlight. *ACS Sustainable Chem. Eng.* **2017**, *5* (10), 9191–9199.

(144) Deng, W.; Zhang, L.; Dong, H.; Chang, X.; Wang, T.; Gong, J. Achieving Convenient CO<sub>2</sub> Electroreduction and Photovoltage in Tandem Using Potential-Insensitive Disordered Ag Nanoparticles. *Chem. Sci.* **2018**, *9* (32), 6599–6604.

(145) Kim, B. J.; Piao, G.; Kim, S.; Yang, S. Y.; Park, Y.; Han, D. S.; Shon, H. K.; Hoffmann, M. R.; Park, H. High-Efficiency Solar Desalination Accompanying Electrocatalytic Conversions of Desalted Chloride and Captured Carbon Dioxide. *ACS Sustainable Chem. Eng.* **2019**, *7* (18), 15320–15328.

(146) Gurudayal; Bullock, J.; Srankó, D. F.; Towle, C. M.; Lum, Y.; Hettick, M.; Scott, M. C.; Javey, A.; Ager, J. Efficient Solar-Driven Electrochemical CO<sub>2</sub> Reduction to Hydrocarbons and Oxygenates. *Energy Environ. Sci.* **2017**, *10* (10), 2222–2230.

(147) Wang, L.; Sofer, Z.; Pumera, M. Will Any Crap We Put into Graphene Increase Its Electrocatalytic Effect? *ACS Nano* **2020**, *14* (1), 21–25.

(148) Zhou, X.; Xiang, C. Comparative Analysis of Solar-to-Fuel Conversion Efficiency: A Direct, One-Step Electrochemical CO<sub>2</sub> Reduction Reactor versus a Two-Step, Cascade Electrochemical CO<sub>2</sub> Reduction Reactor. *ACS Energy Lett.* **2018**, *3* (8), 1892–1897.

(149) Higgins, D.; Hahn, C.; Xiang, C.; Jaramillo, T. F.; Weber, A. Z. Gas-Diffusion Electrodes for Carbon Dioxide Reduction: A New Paradigm. *ACS Energy Lett.* **2019**, *4* (1), 317–324.

- (150) Szczeny, J.; Ruff, A.; Oliveira, A. R.; Pita, M.; Pereira, I. A. C.; De Lacey, A. L.; Schuhmann, W. Electroenzymatic CO<sub>2</sub> Fixation Using Redox Polymer/Enzyme-Modified Gas Diffusion Electrodes. *ACS Energy Lett.* **2020**, *5*, 321–327.
- (151) Liu, K.; Smith, W. A.; Burdyny, T. Introductory Guide to Assembling and Operating Gas Diffusion Electrodes for Electrochemical CO<sub>2</sub> Reduction. *ACS Energy Lett.* **2019**, *4* (3), 639–643.
- (152) Liu, J.; Liu, B.; Ren, Y.; Yuan, Y.; Zhao, H.; Yang, H.; Liu, S. Hydrogenated Nanotubes/Nanowires Assembled from TiO<sub>2</sub> Nanoflakes with Exposed {111} Facets: Excellent Photo-Catalytic CO<sub>2</sub> Reduction Activity and Charge Separation Mechanism between (111) and (111) Polar Surfaces. *J. Mater. Chem. A* **2019**, *7* (24), 14761–14775.
- (153) Wan, L.; Zhou, Q.; Wang, X.; Wood, T. E.; Wang, L.; Duchesne, P. N.; Guo, J.; Yan, X.; Xia, M.; Li, Y. F.; Jelle, A. A.; Ulmer, U.; Jia, J.; Li, T.; Sun, W.; Ozin, G. A. Cu<sub>2</sub>O Nanocubes with Mixed Oxidation-State Facets for (Photo)Catalytic Hydrogenation of Carbon Dioxide. *Nat. Catal.* **2019**, *2* (10), 889–898.
- (154) Gao, C.; Meng, Q.; Zhao, K.; Yin, H.; Wang, D.; Guo, J.; Zhao, S.; Chang, L.; He, M.; Li, Q.; Zhao, H.; Huang, X.; Gao, Y.; Tang, Z. Co<sub>3</sub>O<sub>4</sub> Hexagonal Platelets with Controllable Facets Enabling Highly Efficient Visible-Light Photocatalytic Reduction of CO<sub>2</sub>. *Adv. Mater.* **2016**, *28* (30), 6485–6490.
- (155) Chen, Q.; Chen, X.; Fang, M.; Chen, J.; Li, Y.; Xie, Z.; Kuang, Q.; Zheng, L. Photo-Induced Au-Pd Alloying at TiO<sub>2</sub> {101} Facets Enables Robust CO<sub>2</sub> Photocatalytic Reduction into Hydrocarbon Fuels. *J. Mater. Chem. A* **2019**, *7* (3), 1334–1340.
- (156) Wu, Y. A.; McNulty, I.; Liu, C.; Lau, K. C.; Liu, Q.; Paulikas, A. P.; Sun, C. J.; Cai, Z.; Guest, J. R.; Ren, Y.; Stamenkovic, V.; Curtiss, L. A.; Liu, Y.; Rajh, T. Facet-Dependent Active Sites of a Single Cu<sub>2</sub>O Particle Photocatalyst for CO<sub>2</sub> Reduction to Methanol. *Nat. Energy* **2019**, *4* (11), 957–968.
- (157) Zhao, Y.; Wei, Y.; Wu, X.; Zheng, H.; Zhao, Z.; Liu, J.; Li, J. Graphene-Wrapped Pt/TiO<sub>2</sub> Photocatalysts with Enhanced Photo-generated Charges Separation and Reactant Adsorption for High Selective Photoreduction of CO<sub>2</sub> to CH<sub>4</sub>. *Appl. Catal., B* **2018**, *226*, 360–372.
- (158) Xia, C.; Zhu, P.; Jiang, Q.; Pan, Y.; Liang, W.; Stavitski, E.; Alshareef, H. N.; Wang, H. Continuous Production of Pure Liquid Fuel Solutions via Electrocatalytic CO<sub>2</sub> Reduction Using Solid-Electrolyte Devices. *Nat. Energy* **2019**, *4* (9), 776–785.
- (159) Kong, Z. C.; Liao, J. F.; Dong, Y. J.; Xu, Y. F.; Chen, H. Y.; Kuang, D.-B.; Su, C. Y. Core@shell CsPbBr<sub>3</sub>@zeolitic Imidazolate Framework Nanocomposite for Efficient Photocatalytic CO<sub>2</sub> Reduction. *ACS Energy Lett.* **2018**, *3* (11), 2656–2662.
- (160) Kecszenovity, E.; Endrödi, B.; Tóth, P. S.; Zou, Y.; Dryfe, R. A. W.; Rajeshwar, K.; Janáky, C. Enhanced Photoelectrochemical Performance of Cuprous Oxide/Graphene Nanohybrids. *J. Am. Chem. Soc.* **2017**, *139* (19), 6682–6692.
- (161) Kecszenovity, E.; Endrödi, B.; Pápa, Z.; Hernádi, K.; Rajeshwar, K.; Janáky, C. Decoration of Ultra-Long Carbon Nanotubes with Cu<sub>2</sub>O Nanocrystals: A Hybrid Platform for Enhanced Photoelectrochemical CO<sub>2</sub> Reduction. *J. Mater. Chem. A* **2016**, *4* (8), 3139–3147.
- (162) Kormányos, A.; Hursán, D.; Janáky, C. Photoelectrochemical Behavior of PEDOT/Nanocarbon Electrodes: Fundamentals and Structure-Property Relationships. *J. Phys. Chem. C* **2018**, *122* (25), 13682–13690.
- (163) Osterloh, F. E. Inorganic Nanostructures for Photoelectrochemical and Photocatalytic Water Splitting. *Chem. Soc. Rev.* **2013**, *42*, 2294–2320.
- (164) Rajeshwar, K. Electron Transfer at Semiconductor-Electrolyte Interfaces. *Electron Transfer in Chemistry*; Balzani, V., Ed.; Wiley-VCH: Weinheim, 2001.
- (165) Boettcher, S. W.; Spurgeon, J. M.; Putnam, M. C.; Warren, E. L.; Turner-Evans, D. B.; Kelzenberg, M. D.; Maiolo, J. R.; Atwater, H. A.; Lewis, N. S. Energy-Conversion Properties of Vapor-Liquid-Solid-Grown Silicon Wire-Array Photocathodes. *Science* **2010**, *327* (5962), 185–187.
- (166) Warren, E. L.; Atwater, H. a.; Lewis, N. S. Silicon Microwire Arrays for Solar Energy-Conversion Applications. *J. Phys. Chem. C* **2014**, *118* (2), 747–759.
- (167) Goodey, A. P.; Eichfeld, S. M.; Lew, K.-K.; Redwing, J. M.; Mallouk, T. E. Silicon Nanowire Array Photoelectrochemical Cells. *J. Am. Chem. Soc.* **2007**, *129* (41), 12344–12345.
- (168) Panayotov, D. A.; Frenkel, A. I.; Morris, J. R. Catalysis and Photocatalysis by Nanoscale Au/TiO<sub>2</sub>: Perspectives for Renewable Energy. *ACS Energy Lett.* **2017**, *2* (5), 1223–1231.
- (169) Negrín-Montecelo, Y.; Comesaña-Hermo, M.; Khorashad, L. K.; Sousa-Castillo, A.; Wang, Z.; Pérez-Lorenzo, M.; Liedl, T.; Govorov, A. O.; Correa-Duarte, M. A. Photophysical Effects behind the Efficiency of Hot Electron Injection in Plasmon-Assisted Catalysis: The Joint Role of Morphology and Composition. *ACS Energy Lett.* **2020**, *5* (2), 395–402.
- (170) Creel, E. B.; Corson, E. R.; Eichhorn, J.; Kostecki, R.; Urban, J. J.; McCloskey, B. D. Directing Selectivity of Electrochemical Carbon Dioxide Reduction Using Plasmonics. *ACS Energy Lett.* **2019**, *4* (5), 1098–1105.
- (171) Spittler, M. T.; Modestino, M. A.; Deutsch, T. G.; Xiang, C. X.; Durrant, J. R.; Esposito, D. V.; Haussener, S.; Maldonado, S.; Sharp, I. D.; Parkinson, B. A.; Ginley, D. S.; Houle, F. A.; Hannappel, T.; Neale, N. R.; Nocera, D. G.; McIntyre, P. C. Practical Challenges in the Development of Photoelectrochemical Solar Fuels Production. *Sustain. Energy Fuels* **2020**, *4* (3), 985–995.
- (172) Xu, P.; Huang, T.; Huang, J.; Yan, Y.; Mallouk, T. E. Dye-Sensitized Photoelectrochemical Water Oxidation through a Buried Junction. *Proc. Natl. Acad. Sci. U. S. A.* **2018**, *115* (27), 6946–6951.
- (173) Tembhumne, S.; Nandjou, F.; Haussener, S. A Thermally Synergistic Photo-Electrochemical Hydrogen Generator Operating under Concentrated Solar Irradiation. *Nat. Energy* **2019**, *4* (5), 399–407.
- (174) Verma, S.; Lu, S.; Kenis, P. J. A. Co-Electrolysis of CO<sub>2</sub> and Glycerol as a Pathway to Carbon Chemicals with Improved Technoeconomics Due to Low Electricity Consumption. *Nat. Energy* **2019**, *4* (6), 466–474.
- (175) Salvatore, D.; Berlinguette, C. P. Voltage Matters When Reducing CO<sub>2</sub> in an Electrochemical Flow Cell. *ACS Energy Lett.* **2020**, *5* (1), 215–220.
- (176) Castro, S.; Albo, J.; Irabien, A. Photoelectrochemical Reactors for CO<sub>2</sub> Utilization. *ACS Sustainable Chem. Eng.* **2018**, *6* (12), 15877–15894.

# Hybrid FeNiOOH/ $\alpha$ -Fe<sub>2</sub>O<sub>3</sub>/Graphene Photoelectrodes with Advanced Water Oxidation Performance

Attila Kormányos,\* Egon Kecsenovity, Alireza Honarfar, Tönu Pullerits, and Csaba Janáky\*

In this study, the photoelectrochemical behavior of electrodeposited FeNiOOH/Fe<sub>2</sub>O<sub>3</sub>/graphene nanohybrid electrodes is investigated, which has precisely controlled structure and composition. The photoelectrode assembly is designed in a bioinspired manner where each component has its own function: Fe<sub>2</sub>O<sub>3</sub> is responsible for the absorption of light, the graphene framework for proper charge carrier transport, while the FeNiOOH overlayer for facile water oxidation. The effect of each component on the photoelectrochemical behavior is studied by linear sweep photovoltammetry, incident photon-to-charge carrier conversion efficiency measurements, and long-term photoelectrolysis. 2.6 times higher photocurrents are obtained for the best-performing FeNiOOH/Fe<sub>2</sub>O<sub>3</sub>/graphene system compared to its pristine Fe<sub>2</sub>O<sub>3</sub> counterpart. Transient absorption spectroscopy measurements reveal an increased hole-lifetime in the case of the Fe<sub>2</sub>O<sub>3</sub>/graphene samples. Long-term photoelectrolysis measurements in combination with Raman spectroscopy, however, prove that the underlying nanocarbon framework is corroded by the photogenerated holes. This issue is tackled by the electrodeposition of a thin FeNiOOH overlayer, which rapidly accepts the photogenerated holes from Fe<sub>2</sub>O<sub>3</sub>, thus eliminating the pathway leading to the corrosion of graphene.

in the form of chemical bonds.<sup>[1]</sup> Design of semiconductor (SC)-based nanocomposite materials has come to the forefront of research during recent years. In these studies, the various elementary steps of the PEC process—such as light absorption (exciton formation), the transport, and transfer of the photogenerated charge carriers—can be separated.<sup>[2–4]</sup> This approach is inspired by natural photosynthesis where CO<sub>2</sub> and H<sub>2</sub>O is converted into chemicals in a complex, multi-step process (each of them facilitated by different subsystems) using the energy of sunlight.<sup>[5]</sup> This strategy seems necessary, since no single material was discovered so far, which would simultaneously fulfill all requirements that are necessary to drive PEC processes (such as hydrogen evolution, CO<sub>2</sub> reduction, and water oxidation) efficiently and cost-effectively.<sup>[6,7]</sup>

One of the most extensively studied n-type SC photoelectrodes is hematite ( $\alpha$ -Fe<sub>2</sub>O<sub>3</sub> denoted as Fe<sub>2</sub>O<sub>3</sub> in the following), due to its narrow bandgap ( $E_{\text{BG}} = 2.0\text{--}2.2$  eV), and appropriate valence band (VB) position to drive the PEC water oxidation process.<sup>[8–11]</sup> Additionally, it is non-toxic, abundant, and stable in alkaline solutions.<sup>[12–14]</sup> Although, a maximum of 16.8% solar-to-hydrogen conversion efficiency can be calculated from the bandgap,<sup>[8,15]</sup> real device performances are still far behind.<sup>[16]</sup> The low charge carrier mobility ( $<1$  cm<sup>2</sup> V<sup>-1</sup> s<sup>-1</sup>),<sup>[13]</sup> and short charge carrier lifetime<sup>[15]</sup> together result in small charge carrier diffusion length (2–4 nm).<sup>[17,18]</sup> This means that the majority of photogenerated charge carriers are lost before they could reach the substrate in the electrolyte solution. On top of this, low absorption coefficient<sup>[19]</sup> and sluggish water oxidation kinetics further limits the efficiency of the overall PEC process.

Several strategies have been employed to overcome these issues, among which doping and nanostructuring are the two most prominent. For example, doping of Fe<sub>2</sub>O<sub>3</sub> with various elements—such as Si,<sup>[20]</sup> Ti,<sup>[13]</sup> Mo,<sup>[21]</sup> and Sn<sup>[22]</sup>—can significantly increase the charge carrier mobility and concentration. Nanostructured hematite architectures improved the relative volume of the space-charge layer in comparison to the bulk, which resulted in reduced charge carrier recombination and thus in higher photocurrents.<sup>[23]</sup> One very interesting approach is the combination of hematite with plasmonic gold nanohole array, which resulted in a tenfold increase of the

## 1. Introduction


Photoelectrochemical (PEC) solar fuel generation is considered as a potential one-step strategy to store the energy of sunlight

Dr. A. Kormányos, E. Kecsenovity, Prof. C. Janáky  
Department of Physical Chemistry and Materials Science  
University of Szeged  
Szeged H-6720, Hungary  
E-mail: attila.kormanyos@chem.u-szeged.hu; janaky@chem.u-szeged.hu

A. Honarfar, Prof. T. Pullerits  
Chemical Physics and NanoLund  
Lund University  
Box 124 Lund 22100, Sweden

Prof. C. Janáky  
ELI-ALPS  
ELI-HU Non-Profit Ltd.

Wolfgang Sandner utca 3, Szeged H-6728, Hungary

 The ORCID identification number(s) for the author(s) of this article can be found under <https://doi.org/10.1002/adfm.202002124>.

© 2020 The Authors. Published by WILEY-VCH Verlag GmbH & Co. KGaA, Weinheim. This is an open access article under the terms of the Creative Commons Attribution-NonCommercial License, which permits use, distribution and reproduction in any medium, provided the original work is properly cited and is not used for commercial purposes.

DOI: 10.1002/adfm.202002124



**Table 1.** PEC performance of state-of-the-art hematite photoelectrodes and PEC performance of the best electrodeposited hematite photoelectrodes.

Name	Synthesis method	Photocurrent density	IPCE ( $\lambda = 500$ nm)	Ref.
$\alpha$ -Fe <sub>2</sub> O <sub>3</sub> nanorods with TiO <sub>2</sub> overlayer and Co-Pi catalyst	Chemical bath deposition	6 mA cm <sup>-2</sup> at 1.23 V vs RHE in 1 M KOH, 100 mW cm <sup>-2</sup> AM 1.5G illumination	≈5%	[41]
Ru-doped $\alpha$ -Fe <sub>2</sub> O <sub>3</sub> nanorods	Doctor blading	5.7 mA cm <sup>-2</sup> at 1.23 V versus RHE in 1 M NaOH, 100 mW cm <sup>-2</sup> AM 1.5G illumination	43%	[42]
Interconnected $\alpha$ -Fe <sub>2</sub> O <sub>3</sub> nanosheets with Ag NPs and Co-Pi	Anodization	4.68 mA cm <sup>-2</sup> at 1.23 V versus RHE in 1 M NaOH, 100 mW cm <sup>-2</sup> AM 1.5G illumination	≈10%	[43]
Nanostructured $\alpha$ -Fe <sub>2</sub> O <sub>3</sub> with IrO <sub>2</sub> NPs	Atmospheric pressure chemical vapor deposition	≈3 mA cm <sup>-2</sup> at 1.23 V versus RHE in 1 M NaOH, 100 mW cm <sup>-2</sup> AM 1.5G illumination	≈22%	[23]
Nanostructured $\alpha$ -Fe <sub>2</sub> O <sub>3</sub>	Electrodeposition	1.6 mA cm <sup>-2</sup> at 1.6 V versus RHE in 1 M NaOH, 100 mW cm <sup>-2</sup> AM 1.5G illumination	–	[44]
Nanostructured Zn-, and Ti-doped $\alpha$ -Fe <sub>2</sub> O <sub>3</sub>	Electrodeposition	1.5 mA cm <sup>-2</sup> at 1.23 V versus RHE in 1 M NaOH, 100 mW cm <sup>-2</sup> 300 W Xe lamp	≈2.5%	[13]
Nanostructured Ti-, and Zr-doped $\alpha$ -Fe <sub>2</sub> O <sub>3</sub> with Co(NO <sub>3</sub> ) <sub>2</sub>	Electrodeposition	≈0.6 mA cm <sup>-2</sup> at 1.23 V versus RHE in 1 M KOH, 100 mW cm <sup>-2</sup> AM 1.5G illumination	≈3%	[19]

PEC performance compared to a low-performing bare hematite sample.<sup>[24]</sup>

SCs can be combined with various nanostructured carbon materials (such as graphene<sup>[25]</sup> or carbon nanotubes)<sup>[26]</sup> to facilitate the separation and transport of the photogenerated charge carriers, leading to enhanced PEC behavior. An additional advantage of this synergistic combination is the improved photostability of the hybrids compared to their pristine SC counterparts.<sup>[26]</sup> This concept has been already applied for various inorganic SC, such as ZnO,<sup>[27]</sup> TiO<sub>2</sub>,<sup>[28]</sup> BiVO<sub>4</sub>,<sup>[29]</sup> and Cu<sub>2</sub>O,<sup>[25,26]</sup> etc. There are also few examples, where Fe<sub>2</sub>O<sub>3</sub> was combined with nanocarbons, such as reduced graphene oxide,<sup>[30–32]</sup> graphene,<sup>[11,33,34]</sup> carbon nanotubes,<sup>[35]</sup> and carbon quantum dots.<sup>[36]</sup> Interestingly, in most of these studies, the nanocarbon component is located on the top of the Fe<sub>2</sub>O<sub>3</sub> layer,<sup>[11,30,32]</sup> thus the enhanced PEC behavior is rooted in the passivation of the surface states of Fe<sub>2</sub>O<sub>3</sub> by the nanocarbon overlayer, thereby decreasing surface recombination. The sluggish water oxidation kinetics can be alleviated by the deposition of co-catalyst overlayers such as Co-Pi,<sup>[18]</sup> FeOOH,<sup>[37]</sup> NiOOH,<sup>[38]</sup> NiFeO<sub>x</sub>,<sup>[39]</sup> Ir,<sup>[40]</sup> and IrO<sub>2</sub>.<sup>[23]</sup> Notably, the term “co-catalyst” is used in a broader sense here, as a surface layer that helps to improve the performance of the photoelectrode. Its contribution can be either accelerating the kinetics of the water oxidation reaction; or the passivation the surface states suppressing recombination. Irrespective from the mechanism, both of these contribution results in higher photocurrent density compared to the pristine semiconductor counterpart. As a result of the complex structural-, and surface modifications, PEC performance of hematite photoelectrodes has been greatly improved over the years. The state-of-the-art systems are presented in **Table 1**.

Considering the presented improvements in the above studies, Fe<sub>2</sub>O<sub>3</sub> seems to be an ideal candidate to demonstrate the effect of the various components (e.g., dopants, conductive nanoscaffolds, co-catalyst overlayers) on the PEC performance, and to precisely identify the exact role of each component. Specifically, the charge carrier dynamics of Fe<sub>2</sub>O<sub>3</sub> has been extensively studied by both ex situ and in situ transient absorption spectroscopy (TAS) measurements.<sup>[20,45–47]</sup> Contrastingly, there are only two studies on the charge carrier dynamics of Fe<sub>2</sub>O<sub>3</sub>/nanocarbon nanocomposites,

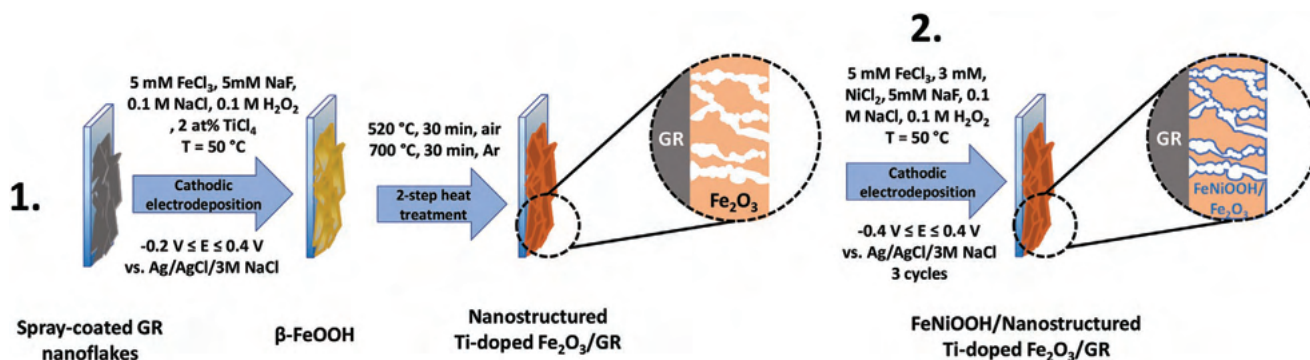
where the charge carrier lifetime was greatly increased either by the reduced graphene oxide under,<sup>[30]</sup> or graphene (GR) overlayer.<sup>[11]</sup> However, no detailed quantification of the measured data can be obtained from these reports. In general, to the best of our knowledge, there is no comprehensive study, where the effect of multiple constituents of a Fe<sub>2</sub>O<sub>3</sub> based hybrid electrodes on the charge carrier dynamics were simultaneously probed on a broad timescale. Such exercise is indeed necessary to follow all events from the charge carrier separation, through the transport, to transfer, and recombination processes.<sup>[48]</sup>

In this work we investigated the PEC behavior of FeNiOOH/Fe<sub>2</sub>O<sub>3</sub>/GR nanocomposite photoelectrodes, synthesized by electrodeposition. Electrodeposition allowed to assemble the three-component nanohybrid in a precise manner, where both structural-, and morphological attributes were carefully controlled. We investigated the effect of the Fe<sub>2</sub>O<sub>3</sub>/GR ratio as well as that of the co-catalyst loading on the PEC properties. While the highest measured photocurrent was 1.2 mA cm<sup>-2</sup> in the case of the pristine Fe<sub>2</sub>O<sub>3</sub> electrode, 2.5 and 3.1 mA cm<sup>-2</sup> photocurrents were harvested for its GR-, and co-catalyst-containing counterparts. Finally, the effect of each component on the charge carrier dynamics was identified by PEC, TAS, and intensity-modulated photocurrent spectroscopy (IMPS) measurements.

## 2. Results and Discussion

### 2.1. Electrodeposition of Fe<sub>2</sub>O<sub>3</sub>/GR Nanocomposites

The Fe<sub>2</sub>O<sub>3</sub>/GR nanocomposite photoelectrodes were synthesized in three steps: i) spray-coating of GR on FTO, ii) electrodeposition of  $\beta$ -FeOOH on GR, iii) two-step heat treatment of  $\beta$ -FeOOH/GR to yield Fe<sub>2</sub>O<sub>3</sub>/GR (**Scheme 1**). In the first step, GR nanoflakes were spray-coated on a FTO-coated glass, from their ethanol-based suspension. This process resulted in an interconnected nanocarbon network on the surface of the substrate electrode. The amount of the spray-coated GR was held constant throughout this study, namely: the electrochemically accessible surface area of GR was approximately three-times higher compared to a bare FTO electrode. Prior to the electrodeposition



**Scheme 1.** Schematic illustration of synthesis methods applied for the preparation of the nanohybrid electrodes samples: 1) cathodic electrodeposition of  $\text{Fe}_2\text{O}_3$  and 2) surface decoration with  $\text{FeNiOOH}$  co-catalyst. Detailed description of the methods can be found in the Experimental Section.

of  $\beta\text{-FeOOH}$ , a conditioning step was carried out in the electrodeposition solution to ensure the proper wetting of the GR nanoflakes and to remove any entrapped gas from the layer (potential cycling in a range where no Faradaic event occurs). This step was followed by the electrodeposition of  $\beta\text{-FeOOH}$  on the GR surface. Electrodeposition was chosen as a synthesis tool due to its beneficial features, most importantly: i) it allows high control over the thickness and morphology of the electrodeposited film, ii) it is faster compared to other synthesis methods, such as atomic layer deposition or solid state synthesis, iii) it is possible to homogeneously coat rough and complex surfaces, iv) the  $\text{Fe}_2\text{O}_3$  layer inherently deposits on the GR surface, and thus an intimate contact forms between them. The thickness of  $\text{Fe}_2\text{O}_3$  (in other words, the composition of the hybrid electrodes) was precisely tuned by varying the electrodeposition charge density. Pristine  $\text{Fe}_2\text{O}_3$  layers were also synthesized on bare FTO as a comparison. Since the thickness of  $\text{Fe}_2\text{O}_3$  can greatly influence PEC properties (e.g., insufficient light absorption for thin layers, higher degree of recombination for thicker layers) synthesis conditions were chosen in a way to make results obtained for bare  $\text{Fe}_2\text{O}_3$  and its GR-containing counterparts fully comparable. Thus, electrodeposition charge densities were normalized by the real surface area, thus the  $\text{Fe}_2\text{O}_3$  layer thicknesses were identical both in the case of the pristine and the GR-containing photoelectrodes. The final step was the heat treatment of the electrodes under air/Ar (in the case of the nanostructured electrodes) to transform  $\beta\text{-FeOOH}$  to  $\alpha\text{-Fe}_2\text{O}_3$ . All synthesis steps along with the experimental conditions are summarized in Scheme 1.

Elemental composition of  $\text{Fe}_2\text{O}_3$  surface was determined with X-ray photoelectron spectroscopy (XPS). According to the survey scans (Figure S1, Supporting Information), all  $\text{Fe}_2\text{O}_3$  samples contain Fe, O, Ti, and Sn (besides adventitious carbon). To quantify the amount of each element, high resolution scans were also recorded (Figure S2, Tables S1 and S2, Supporting Information). The surface of the  $\text{Fe}_2\text{O}_3$  sample mostly consist of O atoms (79.8 at%), which is followed by Fe (16.3 at%). The amount of Ti was around 3.0 at%. The positions of the Ti 2p peaks suggest that Ti is present in the sample as  $\text{Ti}^{4+}$ . Similar conclusions apply for Sn, which is present in as small amount as 0.9 at%. The presence of Sn can be explained by the temperature of the second heat treatment step, which allowed the diffusion of Sn from the underlying FTO to the  $\text{Fe}_2\text{O}_3$  lattice.<sup>[22,49]</sup>

Morphological characteristics of the bare  $\text{Fe}_2\text{O}_3$ , GR, and the nanocomposite films were first studied by scanning electron

microscopy (SEM). Images taken of pristine  $\text{Fe}_2\text{O}_3$  are presented in Figure S3, Supporting Information. The nanostructured  $\text{Fe}_2\text{O}_3$  layer consists of granular, oval-shaped particles, with an average size of  $\approx 100$  nm, homogeneously coating the FTO surface, similarly to precedent literature.<sup>[50,51]</sup> The GR nanoflakes covered the FTO surface (Figure 1A). The average flake size was  $1090 \pm 50$  nm. The morphology of the  $\text{Fe}_2\text{O}_3/\text{GR}$  nanocomposites strongly depended on the composition. At high  $\text{Fe}_2\text{O}_3$  loading ( $450 \text{ mC cm}^{-2}$ ), for example, the GR nanoflakes were mostly and homogeneously covered by  $\text{Fe}_2\text{O}_3$  (Figure 1B). For layers, containing less  $\text{Fe}_2\text{O}_3$  ( $Q_{\text{ED}} = 70 \text{ mC cm}^{-2}$ ) islands were formed, leaving the surface of the nanoflakes partially exposed. If the amount of  $\text{Fe}_2\text{O}_3$  was more than  $450 \text{ mC cm}^{-2}$ , all gaps among the nanoflakes were filled with  $\text{Fe}_2\text{O}_3$ , showing a similar morphology as in the case of the pristine  $\text{Fe}_2\text{O}_3$  photoelectrode. To estimate the average layer thickness ( $Q_{\text{ED}} = 450 \text{ mC cm}^{-2}$ ) of both systems, cross-section SEM images were recorded (Figure S4, Supporting Information), which revealed layer thicknesses of  $220 \pm 40$  and  $440 \pm 90$  nm for the  $\text{Fe}_2\text{O}_3$  and  $\text{Fe}_2\text{O}_3/\text{GR}$  films, respectively.

Transmission electron microscopy (TEM) images further confirmed the composite formation, as both the  $\text{Fe}_2\text{O}_3$  nanocrystals and the underlying GR nanoflakes are visible (Figure 1D–F). HR-TEM revealed lattice fringes in the case of the  $\text{Fe}_2\text{O}_3$  nanoparticles, suggesting high crystallinity all the way to the edges of the particles. Interplanar spacings of 0.370 and 0.260 nm were determined, corresponding to the [012] and [110] lattice planes of  $\alpha\text{-Fe}_2\text{O}_3$ , respectively.<sup>[50]</sup>

Figure 2A compares the Raman spectra recorded for the  $\text{Fe}_2\text{O}_3/\text{GR}$  nanocomposite sample and its pristine components. All Raman-active bands are present on the spectrum of GR (Figure 2A, blue curve; Table S3, Supporting Information).<sup>[52]</sup> The small D/G ratio (0.158) and the position of the 2D band ( $2688 \text{ cm}^{-1}$ ) implies that few-layer graphene flakes are present in our samples.<sup>[52]</sup> In the case of the  $\text{Fe}_2\text{O}_3$  film (Figure 2A, red curve) five out of the seven characteristic bands can be identified, further confirming the chemical nature of the deposit. Bands centered at 220 and  $504 \text{ cm}^{-1}$  are corresponding to the  $A_{1g}$  modes, while the ones, appeared at 288, 401, and  $613 \text{ cm}^{-1}$  are originated from the  $E_g$  modes of  $\alpha\text{-Fe}_2\text{O}_3$ .<sup>[53]</sup> Since  $\text{Fe}_2\text{O}_3$  is an antiferromagnetic material, collective spin movement can be excited in it (this is called a magnon). The band centered at  $1315 \text{ cm}^{-1}$  corresponds to a two-magnon scattering,

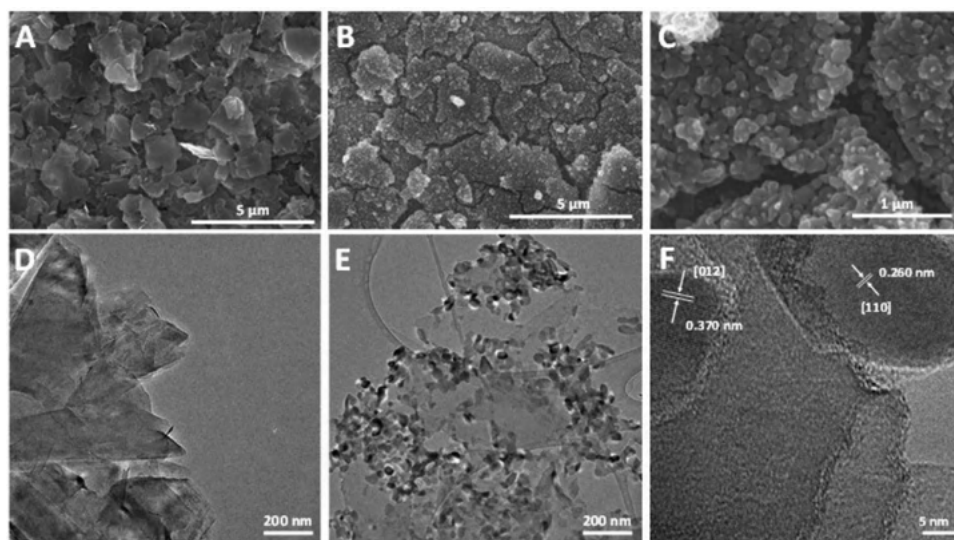


**Figure 1.** SEM images captured for A) GR-coated FTO, B)  $\text{Fe}_2\text{O}_3/\text{GR}$  nanocomposite photoelectrode ( $Q_{\text{ED}} = 450 \text{ mC cm}^{-2}$ ), and for C) the same sample as (B) at higher magnification. TEM images taken for D) GR nanoflakes, E)  $\text{Fe}_2\text{O}_3/\text{GR}$  nanocomposite ( $Q_{\text{ED}} = 450 \text{ mC cm}^{-2}$ ), and F) for the same sample as (E) at higher magnification.

which appeared from the interaction of two magnons created on antiparallel close spin sites.<sup>[54]</sup> As for the  $\text{Fe}_2\text{O}_3/\text{GR}$  nanocomposite electrode, all bands assigned both to GR and  $\text{Fe}_2\text{O}_3$  are present on the spectrum (Figure 2A, red curve). Moreover, the presence of the  $\text{D}+\text{D}'$ ,  $2\text{D}$ ,  $\text{D}+\text{D}'$ , and  $2\text{D}'$  bands in the nanocomposite is a direct proof that GR did not get oxidized during the synthetic procedure.<sup>[55]</sup> Finally, Raman bands of  $\text{Fe}_2\text{O}_3$  are slightly (an average of  $5 \text{ cm}^{-1}$ ) blue-shifted in the nanocomposite, implying an interaction between GR and  $\text{Fe}_2\text{O}_3$ .

## 2.2. Optical and Photoelectrochemical Properties

Optical properties of  $\text{Fe}_2\text{O}_3$  and  $\text{Fe}_2\text{O}_3/\text{GR}$  films were studied by UV-vis spectroscopy (Figure 2B). Three absorption features can be observed on the spectrum of bare  $\text{Fe}_2\text{O}_3$ , originating from the ligand  $d-d$  and from the direct  $\text{O}2\text{p} \rightarrow \text{Fe}4\text{s}$  transitions.<sup>[47,56]</sup> As for  $\text{Fe}_2\text{O}_3/\text{GR}$ , the only difference is a non-characteristic absorption, shifting the baseline throughout the whole spectral

range.<sup>[57]</sup> Tauc analysis was performed (Figure 2C),<sup>[58,59]</sup> and indirect bandgaps of 2.11 and 2.12 eV were calculated, in good agreement with literature values.<sup>[60]</sup>

To estimate PEC water oxidation performance, linear sweep photovoltammograms (LSV) were recorded in 1 M NaOH solution (Figure 3A). Three major conclusions can be promptly made by looking at these photovoltammograms: i) significantly higher photocurrents were harvested in the case of the GR-containing layer, ii) dark currents start to develop earlier, and iii) the onset potential slightly shifted ( $\approx 200 \text{ mV}$ ) toward more positive potentials in the case of the nanocomposite sample. This last phenomenon can be explained by the difference between the interfaces with the underlying FTO electrode surface. While the  $\text{Fe}_2\text{O}_3/\text{FTO}$  is a semiconductor/semiconductor junction, the  $\text{Fe}_2\text{O}_3/\text{GR}$  contains a semiconductor/metal interface. In addition, the temperature of the second heat treatment step ( $700 \text{ }^\circ\text{C}$ ) is high enough for Sn to diffuse into the  $\text{Fe}_2\text{O}_3$  structure, thus additionally doping it (see XPS results below). According to the literature, this slightly shifts onset potentials as well as increases the photocurrent.<sup>[22,49]</sup> The

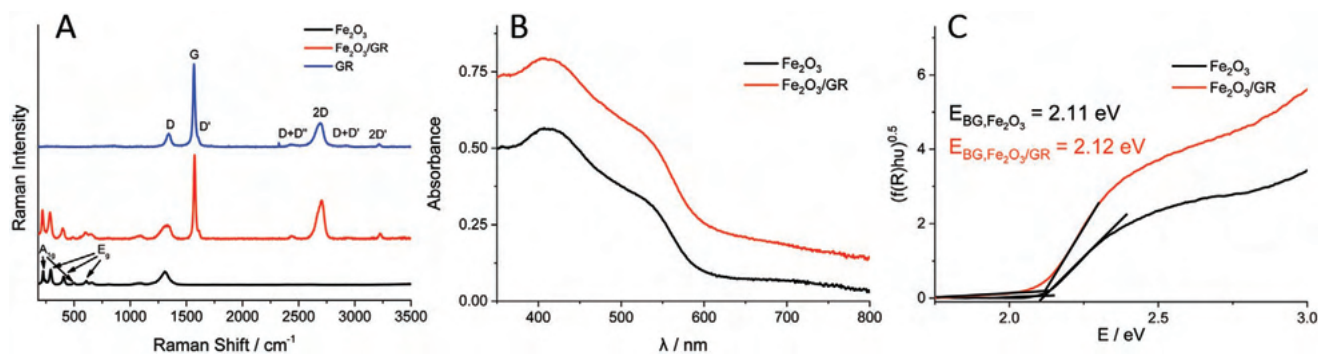


**Figure 2.** A) Raman spectra recorded for  $\text{Fe}_2\text{O}_3$ , GR and  $\text{Fe}_2\text{O}_3/\text{GR}$  thin films.  $Q_{\text{ED}}$  was  $450 \text{ mC cm}^{-2}$  in both cases. B) UV-vis spectra recorded for  $\text{Fe}_2\text{O}_3$  and  $\text{Fe}_2\text{O}_3/\text{GR}$  thin films. Similar compositions were used as for (A). C) Tauc plots constructed from diffuse reflectance spectra recorded for  $\text{Fe}_2\text{O}_3$  and  $\text{Fe}_2\text{O}_3/\text{GR}$  thin films.

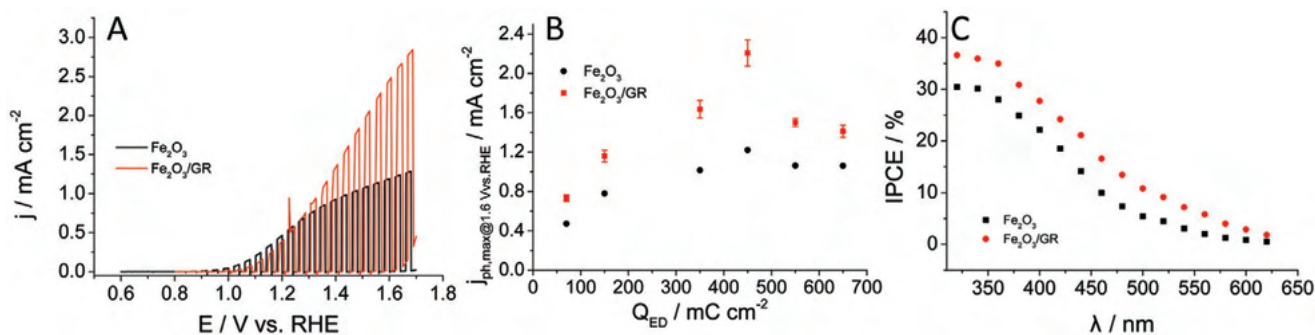


**Figure 3.** A) Photovoltammograms recorded for  $\text{Fe}_2\text{O}_3$  and  $\text{Fe}_2\text{O}_3/\text{GR}$  films in 1 M NaOH under  $100 \text{ W cm}^{-2}$  simulated AM 1.5 solar light.  $Q_{\text{ED}} = 450 \text{ mC cm}^{-2}$ ,  $v = 2 \text{ mV s}^{-1}$ ,  $f_{\text{illumination}} = 0.1 \text{ Hz}$ . B) Maximum photocurrents read from the set of photovoltammograms presented in Figure S5, Supporting Information. Error bars were calculated from at least three individual measurements on different electrodes. C) IPCE curves recorded for  $\text{Fe}_2\text{O}_3$  and  $\text{Fe}_2\text{O}_3/\text{GR}$  photoelectrodes in 1 M NaOH solution, applying 1.5 V versus RHE bias potential.  $Q_{\text{ED}} = 450 \text{ mC cm}^{-2}$ .

presence of GR nanoflakes in the electrode architecture hampers such a diffusion process.

The PEC behavior of nanohybrid electrodes of six different compositions was studied (Figure S5, Supporting Information). A maximum of  $1.2 \text{ mA cm}^{-2}$  photocurrent was measured for  $\text{Fe}_2\text{O}_3$  layers (Figure 3B), which value is in the range of the best-performing photoelectrodes prepared by electrodeposition.<sup>[19,50,61]</sup> Most importantly, all  $\text{Fe}_2\text{O}_3/\text{GR}$  nanocomposite photoelectrodes greatly outperformed their pristine  $\text{Fe}_2\text{O}_3$  counterparts. A maximum trend can be observed as a function of  $\text{Fe}_2\text{O}_3$  loading, both for the pristine and the GR-containing system. Two times higher photocurrents were measured compared to the bare  $\text{Fe}_2\text{O}_3$  ( $2.5$  vs  $1.2 \text{ mA cm}^{-2}$ ) for nanocomposite layers with the optimal composition ( $Q_{\text{ED}} = 450 \text{ mC cm}^{-2}$ ). To the best of our knowledge, no electrodeposited  $\text{Fe}_2\text{O}_3$ -based photoelectrode showed such PEC behavior so far (see Table 1 for comparison).

Figure 3C shows the photoaction spectra recorded for the best-performing  $\text{Fe}_2\text{O}_3$  and  $\text{Fe}_2\text{O}_3/\text{GR}$  photoelectrodes. The characteristics of the two curves are similar, with higher incident photon-to-charge conversion efficiency (IPCE) values in the case of the nanocomposite electrode. IPCE curves were integrated across the AM 1.5G solar spectrum (Figure S6, Supporting Information). The integrated maximum photocurrent values are very close to the ones measured in the photovoltammetry experiments (Table S4, Supporting Information), which further confirms the validity of the recorded photocurrent values. The IPCE values are comparable to the ones, obtained for Ti-doped hematite layers by others,<sup>[62]</sup> but a higher bias was applied in this study ( $1.5 \text{ V vs RHE}$ ). The cutoff region of the two curves are similar ( $E_{\text{cutoff}} \approx E_{\text{BG}} \approx 2 \text{ eV}$ ), indicating that the wavelength range of photoactivity has not broadened in the case of the  $\text{Fe}_2\text{O}_3/\text{GR}$  photoelectrodes. This means that the origin of the enhanced PEC behavior is rooted in the enhanced charge carrier separation and transport (i.e., the enhanced non-characteristic absorption in Figure 2B does not result in any photocurrent).

To glean insights on the electrical properties of the nanohybrid electrodes, electrochemical impedance spectroscopy (EIS) measurements were performed. Figure S7, Supporting Information, shows the Nyquist plots constructed from data collected at open circuit conditions for both  $\text{Fe}_2\text{O}_3$  and  $\text{Fe}_2\text{O}_3/\text{GR}$ .

In the case of  $\text{Fe}_2\text{O}_3$ , a distinct semicircle can be identified in the high-frequency range, assigned to an electron-transfer limited process, whereas the linear part, observed in the lower-frequency range corresponds to the diffusion-limited electron-transfer process.<sup>[63]</sup> The semicircle portion has visibly shrunk in the case of the nanocomposite layers. By fitting the semicircle portion, information can be gained on the series resistance ( $R_s$ ) and on the charge transfer resistance ( $R_{\text{ct}}$ ).  $R_s$  is similar for the two systems. As for  $R_{\text{ct}}$ , one order of magnitude smaller value was calculated for the nanohybrid sample. This phenomenon has been already discussed and elucidated in the literature for other metal-oxide/nanocarbon systems:<sup>[28,64]</sup> by electrodepositing a metal-oxide on a conductive nanocarbon network, the electric conductivity of the nanocomposite layers becomes better, compared to the pristine metal-oxides. This results in improved charge carrier transport and thereby also in suppressed charge carrier recombination explaining the higher photocurrents in the case of the  $\text{Fe}_2\text{O}_3/\text{GR}$  layers.

### 2.3. Transient Absorption Spectroscopy

To understand photoinduced charge carrier dynamics in the photoelectrodes, transient absorption spectroscopy was employed. This method provides information about formation and dynamics of photoinduced charge carriers in the time range from sub-picoseconds to nanoseconds. Time-resolved transient absorption kinetics measured at 800 nm for the bare  $\text{Fe}_2\text{O}_3$ ,  $\text{Fe}_2\text{O}_3/\text{GR}$ , and for the  $\text{FeNiOOH}$  co-catalyst decorated sample, are presented in Figure 4. The loading of the  $\text{Fe}_2\text{O}_3$  layer was identical for all samples ( $Q_{\text{ED}} = 450 \text{ mC cm}^{-2}$ ) which corresponds to about 220 nm thickness. The measurements were carried out in ex situ conditions (i.e., without any electrolyte and applied bias).

Each kinetic trace was normalized to the maximum and fitted by three-exponential decay function (see Supporting Information). Results of the fitting are summarized in Table 2.

The main features of the transient absorption spectrum and the kinetics are consistent with the earlier studies (see an example for the TA spectrum of  $\text{Fe}_2\text{O}_3$  in Figure S10, Supporting Information).<sup>[45,47]</sup> After excitation, an induced negative

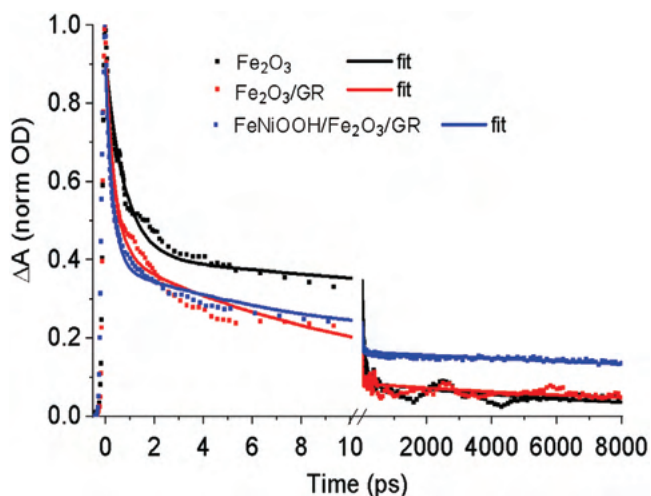


**Figure 4.** Ex situ transient absorption kinetics at  $\lambda = 800$  nm for  $\text{Fe}_2\text{O}_3$ ,  $\text{Fe}_2\text{O}_3/\text{GR}$ ,  $\text{FeNiOOH}/\text{Fe}_2\text{O}_3/\text{GR}$  photoelectrodes following  $\lambda = 400$  nm (3.1 eV) 400  $\mu\text{W}$ , 400  $\mu\text{m}$  spot diameter, 500 kHz repetition rate laser pulse excitation.  $\text{Fe}_2\text{O}_3$  loading is identical for all samples (i.e.,  $Q_{\text{ED}} = 450$   $\text{mC cm}^{-2}$ ).

absorption peak around 530 nm is due to the bleach of  $\text{Fe}_2\text{O}_3$  absorption band, and a broad positive band (which extends to the near IR region) originates from photo-generated free charges in  $\text{Fe}_2\text{O}_3$ . Interestingly, the trend observed on the decay traces for the GR-containing samples is notably comparable to its pristine and co-catalyst-coated counterparts. The TA kinetics, measured at 800 nm, have a significant sub-ps component for all samples regardless of the presence of GR or  $\text{Fe}_2\text{O}_3$  loading. The component corresponds to hot carrier cooling, which is independent of the presence of graphene. In tens of ps time range, GR leads to faster decay of the signal due to the free charges. We attribute this speeding up to the more efficient injection of charges due to the increased photoelectrode surface area provided by the graphene. Graphene can attract both holes and electrons. In contrast to the ten ps time scales, the lifetime of the ns component is somewhat prolonged due to the presence of graphene in the photoelectrode composite. Decorating the  $\text{Fe}_2\text{O}_3$  surface

**Table 2.** Fitting parameters of the transient absorption kinetics in Figure 4.

	$\text{Fe}_2\text{O}_3$	$\text{Fe}_2\text{O}_3/\text{GR}$	$\text{FeNiOOH}/\text{Fe}_2\text{O}_3/\text{GR}$
$A_1$	$0.5 \pm 0.01$ (55%)	$0.5 \pm 0.01$ (55%)	$0.5 \pm 0.02$ (58%)
$t_1$	$0.8 \pm 0.05$ ps	$0.4 \pm 0.05$ ps	$0.3 \pm 0.02$ ps
$A_2$	$0.32 \pm 0.01$ (35%)	$0.35 \pm 0.05$ (36%)	$0.2 \pm 0.04$ (24%)
$t_2$	$51 \pm 3$ ps	$10 \pm 0.5$ ps	$9.87 \pm 0.47$ ps
$A_3$	$0.08 \pm 0.01$ (10%)	$0.08 \pm 0.01$ (9%)	$0.16 \pm 0.01$ (18%)
$t_3$	$9000 \pm 1000$ ps	$14\,000 \pm 2000$ ps	$40\,000 \pm 4000$ ps

with a co-catalyst provides an additional channel to extract holes before they can recombine with the electrons. In presence of the  $\text{FeNiOOH}$  co-catalyst, the amplitude of the long nano-second component of the charge carrier lifetime is increased to almost 20% which is significantly higher compared to the amplitude obtained for  $\text{Fe}_2\text{O}_3$  and  $\text{Fe}_2\text{O}_3/\text{GR}$ . We thereby conclude that the  $\text{FeNiOOH}$  layer effectively attracts holes from the underlying  $\text{Fe}_2\text{O}_3$  film, leading to a superior PEC performance. Similar experiments have been carried out on photoelectrodes with different compositions and very similar trends were found on the  $t_3$  values. These data further support the hypothesis made according to the photostability results (see below), that significant portion of the photogenerated holes are transported to GR, thus oxidizing it. This process can be alleviated by the proper co-catalyst coating on the surface.

## 2.4. Photostability

To probe the photostability of the photoelectrodes, chronoamperometry measurements were carried out for two hours under continuous solar illumination (Figure 5A). While  $\text{Fe}_2\text{O}_3$  remained stable in the timeframe of the experiment, the photocurrents recorded for  $\text{Fe}_2\text{O}_3/\text{GR}$  decreased substantially within 40 min, approaching the values recorded for  $\text{Fe}_2\text{O}_3$ . It is clear from this comparison that this decrease must be tied to the degradation of the underlying GR scaffold upon applying positive bias and illumination. To probe the disappearance of GR

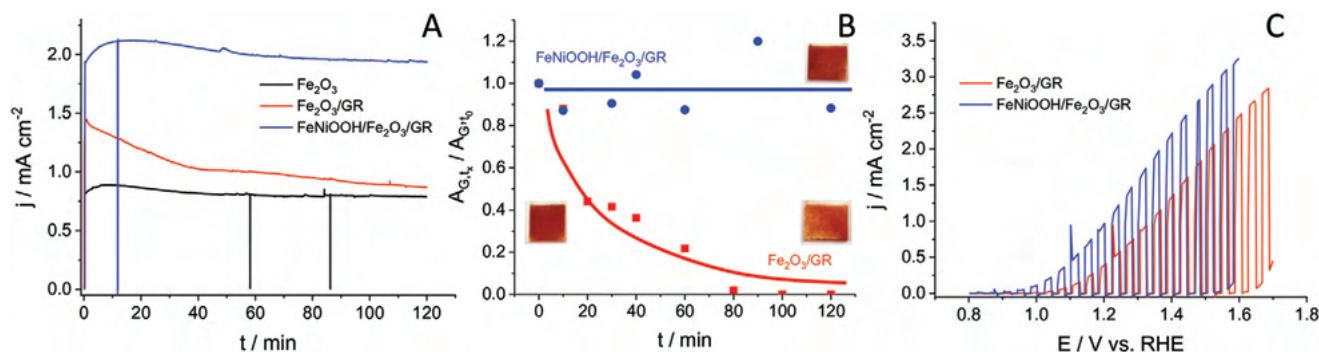


**Figure 5.** A) Long-term chronoamperometry measurements performed in 1 M NaOH solution saturated with Ar, applying  $E = 1.45$  V versus RHE potential and under 100  $\text{mW cm}^{-2}$  AM 1.5 simulated sunlight. The vertical lines show the current drop upon interrupting the illumination. B) Change in the normalized area of the G band of GR in time. Values were determined by integrating the G band intensity in the Raman spectra presented in Figure S8A,B, Supporting Information, and normalizing these values with area of the G band at  $t = 0$  min. Two lines were added to guide the eye of the reader. C) LSV curves recorded for  $\text{Fe}_2\text{O}_3/\text{GR}$  and  $\text{FeNiOOH}/\text{Fe}_2\text{O}_3/\text{GR}$  thin films in 1 M NaOH under 100  $\text{W cm}^{-2}$  simulated AM 1.5 sunlight.  $Q_{\text{ED}} = 450$   $\text{mC cm}^{-2}$ ,  $v = 2$   $\text{mV s}^{-1}$ ,  $f_{\text{illumination}} = 0.1$  Hz.

from the hybrid electrode, Raman spectra were recorded periodically (for experimental details please see Supporting Information) during the long-term photoelectrolysis experiment (Figure S8A, Supporting Information; Figure 5B). The spectra were recorded every 10 min in the first hour and every 20 min in the second hour. The presence of GR was followed by monitoring the intensity of the G band on the spectra. Clearly, this band vanished within the first hour (Figure S8A, Supporting Information). To quantify this observation, G band area was integrated for all spectra and it was normalized with the value calculated for  $t = 0$  min (Figure 5B). The normalized area of the G band decreased monotonously, and completely vanished after 80 min, confirming the disappearance of the underlying GR layer. Our observation invokes a rather uncomfortable question about the applicability of nanocarbon-containing electrodes in oxidative processes, since the widely accepted consensus is that such corrosion should not occur. There are few among the many reports on semiconductor/nanocarbon nanocomposites, however, which describe a similar effect.<sup>[65,66]</sup> Upon illumination, either the formed reactive species (OH<sup>•</sup> radicals) oxidized GR, or after charge separation, a fraction of the photogenerated holes are not transported toward the electrode/electrolyte interface, but rather to GR, which subsequently gets directly oxidized.

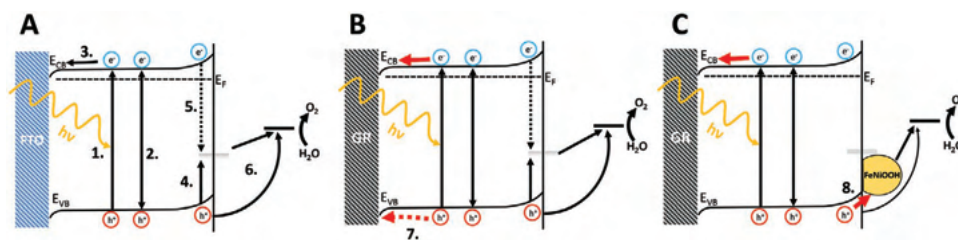
## 2.5. Synthesis and PEC Behavior of FeNiOOH/Fe<sub>2</sub>O<sub>3</sub>/GR Photoelectrodes

One viable option to tackle photostability issues is to deposit a co-catalyst layer on top of Fe<sub>2</sub>O<sub>3</sub>. By doing so, in theory, the vast majority of the photogenerated holes are rapidly transferred to the co-catalyst, which might successfully prevent the corrosion of GR. We chose amorphous mixed FeOOH and NiOOH as co-catalyst (abbreviated as FeNiOOH in the following), which was electrodeposited on Fe<sub>2</sub>O<sub>3</sub>/GR after the second heat treatment step (see Scheme 1 and the Experimental Section for further details). Both FeOOH and NiOOH are well-known water oxidation catalysts and have been widely applied as co-catalyst overlayers to boost the PEC performance of various metal oxide photoelectrodes.<sup>[37,38,67–70]</sup> In most of these studies, however, either only one of them was used<sup>[38,70]</sup> or they were deposited on top of each other as separate layers.<sup>[68,69]</sup> In our case, mixed FeOOH and NiOOH were synthesized in a single step by electrodeposition (instead of the more popular photodeposition). The main advantage of this method is that FeOOH and NiOOH are simultaneously deposited on the electrode surface and their ratio can be easily tuned by the variation of the concentration of the Fe, and Ni salts in the electrodeposition solution.<sup>[37,71]</sup> To determine the exact composition of the FeNiOOH layer, XPS measurements were performed. Survey scans proved the presence of O, Fe, and Ni in the sample (Figure S1, Supporting Information). After collecting and evaluating the high resolution scans (Figure S2, Tables S1 and S2, Supporting Information), the following elemental composition was determined: 83, 16, and 1 at% for O, Fe, and Ni, respectively. The most important conclusion from these numbers is that the Fe:Ni ratio differs from the one expected from the experimental conditions (Fe:Ni 5:3), and thus the formed coating is not stoichiometric.

Additionally, the position and intensity of the O 1s peaks suggest that O atoms in the sample are mostly in the form of hydroxide (71.0%), which is a bit more than two-times higher than in the case of the pristine Fe<sub>2</sub>O<sub>3</sub> sample. Based on this data it can be safely concluded that the electrodeposited FeNiOOH overlayer consists of mixed FeOOH and NiOOH.

Figure 5C shows LSV traces, recorded for Fe<sub>2</sub>O<sub>3</sub>/GR and its FeNiOOH-decorated counterpart. The onset potential has notably shifted to the cathodic direction (approximately 160 mV) in parallel with the 40% increase of the maximum photocurrent, reaching photocurrents as high as 3.1 mA cm<sup>-2</sup>. A notable improvement was also observed for the IPCE values, however, the wavelength-range of absorption did not change (Figure S6B, Supporting Information). The effect of the co-catalyst on the photostability of the Fe<sub>2</sub>O<sub>3</sub>/GR electrode was even more striking (blue curve in Figure 5A). The photocurrents remained stable in the course of the two-hour photoelectrolysis in contrast to the previously experienced rapid decrease. Raman spectra were also taken during this measurement (Figure S8B, Supporting Information). The G band corresponding to the presence of GR is clearly visible even at the end of the two-hour electrolysis. Data were quantified similarly as in the case of the Fe<sub>2</sub>O<sub>3</sub>/GR electrode (Figure 5B) revealing that the normalized area of the G band (thus the amount of GR in the sample) did not change significantly during the measurement. According to the PEC and Raman data, we conclude that by depositing FeNiOOH co-catalyst layer on the surface of Fe<sub>2</sub>O<sub>3</sub>/GR photoelectrode, the effect of the GR framework on the PEC properties was preserved (even slightly improved), in parallel with the protection of the underlying GR from corrosion. To further verify that the measured photocurrents are a result of PEC water oxidation, the concentration of the evolved oxygen was measured with a Clark-type O<sub>2</sub> sensor (Figure S9, Supporting Information). A Faradaic efficiency, close to 100% was calculated over the course of the three hour measurement employing a FeNiOOH /Fe<sub>2</sub>O<sub>3</sub>/GR photoelectrode.

The effect of FeNiOOH on the charge carrier transfer and recombination characteristics was further studied with IMPS.<sup>[72,73]</sup> Figure S11, Supporting Information, shows a set of IMPS spectra recorded from the FeNiOOH/Fe<sub>2</sub>O<sub>3</sub>/GR and the corresponding Fe<sub>2</sub>O<sub>3</sub> and Fe<sub>2</sub>O<sub>3</sub>/GR electrodes applying a set of potentials ranging from 0.8 to 1.55 V versus RHE. An almost perfect circle can be observed at the least positive potentials, meaning that the measured steady-state photocurrent (low frequency intercept, LFI) is close to zero, thus surface recombination dominates the PEC behavior of the system.<sup>[72]</sup> LFI shifts away from zero by the increasing potential along with the increase of the high frequency intercept (corresponding to the maximum harvestable photocurrent, if no recombination occurs). Additionally, the diameter of the semicircle in the upper quadrant, gradually decreases meaning that the applied potential has significantly influenced the equilibrium between the charge carrier transfer and recombination. In the case of the FeNiOOH-decorated sample, no semicircle can be identified in the upper quadrant above 1.4 V versus RHE, suggesting that charge carrier transfer is the dominating process.<sup>[73]</sup> The semicircle in the upper quadrant was shrunk, but never diminished in the case of both co-catalyst-less samples.



**Scheme 2.** Simplified models of the elementary processes occurring in the case of a A)  $\text{Fe}_2\text{O}_3$ , B)  $\text{Fe}_2\text{O}_3/\text{GR}$ , and C)  $\text{FeNiOOH}/\text{Fe}_2\text{O}_3/\text{GR}$  photoelectrode. Elementary processes are: 1) absorption of a photon and generation of an electron-hole pair, 2) nonradiative recombination of an electron-hole pair, 3) electron transport toward the back contact, 4) trapping of holes in surface states, 5) electron-hole recombination in surface states, 6) hole-transfer from the valence band and from the surface states to the electrolyte, 7) hole-transport toward the graphene framework, and 8) hole-transport to the  $\text{FeNiOOH}$  co-catalyst overlayer.

In the following, kinetic parameters were determined from the measured IMPS spectra and plotted versus the applied potential (Figure S12, Supporting Information). Specifically, rate constants, corresponding to charge carrier transfer ( $k_{tr}$ ) and surface recombination ( $k_{sr}$ ) were determined. The  $k_{tr}$  values, calculated for the  $\text{Fe}_2\text{O}_3$  and  $\text{Fe}_2\text{O}_3/\text{GR}$  imply that GR had no obvious influence on the charge carrier transfer characteristics. On the other hand,  $k_{sr}$  values were notably higher, but only up to 1.5 V versus RHE where it drastically dropped in the case of the  $\text{Fe}_2\text{O}_3/\text{GR}$  electrode. When the  $\text{FeNiOOH}$  co-catalyst was present on the electrode surface,  $k_{tr}$  were almost identical to the ones, obtained for  $\text{Fe}_2\text{O}_3$ . This is rather peculiar, since if  $\text{FeNiOOH}$  would behave as a co-catalyst, one would expect a drastic change in the  $k_{tr}$  values. Instead of that, significantly smaller  $k_{sr}$  values were found, indicating suppressed charge carrier recombination. The effect of low  $k_{sr}$  values has also manifested in the charge transfer efficiency, thus the highest values were determined for the  $\text{FeNiOOH}/\text{Fe}_2\text{O}_3/\text{GR}$  electrode (Figure S12C, Supporting Information). From these observations one can conclude that role of  $\text{FeNiOOH}$  is to passivate the  $\text{Fe}_2\text{O}_3$  surface against recombination (reduced Fermi-level pinning and increased band-bending at the surface), rather than activating it for water oxidation. This phenomenon has been also observed and discussed in detail for  $\text{Co-Pi}$ <sup>[74]</sup> and even for  $\text{FeNiO}_x$ <sup>[39]</sup> co-catalyst overlayers.

### 3. Conclusions

We have shown that electrodeposition allows the synthesis of complex photoelectrode architectures with precisely controlled structure and composition. The photoelectrode assembly followed a bioinspired design, where the different components have different function.  $\text{Fe}_2\text{O}_3$  was responsible for light absorption, the GR framework ensured proper charge transport, while the  $\text{FeNiOOH}$  overlayer retained recombination at the surface states through passivation. Photocurrent densities were 2.6 and 1.3 times higher compared to the respective single- and two-component counterparts, and most important, exceeded all precedent literature data for electrodeposited hematite based photoelectrodes. TAS measurements revealed 1.5 times increase in hole-lifetime in the case of the  $\text{Fe}_2\text{O}_3/\text{GR}$  layers compared to the bare  $\text{Fe}_2\text{O}_3$ . Introducing a carbon component to a photoanode, however, raised an additional concern, namely that the photogenerated holes can oxidize the underlying nano-

carbon framework (as confirmed by Raman spectroscopy). By adding a third component to the system (i.e., an  $\text{FeNiOOH}$  overlayer), we were able to suppress the corrosion of the nano-carbon matrix, while all the benefits gained by the presence of GR were still present. Rate constants, corresponding to charge transfer were not affected by the presence of the co-catalyst. Contrastingly, the addition of  $\text{FeNiOOH}$  to the hematite/graphene system has greatly decreased the surface recombination. Our hypothesis of the processes occurring in the investigated systems are presented in **Scheme 2**.

For the pristine  $\text{Fe}_2\text{O}_3$ , photogenerated holes can oxidize water either directly from the valence band, or from the surface states, where they can also recombine with electrons from the conduction band (Scheme 2A). When GR nanoflakes are present (Scheme 2B), two additional processes occur: better transport of photogenerated electrons toward the back contact, due to the highly conductive nature of graphene and some of the photogenerated holes can also be transported to graphene and oxidize it (note the metallic nature of graphene). Finally, if the surface of  $\text{Fe}_2\text{O}_3$  is decorated with a material, which passivates the surface states, holes can be rapidly transported to the co-catalyst (or surface passivating agent) and to the substrate (Scheme 2C). Since the electrodeposited  $\text{FeNiOOH}$  layer is thin and porous, a small fraction of holes might be also transferred directly from the valence band of exposed hematite. Most importantly, because of the rapid hole-transfer to  $\text{FeNiOOH}$ , the pathway leading to the corrosion of graphene is successfully eliminated.

### 4. Experimental Section

**Materials:** Iron (III) chloride ( $\text{FeCl}_3$ , Sigma-Aldrich), nickel (II) chloride ( $\text{NiCl}_2$ , Sigma-Aldrich), sodium chloride ( $\text{NaCl}$ , VWR), sodium fluoride ( $\text{NaF}$ , VWR), sodium hydroxide ( $\text{NaOH}$ , VWR), potassium chloride ( $\text{KCl}$ , VWR), potassium hexacyanoferrate(II) trihydrate ( $\text{K}_4[\text{Fe}(\text{CN})_6] \cdot 3\text{H}_2\text{O}$ , Fluka), potassium hexacyanoferrate(III) ( $\text{K}_3[\text{Fe}(\text{CN})_6]$ , Reanal), sodium sulfate anhydrous ( $\text{Na}_2\text{SO}_4$ , VWR), hydrogen peroxide ( $\text{H}_2\text{O}_2$ , 30%, VWR), titanium tetrachloride ( $\text{TiCl}_4$ , Honeywell), acetone (VWR), ethanol (VWR), and graphene powder (Elicarb Premium Graphene Powder) were of analytical grade and used without further purification. Argon ( $\text{Ar}$ , 99.995%) gas was purchased from Messer. Fluorine-doped tin-oxide-coated glass (FTO, TEC15, Sigma-Aldrich) was used as a substrate. All solutions were prepared using ultrapure deionized water (Millipore Direct Q3-UV, 18.2 M $\Omega$  cm).

**Nanocomposite Synthesis:** First, the GR-dispersion ( $c = 2 \text{ mg mL}^{-1}$  in ethanol), which was sonicated for 30 min prior to use, was spray-coated

on a preheated ( $T = 140\text{ }^{\circ}\text{C}$ ) FTO electrode, using an Alder AD320 type airbrush and a homemade spray-coater robot operated with 1 bar compressed air pressure. To remove the residual traces of the solvent and to enhance adhesion of GR, the films were heat-treated in an oven at  $180\text{ }^{\circ}\text{C}$  for 1 h. The nanocarbon loading was monitored by a Mettler Toledo XPE-26 type analytical microbalance.

As a next step,  $\text{Fe}_2\text{O}_3$  was electrodeposited on the surface of the FTO or GR-coated FTO electrodes. All electrochemical syntheses and measurements were performed using an Autolab PGSTAT302 potentiostat/galvanostat. Nanostructured Ti-doped  $\text{Fe}_2\text{O}_3$  thin films were synthesized using a cathodic electrodeposition procedure adapted from the literature.<sup>[13,71]</sup> A one-compartment, three-electrode electrochemical cell was employed. FTO or GR-coated FTO was used as a working electrode, an Ag/AgCl/3 M NaCl as a reference, and a Pt sheet as a counter electrode. The deposition electrolyte solution contained 5 mM  $\text{FeCl}_3$ , 5 mM NaF, 0.1 M NaCl, 0.1 M  $\text{H}_2\text{O}_2$ , and 2 at%  $\text{Ti}^{4+}$  (added from the aqueous solution of 1 M  $\text{TiCl}_4$ ), which was gently stirred during the synthesis. To protect the spray-coated GR layer from peeling off from the FTO substrate, the concentration of  $\text{H}_2\text{O}_2$  was reduced from 1 to 0.1 M compared to the originally published recipe. Potentiodynamic electrodeposition of  $\text{Fe}_2\text{O}_3$  was carried out at  $50\text{ }^{\circ}\text{C}$  cycling the potential between  $-0.2$  and  $0.4\text{ V}$  using  $200\text{ mV s}^{-1}$  sweep rate. The thickness of the deposited thin films was controlled by the passed charge during the synthesis. After electrodeposition, thin films were thoroughly washed with deionized water and dried under air at room temperature.  $\beta\text{-FeOOH}$  was converted to crystalline  $\alpha\text{-Fe}_2\text{O}_3$  by annealing at  $520\text{ }^{\circ}\text{C}$  under air ( $\Delta T = 5\text{ }^{\circ}\text{C min}^{-1}$ ) for 30 min, which was followed by another heat treatment under Ar at  $700\text{ }^{\circ}\text{C}$  ( $\Delta T = 5\text{ }^{\circ}\text{C min}^{-1}$ ) for 30 min. The purpose of this second heat treatment step was to enhance crystallinity, and it was carried out under Ar to protect the underlying GR layer from oxidation. To characterize the coverage of GR after the synthesis a set of CVs were recorded in a solution containing 5–5 mM  $\text{K}_4[\text{Fe}(\text{CN})_6]$  and  $\text{K}_3[\text{Fe}(\text{CN})_6]$  and 1 M KCl (Figure S13, Supporting Information). Peaks corresponding to the oxidation/reduction of the  $\text{Fe}^{2+}/\text{Fe}^{3+}$  ions were clearly visible on the CV recorded for GR. No peaks were visible on the pristine  $\text{Fe}_2\text{O}_3$  electrode, while slightly higher currents could be seen in the case of the  $\text{Fe}_2\text{O}_3/\text{GR}$  sample. According to this measurement, it was concluded that the GR layer was mostly covered with  $\text{Fe}_2\text{O}_3$  after the synthesis.

**Electrodeposition of FeNiOOH on the Nanocomposite Electrodes:** To prepare FeNiOOH-decorated  $\text{Fe}_2\text{O}_3$  and  $\text{Fe}_2\text{O}_3/\text{GR}$  electrodes, a modified version of the previously described cathodic electrodeposition procedure was employed.<sup>[37]</sup> The deposition electrolyte solution contained 5 mM  $\text{FeCl}_3$ , 3 mM  $\text{NiCl}_2$ , 5 mM NaF, 0.1 M NaCl, and 0.1 M  $\text{H}_2\text{O}_2$ , stirred gently during the synthesis. The potential was cycled between  $-0.49$  and  $0.41\text{ V}$  using  $200\text{ mV s}^{-1}$  sweep rate. Temperature of the deposition solution was kept at  $50\text{ }^{\circ}\text{C}$ . Three cycles gave the highest enhancement in the PEC performance.

**Morphological and Structural Characterization:** A Hitachi S-4700 field emission SEM was operated at an accelerating voltage of 10 kV. TEM images were recorded by using a FEI Tecnai G2 20 X-Twin type instrument, operating at an acceleration voltage of 200 kV. Raman spectra were recorded on a DXR Raman Microscope using a green laser ( $\lambda = 532\text{ nm}$ ), operating at 6.25 mW laser power. UV–vis spectra were recorded on a Shimadzu UV-3600 Plus spectrophotometer in between 300 and 800 nm both in absorbance and reflectance mode. Diffuse reflectance spectra were recorded to construct the Tauc plots. XPS was performed with a SPECS instrument equipped with a PHOIBOS 150 MCD 9 hemispherical analyzer. The analyzer was in FAT mode with 40 eV pass energy (survey scans) and 20 eV pass energy (high resolution scans). The Al K $\alpha$  radiation ( $h\nu = 1486.6\text{ eV}$ ) of a dual anode X-ray gun was used as an excitation source and operated at 150 W power. Ten scans were averaged to get a single high-resolution spectrum, while 20–30 scans were averaged to get a single survey scan. The adventitious carbon peak was at 284.8 eV in all cases. For spectrum evaluation, CasaXPS commercial software package was used.

**Photoelectrochemical Measurements:** LSVs were recorded in a sealed, custom-designed one-compartment, three-electrode quartz cell.  $\text{Fe}_2\text{O}_3$ ,

$\text{Fe}_2\text{O}_3/\text{GR}$ , and  $\text{FeNiOOH}/\text{Fe}_2\text{O}_3/\text{GR}$  on the FTO substrate were used as working electrode, while a Pt sheet and Ag/AgCl/3 M NaCl were employed as counter, and reference electrodes, respectively. The applied light source was a Newport LCS-100 type solar simulator operated at full output. The radiation source was placed 18 cm away from the illuminated working electrode surface ( $100\text{ mW cm}^{-2}$  flux), which was irradiated through a quartz window. The cell contained an aqueous solution of 1 M NaOH which was saturated with Ar. Photovoltammograms were recorded using  $2\text{ mV s}^{-1}$  potential sweep in parallel with periodically interrupted irradiation (0.1 Hz). Oxygen content was monitored during long term measurements by an Orion 3 Star Clark-type oxygen sensor. Calibration of the sensor was performed in DI water, which was saturated with air for one hour and gently stirred prior to the measurement.

IPCE measurements were carried out on a Newport Quantum Efficiency Measurement System (QEPVSI-B) in a single compartment, three-electrode quartz electrochemical cell.  $\text{Fe}_2\text{O}_3$ ,  $\text{Fe}_2\text{O}_3/\text{GR}$ , and  $\text{FeNiOOH}/\text{Fe}_2\text{O}_3/\text{GR}$  on the FTO substrate were used as working electrode, while a Pt sheet and Ag/AgCl/3 M NaCl were employed as counter- and reference electrodes, respectively. The wavelength range was 300–660 nm ( $\Delta\lambda = 20\text{ nm}$  step size). The solution was 1 M NaOH saturated with Ar. The electrodes were held at 0.55 V constant potential during the measurements.

Electrochemical impedance spectra of the pristine  $\text{Fe}_2\text{O}_3$  and  $\text{Fe}_2\text{O}_3/\text{GR}$  layers were recorded in a 1 M NaOH solution saturated with Ar, at OCP, in the 0.1 Hz to 20 kHz frequency range, using a sinusoidal excitation signal (10 mV RMS amplitude). The semicircle portion of each spectrum was fitted using the Nova Software of the Autolab Instrument.

**Intensity-Modulated Photocurrent Spectroscopy:** IMPS was performed on the photoelectrodes using the same cell and electrode setup as described in the case of the photovoltammetry and IPCE measurements but using an AUTOLAB PGSTAT302N potentiostat/galvanostat equipped with an FRA32 module (Metrohm-Autolab) and a LED driver kit (Metrohm-Autolab). Spectra were recorded in the 20 kHz to 0.1 Hz frequency range applying a sinusoidal intensity modulation and bias illumination from a 470 nm blue LED. The amplitude of the modulation was 10%, while the linearity was tested and confirmed by using Lissajous plots. Normalization of the measured signal was carried out by determining the number of the incident photons employing a calibrated silicon photodiode (Thorlabs) and assuming that the LED is monochromatic at its wavelength maximum. From this, the corresponding maximum photocurrent was calculated using the assumption that one photon generates one electron–hole pair.

**Transient Absorption Spectroscopy:** Spitfire Pro (Spectra Physics) amplified laser system was used for transient absorption experiments. The excitation wavelength was 400 nm with average power 400  $\mu\text{W}$ , pulse length 100 fs, and repetition rate 500 Hz. Second harmonic of the amplifier output was generated in BBO crystal and used as pump pulses with central wavelength of 400 nm. For the probe at 800 nm the attenuated amplifier pulses were directly used. The decay traces were fitted by 3 exponential decay function as the main model for the time delayed after 50 fs by using Origin software.

## Supporting Information

Supporting Information is available from the Wiley Online Library or from the author.

## Acknowledgements

This collaborative research received funding from the European Research Council (ERC) under the EU's Horizon 2020 research and innovation program (A.K., E.K., and C.J., Grant Agreement No. 716539). ELI-ALPS is supported by the EU and co-financed by the European Regional Development Fund (GOP-1.1.1-12/B-2012-000, GINOP-2.3.6-15-2015-00001). The authors are grateful for the support from LaserLab



Europe, through campaign LLC002478]. A.H. and T.P. acknowledge financial support from Swedish Research Council and the Swedish Energy Agency. The authors thank Dr. Gergely Ferenc Samu (University of Szeged) for his help with the TA measurements in Lund and the XPS measurements in Szeged, and Dr. Báborka Janáky-Bohner for her support in the manuscript preparation.

## Conflict of Interest

The authors declare no conflict of interest.

## Keywords

composite materials, interface engineering, photoelectrochemistry, solar fuels, transient absorption spectroscopy

Received: March 6, 2020

Revised: May 7, 2020

Published online: June 25, 2020

- [1] N. Lewis, D. Nocera, *Proc. Natl. Acad. Sci. USA* **2006**, *103*, 15729.
- [2] J. Li, N. Wu, *Catal. Sci. Technol.* **2015**, *5*, 1360.
- [3] C. Janáky, K. Rajeshwar, *Prog. Polym. Sci.* **2015**, *43*, 96.
- [4] C. Janáky, E. Kecszenovity, K. Rajeshwar, *ChemElectroChem* **2016**, *3*, 181.
- [5] M. R. Wasielewski, *Chem. Rev.* **1992**, *92*, 435.
- [6] K. Rajeshwar, A. Thomas, C. Janáky, *J. Phys. Chem. Lett.* **2015**, *6*, 139.
- [7] I. Roger, M. A. Shipman, M. D. Symes, *Nat. Rev. Chem.* **2017**, *1*, 0003.
- [8] C. Lohaus, A. Klein, W. Jaegermann, *Nat. Commun.* **2018**, *9*, 4309.
- [9] C. Lohaus, C. Steinert, J. Brötz, A. Klein, W. Jaegermann, *Adv. Mater. Interfaces* **2017**, *4*, 1700542.
- [10] I. S. Cho, H. S. Han, M. Logar, J. Park, X. Zheng, *Adv. Energy Mater.* **2016**, *6*, 1501840.
- [11] S. A. Carminati, A. do Nascimento Barbosa, A. L. M. de Freitas, F. L. Freire, F. L. Souza, A. F. Nogueira, *J. Catal.* **2019**, *372*, 109.
- [12] D. A. Grave, N. Yatomi, D. S. Ellis, M. C. Toroker, A. Rothschild, *Adv. Mater.* **2018**, *30*, 1706577.
- [13] N. Mirbagheri, D. Wang, C. Peng, J. Wang, Q. Huang, C. Fan, E. E. Ferapontova, *ACS Catal.* **2014**, *4*, 2006.
- [14] B. Klahr, S. Gimenez, F. Fabregat-Santiago, J. Bisquert, T. W. Hamann, *Energy Environ. Sci.* **2012**, *5*, 7626.
- [15] K. Sivula, F. Le Formal, M. Grätzel, *ChemSusChem* **2011**, *4*, 432.
- [16] C. Li, Z. Luo, T. Wang, J. Gong, *Adv. Mater.* **2018**, *30*, 1.
- [17] S. Kment, F. Riboni, S. Pausova, L. Wang, L. Wang, H. Han, Z. Hubicka, J. Krysa, P. Schmuki, R. Zboril, *Chem. Soc. Rev.* **2017**, *46*, 3716.
- [18] B. Iandolo, B. Wickman, I. Zorić, A. Hellman, *J. Mater. Chem. A* **2015**, *3*, 16896.
- [19] R. Franking, L. Li, M. A. Lukowski, F. Meng, Y. Tan, R. J. Hamers, S. Jin, *Energy Environ. Sci.* **2013**, *6*, 500.
- [20] C. A. Mesa, A. Kafizas, L. Francàs, S. R. Pendlebury, E. Pastor, Y. Ma, F. Le Formal, M. T. Mayer, M. Grätzel, J. R. Durrant, *J. Am. Chem. Soc.* **2017**, *139*, 11537.
- [21] A. Cots, D. Cibrev, P. Bonete, R. Gómez, *ChemElectroChem* **2017**, *4*, 585.
- [22] Y. Ling, G. Wang, D. A. Wheeler, J. Z. Zhang, Y. Li, *Nano Lett.* **2011**, *11*, 2119.
- [23] S. D. Tilley, M. Cornuz, K. Sivula, M. Grätzel, *Angew. Chem., Int. Ed.* **2010**, *49*, 6405.
- [24] J. Li, S. K. Cushing, P. Zheng, F. Meng, D. Chu, N. Wu, *Nat. Commun.* **2013**, *4*, 1.
- [25] E. Kecszenovity, B. Endrődi, P. S. Tóth, Y. Zou, R. A. W. Dryfe, K. Rajeshwar, C. Janáky, *J. Am. Chem. Soc.* **2017**, *139*, 6682.
- [26] E. Kecszenovity, B. Endrődi, Z. Pápa, K. Hernádi, K. Rajeshwar, C. Janáky, *J. Mater. Chem. A* **2016**, *4*, 3139.
- [27] S. Yin, X. Men, H. Sun, P. She, W. Zhang, C. Wu, W. Qin, X. Chen, *J. Mater. Chem. A* **2015**, *3*, 12016.
- [28] B. Endrődi, E. Kecszenovity, K. Rajeshwar, C. Janáky, *ACS Appl. Energy Mater.* **2018**, *1*, 851.
- [29] Y. H. Ng, A. Iwase, A. Kudo, R. Amal, *J. Phys. Chem. Lett.* **2010**, *1*, 2607.
- [30] F. Meng, J. Li, S. K. Cushing, J. Bright, M. Zhi, J. D. Rowley, Z. Hong, A. Manivannan, A. D. Bristow, N. Wu, *ACS Catal.* **2013**, *3*, 746.
- [31] A. G. Tamirat, W.-N. Su, A. A. Dubale, C.-J. Pan, H.-M. Chen, D. W. Ayele, J.-F. Lee, B.-J. Hwang, *J. Power Sources* **2015**, *287*, 119.
- [32] S. D. A. Carminati, F. L. Souza, A. F. Nogueira, *ChemPhysChem* **2016**, *17*, 170.
- [33] S. Rai, A. Ikram, S. Sahai, S. Dass, R. Shrivastav, V. R. Satsangi, *RSC Adv.* **2014**, *4*, 17671.
- [34] L. He, L. Jing, Z. Li, W. Sun, C. Liu, *RSC Adv.* **2013**, *3*, 7438.
- [35] J. Y. Kim, J. W. Jang, D. H. Youn, J. Yul Kim, E. S. Kim, J. S. Lee, *RSC Adv.* **2012**, *2*, 9415.
- [36] B. Y. Yu, S. Y. Kwak, *J. Mater. Chem.* **2012**, *22*, 8345.
- [37] J. Deng, X. Lv, H. Zhang, B. Zhao, X. Sun, J. Zhong, *Phys. Chem. Chem. Phys.* **2016**, *18*, 10453.
- [38] A. G. Tamirat, W.-N. Su, A. A. Dubale, H.-M. Chen, B.-J. Hwang, *J. Mater. Chem. A* **2015**, *3*, 5949.
- [39] J. E. Thorne, J. W. Jang, E. Y. Liu, D. Wang, *Chem. Sci.* **2016**, *7*, 3347.
- [40] W. Li, S. W. Sheehan, D. He, Y. He, X. Yao, R. L. Grimm, G. W. Brudvig, D. Wang, *Angew. Chem., Int. Ed.* **2015**, *54*, 11428.
- [41] T. H. Jeon, G. Moon, H. Park, W. Choi, *Nano Energy* **2017**, *39*, 211.
- [42] X. Guo, L. Wang, Y. Tan, *Nano Energy* **2015**, *16*, 320.
- [43] P. Peerakiathajohn, J.-H. Yun, H. Chen, M. Lyu, T. Butburee, L. Wang, *Adv. Mater.* **2016**, *28*, 6405.
- [44] Y. W. Phuan, M. N. Chong, T. Zhu, S.-T. Yong, E. S. Chan, *Mater. Res. Bull.* **2015**, *69*, 71.
- [45] S. R. Pendlebury, X. Wang, F. Le Formal, M. Cornuz, A. Kafizas, S. D. Tilley, M. Grätzel, J. R. Durrant, *J. Am. Chem. Soc.* **2014**, *136*, 9854.
- [46] F. Le Formal, S. R. Pendlebury, M. Cornuz, S. D. Tilley, M. Grätzel, J. R. Durrant, *J. Am. Chem. Soc.* **2014**, *136*, 2564.
- [47] Z. Huang, Y. Lin, X. Xiang, W. Rodríguez-Córdoba, K. J. McDonald, K. S. Hagen, K.-S. Choi, B. S. Brunschwig, D. G. Musaev, C. L. Hill, D. Wang, T. Lian, *Energy Environ. Sci.* **2012**, *5*, 8923.
- [48] T. Le Bahers, K. Takanabe, *J. Photochem. Photobiol., C* **2019**, *40*, 212.
- [49] O. Zandi, A. R. Schon, H. Hajibabaei, T. W. Hamann, *Chem. Mater.* **2016**, *28*, 765.
- [50] N. Mirbagheri, D. Wang, C. Peng, J. Wang, Q. Huang, C. Fan, E. E. Ferapontova, *ACS Catal.* **2014**, *4*, 2006.
- [51] R. L. Spray, K.-S. Choi, *Chem. Mater.* **2009**, *21*, 3701.
- [52] A. C. Ferrari, D. M. Basko, *Nat. Nanotechnol.* **2013**, *8*, 235.
- [53] A. M. Jubbs, H. C. Allen, *ACS Appl. Mater. Interfaces* **2010**, *2*, 2804.
- [54] D. L. A. de Faria, V. S. Silva, M. T. de Oliveira, *J. Raman Spectrosc.* **1997**, *28*, 873.
- [55] J.-B. Wu, M.-L. Lin, X. Cong, H.-N. Liu, P.-H. Tan, *Chem. Soc. Rev.* **2018**, *47*, 1822.
- [56] S. Shen, S. A. Lindley, X. Chen, J. Z. Zhang, *Energy Environ. Sci.* **2016**, *9*, 2744.
- [57] G. Wang, X. Shen, J. Yao, J. Park, *Carbon* **2009**, *47*, 2049.
- [58] P. Małucha, M. Pacia, W. Macyk, *J. Phys. Chem. Lett.* **2018**, *9*, 6814.
- [59] J. Tauc, *Mater. Res. Bull.* **1968**, *3*, 37.
- [60] B. Iandolo, B. Wickman, I. Zorić, A. Hellman, *J. Mater. Chem. A* **2015**, *3*, 16896.
- [61] Y. W. Phuan, W.-J. Ong, M. N. Chong, J. D. Ocon, *J. Photochem. Photobiol., C* **2017**, *33*, 54.

- [62] P. S. G. Bassi, T. Sritharan, L. H. Wong, *J. Phys. D: Appl. Phys.* **2018**, 51, 473002.
- [63] S. H. Aboutalebi, A. T. Chidembo, M. Salari, K. Konstantinov, D. Wexler, H. K. Liu, S. X. Dou, *Energy Environ. Sci.* **2011**, 4, 1855.
- [64] W.-D. Zhang, B. Xu, L.-C. Jiang, *J. Mater. Chem.* **2010**, 20, 6383.
- [65] J. G. Radich, A. L. Krenselewski, J. Zhu, P. V. Kamat, *Chem. Mater.* **2014**, 26, 4662.
- [66] J. G. Radich, P. V. Kamat, *ACS Nano* **2013**, 7, 5546.
- [67] A. Tsyganok, D. Klotz, K. D. Malviya, A. Rothschild, D. A. Grave, *ACS Catal.* **2018**, 8, 2754.
- [68] D. K. Lee, K. S. Choi, *Nat. Energy* **2018**, 3, 53.
- [69] T. W. Kim, K.-S. Choi, *Science* **2014**, 343, 990.
- [70] K. George, X. Zhang, A. Bieberle-Hütter, *J. Chem. Phys.* **2019**, 150, 041729.
- [71] R. Schrebler, K. Bello, F. Vera, P. Cury, E. Muñoz, R. del Río, H. G. Meier, R. Córdova, E. A. Dalchiele, *Electrochem. Solid-State Lett.* **2006**, 9, C110.
- [72] L. M. Peter, J. Li, R. Peat, H. J. Lewerenz, J. Stumper, *Electrochim. Acta* **1990**, 35, 1657.
- [73] L. M. Peter, *Chem. Rev.* **1990**, 90, 753.
- [74] C. Zachäus, F. F. Abdi, L. M. Peter, R. van de Krol, *Chem. Sci.* **2017**, 8, 3712.



# Operando cathode activation with alkali metal cations for high current density operation of water-fed zero-gap carbon dioxide electrolyzers

B. Endrődi<sup>1</sup>✉, A. Samu<sup>1</sup>, E. Kecsenovity<sup>1</sup>, T. Halmágyi<sup>1</sup>, D. Sebők<sup>2</sup> and C. Janáky<sup>1,3</sup>✉

**Continuous-flow electrolyzers allow CO<sub>2</sub> reduction at industrially relevant rates, but long-term operation is still challenging. One reason for this is the formation of precipitates in the porous cathode from the alkaline electrolyte and the CO<sub>2</sub> feed. Here we show that while precipitate formation is detrimental for the long-term stability, the presence of alkali metal cations at the cathode improves performance. To overcome this contradiction, we develop an operando activation and regeneration process, where the cathode of a zero-gap electrolyser cell is periodically infused with alkali cation-containing solutions. This enables deionized water-fed electrolyzers to operate at a CO<sub>2</sub> reduction rate matching those using alkaline electrolytes (CO partial current density of 420 ± 50 mA cm<sup>-2</sup> for over 200 hours). We deconvolute the complex effects of activation and validate the concept with five different electrolytes and three different commercial membranes. Finally, we demonstrate the scalability of this approach on a multicell electrolyser stack, with an active area of 100 cm<sup>2</sup> per cell.**

The capture, storage and utilization of carbon dioxide (CO<sub>2</sub>) has entered centre stage in the past decade<sup>1</sup>. Among other strategies, notable attention is devoted to its electrochemical valorization<sup>2,3</sup>, allowing simultaneous decrease in the amounts of CO<sub>2</sub> emitted and the production of raw chemicals, such as carbon monoxide (CO) or formic acid (HCOOH). Employing renewable electricity, the industrial implementation of this technology might be a step in closing the artificial carbon cycle<sup>4,5</sup>. For industrialization, however, several requirements must be fulfilled simultaneously, such as operation at high current density (*j*), high energy efficiency (EE), high product selectivity (Faradaic efficiency, FE) and long-term stability<sup>6,7</sup>. Besides the catalysts<sup>8,9</sup>, electrolyser cell design is equally important in determining these parameters<sup>10</sup>.

To achieve high reaction rate, CO<sub>2</sub> reduction (CO<sub>2</sub>R) must be performed in continuous-flow electrolyzers, encompassing gas diffusion electrodes (GDEs). In such devices, CO<sub>2</sub> gas is fed through a porous cathode support to the catalyst (which together form the GDE)<sup>11,12</sup>. This leads to a thin hydrodynamic boundary layer (a few tens of nm) through which CO<sub>2</sub> must diffuse to reach the catalyst (in contrast to aqueous solutions), allowing high current density operation<sup>12</sup>. Two different types of low-temperature electrolyser cells are widely applied: fuel-cell-like (zero-gap) set-ups, operating without liquid catholyte, where catalyst layers are only separated by a membrane; and microfluidic cells, with continuous liquid electrolyte feed(s). In the latter case, either separate anolyte and catholyte are fed to membrane-separated electrodes, or one solution flows between the anode and the cathode<sup>2</sup>.

In microfluidic cells, highly alkaline conditions allow high current density (>1 A cm<sup>-2</sup>) production of CO<sup>13</sup>, ethylene<sup>14,15</sup>, methane<sup>16,17</sup> and multi-carbon products<sup>18</sup>. While these results are very promising, the scale-up of microfluidic electrolyzers seems challenging<sup>2</sup>. In our opinion, the use of zero-gap electrolyser cells is more promising for industrial applications. Such set-ups also offer a straightforward implementation of alternative anode reactions,

such as glycerol oxidation, to form high-value products on both electrodes, with high EE<sup>19–21</sup>.

Anion-exchanging polyelectrolyte membranes (AEM) are typically used as separators in zero-gap electrolyser cells to avoid high local H<sup>+</sup> concentration and therefore excessive H<sub>2</sub> evolution on the cathode. The direction of ion conduction is from the cathode to the anode (through the membrane), which is maintained partially by the electrogenerated OH<sup>-</sup> ions, but mostly by CO<sub>3</sub><sup>2-</sup> and HCO<sub>3</sub><sup>-</sup> ions formed in the reaction of CO<sub>2</sub> and OH<sup>-</sup> (refs. <sup>22,23</sup>). Consequently, AEM-based operation should be independent of whether an alkaline solution or pure water is fed to the anode (given that the anode catalyst functions in both media). Still, in contrast to the wealth of alkaline studies<sup>10,22–26</sup>, to the best of our knowledge, there is no study in the literature where a zero-gap electrolyser cell with a commercial membrane is operated with water anolyte at high CO<sub>2</sub>R current. In one single study, high current density was ensured using an experimental membrane<sup>27</sup>.

In this study, our aim was to understand which parameters dictate high reaction rate and product selectivity in AEM-based zero-gap electrolyzers and why it is generally required to use concentrated alkaline anolytes<sup>28</sup>. Cation cross-over from the anode to the cathode was identified as a major contributor to the high performance, but it also resulted in precipitate formation in the cathode GDE. To turn this challenge into an opportunity, we designed a scalable process and experimental set-up to operate electrolyser cells with different commercial membranes and pure water anolyte at high current density, by periodically infusing the cathode with different alkali cation-containing solutions.

## Performance fading due to precipitate formation

After longer operation of a zero-gap electrolyser cell (Fig. 1a and Supplementary Fig. 1) with alkaline anolyte, salt precipitates at the cathode, gradually decreasing its performance<sup>24,25,29</sup>. We also experienced this phenomenon (Supplementary Note 1) in the form of

<sup>1</sup>Department of Physical Chemistry and Materials Science, Interdisciplinary Excellence Centre, University of Szeged, Szeged, Hungary. <sup>2</sup>Department of Applied and Environmental Chemistry, Interdisciplinary Excellence Centre, University of Szeged, Szeged, Hungary. <sup>3</sup>ThalesNanoEnergy Zrt, Szeged, Hungary. ✉e-mail: [endrődib@chem.u-szeged.hu](mailto:endrődib@chem.u-szeged.hu); [janaky@chem.u-szeged.hu](mailto:janaky@chem.u-szeged.hu)

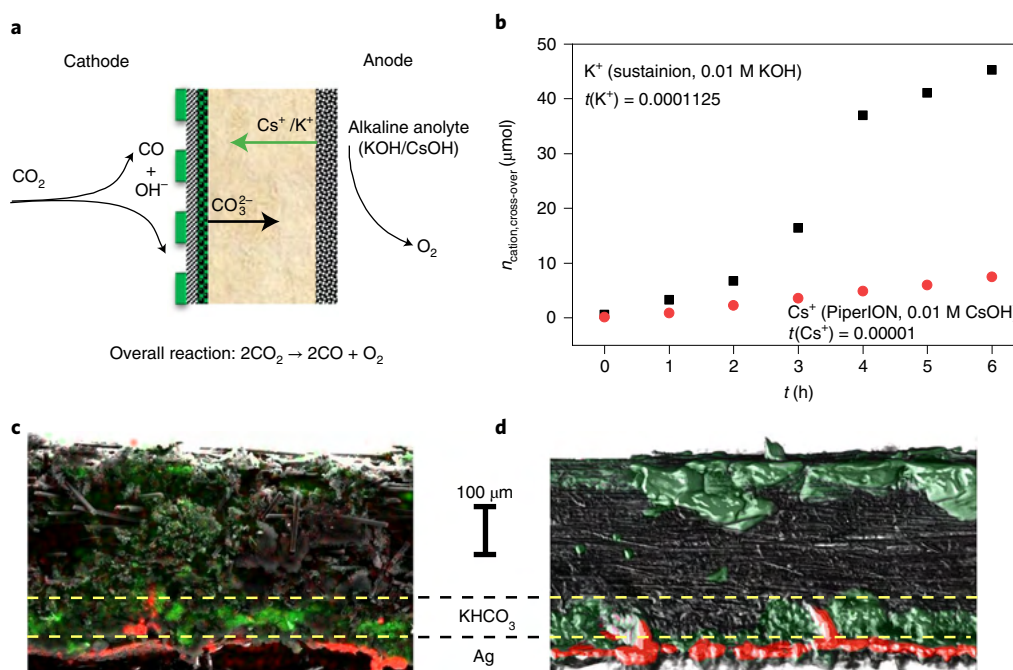


**Fig. 1 | Unintended cation cross-over and precipitate formation in alkaline anolyte-fed zero-gap  $\text{CO}_2$  electrolyzers.** **a**, Schematic illustration of the operation of an AEM-separated zero-gap  $\text{CO}_2$  electrolyser cell with alkaline anolyte. **b**, Ion-chromatographic quantification of  $\text{K}^+$  and  $\text{Cs}^+$  cross-over through different commercially available AEMs during  $\text{CO}_2$  electrolysis in a zero-gap electrolyser cell. **c,d**, Cross-section SEM-EDX (**c**) and micro-CT images (**d**) of a GDE after continuous  $\text{CO}_2$  electrolysis in a zero-gap cell ( $T = 50^\circ\text{C}$ , 1 M KOH anolyte,  $\Delta U = 3.0\text{ V}$ ). The red and green colours in the SEM-EDX and micro-CT images represent Ag and K atoms, respectively. Experiments were repeated on separate cell assemblies independently three times, with similar results.

continuous product formation current decrease (Supplementary Fig. 2a) and/or pressure build-up. The formation of  $\text{KHCO}_3$  and  $\text{K}_4\text{H}_2(\text{CO}_3)_3 \cdot 1.5\text{H}_2\text{O}$  precipitate (Supplementary Fig. 2b) was confirmed by X-ray diffraction analysis and subsequent Rietveld refinement (Supplementary Fig. 2c). The second compound typically forms through the  $\text{CO}_2$  sorption of  $\text{K}_2\text{CO}_3$ , when large excess of  $\text{CO}_2$  is available<sup>30,31</sup>. This precipitate forms because of the unintended cation cross-over through the AEM from the anolyte to the cathode (as verified by ion chromatography (Fig. 1b)), where it reacts with the  $\text{CO}_2$  feed and the electrogenerated  $\text{OH}^-$ .

Scanning electron microscopy–energy-dispersive X-ray micro-analysis (SEM–EDX) and computed microtomography (micro-CT) studies revealed that precipitation occurs not only on the backside of the GDE (that is, in the gas flow channels), but also in its deeper regions (Fig. 1c). A compact layer of the precipitate was observed in the microporous layer and at the junction of the microporous and macroporous layers (see Supplementary Figs. 3–5, and discussion therein). This hampers  $\text{CO}_2$  from reaching the catalyst surface, explaining the continuously decreasing product formation rate (Supplementary Fig. 6).

The state-of-the-art method to overcome this issue is to rinse the cathode with water<sup>24,32,33</sup>. The performance of the cell, however, cannot be fully restored using this method, as water can only wash the deposits from the backside of the GDE, and cannot penetrate the hydrophobic gas diffusion layer (GDL), unless excessive force (pressure) is applied. Such pressure would in turn damage the GDE structure, causing electrode flooding<sup>24,34</sup>. Decreasing the anolyte concentration extends the operation to prolonged timescales. The cross-over of  $\text{K}^+$  or  $\text{Cs}^+$  ions (Fig. 1b), and the consequent precipitate formation and performance fading still occur (see Supplementary Fig. 6 and discussion therein). Increasing the humidity of the  $\text{CO}_2$  gas stream is another alternative mitigation strategy, but it changes the overall operation of the cell<sup>24,29</sup>. An elegant

solution to this problem would be to operate such electrolyser cells with pure water anolyte, inherently preventing precipitate formation in the cathode GDE.

### Operation of $\text{CO}_2$ electrolyzers with pure water anolyte

Using pure water as anolyte instead of 0.1 M KOH the current density drops to one-third ( $100\text{ mA cm}^{-2}$  versus  $300\text{ mA cm}^{-2}$ ; Supplementary Fig. 7a). This large difference appears also in the low frequency limit of the impedance spectra (Supplementary Fig. 7b), which is a measure of the derivative of the current–voltage curve. In contrast, the high frequency limits do not differ much, being around  $1\ \Omega\text{ cm}^2$  for both, which is comparable with the values reported for similar systems<sup>10,27</sup>. This value is related to the total cell resistance, including the membrane, the contribution of which to the total impedance spectra was found to be ohmic in our control experiments (Supplementary Note 2 and Supplementary Fig. 8). The similarity in this value is not surprising, since the membrane conductance is mostly affected by the operational conditions and the charge-transporting ions<sup>35,36</sup>. Analysing the anode gas composition and the complete mass balance of the process,  $\text{CO}_3^{2-}$  was identified as the majority charge carrier through the AEM, irrespective of the anolyte used (Supplementary Note 3 and Supplementary Fig. 9). The transference number of the cations remains in the range  $10^{-4}$ – $10^{-5}$  for both  $\text{Cs}^+$  and  $\text{K}^+$ , which practically excludes their contribution to the membrane conductivity (see Fig. 1b and related discussion in Supplementary Note 4).

As both the membrane resistance and the charge carriers are the same in the two cases, the big difference in the currents with and without KOH in the anolyte must be attributed to changes at the cathode and/or anode interfaces. With pure water anolyte, two arcs can be observed on the impedance spectra (Supplementary Fig. 7b). In general, these are due to interfacial capacitances and charge transfer resistances on any of the electrodes; their exact origin is

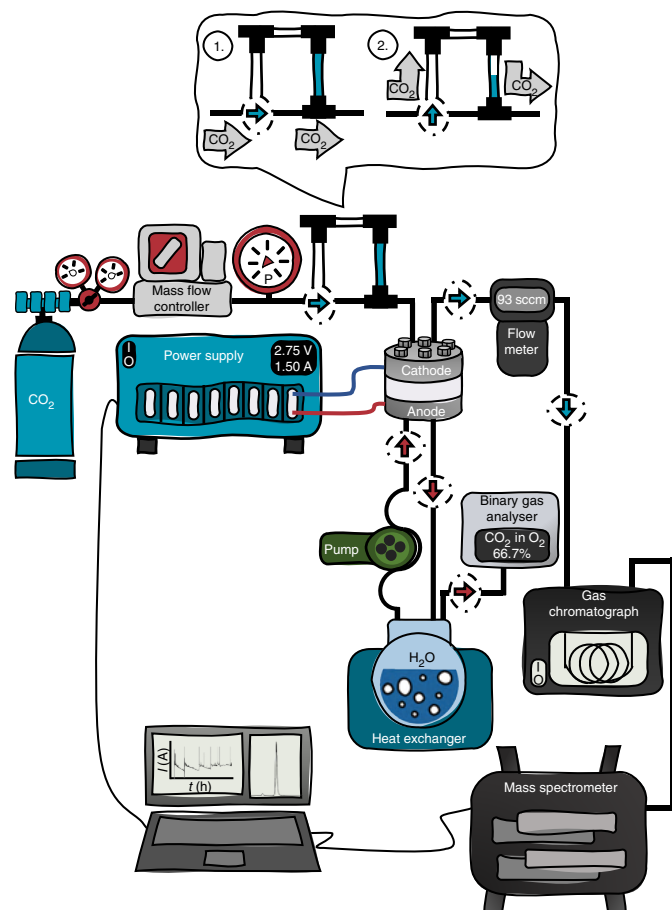


**Fig. 2 | Schematic piping and instrumentation diagram of the test framework employed.** In the inset (top), '1' shows the default positions of the manual valves, forming a continuous gas path to the cell and bypassing the activation loop. Turning the valves into position '2', the gas is driven through the activation loop, carrying the activation fluid into the cell.

beyond the present scope of this study. Notably, the sum of the spans ('diameters') of these arcs is about three times larger when the cell is operated with pure water anolyte instead of 0.1 M KOH, indicating a higher total charge transfer resistance of the electrode processes. Notably, in a zero-gap cell the effect of the membrane and the catalyst/ionomer layer cannot be fully separated. In all our analyses, we consider the ionomer and the catalyst/ionomer/membrane interfaces to belong to the 'catalyst' and not to the membrane.

### Activating the cathode catalyst by infusion with alkali cation-containing solutions

Considering the results of previous studies on the promoting effect of alkali cations in electrochemical  $\text{CO}_2\text{R}$ <sup>37–44</sup>, cation permeation through the membrane from the anolyte might contribute to achieving high reaction rates (this is absent in the case of water-based operation). In microfluidic electrolyzers operating with liquid catholyte, alkali ions are inherently present around the cathode catalyst, which might (partly) explain why these systems outperform their zero-gap counterparts in terms of the achievable current densities<sup>13,45</sup>. Furthermore, a long activation period (~60 min) was observed for zero-gap cells operated with dilute alkaline anolytes (Supplementary Fig. 10), indicating that cations slowly crossing the AEM (note the small transference number in Fig. 1b) and reaching the cathode surface have a boosting effect on the operation.

To validate this notion, we designed a process and an experimental set-up allowing the injection of electrolyte solutions into the  $\text{CO}_2$  feed, which is, in turn, pushed through the cathode GDE by the gas stream (Fig. 2). This solution infusion method (referred to hereafter as 'regeneration') allows the efficient removal of the precipitate potentially formed in the GDE (Fig. 1c), and also introduces alkali metal cations to the cathode (referred to hereafter as 'activation'). Repeatedly performing the activation, each new portion of the solution dissolves any precipitate from the GDE that is incidentally formed in/after the previous activations. During the solution infusion, the  $\text{CO}_2$  gas feed pushes the 'solution plug' through the cell, and therefore there is only a limited contact area between the solution and the gas where precipitate might form in situ. This leads to a constant presence of the activating ions at the cathode GDE, but avoids accumulation.

To enable the electrolyte solution to reach the catalyst layer, the composition of the solvent mixture must be tailored to the wetting properties of the GDE. Contact angles were determined for a series of solvent mixtures (Fig. 3a). As the GDL in our case is a hydrophobic carbon paper, a solvent mixture of 25 v/v% isopropanol in water was employed for further studies. This wets the GDE properly without dissolving its polytetrafluoroethylene (PTFE) content or damaging the AEM (at least within the studied timeframe), and it dissolves the studied salts.

Upon activating the cathode GDE with 10 cm<sup>3</sup> (approximately 50 times the free volume of the cathode compartment) of 0.5 M KOH solution, and meanwhile operating the electrolyser cell with pure water anolyte, a threefold increase in the CO formation rate ( $j_{\text{CO}}$ ) was observed (Fig. 3b–d). For the PiperION membrane (Fig. 3c),  $j_{\text{CO}} = 500\text{--}550 \text{ mA cm}^{-2}$  represents higher current density than the state-of-the-art water anolyte-operated  $\text{CO}_2$  electrolyser cell<sup>27</sup>. The current does not drop after the activating solution leaves the cell, but remains relatively stable, with a slow decay (discussed later). Importantly, this effect was very similar for three commercial membranes (Sustainion X37-50, PiperION TP-85, Fumasep FAB-PK-130) of very diverse chemical composition, thickness, etc. Except for a short transient period, the CO formation selectivity does not drop upon excess liquid injection in the cathode compartment, and it even increases for Sustainion (Fig. 3b, from 70 to 85% FE) and PiperION (Fig. 3c, from 55 to 85% FE) membrane-containing cells.

For comparison, we performed similar activation experiments with pure aqueous solutions (that is, no isopropanol content). A less pronounced activation was seen, albeit with very large variance (Supplementary Fig. 11). This is rooted in the hydrophobicity of the GDE, which only allows the aqueous activation solution to reach the catalyst surface if numerous imperfections (for example, cracks) are present in the structure. Again, tailoring the solvent mixture is crucial for wetting the deeper regions of the GDE without damaging its structure.

Another important aspect is the necessity of the electric field during the activation: if we inject the activation solution without polarization and start the electrolysis subsequently, there is only a minor current increase. This indicates that, beyond simple physical interactions, electrosorption of the cations on the negatively polarized Ag catalyst particles might be a major contributor.

### Mechanism of the activation process

Performing the cathode activation on the water-fed cell increases the current to a level almost identical to that measured with 0.1 M KOH anolyte (Fig. 4a). While the high-frequency impedance of the water-fed cell remains unchanged, the gross charge transfer resistance decreases to a similar value to that detected with alkaline anolyte (Fig. 4b and Supplementary Fig. 12, with further discussion in Supplementary Note 5). As the same anode catalyst ( $\text{IrO}_x$ ) is routinely employed in proton-exchange membrane water electrolyzers at high current densities ( $1\text{--}3 \text{ A cm}^{-2}$ )<sup>46</sup>, it is reasonable to assume

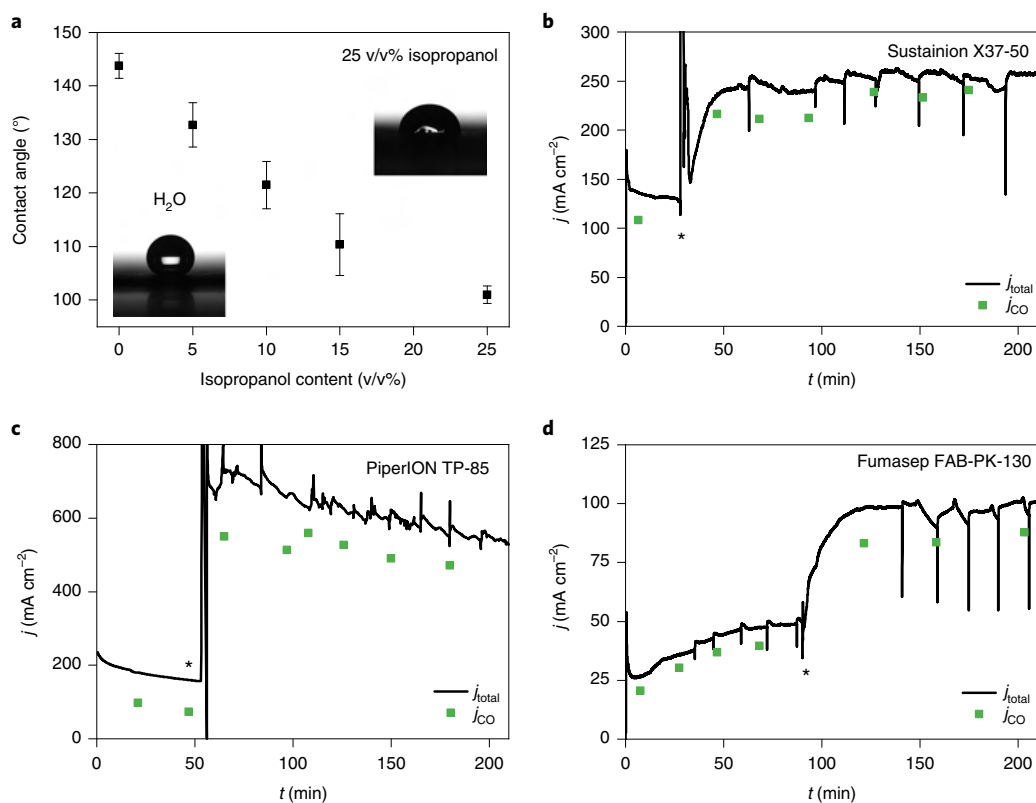


**Fig. 3 | Cathode activation using different commercially available AEMs. a**, Contact angles of different water/isopropanol solvent mixtures on the microporous side of a Sigracet 39BC GDL. **b–d**, Chronoamperometric curves and CO formation partial current densities ( $T_{cathode} = 60\text{ }^{\circ}\text{C}$ ,  $12.5\text{ cm}^3\text{ cm}^{-2}\text{ min}^{-1}$   $\text{CO}_2$  feed rate, pure water anolyte) measured using Sustainion X37-50 ( $\Delta U = 3.1\text{ V}$ ) (**b**), PTFE-reinforced 15- $\mu\text{m}$  thick PiperION TP-85 ( $\Delta U = 3.2\text{ V}$ ) and Fumasep FAB-PK-130 ( $\Delta U = 3.1\text{ V}$ ) AEMs (**c**). Solutions of  $10\text{ cm}^3$  of  $0.5\text{ M KOH}$  (for **b** and **d**) or  $0.5\text{ M CsOH}$  (**c**) in 1:3 isopropanol/water mixture were used to activate the cathode at the times marked with asterisks in the figures. Experiments were repeated on separate cell assemblies independently at least three times, with similar results. The values in **a** are the mean value of three independent measurements, together with the calculated standard deviations.

that this difference is mostly related to the cathode catalyst. To safely exclude the contribution of the anode process (Supplementary Note 6), we have recorded polarization curves of  $\text{IrO}_x$ /PiperION ionomer layers in different electrolyte solutions (that is,  $\text{NaOH}$ ,  $\text{KOH}$ ,  $\text{CsOH}$ ; Supplementary Fig. 13a). The polarization curves overlap, showing that the electroactivity of  $\text{IrO}_x$  is not affected by these cations detectably. This confirms that the eventual penetration of small amounts of the activation solution to the anode side cannot be responsible for the enhanced performance.

The activation is fully reversible: rinsing the cathode GDE with an isopropanol/water mixture (without any dissolved electrolyte) in the absence of polarization restores the current to its initial low value within 1 min, which can be increased again by repeating the activation (Fig. 4c). This repeatable instantaneous activation–deactivation further suggests that the performance enhancement is mostly related to the change in the cathode reaction kinetics. If the electrolyte penetration to the anode side (upon activation) were a major contributor, a single rinsing of the cathode side could not have such a rapid effect. Additional control experiments were carried out without anolyte recirculation, to avoid the possible accumulation of cations or change in the pH. The activation phenomenon occurred in these cases as well (Supplementary Fig. 13b). All these observations together imply that the activation mostly affects the cathode interface.

To take a closer look at processes occurring during activation, we followed the product stream composition in quasi-real time via mass spectrometry, while also monitoring the pressure in the  $\text{CO}_2$

inlet piping (Fig. 4d). The pressure trace shows that it takes about 50 seconds for the activating solution to leave the cell (indicated by a rapid pressure drop after the initial increase). While the cathode compartment is filled with the activation fluid it is deprived of  $\text{CO}_2$ , resulting in high  $\text{H}_2$  formation rate and decreased  $\text{CO}_2$  and  $\text{CO}$  partial pressures in the product gas stream (lower panel of Fig. 4d). When the liquid leaves the cell, the  $\text{CO}$  partial pressure (hence  $j_{\text{CO}}$ ) immediately increases, and meanwhile the  $\text{H}_2$  concentration decreases. Both stabilize in 2 minutes after the activation, demonstrating that the activation is instantaneous (and therefore related to the cathode GDE and its interface with the AEM). Finally, the activated state does not diminish rapidly, which would be expected if entrapped cations leaving the AEM were mostly responsible for the activation, as their amount could only be finite in the thin membranes.

### Factors determining the efficiency of the cathode activation

The activation process influences the pH and ionic strength at the cathode (at least temporarily), and the infused ions can also adsorb onto the catalyst surface. To separate the effects of these parameters, we performed two sets of experiments: one in which different alkali metal hydroxides (that is, different cations) were employed (Fig. 5a and Supplementary Fig. 14a,c), and another in which solutions with constant  $\text{K}^+$  concentration, but with different anions, were injected (Fig. 5b and Supplementary Fig. 14b,d). The activation becomes more pronounced in the order  $\text{NaOH} \ll \text{KOH} < \text{CsOH}$ ,

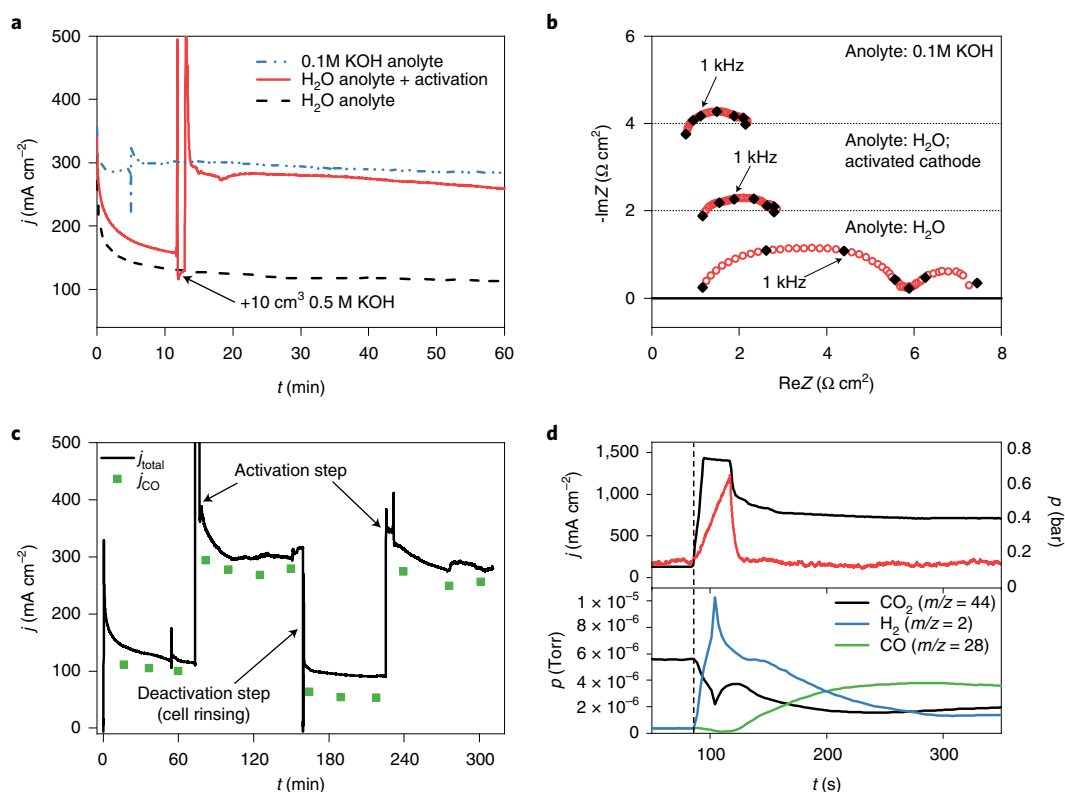


**Fig. 4 | Mechanism and reversibility of cathode activation.** **a, b**, Chronoamperometric curves (**a**) and EIS spectra (**b**) recorded before and after activating the cathode GDE with  $10 \text{ cm}^3$  of 0.5 M KOH solution in 1:3 isopropanol/water mixture (Sustainion membrane,  $\Delta U = 3.1 \text{ V}$ ,  $T_{\text{cathode}} = 60 \text{ }^\circ\text{C}$ ,  $12.5 \text{ cm}^3 \text{ cm}^{-2} \text{ min}^{-1}$   $\text{CO}_2$  feed rate). ReZ and ImZ denote the real and imaginary components of the impedance (Z). **c**, Chronoamperometric curve and CO formation partial current density measured under identical conditions as in **a**. The cathode GDE was activated at the marked times with  $10 \text{ cm}^3$  of 0.5 M KOH solution in 1:3 isopropanol/water mixture, while it was rinsed with  $10 \text{ cm}^3$  of 1:3 isopropanol/water mixture to deactivate it. **d**, Time-resolved current density and product stream composition change during, and immediately after, activating the electrolyser cell (with  $3 \text{ cm}^3$  of 1 M CsOH solution in 1:3 isopropanol/water mixture,  $\Delta U = 3.2 \text{ V}$ ,  $T_{\text{cathode}} = 60 \text{ }^\circ\text{C}$ ,  $12.5 \text{ cm}^3 \text{ cm}^{-2} \text{ min}^{-1}$   $\text{CO}_2$ , PiperION membrane). In the upper panel, the pressure in the  $\text{CO}_2$  inlet pipe during activation is indicated. Experiments were repeated on separate cell assemblies independently at least three times, with similar results.

whether considering the  $j_{\text{CO}}$  values (Fig. 5a), the onset voltage or the slope of the linear sweep voltammetry curves (Supplementary Fig. 14a) or the decrease in the arc diameter in the impedance spectra (Supplementary Fig. 14c). As the pH and ionic strength of these solutions are identical, these measurements directly prove the promoting effect of  $\text{K}^+$  and  $\text{Cs}^+$  ions, and the less considerable effect of  $\text{Na}^+$  ions in the electrochemical  $\text{CO}_2\text{R}$ , in accordance with theoretical<sup>37,41,42</sup> and experimental results<sup>38–40,43,44</sup>. The same trend was found when operating the same cell with NaOH, KOH and CsOH anolytes (Supplementary Fig. 15).

To investigate the effect of the local pH change caused by the activation, solutions of different potassium salts were infused. Although some differences can be seen, they are less striking compared to the case of different cations (Fig. 5b and Supplementary Fig. 14b,d). The current density increase followed the order  $\text{KNO}_3 < \text{K}_2\text{CO}_3 < \text{KOH}$ , suggesting that the effect of the local pH during the activation cannot be fully ruled out. The same trend was found for the double-layer capacitance of the catalyst/ionomer layer studied in the solution of these salts (Supplementary Fig. 16). These differences might stem from the pH-dependent structure of the ionomer (it is a polyelectrolyte) or from the differences in the double-layer structure (and therefore the specific capacitance) in the different solutions. In any case, this can affect the cation adsorption process during the transient period of infusion, and, in turn, the amount of adsorbed alkali metal cations.

The activation efficiency scales with the concentration (up to 0.5 M, Supplementary Fig. 17) and volume (up to  $2 \text{ cm}^3$ , Supplementary Fig. 18) of the electrolyte solution. Finally, the

membrane and gross interfacial charge transfer resistance decreases continuously with the increasing temperature (Supplementary Fig. 19), indicating room for further performance enhancement through careful process engineering.

### Long-term operation

Long-term electrolysis with pure water feed at the anode was performed with a PiperION membrane-containing cell for 224 hours (Fig. 6a,b). Meanwhile the cathode was activated with  $5 \text{ cm}^3$  of 1.0 M CsOH solution after every 12 hours. The initial (before activation) measured  $j_{\text{CO}} \approx 120 \text{ mA cm}^{-2}$  increased to  $j_{\text{CO}} \approx 350 \text{ mA cm}^{-2}$  after the first activation. This increased further when the activation was repeated after 24 and 36 hours, and subsequently it remained stable at  $j_{\text{CO}} = 420 \pm 50 \text{ mA cm}^{-2}$  (with  $\sim 90\%$   $\text{FE}_{\text{CO}}$ ) for over 200 hours (eight days) of continuous operation. The regular spikes on the chronoamperometric curve (every 12 hours) belong to the activation processes (Fig. 6a), while the initial spikes (in the first 25 hours) represent irregular water release from the cell. Clearly, there is an initial period when the water management of the cell stabilizes. The  $\text{FE}_{\text{CO}}$  first decreases during the activation steps, as the large transient current is associated with the increased  $\text{H}_2$  evolution (see also Fig. 4d).  $\text{FE}_{\text{CO}}$  is then restored (or even increased), while  $j_{\text{CO}}$  increases compared to its value before activation. The single-pass conversion was calculated to be 23% (see calculations in Supplementary Note 7), about 11 times larger than that of the reported state-of-the-art water-based  $\text{CO}_2$  electrolyser<sup>27</sup>. A similar experiment was performed with the Sustainion X37-50 membrane, where the electrolyser

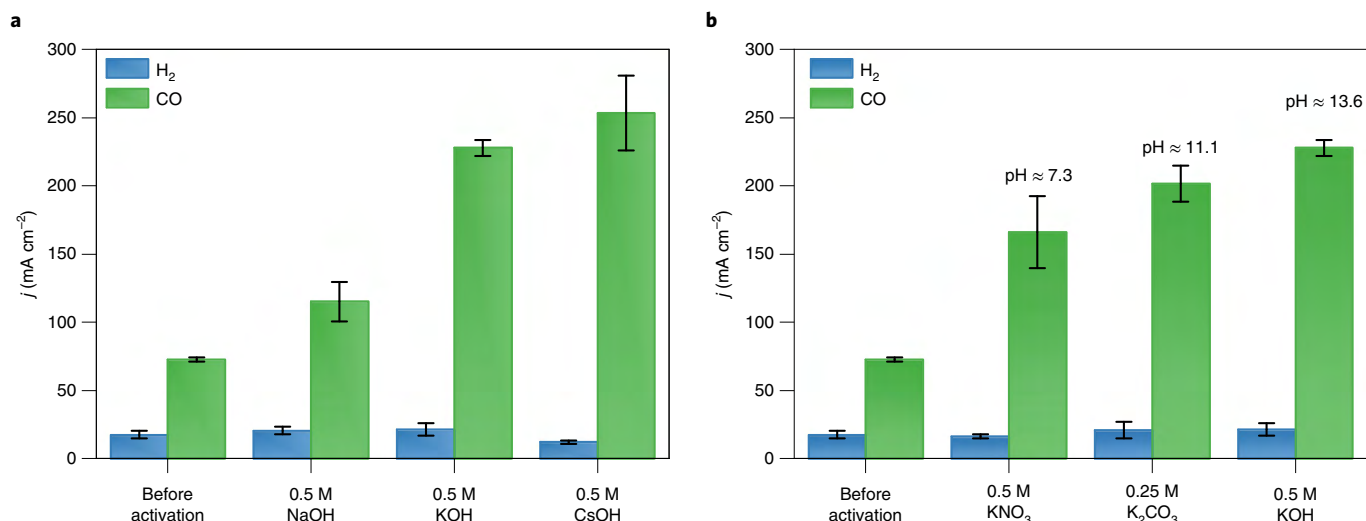


**Fig. 5 | Deconvolution of the complex effect of the activating electrolyte.** **a, b**, Partial current densities for CO and H<sub>2</sub> production during constant-voltage electrolysis with water analyte, after cathode activation using 10 cm<sup>3</sup> solution (in 1:3 isopropanol/water mixture) of different alkali metal hydroxides ( $c=0.5$  M) (**a**) and different potassium salts ( $c(K^+)=0.5$  M) (**b**). The cell was operated at  $\Delta U=3.1$  V,  $T_{\text{cathode}}=60$  °C with  $12.5$  cm<sup>3</sup> cm<sup>-2</sup> min<sup>-1</sup> CO<sub>2</sub> feed rate, using a Sustainion membrane in the cell. The plotted values are the mean from three gas composition measurements (gas chromatography analysis), together with the calculated standard deviations. All experiments were repeated independently on separate cell assemblies three times, with similar results.

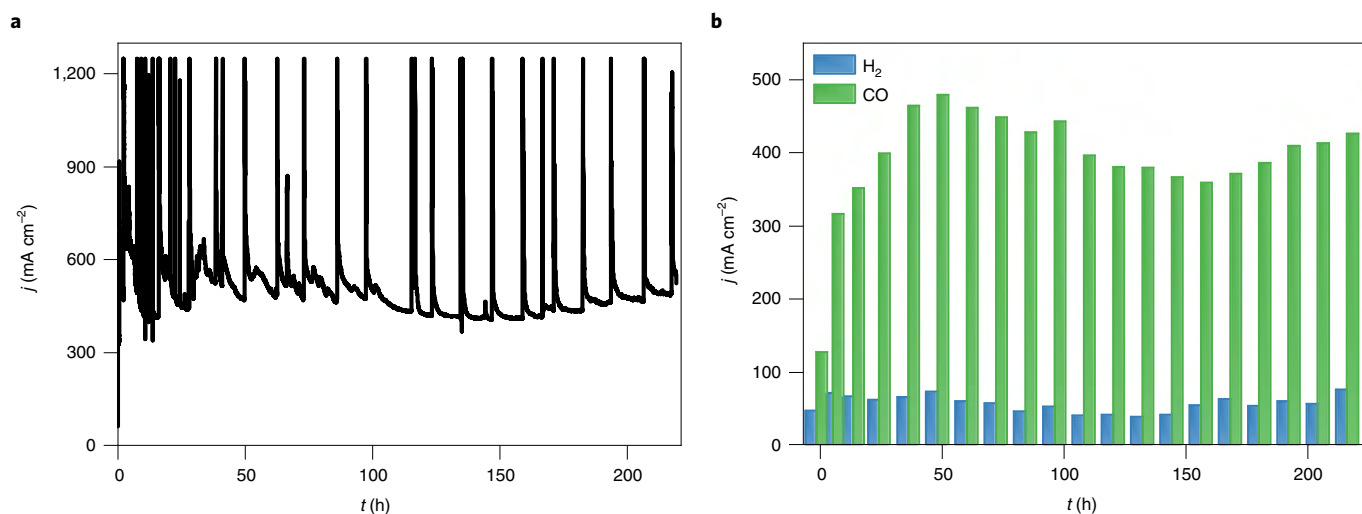


**Fig. 6 | Long-term operation of a CO<sub>2</sub> electrolyser with water analyte and periodic activation.** **a, b**, Total current density (**a**) and CO and H<sub>2</sub> partial current densities (**b**) during constant-voltage electrolysis, using a PTFE-reinforced 15-μm thick PiperION TP-85 membrane-separated cell ( $\Delta U=3.2$  V,  $T=60$  °C water analyte,  $12.5$  cm<sup>3</sup> cm<sup>-2</sup> min<sup>-1</sup> CO<sub>2</sub> feed rate). The cathode was activated with 5 cm<sup>3</sup> of 1 M CsOH solution in 1:3 isopropanol/water mixture after every 12 h of the electrolysis. Long-term experiments (over 100 h) were repeated on separate cell assemblies independently five times, with similar results.

was operated for 10 hours. After activation, the  $j_{\text{CO}}$  increased from  $120$  mA cm<sup>-2</sup> to  $220$  mA cm<sup>-2</sup>, which has not changed in the first five hours, followed by a slight decrease to  $j_{\text{CO}} \approx 200$  mA cm<sup>-2</sup> (Supplementary Fig. 20).

Importantly, no physical precipitate formation was observed in the cells, which were activated repeatedly (see an example for a cell operated for over 100 hours in Supplementary Note 8 and Supplementary Fig. 21). The lack of precipitate formation is attributed to the inherent nature of the activation process, where the applied solvent mixture can dissolve and remove the previously formed precipitate crystals. Therefore, while a small amount of alkali cations is present after the activation, no accumulation occurs.

The presence of cations in the cathode GDE can also be ensured by other methods. For example, controlled cross-over from the anolyte can provide the proper amount of alkali cations to the cathode, especially if combined with periodic regeneration of the cathode with the proper solvent mixture (Supplementary Fig. 6). As a further example, the Ag catalyst layer can be deposited from alkali metal ion-containing suspensions. In this way, the promoter ions are inherently present on the catalyst surface and within the ionomer layer. The electrochemical performance and impedance spectrum of the electrolyser cell assembled with this catalyst layer, and operated with water analyte, are similar to those of the activated cells, presented previously. The performance, however, decreased



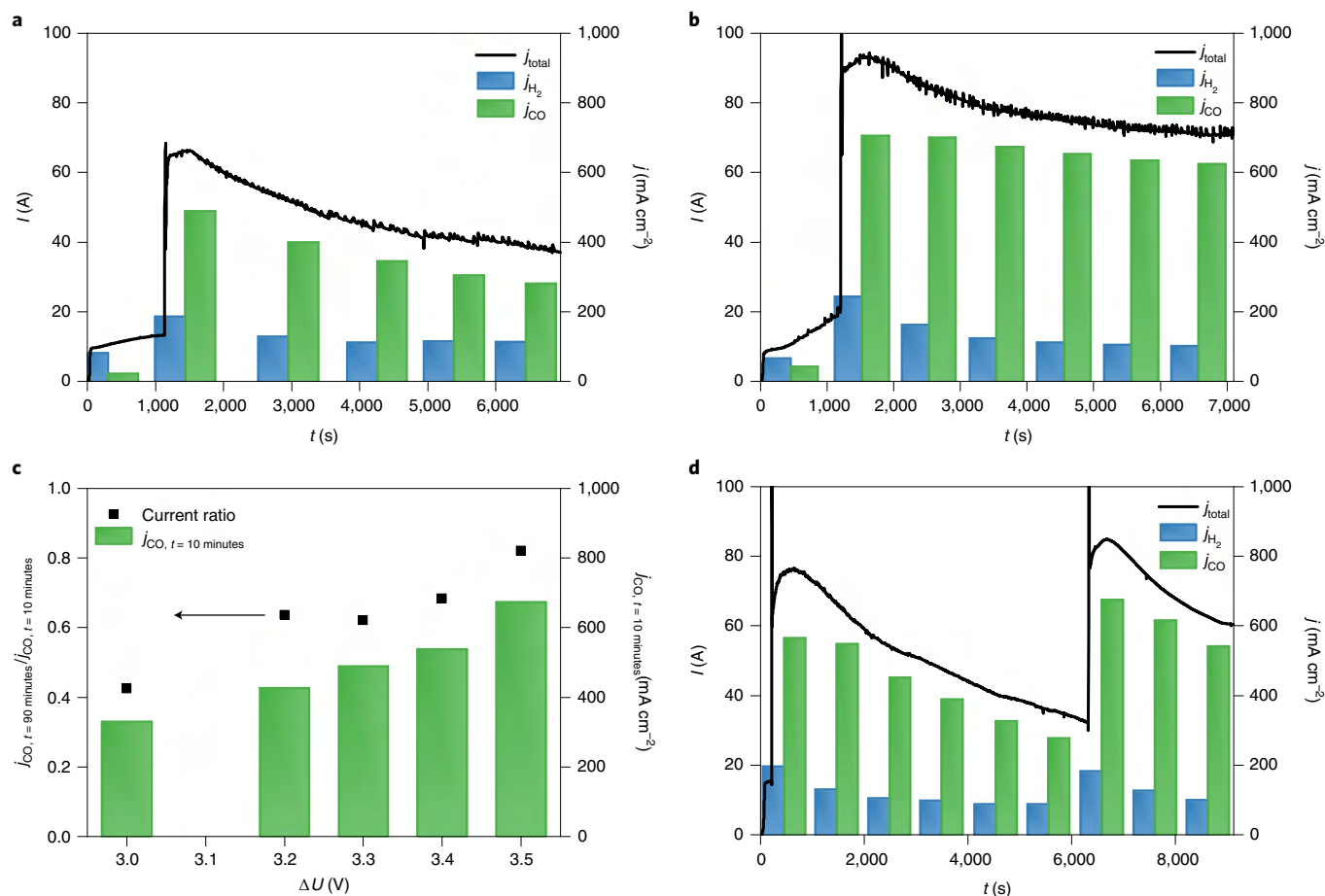


**Fig. 7 | Cathode activation experiments in larger electrolyser cells and stack.** **a, b**, Chronoamperometric measurements on a single-layer electrolyser cell of area  $A = 100 \text{ cm}^2$  ( $T = 60^\circ \text{C}$ , water anolyte,  $12.5 \text{ cm}^3 \text{ cm}^{-2} \text{ min}^{-1}$   $\text{CO}_2$  feed) at  $\Delta U = 3.3 \text{ V}$  (**a**) and  $\Delta U = 3.5 \text{ V}$  (**b**). **c**,  $\text{CO}$  partial current densities 10 min after performing the cathode activation ( $20 \text{ cm}^3$  of  $1 \text{ M CsOH}$  solution in  $1:3$  isopropanol/water mixture) and the ratio of  $\text{CO}$  formation partial current densities 90 and 10 min after performing the cathode activation, recorded at different cell voltages. **d**, Chronoamperometric measurement on a three-layer electrolyser cell stack of  $A = 100 \text{ cm}^2$  ( $T = 60^\circ \text{C}$ , water anolyte,  $12.5 \text{ cm}^3 \text{ cm}^{-2} \text{ min}^{-1}$   $\text{CO}_2$  feed, cathode activation with  $60 \text{ cm}^3$  of  $1 \text{ M CsOH}$  solution in  $1:3$  isopropanol/water mixture) at  $\Delta U = 9.9 \text{ V}$ . Experiments were repeated on separate cell assemblies independently three times, with similar results.

with time, as the  $\text{K}^+$  ions gradually leached out from the catalyst layer (Supplementary Fig. 22).

### Operating larger cells and cell stacks with water anolyte

The scalability of the cathode activation approach was demonstrated on a cell having an active surface area of  $100 \text{ cm}^2$ , and on a three-layer electrolyser stack formed therefrom (Fig. 7 and Supplementary Fig. 23). The cathode activation boosted the  $j_{\text{CO}}$  in all experiments, and  $j_{\text{CO}}$  also increased gradually with the applied cell voltage (Fig. 7a–c). Importantly,  $j_{\text{CO}} = 450 \text{ mA cm}^{-2}$  was measured at  $\Delta U = 3.2 \text{ V}$  (Fig. 7c), which rivals the results recorded on our smaller cell (Figs. 3c and 6). This value further increased to  $j_{\text{CO}} = 650 \text{ mA cm}^{-2}$  at  $\Delta U = 3.5 \text{ V}$  (Fig. 7b), which is close to the best value measured in the same electrolyser cell using  $0.1 \text{ M CsOH}$  anolyte<sup>10</sup>. Importantly, the rate of the current decay after the activation decreased with the increasing cell voltage (that is, the effect of activation lasts longer at higher cell voltages (Fig. 7c)). This again confirms that the activation occurs via the electrosorption of the cations at the negatively polarized cathode.

The activation was also performed in a three-cell stack at  $\Delta U = 9.9 \text{ V}$  stack voltage (Fig. 7d), translating to  $\Delta U = 3.3 \text{ V}$  cell voltage for comparability with the single cell. The activation increased  $j_{\text{CO}}$  to over  $500 \text{ mA cm}^{-2}$ , a current density even slightly higher than that measured in the single-layer cell (Fig. 7a). One key challenge

during scale-up is the increased resistance of the cell (stack) against the flow of gas and the activation fluid during infusion. Therefore, we have monitored the pressure build-up on the cell (cell stack). It was indeed higher than in the case of the small cell ( $0.8 \text{ bar}$  for the small cell,  $\sim 2 \text{ bar}$  for the large cell and  $\sim 3 \text{ bar}$  for the cell stack, see Supplementary Fig. 22), but not detrimental at all. Finally, the cell design was not optimized for this activation process, leaving a lot of room for improvement. In this regard, scale-up and optimization of such electrolyser stacks are ongoing (see Supplementary Fig. 23 for a stack of size  $1,000 \text{ cm}^2$  per cell).

### Conclusions

We uncovered some microscopic/mechanistic reasons behind the performance fading in zero-gap  $\text{CO}_2$  electrolyser cells. SEM–EDX and micro-CT analysis confirmed the formation of alkali metal bicarbonate and mixed carbonate–bicarbonate plaques within the cathode GDE of cells operating with alkaline anolyte, hindering  $\text{CO}_2$  gas from reaching the catalyst surface. In an apparent contradiction to this, we identified the presence of alkali metal ions on the cathode catalyst surface to be a major contributor for high current density  $\text{CO}_2$  reduction. To overcome this ambiguity, we developed an operando activation method, where the cathode of pure water anolyte-fed  $\text{CO}_2$  electrolyser cell is infused periodically with different alkali cation-containing solutions with proper

wetting properties. We have shown that the activation predominantly affects the cathode chemistry and has negligible effect on the anode process and the AEM properties.

The presented proof-of-concept demonstrates scalable water-fed electrolyser cells operating at CO<sub>2</sub> reduction rates matching those using alkaline electrolytes ( $j_{CO}$  of  $420 \pm 50$  mA cm<sup>-2</sup>) over prolonged times (over 200 hours). The activation is repeatable, implying that the observed slow current decrease over time is not caused by any degradation mechanism, but by the continuous desorption and leaching of the alkali cations from the cathode catalyst layer during operation. The rate of performance decay depends on the cathode GDE composition (for example, ionomer composition and content, thickness and porosity) and on operational parameters, such as humidification of the CO<sub>2</sub> stream, water cross-over through the membrane, cell voltage, temperature, current density, etc. Optimizing these parameters is a major engineering task, which in turn might bring a big reward: the ability to operate zero-gap CO<sub>2</sub> electrolyser cells with pure water anolyte at high current density, with negligible maintenance requirements. Such studies are in progress in our laboratory, together with further scaling-up of the technology.

## Methods

**Materials.** All chemicals were purchased from commercial suppliers (Sigma-Aldrich, VWR International), and were of at least analytical grade and were used without further purification. MilliQ grade ( $\rho = 18.2$  M $\Omega$  cm) ultrapure deionized water was used to prepare all the solutions.

**Electrode preparation.** Silver nanoparticles ( $d_{avg} < 100$  nm, Sigma-Aldrich) were dispersed in a 1:1 isopropanol/water mixture at a concentration of 25 mg cm<sup>-3</sup>, together with 15 wt% ionomer, matching the membrane used (Sustainion XA-9, Fumion FAA-3, PiperION I-46). As for the anode catalyst, IrO<sub>x</sub> nanoparticles (Fuel-Cell Store) were dispersed in an identical solvent mixture and ionomer concentration, but with a concentration of 20 mg cm<sup>-3</sup>. The IrO<sub>x</sub> dispersion was homogenized in a regular ultrasonic bath for 20 min (keeping the bath temperature below 35°C), while a high-power immersion sonotrode was used to disperse the Ag nanoparticles.

The Ag dispersion was spray-coated on Sigracet 39BC carbon GDLs preheated on a hotplate at 100°C, using a hand-held airbrush and compressed air carrier gas (~100 cm<sup>3</sup> min<sup>-1</sup>). The anode catalyst was spray-coated similarly, on a porous titanium frit. The cathode catalyst loading was  $1.0 \pm 0.1$  mg cm<sup>-2</sup> for the measurements with the PiperION membrane, and it was  $3.0 \pm 0.1$  mg cm<sup>-2</sup> for the other systems, while the anode catalyst amount was  $1.0 \pm 0.1$  mg cm<sup>-2</sup>.

Commercially available AEMs were used to separate the anode and the cathode chambers (Class T X37-50 Sustainion (50- $\mu$ m thickness) from Dioxide Materials; Fumasep FAB-PK-130 (130- $\mu$ m thickness) from FUMATECH BWT; PTFE-reinforced 15- $\mu$ m thick PiperION TP-85 from W7energy). The membranes were ion-exchanged before use for 24 hours in the respective 1 M alkaline solution (NaOH/KOH/CsOH), which was exchanged to a fresh solution after the first 5 hours.

**Zero-gap electrolyser cells.** All experiments presented in this paper were performed in zero-gap electrolyser cells. These consist of (from bottom to top in Supplementary Fig. 1): an anode current collector on which an anolyte flow pattern was formed, a porous Ti frit with catalyst layer on its side in direct contact with the AEM, held in place by a spacer element, an AEM (different membranes were used in our measurements, as described in the manuscript), a GDE with its catalyst layer facing the membrane, a spacer element to set the compression ratio of the GDE and a cathode current collector with a concentric flow pattern with a central inlet, and an outlet on the perimeter of the flow pattern. The electrolyser elements were assembled directly on top of each other and were held together by six bolt screws (3 Nm torque was applied). The active surface is circular, of diameter 3.2 cm, resulting in a geometrical surface of area,  $A = 8$  cm<sup>2</sup>, the value of which was used to normalize the current values reported here. A larger ( $A = 100$  cm<sup>2</sup>) cell was also used to demonstrate the scalability of our approach. The design of this cell is very similar to its smaller counterpart, but instead of being spherical, it is rectangular in shape. A stack containing three cells was connected in series electrically and in parallel with regards to gas distribution<sup>10,24</sup>.

**Test framework.** The test framework (Fig. 2) was based on our previously reported experimental set-up<sup>24</sup>. Briefly, the CO<sub>2</sub> feed rate was controlled with a Bronkhorst F-201C type mass-flow controller, while an Agilent ADM flow meter was used to measure the flow rate of the gas outlet. The accuracy of this measurement was confirmed by repeating these measurements with the classical bubble-soap method periodically. The gas flow rate was normalized with the surface area of

the cell (hence the units of cm<sup>3</sup> cm<sup>-2</sup> min<sup>-1</sup>). The CO<sub>2</sub> gas was passed through a temperature-controlled humidifier before entering the cell. An extra loop was inserted before the electrolyser to be able to inject electrolyte solutions into the gas stream. This activation loop can be bypassed by turning two three-way valves. After filling the loop with the respective electrolyte solution, it can be injected into the gas stream by turning these two valves. The pressure of the CO<sub>2</sub> in the electrolyser was measured using a digital pressure gauge. The anolyte was circulated in the anode compartment using a peristaltic pump. The electrochemical measurements were performed using a Biologic VMP-300 type instrument, equipped with electrochemical impedance spectroscopy (EIS)- and high current (up to 10 A) booster options. All the experiments presented here (including the EIS measurements) were performed using the potentiostat with the booster connected. For the measurements with the larger electrolyser cell and stack, a programmable power supply (TDK-Lambda GEN-15-220) was used.

The measurements were conducted in a two-electrode set-up, and the total cell voltage is given as the voltage difference between the anode and the cathode (hence the positive values). The absolute value of the current/current density is shown (positive values) in all figures. No *IR* correction was applied on the voltage values presented throughout the manuscript. EIS spectra have been taken at constant cell voltage with added 10 mV r.m.s. perturbation in the frequency range 100 kHz down to 0.1 Hz, with 10 points per frequency decade. The self-consistency of the EIS data was checked by performing Kramers–Kronig tests. Impedance spectra are presented in the form of complex-plane plots ('Nyquist plots') where the points of  $f = 10^k$  Hz frequencies (where  $k$  is an integer,  $-1 \leq k \leq 5$ ) are marked. To help in distinguishing spectra they are shifted along the ordinate.

The composition of the cathode product stream was analysed using a Shimadzu GC-2010 Plus type instrument, equipped with a barrier discharge ionization (BID) detector. A Restek ShinCarbon ST column was employed for the separation with 6.0 grade helium carrier gas. An automatized six-port valve was used to take samples at regular time intervals. In certain experiments the product stream composition was simultaneously monitored using an *m/z* analyser (SRS UGA200) equipped with an atmospheric sampling capillary. This technique allowed the quasi-real-time determination of the product composition, hence providing time-resolved information on the processes occurring during and immediately after cathode activation. The anode gas composition was analysed with a BGA-244 type Binary Gas Analyser (Stanford Research Systems), to monitor the CO<sub>2</sub>/O<sub>2</sub> ratio.

**Membrane impedance measurements.** A Zahner Im6e type instrument was used to characterize the membrane impedance in a four-electrode cell (Supplementary Fig. 8a). The EIS spectra were recorded in galvanostatic mode ( $I = 0$ ), with 1 mA perturbation amplitude, from 100 kHz to 1 Hz, recording twice 8 points per decade.

**Contact angle measurements.** An EasyDrop (Krüss) type instrument was used to measure the wetting properties (that is, contact angles) of different solvent mixtures on the microporous side of the Sigracet 39BC GDL used. A drop of the solvent mixture was formed on the plate with the use of a syringe. Using the CCD camera of the goniometer, the drop contour of the captured photographs was analysed.

**X-ray micro-computed tomography analysis.** A Bruker SkyScan 2211 Multiscale X-ray Nanotomograph (Bruker) instrument was used to record micro-CT images. The three-dimensional structure of the samples was scanned using an 11-megapixel CCD detector by applying a source voltage of 70 kV and current of 400  $\mu$ A (in microfocus mode, with a resolution of 1  $\mu$ m per pixel). NRecon reconstruction software (Skyscan, Bruker) was used to reconstruct the projected images, while the CTAn and CTvox software (Skyscan, Bruker) were applied to carry out the image segmentation and visualizing the 3D-rendered objects, respectively.

**SEM–EDX analysis.** A Hitachi S-4700 scanning electron microscope (SEM) coupled with a Röntec EDX detector was used to take images of the GDEs. The microscope was operated at 10 kV acceleration voltage.

**X-ray diffraction measurements.** X-ray diffraction patterns were obtained using a Bruker D8 ADVANCE X-ray diffractometer, applying CuK $\alpha$  ( $\lambda = 1.5418$  Å) radiation. Rietveld refinement was carried out to quantify the phase composition of the obtained materials.

**Ion chromatography measurements.** To gain direct proof on the K<sup>+</sup> and Cs<sup>+</sup> cross-over through the AEM, electrolysis experiments were performed with 0.01 M KOH and 0.01 M CsOH anolytes at 60°C, and the humid gas leaving the cell was collected in a mechanical liquid/gas separator, initially filled with 10 cm<sup>3</sup> of pure water. The K<sup>+</sup> or Cs<sup>+</sup> concentration of the fluid in this water separator was then monitored during electrolysis by using ion chromatography (Fig. 1b). All ion chromatography measurements were performed using a Shimadzu ion-chromatographic system, consisting of a high pressure chromatographic module (LC-20AD SP), an eluent degas module (DGU-20A5R), an autosampler (SIL-20AC), a conductivity detector for non-suppressed conductivity measurements (CDD-10A VP), a column oven to maintain constant 40°C temperature (CTO-20C) and a Shodex IC YS-50 column. Methanesulfonic acid (4 mM) was used as eluent with a flow rate of 1.0 cm<sup>3</sup> min<sup>-1</sup>, and the sample volume was 50  $\mu$ l.

## Data availability

The authors declare that all data supporting the findings of this study are available within the paper and Supplementary Information files. Source data are provided with this paper.

Received: 31 July 2020; Accepted: 8 March 2021;

Published online: 19 April 2021

## References

- Hepburn, C. et al. The technological and economic prospects for CO<sub>2</sub> utilization and removal. *Nature* **575**, 87–97 (2019).
- Endrődi, B. et al. Continuous-flow electroreduction of carbon dioxide. *Prog. Energy Combust. Sci.* **62**, 133–154 (2017).
- Weekes, D. M., Salvatore, D. A., Reyes, A., Huang, A. & Berlinguette, C. P. Electrolytic CO<sub>2</sub> reduction in a flow cell. *Acc. Chem. Res.* **51**, 910–918 (2018).
- De Luna, P. et al. What would it take for renewably powered electrosynthesis to displace petrochemical processes? *Science* **364**, eaav3506 (2019).
- He, J. & Janáky, C. Recent advances in solar-driven carbon dioxide conversion: expectations versus reality. *ACS Energy Lett.* **5**, 1996–2014 (2020).
- Jouny, M., Luc, W. & Jiao, F. General techno-economic analysis of CO<sub>2</sub> electrolysis systems. *Ind. Eng. Chem. Res.* **57**, 2165–2177 (2018).
- Verma, S. et al. A gross-margin model for defining technoeconomic benchmarks in the electroreduction of CO<sub>2</sub>. *ChemSusChem* **9**, 1972–1979 (2016).
- Schreier, M. et al. Solar conversion of CO<sub>2</sub> to CO using Earth-abundant electrocatalysts prepared by atomic layer modification of CuO. *Nat. Energy* **2**, 17087 (2017).
- Arán-Ais, R. M., Scholten, F., Kunze, S., Rizo, R. & Roldan Cuenya, B. The role of in situ generated morphological motifs and Cu(I) species in C<sub>2+</sub> product selectivity during CO<sub>2</sub> pulsed electroreduction. *Nat. Energy* **5**, 317–325 (2020).
- Endrődi, B. et al. High carbonate ion conductance of a robust PiperION membrane allows industrial current density and conversion in a zero-gap carbon dioxide electrolyzer cell. *Energy Environ. Sci.* **13**, 4098–4105 (2020).
- Liu, K., Smith, W. A. & Burdyny, T. Introductory guide to assembling and operating gas diffusion electrodes for electrochemical CO<sub>2</sub> reduction. *ACS Energy Lett.* **4**, 639–643 (2019).
- Burdyny, T. & Smith, W. A. CO<sub>2</sub> reduction on gas-diffusion electrodes and why catalytic performance must be assessed at commercially-relevant conditions. *Energy Environ. Sci.* **12**, 1442–1453 (2019).
- Bhargava, S. S. et al. System design rules for intensifying the electrochemical reduction of CO<sub>2</sub> to CO on Ag nanoparticles. *ChemElectroChem* **7**, 2001–2011 (2020).
- Kibria, M. G. et al. A surface reconstruction route to high productivity and selectivity in CO<sub>2</sub> electroreduction toward C<sub>2+</sub> hydrocarbons. *Adv. Mater.* **30**, 1804867 (2018).
- Ma, W. et al. Electrocatalytic reduction of CO<sub>2</sub> to ethylene and ethanol through hydrogen-assisted C–C coupling over fluorine-modified copper. *Nat. Catal.* **3**, 478–487 (2020).
- De Gregorio, G. L. et al. Facet-dependent selectivity of Cu catalysts in electrochemical CO<sub>2</sub> reduction at commercially viable current densities. *ACS Catal.* **10**, 4854–4862 (2020).
- Wang, X. et al. Efficient methane electrosynthesis enabled by tuning local CO<sub>2</sub> availability. *J. Am. Chem. Soc.* **142**, 3525–3531 (2020).
- García de Arquer, F. P. et al. CO<sub>2</sub> electrolysis to multicarbon products at activities greater than 1 A cm<sup>-2</sup>. *Science* **367**, 661–666 (2020).
- Verma, S., Lu, S. & Kenis, P. J. A. Co-electrolysis of CO<sub>2</sub> and glycerol as a pathway to carbon chemicals with improved technoeconomics due to low electricity consumption. *Nat. Energy* **4**, 466–474 (2019).
- Na, J. et al. General technoeconomic analysis for electrochemical coproduction coupling carbon dioxide reduction with organic oxidation. *Nat. Commun.* **10**, 5193 (2019).
- Vass, Á., Endrődi, B. & Janáky, C. Coupling electrochemical carbon dioxide conversion with value-added anode processes: an emerging paradigm. *Curr. Opin. Electrochem.* **25**, 100621 (2021).
- Larrazábal, G. O. et al. Analysis of mass flows and membrane cross-over in CO<sub>2</sub> reduction at high current densities in an MEA-type electrolyzer. *ACS Appl. Mater. Interfaces* **11**, 41281–41288 (2019).
- Ma, M. et al. Insights into the carbon balance for CO<sub>2</sub> electroreduction on Cu using gas diffusion electrode reactor designs. *Energy Environ. Sci.* **13**, 977–985 (2020).
- Endrődi, B. et al. Multilayer electrolyzer stack converts carbon dioxide to gas products at high pressure with high efficiency. *ACS Energy Lett.* **4**, 1770–1777 (2019).
- Wang, R. et al. Maximizing Ag utilization in high-rate CO<sub>2</sub> electrochemical reduction with a coordination polymer-mediated gas diffusion electrode. *ACS Energy Lett.* **4**, 2024–2031 (2019).
- Kaczur, J. J., Yang, H., Liu, Z., Sajjad, S. D. & Masel, R. I. A review of the use of immobilized ionic liquids in the electrochemical conversion of CO<sub>2</sub>. *J. Carbon Res.* **6**, 33 (2020).
- Yin, Z. et al. An alkaline polymer electrolyte CO<sub>2</sub> electrolyzer operated with pure water. *Energy Environ. Sci.* **12**, 2455–2462 (2019).
- Gabardo, C. M. et al. Combined high alkalinity and pressurization enable efficient CO<sub>2</sub> electroreduction to CO. *Energy Environ. Sci.* **11**, 2531–2539 (2018).
- Wheeler, D. G. et al. Quantification of water transport in a CO<sub>2</sub> electrolyzer. *Energy Environ. Sci.* **13**, 5126–5134 (2020).
- Zhao, C., Chen, X. & Zhao, C. Carbonation behavior of K<sub>2</sub>CO<sub>3</sub> with different microstructure used as an active component of dry sorbents for CO<sub>2</sub> capture. *Ind. Eng. Chem. Res.* **49**, 12212–12216 (2010).
- Chioyama, H., Luo, H., Ohba, T. & Kanoh, H. Temperature-dependent double-step CO<sub>2</sub> occlusion of K<sub>2</sub>CO<sub>3</sub> under moist conditions. *Adsorpt. Sci. Technol.* **33**, 243–250 (2015).
- Verma, S. et al. Insights into the low overpotential electroreduction of CO<sub>2</sub> to CO on a supported gold catalyst in an alkaline flow electrolyzer. *ACS Energy Lett.* **3**, 193–198 (2018).
- Kudo, Y. et al. Carbon dioxide electrolytic device and carbon dioxide electrolytic method. US patent 20180274109A1 (2018).
- Leonard, M. E., Clarke, L. E., Forner-Cuenca, A., Brown, S. M. & Brushett, F. R. Investigating electrode flooding in a flowing electrolyte, gas-fed carbon dioxide electrolyzer. *ChemSusChem* **13**, 400–411 (2020).
- Liu, Z., Yang, H., Kutz, R. & Masel, R. I. CO<sub>2</sub> electrolysis to CO and O<sub>2</sub> at high selectivity, stability and efficiency using sustainin membranes. *J. Electrochem. Soc.* **165**, J3371–J3377 (2018).
- Luo, X., Rojas-Carbonell, S., Yan, Y. & Kusoglu, A. Structure-transport relationships of poly(aryl piperidinium) anion-exchange membranes: effect of anions and hydration. *J. Memb. Sci.* **598**, 117680 (2020).
- Ringe, S. et al. Understanding cation effects in electrochemical CO<sub>2</sub> reduction. *Energy Environ. Sci.* **12**, 3001–3014 (2019).
- Resasco, J. et al. Promoter effects of alkali metal cations on the electrochemical reduction of carbon dioxide. *J. Am. Chem. Soc.* **139**, 11277–11287 (2017).
- Lobaccaro, P. et al. Effects of temperature and gas-liquid mass transfer on the operation of small electrochemical cells for the quantitative evaluation of CO<sub>2</sub> reduction electrocatalysts. *Phys. Chem. Chem. Phys.* **18**, 26777–26785 (2016).
- Pérez-Gallent, E., Marcandalli, G., Figueiredo, M. C., Calle-Vallejo, F. & Koper, M. T. M. Structure- and potential-dependent cation effects on CO reduction at copper single-crystal electrodes. *J. Am. Chem. Soc.* **139**, 16412–16419 (2017).
- Chen, L. D., Urushihara, M., Chan, K. & Nørskov, J. K. Electric field effects in electrochemical CO<sub>2</sub> reduction. *ACS Catal.* **6**, 7133–7139 (2016).
- Birdja, Y. Y. et al. Advances and challenges in understanding the electrocatalytic conversion of carbon dioxide to fuels. *Nat. Energy* **4**, 732–745 (2019).
- Murata, A. & Hori, Y. Product selectivity affected by cationic species in electrochemical reduction of CO<sub>2</sub> and CO at a Cu electrode. *Bull. Chem. Soc. Jpn* **64**, 123–127 (1991).
- Singh, M. R., Kwon, Y., Lum, Y., Ager, J. W. & Bell, A. T. Hydrolysis of electrolyte cations enhances the electrochemical reduction of CO<sub>2</sub> over Ag and Cu. *J. Am. Chem. Soc.* **138**, 13006–13012 (2016).
- Thorson, M. R., Siil, K. I. & Kenis, P. J. A. Effect of cations on the electrochemical conversion of CO<sub>2</sub> to CO. *J. Electrochem. Soc.* **160**, F69–F74 (2013).
- Carmo, M., Fritz, D. L., Mergel, J. & Stolten, D. A comprehensive review on PEM water electrolysis. *Int. J. Hydrog. Energy* **38**, 4901–4934 (2013).

## Acknowledgements

This project has received funding from the European Research Council (ERC) under the European Union's Horizon 2020 research and innovation programme (grant no. 716539 and 899747, to C.J.). The research was supported by the National Research, Development and Innovation Office (NKFIH) through the FK-132564 project (to E.B.), and by the 'Széchenyi 2020' program in the framework of GINOP-2.2.1-15-2017-00041 project (to C.J.). Financial support for purchasing the CT instrument was also provided by NKFIH through the GINOP-2.3.3-15-2016-00010 project (to C.J.) and D.S.). This project was supported by the János Bolyai Research Scholarship of the Hungarian Academy of Sciences (to B.E. and D.S.). We thank L. Janovák, Á. Balog, G. F. Samu and G. Bencsik at University of Szeged for assistance in contact angle, SEM–EDX, X-ray diffraction (with Rietveld analysis) and ion chromatography measurements, respectively. We also thank T. Pajkossy (Hungarian Academy of Sciences) for his valuable contribution in the design, analysis and interpretation of EIS measurements. We thank P. Kamat (University of Notre Dame) for critical comments on an earlier version of the manuscript and B. Janáky-Bohner for her support in the preparation of the manuscript.

## Author contributions

B.E. and C.J. conceived and supervised the project and designed all experiments. A.S. and T.H. prepared the gas diffusion electrodes and assembled the cells. A.S., T.H. and

E.K. carried out all electrochemical and product analysis experiments. D.S. performed and analysed micro-CT measurements. B.E., E.K. and C.J. designed the electrodes, the electrochemical cells and the electrolyser system. All authors discussed the results and assisted during manuscript preparation.

### Competing interests

Two patent applications have been filed on the continuous-flow electrolysis of CO<sub>2</sub> by some authors of this paper (B.E., A.S., E.K., C.J., all University of Szeged) and their collaborating partner, ThalesNano Zrt. Application numbers: PCT/HU2019/095001 and PCT/HU2020/050033. T.H. and D.S. declare no competing interests.

### Additional information

**Supplementary information** The online version contains supplementary material available at <https://doi.org/10.1038/s41560-021-00813-w>.

**Correspondence and requests for materials** should be addressed to B.E. or C.J.

**Peer review information** *Nature Energy* thanks the anonymous reviewers for their contribution to the peer review of this work.

**Reprints and permissions information** is available at [www.nature.com/reprints](http://www.nature.com/reprints).

**Publisher's note** Springer Nature remains neutral with regard to jurisdictional claims in published maps and institutional affiliations.

© The Author(s), under exclusive licence to Springer Nature Limited 2021